



**18<sup>th</sup> International Conference on  
Sustainable Energy Technologies**

**20-22 August 2019 - Kuala Lumpur - Malaysia**

---

**Sustainable Energy Towards the New Revolution**

---

**Conference Proceedings  
Volume 1**





University of  
Nottingham

UK | CHINA | MALAYSIA



UNIVERSITI SAINS MALAYSIA



Proceedings of the  
**18<sup>th</sup> International Conference on  
Sustainable Energy Technologies**

**SET 2019**

20-22 August 2019  
Kuala Lumpur, Malaysia

Volume 1

Edited by

Professor Saffa Riffat, Dr Yuehong Su,  
Professor Norli Ismail and Dr Mardiana Idayu Ahmad

*SET 2019 Admin Support  
Department of Architecture and the Built Environment  
Faculty of Engineering, University of Nottingham*

© 2019 Copyright University of Nottingham & WSSET

The contents of each paper are the sole responsibility of its author(s); authors were responsible to ensure that permissions were obtained as appropriate for the material presented in their articles, and that they complied with antiplagiarism policies.

Reference to a conference paper:

To cite a paper published in these conference proceedings, please substitute the highlighted sections of the reference below with the details of the article you are referring to:

Author(s) Surname, Author(s) Initial(s), 2019. 'Title of paper'. In: Riffat, Su Ismail, Ahmad. ed., **Sustainable Energy Towards the New Revolution**: Proceedings of the 18th International Conference on Sustainable Energy Technologies, 20-22 August 2019, Kuala Lumpur, Malaysia. University of Nottingham: Buildings, Energy & Environment Research Group. Volume X, pp XX-XX. Available from: [nottingham-repository.worktribe.com/](http://nottingham-repository.worktribe.com/) [Last access date].

ISBN-13: 9780853583318

Version: 10.02.2020

# Foreword

---

The 18<sup>th</sup> International Conference on Sustainable Energy Technologies was a significant international academic event in the domain of world sustainable energy technologies with a theme of '*Sustainable Energy Towards the New Revolution*'. The conference aimed to provide a forum for the exchange of latest technical information, the dissemination of up-to-date research results, and the presentation of major topics including sustainable energy, low carbon technologies, eco-cities, energy security and environmental policy.

Held from August 20<sup>th</sup> – 22<sup>nd</sup> 2019 in Kuala Lumpur, Malaysia, the conference was a collaboration between the World Society of Sustainable Energy Technologies (WSSET), the Universiti Sains Malaysia and University of Nottingham. World-renowned experts and scholars in the area, representatives of prominent enterprises and universities attended to discuss new developments and achievements in the field, as well as promoting academic exchange, application of scientific results, university-industry collaboration and government-industry collaboration.

The papers contained in these proceedings focus on topics such as Energy Storage for the Age of Renewables; Research, Innovation and Commercialisation in Sustainable Energy Technologies; Integrating Planning & Policy, Architecture, Engineering & Economics; Energy and Environment; Engineering Thermo-physics; and Systemic Change for Cities.

About 230 delegates from 30 countries attended SET2019; nearly 400 abstracts were received and 190 papers have been published in the conference proceedings. The proceedings have therefore been divided into three volumes. I hope you enjoy as much as I did the breadth of work you will find in these proceedings.

We would like to thank all participating authors for their contributions to both the conference and to the publishing of this book. We are also indebted to our international scientific committee for their advice and seemingly endless review of papers. We would also like to thank unreservedly Celia Berry, Zeny Amante-Roberts, Dr Mardiana Idayu Ahmad and Professor Dr Norli Ismail for their tireless efforts in making SET2019 one of the most successful conferences we have held. Also a huge thanks to our sponsors First Solar, PCM Products Ltd and Professor Terry Payne.

Professor Saffa Riffat  
Chair in Sustainable Energy Technologies  
President of the World Society of Sustainable Energy Technologies  
Fellow of the European Academy of Sciences  
SET 2019 Chairman

# CONTENTS

Paper Number	Title	Page
#7:	Decarbonising the global electricity sector through demand-side management: a critical and systematic review of policy responses .....	1
#15:	Performance of a small domestic eutectic solder medium temperature latent heat storage system during charging .....	14
#19:	Preparation and electrochemical hydrogen storage performance of sulfonated polysulfone (SPSU) .....	22
#21:	Performance analysis of thermochemical energy storage integrated with heat pump for building applications .....	30
#23:	Market development of PV Solar Home System (SHS) and PV pumping in Yemen .....	43
#25:	Implementation of renewable energy and photovoltaic (PV) system .....	53
#28:	Novel technology of solar assisted domestic hot water (DHW) system with supercooled PCMs .....	64
#31:	Thermal analysis of a low-cost ground heat exchanger using laboratory simulator .....	72
#32:	Modern flow field design to enhance the performance of direct methanol fuel cell .....	82
#35:	Optical-thermal-electrical characteristic and modelling of solar modules .....	95
#36:	Passive design methods for a sustainable house .....	103
#39:	Numerical investigation of mixture generation due to different inlet and outlet positions .....	113
#44:	Experimental study of a portable PV direct-driven variable-speed refrigerator.....	123
#45:	Combined cycle of seawater thermal desalination plant .....	135
#46:	Integration of vacuum multi-effect membrane distillation with adsorption/cooling system.....	145
#47:	Experimental study on the pressure differential at which building air leakage should be measured .....	157
#50:	Thermal conductivity enhancement of phase change materials using aluminium wool.....	167
#51:	Nonsolvent-induced phase separation synthesis of membrane via electro-spraying for desalination .....	176
#52:	Consequence of colour temperature for awareness of security effect in King Mongkut's University of Technology Thonburi .....	183
#54:	Spectrally selective coating for the combination of solar thermal and sky radiative cooling .....	189
#55:	Energy and exergy analysis of a Corum sugar factory .....	195
#59:	Liquid flooded Ericsson cycle heat pump and heat engine system .....	207
#63:	Numerical simulation of water-in-oil emulsions droplets electrostatic coalescence .....	216
#64:	A prototype of thermochemical heat storage system for space heating in building .....	226
#65:	Sound absorption properties of biomass aerogels for building application.....	232
#67:	Bio gasoline production from rubber seed oil using Ni/HY zeolite and Mo/HY zeolite as catalysts .....	243
#69:	Utilisation of the pulse technique in the energy retrofitting to a range of European dwellings .....	252
#70:	Prospect of thermoelectric air conditioner for building application and their building integration methods ..	263
#71:	Performance analysis of sinter waste heat recovery system based on organic Rankine cycle .....	274
#76:	Mathematical modelling and performance analysis of a semi-transparent thin film PV glazing insulated with vacuum layer.....	282
#77:	An innovative semi-transparent thin film PV vacuum glazing .....	297
#78:	Research of air conditioning system in T3 terminal of Dunhuang Airport.....	303
#79:	Thermodynamic analysis of a poly-generation system for electrical power, cooling and desalinated water.....	312
#80:	Optimisation of battery capacity in a DC-power supply system of an office building .....	323
#81:	Spectral characteristics of nanometric absorber: a simple strategy to develop silicon nanostructures for efficient solar energy harvesting.....	333
#83:	Performance optimisation of drag-type vertical axis wind turbine having twisted blades .....	339
#85:	Heat transfer analysis of vacuum insulated windows compared to traditional fenestration technologies ....	349
#87:	Thermal performance evaluation for building application of phase change material blister panels .....	359
#88:	Heat and mass transfer study for the dew-point evaporative cooler with porous layer in wet channel.....	367
#89:	Solar gain mitigation in ventilated tiled roofs by using phase change materials .....	376
#93:	Free piston Stirling engine response to the change in displacer's spring stiffness value .....	387
#96:	Energy management of solar photovoltaic-battery energy systems in buildings .....	397
#97:	Numerical study on trapezoidal solar pond based on a two-dimensional large eddy simulation model .....	405
#99:	Small-scale solar driven mechanical vapour compression desalination system.....	415
#100:	To develop a holistic and affordable toolkit to identify potential energy savings in an existing building: a case study in Taiwan .....	425
#102:	Numerical study of the effect of surface wettability on droplet impact on a spherical surface .....	435
#105:	Synergistic combination of anaerobic digestion and gasification.....	445
#108:	Simulation study and comparative analysis of solar-air dual source heat pump system .....	454
#109:	Measurement and analysis of thermal environment in transition space of veranda .....	463
#111:	Priority and urgency between geothermal and solar photovoltaic in Indonesia's electricity power generation .....	471
#112:	Liquid propellant: catalyst pact pressure drop effect of 50 N green thruster .....	481

#117: Research on air-conditioner energy saving control method based on Q-learning and adaptive constraint network .....	491
#119: Life cycle assessment of wood pellet from para-rubber tree residues.....	498
#120: Investigating supercritical CO <sub>2</sub> power cycle and potential of improvement of turbine leakage characteristics by using barrier gas.....	507
#121: Experimental study on the effect of orientation of vapour grooves on the thermal performance of a novel plate loop heat pipe.....	517
#124: Exploitation of low-grade renewable energy using heat pump technology in China.....	527
#127: Life cycle assessment of microalgae-based pig production system .....	538





---

## #7: Decarbonising the global electricity sector through demand-side management: a critical and systematic review of policy responses

---

Kazeem Alasinrin BABATUNDE<sup>1</sup>, Fathin Faizah SAID<sup>2</sup>, Nor Ghani MD NOR<sup>3</sup>, Moamin A. MAHMOUD<sup>4</sup>, Rawshan Ara BEGUM<sup>5</sup>

<sup>1</sup>Center of Inclusive & Sustainable Development Center, Faculty of Economics and Management, Universiti Kebangsaan Malaysia, 43600 Bangi, Selangor, Malaysia, [alasinrin@siswa.ukm.edu.my](mailto:alasinrin@siswa.ukm.edu.my)

<sup>2</sup>Center of Inclusive & Sustainable Development Center, Faculty of Economics and Management, Universiti Kebangsaan Malaysia, 43600 Bangi, Selangor, Malaysia, [fathin@ukm.edu.my](mailto:fathin@ukm.edu.my)

<sup>3</sup>Center of Inclusive & Sustainable Development Center, Faculty of Economics and Management, Universiti Kebangsaan Malaysia, 43600 Bangi, Selangor, Malaysia, [norghani@ukm.edu.my](mailto:norghani@ukm.edu.my)

<sup>4</sup>Department of Software Engineering, College of Computer Science and Information Technology, Universiti Tenaga Nasional, 43000 Kajang, Selangor, Malaysia, [moamin@uniten.edu.my](mailto:moamin@uniten.edu.my)

<sup>5</sup>Center for Water Cycle, Marine Environment and Disaster Management, Kumamoto University, Kumamoto-shi, 860-8555 JAPAN, [rawshan@kumamoto-u.ac.jp](mailto:rawshan@kumamoto-u.ac.jp)

*The current climate literature on long-term electricity decarbonisation is dominated by global scenarios from Integrated Assessment Models (IAMs), which give special attention to supply-side solutions over demand-side technological options despite the broader range of co-benefits and lesser risk of the latter. To understand the recent state of the art, this study analyses one hundred and three empirical studies on policy instrument evaluations from 1994 to 2018. At first, we find a total of 809 research articles from Web of Science and Scopus databases and eventually analyse 103 empirical peer-reviewed studies based on the inclusion and exclusion criteria from 1994 to 2018. We find that demand-side policy studies are predominantly carried out in Asia, Europe and North America with the US contributing more than one-quarter of the studies reviewed, most of which were published after the president Trump's withdrawal from Paris Agreement (PA). Three types of Demand-Side Management (DSM) are identified with 20 corresponding policy instruments based on six basic categories. Energy saving remains the reason for implementing DSM. Although these policy instruments are promising, they are not always implemented for emissions reduction. Demand-side solutions through policies need to be fully exploited to achieve carbon emission targets from electricity or the overall energy sector.*

*Keywords: climate change; electricity decarbonisation; energy efficiency; energy conservation; demand response*

## 1. INTRODUCTION

That human-related activity sparks global warming is well beyond scientific misunderstanding. Electricity sector alone is responsible for more than 40% of total energy-related CO<sub>2</sub> emissions (IEA, 2018). Since last two decades, emissions from the power industry have been growing annually at 2.3% to a value of 4.3 gigatons (Gt), accounting for about half of the total growth in CO<sub>2</sub> emissions within the same period (IEA, 2018). In sum, the electricity sector now emits nearly 500 grams of CO<sub>2</sub> per kilowatt-hour (g CO<sub>2</sub>/kWh) of energy generated.

Consequently, the carbon intensity of electricity production has been on an upward trend (Ang & Su, 2016; Hinchliffe, Diemen, Heuberger, & Macdowell, 2015). Global carbon emissions from electricity generation increased in 2017 after three years of stagnancy. With the carbon emissions set to rise for the second year running, the European Union has been noticeably decarbonising their power generation. However, much of the growth in emissions is traceable to explosive electricity demand from large developing economies such as China and India. These trends reveal that current efforts to drive CO<sub>2</sub> emissions down from power generation are far from enough.

Electrification in the developing world is growing concurrently with the digitalisation of advanced economies, positioning electricity at the heart of sustainable economic development more than ever. Electric power, according to International Energy Agency (IEA) (IEA, 2018), is increasingly the choice of fuel for meeting companies and household's energy needs leading to growing electricity demand. As witnessed during the 2012 large-scale blackout in eastern and northern India, electricity supply interruptions can be substantially disruptive. It is hard, if not impossible, to think of a sector that is more crucial to the economy than power. But the fast-growing demand for electricity and its increasing coal share in energy mix pose severe and urgent environmental concerns, given the current world population and economic growth trajectory.

The current climate literature on long-term electricity decarbonisation to meet Intended Nationally Determined Contributions (INDCs) is dominated by global scenarios from Integrated Assessment Models (IAMs), which give special attention to supply-side solutions over demand-side technological options. This dominance in the literature is possible because of IAMs' unique ability to link the followings: technology portfolios, mitigation strategies, emission budgets and corresponding warming outcomes (Mundaca, Ürge-Vorsatz, & Wilson, 2018; Wilson, Grubler, Gallagher, & Nemet, 2012). Recent studies reveal how demand-side solutions have been poorly represented in the policy discourse despite the reliance on low energy demand in deep decarbonisation pathways (Rogelj et al., 2015). More so, Demand-side solutions have a full range of benefits and is associated with lesser risk compared to supply-side options: they potentially come along with co-benefits for health (Christoph von et al., 2016), living standard (Vu, Muttaqi, Agalgaonkar, & Bouzardoum, 2018), equity (Ito & Ida, 2018), security (Al-Rubaye, Al-Dulaimi, Mumtaz, & Rodriguez, 2018), system cost (Cui & Li, 2018), and pollution (Ürge-Vorsatz et al., 2016). Demand-side solutions incorporate greater flexibility into the decarbonisation pathways and hence reduce the risk of global disaster (Wilson et al., 2012). To date, we do not fully understand the state of the demand-side policy measures in the context of electricity decarbonisation (Mundaca et al., 2018). Recent literature advocate for more scientific research in the area of demand-side policy evaluations (Creutzig et al., 2016, 2018).

In this study, we systematically review demand-side management literature to strengthen and broaden the evidence based on the role of demand-side policy instruments in reducing carbon emissions and address research gap regarding how these policy instruments can contribute towards achieving deep electricity decarbonisation goal.

## 2. METHODOLOGY

For practitioners and professionals, systematic literature reviews (SLR) can be used to solve managerial and real-life problems by providing evidence-based knowledge through research finding syntheses from a wide range of studies (Briner & Denyer, 2010; Rousseau, Manning, & Denyer, 2008). For academic researchers, SLR can be used to validate models thereby enhancing methodological improvement and accuracy along with the opportunity to identify gaps for further studies (Cherp, Vinichenko, Jewell, Brutschin, & Sovacool, 2018; Schanes, Dobernig, & Gözet, 2018). In this study, a systematic literature review is carried out to characterise relevant studies regarding demand-side policy instruments, define a comparative framework to identify the current state of the art and research gap concerning DSM role in electricity decarbonisation. The most critical phase in conducting SLR is designing a protocol that clearly defines the main aims of the study, exclusion and inclusion criteria and the plan of the analysis (Babatunde, Begum, & Said, 2017). The main research questions addressed in this study are;

- How is DSM research geographically distributed?
- What are demand-side policy instruments being implemented across the world?
- What demand-side policies are being built in response to carbon emissions from the power sector?
- What types of models are being built to assess the impact of demand-side policies?
- What are the main research gaps in line with global emission reduction targets?

## 2.1. Literature review

All research articles with demand-side policy focus and where policy assessment was carried out were identified through two world-renown multidisciplinary bibliographic databases (Martín-Martín, Orduna-Malea, Thelwall, & Delgado López-Cózar, 2018): Scopus and Web of Science (WoS), using the following search strings: "demand-side management" AND "Electricity Demand" AND (polic\* OR measure\* OR intervention\*), ("energy efficiency" OR "energy conservation" OR "Demand response") AND "Electricity Demand" AND (polic\* OR measure\* OR intervention\*).

A published article is included if: (1) it is a peer-reviewed research article; (2) it is on demand-side policy measure(s) in the electricity sector; and (3) empirical model is applied to assess the policy implications from end-users' perspectives. Studies related mainly to demand-side policy in another industry other than electricity, demand-side technology, elasticity were excluded. Document types such as book, book chapter, conference proceedings, and review are also excluded in favour of article type papers. No date or language restrictions are imposed except the work of Costa and Galvis (2016) which was written in Portuguese but later translated into English. The search was conducted in February 2019 to ensure that all 2018 research articles were considered.

## 2.2 Search engine and output

Confining the search to WoS and Scopus indicates that our review is not exhaustive and represents only a sample of demand-side policy assessment literature. At first, a total of 809 studies were retrieved. At stage two, we glanced through the titles as well as abstracts to choose articles based on the inclusion criteria, 134 are selected and passed through full-text reading, of which, 103 research studies fulfilled the inclusion criteria. Seventy-three are from Scopus and sixty-two from WoS of which thirty-two articles are retrievable from both databases (Figure 1).

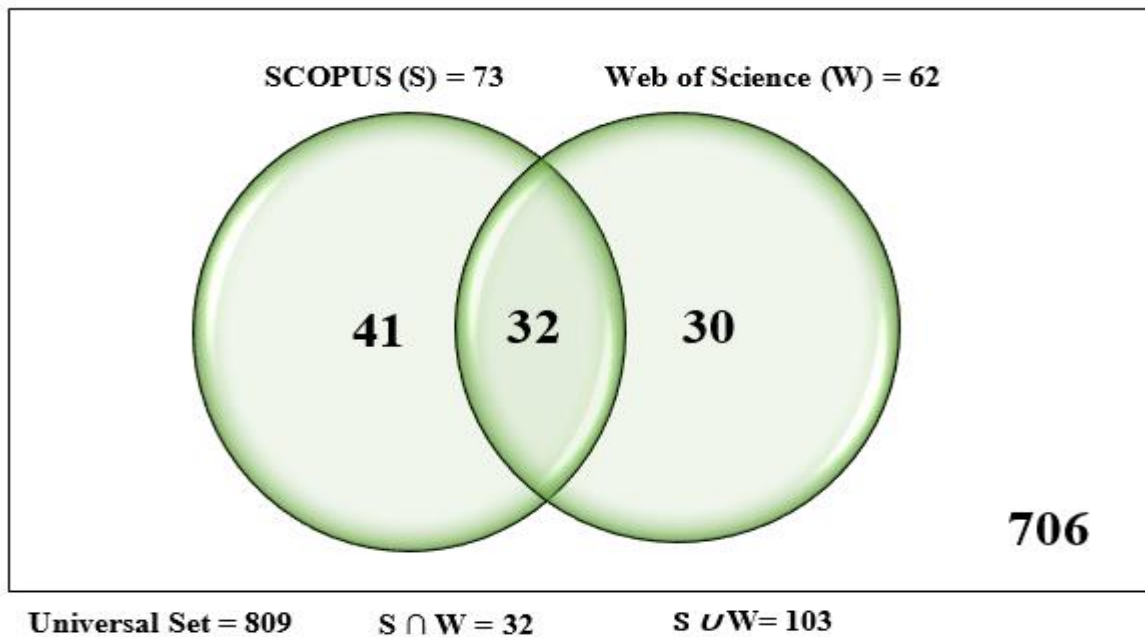


Figure 1: Review article by bibliographic databases

## 2.3 Data extraction

From each included research article, the following information is obtained: title, year of publication, Journal, types of demand-side policies, policy categories, instruments, status and implementer, study location vis-à-vis economic status, geographical regions, end-user sectors, and modelling paradigms.

We analyse each study based on different types of DSM (i.e. energy efficiency, energy conservation and demand response) and classify them into six broad categories (regulatory, price-based, incentive-based, community-based, customer education and voluntary based policies). We further categorise each research article based on the demand-side policy instruments such as time-of-use pricing, block pricing, energy efficiency standard, feed-in tariff, financial incentive, community engagement, and white certificate scheme etc. Finally, we classify each policy-oriented study on whether it is emissions reduction oriented or not.

Based on study location, each article is classified by country and geographical regions of the world to see if there is a regional pattern in the studies reviewed. Six continents classification is used: that is Africa, Asia, Australia/Oceania, Europe, North America, and South America (Figure 2). Based on country's economic development and level of income, research articles are further classified as follow: developing economies, economies in transition, and developed economies; low-income, lower middle income, upper middle income, and high-income.

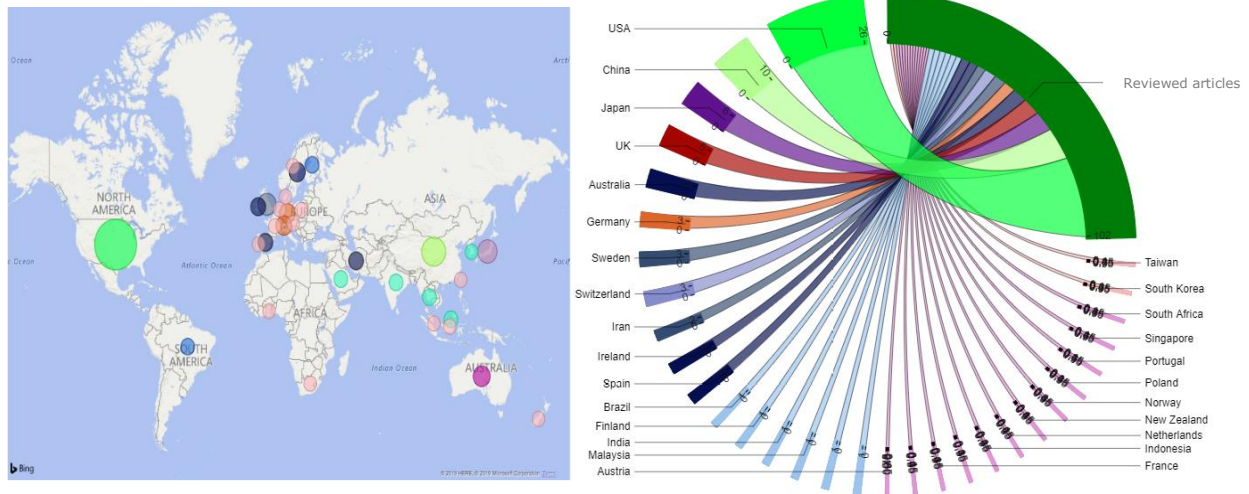


Figure 2: Geographical and country distribution of the reviewed articles

Information concerning the types of methodological approaches deployed in assessing the demand-side policy instruments has been extracted from each study and assigned to the appropriate categories. As a result, the following six modelling paradigms are identified: equilibrium model, optimisation model, simulation model, qualitative model, and experimental model. In addition to the methodological approaches, each article is also grouped based on the targeted electricity end-user sector. This includes residential sector, commercial sector, and the industrial sector. It goes without pointing out that policy can be designed to cut across more than one sector; in this sense, such an article will be assigned to a category we called *crosscutting*.

Finally, over the last three years, the world has been marked by enormous ratification of the Accord de Paris (Paris Agreement) and growing energy decarbonisation (Creti & Nguyen, 2018). However, the withdrawal of the United States from the agreement has come at a critical period of the global struggle against climate change (Nong & Siriwardana, 2018). Of concern is the possibilities of bandwagon effect by other nations (Cooper, 2018; Rhodes, 2017). In this regard, the reviewed studies have been grouped into three separate periods: before Paris Agreement, Paris Agreement year, and after Paris Agreement to find out if the agreement along with U.S. withdrawal has any implication on energy researches.

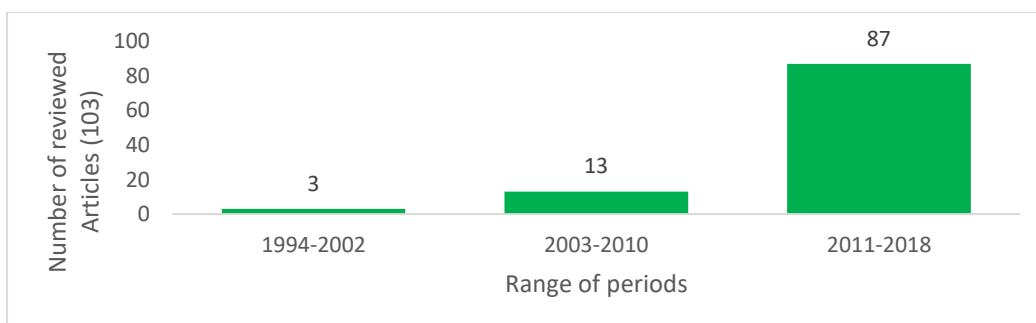


Figure 3: Number of articles per period

### 3. FINDINGS

The earliest study was carried out by Swisher et al. and published in *Energy Policy* (Swisher, Christiansson, & Hedenström, 1994). This was followed by the work of Intarapravich in 1996 (whose research focus was on Thai electricity decarbonisation via energy efficiency and conservation measures) and Waide et al. in 1997 with energy efficiency standard as their primary policy instrument. These two articles were published in *Ambio* and *Energy & Buildings* respectively. Since then, the assessment of demand-side policy instruments has increased rapidly with 13 articles published between 2003 and 2010 and 87 studies from 2011 to the end of 2018 (see Figure 3).

#### 3.1. Author demographics

Given the magnitude of DSM potentials across all countries, policy instruments are expected to be used to overcome its implementation challenges and achieve its broad objective. Hence, a question is asked to identify if research study on demand-side policy assessments concentrates in one country or continent, or if it is a global phenomenon. The huge DSM potential has attracted diverse scholarly research interest from around the world. Majority of the authors are affiliated to institutions in Asia (32%), Europe (32%), and North America (26%) with a total of over 90% of the reviewed studies (Figure 4). In comparison, the whole Africa continent and South America are undoubtedly under-represented despite their huge energy saving potentials (Ouedraogo, 2017; Schaeffer, Cohen, de Aguiar, & Faria, 2009; Silva & Nasirov, 2017) and the magnitude of effects and burden they could shoulder if temperatures were to rise, with the less developed regions likely to be affected the most (Oyeniran & Babatunde, 2015). Our findings attest to the positive responses from world leading CO<sub>2</sub> emitters, as about 87% of DSM studies with emission reduction focus were predominantly conducted in Europe, North America and Asia (Figure 4).

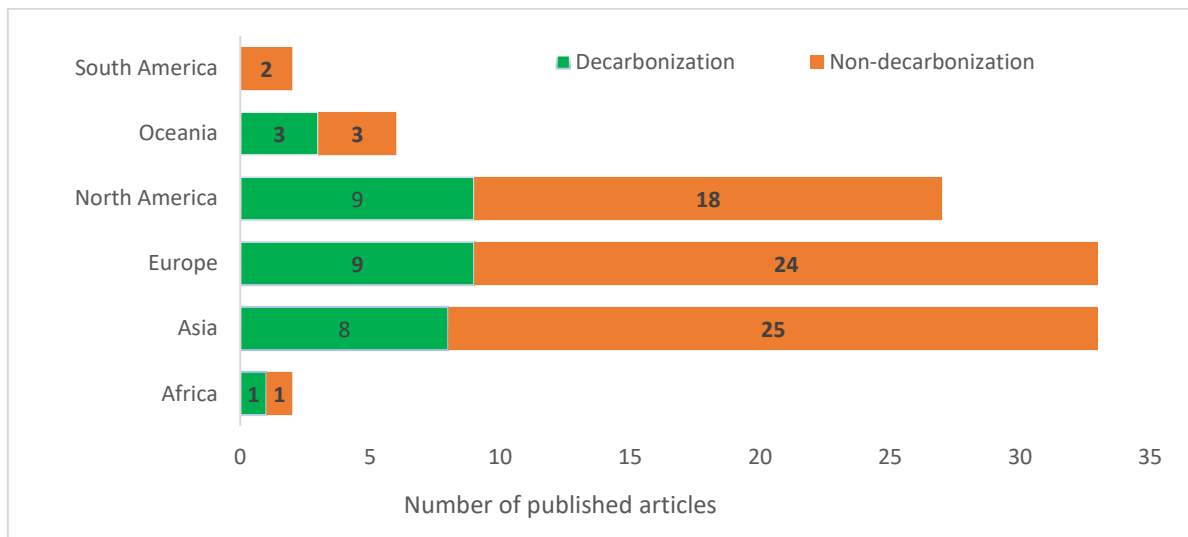


Figure 4: Distribution of studies by regions

Regarding DSM researches by country of affiliations, the United States was the largest source of DSM policy research destination before the Paris Agreement (PA). However, the dominance of the United States has been swept away since then (Figure 5). The percentage of empirical studies coming from institutions within the United States, although, remained at 33% between 1994 to 2015 (the year of the 21st Conference of Parties (COP) held in Paris) has fallen to 20% within 2016–2018 (period after Paris Agreement). More so, the proportion of empirical research from the United Kingdom and Sweden fell from 9% and 7% before PA to 4% and 2% after PA. Only scholars from Germany have not been assessing the demand-side policy measure after PA (Figure 5).

Comparing period before PA with the period after the agreement, an increased number of empirical DSM literature now emanates from institutions in the following countries: China, Australia, Switzerland, Iran, Brazil, Finland, Saudi Arabia, and Malaysia with less than 2% of the total reviewed articles. There is also an upward surge in research interest from academic institutions in 'other' countries (i.e. 13% before PA compared to 16% after PA), indicating an upward trend towards applying DSM most notably with respect to electricity decarbonisation despite US withdrawal from PA (Figure 5).

The information on the distribution of the studies between developed and developing countries is also provided in Figure 5. Despite the leadership of developed countries in term of DSM research outputs with about 67% published articles within the reviewed period, developing countries have shown tremendous research improvement since PA.

The proportion of published studies from developing nations increased from 17% before PA to 45% after PA, while the contributions from developed world fall from 83% before PA to 55% after PA. Meanwhile, the scientific contribution to DSM remained 50/50 contribution between developed and developing countries during the year of the agreement.

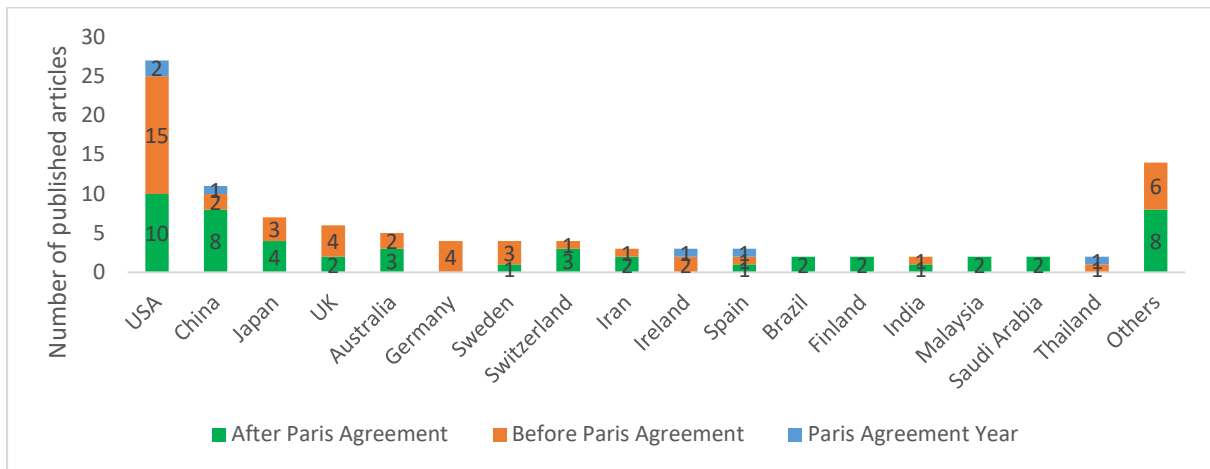


Figure 5: DSM studies by country before and after the Paris Agreement

### 3.2. Articles distribution by journal

This study reviews one hundred and three research articles retrieved from thirty-nine different journal cutting across a wide range of disciplines. The largest recipient of demand-side policy research is from Energy Policy, with around 25.24% of the reviewed articles. This is followed by Applied Energy (5.83%), Energy Journal (5.83%), and IEEE Transactions on Smart Grid (5.83%). The next most popular research destinations are Energy (4.85%), Energy Efficiency (4.85%), Journal of Cleaner Production (3.88%), Energy Economics (3.88%), Energy and Building (3.88%), and Energy Strategy Reviews (2.91%). This is followed by journals with only two published articles: Electric Power Systems Research, Environmental and Resource Economics, IEEE Transactions on Power Systems, Journal of Process Control, and Plos One. A journal that publishes only one article is classified among others (Figure 6).

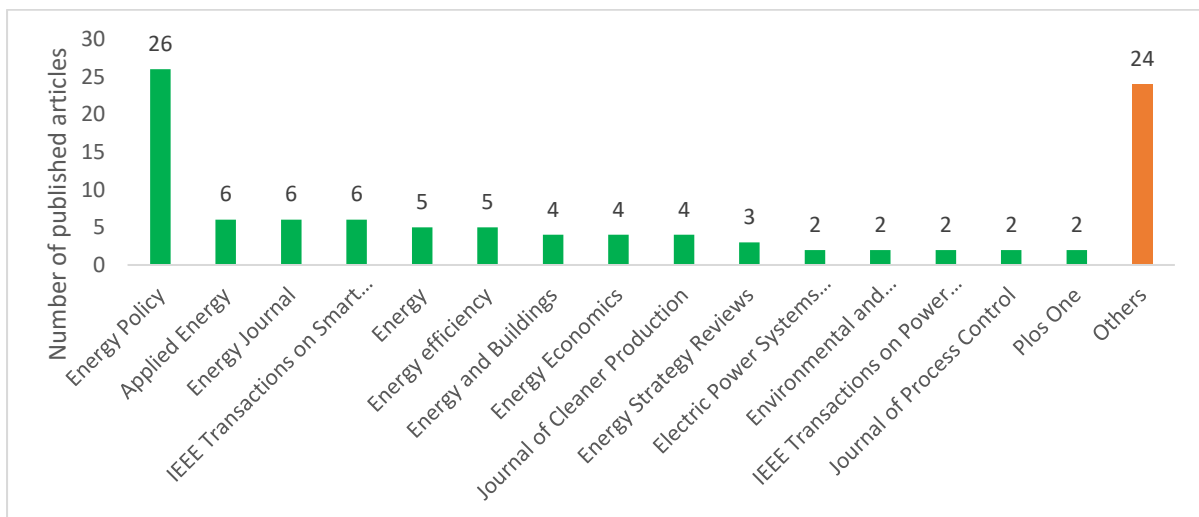


Figure 6: Number of research articles by journal

### 3.3. Demand-side policy instruments

Three types of DSM policies (i.e. demand response, energy conservation, and energy efficiency) have been identified based on six major categories (i.e. community-based, incentive-based, price-based, regulatory, voluntary and education-based policy instruments). Figure 7 shows twenty different policy instruments corresponding to the

three types of DSM based on six policy categories. Information about the status of the policy concerning the country's economic status is considered with about 77% of the reviewed articles assess existing policies, 16% propose new measures and only 7% examine piloted/trial policy of which 85% are conducted in high-income countries, 8.7% in upper middle economies and the remaining 6% are carried out in lower income countries. Research contributions from developing nations improved from 24% in the proposed policy to 37% under the assessment of the existing policies, while the proportion of the research output in developed countries dropped from 76% to 63% under the proposed policy to the on-going policy. The number of empirical studies by policy instruments is provided in Table 1. More than 50% of the reviewed articles focus on demand response, 35% on energy efficiency, and the remaining 15% on energy conservation.

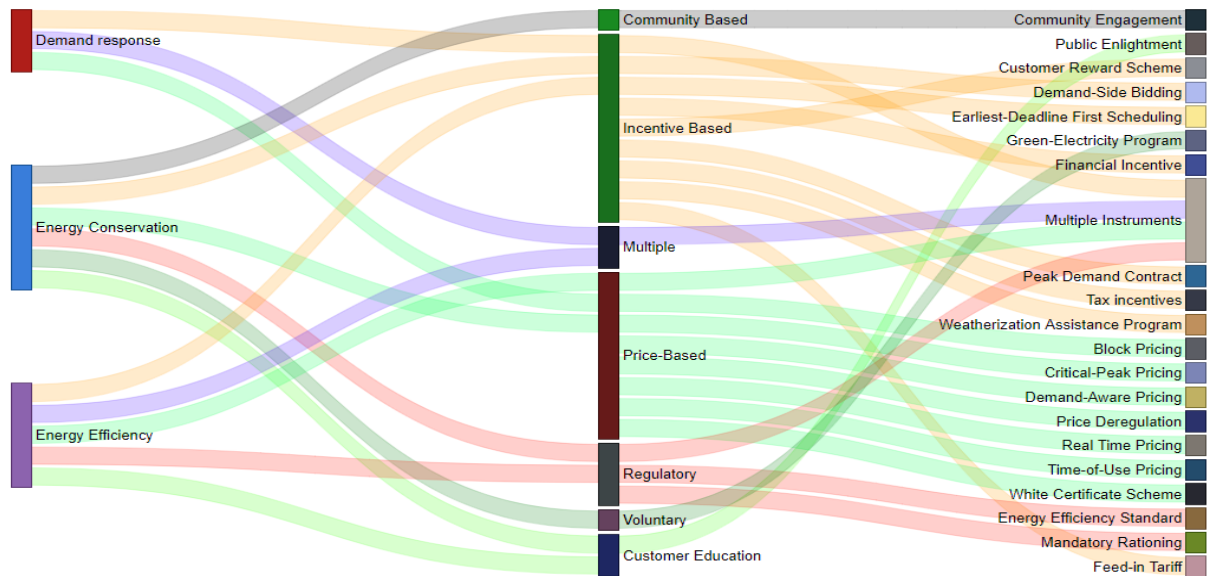


Figure 7: Connections between DSM policies, policy categories and instruments visualised in Sankey diagram

### Demand response Research

Under DR policies, nine kinds of policy instruments have been identified, of which 83% are priced-based, 15% are incentive-based, while the remaining 2% fall under 'multiple categories'. Time-of-use pricing remains the most popular policy, with about 38% of the total DR literature followed by real-time pricing at 11.5%, critical peak pricing at 9.6%, and financial incentive at 6%. Customer reward scheme, demand-aware pricing, demand-side bidding, earliest-deadline-first scheduling, and peak demand contract together account for 9.6% of the DR studies. The remaining 25% are for scientific research that considers more than one policy instruments (Table 1). 25% of the DR published works originate from the United States, followed by China and Japan with 11.5% and 9.6% respectively. In sum, DR policies are usually initiated and implemented for purposes other than electricity emissions reduction, as 88.5% of scientific literature is centred on themes such as peak saving, energy saving, customer welfare among others, while the remaining 11.5% focus on electricity decarbonisation themes.

### Energy Conservation Research

Eight types of policy instruments found in EC literature cut across all six policy categories with price-based (33%) as the highest followed by incentive-based (27%), regulatory (20%), voluntary, customer education and community-based policies all account for 20% of the studies (Table 3). The United States and China lead in deploying EC policy tools, unlike DR, EC policies are geared more towards reducing CO<sub>2</sub> emissions from the electricity sector, as more than 33% of the research focus on electricity decarbonisation.

### Energy Efficiency Research

This review has revealed eight different types of EE policy instruments employed in the literature. Unlike both DR and EC, only four policy categories are found with the majority of the policies being regulatory (39%), followed by incentive (19.4%), customer education (8.3%), and priced-based (8.3%). Studies with more than one policy categories are classified as multiple (25%). Like DR and EC, the United States has the most extensive scientific contribution with one-quarter of the whole EE literature reviewed. This is followed by Germany, the United Kingdom, and Sweden with 11%, 6%, and 6% contributions respectively (table 4). More so, EE policy is mostly designed to

reduce emissions from the power sector. This is evidenced as 53% of EE published articles are assessed based on the policy capacity to reduce emissions from the electric power sector.

Table 1: Number of policy instruments corresponding to DSM types

INSTRUMENTS /TYPES	DEMAND RESPONSE	ENERGY CONSERVATION	ENERGY EFFICIENCY	TOTAL
BLOCK PRICING			4	4
COMMUNITY ENGAGEMENT			1	1
CRITICAL-PEAK PRICING	5			5
CUSTOMER REWARD SCHEME	1			1
DEMAND-AWARE PRICING	1			1
DEMAND-SIDE BIDDING	1			1
EARLIEST-DEADLINE FIRST SCHEDULING	1			1
ENERGY EFFICIENCY STANDARD			13	13
FEED-IN TARIFF			1	1
FINANCIAL INCENTIVE	3	2	3	8
GREEN-ELECTRICITY PROGRAM		1		1
MANDATORY RATIONING		1		1
MULTIPLE INSTRUMENTS	13	3	12	28
PEAK DEMAND CONTRACT	1			1
PRICE DEREGULATION		1	1	2
PUBLIC ENLIGHTMENT		1	3	4
REAL TIME PRICING	6			6
TAX INCENTIVES			2	2
TIME-OF-USE PRICING	20			20
WEATHERIZATION ASSISTANCE PROGRAM		1		1
WHITE CERTIFICATE SCHEME			1	1
<b>TOTAL</b>	<b>52</b>	<b>15</b>	<b>36</b>	<b>103</b>

### 3.4. Research modelling paradigms

Energy modelling is essential before and after designing a demand-side policy, as it can be used to know the likely effectiveness and efficiency of a policy, preventing implementation of poorly designed measures and technological uptakes. Models can also be deployed to evaluate existing policy measure if there is a need for policy adjustments, modifications, or overall turnarounds. In recent years, there has been a significant milestone in modelling development. This success has been partly motivated by the desire to address climate change.

Five types of modelling paradigms have been identified across the literature. Equilibrium model is the most widely used paradigm with about 43% of the reviewed studies, followed by simulation model (27%), optimisation model (19%), experimental model (5%), qualitative model (4%), and the remaining 2% for studies whose model are not explicitly stated (Figure 8). As an ex-post tool, equilibrium model application has been consistent over the study period. The proportion of studies employing the model increased from 33.33% between 1994 and 2002 to 53.85% between 2003 and 2010 and fall to 40.23% between 2011 and 2018. Meanwhile, empirical studies using the optimisation model increased from only one article between 2003 and 2010 to 19 (22%) between 2011 and 2018. However, the dominance of the simulation model has been worn away since the early 2000s. Its application fell significantly from about 67% between 1994-2002 to 39% between 2003 and 2010, and down to 26% between 2011 and 2018. Qualitative and experimental models did not see the light of the day until the works of Strengers (2010) and Bradley et al. (2016), respectively. Since then, scholars' attentions have been drawn to the models with a share of 3.45%, and 5.75% for qualitative and experimental, respectively.



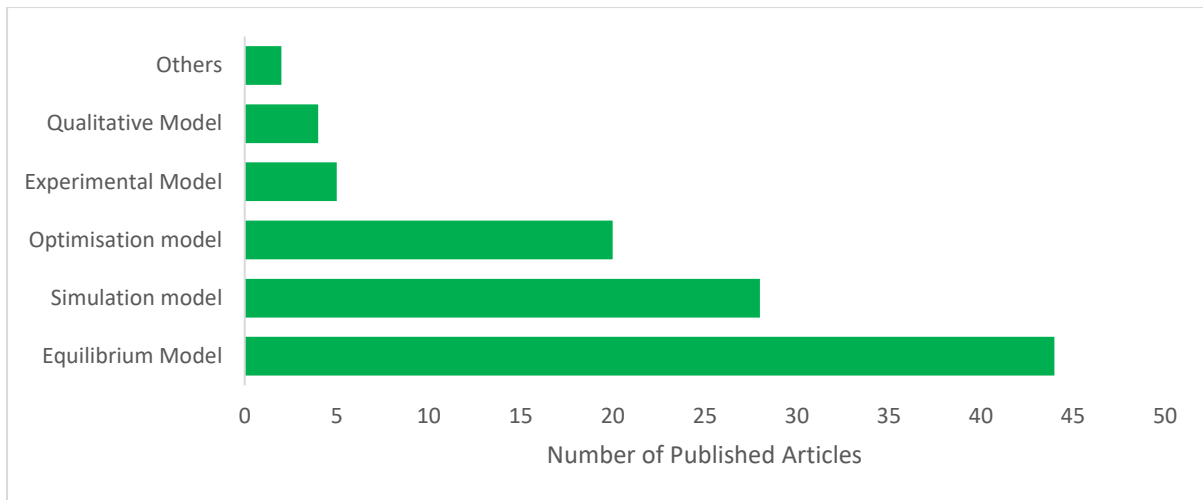


Figure 8: Types of DSM models

### 3.5. Electricity Decarbonisation through DSM

The recent resurgence in DSM efforts has been triggered by growing concerns over shrinking utility reserve margins, fuel price volatility, and above all, climate change. As countries continue to pursue climate and energy policy measures, many pay more attention to the electricity decarbonisation measures, of which demand-side angle is vital. Hence, there is a need for empirical studies on the effectiveness of policy measures (Keay, Rhys, & Robinson, 2012). DSM has evolved tremendously in recent time. First, policymakers and utility companies have come up with innovative policy instruments which are considered in this study. Second, DSM implementers now use the policy measures as a primary tool for achieving deep decarbonisation (Neves, Martins, Antunes, & Dias, 2008) since the corresponding energy saving from policy implementation has been termed “low hanging fruits in the pursuit of climate mitigation” (Carley, 2012).

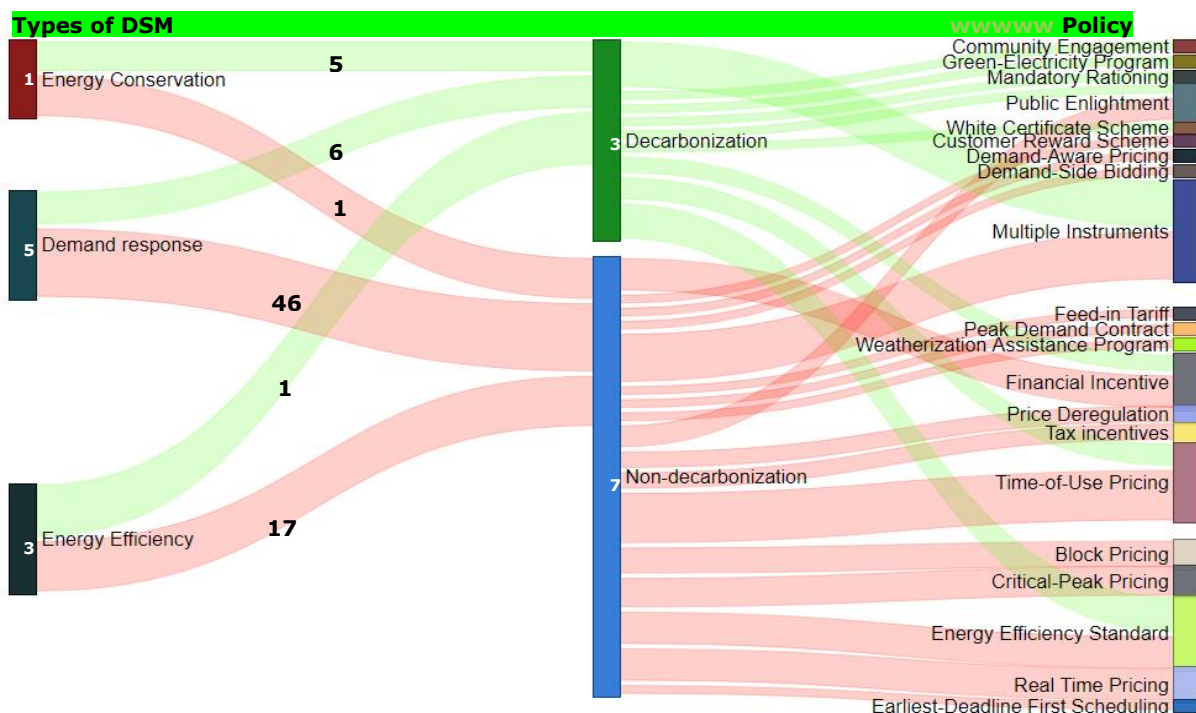


Figure 9: Connections between DSM policies, decarbonisation and policy instruments displayed in the Sankey diagram

DSM has been studied extensively in the scientific literature. However, policymakers’ interests in designing measures with decarbonisation as the central policy trust are low compared to the common goals of DSM. In this, about 71% of published works centre on non-decarbonisation themes, and only 29% concentrate on CO<sub>2</sub> emissions

reduction effectiveness of DSM policies. Different types of DSM policy instruments designed for addressing emissions from the electricity sector are shown in Figure 9. The vast majority of these studies employed multiple instruments (43.3%), followed by energy efficiency standard (23.3%). The first and only researcher to examine DSM as a decarbonisation tool was Intarapavich where he considered demand-side as one of the greenhouse gas mitigation options for the Thai power sector in 1996. Between 2003 and 2010, the number of studies considering demand-side as a decarbonisation tool has increased to 7 (54% of the articles within the period), and 22 published articles between 2011 and 2018, although with a lower proportion of 25% compared to the previous period.

Figure 10 shows the distribution of the articles based on the core demand-side research themes. This study finds that saving/conserving energy remains the central policy focus of DSM with around 22% of papers, followed by CO<sub>2</sub> emissions reduction (20%), Consumer welfare (13.5%), efficiency of energy use (12.6%), peak saving by way of reducing peak demand (12.6%), electricity sustainability (8.7%), cost minimisation of electricity production (5.8%), security of power supply (2.9%), and only one paper consider deferment of plant investment as a theme.

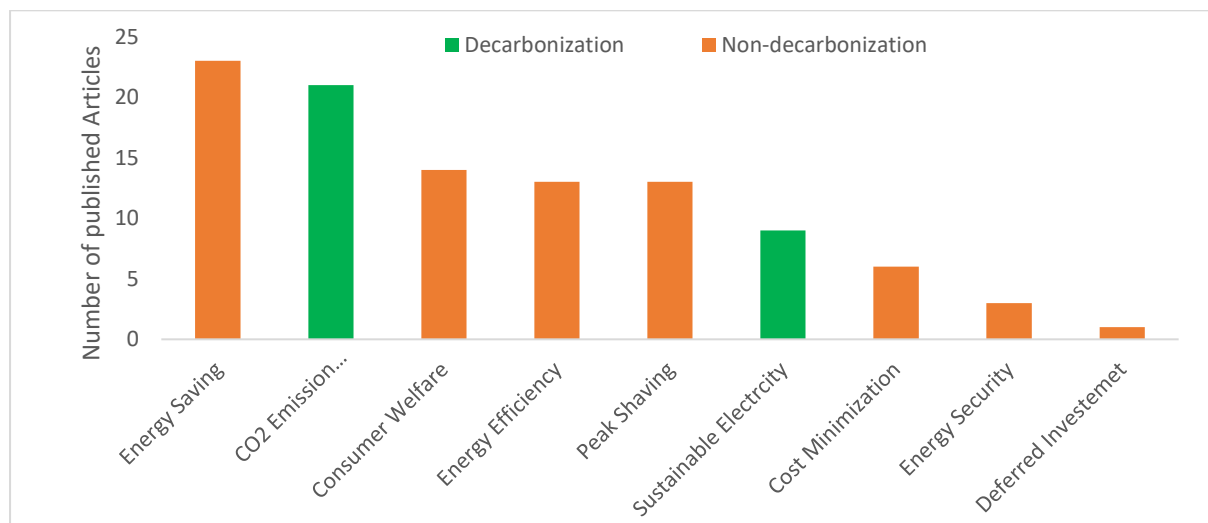


Figure 10: DSM research by themes

#### 4. DISCUSSION AND CONCLUSION

Achieving the Paris Climate Ambitious target of limiting global warming is an enormous but surmountable challenge that spans well beyond supply-side solutions. A fundamental issue according to Creutzig et al. (Creutzig et al., 2018) and Mundaca et al. (Mundaca et al., 2018) is the ongoing evaluation and assessment of different portfolios of policy instruments. By influencing the periods, electricity end-users operate electric devices in such a way that the operations occur more with power generation with low CO<sub>2</sub> emission factors, could propel the direction and pace of decarbonisation pathways and keep PA's 2°C goal within reach (S. J. G. Cooper, Dowsett, Hammond, McManus, & Rogers, 2013). To understand the new state of the art of this field of research, we review one hundred and three empirical studies on policy instrument evaluations between 1994 and 2018. DSM policies are implemented across the world for different reasons, such as decarbonisation (e.g., CO<sub>2</sub> emissions and sustainable electricity) and non-decarbonisation (e.g., energy saving, efficiency, and security, peak saving, consumer welfare, investment deferment and of course cost minimisation). Our results reveal that these policies are always implemented for non-decarbonizing reasons. Energy saving remains one of the main reasons why countries apply DSM (Carroll, Lyons, & Denny, 2014; Sudarshan, 2017) and consumer welfare in term of affordable electricity is cited as another important reason for initiating these policies (Ito & Ida, 2018; Y. Li et al., 2018). In a considerably lesser time compared to other reasons, researchers have cited carbon emissions reduction and sustainable electricity in the form of renewable energy as a policy objective of DSM (Khan, 2018; Trancik, Chang, Karapataki, & Stokes, 2014). Currently, little attention has been paid to DSM policy measures, which are found to be complementarily linked with supply-side solutions.

From a policy perspective, energy efficiency dominated the literature from 1994 to 2010 with energy conservation measures gaining momentum and demand response barely considered in the academic discourse during this period. EE has been a very successful DSM policy option when considering emissions reduction from the electricity sector (Datta & Gulati, 2014; Haeri, Perussi, & Stewart, 2018). Since 2011, demand response measures have overtaken EE policies as the main DSM policy tools. More so, its policy objectives are very diverse and pay more attention to the core DSM issues such as peak saving, energy saving, consumer welfare, (Hayes et al., 2017;

Yalcintas, Hagen, & Kaya, 2015), etc. However, most of DR policies do not always carve in emissions reduction as its primary policy objective. So, it has been described as the primary resource option for peak saving and balancing of electricity demand and supply. But since carbon emissions mainly cause the issue of climate change, comprehensive DR policy design is required to match electricity consumption and generation with low marginal emission factor (Stern, Shober, Tanner, & Dan Violette, 2016).

Another important consideration is that in reality, DSM policies are implemented as policy tool kits rather than a single measure. Despite the benefit of policy combinations, DSM scientific literature is still dominated by stand-alone policy evaluations, with 57% of which come from developed countries while the remaining 43% are conducted in the developing world. This trend could be due to the administrative complexity and cost of implementing multiple DSM policies. The separation of different policy instrument impacts from the pool of measures amid a resurgence of climate change mitigation potential of DSM is another reason why there is more single policy implementation than multiple by countries (Warren, 2015). The following are the countries where policy package has been evaluated: USA (Khezeli & Bitar, 2018), China (L. Li, Yao, Yang, & Zhou, 2018), Japan (Ito & Ida, 2018), Finland (Olkkonen et al., 2017), UK (Granell, Axon, Wallom, & Layberry, 2016), Iran (Derakhshan, Shayanfar, & Kazemi, 2016), and Ireland (Upton, Murphy, Shalloo, Groot Koerkamp, & De Boer, 2015). It is, however, evidence from this analysis that more scientific research is needed in other countries concerning policy package assessment to identify potential policy conflict/Complementarity.

Many papers focus on end-use sectoral analyses such as industrial, commercial, and residential sectors, with the primary aim of providing useful insights into the specific end-user DSM policy inputs. The industrial sector is unarguably responsible for the largest share of electricity demand, and scholars have empirically rolled out a roadmap to its sustainable pathways. However, research in both industrial and commercial sectors, have been undoubtedly under-represented given their shares in the global electricity demand. Conversely, the residential sector receives an overwhelming research interest since 1994, making it the largest DSM research recipient. Meanwhile, one out of every three studies consider all end-use sectors in what is termed as crosscutting. More research is needed in this area especially in both the industrial and commercial sector towards offering purposeful inputs into the national energy policy implementation.

Overall, the top three modelling paradigms researchers used to assess DSM policies are: equilibrium models such as econometrics (Bye, Fæhn, & Rosnes, 2018), discrete choice (Considine & Sapci, 2016), computable general equilibrium (Rodrigues & Linares, 2015) etc.; simulation models such as MAKMAL/TIMES (Blesl, Das, Fahl, & Remme, 2007; Brinker, Birdwell, & Smeenk, 2007), agent-based (Wang, Lin, Liu, Sun, & Wennersten, 2018), scenario-based (Wakiyama & Kuramochi, 2017) etc.; and lastly, optimisation models using linear programming (Vu et al., 2018), mixed integer linear/nonlinear programming (Bego, Li, & Sun, 2014; Lima et al., 2018), dynamic programming (Chen, Wang, Petersen, Tyagi, & Black, 2013), etc. However, the popularity of econometric models is due to its ability not only to predict or measure how electricity consumption changes when the policy is introduced, but it also helps to understand and study the causal mechanisms that propel the policy effect. Furthermore, researchers may want to know if a rise in the price of electricity causes electricity demand to fall. It is easy to set up a regression to examine this relationship, but correlation/relationship does not necessarily imply causation. Therefore, the field of econometrics is fully equipped with capability intended to bring out causation from non-experimental and correlated data. However, since scholars do not content themselves with only optimal prediction makings, but also aim to understand causations, assumptions are required—most crucial of these are linearity and additivity. So, if these are not true, the model becomes invalid and descriptively misleading (Syll, 2018). Therefore, more studies are needed in other modelling paradigms such as simulation model which can be used to understand in which circumstances a policy could succeed/fail, under what conditions and if indeed, the policy will have expected effect.

Many empirical studies on demand-side policy instruments are predominantly conducted in the United States, China, Japan, United Kingdom, Australia, Germany, Sweden, and Switzerland while DSM research in other countries has received little to no interest till date. It is however found that countries like India, France, South Korea, Brazil, and Saudi Arabia are arguably under-represented while nations like Russia and Canada are not represented at all in spite of their contribution to the growth of world electricity demand. For instance, only China and India were responsible for 70% of global electricity growth (3.1%) in 2017. Therefore, DSM policy evaluation is urgently needed to manage the future growth of electricity demand in these countries. The world reached companion and unanimous decision to address the menace of climate change in 2015 during the conference of parties (COP 21) held in Paris. Few years after the agreement comes president Trump's withdrawal from PA, which many consider as an unfortunate and severe setback to the implementation of the INDCs. But contrary to what many expect, more researches have been conducted after Trump's withdrawal declaration with most of them coming from the United States and emerging economies. Our findings dampen the fear of the bandwagon effect of the so-called withdrawal.

These research gaps could have serious implication for achieving ambitious climate targets. For residential end-users, DSM offers the possibility to manage their electricity bills through policy instruments. In the case of commercial and industrial consumers, this would manifest in the form of least cost of production and place them in

more competitive ends from the global market. Apart from reducing the risk of a power outage, government across the world now use DSM to meet climate change mitigation targets.

## 5. ACKNOWLEDGEMENT

The authors significantly acknowledged the financial support from Universiti Kebangsaan Malaysia (UKM) under the grant GUP-2018-015.

## 6. REFERENCES

Babatunde, K. A., Begum, R. A., & Said, F. F. (2017). Application of computable general equilibrium (CGE) to climate change mitigation policy: A systematic review. *Renewable and Sustainable Energy Reviews*, 78(April), 61–71. <https://doi.org/10.1016/j.rser.2017.04.064>

Briner, R. B., & Denyer, D. (2010). Systematic Review and Evidence Synthesis as a Practice and Scholarship Tool. In D. M. Rousseau (Ed.), *The Oxford Handbook of Evidence-Based Management* (pp. 112–129). Oxford: Oxford University Press.

Carley, S. (2012). Energy Demand – Side Management: New Perspectives for a New Era. *Journal of Policy Analysis and Management*, 31(1), 6–32.

Cherp, A., Vinichenko, V., Jewell, J., Brutschin, E., & Sovacool, B. (2018). Integrating techno-economic, socio-technical and political perspectives on national energy transitions: A meta-theoretical framework. *Energy Research and Social Science*, 37(September 2017), 175–190. <https://doi.org/10.1016/j.erss.2017.09.015>

Cooper, M. (2018). Governing the global climate commons: The political economy of state and local action, after the U.S. flip-flop on the Paris Agreement. *Energy Policy*, 118(February), 440–454. <https://doi.org/10.1016/j.enpol.2018.03.037>

Costa, A., & Galvis, J. C. (2016). Demand Side Management Using Time of Use and Elasticity Price. *IEEE Latin America Transactions*, 14(10), 4267–4274. Retrieved from <http://ieeexplore.ieee.org/ielx7/9907/7786295/07786304.pdf?tp=&arnumber=7786304&isnumber=7786295>

Creti, A., & Nguyen, D. K. (2018). “Energy and environment: Transition models and new policy challenges in the post Paris Agreement.” *Energy Policy*, 122, 677–679. <https://doi.org/10.1016/j.enpol.2018.07.048>

Intarapavich, D. (1996). Assessing greenhouse gas mitigation options for the Thai power sector. *Ambio*, 25(4), 233–239. <https://doi.org/10.2307/4314466>

Keay, M., Rhys, J., & Robinson, D. (2012). *Decarbonization of the electricity sector - is there still a place for markets?*

Martín-Martín, A., Orduna-Malea, E., Thelwall, M., & Delgado López-Cózar, E. (2018). Google Scholar, Web of Science, and Scopus: a systematic comparison of citations in 252 subject categories. *Journal of Informetrics*, 12(4), 1160–1177. <https://doi.org/10.1016/J.JOI.2018.09.002>

Neves, L. P., Martins, A. G., Antunes, C. H., & Dias, L. C. (2008). A multi-criteria decision approach to sorting actions for promoting energy efficiency. *Energy Policy*, 36(7), 2351–2363. <https://doi.org/10.1016/j.enpol.2007.11.032>

Nong, D., & Siriwardana, M. (2018). Effects on the U.S. economy of its proposed withdrawal from the Paris Agreement: A quantitative assessment. *Energy*, 159, 621–629. <https://doi.org/10.1016/j.energy.2018.06.178>

Ouedraogo, N. S. (2017). Africa energy future: Alternative scenarios and their implications for sustainable development strategies. *Energy Policy*, 106(April), 457–471. <https://doi.org/10.1016/j.enpol.2017.03.021>

Oyeniran, W. I., & Babatunde, K. A. (2015). Growth Thresholds and Environmental Degradation in Sub-Saharan African Countries: An Exploration of Kuznets Hypothesis. *International Journal of Management, Accounting and Economics*, 2(8), 858–871.

Rhodes, C. J. (2017). US withdrawal from the COP21 Paris Climate Change Agreement, and its possible implications. *Science Progress*, 100(4), 411–419. <https://doi.org/10.3184/003685017x15063357842600>

Rousseau, D. M., Manning, J., & Denyer, D. (2008). Evidence in Management and Organizational Science: Assembling the Field's Full Weight of Scientific Knowledge Through Syntheses. *The Academy of Management Annals*, 2(August), 475–515. Retrieved from <http://ssrn.com/abstract=1309606>

Schaeffer, R., Cohen, C., de Aguiar, A. C. J., & Faria, G. V. R. (2009). The potential for electricity conservation and carbon dioxide emission reductions in the household sector of Brazil. *Energy Efficiency*, 2(2), 165–178. <https://doi.org/10.1007/s12053-008-9033-7>

Schanes, K., Dobernig, K., & Gözet, B. (2018). Food waste matters - A systematic review of household food waste practices and their policy implications. *Journal of Cleaner Production*, 182, 978–991. <https://doi.org/10.1016/j.jclepro.2018.02.030>

Silva, C., & Nasirov, S. (2017). Chile: Paving the way for sustainable energy planning. *Energy Sources, Part B: Economics, Planning and Policy*, 12(1), 56–62. <https://doi.org/10.1080/15567249.2014.977464>

Swisher, J., Christiansson, L., & Hedenström, C. (1994). Dynamics of energy efficient lighting. *Energy Policy*, 22(7), 581–594. [https://doi.org/10.1016/0301-4215\(94\)90077-9](https://doi.org/10.1016/0301-4215(94)90077-9)

Waide, P., Lebot, B., & Hinnells, M. (1997). Appliance energy standards in Europe. *Energy and Buildings*, 26(1), 45–67. [https://doi.org/10.1016/S0378-7788\(96\)01013-4](https://doi.org/10.1016/S0378-7788(96)01013-4)

---

## #15: Performance of a small domestic eutectic solder medium temperature latent heat storage system during charging

---

Ashmore MAWIRE<sup>1\*</sup>, Chidiebere EKWOMADU<sup>1</sup>, Ttotlo LEFENYA<sup>1</sup>, Adedamola SHOBO<sup>2</sup>

<sup>1</sup>Department of Physics and Electronics, North-West University, Mafikeng Campus, Private Bag X2046, Mmabatho 2745, South Africa

<sup>2</sup>Department of Mathematics, Science and Sports Education, University of Namibia, Private Bag 5507, Oshakati, Namibia, Mmabatho 2745, South Africa

\*Corresponding author: ashmore.mawire@nwu.ac.za

*The aim of this study is to evaluate the performance of a packed bed latent heat storage system for domestic medium temperature applications. The packed bed thermal energy storage (TES) system consists of encapsulated eutectic solder (Sn63Pb37) capsules charged up with Sunflower Oil as the heat transfer fluid (HTF). Three charging flow-rates of 4 ml/s, 6 ml/s and 8 ml/s are used to evaluate the charging performance. Temperature profiles along the height of the storage tank, energy rate profiles and exergy rate profiles are used as thermal performance parameters. The lowest flow-rate (4 ml/s) results in a higher degree of thermal stratification along the height of the storage tank and in a lower charging duration. The charging exergy and exergy rates increase with an increase in the flowrate. The highest flow-rate (8 ml/s) shows the highest charging energy and exergy rates. The system is suitable for domestic solar cooking applications to provide heat when the sun is not available.*

*Keywords: charging; eutectic solder; latent heat storage; medium temperature*

## 1. INTRODUCTION

Firewood used to cook food in the rural areas in Africa produces smoke which results in lung related diseases. The rate of deforestation is increased with the cutting of wood, and this results in a poor environmental footprint. Sustainable and renewable energy resources such as solar energy can be used to cater for domestic purposes such as cooking food in developing countries (Mussard and Nydal, 2013). Solar energy has a drawback of intermittency, and it needs to be stored for usage during periods when it is not available, for example at night and during cloudy periods. Thermal energy storage (TES) can offer a short time solution for cooking needs during the night by storing solar thermal energy during daytime and using this stored heat at night (Sharma et al., 2000; Sharma et al., 2005; Hussein et al., 2008; Lecuona et al., 2013). The two main viable options of TES for domestic cooking applications are sensible heat TES (SHTES) and latent heat TES (LHTES). Although SHTES is cheaper and readily available as compared to LHTES, its main drawback is the much lower energy storage density such that larger energy storage tanks are required for usually moderate amounts of thermal energy to be stored. LHTES ensures compact energy storage with the delivery of the stored heat at a controlled temperature for a longer duration since both sensible and latent heat can be extracted from the storage system.

Phase change materials (PCMs) have been recently used in LHTES systems for medium to high temperature applications (Cárdenas and León, 2013). In recent study by Li et al., (2018), a latent heat packed bed storage system was found to be 1.9-2.4 more efficient than a shell and tube latent heat storage configuration for high temperature applications. This justifies more experimental research on medium to high temperature packed bed latent heat storage systems. Recent research on packed bed latent heat storage systems for medium to high temperatures is limited and studies reported mainly used air as the heat transfer fluid (Bellan et al., 2015; Zanganeh et al., 2014; Ma and Zheng, 2017; Peng et al., 2014; Zanganeh et al., 2015; Li et al., 2018; Gimenez-Gavarrell and Fereres, 2017; Peng et al., 2015; Liao et al., 2018). Metallic PCMs are favourable for latent heat storage systems since metals and metal alloys possess a high storage density on a volume basis as well as a substantially higher thermal conductivity. Limited recent work has been done on high temperature metallic PCMs to enhance their understanding (Fernández et al., 2017; Andraka et al., 2015; Fukahori et al., 2016; Nomura et al., 2018; Kotzé et al., 2014; Wang et al., 2006; Zhang et al., 2014).

High temperature metallic PCMs are more appropriate for industrial processes and present safety issues for domestic scale applications like cooking of food, hence medium temperature metallic PCMs (100 °C to 300 °C) using heat transfer fluids are more suitable. There are very limited studies that have appeared in recent years on medium temperature PCMs using heat transfer fluids (Shobo and Mawire, 2017a; Shobo and Mawire, 2017b; Shobo et al., 2017). The use of an oil heat transfer fluid (HTF) instead of air is justified by the fact that a lower pumping power is required, and the design of the storage system is less complicated since fewer pressurized components are required. Sunflower Oil as an HTF has been used recently since it is cheap, food grade, and readily available, non-toxic and possesses characteristics comparable to other commercial HTFs (Mawire et al., 2014; Mawire, 2016). A Tin-Lead based eutectic solder (Sn63/Pb37) is widely available in South Africa, and it has never been used for a latent heat storage application. Energy analysis measures the quantity of the stored energy whereas exergy analysis is measure of the quality of the available energy with reference to the ambient conditions. Irreversibilities in thermodynamic systems occur mainly as heat losses, thus exergy analysis gives a more realistic picture of the performance of a TES system. Exergy performance parameters should thus also be evaluated in TES systems (Jegadheeswaran et al., 2010). Due to the advantages of metallic PCMs mentioned earlier, the aim of the experiment is to evaluate the performance of a eutectic solder metallic PCM based packed bed LHTES system during charging cycles. This study has never been done before using the mentioned PCM, and it will add invaluable information on medium temperature metallic domestic packed bed storage systems.

## 2. EXPERIMENTAL METHOD AND SETUP

Solder wire that was 2 mm thick was inserted into 40 capsules from the top opening until an internal volume 80 % was covered. It was ensured that the solder occupied the maximum volume by pressing the solder wire with a screwdriver. All 40 capsules had approximately the same mass of solder inside them. The total mass of each capsule was measured with an electronic balance before and after inserting the solder wire. Each aluminium capsule had an approximate diameter of 0.05 m and a wall thickness of 0.001 m. The capsules were manufactured as hollow spheres with an opening at the top to allow for inserting of the wire PCM. The volume of the PCM wire in the capsules was about 80 % of the total internal volume of the capsule to allow for thermal expansion. After inserting of the PCM, four capsules had K-thermocouples fixed onto them to measure the PCM temperatures. These thermocouples which extended into the centre of the spheres were fastened on the top of the spheres. The thermocouples acted both as sealing mechanisms and also as temperature monitoring devices. The rest of the PCM capsules were sealed with screw caps. Figure 1 shows a PCM capsule with a screw cap and one with a thermocouple screw cap. The total mass of each capsule was measured before and after encapsulation with an electronic balance to ensure that the capsules had almost the same mass of PCM inside them. Each of the PCM capsule was heated up to its melting point in an oil bath to ensure that there were no PCM leakages before they were put into the storage tank.

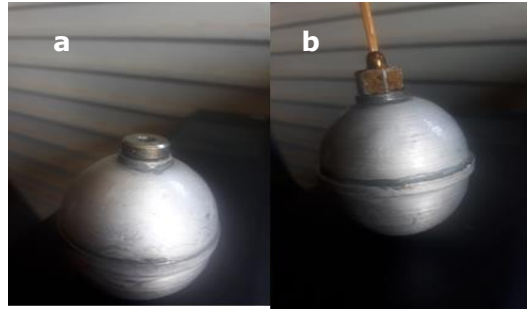


Figure 1: (a) Aluminium PCM capsule with screw cap. (b) Aluminium capsule with thermocouple screw cap.

Thermo-physical properties of the eutectic solder (Sn63/Pb37) obtained from open literature are shown in Table 1. The mass of the solder inside the capsules was around 164 g. The solder has a high thermal conductivity of around 50 W/mK and its latent heat and melting temperatures are reported to be around 52.1 kJ/kg and 183°C respectively. Results obtained from literature were used due to the expensive nature of the measuring equipment. The aim of these experiments was to find the bulk performance of the storage system instead of the thermal properties.

Table 1: Thermo-physical properties of the eutectic solder

Property	Value
Melting Temperature (°C)	183 (Wu et al., 2009, Morando et al., 2014)
Specific Heat Capacity (kJ/kgK)	0.21 (30°C) (Wu et al., 2009)
Phase change enthalpy (kJ/kg)	52.1 (Sn63Pb37 Technical Data Sheet, 2018)
Density(kg/m <sup>3</sup> )	8400 (Wu et al. 2009, Morando et al., 2014)
Thermal conductivity (W/mK)	50 (Morando et al., 2014)
Average mass of PCM in the capsule (g)	164

The main components of the experimental setup are shown in the schematic diagram of Figure 2.

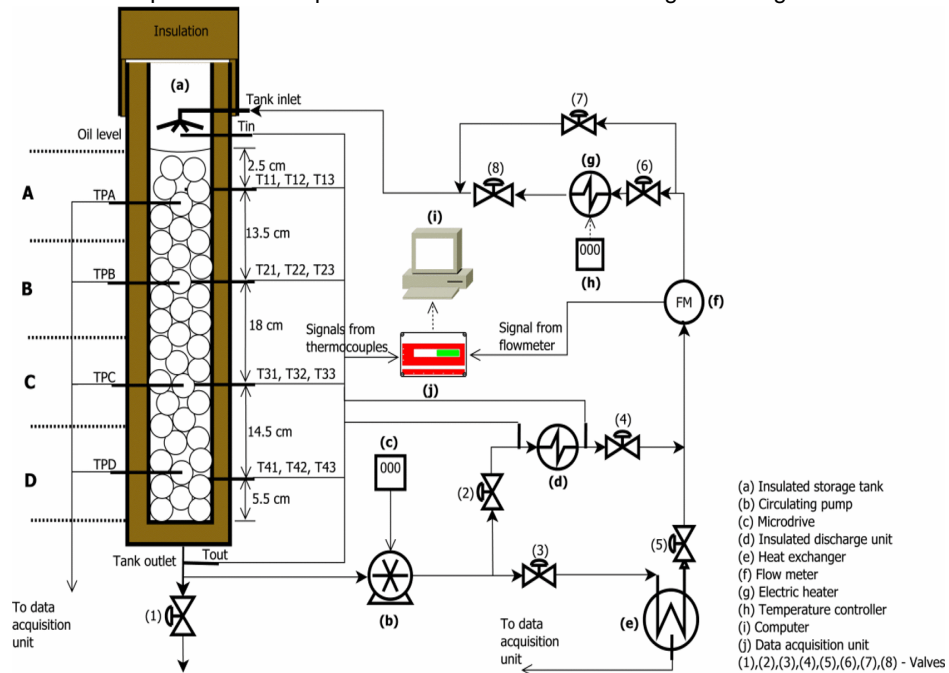


Figure 2: Schematic diagram of experimental setup (Shobo et al., 2017)



Forty spherical eutectic solder PCM capsules of were inserted into the storage tank and the top level capsules were at Level A below the tank's inlet port. Sunflower Oil filled up the void between the capsules up to Level A and the storage tank void fraction was estimated to be around 0.49.

Two electrical spiral coils (power rating: 220V, 900 W each) constituted the heating unit (g) which heated up circulating oil in a copper spiral coil embedded in between the coils. A temperature controller regulated the heating unit. A TZN4S temperature controller (h) (display accuracy:  $\pm 0.3\%$ ) was used to set and control the required maximum temperature. An insulated stainless steel cylindrical storage tank (a) with a diameter of 0.3 m and a height of 0.54 m was used. K-type thermocouples were placed at radial distances of 0.013 m, 0.038 m and 0.064 m to measure the temperature at each axial level of the storage tank (Levels A-D). Four PCM capsules with thermocouples were placed centrally at Levels A-D, to monitor the PCM temperature at each level for the latent heat storage system. The thermocouples were calibrated to an accuracy of around  $\pm 2^\circ\text{C}$ . The voids in the storage tank were filled with around 4 litres of refined Sunflower Oil during the experiments. A magnetic-drive pump (b) was used to circulate Sunflower Oil through the heating unit, while a VLT Micro drive (c) (maximum error: 0.8% of full scale) was used to control the frequency of the pump so as to set a desired flow-rate. A flow meter (maximum operating temperature:  $150^\circ\text{C}$ ) (f) was used to measure the flow-rate of the TES system every 10 s and a heat exchanger (e) was connected directly to the flow meter to cool it down so as not to exceed its maximum operating temperature. An HP 34970 data acquisition unit (j) was connected to the thermocouples and it was used to convert analogue signals to digital signals. A personal computer (i) was used to monitor the temperature profiles of the TES systems and the PCMs, and it recorded data every 10 s.

During the charging cycles valves (1), (2), (4) and (7) were closed while valves (3), (5), (6) and (8) were opened. Charging of the storage system storage was terminated when the bottom temperatures of the storages ( $T_D$ ) were around  $190^\circ\text{C}$  to ensure melting of the PCM at the bottom since this PCM had a melting temperature close to  $183^\circ\text{C}$ . To investigate the effect of the flow-rate, charging experiments were performed with flow-rates of 4 ml/s (low), 6 ml/s (medium) and 8 ml/s (high) respectively at a set heater temperature of  $280^\circ\text{C}$ .

### 3. EXPERIMENTAL THERMAL ANALYSIS

The charging energy rate depends on the inlet and outlet charging temperatures of the storage tank and is expressed as:

$$\text{Equation 1:} \quad \dot{E}_{ch} = \rho_{av} c_{av} \dot{v}_{ch} (T_{chin} - T_{chout})$$

Where:

- $\rho_{av}$  = temperature dependent average density of the oil at the start and end of charging;
- $c_{av}$  = temperature dependent average density of the oil at the start and end of charging;
- $\dot{v}_{ch}$  = volumetric charging flow-rate,  $T_{chin}$  is the inlet charging temperature at the top of the storage tank;
- $T_{chout}$  = outlet charging temperature at the bottom of the storage tank.

The charging exergy rate is given as:

$$\text{Equation 2:} \quad \dot{E}_{xch} = \rho_{av} c_{av} \dot{v}_{ch} \left[ (T_{chin} - T_{chout}) - \left( T_{amb} \ln \frac{T_{chin}}{T_{chout}} \right) \right] \quad (\text{Jegadheeswaran et al., 2010})$$

Where:

- $T_{amb}$  = ambient temperature.

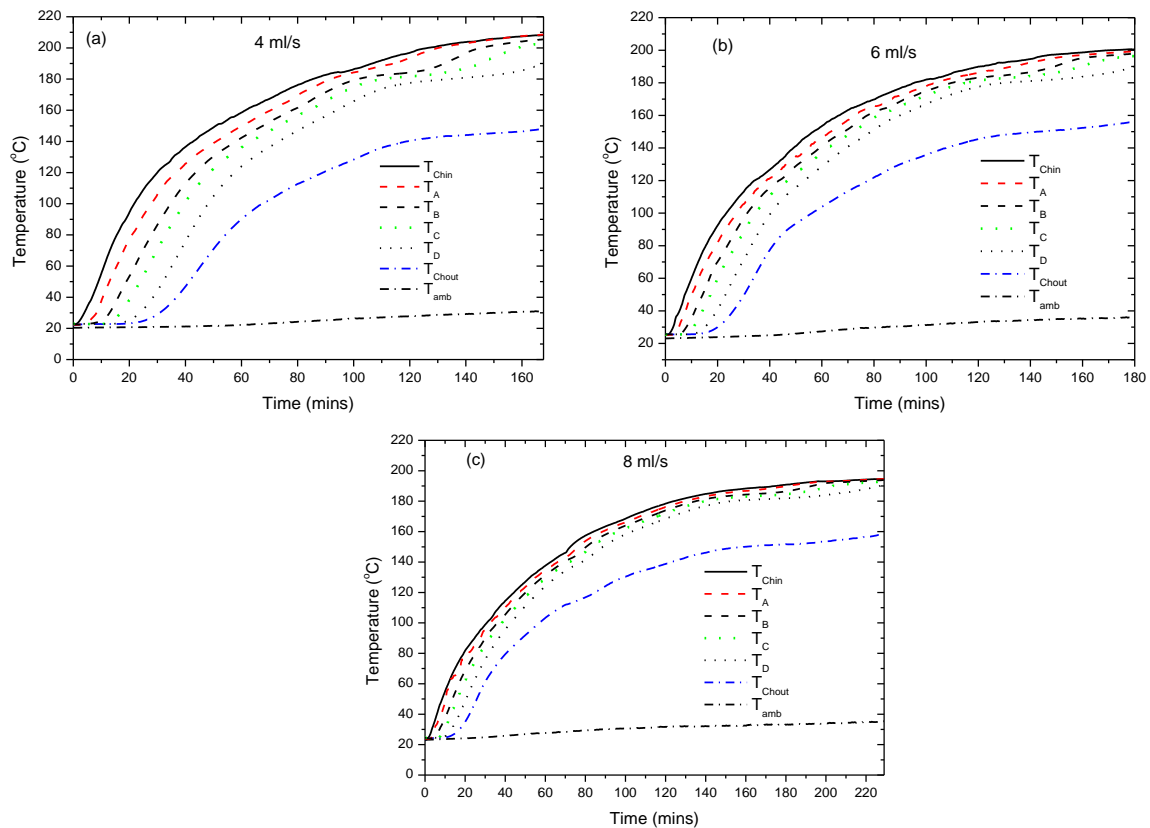
### 4. RESULTS AND DISCUSSION

The effect of the flow-rate on the storage tank temperatures and the charging energy and exergy rates are presented in this section. Figure 3 shows the charging temperature profiles of the storage tank using low (4 ml/s), medium (6 ml/s) and high (8 ml/s) charging flow-rates. The plots show that as the charging flow-rate increases, the charging time increases. A similar effect of an increase of the charging time with the charging flow-rate has been reported by Lugolole et al. (2018) who compared three different sensible heat storage materials in the same storage system. The probable reason for the increase is the increased rate of heat transfer with the higher flow-rate that causes the temperatures inside the storage tank to rise faster such that the associated heat losses are more causing the bottom limiting temperatures to be approached later with the higher flow-rates.

Heat transfer Increases with an increase in the charging flow-rate causing the degree of thermal stratification along of the height of the storage to decrease due to reduced thermal gradients at higher flow-rates. The phase change process is seen to progress from the top to the bottom of the storage since the storage tank is charged from the top to the bottom. The phase change process occurs earlier for the lowest flow-rate (4 ml/s) at around 100 minutes, whereas for the other flow-rates its starts at around 120 minutes (6 ml/s) and 140 minutes, respectively).

The most probable reason is the higher heat transfer rate with the higher flow-rates which induce faster temperature rises consequently also increasing heat losses and the charging times. It is also important to note with the increase in the heat transfer rate induced by increasing the flow-rate, the outlet charging temperature also increases to its highest value at the end of the charging with the highest charging flow-rate (8 ml/s). It seems the lowest charging flow-rate (4 ml/s) results in the best thermal performance in terms of the charging duration. The degree of thermal stratification is also better at the end of charging. This result has also been confirmed by the experiments done by Lugolole et al. (2018). This however, does not directly infer better thermal performance in terms of the charging energy and exergy rates.

Figure 3: Charging temperature profiles at (a) low, (b) medium and (c) high flow-rates for the eutectic solder TES system.



For quantitative and qualitative assessment of the storage performance in a more realistic way, charging energy and exergy rate profiles are presented in Figure 4. The charging energy rate plots (a) show initial rapid rises to peak values with the highest charging flow-rate showing the fastest rise due to the fastest heat transfer rate. The peaks occur at around 20 minutes, 25 minutes and 30 minutes respectively, for 8 ml/s, 6 ml/s and 4 ml/s. These peaks are caused by the initial rise in the inlet temperatures when the bottom of the storage tank is cold during the initial stages of charging inducing larger thermal gradients along the height of the storage tank. As charging progresses, the energy rates drop from the peak values as the bottom becomes hotter and the thermal gradients reduce. The highest peak value of around 820 W is seen with 6 ml/s suggesting that it is the best charging flow-rate since a further increase to 8 ml/s results in a lower peak value. Secondary peak values are seen when charging with the higher flow-rates at around 60 minutes for 6 ml/s and 80 minutes for 8 ml/s. This is possibly due to the drop in rate of rise of the inlet temperatures from around 40 minutes for the 6 ml/s case and from around 70 minutes for the 8 ml/s case (Figure 3 (b) & Fig. 3 (c)). The drop in the rise of the inlet temperatures cause thermal gradients along the height of the storage tank to increase slightly inducing secondary peaks of the energy charging rates for 6 ml/s and 8 ml/s. The drop in the rise of the inlet temperatures is possibly due to phase change transitions at the bottom of the storage tank for higher storage temperatures. The lowest flow-rate with a lower inlet temperature shows no such behaviour. Higher charging energy rates are seen with the highest flow-rate for most of the charging duration from around 80 minutes. This happens even with a lower primary peak value suggesting that it is more beneficial to charge with higher flow-rates to increase the energy charging rates. On the other-hand, the lower flow-rates enable thermal stratification and a charging for a shorter thus the flow-rate should be selected as comprise between obtaining higher charging rates and a shorter charging duration.

Exergy charging rates are lower than the energy charging rates since heat losses are accounted for and the highest flow-rate shows higher values after 70 minutes suggesting it is the best charging flow-rate to obtain better exergy charging rates. The effect of the secondary peak energy rate values is also evident after 40 minutes for 6 ml/s and after 70 minutes for 8 ml/s. Again a compromise should be done at selecting a charging flow-rate that addresses the issues of a shorter charging duration and obtaining reasonably high exergy charging rates.

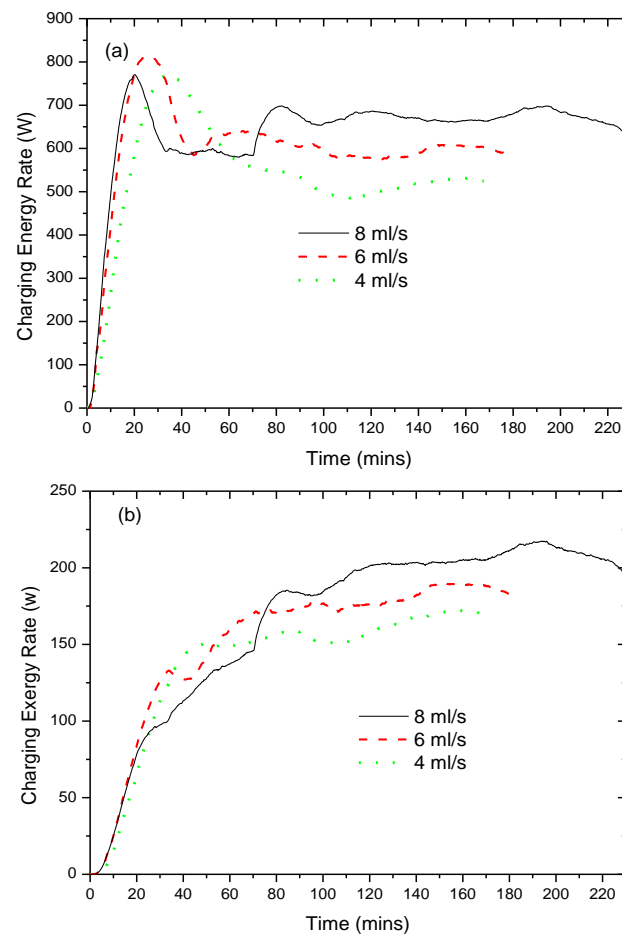


Figure 4: Charging (a) energy rate and (b) exergy rate profiles at different charging flow-rates for the eutectic solder TES system.

## 5. CONCLUSION

A packed bed latent heat storage system consisting of aluminium encapsulated eutectic solder (Sn63Pb37) capsules was experimentally evaluated during charging cycles. Sunflower Oil was used as the heat transfer fluid in the experiments. Charging results were presented in terms of the axial storage tank profiles, the energy rates and the exergy rates using three different charging flow-rates (4 ml/s, 6 ml/s and 8 ml/s). The charging energy and exergy rates increased with the charging flow-rate at the expense of a greater charging duration. The best charging flow-rate was 6 ml/s since it ensured a reasonable duration of charging, reasonable thermal stratification and reasonably high energy and exergy charging rates. The solder can be viable PCM for domestic medium temperature applications since reasonably good results were obtained.

## 6. ACKNOWLEDGEMENT

The authors would like to thank the National Research Foundation (NRF), South Africa for funding to attend and present a paper at this conference under the KIC190214417726 grant. We acknowledge that opinions, findings and conclusions or recommendations expressed in any publication generated by the NRF supported research are our own, and that the NRF accepts no liability whatsoever in this regard.

## 7. REFERENCES

- Andraka CE, Kruizenga AM, Hernandez-Sanchez BA, Coker EN (2015). Metallic phase change material thermal storage for dish Stirling. *Energy Procedia* 69: 726 –36.
- Bellan S, Alam TE, Gonzalez-Aguilar J, Romero M, Rahman MM, Goswami DY, Stefanakos EK (2015). Numerical and experimental studies on heat transfer characteristics of thermal energy storage system packed with molten salt PCM capsules. *Applied Thermal Engineering* 90: 970–79.
- Cárdenas B, León N (2013). High temperature latent heat thermal energy storage: Phase change materials, design considerations and performance enhancement techniques. *Renewable and Sustainable Energy Reviews* 27:724–37.
- Fernández A, Barreneche C, Belusko M, Segarra M, Bruno F, Cabeza LF (2017). Considerations for the use of metal alloys as phase change materials for high temperature applications. *Solar Energy Materials and Solar Cells* 171: 275–81.
- Fukahori R, Nomura T, Zhu C, Sheng N, Okinaka N, Akiyama T (2016). Macro-encapsulation of metallic phase change material using cylindrical-type ceramic containers for high-temperature thermal energy storage. *Applied Energy* 170: 324–28.
- Gimenez-Gavarrell P, Fereres S (2017). Glass encapsulated phase change materials for high temperature thermal energy storage. *Renewable Energy* 107: 497–507.
- Hussein HMS, El-Ghetany HH, Nada SA (2008). Experimental investigation of novel indirect solar cooker with indoor PCM thermal storage and cooking unit. *Energy Conversion and Management* 49: 2237–46.
- Jegadheeswaran S, Pohekar SD, Kousksou T (2010). Exergy based performance evaluation of latent heat thermal storage system: a review, *Renewable and Sustainable Energy Reviews* 14: 2580–95.
- Kotzé JP, von Backström TW, Erens PJ (2014). Simulation and testing of a latent heat thermal energy storage unit with metallic phase change material. *Energy Procedia* 49: 860 – 69.
- Lecuona A, Nogueira N, Ventas R, Rodríguez-Hidalgo M, Legrand M (2013). Solar cooker of the portable parabolic type incorporating heat storage based on PCM. *Applied Energy* 111:1136–46.
- Li M, Jin B, Ma Z, Yuan F (2018). Experimental and numerical study on the performance of a new high temperature packed-bed thermal energy storage system with macro-encapsulation of molten salt phase change material. *Applied Energy* 2018; 221:1–15.
- Liao Z, Zhao G, Xua C, Yang C, Jin Y, Jua X, Du X (2018). Efficiency analyses of high temperature thermal energy storage systems of rocks only and rock-PCM capsule combination. *Solar Energy* 162: 153–64.
- Lugolole R, Mawire A, Lentswe KA, Okello D, Nyeinga K (2018). Thermal performance comparison of three sensible heat thermal energy storage systems during charging cycles. *Sustainable Energy Technologies and Assessments* 30: 37–51.
- Ma F, Zheng P (2017). Investigation on the performance of a high-temperature packed bed latent heat thermal energy storage system using Al-Si alloy. *Energy Conversion and Management* 150: 500–14.
- Mawire A, Taole S, Phori A (2014). Performance comparison of thermal energy storage oils for solar cookers during charging. *Applied Thermal Engineering* 73: 1321–29.
- Mawire A (2016). Performance of Sunflower Oil as a sensible heat storage medium for domestic applications. *Journal of Energy Storage* 5:1–9.
- Morando C, Fornaro O, Garbellini O, Palacio H (2014). Thermal properties of Sn-based solder alloys. *Journal of Materials Science: Materials in Electronics* 25: 3440–47.
- Mussard M, Nydal O (2013). Comparison of oil and aluminum-based heat storage charged with a small-scale solar parabolic trough. *Applied Thermal Engineering* 58: 146–54.

- Nomura T, Yoolerd J, Sheng N, Sakai H, Hasegawa Y, Haga M, Saito, Akiyama T (2018). Microencapsulation of eutectic and hyper-eutectic Al-Si alloy as phase change materials for high-temperature thermal energy storage. *Solar Energy Materials and Solar Cells* 187: 255–62.
- Peng H, Dong H, Ling X (2014). Thermal investigation of PCM-based high temperature thermal energy storage in packed bed. *Energy Conversion and Management* 81: 420–27.
- Peng H, Li R, Ling X, Dong H (2015). Modeling on heat storage performance of compressed air in a packed bed system. *Applied Energy* 160: 1–9.
- Sharma SD, Buddhi D, Sawhney RL, Sharma A (2000). Design, development and performance evaluation of a latent heat storage unit for evening cooking in a solar cooker. *Energy Conversion and Management* 41:1497–508.
- Sharma SD, Iwata T, Kitano H, Sagara K (2005). Thermal performance of a solar cooker based on an evacuated tube solar collector with a PCM storage unit. *Solar Energy* 78: 416–26.
- [Shobo AB, Mawire A (2017a). Experimental comparison of the dynamic operations of a sensible heat thermal energy storage and a latent heat thermal energy storage system. In *Proceedings of 25th Domestic Use of Energy Conference, DUE 2017*; Cape Town, South Africa, April 3-5, 2017: 240–47.
- Shobo AB, Mawire A (2017b). Experimental comparison of the thermal performances of acetanilide, meso-erythritol and an In-Sn alloy in similar spherical capsules. *Applied Thermal Engineering* 124: 871–82.
- Shobo AB, Mawire A, Okello D (2017). Experimental thermal stratification comparison of two storage systems. *Energy Procedia* 142: 3295–3300.
- Sn63Pb37 RA Solder Wire4880–4888 Technical Data Sheet (2018): <https://images-na.ssl-images-amazon.com/images/I/81h+ZhgF19L.pdf>, website accessed 10 January 2018.
- Wang X, Liu J, Zhang Y, Di H, Jiang Y (2006). Experimental research on a kind of novel high temperature phase change storage heater. *Energy Conversion and Management* 47: 2211–22.
- Wu YK, Lin KL, Salam B (2009). Specific heat capacities of Sn-Zn-Based solders measured using differential scanning calorimetry. *Journal of Electronic Materials* 38: 227–30.
- Zanganeh G, Commerford M, Haselbacher A, Pedretti A, Steinfeld A (2014). Stabilization of the outflow temperature of a packed-bed thermal energy storage by combining rocks with phase change materials. *Applied Thermal Engineering* 70: 316–20.
- Zanganeh G, Pedretti A, Haselbacher A, Steinfeld A (2015). Design of packed bed thermal energy storage systems for high-temperature industrial process heat. *Applied Energy* 137: 812–22.
- Zhang G, Li J, Chen Y, Xiang H, Ma B, Xu Z, Ma X (2014). Encapsulation of copper-based phase change materials for high temperature thermal energy storage. *Solar Energy Materials & Solar Cells* 128: 131–37.

---

## #19: Preparation and electrochemical hydrogen storage performance of sulfonated polysulfone (SPSU)

---

Ali SALEHABADI<sup>1</sup>, Mardiana IDAYU AHMAD<sup>2</sup>, Norhashimah MORAD<sup>3</sup>

<sup>1</sup>Environmental Technology Division, School of Industrial Technology, Universiti Sains Malaysia, 11800 Minden, Penang, Malaysia. [alisalehabadi@usm.my](mailto:alisalehabadi@usm.my)

<sup>2</sup>Environmental Technology Division, School of Industrial Technology, Universiti Sains Malaysia, 11800 Minden, Penang, Malaysia. [mardianaidayu@usm.my](mailto:mardianaidayu@usm.my)

<sup>3</sup>Environmental Technology Division, School of Industrial Technology, Universiti Sains Malaysia, 11800 Minden, Penang, Malaysia. [nhashima@usm.my](mailto:nhashima@usm.my)

*Hydrogen storage in solid-state materials is predicted from their tendency to adsorb-desorb hydrogen. The main challenge in the hydrogen storage is to find a new class of materials that can reversibly store hydrogen at high rates under reasonable temperature, pressure and cost conditions. Polymeric materials have recently come to the fore of hydrogen storage technologies because of their high surface area, reversible capacity, and thermo-mechanical stabilities. Here, we report, for the first time, novel hydrogen storage polymer based on sulfonated polysulfone (SPSU) of above 650 mAh/g (~2.3 wt% H) of discharge capacity. Primarily, the SPSU have polymerized from Polysulfone (PSU) in the presence of chlorosulfonic acid (ClSO<sub>3</sub>H). The spectroscopic and elemental analyses confirm the successful sulfonation of PSU. The charge-discharge efficiency of this system exhibits stable sequences with around 97% efficiency, comparable with many benchmark commercial batteries. The results clearly emphasise that the SPSU can be individually assigned as a potential host for hydrogen sorption. Our work will promote the development of low-cost solid-state conductive polymer, as a host for hydrogen sorption.*

*Keywords: hydrogen; energy storage; polymer; discharge capacity; efficiency*

## 1. INTRODUCTION

Decarbonising the power sector, particularly in the developing world, is the most important challenge facing the global energy system over the next 20 years (Zhang, 2017). The environmental concerns and the resource constraints have forced governments to investigate the production of energy from renewable sources. The futuristic technology for energy production and storage are urgently required due to the diminishing stocks of oil and environmental concerns (Sgouridis et al., 2019). Energy conversion is the key input for any proper consideration in energy production and consumption. Hydrogen is a most abundant elements on earth. It is known as a renewable energy carrier with high energy efficiency, and recognised as a clean and safe secondary energy source (Comello and Reichelstein, 2019). The main challenge in this area is the storage of hydrogen at high volumetric and gravimetric density in a small area. Hydrogen molecule has a few electrons; therefore, the intermolecular forces between H-H molecules are weak. It is known that at around 1 atm pressure, the gas condenses to a liquid. Applying an electric discharge through H<sub>2</sub> gas at low pressure result in molecular dissociation, ionisation, recombination, and formation of plasma-add-on (Kato and Nishide, 2018)

Various solid-state materials have been investigated as a host for hydrogen sorption such as hydrides (Millet, 2014; Mohtadi and Orimo, 2017) carbon materials (Pyle et al., 2016; Salehabadi et al., 2018a), metal organic frameworks (MOFs) (Ahmed et al., 2019; Salehabadi et al., 2020) mixed metal oxides (MMOs) (Salehabadi et al., 2019, 2018b), alloys (Wang et al., 2016, 2008), and polymers (Kato and Nishide, 2018), however, few of them are accepted by the US department of energy as a promising host for commercial stationary applications. The mechanism of hydrogen storage in the gas phase occurs in five steps: (a) non-dissociative surface physisorption (desorption); (b) surface dissociative chemisorption (recombination); (c) surface absorption (desorption); (d) transport of hydrogen ad-atoms from sub-surface to bulk regions by diffusion; and (e) phase transformation leads to the precipitation (dissolution).

The polymeric materials have recently attracted much interest due to their structural, thermal and mechanical characteristics. Conductive polymeric materials are capable of producing high power densities at low temperatures (Germain et al., 2009; Rochat et al., 2019). Since the polymeric materials have a mechanical feature as compared to other materials in their fields, large surface area, and tendency to absorb water (especially proton conducting polymers), these materials can be a source for future hydrogen storage systems (Kato et al., 2016). Cross-linked organic polymers and hyper-cross-linked organic polymers are also developed for hydrogen storage systems. The highest specific surface area is reported for hyper-cross-linked polystyrene. In addition, the polymers with intrinsic microporosity (PIMs) have been also devoted for hydrogen storage polymers, in which the pores are formed due to the inefficient packing of rigid polymer subunits (McKeown et al., 2006; Oberoi et al., 2018).

Currently, sulfonated polymers are the most widely used electrolytes in fuel cell technologies due to their high proton conductivity, mechanical properties, chemical and electrochemical stability. However, some deficiencies have prevented their wide range applications such as high cost, low stability at high temperatures, and low conductivity at low humidity. Therefore, alternative studies have been focused on polymerization of new sulfonated polymers like sulfonated polysulfone (SPSU) (Bose et al., 2011).

Polysulfone (PSU) has been achieved an increasing attraction due to its superior thermomechanical stability, moderate cost and commercial availability. In addition, it exhibits resistance towards hydrolysis and oxidation, owing to their structural diphenylene (Casado et al., 2016). Electrochemical study of PSU exhibited an exceeding electrochemical stability profile as compared to other conductive polymers. The sulfonated analog of PSU i.e. sulfonated polysulfone (SPSU) have been polymerized and studied for fuel cell applications (Kim et al., 2016). SPSU can be polymerized either by introducing sulfonic acid groups or the polycondensation of sulfonated monomers. The latter provides a multi-block ionomers, while the former gives low cost randomly sulfonated polymer with high performance (Li et al., 2016).

Up to date, electrochemical hydrogen storage performances of PSU and SPSU have not been considered *via* physisorption. In general, the sulfonated polymers have sufficient conformational flexibility to fill space efficiently. The SPSU with different degree of sulfonation (DS) can be prepared by controlling the molar ratio of the sulfonated agent and polysulfone (PSF), where the ion selectivity and water uptake of the SPSU are highly dependent on DS. For instant, in a typical proton exchange SPSU membrane fuel cell with DS of 62, an ion selectivity of  $4.6 \times 10^3 \text{ S min cm}^{-3}$  is reported that is higher than that of Nafion with DS of 117 ( $4.0 \times 10^3 \text{ S min cm}^{-3}$ ) (Zhang et al., 2019). In addition, the SPSU demonstrates excellent durability in consecutive charging-discharging cycles. The determination of hydrogen storage for SPSU can be measured *via* adsorption measurements or estimation from permeability measurements. Basically, because sulfonation occurs through an electrophilic substitution reaction, therefore, it can be proposed that the electron-rich positions of the aromatic rings will be occupied.

The current study provides the first unique application of sulfonated polysulfone (SPSU), as a main criteria, for physisorbed hydrogen storage. To match the global feature of this polymer, SPSU was polymerized by introducing chlorosulfonic acid to pristine polymer *i.e.* polysulfone (PSU) in order to prepare a low cost and randomly sulfonated

polymer. As the major novelty of this work, the electrochemical hydrogen storage capacity of the SPSU was measured and compared.

## 2. METHODOLOGY

### 2.1. Materials

In the current research, Polysulfone (PSU - average  $M_n \sim 35,000$ , transparent pellets), Dimethylformamide (DMF -  $M_w$  73.09 g/mol), and chloroform ( $\text{CHCl}_3$  -  $M_w$  119.38 g/mol), chlorosulfonic acid ( $\text{ClSO}_3\text{H}$  -  $M_w$  116.52 g/mol) were purchased from Sigma Aldrich (USA) and used without further purification.

### 2.2. Preparation of SPSU

The sulfonation process was carried out in anhydrous conditions under inert atmosphere following the method described by Unnikrishnan et al (Unnikrishnan et al., 2012). In this method, 3.6 g of PSU was primarily dissolved in 36 ml of chloroform by continuous stirring at  $50^\circ\text{C}$  for 12 hours to obtain a clear and viscose solution. Extra amount of chloroform (18 ml) was added to above solution and stirred for 2 hours (Container 1). A solution containing 1.1 ml of chlorosulfonic acid was dissolved in 15 ml of chloroform (container 2) and added slowly into container 1 admixture. The colour of the solution changed to opaque-light-brown, while solidifying over time. The polymerization was terminated after 5-hour of continuous stirring, by addition of water. The precipitated polymer was washed several times with distilled water and dried in a vacuum oven for 24 hours. The reaction mechanism can be proposed as Figure 1.

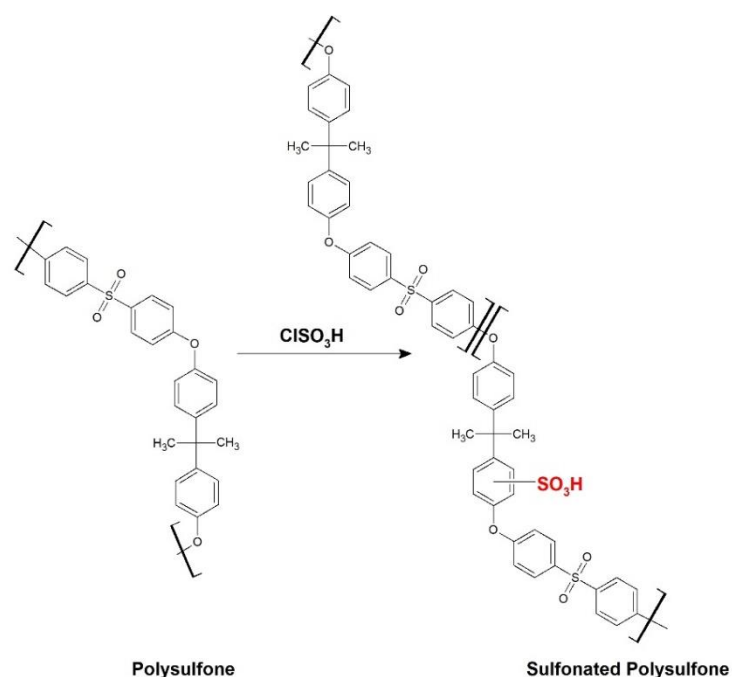


Figure 1: Mechanism of PSU sulfonation.

### 2.3. Characterisation

Hydrogen Nuclear Magnetic Resonance (H-NMR – BRUKER, FT 300 MHz) spectrometer was used in order to confirm the complete sulfonation of the PSU. The samples were dissolved in deuterated dimethyl sulfoxide (D<sub>6</sub>-DMSO). An Energy Dispersive X-ray Spectroscopy, EDX Hitachi S-4300, was used for elemental analysis. Field Emission Scanning Electron Microscopy (FESEM) of the SPSU was carried out using TESCAN-Brno-Czech Republic, 30VP operated at an acceleration voltage of 10 kV. The samples were coated with gold prior to this analysis. The thermal profile of the samples was recorded using a thermogravimetric analyser (TG-DTA Mettler TG-50 analyser) under a nitrogen atmosphere. The samples were heated from ambient temperature to  $900^\circ\text{C}$  at a heating rate of  $20^\circ\text{C}\cdot\text{min}^{-1}$ . The cyclic voltammogram of the SPSU was obtained from the potential applied between a glassy carbon electrode (GCE) (working) and the reference electrode (Ag/AgCl), and the current was measured between the working electrode and the counter electrode (Pt). The CV spectra of the samples were obtained from a probe solution of  $\text{K}_3(\text{Fe}(\text{CN})_6)/\text{K}_4(\text{Fe}(\text{CN})_6)$  in the 0.1 M phosphate buffer solution (pH 7.0), applying a scan rate



of 0.1 V.s<sup>-1</sup>. On the other hand, the electrochemical hydrogen storage performance of SPU and SPSU nanoparticles were measured in a three-electrode setup at room temperature in 6 M KOH electrolyte. The potential of the working electrode (polymers coated on copper foam) was measured with respect to Ag/AgCl reference electrode and Pt counter electrode.

### 3. RESULTS AND DISCUSSION

#### 3.1. Structural analysis

As mentioned before, the PSU was sulfonated via direct sulfonation reaction in the presence of ClSO<sub>3</sub>H. In order to determine the sulfonation profiles of the PSU, <sup>1</sup>HNMR spectrum of the PSU were recorded before and after sulfonation reaction. The samples were primarily dissolved in DMSO-D<sub>6</sub>. Comparison between the proton resonance frequency shifts of the PSU {6.935, 6.956, 7.000, 7.021 (q, 4H), 7.171, 7.239 (d, 2H), 7.866, 7.845 (d, 2H)} and SPSU {6.925 (s, 1H), 7.046 (s, 2H), 7.261 (d, 2H), 7.700 (s, 1H), 7.817, 7.870 (d, 2H)} clearly show an extra proton resonance at 7.700 ppm which is assigned to the presence of -SO<sub>3</sub>H group. The results can be supported by Martos et al (Martos et al., 2015). They reported that the peak associated with the proton adjacent to the new sulfonic acid groups appears at ~7.7 ppm. The presence of the SO<sub>3</sub>H group results in a significant downfield shift of hydrogen as compared to the PSU.

The surface morphology of the SPU and SPSU films were observed by FESEM (Figure 2). The surface morphology of the PSU is highly packed without any roughness and pores (Figure 2a), while the surface of the SPSU is roughened containing several pores (Figure 2b). The pore size of the SPSU film was determined from its respective FESEM micrographs using DigiMizer software. The surface pore size of the SPSU is in the range of 400 – 550 nm. The surface porosity of the polymers is composed of two types of intermolecular voids; network pores and aggregated pores (Figure 2c). The network pores are small interstitial spaces in cross-linked sites, while the aggregated pores are interspaces between the clusters of networks (Cahill et al., 2008). The pores can play an additional role on the hydrogen storage performance of the SPSU.

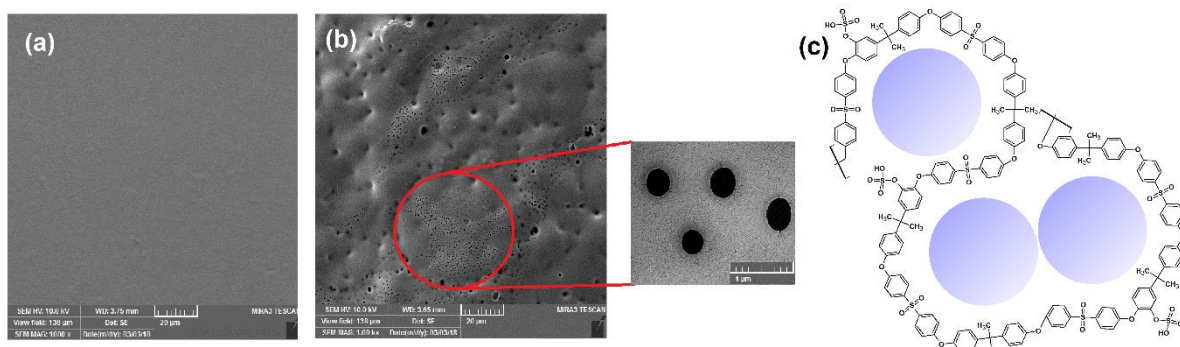


Figure 2: FESEM micrographs of (a) PSU and (b) SPSU; (c) schematic representation of pores in SPSU.

The elemental analysis (EDX) was also affirmed the successful sulfonation of the PSU. The EDX spectrum of SPSU confirms the presence of only carbon (C – 62.26 wt%), oxygen (O – 28.73 wt%), and sulfur (S – 9.02 wt%) in its respective elemental profile. This experimental observation can be supported by literature (Martos et al., 2015). In the PSU, the monomeric unit and SO<sub>3</sub>H have the molecular weights of 442 g/mol, and 80 g/mol, respectively. Therefore, the degree of sulfonation can be calculated using Equation 1;

$$\text{Equation 1: } DS = \frac{\left(\frac{\%S}{100} \times M_m\right) - M_s}{M_s - \left(\frac{\%S}{100} \times M_{SO_3H}\right)}$$

Where:

- DS is degree of sulfonation
- S is elemental weight percentage (wt%) obtained from EDX
- M<sub>m</sub>, M<sub>s</sub>, and M<sub>SO<sub>3</sub>H</sub> represent the molecular weight of the monomer, sulfur
- SO<sub>3</sub>H (g/mol).

The DS of the sample was calculated to be around 0.31.

The thermal stability of the SPSU was studied by TG-DTA (Figures 3a-b). TG-DTA curve of SPSU exhibited a three-step degradation pattern; a weight loss in the range of 50°C to 150°C corresponds to the loss of absorbed water, a weight loss between 250°C and 400°C due to the desulfonation process (evolution of SO<sub>2</sub> and SO gases), and a weight loss above 450°C is related to main chain polymer decomposition. Similar results are reported by Zhang et al (Zhang et al., 2019) on a study of SPSU proton exchange membrane for vanadium redox flow battery. They also reported that the PSU possessed a high thermal stability and no weight loss appears before 500°C.

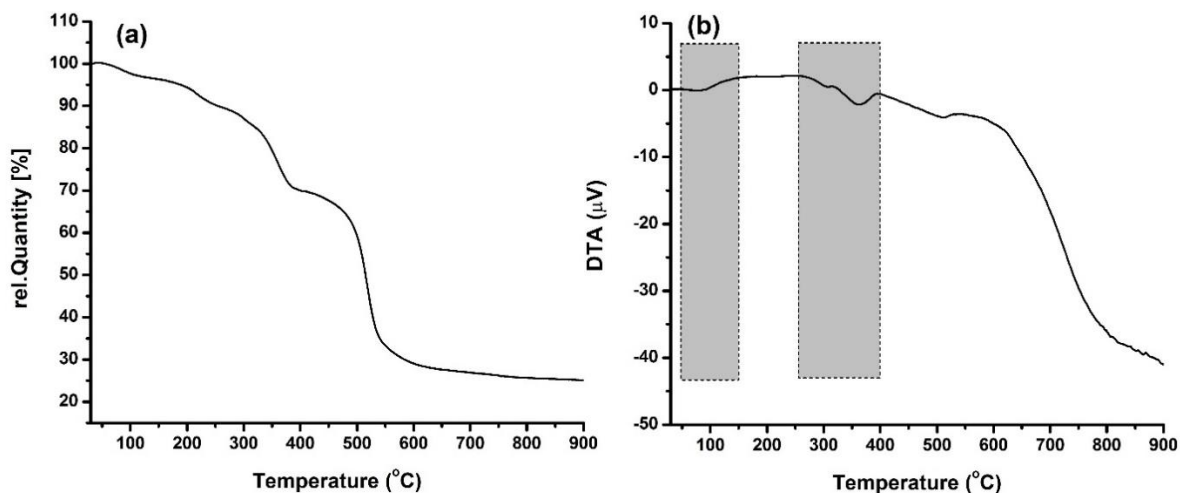


Figure 3: TG-DTA thermograms of SPSU.

### 3.2. Electrochemical properties and hydrogen storage performance

The electrochemical properties of SPSU was traced in a cyclic voltammetry (CV) and its respective charge-discharge curves. Sulfonated polysulfone (SPSU) was coated on a glassy carbon electrode (GCE) and dried overnight before CV analysis. The anodic peak current ( $I_{pa}$ ) of GCE grows at around 45  $\mu$ A, while its respective cathodic peak current ( $I_{pc}$ ) of GCE is at around -46  $\mu$ A. With constant applied scan rate, a wider potential range of the polymer can be observed (-1.6 V / +2.0 V) as compared to GCE (-0.2 V / +0.7 V) (Figure 4a). In the electrochemical response of the SPSU, the redox peaks can be observed which are from electron delocalisation and the growth of a conducting/semi-conductive polymer (Muya et al., 2014). A series of oxidation and reduction currents indicates the capacitive nature of SPSU.

Chronopotentiometry was used in order to evaluate the hydrogen storage capacity of the SPSU. The overall electrochemical reaction process can be ascribed as a reversible phenomenon of charging and discharging processes. The discharge capacity is probably the most important parameter in energy storage systems, which controls the performance of fabricated device. The storage capacity (SC) in a typical charge - discharge sequences can be calculated using Equation 2,

$$\text{Equation 2:} \quad SC = \frac{It_d}{m}$$

Where:

- $I$  is the charge/discharge current (mA),
- $t_d$  is the discharge time (hours)
- $m$  is the mass (g) of the loaded sample

The maximum discharge capacity of the SPSU was obtained to be around 650 mAh/g (2.3% hydrogen content) (Figure 4b). For being competitive, in general, the materials in electrochemical energy storage systems must fulfil the requirements of high discharge capacity, and excellent charge/discharge efficiency (Frackowiak and Béguin, 2001).

The charge/discharge efficiency is defined as the ratio of the energy that can take out of an energy storage system (discharge capacity) divided by the energy put in (charge capacity). Figure 4c displays the maximum charge-discharge curves of the SPSU at room temperature. In the charging curve, two obvious plateaus of potential can be observed indicating at least two different hydrogen adsorption sites (Mulder et al., 2008; Tian et al., 2006). Interestingly, an excellent charge - discharge efficiency of ~97% make SPSU a competitive material for industrial applications.

Up to date, for the storage of hydrogen, the organic polymers have not been widely considered/established as promising materials owing to their structural characteristics, for example, the polymers possess enough conformational and rotational freedom; therefore do not offer high surface areas (McKeown et al., 2006). However, the polymers of intrinsic microporosity (PIMs) are formed by fused-ring subunits, therefore these polymers can provide large amounts of interconnected free volume with large internal surface areas (Ramimoghadam et al., 2016).

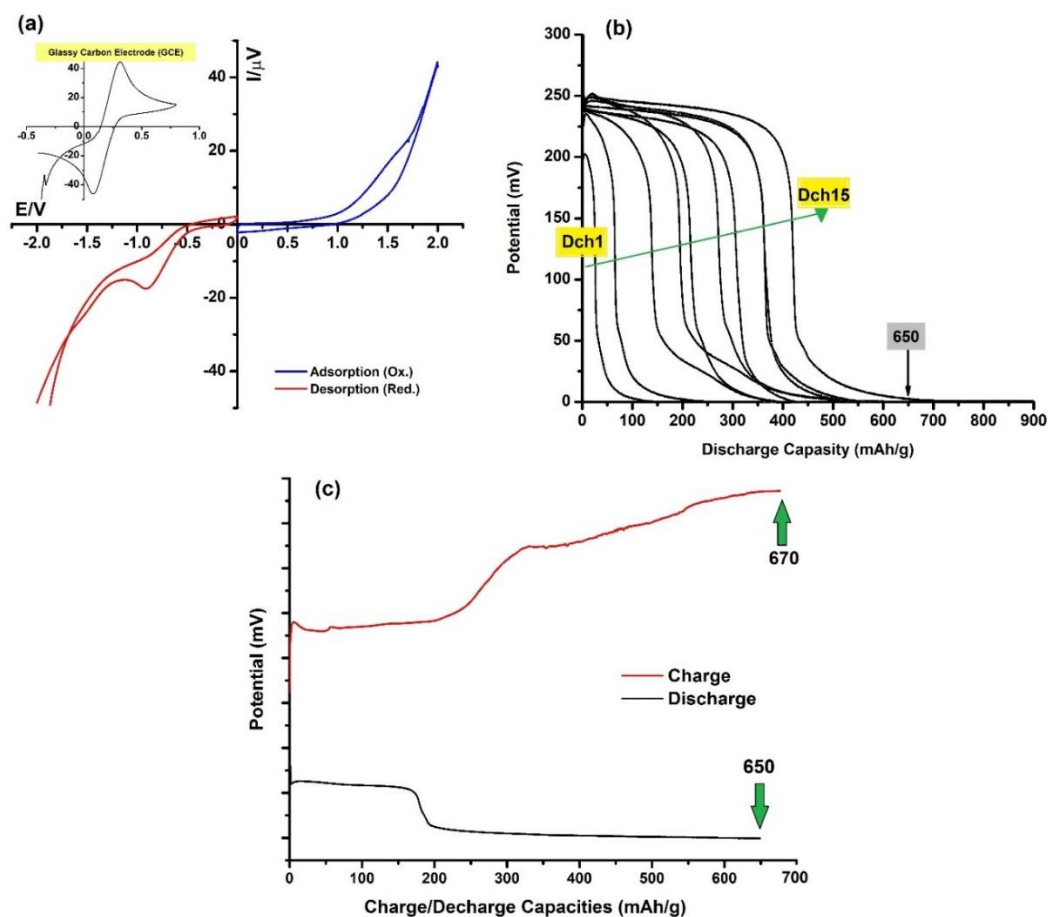


Figure 4: (a) Cyclic voltammogram of SPSU (inset: CV of GCE), (b) Fifteen succeeded discharge capacities of SPSU, and (c) maximum charge – discharge capacities.

#### 4. CONCLUSIONS

Given the anticipated technological advances in exploring novel materials for hydrogen energy storage, the SPSU was successfully polymerized via direct interaction of PSU and  $\text{ClSO}_3\text{H}$ . An extra proton resonance shift at 7.700 ppm - assigned to the presence of  $-\text{SO}_3\text{H}$  group - was affirmed the successfully completed sulfonation of PSU. The HNMR result was supported by elemental analysis, where the degree of sulfonation (DS) was calculated to be around 0.31. The morphological observations were indicating a roughened surface morphology of the SPSU containing pores. The electrochemical features of SPSU confirmed the capacitive nature of SPSU. As the major novelty of this work, the electrochemical hydrogen storage capacity of the SPSU was measured to be around 650 mAh/g (2.3 wt% hydrogen content). It is the first time that a low cost sulfonated polymer is used as host materials for H-sorption. In addition, for being competitive, the SPSU in electrochemical hydrogen storage systems can fulfil the requirements of excellent charge/discharge efficiency (~97%).

#### 5. ACKNOWLEDGEMENT

The authors are grateful to the Universiti Sains Malaysia for supporting this work in the form of postdoctoral fellow.

#### 6. REFERENCES

Ahmed, A., Seth, S., Purewal, J., Wong-Foy, A.G., Veenstra, M., Matzger, A.J., Siegel, D.J., 2019. Exceptional hydrogen storage achieved by screening nearly half a million metal-organic frameworks. *Nat. Commun.* 10, 1568. <https://doi.org/10.1038/s41467-019-09365-w>

- Bose, S., Kuila, T., Nguyen, T.X.H., Kim, N.H., Lau, K., Lee, J.H., 2011. Polymer membranes for high temperature proton exchange membrane fuel cell: Recent advances and challenges. *Prog. Polym. Sci.* 36, 813–843. <https://doi.org/10.1016/j.progpolymsci.2011.01.003>
- Cahill, D.G., Freger, V., Kwak, S.-Y., 2008. Microscopy and Microanalysis of Reverse-Osmosis and Nanofiltration Membranes. *MRS Bull.* 33, 27–32. <https://doi.org/10.1557/mrs2008.11>
- Casado, N., Hernández, G., Sardon, H., Mecerreyes, D., 2016. Progress in Polymer Science Current trends in redox polymers for energy and medicine. *Prog. Polym. Sci.* 52, 107–135. <https://doi.org/10.1016/j.progpolymsci.2015.08.003>
- Comello, S., Reichelstein, S., 2019. The emergence of cost effective battery storage. *Nat. Commun.* 10, 2038. <https://doi.org/10.1038/s41467-019-09988-z>
- Frackowiak, E., Béguin, F., 2001. Carbon materials for the electrochemical storage of energy in capacitors. *Carbon N. Y.* 39, 937–950. [https://doi.org/10.1016/S0008-6223\(00\)00183-4](https://doi.org/10.1016/S0008-6223(00)00183-4)
- Germain, J., Fre, J.M.J., Svec, F., 2009. Nanoporous Polymers for Hydrogen Storage. *Small* 5, 1098–1111. <https://doi.org/10.1002/smll.200801762>
- Kato, R., Nishide, H., 2018. Polymers for carrying and storing hydrogen. *Polym. J.* 50, 77–82. <https://doi.org/10.1038/pj.2017.70>
- Kato, R., Yoshimasa, K., Egashira, T., Oya, T., Oyaizu, K., Nishide, H., 2016. A ketone/alcohol polymer for cycle of electrolytic hydrogen-fixing with water and releasing under mild conditions. *Nat. Commun.* 7, 13032. <https://doi.org/10.1038/ncomms13032>
- Kim, J., Lee, J., You, J., Park, M., Hossain, S. Al, Ho, J., 2016. Materials Horizons Conductive polymers for next-generation energy storage systems : recent progress and new functions. *Mater. Horizons*. <https://doi.org/10.1039/C6MH00165C>
- Li, S., Cui, Z., Zhang, L., He, B., Li, J., 2016. The effect of sulfonated polysulfone on the compatibility and structure of polyethersulfone- based blend membranes. *J. Memb. Sci.* <https://doi.org/10.1016/j.memsci.2016.04.035>
- Martos, A.M., Sanchez, J.Y., Várez, A., Levenfeld, B., 2015. Electrochemical and structural characterization of sulfonated polysulfone. *Polym. Test.* 45, 185–193. <https://doi.org/10.1016/j.polymeresting.2015.06.004>
- McKeown, N.B., Gahnem, B., Msayib, K.J., Budd, P.M., Tattershall, C.E., Mahmood, K., Tan, S., Book, D., Langmi, H.W., Walton, A., 2006. Towards Polymer-Based Hydrogen Storage Materials: Engineering Ultramicroporous Cavities within Polymers of Intrinsic Microporosity. *Angew. Chemie Int. Ed.* 45, 1804–1807. <https://doi.org/10.1002/anie.200504241>
- Millet, P., 2014. Hydrogen storage in hydride-forming materials, in: Iulianelli, A., Basile, A. (Eds.), *Advances in Hydrogen Production, Storage and Distribution*. Woodhead Publishing, UK, pp. 368–409. <https://doi.org/10.1533/9780857097736.3.368>
- Mohtadi, R., Orimo, S., 2017. The renaissance of hydrides as energy materials. *Nat. Rev. Mater.* 2, 16091. <https://doi.org/10.1038/natrevmats.2016.91>
- Mulder, F.M., Dingemans, T.J., Schimmel, H.G., Ramirez-Cuesta, A.J., Kearley, G.J., 2008. Hydrogen adsorption strength and sites in the metal organic framework MOF5: Comparing experiment and model calculations. *Chem. Phys.* 351, 72–76. <https://doi.org/10.1016/j.chemphys.2008.03.034>
- Muya, F.N., Phelane, L., Baker, P.G.L., Iwuoha, E.I., 2014. Synthesis and Characterization of Polysulfone Hydrogels. *J. Surf. Eng. Mater. Adv. Technol.* 4, 227–236. <https://doi.org/10.4236/jsemat.2014.44025>
- Oberoi, A., Nijhawan, P., Singh, P., Oberoi, A.S., Nijhawan, P., Singh, P., 2018. A Novel Electrochemical Hydrogen Storage-Based Proton Battery for Renewable Energy Storage. *Energies* 12, 82. <https://doi.org/10.3390/en12010082>
-

Pyle, D.S., Gray, E.M., Webb, C.J., 2016. Hydrogen storage in carbon nanostructures via spillover. *Int. J. Hydrogen Energy* 41, 19098–19113. <https://doi.org/10.1016/J.IJHYDENE.2016.08.061>

Ramimoghadam, D., Gray, E.M., Webb, C.J., 2016. Review of polymers of intrinsic microporosity for hydrogen storage applications. *Int. J. Hydrogen Energy* 41, 16944–16965. <https://doi.org/10.1016/j.ijhydene.2016.07.134>

Rochat, S., Polak-Krašna, K., Tian, M., Mays, T.J., Bowen, C.R., Burrows, A.D., 2019. Assessment of the long-term stability of the polymer of intrinsic microporosity PIM-1 for hydrogen storage applications. *Int. J. Hydrogen Energy* 44, 332–337. <https://doi.org/10.1016/J.IJHYDENE.2018.02.175>

Salehabadi, A., Ahmad, M.I., Morad, N., Salavati-Niasari, M., Enhessari, M., 2019. Electrochemical hydrogen storage properties of Ce<sub>0.75</sub>Zr<sub>0.25</sub>O<sub>2</sub> nanopowders synthesized by sol-gel method. *J. Alloys Compd.* 790, 884–890. <https://doi.org/10.1016/J.JALLCOM.2019.03.160>

Salehabadi, A., Morad, N., Ahmad, M.I., 2020. A study on electrochemical hydrogen storage performance of  $\beta$ -copper phthalocyanine rectangular nanocuboids. *Renew. Energy* 146, 497–503. <https://doi.org/10.1016/J.RENENE.2019.06.176>

Salehabadi, A., Salavati-Niasari, M., Ghiyasiyan-Arani, M., 2018a. Self-assembly of hydrogen storage materials based multi-walled carbon nanotubes (MWCNTs) and Dy<sub>3</sub>Fe<sub>5</sub>O<sub>12</sub> (DFO) nanoparticles. *J. Alloys Compd.* 745, 789–797. <https://doi.org/10.1016/J.JALLCOM.2018.02.242>

Salehabadi, A., Salavati-Niasari, M., Gholami, T., 2018b. Green and facial combustion synthesis of Sr<sub>3</sub>Al<sub>2</sub>O<sub>6</sub> nanostructures; a potential electrochemical hydrogen storage material. *J. Clean. Prod.* 171, 1–9. <https://doi.org/10.1016/J.JCLEPRO.2017.09.250>

Sgouridis, S., Carbajales-Dale, M., Csala, D., Chiesa, M., Bardi, U., 2019. Comparative net energy analysis of renewable electricity and carbon capture and storage. *Nat. Energy* 4, 456–465. <https://doi.org/10.1038/s41560-019-0365-7>

Tian, Q.-F., Zhang, Y., Sun, L.-X., Xu, F., Tan, Z.-C., Yuan, H.-T., Zhang, T., 2006. Effects of Pd substitution on the electrochemical properties of Mg<sub>0.9-x</sub>Ti<sub>0.1</sub>Pd<sub>x</sub>Ni (x=0.04–0.1) hydrogen storage alloys. *J. Power Sources* 158, 1463–1471. <https://doi.org/10.1016/j.jpowsour.2005.10.068>

Unnikrishnan, L., Madamana, P., Mohanty, S., Nayak, S.K., 2012. Polysulfone/C30B Nanocomposite Membranes for Fuel Cell Applications: Effect of Various Sulfonating Agents. *Polym. Plast. Technol. Eng.* 51, 568–577. <https://doi.org/10.1080/03602559.2012.654580>

Wang, Q., Luo, T., Zhao, Z., Liu, D., Xing, C., Hou, J., Jiang, D., Liu, W., 2016. Effect of ZrH<sub>2</sub> on electrochemical hydrogen storage properties of Ti<sub>1.4</sub>V<sub>0.6</sub>Ni quasicrystal. *J. Alloys Compd.* 665, 57–61. <https://doi.org/10.1016/j.jallcom.2016.01.058>

Wang, Y., Wang, X., Cheng, J.X., Huang, T.S., Murkerjee, S., Kumar, M.P.S., Zhang, W., Srinivasan, S., 2008. Ce<sub>5</sub>Mg<sub>41-x</sub>Ni nanocomposites for electrochemical hydrogen storage. *Dalt. Trans.* 308, 5495. <https://doi.org/10.1039/b801213j>

Zhang, C., 2017. Hydrogen storage: Improving reversibility. *Nat. Energy* 2, 17064. <https://doi.org/10.1038/nenergy.2017.64>

Zhang, Y., Zheng, L., Liu, B., Wang, H., Shi, H., 2019. Sulfonated polysulfone proton exchange membrane influenced by a varied sulfonation degree for vanadium redox flow battery. *J. Memb. Sci.* 584, 173–180. <https://doi.org/10.1016/J.MEMSCI.2019.04.073>

---

---

## #21: Performance analysis of thermochemical energy storage integrated with heat pump for building applications

---

Norhayati MAT WAJID<sup>1</sup>, Abdul Murad ZAINAL ABIDIN<sup>1</sup> Omer SIDDIG<sup>2</sup>, Safa RIFFAT<sup>2</sup>

<sup>1</sup> Energy Efficiency and Renewable Energy Expert Division, Mechanical Engineering Branch, Public Works Department of Malaysia, Menara Kerja Raya, 50480, Kuala Lumpur, Malaysia. [NorhayatiMat.jkr@1govuc.gov.my](mailto:NorhayatiMat.jkr@1govuc.gov.my)  
[abdmurad.jkr@1govuc.gov.my](mailto:abdmurad.jkr@1govuc.gov.my)

<sup>2</sup>Institute of Sustainable Energy, Department of Architecture and Built Environment, University of Nottingham, NG7 2RD, Nottingham, UK. [safa.riffat@nottingham.ac.uk](mailto:safa.riffat@nottingham.ac.uk)  
[siddig.omer@nottingham.ac.uk](mailto:siddig.omer@nottingham.ac.uk)

*The aim of this study is to evaluate the performance during the adsorption and desorption process of a thermochemical energy storage (TES) system integrated with a heat-pump circuit. The chemical reactions of TES produce low-temperature heat, which is then transferred into the room or closed piping system to reduce the room temperature of a building. The low temperature will be used as alternative air-conditioning and will be eliminated or reduce the energy of using the conventional systems that consume high electricity. Furthermore, during the desorption process by using a heat pump, it will be operated during the off-peak hours which the rate of electricity much lower compared to peak hours. In this study, a numerical model was used to determine the regeneration temperature and TES performance. The numerical analysis was carried out using two different cycles; an adsorption cycle and desorption cycle. The operating temperature used in the modelling for charging is 60°C and the discharging is 50°C. In governing the equations on describing the thermal performance of TES, the basic refrigerant circuit of a vapour compression system was used for the adsorption heat pump. From the material synthesising and selection for this study, the material was chosen for this numerical modelling is vermiculite+CaCl<sub>2</sub>. The Engineering Equation Solver (EES) is used for the modelling of regeneration via heat pumps. The modelling was carried using two (2) different type of refrigerant in the heat pump which was the R134a and R1234yf. TES has a higher COP when using R134a compared to R1234yf ranges from 1.44 to 1.98 and 0.33 to 0.48 when the heating temperature is increasing. Other than that, the mass variation change the COP of TES using R134a has higher COP compared to TES using R1234yf ranges from 0.042 to 2.75 and 0.006 to 1.05. However, the desorption time has effect adverse on the COP, the COP of TES of using R134a is lower compared to TES of using R 1234yf ranges from 0.92 to 0.03 and 9.4 to 0.05.*

*Keywords: energy storage; heat pump; performance; building applications*

## 1. INTRODUCTION

The purpose of this paper is to study the theoretical adsorption and desorption process of a thermochemical heat storage system (TES) when integrated with an electric heat clamp, a heat-pump circuit, and using solar energy. A numerical model was used to determine the regeneration temperature and TES performance. The numerical analysis was carried out using two different cycles; an adsorption cycle and a desorption cycle. In governing the equations on describing the thermal performance of THSS, the basic refrigerant circuit of a vapour compression system was used for the adsorption heat pump. This is because the regeneration process is similar to the vapour compression systems which use the R134A (TES-R134a) and R1234yf (TES-R1234yf) as the refrigerant gas. These refrigerant gases were selected based on previous literature aimed towards investigating adoption of low global-warming potential gases for the proposed systems. Furthermore, it has been reported by Zilio, Brown et al. (2011) and Lee and Jung (2012) that R1234yf has four global warming potential (GWP) and zero ozone depletion potential (ODP) compared to the conventional R134a which is 1430 GW (BOC 2019). In this study, both refrigerants were modelled on the desorption process to investigate their effect on the performance of the TES. For the adsorption process, the heat of adsorption is calculated using the adsorption equilibrium which is dependent on the pressure and temperature as in accordance with the Linear Driving Force Method (Aristov, Tokarev et al. 2006, El-Sharkawy, Abdel Meguid et al. 2014). From the material synthesising and selection for this study, the material was chosen for this numerical modelling is vermiculite+CaCl<sub>2</sub>. These composite material was selected due to the high adsorption temperature. At the end of the modelling process, the performance of TES was discussed, and the conclusion was drawn by comparing the three adsorption methods.

## 2. METHODOLOGY

The TES cycle is similar to the basic heat pump cycle in that it consists of two main operational phases, namely adsorption and desorption. The regeneration phase occurs during night hours, when cheap electricity is available under the 'Economy 7' that is more suitable for households with night storage heaters or that use lots of electricity at night. For the electric heating element this model draws on a concept whereby the household use the electric boiler. For the heat pump circuit, the model suggests using a heat pump as the desorption method for the heat storage system for residential. Using solar energy as the heat source may not influence the tariff change. The physical details of the TES-R134a/R1234yf system is illustrated in Figure 1. As the compressor starts to operate, the heat from the refrigerant will desorb the water vapour into the adsorbent pipe and then flow through the evaporator pipe. The latent heat is reversible, and water vapour is stored as a liquid in the adsorbent pipe.

### 2.1. Modelling of transport of heat and adsorbate

The computer modelling for transport of heat and adsorbate is based on the principle of the adsorption heat pipe coupled with the analytical method developed using EES programme. Vermiculite, impregnated with CaCl<sub>2</sub>, was selected to predict the performance of TES. The assumptions on governing the heat balance equation are according to previous modelling (Miyazaki, Akisawa et al. 2009, Zhang, Wang et al. 2011) as listed below:

- i) The temperatures of the adsorbent and adsorbate are assumed to be the same at all times.
- ii) A lump parameter approach is used in the present study to describe the energy and heat balance equations for each element of the adsorption systems.
- iii) The pressure difference between the condenser and the evaporator was neglected.
- iv) The refrigerant adsorbed uniformly in the adsorber and was liquid in the adsorbent.

### 2.2. Adsorption isotherm

The numerical values in calculating this adsorption isotherm is based on the previous model developed by (Miyazaki, Akisawa et al. 2009).

$$q^* = A(T_s) \left[ \frac{P_s(T_w)}{P_s(T_s)} \right]^{B(T_s)} \quad (1)$$

Where

Numerical value for A

$$A(T_s) = A_0 + A_1 T_s + A_2 T_s^2 + A_3 T_s^3 \quad (2)$$

Numerical value for B

$$B(T_s) = B_0 + B_1 T_s + B_2 T_s^2 + B_3 T_s^3 \quad (3)$$

The numerical values of  $A_0 - A_3$  and  $B_0 - B_3$  are provided in Table 1.

Table 1: Value of Parameter used for the adsorption isotherm (Miyazaki, Akisawa et al. 2009)

Parameter	Value
$A_0$	-6.5314
$A_1$	0.072452
$A_2$	$-0.23951 \times 10^{-3}$
$A_3$	$0.25493 \times 10^{-3}$
$B_0$	-15.587
$B_1$	0.15915
$B_2$	$-0.50612 \times 10^{-3}$
$B_3$	$0.5329 \times 10^{-6}$

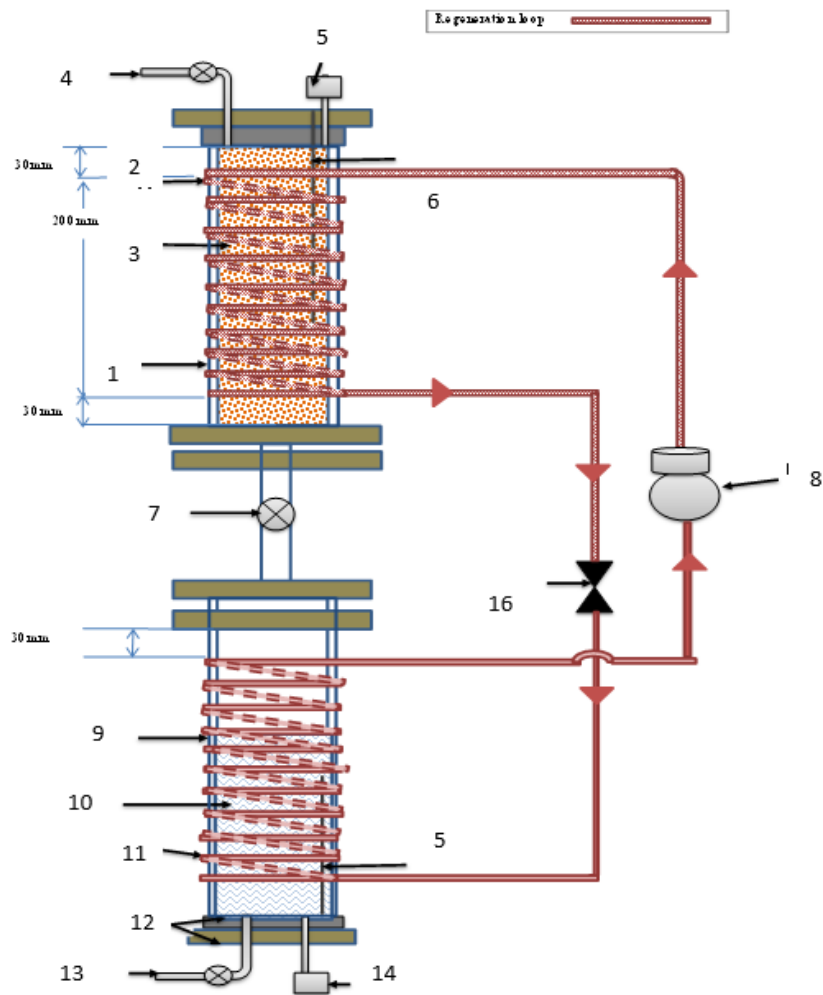


Figure 1: Schematic of TES-R134a/ TES-R1234yf



Table 2: Descriptions of THSS-R134a/1234yf

No	Description	Size
<b>Condenser Section</b>		
	Pipe Type	Cylindrical Borosilicate Glass
1	Condenser Pipe	QVF glass, ID 50mm, maximum pressure 4 barg, maximum temperature :200°C , heat transfer area: 448 cm <sup>2</sup> , thermal conductivity (λ): 1.2 W/m.K), Density (ρ): 2.23 kg/dm <sup>3</sup> , specific heat (cp): 0.8 KJ/kg.K
2	Coil pipe	¼" diameter coil
3	Adsorbent material	50gram Vermiculite +CaCl <sub>2</sub>
4	Valve to vacuum pump	ball valve
5	Pressure sensor	GP pressure transmitter
6	Thermocouple	RTD thermocouple
7	Separation valve	Swagelok ball valve
8	Compressor	miniature DC inverter compressor (ZH2024, Greatcool) displacement of 1.5cm <sup>3</sup> /rev, input power of 220W
<b>Evaporator Section</b>		
	Pipe type	Cylindrical borosilicate Glass
9	Evaporator Pipe	QVF glass, ID 50mm, maximum pressure 4 barg, maximum temperature :200° C , heat transfer area: 448 cm <sup>2</sup> , thermal conductivity (λ): 1.2 W/m.K), Density (ρ): 2.23 kg/dm <sup>3</sup> , specific heat (cp): 0.8 KJ/kg.K
10	Water	100 grams
11	Coil	¼" diameter copper tube coil
12	Flanges	Swagelok flange 50 mm diameter
13	Valve to vacuum pump	Ball valve
14	Pressure sensor	GP pressure transmitter
15	Thermocouple	RTD thermocouple
16	Expansion valve	R134a expansion valve

### 2.3. Adsorption rate

The adsorption rate for the present study is estimated according to (Miyazaki, Akisawa et al. 2009) use of the Linear Driving Force Method (LDF) in equation (4) below.

$$\frac{dq}{dt} = k_s a_v (q^* - q) \quad (4)$$

Where,  $q^*$  is the possible equilibrium amount that adsorbs, for this study its numerical value will be 0.55 based on the experimental results from the vertical adsorbent pipe.  $k_s a_v$  is the overall mass transfer coefficient of the adsorbent or refrigerant pair and can be written as:

$$k_s a_v = \frac{15D_s}{R_p^2} \quad (5)$$

Where,  $R_p$  is the adsorbent particle radius and  $D_s$  is the surface diffusivity and can be expressed by an Arrhenius equation as shown below:

$$D_s = D_{s0} \exp\left(-\frac{E_a}{RT}\right) \quad (6)$$

Where,  $D_{s0}$  is the pre-exponential term,  $E_a$  is the activation energy of surface diffusion. One of the most important conditions for using Equation 6 is that  $D_s$  must be constant (Tien, 1994) The value of  $D_{s0}$  and  $E_a$  were reported as  $2.54 \times 10^{-4}$  m<sup>2</sup>/s and  $4.2 \times 10^4$  J/mol respectively (Sakoda & Suzuki, 1986).

### 2.4. Mass balance of adsorbate

In this study water is used as the adsorbate. Since the quantity of water which exists in the gas phase is negligible in comparison with those in other phases, the mass balance of adsorbate (water) is described as follows (Sakoda and Suzuki 1986)

$$M_s \frac{dq}{dt} + \frac{dM_w}{dt} = 0 \quad (7)$$

Where  $M_s$  is the weight of adsorbent in the adsorbent bed,  $M_w$  is that of water in the evaporator and t is time.

## 2.5. Heat balance in the adsorption cycle

During the adsorption cycle, the movement of heat in the adsorption cycles was considered. Figures 2 & 3 illustrate the vapour transport during the adsorption process. The heat balance of the adsorption pipe and that of adsorbent particles can be expressed as:

$$\frac{d}{dt} (C_s M_s T_s) = Q_{st} \cdot M_s \cdot \frac{dq}{dt} - h_{stp} \cdot A_{stp} \cdot (T_s - T_p) \quad (8)$$

The left part of the model is the heat from the adsorption process through the adsorbent material. The first term from the right provides the heat generated due to the condensation of the desorbed water, while the second term provides the heat rejected to the reactor pipe. The isosteric heat of adsorption  $Q_{st}$ , is thermodynamically derived from the adsorption equilibrium given in Equation 1. Due to the difficulty of the theoretical description of these phenomena and also for the simplification of this model,  $Q_{st}$  was considered constant in this study as 2.8 MJ/kg, which was given in the literature by (Sakoda and Suzuki 1986),

For an adsorbent pipe with heat rejection to ambient, the temperature of the pipe is determined by;

$$\frac{d}{dt} (C_s M_s T_s) = h_{stp} \cdot A_{stp} \cdot (T_s - T_p) - h_a \cdot A_a \cdot (T_p - T_a) \quad (9)$$

Where  $C_s, M_s, T_s$  is the heat capacity, the mass and temperature of the adsorbent material respectively, and  $T_p$  is the temperature of adsorbent pipe,  $h_{stp}, A_{stp}$  are the heat transfer coefficient and area between the adsorbent bed and the adsorbent pipe wall, and  $h_a$  and  $A_a$  are the heat transfer coefficient of the atmosphere and area between the atmosphere and adsorbent pipe wall. For this study, the Euler method is used for solving the numerical integration to determine the temperature of the adsorbent and evaporator pipe according to (Nellis and Sanford 1990).

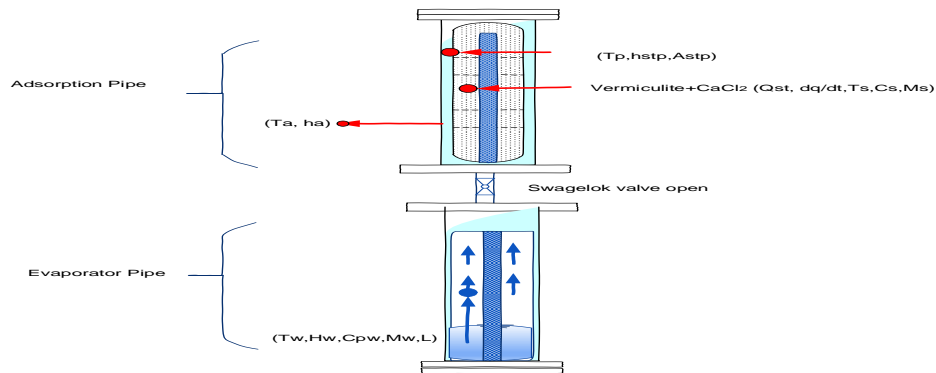
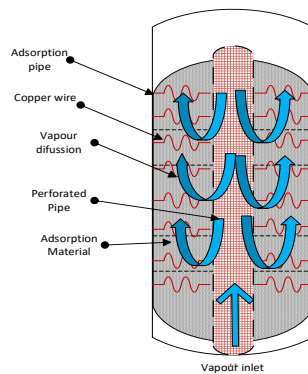


Figure 2: Heat transport of TES during adsorption.



The average temperature of water in the evaporator pipe can be determined by:

$$\frac{d}{dt}(C_w M_w T_w) = h_w \cdot A_w \cdot (T_w - T_a) - L \cdot M_s \cdot \frac{dq}{dt} \quad (10)$$

Right hand side of the equation denote the heat from the evaporator and the left hand side denote the heat transfer from water to ambient.  $L$  is the latent heat of evaporation that is assumed to be equal to  $Q_{st}$  (isosteric heat adsorption). It is necessary to calculate the heat transfer in the water tank, and thus  $h_w$  is determined by some experiments as the temperature drop of a typical water tank. The results showed that the effective heat transfer coefficient  $h_w$  is in the range of 400 - 600  $W/m^2K$  (Riffat, Su et al. 2013).

Figure 3: Detail of vapour diffusion in the adsorption pipe.

#### Parameters adopted in the simulation

The parameters used in this model can be divided into three categories (Table 3) which consist of adsorption properties, the design condition, and operation condition respectively. The adsorbent particles in the adsorbent bed were assumed to transfer only through the heat transfer glass wall. Its corresponding heat transfer area  $A_{stp}$  was regarded as the total surface area of the glass pipe and the heat transfer coefficient,  $h_{stp}$ , was estimated by using the following equation as the approximation (Sakoda and Suzuki 1986):

$$h_{stp} = \frac{k_e}{d/2} \quad (11)$$

Where  $d$  is the average distance between the heat transfer copper wire and  $k_e$  is the effective thermal conductivity of the packed bed, which was estimated at 1.35  $W/m^2K$  by (Tanashev, Krainov et al. 2013). The heat transfer coefficient between the ambient air and the container of the adsorbents ( $h_a$ ), is taken as 1.23  $W/m^2K$ , which is often used as a similar empirical value for composite materials (Miyazaki et al., 2009). The parameter for vermiculite +  $CaCl_2$  is difficult to find in the previous literature. Therefore, some assumptions must be used for this modelling. The activation energy ( $E_a$ ) for vermiculite+ $CaCl_2$  was estimated based on experiments of the dehydration of vermiculite studied by R.Sh.Mikhail et al. (1970) with a reading of 3.7kcal/mole (15 kJ/mole). The isosteric heat adsorption ( $Q_{st}$ ) estimation was based on a previous study done by Aristov et al. (2000), with a reading of 39.4kJ/mole.

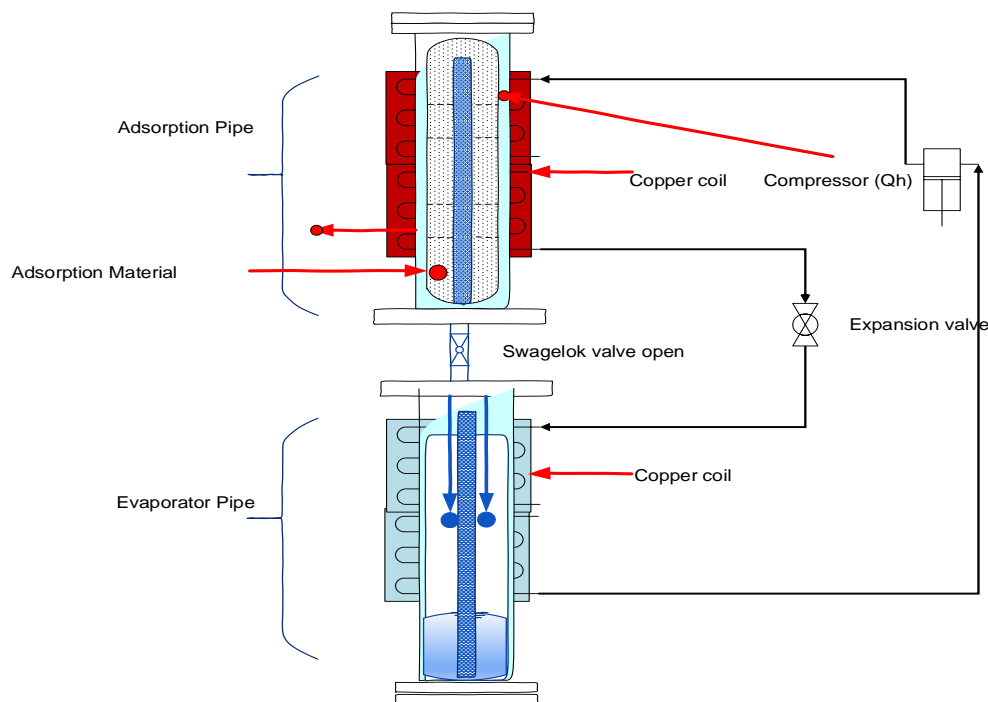


Figure 4: Heat transport of THSS-R134a/R1234yf

Table 3: Simulation physical Data for selected TES material

	Symbols	TES : Vermiculite + CaCl <sub>2</sub> (VCC)	Units	
Adsorption Properties	$q_{\infty}$ (water uptake)	0.55	kg/kg	
	$D_{so}$ (pre-exponential term)	$2.54 \times 10^{-4}$	m <sup>2</sup> /s	
	$E_a$ (activation energy)	$1.5 \times 10^4$	J/mol	
	$Q_{st}$ (isosteric heat of adsorption)	3940	kJ/kg	
	$M_b$ (Mass of adsorbent pipe)	0.75	kg	
	$M_s$ (Mass of adsorbent material)	0.05	kg	
	$M_w$ (Mass of water)	0.1	kg	
	$M_e$ (mass of evaporator pipe)	0.90	kg	
Physical Properties	Length (L)	0.26	m	
	Internal Diameter	0.05	m	
	Outside Diameter	0.055	m	
	Adsorbent bed Cartridge (empty)	0.67	kg	
	Copper pipe	25	Nos turns	
	Fins Spacing	0.01	m	
		$A_{stp}$ (Area of adsorbent cartridge)	0.045	m <sup>2</sup>
		$A_a$ (Area of adsorbent pipe)	0.047	m <sup>2</sup>
		$A_w$ (Area of water cartridge)	0.045	m <sup>2</sup>
		$h_a$ (Heat transfer coefficient between adsorbent pipe and ambient)	1.23	W/m <sup>2</sup> K
		$h_w$ (Heat transfer coefficient in evaporator (water cartridge))	400	W/m <sup>2</sup> K
Operating Conditions	$R_p$ (adsorbent particle radius)	$2.0 \times 10^{-3}$	m	
	$C_p$ (specific heat)	3.06 (Aydin et al., 2015a)	kJ/kgK	
	$T_a$ (ambient temperature)	10	°C	
	$T_{in,ads}$ (initial temperature in adsorbent pipe)	20	°C	
	$T_{in,w}$ (initial temperature in water pipe)	17	°C	
	$T_s$ (adsorbent material temperature)	60	°C	
	$T_{solar}$ (solar collector final temperature)	80	°C	

Movement of heat in the desorption cycle was similarly considered, as shown in Figure 4.

$$\frac{d}{dt}(C_{cp}M_{cp}T_{cp}) = Q_{st}Ms \frac{dq}{dt} - [h_a \cdot A_a \cdot (T_{cp} - T_a)] + Q_H \quad (12)$$

Where RHS denotes the heat in the adsorption pipe, and the first term of LHS is the adsorption heat and heat transfer from the adsorption pipe to ambient.  $Q_H$  is the heat from the heat pump as:

$$Q_H = \dot{m}(h_2 - h_3) \quad (13)$$

This equation is based on the heat pump Carnot cycle, where  $h_2$  is the enthalpy from the refrigerant discharge temperature,  $h_3$  is the enthalpy at the condenser temperature and  $\dot{m}$  is the mass flow rate of refrigerant.

#### The compressor model

The compressor under consideration is a hermetic constant speed compressor, and the mass of refrigerant pumped and circulated by the compressor is given as (Mempouo 2011)

$$\dot{m} = \eta_v \cdot \frac{V_d \eta_v}{v_1} \quad (14)$$

The pumped mass of the refrigerant by the compressor can also be expressed in terms of the rotary speed (N) of the compressor as follows:

$$\dot{m} = \eta_v \cdot \frac{NV_d \eta_v}{60v_1} \quad (15)$$

Where  $V_d$  is the displacement volume rate,  $\eta_v$  the volumetric efficiency of the compressor, and  $v_1$  the specific volume at the inlet of the compressor.

The displacement volume ( $V_d$ ) for a reciprocating-type compressor can be expressed as:

$$V_d = \frac{S_c \pi D_b^2}{4 \times 60} \quad (16)$$

The indicated power for compression can also be calculated in terms of the change of the enthalpy of the refrigerant from the inlet  $h_1$  to outlet  $h_2$  of the compressor as follows:

$$W_{comp} = W_{oi} * \eta_{comp} = \dot{m}_r(h_1 - h_2) \quad (1712)$$

Where  $W_{oi}$  is the total ideal input electric power to the compressor, and  $\eta_{comp}$  is the general efficiency of the compressor.

#### *The expansion valves model*

The throttling process is regarded as the isenthalpic process. The mass flow rate is calculated as follows:

$$\dot{m}_r = k_{ex} \sqrt{2\rho_{in}(p_c - p_{ev})} \quad (18)$$

Where,  $k_{ex}$  is a proportionality constant and is changed as required to maintain the mix of gas and liquid in the evaporator and  $p_c$  and  $p_e$  are the condensing and evaporating pressures (Pa) respectively. The thermostatic expansion valve is modelled as an orifice through which the liquid is expanded from condensing to evaporating pressures. The mass flow rate through it can be correlated according to the Bernoulli equation (Fu, 2014):

$$\dot{m}_r = C_d A \sqrt{2\rho_{in}(p_c - p_{ev})} \quad (19)$$

Where  $\rho_{in}$  is the density of the refrigerant (liquid) at the inlet of the valve ( $\text{kg/m}^3$ ), and  $A$  is the minimum flow area across the orifice.  $C_d$  is the flow coefficient, which depends upon the aperture of the valve. The maximum value is reached when the valve is fully open.  $C_d$  is evaluated through the empirical equation (Fu, 2014):

$$C_d = 0.02 \sqrt{\rho_{in}} + 0.63 v_{out} \quad (20)$$

Where  $v_{out}$  is the specific volume output of refrigerant.

#### *The adsorbent pipe model/condenser coils*

During the regeneration/charging process, the heat from the condenser coils will be transferred to the walls of the adsorbent pipe. The heat in the condenser coils can be determined by the following equation:

$$Q_H = \dot{m}(h_2 - h_3) \quad (21)$$

Where  $\dot{m}$  is the mass flow rate of the refrigerant ( $\text{m}^3/\text{s}$ ),  $h_2$  is the enthalpy heat refrigerant from the discharge pipe of the compressor (kJ/kg), and  $h_3$  is the enthalpy of refrigerant from the outlet of the condenser coils of the system. The enthalpy heat is determined via thermo-physical properties libraries available in the EES software.

#### *The evaporator coils*

The heat from the evaporator coils transferred to the evaporator pipe walls can be determined by:

$$Q_e = \dot{m}(h_1 - h_4) \quad (22)$$

Where  $\dot{m}$  is the mass flow rate of the refrigerant flow in the evaporator ( $\text{m}^3/\text{s}$ ),  $h_1$  is the enthalpy heat from the outlet of the evaporator coils to the compressor (suction) (kJ/kg), and  $h_4$  is the enthalpy heat from the outlet of the expansion valve to the evaporator coils (kJ/kg).

## **2.6. System performance equation**

The system performance of this small prototype was simplified as;

- i. COP of the systems via electrical clamp for desorption

$$COP_1 = \frac{Q_{ads}}{Q_{electric}} \quad (23)$$

- ii. COP of the systems via heat pump circuit for desorption

$$COP_2 = \frac{Q_{ads}}{Q_h} \quad (24)$$

- iii. COP of the heat pump circuit

$$COP_{hp} = \frac{Q_h}{W_c} \quad (25)$$

## 2.7. Numerical result and discussion

### Adsorption process

In this section, the results and discussion are mainly focused on the adsorption process of the TCM materials and their behaviours under the influence of change in saturation pressure ( $P_s$ ) and adsorption uptake ( $dq/dt$ ).

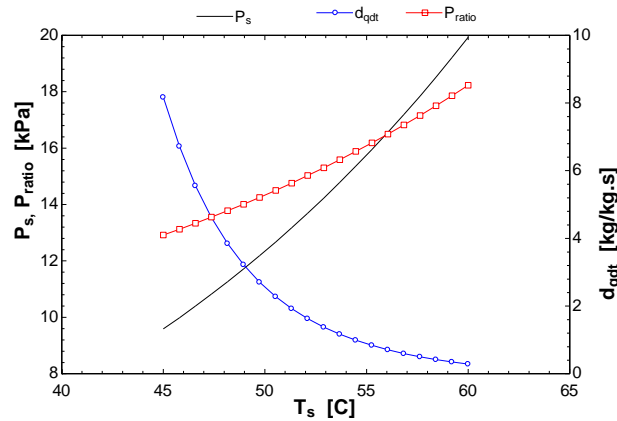


Figure 5: The effect of adsorption temperature vs. adsorption uptake and saturation pressure and pressure ratio.

Figure 5 exhibits the effect of increasing the adsorption material temperature ( $T_s$ ) on saturation pressure and adsorption rate ( $dq/dt$ ). As can be seen from these results, the increase in the adsorption temperature will decrease the adsorption uptake from 8.5kg/kg to 0.28kg/kg. However, the saturation pressure rises from 9kPa to 20kPa. These results suggest that the increase in adsorption temperature will increase the pressure ratio from 9kPa to 20kPa and the adsorption rate will decrease from 8kg/kg to 0.25kg/kg. This is because the reaction will take place during the adsorption cycle when the water vapour is absorbed by the adsorbent material. Therefore, it could be predicted that the adsorbent material temperature will be increased by the increase in adsorption rate during this period.

### Desorption performance of TES using a heat-pump circuit with R134a as refrigerant gas

An analysis has been conducted on the performance of the TES during desorption by using a heat-pump circuit incorporated with the refrigerant gas of R134a. Three possible influential parameters that may affect the TES performance are: the heating temperature effect, the mass of material effect, desorption time effect, have been investigated and discussed below.

#### Heating temperature effect

Figure 6 shows the effect of heating temperature (TH) (R134a) on the adsorption heat and the compressor work. With the assumption of using constant dry mass of TES materials at 50g with 60g of water, the compressor work increases in a positive correlation with the heating temperature. However, the adsorption is expected to be constant throughout the desorption process as no reaction will occur. The heating temperature would also affect the COP system and the COP the heat pump. With the assumption of an ambient temperature ( $T_a$ ) of 10°C, it would be expected that the  $COP_{hp}$  would decrease from 6.15 to 1.33 with the increase in heating temperature rising from 30-60°C, whereas it is expected the  $COP_2$  would rise from 1.44 to 1.98. It can be predicted that as the heating temperature increases, the hydrated composite material will reach semi-equilibrium and lower energy levels will be required to disassociate the water vapour.

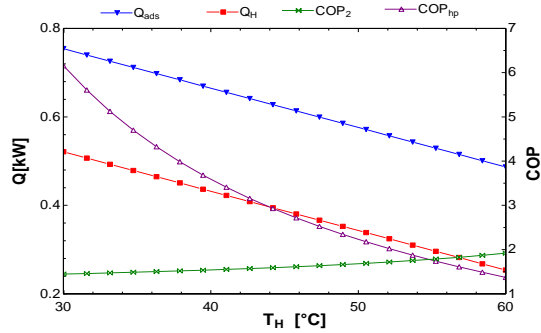


Figure 6: Adsorption heat, condenser heat,  $COP_2$  and  $COP_{HP}$  vs. heating temperature (TES-R134a).

#### Mass of material effect

Figure 7 illustrates the effect of mass adsorbent material effect and predicted that with the assumptions of a heating temperature ( $T_H$ ) of  $60^\circ\text{C}$  and an ambient temperature ( $T_a$ ) of  $10^\circ\text{C}$ , the heat pump heating power ( $Q_H$ ) and the COP of the heat pump will remain constant at  $0.026\text{kW}$  and  $1.41$  respectively. However, the adsorbent heat ( $Q_{ads}$ ) and COP of the systems increased from  $0.27$  to  $17\text{kW}$  and  $0.042$  to  $2.75$  respectively.

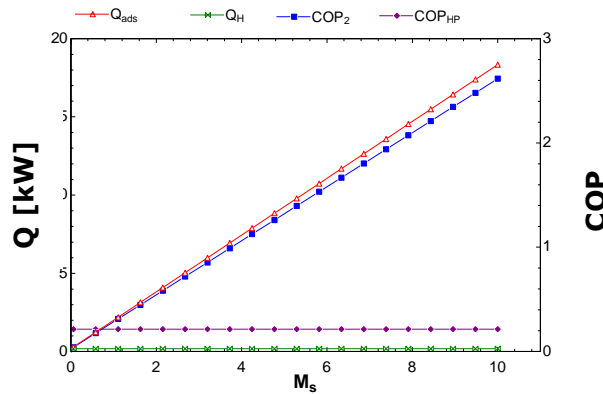


Figure 7: Effect of mass variation to heating power and the COP of the heat pump

#### Desorption time effect

Time dependence during desorption will also have an effect on the  $COP_{HP}$  and  $COP_2$  as shown in Figure 8. With the assumption of the mass of Vermiculite Calcium Chloride at  $0.05\text{kg}$ , the mass of water at  $0.06\text{kg}$ , and with a heat source temperature of  $60^\circ\text{C}$ , the COP of the systems ( $COP_2$ ) and COP of the heat pump ( $COP_{HP}$ ) decreased from  $0.92$  to  $0.03$  and  $1.4$  to  $0.02$  respectively. In this case, the COP of the systems is higher than the COP of the heat pump. Furthermore, the adsorption heat ( $Q_{ads}$ ) decreased from  $0.233\text{kW}$  to  $0.009\text{kW}$ ; as time passed the heat will have been lost to the immediate environment.

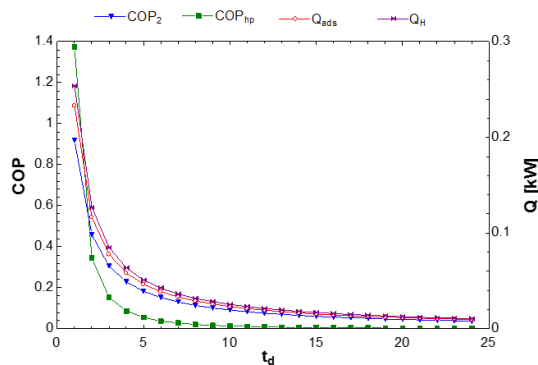


Figure 8: Effect of time on adsorption heat ( $COP_2$ ) and the COP of the heat pump (R134a).

### Desorption Performance of VCC using a Heat-Pump Circuit with R1234yf as the Refrigerant Gas

In this section, an analysis has been conducted on the performance of the TES during desorption using a heat-pump circuit incorporated with the refrigerant gas of R1234yf. Three possibly influential parameters that will affect the TES performance are the heating temperature effect, the mass of material effect and the desorption time effect, all of which have been investigated and discussed below.

#### Heating Temperature Effect

Figure 9 shows the effect of the heating temperature ( $T_H$ ) (R1234yf) on adsorption heat, heat pump heat, the COP of the heat pump ( $COP_{hp}$ ), and the COP of the system ( $COP_2$ ). We can see that the effect of this on the  $COP_{hp}$  is a decrease from 2.66 to 0.93, whereas the  $COP_2$  has increased from 0.32 to 0.48. A higher  $COP_{hp}$  compared to the lower  $COP_2$  is due to the small amount of TES materials using lower heating power than was estimated to be required for the desorption process.

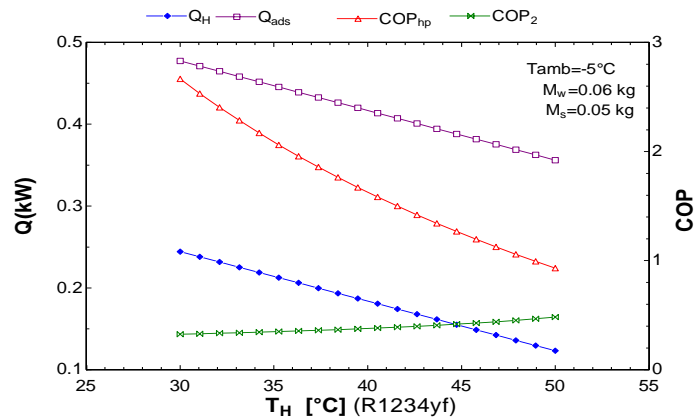


Figure 9: Effect of heating temperature on adsorption heat and compressor work.

#### Mass of Composite Adsorbent Effect

The increase of the TES material mass will increase the adsorption heat due to the increase of potential energy to be extracted from this material. Therefore, as can be seen in Figure 10 with the mass increase, the adsorbent heat ( $Q_{ads}$ ) and the COP of the systems increase between the ranges of 0.28 to 46.6kW and 0.006 to 1.05 respectively. The COP of the heat pump ( $COP_{HP}$ ) and the condenser heat ( $Q_H$ ) remain constant because it is assumed that the heating temperature ( $T_H$ ) and ambient temperature ( $T_a$ ) are constant. However, during desorption, no reaction occurs. Therefore, we can only use this result to compare the effect of a mass increase in the systems quantitatively. However, we predict that if the mass of adsorbent material increases, it will increase the heating power that is required for disassociating the water vapour from the adsorbent material.

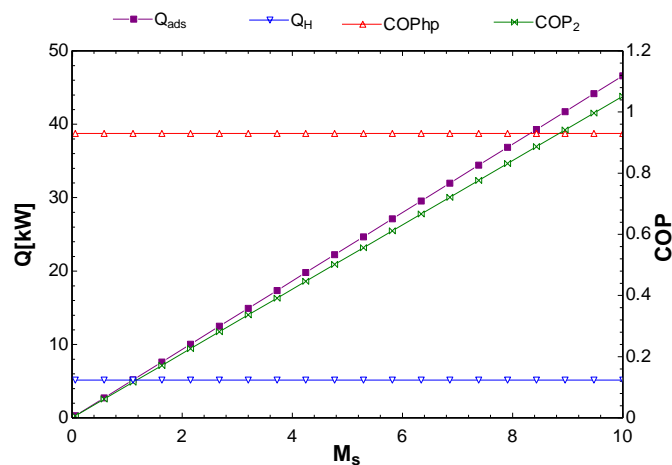


Figure 10: Effect of mass variation on adsorption heat and  $COP_2$ .



### Desorption Time Effect

Time dependence will also have an effect on the  $COP_{hp}$  and  $COP_2$  as shown in Figure 11. With the assumption that the mass of the VCC is 0.05kg and the mass of water is 0.06kg, the COP of the systems ( $COP_2$ ) and the COP of the heat pump ( $COP_{hp}$ ) are decrease from 9.4 to 0.005 and 0.92 to 0.08 respectively. From this result we can see that the COP of the systems is higher than that of the heat pump. The adsorption heat ( $Q_{ads}$ ) and the condenser heat ( $Q_H$ ) have decreased because as time passes the heat is lost to the immediate environment.

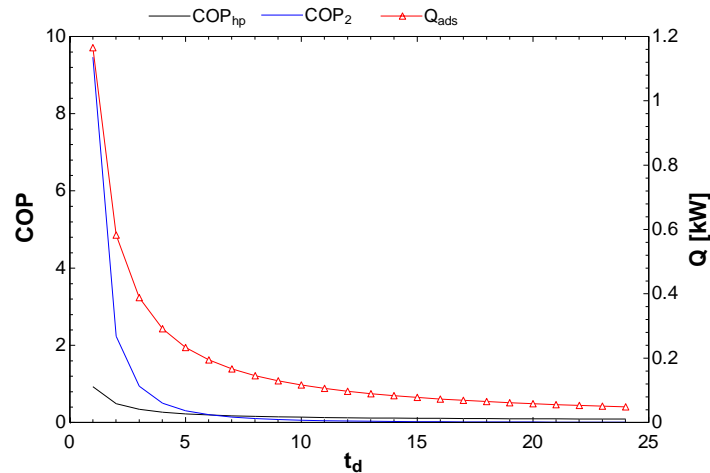


Figure 11: Effect of time on  $COP_2$  and  $COP_{hp}$ .

Table 4: Summary results of all COP from the numerical analysis

Influence Factors	Changing Rate	COP	
		R134a	R1234yf
		$COP_2$	$COP_2$
Heating temperature	30-60°C	1.44 to 1.98	0.33 to 0.48
Mass Variation	2-10kg	0.042 to 2.75	0.006 to 1.05
Desorption time	1-24hr	0.92 to 0.03	9.4 to 0.05

### 3. CONCLUSION

Table 4 summarises the result of COP for all desorption heat source. It can be seen that the increase in heating temperature will increase the COP of the TES system. According to product/power theory, we predicted that the higher power input would have an adverse effect on the COP. Therefore, the decrease in COP when the heating temperature was increased was due to the small amount of mass (0.05kg) applied in the simulation and thus less energy was required for the desorption process. TES has a higher COP when using R134a compared to R1234yf ranges from 1.44 to 1.98 and 0.33 to 0.48 when the heating temperature is increasing. Other than that, the mass variation change the COP of TES using R134a has higher COP compared to TES using R1234yf ranges from 0.042 to 2.75 and 0.006 to 1.05. However, the desorption time has effect adverse on the COP, the COP of TES of using R134a is lower compared to TES of using R 1234yf ranges from 0.92 to 0.03 and 9.4 to 0.05.

### 4. REFERENCES

- Aristov, Y. I., M. M. Tokarev, A. Freni, I. S. Glaznev and G. Restuccia (2006). "Kinetics of water adsorption on silica Fuji Davison RD." *Microporous and Mesoporous Materials* 96(1-3): 65-71.
- BOC. (2019). "Opteon-R1234yf-Brochure410\_124745.pdf." Retrieved 17/6/2019, 2019.
- El-Sharkawy, I. I., H. Abdel Meguid and B. B. Saha (2014). "Potential application of solar powered adsorption cooling systems in the Middle East." *Applied Energy* 126: 235-245.
- Fu, Y. (2014). *Investigation Of Solar Assisted Heat Pump High-rise Residential Buildings.*, University of Nottingham, UK.

Lee, Y. and D. Jung (2012). "A brief performance comparison of R1234yf and R134a in a bench tester for automobile applications." *Applied Thermal Engineering* 35: 240-242.

Mempouo, B. (2011). *Mempouo - 2011 - Investigations of Novel Heat Pump Systems for Low Carbon Homes.pdf*, University of Nottingham, UK.

Miyazaki, T., A. Akisawa, B. B. Saha, I. I. El-Sharkawy and A. Chakraborty (2009). "A new cycle time allocation for enhancing the performance of two-bed adsorption chillers." *International Journal of Refrigeration* 32(5): 846-853.

Nellis, G. and K. Sanford (1990). *Heat Transfer*. United States of America.

Riffat, S., Y. Su and Y. Ding (2013). "Thermochemical cooling system based on adsorption pumping pipe." *International Journal of Low-Carbon Technologies*: ctt055.

Sakoda, A. and M. Suzuki (1986). "Simultaneous Transport of Heat and Adsorbate in Closed Type Adsorption Cooling System Utilizing Solar Heat." *Journal of Solar Energy Engineering* 108(239).

Tanashev, Y. Y., A. V. Krainov and Y. I. Aristov (2013). "Thermal conductivity of composite sorbents "salt in porous matrix" for heat storage and transformation." *Applied Thermal Engineering* 61(2): 401-407.

Tien, C. (1994). *Adsorption Calculations and Modelling*. USA, Butterworth-Heinemann.

Zhang, G., D. C. Wang, J. P. Zhang, Y. P. Han and W. Sun (2011). "Simulation of operating characteristics of the silica gel–water adsorption chiller powered by solar energy." *Solar Energy* 85(7): 1469-1478.

Zilio, C., J. S. Brown, G. Schiochet and A. Cavallini (2011). "The refrigerant R1234yf in air conditioning systems." *Energy* 36(10): 6110-6120.

---

## **#23: Market development of PV Solar Home System (SHS) and PV pumping in Yemen**

---

Ali M. AL-ASHWAL

General Engineering Services, Yemen, amashwal48@gmail.com

*The Saudi-led coalition blockade of Yemen led to a severe scarcity in fuel which led the unavailability of electricity from fossil fuel based sources such as Public Utility and diesel based generators. Therefore, households and other energy consumers looked for all possible ways to get the power supply. Due to the disappearance of fuel, the installation of PV Systems was the best and survival solution. Consequently, rapid diffusion of Photo Voltaic (PV) Solar Home Systems (SHS) took place as well as PV Pumping. As a result of rapid demand increase, the PV SHS market suddenly emerged and experienced very high growth. As a result, most of the traders and even ordinary shops got into the business of selling PV SHS.*

*Before the conflict, PV SHS sales were counted, in best cases, hundreds, now it has jumped up to hundreds of thousands. Thus, a large market for PV SHS was created within a year.*

*This paper examines closely this phenomenon by means of market assessment using a pilot site survey that was performed on households, PV SHS dealers and PV Pumping dealers.*

*Keywords: PV; SHS; renewables*

## 1. INTRODUCTION

Since the start of the war in March 2015, the Saudi Led Coalition has imposed an embargo on many parts of Yemen. All oil products stocks were depleted within 6-8 weeks, resulting in the shutdown of all Public Electricity Corporation (PEC) power stations. Hence Sana'a and many cities and rural areas did not have power from Public Electricity Utility. In addition, the lack of fuel made it difficult to operate private generators. Therefore, households looked for other alternatives for power supply such as Photo Voltaic (PV) Solar Home Systems (SHS). Consequently, rapid diffusion of PV SHS took place, hence the PV SHS market suddenly emerged and experienced a very high growth that most of the traders and even ordinary shops got involved in PV SHS trade. Similarly, PV technology applications were diffused in other sectors like water pumping, shops, clinics, mosques, etc. This subject has been addressed by a number of studies and reports (Badiei, 2018), (Bellini, 2018), (Bodetti, 2019), (Mahmoud, 2017) and (Safia, 2018). Mahmoud (2017) covered well all aspects of the subject. However, the obtained numbers were not properly justified. The other References did not use an analytical approach.

This paper analyses this phenomenon, including market size, future growth and potential of the PV technology industry. The approach used in this work is a pilot site survey that was performed on households, PV SHS dealers and PV Pumping dealers.

The paper starts with a brief discussion of the survey model and survey outcomes. Then direct and estimated calculations are performed. Next Challenges and Value Chain are presented.

## 2. PV SOLAR HOME SYSTEMS (SHS)

A survey was conducted for PV SHS which was based on the following:

- a) A residential quarter located in north-east of Sana'a called Saawan. The quarter contained 190 dwelling units, which is neither a high class nor a poor area, but it is rather a mixture of different levels of living standards. Thus, it is a suitable model for this study.
- b) A sample of 72 traders, PV SHS importers and sellers.

### 2.1. PV SHS dwelling survey

A total of 190 dwelling units represent 190 Households (HH), were the subject of the questionnaire. Out of the 190 HH targeted in the survey, a 149 HH responded to the questionnaire and they confirmed that they used PV SHS. 17 HH confirmed that they have PV SHS, but they didn't want to respond to the questionnaire. 24 HH did not have PV SHS in their houses.

### 2.2. Quantitative outcomes and calculations

The quantitative HH survey results and direct calculations are shown in Table 1. The main takeaway points are summarised below:

- As shown in Figure 1, the majority of PV SHS used 150 Wp panels. The graph has a nearly normal distribution shape.
- The total peak power installed in the HH who responded to the questionnaire was 57.4 kWp.
- From Figure 2 it can be shown that more than 50% of respondents had PV SHS with 300 - 400 Wp. The same could be true for the whole of Yemen.
- The average peak power of PV SHS per HH is 385.235 Wp.
- The diffusion rate is 87.37%, which is considered very high. This includes the HH who have PV SHS but didn't respond to the questionnaire
- The overall average peak power for surveyed houses (190) is 336.574 Wp.
- The total cost for these PV SHS peak power was found in Yemeni Rial; YR38,887,500. This represents an average unit price of YR677.5/ Wp and YR260,990/SHS.
- Due to the significant fall of the value of YR against USD in the second half of 2017 an average of YR300/US\$ over the years 2014 to 2018.
- The unit price of Watt peak for a PV system is US\$2.26/ Wp. and the average unit price for PV SHS is US\$870/SHS.

Table 1: PV SHS dwelling survey results

No	PV Module [Wp]	Panels Quantity	Total Installed [Wp]	No of Surveyed Dwelling Units	
					190
1	50	18	900	HH responded & having SHS	149
2	100	86	8600	HH having PV SHS but not responded	17
3	150	239	35850	HH not having SHS	24
4	200	42	8400	Diffusion Rate	87.37%
5	250	11	2750	Average Wp/HH	385.2349
6	300	3	900	Overall Average Wp/HH	336.574
GRAND TOTAL		399	57400	Total costs PV SHS [YR]	38,887,500

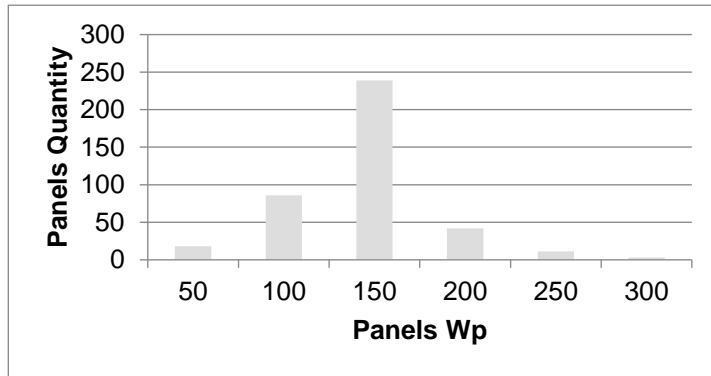


Figure 1: frequency distribution of panel peak power

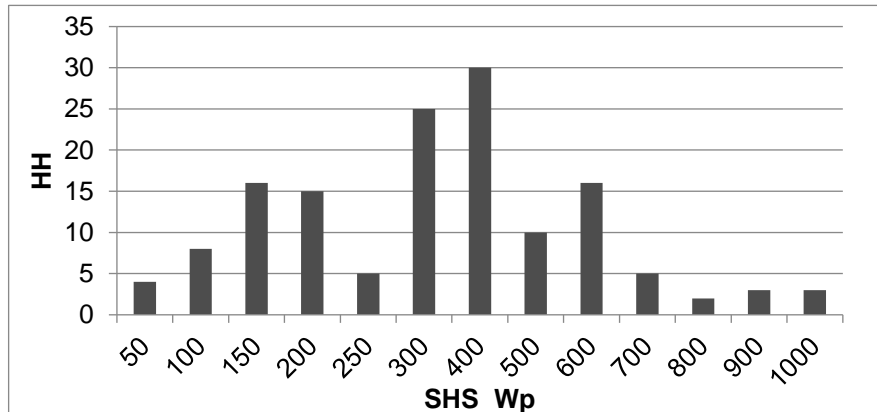


Figure 2: frequency distribution of HH installed power

### 2.3. Estimating installed PV peak power in Yemen

The survey results can be used to estimate the installed PV peak power in Yemen. The following assumptions were used:

- The average dwelling growth rate is calculated from (Central Organization of Statistics, 2009) for years 2004 to 2009.
- HH expenditure on food and non-food goods and services as in (Central Organization of Statistics, 2009) is considered a "financial ability factor".
- Sana'a is assumed to be the "reference" in the estimated calculations for the other areas for the following parameters: Urban Living Factor of Households is referred to "Sana'a City" and Rural Living Factor of Households is referred to "Sana'a rural".
- The diffusion rate of PV SHS for non-embargoed areas is 25% of embargoed ones.
- Peak power of PV systems used by non-HH (shops, clinics, mosques, street light, etc.) is assumed to be 15% of total PV SHS peak power.

In order to perform the required calculations, the following steps were carried out:

- The number of dwellings in 2014 = number of HH in 2009 \* (1+gr)<sup>n</sup> ; where gr is average growth rate; n is number of years; in our case n=5;
- The Financial Ability Factor (FAF), which is the Relative HH expenditure of Urban (FAFu) and Rural (FAFr) areas, with respect to Sana'a City:  

$$FAF = (\text{food and non-food expenditures}) / (\text{Number of Dwelling in 2009} * \text{FAF of Sana'a});$$
- The average PV SHS peak power (AiWp) of different cities and rural areas = (AWp\_of Sana'a)\* FAFu for urban; and (AWp\_of Sana'a)\* FAFr for rural areas;
- The installed peak power of PV SHS for each area = AiWp \* number of dwellings in 2014;
- The total installed peak power of PV SHS in Yemen is the sum of estimated peak power in all Governorates.
- The total number of PV SHS in the country will be the overall average peak power for each governorate\*number HH in that governorate in 2014.
- The total Investment costs of PV systems installed in all governorates for HH and non-HH [Mil.\$] = total installed PV peak power including other users\*unit price of Wp.

An evaluation matrix was constructed to carry out the above calculations. The results are summarised in Table 2.

Table 2: estimated calculation results

Governorates	Urban and Rural Dwellings			Calculated Dwelling		Total Installed MWp
	2009			Urban	Rural	
	Urban	Rural	Total	2014	2014	
Ibb	61,568	294,810	356,377	70,952	339,748	24.40
Abyan	17,809	49,797	67,606	20,524	57,387	17.79
Sana'a City	303,406	5,753	309,159	349,654	6,630	119.92
Al-Baida	15,976	63,448	79,424	18,412	73,120	5.61
Taiz	101,003	346,691	447,694	116,399	399,537	29.01
Al-Jawf	8,204	55,814	64,018	9,454	64,322	1.24
Hajjah	19,701	192,967	212,668	22,704	222,381	8.77
Hodeidah	138,367	282,757	421,125	159,459	325,858	36.39
Hadramout	76,458	86,874	163,332	88,112	100,116	5.99
Dhamar	29,496	197,035	226,531	33,992	227,069	12.70
Shabwah	11,030	49,517	60,546	12,711	57,064	1.77
Sa'adah	14,855	78,072	92,927	17,119	89,973	6.51
Sana'a	4,171	127,865	132,036	4,806	147,355	2.28
Aden	113,092	0	113,092	130,330	0	7.97
Laheg	11,235	119,845	131,079	12,947	138,113	2.03
Mareb	4,541	27,387	31,928	5,233	31,562	0.89
Al-Mahweet	5,337	69,401	74,738	6,150	79,980	2.15
Al-Marah	5,999	8,766	14,765	6,914	10,102	0.84
Amran	21,405	91,795	113,201	24,668	105,788	7.28
Al-Daleh	9,652	60,099	69,751	11,123	69,260	1.64
Reymah	705	56,701	57,406	813	65,344	1.76
Total installed MWp	974,008	2,265,394	3,239,402	1,122,477	2,610,708	291.85
Peak power of PV systems used by non-HH (shops, clinics, mosques, etc.) @ 15% [MWp]						43.78
Total Installed PV peak power including other users @ 15%, but excluding Water Pumping [MWp]						335.63
Total Installed PV peak power including other users @ 15%, including Water Pumping [MWp]						389.75
Total Investment costs of PV systems installed in all governorates for HH and non-HH [Mil.\$]						758.524
Total Investment costs of PV systems installed in the Country including water pumping [Mil.\$]						826.386

These figures show clearly a significant market development for PV technology applications in Yemen. In order to appreciate this development, let us compare the total Installed PV peak power with the total available capacity of electrical power in Yemen. PEC is the sole national Electricity Utility in Yemen. The total available power generation capacity owned by PEC is 960 MW (Public Electricity Corporation, 2014). As seen in Table 2 the total installed PV peak power could reach 335.63 MWp, or 26% of total available generation capacity of the country. This is significantly higher than the average percentage of installed renewable capacity which rarely exceeds 10% in most countries (Solar, 2019).

## 2.4. Questionnaire feedback

As mentioned earlier 149 HH responded to the questionnaire. The questionnaire contains various technical aspects of SHS, such as installation, operation and maintenance. Annexe 1 contains the questionnaire results, as Table 3 summarises HH feedback.

Table 3: Summary of HH Feedback

Question	Feedback	
system installation	By Technicians 93;	By Customer himself 56
Demand satisfaction of SHS capacity	Satisfied: 33;	Unsatisfied: 116
Conducting Maintenance	Doing: 118	Don't: 31
Customer overall Satisfaction	Excellent: 11; V. good: 48; good: 59; satisfactory 19; Unsatisfactory: 9	
SHS Failures leading to a power cut off	Yes: 110	No: 39
Types of Faults	Battery 50%; Panels 30%; controllers and connection 20%.	

It is clear from Table 3 that most of the HH responded positively to PV SHS experience, which took place during the war. However, it should be noted that the failure rate is quite high. However, the majority of HH are satisfied with PV SHS.

## 2.5. Retailers' survey

A total of 72 Retailers of PV SHS systems were surveyed. The questionnaire emphasis was mainly on: company info, PV SHS sales and stock and challenges facing this business. Table 4 contains a summary of PV SHS survey results. Annexe 2 contains detailed survey results. PV SHS sales were not given by the retailers as they consider this data to be commercially sensitive. The top 9 surveyed retailers controlled approximately 50% of the market.

Table 4: retailers survey results

PV SHS Dealers' Survey				
Number of Retailers	Number of Panels in Stock	Peak Power of Panels	Total Peak Power	Largest Market Share [%]
72	81783	50 - 340Wp	17,633,375Wp	11.11; 6.1; 5.2

## 3. PV FOR WATER PUMPING

Groundwater is the main source for domestic usage, drinking and irrigation in Yemen. Due to the lack of fuel during the first year of the conflict, many water authorities and farmers replaced their diesel engine pump systems with PV pumping systems.

### 3.1. Survey and survey outcomes

In order to assess the market development in this area, a survey was performed for PV pumping suppliers. Emphasis was given to the following parameters: company data, location of project, PV peak power [Wp], country of origin and cost. Table 5 summarizes the results of the survey. Unlike the HH SHS market, the largest retailer controls approximately 40% of the market share and the second more than a quarter of the market, indicating that there is less competition in this market sector than in the HH SHS sector.

Table 5: summary of water pumping dealers survey results

Number of Importing Companies	Number of Countries of Origin	Governorates where Pumps Installed	No of Pumps	Peak Power [MWp]	Total Investment [Mil\$]	Largest Market Share [%]
15	15	17	1782	53.746	67,863	39.5; 25.6; 9.7;

It is interesting to notice that the location covers almost all governorates, 17 out of 22. Also, the number of projects and the total peak power given in Table 5 could be greater as there are no official records for PV Pumping traders due to the Country's circumstances. Therefore, it is rational to assume that the capacity is higher by 20%. In other words, the actual total installed peak power for water pumping could reach 65 MWp. From the available price list, the unit price PV pumping system is \$1.262634/Wp. Then the total investment would be \$82M. Annexe 4 contains the results of the survey sorted by market share.

#### 4. CHALLENGES

The instability and war in the country have strongly affected business. Consequently, major difficulties and challenges facing the PV market are created by these circumstances. The following points were taken from dealers' questionnaires, both PV SHS and PV Pumping:

- Continuous devaluation of local currency (YR) against foreign currencies.
- Increased taxes and customs levies; custom charges were doubled in northern and western governorates for goods imported through southern and eastern ports.
- Increased transportation costs.
- Delays at seaports.
- The customers have little knowledge and experience in dealing with the equipment.
- The rapid increase in the inflation rate.
- The restrictions on money transfer outside Yemen by local Banks.
- The price of high-quality PV systems has gone up significantly. The market is full of the low-quality cheap PV system.
- There are no regulations to monitor and control PV system import, hence the competition is not fair.
- There are difficulties in obtaining finance for PV Pumping Projects.
- Imports are almost blocked for years 2017 & 2018.
- Difficulties in opening Letters of Credit.

#### 5. VALUE CHAIN

The value chain structure could look like the one shown in Figure 5.

##### *Manufacturers*

The PV technology industry in Yemen is almost non-existent except for metal frames and PV support structures.

##### *Importers*

In 2015, all ports and airports were closed by the Saudi Led Coalition. Most of the imported goods were delivered to the Country on land by tracks from the Gulf States, mainly the United Arab Emirates (UAE). In that year a rapid increase in demand took place (see Table 6). This situation enabled many businesses to be involved in PV technology.

Table 6 shows the PV systems import trend. Before the war in 2014, the total number of imported PV units from all ports was 24,478 units. Despite the embargo and the closure of the ports due to the war, there was a 10-fold increase in the number of imported units. This dramatic increase took place in order to meet the high increase in demand.

*Table 6: imported PV systems through various ports*

Port of Entry	PV Systems Import (Units)			
	2014	2015	2016	Total
Sea Ports	23,117	143,833	113,797	280,747
Land Ports	1,138	325,386	326,115	652,639
Airports	223	287	00.0	510
Total	24,478	469,506	439,912	933,896

##### *Retailers*

For the same reason, a huge number of retailers became involved in the PV business. Market share, based for SHS, is discussed in Section 3. The largest trader is Assaleh for Trading whose share was 11.11%, which shows healthy competition. The SHS and water pumping trader survey results are summarised in Tables 4 and 5.



## Financing

There is no business model to finance PV projects. However, the financial institutions apply loan conditions that ensure the loans are paid back (Mahmoud, 2017). These conditions are summarized in the following points:

- Private sectors employees should do the following:
  - Sign agreement between the Employer and the financier
  - The Salary of the Employee should be received through the financier
  - Price quotation should be provided
- Civil servants:
  - The loan application must be supported by a guarantor
- Others:
  - They should deposit gold, commercial guarantee or cash as a guarantee.

This procedure reflects the economic and financial crisis created by the war. Consequently, it is not feasible to propose a personal business model, which could replace the above-mentioned procedure, until the war has ended. There are 11 financial institutions engaged in the PV business, see Annexe 3 for more details.

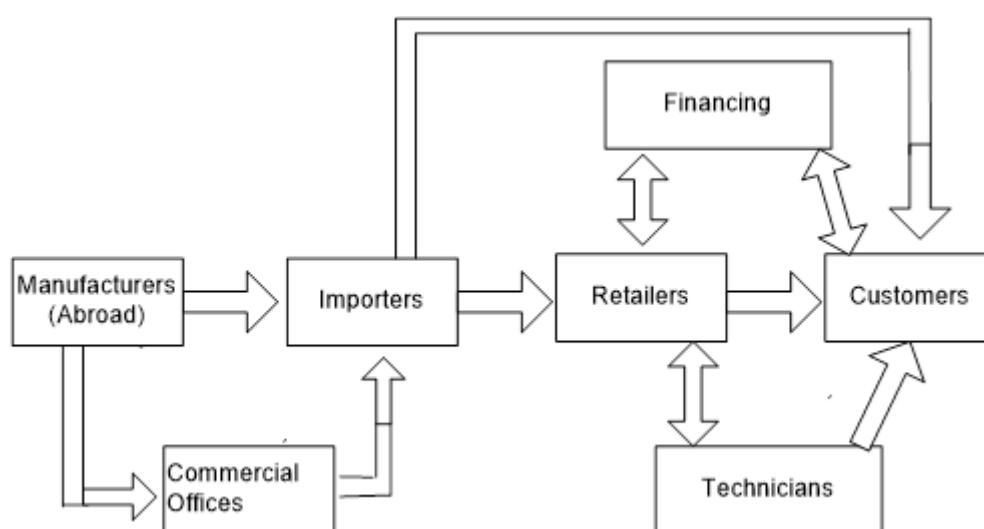


Figure 3: Value chain

## Customers

As mentioned earlier a fast-transitional process of PV market development started in a few months after the conflict. It has resulted in the appearance of a wide spectrum of PV types, technologies, peak powers, manufacturers, countries of origin, prices, etc. in the market. The same phenomenon applies to PV SHS components; like batteries, controllers, inverters, etc.

Furthermore, the rapid increase in demand has led to a mess at the customer end of the Value Chain, for example, high system failure rates, low standard of goods, the big difference of prices, ... etc. This was reflected in the questionnaire results. In addition, 78% of the respondents stated that PV SHS capacity does not satisfy household demand. The failure rates have reached 74%, which is significantly high. On the other hand, 40% of the respondents were highly satisfied.

## 6. CONCLUSIONS

This paper has shown the extraordinary market development of PV technology applications in Yemen. Notwithstanding some of the problems such as the low quality of the PV systems in the market, the quality of the installations is not always up to an acceptable standard and the high prices, people of Yemen have used PV technology to mitigate the effects of the energy crisis.

It has been shown that the contribution of installed PV systems to the overall generation capacity is more than a quarter which is significantly high. It is clear that there is a high potential for further development of PV technology industry in Yemen. Since the diffusion is approximately 90% in Sana'a; it will be economically feasible to apply PV system grid parity when the power sector returns to its normal status.

## 7. REFERENCES

Badiei, S. (2019). A Glimpse of Light in Yemen: Enabling a booming solar industry through entrepreneurship and innovation. [online] World Bank Blogs. Available at: <https://blogs.worldbank.org/arabvoices/glimpse-light-yemen-enabling-booming-solar-industry-through-entrepreneurship-and-innovation> [Accessed 28 May 2019].

Bellini, E. (2018). Yemen sees solar energy grow despite civil war. [online] PV Magazine International. Available at: <https://www.pv-magazine.com/2018/01/24/yemen-sees-solar-energy-grow-amid-civil-war/> [Accessed 28 May 2019].

Bodetti, A. (2019). Solar Power and the Yemeni Civil War. [online] LobeLog. Available at: <https://lobelog.com/solar-power-and-the-yemeni-civil-war/> [Accessed 28 May 2019].

Central Organization of Statistics (2009). Yearly Statistical Book. Sana'a, Yemen: Central Organization of Statistics.

Mahdi, S. (2018). Solar Energy In Yemen: Light Shines Through The Darkness of War | CleanTechnica. [online] CleanTechnica. Available at: <https://cleantechnica.com/2018/09/25/solar-energy-in-yemen-light-shines-through-the-darkness-of-war/> [Accessed 28 May 2019].

Mahmoud, M. et al. 2017. Assessment of the Status of Solar PV in Yemen. The Regional Center for Renewable Energy and Energy Efficiency (RCREEE).

Public Electricity Corporation Annual Report. (2014), Sana'a, Yemen.

Solar. (2019). [online] Available at: <https://www.iea.org/topics/renewables/solar/> [Accessed 2 Jun. 2019].

## 8. ANNEXES

### Annexe 1: HH Questionnaire Outcome

Who did the installation?

By Technicians 93; By Customer himself 56

- Does PV SHS capacity satisfy house demand?  
Yes: 33; No: 116
- Does the customer carry out regular maintenance and checks e.g.:

cleaning	Panel	Controller Monitor		Battery check	
Yes	No	Yes	No	Yes	No
149	0	101	48	104	45

- Over whole Customer Satisfaction

Excellent	11
V. good	48
Good	59
Satisfactory	19
Unsatisfactory	9

- Are there any failures or faults causing PV SHS cut-off?  
Yes: 110; No: 39.
- Type of faults: Battery 50%; Panels 30%; controllers and connection 20%.

## Annexe 2: PV SHS Dealer Survey Results

PV SHS Dealers Survey; Sorted by Greater Market Share				
No	Dealers	Panel Stock	PV [Wp] Stock	Market Share
1	Assaleh for Trading	7000	1960000	11.11%
2	Alwahbani for Trading	4000	1068000	6.06%
3	Alsonaidar for Trading	4000	915000	5.19%
4	Alashwal for Trading	3900	820000	4.65%
5	Yamani & Brothers for Trading	3100	707000	4.01%
6	Aburrijal Corporation	2800	695000	3.94%
7	Computer Engineering World	3700	675000	3.83%
8	Violet flower for PV systems	3100	570000	3.23%
9	Spark Technology	2600	545000	3.09%

## Annexe 3: List of Financial Institutions

1. Small Enterprise Development Fund (SEDF).
2. Yemen Bank for Reconstruction and Development- Islamic Branches.
3. Cooperative and Agricultural Credit Bank-CAC Bank.
4. Tadamon International Islamic Bank.
5. Cooperative and Agricultural Credit Bank- Islamic Branches.
6. International Bank of Yemen.
7. Yemen Commercial Bank.
8. Al-Amal Microfinance Bank.
9. National Microfinance Foundation.
10. Alkuraimi Islamic Microfinance Bank.
11. Azal Islamic Microfinance Program.

#### Annexe 4 PV Pumping Dealers Survey; Sorted by Greater Market Share

No.	Importing Company	Country of Origin	Governorates where Pumps Installed	Pumps	Peak Power	Market Share
				No	[Wp]	
1	Abdullah Ahmed Alsunidar for General Trading	Italia	Al-Hudaydah /Lahj /Amran/Hajjah /Aden /Dhamar	543	21,206,720	39.5%
2	Computer Engineering World	Canada / Italy / Germany / India / Taiwan / China	Al-Hudaydah /Saadah and Different areas	510	13,750,000	25.6%
3	Bin Yassin Trading Est. - Solar energy pumps	Switzerland / India	Al-Hudaydah /Dhamar/Sana'a/Ibb / Lahj	301	5,213,644	9.7%
4	Green Energy Centre	Japan and Denmark	Al-Hudaydah /Sana'a /Dhamer/Hajjah/Ibb/Taiz/Hajjah	57	4,558,600	8.5%
5	Jerusalim for Import	Spain	Al-Hudaydah /Dhamar/Sana'a/Albaidha/ Taiz/Hadramout/Ibb/Mareb/ Rada'a/Hajjah	102	3,809,040	7.1%
6	Alwadi Energy Company	China / India	Hadramout / Valley and Coast	51	1,554,560	2.9%
7	Technical Supplies Center (TSC)	Germany	Al-Hudaydah /Sana'a /Dhamar/Hajjah/Amran /Lahj/Shabwa/Ibb	138	1,235,267	2.3%
8	Ghamdan Trading & Services	China	Al-Hudaydah /Sana'a /Amran/Dhamar/Aldhalea	27	889,790	1.7%
9	Energy Power Int.	China / India	Al-Hudaydah /Lahj	21	623,700	1.2%
10	Systems and Solar Energy Company	China / India	Shabwa, Lahj and Hadramout	14	382,760	0.7%
11	Smart for Technology	Korea/ Malaysia /Germany	Al-Hudaydah /Rada'a /Taiz/Dhamar	6	195,370	0.4%
12	Albasha Power Solution	Italia	Al-Hudaydah /Sana'a /Saadah	6	168,320	0.3%
13	Frist Power	French / Phanzolli / Chinese / United Arab Emirates	Al-Hudaydah /Dhamar	2	82,080	0.2%
14	Ebrahi Ishaq for Trading	Denmark / Italy	Al-Hudaydah /Saadah	2	68,600	0.1%
15	Aidaroods for Solar System	China / India	Abyan.Lahj	2	7,000	0.0%
	Total			1782	53,745,451	

---

## #25: Implementation of renewable energy and photovoltaic (PV) system

### Adopting the Australian ‘Solar Town’ program policies to the UAE local context

---

Sundus SHAREEF<sup>1</sup>, Hasim ALTAN<sup>2</sup>

<sup>1</sup> British University in Dubai, Dubai, UAE, sundusshareef@yahoo.com

<sup>2</sup> University of Sharjah, University City, Sharjah, UAE, hasimaltan@gmail.com

*The environmental policies and the use of renewable energy are at the highest priority of the United Arab Emirates’ (UAE) plans and strategies, and the implementation of clean energy in the country is one of the recent environmental practices that would require more studies and investigation. Conducting this research will offer some valuable analyses and results that could be taking into consideration in the implementation of renewable and solar energy programs further to enacting the environmental legislations and policies to achieve the UAE’s target of reducing CO<sub>2</sub> emissions 70% by 2050. This research aims to explore the capability of implementing the solar panel (PV) system on a large scale by adopting the ‘Solar Town’ program and policies developed by some of the leading countries such as Germany and Australia. Further to this, cost-benefit analysis (CBA) was conducted to find out the benefit and the payback period of implementing this program. By calculating the CBA for each property type within the community, it has been found that the PV energy system could cover an apartment’s electricity consumption with a 1.1 kW surpluses, while it can cover only 60% of a villa’s electricity consumption.*

Keywords: renewable energy; implementing PV; Solar Town; cost-benefit analysis; UAE

## **1. INTRODUCTION**

### **1.1. Background**

Complying with Kyoto Protocol (1997) and the other United Nation agreements on Climate Change, a number of the developed countries founded and began the implementation of the Photovoltaic (PV) panels on large scale (UNFCCC, 1997). One of the successful initiatives is the 'Solar Town' model for producing clean or solar energy on urban scale. The initiative of 'solar town' or 'solar village' was started in Germany in 1997 where the first solar village was established in Bavaria. Wildpoldsried the first solar village producing 321% clean energy more than it needs, and the small agriculture village generating now \$5.7 million from producing the renewable energy every year by selling back to the national grid (Singh, 2015). The village with the population of 2,600 produces a renewable energy using different systems inspired by the village council decided to bring built revenue by building a new industry and over fourteen years, the community equipped nine buildings with solar panels and installed seven windmills (REN21, 2015). Moreover, 190 houses in the village have photovoltaic solar panels on the roof in addition to three small hydro power stations. This industry developed a number of small businesses to service for the installation and the operation of the renewable energy system mentioned. Furthermore, the village council 'Wildpoldsried Innovative Richtungsweisend (WIR)', which means the 'Wildpoldsried Innovative Trend', setting through this initiative, while the council aims to provide and create small businesses to the local surrounding area. The village that is known as 'Klimaschutz' (the Climate Protection) obtained a number of national and international awards for its role in environmental protection, and the village council hosts a tour to explain their experience to the other village's council and visitors.

### **1.2. The Australian 'Solar Town' Program**

The Australian environmental policies and contribution to the climate change mainly was by reducing the GHG emissions, and in line with the concept of clean air, one of the "Cleaner Environment Plan" targets, while the 'Solar Town' (ST) program is one of the large scale renewable energy systems that aimed at producing a large amount of clean energy (Bond, 2011). This is in addition to promoting the sense of ownership and the responsibility against the environment and engaging the locals and communities with the Large Scale Renewable Energy Target (LGRT). The ST program is running in two rounds, the 2014-2015 round and the 2015-2016 round. The Australian government allocated \$2.1 million for the two rounds to support the community's management or organisation to install the renewable energy system on the specific buildings to support the other or the whole community buildings, and to provide clean energy for using solar photovoltaic panels and hot water systems specifically (Australian Government, 2018).

The Australian government has set a clear reference to explain the policies and guidelines, and application procedure for this program; the second round has been improved according to the lessons learned from the first round. The Australian government measures the success of the program by the number of the installed system and the reduction in GHG emissions. They are committed to be fair in distributing funds and studying the case of each community. The funding was provided for only one of the two offered systems: (1) Solar photovoltaic panels or (2) Solar hot water system, and after closing the application for the first round, 20 applications were successful under the first round with funding around \$300k and the government opened the second round application with some revision according to the lessons obtained from the first round. The second round of the solar town program was a revised and an updated version of the first round, and the Australian government provided a detailed guideline to be a reference for the applicants, providing and explaining all the conditions and the forms required to apply for this program (Australian Government, 2018).

### **1.3. The United Arab Emirates (UAE) and environmental actions**

The UAE cities (or Emirates); Abu Dhabi and Dubai have started a serious and rapid steps toward positive contribution to the climate change issues, and as part of Abu Dhabi's vision of 2030 that is already becoming one of the top ten future sustainable cities (DPM, 2019), the capital of the UAE created the local green rating scheme, the Pearl Rating System (PRS) in order to drive the city toward World Sustainable Capital (WSC). It is well known that one of the most important policies for clean environment is the 'Green Building Codes and Regulations'; Green Building Regulations and Rating Systems were developed to eliminate or reduce the negative environmental impact through adopting high environmental standards in design, construction, operations and demolition (GBCA, 2015). This could be achieved by adopting the sustainability attitude in the construction main elements; site selection, energy and water efficiency, operating and management practices, materials and resources management. Furthermore, Dubai rolled out a new building rating system called 'Al Saafat' in 2018, which was developed and issued by Dubai Municipality (DM) as part of Dubai Strategic Plan of 2030 to introduce Dubai as a model of green, healthy city, which follows the highest standards for the sustainable developments (DM, 2019). Since 2012, the implementation of the 'Green Building Regulations and Specifications' of DM became a mandatory requirement for all buildings in the Emirate, and obtaining the 'Green Building Certificate' becomes a condition to obtain the 'Building

Permit' (BP). One of the major requirements in this code is the installation of a renewable energy system - PV panels on the roof of all new projects in Dubai.

The UAE has a great opportunity to benefit from the sun's solar energy according to the location and the weather characteristics of the country. In this study, Dubai was chosen to explore the capability of adopting the 'Solar Town' program. The program goal is to increase the installation and utilisation of the renewable energy on urban scale through developing a partnership involving the different levels of; governmental authorities, local community master developers, local community management, building' owners, householders further to the construction, industry and business sector (MESIA. 2015).

## 2. METHODOLOGY

This research adopted the case study method, interviews, and field observation to obtain the research aim and objectives. The Australian experience in developing the 'Solar Town' initiative was investigated and the policies issued by the Australian Government (Dept. of the Environment and Energy) for this program were further studied to explore the related policies, and how the ST program could be implemented in the UAE / Dubai based case study (Figure 1).

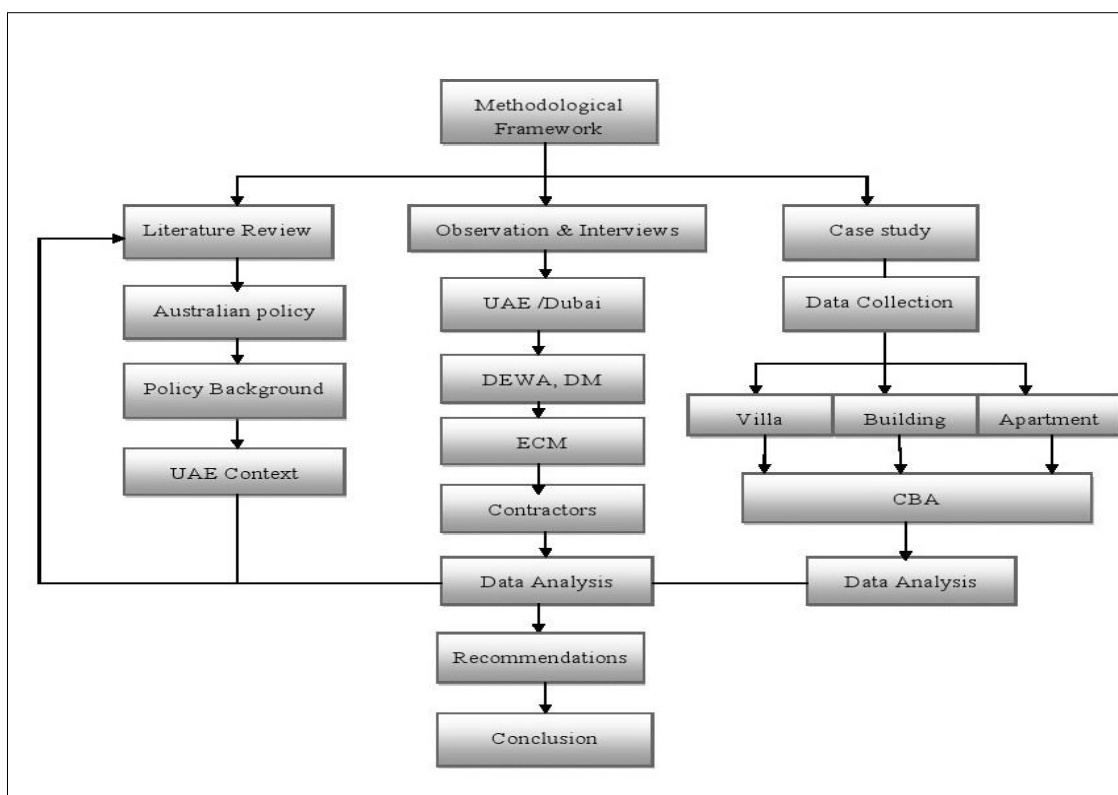


Figure 1: Methodological framework of this research

### 2.1. 'Shams Dubai' Initiative

In December 2014, 'Shams Dubai' (SD) initiative was enacted by H.H. Sheikh Hamdan bin Mohammed bin Rashid Al Maktoum, Crown Prince of Dubai and Chairman of the Dubai Executive Council. SD is one of the smart initiatives that supports the vision of H.H. Sheikh Mohammad bin Rashid Al Maktoum, Vice Minister and Prime Minister of the UAE, the Ruler of Dubai, to lead Dubai into the World Smartest City. The initiative aims to encourage the use of renewable energy by producing the electricity required for the water heater in villas and other type of buildings. The legislation regulations and the guidelines of connecting to the smart grid is operated by Dubai Electricity and Water Authority (DEWA). The initiative encourages householders and building owners to install PV panels to generate their own electricity on site, and the surplus is exported to DEWA's network by connecting these renewable systems to the grid using the smart meter (DEWA, 2018).

During an interview with the manager of solar system program in the headquarters building of DEWA at Al Jadaf, Dubai, the manager stated that the authority issued a list of approved consultants and contractors to work within

this program, and she added that this list is on increase as there is a larger number of consultants and contractors will be evaluated in order to participate in this program. The householder or the building owner should follow a number of steps to get the final approval from the authority to install the Feed-in Tariff solar system. The authority started to proceed with a number of applications, and the program is on development day by day. The program is working according to the feed-in-tariff policy concept, the employee in DEWA Al Quoz, Dubai identified the prices of electricity in the city and the way of calculating the energy produced on site by the consumer. The employee mentioned that DEWA does not pay back for the electricity produced, but rather the amount of the production will be reduced from the consumption amount. In addition to the positive economic and environmental effects of this initiative, it started encouraging new businesses of solar panels sector, selling and maintaining. In the meeting with one of the approved contractors, 'Solar Land Technical Services', the engineer stated that there are some of the projects where the initiative has been installed, and people started to be interested in using renewable energy and solar panels on their roofs to reduce their bills. Hence, this study and the cost-benefit analysis would provide the householders and the building owners a clear perspective of the impact of the use of the renewable energy on the consumption, electricity (i.e. DEWA bill), and the positive environmental impact (DEWA, 2019).

## **2.2. Cost-benefit analysis**

The Cost-Benefit Analysis (CBA) model used to evaluate the feasibility of any investment or project by comparing the total calculated costs with the benefits expected from this investment. It is one of the tools that is used to analyse and assess the feasibility of environmental projects, and it is importance for the decision maker to quantify the advantages (benefits), and the disadvantages (costs) of any project (Alberini, 2010).

The first step of CBA starts with identifications of all costs including Non-Recurring Costs, Operational Costs, Development Costs, and Recurring Costs. The next step is the identification of benefits, which refers to all return or outcome from the alternative system (Martin, 2006). Generally, it is in dollars or local currency, and the benefit covers the following categories; Recurring Benefits, Non-Recurring Benefits, and Non-Quantifiable Benefits. CBA policy varied with type of project or element estimated the main target of this estimation, sometimes, it is a rather complicated procedure because of some items are not traded in markets or some benefits are non-quantified benefits, which needed special valuation techniques (Rolfe, 2011). In this research, the case study apartment is similar to the rest of the building apartments in conditions and average consumption, and therefore the calculation will be conducted on one apartment as an example of the other 24 apartments.

## **2.3. 'Emirates Hills' Community – Dubai-based case study**

To adopt the Australian 'Solar Town' initiative in the UAE, the emirates of Dubai was chosen to explore the capability of implementing this program, and the CBA is conducted to find out the feasibility of implementing this program on an apartment, and at the building's level. The urban planning of Dubai is based on dividing the corridor city into districts, neighbourhoods and communities. Most of these communities are managed by the 'Master Developer' or 'Management Company'. In order to conduct a CBA, a community in Dubai was selected, the neighbourhood is consisting of number of buildings, the consumption of one apartment will be assessed and the feasibility study of installing the solar panels will be evaluated. Furthermore, the CBA of implementing PV panels on the other types of properties in the community will be conducted and analysed. The selected community to examine the opportunity of implementing the ST program is in the 'Emirates Hills' neighbourhood, which is developed by 'Emaar Properties'. The community consists of two types of properties: (1) Villas, and (2) Mid-rise buildings. The mid-rise buildings are G+3 and G+6 stories; a G+3 building is used in this research and explored to assess and evaluate the implementing of photovoltaic panels and connection to the grid, according to the Emaar Community Management (ECM) system where the mid-rise buildings' air conditioning depends on chillers for water cooling, and the total consumption of water heater, lighting and other use are separated from the chillers air conditioning system consumption, as the developer is responsible for the water cooling electricity consumption and the owner is paying annual services to the master developer, 'Emaar Properties'.

A feasibility study is conducted to evaluate and assess the implementation of the renewable energy system, and the calculation of the payback period of installing photovoltaic panels. One apartment from the G+3 mid-rise building is selected, and the results are multiplied by 24 apartments to find system operation of one whole building. The total amount of electricity consumption of each apartment covers; water heating, lighting, air conditioning fan consumption, and other electrical devices used, the consumption excluding the chillers consumption of air conditioning (AC). The site observation showed that the building and roof design could allow to install PV panels, and the installation technique can offer advantages of providing shading to the chillers and increasing cooling unit efficiency.



### 3. DATA COLLECTION AND ANALYSIS

The data of this research collected through the interviews with the people who are officially and directly involved in this program. The interviews cover people from authorities DM and DEWA, community master developer and management such as 'Emaar Community Management (ECM)', contractors and suppliers. During an interview with one of DEWA approved contractors, some of the data required for the CBA was indicated; the engineer mentioned that the average size of the panels used in Dubai is 1.9 - 2.0 m \* 0.9 m. This panel normally produces 250 Watt where the cost of each renewable watt produced is 6.00 Dirham (AED), however according to the SD initiative, calculating the total amount of the energy produced in watts and deducting this value from the consumption value, means DEWA does not offer any price for the energy produced but rather the bill of the producer/consumer is reduced (Dubai Media. 2017).

Figure 2 shows the PV system production compared to the monthly consumption for each property type and as can be seen that the villa consumption is higher than the apartment consumption, as the villa consumption covers the total energy use including the AC consumption, while Figures 3 and 4 show the panel numbers and the initial cost for the two types of the community properties (including the apartment building block); the number of panels and consequently the initial cost for villa is higher than the apartment initial cost. Figure 5 presents a summary of the calculations as results, which are further analysed and discussed in the paper.

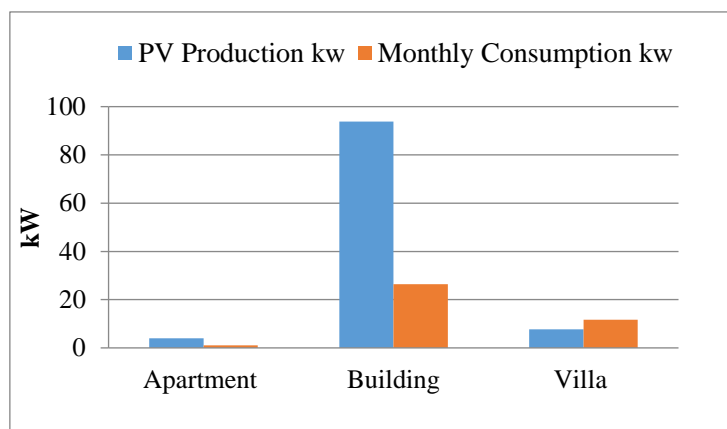


Figure 2: The total PV production compared to the energy consumption for all residential types

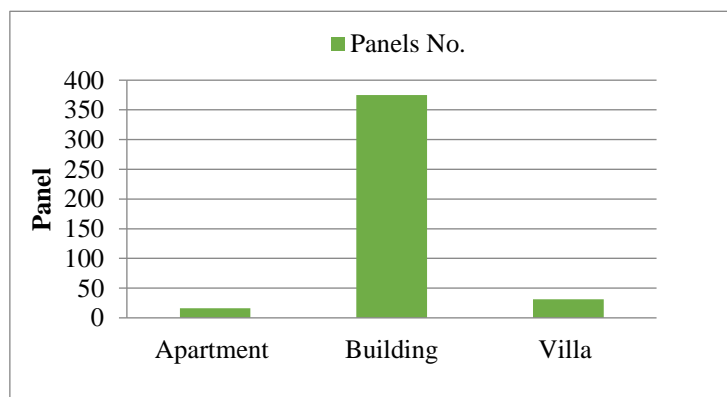


Figure 3: The total number of panels for each property

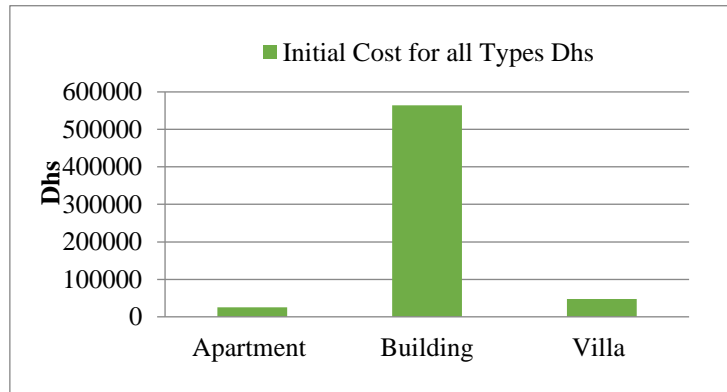


Figure 4: The initial cost for each property system

Property Type	PV Production kw	Monthly Consumption kw	Panels No.	Surplus kw
Apartment	4	1.1	16	2.9
Building	93.75	26.4	375	69.6
Villa	7.75	11.7	31	-3.95

Property Type	Initial Cost of System Dhs	CO2 from Fossil Fuel	CO2 from PV	CO2 Reduction by using PV
Apartment	25500	2400	400	2000
Building	564000	56250	9375	46875
Villa	47500	4650	750	3900

Property Type	Initial Cost of System Dhs	Payback Period years
Apartment	25500	7
Building	564000	6.5
Villa	47500	6.6

Figure 5: Summary of the existing cases calculations

#### 4. RESULTS AND DISCUSSION

The aim of this research was to assess the capability and feasibility of implementing the solar panels on a community scale as a step in adopting the 'Solar Town' model. The cost-benefit analysis of installing solar panels on the selected case study community was evaluated on three levels according to three property types within the community: (1) Apartment, (2) Building, and (3) Villa. The results showed that the maximum production of each apartment is 4.0 kW, which is three times higher than the monthly consumption of 1.1 kW, and the rest of the clean energy produced is 2.9 kW that can be exported to the grid, taking in to consideration that the consumption of an apartment does not include the air conditioning (AC) consumption, according to the regulations of the 'Shams Dubai' program and therefore DEWA will not pay back the surplus of clean energy produced. The authority will transfer these "watts" to the next month consequently. However, the calculation of the case study apartment consumption includes the electricity used for water heating, lighting, (AC fan power) and other electrical devices, and excludes the electricity required for air conditioning (Chillers) as the master developer 'Emaar' is providing this service against a specific yearly service fee calculated by area (sqm). The calculation of the proposed scenario, assuming that the owner has totally independent consumption of DEWA and AC consumption (3.9 kW), shows that installing the PV system will cover the total electricity consumption with a small surplus of 0.1 kW (Figure 6). In this case, the payback period for installing the PV system will be decreased from 7 years to 2 years (Figure 7).

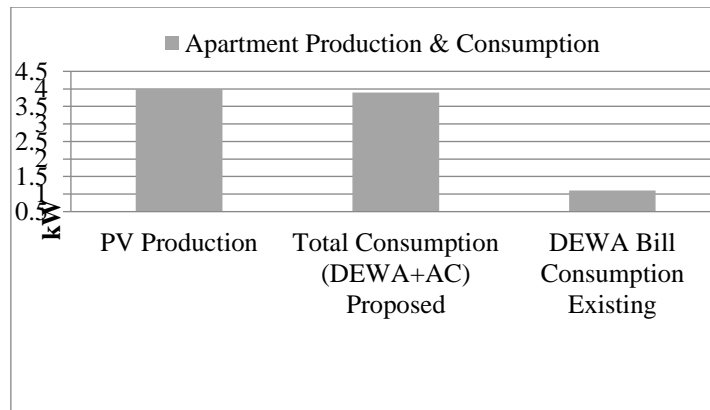


Figure 6: The apartment total electricity consumption and proposed PV production

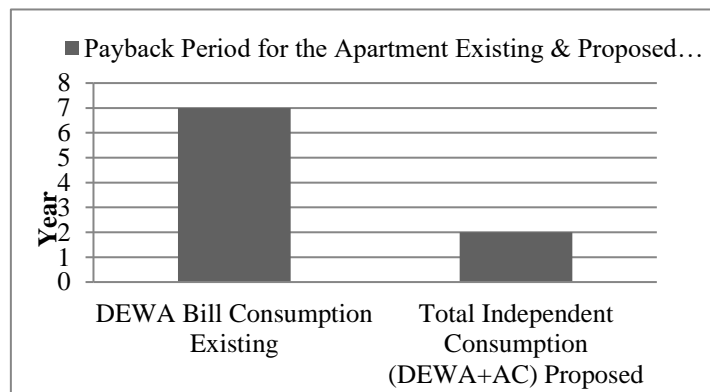


Figure 7: Payback period for the apartment proposed scenario of total electricity consumption

The first proposal of installing PV panels on an apartment by the household (owner or tenant) will not obtain the maximum benefit from installing the system as it will not cover the total payment for electricity use. Furthermore, alteration fee may require from the owner to be paid to the developer as an additional fee. According to the second proposal of conducting a CBA on building scale, the developer takes the full responsibility to install the solar panels on building's roof. As shown by the calculations, the total cost of panels installation is less than the cost required for each apartment separately. This is due to non-separated meter required for each system by DEWA, consequently, the payback period is less for the whole building system installation, and the reduction in consumption will be from the electricity required for air conditioning units (chillers), which is controlled by the developer. Figure 8 shows the clean energy that can be produced by the whole building, i.e. 93.75 kW with respect of the existing energy consumption of each apartment. This energy can cover the total building (24 apartments) monthly DEWA bill, and the variance of 67.35 kW can be used by the master developer to reduce the electricity required for chillers.

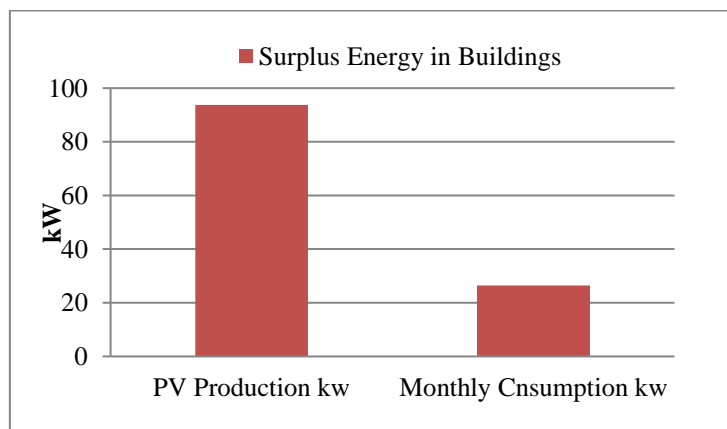


Figure 8: The surplus energy of the building by using PV panels

In the third proposal of installing the panels on villas within the community, the total clean energy production could be directly reduced from the total electricity consumption since the total consumption covers all the electricity consumed by the villa including the air conditioning consumption. Figure 9 shows that the renewable energy produced by a villa can cover 60% of the monthly consumption, and the rest (40%) of the consumption is covered by DEWA electricity. In other words, the onsite energy can reduce the villa electricity bill by 60% if the villa uses the maximum available area on the roof to install the PV system. This result provides an indication that some actions are required to increase the use of renewable energy by the villa owner.

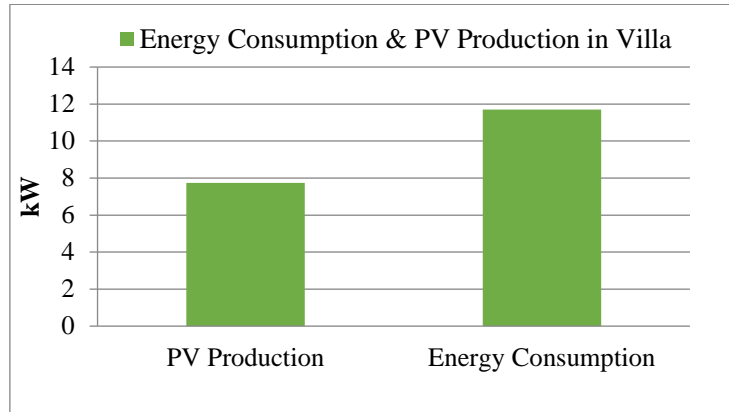


Figure 9: PV production can cover 60% of villa consumption

However, it should be noted the calculations conducted according to the maximum area available on the rooftop to maximize the benefit from solar energy, and it is optional to the developer or the villa owner to use less area and install less number of panels. Figure 10 shows the variation between the energy surpluses in each type.

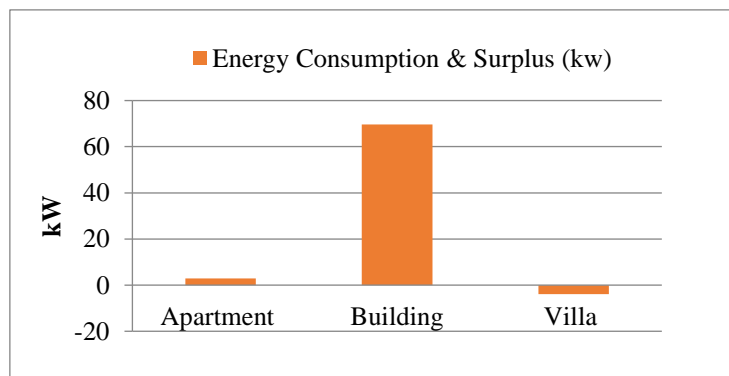


Figure 10: The variation of PV energy surplus between the three property types

Furthermore, there is no major variation in the payback period between the different types of community properties, according to the calculations, and the villa has the less payback period of 6.6 year than the apartment, which is 7 years, taking into consideration that the apartment calculation is according to only DEWA bill consumption (i.e. partial consumption). On the other hand, the total building payback period is 6.5 year, which is less than the individual apartment payback period of 7 years as the initial cost for the building PV system installation is less than the individual apartment system (Figure 11). The variation in the payback period between the apartment, building and villa related to the availability of area in the villa compared to the building and the apartment share of the roof, as the number of panels can be installed in the villa, apartment and building are as follows: 31, 16, and 375 respectively.

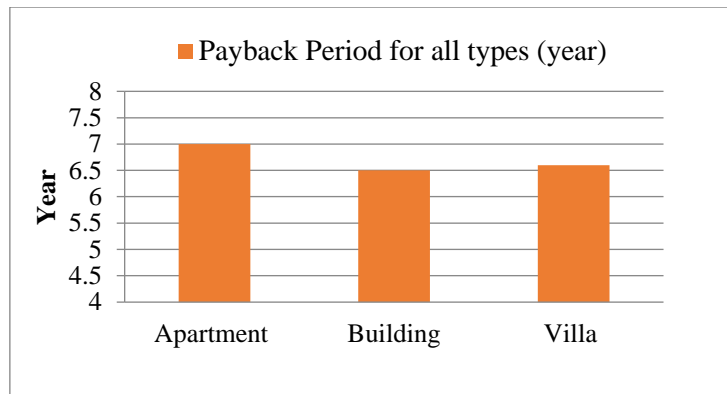


Figure 11: The payback period of the three property types

More than the CBA of installing the PV panels on the community properties, an environmental impact calculation and analysis have been conducted to discover the environmental impact of using the solar panel system. The calculation was conducted according to the reduction in CO<sub>2</sub> emissions that can be obtained by using the calculated number of PV panels for each property comparing the emissions occurred by using the fossil fuel for the same amount of energy produced. The calculation shows that installing the PV panels on the building rooftop to serve the whole building has much more environmental impact than the use for one apartment or one villa scenario, which makes sense as the area of the PV panels will be much more when using the building's roof, and the number of the panels will be installed is much higher than the number of panels will be installed in the apartment or the villa. The reduction in CO<sub>2</sub> emissions for the building, the villa, and the apartment are as follows: 46,875 g, 3,900 g, and 2,000 g respectively (Figure 12).

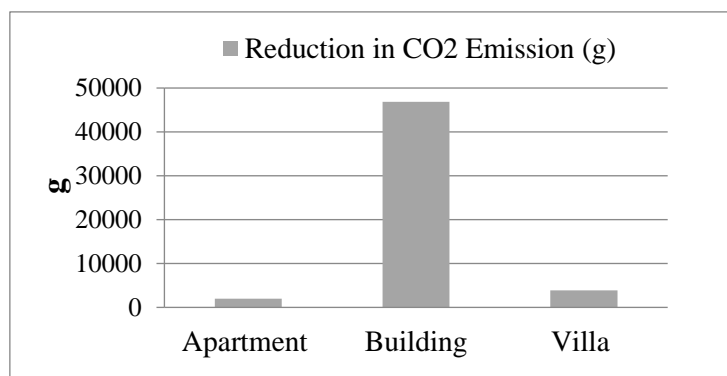


Figure 12: Reduction in CO<sub>2</sub> emissions by using the PV panels for each property type

## 5. CONCLUSIONS

This study evaluated the capability of implementation the Australian program 'Solar Town' within the local context of Dubai, and explored the barriers of implementing the program on urban level. The evaluation of implementing PV panels has been conducted on three levels according to the community property types; (1) apartment, (2) building, and (3) villa. The results showed that installing the system by the apartment will not provide the optimum benefit from the energy produced onsite as the surplus energy, which is about three times higher than the consumption, will be exported to DEWA and calculated for the next month, while the apartment pays a large part of the energy consumption (AC) to the master developer as part of their service fees. According to the economics literature, this represents a type of 'market failure' or 'systematic failure', which requires a governmental intervention to produce or improve the environmental policy to regulate the relation between the stakeholders; master developer, apartment owner and/or tenant, in order to remove the barriers that impedes the large use of renewable energy and solar panels, and to increase the use of clean energy on urban and communities level in Dubai.

Therefore, a scenario was suggested to find the impact of installing the PV panel system in the case study apartment to cover the total consumption (DEWA + AC). The results showed that the PV energy can cover all the consumption of the apartment with small surplus and less payback period of 2 years, but comparing to the villa, the PV solar energy production can cover only 60% of the villa total consumption. This result supports the concept that the high dense areas (such as apartments) are less in energy consumption as they are protected against the solar exposure and solar gain. The obstruction of optimizing the benefits obtained by the apartment owner/tenant

from installing the solar system is indicated as one of the barriers that limited the use of PV panels on large scale. This problem could be overtaken through improving and developing regulations and policies that involve all stakeholders. The urban fabric of Dubai city consists of developed neighbourhoods and communities; this could support the implementation of the program, as the master developer or the community management can implement the program on large scale directly. This is one of the Australian policy conditions for implementing the program and providing funding, as the building should be owned or operated by one owner or organisation. However, the application of this program needs a cooperative effort from the authorities, community developers and individual owners. Furthermore, installing the system by the master developer on all community buildings and other facilities within the community will provide the opportunity to maximize the utilisation of the available area and to generate renewable energy on large scale, further to reducing the installation fees when compared with individual system fees. In this case study, the master developer is responsible for the AC (chillers), and generating the renewable energy on large scale will provide an economic and environmental benefits for the developer, since the developer can use the produced energy to cover the consumption of the chillers, enhancing the community outdoor environment, in addition to the non-quantifiable benefits mentioned before such as enhancing the organisation image.

Moreover, the results showed that installing the system by the villa owners will directly affect the electricity bill as the onsite energy produced will cover 60% of the total monthly consumption and will decrease the depending on the standard electricity. However, all calculations were achieved by calculating the maximum area available for each property and reducing the area provided for PV installation that will consequently reduce the number of panels and the energy produced. The payback period and the reduction in CO<sub>2</sub> emissions were estimated for all property types, and the buildings has the least payback period according to the number of panels that can be installed and the maximum utilisation of the energy produced, while the apartment has the highest payback period as the owner does not obtain the maximum benefit from the energy produced. The CO<sub>2</sub> emission calculations showed that the building offered the highest reduction in CO<sub>2</sub> emissions according to the larger area available for installation and the number of panels that can be installed. Finally, the renewable energy sector in the UAE is a new and promised sector, and further research are required to increase, encourage and develop the use of renewable energy.

## 6. REFERENCES

DPM, 2019. Estidama. Department of Urban Planning and Municipalities, Abu Dhabi. Available at: <https://www.dpm.gov.abudhabi/en/Urban-Planning/Estidama-Program>

Alberini, A. 2010. Cost-benefit Analysis (CBA). Available at: [http://www.ivm.vu.nl/en/Images/CBA1\\_tcm234-161537.pdf](http://www.ivm.vu.nl/en/Images/CBA1_tcm234-161537.pdf)

Australian Government. 2018. Department of the Environment and Energy. Available at: <https://www.environment.gov.au/>

Bond, S. 2011. Barriers and Drivers to Green Buildings in Australia and New Zealand, Property Investment & Finance, (29):4/5, 494-509.

DM. 2019. Dubai Green Building Regulations Practice Guide 2011. Dubai Municipality.

DEWA. 2019. Dubai Electricity and Water Authority. Available at: <https://www.dewa.gov.ae/default.aspx>

DEWA. 2018. Shams Dubai. Dubai Electricity and Water Authority. Available at: <https://new.dewa.gov.ae/en/customer/innovation/smart-initiatives/shams-dubai>

Dubai Media. 2017. Your Guide to Generating Solar Power in Dubai to Slash DEWA Bill. Dubai Emirates 24/7, Available at: <http://www.emirates247.com/news/emirates/your-guide-to-generating-solar-power-in-dubai-to-slash-dewa-bill-2015-03-16-1.584272>

GBCA. 2015. Green Star Rating System. Green Building Council Australia. Available at: <https://www.gbca.org.au/green-star/>

Martin, P. 2006. Dynamic life cycle assessment (LCA) of renewable energy technologies. Renewable Energy, (33), 55-71.

MESIA. 2015. Empowering Solar across the Middle East. Middle East Solar Industry Association. Available at: [www.mesia.com](http://www.mesia.com)

Renewable Energy Network Police for 21st Century (REN21). 2015. Renewable Global Status Report. Available at: <http://new.ren21.net/default.aspx>

Rolfe, J. 2011. Cost benefit analysis – some practical examples. Central Queensland University.

Singh, T. 2015. In habitats, Sustainable Design and Innovation. BBC Magazines, March, (2015). Bristol, UK.

UN. 2005. United Nations General Assembly. The World Summit. Available at: <http://unpan1.un.org/intradoc/groups/public/documents/un/unpan021752.pdf>.

UNFCCC. 1997. United Nations Framework Convention on Climate Change. Available at: [http://unfccc.int/kyoto\\_protocol/items/2830.php](http://unfccc.int/kyoto_protocol/items/2830.php) & [https://en.wikipedia.org/wiki/Kyoto\\_Protocol](https://en.wikipedia.org/wiki/Kyoto_Protocol)

---

## #28: Novel technology of solar assisted domestic hot water (DHW) system with supercooled PCMs

### The characteristics analysis of a selected PCM

---

Yanan ZHANG<sup>1\*</sup>, Cagri KUTLU<sup>1</sup>, Sam GLEDHILL<sup>2</sup>, Adam DICKEN<sup>2</sup>, Zafer URE<sup>2</sup>, Theo ELMER<sup>3</sup>, Andrew CUNNINGHAM<sup>3</sup>, Kitty CUNNINGHAM<sup>3</sup>, Lizhi ZHANG<sup>4</sup>, Guozhong YANG<sup>5</sup>, Huaguan ZHANG<sup>5</sup>, Saffa RIFFAT<sup>1</sup>

<sup>1</sup>Department of Architecture and Built Environment, Faculty of Engineering, University of Nottingham, NG7 2RD  
University Park, Nottingham, UK

<sup>2</sup>Phase Change Materials Products Ltd, Unit 32 Mere View Industrial Estate, Yaxley, Cambridgeshire, UK

<sup>3</sup>Geo Green Power Ltd. Green Barn Costock Road, NG12 5QT, Nottingham, UK

<sup>4</sup>Key Lab of Enhanced Heat Transfer and Energy Conservation, South China University of Technology (SCUT)  
Guangzhou 510640, China

<sup>5</sup>Midea, No. 6 Midea Avenue, Beijiao, Shunde, Foshan City, Guangdong Province, 528311, China

\* Corresponding author: yanan.zhang@nottingham.ac.uk

*In 2018, 28% of energy consumption occurred in domestic building systems. As fuel costs rise, having an efficient and cost effective heating system is one of the main steps to reduce greenhouse gas emissions. Switching to a lower carbon fuel or novel technology to produce hot water offers an alternative way. Phase Change Material (PCM) can be used as heat storage media for a latent heat thermal energy storage system because of its high energy density. In the current application, some PCMs are used as the heat store material with the advantages of self-nucleating properties, high heat of fusion, safe and non-reactive.*

*This paper will indicate a novel domestic hot water (DHW) system. In this technology, various PCM materials have been simulated and tested in DHW systems. PCMs temperature rises when absorb heat. At the time PCMs reach the melting temperature (phase change temperature), they absorb large amounts of heat at an almost constant temperature. Some tests have been done to show the water heating efficiency. According to the water temperature changing record, the highest water temperature was 42.8 °C in the test; and also, in this test, water rose up to the highest temperature in 21 minutes. In the charging process, the lowest melting temperature was 58 °C to melt all the PCM crystal. In the copper coil PCM container unit test, the highest out let water temperature was 44 °C, while the inlet water temperature was 12 °C. The result showed there isn't enough residence time in the coil leads to not enough heat transfer area for it to reach the maximum temperature. The biggest struggle at the moment is to fully access the latent heat of the PCM because of its poor thermal conductivity.*

*Keywords: supercooled PCM; heat battery; solar assisted heat pump; domestic hot water; transient building simulation*



## 1. INTRODUCTION

Phase Change Material (PCM) is a material with high energy density, which is used as energy storage media in latent thermal energy storage systems. It has been classified into two categories: inorganic compounds (e.g. salt hydrates, salts, metals and alloys) and organic compounds (e.g. paraffin, fatty acids/esters and polyalcohol) (Zhang & Fang, 2006). Latent heat storage can be achieved through liquid → solid, solid → liquid, solid → gas and liquid → gas phase changes. However, only solid → liquid and liquid → solid phase changes are practical for PCMs. Initially, it is similar with sensible heat storage (SHS) materials, solid-liquid PCMs temperature rises when absorbing heat. However, when PCMs reach melting temperature (phase change temperature), they absorb large amounts of heat at an almost constant temperature. PCMs continue absorbing heat without a significant rise in temperature until all the material is transformed to the liquid phase. When the ambient temperature falls, the PCMs then solidify and release stored latent heat (Kenisarin & Mahkamov, 2007).

A supersaturated solution is a solution with more dissolved solute than the solvent would normally dissolve in its current conditions. Supersaturation is achieved by dissolving a solute in one set of conditions, then transferring it to other conditions without triggering any release of the solute. Supersaturated solutions are extremely unstable, but often require a triggering event to begin returning to a stable state via the solute coming out of solution. Supersaturated solutions will also undergo crystallisation under specific conditions (Coquerel, 2014; Garskaite et al., 2014). In a normal solution, once the maximum amount of solute is dissolved, adding more solute would cause the dissolved solute to precipitate out (Linnikov, 2014). In the supersaturated condition, the solute will simply precipitate out by a small activation in the solution. It is because supersaturated solution is in a very high energy state and crystallisation can occur by energy releasing, solution will then become a lower energy state. The activation energy comes in the form of a nuclei crystal being added to the liquid solution. This nuclei can be either added from another source or form within the solution due to ion and molecule interactions (Shantz-Hilkes, 2015). A common example of a supersaturated solution is the carbonated beverage. These have much larger amounts of carbon dioxide dissolved than would be possible in normal conditions. The gas is kept dissolved by increased pressure, but immediately begins forming bubbles of released gas where the solution is in contact with its container once that pressure is released through opening the container (Franks et al., 1990). Supersaturated solutions of common substances such as sugar are also possible. Water can dissolve more sugar at higher temperatures, so cooling a carefully prepared solution of fully concentrated sugar water from high temperatures results in a supersaturated solution of sugar. A string or other object placed in the solution gives the sugar crystals a nucleation site, and any object thus inserted slowly develops a coating of solid sugar (Franks et al., 1990; Hartel & Shastry, 1991). Faster and more dramatic reactions are possible with different solutes. For example, the sodium acetate trihydrate can be melt at 58.2 °C and cooled down to become supersaturated solution. They can be stored for very long periods as a liquid, with a high stored energy content, which can be released on any demand (Smith & McBroom, 1992).

Sodium acetate trihydrate is commonly used as reusable gel heating pads (hand warmer). A hand warmer, containing a supersaturated solution of sodium acetate, which releases heat upon crystallisation. When they are heated past the melting point and subsequently allowed to cool, the aqueous solution becomes supersaturated. This solution is capable of cooling to room temperature without forming crystals (Cohen, Soerens, & Amundson, 2011). By pressing on a small mechanical "clicker" within the heating pad that activates the nucleation centres and starts the reaction, a nucleation center is formed, causing the solution to crystallise back into solid sodium acetate trihydrate. In Canbazoğlu et al. study (Canbazoğlu, Şahinaslan, Ekmekyapar, Aksoy, & Akarsu, 2005), disodium hydrogen phosphate dodecahydrate ( $\text{Na}_2\text{HPO}_4 \cdot 12\text{H}_2\text{O}$ ) and sodium thiosulfate ( $\text{Na}_2\text{S}_2\text{O}_3 \cdot 5\text{H}_2\text{O}$ ) are promising PCMs used as a thermal heat storage material. Sodium thiosulfate is a chemical and medication, the supersaturated solution can be activated easily by being struck or heated, it can melt at 48.5 °C and can be decomposed into  $\text{Na}_2\text{SO}_4$  and release  $\text{SO}_2$ . However, most of the PCM supersaturated solutions are not very steady. The change in environment is enough to start crystallisation in supersaturated solution. And also, activation may happen during transportation. Nucleation inhibitor such as Sodium Alginate and  $\text{Na}_2\text{CO}_3$  can be added in the solution to control the formation of crystal. Without nucleation inhibitor, crystals can be formed quickly in the PCM supersaturated solutions with small liquid fluctuations or through physical force. In Cabeza et al. study (Canbazoğlu et al., 2005), starch, cellulose and bentonite are used in the sodium acetate trihydrate as stabilisers and nucleation inhibitor. And also, methylhydroxyethyl-cellulose (MHE-cellulose), and methyl-cellulose (M-cellulose) are used as stabilisers and nucleation inhibitor in industrial purpose. In Harding et al. research (Harding, Pearson, Robinson, Ori, & Lawson, 2014), the kinetic inhibitor is selected from the group consisting of: sodium carboxymethyl cellulose (CSC); gelatine; ethyl cellulose; polyethylene glycol; xanthan gum; glycerol; urea; polysorbate 20; polysorbate 80; polyacrylic acid; sodium pyrophosphate; polyacrylamide; pullulan; poly(vinyl alcohol); and poly(vinyl acetate). In the research, 0.5%wt CSC and 10% potassium acetate were added into sodium acetate trihydrate and the result showed a better stability; however, the nucleation inhibitor of 0.5%wt CMC with 3.33% ethylene glycol did not show a positive result. And also, low toxicity, readily available, and low cost should be considered in the nucleation inhibitor selection.

## 2. INITIAL TESTS

In the domestic hot water (DHW) system application with supercooled PCMs, it is necessary to understand the heat and mass transfer of the PCM materials and PCM pack. And also, it is important to learn the characteristics of the PCM charging and discharging process. Some initial tests have been done to analyse characteristics of the selected PCM.

### 2.1. Discharging and charging process of a PCM pack

Some initial tests have been done to analyse characteristics of the selected PCM. In the PCM bottle pack discharging and charging test (shown in Figure 1), the supercooled solution was 200g, the PCM pack was put in the container with 120g water. One thermocouple was placed in the water to record the temperature, one placed on the surface of the PCM pack, and one put inside the bottle to record the temperature. According to the results record (shown in Figure 2), in the discharging process, the highest water temperature (sensor on the PCM pack surface) was around 40°C which is lower than the PCM bag test, because the heat transfer of the plastic is much lower than PCM bag. It took 30 minutes to reach the highest temperature. In charging process, the PCM materials phase change point was at 55°C. And at that point, the PCM pack surface temperature was about 61°C, and the surrounding water temperature was about 63-64°C, which is much higher than the melting temperature in the PVC PCM bag test charging process.

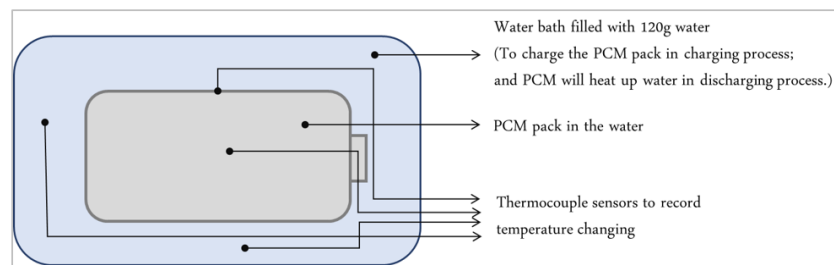


Figure 1: Diagram of PCM pack in discharging and charging process.

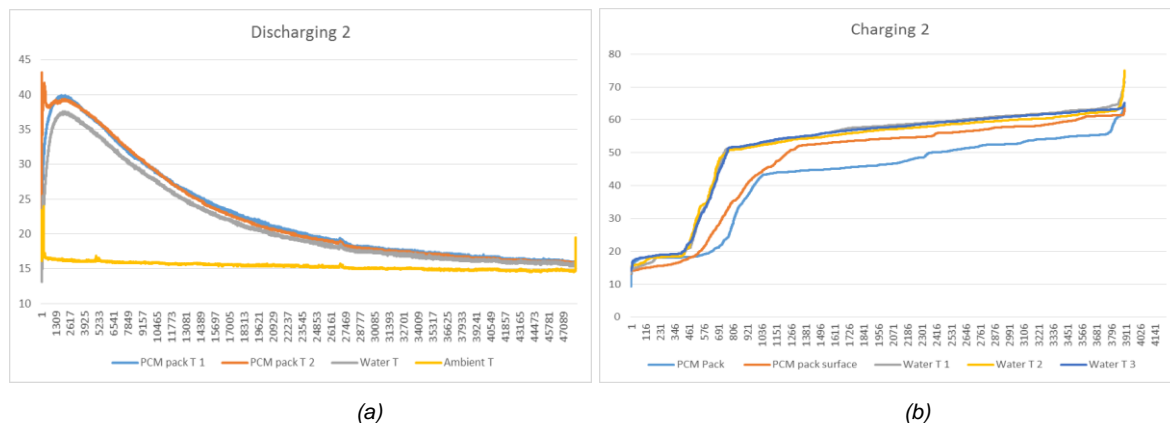


Figure 2: PCM bottle pack (a) discharging and (b) charging tests temperature changing records.

### 2.2. PCM pack test with flowing water

In this test, we used flowing water with a flow rate of 70g/minute to test the heat transfer of the PCM pack. 6 PCM packs were seal on the water container to provide a water flow direction (showed in Figure 3). This test was running for two cycles. After activating all the PCM pack, we used some insulated pad to insulate the reaction box to avoid heat loss.

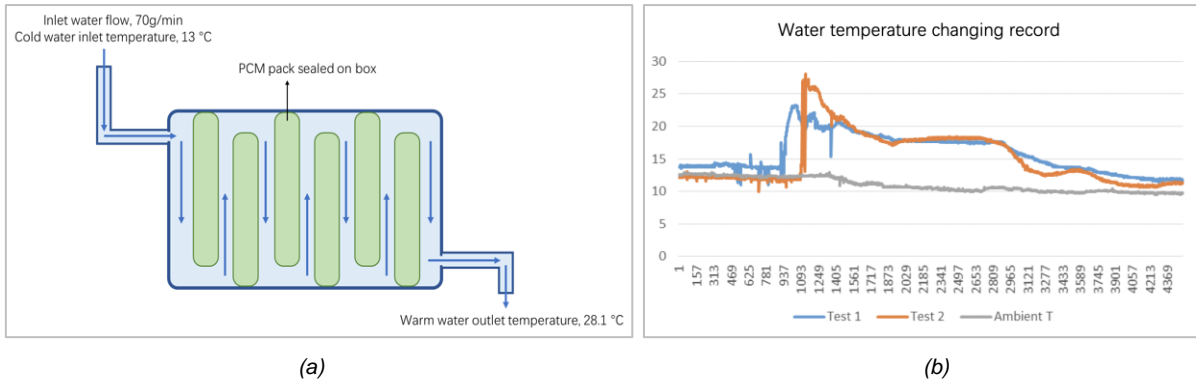


Figure 3: (a) PCM packs test with flowing water; (b) Water temperature record of inlet and outlet water flow in the 1<sup>st</sup> and 2<sup>nd</sup> test cycles.

The ambient temperature was about 12.5°C, and the water flow rate was 70g/min. In the 1<sup>st</sup> test cycle, the highest temperature was 23.3°C (water inlet temperature was 10°C) and it rose up to the highest temperature in 3 minutes. In the 2<sup>nd</sup> test cycle, the highest temperature was 28.1°C and it rose up to the highest temperature in 5 minutes. The results show poor heat transfer, likely due to the HDPE PCM pack acting as a barrier to effective heat transfer.

### 3. PCM STORAGE UNIT WITH COPPER COIL

This current work is an experimental performance of copper coil thermal storage unit filled with PCM (Sodium Acetate supercooled solution). The experimental test is conducted in order to study the characteristics of this PCM during charging and discharging process, and this test will give an idea of how the finalised prototype will work in a hot water heating system. This PCM may charge and discharge large amounts of heat during melting and solidification process, which takes place at near isothermal conditions. This PCM has a relatively low thermal conductivity, therefore the design of a suitable heat exchanger important for the system design as a whole. We have worked out the simulation of this PCM water heating system, and it showed very good results in hot water supply. This study demonstrated that copper coil in storage unit designs are effective to delivering a constant outlet temperature and effective heat transfer with large surface areas. We were studied experimentally this thermal energy storage unit using PCM in the water heat exchanger. The model will be used for hot water heating supply system in building application. This work presents an experimental study of a PCM storage unit for hot water supply application. Two tests of charging and discharging process were studied subject to a fixed water flow rate of 4.2L/hour, and the inlet/outlet temperature of the system. The experiments were focused on the PCM of sodium acetate.

#### 3.1. Experimental set-up

In order to evaluate the performance of the PCM water heating system, an experimental system was set up. The main components of the experimental setup are shown in the photograph of Figure 4 (a)

Figure(a) and the schematic explanation of the operation is shown in Figure 4 (b)

Figure(b). This storage unit is a glass bottle filled with supercooled PCM solution with a single copper coil (internal diameter = 90mm) heat exchanger, it consisted of cylindrical glass container (copper internal diameter = 3mm, length = 1800 mm). The experimental system contains a direct cold water supply at 12°C and a high temperature bath providing hot water at 70°C. The fixed water flow rate is 4.2L/hour. To measure the water temperatures, two thermocouples are placed at the inlet and the outlet of the coil. Two other thermocouples are used to measure the temperatures of the inside PCM solution and ambient air conditions. In both charging and discharging process, the glass container was covered with a layer of insulation to avoid large heat losses.

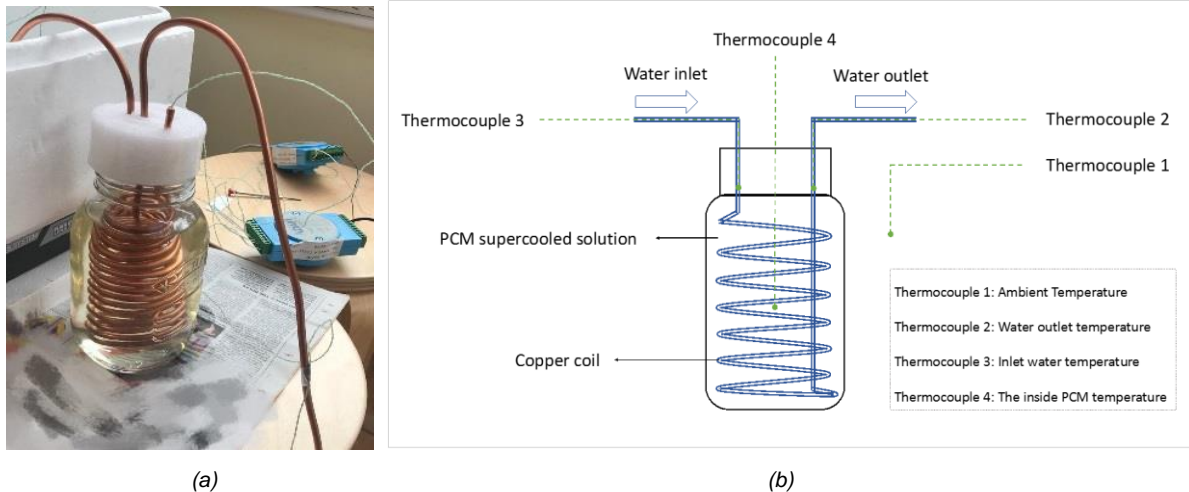


Figure 4: (a) Photograph of the test rig; (b) Diagram of the test rig with thermocouples.

For the discharging process, the components are assembled. First, the glass container is filled with 800g supercooled PCM solution. The copper coil heat exchanger is then submerged in the PCM solution. The data logger is then set to record temperature variations. The temperature variation of the water and PCM during charging and discharging process was recorded every 1 second for all five thermocouples. Cool water is supplied at 12°C with water flow rate of 4.2L/hour. The supercooled PCM is then activated. Photographs showed the heat store PCM was changing gradually (Figure 5). When the outlet and inlet water reaches the same temperature then the experiment can be stopped. The PCM can now be recharged using hot water.

Charging tests were carried out to investigate the melting behaviour and how phase change evolves inside the storage unit. The melting behaviour is observed by taking pictures of the system every 15 minutes. The pictures tracked the motion of the liquid/solid interface (Figure 6). These results demonstrate that PCM melting initiated at the circumferential area of the coil; the closer the PCM is to the coil, the earlier melting commences. In charging/regeneration process, the melting process is initiated by passing the 70°C hot water into the coil with water flow rate of 4.2L/hour. The PCM in the heat storage unit was melted gradually. Photographs showed the heat store PCM was changing gradually in charging process. When the complete fusion of PCM is reached (visual inspection of the PCM status), the hot water supply is stopped and the entire system is allowed to supercool to room temperature.

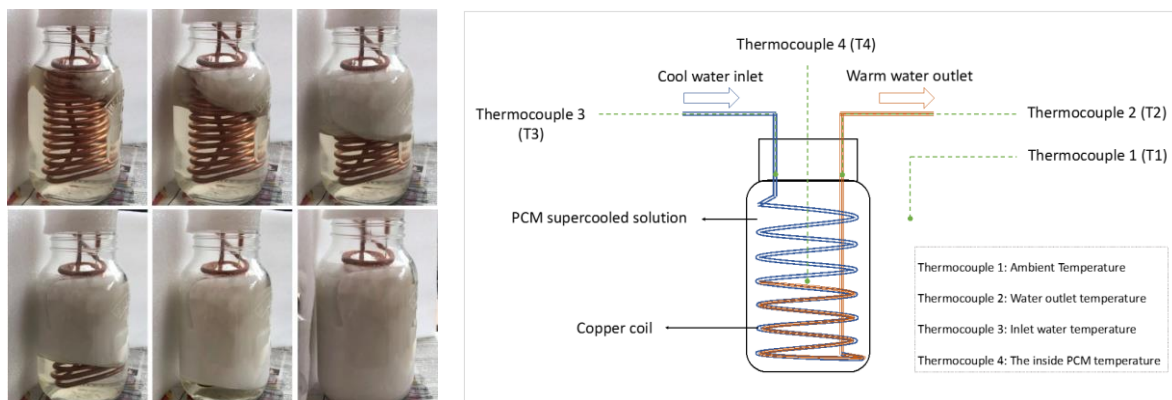


Figure 5: PCM changing with time after active in discharging process

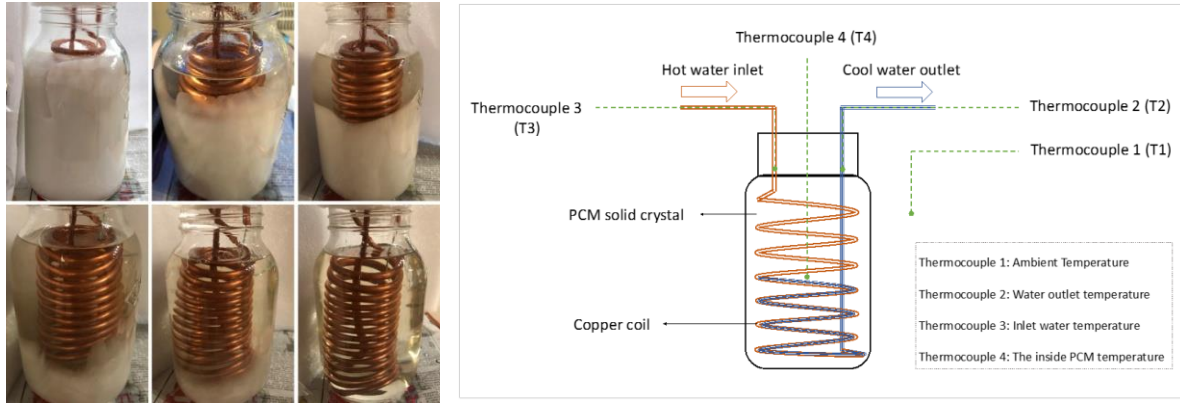


Figure 6: PCM changing with time after supplying hot water in charging process.

### 3.2. Results and discussions

Cold water was supplied from tap water with water flow rate was 4.2L/hour (flow rate was controlled manually by a valve). The inlet water temperature was around 12°C (T3). At beginning of discharging process, PCM solution changed to crystal and reached the maximum temperature within a few seconds. Figure 7 Figure(a) shows temperature variations at four points. Just a few seconds after PCM supercooled solution (800g) was activated, it (T4) reached the highest temperature. The outlet water temperature (T2) rose up to 44°C in about 4 minutes, and the outlet water temperature (T2) stayed above 40°C for approximately 10 minutes. The inlet water temperature (T3) stayed steady at about 12°C and the ambient temperature (T1) was approximately 16°C. The reason why the outlet water temperature cannot reach 50°C is because there isn't enough residence time in the coil and not enough heat transfer area for it to reach the maximum temperature. The biggest struggle at the moment is fully accessing the latent heat of the PCM because of its poor thermal conductivity.

Figure 7 Figure(b) shows PCM heat storage unit in the charging process. Hot water was supplied from a water bath with a flow rate of 4.2L/hour at a temperature (T3) of approximately 70°C. The inlet hot water supplied heat to the PCM heat store unit to melt the PCM. According to Figure 7 Figure(b), the hot water passed through PCM solid from the top, it means that the topside temperature was higher than the bottom of the bottle. So it was difficult to fully melt. Therefore, it will be better to supply the hot water into the base of the unit first so that convection assist the charging process. During the charging process, hot water (T3) was supplied at around 70°C to charging the PCM heat store unit (T4). It can be seen from Figure 7 Figure(b), the PCM complete phase change process at the Phase Change Point, which the PCM liquid (T4) was at a temperature of approximately 59°C, while the outlet water temperature (T2) was slightly higher than the solution temperature (T4). After that point, T2 and T4 showed a rapid temperature increase, meaning that all the solid PCM crystal was completely melted after approximately 90 minutes (1.5 hours).

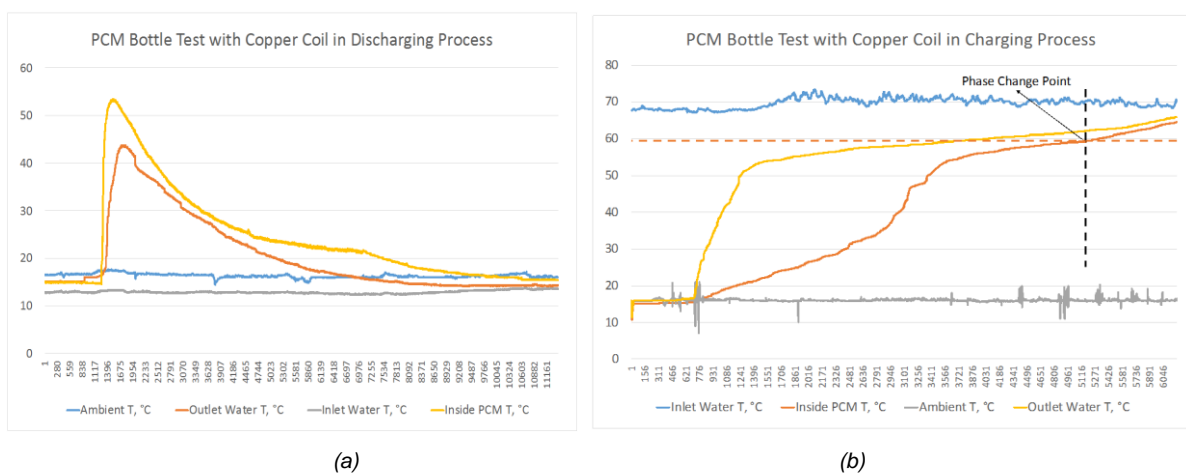


Figure 7: (a) Four thermocouples temperature changing in the discharging process; (b) Four thermocouples temperature changing in the charging process.

#### 4. CONCLUSION

In our selected material - - the sodium acetate trihydrate, can reach 55°C. In the PCM pack discharging test, the highest water temperature (sensor on the PCM pack surface) was around 40°C, because the heat transfer of the plastic is low. It took 30 minutes to reach the highest temperature. In the charging process, the PCM materials phase change point was at 55°C. And at that point, the PCM pack surface temperature was about 61°C, and the surrounding water temperature was about 63-64°C, which is much higher than the melting temperature. In the PCM pack test with 70g/min flowing water, the highest water outlet temperature was 28.1°C while the inlet water was 12.5°C. And it rose up to the highest temperature in 5 minutes. The main issue is the heat transfer of the PCM pack. In the PCM pack test with 70g/min flowing water, the highest water outlet temperature was 28.1°C while the inlet water was 12.5°C. And it rose up to the highest temperature in 5 minutes. The main issue is the heat transfer of the PCM pack.

A PCM heat exchanger for latent heat storage of thermal energy was designed, fabricated, and analysed experimentally. Charging and discharging processes were studied by using a fixed water flow rate, inlet temperature and flow direction. Temperature readings and images of the PCM revealed details of the phase change behaviours in the copper coil PCM heat exchanger. The experimental results show that in the discharging process, the outlet water temperature rose up to the highest temperature at 44°C in 4 minutes, it stayed above 40°C for 10 minutes. The inlet water temperature stayed steady at 12°C, while the ambient temperature was 16°C. Outlet water temperature cannot reach to 50°C because there isn't enough residence time in the coil and not enough heat transfer area for it to reach the maximum temperature. In the charging process, hot water provided a steady temperature at 70°C to charge PCM heat store unit. All the PCM was melt at the Phase Change Point, which the PCM liquid (T4) was at a temperature of about 59°C, while the outlet water temperature was slightly higher than the solution temperature. After that point, T2 and T4 showed a rapid temperature increase, meaning that all the solid PCM crystal were completely melted after approximately 90 minutes. The discharging process was very similar to the charging process. It was also found that a more time should be applied to the liquid in charging process after all the PCM melt, because if there is any crystal left in the liquid, crystallisation will happen when temperature decreases and the liquid will become a saturated solution with crystal on the bottom of the container.

#### 5. REFERENCES

- Canbazoğlu, S., Şahinaslan, A., Ekmekyapar, A., Aksoy, Y. G., & Akarsu, F. (2005). Enhancement of solar thermal energy storage performance using sodium thiosulfate pentahydrate of a conventional solar water-heating system. *Energy and Buildings*, 37(3), 235-242.
- Cohen, J. C., Soerens, D. A., & Amundson, J. D. (2011). Patterned self-warming wipe substrates: Google Patents.
- Coquerel, G. (2014). Crystallization of molecular systems from solution: phase diagrams, supersaturation and other basic concepts. *Chemical Society Reviews*, 43(7), 2286-2300.
- Franks, F., Mathias, S., Hatley, R., Baust, J., Hvidt, A., Chapman, D., & Jaenicke, R. (1990). Water, temperature and life. *Philosophical Transactions of the Royal Society of London B: Biological Sciences*, 326(1237), 517-533.
- Garskaite, E., Gross, K.-A., Yang, S.-W., Yang, T. C.-K., Yang, J.-C., & Kareiva, A. (2014). Effect of processing conditions on the crystallinity and structure of carbonated calcium hydroxyapatite (CHAp). *CrystEngComm*, 16(19), 3950-3959.
- Harding, N., Pearson, P., Robinson, J., Ori, M., & Lawson, M. (2014). Sodium acetate trihydrate formulations: Google Patents.
- Hartel, R. W., & Shastry, A. V. (1991). Sugar crystallization in food products. *Critical Reviews in Food Science & Nutrition*, 30(1), 49-112.
- Kenisarin, M., & Mahkamov, K. (2007). Solar energy storage using phase change materials. *Renewable and sustainable energy reviews*, 11(9), 1913-1965.
- Linnikov, O. (2014). Mechanism of precipitate formation during spontaneous crystallization from supersaturated aqueous solutions. *Russian Chemical Reviews*, 83(4), 343.
- Shantz-Hilkes, C. (2015). From pedagogy to participation progressive youths' paths to formal civic engagement. University of Toronto (Canada).
- Smith, R. A., & McBroom, R. B. (1992). Boron oxides, boric acid, and borates. *Kirk-Othmer Encyclopedia of Chemical Technology*.

Zhang, Z., & Fang, X. (2006). Study on paraffin/expanded graphite composite phase change thermal energy storage material. *Energy Conversion and Management*, 47(3), 303-310.

---

## #31: Thermal analysis of a low-cost ground heat exchanger using laboratory simulator

---

Blaise MEMPOUO<sup>1\*</sup>, Saffa B. RIFFAT<sup>1</sup>, Theo ELMER<sup>2</sup>, Adam DICKEN<sup>3</sup>, Ben ATACK<sup>4</sup>  
Philip TYLER<sup>5</sup>

<sup>1</sup> Architecture, Energy & Environment (AEE) Research Group, Institute of Sustainable Energy Technology, Department of Architecture & Built Environment, University of Nottingham; University Park, NG7 2RD Nottingham, United Kingdom, Tel: +44(0) 1158467132, Fax: +44(0) 1159513159

<sup>2</sup> Geo Green Power Ltd, Green Barn, Costock Road, Wysall, Nottingham, NG12 5QT United Kingdom,

<sup>3</sup>EPS Ltd, Unit 32, Mere View Industrial Estate Yaxley, Cambridgeshire PE7 3HS, UK Tel: +44 (0)1733 243400

<sup>4</sup>Positive Homes Ltd, 7 Clifford Close, Keyworth, Nottinghamshire, NG12 5GZ, UK, Tel: +44 (0) 115983043

<sup>5</sup>Solar Ready Ltd, 11 Ivanhoe Road Finchampstead Berkshire RG40 4QQ,

\*Corresponding author: Blaise.mempouo@nottingham.ac.uk

Shallow depth of ground can be use as heat source in winter, and heat sinks through summer has shown, numerically and experimentally that it is able to produce potential cooling and heating throughout the year. The cooling and heating can be extracted / injected by means of a novel affordable thermal-pipe heat exchanger with heating medium (water/glycol) technique. To exploit effectively the heat capacity of the ground, a heat-exchanger system has to be designed and constructed to facilitate heat transfer to/from the ground. Because of the shallow depth of the soil around the thermal-pipe, the experiment has limitations in rapid change of input parameters. Thus, this paper presents the performance of the thermal-pipe ground heat exchanger (TP-GHE) based on experimental studies using a laboratory simulator. Different input parameters have been investigated such as heat medium (water/glycol) inlet temperature varies from 10 to 11°C, ground temperature ( $T_g$ ) varies from 4 to 12°C and water/glycol flow rate at 0.01– 0.03 kg/s. The actual soil surrounding was created in a plastic tank and nine copper thermal pipes of 1m length and 0.125m pitch between them were used in the simulator. A chiller, was used to maintain the soil temperature constant. Results show that the flow rate of 0.03 kg/s and  $T_{ground}$  of 13 °C gives the highest temperature lift with 6.62 °C or 26.5 % relative to the inlet temperature. The highest heat transfer rate at 308.3 W was obtained at a flow rate of 0.03 kg/s. The experimental results also have been validated with a field test from the industrial partner and were found to be in close agreement with, numerically analysis results.

Keywords: Heat pump, Vertical ground heat exchanger, Thermal pipes GCEs, GSHPs, Ground temperature



## 1. INTRODUCTION

The vertical and horizontal closed loop heat pumps are well-established technology to provide heating and cooling for various type of buildings around the world (Mempou, 2014). Ground source heat pumps (GSHPs) use the earth as winter heat sources and summer heat sinks via a ground heat exchangers (GHEs), typically having seasonal efficiencies of between 350 % and 400 % (Mempou et al, 2017). In the UK, among the key barriers to the technology adoption is the high installation costs of GHEs mainly using ground borehole loops and slinky coils? Giving the size and layout of a typical GSHP installation cost ranges between £13,000 -£20,000 (Franck energy, 2017). Thus, a key priority is to develop economic GHEs having improved heat transfer technology coupled with a rapid installation method. This paper will demonstrate an innovation that will lead to a novel GSHPs technology (EfficientGeoTech) that will tackle the fundamental techno-economic barrier to existing GSHPs. The innovation elegantly addresses the fundamental problem by providing thermal pipes (GHEs) that are cheap to manufacture and install, avoiding expensive and large drilling rigs required for conventional borehole thus, suitable for retrofit applications of homes.

The ground has ability to maintain constant temperature, which is relatively higher than ambient air temperature in winter and lower in summer. Thus, both cooling and heating can be utilised by using GHEs. In addition, the shallow depth of ground was identified to be able to produce sinusoidal temperatures and remain constant at a certain depth throughout the year. During the year, the earth temperature beyond a depth of 1 m is sensitive to the air temperature and solar radiation and the annual fluctuation of the earth temperature extends to a depth of about 10 meters. As a result, the annual temperature variation of the ground at a depth of 10m is between -3°C to 12°C. To exploit effectively the heat capacity of the ground, Ground Heat Exchangers (GHE) has to be designed and constructed to facilitate heat transfer to/from the ground. Because of the shallow depth of the soil around the thermal-pipe, the experiment has limitations in rapid change of input parameters. Thus, this paper presents the performance of the thermal-pipe ground heat exchanger (TP-GHE) based on experimental studies using a laboratory simulator. The overall aims of the project is to investigate the technical feasibility of a low cost heat exchanger that would enable vertical closed loop Ground Source Heat Pump (GSHP) to become economically viable for space heating and cooling in the residential buildings.

In this paper, an experimental system was set up to study the performance of the novel thermal-pipe ground heat exchanger (TP-GHE). The actual soil surrounding the TP-GHE was created in a plastic tank and nine copper thermal pipes of 1m length and 0.125m pitch between them were used in the simulator.

## 2. BACKGROUND

Chow et al reported the most recent work in the earth-air heat exchanger (EAHE) technique (Chow et al., 2011). Bortoloni et al. have conducted the analysis of ground temperature and their results shown that the soil temperature varies from 4°C to 28 °C for depth of 1- metre. Then the temperature changes to 15.5–18 °C as the depth change to 4-metre (Bortoloni et al. 2017). Derbel and Kanoun (2010) have conducted a theoretical and experimental study of the EAHE. A mathematical model for the theoretical study was developed based on circular cross flow heat exchanger with one fluid unmixed. The study had inspired input parameters from Al- Ajmi et al. (2006) and Goswami and Dhaliwal (1985). The model was also tested at different soil thermal conductivities and validated against previous experimental data by Thanu et al. (2001).

In the opinion of the authors, field study is a common practice in analysing performance of GHEs using an experimental approach. The experimental approach is based on the nature of the ground to produce source of energy either for heating or cooling. There are restrictions in time for getting a quick response of the parameters for the field study, which depends more on the nature of the climate. Besides that, in the real application, a GHEs system usually does not need to work continuously over 24 h. When the operation is turned off, the system can be ignored for evaluation and it should be in self-recovery mode. From the opinion of the authors, these are the strong reasons to shift the approach of experimental work from a field study to a laboratory simulator that is more controllable of dependent parameters and has high repeatability of the experiment. Therefore, this paper presents performance of the thermal-pipe ground heat exchanger (TP-GHE) based on experimental studies conducted at the University Of Nottingham in the UK using a full scale laboratory simulator. Different input parameters have been investigated such as heat medium (water/glycol) inlet temperature varies from 10°C to 11°C, ground temperature (T<sub>g</sub>) varies from 4°C to 12°C and water/glycol flow rate at 0.01– 0.03 kg/s.

## 3. MATERIAL AND METHODS

### 3.1. Heat transfer model

The heat transfer process occurred between water/glycol that flows inside the thermal-pipe ground heat exchanger (TP-GHE) and ground surrounding. The heat transfer mechanism of the TP-GHE is related to the process of absorbing and releasing heat to and from the thermal pipe and the surrounding ground as the heat transfer fluid flows through the pipe within the thermal pipe.

Heat transfer between the GHE and the surrounding ground involves a complex mechanism, but heat transfer to the ground is mostly through conduction. The heat-transfer-governing equation used for conduction in the ground is shown in the equation (1) below.

Equation 1: 
$$-\frac{d}{di} \left( \lambda \frac{dT}{di} \right) + \rho c \frac{dT}{dt} + q_i = 0 \quad (i = x, y, z)$$

Where:

- T = the temperature
- $\lambda$  = the thermal conductivity
- $\rho$  = the density
- c = the specific heat capacity
- $q_i$  = the internal heat generation

Fundamentally, the Thermal Response Test (TRT) is conducted in order to evaluate the heat exchange rate through the GHEs. The Thermal Response Test (TRT) is vital for designing ground source heat pumps and seasonal thermal energy storage (STES) systems. Mogensen (1983) first suggested the Thermal Response Test (TRT) at an international conference in Stockholm. Mogensen suggested a simple arrangement in which heat at constant power is injected into (or extracted from) a borehole while the borehole mean temperature is measured. So, a thermal response test (TRT) is used to determine the thermal properties of the ground. There is no direct way to measure ground thermal conductivity and borehole thermal resistance (Gehlin 2002). The TRT can be used to determine the ground thermal conductivity, using a line source or cylindrical source model, by applying constant heat to the equipment.

On the other hand, the thermal performance test (TPT) is used to measure the heat exchange rate of the GHEs under the condition that the inlet temperature is kept constant. Then the heat exchange rate is calculated using equation (2) below.

Equation 2: 
$$Q = M C_{wf} (T_{in} - T_{out})$$

Where:

- $T_{in}$  is the inlet temperature of the fluid
- $T_{out}$  is the outlet temperature of the fluid
- M is the mass flow rate of the fluid
- $C_{wf}$  the specific heat of the working fluid, which is treated as constant, although it can vary as a result of temperature variations in the fluid. In this case, it is reasonable to use an average value based on the average temperature of the cold fluid between the inlet and outlet.

### 3.2. Experimental System

Due to uncontrollable parameters in actual conditions, in order to evaluate the heat exchange rate through the thermal-pipe ground heat exchanger (TP-GHE) the laboratory simulator apparatus (Figure 1) has been used. Conceptually, the simulator has similarities with the actual condition. The setup included a soil/ground chiller, mock-up soil box, heat pump, circulating pump, thermocouples, flow meter, water-tank and water-cooling systems. The set-up was multifunctional; it was able to measure heat exchange and ground thermal conductivity because it was equipped with controllers for both temperature and moisture content.

Figure 1 and Figure 2 show a full schematic diagram of the TP-GHEX lab simulator. The TP-GHEX lab simulator consists of an soil/ground simulator tank with integrated thermal pipes, chiller machine (CM), heat pump, a Loads simulator made of water storage tank (ST) with a thermostat, a water cooler to simulate the Heat distribution System. The temperature inside the soil/ground simulator tank is maintained constant by mean of the CM, which produces chilled water and circulates it into the loop around soil simulator tank. The heat transfer process will occur between the water/glycol inside the Thermal Pipes and soil in the soil/ground simulator tank as the heat is extracted at the evaporator of the heat pump. In order to evaluate the heat rate extracted from the soil/ground two parameters were measured, the masse flow rate using electronic flow meter and temperatures around the monitoring points were made via k-type thermocouples at thirty (30) different points (Figure 1).

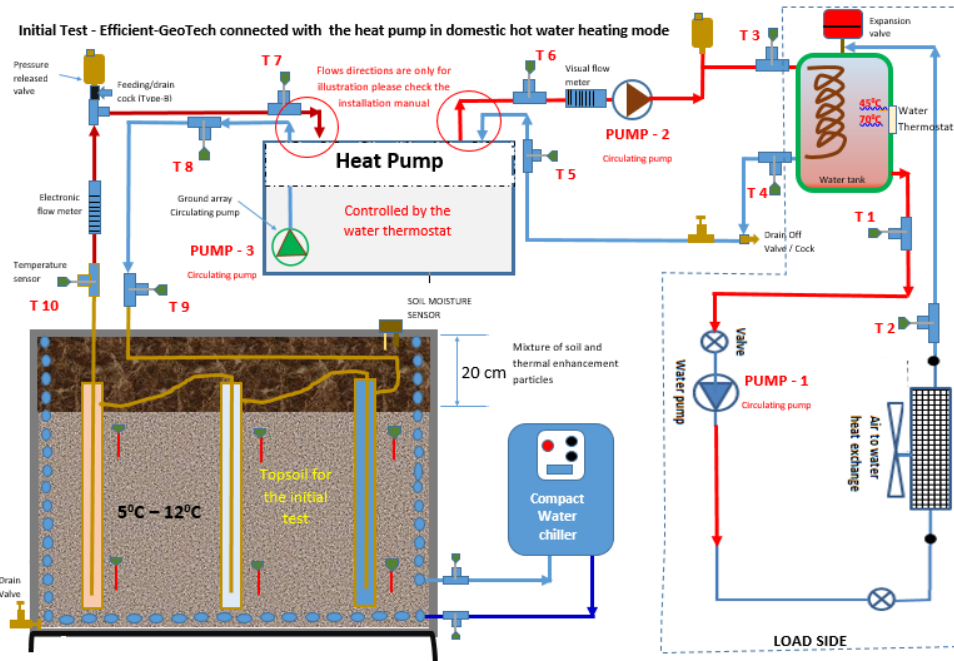


Figure 1: Schematic diagram of the TP-GHE lab simulator.

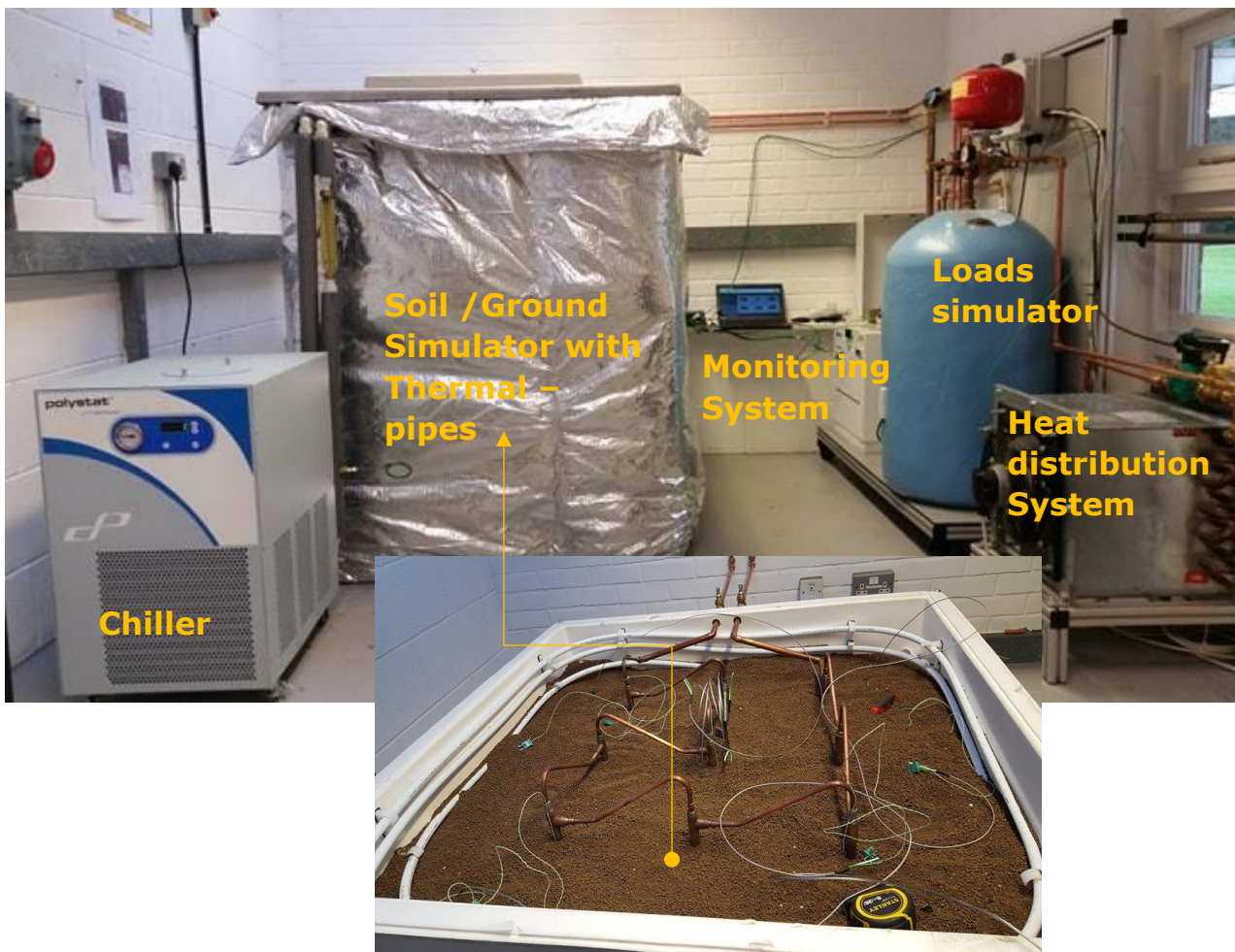


Figure 2: Experimental setup of the Efficient GeoTech Heat pump under investigation

### 3.3. Materials, equipment and procedures

This section describes the materials, equipment needed, and procedures to follow during the investigation. Equipment was installed in order to measure the heat exchange rate of each Thermal-pipe Ground Heat Exchanger (TP-GHE). The setup in the Figure 2 included a soil/ground chiller, mock-up soil box, heat pump, circulating pump, thermocouples, flow meter, water tank and water-cooling systems. The set-up was multifunctional; it was able to measure heat exchange and ground thermal conductivity because it was equipped with controllers for both temperature and moisture content.

#### *The Thermal-pipe Ground Heat Exchanger (TP-GHE)*

The performance of TP-GHEX has been analysed based on parameter and condition settings as tabulated in Table 1. In general, this investigation focused on thermal characteristics and performance of the system by analysing the effects of mass flow rate and ground temperature on the fluid temperature ( $T_f$ ) and the rate of heat transfer ( $Q$ ) of the TP-GHEX.

Table 1: Parameter for TP-GHEX.

Parameter	Values
Outside/inside pipe diameter of the TP-GHEX	15mm / 8mm
Length	1 m
Copper / Thermal conductivity	385 W/m K
Thermal conductivity of soil	1.89 W/m K
Soil Volume x=1m, y=1 m, z=1.2m	1.2 m <sup>3</sup>
Mass flow rate of the water/glycol	0.01– 0.03 kg/s
Ground temperature	4°C , 6°C to 8°C , 10°C and 12°C
Water inlet temperature	-3 °C

#### *Soil/ground simulator tank and chiller*

A Carbon-Fiber Tank (1 m × 1 m × 1.20 m) of 1220 Litres with insulation to reduce heat transfer from the soil to the environment and to maintain a constant temperature in the soil during the Thermal Response Test (TRT) test were used. A commercial disinfected dry soil with the physical and thermal properties (Table 2) were used to fill the carbon-fiber tank. Soils were compacted to a certain density within the Carbon-Fiber Soil Filter Tank and 100m long underfloor heating pipe.

Table 2: Physical and thermal properties of soil.

Parameter	Value
Bulk density,	1.27 g/cm <sup>3</sup>
Thermal conductivity,	0.26 W/m K
Water content,	0 w [%]
Specific heat capacity,	785 c [J kg <sup>-1</sup> K <sup>-1</sup> ]
Thermal diffusivity,	2.57 × 10 <sup>-7</sup> m <sup>2</sup> s <sup>-1</sup>



Figure 3: 25kg Bags of Dry Soil - Sterilised Loam that was used to fill the tank as the soil sample

The physical and thermal properties of Dry Soil-Loam are the most important factors to consider. A commercial dry loam screened to 3mm and sterilised was used, and it was made of 27 % clay content, 35 % Sand Matter, 17 % Silt, and 2.6 Organic matter and 14.4 % others (Figure 4), which was used to fill the carbon-fiber tank.

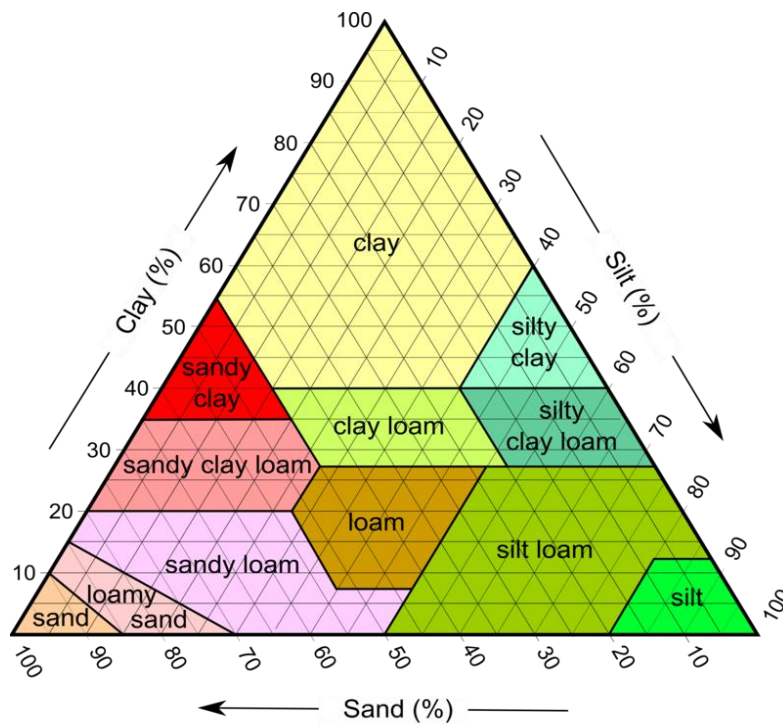


Figure 4: A quality screened Kettering Loam, screened to 3mm and sterilised.

From HanssonKlas et al (2004)'s work summarised in the Figure 5. The thermal conductivity of the Dry Soil-Loam increased with increasing soil water content. The results also shown that the thermal conductivity of the mixt soil used for the test ranged from 0.37 to 1.42 for sandy loam, from 0.37 to 1.90 for loam, from 0.38 to 1.71 for clay loam, and from 0.39 to 0.41 mcal/s.

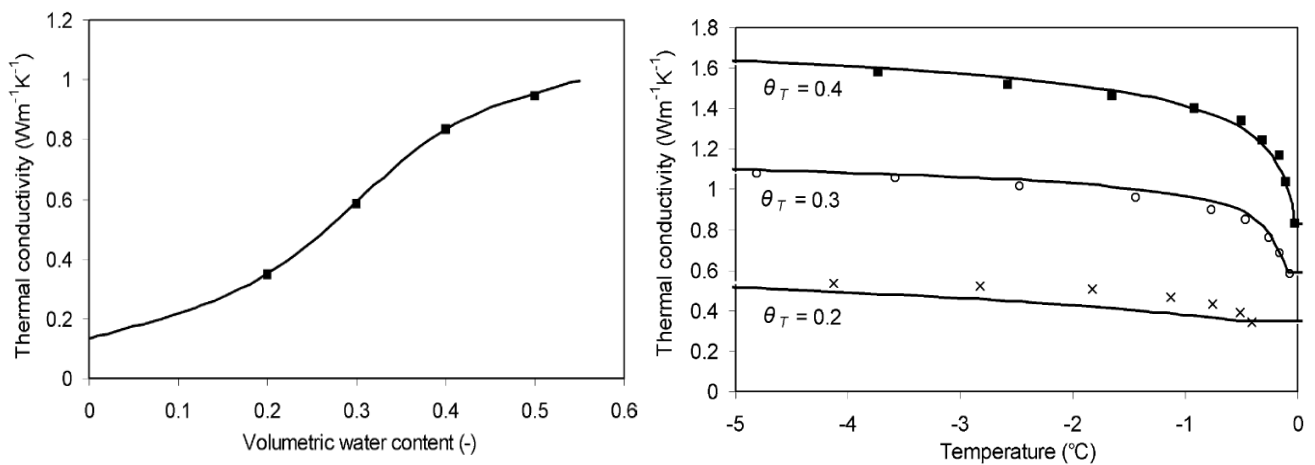


Figure 5: Thermal Properties of Dry Soil-Loam. Source: HanssonKlas et al (2004)

The heat transfer mechanism of the Ground Heat Exchangers is related to the process of absorbing and releasing heat to and from the thermal pipe and the surrounding ground as the heat transfer fluid flows through the thermal pipe. Consequently, the thermal conductivity as a function of soil bulk density for loam is very important factors, since the bulk density increases with compaction and tends to increase with depth. Sandy soils are more prone to high bulk density (see Figure 6).

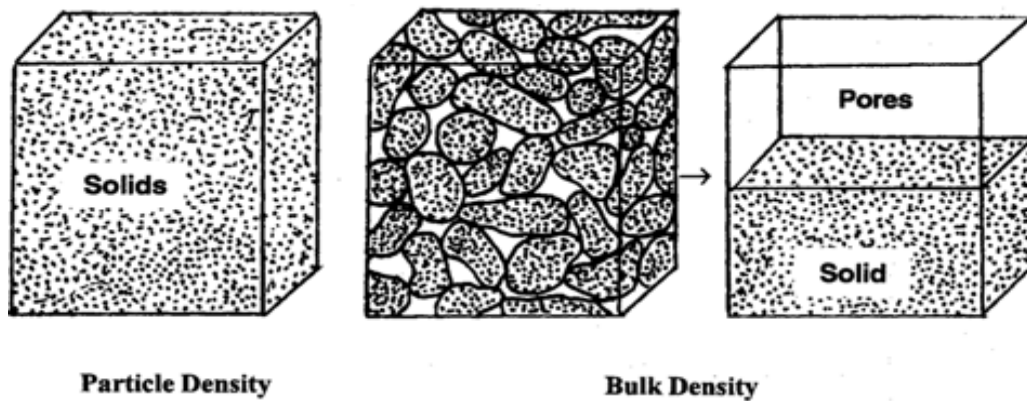


Figure 6: Bulk density is the weight of soil in a given volume, Source: HanssonKlas et al (2004).

### 3.4. Testing procedure and monitoring parameters

The circulating medium in the TP-GHEX is water/glycol, which is pumped out to/from the heat pump by the circulating pump. The flow rate is adjusted by regulating valve. The water/glycol flowing through the regulating valve returns to the heat pump.

When simulate the rig for space-heating using underfloor heating, before standing the test, the temperature T1 (Figure 1) should be kept constant between 40 °C – 45 °C. Also, temperature (T3, T4, T5 and T6) should also be the same or very close to each other less than 1-2°C the same or very close to each other) before standing the test. The Compact Water Chiller should be used to create the testing condition (6°C – 12 °C) in the soil before standing the experiment. Before starting recording data, the water/glycol in the ground loop, so water/glycol could have a consistent temperature (T7, T8, T9 and T10 are the same or very close to each other) before standing the test. When all temperatures are quite stables, the compressor of the heat pump would then be switched on. The rig was then ready to be monitored using the K-type thermocouples at each pipe (Figure 7) at various points (T<sub>p,i,j</sub>), with i the pipe number and j the position (Figure 8).

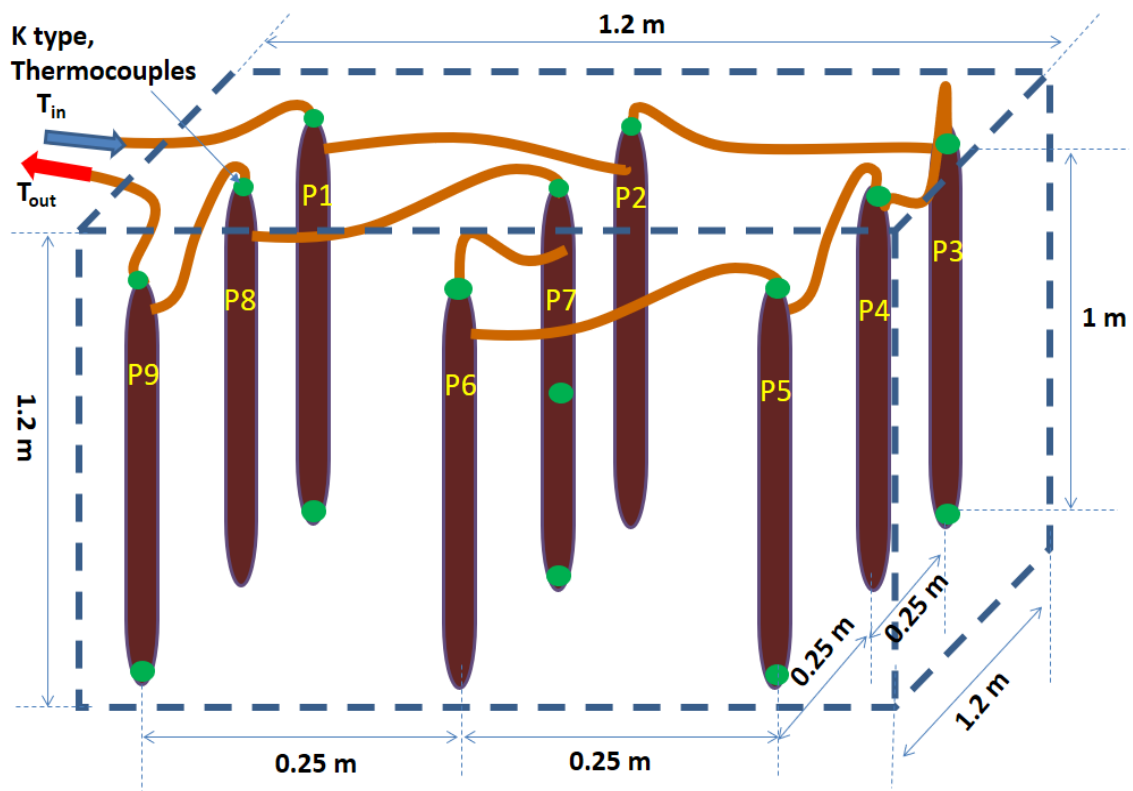


Figure 7: Schematic diagram of the monitoring points of the Soil Thermal Pipe Heat Exchanger

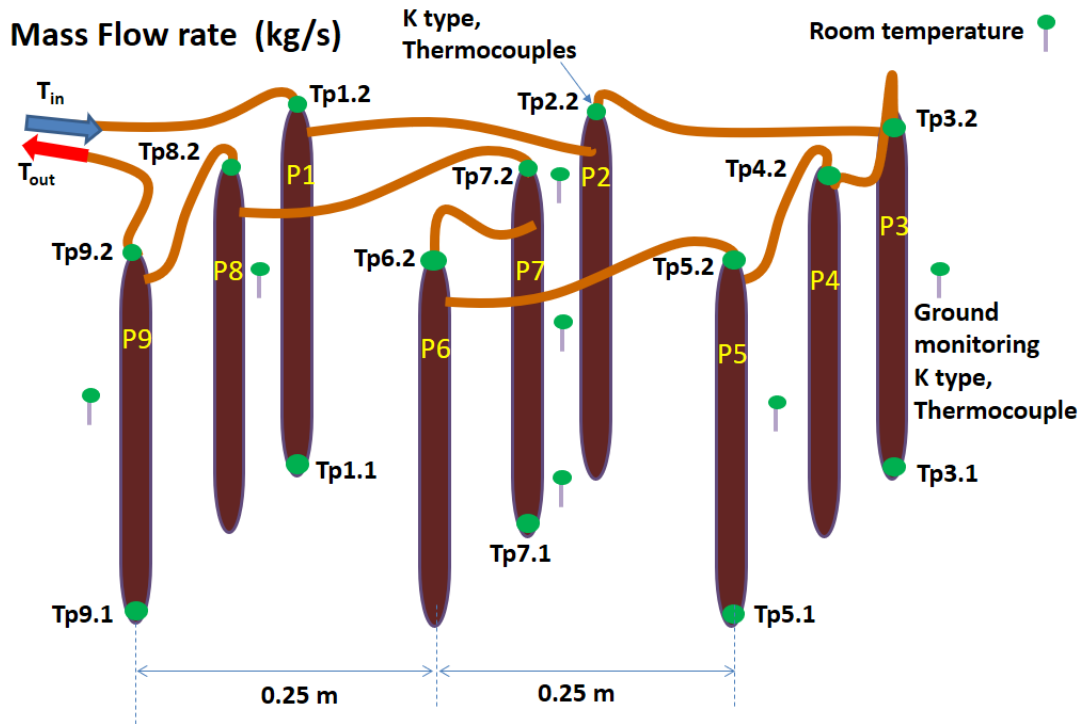


Figure 8: Schematic diagram of the monitoring points of the Soil Thermal Pipe Heat Exchanger.

#### 4. RESULTS

The outlet fluid temperature is the main parameter obtained from the experimental work. There are two different flow rates that were considered in the experiment, which were  $0.2\text{ l/s}$  and  $0.5\text{ l/s}$  (Figure 9). Meanwhile, ground temperature of  $23$ ,  $24$  and  $25\text{ }^\circ\text{C}$  was used for each temperature at  $y=0$  is considered as inlet temperature of the water/glycol. The fluid temperature, increases as the water/glycol flows along the thermal pipe.

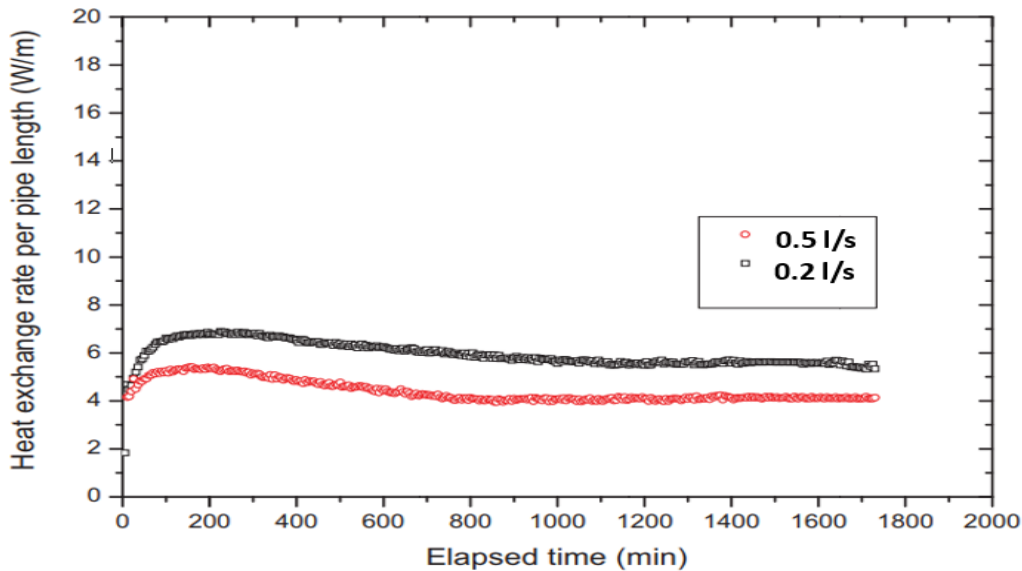


Figure 9: The heat rate of extracted from the Soil Thermal Pipe Heat Exchanger at different flow rate.

The variation between the inlet and outlet temperature was about  $5\text{ }^\circ\text{C}$ , shown in the Figure 10. Meanwhile, at the same setting of  $T_g$  and mass flow rate, the outlet temperature variation with inlet temperature, if the inlet temperature is greater than the ground temperature  $^\circ\text{C}$ , as showed in the figure 16 below, the temperature of the water/glycol drop and the least temperature drop at the outlet of the pipe, which is  $6.46\text{ }^\circ\text{C}$ . The  $T_{out}$  variation

increases as the ground temperature increases from 3 °C to 12 °C as shown in Figure 16. However, the  $T_{out}$  variation for all inlet temperatures tends to reach the ground temperature at the end of the 8.7-metre pipe.

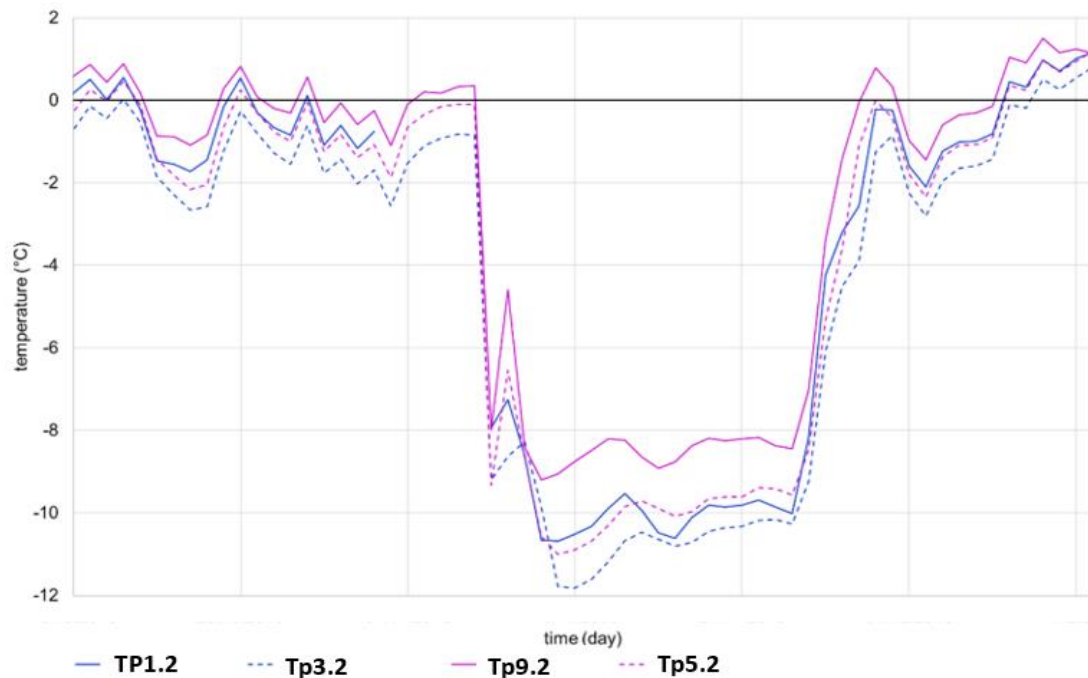


Figure 10: the monitoring temperatures at points  $Tp1.2$ ,  $Tp3.2$ ,  $Tp9.2$  and  $Tp5.2$  of the Soil Thermal Pipe Heat Exchanger.

## 5. CONCLUSION

The temperature of the circulating water/glycol reached a near steady state after 20 h in the TRT. The initial temperature of the soil loam was -3 to 12°C, and the average flow rate of the circulating water was 4–5.55 lpm. The total average heat-exchange rate for the nine (9) TP-GHEs were 290.61W. The average heat-exchange rates per pipe length is between 4.40W/m and 6.02W/m. The heat rate of TP-GHEs is lower than conventional U-tube system; the thermal radius of the U-tube system is greater than that of the TP-GHEs, but very affordable in theme of the cost. The reason for the analysis is that the cost of installing conventional ground heat exchangers. In addition, the effects of the distance between two pipes and thermal interference problems due to the superposition of temperature field interactions need to be investigated in the future work.

## 6. ACKNOWLEDGEMENT

The work of this paper is part of the UK Research and Innovation (UKRI) - Innovate UK project: Low-cost Efficient Ground Source Heat Pump Technology with Enhanced Heat Transfer (EfficientGeoTech). It is gratefully acknowledged that this work is supported by Innovate UK (Réf: 132744). The authors wish to express their acknowledgements to Geo Green Power Ltd and others collaborates for providing their valuable cooperation for this study.

## 7. REFERENCES

- Al-Ajmi, F., Loveday, D.L., Hanby V.I. (2006), The cooling potential of earth–air heat exchangers for domestic buildings in a desert climate, *Build. Environ.* 41 (3) 235–244.
- Ascione, F., Bellia, L., Minichiello, F. (2011), Earth-to-air heat exchangers for Italian climates, *Renew. Energy* 36 (8) 2177–2188.
- Bortoloni, M., Bottarelli, M., Su, Y. (2017), A study on the effect of ground surface boundary conditions in modelling shallow ground heat exchangers, *Appl. Therm. Eng.* 111 (Supplement C) 1371–1377.



- Chow, T.T., Long, H., Mok, H.Y., Li K.W. (2011), Estimation of soil temperature profile in Hong Kong from climatic variables, *Energy Build.* 43 (12) 3568–3575.
- Derbel, H.B.J., Kanoun, O. (2010), Investigation of the ground thermal potential in Tunisia focused towards heating and cooling applications, *Appl. Therm. Eng.* 30 (10) 1091–1100
- Gehlin S. (2002). *Thermal Response Test, Method Development and Evaluation*. Doctoral Thesis 2002:39. Luleå University of Technology. Sweden.
- Goswami, D.Y., Dhaliwal, A.S. (1985), Heat transfer analysis in environmental control using an underground air tunnel, *J. Sol. Energy Eng.* 107 (2) 141–145.
- Hansson, K., Simunek, J., Mizoguchi, M. (2004). Water Flow and Heat Transport in Frozen Soil: Numerical Solution and Freeze-Thaw Applications May 2004 *Vadose Zone Journal* 3(2):693-704. DOI: 10.2113/3.2.693
- Mempouo, B., Riffat, S., Cunningham A. (2017). Low-cost Efficient Ground Source Heat Pump with an Innovative Ground Heat Enhancement Technique. The 16th International Conference on Sustainable Energy Technologies – SET 2017, 19th to 22<sup>nd</sup>
- Mogensen P. (1983). Fluid to Duct Wall Heat Transfer in Duct System Heat Storage. *Proc. Int. Conf. On Subsurface Heat Storage in Theory and Practice*. Stockholm. Sweden, June 6–8, PP: 652-657
- Thanu, N.M., Sawhney, R.L., Khare, R.N., Buddhi D. (2001), An experimental study of the thermal performance of an earth-air-pipe system in single pass mode, *Sol. Energy* 71 (6) 353–364.

---

## #32: Modern flow field design to enhance the performance of direct methanol fuel cell

---

Osama GAMEA<sup>1</sup>, Shinichi OOKAWARA<sup>2</sup>, Mahmoud AHMED<sup>3</sup>

<sup>1</sup>Department of Energy Resources Engineering, Egypt-Japan University of Science and Technology, Alexandria 21934, Egypt. osama.abdelsamea@ejust.edu.eg

<sup>2</sup>Department of Energy Resources Engineering, Egypt-Japan University of Science and Technology, Alexandria 21934  
Department of Chemical Science and Engineering, Tokyo Institute of Technology, Tokyo 152-8552, Japan 21934  
Egypt. mahmoud.ahmed@ejust.edu.eg

<sup>3</sup>Department of Chemical Science and Engineering, Tokyo Institute of Technology, Tokyo 152-8552, Japan  
sokawara@chemeng.titech.ac.jp

*New modifications are added to the serpentine flow field to enhance the performance of direct methanol fuel cell. The modifications are based on increasing the pressure difference between adjacent channels to increase the under-rib flow. The width of flow channel is contracted between parallel channels with different width values of 0.8, 0.6, and 0.4 mm. The height of the flow field is also decreased from 0.8 to 0.4 mm. To determine the performance parameters of newly proposed designs, a three-dimensional single-phase isothermal model is developed, numerically simulated, and validated using experimental measurements. Decreasing contraction width from 0.8 to 0.4 mm achieved an increase in net generated power density by 6% compared with conventional non-contracted configuration. The maximum increase in performance was 25% and it was noticed when decreasing flow field height to 0.4 mm and using contraction width of 0.4 mm. The increase in performance was a result of boosting reactants concentration by enhancing under-rib flow.*

*Keywords: direct methanol fuel cell; flow field configuration; under-rib flow*

## 1. INTRODUCTION

Deep research is conducted to improve power supplies to portable devices as well as large applications. Conventional power generators using fossil fuels are well-established solution for most applications. With the fact of resources depletion, research focused on sustainable power sources. A variety of renewable power sources are considered; wind, solar, tidal, etc. Unfortunately, most renewable power sources are not consistent and depend on environmental conditions and are usually combined with an energy storage device. Lithium-ion batteries are often used for wide range of applications (Zubi *et al.*, 2018). Fuel cells are efficient energy conversion devices that convert chemical energy stored in fuel into electrical energy directly. Due to the nature of operation of fuel cells, they have higher efficiency than conventional power generators (RYAN *et al.*, 2016). Fuel cells are almost noise free, have no harmful emissions, and have a fast start-up. Fuel cells have several classifications and can operate using different fuels. However, hydrogen is the most famous fuel used and has higher power density, methanol has very attractable specifications that prefer its use in certain applications. Due to its liquid nature at room temperature, methanol is easy to store, handle and transport. Direct methanol fuel cell system also has higher energy density compared with lithium-ion batteries and hydrogen fuel cell system (Majumdar, Revankar and Majumdar, 2014; Joghee *et al.*, 2015). For the advantages of direct methanol fuel cell, extensive research is concerned with increasing its efficiency and getting rid of related operating problems. The main target to increase the efficiency of the direct methanol fuel cell is to increase electrochemical reactions activity at both redox reaction sites; anode and cathode. This can be done by finding better catalysts with minimal cost and developing methods to provide uniform high concentration of reactants at reaction sites. Decreasing the overall resistance of the system, decreasing fuel cross over across membrane, and minimizing size and parasitic loads are also considered goals. The research to improve direct methanol fuel cell performance is divided into three main areas; operating parameters, layers chemical composition, and geometrical design of flow field.

Wide research was conducted on flow field design. El-Zoheiry, Mori and Ahmed (2018) increased the performance of direct methanol fuel cell by presenting new technique in modifying spiral flow field patterning. The increase in power density generated resulted from better mass transport process of reactants. El-Zoheiry, Ookawara and Ahmed (2017) managed to decrease the pressure loss through flow field and developed a criteria to enhance the performance of direct methanol fuel cell by using convection enhanced flow fields. Zhang *et al.* (2011) proposed using tapered configuration of the serpentine flow field which increased pressure difference between adjacent channels and supported mass transport process. This modification resulted in increasing output power compared with conventional flow field. Ramin, Sadeghifar and Torkavannejad (2019) tested the effect of adding traps with different lengths and variable frequency on the performance of polymer electrolyte membrane fuel cell. They noted that the added traps achieved higher oxygen diffusivity, higher current and power densities, and more uniform distribution of reactants and temperature over the catalyst layer. Ouellette *et al.* (2017) presented new bio-inspired flow fields to enhance the performance of direct methanol fuel cell. They tested the performance of the proposed leaf and lung flow fields analytically and experimentally. The proposed flow fields had better effect when used at cathode side. They could achieve the best performance when using methanol solution with concentration of 1.00 M. Hyun *et al.* (2006) analysed numerically the performance of direct methanol fuel cell using four flow field configurations; parallel, serpentine, parallel serpentine and zigzag. The analysis concluded that the zigzag flow field performed best with good resistance to the fuel concentration polarisation. Wang *et al.* (2017) studied the effect of flow field configuration on the under-rib convection and pressure drop in polymer electrolyte membrane fuel cells. The numerical study revealed that narrower channels with smaller cross-section enhance the performance of the fuel cell. Heidary and Kermani (2012) numerically investigated the effect of adding indentations in the flow field. They reported that the indentations enhanced the heat and mass transfer process through the flow field. Vijayakumar *et al.* (2012) conducted experimental investigations on the effect of flow field depth on the performance of direct methanol fuel cell. They concluded that decreasing flow field depth enhances the mass transport process of the reactants to a certain limit. Further depth decreasing has a harmful effect due to the increase of methanol crossover and CO<sub>2</sub> bubbles blocking.

The search for the optimum flow field design is growing to achieve the maximum possible performance with minimum cost and power losses. In this research, new flow fields based on serpentine configuration are proposed and the effect of adding contractions and changing flow field height on the direct methanol fuel cell is tested numerically.

## 2. PHYSICAL MODEL

The direct methanol fuel cell is composed of two compartments; anode and cathode. Each compartment includes a flow field, gas diffusion layer, and a catalyst layer with a polymer electrolyte membrane separating them as seen in Figure 1. Reactants enter the fuel cell at both electrodes' flow fields; fuel at anode and oxygen at cathode. The flow fields distribute reactants on the area of the gas diffusion layers. The gas diffusion layers are porous media which control the transport of reactants to the active catalyst layers. The catalyst layer is the place where electrochemical reactions take place; oxidation at anode releasing electrons to external circuit and protons that cross the membrane and reduction at cathode receiving protons from membrane and electrons from external circuit. The proposed design depends on increasing pressure difference between adjacent channels in serpentine

configuration. The domain considered has an area of 31.00x31.00 mm. The channel height is tested for two values; 0.8, and 0.4 mm. The channel width is 1.00 mm with a variable cross-section ( $x$ ) at the connections between adjacent channels as seen in Figure 2. The variable cross-section takes the values of 0.8, 0.6, and 0.4 mm. Other parameters are mentioned in (Table 1

Table).

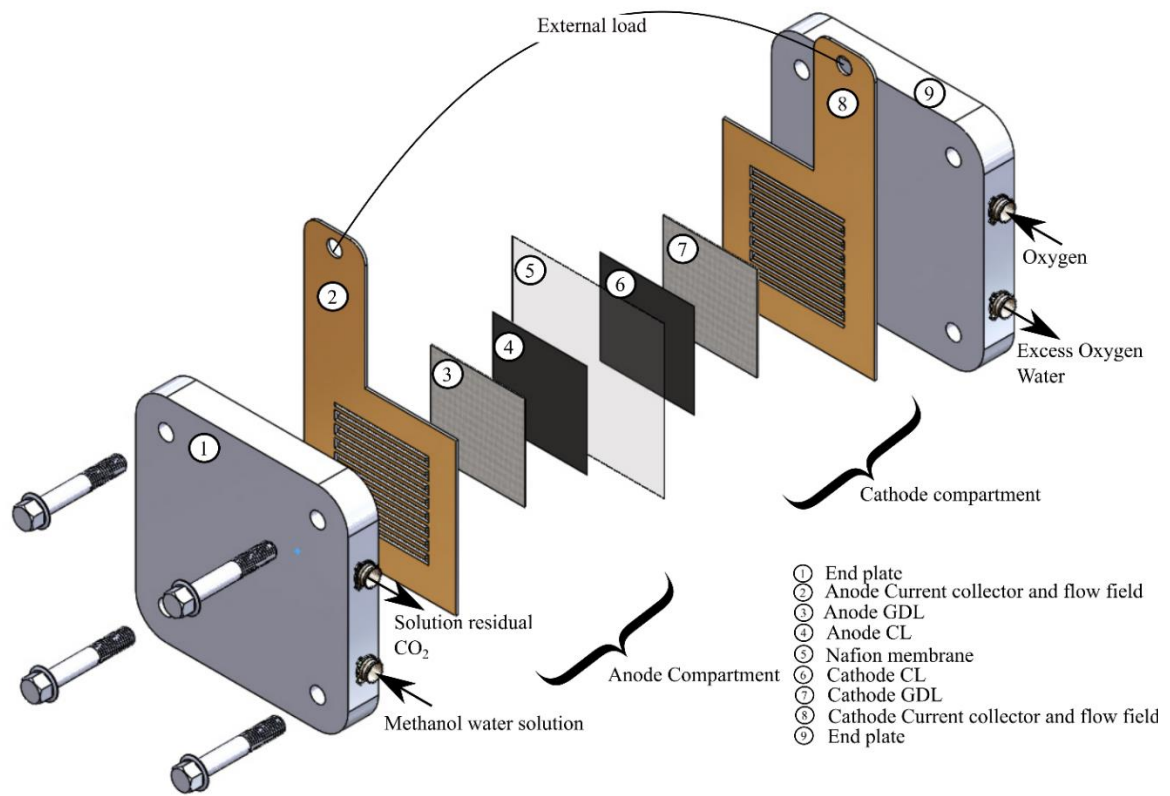


Figure 1: Direct methanol fuel cell components.

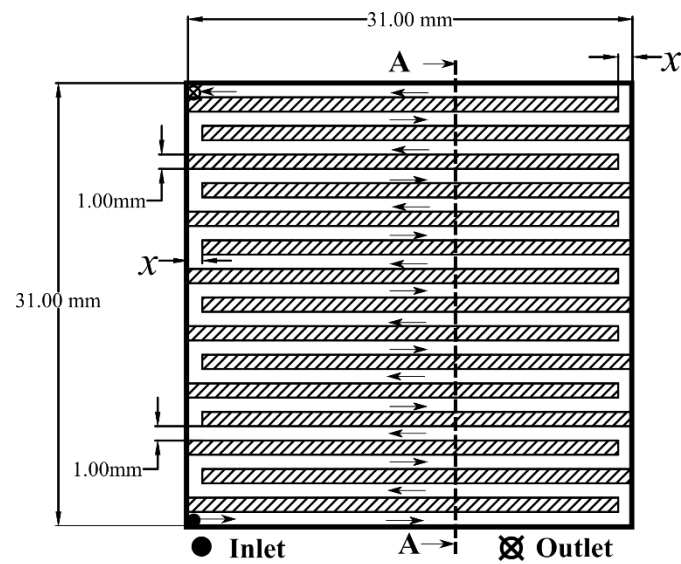


Figure 2: Serpentine flow field design.

Table 1: Design parameters.

Flow field height	0.8 – 0.4 (mm)
Flow field width	1 (mm)
Rib width	1 (mm)
gas diffusion layer thickness	
catalyst layer thickness	0.02 (mm)
Membrane thickness	0.13 (mm)
gas diffusion layer porosity	0.7
catalyst layer porosity	0.3
Membrane porosity	0.3
Nafion volume in catalyst layer	0.4
Permeability of gas diffusion layer	$2 * 10^{-12} (m^2)$
Permeability of catalyst layer	$1 * 10^{-14} (m^2)$
Permeability of the membrane	$2 * 10^{-18} (m^2)$

### 3. THEORETICAL ANALYSIS

The fuel cell technology is a scientific branch with multidisciplinary. To study the effect of flow field geometry on the performance of direct methanol fuel cell, a three-dimensional model is developed. The model accounts for reactants and products flow in flow fields, porous media flow in gas diffusion layers and catalyst layers, electrochemical reactions, and charge transport. For simplicity, acceptable assumptions are considered through the model.

#### 3.1. Model assumptions

- 1) Single phase flow (M. soo Hyun *et al.*, 2006; Wang *et al.*, 2011; Zhang *et al.*, 2011).
- 2) Methanol cross-over is neglected.
- 3) Isothermal operating conditions.
- 4) Homogenous porous domains with isotropic properties.

#### 3.2. Governing equations

Charge conservation through the cell is governed by Ohm's law (Equation 1Equation).

$$\text{Equation 1: Ohm's law} \quad \nabla \cdot (-\sigma \nabla \cdot \varphi) = S$$

Where:

- $\sigma$  = electric conductivity (S/m)
- $\varphi$  = phase potential
- $S$  = current source term (A/m<sup>3</sup>)

The overall electrochemical reaction within the direct methanol fuel cell are mentioned in (Equation 2Equation). Where the relations connecting overpotential and electrochemical reactions at anode and cathode are the Butler-Volmer equation (Equation 3Equation), and the cathodic Tafel equation (Equation 4Equation) (Al-Baghdadi and Al-Janabi, 2007).



Equation 3: Butler-Volmer equation

$$i_a = a_{i_{0a}}^{ref} \left( \frac{C_{MeOH}}{C_{MeOH}^{ref}} \right) \left( \exp \left( \frac{\alpha_a F \eta}{RT} \right) - \exp \left( \frac{-\alpha_c F \eta}{RT} \right) \right)$$

Equation 4: Cathodic Tafel equation

$$i_c = a_{i_{0c}}^{ref} \left( \frac{C_{O_2}}{C_{O_2}^{ref}} \right) 10^{\frac{\eta}{A}}$$

Where:

- $i$  = current production rate (A/m<sup>3</sup>)
- $a_{i_{0a}}^{ref}$  = electrochemical active area per unit catalyst volume, the exchange current density (A/m<sup>3</sup>)
- $C_{MeOH}, C_{O_2}$  = methanol and oxygen concentrations (mol/ m<sup>3</sup>)
- $C_{MeOH}^{ref}, C_{O_2}^{ref}$  = methanol and oxygen reference concentrations (mol/ m<sup>3</sup>)
- $\alpha$  = transfer coefficient
- $F$  = faraday constant (C/mol)
- $\eta$  = overpotential (V)
- $R$  = gas constant
- $T$  = temperature (K)

Free flow in flow fields is governed by continuity (Equation 5Equation), and Navier-Stokes equations (Equation 6Equation ) where porous media flow in gas diffusion and catalyst layers is governed by Brinkmann equations (Equation 7Equation) (Bednarek and Tsotridis, 2017).

Equation 5: Continuity equation

$$\rho \nabla \cdot \mathbf{u} = Q_{br}$$

Where:

- $\rho$  = density (kg/m<sup>3</sup>)
- $\mathbf{u}$  = velocity vector (m/s)
- $Q_{br}$  = mass source term (kg/(m<sup>3</sup>.s))

Equation 6: Navier-Stokes equation

$$\rho(\mathbf{u} \cdot \nabla)\mathbf{u} = \nabla \cdot [-p\mathbf{I} + \mu(\nabla\mathbf{u} + (\nabla\mathbf{u})^T)] + F$$

Where:

- $\square$  = pressure (Pa)
- $\square$  = viscosity (kg/(m.s))
- $\square$  = volume forces (kg/(m<sup>2</sup>.s<sup>2</sup>))

Equation 7: Brinkmann equation

$$\frac{\rho}{\varepsilon_p}(\mathbf{u} \cdot \nabla)\frac{\mathbf{u}}{\varepsilon_p} = \nabla \cdot \left[ -p\mathbf{I} + \frac{\mu}{\varepsilon_p}(\nabla\mathbf{u} + (\nabla\mathbf{u})^T) - \frac{2\mu}{3\varepsilon_p}(\nabla \cdot \mathbf{u})\mathbf{I} \right] - \left( K^{-1}\mu + \frac{Q_{br}}{\varepsilon_p^2} \right)\mathbf{u} + F$$

Where:

- $\varepsilon_p$  = porosity
- $K$  = permeability (m<sup>2</sup>)

Mass transfer in free and porous media is governed by Stefan-Maxwell equations (Equation 8Equation, Equation 9Equation, and Equation Equation10).

Equation 8: Species conservation

$$\nabla \cdot \mathbf{j}_i + \rho(\mathbf{u} \cdot \nabla)\omega_i = R_i$$

Equation 9: Relative mass flux vector

$$\mathbf{j}_i = - \left( \rho\omega_i \sum_k D_{ik} \mathbf{d}_k \right)$$

Equation 10: diffusional driving force

$$\mathbf{d}_k = \nabla x_k + \frac{1}{p} [(x_k - \omega_k)\nabla p - \rho\omega_k \mathbf{g}_k + \omega_k \sum_{l=1}^Q \rho\omega_l \mathbf{g}_l]$$

Where:

- $j_i$  = mass flux vector ( $\text{kg/m}^2\cdot\text{s}$ )
- $\omega_i$  = mass fraction
- $D_{ik}$  = diffusion coefficient ( $\text{m}^2/\text{s}$ )
- $d_k$  = diffusion driving forces ( $1/\text{m}$ )
- $x$  = mole fraction
- $g$  = external force per unit mass ( $\text{m/s}^2$ )

### 3.3. Boundary conditions

- Anode inlet flow rate = 1 mL/min
- Cathode inlet flow rate = 200 mL/min
- Methanol inlet concentration =  $0.5 \text{ mol/m}^3$
- All surfaces are electrically isolated but facing anode current collector which is grounded and facing cathode current collector which is set to cell voltage.

Other operating parameters are mentioned in (Table 2 Table).

Table 2: Operating parameters.

Property	Value
Gas phase dynamic viscosity	$4.05 * 10^{-5} \text{ (kg/ms)}$
Liquid phase dynamic viscosity	$2.03 * 10^{-5} \text{ (kg/ms)}$
gas diffusion layer electric conductivity	$222 \text{ (S/m)}$
Electrolyte conductivity	$9.825 \text{ (S/m)}$
Methanol and water binary diffusion coefficient	$6.69 * 10^{-9} \text{ (m}^2/\text{s)}$
Oxygen and water binary diffusion coefficient	$2.82 * 10^{-5} * (T/308.1)^{1.75} \left(\frac{\text{m}^2}{\text{s}}\right)$
Cell temperature	$75^\circ \text{ C}$
Reference pressure	$1.013 * 10^{-5} \text{ (Pa)}$
Oxygen reference concentration	$0.52 \text{ (mol/m}^3\text{)}$
Methanol reference concentration	$100 \text{ (mol/m}^3\text{)}$
Anode exchange current density	$5 * 10^{-6} \text{ (A/m}^3\text{)}$
Cathode exchange current density	$200 \text{ (A/m}^3\text{)}$
Anode transfer coefficient	$0.5$
Cathode transfer coefficient	$1.2$

## 4. NUMERICAL SOLUTION

Initial guess of concentration is used to get initial current distribution. Then mass and momentum source terms are calculated. After that flow velocity and pressure can be obtained in the computational domain. New concentrations distribution can be calculated and the fully coupled system of equations is solved.

### 4.1. Mesh independence test

A mesh independence test was conducted based on the value of output current for each value of voltage. After four trials with mesh refining, a maximum error of 0.1% was reached at a number of elements of 1,761,408 as seen in (Figure 3Figure).



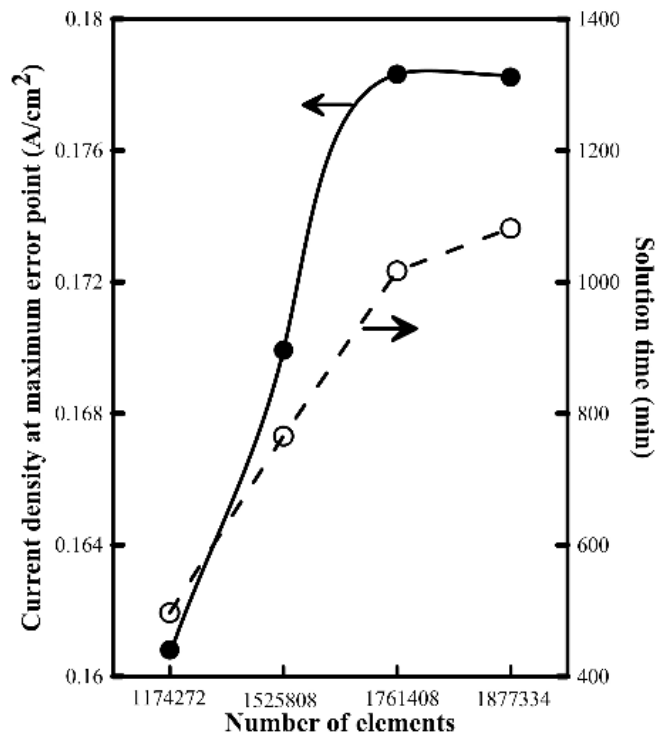


Figure 3: Mesh independence test development.

#### 4.2. Model validation

To validate the used model, comparison between the predicted results' polarisation curve and the measurements of (Vijayakumar *et al.*, 2012) is performed as shown in (Figure 4 *Figure*). The predicted results are obtained using the same geometrical and physical parameters of the described experimental setup. Methanol concentration of 1 M is feed in the anode side at the rate of 4 ml/min while air enters the cathode side at flow rate of 600 cm<sup>3</sup>/min. The experiment tested the performance of the direct methanol fuel cell for two values of flow channel height of 0.8, and 0.4 mm. The model shows good agreement with experimental results for the two cases.

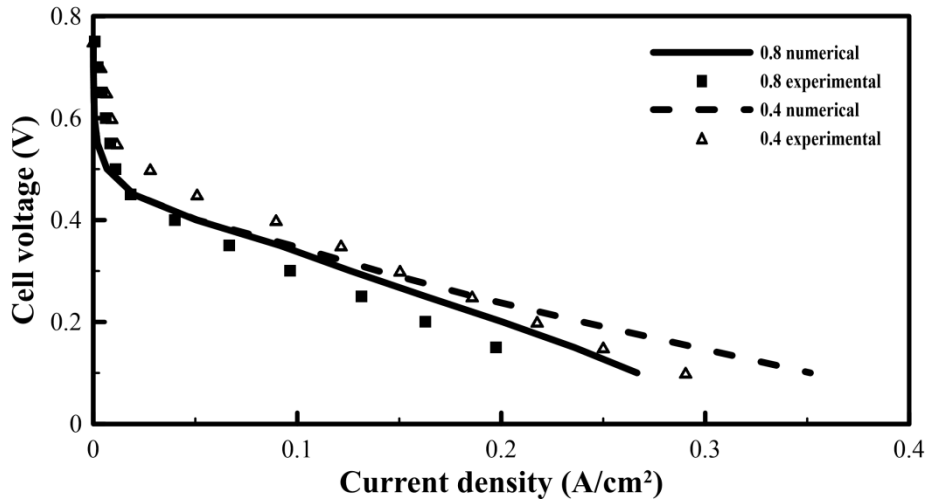


Figure 4: Model validation

## 5. RESULTS

Several performance variables are presented to evaluate the influence of scaling the flow field width on performance.

### 5.1. Pressure distribution

To understand the effect of the modifications on the performance of the fuel cell, pressure difference across ribs between adjacent flow channels is evaluated and plotted in (Figure 5 *Figure*). For each configuration, pressure difference between each two adjacent channels is constant through entire flow field. To define each configuration, height is given letter (h) and contraction value of flow field width is given letter (x) both in millimeters.

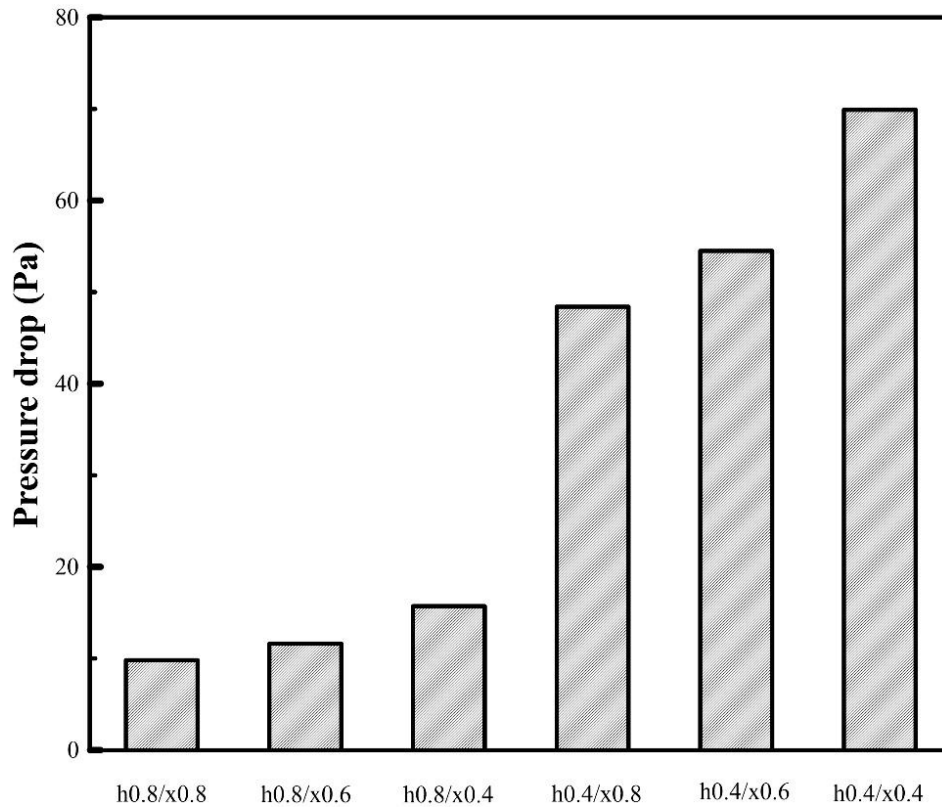


Figure 5: Pressure difference across ribs.

It is noticed that decreasing the width of the flow field between parallel channels increased pressure difference between adjacent channels. Decreasing flow field height also increased total pressure drop and consequently pressure difference between adjacent channels. Increasing pressure drop increases parasitic pumping load. An optimum height should be optimised to balance the benefit of higher under-rib flows without excessive increase in parasitic loads.

## 5.2. Methanol concentration

An efficient flow field would increase the provided reactants to active reaction sites. Local methanol concentration on the surface of the catalyst layer for different flow fields is plotted in (Figure 6Figure).

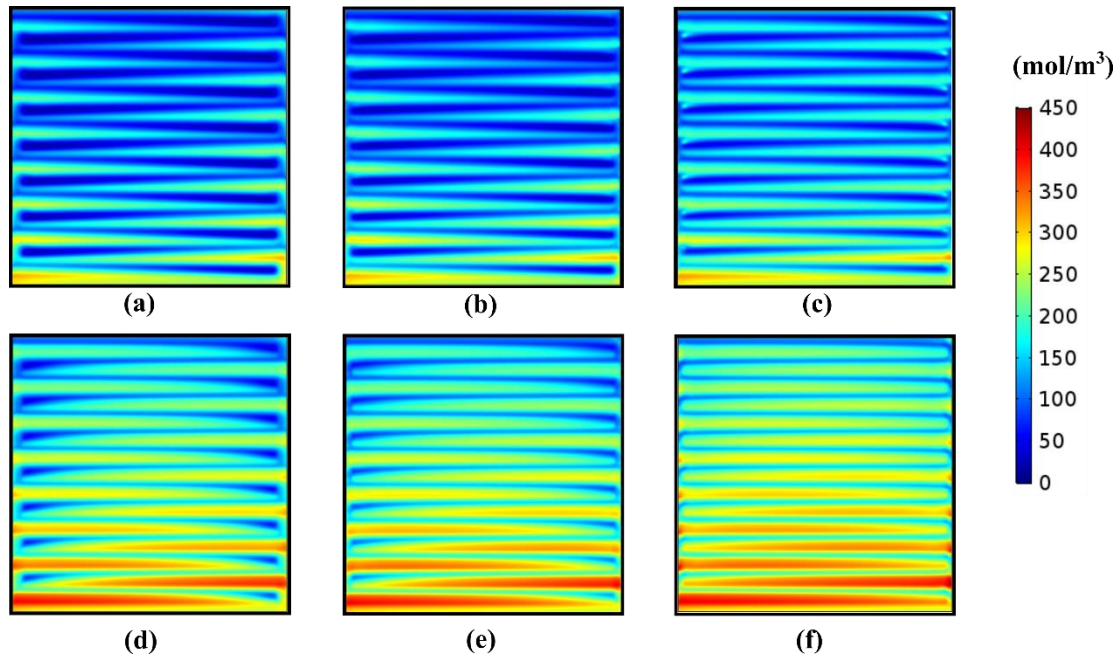


Figure 6: Local methanol concentration.

As can be seen, methanol concentration decreases gradually from inlet to outlet. Decreasing flow field height boosted the methanol concentration by enhancing mass transport through porous layers. The contractions added to flow field bends also had a positive effect as decreasing flow field width at bends from 0.8 to 0.4 mm alleviated methanol concentration provided to the catalyst layer.

### 5.3. Overall performance

To judge the effect of the proposed modifications on the serpentine flow field, the polarisation curve is plotted showing the generated power density for each configuration after deducting pumping loads (Figure 7 Figure).

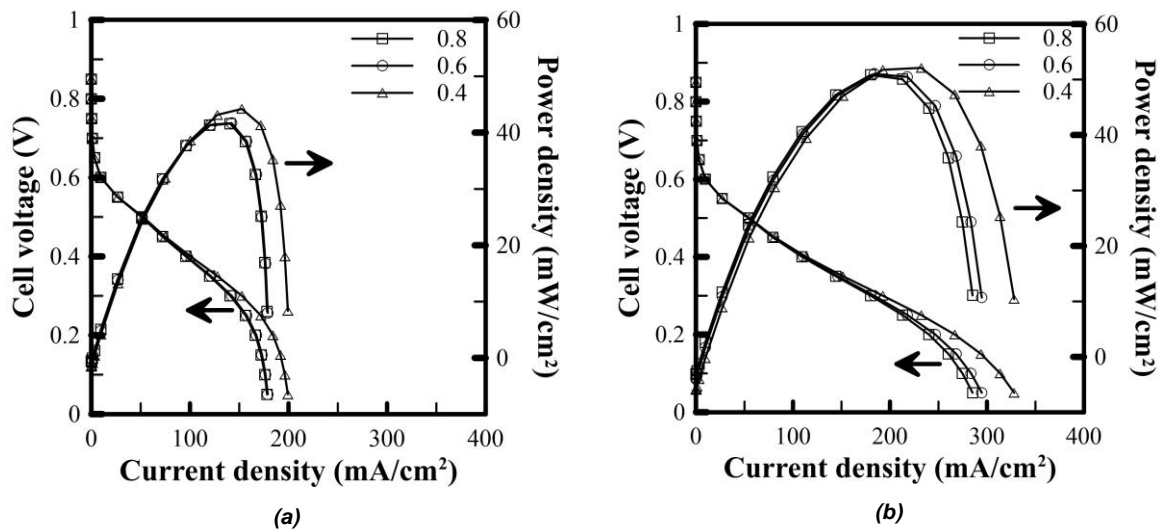


Figure 7: Polarisation curve for different contraction ( $x$ ) value for (a) 0.8 mm height, and (b) 0.4 mm height.

As can be seen, an overall increase in performance is noticed when decreasing flow field height from 0.8 to 0.4 mm as reported by Vijayakumar et al. (2012). Also, an increase in performance is observed with the decrease of the contraction width ( $x$ ) from 0.8 to 0.4 mm for both flow field heights.

## 6. CONCLUSION

A comprehensive three-dimensional single-phase model was used to investigate the effect of adding contraction between adjacent channels in serpentine flow field for direct methanol fuel cell. The contraction width took the values 0.8, 0.6, and 0.4 mm. The flow field height effect on the performance is also tested and took the values 0.8, and 0.4 mm. Decreasing flow field height and decreasing contraction depth increases pressure difference between adjacent channels which increases under-rib flow. The under-rib convection flow enhanced providing methanol with higher concentration to active sites at catalyst layer surface. On the other hand, decreasing flow field height and contraction width increase total pressure drop which increases parasitic pumping loads. An optimisation study should be conducted to find the best values for flow field height and contraction width. An experimental study should also be conducted to visualise the effect of using narrower channels on carbon dioxide bubbles behaviour so as not to cause gas blocking to active reaction sites.

## 7. REFERENCES

- Al-Baghdadi, M. A. R. S. and Al-Janabi, H. A. K. S. (2007) 'Modeling optimizes PEM fuel cell performance using three-dimensional multi-phase computational fluid dynamics model', *Energy Conversion and Management*, 48(12), pp. 3102–3119. doi: 10.1016/j.enconman.2007.05.007.
- Bednarek, T. and Tsotridis, G. (2017) 'Issues associated with modelling of proton exchange membrane fuel cell by computational fluid dynamics', *Journal of Power Sources*. Elsevier B.V, 343, pp. 550–563. doi: 10.1016/j.jpowsour.2017.01.059.
- El-Zoheiry, R. M., Mori, S. and Ahmed, M. (2018) 'Using multi-path spiral flow fields to enhance under-rib mass transport in direct methanol fuel cells', *International Journal of Hydrogen Energy*. Hydrogen Energy Publications LLC, (xxxx). doi: 10.1016/j.ijhydene.2018.11.146.
- El-Zoheiry, R. M., Ookawara, S. and Ahmed, M. (2017) 'Efficient fuel utilization by enhancing the under-rib mass transport using new serpentine flow field designs of direct methanol fuel cells', *Energy Conversion and Management*. Elsevier Ltd, 144, pp. 88–103. doi: 10.1016/j.enconman.2017.04.041.
- Heidary, H. and Kermani, M. J. (2012) 'Performance enhancement of fuel cells using bipolar plate duct indentations', *International Journal of Hydrogen Energy*. Elsevier Ltd, 38(13), pp. 5485–5496. doi: 10.1016/j.ijhydene.2012.10.020.
- Hyun, M. et al. (2006) 'Prediction of anode performances of direct methanol fuel cells with different flow-field design using computational simulation', *Journal of Power Sources*, 157(2), pp. 875–885. doi: 10.1016/j.jpowsour.2006.02.023.
- Hyun, M. soo et al. (2006) 'Prediction of anode performances of direct methanol fuel cells with different flow-field design using computational simulation', *Journal of Power Sources*, 157(2), pp. 875–885. doi: 10.1016/j.jpowsour.2006.02.023.
- Joghee, P. et al. (2015) 'A review on direct methanol fuel cells – In the perspective of energy and sustainability', *MRS Energy & Sustainability*, 2, p. E3. doi: 10.1557/mre.2015.4.
- Majumdar, S. R. and P., Revankar, S. and Majumdar, P. (2014) *Fuel Cells: Principles, Design, and Analysis*, CRC Press. CRC Press. doi: 10.1016/B978-0-12-387709-3.50003-6.
- Ouellette, D. et al. (2017) 'Assessment of different bio-inspired flow fields for direct methanol fuel cells through 3D modeling and experimental studies', *International Journal of Hydrogen Energy*, pp. 1–19. doi: 10.1016/j.ijhydene.2017.06.073.
- Ramin, F., Sadeghifar, H. and Torkavannejad, A. (2019) 'Flow field plates with trap-shape channels to enhance power density of polymer electrolyte membrane fuel cells', *International Journal of Heat and Mass Transfer*. Elsevier Ltd, 129, pp. 1151–1160. doi: 10.1016/j.ijheatmasstransfer.2018.10.050.
- Ryan, O. et al. (2016) *Fuel cell fundamentals*. Third Edit. John Wiley & Sons.

Vijayakumar, R. et al. (2012) 'Effect of anode and cathode flow field depths on the performance of liquid feed direct methanol fuel cells (DMFCs)', *Journal of Applied Electrochemistry*, 42(5), pp. 319–324. doi: 10.1007/s10800-012-0396-2.

Wang, C. et al. (2017) 'The respective effect of under-rib convection and pressure drop of flow fields on the performance of PEM fuel cells', *Scientific Reports*, 7(1), p. 43447. doi: 10.1038/srep43447.

Wang, S. J. et al. (2011) 'Computational simulation and experimental evaluation on anodic flow field structures of micro direct methanol fuel cells', *Applied Thermal Engineering*. doi: 10.1016/j.applthermaleng.2011.05.013.

Zhang, Y. et al. (2011) 'A tapered serpentine flow field for the anode of micro direct methanol fuel cells', *Journal of Power Sources*. doi: 10.1016/j.jpowsour.2010.12.012.

Zubi, G. et al. (2018) 'The lithium-ion battery: State of the art and future perspectives', *Renewable and Sustainable Energy Reviews*, 89(March), pp. 292–308. doi: 10.1016/j.rser.2018.03.002.

---

## #35: Optical-thermal-electrical characteristic and modelling of solar modules

---

Lu SHEN, Tao MA

*School of Mechanical Engineering, Shanghai Jiao Tong University, Shanghai, China*

*The key to improving solar module efficiency is to mitigate the losses during carries' generation, transportation and recombination process and cell to module process. These losses can be classified into optical, thermal and electrical mechanisms, such as the mismatch between energy of incident photo and band gap of semiconductor material, radiation emitted to the environment and structural defects and impurities. Photovoltaic effect refers to conversing solar energy to chemical potential energy and to electricity finally. This paper aims to analyse and quantify the losses and thermal sources generated during this whole conversion process. A comprehensive model which combines the experimental performance parameters and microscopic operation mechanisms is developed, to calculate the optical and electrical losses, heat source generation and ultimate power output efficiency of the solar module under actual operating condition. The results show that, for a real silicon solar module with conversion efficiency at 18.50%, about 66.01% solar energy is lost in carries generation, with remaining 2.29% and 10.91% in transport and recombination process, respectively. Also, about 2.3% of incident energy is lost from cell to module process. Those losses, approximately 62.92%, are transformed into thermal source, which rises the cell temperature. Besides, almost 18.58% of total energy leaves the cell due to multilayer reflection. Furthermore, some suggestions are provided in the end to control losses and improve module performance.*

*Keywords: solar cell; photovoltaic effect; optical-thermal-electrical loss; heat source; cell performance*

## 1. INTRODUCTION

Energy and environmental issue is the focus of common concern in the world today. Solar photovoltaic power generation is considered to be the most attractive and promising technology in renewable energy (You et al., 2013, Ma et al., 2014). According to the well-known Shockley and Queisser (SQ) efficiency limit, the maximum efficiency of solar cell is concerned as 30% (Shockley and Queisser, 1961). For a real solar cell, however, the conversion efficiency is much lower than that and losses are occurred in the whole physical process, including carriers' generation, transportation and recombination (Polman and Atwater, 2012). For a solar module, there are other loss factors from cell to module (CTM), such as reflection and resistance loss in interconnection (Haedrich et al., 2014). Thus, analysis and quantification of losses in solar modules is essential to optimise the module structure and improve electricity efficiency.

In the literature, different methods to quantify and mitigate losses in solar modules have emerged (Hanifi et al., 2018, Yang et al., 2017, Zhang et al.). They analysed the optical losses of solar modules and evaluated the impacts of different approaches to reduce these losses, while other losses, especially heat source, are not mentioned in these research (Schneider et al., 2014, Krauter and Grunow, 2006, Lu and Yao, 2007). Louise et al. (Hirst and Ekins - Daukes, 2011) quantified five intrinsic losses process of solar cell and introduced advanced devices to avoid these losses. Nelson et al. (Nelson et al., 2013) focused on below band-gap and thermalisation (hot carrier) losses and the necessity of hot carrier scattering and the challenge of photon flux are discussed in their research. Intrinsic losses are dominant but in real solar cells, there are more loss mechanisms that influence the final conversion efficiency. To analyse the whole loss mechanisms and thermal sources generation process, an integrated optical-electrical-thermal (OET) model, compromising the accuracy and simplification, is proposed in this paper for solar modules.

## 2. OPTICAL-ELECTRICAL-THERMAL MODELING OF SOLAR MODULE

To figure out these all loss process in solar cells, this paper presents a comprehensive model to analyse and quantify the OET losses at maximum power point in solar cells with the coupled model presented in Figure 1 *Figure* . Firstly, the parameters under standard test condition (STC), such as solar radiation and cell temperature, the optical properties and electrical characteristics of a solar cell are input into the model. With these input, the loss in cell and from cell to module can be calculated. Finally, the difference between total incident energy and loss energy is the power generated indeed. By the way, the OET characterization of solar modules is also available on this model.

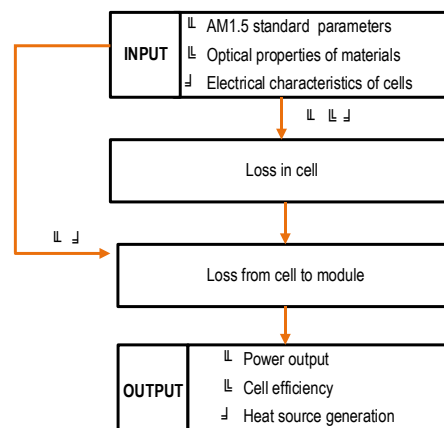


Figure 1: the structure chart of the energy loss model.

### 2.1. Cell loss

#### *Losses in carriers' generation process*

To analyse the losses in carriers' generation process, there are two main losses mechanisms, i.e. transmission/reflection loss and spectral mismatch loss. The reflection and absorption loss usually exist in the interface between air and glass, glass and encapsulant and solar cell, solar cell and back sheet, if a general solar cell is considered (as presented in Figure 2 *Figure* ). The hemispheric global reflection and transmission can be measured by spectrometer or achieved from optical simulation program OPAL 2 (Mcintosh and Baker-Finch, 2012)



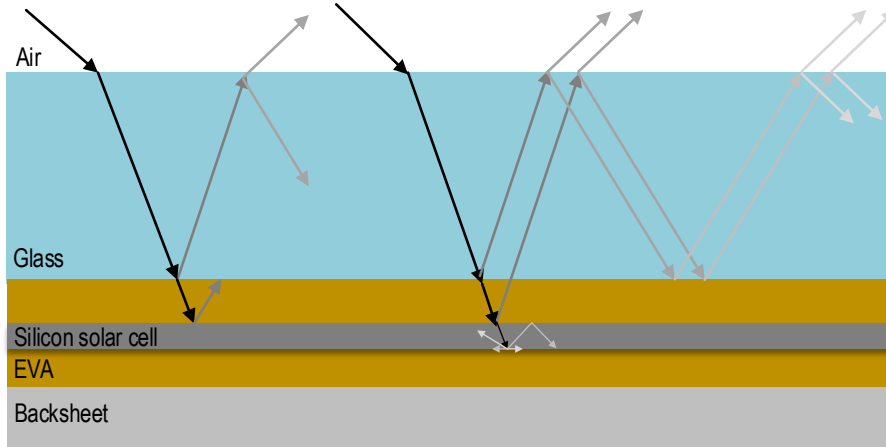


Figure 2: Light path inside the solar cell

By excluding the reflection and absorption losses in solar cell, the rest of total incident photons is assumed to enter the silicon cell, as shown in Equation 1 Equation and Equation 2. After that, there are two factors to limit the carriers' generation rate in silicon, namely sub-bandgap loss and thermalisation loss.

Equation 1: Reflection and absorption losses in solar cell

$$P_{optical}(\lambda) = P_{incident}(\lambda) \cdot R(\lambda) \cdot \alpha(\lambda)$$

Equation 2: The rest of total incident irradiance

$$P_{entering}(\lambda) = P_{incident}(\lambda) - P_{optical}$$

Where:

$P_{optical}(\lambda)$  = reflection and absorption losses (W/m<sup>2</sup>)

$P_{incident}(\lambda)$  = total incident irradiance (W/m<sup>2</sup>)

$P_{entering}(\lambda)$  = the rest of incident irradiance (W/m<sup>2</sup>)

$R(\lambda)$  = global reflection coefficient

$\alpha(\lambda)$  = global transmission coefficients

It is obvious, not every incident photon can contribute to photocurrent. The distribution of photons entering cells is also related to their energy. The energy of one photon depends on its wavelength. Figure 3Figure shows the results caused by photons with different wavelength. Spectral mismatch losses include sub-bandgap and thermalisation losses. The losses due to sub-bandgap and thermalisation mechanisms can be expressed by Equation 3 and Equation 4 respectively:

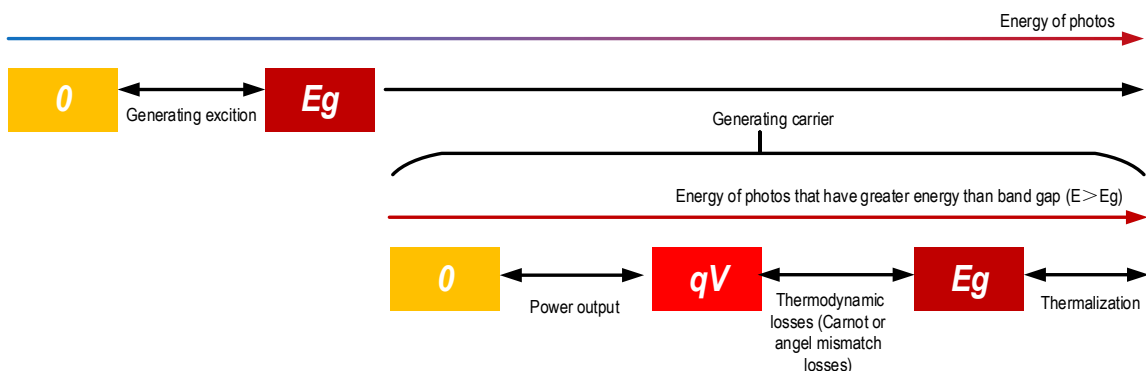


Figure 3: The results caused by photons with different energy levels

Equation 3: Reflection and absorption losses in solar cell

$$Q_{sub-bandgap} = \int_0^{E_g} P_{entering}(E) \cdot PFD(E) dE$$

Equation 4: The rest of total incident irradiance

$$Q_{\text{thermalization}} = \int_{E_g}^{\infty} P_{\text{entering}}(E) \cdot \text{PFD}(E) dE - P_{\text{entering}}(E_g) \cdot \text{PFD}(E_g) \cdot E_g$$

Where:

PFD( $\lambda$ ) = the photon flux density ( $\mu\text{E}$ )  
 $E_g$  = bandgap of semiconductor material (eV)

#### Losses in carriers' transportation process

After generation, the carriers could lose kinetic energy to atoms and lattice in their transportation path, therefore the heat is induced, which is also called series resistance loss. Simultaneously, the shunt resistance loss due to leakage current can be defined as a kind of losses in transportation process as well.

Series and shunt resistance loss can be calculated in the form of Joule heating equation (Equation 5) (Dupré et al., 2017) and Equation 6:

Equation 5: Reflection and absorption losses in solar cell  $Q_{\text{series}} = J_{\text{MPP}}^2 \cdot R_s$

Equation 6: The rest of total incident irradiance  $Q_{\text{shunt}} = \frac{V_{\text{shunt}} + J_{\text{shunt}} \cdot R_s}{R_{\text{sh}}} \cdot \frac{E_g}{q}$

Where:

$R_s$  = series resistance of solar cell ( $\Omega$ )  
 $R_{\text{sh}}$  = shunt resistance ( $\Omega$ )  
 $V_{\text{shunt}}$  = voltage of the shunt path (V)  
 $J_{\text{shunt}}$  = current of the shunt path ( $\text{A}/\text{m}^2$ )

#### Losses in carriers' recombination process

Carriers are generated due to photovoltaic effect; on the other hand, they can be recombined due to radiation and non-radiation recombination at the same time. The main recombination mechanisms in a solar cell are listed in Table 1. Any recombination mechanism, including radiative and non-radiative recombination, has dual impacts to output power. On one side, the shortage of the number of excited charges that could go through external circuit leads the loss of current. For example, as for radiative recombination, the inducement of current loss is the rising dark current. On the other side, the diminishment of generation-recombination balance also reduces the voltage that builds in the cell, which can be called Carnot and angle mismatch loss. Just like other heat engines, the conversion efficiency of a solar cell is limited by Carnot efficient and the hot reservoir, i.e. the Sun. Additionally, according to the Kirchhoff's law, the emission angle is much bigger than absorption angle of a solar cell, which also results in the drop of voltage and heat generation (Kosten and Atwater, 2011).

Table 1: The three main recombination mechanisms in solar cells

The recombination mechanisms	The main result	Degree of influence	Can be avoided?
Radiation recombination	Spontaneous emission recombination Stimulated emission recombination	Photons emission	Dominant loss in ideal semiconductors
Auger recombination	Increasing the kinetic energy of other carriers and rising cell temperature	Dominant loss in intermittent bandgap semiconductor	Related to band structure, cannot be avoided
Shockley Read Hall (SRH) recombination	Surface recombination Grain boundary recombination Bulk recombination	Providing phonons for lattice vibration and rising cell temperature	Dominant loss in actual semiconductor
			Only happen in defect semiconductors and can be avoided

For radiative recombination, the emission loss generating from photon emission can be neglected. Then, the current and voltage drop loss led by non-radiative recombination can be calculated by Equation 7 and Equation 8:

Equation 7: Reflection and absorption losses in solar cell

$$Q_{NRR-\Delta J} = E_g \left( \frac{1}{ERE} - 1 \right) \cdot \frac{2\Omega_{emit}}{c^2 \cdot h^3} \cdot \int_{E_g}^{\infty} \frac{\overline{EQE} \cdot E^2}{\exp\left(\frac{E - q \cdot V_{MPP}}{k \cdot T_c}\right) - 1} dE$$

Equation 8: The rest of total incident irradiance

$$Q_{NRR-\Delta V} = J_{MPP} \cdot \frac{k \cdot T_c}{q} \cdot \ln\left(\frac{1}{ERE_{MPP}}\right)$$

Where:

- ERE = external radiative efficiency
- C = speed of light (2.998\*E8 m/s)
- H = Planck constant (6.63\*E-34 J/s)
- $\Omega_{emit}$  = solid angle of emission
- K = Boltzmann's constant (1.38\*E-23 J/K)
- $\overline{EQE}$  = external quantum weighted average efficiency
- $T_c$  = cell temperature (K)

Then the Carnot and loss can be expressed in Equation 9 and Equation 10:

Equation 9: Reflection and absorption losses in solar cell

$$Q_{NRR-\Delta J} = E_g \left( \frac{1}{ERE} - 1 \right) \cdot \frac{2\Omega_{emit}}{c^2 \cdot h^3} \cdot \int_{E_g}^{\infty} \frac{\overline{EQE} \cdot E^2}{\exp\left(\frac{E - q \cdot V_{MPP}}{k \cdot T_c}\right) - 1} dE$$

Equation 10: The rest of total incident irradiance

$$Q_{NRR-\Delta V} = J_{MPP} \cdot \frac{k \cdot T_c}{q} \cdot \ln\left(\frac{1}{ERE_{MPP}}\right)$$

Where:

- q = elementary charge
- $\Omega_{abs}$  = solid angle of absorption
- $T_s$  = sun temperature (5800K)

## 2.2. Modelling of losses from Cell to module

Reflection loss in interconnection

To calculate the efficiency of PV module, some other factors need to be considered. As depicted in Figure 4, the incident light would be reflected in these inactive areas (Haedrich et al., 2014) Then, the loss power due to reflection of interconnection can be written in Equation 11:

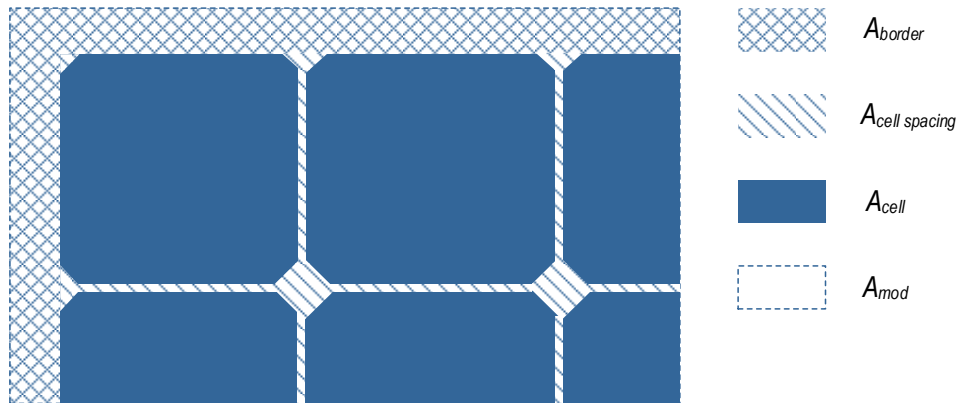


Figure 4: A schematic diagram describing relevant details of the PV module (Haedrich et al., 2014)

Equation 11: Reflection loss in inactive areas.

$$P_{inactive} = P_{cell} \cdot N_s \cdot N_p \cdot \left( 1 - \frac{A_{border} + A_{cell\_spacing}}{A_{mod}} \right)$$

Where:

- $A_{border}$  = the area from module edge to cell edge (m<sup>2</sup>)
- $A_{cell\_spacing}$  = the area between cells (m<sup>2</sup>)
- $A_{cell}$  = the area of silicon wafer (m<sup>2</sup>)
- $A_{mod}$  = total module area (m<sup>2</sup>)
- $P_{cell}$  = the actual output power of individual crystalline silicon cell (W/m<sup>2</sup>)
- $N_s$  = the number of series cell in a module
- $N_p$  = the number of parallel cell in a module

#### Resistive loss in interconnection

Because of the ohmic effect, when the current passes through the interconnect ribbons ((tabbing & stringing), some parts will be dissipated in the form of heat. Such kind of electrical loss depends on the current through the ribbons and the equivalent resistance of the internal connection, which can be calculated by Equation 12 and Equation 13 (Hanifi et al., 2016):

Equation 12: Carnot loss.

$$R_{eff} = \rho_{ribbon} \cdot I$$

Equation 13: Angle mismatch loss.

$$Q_{interconnection} = R_{eff} \cdot I^2$$

Where:

- $\rho_{ribbon}$  = the conductivity of the ribbon
- $R_{eff}$  = the equivalent resistance in the interconnection

### 3. RESULTS AND DISCUSSIONS

Based on the developed OET model, the specific losses of module can be calculated and the results are listed in Table 2

Table and Figure 5. The results show that the loss in carriers' generation process, which refers to the optical and spectral mismatch loss, plays the most important role to restrict the total conversion efficiency. The Carnot loss and angle mismatch loss take up a great proportion as well. Figure 5 (a) shows the proportion of each loss mechanism of the solar module. According to this figure, the carriers' generation, transportation and recombination and CTM loss are 66.01%, 2.29%, 10.91% and 2.30%, respectively, and the resultant efficiency is 18.50%. The energy loss may leave the cell, i.e. reflection loss, or they are converted to heat. It can be also obtained from Figure 5 (b) that almost 63% of incident energy in solar modules is converted to heat and increase cell temperature. Some of these losses are intrinsic and cannot be avoided while the rest can be mitigated with suitable managements. For example, texturing surface and light trapping structure are two promising applications to diminish the reflection and absorption loss. The up-conversion or down-conversion and multi-junction device can contribute to the reduction of loss caused by spectral mismatch. Increasing shunt resistance or decreasing series resistance are also practical mitigation pathways. Minimizing impurity and solid angle mismatch could play an important role as well.

Table 2: Energy distribution and heat source of four samples.

$P_{incident}$ (W/m <sup>2</sup> )	1000	$Q_{Carnot}$ (W/m <sup>2</sup> )	18.81
$P_{optical}$ (W/m <sup>2</sup> )	171.28	$Q_{angle\_mismatch}$ (W/m <sup>2</sup> )	90.16
$P_{entering}$ (W/m <sup>2</sup> )	828.72	$P_{space}$ (W/m <sup>2</sup> )	14.50
$Q_{sub-bandgap}$ (W/m <sup>2</sup> )	168.40	$Q_{resistance}$ (W/m <sup>2</sup> )	8.49
$Q_{thermalization}$ (W/m <sup>2</sup> )	320.41	$P_{output}$ (W/m <sup>2</sup> )	184.99 W
$Q_{series}$ (W/m <sup>2</sup> )	9.39	$Q_{total}$ (W/m <sup>2</sup> )	720.10W
$Q_{shunt}$ (W/m <sup>2</sup> )	13.47	Calculated efficiency (%)	18.50
$P_{emission}$ (W/m <sup>2</sup> )	0.059	Real efficiency (%)	18.30

$Q_{NRR-\Delta J}$ (W/m <sup>2</sup> )	0	Error (%)	1.09
$Q_{NRR-\Delta V}$ (W/m <sup>2</sup> )	0.045		

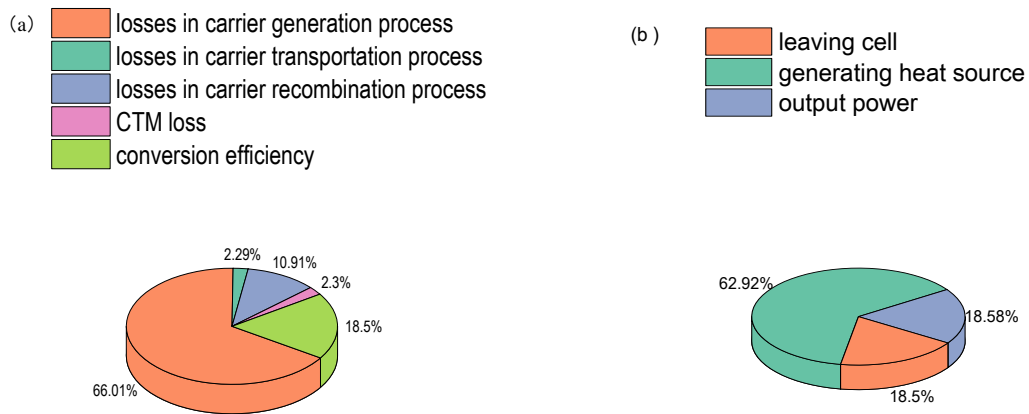


Figure 5: (a) Losses mechanisms in solar modules; (b) The distribution of incident solar radiation in solar modules.

#### 4. CONCLUSIONS

To conclude, this paper presents an OET model to determine and quantify the loss in carriers' generation, transportation and recombination process and cell to module process in the solar module. The results show that, for a real crystalline silicon PV module, about 66.01% solar energy is lost in carries generation, with remaining 2.29%, 10.91% and 2.30% in transport, recombination and cell to module process, respectively. It can also be obtained that 62.92% and 18.58% of incoming solar energy is leaving the cell and generating heat source. For future work, the temperature coefficients of solar cell will be concerned in detail and the thermal resistance model will be built including the heat transfer between the cell and environment.

## 5. REFERENCES

- Dupré, O., Vaillon, R. & Green, M. A. 2017. Specificities of the Thermal Behavior of Current and Emerging Photovoltaic Technologies.
- Haedrich, I., Eitner, U., Wiese, M. & Wirth, H. 2014. Unified methodology for determining CTM ratios: Systematic prediction of module power ☆. *Solar Energy Materials & Solar Cells*, 131, 14-23.
- Hanifi, H., Dassler, D., Schneider, J., Turek, M., Schindler, S. & Bagdahn, J. 2016. Optimized Tab Width in Half-cell Modules ☆. *Energy Procedia*, 92, 52-59.
- Hanifi, H., Pfau, C., Turek, M. & Schneider, J. 2018. A practical optical and electrical model to estimate the power losses and quantification of different heat sources in silicon based PV modules. *Renewable Energy*, 127.
- Hirst, L. C. & Ekins-Daukes, N. J. 2011. Fundamental losses in solar cells. *Progress in Photovoltaics Research & Applications*, 19, 286-293.
- Kosten, E. D. & Atwater, H. A. 2011. Limiting acceptance angle to maximize efficiency in solar cells. *Proceedings of SPIE - The International Society for Optical Engineering*, 8124, 103-112.
- Krauter, S. & Grunow, P. 2006. Optical modelling and simulation of PV module encapsulation to improve structure and material properties for maximum energy yield. *Conference Record of the 2006 IEEE 4th World Conference on Photovoltaic Energy Conversion, Vols 1 and 2*, 2133-+.
- Lu, Z. H. & Yao, Q. 2007. Energy analysis of silicon solar cell modules based on an optical model for arbitrary layers. *Solar Energy*, 81, 636-647.
- Ma, T., Yang, H. & Lu, L. 2014. Development of a model to simulate the performance characteristics of crystalline silicon photovoltaic modules/strings/arrays. *Solar Energy*, 100, 31-41.
- Mcintosh, K. R. & Baker-Finch, S. C. OPAL 2: Rapid Optical Simulation of Silicon Solar Cells. *Photovoltaic Specialists Conference*, 2012.
- Nelson, C. A., Monahan, N. R. & Zhu, X. Y. 2013. Exceeding the Shockley–Queisser limit in solar energy conversion. *Energy & Environmental Science*, 6, 3508-3519.
- Polman, A. & Atwater, H. A. 2012. Photonic design principles for ultrahigh-efficiency photovoltaics. *Nat Mater*, 11, 174-7.
- Schneider, J., Turek, M., Dyrba, M., Baumann, I., Koll, B. & Booz, T. 2014. Combined effect of light harvesting strings, anti-reflective coating, thin glass, and high ultraviolet transmission encapsulant to reduce optical losses in solar modules. *Progress in Photovoltaics*, 22, 830-837.
- Shockley, W. & Queisser, H. J. 1961. Detailed Balance Limit of Efficiency of p-n Junction Solar Cells. *Journal of Applied Physics*, 32, 510-519.
- Yang, Z., Fang, Z., Sheng, J., Ling, Z., Liu, Z., Zhu, J., Gao, P. & Ye, J. 2017. Optoelectronic Evaluation and Loss Analysis of PEDOT:PSS/Si Hybrid Heterojunction Solar Cells. *Nanoscale Research Letters*, 12, 26.
- You, J., Dou, L., Yoshimura, K., Kato, T., Ohya, K., Moriarty, T., Emery, K., Chen, C. C., Gao, J. & Li, G. 2013. A polymer tandem solar cell with 10.6% power conversion efficiency. *Nature Communications*, 4, 1446.
- Zhang, C., Cao, G., Wu, S., Shao, W., Giannini, V., Maier, S. A. & Li, X. Thermodynamic loss mechanisms and strategies for efficient hot-electron photoconversion. *Nano Energy*.

---

## #36: Passive design methods for a sustainable house

---

Shihao ZHANG<sup>1\*</sup>, Qi Xu<sup>2</sup>, Saffa RIFFAT<sup>3</sup>

<sup>1</sup>Department of Architecture and Built Environment, Faculty of Engineering, University of Nottingham, NG7 2RD  
University Park, Nottingham, UNITED KINGDOM  
Shihao.zhang@nottingham.ac.uk

<sup>2</sup>Department of Architecture and Built Environment, Faculty of Engineering, University of Nottingham, NG7 2RD  
University Park, Nottingham, UNITED KINGDOM  
Qi.xu1@nottingham.ac.uk

<sup>3</sup>Department of Architecture and Built Environment, Faculty of Engineering, University of Nottingham, NG7 2RD  
University Park, Nottingham, UNITED KINGDOM  
saffa.riffat@nottingham.ac.uk

\*Corresponding Author

*Rapid growth in world energy usage has caused concern about supply difficulties, energy depletion, and serious environmental impacts. 'Passive design' is design that takes advantage of the environment factors to maintain a comfortable temperature range. It uses 'natural' sources of heating, cooling and ventilation to create comfortable conditions inside buildings, not like conventional sustainable building using the HVAC or the sustainable technologies, such as insulation material to save energy. Passive design enjoys great potential to reduce the carbon emission without other incremental cost compared with traditional house. This paper investigates the current designing practice and experience to minimise the energy consumption of house operation. A substantial investigation into the impact of passive design measures for a case house is covered. This level of understanding is essential if we are to choose rational passive strategies for future sustainable building.*

*Keywords: passive design; sustainable building; low-carbon technology*

## 1. INTRODUCTION

There are severe challenges for the future, such as taking a responsible approach towards nature. In addition, there is the search for an environmentally friendly energy supply that is easy on resources and climate. A further challenge is the search for clean sources of drinking water. Aside from novel and more efficient technologies than are currently in place, additional emphasis will need to be placed on reducing energy and water requirements without decreasing either comfort levels or living standards.

Green buildings are capable of meeting even the most stringent demands for aesthetics and architecture, which is something that the examples given in this research clearly show. Planning these buildings, according to an integrated process, requires the willingness of all those involved: to regard the numerous interfaces as seams of individual assembly sections, the synergies of which are far from being exhausted yet. A holistic and specific knowledge is needed regarding essential climatic, thermal, energy-related, aero-physical and structural-physical elements and product merits which do not end at the boundaries of the individual trades.

In recent years, there has been increasing interest among entrepreneurs and architects seeking to introduce intelligent buildings into the built environment. The passive design applied by architects when designing buildings respond to climate conditions and requirement (Ahmad et al. 2016). They aim to accomplish efficient levels of energy consumption in buildings, to meet national goals. Globally, lighting, heating, cooling and air conditioning are responsible for two fifths of the total world annual energy consumption. Also, devices cause considerable environmental impact (EI) due to the related GHG emission (Omer 2011). Moreover, there is a considerable increase in global energy consumption due to human needs for more comfortable interior environments. Since the approving of the Montreal Protocol, governments are working to phase out the refrigerants that could destroy stratospheric ozone. Therefore, new power resource production is required. There has been a renewed interest in cooling and heating technologies to reduce the EI.

## 2. GREEN BUILDING REQUIREMENTS

Energy consumption patterns depend on local climate conditions, the culture of the citizens and the policies of the country. There is not a single efficient solution suitable for all buildings in the world. Developed countries are developing energy conservation in the building sector in general and in residential buildings. In addition, these countries have systematic Greenhouse Gas (GHG) Emission Reduction policies and criteria defining the band of energy consumption in domestic buildings in kWh/m<sup>2</sup>. The passive house standard includes several criteria, but the main one is the low annual heating demand – not more than 15 kWh/m<sup>2</sup>. Sustainable houses and energy conservation in buildings remain targets for developed countries to address to achieve sustainable environmental and economic development.

Reportedly, about 40% of energy use is consumed by building related industry (Gong & Song 2015). Moreover, the building sector consumes 40% of the world's energy, 16% of the world's fresh water (Ghiaus & Inard 2004) and produces 33% of global GHG emission (Berardi 2016). As for heating and cooling, the energy required is around 40% of the total world annual consumption, involving a great amount of GHG emission (Omer 2013). In the last decades, the development of air conditioning demands a considerable increase in electricity (Chiesa et al. 2014; Omer 2013). In response to these statistics, there is considerable interest in the world, promoting environment protection. All the world governments are creating an awareness of sustainable development by producing environment-friendly design that can use the least energy to satisfy the most comfortable interior environment. Such concepts would account for interactions among the dynamic conditions affecting each building's unique environment (Férey 2000). Because of the need to reducing energy consumption, researchers have proposed several sustainable approaches and energy efficient technology (Berardi 2016). However, the way we are able to integration these high-tech devices are also a barrier for the development of low-carbon house. The prefabricated building would be a key point under the current circumstances. It is extremely important to review that area to identify the realistic way to accomplish it.

### Sustainable design

Sustainable design regards the particular way to construct and operate a building by as much as natural resources, such as the heat, air, passive solar gain and cooling. Through implementing passive design, the use of mechanical system can be reduced by about 80%.

The Passive House standards for Germany require that buildings should satisfy the following requirements:

- The annual heating/cooling demand must not be more than 15 kWh/m<sup>2</sup> per year.



- Total primary energy (source energy for electricity etc.) consumption (primary energy for heating, hot water and electricity) must not be more than 120 kWh/m<sup>2</sup> per year.
- The maximum of 0.6 air changes per hour at 50 Pascals pressure
- Thermal comfort must be met for all living areas year-round with not more than 10% of the hours in any given year over 25°C

In order to achieve the above standards, it is necessary to follow the passive design principles that help reduce the energy demand. Buildings designed to the Passive House standard require a well-insulated building envelope with a ventilation system that can recover heat from the exhaust air. In such a sustainable building, the space heating requirements are no longer so serious. To achieve these low energy targets the building design has to exceed the normal regulatory requirements for insulation and air tightness. Experience, mainly within Germany and Austria, has shown that it is possible and economically viable to build these particular kinds of construction and that they can maintain good air quality and thermal comfort throughout the year.

### 3. DESIGN, CONSTRUCTION, COMMISSIONING AND MONITORING FOR GREEN BUILDINGS

#### 3.1. Buildings

Low-carbon prefabricated housing is another side of the issue of the sustainable house. Nowadays, many governments encourage the low-carbon design, the passive design refer to the architectural strategies applied by the architect and engineering to respond the climate conditions and requirements (Ahmad et al. 2016). 'Low carbon energy buildings', 'eco-houses' and 'green buildings', are terms commonly used by both engineers and architects. Low-carbon houses are intended to reduce the environment impact of the construction. With the help of suitable architectural design, the comfort interior environment can be achieved, which means the need for the energy for the cooling or heating can be deduced. In the most stressful seasons - summer and winter - the indoors temperature should be the primary consideration of the building design (Ochoa & Capeluto 2008). Besides the mechanical improvement through innovation of the ventilation, such as power fans or pump, the natural heat transfer approach is also available, including convection, conduction, radioactivity and evaporation. During the summer season, the cooling strategies should be prepared in three phases to avoid overheating in the interior of building:

- Adjustment of heat gains
- Inhibition of heat gains in the building
- Rejection of heat to heat sinks from the interior of the building (hybrid or natural cooling).

Table 1: the reference for architectural design which the common passive strategies for the components in prefabricated building

Passive Strategies	Reference	Statement
<b>Orientation on building</b>	(Morrissey et al. 2011)	the easiest approach in achieving thermal comfort is the adherence to the oriented buildings
	(Bekkouche et al. 2011)	positioning the house in the right direction is entailed in the central principle during building design
	(Haase & Amato 2009) (Olgay 1967)	solar radiation can be determined by the orientation building alignment corresponding to local climatic conditions to maximise the natural benefit
<b>Building layout (Shape)</b>	(Okeil 2010)	ventilation dependent on the building shape
	(Capeluto 2003)	Self-shading has significant impact on the interior spaces
<b>Building envelope</b>	(Capeluto 2003)	The cooling or heating systems can be economised by adequately sealing the building
	(Radhi 2008)	Residential buildings having decreased window/wall ratio were observed to have reduced energy demand
<b>Walls</b>	(Christian et al. 2006)	The impact of thermal insulation has significant effect on the heat conservation in the building.
<b>Window</b>	(Kamal et al. 2000)	The heat loss from the window account for the 25% of the total energy loss for the building.
	(Cuce & Cuce 2016)	The glazed window not just limited to being more tough, but also the impact of heat transmittance, thermal bridging via glazing, and direct solar gain
<b>Building colour</b>	(Asimakopoulos 1996)	Envelop colour lead for convective heat transfer, leading to quicker cooling down of the textured surface
	(Bouchlaghem 2000)	A decrease in the heat obtained by the building is favoured through passive shading systems.
<b>Solar controls/ Shading elements</b>	(Graves et al. 2001)	Using more natural light is more comfort than the artificial lights. Reduction in use of artificial lights also leads to decrease in heat generated within the building
	(Capeluto et al. 2003)	Adjustable shading devices can reduce the energy consumed for the heat in winter and cooling in summer.
<b>Thermal Mass</b>	(Sidanius et al. 2000)	It is highly advised to use thermal mass to allow the internal condition to be smoother than large outdoor fluctuated temperature.

The requirements for the Passive house require that the airtightness do not exceed 0.6 air changes per hour at 50 Pascals pressure. So the prefabricated components manufactured in factories can promise high accuracy. Also, the accelerated erection on site could promise high accuracy installation:

- Re-market the second-hand components resulting from changes to dwellings or disposal of dwellings.
- Mass production of building components have potential for relocation of dwellings rather than demolition.
- Minimal use of in-situ materials minimises waste on site.

Prefabrication techniques are well suited to these ideas, and could create a concept in flexible, customised design.

### *Prefabricated building*

Prefabricated buildings, in which most of the building components are produced in factories and transported to the construction site for assembly, has become popular worldwide (Zhang et al. 2014). Compared with traditional construction method, this approach is very different from a lot of field, such as the raw processed materials are transferred to the factory other than the construction site directly. In the academic field, there are several terms used to describe the prefabricated building or technology, such as preassembly, modularisation and offsite construction (Song et al. 2005). In the US, the prefabricated house is also named modular housing (Song et al. 2005), offsite production in EU countries (Song et al. 2005) and in the mainland China the name is industrialised housing (Zhang & Skitmore 2012).

After decades of development, the prefabricated building has been extensively utilised in EU countries, but in mainland China, it has just taken its first steps (Zhang & Skitmore 2012; Zhang et al. 2014). With rising consciousness of low-carbon house, the prefabricated house has spread rapidly in China, especially in Beijing and Shanghai to satisfy the housing needs and reduce pollution during construction.

Several benefits of the prefabricated house have been addressed from the academic field (Liu & Ying 2009). However, previous researchers were focusing on the benefit of structural reliability, initial cost reductions and increasing productivity, but there are few researchers paying attention to the environmental benefits of offsite-production house. With the rising need to accomplish a low-carbon society around the world, various green technologies have been promoted as sustainable practice in the global building industry, such as the passive building strategies (Zhang et al. 2011) and sustainable technology (Zhang et al. 2012). The technology is also regarded as a new approach of sustainable construction means for its potential to save energy and raw materials (Zhang et al. 2014). The environment impact of prefabricated building can be significant and can be regarded as a main method to accomplish sustainable development. Thus, it is very important to know how to integrate the relationship between sustainable technology and building components.

### *Building shape and orientation*

The first basic principle in a passive house is the orientation, in which the southern façade of the building should be oriented towards the equator in the northern hemisphere (and the northern façade towards the north in the southern hemisphere).

By facing the longer axis of the building in the east/west direction, the longer dimension of the home faces will be more likely to gain the maximum solar radiation. For that reason, areas which are most frequently used, such as the kitchen and the living room, must be located into this part of the building.

This orientation is also advantageous for summer cooling conditions because it minimises the east-west façades to morning and afternoon sunlight.

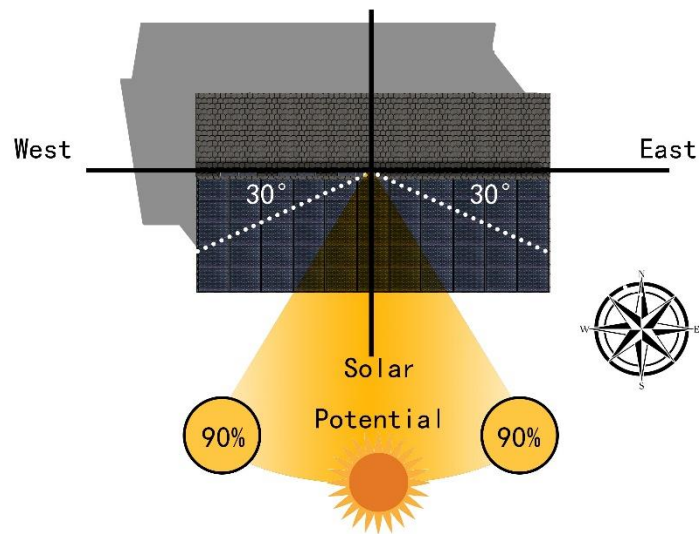


Figure 1: Building shape and orientation

### *Building envelope and shadow*

The study for the envelop of buildings has become the main field of the low-carbon house research for the two thirds of the energy loss in building from the architectural facades (Granadeiro et al. 2013). To some extent, if we could construct a complete envelop system, we could reduce the energy demand. Walls are the main part of building envelope and thermal resistance ( $R$ -value) of the wall have significant impact on the capacity of the heat conservation in building. Thus, increasing the thermal resistance is the main approach for the low-carbon building envelop.

However, this type of shading device is not efficient for the south-west façade at blocking the sun entering inside during morning and afternoon hours, when the sun is low in the sky. It is very important to understand that in summer the peak sun angles comes in June on the 21st during the solstice, but peak temperature and humidity come mostly in August. Therefore, include a fully shade south façade during the summer will also shade the window in autumn and spring, when actually the passive solar heat is needed for heat up the building and keep the house with a comfort temperature. Having say that, for designing a proper shading device it is necessary to understand how the sun moves along the year and which effect its angles have on the building. The altitude and azimuth angles represent the position of the sun in the sky.

Because shading devices can have a huge impact on the building appearance as well as reducing the cooling demand, they must be considered and evaluated at the early stage of the design process, in order to be effective for both technical and visual aspect for being well-integrated in the whole architecture.

There are several type of shading devices, but it is very difficult to make a generalisation of their design. However, some general recommendations have been listed just below:

- to control direct solar radiation in the south facade, use fixed overhangs
- limit the number of east and west windows because they are very difficult to shade compared to the south side. Maybe some consideration of the surrounded landscape, such as type of tree that might be used to shade
- north façade can be out of shading as it receives very little direct solar radiation – interior shading devices, such as Venetian blinds or vertical louvres, might be used in order to control glare, however exterior shadings must be included since the interior ones have already admitted the solar gain in.

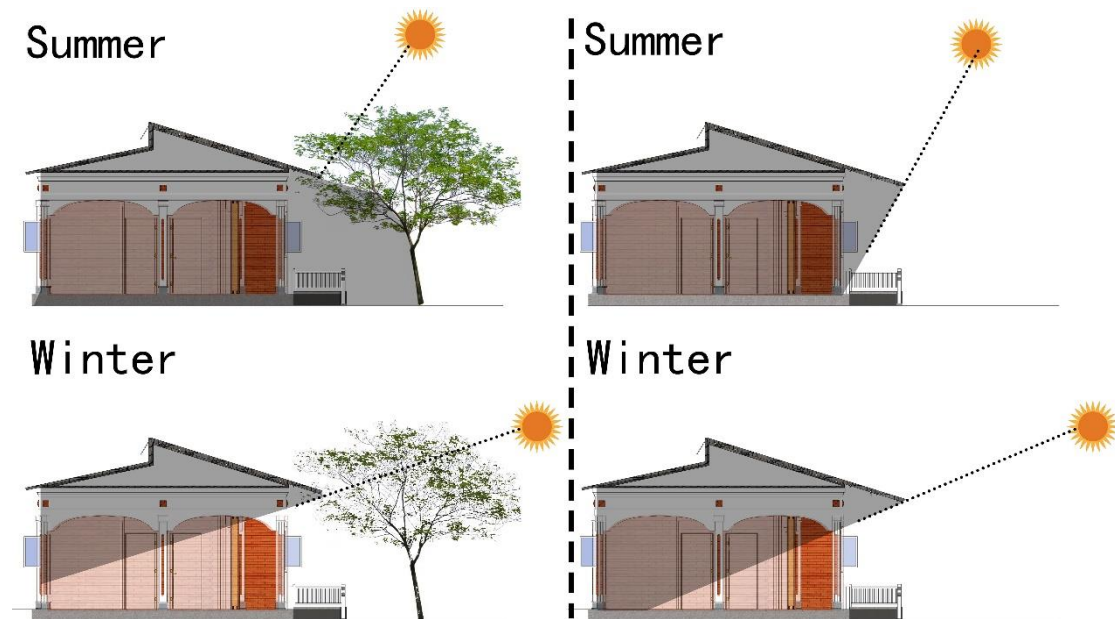


Figure 2: Building shadow

A well-insulated building helps in reducing heat loss during the winter and keeping the house cool during the summer. Insulated materials, so called because they are poor conductors of heat, form a barrier between interior and exterior spaces, by means between warmed interior and cool exterior, and cool interior and hot exterior according to the season. Since insulation is important in warm climate as well as in cold climate, less energy is required to heat houses in cold conditions or cool houses in warm conditions, which results in a good interior temperature along the whole year. Regarding insulation, the heat loss through the construction (walls, floor, basement, ceiling or the roof) is represented by the thermal heat loss coefficient or U-value, which represents how much heat in Watts is lost per m<sup>2</sup> at a standard temperature difference. Insulation materials are normally used in walls, floors and roof because they work by resisting heat flow, which is measured by an R-value (the higher the R-value, the greater the insulation). The R-value changes according to the material type, its density and thickness and it is affected by thermal bridging. Thermal bridging represents the unwanted heat flow that comes inside the building through joints, studs and rafters. Therefore, in order to achieve the best insulation thermal bridges must be avoided.

### Ventilation

Ventilation of building is a vital part of building. In the field of ventilation, we should consider about balancing the frequency of ventilation to fresh the interior air, and making it take less heat during the ventilation. How to balance this demand is key point in the low-carbon building ventilation design.

Windows are a significant source of transmission heat loss or heat gain at different climate zones. As heat lost through windows account about 20% of the total heat loss from an average home in UK. The energy efficiency of window technologies is crucial to overall energy efficiency to reduce fuel energy costs and Carbon emission. Also increasing thermal resistance of window may help to reduce the condensation problem that is a common complaint by customers.

The latest construction designs are now tending to include natural ventilation systems such as wind tower devices into building that help to increase the passage of fresh air through the building, thus decreasing energy consumption (Calautit et al., 2014). The said phenomenon is denoted as '*windcatcher*' owing to its ability to trap the cool wind, from a higher altitude outside the building and directing it towards the interior located at comparatively lower level as per the pertaining wind force (Prajongsan, 2014). Previously, wind catcher has remained a major part of the environmental control strategies and processes. One of such tactics involved shifting from one room to another on either daily or seasonal basis (Passe, 2015).

The wind towers are constructed from mud bricks in different heights and provided with various spaces acting as outlets for winds flowing in different directions (Passe, 2015). The windcatcher operates through two major forces i.e. (1) Buoyancy effect. (2) External wind

Buoyancy effect refers to the difference between internal and external temperatures. This makes the external winds play a considerable role in the functioning of the windcatcher. Moreover, the efficiency of windcatchers are negatively affected by the number of outlets provided in the chamber i.e. more outlets decrease the efficiency. Though, in some locations with no significant winds, having a multi-opening chamber is the most appropriate option (Prajongsan, 2014).

### 3.2. Summary of the sustainable design system

Another important issue regarding sustainable building is the integration of renewable energy systems into the building at the very early stage of the design process. By means that, it is very important to consider which technologies will be more suitable according to the site conditions and the building structure.

A renewable system integrated into the building, such as PVs and Solar Collector, represents a good practice that has many advantageous aspects, such as:

- it works as both building envelope material and energy generator
- it saves in materials and energy costs
- it drastically reduces CO2 emissions
- it actually adds architectural value to the building as well as providing a public expression of sustainable commitment.

An integrated renewable system into the building is used to replace conventional materials on the building envelope, such as the roof, façade or skylights. The integrated systems are increasingly becoming a good practice because the initial cost can be offset by reducing the amount of cost spent for producing and installing building materials. In fact, the systems, mostly PV and in some cases Solar Panels are used to construct part of the building and they are available in several forms. According to the envelope in which they will be integrated, they can be available in different types, such as:

- a thin film solar cell integrated into a flexible polymer roofing membrane suitable for
- flat roofs
- modules roof tiles, solar shingles and panels normally used in pitched roofs
- solar modules mounted on the façade of the building
- (semi)transparent modules used to replace architectural components made with glass, such as windows or skylights, that can work as well as shading.

The core concept of the low-carbon house is the *Open Source and Throttling*. The list of the most common sustainable technologies is shown below. Using Solar system or Heat pump as the sustainable energy resource for operation. Though different, envelope devices, such as vacuum glazing, insulated wall and so on, to keep the interior temperature stable. Those low-carbon technologies have been developed to satisfy this concept.

Table 2: Low-carbon technologies list

Open Source	Heat Pump	Ground Source Heat Pump,
		Air source heat pump
	Solar System	Photovoltaics Panel
		Solar collector
	Wind	Wind turbines
<b>Throttling</b>	Wall	passive solar wall
		structural insulating pane
		Wallboard with latent heat storage
	Windows/Glazing	Vacuum glazing
		Aerogel glazing
		Switchable reflective glazing
		Suspended particle devices (SPD) film
	Roof	Masonry roofs
		Lightweight roofs
		Ventilated and micro-ventilated roofs
		Solar-reflective/cool roofs
		Green roofs
	Ventilation	Heat recovery
		Wind catcher
	Orientation on building	the easiest approach in achieving thermal comfort is the adherence to the oriented buildings
		positioning the house in the right direction is entailed in the central principle during building design

Open Source	Heat Pump	Ground Source Heat Pump,
		solar radiation can be determined by the orientation building alignment corresponding to local climatic conditions to maximise the natural benefit
	Building layout (Shape)	ventilation dependent on the building shape Self-shading has significant impact on the interior spaces
	Building envelope	The cooling or heating systems can be economised by adequately sealing the building Residential buildings having decreased window/wall ratio were observed to have reduced energy demand
	Walls	The impact of thermal insulation has significant effect on the heat conservation in the building.
	Window	The heat loss from the window account for the 25% of the total energy loss for the building. The glazed window not just limited to being more tough, but also the impact of heat transmittance, thermal bridging via glazing, and direct solar gain
	Building colour	Envelop colour lead for convective heat transfer, leading to quicker cooling down of the textured surface
	Solar controls/ Shading elements	A decrease in the heat obtained by the building is favoured through passive shading systems. Using more natural light is more comfort than the artificial lights. Reduction in use of artificial lights also leads to decrease in heat generated within the building Adjustable shading devices can reduce the energy consumed for the heat in winter and cooling in summer.
	Thermal Mas	It is highly advised to use thermal mass to allow the internal condition to be smoother than large outdoor fluctuated temperature.

### 3.3. Monitoring and energy management

Sustainable house stands out though minimizing the energy requirement. However, the sustainable building cannot have the best efficient operation all the time. Actually, the technologies in the building are always in the faulty operation phase. The specific performance is the overheating of the sustainable building. Also, neither house owner, nor the user, do not have idea how much energy needed to maintain the comfortable interior temperature. Thus, there need systems to manage and operate the energy using.

Unfortunately, the tools for managing are not very user-friendly. The management system is always academic and complicated and is therefore rarely used if at all. Whether a given building or system is work in the energy- efficient phase depends on the different application, climate or other influence factors. For example, over 35% energy in Wuhan is for heating, cooling, ventilation and lighting. However, the house in Harbin consumed more energy on heating. The proportion would be up to 50%. It is difficult to forecast the actual energy using.

Aside the above reasons, the insufficient measuring technology equipment is another reason not using all potential for the sustainable building. In addition, the new built building always has the best thermal performance. After years using, the building technology is out of work. Analysis of enormous amount of data is merely done by recording the data by hand. Therefore, a system can automatically compare recorded data and calculated the value is needed. That system is called the energy monitoring system. The system can operate the different technologies according to the climate big data, the data from sensors. Also, the systems can notificate the flaw message to the operator and user. Let them update the setting to get the best performance.

## 4. CONCLUSION

The prefabrication technology will be an essential technology for the future. In past research, people regarded the prefabricated building as an uncomfortable and temporary place for living. In addition, the energy efficiency of previous prefabricated buildings were less than the other building. Thus, the development of prefabricated house is relative lower than the overall level of building industry. However, if we can connect low-carbon technology with the prefabricated building, we can take advantage of the benefits of low-carbon technology and prefabricated buildings to get an ideal house for humans with low-cost and a comfortable interior environment. This research report reviews the literature on principle and application of the prefabricated technology and devices prefabricated in the building, especially on the heat exchange and heat storage in house. It tries to assess the best approaches for integrating low-carbon technology, such as heat pump and heat recovery, into building components. The review work carried out by the authors will assist the development of prefabrication techniques, and therefore, to aid to promote their applications in the UK market.

## 5. REFERENCES

- Ahmad, T., Thaheem, M.J. & Anwar, A., 2016. Developing a green-building design approach by selective use of systems and techniques. *Architectural Engineering and Design Management*, 12(1), pp.29–50. Available at: <http://www.tandfonline.com/doi/full/10.1080/17452007.2015.1095709>.
- Asimakopoulou, D., 1996. *Passive cooling of buildings*, Earthscan.
- Bekkouche, S.M.A. et al., 2011. Introduction to control of solar gain and internal temperatures by thermal insulation, proper orientation and eaves. *Energy and buildings*, 43(9), pp.2414–2421.
- Berardi, U., 2016. A cross-country` comparison of the building energy consumptions and their trends. *Resources, Conservation and Recycling*. Available at: <http://linkinghub.elsevier.com/retrieve/pii/S0921344916300489> [Accessed June 11, 2017].
- Bouchlaghem, N., 2000. Optimising the design of building envelopes for thermal performance. *Automation in Construction*, 10(1), pp.101–112.
- Capeluto, I.G., 2003. Energy performance of the self-shading building envelope. *Energy and buildings*, 35(3), pp.327–336.
- Capeluto, I.G., Yezioro, A. & Shaviv, E., 2003. Climatic aspects in urban design—a case study. *Building and environment*, 38(6), pp.827–835.
- Chiesa, G., Simonetti, M. & Grosso, M., 2014. A 3-field earth-heat-exchange system for a school building in Imola, Italy: Monitoring results. *Renewable Energy*, 62, pp.563–570. Available at: <http://linkinghub.elsevier.com/retrieve/pii/S0960148113004229> [Accessed June 19, 2017].
- Christian, J.E. et al., 2006. Energy Efficiency, SIPS, Geothermal, and Solar PV Used in Near Zero-Energy House. *ASHRAE transactions*, 112(2).
- Cuce, E. & Cuce, P.M., 2016. Vacuum glazing for highly insulating windows: Recent developments and future prospects. *Renewable and Sustainable Energy Reviews*, 54, pp.1345–1347. Available at: <http://dx.doi.org/10.1016/j.rser.2015.10.134>.
- Férey, G., 2000. Building units design and scale chemistry. *Journal of Solid State Chemistry*, 152(1), pp.37–48.
- Ghiaus, C. & Inard, C., 2004. 2 Energy and environmental issues of smart buildings.
- Gong, Y. & Song, D., 2015. Life cycle building carbon emissions assessment and driving factors decomposition analysis based on LMDI-A case study of Wuhan city in China. *Sustainability (Switzerland)*, 7(12), pp.16670–16686.
- Granadeiro, V. et al., 2013. Automation in Construction Building envelope shape design in early stages of the design process : Integrating architectural design systems and energy simulation. *Automation in Construction*, 32, pp.196–209. Available at: <http://dx.doi.org/10.1016/j.autcon.2012.12.003>.
- Graves, H. et al., 2001. *Cooling buildings in London: overcoming the heat island*, BREPress.
- Haase, M. & Amato, A., 2009. An investigation of the potential for natural ventilation and building orientation to achieve thermal comfort in warm and humid climates. *Solar energy*, 83(3), pp.389–399.
- Kamal, A. et al., 2000. Axonal transport of amyloid precursor protein is mediated by direct binding to the kinesin light chain subunit of kinesin-I. *Neuron*, 28(2), pp.449–459.
- Liu, Z. & Ying, H., 2009. Prefabrication construction in residential building of Vanke real estate company China. In *Management and Service Science, 2009. MASS'09. International Conference on*. IEEE, pp. 1–4.
- Morrissey, J., Moore, T. & Horne, R.E., 2011. Affordable passive solar design in a temperate climate: An experiment in residential building orientation. *Renewable Energy*, 36(2), pp.568–577.

- Ochoa, C.E. & Capeluto, I.G., 2008. Strategic decision-making for intelligent buildings: Comparative impact of passive design strategies and active features in a hot climate. *Building and Environment*, 43(11), pp.1829–1839.
- Okeil, A., 2010. A holistic approach to energy efficient building forms. *Energy and buildings*, 42(9), pp.1437–1444.
- Olgay, V., 1967. Bioclimatic orientation method for buildings. *International Journal of Biometeorology*, 11(2), pp.163–174.
- Omer, A.M., 2013. Direct expansion ground source heat pumps for heating and cooling. *International Research Journal on Engineering*, 1(2), pp.27–48. Available at: <http://www.apexjournal.org>.
- Omer, A.M., 2011. Energy and environment: applications and sustainable development.
- Radhi, H., 2008. A systematic methodology for optimising the energy performance of buildings in Bahrain. *Energy and Buildings*, 40(7), pp.1297–1303.
- Sidanius, J. et al., 2000. Social dominance orientation, anti-egalitarianism and the political psychology of gender: an extension and cross-cultural replication. *European Journal of Social Psychology*, 30(1), pp.41–67.
- Song, J. et al., 2005. Considering prework on industrial projects. *Journal of construction engineering and management*, 131(6), pp.723–733.
- Zhang, X., Platten, A. & Shen, L., 2011. Green property development practice in China: Costs and barriers. *Building and Environment*, 46(11), pp.2153–2160. Available at: <http://www.sciencedirect.com/science/article/pii/S0360132311001338> [Accessed June 19, 2017].
- Zhang, X. & Skitmore, M., 2012. Industrialized housing in China: a coin with two sides. *International Journal of Strategic Property Management*, 16(2), pp.143–157.
- Zhang, X., Skitmore, M. & Peng, Y., 2014. Exploring the challenges to industrialized residential building in China. *Habitat International*, 41, pp.176–184. Available at: <http://linkinghub.elsevier.com/retrieve/pii/S0197397513000891> [Accessed June 21, 2017].
- Zhang, X., Wu, Y. & Shen, L., 2012. Application of low waste technologies for design and construction: A case study in Hong Kong. *Renewable and Sustainable Energy Reviews*, 16(5), pp.2973–2979. Available at: <http://www.sciencedirect.com/science/article/pii/S1364032112001141> [Accessed June 19, 2017].



---

## #39: Numerical investigation of mixture generation due to different inlet and outlet positions

---

Hussain Saad ABD<sup>1</sup>, Abdulmunem R. ABDULMUNEM<sup>2, 3</sup>, Mohammed Hassan JABAL<sup>4</sup>

<sup>1</sup> Electromechanical Engineering, University of Technology, Baghdad, Iraq, 50228@uotechnology.edu.iq

<sup>2</sup> Faculty of Mechanical Engineering, Universiti Teknologi Malaysia, 81310 UTM Skudai, Johor, Malaysia, abdulmunemraad@graduate.utm.my

<sup>3</sup> Electromechanical Engineering, University of Technology, Baghdad, Iraq, 50192@uotechnology.edu.iq

<sup>4</sup> Electromechanical Engineering, University of Technology, Baghdad, Iraq, 50124@uotechnology.edu.iq

*Numerical simulation is a method used to carry out a study of the flow characteristics of compressible fluid through different channels. Two approaches using the air as a working substance were used to study the flow characteristics. In the first approach, two inlets and one outlet horizontally in x direction were intended to generate different flow characteristics with the flow properties calculated along diagonal lines inside the channel. In the second approach, one inlet and outlet horizontally with sudden change in the area of the channel was employed. In this research, the flow properties were calculated along the centre line inside the channel and the flow fields have been investigated. A non-linear k- $\epsilon$  model was employed to solve the flow characteristics by using the finite difference method with a curvilinear coordinate system near the dead zone. The k- $\epsilon$  and Reynolds stress model are semi-empirical models based on the equations of transport that contain of dissipation rate ( $\epsilon$ ) as well as turbulent kinetic energy ( $k$ ). The turbulent kinetic energy and its rate of dissipation is derived from the Navier-Stokes equation. In this work, the simulation outcomes of proposed k- $\epsilon$  turbulence model indicated good compatibility with published correlations. In order to get an accurate solution, the value of  $10^{-8}$  for maximum normalised equation residual was considered to be the converging between computation and steady solution. The model applied for flow velocity 30 m/s and the obtained results presented as curves, surface and contours for velocities turbulent kinetic energy, rate of dissipation of turbulent kinetic energy and vortices. The builder model can be utilised for academic purposes since it can be widely used for many physical and engineering applications.*

*Keywords: compressible fluid; mixture generation; CFD; Navier-Stokes*

## 1. INTRODUCTION

Flow characteristics under different inlet and outlet channels through different flow patterns and geometries indicate economic advantages as well as improving design reliability. Several papers have used computational fluid dynamics (CFD) in many industrial applications for example automotive, aerospace, aeronautical, power generation, meteorology, heating and cooling systems, chemical processing and offshore systems. One of the big problems associated with CFD in real applications is the turbulence modelling that is considered a weak point in spite of the progressing in representation of geometry, generation of grid, robust numerical methods along with advanced computational resources (Davidson,2002; Moin *et al.*,1998; Hirsch *et al.*,2009). The three turbulent flow simulation strategies in this paper take in to consideration the principle categories in solution which are, Simulations Large Eddy LES, direct Numerical Simulations DNS and Reynolds Averaged Navier-Stokes (RANS).

## 2. THEORETICAL BACKGROUND

The nonlinear partial-differential equations (PDEs) consisted on two equations which are, Navier-Stokes and transport equations which representing the momentum and mass conservations and  $k$  and  $\epsilon$  for the turbulence model respectively. In order to convert the PDEs into nonlinear algebraic equations set, COMSOL3.5 program was used. In this work, the separated solution algorithm is utilised to obtain the solution rather than collecting all algorithms in a single matrix equation. The iterative process has been employed:

Beginning with the initial “guess” for all the parameters and then the solution be updated, or be allowed to “relax”, throughout the final solution of steady-state.

Velocity and pressure was specified as inlet and outlet respectively for the solution. All channel geometries for both methods as Cartesian co-ordinate system were imported into the COMSOL program in addition to using the turbulent non-Newtonian Power Law model and the model solutions for the Navier-stokes equation at specified velocities. Several iteration loops were specified to solve the nonlinear governing equations before finding a convergent solution. The scheme of upwind first-order is employed to discretize the governing equations set while schemes of finite element were employed to calculate the pressure of cell-face in order to use the segregated solver in COMSOL3.5. Numerical algorithm consisted of sets of pressure and velocity referring to momentum and continuity equations combinations in order to derive a pressure equation at the separated solver.

The system of equations can be summarised by the following basic equations:

Equation 1: for  $K$  (Banerjee *et al.*, 1994; Bandyopadyay and Das,2007)

$$\frac{\partial k}{\partial t} + U_j \frac{\partial k}{\partial x_j} - \frac{\mu_t}{\rho} S^2 - \epsilon + \frac{\partial}{\partial x_j} \left[ \frac{1}{\rho} \left( \mu + \frac{\mu_t}{\sigma_k} \right) \frac{\partial k}{\partial x_j} \right] \quad (1)$$

Equation 2: for  $\epsilon$ :

$$\frac{\partial \epsilon}{\partial t} + U_j \frac{\partial \epsilon}{\partial x_j} = \frac{\epsilon}{k} \left( C_{1\epsilon} \frac{\mu_t}{\rho} S^2 - C_{2\epsilon} \epsilon \right) + \frac{\partial}{\partial x_j} \left[ \frac{1}{\rho} \left( \mu + \frac{\mu_t}{\sigma_\epsilon} \right) \frac{\partial \epsilon}{\partial x_j} \right] \quad (2)$$

Equation 3: Turbulent viscosity is calculated from:

$$\mu_t = \rho C_\mu \frac{k^2}{c} \quad (3)$$

There are 5 free constants:  $\partial k, \partial_c, C_{1c}, C_{2c}, C_\mu$

## 3. OVERVIEW OF THE EQUATION FOR K

The kinetic energy equation includes an additional unknown term as a turbulent fluctuation. Based on Boussinesq assumption, these turbulent fluctuation can be connected with the mean flow [Das *et al.*, 1989, Das *et al.*, 1991).

Equation 4: Common form for model equation of  $k$ .

$$\frac{\partial(\rho k)}{\partial t} + \frac{\partial}{\partial x_i} (\rho k \bar{u}_i) = \frac{\partial}{\partial x_i} \left[ \left( \mu + \frac{\mu_t}{\sigma_k} \right) \frac{\partial k}{\partial x_i} \right] + 2\mu_t \bar{S}_{ij} \cdot \bar{S}_{ij} - \rho \epsilon \quad (4)$$

The Prandtl number  $\sigma_k$  connects the diffusivity of  $k$  to the eddy viscosity. Typically a value of 1.0 is used.

#### 4. OVERVIEW OF THE EQUATION $\epsilon$

In order to find the  $\epsilon$  model equation,  $k$  will be multiplied by  $(\epsilon/k)$  and entering model constants.

Equation 5: Common form for model equation of  $\epsilon$  (Banerjee et al., 1998).

$$\frac{\partial(\rho\epsilon)}{\partial t} + \frac{\partial}{\partial x_i} (\rho\epsilon\bar{u}_i) = \frac{\partial}{\partial x_i} \left[ \left( \mu + \frac{\mu_t}{\sigma_\epsilon} \right) \frac{\partial \epsilon}{\partial x_i} \right] + C_{1\epsilon} \frac{\epsilon}{K} 2\mu_t \bar{S}_{ij} \cdot \bar{S}_{ij} - C_{2\epsilon} \rho \frac{\epsilon^2}{K} \quad (5)$$

The Prandtl number  $\sigma_\epsilon$  connects the diffusivity of  $\epsilon$  to the eddy viscosity. Typically a value of 1.30 is used typically values for the model constants  $C_{1\epsilon}$  and  $C_{2\epsilon}$  of 1.44 and 1.92 are used.

#### 5. NUMERICAL SOLUTION FOR THE MODEL

In this research we take two approaches to study the compressible flow characteristics. A numerical simulation was carried out to study the flow characteristics of compressible flow through different geometrical channels. The air is used as a working substance. Three approaches are used here to analyse the flow characteristics which include velocity distribution, turbulent kinetic energy, viscosity, and pressure behaviour.

In the first approach we take two inlets and one outlet and all flow directions are horizontal i.e. two inlet and one outlet channel to generate different flow characteristics, also the flow properties calculated along diagonal line inside the channel.

In the second approach, we take one inlet and one outlet with a sudden area increase in  $x$  direction, and the flow properties calculated along the centre line inside the channel. The properties of the working substance are given in Table 1.

Table 1: Properties of working substance

rho	1.24[kg/m <sup>3</sup> ]	Density
eta	1.78e-5[Pa*s]	Viscosity
u	30[m/s]	Inlet peak velocity
h step	3.91[cm]	Step height
N	3792	Number of meshes element
Err	10 <sup>-8</sup>	Accepted accumulated error

#### 6. RESULTS AND DISCUSSION

For the application of the mentioned theory of compressible flow through different channels geometry, a numerical solution for the geometry is presented. The solution includes the velocity profile through the channel in terms of arrow contours streamlines and surface velocity under initial velocity 30 m/s, for both approaches after feeding the main program by the mentioned data. Numerical treatments with the system of equations were carried out.

The numerical method used here is a finite element method for solutions. The differential equations for the first approach of the flow velocity distribution are represented in Figure 3 which illustrates the flow velocity in the channel. It is clear that the variation of flow velocity increased at the outlet and reached 80 m/s. The velocity distribution for the second approach (one inlet and one outlet) is represented in Figure 14. The flow velocity decreased near the outlet due to the sudden change in the area of the channel.

Figures 4 and 15 represent the flow field as arrows to show the vector directions of flow inside the channels from inlet to outlet. Figures 5 and 16 give streamlines for the flow; these figures give indications of weak zones and disturbance in the flow field. Figures 6 and 17 illustrate the flow field as contours; the knot equal velocity zone in the flow field inside the channels.

Then take the diagonal line for approach one as show in Figure 7 and study many important flow properties along the line. In Figure 8 the vorticities inside the flow was very clear, it increased to a value 250 (1/s) and then decreased to -50 (1/s). For the second approach (one inlet and one outlet) in Figure 19, the vorticities fluctuated along the centre line due to high

variation in turbulent kinetic energy. In Figures 9 and 10 the turbulent kinetic energy and turbulent viscosity increased in nonlinear behaviour because the governing equations are nonlinear partial differential equations.

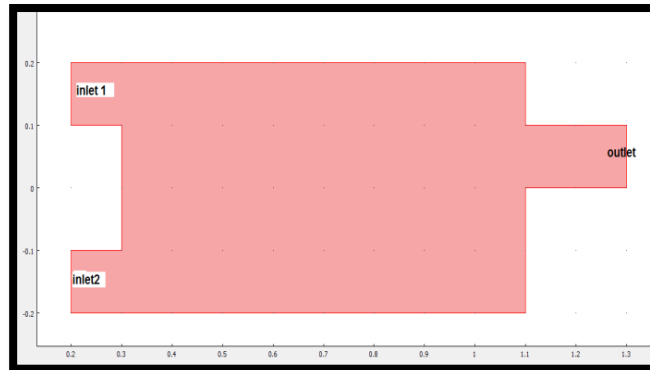


Figure 1: Geometrical shape for proposal approach two with 2 inlet one outlet

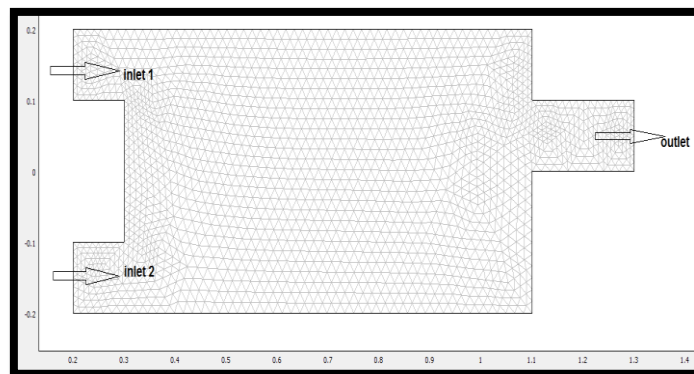


Figure 2: Mesh shape for proposal approach one with 2 inlet one outlet with 3792 elements

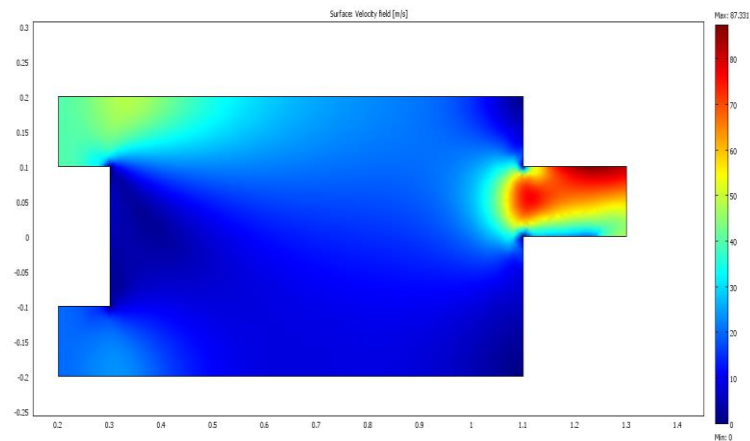


Figure 3: Surface velocity distribution for approach one with 2 inlet and one outlet

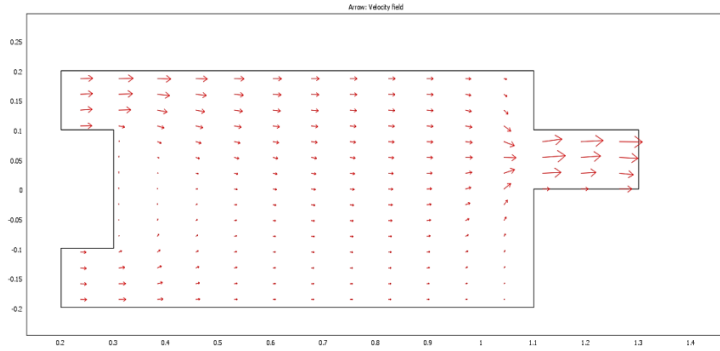


Figure 4: Arrow velocity distribution for approach one with 2 inlet and one outlet

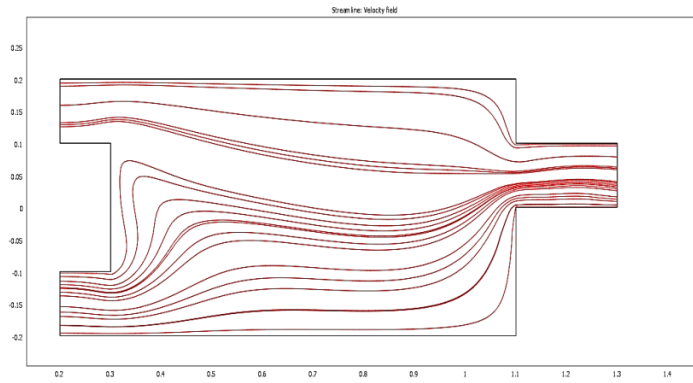


Figure 5: Stream line velocity distribution for approach one with 2 inlet and one outlet

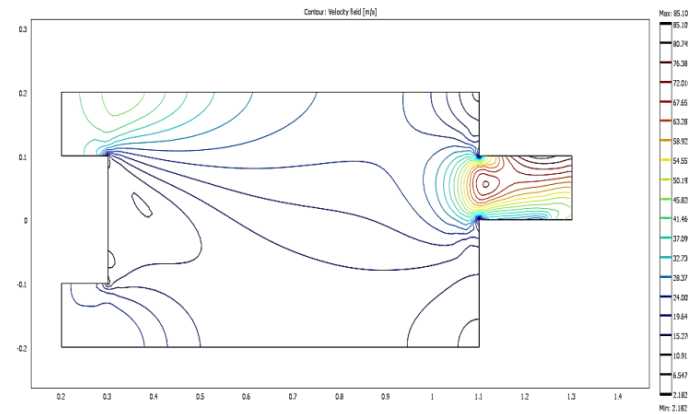


Figure 6: Contour for velocity distribution for approach one with 2 inlet and one outlet

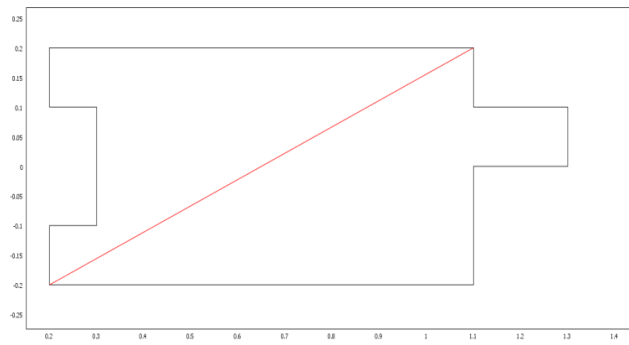


Figure 7: Geometrical shape for approach one with diagonal line

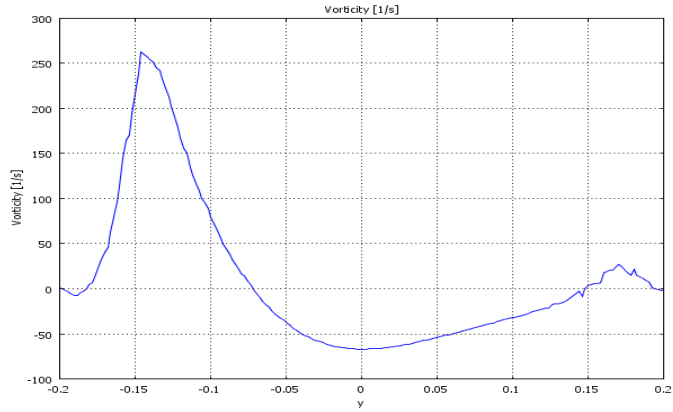


Figure 8: Vorticity variations along the diagonal line in the flow field

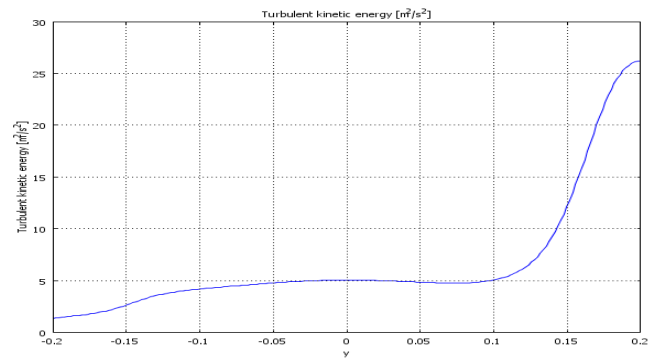


Figure 9: Turbulent kinetic energy variations along the diagonal line in the flow field

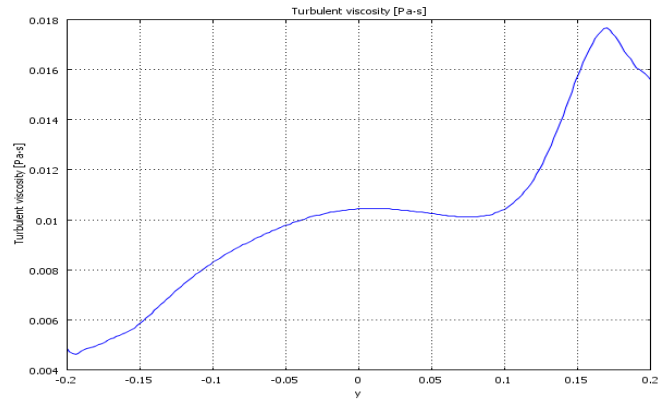


Figure 10: Turbulent viscosity variations along the diagonal line in the flow field

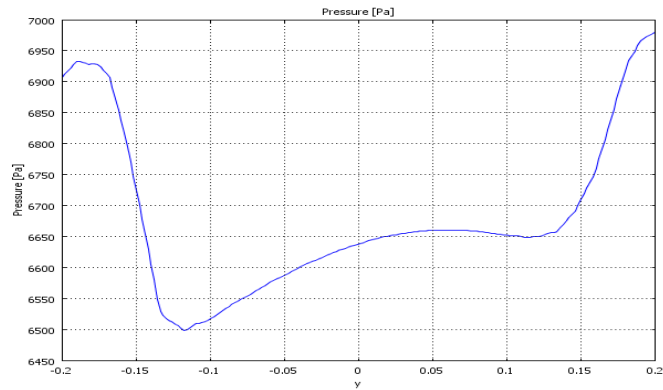


Figure 11: Pressure variations along the diagonal line in the flow field

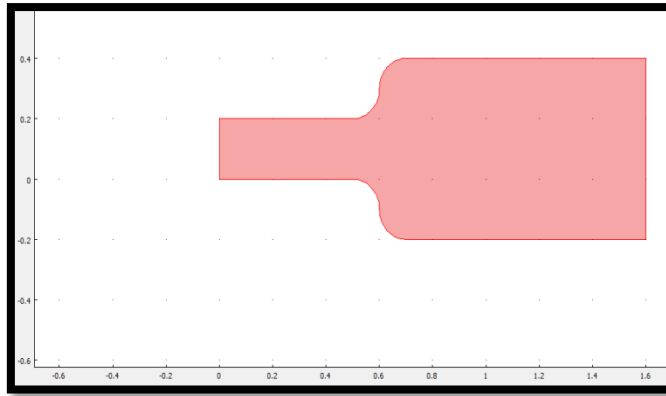


Figure 12: Geometrical shape for approach two with one inlet and one outlet

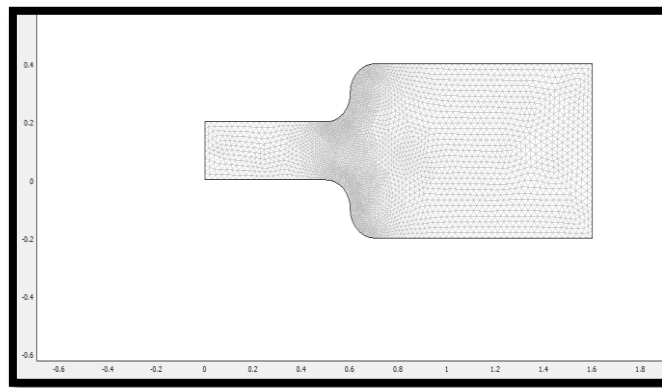


Figure 13: Mesh shape for approach two with one inlet and one outlet with 3680 elements

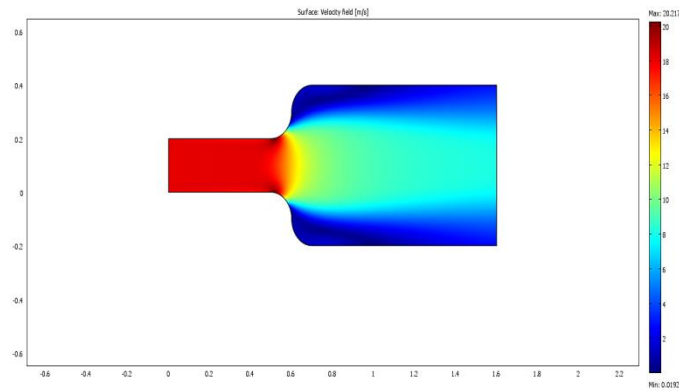


Figure 14: Surface velocity distribution for approach two with one inlet and one outlet

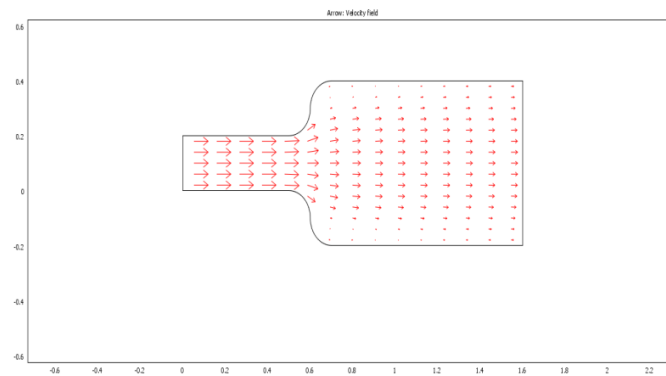


Figure 15: Arrow velocity distribution for approach two with one inlet and one outlet

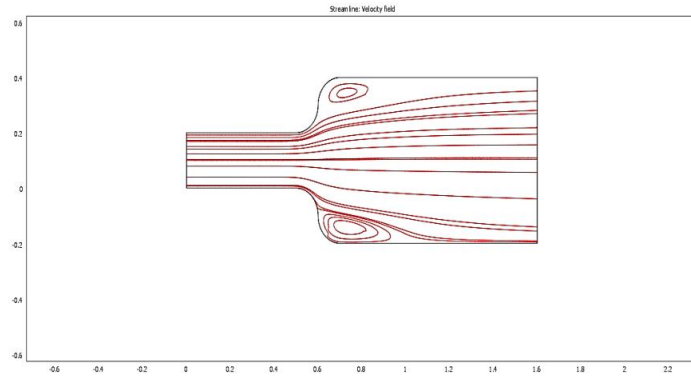


Figure 16: Streamline velocity distribution for approach two with one inlet and outlet

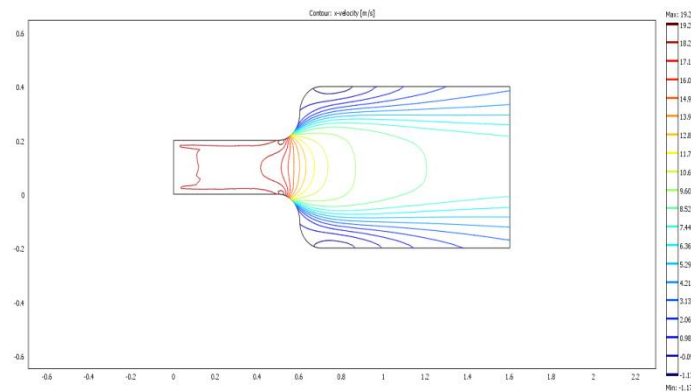


Figure 17: Contour velocity distribution for approach two with one inlet and outlet

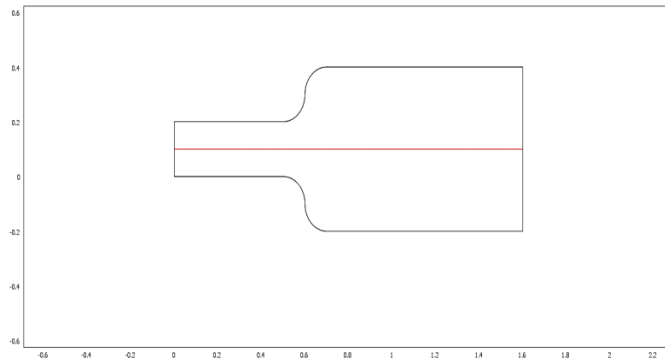


Figure 18: Geometrical shape for approach two

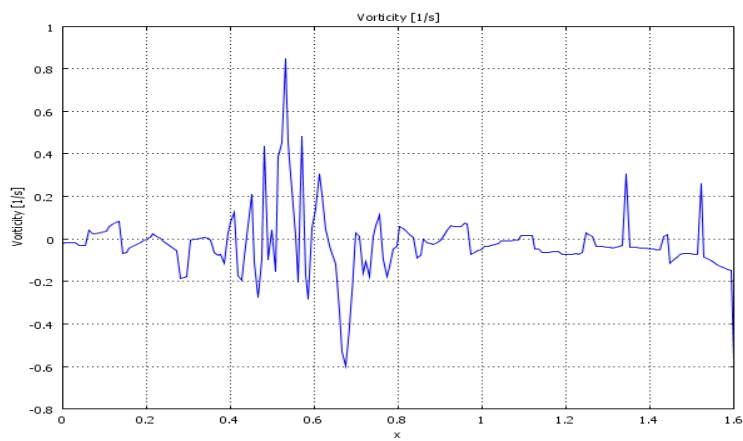


Figure 19: Vorticity variations along the centre line in the flow field



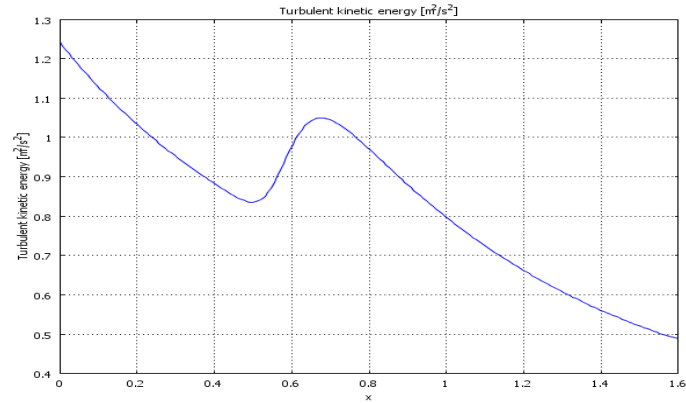


Figure 20: Turbulent kinetic energy variations along the centre line in the flow field

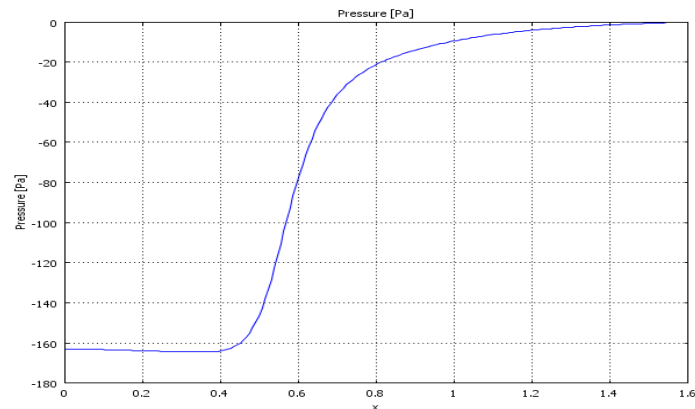


Figure 21: Pressure variations along the centre line in the flow field

## 7. CONCLUSION

From this study, the following can be concluded:

- A non-linear k- $\epsilon$  model can be employed to solve the flow characteristics;
- It can be controlled on the flow characteristics by changing the inlet and outlet channels;
- There are big differences in flow characteristics of compressible fluid by changing the geometric shape of inlet and outlet channels;
- The more significant changes happen at turbulent kinetic energy and turbulent viscosity when we change the inlet and outlet channels.

## 8. REFERENCES

Bandyopadhyay, T.K. and Das, S.K., Non - Newtonian pseudoplastic liquid flow through small diameter piping components, J. Petrol. Sc. & Engg., (2007).

Banerjee, T.K. and Das, S. K., Gas-non- Newtonian liquids flow through globe and gate valves, Chem. Engg. Comm., 167, 133-146. (1998).

Banerjee, T.K., Das, M. and Das, S. K., Non- Newtonian liquid flow through globe and gate valves, Can. J. Chem. Engg., 72, 207-211. (1994).

Das, S. K., Biswas, M. N. and Mitra, A. K., Pressure losses in Two-phase Gas-non-Newtonian liquid flow in horizontal tube, J. Pipelines, 7, 307-325(1989).

Das, S.K., Biswas, M. N. & Mitra, A. K., Non- Newtonian liquid flow in bend, Chem. Eng. J., 45,165-171. (1991).

Davidson, D.L., The role of computational fluid dynamics in process industries. Bridge, 2002. 32(4): p. 9-14.

Hirsch, C. and B. Tartinville, Reynolds - Averaged Navier - Stokes modelling for industrial applications and some challenging issues. *International Journal of Computational Fluid Dynamics*, 2009. 23(4): p. 295-303.

Moin, P. and K. Mahesh, Direct numerical simulation: a tool in turbulence research. *Annual Review of Fluid Mechanics*, 1998. 30(1): p. 539-578.

---

## #44: Experimental study of a portable PV direct-driven variable-speed refrigerator

---

Jie Ji<sup>1</sup>, Yuhe GAO<sup>2</sup>

<sup>1</sup>University of Science and Technology of China, Jijie@ustc.edu.cn

<sup>2</sup>University of Science and Technology of China, gyh1993@mail.ustc.edu.cn

*A portable PV direct-driven variable-speed refrigerator is proposed in this study. The compressor rotation speed of this system was controlled according to the solar irradiation allowing the utilisation efficiency of solar energy could be optimised and the frequently on-off of the compressor caused by the variation of solar irradiation could be avoided. The influence of the control strategy of the compressor speed, the ambient temperature and the internal fan were studied respectively. Compared to the constant-speed refrigerator, the variable-speed refrigerator was able to raise the daily average PV utilisation efficiency by 48.1%, raise the ice production by 99.6% and raise the final net refrigeration quantity by 22.8%. When ambient temperature rose from 20°C to 30°C, the ice production reduced by 23.9% and the final net refrigeration quantity reduced by 10.5%. The application of the internal fan could shorten the time needed for cooling water to 5°C by 39.3%.*

*Keywords: PV refrigeration; direct-driven; variable speed; refrigerator; portable*

## 1. INTRODUCTION

In recent years, there have been growing mobile refrigeration demands in people's outdoor activities such as fishing, medical preservation and mobilisation of troops. Solar refrigeration is a valuable solution of mobile refrigeration due to the positive correlation between the refrigeration demand and the solar irradiation intensity. Loan S et al. reviewed the solar refrigeration technologies showing that solar refrigeration had good perspective because of its energy-saving characteristic. Now, solar refrigeration is attracting more and more attention (Loan, 2013).

There are two kinds of solar refrigeration technologies: solar thermal refrigeration and solar PV refrigeration. The technical and economic comparisons of solar refrigeration systems have been discussed in some research. It has been concluded that solar PV compression refrigeration has the greatest potential to be used in mobile refrigeration. The steady cost reduction of the PV module has promoted the commercialisation of PV compression refrigeration. From 2007 to 2018, the cost of the PV module dropped from 36.0CNY/Wp to 2.5CNY/Wp in China. In addition, the energy efficiency of the PV compression refrigeration is high. Bansal PK et al. compared PV compression refrigeration, PV semiconductor refrigeration and solar absorption refrigeration in energy efficiency and cost. The results indicated that the energy efficiency of PV compression refrigeration was the highest and the cost of production was the lowest. What is more, the solar PV compression refrigeration system is simpler in structure and easier to maintain compared with other solar refrigeration systems (Bansal, 2000).

The PV compression refrigeration systems in previous research used the inverter or the storage battery. The inverters and the heavy storage batteries not only limited the mobility and reduced the energy conversion efficiency of the system, but also were responsible for a significant portion of the capital cost and the maintenance cost (Opoku, 2016). The DC compressors were often used to eliminate the inverter, because the DC compressors could be directly driven by PV panels which supplied direct current (Daffallah, 2017). The storage batteries were often replaced by cold storage systems (Toure, 1999). Though the cold storage system was cheaper than the battery, it was also heavy and limited the mobility of the system. In this paper, the PV refrigerator was constructed without the inverter or the energy storage system. The low temperature in the chamber could also be maintained overnight or during rainy days because the objects frozen in the chamber had the function of cold storage.

The PV compression refrigeration system without the cold storage system cannot make full use of solar energy if it uses a constant-speed compressor. When the compressor speed is set too slow, the compressor cannot make full use of the energy generated by the PV panel. When the compressor speed was set too fast, the compressor cannot start under weak solar irradiation. To raise the utilisation efficiency of solar energy, the DC variable-speed compressor should be adopted. Ekren O et al. evaluated the performance of a DC variable-speed compressor (Ekren, 2013). This DC compressor could be directly driven by PV panels without inverters and the compressor rotation speed could be changed by the controller. Axaopoulos PJ et al. presented a PV powered DC ice-maker which operated without the use of batteries or inverters (Axaopoulos, 2009). To extract the maximum electric power from the PV, the compressor worked in the maximum power tracking (MPT) mode with four compressors used and controlled by a novel dedicated controller. Though this method improved the start-up characteristics of the system, it reduced the utilisation efficiency of the compressor.

In this paper, a PV direct-driven variable-speed refrigerator was studied which was constructed without the inverter or the storage battery. To raise the PV utilisation efficiency and avoid the frequently on-off of the compressor, a novel compressor speed control method was adopted. Differently from the former control methods, the compressor speed was controlled according to the solar irradiation intensity. To speed up the refrigeration, an internal fan was used in the chamber. This system was constructed and experimentally investigated in an enthalpy difference lab so that the system could operate in stable external environment and the experimental results would be more accurate.

## 2. EXPERIMENTAL SETUP AND TEST APPARATUS

### 2.1. Construction of the PV refrigeration system

Figure 1 is the schematic diagram of the experiment rig. The portable PV direct-driven variable-speed refrigerator mainly consisted of a PV panel, a DC refrigerator and the irradiation signal-sensing module. The direct current generated by the PV panel drove the DC compressor directly. In the meantime, the irradiation sensor converted solar irradiation to electrical signal, and the electrical signal was amplified by the Voltage-amplifier. The compressor controller adjusted the compressor rotation speed according to the electrical signal from the Voltage-amplifier. The stronger the solar irradiation was, the faster the compressor speed was so the refrigerator could make full use of the energy generated by the PV panel. There was a fan inside the refrigerator, which could cause forced convection heat exchange and the quick temperature drop of objects in the chamber.

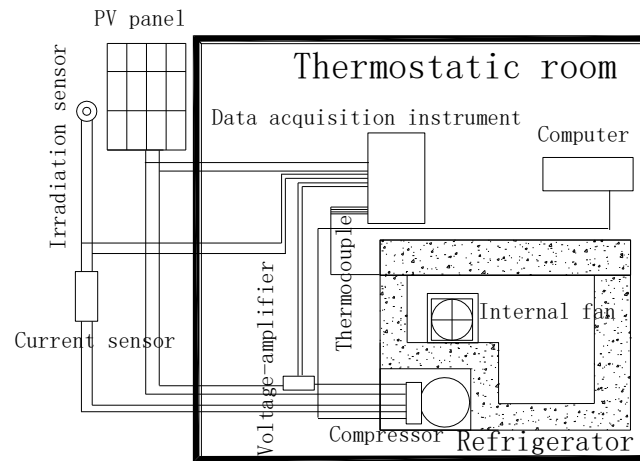


Figure 1: Schematic diagram of the experiment rig

Figure 2 shows the physical map of the experiment rig. A Polysilicon PV panel was used. The PV panel was facing south and the obliquity of it was 35°. To avoid the frequent on-off of the compressor caused by solar irradiation fluctuation, the peak output power of this PV panel was 150W, nearly twice the rated power of the compressor. The maximum power point voltage of this PV panel and the rated voltage of the compressor were both 24V. The compressor was BD-35F DC compressor made by Secop. The rotation speed of this compressor could be adjusted from 2000rpm to 3500rpm. The refrigerant was R134a. This DC refrigerator was rebuilt from a traditional refrigerator.

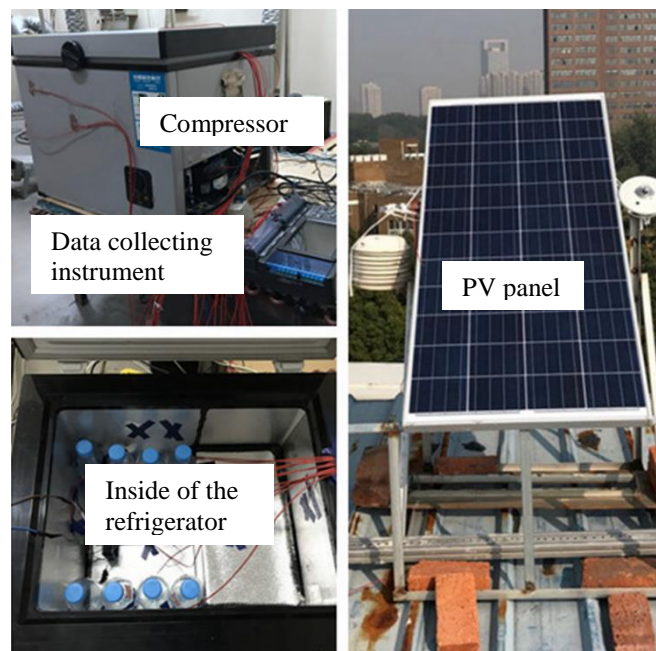


Figure 2: Physical map of the experiment rig

## 2.2. Experimental measurement system

The temperature was measured by T type thermocouple (measurement error:  $\pm 0.5^{\circ}\text{C}$ ); the current and the voltage were measured by the current sensor and the voltage sensor separately (measurement error: 0.1%); solar irradiation was measured by the TBQ-2 type irradiation sensor (measurement error: 2%). The irradiation sensor was placed near the PV panel and parallel with the PV panel. The data was recorded by HIOKI LR8402-21 data acquisition instrument. The frequency of data acquisition was  $1\text{s}^{-1}$ . The final ice production was counted by weighing the ice in the bottles.

The refrigerator was placed in the enthalpy difference lab. Figure 3 shows the picture of the enthalpy difference lab. It consisted of two chambers, the indoor chamber and the outdoor chamber. The air conditioning systems could control the temperature and the humidity of air in two chambers. The air sampling devices sampled air to measure the parameters of air and the air conditioning systems regulated air in two chambers. The refrigerator was placed in the indoor chamber, which was used as a temperature adjustable thermostatic room. The experiment rig was located in Hefei City, Anhui Province.

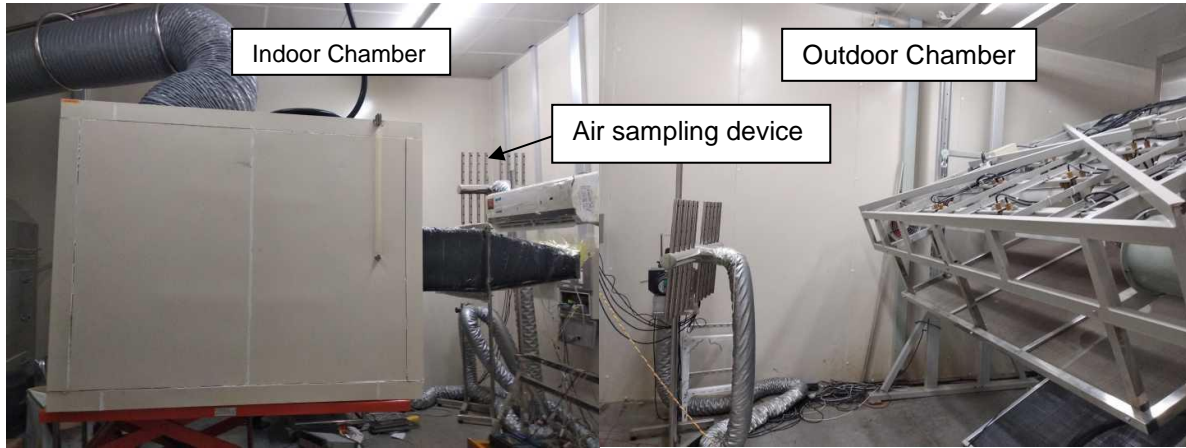


Figure 3: The picture of the enthalpy difference lab

### 3. PERFORMANCE EVALUATION OF THE SYSTEM

The net refrigerating effect of the refrigerator is given by

Equation 1: net refrigerating effect of the refrigerator

$$Q_n = cM(T_1 - T_0) + \gamma m + Q_e$$

Where:

- $Q_n$  = net refrigerating effect of the refrigerator (W)
- $C$  = specific heat of water (J/(kg·°C))
- $M$  = total mass of water in the chamber (kg)
- $T_1$  = initial temperature of water (K)
- $T_0$  = freezing temperature of water (K)
- $\Gamma$  = specific latent heat (J/kg)
- $Q_e$  = other refrigerating effect (W)

The daily average PV utilisation efficiency is given by

Equation 2: daily average PV utilisation efficiency

$$\eta = E / (\eta_e \int I A dt)$$

Where:

- $\eta$  = daily average PV utilisation efficiency
- $E$  = daily energy consumption of the refrigerator (J)
- $\eta_e$  = power generation efficiency of the PV panel
- $I$  = solar irradiation on the PV panel (W/m<sup>2</sup>)
- $A$  = area of the PV panel (m<sup>2</sup>)

The instantaneous PV utilisation efficiency is given by

Equation 3: instantaneous PV utilisation efficiency

$$\eta_i = w/(\eta_e IA)$$

Where:

- $\eta_i$  = instantaneous PV utilisation efficiency
- $w$  = input power of the refrigerator (W)
- $\eta_e$  = power generation efficiency of the PV panel
- $I$  = solar irradiation on the PV panel (W/m<sup>2</sup>)
- $A$  = area of the PV panel (m<sup>2</sup>)

#### 4. RESULTS AND DISCUSSIONS

The experiments were carried out on several sunny days with similar solar irradiation and ambient temperature in October, 2016.

There were two parts to the experiments. In the first part, the DC refrigerator was directly driven by the PV panel. The aim of this part was to study the influences of compressor speed control strategies and ambient temperature on the refrigerator performance. In the second part, the DC refrigerator was placed in a thermostatic room and driven by the DC power supply rather than the PV panel. The aim of this part was to study the influences of the internal fan on the refrigerator performance.

##### 4.1. Performance testing of the DC refrigerator

In the performance testing, the DC refrigerator was driven by the DC power supply, and there were no objects to be frozen in the chamber. The refrigerator was located in the thermostatic room, where air temperature was 20°C. Figure 4 shows the variations of air temperature in the refrigerator with the conversion of the temperature controller. Table 1 shows the gear parameters of the refrigerator. At the beginning, the temperature controller was shifted to gear 1. After 12.4 minutes' operation, temperature of air in the chamber dropped to 1.2°C, and the compressor stopped. Then, air temperature in the chamber rose, until the compressor worked again. The constant on-off of the compressor caused air temperature tremors in every gear. Table 1 shows that tremors of air temperature in the chamber were nearly 4°C, which was a little higher than general demands of tremors 1°C to 3°C. Because the DC compressor was not matched perfectly with other parts of the refrigerator. The lowest air temperature in the chamber could reach -25.9°C so this DC refrigerator could meet many kinds of refrigeration demands.

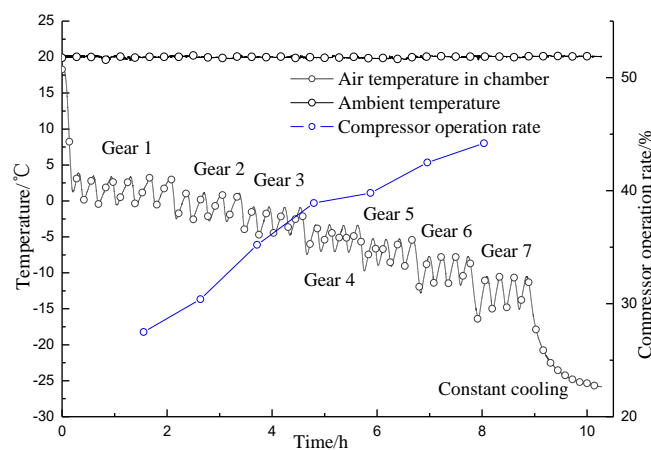


Figure 4: Variations of air temperature in the refrigerator

Table 1: Different gear parameters of the portable PV direct-drive refrigerator

Gear	1	2	3	4	5	6	7	8
Average air temperature in the chamber /°C	1.4	-0.8	-2.8	-5.2	-7.2	-9.7	-12.8	-25.9
Tremors of air temperature in the chamber /°C	4.0	4.0	3.9	3.7	3.7	3.9	4.6	/
Compressor operation rate /%	27.5	30.4	35.2	38.9	39.8	42.5	44.2	100

#### 4.2. The influences of compressor speed control strategies

In this section, the PV panel drove the DC compressor directly. The PV panel was placed outdoor and the DC refrigerator was placed in the thermostatic room where air temperature was 30°C. The temperature controller was shifted to the constant refrigeration mode. There was an internal fan and 8 bottles of water in the chamber. The water in every bottle was 550mL and the initial temperature of water was 30°C. In the first experiment of this section, the compressor rotation speed was adapted to the solar irradiation intensity. The compressor speed ranged from 2000r/min to 3500r/min. In the second experiment, the compressor rotation speed kept 2000r/min. In two experiments, the compressor started when the solar irradiation was strong enough to start the compressor and it stopped when the solar irradiation was not strong enough. The solar irradiations were similar in two experiments.

Figure 5 shows the influence of compressor speed control strategies on the variations of the compressor speed. The total operation times in two experiments were both nearly 8 hours. It could be concluded that the variable-speed refrigerator had good start-up characteristic and it could run under weak solar irradiation. When the compressor stopped, solar irradiation was 244W/m<sup>2</sup> in the variable-speed experiment, which was lower than that in the constant-speed experiment of 273W/m<sup>2</sup>. Because at the end of the variable-speed experiment, the lower chamber internal temperature caused the lower minimum input power of the refrigerator. The compressor speed of the variable-speed refrigerator adapted well to the solar irradiation. At noon, the compressor speed stopped increasing because it had reached the maximum value of 3500r/min.

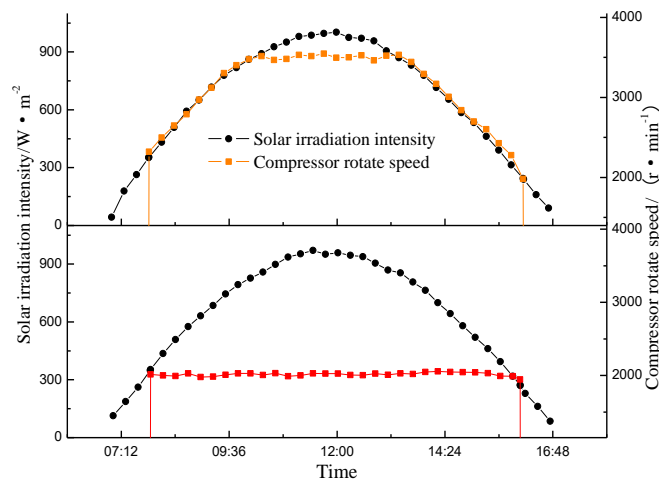


Figure 5: Variations of irradiation intensity and the compressor rotation speed

Figure 6 shows variations of temperature inside the variable-speed refrigerator and the constant-speed refrigerator. The initial temperatures of water and air in the chamber were both 30°C. During the first hour, variations of water temperatures in two experiments were similar. Because the difference between compressor rotation speeds in two experiments was not significant at the beginning. After the first hour, difference between water temperatures started widening with the widening of the difference between compressor rotation speeds. It separately took 4.6h and 5.9h to cool water down to 0°C in the variable speed experiment and the constant speed experiment. When water started freezing at 0°C, air temperature in the chamber stopped dropping. The total ice production was 978g in the variable speed experiment, which was 99.6% more than the total ice production 490g in the constant speed experiment.



The net refrigeration quantity was  $8.82 \times 10^5 \text{J}$  in the variable speed experiment, which was 22.8% more than the net refrigeration quantity  $7.18 \times 10^5 \text{J}$  in the constant speed experiment.

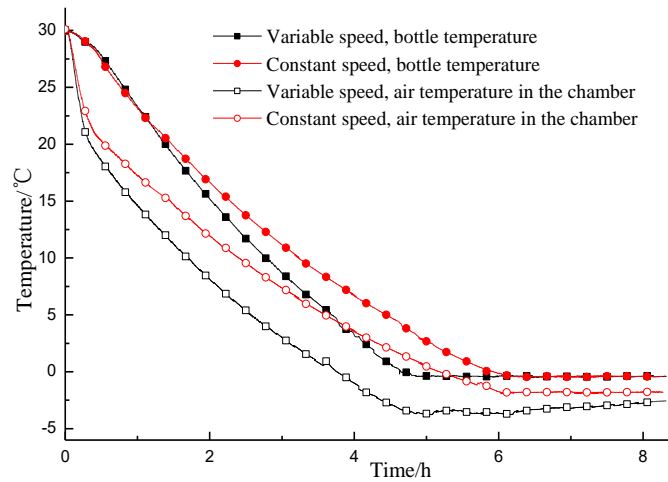


Figure 6: Variations of temperature in the refrigerator with variable speed or constant speed

Figure 7 shows variations of compressor input power of the refrigerator with variable speed or constant speed. The average compressor input power were separately 56.4W and 38.4W in the variable speed experiment and the constant speed experiment. During the first 30 minutes, the compressor input power increased rapidly. Because the input power needed by the compressor increased with the increase of the temperature difference between the evaporator and the condenser, the compressor input power of the refrigerator with constant speed began to reduce. Because the ratio of suction pressure to outlet pressure reduced with the temperature drop in the chamber. The compressor rotation speed did not stop increasing after the first 30 minutes, so the compressor input power did not stop increasing till the input power reached a maximum of 70W. However, the maximum of the compressor input power appeared earlier than the maximum of solar irradiation. Because the compressor input power is not only related with the compressor rotation speed but also related with the state of refrigerant. The speed control strategy has potential for optimisation. The daily energy consumption in the variable speed experiment and the constant speed experiment were separately 0.475kWh and 0.318kWh.

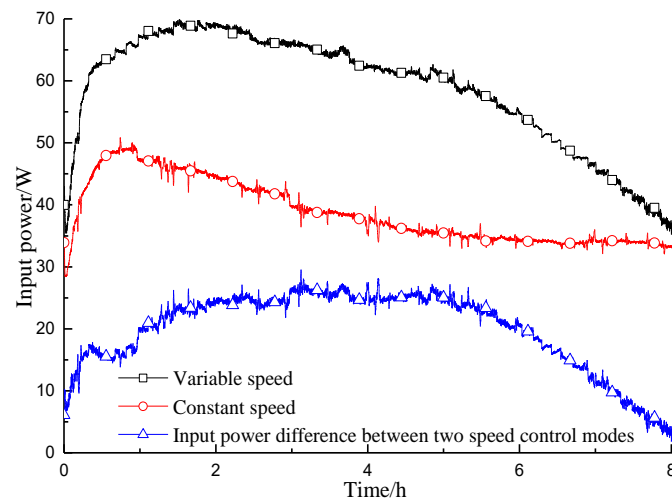


Figure 7: Variations of compressor input power of the refrigerator with variable speed or constant speed

Figure 8 shows variations of the PV utilisation efficiency in two experiments. In the morning and the afternoon, the solar irradiation was not so strong and the refrigerator could make full use of the energy generated by the PV panel. However, at noon, the solar irradiation was so strong that the energy generated by the PV panel was over the demand of the refrigerator. Therefore, the PV utilisation efficiency was lower at noon than in the morning and the afternoon.

The PV utilisation efficiency of the variable-speed refrigerator was higher than that of the constant-speed refrigerator. In the morning and the afternoon, the PV utilisation efficiency of the variable-speed refrigerator was between 80% and 100% and it was between 60% and 80% of the variable-speed refrigerator. At the beginning of operation, due to the variety of the refrigerant state, the PV utilisation efficiency rose rapidly. The average PV utilisation efficiency was 63.7% in the variable speed experiment, which was 48.1% higher than that in the constant speed experiment of 43.0%.

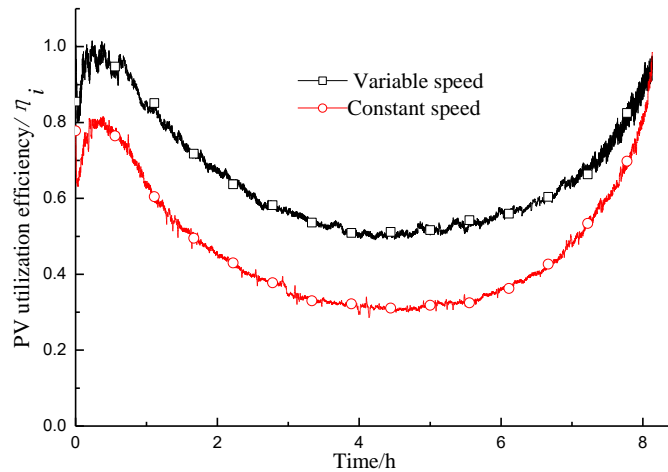


Figure 8: Variations of PV utilisation efficiency with variable speed or constant speed

#### 4.3. The influences of ambient temperature

In this section, the PV panel also drove the DC compressor directly. The PV panel was placed outdoors and the DC refrigerator was placed in the thermostatic room. The temperature controller was shifted to the constant refrigeration mode. There was an internal fan and eight bottles of water in the chamber. There was 550mL water in every bottle and the initial temperature of water was 30°C.

Figure 9 shows variations of irradiation intensity and compressor rotation speed on two consecutive sunny days. Air temperature in the thermostatic room was 30°C in the first experiment and was 20°C in the second experiment. From Figure 6, it can be seen that the solar irradiation in two days were similar so choosing the two days as experimental days was reasonable.

Two experiments all started at 07:50 and finished at 16:00. Solar irradiation intensities were all nearly 350W/m<sup>2</sup> at the beginnings of two experiments and were separately 244W/m<sup>2</sup> and 246W/m<sup>2</sup> at the ends of two experiments. The compressor rotation speeds were all adapted to the solar irradiation intensities in two experiments. It can be seen that the compressor rotation speeds adapted well to the solar irradiation. At nearly 10:10, the compressor reached to the fastest rotation speed of 3500r/min and the compressor kept this rotation speed for nearly 3.5h.

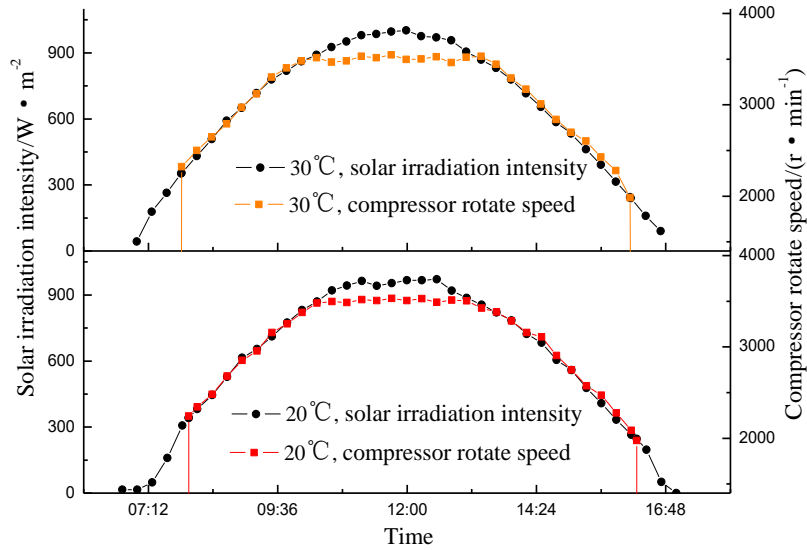


Figure 9: Variations of irradiation intensity and compressor rotation speed

Figure 10 shows variations of temperature in the chamber under different ambient temperatures. It separately took 4.1h and 4.7h to cool water down to 0°C when ambient temperature was 20°C and 30°C. When the water temperature dropped to 0°C, water started to freezing and air temperature in the chamber became constant. Air temperature in the chamber separately dropped to the lowest temperature -4.5°C and -3.8°C under 20°C ambient temperature and 30°C ambient temperature, then, air temperature in the chamber started going up because compressor rotation speed started to slow down with the reduction of irradiation intensity.

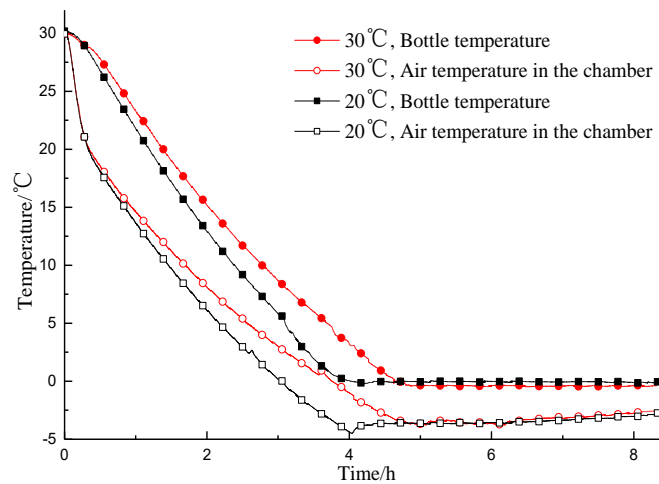


Figure 10: Variations of temperature in the chamber under different ambient temperatures

Total ice production was 1285g under 20°C ambient temperature and it was 978g under 30°C ambient temperature, which was 23.9% less than the former. The net refrigerating effect was  $8.82 \times 10^5 \text{J}$  under 30°C ambient temperature, which was 10.5% lower than that under 20°C ambient temperature of  $9.85 \times 10^5 \text{J}$ . It can be concluded that ambient temperature has great influence on the performance of this PV direct-driven variable-speed refrigerator. So, the adiabatic performance of the refrigerator should be enhanced.

Figure 11 shows variations of PV input power under different ambient temperature. The daily average PV input power was 52.0W under 20°C ambient temperature and 56.4W under 30°C ambient temperature so ambient temperature has limited effect on the PV input power.

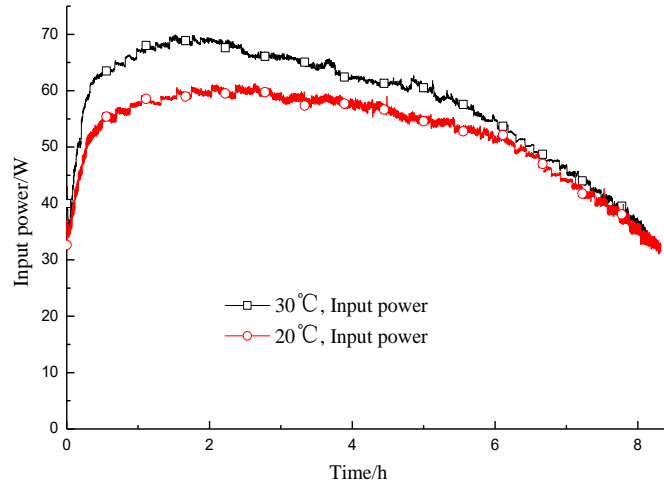


Figure 11: Variations of PV input power under different ambient temperature

#### 4.4. The influences of the internal fan

Figure 12 shows the variations of temperature inside the refrigerator with or without the internal fan. The refrigerator was also driven by the DC power supply, and the internal fan was a small DC fan. In the chamber, there were eight bottles of water to be refrigerated and water in every bottle was 550mL. The ambient temperature was 30°C, and the initial temperature of water in the chamber was 21°C. The temperature controller was shifted to gear 1.

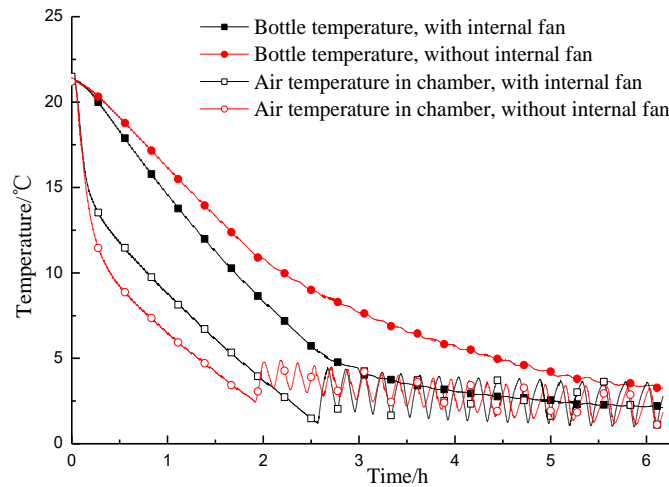


Figure 12: Variations of temperature inside the refrigerator with or without internal fan

It separately took 2.67h and 4.40h to cool water down to 5°C for the refrigerator with the internal fan and the one without the internal fan. After 6h operation, water in the chamber was separately cooled down to 3.4°C and 2.2°C. It can be concluded that the internal fan can speed up the cooling of water so the use of the internal fan can meet the demand of quick temperature drop. It can be seen that the positions of the temperature curves, "Bottle temperature, with internal fan" and "Bottle temperature, without internal fan", are closer than the positions of the other two temperature curves. In the constantly operation period of compressor, air temperature in the chamber with the internal fan was higher than that without the internal fan because the heat transfer between air and water in the chamber with the internal fan was more sufficient.

It took more time for the refrigerator with the internal fan from the beginning of operation to the first stop of the compressor than the one without the internal fan because the internal fan could speed up heat transfer, and it took more time for refrigerant to reach the stop temperature of the temperature controller. The thermometer bulb of the temperature controller was near the evaporator. The internal fan sped up the heat transfer between the evaporator

and air in the chamber, which caused that evaporator temperature to be higher and the air temperature lower. When the compressor first stopped, air temperature in the chamber with the internal fan was lower than that without the internal fan.

In the intermittently operation period of compressor, the compressor operation time rates of internal fan group and without internal fan group were similar, separately 37.9% and 34.8%. It can be concluded that the internal fan had limited effect on the operation of refrigerator in the intermittently operation period. The higher operation time rate of the internal fan group was caused by the better heat transfer in the chamber. Figure 13 shows energy consumption of two experiment groups. The total energy consumption of two experiment groups were separately 0.233kWh and 0.209kWh. The internal fan has limited effect on the energy consumption of the system.

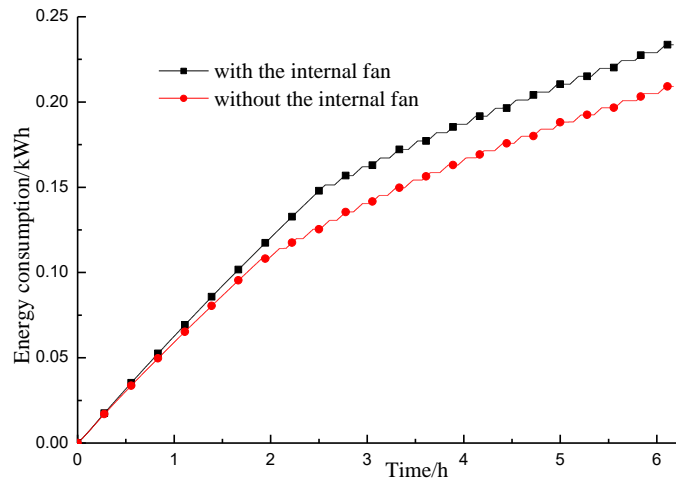


Figure 13: Power consumption of the refrigerator with or without internal fan

Table 2 shows the summary of experiment results.

Table 2: Summary of experiment results

		Ice production	Net refrigerating effect	PV utilisation efficiency
Experiments about the compressor rotation speed control strategy	Variable compressor rotation speed	978 g	$8.82 \times 10^5$ J	63.7%
	Constant compressor rotation speed	490 g	$7.18 \times 10^5$ J	43%
Experiments about the ambient temperature	20°C	1285g	$9.85 \times 10^5$ J	/
	30°C	978g	$8.82 \times 10^5$ J	/
		Duration of cooling water down to 5°C	Compressor operation rate	Energy consumption
Experiments about the internal fan	With internal fan	2.67 h	37.9%	0.233 kWh
	Without internal fan	4.40 h	34.8%	0.209 h

## 5. CONCLUSIONS

A novel portable PV direct-driven variable-speed refrigerator was proposed in this paper and the influences of the compressor speed control strategy, the ambient temperature and the internal fan were experimentally investigated.

- 1) The variable compressor speed control strategy can significantly improve the performance of the PV

direct-driven refrigerator. The PV utilisation efficiency, the ice production and the net refrigerating effect of the variable-speed refrigerator were separately 48.1%, 99.6% and 22.8% higher than that of the constant-speed refrigerator and the speed control strategy still has potential for optimisation.

- 2) The ambient temperature has a big influence on the performance of this portable PV direct-driven variable-speed refrigerator. The net refrigerating effect was  $8.82 \times 10^5 \text{J}$  under  $30^\circ\text{C}$  ambient temperature which was 10.5% lower than that under  $20^\circ\text{C}$  ambient temperature of  $9.85 \times 10^5 \text{J}$ .
- 3) The internal fan has no significant influence on the energy consumption of the refrigerator, but it can significantly raise the cooling rate. It separately took 2.67h and 4.40h to cool water down to  $5^\circ\text{C}$  for the refrigerator with the internal fan and the refrigerator without the internal fan.

## 6. REFERENCES

Axaopoulos PJ, Theodoridis MP, 2009. Design and experimental performance of a PV Ice-maker without battery. *Solar Energy*, 83: 1360-1369.

Bansal PK, Martin A, 2000. Comparative study of vapor compression, thermoelectric and absorption refrigerators. *International Journal of Energy Research*, 24(2): 93-107.

Daffallah KO, Benganem M, Alamri SN, et al., 2017. Experimental evaluation of photovoltaic DC refrigerator under different thermostat settings. *Renewable Energy*, 113: 1150-1159.

Ekren O, Celik S, Noble B, et al., 2013. Performance evaluation of a variable speed DC compressor. *International Journal of Refrigeration*, 36: 745-757.

Loan S, Calin S, 2013. Review of solar refrigeration and cooling systems. *Energy and buildings*, 67: 286-297.

Opoku R, Anane S, Edwin IA, et al., 2016. Comparative techno-economic assessment of a converted DC refrigerator and a conventional AC refrigerator both powered by solar PV. *International Journal of Refrigeration*, 72: 1-11.

Toure S, Fassinou WF, 1999. Cold storage and autonomy in a three compartments photovoltaic solar refrigerator: experimental and thermodynamic study. *Renewable Energy*, 17: 587-602.

---

## #45: Combined cycle of seawater thermal desalination plant

---

Ashraf HASSAN

*Qatar Environment and Energy Research Institute, Hamad Bin Khalifa University, Qatar Foundation, Doha, Qatar, [ahassan@hbku.edu.qa](mailto:ahassan@hbku.edu.qa)*

*In this work, the multi-stage flash (MSF) process and the multiple-effect distillation (MED) process are combined together using thermal vapor compressor (TVC) to form a combined cycle of distillation (CCD) plant to produce desalted water with high-gain output ratio (GOR). The technologies of MSF, MED and TVC have already been proven and are available as commercial plants in international markets in many countries where the combination is called combined cycle of distillation (CCD) plant. The CCD system has a special coupling and configuration that uses nine stages of MSF process, seven Effects of MED process and two apparatus of TVC. Stage #6 has a special configuration to adapt the new configuration. The capital cost of the CCD plant decreased by increasing the GOR and by decreasing the number of MSF stages. The design of CCD plant includes some modification on the conventional design of MSF and MED plants. The following are the main features of CCD plant, with the GOR able to reach around 20 and specific power consumption decreasing to less than 3.5 kWh/m<sup>3</sup>. The calculations, results and drawings have been generated and proven using the following three types of software: Engineering Equation Solver (main program), Matlab R2016b and Microsoft Developer Studio (FORTRAN power Station 4.0).*

*Keywords: combined cycle of distillation plant, multi stage flash, multiple effect distillation, thermal vapor compressor*

## 1. INTRODUCTION

The thermal efficiency of thermal water desalination plants is quantified by the Gain Output Ratio (GOR) defined as the quantity of distillate produced per unit of heating steam used. Figure 1 shows sets of global trends of GOR for many plants all over the world, which the maximum GOR of multi stage flash (MSF) process and multiple effect stage flash (MED) plants scattered between 8-9 and 8-11, respectively.

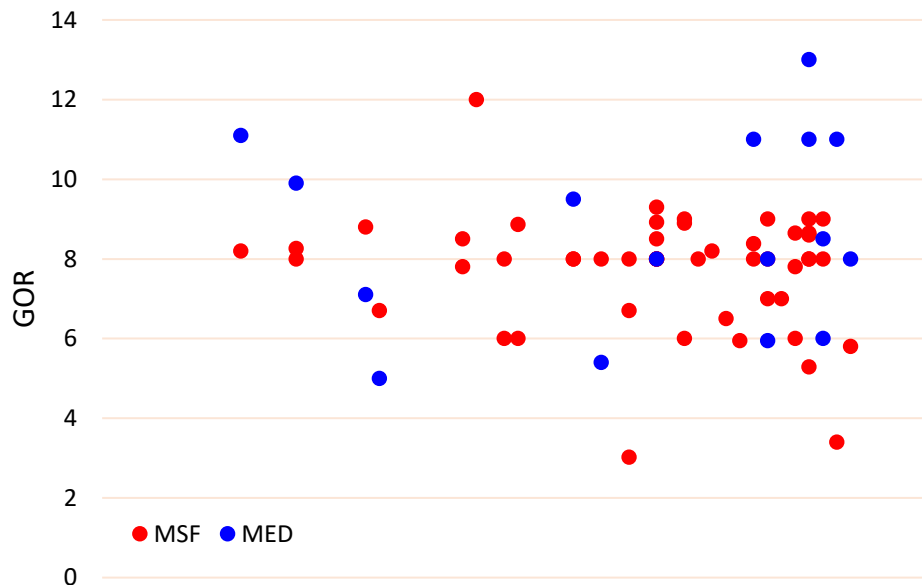


Figure 1: Sets of global GOR for MSF and MED plants since 1970 (source: DesalData 2016)

Recent installed power plants all over the world are using combined cycle (CC) power plant (Darwish *et al.*, 2016). The CC cycle consists of gas turbine (GT), heat recovery steam generators (HRSG), and steam turbine (ST). In these plants, GTs produce electric power (EP) and its hot gas exhaust operates the HRSG to generate steam. The steam is supplied to ST to generate more EP, and its extracted (or discharged) steam is directed to a thermally-operated desalting plant (DP), e.g. multi-stage flash (MSF) or multi-effect thermal vapor compression producing desalted seawater (DW). A plant producing both EP and DW is called a co-generation power desalting plant.

The present work relates to thermal desalination processes using MSF and multiple effect distillation (MED) evaporators coupled with thermal vapour compressor (TVC). In distillation processes, seawater is heated to evaporate pure water that is subsequently condensed. The performance of distillation processes increases with increasing number of chambers/evaporators. TVC coupled with MED process to increase its performance. The current MSF plants consist of 20-24 stages to achieve about GOR less than 9, while the current MED plants consist of 6-8 effects to give the value of GOR about 11 or less.

Zeitoun *et al.* (Zeitoun, Alansary and Nuhait, 2016b) filed a patent for desalination system for MSF process and TVC, which the system modified by replacing the condenser in the last stage with a TVC to transfer vapour to the first stage. Each stage having a flashing section extending vertically, a condensing section extending horizontally to overlay the flashing section of the next succeeding stage, and a demister. Zeitoun *et al.* (Zeitoun, Alansary and Nuhait, 2016a) filed another patent on MED desalination system. The MED system includes a housing having a heating box, a plurality of vessels, a plurality of heat rods within each of the vessels, and a condenser unit. A separator wall separates each vessel. Each heat rod extends through one of the separator walls, such that each heat rod has a first end extending into one vessel and a second end extending into an adjacent vessel.

El-Sayed (El-Sayed, 2017) filed a patent on combination MED system and MSF system. The combination MED and MSF evaporation system integrates a MSF system with a MED system such that the flashing temperature range of MSF process is shifted upward on the temperature scale (e.g., 70-120°C), while the MED process operates in the lower temperature range (e.g., below 70°C). The MSF system includes a plurality of flash evaporation/condensation stages, such that the MSF evaporation system receives a stream of seawater or brine after being preheated by feed heaters of MED system. The MED system includes a plurality of evaporation/condensation effects, such that the MED evaporation system receives the heated concentrated brine from MSF system. While, the brine heater connected in between MSF system and the boiler.

The choice of thermal vapour compressor to transform the thermal energy of motive steam will primarily depend on the final vacuum to be achieved (Hassan and Darwish, 2014). The net result of these energy transformations is



an increase of the absolute pressure of the mixture on discharge to several times the pressure at which it entered the ejector inlet. The performance formula of mixing ratio is used to this work.

The high cost of desalted seawater (DW) calculated in this paper calls for the use of more energy efficient desalting system such as the seawater reverse osmosis (SWRO) system in place of the multistage flash (MSF) and multi effect thermal vapour compression (METVC) methods presently used. Both MSF and METVC use thermal energy of about 270 kJ/m<sup>3</sup> and pumping energy of 2–4 kWh/m<sup>3</sup>. When added to the pumping energy, it gives the specific consumed energy of more than 20 kWh/m<sup>3</sup>, compared to 4–5 kWh/m<sup>3</sup> for SWRO system (Darwish, Abdulrahim and Hassan, 2016). All newly built power plants in Qatar are using combined cycle (CC), due to good reasons, including low capital cost, less negative environmental impact when natural gas (NG) is used as fuel, and significantly higher efficiency 44–55% in the high-temperature environment in the Gulf Cooperation Council at full load.

## 2. DESCRIPTION OF COMBINED CYCLE OF DISTILLATION PLANT

The combined cycle of distillation (CCD) plant comprises of 9 stages of multi stage flash (MSF) system (from 1 to 9) and 7 effects of multiple effect distillation (MED) system (from 10 to 16), as shown in Figure 2. Both systems are coupled together with using two thermal vapour compressors (TVC). The discharged steam of TVC<sub>MSF</sub> is used as heat source in the brine heater of MSF system, which the motive steam of TVC is coming from the power plant while the entrained vapour is sucked from the generated vapour of stage #6 and flash box #6. While the TVC<sub>MED</sub> is providing the discharged steam into the effect #10 of MED system, which the motive steam is coming from the power plant and the entrained vapour is coming from last effect #16.

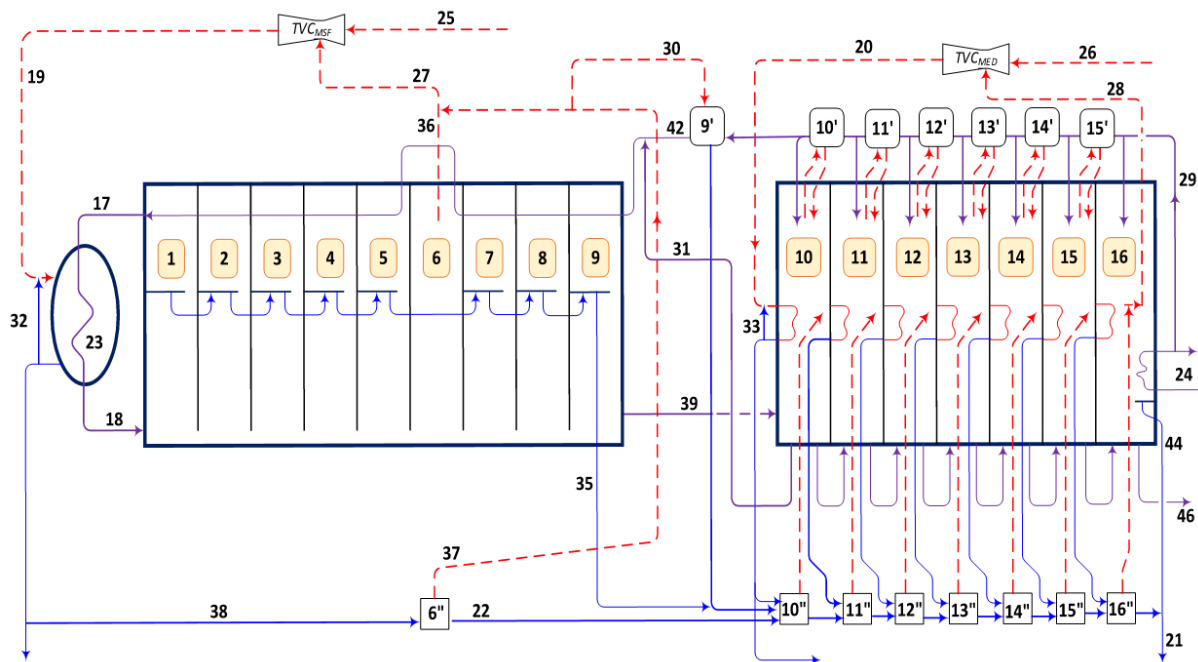


Figure 2: Layout of the combined cycle of distillation (CCD) plant

Stage #9 discharges the brine into effect #10 at sudden reduction in pressure to generate some vapour. While, the brine of effect #10 is split into two lines, the 1<sup>st</sup> one will pass into the next effect for flashing in and the 2<sup>nd</sup> one is recycled to mix with the warmed feed water of preheater #9' to form the recycled feed water for MSF stages. The accumulated condensed water in stage #9 will get out of the stage to flash into flashing box #10''.

The seawater passed into the last effect #16 to condense the remained vapour there, as the warmed seawater will be rejecting again to the sea. While before discharging the warmed seawater into the sea, a makeup water will be used to feed the MED effects and MSF stages through passing of number of the preheaters to raising the feed water temperature.

Table 1 shows the operating input values that used in the heat and mass balance calculations to know how much distillate water can be produced if each TVC used 1 kg/s as a motive steam. The configuration of the operational conditions of TVCs are shown in Table 2 using the performance formula by Equation 1. The mixing ratio ( $Mr$ ) can be calculated as a function of the compression ratio ( $Cr$ ) and expansion ratio ( $ER$ ) as determined in Equation 1. The mixing ratio ( $Mr = Mms/Ment$ ) of the outlet steam depends on the compression ratio ( $Cr = Pd/Ps$ ) and expansion ratio ( $Er = Pms/Ps$ ). Where,  $Mms$  is the flow rate of motive steam,  $Ment$  is the flow rate of entrained vapour,  $Pd$  is

the discharge pressure of mixed steam,  $P_s$  is the suction pressure of entrained vapour and  $P_{ms}$  is the motive steam pressure (Hassan and Darwish, 2014).

Table 1: The used input values

Item #	Temperature, °C	Pressure, bar	Salinity, ppm	Flow Rate, kg/s	Vapour Fraction
Line 24	35	--	45000	--	0
Line 18	109.2	--	--	--	0
Brine of stage #16	44	--	--	--	0
Brine of effect #10	66	--	--	--	0
Brine of stage #9	73.22	--	--	--	0
Line 25	--	20	--	1	1
Line 26	--	6	--	1	1

Table 2: Operating conditions of the thermal vapour compressors

Item	$TVC_{MSF}$	$TVC_{MED}$
Mass flow of entrained vapour, kg/s	0.5083	0.5707
Expansion ratio	35.64	69.36
Compression ratio	3.3	3.5
Mixing ratio	1.967	1.752
Discharged temperature, °C	140.8	107
Discharged pressure, bar	1.852	0.3028

Equation 1:

$$Mr \left\{ \begin{array}{l} = -1.611 + 11.033 * LN(Cr) + 13.528 / Er - 14.934 * LN(Cr)^2 - 34.440 / Er^2 - 48.477 * LN(Cr) / Er \\ \quad + 6.462 * LN(Cr)^3 + 29.970 / Er^3 + 70.811 * LN(Cr) / Er^2 + 46.959 * LN(Cr)^2 / Er \\ \quad , at 2 \leq Er < 10 \\ = -3.208 + 3.933 * Cr + 27.236 / Er - 1.192 * Cr^2 - 141.423 / Er^2 - 22.546 * Cr / Er + 0.126 * Cr^3 \\ \quad + 348.507 / Er^3 + 41.796 * Cr / Er^2 + 6.440 * Cr^2 / Er \\ \quad , at 10 \leq Er < 100 \\ = -1.934 + 2.153 * Cr + 113.491 / Er - 0.522 * Cr^2 - 14735.965 / Er^2 - 31.852 * Cr / Er + 0.048 * Cr^3 \\ \quad + 900786.045 / Er^3 - 495.582 * Cr / Er^2 + 10.025 * Cr^2 / Er \\ \quad , at Er \geq 100 \end{array} \right.$$

Where:

- Mr = mixing ratio (motive steam flow rate per entrained vapour flow rate)
- Cr = compression ratio (discharge pressure per suction pressure)
- Er = expansion ratio (motive steam pressure per suction pressure)

In MSF stages, the heated seawater (42) and recycled brine (31) are mixing together then passing through tubes into each evaporator chamber from stage #9 to stage #1 except stage #6, where it progressively heated. The heated seawater (17) is heated to the maximum temperature in the brine heater (23) by the heating steam source (19) and adapted its thermal conditions by desuperheater (32), which the function of the desuperheater is to pump a controlled stream of the condensate to control steam temperature. Subsequently, the heated brine (18) flows through nozzles into the stage #1, which is maintained at a pressure slightly lower than the saturation pressure of the incoming stream. As a result, a small fraction of the brine flashes forming pure vapour. The generated vapour passes through a demister in the upper part of the stage, where it condensed on the outer surface of the horizontal condensing brine tubes and is collected in a distillate tray. The heat transferred by the condensation warms the incoming feed water as it passes through that stage. The remaining brine passes through successively through all MSF stages at progressively lower pressures, where the process is repeated. As well, the hot distillate flows from stage #1 to stage #9 and cools itself by flashing a portion into steam which is re-condensed on the outside of the tube bundles. The collected distillate (35) flows at stage #9 and flashes into flashing box #10", while the remaining brine (39) by stage #9 will pass into effect #10. The same amount of the entrained vapour (27) mixes, as a condensate, will flash into the flashing box #6".

The main part of the generated vapour (36) of stage #6 and the flashed vapour (37) of flash box #8", both are entrained together by  $TVC_{MSF}$  as mentioned above to mix with the motive steam and then discharging into the brine heater. The remained vapour (30) passes for heating the seawater into preheater (9') and then to raise its

temperature. Meanwhile, the vapour formed in the effect #16, is entrained by  $TVC_{MED}$  to mix with the motive steam then discharge into the horizontal tubes of effect #10 as the final condenser will condense the rest of the generated vapour.

In  $MED$  effect, the  $TVC_{MED}$  provides the effects with a heating steam (20), which it mixes with a condensate in the desuperheater (33) then used as a heating steam into the effect #10 causing the evaporation of the sprayed feed water. The generated vapour passes through the preheater (10') then introduced into the following effect. In each effect, the generated vapour is condensed in the horizontal tubes and heat of the condensation derived from it is utilized to evaporate the sprayed feed water on the outer surface of the tubes. The remaining part of the sprayed feed water is fall down as a brine at higher temperature and salinity then flashes into the next effect, and so on.  $TVC_{MED}$  will entrain a part of the generated vapour (28) in the last effect #16, while the final condenser will condense the remaining vapour (44) using the cold seawater (24). The exit-warmed seawater of the final condenser divides into two streams; the first stream (29) is used to feed the  $MED$  effects and  $MSF$  stages; and the second will reject into the sea after mixing with the final discharged brine (46).

The stream (39) of the discharged brine flashes into the effect #10 and used as a one of heating sources for the next effect #11. In the effect #10, the remained brine of the sprayed feed water and the stream of (39) will flow outside the effect #10 and divides into two streams; the first stream (31) will be recycled and mixed with the stream (42) to form the recycled flow of  $MSF$  stages; while the second stream will flashed into the next effect #11. In flash box #10", four condensed streams are collected to flash in. The four streams are the condensate (22) of the flash box #6", the condensate (30), condensate (35) and the same amount of entrained vapour (28) from the condensate (20) plus (33). The flashed vapour will mix with the generated vapours in effect #10 to raise the temperature of the feed water and as a heat source for the next effect. The remaining condensate of flash box #10" will flash into the next flash box #11", and so on. In the final condenser, the seawater (24) condenses the vapour in the last effect #16 and during the condensation process of vapour, the temperature of the seawater increases. A stream (29) of the heated seawater used to provide the  $MED$  effects with the required feed water, from #16 to #10, where the feed water passes through the number of preheaters to increase its temperature. Another part (42) of the warmed seawater will pass through the preheaters to makeup  $MSF$  stages.

### 3. DISCUSSION AND RESULTS

As mentioned above, the main systems of CCD plant includes 9 stages of  $MSF$  process, 7 effects of  $MED$  process and 2  $TVC$  to provide the heat sources for brine heater and 1<sup>st</sup> effect of  $MED$ . In  $MSF$  stages, the generated vapour at the condition of stages #6 is designed to entrain by  $TVC_{MSF}$ . Although the generated vapours by stage #6 and by flashing box #6" are used as a part of heat source to reduce the value of motive steam for the brine heater, they returned again to accumulate as condensate with other condensed vapours. While, the discharged brine from stage #9 will be used to flash into effect #10, which the generated vapour will be mixed with the generated vapour by spayed feed and the generated vapour by flashing box #10" and then all the three vapours are used as a heating vapour for the next effect #11. Therefore, the generated vapour by effect #11 is rapidly increased, as shown in Figure 3.

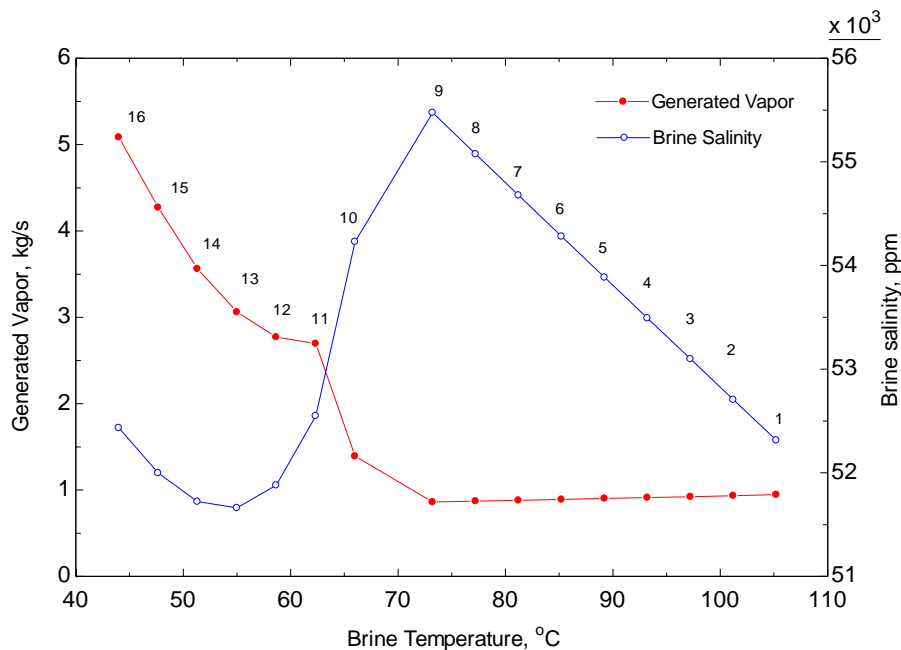


Figure 3: The distribution of generated vapour and brine salinity per each stage/effect as function of brine temperature

Table 3 shows the operating conditions of all CCD stages and effects. The generated vapour in MSF stages decreased sequentially, while in MED increased rapidly starting from effect #11 until last effect due the increasing the sources of heating vapours in the horizontal tubes. Therefore and due to the behaviour of the generated vapour, the brine salinity in MSF stages will slightly increase from stages #1 to stage #9, while the brine salinity starting from effect #10 to last effect has decreased, as shown in Figure 3.

Table 3: Operating conditions of MSF stages and MED effects

	$T_b, ^\circ\text{C}$	$M_{gv}, \text{kg/s}$	$S_b, \text{ppm}$
Stage #1	105.2	0.9459	52314
Stage #2	101.2	0.9345	52706
Stage #3	97.22	0.9233	53098
Stage #4	93.22	0.9123	53491
Stage #5	89.22	0.9016	53886
Stage #6	85.22	0.8910	54281
Stage #7	81.22	0.8806	54678
Stage #8	77.22	0.8705	55076
Stage #9	73.22	0.8605	55475
Effect #10	66.00	1.392	54229
Effect #11	62.33	2.696	52549
Effect #12	58.67	2.772	51879
Effect #13	55.00	3.061	51661
Effect #14	51.33	3.562	51722
Effect #15	47.67	4.272	51997
Effect #16	44.00	5.085	52433

The recycled flow in the tubes bundle of MSF stages and brine heater can be calculated using Equation 2, while the generated vapour and brine salinity per each stage of MSF can be determined using Equation 3 and Equation 4, respectively. The resources of heating vapour in the horizontal tubes in effect #11 can calculated by Equation 5, which consists of three types of generated vapours.

$$\text{Equation 2: } M_{rec} = (M_{ms,msf} + M_{ent,msf} + M_{desup}) \frac{E_d - E_{sf}}{C_p (T_{TBT} - T_{f,1})}$$

$$\text{Equation 3: } M_{gv,i}|_{msf} = \frac{M_{b,i-1} C_p (T_{b,i-1} - T_{b,i})}{h_{g,i} - C_p T_{b,i}}$$

$$\text{Equation 4: } S_{b,i}|_{msf} = \frac{M_{b,i-1} S_{b,i-1}}{M_{b,i}}$$

$$\text{Equation 5: } M_{hs,11}|_{med} = M_{gv,10}|_{med} + M_{fb\_v,10} + M_{f\_v,10}$$

$$\text{Equation 6: } GOR = \frac{M_{prod}}{M_{hs}}$$

Where:

- $M_{b,rec}$  is the value of (41) the flow rate of recycled part of the (39)
- $M_{b,g}$  is the value of (39) the flow rate of the discharged brine from stage #9
- $M_{prod}$  is the water production rate of the CCD plant
- $M_{hs}$  is the consumption rate of the heating steam from an external source (power plant)

The gain output ratio (*GOR*) used to measure the performance of the desalination processes of *CCD* plant as defined in Equation 6. The part of warmed seawater that used to feed the *MED* effects can be affected on the *CCD* plant performance, which increasing backup feed water consumption into *MED* will increase the *GOR* but also will increase the *SPC*. Figure 4 shows effect of changing of feed water flow rate of *MED* effects from 50 kg/s to 300 kg/s on *GOR* and *SPC*, where the *GOR* changed from 16.91 to 19.01, respectively. While the *SPC* is increased from 2.483 kWh/m<sup>3</sup> at 50 kg/s, to 3.356 kWh/m<sup>3</sup> at 300 kg/s.

As in the most locations in the Gulf Countries, the salinity of seawater is 45000 ppm as the recycled feed water for *MSF* stages is about 51924 ppm. As shown in Figure 2 and mentioned in Table 3, the brine salinity will change from 52314 ppm in stage #1 to 55475 ppm in stage #9. Since the discharged brine of stage #9 will mix with the brine of *MED* effect #10 of low salinity, then the brine lowered to 51661 ppm at effect #13 and increased to 52433 ppm in last effect. Meanwhile, Figure 5 shows the effect of feed water flow rate of warmed seawater that discharged from the final condenser on the brine salinity. At lower flow rate less than 100 kg/s of feed water, the salinity of *MED* effects could reach to dangerous values higher than 70,000 ppm.

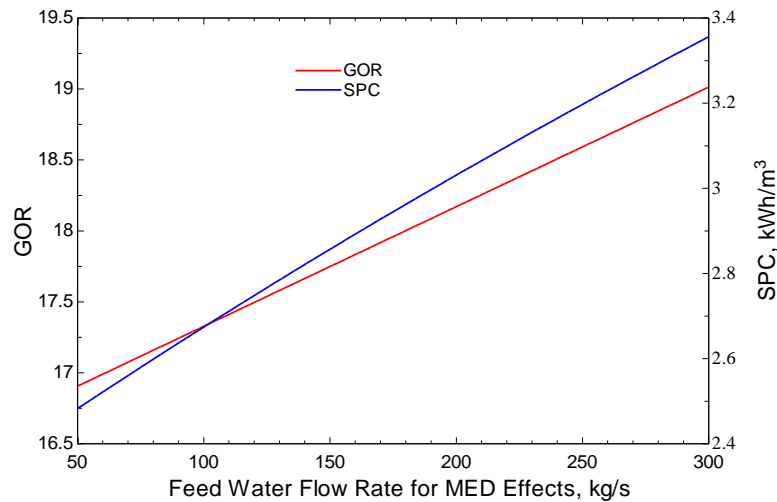


Figure 4: Effect of the feed water flow rate on *GOR* and specific power consumption

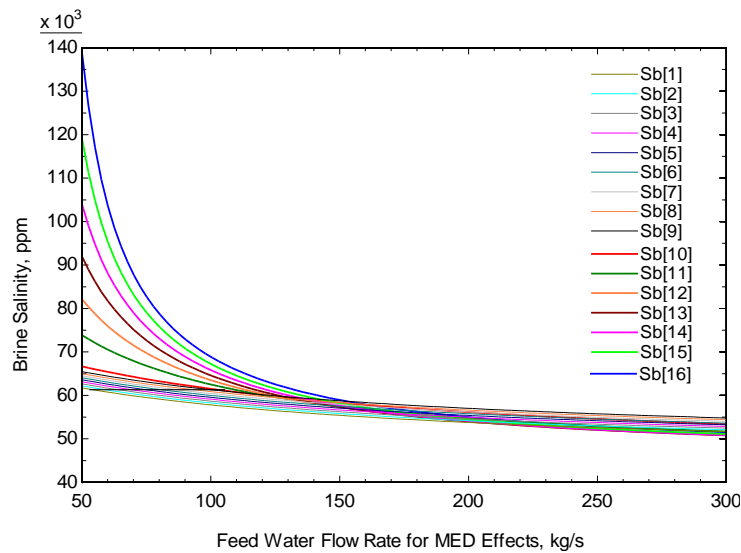


Figure 5: Effect of the feed water flow rate on the brine salinity

Efficiency of the boiling process to generate vapour is higher than the efficiency to generate vapour by flashing. Therefore, the coupling between *MSF* and *MED* plants in *CCD* design is based on flashing the brine of *MSF* process in *MED* effects to generate more vapour then used it as a heat source in next effects. In addition, the higher temperature difference will generate much vapour flow rate. The temperature difference in *MSF* stages is 4.0°C, while the brine temperatures if stage #9 and effect #10 are 73.22°C and 66.00°C, as mentioned in Table 1. Therefore, the discharged brine by stage #9 will generate more vapour in effect #10 than that generated in previous stages, respectively as shown in Table 3. Figure 6 shows parametric results to study the effect of brine temperature of stage #9 on the plant performance. Brine temperature of stage #9 is tested from 68°C to 78°C. As a result, more vapour will be generated in *MED* effects and so the distilled water flow rate of *CCD* plant will increase. In addition,

the GOR of the CCD plant will increase from 14.82 at 68°C to 22.05 at 78°C. Figure 7 shows the effect of increasing the brine temperature of stage #9 leads to decrease the SPC due to increasing the distilled water flow rate of CCD plant.

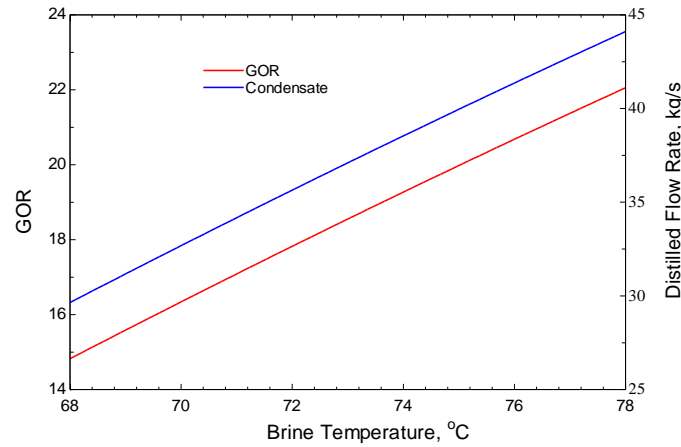


Figure 6: Effect of brine temperature of MSF stage #9 on the GOR and condensate flow rate

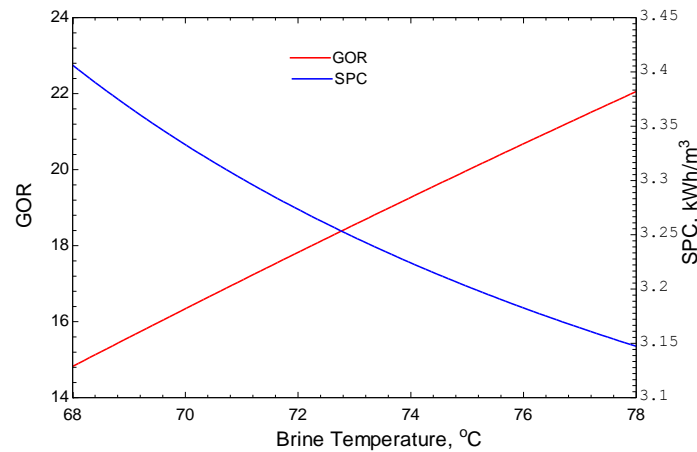


Figure 7: Effect of brine temperature of MSF stage #9 on the GOR and SPC

#### 4. CONCLUSIONS

As mentioned above, the CCD plant is a combination between MSF process, MED process and TVC apparatus. A CCD plant includes a plurality of multi stage flash evaporators, a plurality of multiple effect distillation evaporators, and a plurality of thermal vapour compressors. The thermal vapour compressors thermally energize the multi stage flash evaporators and the multiple effect distillation evaporators. A coupling system installed to provide the CCD plant more flexibility in operation to integrate MSF, MED and TVC. The following are the main features of CCD plant:

1. The CCD plant represents a breakthrough GOR to produce fresh water using hybrid thermal desalination plants.
2. Specific electric power consumption reached to less than 3.5 kWh/m<sup>3</sup>.
3. The water production cost will be decreased due to increasing the distillate water production and due to decreasing the capital cost by reducing the number of stages of MSF.

#### 5. APPENDIX

$$\text{Equation 7: } P_{sat} = \exp \left( 11 + 0.0068 - \frac{3052.027}{273.15 + T_v} - \frac{451032}{(273.15 + T_v)^2} + \frac{2.308 \times 10^7}{(273.15 + T_v)^3} \right) \times 0.981$$

$$\text{Equation 8: } h_f = -0.034 + 4.21 * T_v - 6.2 * 10^{-4} * T_v^2 + 4.5 * 10^{-6} * T_v^3$$

Equation 9: 
$$h_{fg} = 2501.9 - 2.41 * T_v + 1.2 * 10^{-3} * T_v^2 - 1.6 * 10^{-5} * T_v^3$$

Equation 10: 
$$h_g = 2501.69 + 1.807 * T_v + 5.088 * 10^{-4} * T_v^2 - 1.1221 * 10^{-5} * T_v^3$$

Equation 11:

$$T_{sat} \left\{ \begin{array}{ll} = -2103.5 * P_v^6 + 6456.5 * P_v^5 - 7980.7 * P_v^4 + 5133.3 * P_v^3 & \\ \quad - 1885.3 * P_v^2 + 452.16 * P_v + 14.941 & , 0.1 \leq P_v \leq 0.8 \\ = 2.207 * P_v^3 - 15.89 * P_v^2 + 52.805 * P_v + 60.491 & , 0.9 \leq P_v \leq 2.3 \\ = -0.00000008 * P_v^6 + 0.0006 * P_v^5 - 0.0192 * P_v^4 + 0.3304 * P_v^3 & \\ \quad - 3.3931 * P_v^2 + 24.569 * P_v + 82.798 & , 2.4 \leq P_v \leq 5.4 \\ = 0.0065 * P_v^3 - 0.3755 * P_v^2 + 9.9958 * P_v + 111.06 & , 5.5 \leq P_v \leq 20.5 \end{array} \right.$$

## 6. NOMENCLATURE

Abbreviations		Subscription	
$C_r$	Compression ratio	$b$	Brine
$E$	Enthalpy, kJ/kg	$d$	Discharge
$E_r$	Expansion ratio	$f$	Fluid
$GOR$	Gain output ratio	$f_v$	Flashed vapor by brine
$h$	Enthalpy, kJ/kg	$fb_v$	Flashed vapor by distillate in the flashing boxes
$M$	Mass flow rate, kg/s	$fg$	Latent heat
$M_r$	Mixing ratio	$g$	Gas
$P$	Vapor pressure, bar	$gv$	Generated vapor
$S$	Brine salinity, ppm	$hs$	Heating steam
$T$	Temperature, °C	$med$	Multiple effect distillation
		$msf$	Multi stage flash
		$prod$	Production
		$rec$	recycle
		$sat$	Saturation
		$sf$	Saturation fluid
		$v$	Vapor

## 7. REFERENCES

Darwish, M. A. *et al.* (2016) 'Retrofitting the combined-cycle producing electric power and desalted seawater to include district cooling in GCC', *Desalination and Water Treatment*, 57(12), pp. 5331–5344. doi: 10.1080/19443994.2015.1007172.

Darwish, M. A., Abdulrahim, H. K. and Hassan, A. S. (2016) 'Realistic power and desalted water production costs in Qatar', *Desalination and Water Treatment*, 57(10), pp. 4296–4302. doi: 10.1080/19443994.2014.992977.

El-Sayed, E. (2017) 'US 9,539,522 B1'.

Hassan, A. S. and Darwish, M. A. (2014) 'Performance of thermal vapor compression', *Desalination*, 335(1). doi: 10.1016/j.desal.2013.12.004.

Zeitoun, O., Alansary, H. and Nuhait, A. (2016a) 'US 9,309,129 B1'.

Zeitoun, O., Alansary, H. and Nuhait, A. (2016b) 'US 9,393,502 B1'.



---

## #46: Integration of vacuum multi-effect membrane distillation with adsorption/cooling system

---

Ashraf HASSAN<sup>1\*</sup>, Raya AL-DADAH<sup>2</sup>, Saad MAHMOUD<sup>2</sup>, Hassan FATH<sup>3</sup>, Eman HUSSEIN<sup>2</sup>, Nourhan GENIDI<sup>1</sup>

<sup>1</sup>Qatar Environment and Energy Research Institute, Hamad Bin Khalifa University, Qatar Foundation, Doha, Qatar

<sup>2</sup>University of Birmingham, Birmingham, UK

<sup>3</sup>Egypt-Japan University of Science and Technology, Alexandria, Egypt

\*Corresponding author: [ahassan@hbku.edu.qa](mailto:ahassan@hbku.edu.qa)

*This paper addresses the integration of vacuum multi-effect membrane distillation (VMEMD) with adsorption (AD) unit using metal organic frameworks (MOF) adsorbent material to produce potable water and cooling water. VMEMD is a combination of the two concepts of vacuum membrane distillation (VMD) and multi-effect distillation (MED), where permeate side is vacuumed yielding lower vapour pressure than in the feed side thus generating the distillation process. Such technology can effectively exploit the vacuum conditions associated with the adsorption process yielding higher potable water production rates. The AD unit is a heat-driven technology that can be used to generate potable water and cooling through adsorption / desorption of water vapour by a porous adsorbent material. Metal Organic Framework (MOF) is a new class of porous material with high surface area (up to 5500m<sup>2</sup>/g), superior adsorption characteristics and large porosity. Aluminium Fumarate is an MOF material that was shown to have water vapour adsorption characteristics superior to those of silica gel and zeolite. The CPO-27(Ni) was found to be more suitable for applications working at a low evaporation temperature (5°C) and high regeneration temperature (≥90°C), while aluminum fumarate showed a superior performance at a higher evaporation temperature (20°C) and low regeneration temperature (70°C).*

*Keywords: vacuum membrane distillation, adsorption, solar linear Fresnel collector*

## 1. INTRODUCTION

Generally, the membrane distillation (MD) processes divided into four different types; direct contact membrane distillation, air-gap membrane distillation, sweeping gas membrane distillation, and vacuum membrane distillation (VMD). Most of these technologies have been tested either in laboratory bench-scale or in small-scale pilot test units. In MD, the vapor transport occurs in three steps: (i) evaporation from the hot liquid feed concentrate, (ii) vapor transport through the porous membrane, and (iii) condensation to a cold liquid permeate (Hassan *et al.*, 2016; Hassan and Fath, 2017). The temperature difference across the two sides of the hydrophobic membrane leads to a partial pressure difference that causes water to evaporate and vapor transport. Due to high surface tension of the polymeric membrane materials, liquid water is prevented from entering the membrane pores, while molecular water in the vapor phase can pass through. Water vapor transfers across the hydrophobic membrane and are condensed or removed as a vapor from the permeate side of the membrane module. Since the liquid does not transport across hydrophobic membrane, dissolved ions are completely rejected by membrane (El-Zanati and El-Khatib, 2007).

The advantages of MD lie in its simplicity, the need for only small temperature differences and nearly 100% rejection of dissolved solids (Chen, Ho and Yeh, 2009). Furthermore, the low energy demand systems in MD processes can be equipped with renewable energy equipment such as solar collectors and solar distillers. The mass transfer of MD can be interpreted by three fundamental mechanisms: molecular diffusion, Knudsen diffusion and Poiseuille flow or the combination between them known as a transition mechanism (Zhang *et al.*, 2016).

Adsorption desalination technology has shown potential as a possible alternative for other desalination technologies (Youssef, Mahmoud and AL-Dadah, 2015, 2016). This technology can utilize low temperature waste heat to produce two useful effects; desalination and cooling. Silica gel has been used as water adsorbent for a number of cooling applications including combined power, heating and cooling, automotive air conditioning and solar powered cooling systems (Rezk *et al.*, 2012). Adsorption occurs when ever a solid surface resides with a gas or liquid: it is defined as the enrichment of material or increase in the density of the fluid near an interface (Alsaman *et al.*, 2016). Adsorption deals with the process in which molecules accumulates in the interfacial layer, but desorption is the converse process.

Metal Organic Frameworks (MOFs) are new micro-porous materials with exceptional high porosity, uniform pore size, well-defined molecular adsorption sites and large surface area (up to 5500 m<sup>2</sup>/g) (Rezk *et al.*, 2013). Currently, limited MOF materials with high water adsorption capabilities and hydrothermal stability are available on a large scale. Two MOF materials, namely CPO-27(Ni) and aluminum fumarate, have been identified to have a high hydrothermal stability, high water uptake of 0.47 g<sub>H<sub>2</sub>O</sub>/g<sub>ads</sub> and 0.53 g<sub>H<sub>2</sub>O</sub>/g<sub>ads</sub> at a relative pressure of 0.9 and are commercially available (Elsayed *et al.*, 2016).

A great potential offers for the mentioned (aluminum fumarate and CPO-27(Ni)) for various adsorption applications. Increasing the condensation temperature was found to be detrimental to the performance of the two materials. The CPO-27(Ni) was found to be more suitable for applications working at a low evaporation temperature (5°C) and high regeneration temperature (≥90°C), while aluminum fumarate showed a superior performance at a higher evaporation temperature (20°C) and low regeneration temperature (70°C) (Elsayed *et al.*, 2016).

## 2. SYSTEM DESCRIPTION

Integration of VMEMD and AD system consists of the main subsystems; VMEMD system, AD system, Chilled water system, feed water system, heating water system and cooling water system. **Error! Reference source not found.** gives a rough overview over the main components of the system. The designed system of VMEMD process is a combination of the two concepts of vacuum membrane distillation (VMD) and multi effect distillation (MED). It divides a feed stream, distillate stream of very pure water and the brine stream, which shows a higher concentration of dissolved agents than the feed. While the feed water can be heated through its passing into two shell and tube heat exchangers (feed water (FW) preheater and VMD FW heater) utilizing the internal heat to drive this process at a temperature level of 50°C - 80°C as the distillate steam will pass through a condenser then into the product tank.

The warmed brine of VMEMD will loss most of its internal heating through passing the pre-cooler and then used as a feed water in AD cycle to produce another source of distillate water. In the evaporator, the vapor space is working under very vacuum pressure and the cold brine sprays onto horizontal tubes as the chilled water will pass into the horizontal tubes to be cooler to use in cooling the buildings. Part of the sprayed brine will convert into vapor while the rest will be discharging out the evaporator to cool the brine of VMEMD in the pre-cooler.

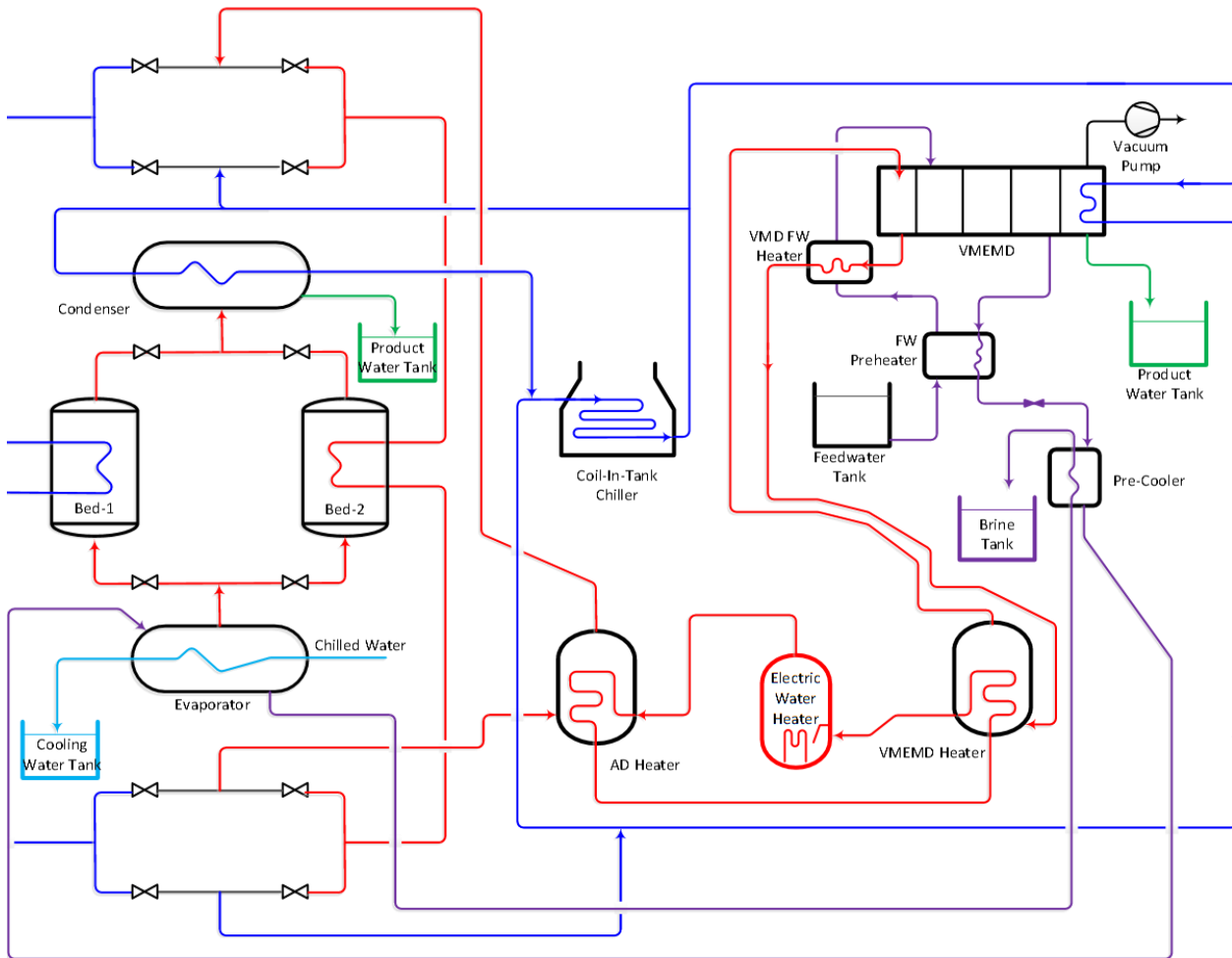


Figure 1: Layout of Integration of VMEMD with AD System

The AD subsystem comprises the following components such as two beds, evaporator, condenser and a set of controlling valves. At the same time, the two beds are working with two opposite modes, so when the Bed-1 works under adsorption mode, Bed-2 works under desorption mode, and vice versa. In adsorption mode, the generated vapor by evaporator will be absorbed by Bed-1 or Bed-2 at different times as a liquid on the outer surface of the absorbent material. While in desorption mode, external heat source uses to evaporate the adsorbed vapor on the absorbent material and then the regenerated vapor will pass towards the condenser to condense and collect in a tank as a product water. Once the regenerated vapor is released into condenser, the valves of heat source will be closed and the valves of cold water will open to adapt the bed to be ready to start the adsorption mode again, and so on.

Hence, the evaporator is working under very low vacuum pressure and the adsorbent materials in the Beds adsorb the generated vapor, the working temperature in the vapor space can be controlled to be less than 20°C. Therefore, chilled water can pass in-tubes in the evaporator to be cooler, collect in a tank and then distribute it as a cooling water.

The heating system is designed through using an electrical water heater to provide the system with required heat sources at different values of temperature, flow rate and pressure. While, the cooling water system is designed to use coil-in-tank chiller to condense the vapor in the vapor condensers and to adapt the Beds to be ready for adsorption mode. Finally, the feed water system is required to manage the circulation of water flows at different conditions of temperature, flow rate, pressure and salinity. Since, there is no consumption of chemical materials in the system; therefore, the feed water has the ability to mix the product water with brine in the feed water tank again.

### 3. VACUUM MEMBRANE DISTILLATION SYSTEM MODELING AND ANALYSIS

The VMEMD system is designed to suit integration with AD system and be able to produce 750 kg/day. The function of water riser in VMEDD is to rise the feed water temperature up to 80°C. The VMEMD feed water is preheated through two heat exchangers to rise its temperature to reach 50°C before entering the VMEMD water riser. The feed water passes through 3-chambers of VMEMD, where part of it evaporates and migrates through the hydrophobic micro porous Polytetrafluoroethylene flat membranes then followed by condensation as distilled water. Due to high surface tension of the polymeric membrane materials, liquid water is prevented from entering the membrane pores, while molecular water in the vapor phase can pass through. The generated vapor will suck into vacuum channel at lower pressure then condensed in the condenser to form a fresh water product. The rejected brine of the VMEMD is used as feed water of the AD evaporator. The VMEMD system comprises hot channel, membrane sheet, and vacuum side. In hot channel, the feed water bulk temperature will be decreased on the membrane surface as the concentration will be increased due to transmembrane of the permeate vapor through the membrane. The vacuum pump create a vacuum pressure and the permeate vapor stripped away and condensed into liquid in the condenser.

For VMEMD, the vapor transport occurs in three steps; (i) evaporation from the hot saline feed, (ii) vapor transport through the porous membrane, and (iii) condensate the transported vapor in outside condenser, which the vacuum is created through a vacuum pump. The temperature difference across the two sides of the hydrophobic membrane leads to a pressure difference that causes water to evaporate. Equation 1 represents the time dependent transmembrane flux ( $J_m$ ) along the membrane length, which it divided into a mesh with  $i$  steps. The influence of the pressure conditions across the membrane's surface is more significant on the permeate flux.

Equation 2 represents the conduction heat transfer rate through the membrane material while Equation 3 was used to calculate the total heat transferred by VMD. The membrane surface temperature ( $T_{f,m}$ ) can be determined by the flow bulk temperature and the coefficient of heat transfer, as shown in Equation 4. The time-dependent of the mass flow rate in the hot channel can be determined by Equation 7.

$$\text{Equation 1:} \quad \frac{\partial}{\partial t} J_m(i) = B \frac{\partial}{\partial t} (P_{f,m}(i) - P_{vac})$$

$$\text{Equation 2:} \quad \frac{\partial}{\partial t} q_m(i) = K_{cond} \frac{\partial}{\partial t} (T_{f,m}(i) - T_p)$$

$$\text{Equation 3:} \quad \frac{\partial}{\partial t} q_{out}(i) = \frac{\partial}{\partial t} (J_m(i) h_{fg,f}(i)) + \frac{\partial}{\partial t} q_m(i) - \frac{\partial}{\partial t} (J_m(i) (h_{f,b}(i) - h_{f,m}(i)))$$

$$\text{Equation 4:} \quad \frac{\partial}{\partial t} T_{f,m}(i) = \frac{\partial}{\partial t} T_{f,b}(i) - \frac{1}{H_f} \frac{\partial}{\partial t} q_{out}(i)$$

$$\text{Equation 5:} \quad \frac{\partial}{\partial t} h_{f,m}(i) = 4210.8 \frac{\partial}{\partial t} T_{f,m}(i) - 1.24 T_{f,m}(i) \frac{\partial}{\partial t} T_{f,m}(i) + 0.0134 T_{f,m}(i) \frac{\partial}{\partial t} T_{f,m}(i)$$

$$\text{Equation 6:} \quad \frac{\partial}{\partial t} h_{f,b}(i+1) = \frac{\partial}{\partial t} h_{f,b}(i) - dA \frac{\partial}{\partial t} \left( \frac{q_{out}(i)}{m_f(i)} \right)$$

$$\text{Equation 7:} \quad \frac{\partial}{\partial t} \dot{m}(i) = \dot{m}(i-1) - J_m(i-1) * dA$$

Where:

- $J_m$  is the permeate flux, kg/m<sup>2</sup>.s
- $B$  is the membrane water permeability coefficient, kg/m<sup>2</sup>.s.Pa
- $P$  is the pressure, kPa
- $q$  is the heat flux, W/m<sup>2</sup>

In VMEMD system, the mass transfer controlled by the heat transfer in the feed boundary. Local heat and mass fluxes calculated along the membrane length because of high local heat transfer coefficient in the inlet region and

thin thermal boundary. The simulation of the temperature distribution along the membrane length of fluid bulk temperature, membrane surface temperature and the vacuum temperature are plotted in Figure 2, which the 6.4 m of membrane length (four VMEMD effects with 1.6 m each) with 80°C inlet feed water temperature selected. The model shows the simulation of decreasing the transmembrane flux across the membrane due to the decreasing membrane surface temperature along the VMEMD module channel. Temperature polarization (TP) will take into condensation at high feed temperature and low feed velocity.

The flow in hot channel can be simulated in one-dimensional of length. The mesh (cell) is addressed in z-direction along the membrane length, which is divided into 50 cells. In each cell, the governing partial differential equations of mass, momentum and energy conservation are determined and solved. Figure 3 shows the steady state results of transmembrane flux behavior in the hot channel along the membrane surface as function with different values of the inlet feed water temperature.

The hot water system comprises of an electric heater and two water heaters. Figure 4 shows the simulation of mass and heat balance for the overall systems, the hot water system will provide the adsorption cycle and VMEMD cycle with the required thermal power in the form of pressurized hot water up to 140°C and 90°C, respectively. The VMEMD feeds with feed water at flow rate and temperature of 1960 kg/d and 30°C, respectively that the feed water will preheating gradually to reach to 86°C. The VMEMD will produce 758 kg/d and 1202 kg/d as fresh water and brine water at 37.6°C and 48°C, respectively. The brine will cold and used as a feed water in AD system at 16.5°C. Therefore, the recovery ratio of VMEMD will be 38.7.

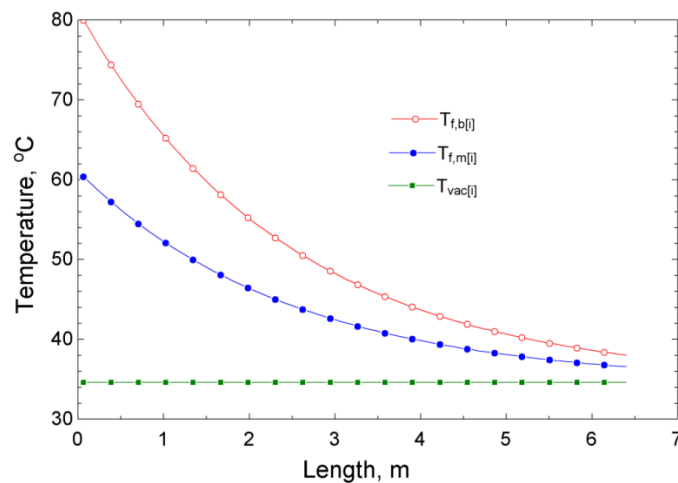


Figure 2: Module temperatures distribution as function of the membrane length

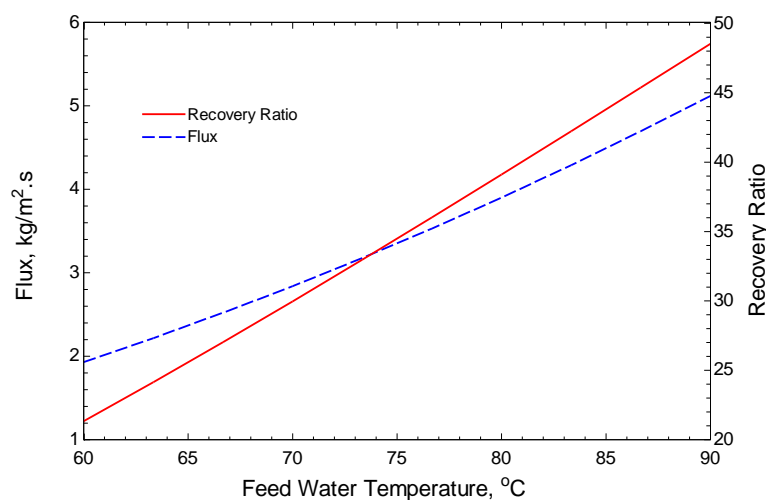


Figure 3: Flux distribution along the membrane length as function of feed water temperature

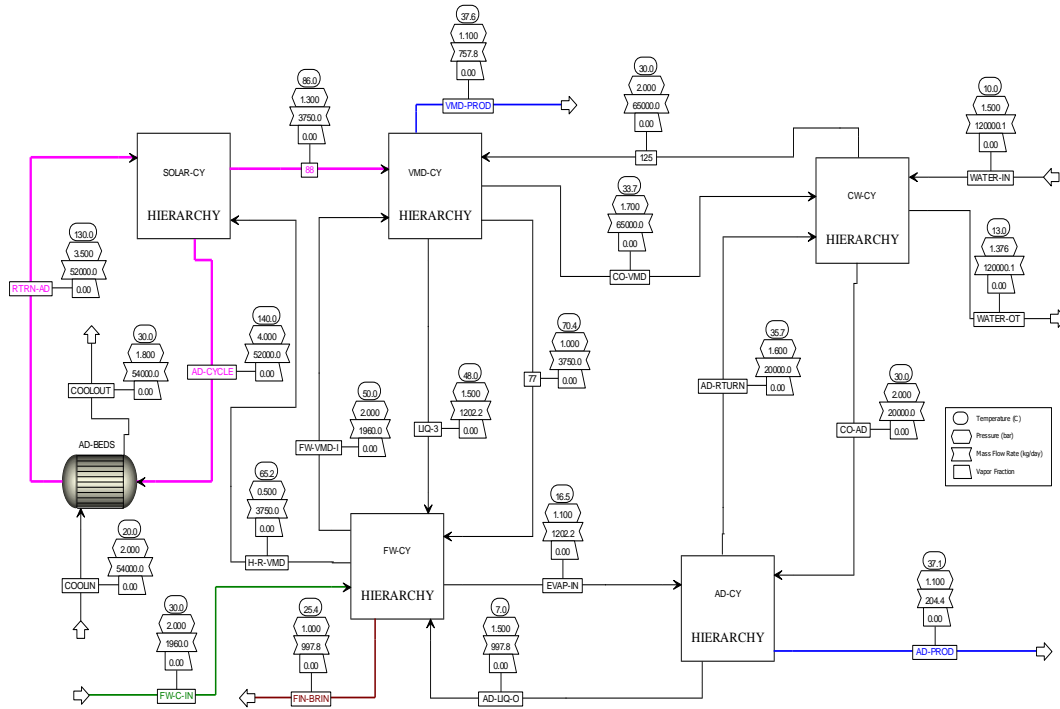


Figure 4: The simulation of solar adsorption/desalination systems

#### 4. ADSORPTION SYSTEM MODELING AND ANALYSIS

Figure 5 shows a schematic diagram of a 2-bed adsorption system consisting of four main components, which are; adsorber bed, desorber bed, evaporator and condenser. The distilled water cycle starts by simultaneous evaporation and adsorption processes as brine evaporates and the adsorbent material in the adsorber bed adsorbs the resulting water vapour. During adsorption process, cooling water is supplied to the adsorbing bed to absorb the associated released heat of adsorption. As a result of evaporation in the evaporator, cooling effect is produced and appears as cooler chilled water at outlet from evaporator. To regenerate the adsorbed water vapour in the bed, hot fluid is supplied to the bed to desorb the water vapour, which is then condensed by the flow of cooling water in the condenser. The collected condensate from the bottom of the condenser is the produced fresh water which is then pumped out from the condenser and stored in tanks.

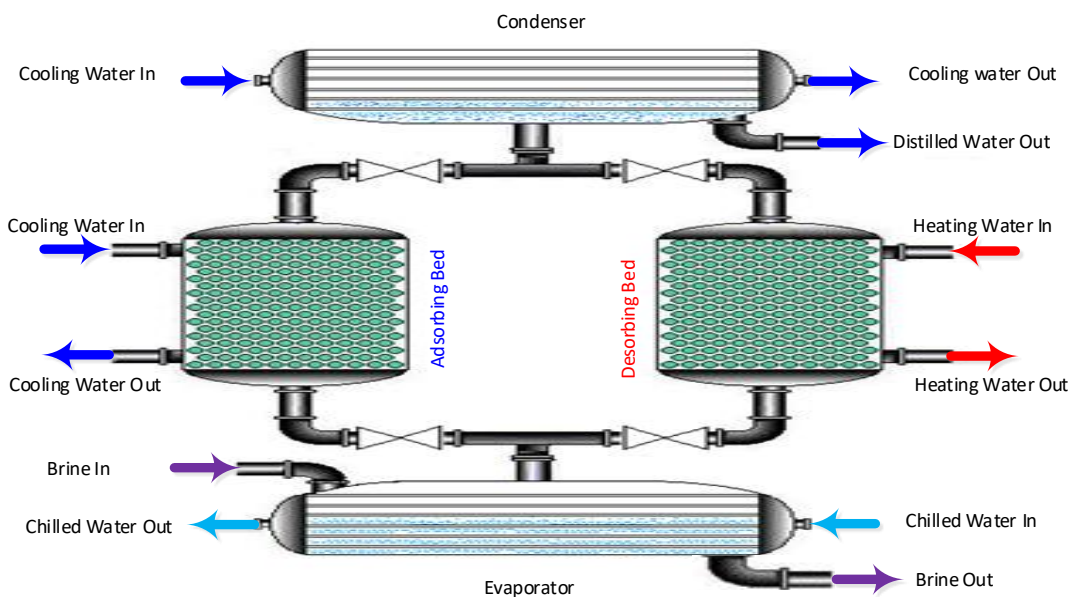


Figure 5: Schematic diagram of the adsorption system

Figure 6 shows four materials water adsorption isotherms of MIL-101(Cr), MIL-100(Fe), and aluminum fumarate, which they exhibited a type-IV adsorption isotherm. While CPO-27(Ni) exhibited type I adsorption isotherm. The figure shows that at low partial pressure, the water uptake was low due to the hydrophobicity of the organic linker, but a steep increase in the water uptake took place at higher relative pressure range due to the accumulation of the adsorbed water molecules inside the pores of the material. Finally, the uptake either continued to increase as in case of aluminum fumarate or reached a plateau as in case of MILs to reach the maximum value.

For CPO-27(Ni), the water adsorption mechanism differs from the other three materials as CPO-27(Ni) exhibited a type-I adsorption isotherm reaching 81% of its capacity at a very low relative pressure and then a plateau reaching its maximum uptake of  $0.47 \text{ g}_{\text{H}_2\text{O}} \cdot \text{g}_{\text{ads}}^{-1}$  at a relative pressure of 0.9. This performance is due to the presence of unsaturated metal centers (UMCs) existing in some MOF structures. These UMCs are metal binding sites formed after the removal of axial ligands from metal atoms attracting water molecules and offering extra binding sites to the guest molecules, especially at low-pressure values (Wang and Ng., 2005; K. C. Ng *et al.*, 2012). The performance of cyclic water uptake is mainly determined by four operating temperatures, which are desorption, adsorption, evaporation and condensation temperatures. In this study, the adsorption and condensation temperatures are fixed at  $30 \text{ }^\circ\text{C}$ , while two evaporation temperature values  $10 \text{ }^\circ\text{C}$  and  $20 \text{ }^\circ\text{C}$  and two desorption temperatures  $90 \text{ }^\circ\text{C}$  and  $130 \text{ }^\circ\text{C}$  were used. Table 1 shows performance of MOF materials at various operating conditions with the following results:

- MIL-101(Cr) was significantly dependent on the evaporation temperature but less profoundly on the desorption temperature.
- CPO-27(Ni) was found to be significantly dependent on desorption temperature with no significant dependency on the evaporation temperature.
- Aluminum Fumarate was found to be significantly dependent on the evaporation temperature with no dependency on the desorption temperature.
- MIL-100(Fe) was found to be significantly dependent on the evaporation temperature with no dependency on the desorption temperature.

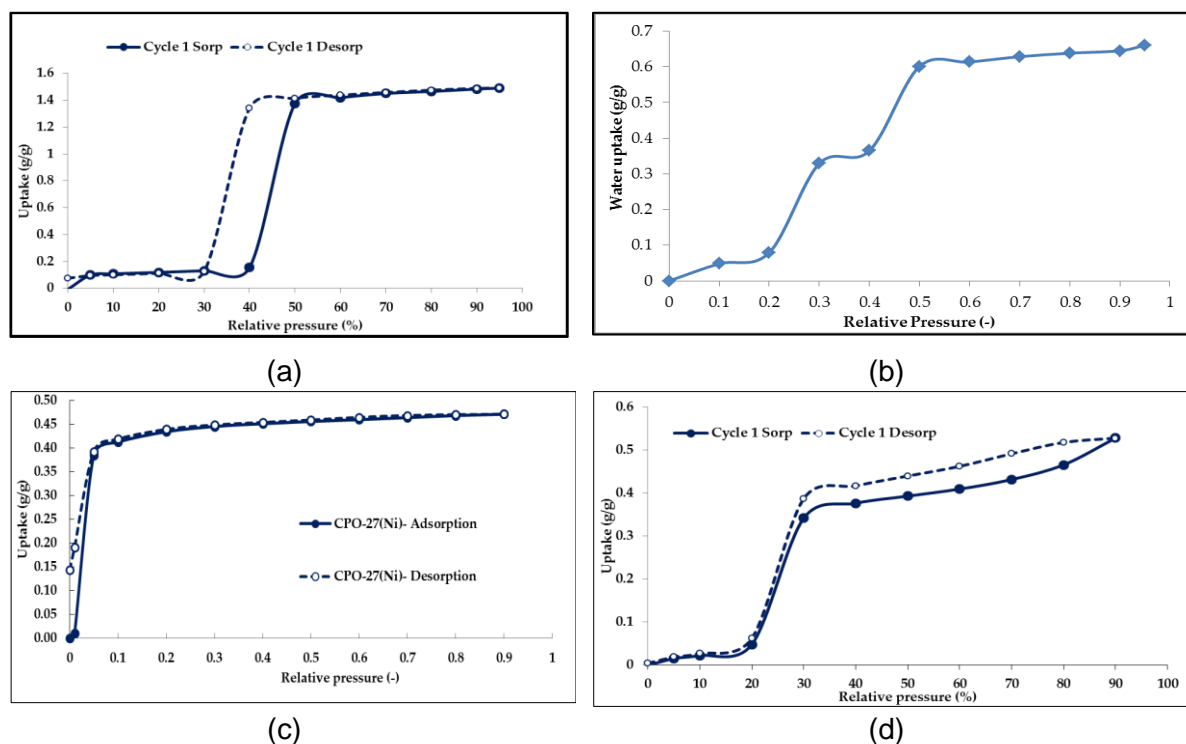


Figure 6: Water uptake of (a) MIL-101(Cr), (b) MIL-100(Fe), (c) CPO-27(Ni) and (d) aluminum fumarate

Table 1: Cyclic\* uptake (g/g) of different MOF materials at various operating conditions

Material	Evaporation Temperature, °C	Desorption Temperature	
		90 °C	130 °C
MIL-101(Cr)	10 °C	0.0396	0.0966
	20 °C	1.236	1.293
CPO-27(Ni)	10 °C	0.1806	0.4459
	20 °C	0.1847	0.45
Aluminum Fumarate	10 °C	0.27557	0.2851
	20 °C	0.3875	0.397
MIL-100(Fe)	10 °C	0.26	0.28
	20 °C	0.54	0.547

\* The adsorption temperature and condensation temperature is 30°C.

Figure 7 shows the schematic diagram of the adsorption cycle generated using Aspen Adsorption software, it consists of two gas beds, six void tanks, six valves, feed stream and product stream, taking into consideration connecting the pressure setters (feed/product streams & voids) and flow setters (valves & beds) in an alternating manner. The model was simulated for three cycles. Each cycle will last for 1400 second, and will be controlled by four steps in the cycle organizer, time driven option with the below specifications of each step were initially selected/manipulated as per the experimental conditions followed in UoB:

- Step 1. Preheating of Bed 1 and Precooling of Bed 2: at 30 sec.
- Step 2. Desorption of Bed 1 and Adsorption of Bed 2: at 700 sec.
- Step 3. Precooling of Bed 1 and Preheating of Bed 2: at 730 sec.
- Step 4. Adsorption of Bed 1 and Desorption of Bed 2: at 1400 sec.

Which:

- Preheating Bed 1/Precooling Bed 2: where all valves are closed and the temperature will be ramped from the  $T_{cw}= 30^{\circ}\text{C}$  to  $T_{hw}= 90^{\circ}\text{C}$  for bed 1 and vice versa for bed 2, and accordingly the gas/adsorbent thermal conductivity will be changed.
- Desorption Bed1/Adsorption Bed 2: heating water will be supplied through the jacket heat exchanger in bed 1 to release the adsorbed water vapor and VP1 will be opened to connect bed 1 to the product tank, which used to accumulate the produced water vapor. On the contrary, VF2 will be opened to connect bed 2 to the feed stream and cooling water will be supplied to absorb the exothermic heat during adsorption.
- Precooling Bed 1/Preheating Bed 2: where all valves are closed and the temperature will be ramped from the  $T_{cw}= 90^{\circ}\text{C}$  to  $T_{hw}= 30^{\circ}\text{C}$  for bed 1 and vice versa for bed 2, and accordingly the gas/adsorbent thermal conductivity will be changed.
- Adsorption Bed1/Desorption Bed 2: VF1 valve will be opened to connect bed 1 to the feed stream and cooling water will be supplied to absorb the exothermic heat during adsorption. On the other side, heating water will be supplied through the jacket heat exchanger in bed 2 to release the adsorbed water vapor and VP2 will be opened to connect bed 2 to the product tank.



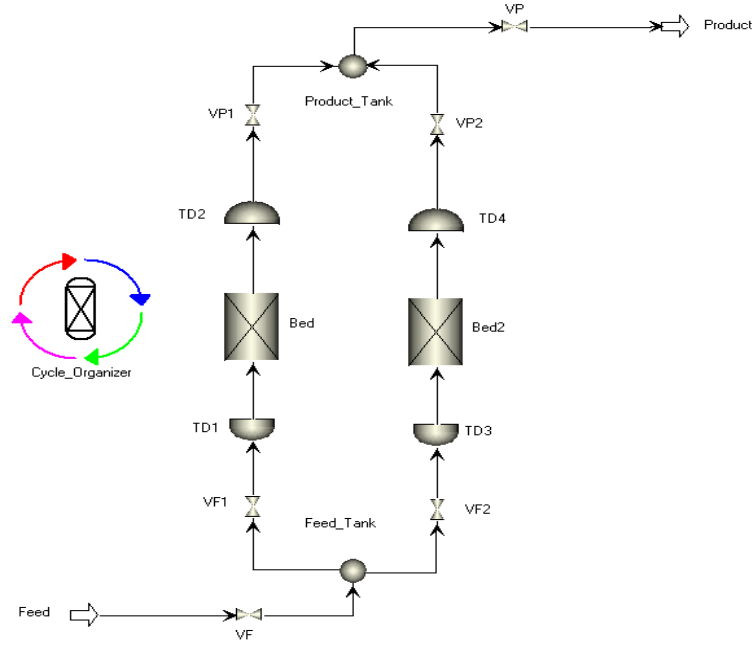


Figure 8: Schematic diagram of adsorption cycle

Energy, salt and mass balance equations are solved to get evaporator, condenser, adsorber and desorber beds temperatures besides evaporator seawater mass and salt concentration for the fluids of Figure 5. These set of equations are listed below.

Energy balance of the evaporator:

$$\text{Equation 8:} \quad \frac{\partial}{\partial t} M_{brine} (T_{br,in} - T_{br,out}) = \frac{\partial}{\partial t} \dot{m}_{ads} T_{ads} - \dot{m}_{ch} \frac{\partial}{\partial t} (T_{ch,in} - T_{ch,out})$$

Mass balance of the evaporator:

$$\text{Equation 9:} \quad \frac{\partial M_{br}}{\partial t} = \dot{m}_{br,in} - \dot{m}_{br,out} - \dot{m}_{vap,ads}$$

Salt balance of the evaporator:

$$\text{Equation 10:} \quad \dot{m}_{br,in} S_{br,in} = \dot{m}_{br,out} S_{br,out}$$

Where:

- $M_{brine}$  is brine mass in the evaporator, kg
- $\dot{m}$  is mass flow rate, kg/s
- $S$  is salt concentration, ppm

The energy required to adapt the beds for adsorption or desorption process can be determined using Equations 11 and 12, while the energy required for vapor condensation process inside the condenser, Equation 13.

Adsorption bed, energy balance equation:

$$\text{Equation 11} \quad : Q_c|_{ads} = \dot{m}_{cw} Cp (T_{cw,out} - T_{cw,in}) + M_a Q_{st} \frac{\partial C_{ads}}{\partial t} = (M_a Cp_a + M_{hx} Cp_{hx}) \frac{\partial T_{ads}}{\partial t}$$

Desorption bed, energy balance equation:

$$\text{Equation 12:} \quad Q_h|_{des} = \dot{m}_{hw} Cp (T_{hw,in} - T_{hw,out}) + M_a Q_{st} \frac{\partial C_{des}}{\partial t} = (M_a Cp_a + M_{hx} Cp_{hx}) \frac{\partial T_{des}}{\partial t}$$

Condenser energy balance equation:

$$\text{Equation 13:} \quad Q_{cond} = \dot{m}_{cw} Cp (T_{cw,out} - T_{cw,in}) = M_a h_{fg} \frac{\partial C_{des}}{\partial t}$$

Two key performance indicators are used to compare cycle outputs at different operating conditions. As this cycle

is producing fresh water and cooling, these parameters are specific daily water production (SDWP) and specific cooling power (SCP) which are calculated using Equations 6-7.

Equation 14: 
$$SDWP = \int_0^{t_{cycle}} \frac{\dot{m}_{cond} Cp}{h_{fg} M_{ads}} (T_{cond,out} - T_{cond,in}) dt$$

Equation 15: 
$$SCP = \int_0^{t_{cycle}} \frac{\dot{m}_{chilled} Cp}{M_{ads}} (T_{chilled,in} - T_{chilled,out}) dt = \frac{Q_{evap}}{M_{ads} t_{cycle}}$$

Equation 16: 
$$Q_{st} = \rho_s Cp c \frac{\partial T_s}{\partial t}$$

The thermodynamic modelling of AD cycle carried out using 20 kg of aluminum fumarate packed in the adsorber beds of a two-bed adsorption system can produce the desalinated water of 204 kg/d and cooling rate of 5kW. Figure 8 shows the temperature profiles of the two beds and the adsorbent material (MOF) for the AD system where the two beds alternate the functional modes between adsorption/desorption. Bed 1 starts with preheating step with a duration of 30 seconds, where water temperature inside the HE tubes will be increased from 30 °C to 90°C, thus the temperature of the adsorbent material will be increased as well. Then, during the desorption step that last for 670 seconds, the adsorbent material temperature will continue to increase to reach about 75 °C as a result of the continuous circulation of hot water inside the HE tubes to regenerate the adsorbed vapor. In order to cool the bed to start the adsorption step, precooling step is required where cooling water at 30°C will be circulated in the HE for 30 seconds. Adsorption step will start after the precooling step where the temperature of the adsorbent material will be about 40°C. Bed 2 will follow the same steps but in reverse sequence as shown in Figure 8(b).

Figure 9 shows the concentration profiles of the vapor in Bed 2 along the vertical direction of the Bed height, where the most vapor is concentrated in the first one-third of the Bed height. Figure 10 presents the inlet temperature profiles of adsorption/desorption heat exchangers for two beds for three sequential cycles, alternating between adsorption and desorption modes, which the inlet temperature of HEs are changing from 30°C to 90°C whatever the number of cycles.

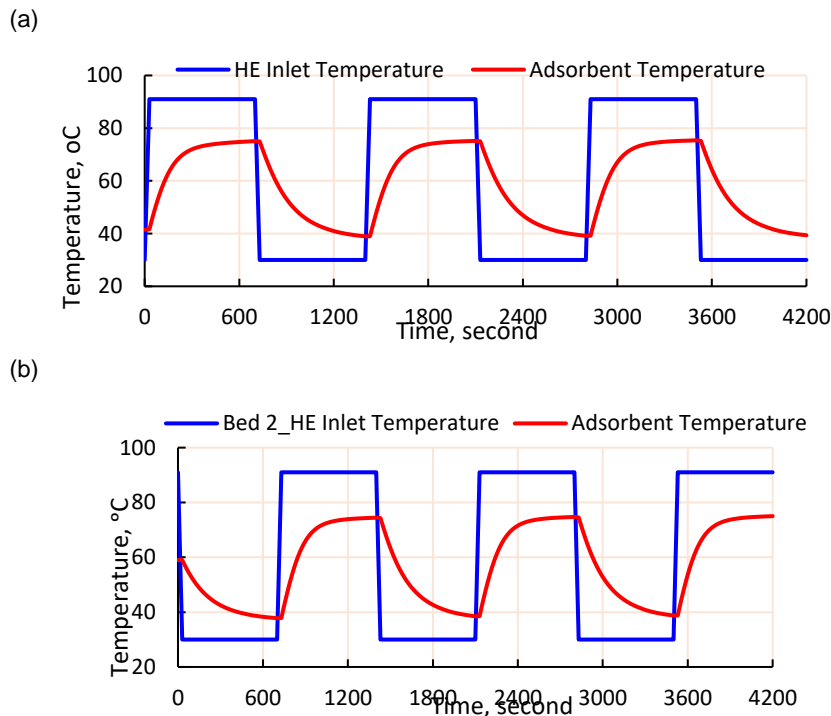


Figure 8: Solid temperature profiles for two beds during the four steps; (a) for Bed 1 and (b) for Bed2

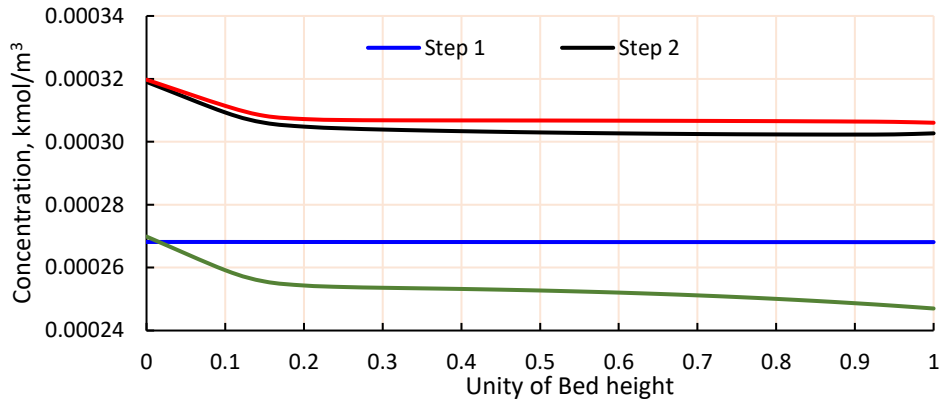


Figure 9: Concentration profiles of Bed 2 during the four steps along the Bed height

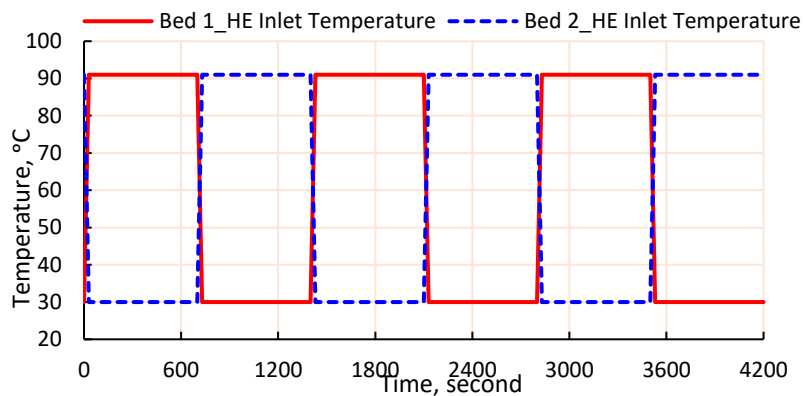


Figure 10: Temperature profiles of adsorption/desorption Beds

## 5. CONCLUSIONS

The main results of the system can be summarised as following:

- The pilot plant recovery ratio can be reached to more 50%, which the production of VMEMD system and the AD system can be reach to 750 kg/d and 200 kg/d, respectively.
- CPO-27(Ni) was found to be significantly depends on desorption temperature with no significant dependency on the evaporation temperature.
- Aluminum Fumarate was found to be significantly depends on the evaporation temperature with no dependency on the desorption temperature.
- The calculated power consumption can be lowered to 3.9 kWh/m<sup>3</sup>.
- Producing cooling water for towers.
- The system of VMEMD and AD is environmentally friendly, which there is no CO<sub>2</sub> emission and no harm upon ecosystems or the environment.

## 6. NOMENCLATURE

Abbreviations		Subscription	
<i>m</i>	Mass flow rate, kg/s	<i>b</i>	Brine or bulk
<i>A</i>	Area, m <sup>2</sup>	<i>br</i>	Brine
<i>c</i>	Uptake, kg <sub>water</sub> /kg <sub>ads</sub> .day	<i>ch</i>	Chilled water
<i>h</i>	Enthalpy, kJ/kg	<i>cw</i>	Cooling water
<i>J</i>	Flux, kg/m <sup>2</sup> .s	<i>d</i>	Discharge
<i>K</i>	Thermal conductivity, W/m.K	<i>f</i>	Fluid
<i>M</i>	Mass, kg		

$P$	Pressure, bar	$fg$	Latent heat
$S$	Salinity, ppm	$hw$	Hot water
$SCP$	Specifying cooling power, kW/kg	$m$	membrane
$SDWP$	Specific daily water production, m <sup>3</sup> /m <sup>3</sup> .day	$vap$	Vapor
$T$	Temperature, °C		

## 7. ACKNOWLEDGEMENT

The project is funding by Qatar National Research Fund (QNRF) entitled “Development of Solar Driven Adsorption Water Desalination / Cooling System Using Advanced Metal Organic Framework Material” and coded as “NPRP9-028-2-012”.

## 8. REFERENCES

Alsaman, A. S. *et al.* (2016) ‘A state of the art of hybrid adsorption desalination-cooling systems’, *Renewable and Sustainable Energy Reviews*. Elsevier, 58, pp. 692–703. doi: 10.1016/j.rser.2015.12.266.

Chen, T. C., Ho, C. D. and Yeh, H. M. (2009) ‘Theoretical modeling and experimental analysis of direct contact membrane distillation’, *Journal of Membrane Science*, 330(1–2), pp. 279–287. doi: 10.1016/j.memsci.2008.12.063.

El-Zanati, E. and El-Khatib, K. M. (2007) ‘Integrated membrane -based desalination system’, *Desalination*, 205(1–3), pp. 15–25. doi: 10.1016/j.desal.2006.03.548.

Elsayed, E. *et al.* (2016) ‘Aluminium fumarate and CPO-27(Ni) MOFs: Characterization and thermodynamic analysis for adsorption heat pump applications’, *Applied Thermal Engineering*. Elsevier Ltd, 99, pp. 802–812. doi: 10.1016/j.applthermaleng.2016.01.129.

Hassan, A. S. *et al.* (2016) ‘Dynamic performance of vacuum membrane distillation system’, *Desalination and Water Treatment*, 57(48–49), pp. 23196–23205. doi: 10.1080/19443994.2015.1099330.

Hassan, A. S. and Fath, H. E. S. (2017) ‘Numerical Dynamic Simulation Of Vacuum Membrane Distillation Plant’, in *4 TH INTERNATIONAL CONGRESS ON TECHNOLOGY ENGINEERING & SCIENCE*. Kuala Lumpur, Malaysia.

K. C. Ng *et al.* (2012) ‘Study on a waste heat-driven adsorption cooling cum desalination cycle’, *International Journal of Refrigeration*, 35, pp. 685–693.

Rezk, A. *et al.* (2012) ‘Characterisation of metal organic frameworks for adsorption cooling’, *International Journal of Heat and Mass Transfer*. Elsevier Ltd, 55(25–26), pp. 7366–7374. doi: 10.1016/j.ijheatmasstransfer.2012.07.068.

Rezk, A. *et al.* (2013) ‘Investigation of Ethanol/metal organic frameworks for low temperature adsorption cooling applications’, *Applied Energy*. Elsevier Ltd, 112, pp. 1025–1031. doi: 10.1016/j.apenergy.2013.06.041.

Wang, X. and Ng., K. C. (2005) ‘Experimental investigation of an adsorption desalination plant using low-temperature waste heat’, *Applied Thermal Engineering*, 25, pp. 2780–9.

Youssef, P. G., Mahmoud, S. M. and AL-Dadah, R. K. (2015) ‘Performance analysis of four bed adsorption water desalination/refrigeration system, comparison of AQSOA-Z02 to silica-gel’, *Desalination*. Elsevier B.V., 375, pp. 100–107. doi: 10.1016/j.desal.2015.08.002.

Youssef, P. G., Mahmoud, S. M. and AL-Dadah, R. K. (2016) ‘Numerical simulation of combined adsorption desalination and cooling cycles with integrated evaporator/condenser’, *Desalination*. Elsevier B.V., 392, pp. 14–24. doi: 10.1016/j.desal.2016.04.011.

Zhang, Y. *et al.* (2016) ‘Numerical simulation of 3D hollow-fiber vacuum membrane distillation by computational fluid dynamics’, *Chemical Engineering Science*, 152, pp. 172–185. doi: 10.1016/j.ces.2016.05.040.

---

## #47: Experimental study on the pressure differential at which building air leakage should be measured

---

Alan VEGA PASOS<sup>1</sup>, Xiaofeng ZHENG<sup>2</sup>, Mark GILLOTT<sup>3</sup>, Christopher J. WOOD<sup>4</sup>

<sup>1</sup> Buildings, Energy and Environment, Research Group, Faculty of Engineering, University of Nottingham, University Park, Nottingham, NG7 2RD, United Kingdom, alan.vegapasos@nottingham.ac.uk

<sup>2</sup> Buildings, Energy and Environment, Research Group, Faculty of Engineering, University of Nottingham, University Park, Nottingham, NG7 2RD, United Kingdom, xiaofeng.zheng@nottingham.ac.uk

<sup>3</sup> Buildings, Energy and Environment, Research Group, Faculty of Engineering, University of Nottingham, University Park, Nottingham, NG7 2RD, United Kingdom, mark.gillott@nottingham.ac.uk

<sup>4</sup> Buildings, Energy and Environment, Research Group, Faculty of Engineering, University of Nottingham, University Park, Nottingham, NG7 2RD, United Kingdom, christopher.wood@nottingham.ac.uk

*Air infiltration represents up to one third of the energy losses in a building. Air leakage is the parameter that has the biggest effect on air infiltration. Currently the Air Leakage Rate (ALR) is measured by means of a (de) pressurisation technique and is quoted at 50 Pa of pressure difference. Some research has shown that building air leakage occurs at low pressure differences, in the range of 1 -10 Pa. To get an ALR at low pressures, the pressurisation test result must be extrapolated; large uncertainty is created through this process. Other novel method (Pulse) measures the air leakage rate and quotes it at 4 Pa. This study aims to measure the pressure difference in four facades of a test house in Nottingham, United Kingdom. Differential pressure transducers measured indoor-outdoor pressure differences for a six-day period. Air leakage tests were also carried out with the wind speed, indoor and outdoor temperatures being monitored on site. Results showed that the majority of the pressure difference in the tested house occurred between 3.5 and 4.5 Pa even when high wind gusts (up to 9 m/s) were present. The distribution of the measured pressure differences follows a normal (Gaussian) distribution. The calculated mean pressure difference was close to 3 Pa, which agrees with authors saying that air leakage occurs in the range of 1 – 10 Pa under natural (environmental) conditions. This suggests that a technique that measures and quotes ALR at 4 Pa should deliver more representative results.*

*Keywords: air infiltration; air leakage; air permeability; pressure difference in buildings*

## 1. INTRODUCTION

Buildings represent 40% of energy consumption in the EU, a similar figure is drawn in the rest of the world (Lapillonne, et al., 2015). Heat losses due to air infiltration represent up to one third of the energy losses in a building (Energy Saving Trust, 2006). This air infiltration ( $m^3/s, h^{-1}$ ) is the “non-intended” ventilation through gaps and cracks in the building fabric (Santamouris & Asimakopoulos, 1996). The most important parameter affecting air infiltration is the air leakage rate (ALR,  $m^3/s$ ), ALR is the airflow through the building fabric measured at a given pressure difference, most commonly 50 Pa (Etheridge, 2012).

When wind acts on the envelope of a building an indoor-outdoor pressure differential is created. Different facades will have different pressure differentials due to the wind direction; therefore a pressure difference field will be created around the building. A different pressure differential is created with the changes in temperature and the buoyancy effect. Infiltration and air leakage occur due to a combination of these pressure differentials acting at the same time (Jones, et al., 2013).

Air leakage rate, when referenced by building volume and envelope area, is called air permeability ( $m^3h^{-1}m^{-2}$ ). Air permeability is the metric used in the United Kingdom. To measure the permeability of a building, the most common method is to pressurise or depressurise a building using a large fan mounted in a doorway. The pressure differences from the measurements are typically taken between 10 to 60 Pa. The air flow and the indoor-outdoor pressure difference are measured through a flow meter and a pressure gauge respectively. The outcome is a permeability value quoted at 50 Pa of pressure difference (The British Standards Institution, 2015; Anderson, 1995; Energy Conservatory, n.d.). This pressurisation method is most commonly known as “blower door” and has been used and developed for more than 40 years. Many countries include the blower door as the standard method to measure the air leakage rate (RDH Building Engineering Ltd, 2013). A photo of a typical Minneapolis blower door model 4 is given in image 1a.

A question, which arises from the use of the blower door is: why do we measure quoting at 50 Pa? The answer is to minimise the effects and the noise created by wind and buoyancy effects occurring naturally. Nevertheless, it is known that air leakage and air infiltration occur in much lower pressure differences. This creates a great uncertainty when extrapolating from high to low pressure (Cooper & Etheridge, 2007).

On the other hand, a different technique to measure ALR is the Pulse technique (Cooper & Etheridge, 2007; Cooper & Zu, 2011; Cooper, et al., 2014; Cooper, et al., 2016). Pulse creates an instant pressure rise in the building's enclosure from the release of compressed air. The rise is measured by a pressure transducer. The ALR (or permeability) is quoted at 4 Pa and the pressure covered by the measurements of Pulse are in the range of 0 – 10 Pa. The main advantage of the Pulse technique (compared with the standard pressurisation method) is that it maintains the building integrity, the envelope is non-stressed and the building does not have to experience an increased pressure differential; these features are regarded as a potential disadvantage. Nevertheless, Pulse lacks a process of development and is not included in any legislation. A photo of the Pulse equipment available for commercial distribution is included in Figure 1b.

There is an ongoing debate concerning the consequences of changing the pressure difference conditions and whether it is feasible to include a different method that does not include a prolonged pressure change in the building; that is why the objective of this study is to measure the pressure difference in a test house through different wind (high and low velocities) and temperature (changing temperature difference) conditions, in order to make informed decisions on which method to use when measuring the air leakage rate.



a)



b)

Figure 1. Air leakage measuring techniques a) blower door for the pressurisation method and; b) Pulse technique equipment.

## 2. METHOD

This experimental study is part of a larger project involving the measurement and correlation of air infiltration, air leakage and environmental conditions. A house located in the University of Nottingham's University Park campus was used to conduct different experiments. The building under test is a three bed detached house built with innovative construction materials, which is part of the Creative Energy Homes in the University of Nottingham.

The house is a two storey - detached property. The main façade is facing south to an open green space with a number of trees 30 meters away; the other three sides of the house have a regular suburban neighbouring area (Figure 3b). Six different thermal zones were defined, four in the top floor and two in the ground floor. Figures 2a and 2b depict the house and the organisation of the equipment; furthermore, the figure shows the location of pressure tapings, the points were positioned in each façade. An important part of this experiment was to measure the wind speed occurring near the test house, therefore an anemometer (Wind Speed low inertia cup and wind vane WSD1%) was placed in a nearby house located circa 10 metres from the test house. Figure 3a shows the south façade of the test house and Figure 3b shows how the house is located and its neighbouring environment, furthermore, it shows the location of the utilised anemometer.



Figure 2. Top floor (left) and ground floor (right) of the test house; orange dots represent the places where the pressure tapings were allocated; the purple dot is where the pressure references was allocated, blue and red dots, represent a different experiment

The wind speed was measured at eaves height using an anemometer located 10 meters away from the test house. Internal and external temperature difference was measured using PT-100 resistance temperature sensors (-200 - 850°C) with two measuring outside the house and one located in each of the defined thermal zones. To enhance the temperature difference, several fan heaters were used in different parts of the house. The wind speed was measured every second and recorded in a data logger. Due to equipment restrictions, only an approximate wind speed could be measured, the maximum sampling speed of the anemometer was one count per second, every count represented 1.493 m/s of wind speed. In addition, the fact that the anemometer was placed slightly apart of the test house, made the authors expect a delay in the wind effect to be reflected in the pressure transducers, compared to the measurements made by the anemometer, depending on the wind direction.

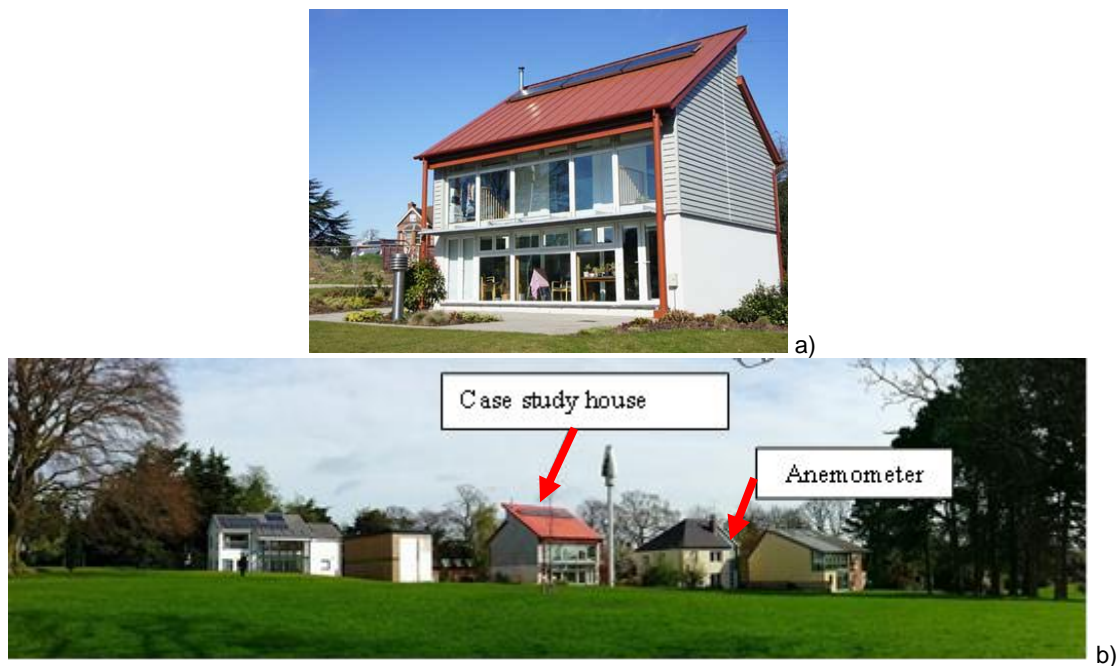


Figure 3. a) Test house, south or main façade, and; b) location of the house within its neighbouring environment.



To also account the buoyancy effect, the indoor temperature was modified using fan heaters, the temperature of the house was raised up to 23°C from 17:00 to 00:00 hours every test day, monitored with the temperature sensors located across the test house. This simulates an occupied house, and enhances the temperature difference. The tests were carried out in the winter of 2018, therefore the expected temperature difference was above 15 K.

Five +/-20 Pa differential pressure transducers FCO-44 (Figure 4) were located on each façade of the building (North, East, South and West), and one in the highest indoor point of the building. All the pressure transducers have the same reference located in zone 5 of the test house. Each FCO-44 has a tube connected to the corresponding façade and other connected to the reference point. Furthermore, all the FCO-44 were connected to a data logger which was logging every second. Each pressure transducer was sampling at a 1 second rate and the data was logged in a data logger.



Figure 4. Differential pressure transducers used, one for each façade and one at the highest indoor point and; North pressure tapping.

The calculation and analysis process investigates the effect of wind and temperature difference changes in the outdoor-indoor pressure difference. With this information it is possible to define the pressure difference at which natural conditions of air infiltration and air leakage occur. In addition, it was possible to perform a quick analysis on whether it is feasible to use pressure transducers as a substitute for measuring the environmental conditions when measuring a building's air leakage rate.

All the experimentation was carried from the 23rd to the 28th of February 2018. A summary of the equipment used can be found in Table 1.

Table 1. Equipment used

Measurement	Equipment
Wind speed	Wind Speed low inertia cup and wind vane WSD1%
Temperature	Temperature sensors PT100 RTD
Pressure difference	+/-20 Pa Differential pressure transducers FCO-44
Data logging	Data logger DT-85 data taker
Other	Fan heaters

### 3. RESULTS AND DISCUSSION

From the 23rd to the 28th of February 2018 when the experiments where performed, different wind and temperature conditions were captured. The first analysis made was the effect of temperature changes in the pressure difference. A quick analysis showed that it is difficult to capture a pressure difference only related to indoor-outdoor temperature difference. This is because the wind was changing speed (despite low magnitude) and direction and drives immediate changes in pressure, while the temperature difference takes longer to change the pressure difference.

It is important to mention that all the outdoor pressure tapings were set at similar heights, therefore it was not possible to measure outdoor temperature stratification. The pressure tapping located indoors showed little variation in pressure difference probably because the height difference was less than 6 meters.

On the other hand, if only wind speed is considered, it was seen that wind gusts were captured by the pressure transducers between 3 to 5 seconds after they were captured by the anemometer. Figure 5 presents an example of these findings, the graph shows an eleven minute period when wind gusts were captured by the anemometer. The figure shows the pressure difference and wind speed in the east façade located in the windward side.

From all the measurements of both, wind and pressure difference, the data containing high wind speeds was separated from the rest, as a result short periods were considered to analyse how wind gusts are captured in terms of pressure difference. This is important because wind gusts make measuring the air leakage rate more difficult due to a sudden change of pressure difference (Kraniotis, et al., 2014).

A positive peak in pressure difference was recorded few moments after the wind gust was captured in the anemometer. Authors believe that this time delay of 3 to 5 seconds is because of the distance between the anemometer and the test house. Similar results were found for each of the façades, with the difference that in the leeward side of the building the pressure peaks were found in the negative side.

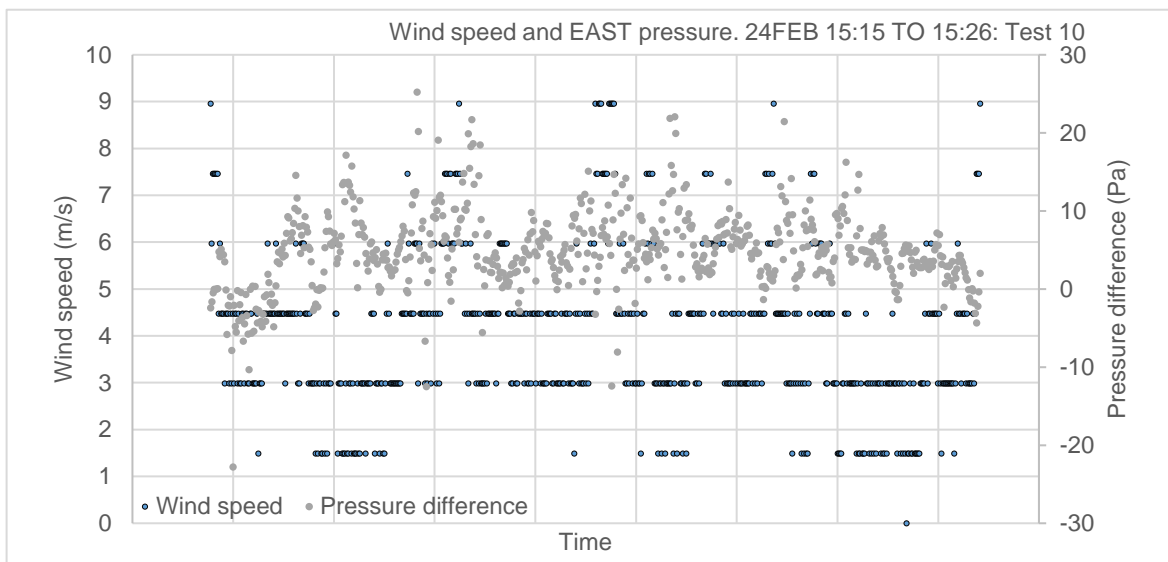


Figure 5. Wind speed and pressure difference in the east façade of the building during a eleven minute time on the 24<sup>th</sup> of February 2018.

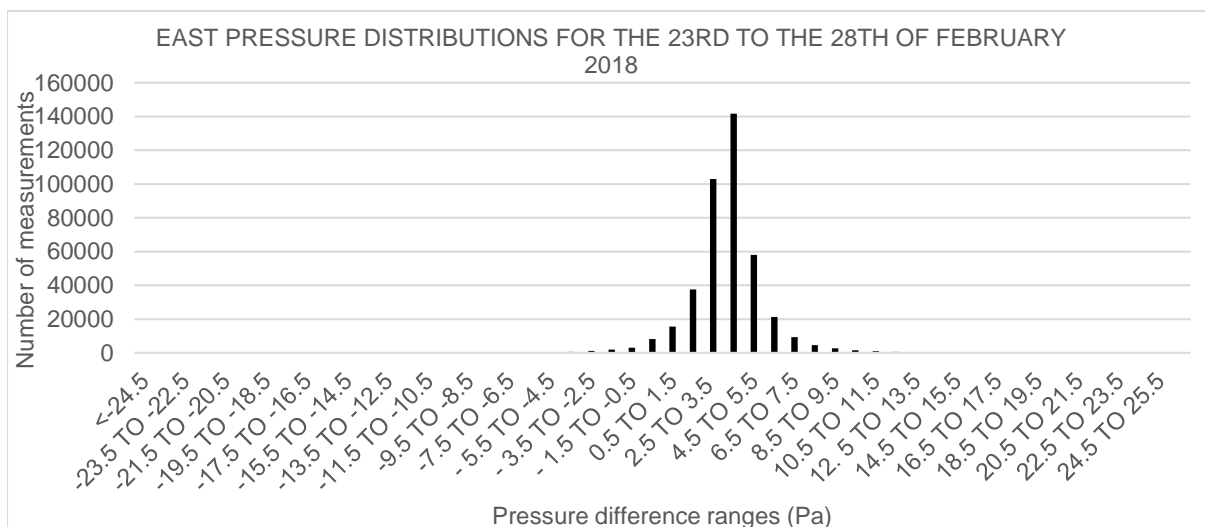


Figure 6: Pressure distributions in the East façade of the test house from the 23rd to the 28th of February 2018.

These results showed that the pressure transducers can be used to correlate the pressure difference, and to be used as an alternative when measuring ALR, regardless of the method used. Furthermore, pressure transducers can be correlated with the wind speed to determine a different way to account for the wind acting on the building's envelope, however, this is not part of the scope of this study. In addition, results showed how the pressure difference changes with time.

High wind speeds are not always present and wind gusts occur in a fraction of a second. That is why an analysis of all the measurements from the 23rd to the 28th of February 2018 was made, as shown in Figure 6. It can clearly be seen that for this period, where different weather conditions were captured, the majority of the pressure differences captured in the windward façade (east) are in the range of 3.0 to 4.5 Pa. Measurements on facades exposed to direct wind (windward) showed similar results, on leeward facades the pressure differentials were lower (1.5-2.5 Pa).

The mean pressure differences in all four facades of the test house for all the measurements taken is 3.17 Pa with an standard error of  $\pm 0.0022$  Pa, however, the most repeated value of Figure 5 is the range covering between 3.5 and 4.5 Pa, this was valid for the windward side of the house.

As mentioned before, wind gusts are regularly a problem when measuring ALR due to their effect in the background pressure. If the same period as in Figure 5 is selected, and the results are arranged, two major findings can be found: first, the pressure differences on each façade follow a normal distribution and; second, that most of the pressure differences occur between 1.5 to 5.5 Pa of pressure difference. Figures 7a, 7b, 7c and, 7d show the distribution of pressure differences (Pa) of every façade tested for an eleven minutes period on the 24th of February 2018 when high wind (velocities up to 9 m/s) was hitting the test house. Similar analyses were made for different periods when high winds were acting on the faces of the building, the results were all consistent with these findings, these are given in Table 2 and 3 which show three selected high wind periods on which a similar analysis (as the one given for Figure 7) was done.

The statistical figures from different periods when wind gusts were captured are summarised in Table 2.

Table 2. Statistical figures from measured pressure differences when wind gusts were captured by the anemometer.

Test	Feb 24 <sup>th</sup> 15:15-15:26				Feb 25 <sup>th</sup> 17:07-17:17				26 <sup>th</sup> Feb 14:31-14:41				Average
	E	N	S	W	E	N	S	W	E	N	S	W	
Facade Average pressure difference (Pa)	4.86	1.01	2.49	2.50	3.68	1.34	3.53	3.14	4.33	2.29	3.25	2.64	2.92
Standard error	0.19	0.12	0.09	0.12	0.11	0.07	0.05	0.07	0.09	0.06	0.04	0.05	0.09

The mean pressure difference for these periods is  $2.92 \pm 0.09$  Pa, it is clearly seen that for the leeward façade (north) the pressure difference is less than those in where the wind is directly hitting the envelope of the building. The most repeated ranges vary from façade to façade, for the three periods of high gusts these are shown in Table 3.

Table 3. Most repeated ranges of pressures when wind gusts were captured.

Test	Feb 24 <sup>th</sup> 15:15-15:26				Feb 25 <sup>th</sup> 17:07-17:17				Feb 26 <sup>th</sup> 14:31-14:41			
	E	N	S	W	E	N	S	W	E	N	S	W
Most repeated range (Pa)	3.5	0.5	1.5	2.5	2.5	0.5	3.5	2.5	3.5	1.5	3.5	2.5
	4.5	1.5	2.5	3.5	3.5	1.5	4.5	3.5	4.5	2.5	4.5	3.5

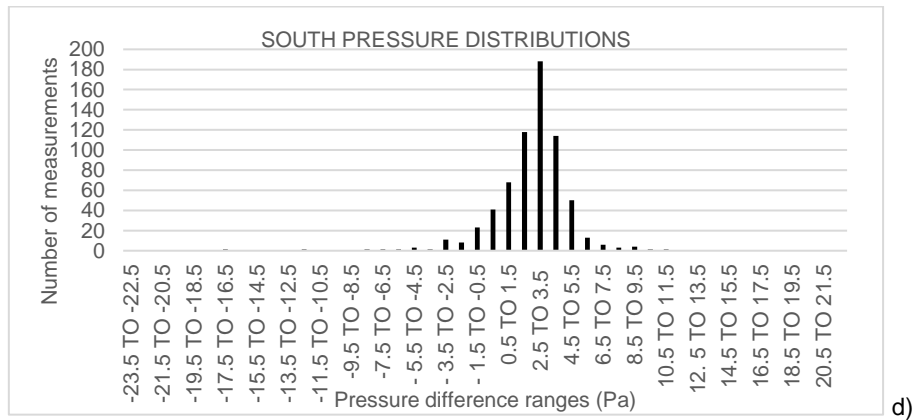
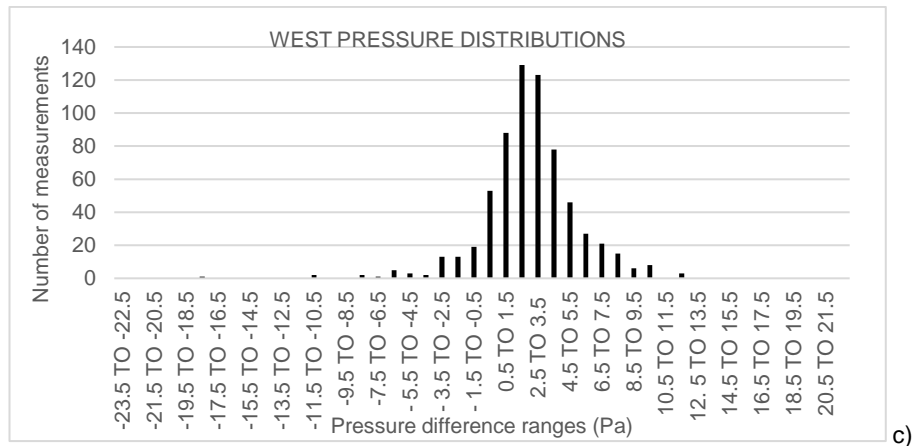
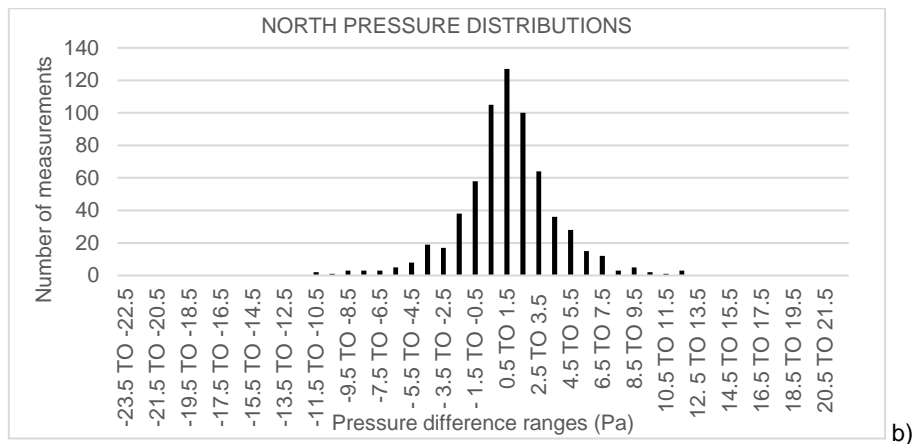
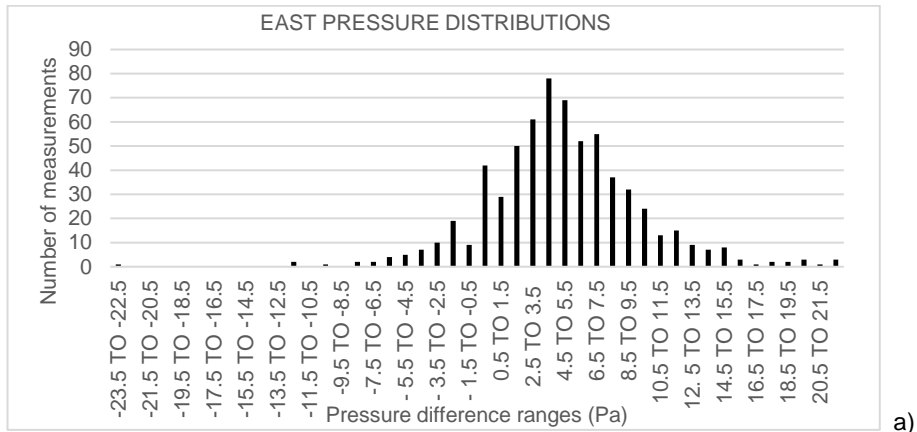


Figure 7. Pressure difference distribution on the 24<sup>th</sup> of February 2018 from 15:15 to 15:26 when wind gusts were captured in a) east, b) north, c) west and, d) south facades of the test house.

From what is presented in Tables 2 and 3, it can be concluded that the majority of the pressure differences occur in this house between 1.5 and 4.5 Pa. These results found, strongly agree with Cooper and Etheridge (2007) who mentioned that “natural conditions” at which air leakage and air infiltration occur is near the 4 Pa. Authors suggest that the measured ALR quoted at 4 Pa should reduce the uncertainty created by the extrapolation from high to low pressure. The Pulse technique measures quotes and measures ALR at 4 Pa. It is fully recommended to continue the development and revision of such technique to provide more accurate ALR measurements, than the ones commonly obtained nowadays with the blower door method.

#### 4. CONCLUSIONS

During the last week of February 2018, measurements of pressure difference in a test house in Nottingham, United Kingdom were made. The objective was to have more information to make decisions about which technique to use to measure the air leakage rate (ALR).

Results showed that wind gusts were captured by the pressure transducers after a time delay of less than 5 seconds, which is probably due to the distance between the anemometer and the test house.

The major result was that natural conditions at which air leakage and air infiltration occur is mostly between 3.5 and 4.5 Pa of pressure difference for a windward façade and 0.5-2.5 for leeward facades. The mean pressure difference calculated in a 5 day period was 3.17 Pa. This may suggest that a technique that measures and quotes ALR at 4 Pa could deliver results without the uncertainty created from extrapolation, compared to those quoting results at a high pressure difference.

It is recommended that the Pulse technique continues its R&D development due to the advantage found in this experimental study. Future work include the analysis and distribution of pressure differences when airtightness is being measured, and; the calculation of uncertainty when infiltration is predicted from Pulse and the standard pressurisation methods.

#### 5. ACKNOWLEDGEMENT

Part of this work was funded by the Mexican Council of Science and Technology (CONACYT), and The European Union's Horizon 2020 research and innovation programme under grant agreement No 637221. [‘Built2Spec’: [www.built2spec-project.eu/](http://www.built2spec-project.eu/)]

#### 6. REFERENCES

- Anderson, A., 1995. “The History of the Blower Door”. *Home Energy Magazine Online*. [Online] Available at: <http://homeenergy.org/show/article/year/1995/id/1171>
- Cooper, E. & Etheridge, D., 2007. Determining the Adventitious Leakage of Buildings at Low Pressure, Part 1: Uncertainties. *Building Services Engineers Research Technology*, Volume 28, pp. 71-80.
- Cooper, E. & Etheridge, D., 2007. Determining the Adventitious Leakage of Buildings at Low Pressure, Part 2: Pulse Technique. *Building Services Engineers Research Technology*, Volume 28, pp. 81-96.
- Cooper, E. et al., 2014. *A Nozzle Pressurization Technique for Measurements of Building Leakage at Low Pressures*. Poznan, Poland, s.n.
- Cooper, E. et al., 2016. Field Trialling of a New Airtightness Tester in a Range of UK homes. *International Journal of Ventilation*, 18(1), pp. 1-18.
- Cooper, E. & Zu, Y., 2011. *A Nozzle Pulse Pressurisation Technique for Measurement of Building Leakage at Low Pressure*. Istanbul, Turkey, s.n.
- Energy Conservatory, n.d. *Minneapolis Blower Door Operation Manual for Model 3 and Model 4 Systems..* [Online] Available at: <http://dev.energyconservatory.com/wp-content/uploads/2014/07/Blower-Door-model-3-and-4.pdf>. [Accessed 2017].

Energy Saving Trust, 2006. *Good Practice Guide 268- Energy efficient ventilation in dwellings - a guide for specifiers*. London, UK.: Energy Saving Trust.

Etheridge, D. W., 2012. *Natural ventilation of buildings: theory, measurement and design*. UK.: Wiley and Sons.

Jones, B. et al., 2013. The effect of party wall permeability on estimations of infiltration from air leakage. *International Journal of Ventilation*, 12(1), pp. 17-29.

Kraniotis, D., Thiis, T. & Aurlen, T., 2014. A Numerical study on the impact of wind gust frequency on air exchanges in buildings with variable external and internal leakages. *Buildings*, 4(1), pp. 27-42.

Lapillonne, B., Pollier, K. & Samci, N., 2015. Energy efficiency trends for households in the EU.. pp. 1-51.

RDH Building Engineering Ltd., 2013. *Air Leakage Control in Multi-Unit Residential Buildings*, Vancouver, Canada: Canada Mortgage and Housing Corporation.

Santamouris, M. & Asimakopoulos, D., 1996. *Passive Cooling of Buildings*. s.l.:James & James (Science Publishers) Ltd..

The British Standards Institution, 2015. *BS EN ISO 9972:2015 Thermal Performance of Buildings - Determination of Air Permeability of Buildings- Fan Pressurization Method*, United Kingdom: BSI Standards.

---

## #50: Thermal conductivity enhancement of phase change materials using aluminium wool

---

Adam DICKEN<sup>1</sup>, Zafer URE<sup>2</sup>

<sup>1</sup> Phase Change Material Products Limited, Unit 32, Mere View Industrial Estate, Yaxley, Cambridgeshire, PE7 3HS, UK, adam.dicken@pcmproducts.net

<sup>2</sup> Phase Change Material Products Limited, Unit 32, Mere View Industrial Estate, Yaxley, Cambridgeshire, PE7 3HS, UK, z.ure@pcmproducts.net

*Phase change materials (PCM) offer a solution to bridging the energy gap between energy use and energy availability. These materials store energy in the form of latent heat, which is the heat required to convert a solid into a liquid, without a change in temperature. This physical process is completely reversible and allows energy to be stored in a dense, safe and convenient way. One of the major drawbacks which limits the practical application of many organic PCMs is their low thermal conductivity, many researchers have lead focused investigations into a number of thermal conductivity promoters to help improve their thermal characteristics, but very few have been commercially viable. This paper presents a practical study on the thermal conductivity enhancement of organic phase change material using randomly packed aluminium wool and discusses the practical reality of applying this technology. A number of composite PCM samples were created, each using the same base PCM and different weight percentages of thermal conductivity promoter. The composite PCMs were tested using differential scanning calorimetry (DSC), T-history method and the thermal conductivity was measured. The performance of each composite PCM was then compared and discussed. It was found that composite PCM had an improvement in thermal conductivity by up to 70.8%. Their freezing and melting rates improved by up to 167.7% and 68% respectively. This gain in thermal performance was at the expense of the samples latent heat capacity.*

*Keywords: energy management, energy storage, phase change materials, thermal conductivity promoter*

## 1. INTRODUCTION

An ideal candidate phase change material (PCM) would have a number of properties and features including: a small phase transition range; high volumetric heat capacity; high thermal conductivity; uniform freezing and melting; rapid crystallisation; completely reversible freeze-melt cycles; no degradation after repeated phase transitions; compatible with plastics such as HDPE, GRP and metals for encapsulation; non-toxic, non-flammable, non-hazardous and non-corrosive; low cost with readily available components; and a phase transition temperature which is in accordance with the operating temperature range of the system. The ideal PCM has yet to be found; however, in any given engineering application the PCM that matches the most of these criteria is selected.

Organic phase change materials are made up of materials such as waxes, paraffin and fatty alcohols. These PCMs often exhibit a small phase transition range and a high heat capacity; however, they suffer from having poor thermal conductivity. This poor thermal conductivity leads to poor heat transfer as described by Fourier's Law. By increasing the thermal conductivity of a substance the rate of heat transfer will increase, which in this case leads to faster charging and discharge rates for thermal energy storage (TES). From a commercial perspective, the market has a strong desire for faster charging and discharging rates within PCM TES for an acceptable price. The introduction of using a thermal conductivity promoter within phase change materials has been the subject of numerous studies that go back a number of decades, the resulting PCM being known as composite PCM. The focus of this work has surrounded aluminium-based thermal conductivity promoters. Recently, materials such as diamond foam; metallic foams; graphite nanoplatelets; copper nanowire aerogel; carbon fibres; and most commonly expanded graphite have been used as thermal conductivity promoters. The question of how to apply these promoters is not only based on the materials thermal properties, but also their shape, chemical make-up and configuration. As these shapes become more complex; the cost of manufacturing increases exponentially, as does the expertise required to produce these advanced materials, leading to the commercial practicality suffering. Aluminium wool is a highly conductive; compatible; cheap and readily available material which could potentially be an effective thermal conductivity promoter.



*Figure 1: Close-up picture of the structure of aluminium wool*

Figure 1 illustrates how the thin, chaotic, strands of aluminium create a web of intersecting material. This offers a network, through which heat can easily conduct and diffuse. In addition, these thin strands present a high heat transfer area, which further improves heat flow through the composite PCM. A common drawback of many thermal conductivity promoters is that any they must be functionalised, otherwise they can separate from their solution and their effectiveness can drop dramatically. One of the benefits of aluminium wool is that it does not require functionalisation; it can be bent and compressed to take a desired configuration, which it will retain. Often, PCM functionalisation leads to a reduced latent heat capacity; however, in this case the only loss in latent heat capacity is due to the loss of PCM volume because of the presence of aluminium wool. In this paper, thermal conductivity improvement of PlusICE A44 as a PCM using aluminium wool was investigated. The effect of the thermal conductivity enhancement was investigated experimentally; in addition, the latent heat capacities were measured by DSC analysis technique and the phase transition time was estimated experimentally using the T-history method. These results were then compared to that of pure A44.



## 2. EXPERIMENTAL RESULTS

### 2.1. Preparation of A44 and aluminium wool composite PCMs

Four samples of PCM were tested, using A44 phase change material from Phase Change Materials Products Limited as the baseline material. The different composite PCM will be tested on a volumetric basis; therefore, 43cm<sup>3</sup> was selected as the test volume. Their respective compositions are as shown in Table 1.

Table 1: Composite PCM composition

Component	Sample 1	Sample 2	Sample 3	Sample 4
Aluminium wool (g)	0.00	1.46	3.52	5.60
Aluminium wool (wt%)	0.00	4.3	10.0	15.3
A44 phase change material (g)	32.68	32.30	31.69	31.10
A44 phase change material (wt%)	100	95.7	90.0	84.7
Total weight of composite PCM (g)	32.68	33.76	35.21	36.70

These composite PCMs were prepared by weighing out the necessary quantity of aluminium wool into a container. It could then be manipulated inside the container to ensure that it is evenly distributed. A44 was then melted and poured into the container, filling all the void space between the aluminium wool strands.



Figure 2: Aluminium wool composite PCM in containers

Figures 2a, 2b, 2c and 2d show samples 1, 2, 3 and 4 respectively. It illustrates that the increasing fractions of the aluminium thermal conductivity promoter is visible to the observer and the random nature of the aluminium strands. Figure 2d shows that there is a relatively small amount of void space between strands compared to that of Figure 2b, further compression of the aluminium wool becomes difficult without mechanical assistance, suggesting that beyond 15wt% aluminium wool composite PCM would be more difficult to achieve.

### 2.2. Thermal conductivity measurement

The thermal conductivity of each sample was determined by using a KD2 Pro Thermal Properties Analyser. The samples were heated above their phase transition region and the SH-1 sensor was inserted into the liquid PCM. The PCM was allowed to cool to room temperature of approximately 18°C; six measurements of thermal conductivity were taken and averaged. As shown in Table 2, there is a clear trend that increasing weight fractions of aluminium wool thermal conductivity promoter lead to an increasing thermal conductivity in the composite PCM; however, this will be at the expense of the composite's latent heat capacity. This is due to the aluminium promoter not offering any latent heat storage at the target temperature for this PCM.

Table 2: Composite PCM thermal conductivity

Property	Sample 1	Sample 2	Sample 3	Sample 4
Average thermal conductivity (W/mK)	0.288	0.356	0.468	0.492
Change compared to baseline (%)	0.0	+23.7	+62.5	+70.8

Figure 3 illustrates the link between increasing amounts of aluminium wool and the thermal conductivity of the sample. It appears that there is a rough linear relationship between thermal conductivity and the weight percentage of the aluminium wool. Even at relatively low weight fractions of 4.3%, the thermal conductivity promoter appears to have a large effect on the thermal conductivity of the composite, with sample 2 exhibiting a 23.7% increase in thermal conductivity. The drawback, as previously discussed, is the resulting loss in latent heat capacity; however, due to the high density of aluminium relative to that of the A44 PCM the latent heat capacity loss will likely be minimal. Further analysis of the samples will determine how impactful the increase in thermal conductivity is on performance at a macroscale and the latent heat storage potential of the PCM.

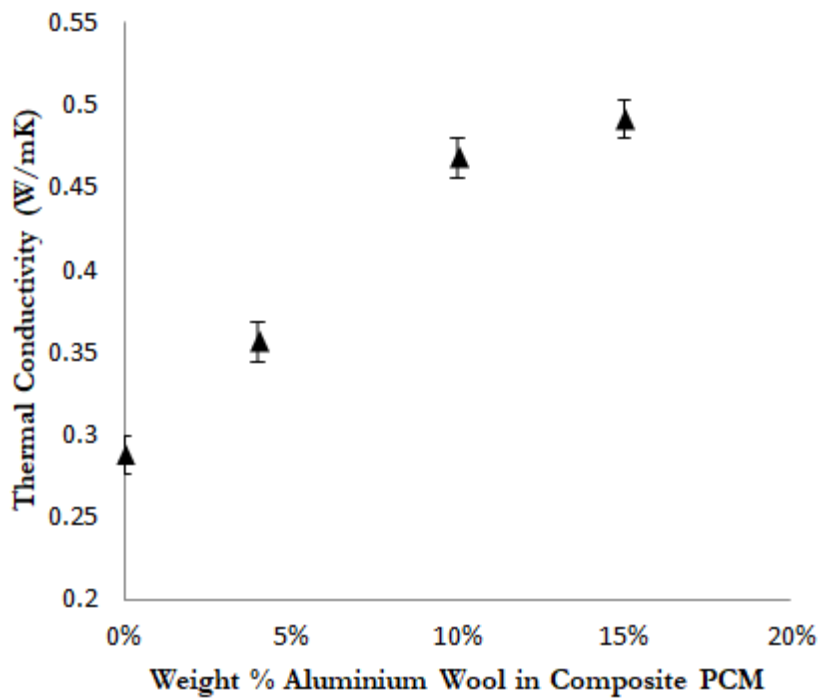


Figure 3: Comparison of the thermal conductivity and percentage of aluminium wool in composite PCM

### 2.3. Determination of thermal properties

Differential scanning calorimetry (DSC) analysis technique is a valuable tool for determining the latent heat storage potential of a given substance. In this study, the experiments were performed using a DSC823e from Mettler Toledo under a nitrogen atmosphere, supplied at a rate of 100 ml/min. The heating rate was 10 K/min. Dynamic samples masses were taken to be analysed between a temperature range of 10 - 95°C. Figure 4a, 4b, 4c and 4d show the DSC results for the samples 1, 2, 3 and 4 respectively. The numerical results are summarised as shown in Table 3.

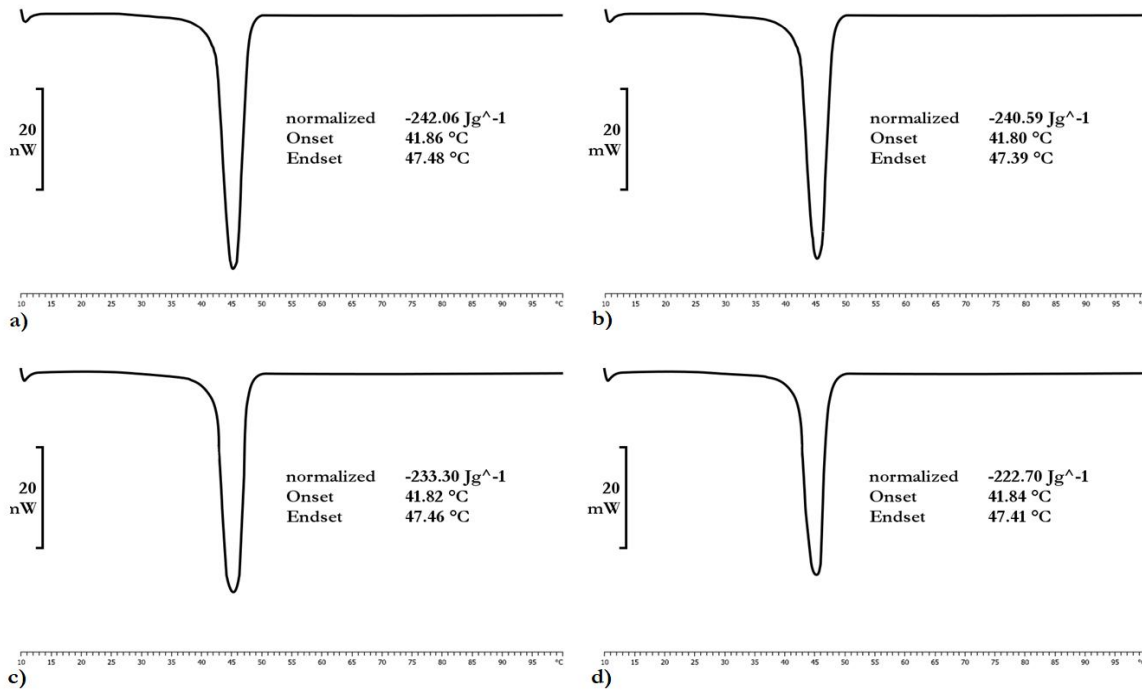


Figure 4: Results from differential scanning calorimetry

Table 3: Composite PCM latent heat capacity comparison

Property	Sample 1	Sample 2	Sample 3	Sample 4
Latent heat capacity (kJ/kg)	242.06	240.59	233.30	222.70
Change compared to baseline (%)	0.0	-0.61	-3.03	-4.55

As shown in Figure 4a, the DSC for pure A44 shows a very narrow peak, suggesting that it has a small phase transition range. It has a latent heat capacity of 242.06 kJ/kg. Figure 4b shows the DSC for sample 2, as anticipated there is a corresponding drop in the latent heat capacity of the sample; which is related to the corresponding weight percentage of PCM in the composite. The latent heat capacity of sample 2 is 240.59 kJ/kg. This trend continues in the other samples, with samples 3 and 4 having reduced latent heat capacities of 233.30 kJ/kg and 222.70 kJ/kg respectively. Table 3 further illustrates the change in latent heat capacity for each sample compared to the base PCM. The latent heat capacities of the samples show a strong negative correlation with the increasing fraction of aluminium wool within the composite.

## 2.4. Determination of phase transition time

By modifying the T-history method, experiments can be run simultaneously to observe the temperature changes of all samples under the same conditions. This allows the changes in freezing and melting rates to be observed, as well as confirming the phase transition region and the presence of subcooling at a larger, macro-scale. By comparing the freezing and melting times, the effects on the effective thermal conductivity presented by the introduction of the thermal conductivity promoter can be better understood. A number of conditions have been set to ensure that the test is fair, including: sample volume; container type and material and ambient conditions to ensure the same  $\Delta T$  is presented at the beginning of each test.

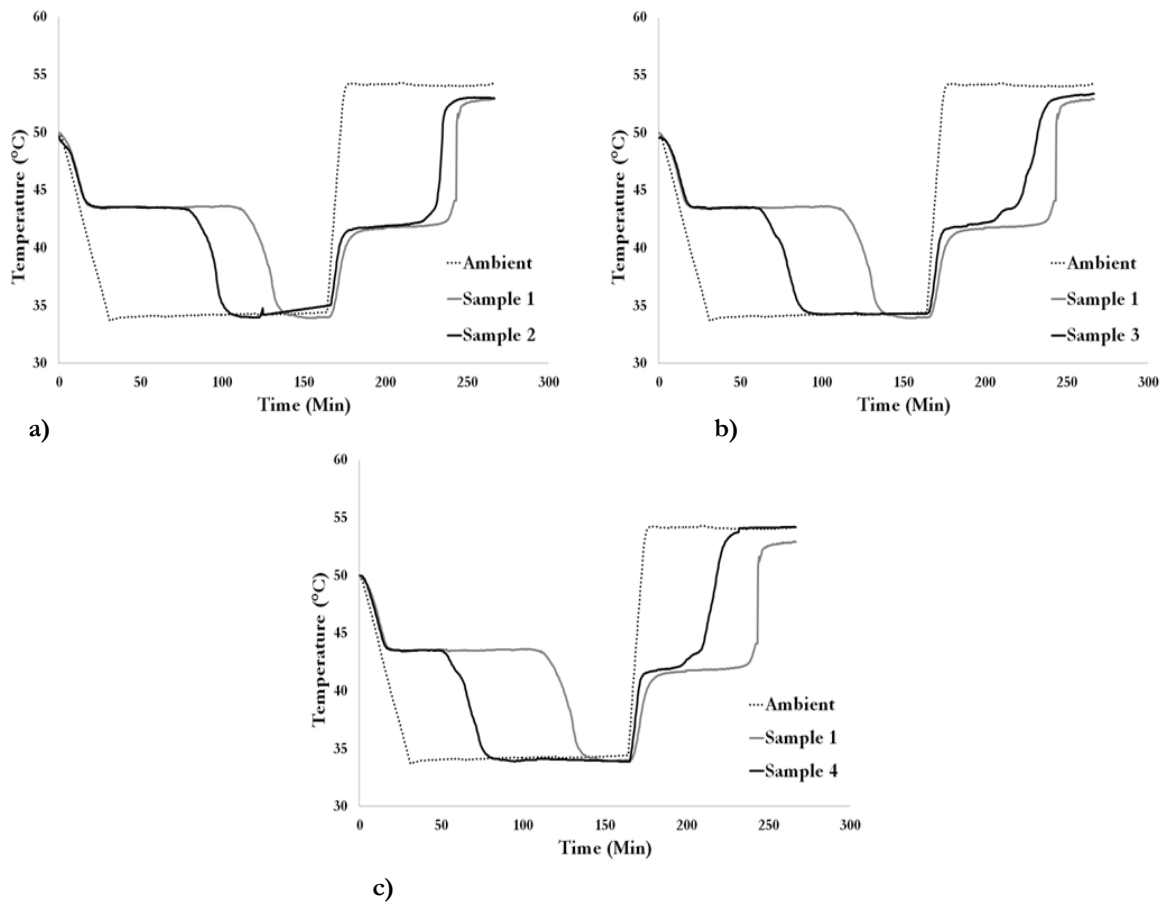


Figure 5: T-history results

Figure 5a shows the simultaneous T-history method results for samples 1 and 2. This offers a direct comparison between the freezing and melting of the baseline PCM and composite PCM. Figures 5b and 5c show the simultaneous T-history method results comparing sample 1 with sample 3 and sample 4 respectively. On observation, the shorter freezing and melting plateaus presented by the composite PCM in all tests indicate that the freezing and melting rates are increased. Even when considering the marginally different latent heat capacities, the composite PCMs appear to have a much faster freeze-melt time.

Table 4: Numerical analysis of T-history method results

Property	Sample 1	Sample 2	Sample 3	Sample 4
Onset of freezing (min)	20.0	20.0	20.0	20.0
Endset of freezing (min)	107.0	79.5	61.0	52.5
Onset of melting (min)	179.5	175	175.5	174.5
Endset of melting (min)	240	227.5	219.5	210.5
Rate of freezing compared to Sample 1 (%)	+0.0	+46.2	+112.2	+167.7
Rate of melting compared to Sample 1 (%)	+0.0	+15.2	+37.5	+68.1

Table 4 illustrates the findings from the T-history method in a quantitative manner, showing the change in the rate of freezing and melting. These results show a strong correlation between the weight fraction of aluminium wool and the rate of both freezing and melting. Even at the low weight fraction of 4%, there is a large improvement in the freezing and melting rate of 46.2% and 15.2% respectively. As the weight fraction of aluminium wool increases to approximately 10% in sample 3, there is an increase in the freezing and melting rate of 112.2% and 37.5% respectively. Sample 4 has been shown to have the highest thermal conductivity of all PCM tested during these experiments, this was reflected in its performance during this test, exhibiting a freezing rate improvement of 167.7% and melting rate improvement of 68.1%. These results further illustrate the impact of improved thermal conductivity on the macro-scale phase transition time.

### 3. DISCUSSION

#### 3.1. Compatibility of aluminium wool with organic PCM

Aluminium is fully compatible with all common organic PCM components. The aluminium wool is distributed as evenly as possible; however, the composite still is not entirely homogenous. The densities of samples 1, 2, 3 and 4 are 760, 785, 819 and 853 kg/m<sup>3</sup> respectively. This suggests that greater weight fractions of aluminium promoter within a composite PCM will lead to a heavier TES system, assuming the systems are of the same volume. Following numerous freeze-melt cycles, the aluminium wool has proven to be shape-stable and not separate from the PCM component, this mechanical robustness should allow the composite PCM to be beneficial in a greater number of applications. There were some concerns that the higher density of aluminium would lead to the wool settling; however, even after 120h at temperatures over the melting point of A44, the promoter did not settle out and the composite PCM showed a near homogenous state. It appears that, whilst being ductile, the aluminium can resist the compressive stress created by the surrounding PCM and therefore maintains its shape.

#### 3.2. Thermal conductivity improvement

Figure 3 shows the variation of thermal conductivity with different weight fractions of aluminium wool present. This indicates that increasing weight fractions of aluminium lead to increased thermal conductivity. A relationship between the thermal conductivity and weight fraction of aluminium can easily be drawn from Figure 3 as follows:

*Equation 1: Relationship between thermal conductivity and weight fraction of aluminium*  $y = 1.4181x + 0.2982 (R^2 = 0.9547)$

Where:

y = thermal conductivity (W/mK)  
x = weight fraction of aluminium wool

Thermal conductivities of the composite PCM with weight fractions of 4.3%, 10.0% and 15.3% aluminium wool indicated that the thermal conductivity of A44 (0.288 W/mK) increased by 23.7%, 62.5% and 70.8% respectively. This was attributed to the high thermal conductivity of aluminium. The results indicated that the thermal conductivity could be further improved by even greater weight fractions of aluminium; however, it becomes difficult to compress the aluminium wool further without mechanical assistance. Increasing the amount of aluminium beyond 15wt% would further decrease the latent heat capacity of the composite due to the decrease in weight fraction of A44 present in the composite. The high thermal conductivity of the composite PCM make this much more attractive than pure A44 for systems that require a faster thermal response time.

#### 3.3. Thermal properties of A44/aluminium wool composite PCM

DSC analysis was conducted to investigate the influence of aluminium wool on the latent heat storage capacity of A44 and the composite PCM. The DSC curves in Figure 4 were taken as a reference to evaluate the change in thermal properties of composite PCM. It shows that increasing weight fractions of aluminium wool leads to a decrease in the latent heat storage; the latent heat storage of A44 (242.06 kJ/kg) was reduced in each composite PCM to 240.59 kJ/kg, 233.30 kJ/kg and 222.70 kJ/kg for the PCM with weight fractions of 4.3%, 10.0% and 15.3% aluminium wool respectively. This illustrates the resulting latent heat capacity losses of 0.61%, 3.03% and 4.55% for each composite PCM respectively. This performance loss, whilst noteworthy is relatively small and this satisfactory latent heat capacity means it is still suitable for TES applications.

### 3.4. Comparison of freezing and melting time of composite PCM with baseline

This marked improvement in thermal conductivity was further tested by comparing the freezing and melting times of the composite PCM with that of A44. This improvement in times can be observed in Figure 5. Composite PCM with weight fractions of 4.3%, 10.0% and 15.3% aluminium wool indicated that the freezing time of A44 (87min) decreased by 31.6%, 52.9% and 62.6% respectively; and the melting time of A44 (60.5min) decreased by 13.2%, 27.3% and 40.5% respectively. This is due to the enhanced heat transfer by higher thermal conductivity and increased thermal diffusivity. The reduction in these phase transition times confirmed the improvement of thermal conductivity in the composite PCM. This would mean that the composite PCM could absorb any heat supplied more rapidly from a heat source compared with pure organic PCM; furthermore, it would release energy faster leading to a more agile TES system.

## 4. CONCLUSIONS

Thermal conductivity of the A44 was efficiently improved using aluminium wool thermal conductivity promoter. In addition, it acted as a heat diffusion promoter. The results clearly indicate a linear relationship between thermal conductivity and the weight fraction of aluminium wool. The variation in thermal conductivity improvement of A44 was caused by differences in homogeneity within the composite PCM, due to the chaotic nature of the aluminium wool strands. The thermal conductivity improvement of pure A44 was also tested by examining the freezing and melting times of pure A44; A44/Al (95.7/4.3wt%); A44/Al (90.0/10.0wt%); and A44/Al (84.7/15.3wt%) composite PCM. The reduction of the melting times of composite PCM with respect to both the freezing and melting time confirmed the thermal conductivity improvement of A44. This result also proved that the heat transfer rate of composite PCM were markedly higher than that of pure A44, this being owed to the presence of aluminium, which has a high thermal conductivity. Furthermore, the effects of aluminium wool thermal conductivity promoter on the latent heat capacity of pure A44 were investigated by DSC analysis. Results from the DSC indicated that the decrease in latent heat capacity of the composite PCM due to the presence of the promoter was minimal, meaning that the composite PCM had latent heat storage capacity that could be considered useful for thermal energy storage applications. As a result, aluminium wool can be considered an effective thermal conductivity and heat diffusion promoter to improve the thermal performance of A44, without greatly reducing its latent heat storage capacity as shown by Table 5, which summarises all key findings.

Table 5: Key results summary

Property	Sample 1	Sample 2	Sample 3	Sample 4
Aluminium wool fraction (%)	0	4.3	10.0	15.3
Average thermal conductivity (W/mK)	0.288	0.356	0.468	0.492
Thermal conductivity change (%)	0.0	+23.7	+62.5	+70.8
Latent heat capacity (kJ/kg)	242.06	240.59	233.30	222.70
Latent heat capacity change (%)	0.0	-0.61	-3.03	-4.55
Rate of freezing compared to sample 1 (%)	+0.0	+46.2	+112.2	+167.7
Rate of melting compared to sample 1 (%)	+0.0	+15.2	+37.5	+68.1

With respects to the real-world application of this composite PCM, it was found to be both easy to handle and simple to produce in comparison to the majority of alternative PCM enhancement methods. This simplicity lends itself to the technology being both cheap and accessible, both of which are important for engineering projects at scale, as end-users must believe that the technology is the right choice and the right price. Thermal energy storage systems often have a return on investment of approximately 3–7 years depending on application, therefore any composite or enhanced PCM that is applied must lead to an appreciable benefit whilst remaining economically viable for the given application. In the case of aluminium wool composite PCM, it has proven to have a number of the ideal PCM characteristics discussed previously, whilst remaining economically attractive.

## 5. REFERENCES

- Chaichan, M, 2015. Using aluminium powder with PCM (paraffin wax) to enhance single slop solar water distiller productivity in Baghdad - Iraq winter weathers. *International Journal of Renewable Energy Research*, Volume 5, pages 251-257.
- Fan, L, 2011. Thermal conductivity enhancement of phase change materials for thermal energy storage: A review. *Renewable and Sustainable Energy Reviews*, Volume 15, pages 24-46.
- Lin, Z, 2019. Thermal enhancement and shape stabilization of a phase-change energy-storage material via copper nanowire aerogel. *Chemical Engineering Journal*, Volume 373, pages 857-869.
- Long, Z, 2019. Thermal conductivity enhancement of phase change materials with 3D porous diamond foam for thermal energy storage. *Applied Energy*, Volumes 233-234, pages 208-219.
- Nazir, H, 2019. Recent developments in phase change materials for energy storage applications: A review. *International Journal of Heat and Mass Transfer*, Volume 129, pages 491-523.
- Solé, A, 2013. Review of the T-history method to determine thermophysical properties of phase change materials (PCM). *Renewable and Sustainable Energy Reviews*, Volume 26, pages 425-436.
- Yinping. Z, 1999. A simple method, the T-history method, of determining the heat of fusion, specific heat and thermal conductivity of phase-change materials. *Measurement Science and Technology*, Volume 10, pages 201-205.

---

# #51: Nonsolvent-induced phase separation synthesis of membrane via electro-spraying for desalination

---

Qian-wen SU, Li-Zhi ZHANG, Saffa RIFFAT

<sup>1</sup> Environmental Key Laboratory of Enhanced Heat Transfer and Energy Conservation of Education Ministry, School of Chemistry and Chemical Engineering, South China University of Technology, Guangzhou 510641, China. Ceqianwen.su@mail.scut.edu.cn

<sup>2</sup> Environmental Key Laboratory of Enhanced Heat Transfer and Energy Conservation of Education Ministry, School of Chemistry and Chemical Engineering, South China University of Technology, Guangzhou, China

<sup>3</sup> Environmental Technology Faculty of Engineering, Department of Architecture & Built Environment, University of Nottingham, University Park, Nottingham, NG7 2RD, UK, Saffa.riffat@nottingham.ac.uk

Superhydrophobic membranes with excellent water repellence property are good candidates for membrane distillation. In the field of polymer membranes, nonsolvent-induced phase separation (NIPS) is a common strategy to produce porous structures after the removal of solvents. Inspired by the theoretical research, we have reported a facile method to fabricate a superhydrophobic microporous membrane for desalination which combined nonsolvent-induced phase separation (NIPS) and electro-spraying. In this paper, a novel poly(vinylidene fluoride) (PVDF) membrane with a micro/nanoscale hierarchical structure has been prepared. Before electro-spraying, an appropriate amount of nonsolvent which did not cause phase separation was mixed with polymer solution. During the electro-spraying, the composition changed, and phase separation occurred owing to the volatility of solvent and nonsolvent, thus creating porous structures with high permeability and a contact angle of 152.4°, which were ideal for direct contact membrane distillation (DCMD) application. By changing the composition of three phase, different membrane morphology could be obtained. The resultant nanofibrous membranes exhibited high permeability and superhydrophobicity. The facile and scalable strategy might be applied to fabricate superhydrophobic and highly permeable membranes for desalination applications.

Keywords: superhydrophobicity; PVDF; electro-spraying; nonsolvent; desalination



## 1. INTRODUCTION

The availability of fresh water is one of the world's greatest challenges. Meanwhile, the growing population, industrialisation and Global warming is further exacerbating water shortages (Elimelech and Phillip, 2011). Membrane-based seawater separation is one of the most promising desalination methods, which can relieve pressure on water supply by conversion of seawater into fresh water. Reverse osmosis (RO) is widely applied due to its lower energy consumption compared with thermal distillation over a period. However, owing to its inherent drawbacks of requiring high voltage equipment, membrane distillation (MD) has gradually become a high-efficiency technique driven by vapour pressure difference on both sides of the membrane (Dudchenko et al., 2017). In general, high permeability and low energy consumption are important indices to evaluate a successful desalination. However, membrane distillation is limited by membrane wetting and low permeate flux in actual operation. Therefore, it is key to fabricate membranes with high permeability and superhydrophobicity by designing appropriate membrane pore size and modification (Lee et al., 2016). A hierarchical micro/nanostructure is necessary to fabricate a superhydrophobic surface. Generally, there are two methods of blending and coating to improve the roughness of the membrane, then modified by low-surface-energy materials. However, blending often suffers from inhomogeneous dispersity of the nanoparticles, while coating also confronts low permeability owing to the increase of membrane thickness and the reduction of membrane pore size. For these purposes, researchers have made many efforts to improve the dispersity and permeate flux. Regrettably, these methods often involve complicated chemical modification which are hard to achieve mass production (Li et al., 2015; Liao et al., 2014). Hence, it is necessary to design a superhydrophobic membrane via a simple method.

The electrospinning technique is a direct method to fabricate micro/nanoscale structures (Nejati et al., 2015; Tabatabaei et al., 2008). Jiang et al. (2004) prepared polystyrene (PS) surfaces using PS/DMF solutions of different concentrations by a simple electro-hydrodynamics (EHD) technique, which is the first time hydrophobicity has been achieved without any modification (Jiang et al., 2004). However, owing to the formation of compact microspheres, the method is often used as a coating to achieve water repellence. Jiang et al. also fabricated superhydrophobic microporous poly (vinylidene fluoride) (PVDF) membranes via a high-humidity induced electrospinning process (Jiang et al., 2018). Regrettably, the method is not suitable for the preparation of hollow fibre membranes. Besides, the permeability is too low to meet the requirement of water yield. In the field of polymer membranes, nonsolvent-induced phase separation (NIPS) is a common strategy to produce porous structures after the removal of solvents. (Srinivasarao et al., 2001) Inspired by the theoretical research, we have reported a facile method to fabricate a superhydrophobic microporous membrane for desalination which combined NIPS and electrospinning. Before electrospinning, an appropriate amount of nonsolvent which did not cause phase separation was mixed with polymer solution. During the electrospinning, the composition changed, and phase separation occurred owing to the volatility of solvent and nonsolvent, thus creating porous structures. (Qi et al., 2009) The microsphere/fibre porous structure was formed by a simple electrospinning technique from solutions in which a good solvent (N-methyl-2-pyrrolidone, NMP), a nonsolvent (H<sub>2</sub>O), and polymer (PVDF) were premixed. By changing the composition of three phase, different membrane morphology can be obtained. The resultant nanofibrous membranes exhibited high permeability and superhydrophobicity.

## 2. EXPERIMENTAL SECTION

### 2.1. Materials

Poly (vinylidene fluoride) (PVDF, FR904) was purchased from Shanghai 3F New Materials Technology Co., N-methyl-2-pyrrolidone (NMP) and ethanol were obtained from Guangzhou Qianhui Co., 1H, 1H, 2H, 2H-Perfluorodecyltrichlorosilane (FDTS) was purchased from Sigma-Aldrich, China. Deionised water (DW) was obtained from our laboratory.

### 2.2. Membrane fabrication process

Two steps were taken to fabricate the superhydrophobic and permeable membrane: (1) Electrospinning process. PVDF was mixed with solvent (NMP) and nonsolvent (H<sub>2</sub>O) at different ratios and stirred at 65 °C for 12 h to obtain homogeneous solutions. Then the solutions were kept at 25 °C for 12 h to remove bubbles. The solution was fed into a syringe and ejected through a metallic needle, with a feed rate of 1.28 m<sup>3</sup>/h. the needle tip was connected to a high voltage of 12 kV, and a piece of aluminium foil was used to collect the fibres with a tip-to collector of 15 cm. All the experiments were carried out at 20~25 °C and a relative humidity of 50~60%. The membranes by spinning were immersed in deionised water at 70 °C for 2 h to remove the residual solvent and then dried at room temperature for later use; (2) superhydrophobic modification. The prepared membranes were immersed in fresh FDTS solutions (FDTS/ethanol, 1/99, v/v) for 24 h and rinsed by ethanol. Finally, the membranes were dried at room temperature for further experiments. For simplicity, the membranes were marked as M1, M2, M3, M4 and M5, respectively.

### 2.3. Membrane Characterisation

The morphologies of membranes were characterised using scanning electron microscopy (Hitachi S-4800, Japan). Water contact angle measurements were conducted on a Data-physics OCA 40 (Germany) at room temperature using a water droplet of 3  $\mu\text{L}$ . An average value was adopted from the measurements at least five times at different locations of the same membrane. The pore sizes were measured via a bubble point method using a pore size analyser (3H-2000PB). The roughness of the membranes was characterised by an atomic force microscopy (AFM) (BMT EXPERT, Germany) with size of 5  $\mu\text{m} \times 5 \mu\text{m}$ . The membrane crystalline structure and infrared spectroscopies were characterised by X-ray diffraction (XRD, Bruker D8 advance, Germany) and Bruker Hyperion FT-IR spectrometer, respectively.

### 2.4. Phase behaviours of the solutions

Phase separation of the solutions was obtained from varying compositions of PVDF, NMP,  $\text{H}_2\text{O}$ . The different ratios of solutions were mixed at 65  $^\circ\text{C}$  for magnetic stirring obtain homogeneous solutions. The solutions that were in the steady state at room temperature kept transparent, while the solutions that were in the unstable status turned to be cloudy gradually owing to the occurrence of phase separation. The liquid-liquid demixing boundary at room temperature was obtained by the cloud point method.

## 3. RESULTS AND DISCUSSION

### 3.1 Phase separation mechanism of PVDF/NMP/ $\text{H}_2\text{O}$ system

The mutual affinity of PVDF and NMP/ $\text{H}_2\text{O}$  can be estimated by Hansen's solubility ( $\delta_i$ ) (Hansen, 2002). During nonsolvent induced phase separation, solvent and nonsolvent played important roles in determining the morphology and property of the membrane. The  $\Delta G^E$  (the change of the free energy of mixing) values of NMP with PVDF were the lowest of the common solvent, which was indicative of the good compatibility and strong interaction between NMP and PVDF. Therefore, NMP was used as the solvent for the ternary system. The ternary system refers to a three-component system (solvent: NMP, non-solvent:  $\text{H}_2\text{O}$ , polymer: PVDF). Generally, the value of  $\delta_i$  for  $\text{H}_2\text{O}$  was much bigger than other nonsolvent, which suggested that the thermodynamic stability of the PVDF/NMP/nonsolvent systems had the following sequence:  $\text{H}_2\text{O} < \text{MeOH} < \text{EtOH} < \text{IPA}$ . In other words, only a very small amount of water can be used to disturb the equilibrium phase of the solution. Therefore, water was used as the nonsolvent for the ternary system. Considering this, different ratios of ternary system are mixed to investigate the thermodynamic properties of the polymer/solvent/nonsolvent mixture.

During electrospinning process, a sample solution solidifies accompanying evaporation of solvents and the films was formed on the collector when a high voltage was applied. In this study, since the ternary systems contained nonsolvent ( $\text{H}_2\text{O}$ ), solvent (NMP) and polymer (PVDF), the effect of phase separation on the morphology of membrane during solvent evaporation was worthy of discussion. To elucidate the formation mechanism of porous microspheres, the phase diagram of the PVDF/NMP/ $\text{H}_2\text{O}$  ternary system was examined as shown in Figure 1. Two regions were divided by liquid-liquid demixing line determined by the compositions of solutions. The solutions in region I were homogeneous while those in region II was separated into phases. During electrospinning process, owing to the solvent and nonsolvent evaporation, the solution separated into two phases (polymer-rich and solvent-rich phases) and crossed the liquid-liquid demixing line. Therefore, the metastable solution underwent solid-liquid (S-L), liquid-liquid (L-L) or simultaneous phase separation mechanisms. With the increase of water, the solution in the unstable status turned to be cloudy. The final morphology of the membrane via electrospinning was determined by volatility of solvents and the degree of phase separation.

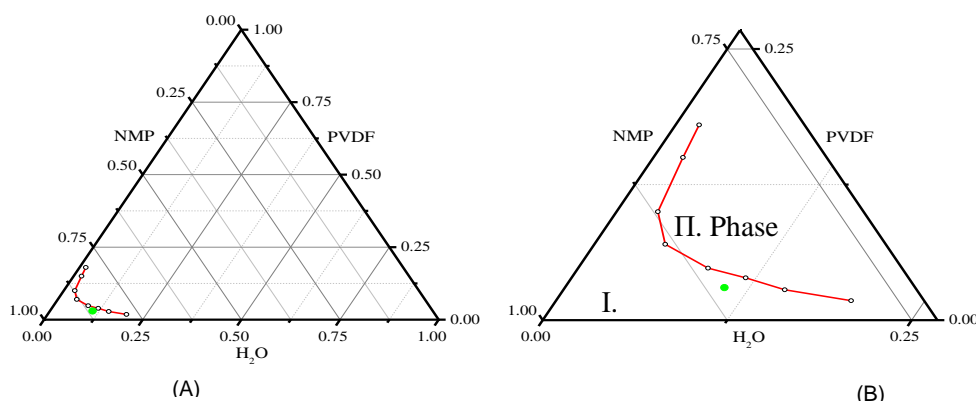


Figure 1. Phase diagram of the ternary system.

### 3.2. Surface Morphologies of membranes

Figure 2 showed the surface morphologies of the different membranes. Figure 2(a) showed the fibre structures and micropores. Generally, the polymer droplets overcame the surface tension to form jet streams, and eventually landed on the receiver to form fibres under high-voltage field. Some pores were formed on the surface of the fibre, which mainly resulted from the evaporation of solvents in the spinning process. Compared with Figure 2(a), as the polymer concentration decreased, fibres gradually transformed to microspheres, forming a microsphere-fibre interlinked structure. In the spinning process, competition between electrical force and surface tension decides the morphology of the membrane. With dilute solutions, the electrical force was not enough to sustain the elongation the jet streams, leaving the nozzle shrinks to droplets and ultimately forming microspheres. However, as an organic solvent with a high boiling point of 203 °C. NMP was hard to evaporate in air, thus forming flattened microspheres and fibres adhesion. When adding water into the polymer solution, phase separation occurred owing to the solvent and nonsolvent evaporation. Microsphere was interlinked with nanofibers in a stable 3D network in Figure 2(c). Some pores were formed on the surface of the microspheres caused by the evaporation of solvents in the spinning process in Figure 2(c). As the water content increased, the number of the microspheres increased, and the size gradually became uniform. The average diameter of the microspheres was 5.45  $\mu\text{m}$  with a pore size of 100 nm in Figure 2(d). Finally, after modification by FDTS, the surface energy of the membrane is lower. The average diameter increased from 5.45  $\mu\text{m}$  to 5.62  $\mu\text{m}$ . In Figure 2(e), a micro/nanoscale hierarchical structured surface was formed, which was helpful to improve the hydrophobicity of the membrane.

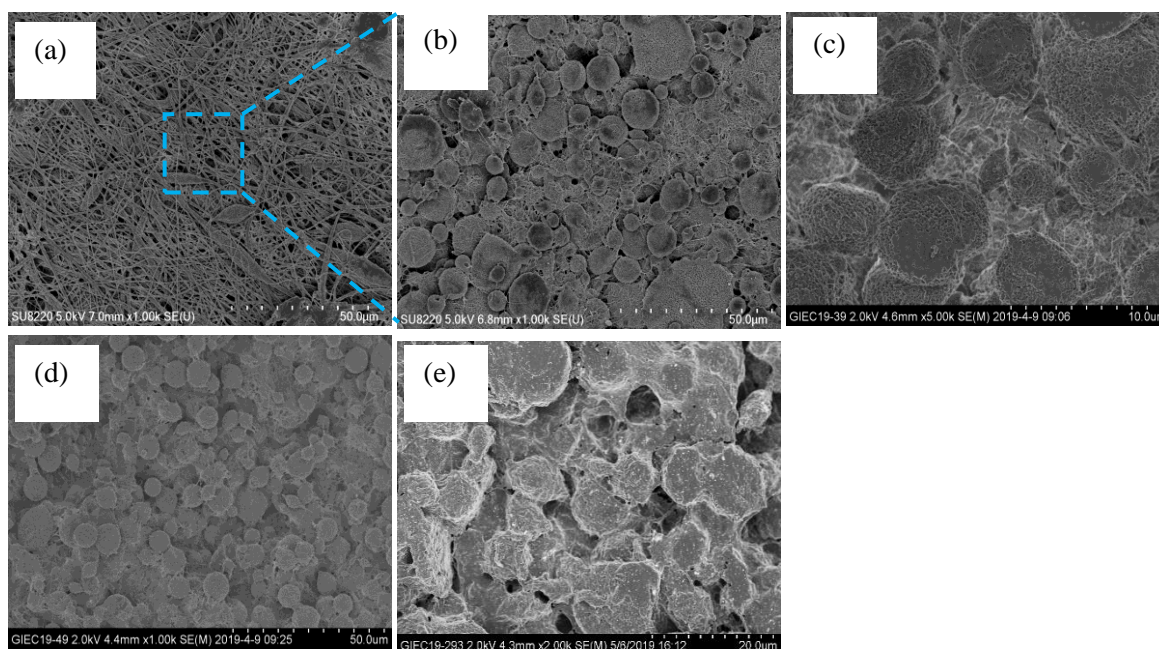


Figure 2: Surface scanning electron microscopy (SEM) images of (a) M1, (b) M2, (c) M3, (d) M4 and (e) P-M4, respectively.

### 3.3. Surface Morphologies of membranes

The contact angles of membranes were measured in Figure 3. Owing to the plane structure of nanofibers, M1 had the smallest contact angle. After the reduction of the polymer content, flatted microsphere structure was formed with a higher contact angle than M1. When adding water into the polymer solution. The number of microspheres increased with a higher contact angle. After modification by FDTS, a micro/nanoscale hierarchical structured superhydrophobic membrane was formed with a contact angle of 152.4°.

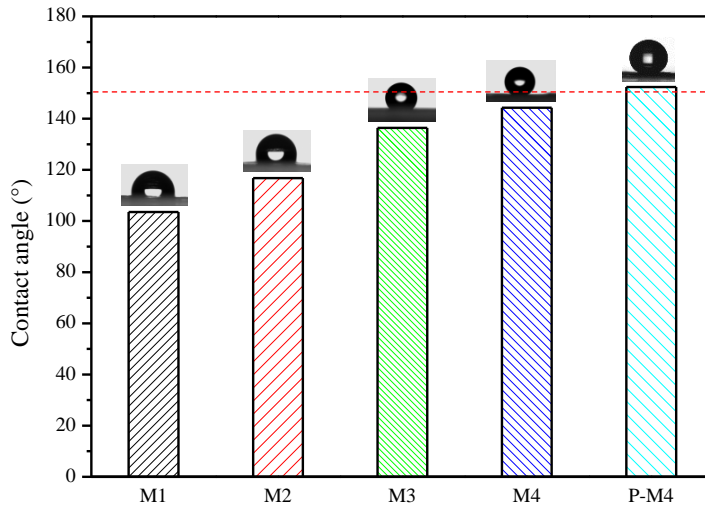


Figure 3. Hydrophobic degrees of different membranes. (A) Water contact angle of the membranes.

Apart from the wettability, the effect of PVDF concentration on the membrane pore size and distribution was also investigated. As shown in Figure 4, the pore size distributions of these PVDF membranes varied from 0.5~1  $\mu\text{m}$ . The membrane properties were concluded in Table 1. For M1 and M2, the pore size decreased as the polymer concentration decreased. The result may come from the change of membrane structure from nanofibers to microspheres. For M3 and M4, the pore size increased as water content increased. The result may come from nonsolvent evaporation in the spinning process. After modification by FDTs, the pore size decreased slightly owing to the coating material. Similarly, with changing the composition of membrane, the porosity decreased slightly from 77.4% to 63.8%. Although other factors such as the presence of surfactants in the solution can make the membrane wet, the major contributor to membrane wetting was fouling. Therefore,  $\text{LEP}_w$  increases from 65.54 KPa to 345.96 KPa, which showed better hydrophobicity and MD efficiency. (Gryta and Grzechulska-Damszel, 2009)

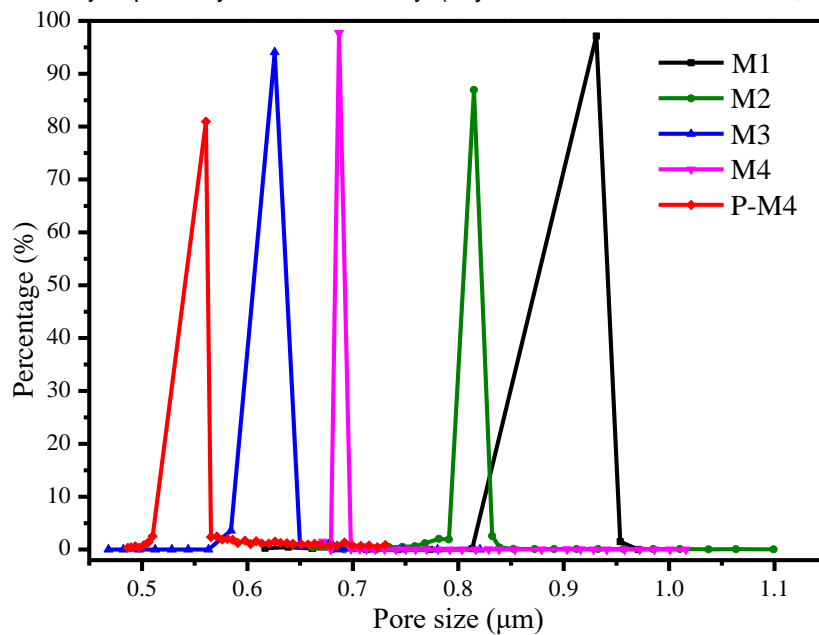


Figure 4. Microporous structure of different membranes.

Table 1. Information about the liquid entry pressure, pore diameter, porosity, contact angle, roughness and the membranes.

Membrane	Maximum pore size / $\mu\text{m}$	Porosity /%	Minimum pore size / $\mu\text{m}$	Average pore diameter / $\mu\text{m}$	$\text{LEP}_w$ (KPa)	Contact angle /degree	Roughness /nm
M1	1.0376	77.4	0.6168	0.9215	65.54	103.5	38.2
M2	1.0990	65.9	0.6617	0.8158	119.54	116.8	59.1
M3	0.8206	76.1	0.5844	0.6341	257.56	136.5	67.3
M4	1.0159	64.9	0.6716	0.6926	232.91	144.3	111
P-M4	0.7378	63.8	0.4865	0.5625	349.96	152.4	125

### 3.4. Analysis of surface structure

The ATR-FTIR spectra of membranes showed the change of functional groups. As shown in Figure 5(A), all membranes exhibited typical peaks of  $\alpha$  phase at 614, 760, and 975  $\text{cm}^{-1}$ . For M2 and M3, a C=O peak at 1720  $\text{cm}^{-1}$  occur, which indicated residual solvent of NMP. With adding more water into polymer solutions such as M4 and P-M4, residual solvents disappeared determined by volatility of solvents and the degree of phase separation. After modification by FDTS, the intensity of the peak at 1404  $\text{cm}^{-1}$  increased, which meant the increase of  $-\text{CF}_2$  group. Therefore, the hydrophobicity of the membrane was better than M4. Positively charged silica nanoparticles were tethered to these fluorocarbon groups via electrostatic interaction to produce membranes with superhydrophobic surfaces.

The membrane polymorphs was investigated by XRD. As shown in Figure 5(B), all membranes exhibited similar diffraction peaks at 18.4° and 20.2°, which corresponded to (0 2 0), (1 1 0) planes of PVDF crystals in the  $\alpha$  phase, respectively. The results showed that the non-polar  $\alpha$  phase was dominant in the PVDF membranes prepared from electrospinning. After adding water, the diffraction peaks changed from 18.4° to 17.8°. According to Bragg eq. ( $(2d) \sin \theta = \lambda$ ), (Bourlinos and Gournis, 2003), the value increases as  $\theta$  decreased, which showed that the lattice expanded. The reason could be that fluorine atom with a large atomic radius replaced hydrogen atom with a small atomic radius. In the  $\alpha$  phase, the polymer chains were arranged in a TGTG' conformation. Thus, the dipole moments of the crystal stacks were arranged in alternating directions, making it non-polar. (Andrew and Clarke, 2008) For PVDF membranes dominated by non-polar phase, the interactions between the membrane surface and polar water molecules were weak, thus increasing the hydrophobicity of the membrane further.

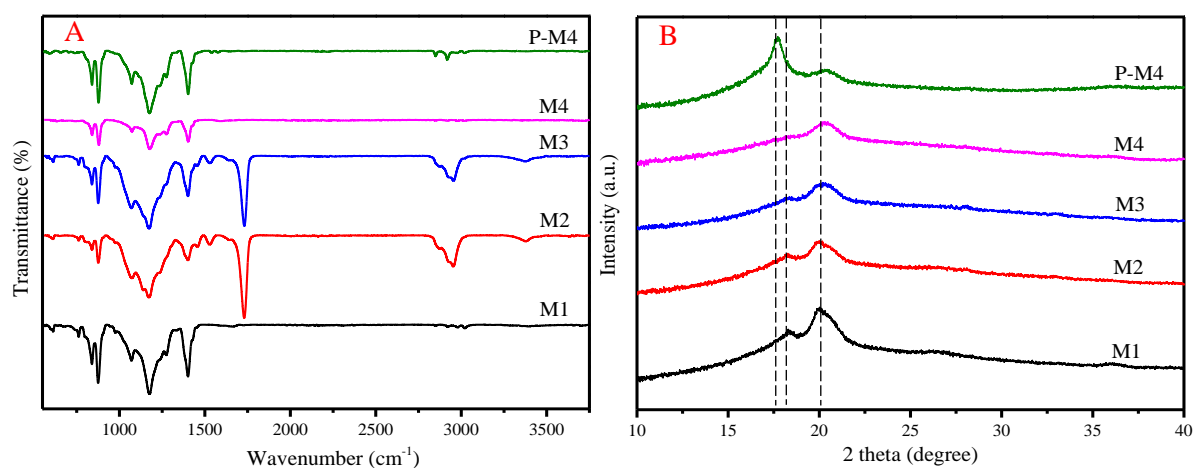


Figure 5. Structural properties of the membranes examined by ATR-FTIR (A) and XRD (B).

## 4. CONCLUSION

In summary, a novel microporous PVDF membrane was fabricated through a nonsolvent-induced phase separation electrospinning method. The unique microsphere-fibre hierarchical structure and modification by low surface energy materials (FDTS) endowed the PVDF membrane with superhydrophobicity. The average diameter increased from 5.45  $\mu\text{m}$  to 5.62  $\mu\text{m}$ . The relationship between porous structure and permeability was investigated in detail. The membrane with optimised wettability and pore structure showed hydrostatic pressure of 349.96 KPa. The facile preparation process and excellent performance of our membrane have shown great potential for desalination.

## 5. REFERENCES

- Andrew, J. S.; Clarke, D. R., 2008. Effect of Electrospinning on the Ferroelectric Phase Content of Polyvinylidene Difluoride Fibers. *Langmuir*, 24, 670-672.
- Bourlinos, A. B.; Gournis, D.; Petridis, D.; Szabo, T.; Szeri, A.; Dekany, I., 2003. Graphite Oxide: Chemical Reduction to Graphite and Surface Modification with Primary Aliphatic Amines and Amino Acids. *Langmuir*, 19, 6050-6055.
- Dudchenko, A. V.; Chen, C.; Cardenas, A.; Rolf, J.; Jassby, D., 2017. Frequency-dependent Stability of CNT Joule Heaters in Ionizable Media and Desalination Processes. *Nat. Nanotechnol.*, 12, 557.

Elimelech, M.; Phillip, W. A., 2011. The Future of Seawater Desalination: Energy, Technology, and the Environment. *Science*, 333, 712.

Gryta, M.; Grzechulska-Damszel, J.; Markowska, A.; Karakulski, K., 2009. The Influence of Polypropylene Degradation on the Membrane Wettability During Membrane Distillation. *J. Membr. Sci*, 326, 493-502.

Hansen, C. M., 2002. Hansen solubility parameters: a user's handbook. The US: CRC press.

Jiang, L.; Zhao, Y.; Zhai, J., 2004. A lotus-leaf-like superhydrophobic surface: A Porous Microsphere/nanofiber Composite Film Prepared by Electrohydrodynamics. *Angew. Chem. Int. Edit*, 43, 4338-4341.

Jiang, G.; Luo, L.; Tan, L.; Wang, J.; Zhang, S.; Zhang, F.; Jin, J., 2018. Microsphere-Fiber Interpenetrated Superhydrophobic PVDF Microporous Membranes with Improved Waterproof and Breathable Performance. *Acs Appl. Mater. Interfaces*, 10, 28210-28218.

Lee, J.; Boo, C.; Ryu, W.-H.; Taylor, A. D.; Elimelech, M., 2016. Development of Omniphobic Desalination Membranes Using a Charged Electrospun Nanofiber Scaffold. *ACS Appl. Mater. Interfaces*, 8, 11154-11161.

Li, X.; Yu, X.; Cheng, C.; Deng, L.; Wang, M.; Wang, X., 2015. Electrospun Superhydrophobic Organic/Inorganic Composite Nanofibrous Membranes for Membrane Distillation. *Acs Appl. Mater. Interfaces*, 7, 21919-21930.

Liao, Y.; Loh, C.-H.; Wang, R.; Fane, A. G., 2014. Electrospun Superhydrophobic Membranes with Unique Structures for Membrane Distillation. *Acs Appl. Mater. Interfaces*, 6, 16035-16048.

Nejati, S.; Boo, C.; Osuji, C. O.; Elimelech, M., 2015. Engineering Flat Sheet Microporous PVDF Films for Membrane Distillation. *J. Membr. Sci*, 492, 355-363.

Qi, Z.; Yu, H.; Chen, Y.; Zhu, M., 2009. Highly Porous Fibers Prepared by Electrospinning a Ternary System of Nonsolvent/solvent/poly(L-lactic acid). *Mater. Lett*, 63, 415-418.

Srinivasarao, M.; Collings, D.; Philips, A.; Patel, S., 2001. Three-dimensionally Ordered Array of Air Bubbles in a Polymer Film. *Science*, 292, 79-83.

Tabatabaei, S. H.; Carreau, P. J.; Ajji, A., 2008. Microporous Membranes Obtained from Polypropylene Blend Films by Stretching. *J. Membr. Sci*, 325, 772-782.

---

## #52: Consequence of colour temperature for awareness of security effect in King Mongkut's University of Technology Thonburi

---

Preecha AREGAROT<sup>1</sup>, Kuskana KUBAHA<sup>2</sup>, Sureeluk THINA<sup>3</sup>

<sup>1</sup>Energy Management Technology, School of Energy Environment and Materials, King Mongkut's University of Technology Thonburi, preecha.are@kmutt.ac.th

<sup>2</sup>Energy Management Technology, School of Energy Environment and Materials, King Mongkut's University of Technology Thonburi, kuskana.kub@kmutt.ac.th

<sup>3</sup>Office of Building and Ground Management, King Mongkut's University of Technology Thonburi, sureeluk.thina@gmail.com

At King Mongkut's University of Technology Thonburi (KMUTT), the pedestrian ways are the main routes between building entry points for people both day and night. When designing pedestrian ways, designers must be aware of safe paths, slope, floor texture and include ample light at night time. Lighting in particular can enhance visibility and thereby engender a sense of security. Therefore, insufficient illumination on pedestrian ways is of great concern. The Thai government supports a budget related to lighting improvement in the university by using LED lamps on pedestrian ways. This project aims to help reduce energy consumption in KMUTT: by changing from 250 watts metal-halide lamps to 75 watts LED lamps, the energy consumption was reduced from 282,510 to 70,627.5 kWh; a 75% decrease. Not only was energy saved, but people's perception of security was changed after the colour temperature changed from 1,850K. to 4,000K. When conducting a questionnaire survey of 30 participants of different age and gender, participants were tested by walking around KMUTT then stopped at each station and answering questions. One-way analysis of variance (ANOVA) was used to determine statistical differences of illumination. The results of this study show the differentiation of security perception. Subjects feel unfamiliarity when they stayed at station 3 and 4. Then station 3 ( $F(3.614) = 3.156, p < 0.026 < 0.05$ ) and station 4 ( $F(4.328) = 8.381, p < 0.013 < 0.05$ ). The subjects feel unsecure when stopping at station 2, station 3, station 4, and station 6. There were significant results on station 2 ( $p < 0.00$ ), station 3 ( $p < 0.00$ ), station 4 ( $p < 0.010$ ) and station 6 ( $p < 0.00$ ). In conclusion, colour temperature affects familiarity and pedestrians' feeling of security. Significant results ( $sig. > 0.00 > 0.05$ ) can be analysed that subjects feel familiarity with Daylight (LED) more than Warm (metal-halide) stations.

Keywords: LED lighting; energy consumption; colour temperature; security

## 1. INTRODUCTION

Street lighting for pedestrians at King Mongkut's University of Technology Thonburi (KMUTT) has changed over time according to the context of the university. The university feels it is important to standardise the brightness on roads and lighting can also increase the feeling of safety for pedestrians at night (Appleton, 1975). Good lighting can determine the environment and improve the sense of safety at night and the perception and impact on people within KMUTT. There has been plenty of research and guidelines relating to lighting design on pedestrian ways to generate illuminance, and relationships between peoples perception and illumination levels that affect the feeling of safety. Lighting influences people's perceived safety at night (Siyuan & Minitai, 2010) and the environment context will differ with user experience, e.g. with insufficient light, the familiarity with the area, gender and age. Research has found that lighting problems relate to a sense of security for pedestrians (Arut Sawatronnapat, 2555). The study show the results of the research and survey about pedestrian's sense of security while walking around the six experimental stations with warm light and day light scenes.

The campus setting and infrastructure information will provide the basic information of the university's consideration towards green environment. This indicator also shows if the campus deserves to be called a Green Campus. The aim is to trigger the participating universities to provide more spaces for greenery and to safe guard the environment, as well as the development of sustainable energy. KMUTT is one of the Science and Technology Universities in Thailand which builds capability to be a role model on energy and environmental management in Thailand and integrates all activities including teaching and research. KMUTT has adopted the goal to be a Green University and since 2005 has focused on energy, environment and safety, and has set up an Energy Environment and Safety Office to take responsibility for the system development and implementation. Sustainability is one of the major challenges of current and future generations of students & staff. KMUTT plans to educate students and encourage them to learn outside of classrooms and to transform its campuses to be an ideal environment for developing innovative solutions to and awareness of relevant problems thereby improving the world for current and future generations. According to Sustainable Development Goal 2030 (SDG, 2030), KMUTT has been committed to be a Green University for SDG 2030 since 2017, complying with the national agenda. KMUTT has a responsibility to contribute to the global and national sustainability agenda and to promote the development of sustainability leadership on our campus. The university has an additional responsibility to encourage students to do their part to protect the environment and natural systems.

## 2. METHODS

This study aims to investigate the quality of pedestrian lighting around the campus. The first section calculates energy consumption before and after changing lightbulbs from metal halide to LED lamps. This includes the break-even point for the budget and electrical costs. Section two studies the human side and sense of security. This is in two parts: the first is to find 30 locations with 15 scenes to be lit by metal halide and 15 by LED. Pictures of these were used for an on-line rating test. Then using the top six highest scores from an online questionnaire with three scenes being metal halide and three being LED scenes for part 2. Part 2 of the study is about the feeling of security in people walking in the six locations. The study focused on people's perceived safety in the university environment and their fear of crime (show in Figure 1). In the test areas, the subjects walked in a loop and during questioning, subjects stood 4m away from the surveyor who stood in unclear vision in dark clothing at night.



Figure 1: Mapping locations around in KMUTT campus.





Figure 2: Station 1-6 stations in locations around campus.

### 3. RESULTS

#### 3.1. Part 1

With Government support, the budget for the university to change pedestrian lighting from metal halide to LED lamps was carried out in two phases as shown in Table 1. In phase 1, 165 lamps were changed and in phase 2, 50 lamps and the colour temperatures were changed from Correlated Colour Temperature 4,000K  $\pm$  500. Power usage changed from 250 Watts to 75 Watts. Table 1 shows the results: phase 1 after changing lamps to LED, the difference in electricity fees is 1,051,529 THB, approximately 262,882.1 THB. Electricity charge is decrease 76%. In phase 2 after charging 50 LED lamps, the difference is 318,645 THB, approximately 79,661.25 THB. The cost of electricity decreased by 75%. The break-even point from phase 1 is 3.29 years and phase 2 is 2.8 years.

Table 1: The table is showing about energy consume including breakeven point.

Energy consumes (kWh.)			Electricity charge.		
Phase I	Before	216,810.00	1,051,529.00	Budget (THB)	2,600,000.00
165 (Lamps)	After	54,202.50	262,882.10	Break-even / years.	3.29
Phase II	Before	65,700.00	318,645.00	Budget (THB)	675,000.00
50 (Lamps)	After	16,425.00	79,661.25	Break-even / years.	2.82

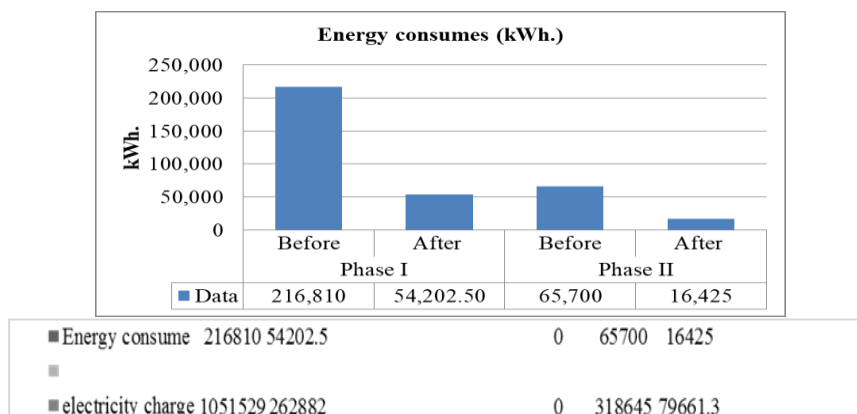


Figure 3: Comparison of energy consumption before changing pedestrian's light metal halide to LED (Phase 1 and 2).

### 3.2. Part 2

This section describes the study of the psychology of the pedestrian user walking at night time. There is literature showing that people feel most safe when they can recognise another pedestrian's face clearly (Wu & Kim, 2016). Lin & Fotios (2016) suggest that 4m is the shortest distance for subject recognition, thus in this test we try to stimulate the feeling of insecurity for the subject during their walk and stop at each station. There are 2 parts in this survey: part 1 is to find 20 places in main campus where there are hiding places compounded with buildings, trees and signage blocking the location, then select 6 places after online questionnaire with the highest score.

The second part takes six selected stations as shown in Figure 2. Test subjects were asked to walk to a station by a random loop, then to stand face-to-face with the questioner at about 4m apart to simulate unclear vision for the subject, and to answer a questionnaire, four questions at each station. The questionnaire was in two parts. The first part asked for personal information and the second was a 6-point Semantic Differential scale to define feelings, the scoring ranged from most to least (1-6) (Table 2.) They were defining feelings of familiarity and feeling of secure and the experiments were conducted between 6 and 20 October 2017. The subjects were university members and outsider people, men and women aged 18-60 years, all of them were of Thai nationality.



Figure 4: The example scene from subjects viewing during testing.

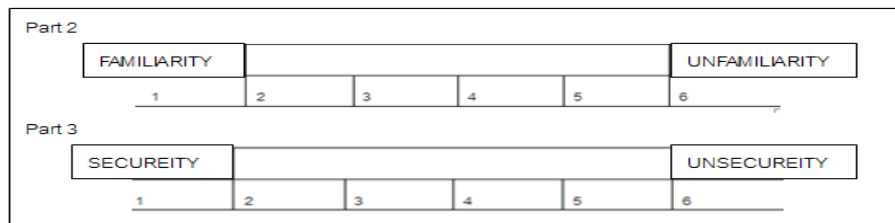


Figure 5: Semantic scale for subject to define their feeling during test in each station (questionnaire part 2, 3).

Experiment 1 concerned the effect of familiarity and security in pedestrian with other people. The result of familiarity and security in six stations are summarised in Table 2. The study set 1 condition control (1 stranger with unclear face standing in front of a subject at 4m.) After data repeated by One-way ANOVA, we found a significant result at station 3 and station 4 indicating that the subjects felt unfamiliarity when they stood at these stations. There are station 3 ( $F(3.614) = 3.156, p < 0.026 < 0.05$ ) and station 4 ( $F(4.328) = 8.381, p < 0.013 < 0.05$ ).

Concerning the feeling of security, we are found a significant on station 2, station 3, station 4 and station 6. There are station 2  $p < 0.00$ , station 3  $p < 0.00$ , station 4  $p < 0.010$  and station 6  $p < 0.00$ . This indicates that subjects felt insecure when at those stations. However, we did not find a significant difference between familiarity of insider and outsider subjects with stations in the experiment.

Table 2: Mean and standard deviation with Familiarity and Security score from six stations (experiment 1).

Experiment 1	Station 1	Station 2	Station 3	Station 4	Station 5	Station 6
Familiarity	4.23 (0.30)	5.33 (0.20)	4.83 (0.19)*	4.50 (0.29)*	4.60 (0.32)	4.93 (0.27)
Security	4.37 (0.18)	2.33 (0.23)*	2.50 (0.22)*	3.40 (0.18)*	3.77 (0.23)	3.17 (0.24)*

\*Significant  $p < 0.05$

Experiment 2 concerned the effect of colour temperature on familiarity and security of pedestrians. From summarize of color temperature group. It's showing the significant between familiarity with Daylight (LED) (4,000K  $\pm$  500) stations more than Warm (metal halide) (1,850 K) stations (sig >0.00>0.05). However in term of security feeling, subjects. There are insignificant, that mean LED and metal halide do not influence the sense of security of subject. There are result of familiarity and security with color temperature is summarized in Table 3.

Table 3: Mean and standard deviation with Familiarity and Secure for each colour temperature.

Experiment 2	Day Light (LED)(4,000K <sup>1</sup> $\pm$ 500)	Warm (metal halide)(1,850 K <sup>1</sup> )
Familiarity	4.80 (0.14)*	4.68 (0.17)
Security	3.96 (0.15)	3.56 (0.13)

\*Significant  $p < 0.05$ , <sup>1</sup> Correlated Colour Temperature.

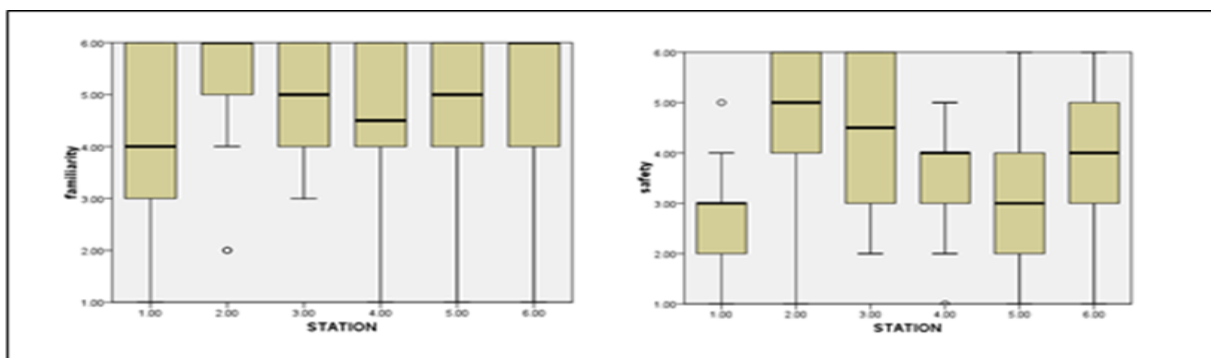


Figure 6: The dissipative diagram between Stations and feelings of Familiarity and Security.

#### 4. DISCUSSION

From the study we are found that factors like being a member of the university or an outsider does not influence the feeling of familiarity. Experiment one concerned the effect of familiarity and security in pedestrian with people. The result of familiarity and security in six stations are Security feeling, we found significance at stations 2, 3, 4 and 6. This means that subjects felt unsecure when standing at those stations. However, we did not finding a significant difference between familiarity of insider and outsider subjects with stations in the experiment. Experiment 2 concerned the effect of colour temperature on the familiarity and security of pedestrians. The survey showed a significant difference between feelings of familiarity in Daylight (LED) more than Warm (metal halide) lighting. However, in term of feelings of security, there are insignificant differences indicating that LED and metal halide lighting does not influence the sense of security in the subject. There are result of familiarity and security with colour temperature.

Literature and research support the notion that more factors should be considered in night light for pedestrians. Then the situation is relating to the city of Melbourne (2002) states that white light has more effect on the human eye than yellow light. There is not only lighting, the environment is relating to sense of security in people. Fisher & Nasar (1992) is suggest about atmosphere, amount light, human and environment is relate to safety feeling including (Loewen, L. J., Steel, G. D., & Suedfeld, P. (1993).

Yao et al. (2009) suggests that the pedestrian environment with sparse lighting caused by shadows can evoke a reaction of fear in people. Also Fisher & Nasar (1992) suggest that an environment can influence perceived safety by the obstruction of people's vision from things such as trees, buildings and signage.

#### 5. ACKNOWLEDGEMENT

This research was supported by [Building and Ground Management Institute, Research, Innovation and Partnerships, King Mongkut's University of Technology Thonburi (KMUTT). We are thankful to our colleagues who provided expertise (Mr.Prapon Ruengvuthchanaphuech)] that greatly assisted the research, although they may not agree with all of the interpretations provided in this paper.

## 6. REFERENCES

Appleton, J. (1975). *The experience of place*. London: Wiley.

Atici, C., Özçelebi, T., & Lukkien, J. J. (2011). System architecture for road lighting. In *Proceedings of the 2011 IEEE International Conference on Consumer Electronics* (pp. 681e682). <http://dx.doi.org/10.1109/ICCE.2011.5722807>.

Fotios SA, Raynham P. (2011) Correspondence: Lighting for pedestrians: Is facial recognition what matters *Lighting Research and Technology* 2011; 43: 129–130.

Fotios SA, Goodman T. (2012) Proposed UK guidance for lighting in residential roads. *Lighting Research and Technology* 2012; 44: 69–83.

Green P, Rao V. (1970) Rating scales and information recovery- how many scales and response categories to use *Journal of Marketing* 1970; 3: 33–39.

Nasar, J. L., Fisher, B., & Grannis, M. (1993). Proximate physical cues to fear of crime. *Landscape and Urban Planning*, 26, 161 -178.

Nasar, J. L., & Jones, K. M. (1997). Landscapes of fear and stress. *Environment and Behavior*, 29, 291-323.

Loewen, L. J., Steel, G. D., & Suedfeld, P. (1993). Perceived safety from crime in the urban environment. *Journal of Environmental Psychology*, 13, 323-.331.

Yao Q, Sun Y, Lin Y. (2009) Research on facial recognition and color identification under CMH and HPS lamps for road lighting. *Leukos* 2009; 6: 169-178.

---

## #54: Spectrally selective coating for the combination of solar thermal and sky radiative cooling

---

Bin ZHAO<sup>1</sup>, Mingke HU<sup>2</sup>, Xianze AO<sup>3</sup>, Nuo CHEN<sup>4</sup>, Gang PEI<sup>5\*</sup>

*Department of Thermal Science and Energy Engineering, University of Science and Technology of China,  
230027 Hefei, China,*

*<sup>1</sup>zb630@mail.ustc.edu.cn*

*<sup>2</sup>hmk@ustc.edu.cn*

*<sup>3</sup>aoxianze@mail.ustc.edu.cn*

*<sup>4</sup>chenuo@mail.ustc.edu.cn*

*<sup>5\*</sup> Corresponding author: peigang@ustc.edu.cn*

*Sky radiative cooling (RC) has drawn much attention recently for its potential as a passive cooling method for energy harvesting and thermal management. Sky RC primarily relies on the “atmospheric window” with a high transparency for electromagnetic wave from 8 to 13  $\mu\text{m}$ , allowing some of the heat to effectively escape to the colder universe. In this study, a spectrally selective coating is proposed and designed for the combination of daytime solar thermal (ST) conversion and nocturnal sky RC. Optical simulation is conducted, and results show that the proposed coating has a high solar absorptivity of approximately 0.92 and a strong thermal emissivity only in the “atmospheric window” with an average value of 0.86. Moreover, the performance of the ST conversion and the nocturnal sky RC of the proposed coating is evaluated by thermal analysis. The predicted results show that the proposed coating can be passively cooled to approximately 10 °C below ambient air temperature during night-time and can be heated to 73.4 °C higher than ambient air temperature by solar radiation. In summary, this work provides a new way of hybrid utilisation for solar energy and nocturnal sky RC.*

*Keywords: spectrally selective coating; solar thermal; sky radiative cooling; integration*

## 1. INTRODUCTION

Radiative cooling (RC) releases heat to a relatively cold universe and creates a local cold source for energy harvesting passively. This unique mechanism primarily relies on the “atmospheric window,” which has high transparency for electromagnetic wave at the wavelength from 8 to 13  $\mu\text{m}$ , allowing some heat to effectively escape to the relatively cold universe (Zhao et al., 2019a).

The development of RC has been focused on night-time in previous studies. Emitters with narrow high emissivity only within the atmospheric window (e.g., photonic emitters (Hossain et al., 2015) and micro/nano-particle based film (Gentle and Smith, 2010)) or the entire mid-infrared wavelength band (e.g., black paint (Hamza et al., 1995) and bulk silica (Kou et al., 2017)) are all good candidates of efficient night-time RC (NRC). The investigation of NRC is not limited to emitters, but also extends to real applications, such as building-integrated NRC systems, to obtain sub-ambient cooling effects. For example, Parker and Sherwin (Parker and Sherwin, 2008) proposed a concept of *NightCool building* that uses the NRC method to decrease the building’s electricity demand for space cooling. A long-term experiment showed that the average energy saving of *NightCool building* can reach 15%, which indicates that NRC has the potential to provide cooling and save energy for buildings.

Daytime radiative cooling (DRC) has been a popular research topic in recent years, and the sub-ambient cooling phenomena have been obtained by RC even under direct sunshine. The commonly used methods to achieve DRC is by using a spectrally selective emitter with low solar absorption and strong thermal emission. In 2014, a sub-ambient DRC was experimentally demonstrated by Raman (Raman et al., 2014) by using a photonic emitter with a high solar reflection of 97% and a strongly selective thermal emission with the atmospheric window. Since then, various kinds of spectrally selective emitters, including glass-polymer metamaterial (Zhai et al., 2017), hierarchically porous polymer (Mandal et al., 2018), and cooling wood (Li et al., 2019), have been developed for efficient DRC.

The abovementioned NRC and DRC methods only have a single function and can only be used for cooling. In our previous studies (Hu et al., 2018, 2016; Zhao et al., 2019c, 2019b, 2018, 2017), we proposed a novel concept by integrating the RC mechanism into existing solar collection methods to simultaneously achieve a cooling phenomenon and harvest solar energy. In this study, a spectrally selective coating is designed to combine solar thermal (ST) and NRC, i.e., ST-NRC. The ST-NRC coating needs high solar absorption for ST conversion and strong thermal emission only within the atmospheric window for cooling by NRC. The combined optical and thermal simulation is conducted to evaluate the potential of the proposed coating for ST-NRC hybrid utilisation.

## 2. OPTICAL DESIGN OF THE ST-NRC COATING

The schematic of the ST-NRC hybrid utilisation and the proposed ST-NRC coating is presented in Figure 1. ST-NRC coating can obtain heat energy by ST conversion at daytime and gain cooling energy by NRC at night-time. The proposed ST-NRC coating consists of four layers designed on top of a substrate. The bottom three layers are responsible for selective solar absorption, and this structure is a typical kind of solar-selective coating called nickel-aluminum oxide (Ni-Al<sub>2</sub>O<sub>3</sub>) coating (Li et al., 2012). The top layer of polydimethylsiloxane (PDMS) primarily assists in optimising spectrally selective thermal emission in the mid-infrared wavelength band.

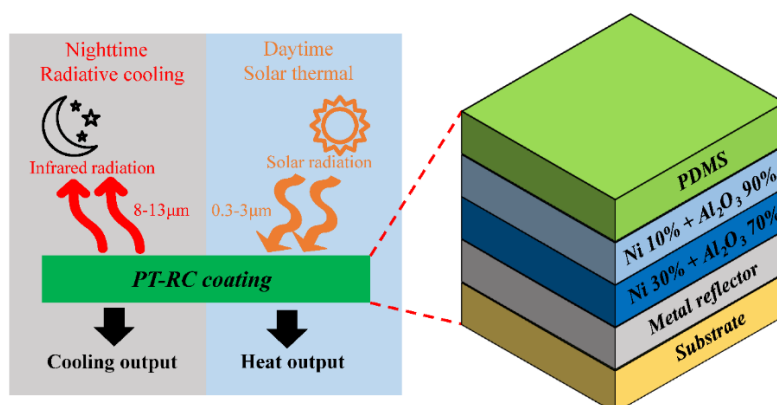


Figure1: Schematic of ST-NRC hybrid utilisation and proposed ST-NRC coating

The spectral properties of the proposed ST-NRC coating were numerically calculated and optimised. During simulation, silver (Ag) was selected as the metal reflector. The spectral-dependent complex optical constants of Ni, Al<sub>2</sub>O<sub>3</sub>, Ag, and PDMS were adopted from the literature (Lee and Luo, 2019; Palik, 1985; RefractiveIndex, 2019). The effectively complex optical constants of the mixing layer of Ni-Al<sub>2</sub>O<sub>3</sub> were determined by using the Bruggeman

model (Niklasson et al., 1981) as follows:

$$f \frac{\xi_{Ni} - \xi_{Ni-Al_2O_3}}{\xi_{Ni} + \xi_{Ni-Al_2O_3}} + (1-f) \frac{\xi_{Al_2O_3} - \xi_{Ni-Al_2O_3}}{\xi_{Al_2O_3} + \xi_{Ni-Al_2O_3}} = 0, \quad (1)$$

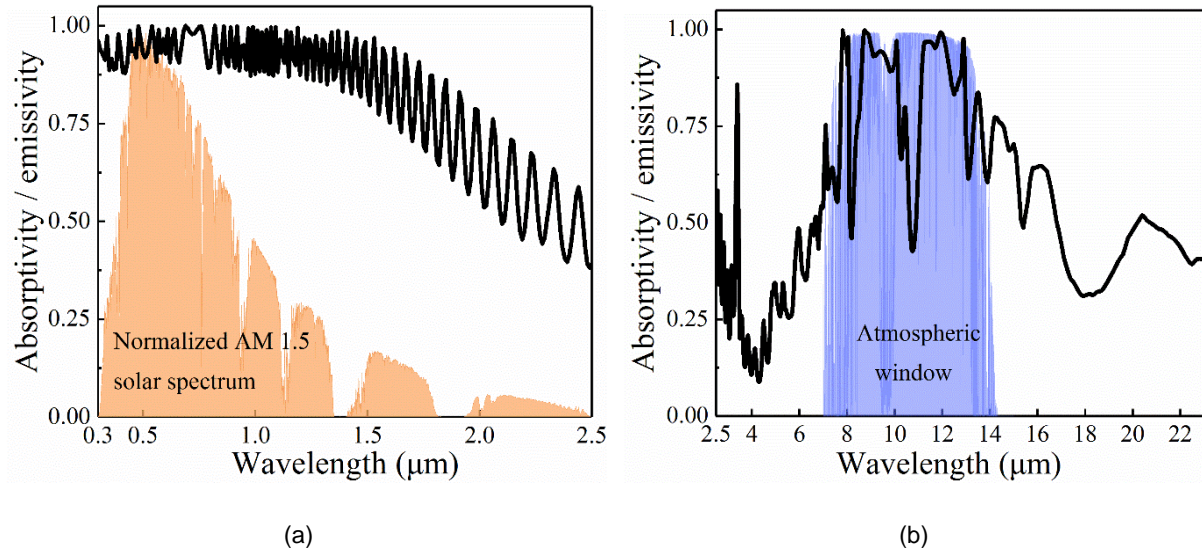
Where:

- $\xi$  = complex permittivity
- $f$  = the filling factor of Ni in the Ni-Al<sub>2</sub>O<sub>3</sub> layer.

The optimised spectral absorptivity/emissivity of the proposed ST-NRC coating is shown in Figure 2, and the corresponding thickness of each layer is given in Table 1. As shown in Figure 2, the proposed ST-NRC has high solar absorption in the solar radiation band with a weighted absorptivity of 0.92, and it has a strongly selective thermal emission within the atmospheric window with an average emissivity of 0.86.

*Table 1. Thickness of each layer of ST-NRC coating*

Name	Thickness (nm)
PDMS	18600
Ni 10% + Al <sub>2</sub> O <sub>3</sub> 90% ( $f=0.1$ )	107
Ni 30% + Al <sub>2</sub> O <sub>3</sub> 70% ( $f=0.3$ )	88
Metal reflector (Ag)	120



*Figure 2: Calculated spectral absorptivity/emissivity of the proposed ST-NRC coating at (a) solar radiation band and (b) infrared band, with a normalised AM 1.5 solar spectrum and a typical transmittance curve of the atmospheric window plotted as a reference.*

### 3. THERMAL ANALYSIS

The thermal performance of the proposed ST-NRC for daytime ST and NRC was evaluated by using a fundamental thermal simulation model, which was originally developed for DRC (Raman et al., 2014). The temperature of the ST-NRC coating was determined by solving the heat balance equation

$$q_{rad} - q_{sun} - q_{atm} - q_{con} = 0, \quad (2)$$

Where:

- $q_{rad}$  = the power radiated by the coating;

- $q_{sun}$  and  $q_{atm}$  = the coating's absorbed power from the sun and atmosphere, respectively;
- $q_{con}$  = the power from the ambient environment to the ST-NRC coating via a convection and conduction process.

The power radiated by the coating, which is defined as  $q_{rad}$ , can be expressed as

$$q_{rad} = 2\pi \int_0^{\infty} \int_0^{\frac{\pi}{2}} \varepsilon(\lambda, \theta) I_b(\lambda, T) \sin\theta \cos\theta d\theta d\lambda, \quad (3)$$

Where:

- $\varepsilon(\lambda, \theta)$  = the directional spectral emissivity of the ST-NRC coating
- $I_b(\lambda, T)$  = the spectral radiance of a blackbody at temperature  $T$ .

The power absorbed by the coating from the atmosphere, which is defined as  $q_{atm}$ , can be calculated as follows:

$$q_{atm} = 2\pi \int_0^{\infty} \int_0^{\frac{\pi}{2}} \alpha(\lambda, \theta) \varepsilon_{atm}(\lambda, \theta) I_b(\lambda, T) \sin\theta \cos\theta d\theta d\lambda, \quad (4)$$

Where:

- $\alpha(\lambda, \theta)$  = the direction spectral absorptivity of the ST-NRC coating, which is equal to  $\varepsilon(\lambda, \theta)$  according to Kirchhoff law;
- $\varepsilon_{atm}(\lambda, \theta)$  = the directional spectral emissivity of atmosphere

The directional spectral emissivity of atmosphere can be estimated as (Raman et al., 2014):

$$\varepsilon_{atm}(\lambda, \theta) = 1 - \tau(\lambda, 0)^{1/\cos\theta},$$

Where:

- $\tau(\lambda, 0)$  = the normal transmittance of the atmosphere.

The power absorbed by the coating from the sun and the power from the ambient environment to ST-NRC coating via convection and conduction process, defined as  $q_{atm}$  and  $q_{con}$  respectively, can be expressed as

$$q_{sun} = \alpha_{eff} G, \quad (5)$$

$$q_{con} = h(T_a - T), \quad (6)$$

Where:

- $\alpha_{eff}$  = the AM 1.5 solar spectrum-weighted absorptivity of the ST-NRC coating;
- $G$  = the total solar radiation power;
- $T_a$  and  $T$  = the temperature of ambient air and ST-NRC coating, respectively;
- $h$  = the overall heat transfer coefficient, which is set to  $5 \text{ W}\cdot\text{m}^{-2}\cdot\text{K}^{-1}$  for simulation in this study.

The temperature of ST-NRC was determined on the basis of the above mathematical model. The results are given in Figure 3. The data about solar radiation power and ambient temperature were measured at Hefei, China on April 16, 2018. The normal transmittance of the atmosphere is assumed to be unchanged over the day. The corresponding data were obtained from the literature ("MODTRAN," 2019).



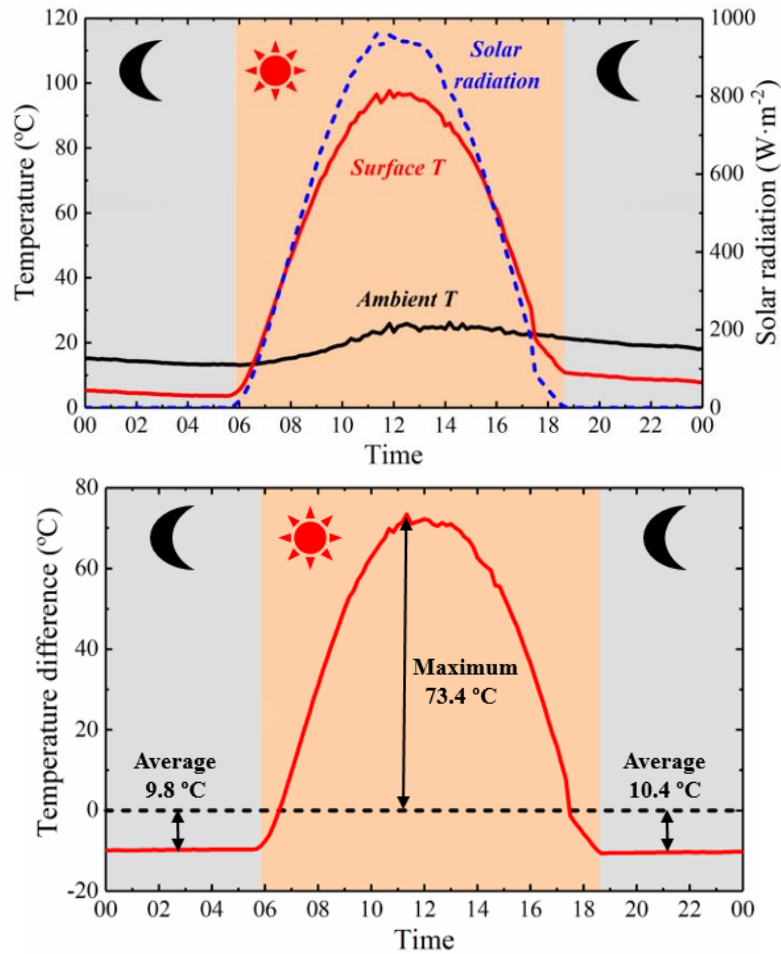


Figure 3. Simulated temperature of ST-NRC coating (red curve) with ambient temperature (black curve) and solar radiation power (blue curve) plotted as references.

Figure 3 shows the proposed ST-NRC coating can achieve daytime ST conversion and NRC. For example, the ST-NRC coating can be passively cooled to approximately 10 °C below ambient air temperature during night-time, and the coating can be heated to 73.4 °C higher than ambient air temperature by sunshine.

#### 4. CONCLUSION

A spectrally selective coating is proposed and designed for the hybrid utilisation of ST and NRC (i.e., ST-NRC). The solar absorptivity of the designed ST-NRC coating is approximately 0.92, and the coating's average emissivity within the atmospheric window is nearly 0.86. The results of thermal analysis reveal that the ST-NRC coating can be heated to 73.4 °C higher than ambient air temperature at daytime and can be passively cooled to approximately 10 °C below ambient air temperature during night-time, indicating that the proposed ST-NRC coating has the potential to harvest solar energy by ST and provide cooling by NRC.

#### 5. ACKNOWLEDGEMENT

This work has been supported by the National Natural Science Foundation of China (NSFC 51776193 and 51761145109).

#### 6. REFERENCES

- Gentle, A.R., Smith, G.B., 2010. Radiative heat pumping from the Earth using surface phonon resonant nanoparticles. *Nano Lett.* 10, 373–379.
- Hamza, A., Taha, I.M.S., Ismail, I.M., 1995. Cooling of water flowing through a night sky radiator. *Sol. Energy* 55, 235–253.

- Hossain, M.M., Jia, B., Gu, M., 2015. A metamaterial emitter for highly efficient radiative cooling. *Adv. Opt. Mater.* 3, 1047–1051.
- Hu, M., Pei, G., Wang, Q., Li, J., Wang, Y., Ji, J., 2016. Field test and preliminary analysis of a combined diurnal solar heating and nocturnal radiative cooling system. *Appl. Energy* 179, 899–908.
- Hu, M., Zhao, B., Ao, X., Zhao, P., Su, Y., Pei, G., 2018. Field investigation of a hybrid photovoltaic-photothermic-radiative cooling system. *Appl. Energy* 231, 288–300.
- Kou, J. long, Jurado, Z., Chen, Z., Fan, S., Minnich, A.J., 2017. Daytime radiative cooling using near-black infrared emitters. *ACS Photonics* 4, 626–630.
- Lee, E., Luo, T., 2019. Black body-like radiative cooling for flexible thin-film solar cells. *Sol. Energy Mater. Sol. Cells* 194, 222–228.
- Li, T., Zhai, Y., He, S., Gan, W., Wei, Z., Heidarinejad, M., Dalgo, D., Mi, R., Zhao, X., Song, J., Dai, J., Chen, C., Aili, A., Vellore, A., Martini, A., Yang, R., Srebric, J., Yin, X., Hu, L., 2019. A radiative cooling structural material. *Science* (80- ). 364, 760–763.
- Li, Z., Zhao, J., Ren, L., 2012. Aqueous solution-chemical derived Ni-Al  $2O_3$  solar selective absorbing coatings. *Sol. Energy Mater. Sol. Cells* 105, 90–95.
- Mandal, J., Fu, Y., Overvig, A.C., Jia, M., Sun, K., Shi, N.N., Zhou, H., Xiao, X., Yu, N., Yang, Y., 2018. Hierarchically porous polymer coatings for highly efficient passive daytime radiative cooling. *Science* (80- ). 362, 315–319.
- MODTRAN, 2019. URL [http://modtran.spectral.com/modtran\\_home#plot](http://modtran.spectral.com/modtran_home#plot) (accessed 4.1.19).
- Niklasson, G.A., Granqvist, C.G., Hunderi, O., 1981. Effective medium models for the optical properties of inhomogeneous materials. *Appl. Opt.* 20, 26.
- Palik, E.D., 1985. Handbook of optical constants of solids, Handbook of Optical Constants of Solids. Academic press.
- Parker, D.S., Sherwin, J.R., 2008. Evaluation of the NightCool Nocturnal Radiation Cooling Concept : in Scale Test Buildings Stage Gate 1B.
- Raman, A.P., Anoma, M.A., Zhu, L., Rephaeli, E., Fan, S., 2014. Passive radiative cooling below ambient air temperature under direct sunlight. *Nature* 515, 540–544.
- RefractiveIndex, 2019. Refractive Index. URL <https://refractiveindex.info/>
- Zhai, Y., Ma, Y., David, S.N., Zhao, D., Lou, R., Tan, G., Yang, R., Yin, X., 2017. Scalable-manufactured randomized glass-polymer hybrid metamaterial for daytime radiative cooling. *Science* (80- ). 355, 1062–1066.
- Zhao, B., Hu, M., Ao, X., Chen, N., Pei, G., 2019a. Radiative cooling: A review of fundamentals, materials, applications, and prospects. *Appl. Energy* 236, 489–513.
- Zhao, B., Hu, M., Ao, X., Chen, N., Xuan, Q., Jiao, D., Pei, G., 2019b. Performance analysis of a hybrid system combining photovoltaic and nighttime radiative cooling. *Appl. Energy* 252, 113432.
- Zhao, B., Hu, M., Ao, X., Huang, X., Ren, X., Pei, G., 2019c. Conventional photovoltaic panel for nocturnal radiative cooling and preliminary performance analysis. *Energy* 175, 677–686.
- Zhao, B., Hu, M., Ao, X., Pei, G., 2017. Conceptual development of a building-integrated photovoltaic–radiative cooling system and preliminary performance analysis in Eastern China. *Appl. Energy* 205, 626–634.
- Zhao, B., Hu, M., Ao, X., Xuan, Q., Pei, G., 2018. Comprehensive photonic approach for diurnal photovoltaic and nocturnal radiative cooling. *Sol. Energy Mater. Sol. Cells* 178, 266–272.

---

## #55: Energy and exergy analysis of a Corum sugar factory

---

Ali KILICARSLAN<sup>1</sup>, Gultekin YILDIZ<sup>2</sup>

<sup>1</sup> Hitit University-Department of Mechanical Engineering, 19030 Corum, TURKEY. alikilicarslan@hitit.edu.tr

<sup>2</sup>Corum Provincial Health Directorate, Corum, TURKEY. yildiz.gultekin@gmail.com

*In this study, it is aimed to carry out the energy and exergy analyses of the sections of turbine and refinery in Çorum Sugar Factory-Turkey, established in 1991. The analyzed units at the factory are units of where steam and electricity are generated and the units next to these units, namely, five evaporators that use the steam. In terms of the integrity of the plant, other units of the plant where sugar beet is processed are briefly mentioned. Although the technology currently used in the factory is old, it is being used most effectively. The best indicators of this situation are results of the measurements and evaluations. At the entire plant, 84% energy efficiency and 51% exergy efficiency of produced steam is obtained. According to the obtained results, the maximum percentage rate of irreversibility is 67% at the boiler and turbine section. The total irreversibility rate happens at 24% in the evaporators and the overall irreversibility percentage of factory happens as 49%. Together with the electrical energy produced by the natural gas fired steam turbine at the factory, there cycling of waste steam in other processes and the effect of it on the profitability of the factory are examined. The energy and exergy efficiency, in other words efficient usage of energy, is very important in such a large company. Large enterprises in the food sector to carry out such a study has shed light on increasing profitability and making more accurate investment.*

*Keywords: sugar plant; energy; exergy; irreversibility; electricity production*

## 1. INTRODUCTION

The sources of fossil fuels have been diminishing at an increasing rate. Therefore, the systems producing energy by using fossil fuels should be analyzed very effectively in order to increase the efficiency and decrease the losses. The first law of thermodynamics, in other words, the conservation of energy, is not enough to analyze the systems and the second law analysis of the thermal systems is also necessary in order to evaluate the systems effectively. Sugar plant that uses either sugar cane or sugar beet occupies an important place in food sector. Steam cycles, namely, Rankine cycles, are used in sugar plants to produce power and electricity.

Substances are physically stable and chemically balanced in nature. Formation of work is not possible without physical or chemical interaction against each other. Energy and exergy are emerging as a result of this interaction. According to the rules of thermodynamics, energy is a unit that can be transformed into other forms. Energy conversion, that is, transformation of an energy form into other energy forms becomes useful and utility. There is much energy transformation form, heat-electricity, kinetic-electrical, chemical-heat, electricity-heat etc. heat, etc. In these transform, the amount of energy and mass are in direct proportion and a very important measure. In a system with continuous flow, energy and exergy analyses are done as physically and chemically by using the mass balance equation for a control volume.

There are studies aiming to investigate these cycles from the first and second laws of thermodynamic point of view in the literature. Some studies are summarized below.

Energy and exergy analysis of a sugar factory in India, having a capacity of 5000 tons crushed per day, were carried out and the available evaporators are modified in order to decrease the mass flow rate of steam. It was claimed that the steam consumption and exergy losses were decreased by 9 T/h and 48 %, respectively. It was also mentioned that the optimum superheat temperature of the backpressure turbine including single extraction was 600 °C (Ram and Banerjee, 2003). Exergy and energy analysis of a cogeneration power plant of a sugar factory employing backpressure and extraction condensing steam turbine was carried out in terms of steam inlet pressure. The effect of steam inlet pressure on the energy and exergy efficiencies and exergy loss was observed and compared for both backpressure steam turbine cogeneration plant and condensing steam turbine cogeneration plant. It was resulted that the backpressure steam turbine cogeneration plant, an energy efficiency of 0.863 and energy efficiency of 0.307, is more efficient than the condensing steam turbine cogeneration plant (Kamate and Gangavati, 2009). Energy and exergy analyses of a sugar factory in Turkey were carried out and the optimization of these analyses was also performed. Different scenarios were employed in order to find the optimum values of energy and exergy efficiencies and the optimum values were to be found 48.7% for energy efficiency and 31.7% for exergy efficiency (Taner and Sivrioglu, 2015). Energy, exergy and thermo-economic analyses of a sugar factory located in Turkey were carried out by using the real data with respect to the three scenarios. It was found that the power generated by the power plant was increased while the simple repayment period was decreased by applying the third scenario when it is compared to the current situation. It was resulted that the power, simple repayment period and unit exergy cost of the power plant were 14 MW, 4.32 years and 3.142 \$ / kW, respectively (Taner and Sivrioglu, 2015). Exergy analysis of a sugar factory having a capacity of 250 ton per hour sugar mill was carried out by using Aspen Plus simulation program. It was observed that the exergy destruction and second law efficiency of the factory is 217.3MJ per ton of cane crushed and 9.7%, respectively. It was also found that the maximum exergy destruction occurred in the evaporation unit (Dogbe et al., 2018). From the aspects of the first and second law of thermodynamics, the cogeneration thermal power plant in India was analyzed to investigate the parameters of the energy and exergy efficiencies, energy loss and exergy destruction and the effect of the moisture content of bagasse on these parameters was also observed. It was observed that the maximum energy loss and exergy destruction occurred in the boiler furnace using the bagasse moisture content of 50 % as fuel 23.021 % and 68.219 %, respectively. It was also observed that the energy and exergy efficiencies of cogeneration power plant would be increased 3.66 % by energy and 3.02 % by exergy in case of decreasing the bagasse moisture content from 50 % to 0 % (Sing, 2019). The effect of eight operating parameters including imbibition water, syrup DS concentration, recycling in A-pan, B-pan or C-pan, massecuite temperature in A, B or C on the defined energy indicators was observed by means of a MATLAB simulation code in a sugar factory using sugar cane as a raw material. It was observed that the parameters, namely, the elevated imbibition water use and A-massecuite recycling had a more dominant than others, approximately 79% on the overall steam used (Mkwananzi et al., 2019).

Most of the studies in the literature, the energy and exergy analyses of the sugar plants that use sugar cane as a raw material were carried out, but the sugar beet is used as a raw material in the sugar plant in this study. The energy and exergy analyses are extensively carried out. The cycle and Grassmann diagrams are also presented in detail in this study.

## 2. THERMODYNAMIC ANALYSIS

In order to understand the system, it is necessary to see all stages both visually and schematically. To see stages explained above and illustrated with pictures, schematic representation is given in Figure 1. In fact, there are also more complex process than this schematic, where only the steam and energy related parts are discussed. The parts described above for sugar production are given in this schematic. In the following, for the thermodynamic analysis, the boiler, turbine section and evaporators are considered separately. In total, 5 continuous flow control volumes were regulated and analyzed by calculating the energy, exergy and irreversibility of a volume. In addition, in accordance with the rules of thermodynamic the efficiencies were calculated.

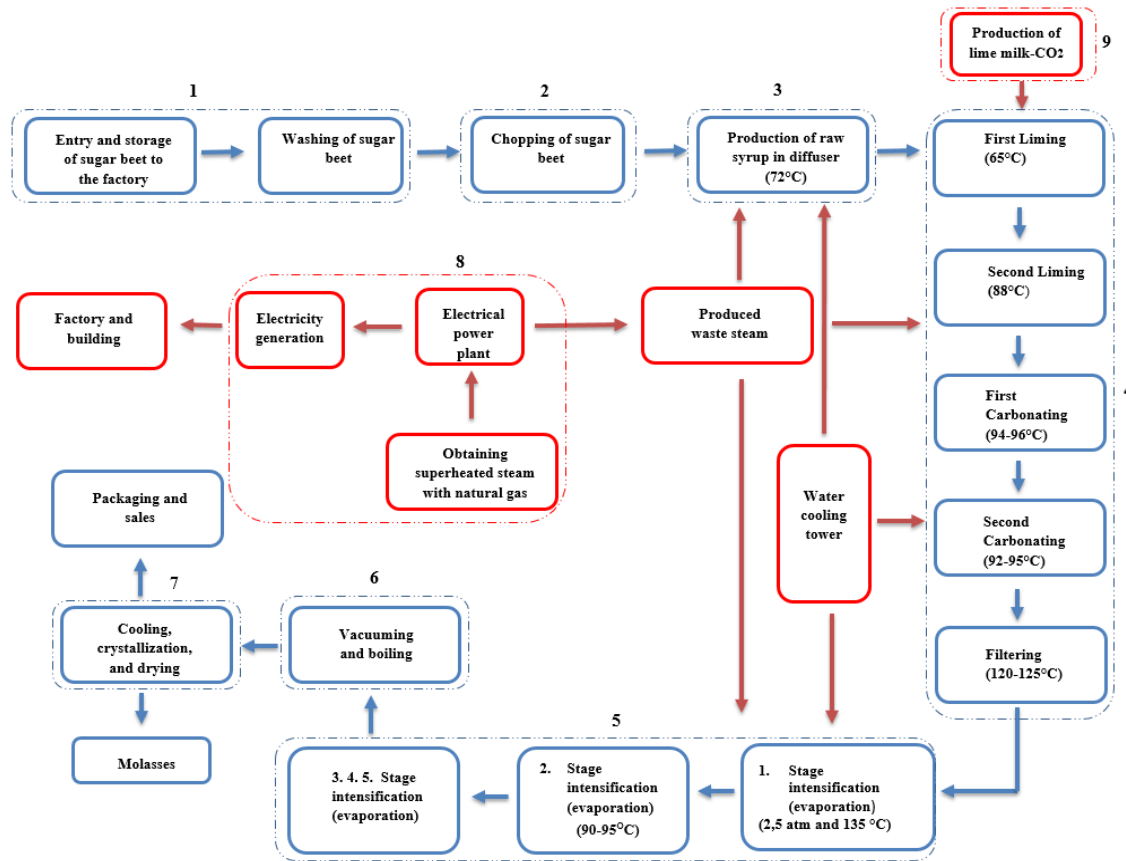


Figure 1: Schematics of sugar factory processes

### 2.1. Energy analysis

In order to perform energy analysis, the mass flow rates at the inlets and outlets of the control volumes should be determined. Mass balance for a control volume can be written as (Çengel ve Boles, 2013):

$$\text{Equation 1: } \frac{dm_{CV}}{dt} = \sum \dot{m}_i - \sum \dot{m}_o$$

Where:

- $\frac{dm_{CV}}{dt}$  = change of mass with respect to the time within a control volume,
- $\dot{m}_i$  = mass flow rate of the fluid entering the control volume and
- $\dot{m}_o$  = mass flow rate of the fluid exiting the control volume.

It is necessary to determine the energy inputs and outputs and to divide them into sections. The mass flow rate, temperature and pressure data at the inlets and outlets of these sections should be obtained. By neglecting the kinetic and potential energies, the energy equation for a control volume can be expressed as:

$$\text{Equation 2: } \frac{dE_{CV}}{dt} = \sum \dot{m}_i h_i - \sum \dot{m}_e h_e + \dot{Q}_{CV} - \dot{W}_{CV}$$

Where:

- $\frac{dE_{KH}}{dt}$  = change of energy with respect to the time within a control volume
- $h_i$  = enthalpy of the fluid at the control volume inlet
- $h_e$  = enthalpy of the fluid at the control volume outlet
- $\dot{Q}_{CV}$  = heat transfer rate to the control volume
- $\dot{W}_{CV}$  = power done by a control volume.

The control volume consists of two parts. First, the boiler and turbine section where the first energy is produced, the other is the factory and the refinery part where the beet is chopped, the syrup is produced and the refined and the crystal sugar is produced. According to the conservation law of energy which is the 1st law of thermodynamics, it is necessary that ensuring balance of inlet and outlet mass. The steam cycle of the factory and refinery is shown schematically in Figure 1. Accordingly, in order to be able to perform thermodynamic analysis, the stages shown in Figure should be analyzed in sections by dividing them into control volumes. According to this:

1. Control Volume: the volume of the Boiler and turbine section (Figure 2),
2. Control Volume: 1A and 1B first evaporator and connected units (Figure 3),
3. Control Volume: 2A and 2B second evaporator and connected units (Figure 4),
4. Control Volume: 3A and 3B third evaporator and connected units (Figure 5),
5. Control Volume: fourth and fifth evaporators and connected units (Figure 6).

As a result, five control volumes were formed.

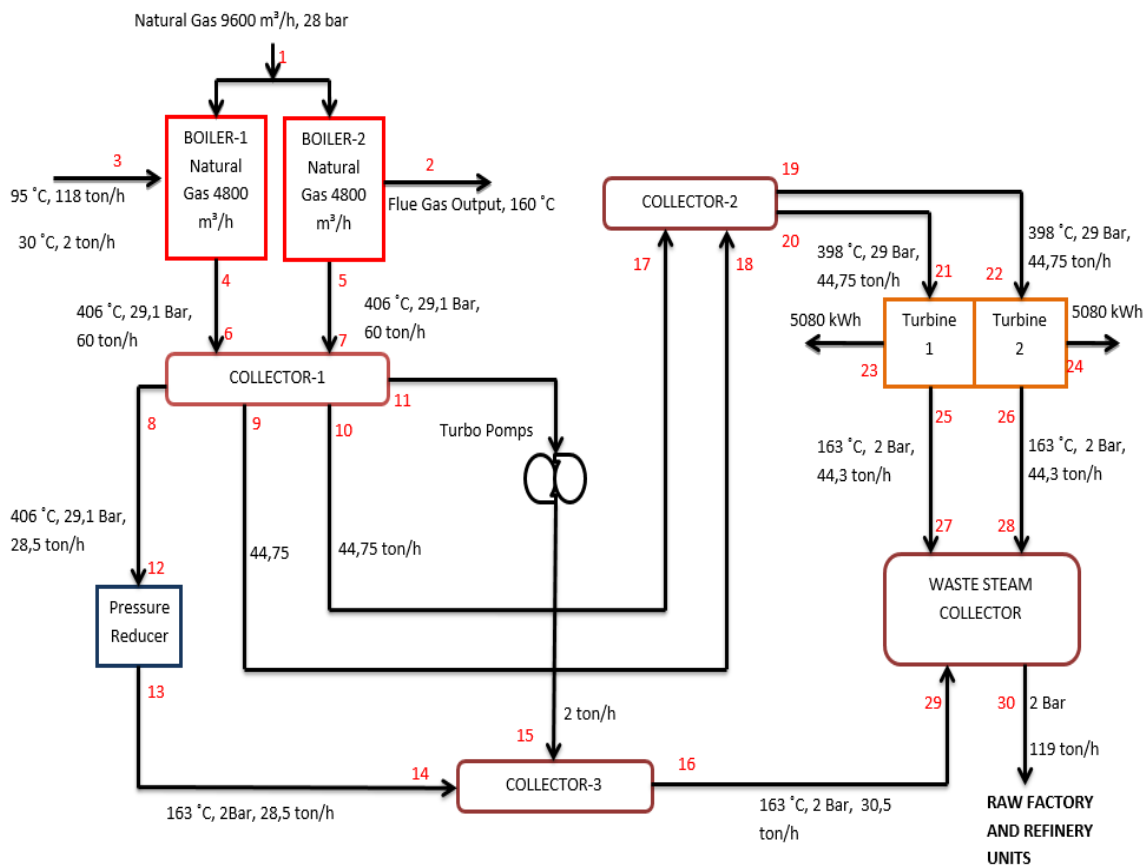


Figure 2: The distribution of the steam boiler and turbine section

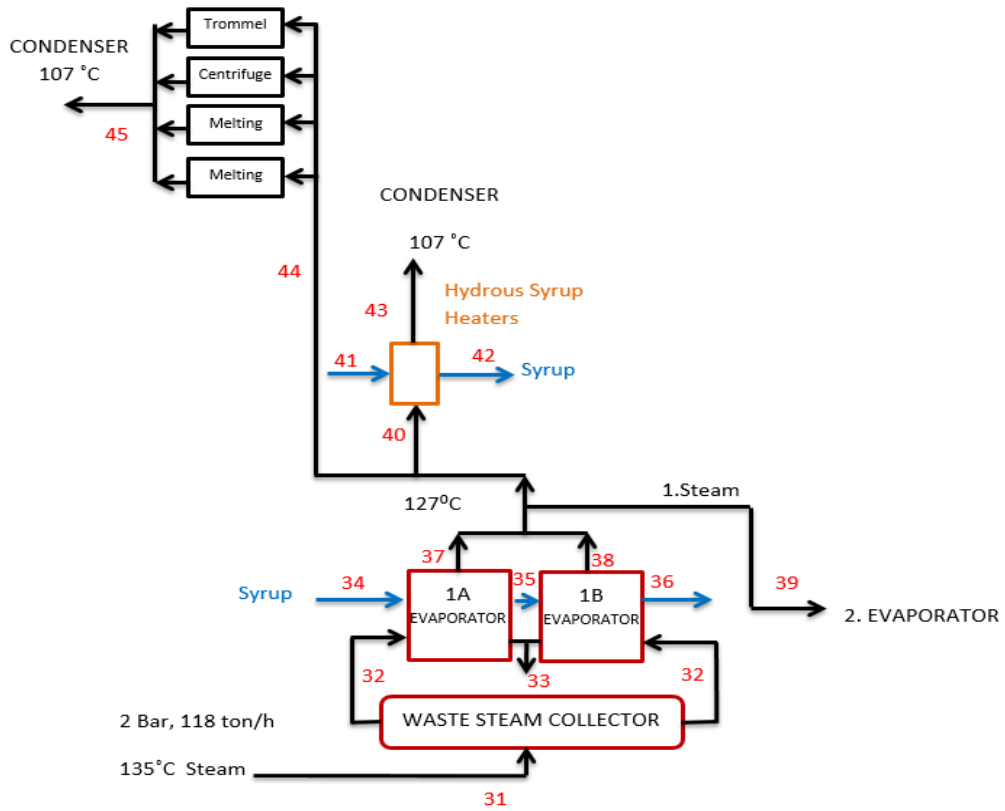


Figure 3: First evaporator steam distribution

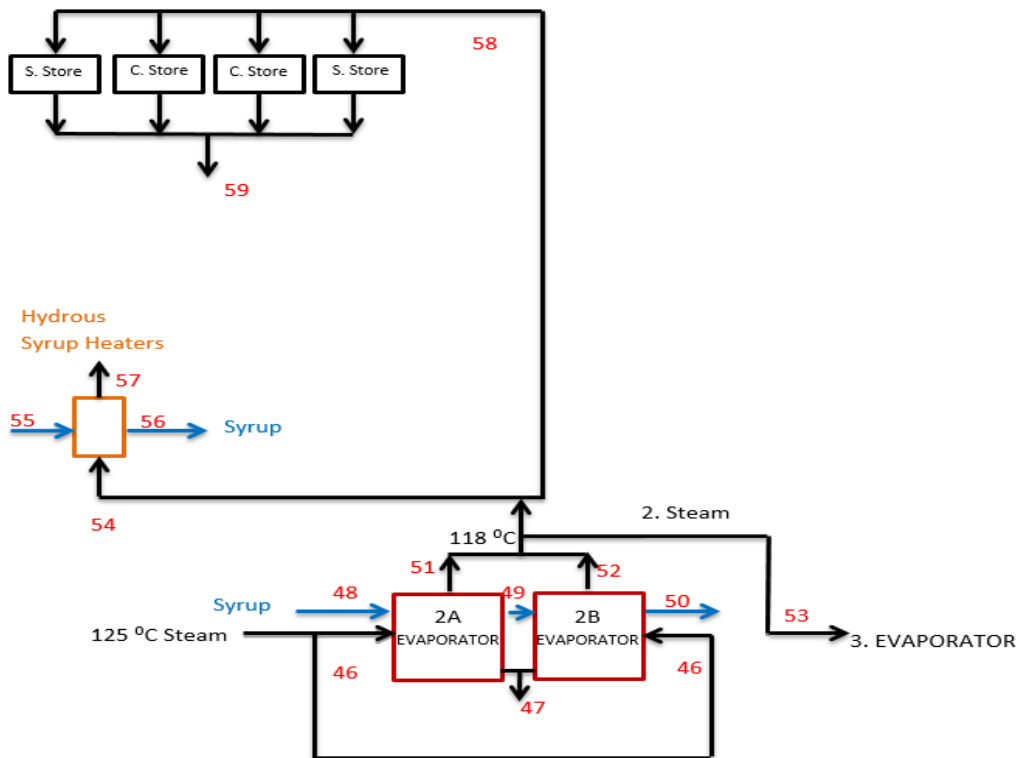


Figure 4: Second evaporator steam distribution

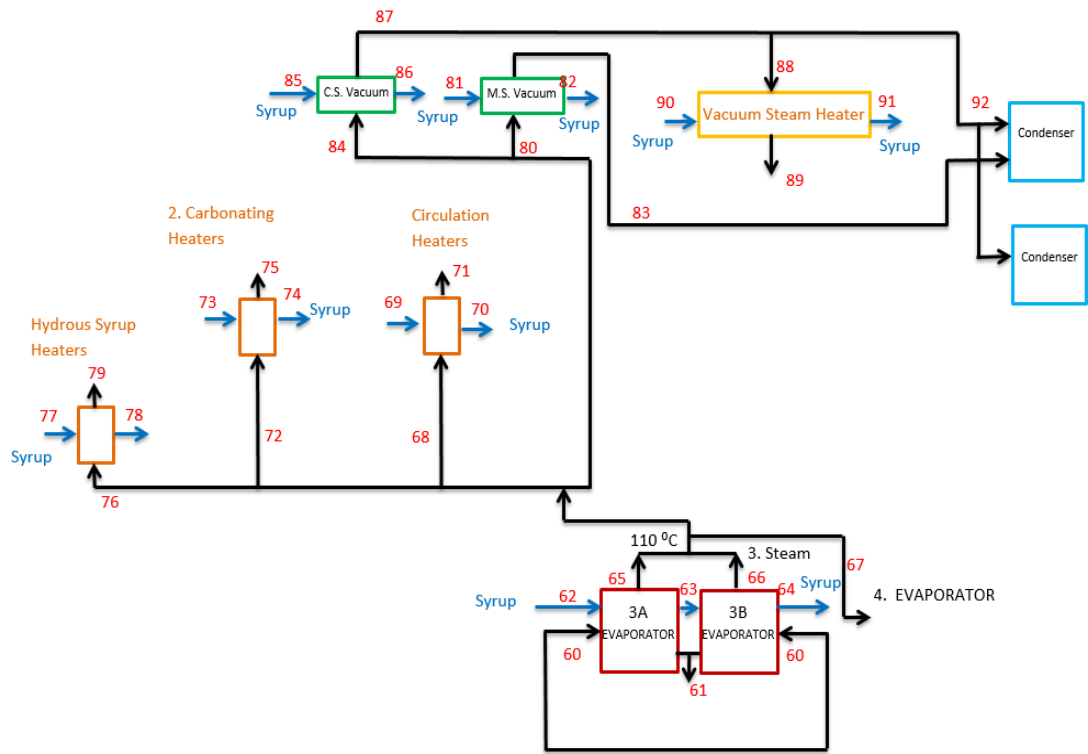


Figure 5: Third evaporator steam distribution

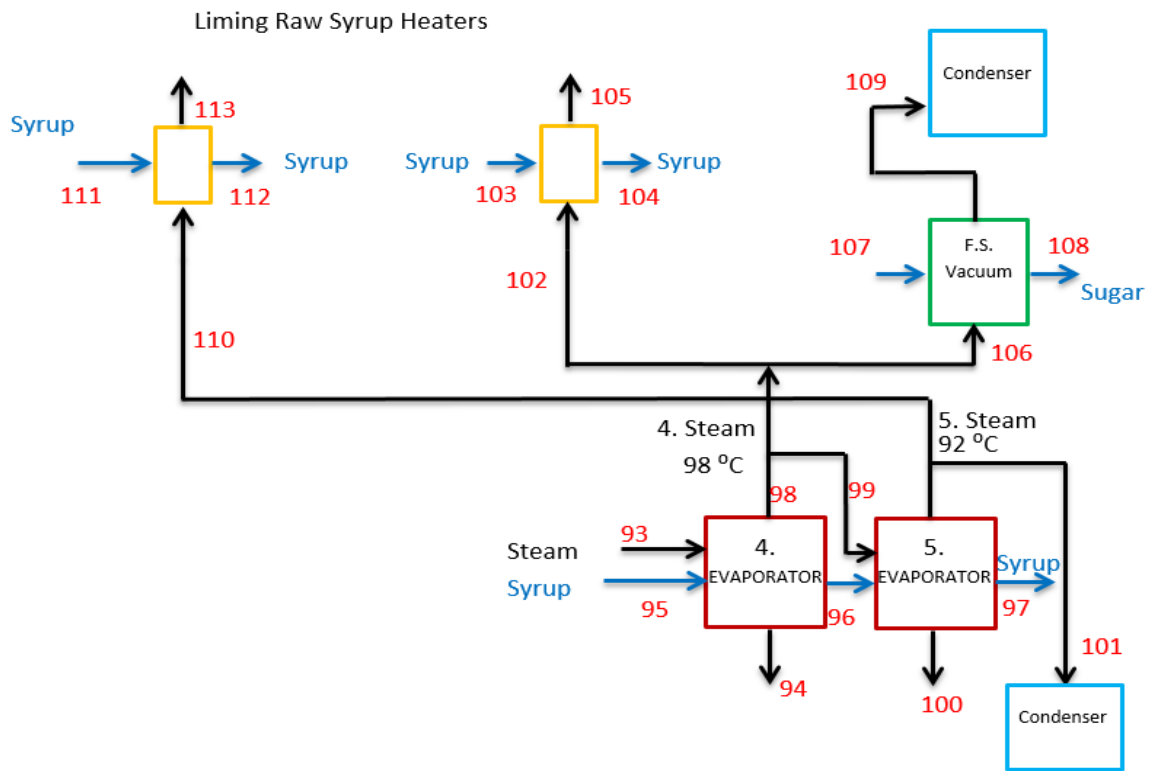


Figure 6: Fourth and fifth evaporators steam distribution



## 2.2. Exergy analysis

As previously stated, the expression of exergy is evaluated within the scope of the second law of Thermodynamics. More efficient use of energy resources can only be explained by the understanding of exergy. To calculate exergy, some parameters need to be known. For example, "dead state" expresses the balance of the system or matter with the environment. Therefore, pressure and temperature of the environment; pressure and temperature of the system, speed, and environment-based values such as height values need to be known. In the second law of thermodynamics, the equations of entropy balance and exergy balance should be considered together.

The entropy balance for a control volume can be written as (Borgnakke, 2009),

$$\text{Equation 3:} \quad \frac{dS_{CV}}{dt} = \sum_i \dot{m}_i s_i - \sum_e \dot{m}_e s_e + \sum_j \frac{\dot{Q}_{CV}}{T} + \dot{S}_{gen,j}$$

Where:

- $\dot{S}_{gen}$  = total entropy generated per unit time
- $\frac{dS_{CV}}{dt}$  = change of entropy per unit time entropy within the control volume
- $\frac{\dot{Q}_{CV}}{T}$  = entropy transfer caused by the heat transfer at the surrounding boundary
- $s$  = specific entropy of the fluid at the inlet or outlet conditions.

Exergy balance for a control volume can be written as (Moran, 2004).

$$\text{Equation 4:} \quad \frac{dE_{x,CV}}{dt} = \sum_i \dot{m}_i e_x - \sum_e \dot{m}_e e_x + \sum \left(1 - \frac{T_0}{T_j}\right) \dot{Q}_{CV} - \left(\dot{W}_{CV} - P_0 \frac{dV_{CV}}{dt}\right) - \dot{I}$$

Where:

- $\dot{I}$  = irreversibility rate
- $\frac{dE_{x,CV}}{dt}$  = change of exergy per unit time within the control volume
- $\frac{dV_{CV}}{dt}$  = change of volume with respect to time within the control volume
- $P_0$  = pressure of the fluid at environment air conditions
- $T_0$  = temperature of the fluid at environment air conditions
- $e_x$  = specific flow exergy of the fluid at the inlet or outlet conditions.

In case of neglecting the kinetic and potential exergies, the flow exergy  $e_x$  can be written as:

$$\text{Equation 5:} \quad e_x = (h - h_0) - T_0(s - s_0)$$

According to the Guy Stodola Theorem, irreversibility rate  $\dot{I}$  can be expressed as (Bejan, 1996):

$$\text{Equation 6:} \quad \dot{I} = T_0 \dot{S}_{gen}$$

Where:

- $h_0$  = enthalpy at environment air conditions
- $s_0$  = entropy at environment air conditions.

Depending on these values, physical, potential and kinetic exergy values of the system are calculated. In addition, molar and standard chemical exergy should be calculated according to the proportion of pure substances forming the components of the substance. Molar chemical exergy of a gas  $e_{kim}^e$  can be expressed as (Moran, 2004),

$$\text{Equation 7:} \quad e_{kim}^e = \sum y_i e_i + \bar{R} T_0 \sum y_i \ln y_i$$

Where  $e_i$  is the standard chemical exergy of a gas,  $y_i$  is the molar ratio of gas in a gas mixture and  $\bar{R}$  is the universal gas constant.

The sum of all the exergies found constitutes the total exergy of the system or substance. In some cases, the potential and kinetic exergy may be negligible because they are too small amount and in the same way the amount of other exergy may be neglected.

In this system, the temperature of the steam obtained in each stage evaporator decreases and the dry matter ratio of raw syrup increases. At the factory, steam is produced at different pressure and temperature to be used in all units working with steam energy. In the evaporators, the syrup transition process, the heat transfer area and the heat transmission coefficients are of great importance here in terms of efficiency.

### 3. RESULTS AND DISCUSSION

The real data was collected from a sugar factory operating in Corum, Turkey and then it was evaluated by using the main equations described above. The results are represented in the forms of Grassman diagrams and tables in the following sections.

Figure 7 shows the Grassman diagram of boiler and turbine section. As it is depicted in Figure 7, the rate of irreversibility is very high, about 65% as it is compared to the exergy output. This is due to the fact that the chemical exergy is predominant in the natural gas components, and that a large part of the irreversibilities exist in the combustion section. In all works, the same situation exists in natural gas and power plants. In addition, although the heat from the chimney is evaluated in addition to the heat obtained from the two phases, the efficiency remains below 50%. In fact, although electricity production with natural gas is not a very efficient production method, it is a very common method.

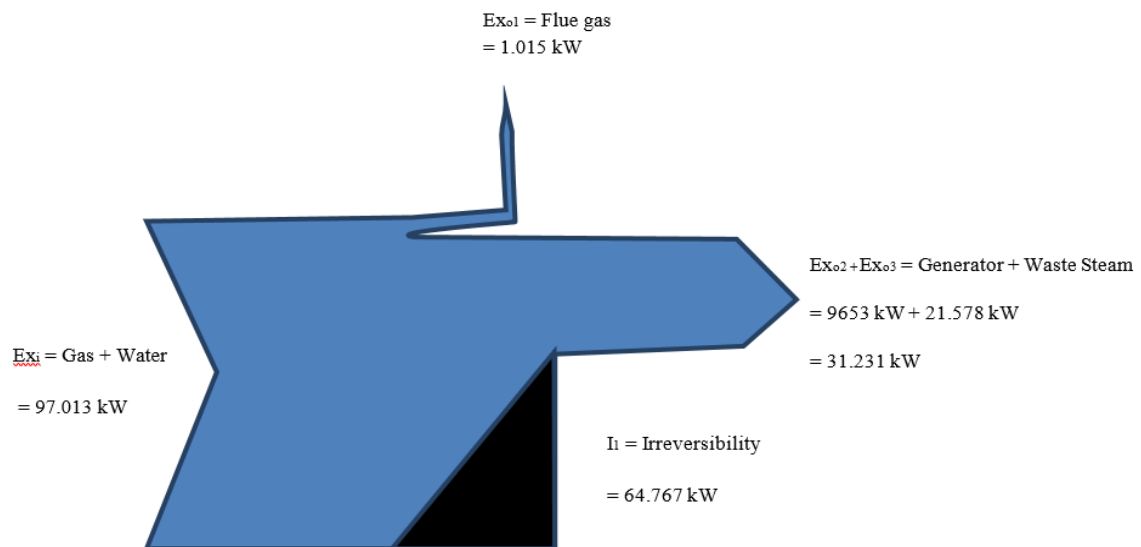


Figure 7: Boiler and turbine section exergy Grassmann diagram

Figure 8 depicts the Grassmann diagram of first evaporator. At the inlet of the evaporator, the mixture of steam and syrup exists. At the exit of the evaporator, the mixture of steam and syrup exists but some of water in the mixture is separated from the mixture by means of evaporation. The amount of irreversibility is very low as it is compared to the exergy output. As it is shown in Figure 8, the irreversibility rate is 3508 kW while the exergy output including syrup and steam is 20308 kW. At the first stage of evaporation, the exergy of the saturated vapor, approximately 10 % of the exergy output, is 2344 kW.

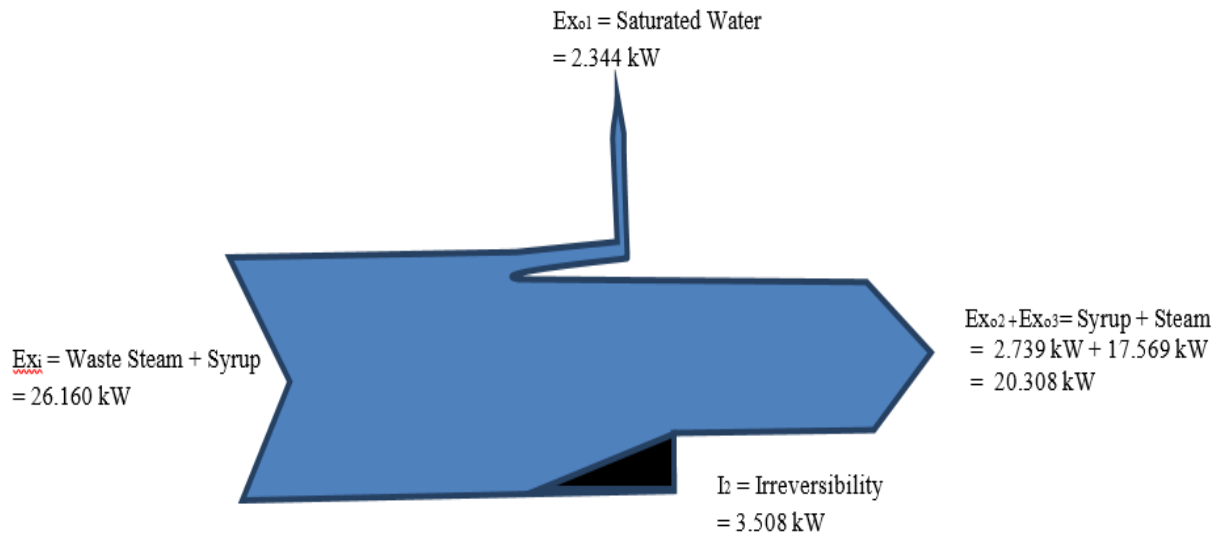


Figure 8: First evaporator exergy Grassmann diagram

Figure 9 shows the Grassmann diagram of second evaporator. Like first evaporator, the inlet and outlet of the second evaporator include the same mixture such as syrup and steam. As it depicted in Figure 8, the irreversibility rate is 9084 kW and it is much more than the one in the first evaporator. The ratio of irreversibility rate to the input exergy for the second evaporator is 38.12% while the ratio for the first evaporator is 13.40%. The exergy of the saturated vapor at the exit of the second evaporator is less than the one at the exit of the first evaporator.

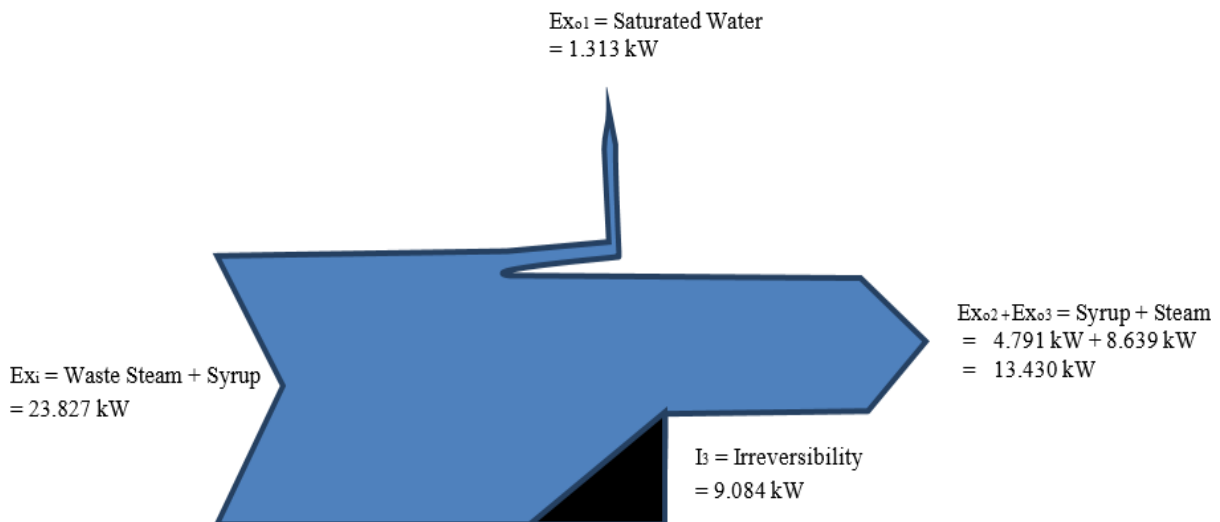


Figure 9: Second evaporator exergy Grassmann diagram

The Grassmann diagram of third evaporator is shown in Figure 10. As it is shown from Figure 10, some sugar exists in addition to the syrup and steam. The exergy of the sugar can be ignored as it is compared to the exergies of the syrup and steam. The irreversibility in the third evaporator is less than the one in the second evaporator, but it is more than the in the first evaporator. The ratio of exergy of the steam to the syrup during the first stage of the evaporation in the product is 6.41 and the ratio during the second stage of the evaporation in the product is 1.8. The ratio continues to decrease and it becomes 0.15 at the third evaporator.

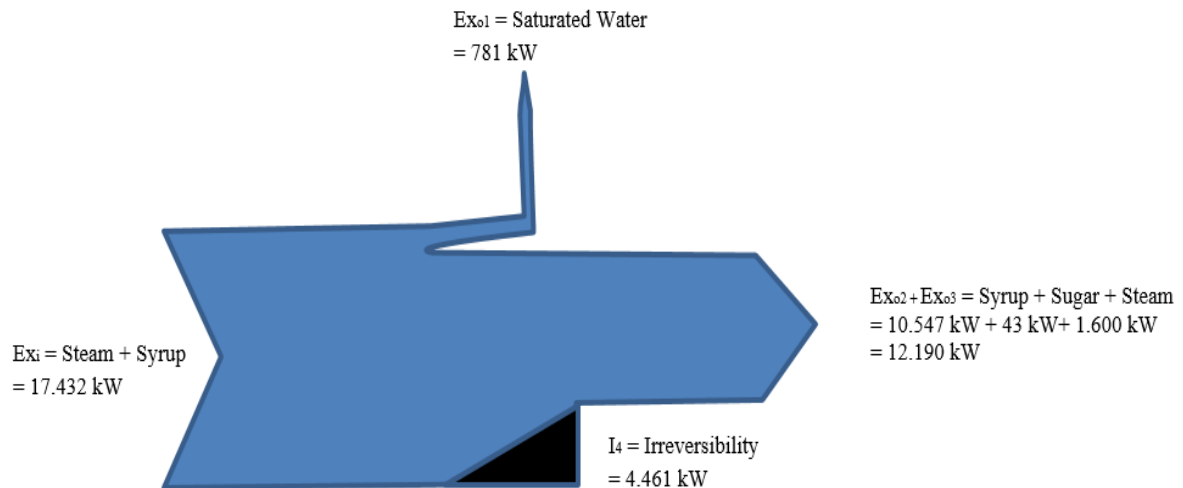


Figure 10: Third evaporator exergy Grassmann diagram

The last stage of the evaporation occurs at the fourth and fifth evaporators and the Grassmann diagram of this stage is depicted in Figure 11. There is no steam any more in the products. The last product is syrup and molasses. Molasses, refining from sugar beet, including 45% and 50% sugar. The exergies, including the inlet and outlet, at the last stage are very low because the most of the exergies were consumed during previous evaporation stages. The ratio of irreversibility rate to the input exergy for the second evaporator is 19.25%. The ratio of exergy of saturated water to the total exergy at the outlet of the evaporation process is 11.5 % for the first evaporator, 9.77 for the second one, 6.4 for the third one and 8.1 for the last one. This ratio normally decreases as the number of evaporation process increases, but the ratio of last stage of evaporation is higher than the third stage. This is because of converting to the saturated water at the last stage.

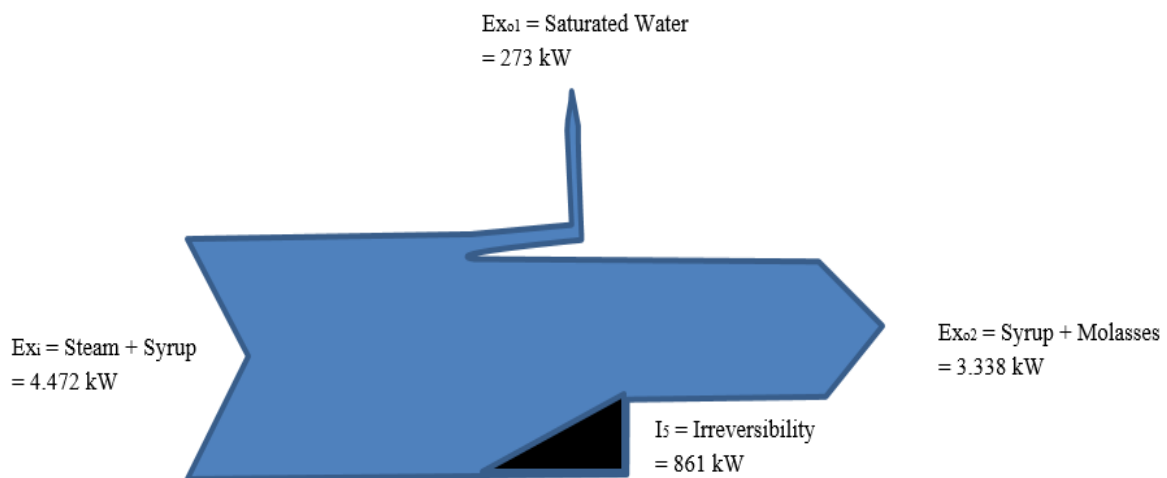


Figure 11: Fourth and fifth evaporators exergy Grassmann diagram

Table 1 shows the exergies at the inlet and outlet of the elements including boiler, turbines and evaporators. In addition to these, it also shows the irreversibilities of the elements and the ratio of the irreversibility of the elements to the total irreversibility. As it is seen from Table 1, the maximum amount of irreversibilities, the irreversibility ratio about 78%, occur in the turbine and boiler section this is because of inefficient combustion and sudden expansion in turbine. The minimum irreversibility ratio, around 1%, occurs in the fourth and third evaporators. The reason for this, the heat transfer at a finite temperature difference decreases too much as it is compared to the other evaporators. The irreversibility ratio difference between the first evaporator and third evaporator is very low.

Table 1: Exergy Quantities and Irreversibility Rates

	Exergy Inlet	Exergy Outlet	Irreversibility	Irreversibility Ratio
Boiler and Turbine	99.887	35.270	64.617	78,794
First Evaporator	26.160	22.652	3.508	4,250
Second Evaporator	23.827	14.742	9.084	11,006
Third Evaporator	17.432	12.971	4.461	5,405
Fourth and Third Evaporators	4.472	3.611	861	1,043
Total Amount	168.904	86.222	82.531	100

#### 4. CONCLUSION

Through this study, the exergies and irreversibilities of all stages in turbine and refinery systems was determined. The most used parts of the steam energy or places where heat loss are highest is determined and according to that alternative studies can be done. Exergy efficiency is always lower than the energy efficiency value. The reason for this, at the analysis of the efficiency according to the first law, irreversibility and quality of energy are not taken into account. Where the irreversibility value is high, there are places where finite temperature differences are high. The boiler feed water is not preheated. If the boiler feed water is preheated with flue gas, the exergy efficiency would increase. Turbine and boiler section which has the highest irreversibility, significantly reduces the overall efficiency of the plant. Here, the reason why exergy loss is more than energy loss is that there are more irregularities such as chemical energy at combustion, heat energy and internal energy. The irreversibility ratio of the first and 3rd evaporators are close to each other and the 2nd evaporator irreversibility ratio are higher than the other evaporators. The reason for this is that the vapor produced in the 2nd evaporator is not used very much and the heat losses are high. At the 4th and 5th evaporators, efficiency is low due to make operation at low temperature and low pressure and because of being end-use place of steam.

In the repair and maintenance works carried out every year, parts of the campaign season, which are damaged by excessive heat and cause an increase in heat loss, are renewed. It is necessary to select the most suitable material taking into account costs for this renewal. In all cases there will be efforts to improve. The things to do for this sugar factory may be listed as follows:

- By taking advantage of technological developments, the factory should revise and by taking into account costs, the technical specifications of the materials to be used in maintenance should be determined in the figure, which is best suited to the purpose.
- In heat exchangers used in evaporators, it will be appropriate to use waste vapor less but at high temperatures by increasing the heat flow.
- Optimum amount of steam and electricity should be produced daily during the campaign time in accordance with automation system.
- Recycling of heat from flue gas can be achieved. For example, heating the boiler inlet water or pre-heating the incoming natural gas.

## 5. REFERENCES

Bejan A., 1996, Entropy Generation Minimization, CRC Press.

Borgnakke C., Sonntag R.E., 2009, Fundamentals of Thermodynamics, Seventh Edition. Wiley.

Çengel Y., Boles M. A., 2013, Thermodynamics: An Engineering Approach, Seventh Edition, McGraw Hill.

Dogbe, E.S., Mandegari, M.A., Görgens, J.F., 2018. Exergetic diagnosis and performance analysis of a typical sugar mill based on Aspen Plus® simulation of the process. *Energy*, 145, 614-625.

Kamate, S.C., Gangavati, P.B., 2009. Exergy analysis of cogeneration power plants in sugar industries. *Applied Thermal Engineering*, 29, 1187–1194.

Mkwananzi, T., Mandegari, M., Görgens, J.F., 2019. Disturbance modelling through steady-state value deviations: The determination of suitable energy indicators and parameters for energy consumption monitoring in a typical sugar mill. *Energy* 176, 211-223.

Moran, Micheal J., Shapiro, Howard N., 2004, Fundamentals of Engineering Thermodynamics, 5. Edition, Wiley, p. 659

Ram, J.R., Banerjee, R., 2003. Energy and cogeneration targeting for a sugar factory. *Applied Thermal Engineering*, 23, 1567–1575.

Taner, T., Sivrioglu, M., 2015. Energy exergy analysis and optimization of a model sugar factory in Turkey. *Energy*, 93, 641-654.

Taner, T., Sivrioglu, M., 2017. A techno-economic & cost analysis of a turbine power plant: A case study for sugar plant. *Renewable and Sustainable Energy Reviews*, 78, 722–730.

---

## #59: Liquid flooded Ericsson cycle heat pump and heat engine system

---

Chris BENSON

*University of Nottingham, Department of Architecture and the Built Environment  
Chris.Benson@Nottingham.ac.uk*

*The Ericsson cycle modified with a novel implementation of the liquid flooding concept is presented. With liquid flooding, the effective surface area of the compression and expansion processes is greatly increased, allowing near isothermal processes, allowing the ideal, reversible system to approach Carnot efficiency. Modelling was conducted using an EES and Modelica based model. The system is improvement on early proposed Ericsson liquid flooded cycle arrangements shows marked improvements in the non-ideal case of irreversible components and other system losses. Modelled systems include Ericsson heat pumps and heat engines for possible application to domestic applications such as hot water heating, refrigeration, and mCHP/mCSP type devices.*

*Keywords: heat pump; heat engine; Ericsson cycle; liquid flooding; mCHP; mCSP; waste heat*

## 1. INTRODUCTION

With the rapidly increasing threat posed by global warming and climate change, there is a growing interest in clean and efficient energy sources such as solar and wind power generation. While these will become major sources of power, efficient use of this power is paramount. Buildings account for 36% of global energy use and 39% of carbon emissions, of which space heating accounts for 30%. (UN Report 2017). While electric heating may allow use of solely green sourced electrical energy, a much more efficient method to create heat is through the use of heat pumps, where the heat of even low temperature ambient air or other source is upgraded, creating 2-4 times the amount of heat with the same electricity of a purely electric heating system. While heat pumps are highly efficient for upgrading heat, the majority use working fluids of HFCs with 2000-4000 the global warming potential as CO<sub>2</sub>. By treaty these fluids must be eliminated, yet few satisfactory alternatives exist. The immediate need of high efficiency, HFC free heat pumps system is paramount.

## 2. ERICSSON CYCLE

The Ericsson external heat engine is a closed cycle system that, in the ideal form, achieves Carnot efficiency, the highest possible between two heat sinks. The cycle consists of the following segments: Isothermal compression, isobaric heat addition, isothermal expansion, and isobaric heat rejection. The working fluid of the cycles can be Helium, Hydrogen, Nitrogen, or even air; it does not require HFCs. The isothermal compression and expansion segments require the fluid to take in or expel heat, normally through the chamber walls. The isobaric heat addition and rejection is normally in the form of a counter flow heat exchanger, allowing the cycle to recuperate the heat energy of the cycle. Importantly, the volume of a well-insulated counter flow heat exchanger or 'recuperator' does not affect the cycle performance, allowing a large recuperator, which is a significant advantage, unlike the Stirling cycle, which is commonly associated with the Ericsson cycle. While the Ericsson heat engine cycle creates a shaft power output, run in the reverse thermodynamic direction, shaft power can drive the system to create a heat pump and mechanically move heat in the opposite direction as the natural flow of heat. This Ericsson cycle heat pump also, in the ideal form, achieves Carnot efficiency, the highest possible for a heat pump.

As with all gas cycles, the mechanical implementation of the ideal cycle presents significant engineering challenges. While the recuperator is a counter-flow heat exchanger with commercial versions achieving >95% effectiveness, isothermal compression and expansion of the working fluid is not possible in mechanical systems due to the limited surface area for conduction and limited time of the process. Additionally, as with all gas cycles, the Ericsson cycle is extremely sensitive to the efficiencies of the compressor and expander (Lemort, 2008).

## 3. LIQUID FLOODED ERICSSON CYCLE SYSTEMS

Compression and expansion segments of the ideal Ericsson cycle are isothermal yet in practice are more adiabatic, forming a quasi-isothermal segment at best. This is due to non-infinite time of the segment and insufficient heat exchange of the working fluid to the chamber and ambient. Many expander and compressor designs have been explored in attempts to create chambers with sufficient conduction surface, yet with increase in surface area, there is the corresponding increase in seal length, and thus friction (Igobo, 2014). The efficiency gains of approaching isothermal segments is countered by the increase in seal friction, making the concept of very large surface areas at best very challenging and cost prohibitive for any commercially viable system.

An alternative method to approach isothermal compression and expansion is through the use of liquid flooding of the volumetric chambers. While it is somewhat common to inject 1-5% by mass of liquid into compressors and expanders to increase sealing effectiveness, it is also known that by increasing the flooding, that is the relative ratio of liquid to gas mass, compressor work can be minimized as the compression becomes more isothermal. To optimize the concept to approach isothermal segments, the liquid heat capacity needs to be significantly higher than the gas. During the segments, depending on the liquid-gas ratio, the gas approaches isothermal compression or expansion as the heat energy is exchanged with the incompressible liquid. The liquid is chosen to remain liquid throughout the cycle process. In effect, liquid flooding increases the heat exchange surface area to the gas, allowing isothermal segments and large system efficiency gains.

The concept of liquid flooding applied to the compressor and expander of an Ericsson cycle was explored by Hugenroth (Hugenroth, 2006) to overcome the substantial difficulties of achieving isothermal segments. While the development concentrated on a small heat pump system using paired scroll compressor and expanders as a small refrigeration unit, the theoretical work of the Liquid Flooded Ericsson Cycle (LFEC) developed applies to and Ericsson heat engine as well.



### 3.1. Theoretical LFEC modelling

An analytic model was developed from the original work of Hugenroth for the compression and expansion volume with gas-liquid fluid mixture within. Standard thermodynamic relations are used to determine the resultant power and temperature changes of the fluid during compression and expansion. The compression chamber is considered a rigid, sealed container with heat added or removed to the fluid in accordance with the first law of thermodynamics. Nitrogen, the working fluid of the modelling presented, is modelled as an ideal gas. The equations below apply to both compression and expansion with negative work for compression and positive work for expansion, consistent with the convention adopted here that all energy flows into a control volume are positive and all energy flows out are negative.

Starting with the energy of the gas and liquid in the volumetric chamber, Equation 1. By definition, Equation 2 follows, and thus, Equation 3.

$$\text{Equation 1:} \quad \delta Q = dU = du_g m_g + du_l m_l$$

$$\text{Equation 2:} \quad du = dT c_v$$

$$\text{Equation 3:} \quad dU = m_g c_{v,g} dT + m_l c_l dT$$

Where:

- $U$  = internal energy
- $M$  = mass (g: gas, l: liquid)
- $T$  = temperature
- $c_v$  = constant volume heat capacity
- $c_l$  = heat capacity of liquid (treated as incompressible)

Rearranging gives Equation 4, where  $C_{v,f}$  is the effective constant volume specific heat and is the average specific heat of the fluid mix weighted by the respective masses. The same approach is used to give  $C_{p,f}$ , the effective constant pressure specific heat, Equation 5. These can be combined as the ratio of specific heat of an ideal gas, to give the isentropic exponent of the combined liquid and gas in the volumetric chamber, Equation 6., that is Equation 5 divided by Equation 4. From this, it can be seen that an ideal gas with a constant specific heat ratio of  $k$  that is undergoing a compression or expansion process in thermal equilibrium with an incompressible liquid having a constant specific heat behaves exactly like an ideal gas having a constant specific heat equal to  $k^*$ .

$$\text{Equation 4:} \quad c_{v,f} = \frac{m_g c_{v,g} + c_l m_l}{m_g}$$

$$\text{Equation 5:} \quad c_{p,f} = \frac{m_g c_{p,g} + c_l m_l}{m_g}$$

$$\text{Equation 6:} \quad k_f = \frac{m_g c_{p,g} + c_l m_l}{m_g c_{v,g} + c_l m_l}$$

With the theoretical development above, the LFEC can be modelled in the same method as a cycle with ideal gas. To observe the effect of liquid the dimensionless term, Capacitance Rate Ratio is introduced as Equation 7. In this, the ratio of liquid to gas capacitance is weighted by the mass flow of each. Equation 8 is the relative ratio of fluid temperatures during compression.

$$\text{Equation 7:} \quad \gamma_{CR} = \text{Capacitance Rate Ratio} \equiv \frac{\dot{m}_l c_l}{m_g c_{p,g}}$$

$$\text{Equation 8:} \quad \frac{T_2}{T_1} = \left( \frac{P_2}{P_1} \right)^{\frac{k_f - 1}{k_f}}$$

Where:

- $T_1$  = inlet temperature
- $T_2$  = outlet temperature
- $P_1$  = start pressure
- $P_2$  = end pressure

#### 4. LIQUID FLOODING

Nitrogen was chosen for the working fluid (gas) of the Ericsson cycle, both as a heat engine and heat pump. In modelling, this was treated as an ideal gas. Duratherm LT was chosen as the liquid flooding fluid for both heat pump and lower temperature heat engine applications. Fluid properties are detailed in Table 1. The Duratherm LT fluid model was developed from the manufacturer's tabular data by linear regression, creating polynomials for use in the EES models. Duratherm LT is suitable for applications from -29C to 315C. Other liquids may be used as research continues.

Table 1: Gas and liquid properties

Fluid	Density [ kg/m <sup>3</sup> ]	Heat Capacity [ J/kgK ]
Nitrogen	1.16	1040
Duratherm LT	811.18	2139

Temperature: 300K, Pressure: 1 bar

The mass of the respective gas and liquid (left) with the Capacitance Rate Ratio (right) as a function of mass ratio is shown in Figure 1. An Ericsson heat engine model shows Capacitance Rate Ratios of the compressor (5C) and expander (300C) are different due to the heat capacity of both the liquid and gas being a function of pressure and temperature.

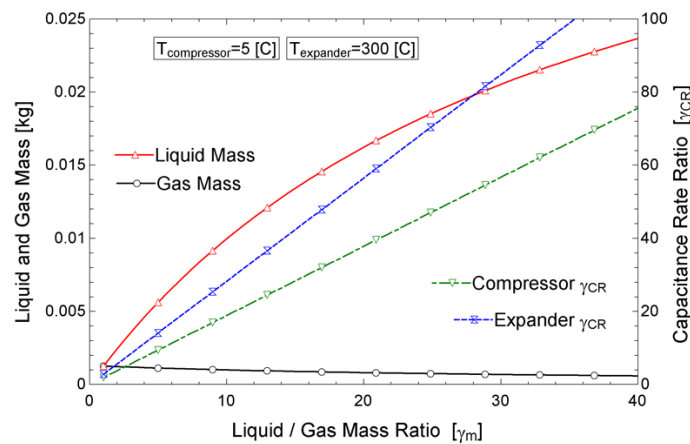


Figure 1: Liquid - gas relationships

The effect of liquid flooding of a compressor and expander is shown in Figure 2, where the capacitance ratio (Equation 7) is increased and the relative temperature is observed (Equation 8) with different fluid pressures. It can be seen with increasing flooding ratio, the compression and expansion processes approach isothermal. The effect is decreased with increased compression (CR) and expansion ratios (ER). It can be seen that a capacitance ratio of  $\gamma_{CR} = 15$ , the outlet temperature is within 0.5% of the inlet temperature, essentially isothermal. It is shown later that values of  $\gamma_{CR} = 50-60$  are optimal for the applications of the proposed system.

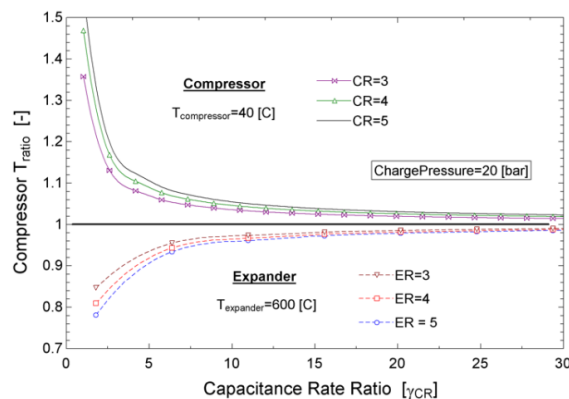


Figure 2: Liquid Flooding and Isothermalities

The effect of liquid flooding and the work required for compression can be seen in Figure 3. In this, the work with respect to adiabatic work of the compressor is minimized with  $\gamma_{CR} = 4$ . With increasing flooding, work increases, where the compressor essentially become a liquid pump and associated work increasing with liquid mass flow. The work required for compression can be optimized, but it will be seen, cycle optimisation results in higher flooding ratios of the compressor. This is well known in industry where flooding is used to minimize work of compression.

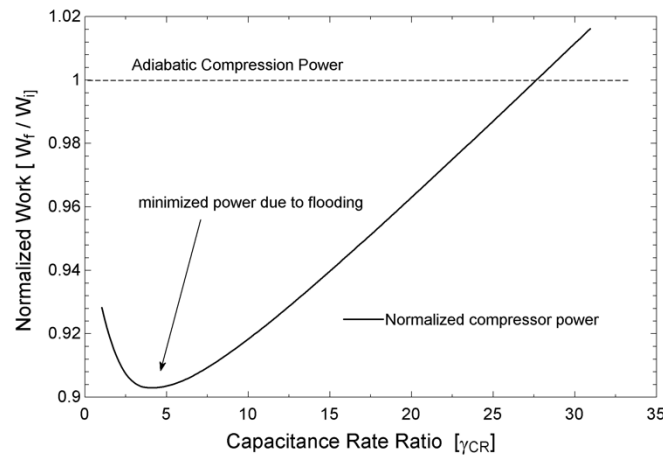


Figure 3: Compressor Work with Flooding

#### 4.1. LFEC system arrangement

The LFEC system arrangement developed by Hugenroth is shown in Figure 4. This was the configuration first developed as a heat pump cooler. The same arrangement was later used in an Ericsson heat engine development of a micro-Concentrated Solar Power (mCSP) system (Nelson, 2014).

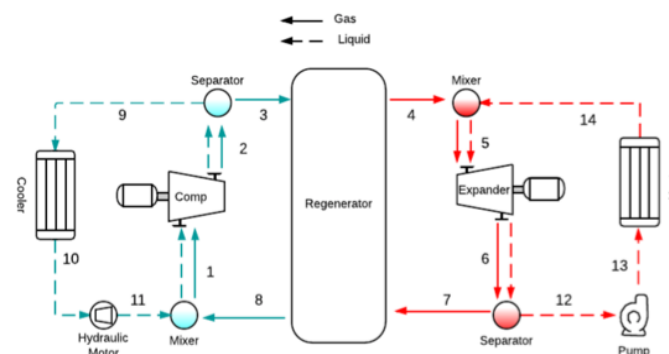


Figure 4: LFEC System Arrangement

In this there are three fluid loops; the working gas loop of the Ericsson cycle (1-8), the compressor liquid flooding loop (1-2, 9-11) and the expander fluid loop (5-6, 12-14). The separate liquid and working gas fluid loops were used since a suitable recuperator that can tolerate the gas and liquid counter flow were not available. While an additive manufacturing recuperator would allow such flows, the cost is prohibitive. For the system, commercial, off the shelf heat exchangers, pumps, hydraulic motors were used. Bespoke fluid separators were fabricated. Scroll compressors, which can be modified to perform as expanders are known to tolerate high ratios of liquid, where used in this system.

$$\text{Equation 9:} \quad \text{Second Order Efficiency} = \eta_{\text{Carnot}} = \frac{\text{COP}_{\text{System}}}{\text{COP}_{\text{Carnot}}}$$

In order to quantify system performance, Second Order Efficiency is used, defined in Equation 9. The LFEC system, modelled with ideal components, achieves Second Order Efficiency greater than 0.9, yet with actual component efficiencies of the scroll compressors, pressure and heat losses, the actual system showed fundamental issues with the concept and implementation. The primary issue was extreme sensitivity of closed cycle systems to the limited isentropic efficiency of the scroll systems, less than 0.7. This was compounded by the fluid routing system, pumps, separators and associated routing pressure losses. The compressor fluid loop (1-2, 9-11) included a

hydraulic motor which allowed fluid, pumped by the compressor, to return to the low-pressure side, incurring losses due to inefficiencies. The expander fluid loop (5-6, 12-14) includes a pump, required to pump liquid from low pressure to high, incurring significant work ( $w = v_l (P_f - P_i)$ ). Additionally, in the LFEC test system, fluid lines up to 1.2m in length were used between elements, incurring pressure drops. All of this resulted in systems with second order efficiencies less than 0.15 and in the case of the cooler, suited only for very limited temperature ranges.

## 5. PROPOSED LIQUID FLOODED ERICSSON CYCLE SYSTEM

The promise of a liquid flooded Ericsson system has led to the proposed system shown in Fig 5. This system is an attempt to overcome the limitations of the previous LFEC system and create a simple system applicable to both heat engine and heat pump systems. In this a newly developed counter-flow heat exchanger is used that allows concurrent flow of both liquid and gas and achieves an effectiveness >90%, which will be detailed in a follow-on work. The flows of liquid and gas are shown separate for modelling yet in the recuperator, run together. This recuperator arrangement allows the elimination of the many ancillary elements of the LFEC system (Figure 4) and greatly increases the system efficiency possible. The simple diaphragm or gear pumps move liquid from the recuperator to the compressor or expander; they do not require pumping work across the low- and high-pressure sides of the cycle as in the original LFEC system and thus avoid the associated work. The system was modelled with a constant flow enthalpy energy effectiveness heat exchanger models using Engineering Equation Solver (EES) (Klein, 2009). The new proposed arrangement simplifies fluid routing to allow significantly higher flooding ratios than the previous LFEC. In comparing the EES optimized cycles as a domestic hot water heater (5C expander, 65C compressor), using realistic efficiency of components and heat exchangers, the proposed cycle optimized to a 2<sup>nd</sup> Order efficiency of 0.56 with capacitance rate ratio of 66 as opposed to the LFEC which was 2<sup>nd</sup> Order Efficiency 0.19 with gamma CR = 8.6, showing the proposed system allows significantly greater liquid flow and greater system efficiency, as shown in Figure 6.

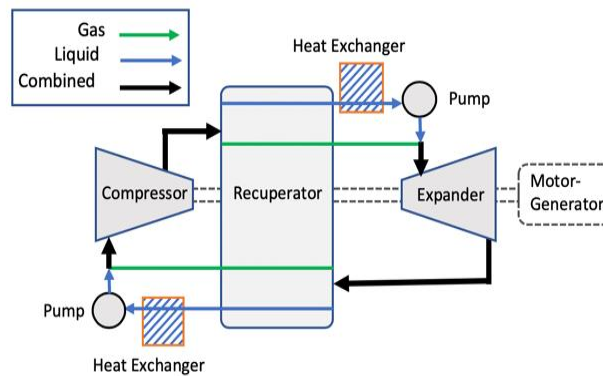


Figure 5: Proposed LF Ericsson Cycle System

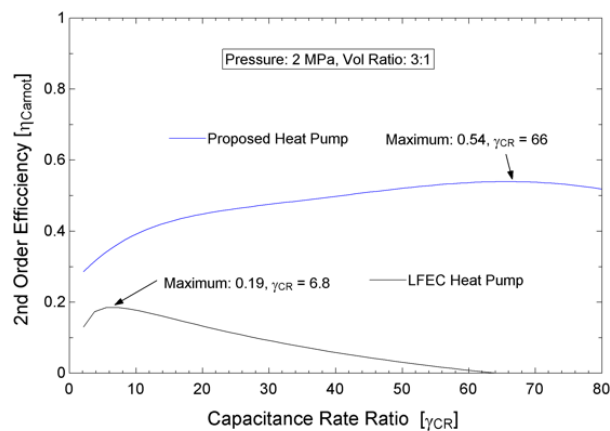


Figure 6: Proposed and LFEC Comparison

## 5.1. Geometry

While scroll compressors tolerate liquid and can be used for this application, their limited isentropic efficiency and complex entry and exit fluid routing requirements made them less than ideal. Newly developed compressor-expander systems are much more suited for the application and can tolerate significant liquid mass. For the proposed system, a compressor-expander system as shown in Figure 7 will be used. This consists of an outer housing and inner drum which oscillates inside. The rotor inside the drum creates two pair of double acting volumetric spaces which results in volume cycling as shown in Figure 8. The system will be detailed in a later paper. The design uses clearance seals which are enhanced with liquid flooding to allow minimal frictional losses yet required pressure sealing. Currently, a very similar system at the TRL6 level is achieving isentropic efficiencies greater than 90% and it is expected that this system will achieve similar.

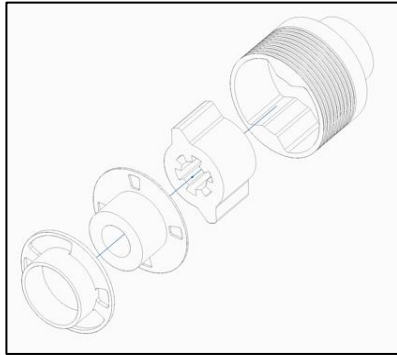


Figure 7: Compressor expander

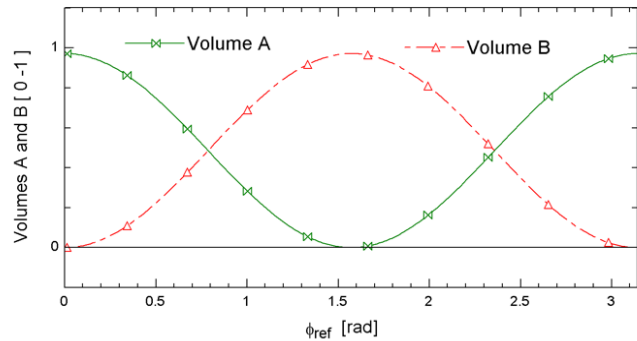


Figure 8: Volume cycling

## 6. CYCLE CHARACTERISTICS

The proposed cycle sensitivity to compressor and expander isentropic efficiencies is shown in Figure 9, which is similar to all gas systems. It can be seen that any increase in efficiency would be beneficial; compressor and expander efficiencies near 0.9 allow commercial viability of such a system. A similar, yet linear efficiency improvement can be had with increase in recuperator effectiveness. The proposed novel dual phase (liquid and gas flow) recuperator models with effectiveness greater than 90%, again allowing a commercially viable heat pump or heat engine.

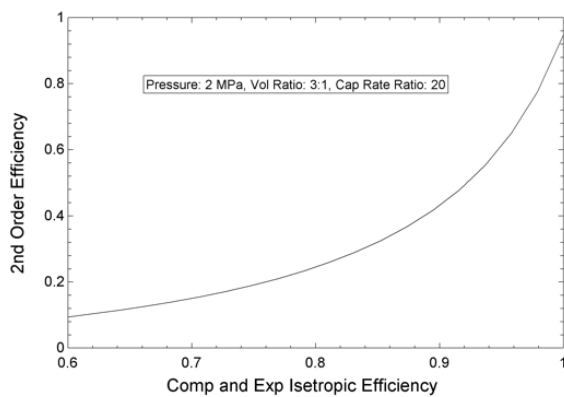


Figure 9: Compressor Expander Efficiency

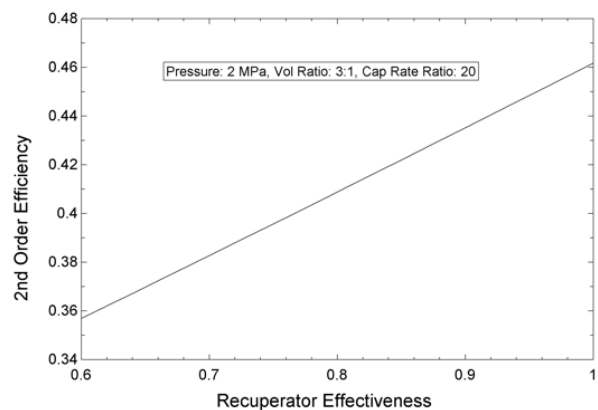


Figure 10: Recuperator Effectiveness

## 7. APPLICATIONS

The proposed liquid flooded Ericsson system arrangement can be applied as a heat engine or heat pump. While the proposed geometry of the compressor/expander system of the does not scale beyond the 4kW<sub>thermal</sub> heat pump or 10kW<sub>thermal</sub> heat engine, this size range is ideal suited for domestic and small business applications such as domestic hot water heat pumps, GSHP, ASHP, and as heat engines such as mCSP and mCHP systems. An additional advantage of the liquid flooding system is that the liquid flooding fluid can be routed for the application,

such as cooling heat transfer fluid circuits or to outside ambient radiators, eliminating the need for those additional systems. Suitable liquid flooding fluids are available for both low, cryogenic (-150C) and high temperature (<900C) applications.

The modelled performance of the proposed system as domestic hot water heat pump (ambient 5C, hot water outlet 65C) is shown in Figure 11. In this the performance of the new proposed system is compared to the original LFEC system with the additional fluid systems. This is shown for a range of compressor/expander and heat exchanger efficiencies/effectiveness (0.7 – 0.9) shows the marked improvement compared to the original LFEC concept. Additional improvements through optimization of fluid flooding ratios and compressor-expander volume ratios show a realizable second order efficiency of 0.65 is possible with system development.

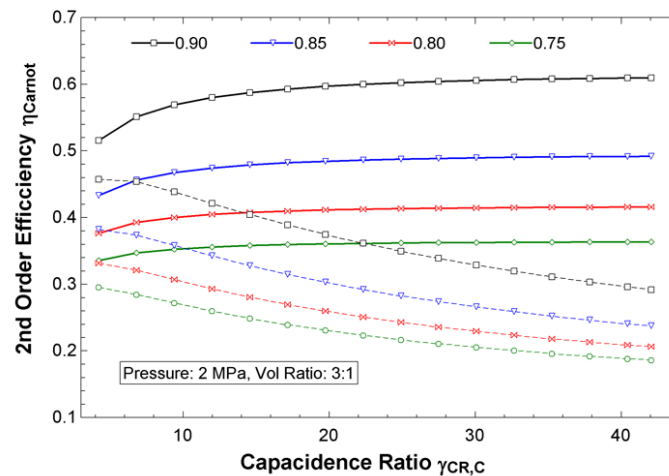


Figure 11: Domestic Hot Water Heat Pump

## 8. CONCLUSION

Ericsson cycle systems in their ideal form are ideal for application in the built environment where their high theoretical efficiency and HFC free working fluid would provide an immediate alternative to lower efficiency vapour compression cycle systems with HFCs. Yet actual mechanical systems have proven unable to deliver the efficiency required. Liquid flooding provides a path to commercially viable system. While the initial liquid flooding arrangements had significant shortcomings in efficiency and simplicity, the proposed system shows potential through modelling to be applicable both as a heat pump with applications such as hot water heater, GSHP, ASHP, and coolers, and as a heat engine for applications such as mCSP systems. The proposed system relies on a novel recuperator and compressor, and expander system that are still in development. The outcome of the current develop project will yield a heat pump and heat engine demonstration system.

## 9. ACKNOWLEDGEMENT

The authors wish to acknowledge the financial support of the UK Engineering and Physical Research Council (EPSRC, grant No. EP/R000182/1)

## 10. REFERENCES

DuraTherm LT Fluid Data, DuraTherm Heat Transfer Fluids Corp, Lewiston NY, USA <https://durathermfluids.com/products/duratherm-lt/>

Hugenroth, J et al, 2006, Liquid-flooded Ericsson cycle cooler Part 1- thermodynamic analysis, International Refrigeration and Air Conditioning Conference, Purdue <https://docs.lib.purdue.edu/iracc/823/>

Hugenroth, J, 2006, PhD Thesis, Liquid Flooded Ericsson Cycle Cooler, Purdue University, <https://docs.lib.purdue.edu/dissertations/AAI3287416/>

Igobo, O., & Davies, P. A. 2014, Review of low-temperature vapour power cycle engines with quasi-isothermal expansion. *Energy*, 70, 22-34. <https://doi.org/10.1016/j.energy.2014.03.123>

Klein, S.A., EES – Engineering Equation Solver, Version 10.668, 28 July 2019  
F-Chart Software, <http://fchart.com>

Lemort, V, et al, 2008, Analysis of Liquid-Flooded Expansion Using a Scroll Expander, International Compressor Engineering Conference, <https://pdfs.semanticscholar.org/ab33/16f83c1a1e80d240b0c85275717771589903.pdf>

Nelson, A, 2014, High temperature flooded expansion for solar thermal power generation, MSc Thesis, Purdue. [https://docs.lib.purdue.edu/cgi/viewcontent.cgi?article=1484&context=open\\_access\\_theses](https://docs.lib.purdue.edu/cgi/viewcontent.cgi?article=1484&context=open_access_theses)

UN Global Status Report, 2017, Towards a zero-emission, efficient, and resilient buildings and construction sector, [https://www.worldgbc.org/sites/default/files/UNEP%20188\\_GABC\\_en%20%28web%29.pdf](https://www.worldgbc.org/sites/default/files/UNEP%20188_GABC_en%20%28web%29.pdf)

---

## #63: Numerical simulation of water-in-oil emulsions droplets electrostatic coalescence

---

Xiangzhi ZHANG<sup>1</sup>, Yong SHI<sup>1</sup>, Yong REN<sup>1</sup>, Yuying YAN<sup>1,2</sup>

<sup>1</sup>Research Centre for Fluids and Thermal Engineering, University of Nottingham Ningbo China, 315100 Ningbo China, Xiangzhi.ZHANG2@nottingham.edu.cn

<sup>2</sup>Fluids and Thermal Engineering Research Group, Faculty of Engineering, University of Nottingham, NG7 2RD University Park, Nottingham, UNITED KINGDOM, yuying.yan@nottingham.ac.uk

*Phase separation of crude oil is a vital and common problem in the petroleum industry, and electric field assisted water droplets coalescence is regarded as one of the most efficient demulsification approaches. The correlative principles about electrohydrodynamics have been developed accompanied by experiments. In this study, we adopt the phase field method to develop a multi-field coupling multiphase model with the impact of an electric field. The Poisson equation is used to characterise the electric potential distribution, the Navier-Stokes equations modified with additional electrokinetic effect source terms are used to characterise the laminar flow in a channel, and the moving interface is tracked by solving the Cahn-Hilliard equations. Subsequently, the model is employed to simulate the flow of emulsions in a channel and the coalescence of water droplets stimulated by an applied electric field. The journey of oil-water interphase shows that the whole process of electrocoalescence is explicitly separated into the approaching stage and aggregating stage. Among those various electrokinetic mechanisms, the dipole-dipole interaction plays a dominant role in facilitating the coalescence of droplets. The dielectrophoresis caused by the non-uniformity of electric fields has both positive and negative effects on the enhancement of electrocoalescence. The simulation about the Poiseuille flow driven by pressure gradient shows that the flow velocity decreases with the increase of electric intensity and zeta potential. It is acquired that the resistance effect of the electric double layer gives rise to a flow rate loss, which indicates the necessity to research the material properties of fluids and wall surface in the future.*

*Keywords: phase separation, water-in-oil emulsions, electrocoalescence, phase field*



## 1. INTRODUCTION

Phase separation of oil-water mixture is one of the most common and critical problems in the petroleum industry. A typical example is the water component remaining in crude oil can deteriorate the downstream processes in different ways, i.e. the corrosion of equipment, the complications caused by increased viscosity, deactivation of catalysts, and perhaps some unwanted reactions (Kwon et al., 2010). Historically, the technology for electrocoalescence was invented for the petroleum-related industries in California, and it has been widely employed in the separation of aqueous phase dispersed in dielectric oil phase with a significantly lower permittivity than that of the dispersed phase (Eow et al., 2001). Apart from electrocoalescence, currently available demulsification approaches in practice are gravity settling, heat treatment, ultrasonic wave demulsification, magnetic field demulsification, membrane separation, high-speed centrifugal separation, microwave irradiation demulsification, and chemical or biological demulsification, etc. (Zolfaghari et al., 2016, Stewart et al., 1983, Li et al., 2014, Yang et al., 2009, Lemos et al., 2010, Arnaud, 2005). Each of these methods has its own superiorities and drawbacks. Comprehensively, electrocoalescence is generally considered as an effective phase separation technique in industries since it is relatively more eco-friendly, energy-conserving and expense-saving (Ptasinski and Kerkhof, 1992).

The principle of electrocoalescence is applying an electric field across the suspension of immiscible liquids may stimulate adjacent droplets to coalesce, thus increasing droplets size and break the quasi-equilibrium of emulsions, which leads to phase separation (Luo et al., 2016). Pearce (Pearce, 1954) divided the process into two steps as the alinement of water droplets chains and the coalescence of adjacent droplets. When conductive particles are immersed in a liquid with relatively higher resistivity, a chain of droplets would appear and form a conducting path, which acts as a local short circuit. The chain of droplets is formed by forces which originate in the potential differences between the droplets, and the chain is subjected to the electric field. Then, the thin oil films between the drops will be disrupted due to puncturing of the oil layers between adjacent droplets. Lewis (Lewis, 1934) drew attention to the phenomenon of droplets coalescence and he suggested that the two factors to this step are the breakdown of the film between droplets and the force between droplets. Chokkalingam et al. (Chokkalingam et al., 2014) pointed that the mechanism of demulsification is that the differences in conductivity and permittivity of the dispersed phase and continuous phase destabilise the interface, which leads to the deformation of droplet and interface. Hereafter, surfactant molecules at the interfaces are displaced or realigned, eventually leading to electrocoalescence (Mousavichoubeh et al., 2011).

Since the whole process is complex and various subjects (i.e. multiphase flow, thermodynamics and heat transfer, electromagnetism, electrohydrodynamics) are involved, it is essential to clarify the roles of associated physical phenomena and induced forces that act in electrocoalescence. In this study, we attempt to develop a reliable multi-field coupling model to simulate the coalescence of water droplets under the impact of an electric field. Based on the model, we then investigate the influence of electric intensity and zeta potential on multiphase flow and phase interaction.

## 2. APPROACH

In this section, we first review the various mechanisms might take effect in electrocoalescence provided by scholars previously. Then we adopt a phase field method to build a multiphase flow model aims to simulate the flow of water-in-oil emulsions in a channel. The impact of an applied electric field on water droplets coalescence can be studied through the method of numerical simulation.

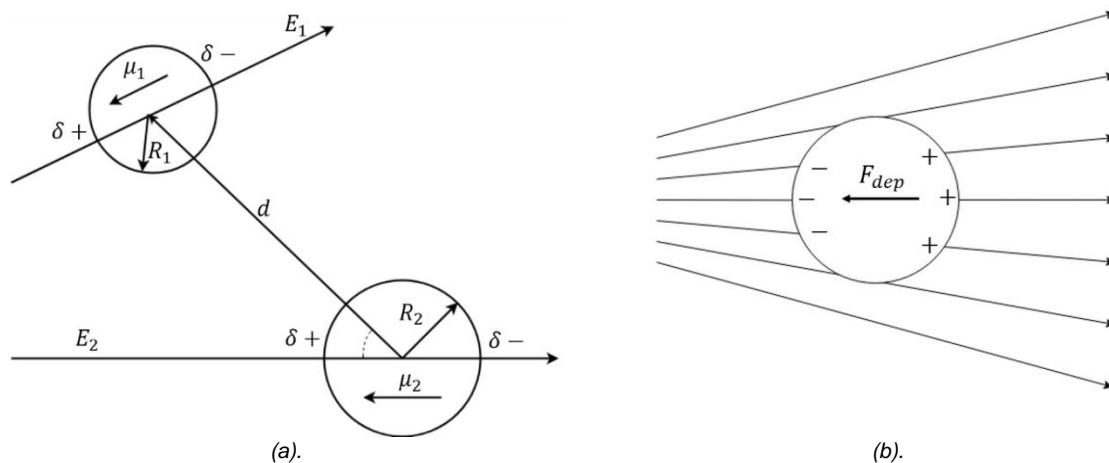


Figure 1: (a). Sketch of dipole-dipole force on circular droplets, (b). Sketch of dielectrophoretic force.

## 2.1. Electrostatic coalescence mechanisms

Generally, the coalescence phenomenon is described as the gathering of several individually manageable sub-processes (Zdravkov et al., 2003). In the first stage, the fluid motion plays a dominant role in bringing two droplets in close proximity. Subsequently, coalescence is promoted by field-induced attraction force, accompanied by the deformation of phase interfaces (Lundgaard et al., 2006). During the electrocoalescence process, the dispersed aqueous phase exhibit several diverse tendencies of migration and aggregation under the effect of the electric field. Among them, dipole coalescence, oscillation coalescence, electrophoresis, and dielectrophoresis are contributing to the coalescence of water droplets, while electrically induced dispersion also exists in the meantime, which greatly increases the complexity of the process.

### *Dipole coalescence*

In practical applications, impurities (such as acid, alkali, and salt) are often dissolved in the aqueous phase that the induced polarisation charges generate at the ends and form a dipole. Under the action of polarisation force, droplets approach each other, thus exhausting the oil film between these two droplets. Charles et al. (Charles and Mason, 1960) found a critical value that the oil film will burst immediately when the space of adjacent droplets reaches the critical value and the droplets will merge to a larger one. Since the dipole-dipole interaction plays a predominant role (Peng et al., 2016) in the attraction stage of electrocoalescence, it will be discussed especially in the following section.

### *Oscillation coalescence*

Water droplets can form induced dipoles under the effect of electric fields, and both ends of each dipole will generate a pair of two tensions, which are equal but in opposite directions. Under the tensions, droplets could be stretched into prolate spheres (Taylor, 1988). When the externally applied electric field changes periodically (AC or pulsed DC), the ions will impinge on the interface film and the repeated stretching deformation of droplets take place periodically. The periodic oscillation might increase the probability of collision and enhance the kinetic energy, thus weakening the mechanical strength of the interfacial film (Torza et al., 1971). Bailes and Dowling (Bailes and Dowling, 1985) suggested the electric field intensity and frequency are the two main factors to influence the vibration and oscillation coalescence.

### *Electrophoresis*

Electrophoresis is the migration of dispersed phase carrying a net charge, which is mainly encountered in uniform DC fields. Ultimately, it is caused by the presence of a charged phase interface, where an external electric field exerts an electrostatic Coulomb force. Due to the competition of electromigration and diffusion, the surface charge attracts the mobile counter-ions, thus forming an electric double layer (EDL) on the surface that partially shields the surface charge. Because the electrostatic Coulomb force is balanced by Stokes' drag, the velocity keeps constant, which is characterized by electrophoretic mobility (Luo et al., 2016). In most cases, crude oils are slightly conductive (about  $10^{-9}$ ~ $10^{-7}$  S·m<sup>-1</sup>), the electrophoretic attraction is therefore restricted to adjacent charged droplets with opposite polarity.

### *Dielectrophoresis*

Primarily, dielectrophoresis rises from the non-linear interaction applied on an extended dipole body subjected to a non-uniform electric field and surrounded by a dielectric medium. Driven by dielectrophoretic force, water droplets can migrate to regions with large potential gradient, thus increasing the local density of aqueous phase and enhancing the coalescence probability. According to the classical Maxwell-Wagner theory (Jones, 2003), the time-averaged dielectrophoretic force acting on a spherical droplet suspended in a dielectric medium has been acquired (Equation 1). Considering the permeability of the conductive dispersed phase and dielectric continuous phase, dielectrophoretic forces induced by an applied divergent field are indeed weak to facilitate the coalescence of water droplets (Peng et al., 2016).

Equation 13: Expression of dielectrophoretic force.

$$F_{dep} = 2\pi R^3 \varepsilon_d K_\varepsilon \nabla |E|^2$$

Where:

- $F_{dep}$  = dielectrophoretic force (N/m<sup>3</sup>)
- $R$  = radius of droplet (m)
- $\varepsilon_d$  = permittivity of dispersed phase (F/m)
- $K_\varepsilon$  = Clausius-Mossoti factor (1)

## Electrically induced dispersion

When the applied electric field is large enough and exceeds a critical value, the voltage will be rapidly increased and the water droplets will be overstretched under the forces. As electrically induced dispersion can significantly neutralise the coalescence effects, it should be avoided in practical applications.

### 2.2. Dipole-dipole interaction

In emulsions, neutral droplets without polarisation charges in oil could generate induced dipoles under the electric field, and each induced dipole carries equal but opposite charges at both ends (Ceolho and Lv, 1984). Equation 2 shows the expression of induced dipole moment (Ye et al., 2004).

$$\text{Equation 2: Electric field induced dipole moment.} \quad \mu_i = 4\pi\epsilon_c R_i^3 K_\epsilon \left(1 - \frac{b}{R_i}\right)^3 E$$

Where:

- $\mu_i$  = induced dipole moment of each droplet (C·m)
- $\epsilon_c$  = permittivity of continuous phase (F/m)
- $R_i$  = radius of each droplet (m)
- $K_\epsilon$  = Clausius-Mossotti factor (1)
- $b$  = measure of the eccentricity of the droplet (m)
- $E$  = electric field intensity (V/m)

Via the action of dipole moments, the pair of induced dipoles would produce interactive electric field forces to attract mutually. The resulting interaction force, affected by the inhomogeneous field created by their own dipolar moment, is always negligible at a long distance but it increases rapidly when the droplets are brought in close proximity (Eow and Ghadiri, 2003).

$$\text{Equation 3: Field energy of electrostatic interaction between two droplets.} \quad W_d = -\frac{\mu_1 \mu_2}{4\pi\epsilon_c d^3} (3\cos^2\theta - 1)$$

Where:

- $W_d$  = field energy of electrostatic interaction (N/m<sup>2</sup>)
- $\mu_1, \mu_2$  = induced dipole moment of each droplet (C·m)
- $\epsilon_c$  = dielectric constant of the continuous phase (F/m)
- $d$  = distance between droplet centres (m)
- $\theta$  = angle of dipoles (rad)
- In point-dipole approximation, considering the permittivity of each phase that  $\epsilon_c \ll \epsilon_d$ , the radial electric field force between the two droplets is obtained (Peng et al., 2016).

$$\text{Equation 4: Radial electric field force} \quad F_r = -\frac{\partial W_d}{\partial r} \Big|_{r=d} = -\frac{6\pi\epsilon_c R_1^3 R_2^3 E^2}{d^4} (3\cos 2\theta + 1)$$

Droplets could be stretched to approximately prolate sphere, due to the effect of applied electric fields. The polarisation induced mechanical stresses at the interface is expressed through the Maxwell stress tensor in symbolic form (Equation 5) (Griffiths, 2005). Based on it, Gong et al. (Gong et al., 2009) derived the radial electric field force (Equation 6).

$$\text{Equation 5: Polarisation induced stress tensor.} \quad \boldsymbol{\sigma} = \epsilon_c \mathbf{E} \otimes \mathbf{E} - \frac{1}{2} \epsilon_c (\mathbf{E} \cdot \mathbf{E}) \mathbf{I}$$

Where:

- $\epsilon_c$  = dielectric constant of the continuous phase (F/m)
- $\boldsymbol{\sigma}$  = Maxwell stress tensor in electrostatics (N/m<sup>3</sup>)
- $\mathbf{E}$  = electric field intensity (V/m)
- $\mathbf{I}$  = identity tensor (1)

$$\text{Equation 6: Dipole-dipole interaction force.} \quad \begin{pmatrix} F_r \\ F_\theta \end{pmatrix} = \epsilon_c b_2^2 \lambda^2 E^2 \cdot \begin{bmatrix} \cos\theta & \sin\theta \\ -\sin\theta & \cos\theta \end{bmatrix} \begin{pmatrix} K_1 \\ K_2 \end{pmatrix}$$

Where:

- $F_r$  = radial electric field force (N/m<sup>3</sup>)
- $F_\theta$  = tangential electric force (N/m<sup>3</sup>)
- $\varepsilon_c$  = dielectric constant of the continuous phase (F/m)
- $b_2$  = minor semiaxis of the second droplet (m)
- $\lambda$  = stretching ratio of droplet (1)
- $K_1, K_2$  = coefficients of force (1)

### 2.3. Governing equations and boundary conditions

Far-sightedly, the developed model aims at investigating the factors in various aspects that influence the performance of electrocoalescence. In this part, a typical design is discussed, where the multiphase flow of water-in-oil emulsions enters a channel equipped with alternating electrodes arranged along the wall. Figure 2 shows the structure of the channel and the electrodes configuration.

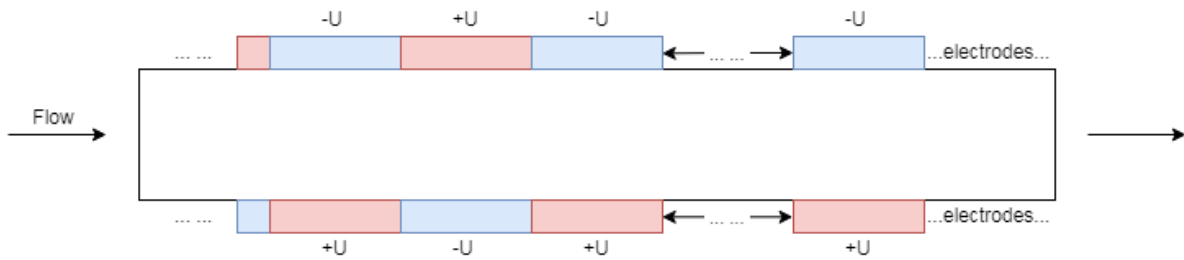


Figure 2: Sketch of the flow channel and electrodes configuration

#### Electrostatics

The electrostatics equation is often used to compute the electric field, electric displacement field, and potential distributions in dielectrics on conditions when the electric charge distributions are explicitly prescribed by solving Gauss' Law (Equation 7) for the electric field using the scalar electric potential as the dependent variable.

Equation 7: Gauss' Law of the electric field.  $\nabla \cdot (\varepsilon_0 \varepsilon_r \nabla U) = -\rho_e$

Where:

- $\varepsilon_0$  = vacuum permittivity (8.8541×10<sup>-12</sup>F/m)
- $\varepsilon_r$  = relative permittivity (1)
- $U$  = electrical potential (V)
- $\rho_e$  = local charge density (C/m<sup>3</sup>)

The boundary condition for all non-electrode surfaces (including channel inlet and outlet) is  $\frac{\partial U}{\partial n} = 0$ , while the applied electric potential on positive electrode surfaces are prescribed as  $U = U_e$  and  $U = -U_e$  on negative electrode surfaces.

#### Laminar flow

The continuity equation and the Navier-Stokes equation for incompressible viscous fluids are used to characterise the flow field (Equation 8). In which,  $\rho$  and  $\mu$  are the density and viscosity of the two phases, defined as  $\rho = \varphi \rho_d + (1 - \varphi) \rho_c$ , and  $\mu = \varphi \mu_d + (1 - \varphi) \mu_c$ . The subscript  $d$  denotes the dispersed phase, while the subscript  $c$  denotes the continuous phase.

Equation 8: Navier-Stokes equations for incompressible viscous fluids.  $\nabla \cdot \mathbf{V} = 0$   
 $\rho \left( \frac{\partial \mathbf{V}}{\partial t} + (\mathbf{V} \cdot \nabla) \mathbf{V} \right) = \nabla \cdot [-p \mathbf{I} + \mu (\nabla \mathbf{V} + (\nabla \mathbf{V})^T)] + \mathbf{F}$

Where:

- $\mathbf{V}$  = velocity field (m/s)
- $\mathbf{I}$  = identity tensor (1)
- $\mathbf{F}$  = volume force (N/m<sup>3</sup>)
- $p$  = pressure (Pa)
- $\rho$  = density (kg/m<sup>3</sup>)
- $\mu$  = dynamic viscosity (Pa·s)
- $\varphi$  = volume fraction of dispersed phase (1)

$\mathbf{F}$  is the volume force source term. In this case, the dominant volume force includes the dipole-dipole interaction force (Equation 9).

Equation 9: Dipole-dipole interaction force.

$$\begin{pmatrix} F_x \\ F_y \end{pmatrix} = \nabla \cdot \begin{bmatrix} \frac{1}{2} \varepsilon_0 \varepsilon_r (E_x^2 - E_y^2) & \varepsilon_0 \varepsilon_r E_x E_y \\ \varepsilon_0 \varepsilon_r E_x E_y & -\frac{1}{2} \varepsilon_0 \varepsilon_r (E_x^2 - E_y^2) \end{bmatrix}$$

The inlet boundary is fully developed flow with an average velocity, while the outlet is a suppress backflow pressure boundary. The boundary condition of the wall is dealt with an electroosmotic velocity, which describes the movement of the electric double layer (Equation 10).

Equation 10: Helmholtz-Smoluchowski relationship.

$$\begin{aligned} \mathbf{u}_{slip} &= \mu_{eo} \mathbf{E}_t \\ \mu_{eo} &= -\frac{\varepsilon_0 \varepsilon_r \zeta}{\mu} \end{aligned}$$

Where:

- $\mathbf{u}$  = electroosmotic velocity (m/s)
- $\mathbf{E}_t = \mathbf{E} - (\mathbf{E} \cdot \mathbf{n})\mathbf{n}$  = electric field tangential to the wall (V/m)
- $\mathbf{n}$  = unit normal vector (1)
- $\mu_{eo}$  = electroosmotic mobility (m<sup>2</sup>/V·s)
- $\varepsilon_0$  = vacuum permittivity (8.8541×10<sup>-12</sup>F/m)
- $\varepsilon_r$  = relative permittivity (1)
- $\zeta$  = zeta potential (V)

#### Phase field

The phase field method is a widely used approach to solve multiphase flow problems, where the interfacial layer is governed by a dimensionless phase field variable  $\phi$ , which is a function of the volume fraction of  $\varphi$ :  $\phi = 1 - 2\varphi$  (Amiri and Hamouda, 2013). Cahn-Hillard equations are used to track the moving interface (Equation 11).

Equation 11: Cahn-Hillard phase field equations.

$$\begin{aligned} \frac{\partial \phi}{\partial t} + \mathbf{V} \cdot \nabla \phi &= \nabla \cdot \gamma \nabla G \\ \gamma &= \chi \varepsilon_{pf}^2 \\ G &= \lambda \left[ -\nabla^2 \phi + \frac{\phi(\phi^2 - 1)}{\varepsilon_{pf}^2} \right] \\ \lambda &= \frac{3\varepsilon_{pf}\sigma}{2\sqrt{2}} \end{aligned}$$

Where:

- $\phi$  = phase field variable (1)
- $\gamma$  = mobility parameter to determine the time scale (m<sup>3</sup>·s/kg)
- $G$  = chemical potential (Pa)
- $\chi$  = mobility tuning parameter (m·s/kg)
- $\varepsilon_{pf}$  = capillary width (m)
- $\lambda$  = mixing energy density (N)
- $\sigma$  = surface tension coefficient (N/m)

The wetted wall boundary condition is set by assuming a contact angle  $\theta_w$  (Equation 12).

Equation 12: Assumption of wetted wall boundary condition.

$$\mathbf{n} \cdot \frac{\gamma\lambda}{\epsilon_{pf}^2} \nabla\psi = 0$$

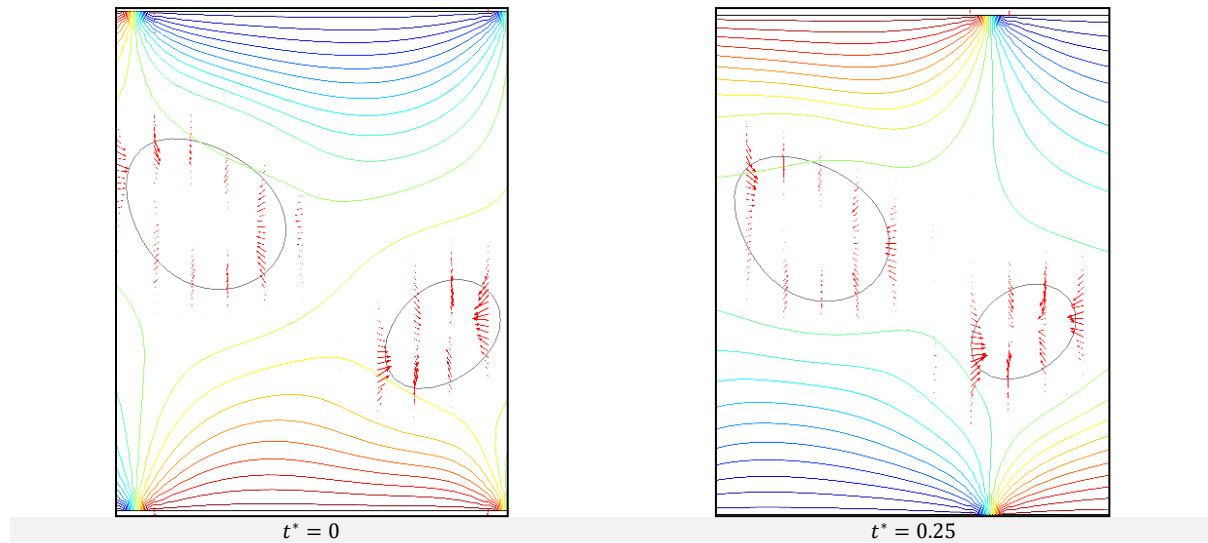
$$\mathbf{n} \cdot \epsilon_{pf}^2 \nabla\phi = \epsilon_{pf}^2 \cos(\theta_w) |\nabla\phi|$$

Where:

- $\mathbf{n}$  = unit normal vector (1)
- $\theta_w$  = contact angle (rad)

### 3. RESULTS AND DISCUSSION

In this study, a phase field model of multiphase electrohydrodynamic flow is developed to simulate the process of electrocoalescence. Figure 3 shows the time evolution for two droplets coalescence facilitated by a non-uniform electric field ( $E = 500V/cm$ ) generated by alternating electrodes (showed in Figure 2). According to Figure 3, the whole process of electrocoalescence is explicitly separated into two stages (approaching and aggregation). Initially, the two droplets have a circular shape before they enter the electric field region. Polarised by the electric field, the two droplets undergo the electric force acting on them. Due to induced dipoles, each one droplet is attracted by the other, which makes them deform into non-symmetric prolate ellipsoids. With the approaching of droplets, the oil film between them is drained and coalescence takes place. The electric field at the central axis is vigorous around the centre of each electrode plate and decreases when approaching the demarcation points, where the highly distorted local field generates a dielectrophoretic force which has a tendency to break up the droplets. Hence, the non-uniformity of electric fields with such kind of electrodes configuration have an adverse effect on coalescence, which will compromise the overall separation efficiency.



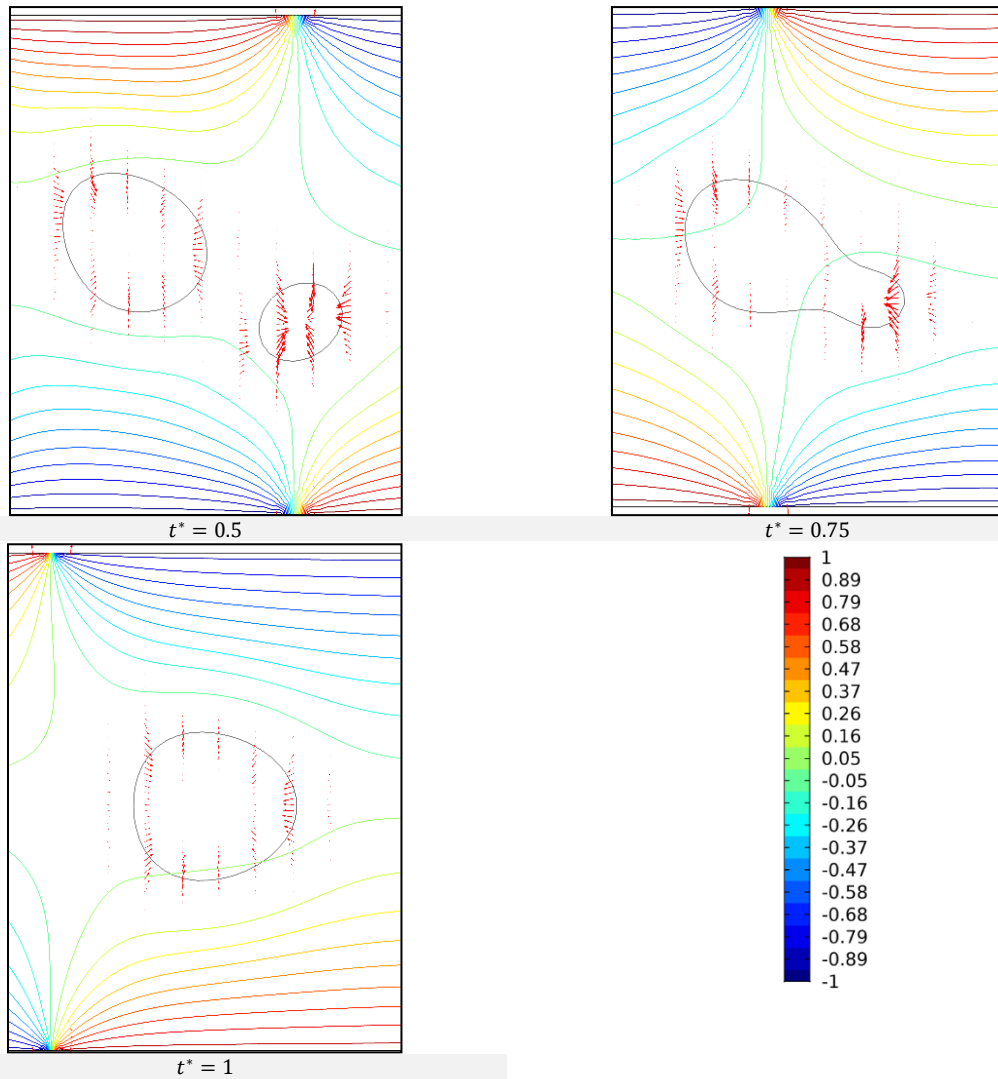


Figure 3: Process of droplets coalescence enhanced by an electric field, the color legend shows the dimensionless electric potential  $U^* = U/U_e$  ( $U_e$  is the electric potential of positive electrode), the dimensionless time  $t^* = t/\tau$  ( $\tau$  is the stay time of droplets in channel), and the arrows represent the applied forces acting on droplets.

To discuss the electric field effects quantitatively, the impacts of electric intensity and zeta potential on Poiseuille flow driven by pressure gradient have also been investigated. Figure 4 shows the flow velocity and the absolute value of  $\partial^2 v^*/\partial y^{*2}$  decrease with the increase of electric intensity and zeta potential. It could be presumed that the resistance effect of the electric double layer gives rise to this phenomenon, which results in flow rate loss in microchannel (Gong and Wu, 2006). The electrolyte flow in the channel driven by pressure gradient carries electric charge of the electric double layer, and the streaming current produces an electrical potential difference opposite to the flow direction, causing a loss of velocity. As the physical interaction of insulated solid wall and electrolytic liquid is the main source of additional resistance, the material of channel and the associated properties of emulsions should be taken into consideration.

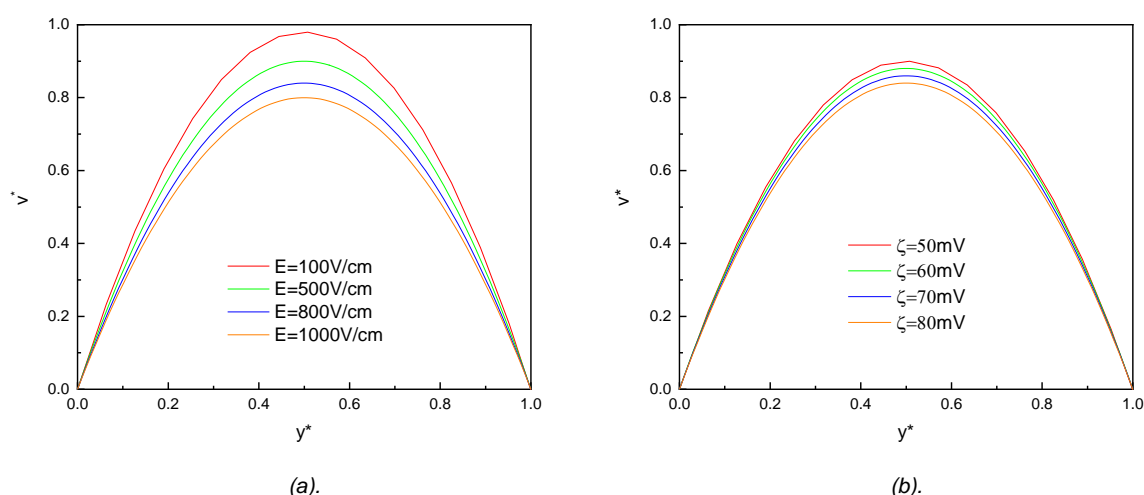


Figure 4: (a). Velocity distribution with varying electric intensity,  $\zeta = 50\text{mV}$ , (b). Velocity distribution with varying zeta potential,  $E = 50\text{mV}$ ;  $v^*$  is the dimensionless velocity,  $y^*$  is the dimensionless length scale.

#### 4. CONCLUSION

In this study, we adopt the phase field method to build a flow model of oil-water mixture under the impact of electric fields, which is then used to simulate the water droplets coalescence enhanced by electric fields. The mechanisms potentially contributing to electrocoalescence have been investigated and it is found that the dipole-dipole interaction plays a dominant role in promoting the coalescence. On top of that, we have also acquired that zeta potential and electric intensity may counteract pressure gradient driven Poiseuille flow due to the additional resistance originates from the streaming current. The result shows the non-uniformity of electric fields have both positive and negative effects on facilitating the electrocoalescence, which should be researched comprehensively in the future. Furthermore, the phase interaction and interfacial mechanisms should be researched further as they are of essential importance especially when the magnitude arrives at a microscale.

#### 5. REFERENCES

- Amiri, H. A. & Hamouda, A. A. 2013. Evaluation of level set and phase field methods in modeling two phase flow with viscosity contrast through dual-permeability porous medium. *International Journal of Multiphase Flow*, 52, 22-34.
- Arnaud, J. 2005. Methods and apparatus for oil demulsification and separation of oil and suspended solids from produced water. Google Patents.
- Bailes, P. & Dowling, P. 1985. The production of pulsed EHT voltages for electrostatic coalescence. *Journal of Electrostatics*, 17, 321-328.
- Ceolho, R. & LV, J. 1984. Dielectric Physics. Science Press, Beijing, China.
- Charles, G. E. & Mason, S. G. 1960. The mechanism of partial coalescence of liquid drops at liquid/liquid interfaces. *Journal of Colloid Science*, 15, 105-122.
- Chokkalingam, V., Ma, Y., Thiele, J., Schalk, W., Tel, J. & Huck, W. T. 2014. An electro-coalescence chip for effective emulsion breaking in droplet microfluidics. *Lab on a Chip*, 14, 2398-2402.
- Eow, J. S. & Ghadiri, M. 2003. Motion, deformation and break-up of aqueous drops in oils under high electric field strengths. *Chemical Engineering and Processing: Process Intensification*, 42, 259-272.
- Eow, J. S., Ghadiri, M., Sharif, A. O. & Williams, T. J. 2001. Electrostatic enhancement of coalescence of water droplets in oil: a review of the current understanding. *Chemical engineering journal*, 84, 173-192.
- Gong, H., Song, S. & Peng, Y. 2009. Theoretical calculations of electrostatic force between ellipsoidal drops in W/O emulsion [J]. *Journal of the Chemical Industry and Engineering Society of China*, 7.



- Gong, L. & Wu, J.-K. 2006. Resistance effect of electric double layer on liquid flow in microchannel. *Applied Mathematics and Mechanics*, 27, 1391-1398.
- Griffiths, D. J. 2005. Introduction to electrodynamics. AAPT.
- Jones, T. B. 2003. Basic theory of dielectrophoresis and electrorotation. *IEEE Engineering in medicine and Biology Magazine*, 22, 33-42.
- Kwon, W.-T., Park, K., Han, S. D., Yoon, S. M., Kim, J. Y., Bae, W. & Rhee, Y. W. 2010. Investigation of water separation from water-in-oil emulsion using electric field. *Journal of Industrial and Engineering Chemistry*, 16, 684-687.
- Lemos, R. C., Da Silva, E. B., Dos Santos, A., Guimaraes, R. C., Ferreira, B. M., Guarnieri, R. A., Dariva, C., Franceschi, E., Santos, A. F. & Fortuny, M. 2010. Demulsification of water-in-crude oil emulsions using ionic liquids and microwave irradiation. *Energy & Fuels*, 24, 4439-4444.
- Lewis, W. 1934. On adherence and coalescence in emulsions. *Transactions of the Faraday Society*, 30, 958-967.
- Li, S., Li, N., Yang, S., Liu, F. & Zhou, J. 2014. The synthesis of a novel magnetic demulsifier and its application for the demulsification of oil-charged industrial wastewaters. *Journal of Materials Chemistry A*, 2, 94-99.
- Lundgaard, L., Berg, G., Ingebrigsten, S. & Atten, P. 2006. Emulsions and emulsion stability. Vol. 132. CRC Press, Ch. Electrocoalescence for oil-water separation: Fundamental aspects.
- Luo, S., Schiffbauer, J. & Luo, T. 2016. Effect of electric field non-uniformity on droplets coalescence. *Physical Chemistry Chemical Physics*, 18, 29786-29796.
- Mousavichoubeh, M., Ghadiri, M. & Shariaty-Niassar, M. 2011. Electro-coalescence of an aqueous droplet at an oil-water interface. *Chemical Engineering and Processing: Process Intensification*, 50, 338-344.
- Pearce, C. 1954. The mechanism of the resolution of water-in-oil emulsions by electrical treatment. *British Journal of Applied Physics*, 5, 136.
- Peng, Y., Liu, T., Gong, H. & Zhang, X. 2016. Review of the Dynamics of Coalescence and Demulsification by High-Voltage Pulsed Electric Fields. *International Journal of Chemical Engineering*, 2016.
- Ptasinski, K. & Kerkhof, P. 1992. Electric Field Driven Separations: Phenomena and Applications. *Separation science and technology*, 27, 995-1021.
- Stewart, A., Gray, N., Cairns, W. & Kosaric, N. 1983. Bacteria-induced de-emulsification of water-in-oil petroleum emulsions. *Biotechnology letters*, 5, 725-730.
- Taylor, S. E. 1988. Investigations into the electrical and coalescence behaviour of water-in-crude oil emulsions in high voltage gradients. *Colloids and Surfaces*, 29, 29-51.
- Torza, S., Cox, R. & Mason, S. 1971. Electrohydrodynamic deformation and bursts of liquid drops. *Philosophical Transactions of the Royal Society of London. Series A, Mathematical and Physical Sciences*, 269, 295-319.
- Yang, X.-G., Tan, W. & Tan, X.-F. 2009. Demulsification of crude oil emulsion via ultrasonic chemical method. *Petroleum Science and Technology*, 27, 2010-2020.
- Ye, Q., Li, J. & Zhang, J. 2004. A displaced dipole model for a two-cylinder system. *IEEE transactions on dielectrics and electrical insulation*, 11, 542-550.
- Zdravkov, A., Peters, G. & Meijer, H. 2003. Film drainage between two captive drops: PEO-water in silicon oil. *Journal of colloid and interface science*, 266, 195-201.
- Zolfaghari, R., Fakhru'l-Razi, A., Abdullah, L. C., Elnashaie, S. S. & Pendashteh, A. 2016. Demulsification techniques of water-in-oil and oil-in-water emulsions in petroleum industry. *Separation and Purification Technology*, 170, 377-407.

---

## #64: A prototype of thermochemical heat storage system for space heating in building

---

Yanan ZHANG<sup>1</sup>, Auwal DODO<sup>2</sup>, Yijun YUAN<sup>3</sup>, Saffa RIFFAT<sup>4</sup>

<sup>1</sup>Department of Architecture and Built Environment, University of Nottingham, Nottingham, NG7 2RD, UK, [yanan.zhang@nottingham.ac.uk](mailto:yanan.zhang@nottingham.ac.uk)

<sup>2</sup>Department of Architecture and Built Environment, University of Nottingham, Nottingham, NG7 2RD, UK, [auwal.dodo@nottingham.ac.uk](mailto:auwal.dodo@nottingham.ac.uk)

<sup>3</sup>Department of Architecture and Built Environment, University of Nottingham, Nottingham, NG7 2RD, UK, [yijun.yuan@nottingham.ac.uk](mailto:yijun.yuan@nottingham.ac.uk)

<sup>4</sup>Department of Architecture and Built Environment, University of Nottingham, Nottingham, NG7 2RD, UK, [saffa.riffat@nottingham.ac.uk](mailto:saffa.riffat@nottingham.ac.uk)

*Energy storage is the capture of energy produced at one time for use at a later time. It comes in multiple forms, such as chemical energy, electrical power, elevated temperature, latent and sensible heat, kinetic and gravitational potential energy. Thermochemical energy is used to drive a reversible endothermic chemical reaction, storing energy as chemical potential, and it is cost effective methods to provide a thermal comfort to improve living condition for people. Thermochemical energy storage (TES) materials normally have very high energy density and low regeneration temperature for energy saving. Solar energy is a very good heat source for the thermochemical energy storage system for regeneration in this project.*

*In this project, V-MgSO<sub>4</sub>-CaCl<sub>2</sub> has been chosen as the optimal TES material for use in our prototype, based on previous tests and analysis. V-MgSO<sub>4</sub>-CaCl<sub>2</sub> shows the highest energy density of 1173.5kJ/kg and the lowest regeneration temperature of 62 °C. In this prototype, the operation condition was under a low relative humidity level (60%) with the highest reaction temperature at about 37.44 °C for more than 3.5 hours. The COP of the TES system for heating reaction was 1.11.*

*Keywords: Thermochemical heat storage; heat storage; space heating; thermochemical heat storage materials; prototype*

## 1. INTRODUCTION

Fossil fuel consumption leads to a significant global warming and rising sea level. Thermochemical energy storage (TES) technologies can be an alternative to conventional thermal heat storage because of the high energy density, low heat loss, low regeneration temperature and low volume requirement. Stored energy can be used later to fill the gap between energy demand and supply. Researches have shown significant advantages: TES is more energy efficient and environmentally friendly and is identified as chemical storage. The energy density of thermochemical materials is two times higher than latent energy storage, and 8-10 times higher than sensible energy storage materials. TES is an advanced technology to address the time difference between energy demand and production in building servicing systems.

Thermochemical materials provide a promising solution to achieve a long-term 100% renewable energy economy. The systems are simple in design, fabrication and operation. In the MERITS project (de Jong, 2016), Jong showed  $\text{Na}_2\text{S}$  had a heat storage density of  $0.14 \text{ GJ/m}^3$ . Development has been done to improve the heat storage density by enhancing vapour and heat transport level. However,  $\text{Na}_2\text{S}$  has the risk of corrosion and reaction and a hazard of  $\text{H}_2\text{S}$  emissions. Liu et al. demonstrated  $\text{CaCl}_2$  as an industrial waste heat filter (mesoporous ceramic honeycomb filter) to absorb high temperature waste heat and provide a low-temperature waste exhaust (Jiang et al., 2016) (Donkers, Sögütöglu, Huinink, Fischer, & Adan, 2017). Results show that the storage density for heating was  $0.27 \text{ GJ/m}^3$ . In Aristov et al. studies (Aristov, Restuccia, Tokarev, Buerger, & Freni, 2000), selective water sorbents (SWSs) in sorption system can provide very high COP of 0.7-0.8 for cooling and 1.6-1.8 for heating. Compared with other materials, vermiculite with  $\text{CaCl}_2$  can exchange large water during the process (a very high water uptake ratio and also a higher energy density). Vermiculite with  $\text{CaCl}_2$  showed a very good water uptake of  $1.13 \text{ g/g}$  and can be widely used in the sorption systems (Aristov, Restuccia, Tokarev, & Cacciola, 2000). In Brancato's study (Brancato, 2018), a system with the composite of vermiculite +  $\text{LiCl}$  was developed for thermal energy storage applications. Thermal storage capacity was about  $2.15 \text{ kJ/kg}$  in the seasonal term storage system. Furthermore, as the host matrix, vermiculite has been confirmed slowdown sorption dynamics, allowing the reaction process to be more easily controlled, and supplying energy when it is necessary.

Energy storage accumulates generated energy for later use. It comes in multiple forms, such as chemical energy, electrical potential energy, gravitation potential energy, radiation, latent heat and kinetic power. There is generally a lot of solar energy in summer or at daytime, but more heating is needed in winter and at night. That is why energy storage system are required. Thermochemical energy storage (TES) can be a promising advanced technology in addressing massive energy use for heating and cooling in building application. Such systems can be an alternative to the conventional energy system because of the lower heat loss, higher energy density of the materials, more efficient and environmentally friendly. In this project, a novel open system of thermochemical energy is demonstrated, and different high energy density storage salts (e.g.  $\text{CaCl}_2$ ,  $\text{MgSO}_4$ ,  $\text{LiNO}_3$ , and  $\text{MgCl}_2$ ) with host matrix such as vermiculite and advanced carbon were used as thermochemical heat storage (THS) materials. The aim of this project is to characterise different composites to find better performing materials with higher energy density, lower heat loss, next regeneration temperature, higher temperature lift in reaction process and higher system efficient. Some modification has been done on these results that indicate that vermiculite-based composite with  $\text{MgSO}_4$  and  $\text{CaCl}_2$  as energy storage spices showed the best performance in the system and presented the optimal option. The modified model offers a higher accuracy and efficiency than the simplified model.

In this project, the salt impregnated composite materials are used as the TES materials, and the energy density was analysed to identify the optimal material. V- $\text{MgSO}_4$ - $\text{CaCl}_2$  was selected because of its high energy density. Other characteristics such as high energy density, low regeneration temperature and high moisture uptake should be taken into consideration when we choose a good thermochemical energy storage material. The open thermochemical energy storage system was built for the materials test, which is a simple prototype in lab, using a fan with heater as the low temperature heat source for regeneration. A humidifier was used to add moisture to the air supply. In the discharging/reaction process, moist air goes through the materials and is adsorbed. Exothermic materials release heat when combined with water moisture. The system provides dry and hot air for buildings. For the charging/regeneration process, hot air at  $90^\circ\text{C}$  for drying the materials. The PID control was installed for temperature control to avoid overheating because in the real prototype we will use the low temperature source to instead of the heater and fan.

## 2. EXPERIMENT DESIGNS FOR THE OPEN THERMOCHEMICAL HEAT STORAGE PROTOTYPE

This test rig system is consisted of the aluminium reactor, an air blower, a heat exchanger, an air humidifier, aluminium pipes and humidity and thermocouple sensors (see Figure 1). The main purpose was to test the selected materials for thermochemical energy system and analyse what materials prove to yield best results. The materials tested in the previous test rig included vermiculate combined with different salts (SIM):  $\text{MgSO}_4$ - $\text{LiCl}$ ,  $\text{MgSO}_4$ - $\text{CaCl}_2$ , and  $\text{CaCl}_2$ - $\text{LiCl}$ . Each testing consisted of discharging and charging measuring. V- $\text{MgSO}_4$ - $\text{CaCl}_2$  was selected as the best thermochemical heat storage material for the testing in the prototype. Compared with the

results in the previous test, V-MgSO<sub>4</sub>-CaCl<sub>2</sub> is the optimal choice for thermochemical heat storage material because of its lower regeneration temperature and higher reaction temperature. The chosen thermochemical heat storage material were used in the prototype to check the availability of space heat supply.

## 2.1. Experiment rig set-up

A vertical cylinder tank was used as the reaction body and a fan with heater was used to provide warm air (90 degree C) in the regeneration process. A PID controller was installed after the fan heater to control the hot air temperature in case of overheating. A humidifier supplied moist air for the reaction during discharging process. Seven tubes with fins were installed inside the reaction body, all the materials (16kg) were filled inside the fins, and there were many holes on the tubes to let the moisture air go through the tube and release to the materials. Moist air went through the materials and exhausted through the air outlet tube. Chemical reaction (Hydration reaction):

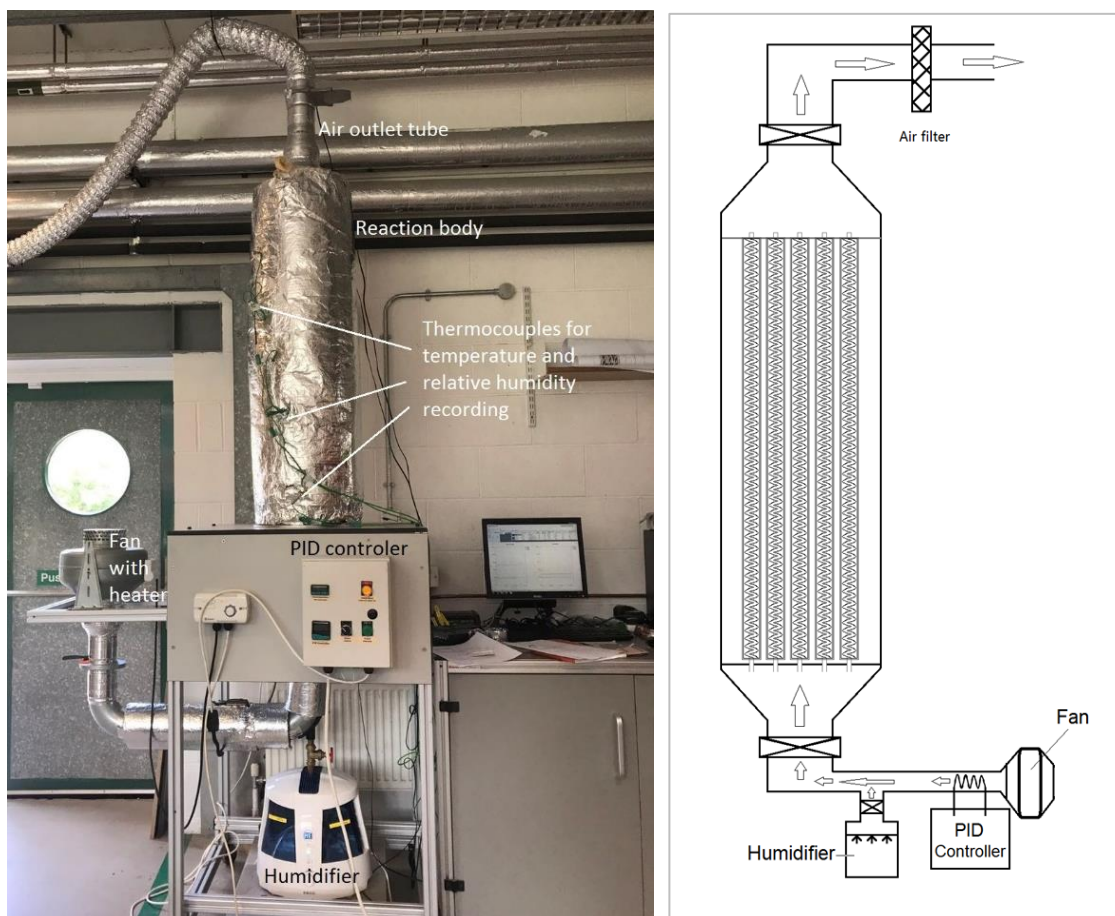
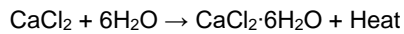


Figure 1: Open system for thermochemical energy storage materials test rig.

All the detail information of the components of the test rig are shown in Table 1 below:

Table 1: Components of the prototype and the parameters.

Components	Specifications	Purpose
Air Fan	Air flow rate: 0.16 m/s	For air inlet.
Humidifier	Power: 47W	To provide moisture for the THS material.
Electrical heating element	Power: 35W	To heat and dry the air before the reactor inlet
PID controller	0.53 kWh	To control charging temperature, which was 90°C for this testing.
Thermocouple sensors		To monitor the temperature and relative humidity changing during the operation.
THS material	MgSO <sub>4</sub> -CaCl <sub>2</sub> , weight ratio is 1:2	Used for thermochemical energy storage to store energy inside as an energy storage media.
Aluminium (casing) reactor	Aluminium reactor with the well insulation	The reactor where discharging and charging occurs.
Pipes	Regeneration T: 90°C Aluminium pipes with the well insulation	To direct the airflow and minimise heat losses.

## 2.2. Experiment description

The whole prototype was 60kg with 16kg vermiculite-MgSO<sub>4</sub>-CaCl<sub>2</sub>. The ratio of each component is 1:1:2 (vermiculite : MgSO<sub>4</sub> : CaCl<sub>2</sub>). Before starting the test, hot air at 90°C was supplied to dry materials for 48 hours, then the rig was sealed and allowed to cool for 24 hours. Data recording was started 30 minutes before the supply of moist air commenced, then the discharging process was started. In the discharging/reaction process, moist air goes through the material and is adsorbed. Exothermic materials release heat when combined with water moisture and the system provides dry and warm air for building. The relative humidity level at the inlet was about 60%. The moist air was supplied for 3 hours and the results were checked. For the charging/regeneration process, a fan with heater providing 90°C temperature was used for drying the materials. The PID control was installed to control temperatures to avoid overheating.

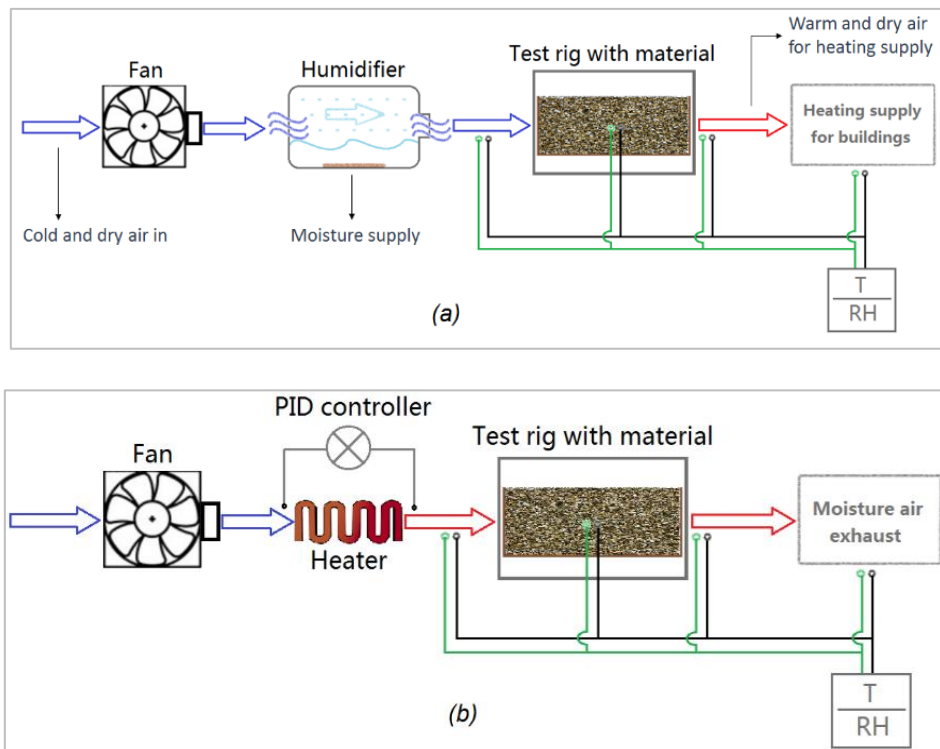


Figure 2: (a) Discharging cycle in open loop thermochemical energy storage system; (b) Charging cycle in open loop thermochemical energy storage system.

### 3. RESULTS AND ANALYSIS

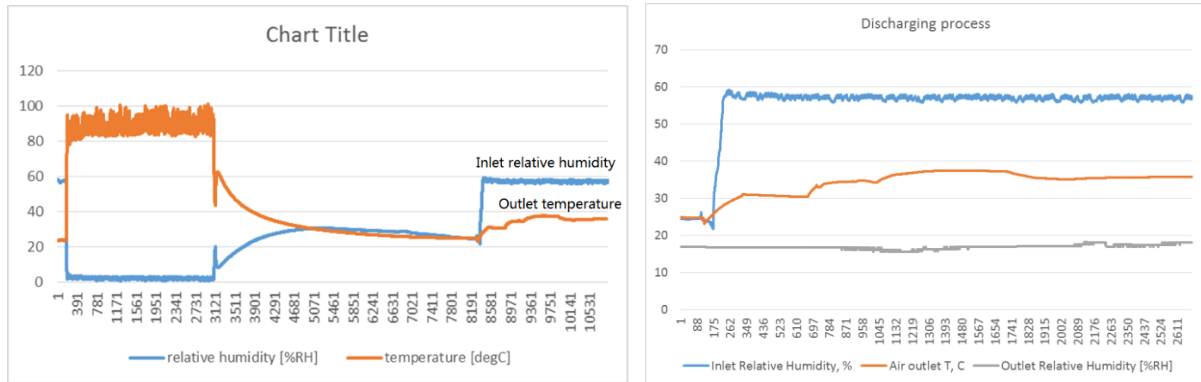


Figure 3: (a) The reading results of charging and discharging process of the test; (b) The reading results of discharging process of the test.

According to the record readings, results showed that the V-MgSO<sub>4</sub>-CaCl<sub>2</sub> temperature increased to the highest temperature of 37.44°C after moisture supply in 22 minutes. The temperature remained above 30°C for 3 hours and 15 minutes without showing a drop in temperature indicating that it can retain heat for some time. At the same time, the outlet relative humidity level was about 17% indicating that most of the air moisture was adsorbed by the TES materials.

The fan velocity is 0.16 m/s and the diameter is 0.1m (equals to 0.0078m<sup>2</sup> \* 0.16m/s \* 1.29kg/m<sup>3</sup> = 0.00162 kg/s, air density is 1.29kg/m<sup>3</sup>). The power of the heat fan is 47W.

The warm air weight was 0.00162kg/s\*(3 hours \*3600s+15min \*60s) = 18.95kg, which equals to 14.7m<sup>3</sup>.

Specific heat capacity (Cp) of air is 1.006 kJ/kgC.

Using heat transfer formula, for every second:

$$Q_c = C_p * m_a * \Delta T = 1.006 \text{ kJ/kgC} * 0.00162\text{kg} * \Delta T$$

Using every second reading to calculate the total energy generate:  $Q_{c-total} = 62 \text{ kWs}/3600\text{s/h} = 0.017 \text{ kWh}$ .

Fan energy consumption is  $E_f = 47\text{W} * 3.2 \text{ h} = 0.15\text{kWh}$ .

The COP is the ratio of the heat release to surrounding environment plus the input work to the input work:

$$COP = \frac{Q_c + E_f}{E_f} = \frac{0.017\text{kWh} + 0.15\text{kWh}}{0.15\text{kWh}} = 1.11$$

### 4. CONCLUSIONS AND FUTURE WORKS

In the prototype test, 16 kg V-MgSO<sub>4</sub>-CaCl<sub>2</sub> was placed in the reactor. After one cycle test, the highest outlet temperature was 37.44 ° C with a reaction COP of 1.11, which did not reach the high temperature we expected (above 40 degree C). The inlet relative humidity level was about 60% and the outlet relative humidity level was about 17%, which means that the TES materials have a very good water uptake capacity. Because the hole under the bottom of the reactor is too small that the moisture air cannot go through the rig completely, some of the moisture air escape from the gap of the humidifier, so the humidity level cannot reach 90%. In the next step, we will expend the hole to make them larger for the moisture air going through the tube to inject into the materials. After the 1<sup>st</sup> step test in the prototype, we modified the humidifier to be installed in front of the fan to increase moisture transfer and reduce moisture leakage. The flat pan in the bottom of the rig is used to provide the moisture transfer and fix the tubes inside the rig test body. More holes can supply more moisture air to rise the relative humidity level. Hence, a flat pan with more holes will be replaced the old one to provide more access for moisture air goes pass the reaction body.

## 5. REFERENCES

Aristov, Y. I., Restuccia, G., Tokarev, M., Buerger, H.-D., & Freni, A. (2000). Selective water sorbents for multiple applications. 11. CaCl<sub>2</sub> confined to expanded vermiculite. *Reaction Kinetics and Catalysis Letters*, 71(2), 377-384.

Aristov, Y. I., Restuccia, G., Tokarev, M., & Cacciola, G. (2000). Selective water sorbents for multiple applications, 10. Energy storage ability. *Reaction Kinetics and Catalysis Letters*, 69(2), 345-353.

Brancato, V., Gordeeva, L. G., Sapienza, A., Palomba, V., Vasta, S., Grekova, A. D., ... & Aristov, Y. I. (2018). Experimental characterization of the LiCl/vermiculite composite for sorption heat storage applications. *International Journal of Refrigeration*.

de Jong, A. J., van Vliet, L., Hoegaerts, C., Roelands, M., & Cuypers, R. (2016). Thermochemical heat storage—from reaction storage density to system storage density. *Energy Procedia*, 128-137.

Donkers, P., Sögütoglu, L., Huinink, H., Fischer, H., & Adan, O. (2017). A review of salt hydrates for seasonal heat storage in domestic applications. *Applied Energy*, 199, 45-68.

Jiang, J., Chan, A., Ali, S., Saha, A., Haushalter, K. J., Lam, W.-L. M., . . . Mahon, S. B. (2016). Hydrogen sulfide—mechanisms of toxicity and development of an antidote. *Scientific reports*, 6, 20831.

---

## #65: Sound absorption properties of biomass aerogels for building application

---

Yixin WANG<sup>1</sup>, Yuehong SU<sup>1</sup>, Fatang JIANG<sup>1,2\*</sup>, Saffa RIFFAT<sup>1\*</sup>

<sup>1</sup> Faculty of Engineering, University of Nottingham, University Park, Nottingham, NG7 2RD, UK;

<sup>2</sup> School of Bioengineering and Food Science, Hubei University of Technology, Wuhan 430068, China;

*This study presents the preparation and property characterisation of biomass aerogels as sound absorption building materials. As innovatively sustainable porous materials, four natural, degradable bio-polymers (gelatine, starch, wheat straw, and konjac glucomannan) were chosen as the raw materials to prepare the environmentally friendly biomass aerogels with sound absorption property, through the efficient freeze drying method combined with a sol-gel process. Results indicated that the four components may have different effects on the aerogel pore structure, and the aerogel formula was thus optimised to reach the best sound absorption, and the sound adsorption mechanism was analysed. Appropriate addition of gelatine and starch components could enhance mechanical properties proved by texture profile analysis, and also possibly contributed to the formation of through-hole structures enhancing sound absorption performance verified by microstructure images of biomass aerogels. The presence of wheat straw may cause pore shape changes of biomass aerogel due to the special multi cavities structure. Konjac glucomannan with high flexibility and linearity may work as the aerogel skeleton material. Within the experimental range, biomass aerogel with the optimised formula had an average sound efficiency 0.352, density 0.047 g/cm<sup>3</sup> and porosity 94.46 ± 0.04%. It shows better sound absorption performance than traditional sound absorption cotton (average sound efficiency 0.225). The decomposition temperature of biomass aerogels has been determined to be 282.06 to 354.94°C. These results demonstrate the high sound absorption potential of biomass aerogels for building applications.*

*Keywords: biomass aerogels; natural; sound absorption; building applications*



## 1. INTRODUCTION

In 1972, the World Health Organization announced that noise is a kind of pollutant. Currently, the noise was considered as the most widespread and hardest controlled environment pollution (Bronzaft, 2010; Chen, 2014). Noise can cause negative health effects and has become to one of the three major pollution problems in the world. It will not only affect the human hearing system but also cause some health problems such as high blood pressing (Schmidt, 2015) and increased physiologic stress (Seidman, 2010; Tzivian, 2015). Apart from the influence on human health (Matheson, 2003), noise can accelerate the aging of buildings and machinery, affecting the accuracy of the equipment. Therefore, acoustic insulation materials which can be used in different fields are urgently needed. There is a large number of special sound absorbing materials appeared (Arenas, 2010; Koruk, 2015; Liu, 2016; Hung, 2014).

Currently, there are many types of sound absorbing materials, such as glass fibre (Wang, 2001), metal fibre (Azevedo, 2005), polyethylene foam (Zhao, 2015), ceramic (Wu, 2014), rock (Jamshaid, 2016) and glass wool (Azevedo, 2005) and so on. According to the structure, it can be divided into two categories: porous sound absorbing materials (Sgard, 2005; Rey, 2012; Cao, 2018) and resonant sound absorbing materials (Meng, 2012; Merkel, 2015). For porous sound absorption materials, it has a large number of tiny porous structures, which penetrate each other and communicate with the outside through the surface pores, called open porous. There are two types of open porous, which have great sound absorption properties, one of them opens only at one end called "blind", the other one is open at both ends and known as "through" (Arenas, 2010). Currently, the sound absorbing materials commonly used in the market have some defects. For example, sponges have excellent sound absorbing properties often used in recording studios. However, it has poor damping effect and it is easy to absorb dust; Glass fibres commonly used as sound absorption materials, was formed with good sound insulation property as well as fragile performance which will cause damage to the lungs if inhaled by the human. A new porous material appeared in 1931, Kistler invented an aerogel with a three-dimensional porous structure, which was derived from a gel where the liquid component of the gel has been replaced by gas, forming a solid with extremely low density and a large number of porous (Kistler, 1931). Insisting on low carbon and environment-friendly idea, green and sustainable biomass aerogels have attracted a lot of interests from researchers (Robitzer, 2011).

As one highly potential biomass sources, natural polysaccharide or their derivatives are widely used because of non-toxicity, sustainability and biodegradability. Konjac glucomannan (KGM) is an edible polysaccharide found in the tuber of *amorphophallus konjac* plant (Nair, 2011) with high molecular weight (Williams, 2002) ( $6.8 \times 10^5$ – $9 \times 10^6$ ) and high viscous property (30000 mPa·s, 1%, w/v). With the  $\beta$ -1,4 glycosidic bonds, KGM composed by  $\beta$ -D-glucose and  $\beta$ -D-mannose with the molar ratio about 2:3 or 1:1.16, while the  $\beta$ -1,3 glycosidic bonds exist through the branched structure (Davé, 1997). Starch, an edible, renewable agricultural product is usually used in food or other industrial products (Kenar, 2014). Wheat is cultivated in over 115 nations in the world, produced numerous wheat straw which can be used as sound absorption materials (Zou, 2010; Saadatnia, 2008). Gelatin widely occurs in skin and bone has a special polypeptide, which is formed by both cationic and anionic along with hydrophobic groups (Elzoghby, 2013). KGM (Wang, 2018; Ni, 2016), starch (García-González, 2012; Druel, 2017; Ubeyitogullari, 2018), wheat straw (Wan, 2015; Wang, 2018) and gelatine (Wang, 2016; Jiang, 2019) are widely used for several industrial applications in the field of functional materials because of its biodegradability and biocompatibility. According to the previous research (Wang, 2018), we have constructed a new system to develop biomass aerogels for sound absorption materials.

## 2. EXPERIMENTAL

### 2.1. Materials preparation

The dry wheat straw was obtained from a local farm in Wuhan. After cut into a small segment, the wheat straw was cleaned several times until there are no impurities existed. The wheat straw segment was dried in 90°C oven, minced in the grain crusher and then sieved through the 160 mesh Tyler screen (pore size 94  $\mu$ m). Konjac glucomannan (KGM) is purchased from Hubei Konson Konjac Gum Co., Ltd (Wuhan, China). Gelatine was purchased from Sinopharm Chemical Reagent Co., Ltd. (Shanghai, China). Potato starch was purchased from Wuhan Lin He Ji Food Co., Ltd. (Wuhan, China).

### 2.2. Biomass aerogel preparation

The preparation of biomass aerogels was based on an invention patent of Licheng Biological Technology in China. Gelatine (0-1.5%, w/v) were weighted and added in 50 mL beaker with 20 mL double-distilled water. After half an hour heating in a water bath at 60°C, gelatine was entirely dissolved with the stir of glass rod. The rest of 80 mL double-distilled water was put in a 250 mL beaker with the 90°C bath water heating. The KGM powder (0.5-1.5%, w/v) or KGM powder, wheat straw powder (0.5%-1.5%, w/v) and starch (1%-3%, w/v) was slowly added under constant stirring at 600 rpm, and the dissolved gelatine solution was drained into a 250 mL beaker along with a glass rod. After sealing the beaker mouth with plastic film, the mixture was stirred for 1 h, then poured into a 6 well

plate (diameter 34.8 mm, height 18 mm), and immediately placed in a 4°C refrigerator as pre-freeze for 2 h. The freeze drying process obtains two steps, frozen in an ultra-low temperature freezer (DW-FL262, Rowsen, China) at -25°C for 10 h and dried in a freeze dryer (FD-1A-50, Boyikang, China) at -55°C under a vacuum of 1 Pa for 24 h. The biomass aerogels (diameter 34.8 mm, height 10 mm) were obtained. In order to simplify the description of biomass aerogels, all samples were coded in the form of K0S0G0WS0 (K, S, G, WS represents konjac glucomannan, potato starch, gelatine and wheat straw, respectively), and the number after K, S, G, WS indicates the weight volume percent of origin biomass sol. Prior to the tests, all samples were stored in a dryer with silica gel beads. Before the sound absorption test, biomass aerogel samples were cut into two sizes, diameter 30 mm and diameter 96 mm with the same height 10 mm.

### 2.3. Characterisation of biomass aerogels

#### *Dry density*

The prepared biomass aerogels were measured by the analytical balance and Vernier calliper. All tests were repeated 4 times and the dry density ( $\rho$ ) was calculated with the following Equation 1:

$$\text{Equation 1: } \rho = \frac{m}{V}$$

Where:

- m = weight of biomass aerogels
- V = volume of biomass aerogel samples

#### *Estimation of porosity*

Porosity is an important indicator for determining the structure of biomass aerogels. In this research, the porosity method referred to Shi et al (Shi, 2013). First, dry biomass aerogels were weighted with the mass of  $m_0$ , then completely immersed in a container with ethanol and weighted in total ( $m_1$ ). The container with biomass aerogels and ethanol was placed under a vacuum desiccator and evacuated until no air bubble coming out of biomass aerogels. After the vacuuming process, biomass aerogels were taken out, the containers with residual ethanol were weighted and the mass was recorded as  $m_2$ . Each test was repeated with 4 parallel samples. The porosity of biomass aerogels was calculated as Equation 2:

$$\text{Equation 2: } \text{Porosity} = \frac{\text{Weight of ethanol in sample}}{\text{Total weight of sample and ethanol}} = \frac{m_1 - m_2 - m_0}{m_1 - m_2} \times 100\%$$

#### *Scanning electron microscope and morphology test*

Prior to SEM test, biomass aerogels was cut into 5 mm x 5 mm x 1 mm small cubes with a sharp razor blade. The cube piece samples were fixed on the electron microscope sample stage with conductive glue, and then the surface needs to be observed were coated with gold particles (Bio-Rad type SC 502, JEOL Ltd, Japan) by sputtering for 60 s. The microstructure of biomass aerogels was observed at a magnification of 50X, 100X and 1000X using an accelerated voltage of 30kV.

#### *Texture profile analysis*

The mechanical properties of biomass aerogels were tested by a texture analyser (TA. XT. Plus, Stable Micro Systems, Surrey, UK) through double compression test using a 30kg load cell and a discoidal probe (d=100mm, compression plate type: 10585). The test detailed parameters are as follows: test compression ratio: 60mm / min; compression percentage: 30%; trigger force set to 1.00N in automatic mode. The compressive strength of the samples in the compression test was defined as the maximum stress during the test. Each test was repeated with 4 parallel samples. The stress ( $\sigma$ ) is calculated by the following standard equation:

$$\text{Equation 3: } \sigma = \frac{F}{S_0}$$

Where:

- F = force on the surface of samples.

### *Thermogravimetric analysis (TGA)*

The thermogravimetric test was measured using a Netzsch TG 209 (Thermogravimetric Analyzer, Nexi, Germany). The freeze-dried composite biomass aerogel sample was pulverised by a pulveriser before testing. The sample was heated from 25 °C to 600 °C at a heating rate of 20 °C / min under a nitrogen flow rate of 20 mL/min, and the weight loss curve was recorded.

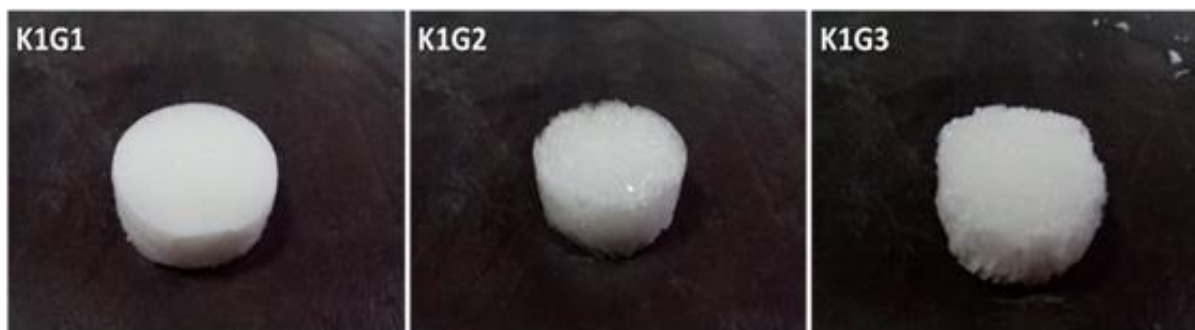
### *Sound absorption coefficient measurement*

The sound absorption coefficient of biomass aerogels was measured at room temperature using an Impedance Tube AWA6122A (Hangzhou Aihua Instruments, China). The biomass aerogels were cut into two different sizes (Diameter 30 mm, height 10 mm and diameter 96 mm, height 10 mm) to test the sound absorption coefficient at the frequency of 125, 250, 500, 1000, 2000 and 4000 Hz. Noise reduction coefficient (NRC) is the average sound absorption coefficient at six different frequencies.

## **3. RESULTS AND DISCUSSION**

### **3.1. Impact of gelatine and wheat straw on the aerogels structure**

It was found that an unusual phase separation was manifested in the KGM/gelatine hydrogels with the KGM addition at 1.5% (w/v). And this phenomenon was discovered by Jennifer C. Harrington (Harrington, **2009**)<sup>40</sup> in 2009. Based on these results, a preliminary experiment was designed with the KGM addition of 1% (w/v) and gelatine concentration increased from 1% to 3%. It can be found from images (as shown in Figure 1) that the appearance of K1G1 and K1G2 is uniform, but when the concentration increased to 3%, the inhomogeneous surface appeared. It has been certificated in our previous research that the existence of gelatine contributes to the amount of open pore structure with large size. These results are consistent in SEM images in Figure 2. With gelatine concentration increased from 1% to 3% (w/v), the pore size of KGM/gelatine aerogels gradually increased. However, when the addition of gelatine increased to 3% (the total solid content doubled), the pore wall of biomass aerogels (K1G3) became thicker leading to the tighter pore structure. Meanwhile, a number of tiny pores formed.



*Figure 1: Digital photograph of KGM/gelatine aerogels*

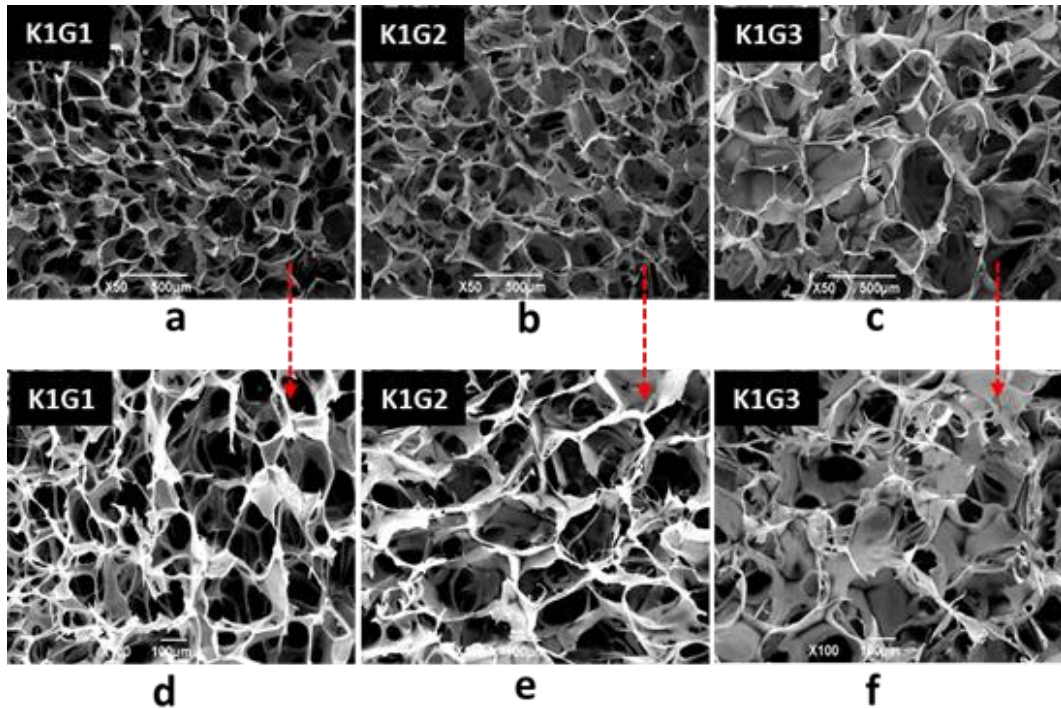


Figure 2: SEM observations of KGM/gelatin aerogels with different concentration with two magnifications (50X and 100X)

Results revealed that the aerogels display three-dimensional network structure (Figure. 3). For biomass aerogels, the KGM molecules act as a skeleton, and the pores are relatively big, spherical and uniform. The presence of wheat straw causes the shape changes of ice crystal formed during freezing, which could affect the distribution of pore size, shape and the connectivity of the porous network. The pure KGM aerogels pore is relative spherical and uniform after wheat straw addition, the aerogel pore was changed from polygons into an irregular shape. Besides, wheat straw can also provide many micron-scale pores due to their multi-cavities as shown in Figure 3.

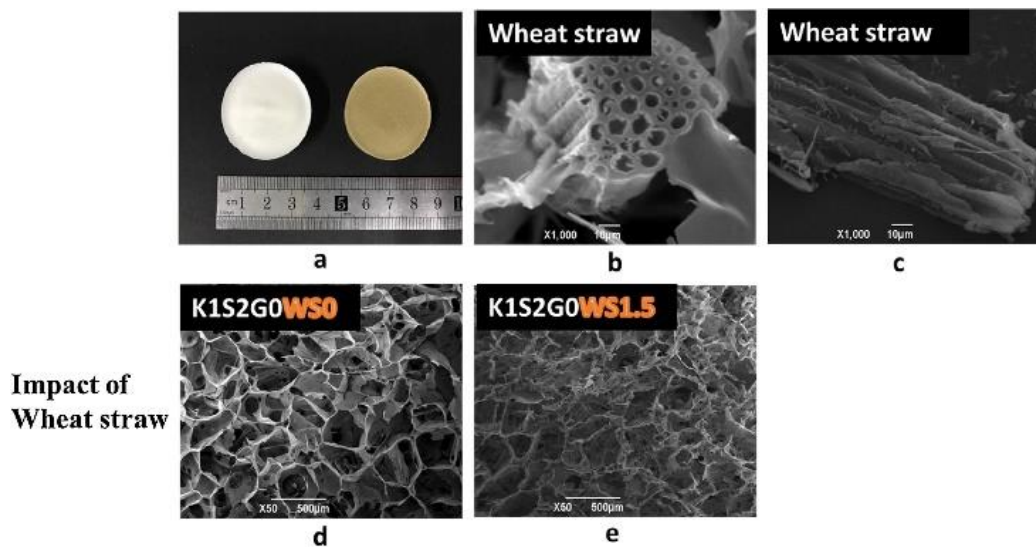


Figure 3: Images of biomass aerogels with and without wheat straw (a), wheat straw (b, c) and SEM observation of biomass aerogels (d, e) (Wang, 2018).

### 3.2. Impact of starch on the mechanical properties of biomass aerogels

Referring to our previous work, pure KGM aerogels have poor mechanical strength. Aerogels are usually used in a specific practical application requiring high compressive stress. Therefore, the mechanical properties of the KGM aerogels were improved by adding starch due to its special branched structure. According to previous experiment

(Wang, 2018) (Figure 4), it has been concluded that the starch addition of 1%, 2%, 3%, 4% can bring improvement of stress by 161%, 956%, 1505%, and 2788%, respectively, compared to the K1 aerogel. However, too high starch concentration does not benefit to the sound absorption capability for the dense pore structure. Therefore, a suitable range of starch addition was selected from 1% to 3%.

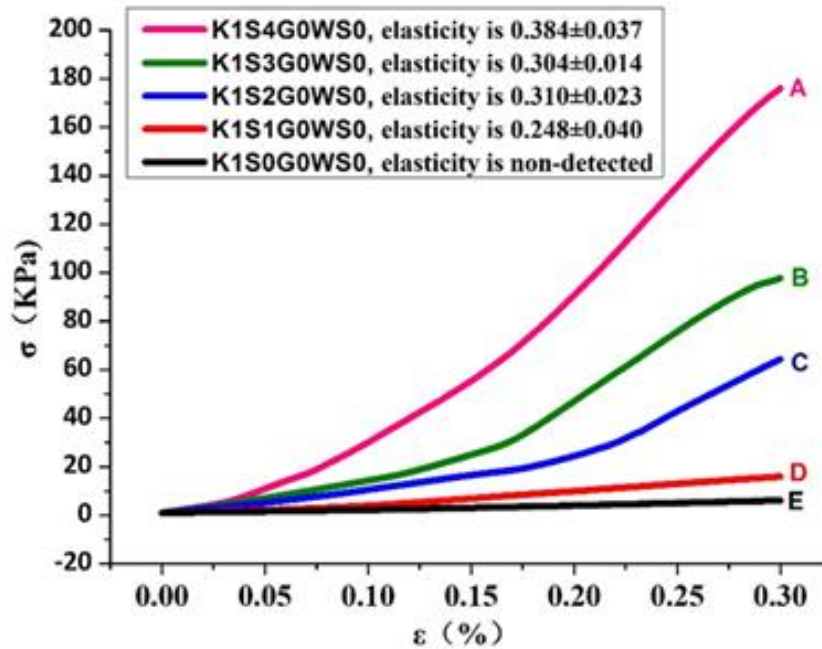


Figure 4: Stress-strain curves for KGM/Starch aerogels with different starch concentration (Wang, 2018).

### 3.3. Sound absorption property

Based on the characteristic of selected raw materials and above discussion, an L9 (3)<sup>4</sup> orthogonal array test was executed and the impact of different components and concentrations on the sound absorption coefficient were analysed. The optimised biomass aerogels formula was obtained. Nine different biomass aerogels were designed through three levels (different concentration) and four factors (four different raw materials). K1S1G1WS1, K1.5S1G0.5WS1.5 and K1.5S2G1WS0.5 were selected from the orthogonal experiments to compare the cross profile and surface by SEM images. With the addition of wheat straw, the pore structure became complex, as shown in Figure 5. The comparison of surface microstructure images between four different samples has been shown in Figure 5. For the low total solid content, K0.5S1G00WS0.5 composed of large size pore structure which connected to each other presenting full through-hole structure. Sound waves are easier to pass through the full through-hole structure with low flow resistance, leading to less sound energy loss. Therefore, the sound absorption performance of K0.5S1G00WS0.5 was poor though the pore structure of K1.5S1G0.5WS1.5, K1.5S2G1WS0.5 and K1S1G1WS1 were gradually increased (Figure 5 d, f, b), adjusted by the amount of gelatine and starch. With the appropriate addition of starch, the concentration of gelatine was positively related to the number of through pores. A significant difference was shown in Figure 6 that K1S2G0WS1.5 has some close pores in the surface, while K1S1G1WS1 has a large number of through pores distributing in the surface.

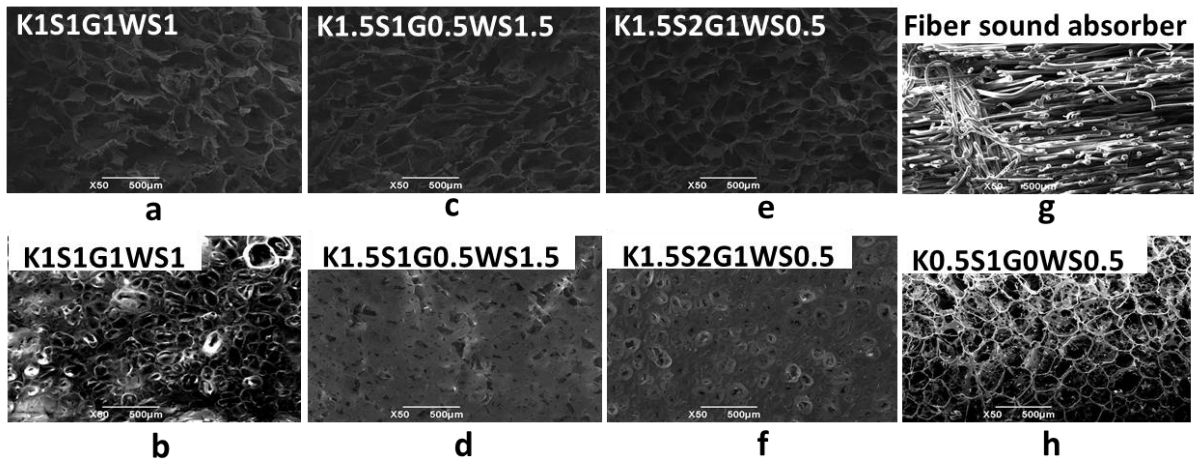


Figure 5: Sectional (a, c, e) and surface (b, d, f, h) SEM observations of composite aerogels with different proportions and traditional sound-absorbing fibreboards (g)

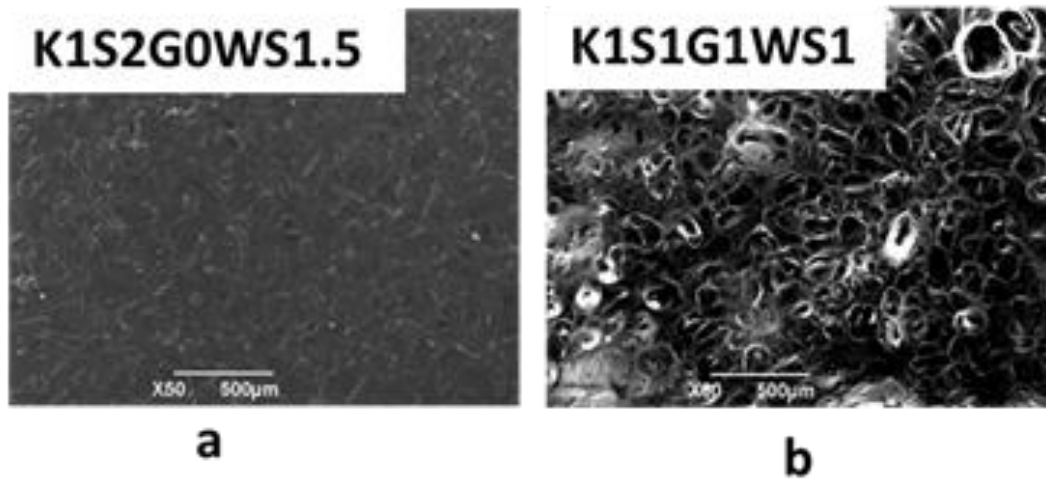


Figure 6: Surface SEM observations of composite aerogels with best thermal insulation properties (a) and through-hole (b)

The higher sound absorption coefficient was observed among different biomass aerogels. Based on the sound absorption coefficient test results of 9 different biomass aerogels, k and Range values were calculated out and the results indicated the impact of ingredients concentration on the sound absorption coefficient followed the order: gelatin > starch > KGM > wheat straw. The optimised biomass aerogels formula with good sound absorption ability was calculated to be K1S2G1WS1.5. To confirm this, K1S2G1WS1.5 aerogels were prepared and its density and porosity were  $0.047 \text{ g/cm}^3$  and  $94.46 \pm 0.0383\%$ , respectively. The sound absorption coefficient of K1S2G1WS1.5 was measured to be 0.352, a little higher than K1S1G1WS1 (0.334). Compared with K1S1G1WS1, the increasing of starch and wheat straw may enhance sound absorption ability. The higher concentration of starch could increase the bulk density and the higher content of wheat straw could bring higher porosity.

Table 1: Analysis of L9 (3)<sup>4</sup> sound efficiency test results

Sample code	KGM	Starch	Gelatin	Wheat straw	The average sound absorption coefficient
K0.5S1.0G0WS0.5	0.5	1.0	0	0.5	0.268
K0.5S2.0G0.5WS1.0	0.5	2.0	0.5	1.0	0.295
K0.5S3.0G1.0WS1.5	0.5	3.0	1.0	1.5	0.285
K1.0S2.0G0WS1.5	1.0	2.0	0	1.5	0.310
K1.0S3.0G0.5WS0.5	1.0	3.0	0.5	0.5	0.296
K1.0S1.0G1.0WS1.0	1.0	1.0	1.0	1.0	0.335
K1.5S3.0G0WS1.0	1.5	3.0	0	1.0	0.114
K1.5S1.0G0.5WS1.5	1.5	1.0	0.5	1.5	0.315
K1.5S2.0G1.0WS0.5	1.5	2.0	1.0	0.5	0.324

k1	0.28267	0.23067	0.30567	0.29600
k2	0.31333	0.30200	0.30967	0.05056
K3	0.25100	0.31433	0.23167	0.30333
Range	0.06233	0.08367	0.07800	0.05567
Optimal level	G > S > KGM > WS			
Major factor (w/v)	1%	2%	1%	1.5%
Optimised formula	K1S2G1WS1.5			0.352

Table 2: Aerogels formulae and porosity, density testing results

Sample	Porosity (%)	Density (g/cm <sup>3</sup> )
K0.5S1.0G0WS0.5	97.17 ± 0.03	0.0201 ± 0.0002
K0.5S2.0G0.5WS1.0	93.76 ± 0.09	0.0410 ± 0.0006
K0.5S3.0G1.0WS1.5	94.28 ± 0.08	0.0524 ± 0.0015
K1.0S2.0G0WS1.5	93.28 ± 0.06	0.0409 ± 0.0013
K1.0S3.0G0.5WS0.5	92.65 ± 0.05	0.0506 ± 0.0001
K1.0S1.0G1.0WS1.0	94.43 ± 0.04	0.0358 ± 0.0010
K1.5S3.0G0WS1.0	92.49 ± 0.07	0.0471 ± 0.0015
K1.5S1.0G0.5WS1.5	93.80 ± 0.05	0.0392 ± 0.0006
K1.5S2.0G1.0WS0.5	94.40 ± 0.02	0.0437 ± 0.0008
K1S2G1WS1.5(Optimised formula)	94.46 ± 0.04	0.0470 ± 0.0005

After the orthogonal formula assay, the sound absorption coefficient, density and porosity were tested. From the sample listed in Table 1 and 2, we selected three biomass aerogels with better sound absorption performance (K1S2G1WS1, K1.5S2G2WS0.5 and K1.5S1G0.5WS1.5) to analyse the impact of pore structures on sound absorption coefficient. Biomass aerogels with good sound absorption performance have high porosity and low density, porosity was around 93% to 94% and the density is about 0.35 to 0.45 g/cm<sup>3</sup>. Under certain thickness (1 cm), porosity and density are the important factors influencing sound absorption performance. With the appropriate density and porosity, sound waves are subjected to flow resistance as they pass through the pores, consuming acoustic energy. Meanwhile, with high porosity, such as K0.5S1G0WS0.5, the friction between the sound wave and pore structure was limited leading to low sound energy conversion efficiency.

The sound absorption coefficient curves showed the samples had excellent sound absorption performance in medium-high frequency. In Figure 7, the sound absorption coefficient was about 0.1 at 500 Hz 0.8 at 4000 Hz. Compared with traditional fiber cotton sound absorbing board (the average sound absorption coefficient 0.225), the biomass aerogels showed significant excellent characteristics.

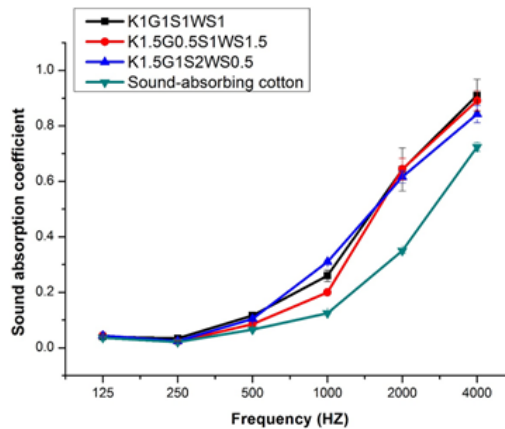


Figure 7: Sound absorption efficiency of composite aerogels (K1S1G1WS1, K1.5S1G0.5WS1.5, K1.5S2G1WS0.5) and sound absorbing board

### 3.4. Mechanical property

On the results of sound absorption performance, three representative samples were selected to test the mechanical properties. From the stress-strain curves as Figure 8, K1.5S2G1WS0.5 showed best compressive strength, nearly 3 times higher than the compressive strength of K1.5S1G0.5WS1.5. Starch is the factors affecting the mechanical properties of biomass aerogels.

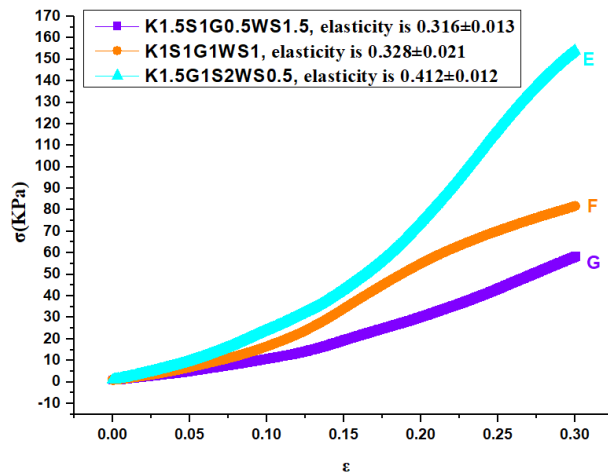


Figure 8: Stress-strain curves for composite aerogels prepared from the different constitution

### 3.5. Thermogravimetric analysis

TG curves (Figure 9) and detail data (Table 3) indicated the biomass aerogels were decomposed in two steps. At around 100°C, the first stage of mass loss appeared, caused by the dehydration of biomass aerogels. With the porous structure and hydrophilic properties, there was still some water in biomass aerogels. The second mass loss stage is caused by the pyrolysis of polysaccharides and protein. The mass loss stage for K1S1G1WS1 was from 282.06–354.94 °C. The thermal stability of biomass aerogels was good.

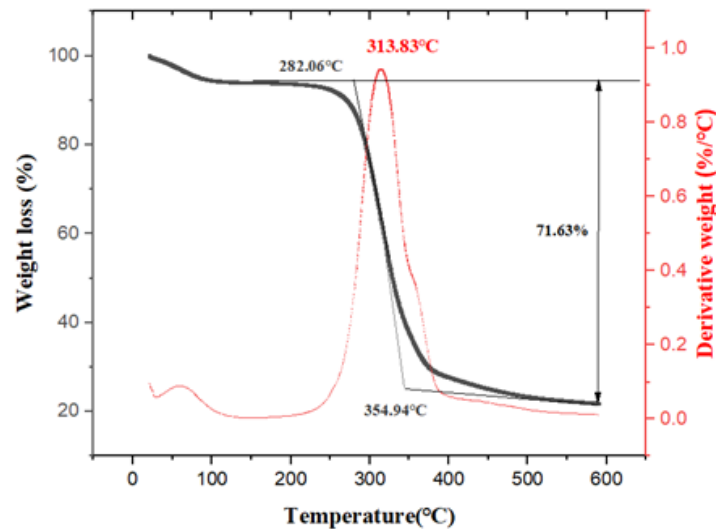


Figure 9: TGA of composite aerogels

Table 3: Parameters obtained from TG curves

Sample	EIDT/ °C	EEDT/ °C	Mass loss until 600°C /%	T <sub>v-max</sub> / °C
K1S1G1WS1	282.06	354.94	71.63%	313.83

Where: EIDT presents: epitaxial initial decomposition temperature; EEDT presents: epitaxial end decomposition temperature; T<sub>v-max</sub> presents: temperature of maximum thermal decomposition velocity.



## 4. CONCLUSION

Biomass aerogels were prepared via the freeze-drying method. The microstructure of aerogels was observed by SEM. The sound absorption coefficient of biomass aerogels has been tested. The optimised biomass aerogel sample for sound absorption was determined to be K1S2G1WS1.5, with its average sound absorption coefficient 0.352, density 0.047 g/cm<sup>3</sup> and porosity 94.46 ± 0.04%. The contribution of different components and their concentration on sound absorption property, density and porosity have been investigated. The SEM images showed the appropriate addition of gelatin and starch could improve the performance of sound absorption with the specific pore structure in biomass aerogels. The texture test and TG test evaluated the application potential of biomass aerogels. Results from the study demonstrate the possibility of biomass aerogels as sound absorption material in building applications.

## 5. REFERENCES

- Arenas, J. P.; Crocker, M. J., Recent trends in porous sound-absorbing materials. *Sound & vibration* **2010**, *44* (7), 12-18.
- Azevedo, L. J.; Nabuo, M. In *Sound absorption of sisal fiber panels*, INTER-NOISE and NOISE-CON Congress and Conference Proceedings, Institute of Noise Control Engineering: 2005; pp 1806-1811.
- Bronzaft, A. L.; Hagler, L., Noise: The Invisible Pollutant that Cannot Be Ignored. In *Emerging Environmental Technologies, Volume II*, Shah, V., Ed. Springer Netherlands: Dordrecht, 2010; pp 75-96.
- Cao, L.; Fu, Q.; Si, Y.; Ding, B.; Yu, J., Porous materials for sound absorption. *Composites Communications* **2018**, *10*, 25-35.
- Chen, D. R.; Chang, X. H.; Jiao, X. L., Chapter 22 - Aerogels in the Environment Protection. In *The Role of Colloidal Systems in Environmental Protection*, Fanun, M., Ed. Elsevier: Amsterdam, 2014; pp 573-591.
- Davé, V.; McCarthy, S. P., Review of konjac glucomannan. *Journal of environmental polymer degradation* **1997**, *5* (4), 237.
- Druel, L.; Bardl, R.; Vorwerg, W.; Budtova, T., Starch Aerogels: A Member of the Family of Thermal Superinsulating Materials. *Biomacromolecules* **2017**, *18* (12), 4232-4239.
- Elzoghby, A. O., Gelatin-based nanoparticles as drug and gene delivery systems: Reviewing three decades of research. *Journal of Controlled Release* **2013**, *172* (3), 1075-1091.
- García-González, C. A.; Uy, J. J.; Alnaief, M.; Smirnova, I., Preparation of tailor-made starch-based aerogel microspheres by the emulsion-gelation method. *Carbohydrate Polymers* **2012**, *88* (4), 1378-1386.
- Hung, T.-C.; Huang, J.-S.; Wang, Y.-W.; Lin, K.-Y., Inorganic polymeric foam as a sound absorbing and insulating material. *Construction and Building Materials* **2014**, *50*, 328-334.
- Jamshaid, H.; Mishra, R., A green material from rock: basalt fiber – a review. *The Journal of The Textile Institute* **2016**, *107* (7), 923-937.
- Kenar, J. A.; Eller, F. J.; Felker, F. C.; Jackson, M. A.; Fanta, G. F., Starch aerogel beads obtained from inclusion complexes prepared from high amylose starch and sodium palmitate. *Green Chemistry* **2014**, *16* (4), 1921-1930.
- Kistler, S. S., Coherent expanded aerogels and jellies. *Nature* **1931**, *127*, 741-741.
- Koruk, H.; Genc, G., Investigation of the acoustic properties of bio luffa fiber and composite materials. *Materials Letters* **2015**, *157*, 166-168.
- Liu, Z.; Zhan, J.; Fard, M.; Davy, J. L., Acoustic properties of a porous polycarbonate material produced by additive manufacturing. *Materials Letters* **2016**, *181*, 296-299.
- Matheson, M. P.; Stansfeld, S. A., Noise pollution: non-auditory effects on health. *British Medical Bulletin* **2003**, *68* (1), 243-257.

- Meng, H.; Wen, J.; Zhao, H.; Wen, X., Optimization of locally resonant acoustic metamaterials on underwater sound absorption characteristics. *Journal of Sound and Vibration* **2012**, *331* (20), 4406-4416.
- Merkel, A.; Theocharis, G.; Richoux, O.; Romero-García, V.; Pagneux, V., Control of acoustic absorption in one-dimensional scattering by resonant scatterers. *Applied Physics Letters* **2015**, *107* (24), 244102.
- Nair, S. B.; Jyothi, A. N.; Sajeev, M. S.; Misra, R., Rheological, mechanical and moisture sorption characteristics of cassava starch-konjac glucomannan blend films. *Starch - Stärke* **2011**, *63* (11), 728-739.
- Ni, X.; Ke, F.; Xiao, M.; Wu, K.; Kuang, Y.; Corke, H.; Jiang, F., The control of ice crystal growth and effect on porous structure of konjac glucomannan-based aerogels. *Int J Biol Macromol* **2016**, *92*, 1130-1135.
- Rey, R. d.; Alba, J.; Arenas, J. P.; Sanchis, V. J., An empirical modelling of porous sound absorbing materials made of recycled foam. *Applied Acoustics* **2012**, *73* (6), 604-609.
- Robitzer, M.; Renzo, F. D.; Quignard, F., Natural materials with high surface area. Physisorption methods for the characterization of the texture and surface of polysaccharide aerogels. *Microporous and Mesoporous Materials* **2011**, *140* (1), 9-16.
- Saadatnia, M.; Ebrahimi, G.; Tajvidi, M. In *Comparing sound absorption characteristic of acoustic boards made of Aspen particles and different percentage of Wheat and Barely straws*, 17th world conference on Non-destructive Testing, 2008.
- Schmidt, F.; Kolle, K.; Kreuder, K.; Schnorbus, B.; Wild, P.; Hechtner, M.; Binder, H.; Gori, T.; Münzel, T., Nighttime aircraft noise impairs endothelial function and increases blood pressure in patients with or at high risk for coronary artery disease. *Clinical Research in Cardiology* **2015**, *104* (1), 23-30.
- Seidman, M. D.; Standring, R. T., Noise and Quality of Life. *International Journal of Environmental Research and Public Health* **2010**, *7* (10), 3730-3738.
- Sgard, F. C.; Olney, X.; Atalla, N.; Castel, F., On the use of perforations to improve the sound absorption of porous materials. *Applied Acoustics* **2005**, *66* (6), 625-651.
- Tzivian, L.; Winkler, A.; Dlugaj, M.; Schikowski, T.; Vossoughi, M.; Fuks, K.; Weinmayr, G.; Hoffmann, B., Effect of long-term outdoor air pollution and noise on cognitive and psychological functions in adults. *International Journal of Hygiene and Environmental Health* **2015**, *218* (1), 1-11.
- Ubeyitogullari, A.; Brahma, S.; Rose, D. J.; Ciftci, O. N., In Vitro Digestibility of Nanoporous Wheat Starch Aerogels. *Journal of Agricultural and Food Chemistry* **2018**, *66* (36), 9490-9497.
- Wan, C.; Lu, Y.; Jiao, Y.; Jin, C.; Sun, Q.; Li, J., Fabrication of hydrophobic, electrically conductive and flame-resistant carbon aerogels by pyrolysis of regenerated cellulose aerogels. *Carbohydrate Polymers* **2015**, *118*, 115-118.
- Wang, C.-N.; Torng, J.-H., Experimental study of the absorption characteristics of some porous fibrous materials. *Applied Acoustics* **2001**, *62* (4), 447-459.
- Wang, Y.; Wu, K.; Xiao, M.; Riffat, S. B.; Su, Y.; Jiang, F., Thermal conductivity, structure and mechanical properties of konjac glucomannan/starch based aerogel strengthened by wheat straw. *Carbohydr Polym* **2018**, *197*, 284-291.
- Williams, P. A.; Phillips, G. O.; Crosby, G., Managing healthy levels of Blood glucose and cholesterol with konjac flour. **2002**.
- Wu, G.; Li, R.; Yuan, Y.; Jiang, L.; Sun, D., Sound absorption properties of ceramic hollow sphere structures with micro-sized open cell. *Materials Letters* **2014**, *134*, 268-271.
- Zhao, T.; Yang, M.; Wu, H.; Guo, S.; Sun, X.; Liang, W., Preparation of a new foam/film structure poly (ethylene-co-octene) foam materials and its sound absorption properties. *Materials Letters* **2015**, *139*, 275-278.
- Zou, Y.; Huda, S.; Yang, Y., Lightweight composites from long wheat straw and polypropylene web. *Bioresource Technology* **2010**, *101* (6), 2026-2033.

---

## #67: Bio gasoline production from rubber seed oil using Ni/HY zeolite and Mo/HY zeolite as catalysts

---

Muhammad SYAAMIL<sup>1</sup>, Mariam AMEEN<sup>2</sup>, Haswin KAUR<sup>3</sup>, Suzana YUSUP<sup>4</sup>, Mohammad Tazli AZIZAN<sup>5</sup>, Aqsha AQSHA<sup>6</sup>

*Centre of Bio-fuel and Biochemical Research (CBBR), Institute of Sustainable Living (ISL), Department of Chemical Engineering, Universiti Teknologi PETRONAS, Perak, Malaysia,*

<sup>1</sup>syaamilsaad@gmail.com

<sup>2</sup>mariam.ameenkk@gmail.com

<sup>3</sup>haswin.kaur@gmail.com

<sup>4</sup>drsuzana\_yusuf@utp.edu.my

<sup>5</sup>tazliazizan@utp.edu.my

<sup>6</sup>aqsha@utp.edu.my

*Crude rubber seed oil was used in this study to determine the ability of the oil to produce bio gasoline. Catalytic cracking of rubber seed oil over zeolites of HY supporting Ni and Mo catalysts was carried out with limited amount of research of bio gasoline production from rubber seed oil. The objective of the study is to investigate the effect of metal loading on bio gasoline yield and composition. Nickel and Molybdenum were chosen as the metallic function of the catalysts due to hydro processing catalysts. Three different metal loadings of Ni and Mo were studied which are 3%, 12% and 15 % to investigate the effect of different amount of metal on the catalytic activity for hydrocracking of rubber seed oil into bio gasoline products. All the catalysts were subjected to characterisation techniques such as BET, H<sub>2</sub>TPR, FESEM to understand the physicochemical properties of the catalysts. At initial condition, the variables are fix at 400°C, 4 grams of catalyst, 1atm pressure under nitrogen flow for 3 hours reaction time in hydrocracker reactor for initial screening of the catalysts. The conversion of rubber seed oil into bio gasoline components were measured ranging from C5-C12 hydrocarbons. Among all the metal loadings of both metals, 3% Nickel on HYZ was found to be the most efficient due to highest conversion of rubber seed oil into bio gasoline. This is due to the high surface area, large pore size and pore volume. The screened catalysts i.e. 3 wt% Ni/H-Zeolite was chosen for optimisation of temperature. The effect of temperature was observed by increasing temperature from (300-500°C). The optimised temperature was observed at 400°C at which bio gasoline relative composition was 43.15%. The results proved that rubber seed oil has high potential to be utilised as an alternative energy resource for bio gasoline production.*

*Keywords: bio gasoline; rubber seed oil; catalytic cracking; catalysts screening; optimization of temperature*

## 1. INTRODUCTION

Alternatives to fossil fuel have been developed to tackle the natural resource depletion since last decades. Crops and seeds oil from various plants are becoming subjects of research due to the high contents sugar and oil. Until now, oil extracted from vegetables also shows promising results on production of renewable fuels. However, due to the argument over food vs. fuel, research has been focused on non-edible food crops, and these non-edible crops are considered as source of renewable fuels production (Ameen et al., 2017b, Ameen et al., 2019b, Ameen et al., 2019a, Arun et al., 2015). Among the various feedstock, non-edible oil such as rubber seed oil was found one of the potential sources for biofuel production and have been research since early 20<sup>th</sup> century (Ahmad et al., 2014, Ameen et al., 2019a, Ameen et al., 2019b, Bokhari et al., 2016a, Bokhari et al., 2016b, Dhawane et al., 2018, Ameen et al., 2017a). Due to large scale plantation of rubber especially in South East Asia, rubber seed is considered as one of the major source for the production of biofuels after palm oil (Widyarani et al., 2014). Production of rubber from Malaysia, Indonesia and Thailand combined covers two third rubber harvested area of the world (Widyarani et al., 2014). This open the opportunity of benefiting the part of the rubber tree which was known before as profitless product. With abundant sources of rubber trees in Malaysia, the raw material supply of rubber seed would be an advantageous for the continuation of biofuels project. Generally, there are various process that can be used to produce biofuels from non-edible oil, including conventional process such as transesterification, and advanced techniques such as hydrotreating, pyrolysis and hydrocracking. Catalytic cracking is a process of converting long chain hydrocarbons to lower molecular weight hydrocarbon compounds in the presence of catalyst. In fact, this process is homologous to petroleum refinery process which is widely used to produce saturated hydrocarbons mainly gasoline, jet fuels and diesel range hydrocarbons (Speight, 2019). There are several researches on conversion of edible oil to bio-gasoline such as sunflower oil, rapeseed oil, vegetable oil, canola oil as well as palm oil (Al-Sabawi et al., 2012). However, food scarcity due to utilisation of edible oil as sources for bio-gasoline production were argued and need to be minimised (Ahmad Fadzil Ahmad Shuhaili, 2016, Al-Sabawi et al., 2012). Therefore, the production of bio-gasoline from edible oils are limited and only can be produce in low amount. Rubber seed oil however is non-edible and has no major application, is found to be very suitable for exploration in bio-gasoline production.

Catalyst design is an important part of catalytic cracking, it mainly depends on physiochemical properties of the catalysts such as acidity, surface area, particle size and crystallite structure. It is well known that solid acid catalysts are most promising catalysts, used for cracking of long chain hydrocarbons into small chain hydrocarbons due to high acidity. Zeolite was known for its properties that can sort molecules mainly based on size exclusion, due to the regular pore structure of molecular dimensions. In previous studies, Nickel and Cobalt are widely used in hydrocracking process to produce biofuels, along with few other catalysts. Therefore, zeolite family has been widely used for catalytic cracking of triglycerides into bio gasoline. There are several types of zeolites such as ZSM-5, Y-zeolite, Zeolite Beta, and USY zeolite depending on their frame structure and acidity, pore size and pore volume (Li et al., 2015, Ameen et al., 2017b). Therefore, proper catalysts design, and metal loading is important for catalytic cracking (Phimsen et al., 2017). Other important factor is operating parameters such as temperature, pressure and weight hourly space velocity. Several studies have been performed to optimise the reaction parameters for bio gasoline production using different catalysts and different feedstock (Al-Sabawi et al., 2012, Corma et al., 2007, Jamil et al., 2014, Speight, 2019). It is well reported that temperature and weight hour space velocity are most influential factors. Therefore, utilisation of new catalyst design and feedstock can change the optimised conditions and composition of bio gasoline (Zandonai et al., 2016, Jamil et al., 2014).

In the present study, the process highlighted for the production of bio-gasoline from rubber seed oil via catalytic cracking. The catalytic cracking of rubber seed oil involves mainly types of catalysts (mostly zeolites) and metal loading as well as operating parameters. However, in the production of bio gasoline, Ni and Mo are rarely use especially with rubber seed oil as raw material. In this study, the in cooperation of Ni and Mo over H-Yzeolite as monometallic catalyst are investigated and subjected to determine the optimum temperature for a higher relative bio-gasoline composition from rubber seed oil using GC-FID. The objectives of this study are to characterise and screen the Ni/HY zeolite and Mo/HY zeolite catalysts among different metal loading for the catalytic cracking of rubber seed oil and best metal loading catalyst is selected to determine the optimum temperature for highest conversion of rubber seed oil and relative composition of bio gasoline.

## 2. METHODOLOGY

The research methodology includes the catalysts preparation with different metal loadings, screening of the catalysts for catalytic reaction of rubber seed oil and optimisation of temperature over screened catalyst.

### 2.1. Catalyst preparation

Three sets of catalysts were prepared by conventional wet impregnation method. All the catalysts denoted as xNi/HY zeolite and xMo/HY zeolite, where "x" is metal loading 3, 12, and 15 wt% of metal (Ni or Mo). The

corresponding series of catalysts were prepared using  $\text{Ni}(\text{NO}_3)_2 \cdot 6\text{H}_2\text{O}$  and  $(\text{NH}_4)_6\text{Mo}_7\text{O}_{24}$  (with predetermined amount of wt% of Ni and Mo) as precursors of Ni and Mo respectively. The aqueous solutions of  $\text{Ni}(\text{NO}_3)_2 \cdot 6\text{H}_2\text{O}$  were prepared in de-ionized water separately for each formulation. The aqueous solutions of Ni and Mo salts were prepared and doped with predetermined amount of H-Y zeolite as support with continuous stirring of (350 rpm) for 4 h at room temperature. The obtained solutions were dried at 120°C for 12 h in dry oven and calcined at 550°C for 6 h. All the prepared catalysts were subjected to characterisation techniques.

## 2.2. Catalyst characterisation

All the catalysts formulations have been characterised by FESEM, EDX and dot mapping, to evaluate the morphology and metal distribution, BET analysis by ASAP 2020 for surface area, pore volume and pore size determination and hydrogen temperature program reduction for reduction to determine the activation temperature of the catalysts.

## 2.3. Catalyst screening

Prior to the screening of the catalysts, all the catalysts were subjected to the reduction process. The reduction temperature of the catalysts was determined using hydrogen temperature program reduction. All the catalysts were reduced under purified hydrogen gas at 600°C with flow rate of 50 mL/min for 2 hours in a continuous fixed bed reactor. After reduction process, the reactor was purged with nitrogen for 3 h in order to avoid the hydrogen interference during catalytic cracking reaction. The reaction conditions for screening of the catalysts were set as 350°C, WHSV 4 h<sup>-1</sup>, pressure 1 bar and reaction time 3 h in hydrocracker reactor. The higher WHSV and lower temperature was selected in order to observe the conversion of rubber seed oil at minimum contact time. When reaction conditions were stabilised, rubber seed oil was poured into a beaker and was pre-heated gently to ensure a homogenous mixture of oil rubber seed oil and pump with help of HPLC pump with flow rate of 0.245 mL/min into the reactor. The products obtained were analysed through GC-FID based on carbon number.

## 2.4. Temperature optimisation of catalytic cracking of rubber seed oil

Among all the variables such as temperature, pressure, WHSV, temperature was observed to be the most influential factor that influenced the hydrocracking as reported (Doronin et al., 2012, Zheng et al., 2017). Among all the catalysts the 3 wt% Ni/H Y zeolite was chosen as the best catalyst for gasoline composition. The optimisation of temperature runs was performed at 300-500°C for 3 h. For all samples obtained during process optimisation were analysed for comparison of the highest hydrocarbon in gasoline range. 4 grams of catalyst of 3% Ni on HY zeolite catalyst that has been used under the similar reaction condition keeping constant other reaction parameters such as WHSV 4 h<sup>-1</sup>, pressure 1 bar and temperature varied from 300-500°C using 4 grams of the catalysts. After reaction performed the product was collected at room temperature (25°C). All the liquid products obtained were analysed using GC-FID ASTM D2887 method.

## 2.5. Product analysis

Gas Chromatography-Flame Ionization Detector (GC-FID) was used to determine the formation of bio gasoline in the oil sample. GC-FID was chosen because of the ability to detect desired compounds with accuracy. The hydrocarbons that are interested in ranged from C5-C12 which represents gasoline compounds. The method used was an oven ramp, with temperature of 100°C as initial temperature. From 70 – 150°C, 5°C/min was the increment and 30°C until 200°C. A holdup of 10 minutes with 5°C/min increment from temperature of 200 to 300°C. A split injector of 10:5:1 was fixed with temperature detector for GC-FID set at 300°C.

# 3. RESULTS AND DISCUSSION

## 3.1. Characterisation of Catalyst

Table 1 illustrates the textural properties of synthesised catalysts i.e. surface area, pore size, and pore volume, using N<sub>2</sub> adsorption isotherms method. It is predefined that with increase of wt% of Ni and Mo loading, surface area significantly decreases whereas, pore size, and pore volume increase to some extent. The reduction in surface area, possibly due to blockage of zeolite channels by metal oxides. These observations are in agreement with the reduction of surface area for impregnated Ni/HY zeolite catalysts attributed from literature (Lin et al., 2014). Whereas, increment of pore size and pore volume is mainly due to insertion of metal oxide into the pores of zeolite channels which possess strong binding energy. It obvious from Table 1 that metal oxides due to their particle size always behave differently, as compared to Ni loading on to the zeolite support Mo loading significantly affected the pore size and pore volume, which is in favour of hydrocracking reactions. Higher surface area, larger pore volume and pore size (mesoporous range i.e. 2-50 nm) helps to accelerate the rate of adsorption and desorption

phenomena particularly long chain fatty acids or triglycerides. From the isotherm linear plot obtained in Figure 1, nitrogen gas was flowed to determine the adsorption and desorption rate on the catalyst. Result obtained from Figure 1 has shown 3% Ni has the highest adsorption and desorption rate, followed by 12% Ni, 15% Ni, 3% Mo, 15% Mo and 12% Mo. High adsorption rate is caused by mesoporous pore size. The hysteresis type (IV) is observed among all the catalysts. The pore structure is probably representing here as narrow slit shape. Which is evident from FESEM analysis discussed later in this section. The overview on BET surface area and physical adsorption and desorption property revealed that the present structure might be favourable for the conversion bulky molecular structure of rubber seed oil to small chain hydrocarbons present in gasoline.

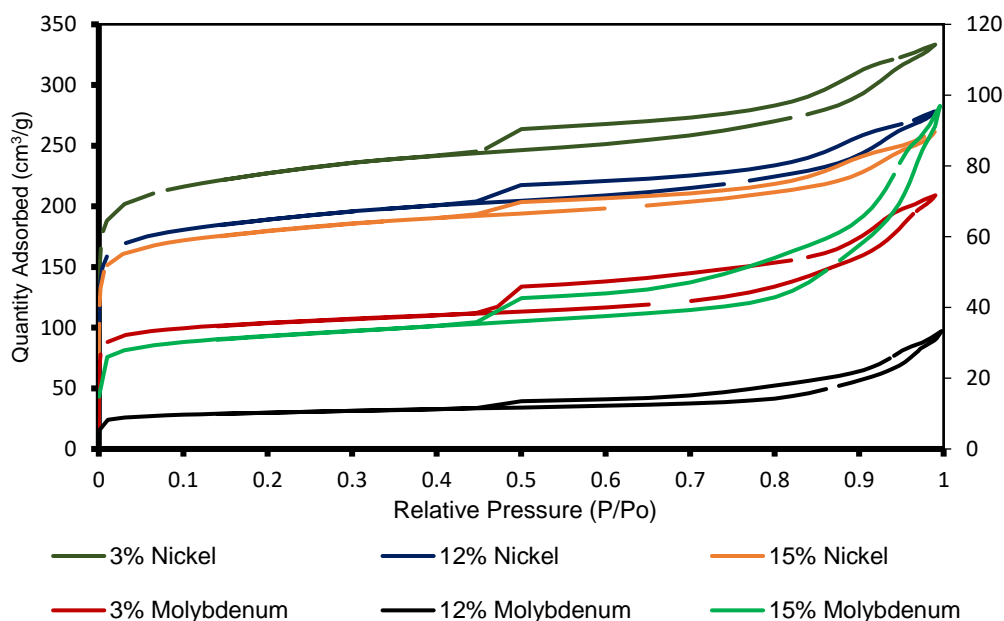


Figure 1: Isotherm linear plot for 3 wt% 12 wt% and 15 wt% of Nickel and Molybdenum on HYZ catalyst

Table 1: Properties of catalyst pore structure

Catalyst	BET surface area (m <sup>2</sup> /g)	Pore Volume (cm <sup>3</sup> /g)	Pore Size (nm)
HYZ	794.57	0.51	2.63
3% Ni	745.17	0.51	2.77
12% Ni	619.82	0.42	2.73
15% Ni	586.61	0.39	2.71
3% Mo	339.08	0.31	3.73
12% Mo	298.99	0.13	5.55
15% Mo	105.17	0.13	5.24

Figure 2 shows the morphology and textural properties of all Ni/HY zeolite and Mo/HY zeolite catalysts. The crystalline structure of the catalyst was observed to be evenly dispersed with very less agglomeration in low metal loadings. This might promote the higher surface area of the catalyst for higher catalytic cracking. It is clear from the FESEM images of 3% Mo/HY zeolite morphology in Figure 2, that it is observed to be almost indistinguishable to 3% Ni/ HY zeolite due to evenly distributed metal particles over the support HY zeolite. Similarly, 12 wt% Ni conversely contains small crystalline structure embedded on the surface of the support and the structure of the catalyst that is uneven compared to both 3 wt% of Ni and Mo loading. This is mainly due to the blockage of the pores of the HY zeolite channels that ultimately reduces adsorption surface area. Whereas, comparing the 12% Mo/ HY zeolite catalyst with homologue of Ni loading is more evenly distributed but the slight agglomeration might decrease the activity of the catalysts. Similar results were observed in 15 wt% loading Ni and Mo with high agglomeration of particles which is evidence from dot mapping of respective catalysts. Figure 2 shows 15% Ni agglomerated the most among the other Nickel catalyst reduced the surface area which could cause low conversion of rubber seed oil into gasoline. Figure 2 shows dot-mapping inset EDX spectra of all synthesised catalysts respectively. This is noticeable from the FESEM images that the Ni particles are homogeneously dispersed over the external surface of HY zeolite. FESEM images shows NiO exists in cubic and Mo exists in orthorhombic structures and relatively large particle size over the external surface of the zeolite which shows that impregnation of Ni and Mo did not affect the morphology of zeolite. EDX spectra also confirmed the Ni and Mo dispersion

consistently, even with low metal loading. The homogeneous dispersion can be observed in dot-mapping images of all catalysts. The slightly homogenous dispersion of metal particle on the surface of catalysts may enhanced the catalytic properties due to serving H atom for hydrogenation reaction as it evident from literature that the Ni particle embedded within the channels of zeolite blocked the pore volume, reduced the surface area and slightly increased the pore size (Subsadsana and Ruangviriyachai, 2016).

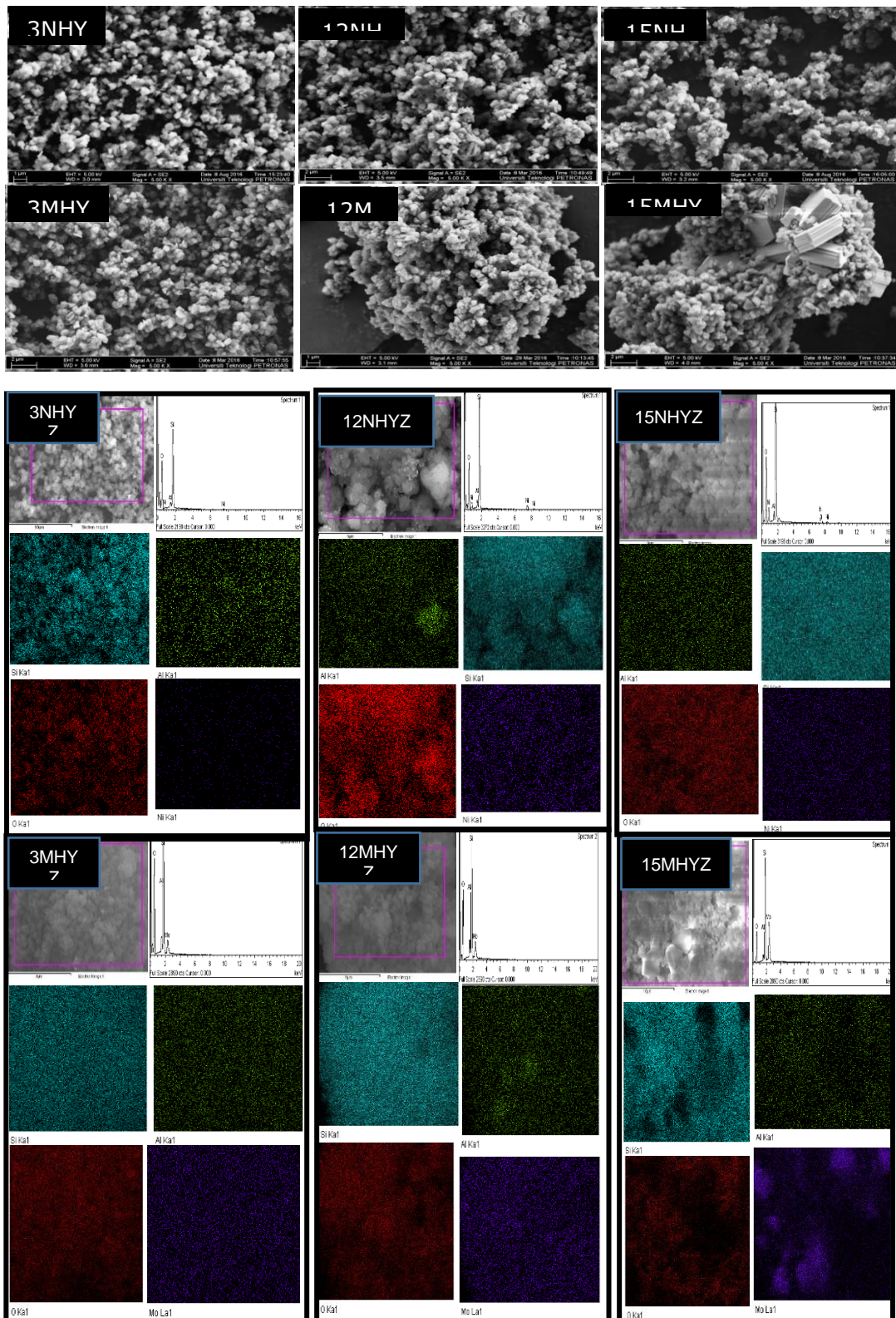


Figure 2: FESEM, EDX and dot mapping result for synthesised catalyst: 3NHYZ, 12NHYZ, 15NHYZ for 3, 12, 15 wt% of Ni/HYZ and 3MHYZ, 12MHYZ and 15MHYZ for 3, 12, and 15wt. Mo/HYZ.

Figure 3 shows the temperature program reduction ( $H_2$ TPR) determined using freshly calcined Ni/HY zeolite and Mo/ HY zeolite catalysts with 3 wt%, 12 wt% and 15 wt% Ni and Mo doped over HY zeolite catalysts. All catalysts established the similar range of water desorption in TPR peaks around 100°C. The peaks in the temperature range of 100 to 150°C agrees to desorption of adsorbed water. While, the peak at 385°C is assigned to the reduction of bulk NiO to  $Ni^{+2}$  ion which shows the weak interaction with support (Mlinar et al., 2012). This weak interaction attributes that the NiO particles are mainly located on the outside of zeolite channels as reported in the literature (Lin et al., 2014). The other shoulder peak in the range of 470-600°C relates to the strong interaction of fewer NiO particles with support (Maia et al., 2010). This higher reduction peak corresponds to NiO particles which are embedded into the channels of HY zeolite that is evidence from increment of pore size and reduction of surface area. Therefore, the higher temperature is required to reduce NiO particles. These facts are clear from the literature that Ni is mostly present in NiO form which is reducible at lower reduction temperature. Metal loading significantly enhanced the hydrogen consumption from 3 wt% to 12 wt% as it is shown in detectors signals in TPR results. In the same way Mo loading catalysts showed similar results of Ni loading. The reduction temperature of first peak at 570°C represents the reduction of  $MoO_3$  (VI) to  $Mo_2O_3$  (V). This peak shifted slightly lower in 12 wt% Mo and 15 wt% Mo loading from 570°C to 550°C. This slight shift might be due to weak binding energy between metal and support. In contrast, the pore size of Mo based catalysts showed significant increase in pore size with increase of Mo loading. The increment of pore size should relatively show higher reduction temperature. However, this slight decrease in reduction temperature shows that might be Mo is present in more than one oxidation state i.e. MoO (IV). However, lower reduction temperature favours the lower particle size and homogenous dispersion of metals over the surface. In the present study, the presence of metal particles over the surface may favour the catalytic cracking (Kim, 1996).

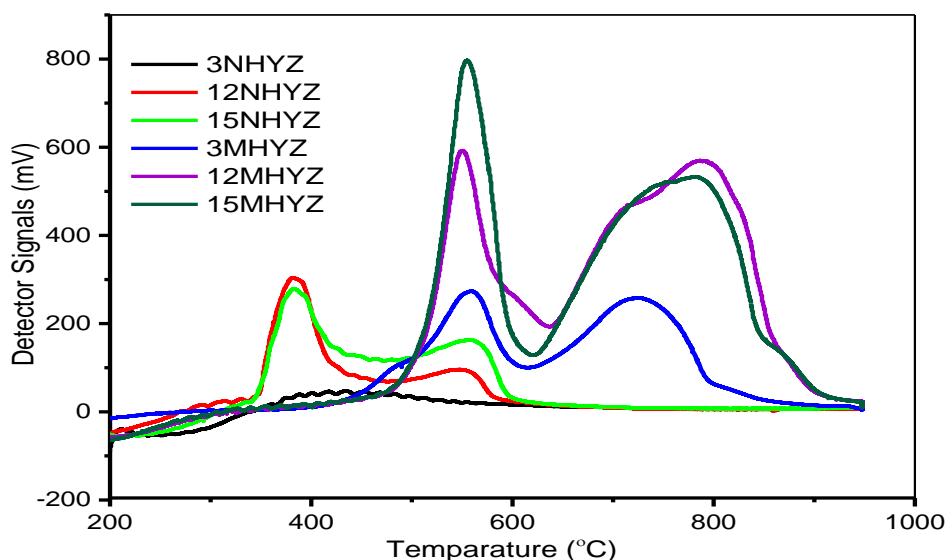


Figure 3:  $H_2$ TPR of all the synthesised catalysts: (3NHYZ) 3% Ni/HYZ, (12NHYZ) 12% Ni/HYZ, (15NHYZ) 15% Ni/HYZ, (3MHYZ) 3% Mo/HYZ, 12% Mo/HYZ, (12MHYZ) and (15MHYZ) 15% Mo/HYZ.

### 3.2. Catalyst screening

The catalytic cracking of rubber seed oil to produce gasoline range hydrocarbon was conducted over Ni and Mo supported HY Zeolite catalysts using different metal loadings i.e. 3, 12, and 15 wt%. Initially all the catalysts were screened based on gasoline range hydrocarbon relative ratio. Among all the catalysts formulation the lowest metal loading of Ni i.e. 3 wt% Ni/ HY zeolite was found with high content of gasoline range hydrocarbons analysed by GC-FID as shown in Figures 4 and 5. It can be observed from data that production of bio gasoline does not affected by metal loading. The most influential property of the catalysts is surface area, Ni with lowest metal loading having highest surface area pronounced with higher catalytic activity with production of 66.6% gasoline relative ratio at 100% triglycerides conversion. However, similar results were obtained with Mo with lowest metal loading of 3 wt% with gasoline relative ratio of (60.66%). However, the with increase of Ni loading the catalytic activity decreases in both type metal loadings, this might be due to reduction in surface area or agglomeration of particles as it can be seen clearly in FESEM and dot mapping images. Comparing Ni and Mo loading effect, it is clear from their catalytic activity that Mo due to large particle size compare to Ni, showed significantly decrease in gasoline relative ratio. Therefore, It can be clearly stated that catalyst with high surface area, low agglomeration and higher acidity play an important role in catalytic cracking of rubber seed oil.



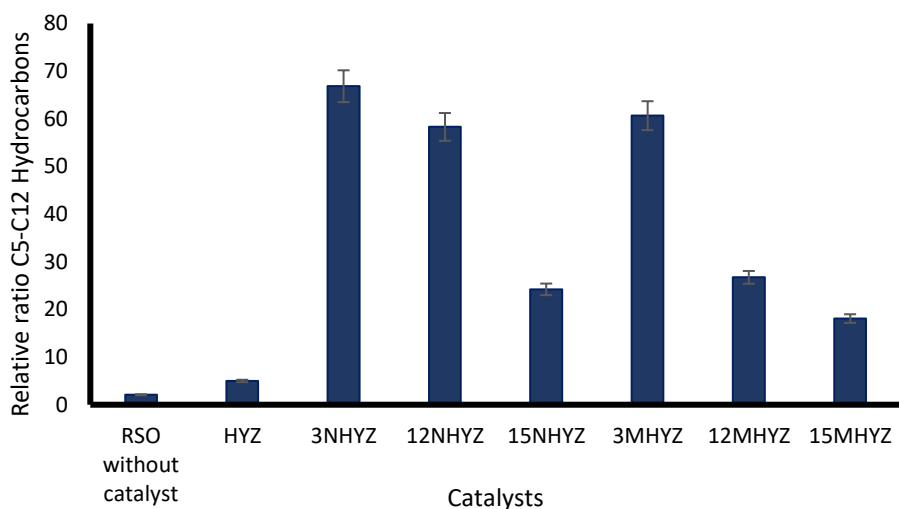


Figure 4: Percentage of C5-C12 for blank RSO and oil sample with different catalyst

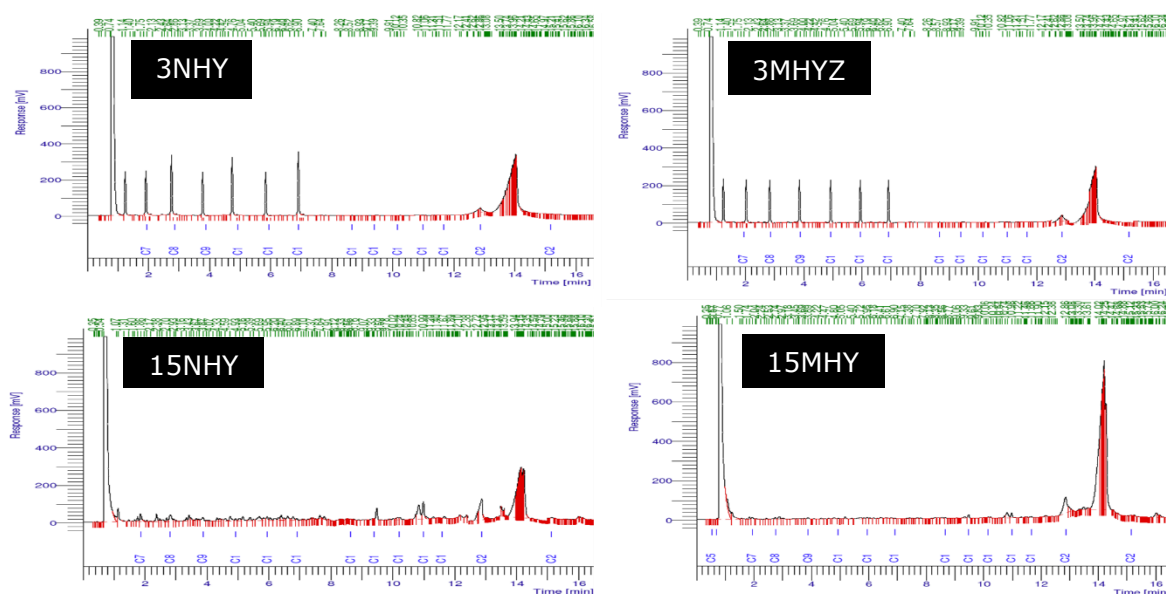


Figure 5: GC-FID spectra of 3 wt% Ni / HY zeolite (3NHYZ), 3 wt% Mo/ HY zeolite (3MHYZ), 15 wt% Ni / HY zeolite (15NHYZ) and 15 wt% Mo / HY zeolite (15MHYZ).

### Optimisation of Temperature

Temperature is one of the most influential factors to produce bio gasoline i.e. desired hydrocarbons with range of C5-C12. For the optimisation of temperature, five different temperatures were selected from 300°C to 500°C for catalytic reaction over 3 wt% Ni/HY zeolite. The effect of temperature is shown in Figure 6, temperature that has the highest conversion towards the selected carbon range is 400°C. To further support the result, comparison in study was done with (Li et al., 2015) on jet fuel production (carbon range of C8-C16) using Ni/HYZ. The yield of alkanes of jet range and aromatics increases to 40.5% when the temperature of reaction were brought up to 390°C and further increase when it is brought up to 400°C (Li et al., 2015). This change in characteristics occurs due to the reaction pathway converting from oligomerization to cracking reaction. When the temperature increase to 410°C, yield of alkane decreased to 31% due to the alkane portion conversion to aromatic compounds (Li et al., 2015). In contrast on the production of jet fuel, the target range of carbon in this project limits to only C12. Stated short chain hydrocarbons (C8-C12) have higher selectivity compared long chain hydrocarbons (C12-C16) if the temperature of reaction is maintained at 410 and 430°C and it is justified due to the severe cracking process (Li et al., 2015). Thus, the optimal temperature for the catalytic reaction of RSO is optimised as 400°C. The temperature above 400°C relatively give more aromatic hydrocarbons that ultimately reduced the gasoline range hydrocarbons. Temperature below 400°C is significant to produce diesel range hydrocarbons.

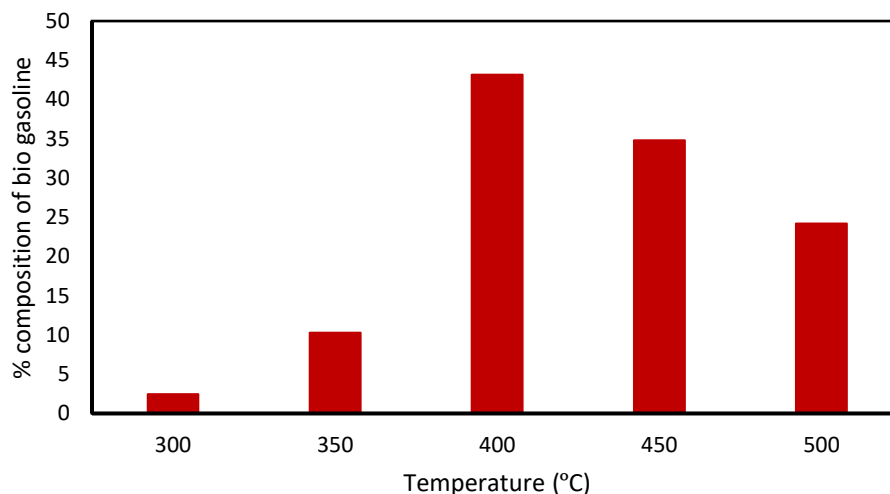


Figure 6: Temperature effect on gasoline composition

#### 4. CONCLUSION

Catalytic cracking is a key process in producing bio gasoline from vegetable oil. Non-edible type of vegetable oil i.e. rubber seed oil was chosen as feedstock. The effect of metal loading was investigated to produce biogasoline. Among all the metal loadings i.e. 3, 12, and 15 wt% of Ni and Mo over HY zeolite, 3 wt% Ni was found to be more active compared to others with 66.84% of C5-C12 relative ratio gasoline. The higher catalytic activity is mainly due to the higher surface area and low agglomeration of metal particles. The temperature optimised was found to be 400°C with less aromatic hydrocarbons over 3 wt% Ni/HY zeolite, which indicates that metal loading does not affect significantly on gasoline production, only the higher surface area and homogenous dispersion, large pore size and pore volume significantly influenced the hydrocracking reaction.

#### 5. ACKNOWLEDGEMENT

Authors would like to thank, Yayasan Universiti Teknologi PETRONAS, Perak, Malaysia and Ministry of Higher Education (MOHE) for funding this project (YUTP-0153AA-A91) and FRGS (015-13 AB-K83) respectively. Author also acknowledge the Funding from Ministry of Education Malaysia for Higher Institution Centre of Excellence (HiCoE) (015MAO-052) to continue the ongoing research projects.

#### 6. REFERENCES

- Ahmad, J., Yusup, S., Bokhari, A. & Kamil, R. N. M. 2014. Study of fuel properties of rubber seed oil based biodiesel. *Energy Conversion and Management*, 78, 266-275.
- Al-Sabawi, M., Chen, J. & Ng, S. 2012. Fluid Catalytic Cracking of Biomass-Derived Oils and Their Blends with Petroleum Feedstocks: A Review. *Energy & Fuels*, 26, 5355-5372.
- Ameen, M., Azizan, M. T., Ramli, A., Yusup, S. & Abdullah, B. 2019a. The effect of metal loading over Ni/ $\gamma$ -Al<sub>2</sub>O<sub>3</sub> and Mo/ $\gamma$ -Al<sub>2</sub>O<sub>3</sub> catalysts on reaction routes of hydrodeoxygenation of rubber seed oil for green diesel production. *Catalysis Today*.
- Ameen, M., Azizan, M. T., Ramli, A., Yusup, S. & Alnarabiji, M. S. 2019b. Catalytic hydrodeoxygenation of rubber seed oil over sonochemically synthesized Ni-Mo/ $\gamma$ -Al<sub>2</sub>O<sub>3</sub> catalyst for green diesel production. *Ultrasonics Sonochemistry*, 51, 90-102.
- Ameen, M., Azizan, M. T., Yusup, S. & Ramli, A. 2017a. Hydroprocessing of Rubber Seed Oil over Ni-Mo/ $\gamma$ -Al<sub>2</sub>O<sub>3</sub> for the Green Diesel Production. *CHEMICAL ENGINEERING*, 61.
- Ameen, M., Azizan, M. T., Yusup, S., Ramli, A. & Yasir, M. 2017b. Catalytic hydrodeoxygenation of triglycerides: An approach to clean diesel fuel production. *Renewable and Sustainable Energy Reviews*, 80, 1072-1088.

- Arun, N., Sharma, R. V. & Dalai, A. K. 2015. Green diesel synthesis by hydrodeoxygenation of bio-based feedstocks: Strategies for catalyst design and development. *Renewable and Sustainable Energy Reviews*, 48, 240-255.
- Bokhari, A., Chuah, L. F., Yusup, S., Klemeš, J. J. & KamiL, R. N. M. 2016a. Optimisation on pretreatment of rubber seed (*Hevea brasiliensis*) oil via esterification reaction in a hydrodynamic cavitation reactor. *Bioresource Technology*, 199, 414-422.
- Bokhari, A., Yusup, S., Chuah, L. F. & KamiL, R. N. M. 2016b. Vacuum Distilled Post Blend Crude Palm and Rubber Seed Oil Methyl Esters: Optimisation and Parametric Studies. *Procedia Engineering*, 148, 479-486.
- Corma, A., Huber, G. W., Sauvanaud, L. & O'connor, P. 2007. Processing biomass-derived oxygenates in the oil refinery: Catalytic cracking (FCC) reaction pathways and role of catalyst. *Journal of Catalysis*, 247, 307-327.
- Dhawane, S. H., Kumar, T. & HaldER, G. 2018. Process optimisation and parametric effects on synthesis of lipase immobilised carbonaceous catalyst for conversion of rubber seed oil to biodiesel. *Energy Conversion and Management*, 176, 55-68.
- Doronin, V. P., Potapenko, O. V., Lipin, P. V., Sorokina, T. P. & Buluchevskaya, L. A. 2012. Catalytic cracking of vegetable oils for production of high-octane gasoline and petrochemical feedstock. *Petroleum Chemistry*, 52, 392-400.
- Jamil, F., Bawadi, A., Ahmad, M. M., Inayat, A. & YusuP, S. Catalytic Cracking of Synthetic Bio-Oil: Kinetic Studies. *Applied Mechanics and Materials*, 2014. Trans Tech Publ, 259-262.
- Kim, M.-C. K. A. K.-L. 1996. A Role of Molybdenum and Shape Selectivity of Catalysts in Simultaneous Reactions of Hydrocracking and Hydrodesulfurization. *Korean J. of Chem Eng*, 13, 1-6.
- Li, T., Cheng, J., Huang, R., Zhou, J. & Cen, K. 2015. Conversion of waste cooking oil to jet biofuel with nickel-based mesoporous zeolite Y catalyst. *Bioresource Technology*, 197, 289-294.
- Lin, T. J., Meng, X. & Shi, L. 2014. Ni-exchanged Y-zeolite: An efficient heterogeneous catalyst for acetylene hydrocarboxylation. *Applied Catalysis A: General*, 485, 163-171.
- Maia, A. J., Louis, B., Lam, Y. L. & Pereira, M. M. 2010. Ni-ZSM-5 catalysts: Detailed characterization of metal sites for proper catalyst design. *Journal of Catalysis*, 269, 103-109.
- Mlinar, A. N., Baur, G. B., Bong, G. G., Getsoian, A. B. & Bell, A. T. 2012. Propene oligomerization over Ni-exchanged Na-X zeolites. *Journal of Catalysis*, 296, 156-164.
- Phimsen, S., Kiatkittipong, W., Yamada, H., Tagawa, T., Kiatkittipong, K., Laosiripojana, N. & Assabumrungrat, S. 2017. Nickel sulfide, nickel phosphide and nickel carbide catalysts for bio-hydrotreated fuel production. *Energy Conversion and Management*, 151, 324-333.
- Speight, J. G. 2019. Chapter 9 - Catalytic Cracking Processes. In: Speight, J. G. (ed.) *Heavy Oil Recovery and Upgrading*. Gulf Professional Publishing.
- Subsadsana, M. & Ruangviriyachai, C. 2016. Effect of NiW Modified HZSM-5 and HY Zeolites on Hydrocracking Conversion of Crude Palm Oil to Liquid Hydrocarbons. *Oriental Journal of Chemistry*, 32, 839-844.
- Widyarani, Ratnaningsih, E., Sanders, J. P. M. & BruinS, M. E. 2014. Biorefinery methods for separation of protein and oil fractions from rubber seed kernel. *Industrial Crops and Products*, 62, 323-332.
- Zandonai, C. H., Yassue-Cordeiro, P. H., Castellã-Pergher, S. B., Scaliante, M. H. N. O. & Fernandes-Machado, N. R. C. 2016. Production of petroleum-like synthetic fuel by hydrocracking of crude soybean oil over ZSM5 zeolite – Improvement of catalyst lifetime by ion exchange. *Fuel*, 172, 228-237.
- Zheng, Q., Huo, L., Li, H., Mi, S., Li, X., Zhu, X., Deng, X. & SheN, B. 2017. Exploring structural features of USY zeolite in the catalytic cracking of *Jatropha Curcas* L. seed oil towards higher gasoline/diesel yield and lower CO<sub>2</sub> emission. *Fuel*, 202, 563-571.

---

## #69: Utilisation of the pulse technique in the energy retrofitting to a range of European dwellings

---

Xiaofeng ZHENG<sup>\*1</sup>, Edward COOPER<sup>2</sup>, David TETLOW<sup>1</sup>, Mark GILLOT<sup>1</sup>, Saffa RIFFAT<sup>1</sup>,  
Shin-Ku LEE<sup>3</sup>, Christopher WOOD<sup>1</sup>

<sup>1</sup> Building, Energy and Environment Research Group, Faculty of Engineering, University of Nottingham,  
University Park, Nottingham NG7 2RD, UK xiaofeng.zheng@nottingham.ac.uk

<sup>2</sup> Department of Architecture and Built Environment, Faculty of Science and Engineering, University of  
Nottingham Ningbo China, 199 Taikang East Road, Ningbo 315100, China

<sup>3</sup> Research Centre for Energy Technology and Strategy, National Cheng Kung University No.1, University Rd,  
Tainan 701, Taiwan, ROC

*There has been increased focus on the energy use in the buildings as it contributes up to 50% of global energy consumption in the developed countries. The importance of airtightness test in buildings has long been recognised due to the potentially large energy savings associated with good envelope airtightness. Moreover, good envelope airtightness makes it easy to control the indoor environment and achieve effective and efficient ventilation. Therefore, building airtightness should be used as an important indicator of building energy performance and indoor environment quality in the process of building energy retrofitting. The Pulse technique has been used to monitor the airtightness level of a range of European dwellings that went through energy retrofitting. About 10%-50% improvement on envelope airtightness has been demonstrated in most of the dwellings with one exception where the house became leakier. Lessons were learnt on issues that are potentially present in the process of house energy retrofitting.*

Keywords: energy retrofitting; building airtightness; blower door; the Pulse technique

## 1. INTRODUCTION

As the impact of global warming is causing great concern globally, it has become highly pressing to cut down CO<sub>2</sub> emission in the building sector, which contributes up to 40% of global energy consumption and this figure goes up to 50% in the developed countries (UNEP, 2009; Lombard, 2008; International Energy Agency, 2013; Orme, 2001). Hence, it is essential to keep the energy consumption of buildings at a low level in order to decarbonise the building sector. The Climate Change Act requires the UK to achieve 80% reduction in greenhouse gas emissions by 2050 relative to 1990. By 2015, 38% reduction in emissions relative to 1990 has been achieved but mostly in the power sector as a result of reduced use of coal and increased generation of electricity from renewables, with little progress in other sectors (Committee on Climate Change, 2016). For instance, there has been slow uptake of low-carbon technologies/behaviours and the improved fuel efficiency in the transport sector has been offset by increased demand for travel as the economy has grown and fuel prices have fallen. Moving forward, to maintain the same progress rate in the emission reduction, efforts need to be made in multiple sectors. Analysts have suggested a complete decarbonisation of the building stock by 2050 seems to be a more realistic approach given the difficulty of reducing emissions in other sectors.

It was reported there were over 26 million homes in the UK housing stock ranging from the largest Elizabethan mansion to the smallest purpose-built flat (House of Commons, 2007-08). The carbon emission from them hit 41.7 million tonnes in 2004, representing more than a quarter of the UK's emissions of the main greenhouse gas driving climate change (Department for Communities and Local Government, 2006). To meet government targets, domestic emissions need to fall to 17 million tonnes p.a. by 2050. Space and water heating are responsible for up to 73% of the domestic emissions. Due to the global warming, there might be reduced demand in heating but it could be offset by the increased cooling demand in summer. Hence, the majority of domestic emissions is still caused by space heating/cooling and water heating. In the EU, the residential sector accounts for 25% of the yearly final energy consumption (Ec.europa.eu, 2017) and is the one of the largest energy consumers. To reduce the carbon emissions and its associated environmental impact, Energy Efficiency Directive (European Parliament and the Council of the European Union, 2012) and Energy Performance of Building Directives (European Parliament and the Council of the European Union, 2010) were introduced by the EU.

It was suggested by several studies (Ballarini, 2017; Baldini, 2017; Subramanyam, 2017; Santin, 2012; Monteiro, 2017) that there is a great potential of enhancing the energy efficiency of residential sector, which can be achieved by reducing the energy demand through energy retrofitting, utilising more energy efficient appliances and technical systems as well as changing the user behaviours. In the building retrofits, the potential of cutting down carbon emission in the building sector is justified by the aged and energy inefficient building stock of the EU, with two-thirds of the existing buildings having been built before there were any energy performance standards (European Commission, 2016). Due to the aforementioned unique characteristics of building stocks in EU, energy retrofits are promoted across the EU member states by the European Directives to improve the energy efficiency of existing buildings. However, there has been little uptake on the energy retrofitting due to many issues, including financial, social, informational and educational challenges (Monteiro, 2017; IEA, 2010). For instance, the high upfront cost and long cost recovery period can make the house retrofitting financially unattractive. Tolerance to disruption caused by energy retrofitting, unexpected delays or complications can cause considerable stress. Negative attitudes can develop towards a refurbishment experience due to technological faults or internal disputes leading to problems with workmanship (Crosbie, 2010).

Generally, a number of measures can be taken to retrofit buildings, which usually include installation of fabric insulation (such as external wall insulation), utilisation of energy efficient systems and appliance (such as more efficient boiler and lightings) and improvement of building airtightness, etc. The overall objectives are to improve the building energy efficiency, indoor environment quality (Milne, 2000; Maidment, 2014; Banfill, 2012) and building durability. In order to achieve these targets, it is essential to reduce the building energy demand by obtaining a thermal resistant and airtight building fabric as a good starting point.

The relative proportion of energy losses associated with air infiltration has increased as the building thermal insulation has been improved over the last few decades. Building energy consumption caused by building infiltration takes 13%-30% of the overall heating energy, 4-14% of cooling load (Emmerich, 1998; Jokisalo, 2009; Raman, 2014; Keast, 1979; Ross, 1978). Building infiltration is fundamentally determined by airtightness, which also affects the building ventilation. Therefore, a good building airtightness is desirable from the energy's standpoint. However, the indoor air quality would be compromised if the indoor contaminant is not diluted quickly enough by the infiltration. A purpose-designed ventilation strategy is required in this case in order to provide sufficient fresh air to occupants. Another significant factor, which is usually overlooked in comparison to energy consumption and indoor air quality, is the long-term effect caused by the moisture transportation that is largely influenced by the airtightness. A poor airtightness affects the lifespan of building structure by allowing the unconditioned air to penetrate through building fabric, condense in the building envelope and deteriorate the building fabric. It also establishes a suitable environment for the growth of mould, which is potentially another source of contaminant to indoor environment. Therefore, it is important to monitor the airtightness during domestic energy retrofits to make sure the pre-defined

target is met and the right ventilation strategy is taken, especially considering good airtightness is necessary to achieve efficient operation of MVHR (Banfill, 2012).






The purpose of the EU-funded Holistic Energy Retrofit Building (HERB) project is to develop new retrofit technologies that can be applied to buildings with the aim to save 80% on energy consumption and 60% on carbon emissions, this being combined with the retrofit of the dwellings and a range of pre and post monitoring. The airtightness of a range of dwellings in the UK, Netherlands, Portugal, Greece and Italy was monitored at the pre and post retrofit stages to see how the retrofits affect the building airtightness.

## 2. METHODOLOGY

This section introduces how the airtightness tests to the dwellings have been carried out through the whole retrofitting cycle, using both pulse technique and steady pressurisation method, how the testing data is analysed, compared and correlated with each other. In order to maintain a good indoor air quality for occupants' health and comfort, the formation of mould and accumulation of indoor pollutants, such as body odours, cooking smells, volatile organic compounds and moisture need to be minimised. This can be done by taking a number of measures, including elimination of excessive exchange of indoor conditioned air and outdoor air, installation of fabric insulations (wall, roof and floor) and deployment of a correct ventilation strategy. Traditionally, the houses built in the UK are less airtight than those built in many other territories in Europe. For all the retrofitted dwellings herein, the natural ventilation, which is the original ventilation strategy, was retained for various reasons but mainly due to the cost consideration because most of the involved dwellings were occupied by people on low incomes and those need social support. Hence, it was not necessary to achieve an airtightness level that is below  $3 \text{ m}^3/\text{h}/\text{m}^2$ , which is required by the scenario when a MVHR is installed, but aimed for the regulatory level set by the UK's building regulation, which is  $10 \text{ m}^3/\text{h}/\text{m}^2$ .

The airtightness test campaign was undertaken over three years during which the dwellings had been through various retrofitting process. In the meanwhile, the research and development on the pulse technique had been ongoing in order to develop the commercial application. Therefore, pulse prototypes in a few iterations were utilised in this testing campaign. They are summarised in Table 1. The full iterations of the pulse development is described in Zheng (2018) and Zheng (2019). During the period of the testing campaign, two main changes occurred. The first one was the use of lightweight composite air tank with oil-free double piston compressor to replace the original heavy and noisy oil-based semi industrial compressor. Hence, the portability of the unit is improved and it is quieter to operate. The other change is the simplification of the laboratory type control and sensing equipment into a control box, which made the setup of the power supply and data acquisition for the pulse unit much simpler and the operation of the pulse test can be completed through button operations. Therefore, the error caused by the human operation can be minimised.

Table 1: Pulse prototypes used for testing during retrofit

Developmental stage	Prototype 1 (2010-2013)		Prototype 2 (2013-2015)
Photo			
Control unit			
Properties	No.2, 4, 5, 7, 8, 10	No.1, No.2, No.3, 5, 7, 8, 10	No.6,
Note	Please refer to Table for the property ID used in this table.		

The schematic diagram of the Pulse unit is illustrated by Figure 1. The pulse generation is achieved by opening the solenoid valve for a short period (typically 1.5 seconds). The pressure difference across building envelope and the pressure inside compressor tank are measured by differential pressure transducer and pressure transducer, respectively. At a sampling rate of 200Hz, the data is recorded by a laptop using a BNC box and A/D converter. More technical details are introduced in by Cooper (2007). Further developments were made to improve the overall system design, integrity and operability, which were then verified in experimental studies (Cooper, 2016; Zheng, 2019a).

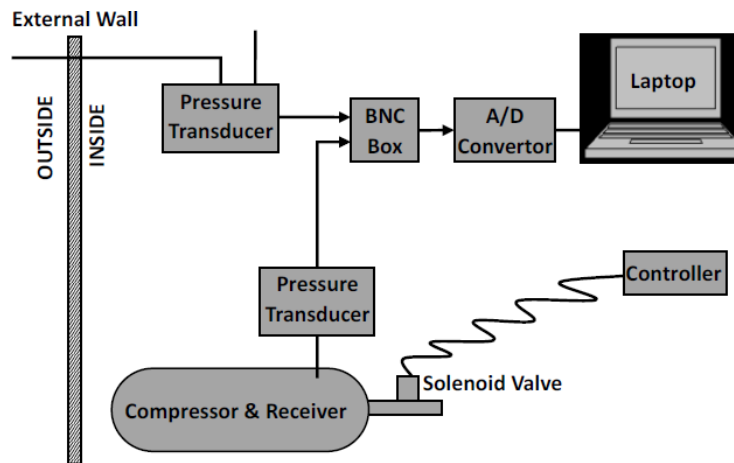


Figure 1: Schematic diagram of the nozzle-based Pulse unit

Prior to testing, all the houses were prepared according to the UK's Air Tightness Testing and Measurement Association's Technical Standard L1 (ATTMA Technical standard L1, 2016) for measuring air permeability of building envelopes in dwellings. The blower-door tests followed the guidelines set out in ATTMA TSL1 and the BS EN: 13829, which has been superseded by BS EN ISO 9972 (BSI Standards Publication, 2015). As such, the results should be comparable with those carried out for demonstrating compliance with the UK Building Regulations. The tests were conducted with the fan mounted in a suitable doorway, as shown in Figure 2, and under both pressurisation and depressurisation. A Minneapolis model 3 blower door was used for the blower door testing.

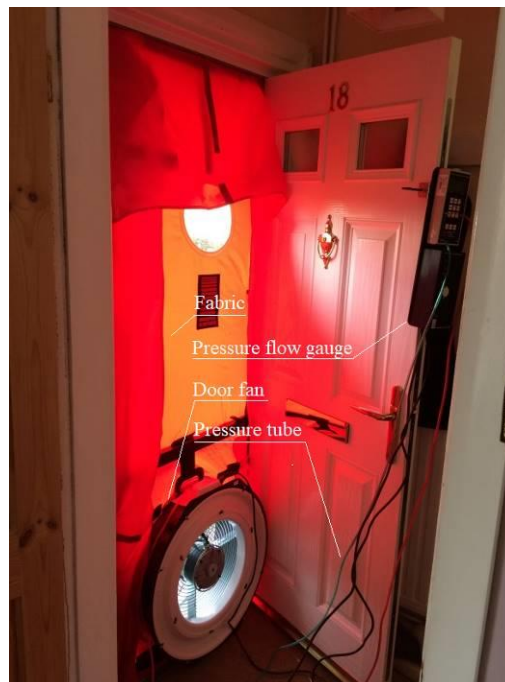


Figure 2: The setup of blower-door

Same with the new construction, it is not uncommon to see the performance gap between the design and as-retrofitted stage in the retrofit. In order to deliver an effective retrofit where the gap is minimised, it is essential to not only adopt an effective and accurate management strategy, but also carry out quality checks at the key retrofit stages where the important measures are taken, such as upgrade of windows, modification of building fabrics and installation of HVAC services and lighting system. As an important indicator of the installation and construction quality, ideally building airtightness should be monitored at the key stages throughout the whole retrofitting process to ensure the effectiveness of each measures taken and the predefined target is met. For instance, some of the upgrades to the external fabric and glazing have multiple benefits in that they contribute to reduced infiltration rates as well as conduction losses (Banfill, 2012). Measuring the changes in the building's air permeability allows the

combined effect of these improvements to be assessed as a series of retrofit measures. However, it was only carried out before and after the retrofit in this study due to various reasons, including limited access to dwellings, delayed work schedules and withdrawal of participation.

The retrofitting process involved with multiple partners across various countries in Europe. Each partner was responsible for developing their own retrofit plan according to their user requirement, local building regulations and financial condition. In total, seven partner countries provides demonstration sites for energy retrofit and were involved in the retrofit. Table 2 lists the retrofitting plan made according to the user requirement, climate characteristic, building energy profile and market condition.






Table 2: Indicative plan of technologies to be considered in the retrofit plan

Country	Building fabric	Lighting	Ventilation	Power/hot water generation	Heat generation
UK	Aerogel or starch microporous materials for internal insulation and surface coating of exterior, Vacuum insulation panel and smart windows	Integrated light pipes	Natural ventilation	Solar thermal and/or PV panels for roof integration	Heat pumps
Italy	Aerogel or starch microporous materials for internal insulation and surface coating of exterior	Energy efficient lighting	Natural ventilation and passive heating/cooling	Solar thermal for roof and/or PV panels for facade integration	Heat pumps
Portugal	Smart windows and surface coating	Energy efficient lighting	Natural ventilation and passive heating/cooling or heat pumps for heating and cooling	Solar thermal and/or PV panels	N/A
Greece	Smart windows and surface coating	Energy efficient lighting	Natural ventilation and passive heating/cooling or heat pumps for heating and cooling	Solar thermal and/or PV panels	N/A
Netherlands	Aerogel or starch microporous materials for internal insulation and surface coating of exterior	Energy efficient lighting	Energy efficient HVAC	Solar thermal and/or PV panels	N/A

### 3. CASE STUDY BUILDINGS AND SETUP

All the properties except No.8 are dwellings that were provided by the local council in each city for the people with low-income. Three of them are semi-detached house, one is an end-terraced house and all the rest are apartments. They have various sizes and leakage levels. The volume of the case study buildings ranges from 136 m<sup>3</sup> to 398 m<sup>3</sup> and the leakage level of them prior to the retrofit ranged from 5 to 20 m<sup>3</sup>h<sup>-1</sup>m<sup>-2</sup>.

Table 3: Dwellings that were subject to the retrofit and airtightness-tested

				
No.1-SD	No.2-SD	No.3-ET	No.4-(I) flat 1	No.5-(I) flat 2
				
No.6 (G) flat 1	No.7 (G) flat 2	No.8 (N) Detached	No.9 (P) flat 1	No.10 (P) flat 2

Note: Great Britain (GB), Italy (I), Greece (G), the Netherlands (N) and Portugal (P)



To illustrate how the Pulse unit was set up during testing, Figure 3 shows a few examples in some of the testing dwellings in the UK, Italy, the Netherlands and Greece. The Pulse unit, comprised of control unit and a compressor with a 50-litre air tank, was placed in the centre of the test dwelling. The control unit was brought by the tester and the compressor at each location was prepared by the local project partner.



Figure 3: Setup of the Pulse unit in some of test dwellings

## 4. TEST RESULTS

### 4. 1. Airtightness test (pre vs. post)

Table 4 lists the ten properties that were subjected to airtightness testing during the retrofit process; they are located in five countries: Great Britain (GB), Italy (I), Greece (G), the Netherlands (N) and Portugal (P). In all the ten buildings, the Pulse test was carried out at both stages, while only three properties had both the Pulse and blower door tests at the before and after stages. Due to timing, resource and access issues the remaining properties did not have the blower door performed at the post-retrofit stage (or if it did, the result is unknown to the authors) Therefore, in order to make the results more comparable, the discussion will be focused on results given by the Pulse tests.

Table 4: Dwellings subjected to testing and the testing scenario

Stage	Pre-retrofit test		Post-retrofit test	
	Pulse test	Blower door test	Pulse test	Blower door test
No.1 (GB) Semi detached	Yes	Yes on the same day	Yes	Yes on the same day
No.2 (GB) semi detached	Yes	Yes on the same day	Yes	Yes on the same day
No.3 (GB) Terraced	Yes	Yes on the same day	Yes	Yes on the same day
No.4 (I) flat 1	Yes	Yes on different days	Yes	unknown
No.5 (I) flat 2	Yes	Yes on different days	Yes	unknown
No.6 (G) flat 1	Yes	Tracer gas	Yes	unknown
No.7 (G) flat 2	Yes	Tracer gas	Yes	unknown
No.8 (N) Semi-detached	Yes	Yes on the same day	Yes	Unknown
No.9 (P) flat 1	Yes	No	Yes	No
No.10 (P) flat 2	Yes	No	Yes	No

Figure 4 shows the air permeability level of the dwellings measured by the Pulse technique before and after the retrofit. Different from a widely-held belief in the UK that British houses are among the leakiest in the western world

(DECC, 2011), the dwellings in Britain tested in this study are interestingly the most airtight among them all. When converted to the air permeability at 50 Pa ( $Q_{50}$ ) using the empirical ratio 5.30 (Orme, 2001; Jokisalo, 2009), two British dwellings met the requirement of airtightness set by the UK building regulations for new builds (below 10  $m^3/h/m^2$ ). While all dwellings in other countries except flat 2 in Italy have a  $Q_{50}$  that is greater than 10  $m^3/h/m^2$ . After the retrofit, improvement of envelope airtightness in percentage difference in comparison with the pre-retrofit stage is also illustrated in Figure 4. In most of the dwellings, an improvement (8%-50%) on the envelope airtightness was achieved. The dwellings from No.4 to No.9 had the highest improvement in airtightness, over 40%. For the dwelling No.1, 2 and 10, the improvement on the airtightness is much lower. For the dwelling 1 and 2, the airtightness level prior to the retrofit was already very low, just above 5  $m^3/h/m^2$ , which left small margin for improvement. For the property 10, the dwelling was very leaky before retrofit and that suggests the improvement could have been greater. The exception was with dwelling No.3 which had leakier envelope after the retrofit work was completed. It was found out plasterboards on some walls were broken during the retrofitting process but not repaired afterwards, as shown in Figure 5. It suggests some installations carried out during the retrofit process might have caused some damage to the fabric. It was not notified to the management team afterwards and it was difficult to trace back the retrofit work due to the absence of clear communication and overall responsibility. That led to a gap between the predefined target and as-retrofit performance. Nevertheless, the improvement on airtightness achieved in this study is much less than what was claimed in an early study (Lowe, 1997). Hence, this suggests the potential of improving the building airtightness was not fully realised and a better quality control strategy should be adopted in the retrofit process in order to make sure the measures taken at the key retrofitting stages to deliver a good quality of installation and remediation.

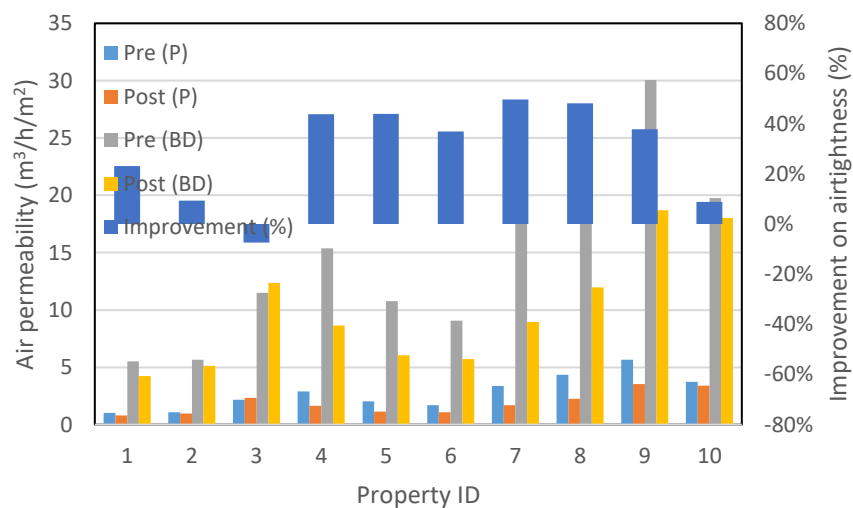


Figure 4: Air permeability at 4 Pa ( $Q_4$ ) and 50 Pa ( $Q_{50}$ ) and improvement on airtightness in the retrofitted dwellings (Note: (P) and (BD) stand for the Pulse test and blower door test)

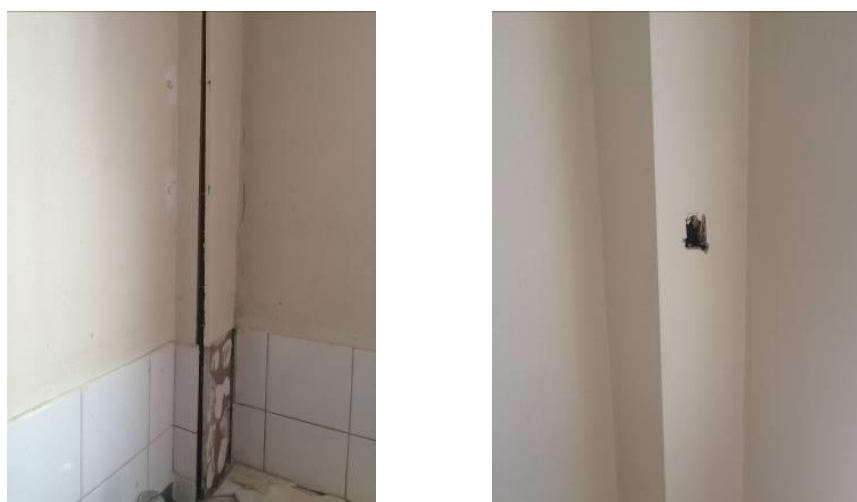


Figure 5: Defects in building fabric in property 3 after the retrofit

## 4.2. Thermography

Research carried out by BRE on 35 houses (Stephen, 2000) pre- and post-sealing of components indicated in the whole house air leakage, 16% was contributed by the unintended gaps in openable windows and doors, 13% was contributed by loft hatch, window and door surrounds and permanent vents and 71% was contributed by gaps and cracks in the building envelope.

In this section, building diagnostic using a thermal image camera is introduced to illustrate the typical locations of building leakage pathways. This was done with the aid of a blower door fan, which was used to create a pressure difference across the building envelope in the presence of temperature difference around 10 °C. Hence, central heating was turned on in advance to establish the required temperature difference between indoor and outdoor air when thermal image camera is used for capturing the trail of incoming cold outdoor air. The incoming air, with lower temperature, comes into the house at a certain speed driven by the established pressure difference. The air stream cools down the surfaces near the leakage pathways by “brushing” the surfaces and is reflected as a trail of cold air stream in thermal image camera. The temperature contrast can be seen through a thermal image camera, an example is shown in Figure 6.

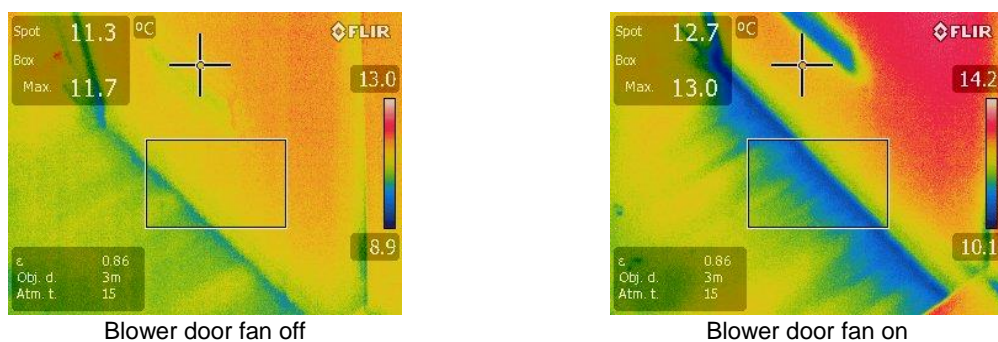
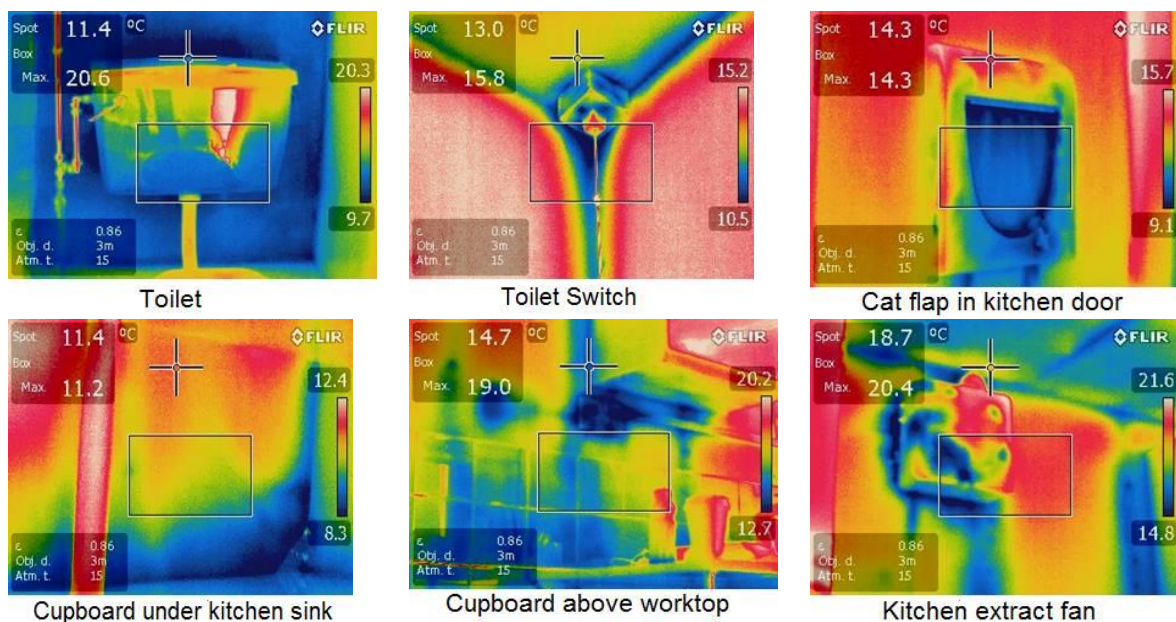


Figure 6: Trail of cold air stream through leakage pathway at the basement door

To illustrate the typical locations of leakage pathways in a dwelling, Figure 7 shows the locations of leakage pathways identified by the thermal image camera in the house No.3. The thermal images show that the locations are mainly at the service penetrations, junctions between wall and wall, wall and ceiling, wall and floor, wall and windows/doors. It needs to be noted that some of the cold areas, on the wall for instance, are resulted from poor insulation. The findings were summarised in a report, which was then provided to the retrofit team for further action. In the report, the leakage pathways were not individually quantified but provided a qualitative indication on the retrofit approach that should be taken to repair the existing defects in the envelope to obtain a more airtight fabric.



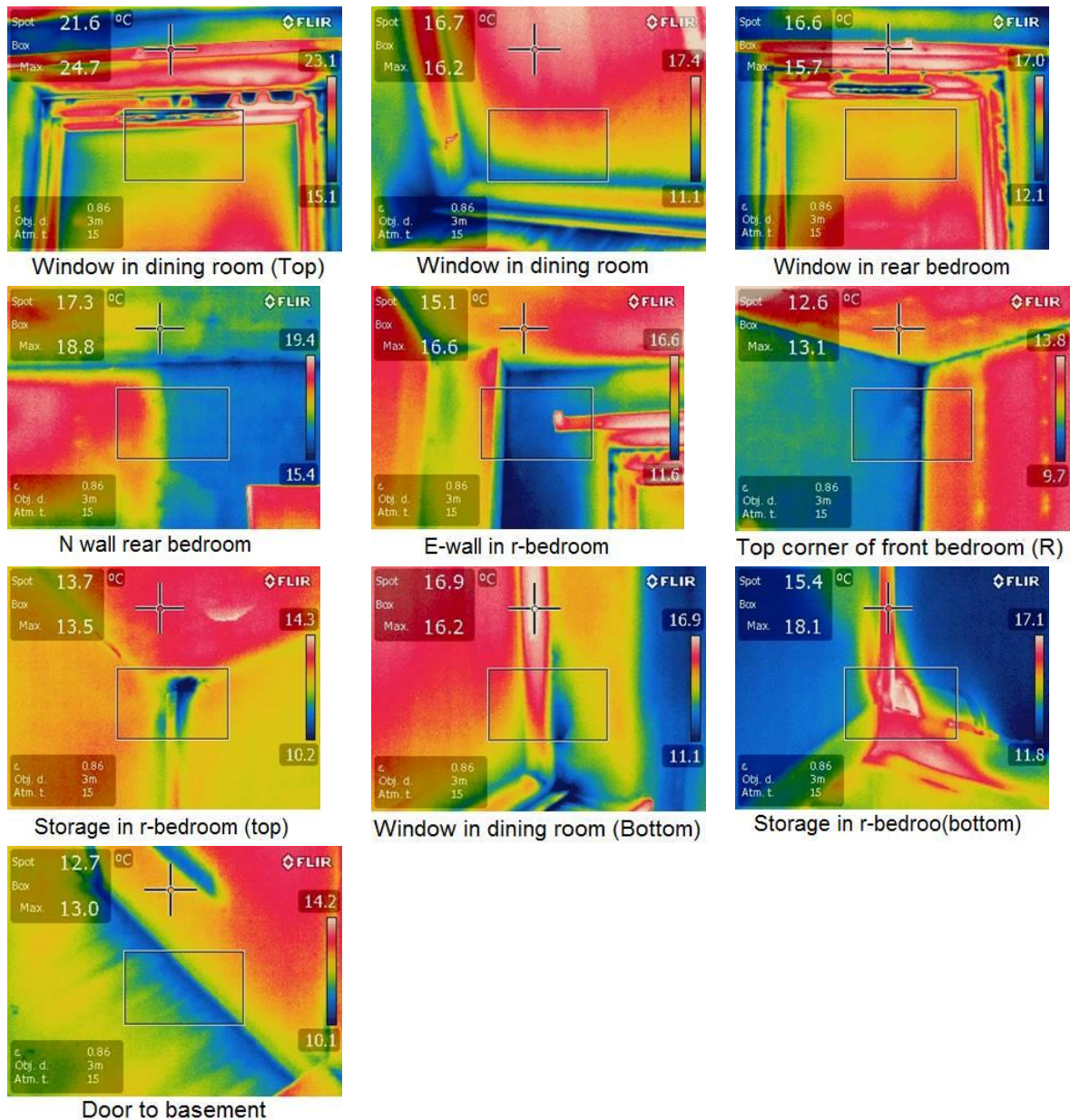


Figure 7: Location of the leakage pathways in house No.3 before retrofit

## 5. CONCLUSIONS

This paper introduces an experimental study on how the airtightness of a range of European dwellings changed when they went through the process of energy retrofitting. The test dwellings were comprised of houses and apartments in countries with temperate and Mediterranean climates, where the buildings are designed to have various leakage characteristics to match the local climate and user behaviours. The results showed that the air leakage of most test dwellings has been decreased by 8% to 50%, which indicated the retrofit measures had a positive impact on the building envelope airtightness. The  $Q_{50}$  of most dwellings are higher than  $5\text{m}^3/\text{h}/\text{m}^2$ , which is a level where MVHR is not required, suitable for natural ventilation. One dwelling became leakier after retrofit. The cause of it was attributed to damages in the plasterboard during the retrofitting process and it was not repaired afterwards. That led to a gap between the predefined target and as-retrofit performance. This suggests a better communication and a clear overall responsibility on the quality of retrofit tasks are required to eliminate the occurrence of this. In comparison with other studies, the result on the improvement of the airtightness achieved in this retrofit suggests that there is a potential to achieve greater improvement on the envelope airtightness. Adopting the measurement at the key stages where the retrofit measures are taken would be a crucial and effective way of achieving better quality control. That would not only effectively audit the quality of the overall retrofitting process but also define a clear responsibility for each individual party that is involved at different stages of the process. The necessity of adopting this approach shows a greater significance in the context of retrofitting/ constructing buildings

towards low/zero carbon level, which needs a well-defined airtightness target in order to minimise the heat losses caused by building infiltration and achieve a required performance in operating MVHR systems.

## 6. ACKNOWLEDGEMENT

The authors gratefully acknowledge funding received from: the European Union's Seventh Programme for research, technological development and demonstration under grant agreement No 314283. ['HERB']; and the Innovate-UK programme for 'Scaling Up Retrofit' under project No: 101609. ['PULSE': [www.pulseairtest.com/](http://www.pulseairtest.com/) .

## 7. REFERENCES

ATTMA Technical standard L1. Measuring air permeability in the envelopes of dwellings. The Air Tightness Testing & Measurement Association (2016).

Baldini M, Trivella A. Modelling of electricity savings in the Danish households sector: from the energy system to the end-user. *Energy Efficiency* 2017; 1-19.

Ballarini I, Corrado V, Madonna F, Paduos S, Ravasio F. Energy refurbishment of the Italian residential building stock: energy and cost analysis through the application of the building typology. *Energy Policy* 2017; 105:148-160.

Banfill, P. Simpson, S., Haines, V., Mallaband, B. (2012) Energy-led retrofitting of solid wall dwellings: technical and user perspectives on airtightness", *Structural Survey*, Vol. 30 Issue: 3, pp.267-279, <https://doi.org/10.1108/02630801211241829>.

BS EN ISO 9972. Thermal performance of buildings-Determination of air permeability of buildings-Fan pressurisation method. BSI Standards Publication (2015).

Committee on Climate Change. Meeting Carbon Budgets-2016 Progress Report to Parliament. Available from: <https://www.theccc.org.uk/wp-content/uploads/2016/06/2016-CCC-Progress-Report.pdf>

Cooper, E.W. and Etheridge, D.W. Determining the adventitious leakage of buildings at low pressure. Part 1: uncertainties *Building Serv. Eng. Res. Technol.* (2007), 28, pp.71-80.

Cooper, E., Zheng, X., Wood, C., Gillot, M., Tetlow, D., Riffat, S. & De Simon, L. 2016. Field trialling of a pulse airtightness tester in a range of UK homes. *International Journal of Ventilation*, 1-18.

Crosbie, T. and Baker, K. (2010) Energy efficiency interventions in housing: Learning from the inhabitants, *Building Research & Information*, vol. 38 (1), pp.70-79

Database - Eurostat [Internet]. Ec.europa.eu. 2017. Available from: <http://ec.europa.eu/eurostat/data/database>

DECC. The Green Deal and energy company obligation consultation document, [https://www.gov.uk/government/uploads/system/uploads/attachment\\_data/file/42980/3607-green-deal-energy-company-ob-cons.pdf](https://www.gov.uk/government/uploads/system/uploads/attachment_data/file/42980/3607-green-deal-energy-company-ob-cons.pdf) (2011, accessed 1 June 2014).

Department for Communities and Local Government, Review of the Sustainability of Existing Buildings, November 2006.

Emmerich, S.J., Persily, A.K., Energy impacts of infiltration and ventilation in U.S. office buildings using multizone airflow simulation. *IAQ and Energy* 98 (1998), pp.191-203.

European Commission. Putting energy efficiency first: consuming better, getting cleaner. Fact Sheet, Brussels; 2016.

European Commission. Directive of the European Parliament and of the Council amending Directive 2012/27/EU on energy efficiency. Brussels; 2016.

European Parliament and the Council of the European Union. 2012/27/EU, Energy Efficiency Directive, Brussels; 2012.

European Parliament and the Council of the European Union. 2010/31/EU, Energy Performance of Buildings Directive (EPBD recast), Brussels; 2010.

House of Commons, Existing Housing and Climate Change—seventh report of session 2007-08. Available from: <http://www.publications.parliament.uk/pa/cm200708/cmselect/cmcomloc/432/432i.pdf>

IEA. Energy Efficiency Governance Handbook. France; 2010.

International Energy Agency, 2013. Transition to Sustainable Buildings-Strategies and Opportunities to 2050. Available from: <http://www.iea.org/Textbase/npsum/building2013SUM.pdf>

- Jokisalo, J., Krunitski, J., Korpi, M., Kalamees, T., Vinaha, J. Building Leakage, infiltration, and energy performance analyses for Finnish detached houses. *Building and Environment* (2009), 44, pp.377-387.
- Keast, D.N., Pei, H.S. The use of sound to locate infiltration openings in buildings. *Proceedings ASHRAE/DOE Conference "Thermal performance of the exterior envelopes of buildings"*, Florida, December 3-5. 1979
- Lombard, L., Ortiz, J., Pout, C. A review on buildings energy consumption information. *Energy and Buildings* 40 (2008) 394-398.
- Lowe, R.J., Johnston, D and Bell, M. Airtightness in UK dwellings: a review of some recent measurements. (1997) Available from: <https://www.aivc.org/sites/default/files/airbase.10669.pdf>
- Maidment C.D., Jones C.R., Webb T.L., Hathway E.A., Gilbertson J.M. The impact of household energy efficiency measures on health: A meta-analysis. *Energy Policy*, Volume 65, February 2014, pp. 583-593.
- Milne G, Boardman B. Making cold homes warmer: the effect of energy efficiency improvements in low-income homes: a report to the Energy Action Grants Agency Charitable Trust *Energy Policy* 2000; 28: 411–24.
- Monteiro, C., Causone, F., Cunha, S., Pina, A., Erba, S. Addressing the challenges of public housing retrofits. *Energy Procedia* 134 (2017) 442-451.
- Orme M. Estimates of the energy impact of ventilation and associated financial expenditures. *Energy and Buildings* 2001; 33: 199/205.
- Raman, G., Chelliah, K., Prakash, M., Muehleisen, R.T., Detection and quantification of building air infiltration using remote acoustic methods. *Internoise 2014 Melbourne, Australia*, 16-19 November
- Ross, H. "Air Infiltration," Lecture at Public Meeting, DoE, Division of Building and Community Systems, Architectural and Engineering Systems Branch, 21 September 1978.
- Santin O. Occupant behaviour in energy efficient dwellings: evidence of a rebound effect. *Journal of Housing and the Built Environment* 2012; 28: 311-327.
- Stephen RK. Airtightness in UK dwellings. *Building Research Establishment (BRE) Information Paper IP/1/00*. Watford: HIS BRE Press, 2000.
- Subramanyam V, Kumar A, Talaei A, Mondal MAH. Energy efficiency improvement opportunities and associated greenhouse gas abatement costs for the residential sector. *Energy* 2017; 118:795-807.
- UNEP. Buildings and Climate Change, Summary for Decision-Makers. Sustainable Buildings & Climate Initiative, 2009. Available from: <http://www.unep.org/sbci/pdfs/SBCI-BCCSummary.pdf>
- Zheng, X.F., Cooper, E., Zu, Y.Q., Gillott, M., Tetlow, D., Riffat, S., Wood, C.J. 2018. Experimental studies of a pulse pressurisation technique for measuring building airtightness. In: 17th International Conference on Sustainable Energy Technology, 21-23 August 2018, Wuhan, China.
- Zheng, X.F., Cooper, E., Zu, Y.Q., Gillott, M., Tetlow, D., Riffat, S., Wood, C.J. Experimental Studies of a Pulse Pressurisation Technique for Measuring Building Airtightness. *Future Cities and Environment* (2019), 5(1): 10, 1–17 DOI: <https://doi.org/10.5334/fce.66>
- Zheng, X., Cooper, E., Mazzon, J., Wallis, I. & Wood, C. J. 2019a. Experimental insights into the airtightness measurement of a house-sized chamber in a sheltered environment using blower door and pulse methods. *Building and Environment*, volume 162. <https://doi.org/10.1016/j.buildenv.2019.106269>

---

## #70: Prospect of thermoelectric air conditioner for building application and their building integration methods

---

Xiaoli MA<sup>1\*</sup>, Han ZHAO<sup>2</sup>, Xudong ZHAO<sup>3</sup>, Guiqiang LI<sup>4</sup>, Samson SHITTU<sup>5</sup>

<sup>1</sup>School of Engineering and Computer Science, University of Hull, UK, HU6, 7RX. x.ma@hull.ac.uk;

<sup>2</sup>Green Building & Low-carbon Technology Development Center, Atlantic House, Imperial Way, Reading, UK, RG2 0TD. hzhaoh1@gmail.com

<sup>3</sup>School of Engineering and Computer Science, University of Hull, UK, HU6, 7RX. Xudong.zhao@hull.ac.uk;

<sup>4</sup>School of Engineering and Computer Science, University of Hull, UK, HU6, 7RX. Guiqiang.Li@hull.ac.uk;

<sup>5</sup>School of Engineering and Computer Science, University of Hull, UK, HU6, 7RX. S.Shittu@2016.hull.ac.uk

\*Corresponding author

*The refrigerants used in conventional vapour-compression air conditioning systems have detrimental effects on the global environment. Phasing-down hydrofluorocarbon (HFC) refrigerants for HVAC equipment over the next 20 years has been proposed and the refrigerants are undergoing a massive shift globally. In this aspect, the thermoelectric technology has attracted considerable attentions as its ability to directly convert between thermal and electrical energy using a simple solid-state semiconductor device, offering sustainable solution in various fields. This paper presents a prospect of the thermoelectric air conditioning technology for building applications. Recent advances in thermoelectric materials, thermoelectric module and thermoelectric heating/cooling system design, which would provide the potential to greatly improve the COP of the thermoelectric air conditioner, are reviewed. Utilising the waste heat of the thermoelectric system for domestic applications and for improving the overall COP of the system is discussed. It is prospected that the thermoelectric air conditioner would be competitive or superior to the conventional ones regarding to its energy efficiency with the development of the thermoelectric technologies. In addition, the thermoelectric systems have the advantages of be a very compact flat unit and are easy to be integrated into the building structure. The paper also proposes a novel multifunctional thermoelectric building energy façade system that integrates a thermoelectric heat pump unit into a double-skin façade to provide heating and cooling, heat recovery ventilation and domestic hot water or drying services for buildings, based on the waste heat utilisation. Except for integration into façade, several additional building integration methods of the system are also proposed and shown schematically.*

*Keywords: Thermoelectric, air conditioner; COP; waste heat utilisation; building integration*

## 1. INTRODUCTION

Thermoelectrics can enable direct energy conversion between heat and electricity, based on thermoelectric effects, which has been considered as a green and sustainable solution to the global energy dilemma. A thermoelectric module is a simple solid-state device that converts electrical energy into thermal energy or the reverse. As shown in Figure 1, it consists of a number of couples of p- and n-type semiconductor strips sandwiched between two ceramic plates, connected electrically in series and thermally in parallel. When supplied with a suitable electric current they can provide either cooling or heating depending on the direction of the current. Heat generation or absorption rates are proportional to the magnitude of the current and also the temperature of the hot and cold side. The amount of heat removed by the hot side corresponds to the cooling effect and the electrical power input.

The thermoelectric modules are reliable energy converters and have no noise or vibration as there are no mechanical moving parts. They have small size and are light in weight. As heat pumps, they are friendly to the environment as CFC gas or any other refrigerant gas is not used. Due to these advantages, the thermoelectric devices found a large range of applications in recent decades, including cooling electronic devices, refrigerator and air conditioner, power generation and thermal energy sensors, etc (Riffat et al, 2003).

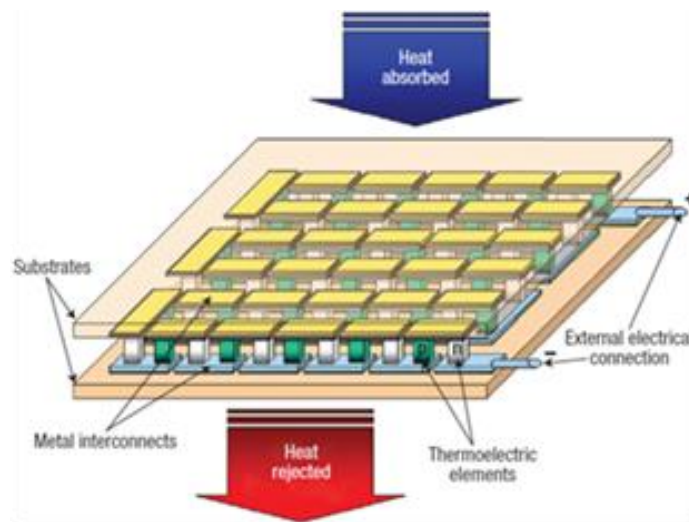


Figure 1: Thermoelectric module

Any thermoelectric device has a given operating temperature range beyond which its operation may cease. For cooling/heating applications, all thermoelectric modules require heat sinks in order to dissipate the energy generated or absorbed at the two junctions. A thermoelectric cooling/heating unit is therefore composed of three basic components, the thermoelectric module, the heat dissipater at the hot side of the module and the cooling component at the cold side of the module, as shown in Figure 2.

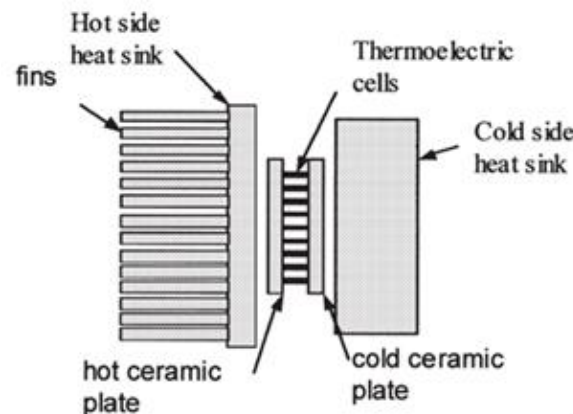


Figure 2: Basic components of a thermoelectric cooling/heating system



Conventional mechanical air conditioning systems are energy intensive and currently dominate the HVAC market. The refrigerants used in conventional vapour-compression air conditioning systems have detrimental effects on the global environment. Phasing-down hydrofluorocarbon (HFC) refrigerants for HVAC equipment over the next 20 years has been proposed and the refrigerants are undergoing a massive shift globally (Ortlieb et al, 2017). Although alternative refrigerants with low global warming potential (GWP) will partially solve the problems, a long-term complete solution is to move building HVAC systems away from vapour compression technologies (Tan et al, 2015). In recent years, the thermoelectric (TE) technology has attracted considerable attention from various research areas as its ability to directly convert between thermal and electrical energy using a simple solid-state semiconductor device offers sustainable solution in various fields (Park, et al, 2016). A TE air conditioning system has many advantages including fully environmentally friendly; requires no refrigerant; requiring no periodic replenishment; substantially less maintenance; compact in size and light in weight; high reliability with no moving parts (except for small fans); no noise or vibration; long life span; able to withstand severe environments; easy to integrate into existing building structure; and more importantly, it can be powered by direct current (DC) electric sources, such as photovoltaic (PV) cells and fuel cells. However, the existing TE air conditioning systems have low Coefficient of Performance (COPs) for space cooling that limits its application for domestic air conditioning. Literature review found few researches in the TE building space cooling (Zhao et al, 2014; Gillott M et al, 2010; He W et al, 2013; Alomair M et al, 2015; Liu Z et al, 2015). Currently the most efficient TE space cooling system in research has an average cooling COP of 0.87, with the maximum cooling COP of 1.22 (Zhao et al, 2014).

Generally, the low COPs of the TE air conditioners were caused by a few problems, i.e. low figure of merit (ZT) of the thermoelectric materials, inefficient TE module design and inappropriate cooling system design. With the development of TE materials and TE technologies in recent decade, the above existing problems could be overcome and a highly efficient TE air conditioner is prospected. In addition, recent development in TE material with obviously reduced cost would provide TE Air conditioners with greatly reduced cost. Furthermore, utilising the high density waste heat produced by the TE cooling system for domestic applications would be an ideal way to enhance the overall efficiency of TE system operation. However, researches in utilisation of the waste heat of thermoelectric system is rare (He W et al, 2013), and this system is ineffective in removal of the waste heat from the thermoelectric unit and results in a low cooling COP of 0.45.

The paper presents an overview of the current advance of the TE technologies that would provide a potential to greatly improve the COPs and reduce the costs of the TE air conditioning systems, which would promote the public acceptance of the TE air conditioners.

The paper also proposes a novel multifunctional thermoelectric building façade system. This system smartly integrates a TE heat pump unit into a double-skin ventilated façade. The system sets multifunction in one, it provides heating/cooling and ventilation for buildings, and the high density waste heat produced in the cooling mode (predicted >60°C) is directly utilised to provide domestic hot water or drying (clothing or other goods) services. The system has the capability of performing heat recovery ventilation or recovering heat from domestic waste water to use as a part of heat source of the TE heat pump in heating mode. The system with this structure therefore would have the potential of greatly enhanced overall COP, in addition to the advance in recent TE material and TE technology. Furthermore, the system is very easy to be integrated into the building structure, various methods on integration of the system into buildings are introduced schematically.

## **2. OPTIMISATION OF THE THERMOELECTRIC COOLING/HEATING SYSTEM DESIGN**

At present, the COP of a thermoelectric cooler is typically < 0.5. However, it has been reported that a well-designed (small cooler) system can achieve a COP to be > 2 ([www.analogtechnologies.com](http://www.analogtechnologies.com)). The well designed system should have optimum design/selection of the following items according to its operating conditions, include: (1) selection of the optimum TE material (ZT) by balancing its efficiency (judged by ZT) availability and cost. (2) Optimisation of the geometrics of thermoelectric elements; (3) optimisation of the heat dissipate/transport components; (4) optimisation of the operating DC current. Recent development in TE material, TE module geometry design, heat removing and dissipating technologies would benefit the TE cooling/heating system design to further enhance the COP of the system.

### **2.1 Recent advance in thermoelectric materials**

The material used in construction of a TE cooling system plays an important role in controlling the performance of these devices. The TE performance is closely related to the figure of merit of thermoelectric materials, ZT. A good thermoelectric material should have high primary criterion of merit ZT. A high ZT requires low thermal conductivity but high electrical conductivity (Twaha et al, 2016). Conventional thermoelectric materials are bulk alloy materials such as Bi<sub>2</sub>Te<sub>3</sub>, PbTe, SiGe and CoSb<sub>3</sub>, among which Bi<sub>2</sub>Te<sub>3</sub> is the most commonly used one for a long time. They usually process a ZT value less than one (Bell L E et al, 2008).

It was reported that if the average ZT reaches two, domestic and commercial solid-state heating, ventilating and air-cooling systems using thermoelectric material would become practical (Bell L E et al, 2008). The recent advances in thermoelectric material make it possible to significantly improve ZT factor through nanotechnology. Two primary approaches are bulk samples containing nanoscale constituents and low dimensional materials. New thermoelectric materials with larger ZT factor values may intrigue a breakthrough in various application areas for thermoelectric devices. It was reported that the best commercial thermoelectric materials recently have ZT values around 1.0 (Zhao et al, 2014). The highest ZT value in research is about 3, reported by Harman in 2005 (Harman T C et al, 2005). Other best reported thermoelectric materials have figure of merit values of 1.2-2.6 at certain temperature (Zhao D et al, 2014; He W et al, 2015), Table 1 lists a selection of the reported high figure of merit thermoelectric materials.

Table 1: A selection of high figure of merit thermoelectric materials

Material	Type (a)	ZT value	Temperature
Bi-doped PbSeTe/PbTe (QDSL)	n-type	3	550K
In <sub>0.2</sub> Ce <sub>0.15</sub> Co <sub>4</sub> Sb <sub>12</sub> Skutterudite	n-type	1.43	800K
(Bi <sub>0.25</sub> Sb <sub>0.75</sub> ) <sub>2</sub> Te <sub>3</sub>	p-type	1.27	298K
Bi <sub>2</sub> (Te <sub>0.94</sub> Se <sub>0.06</sub> ) <sub>3</sub>	n-type	1.25	298K
K <sub>0.95</sub> Pb <sub>20</sub> Sb <sub>1.2</sub> Te <sub>22</sub>	n-type	~1.6	750K
PbTe-SrTe	p-type	1.7	~800K
Binary crystalline In <sub>4</sub> Se <sub>3-8</sub>	n-type	1.48	~705K
AgPb <sub>m</sub> SbTe <sub>2+m</sub>	n-type	~2.2	800K
Bi <sub>2</sub> Se <sub>0.5</sub> Te <sub>2.5</sub>		1.28	Room temperature
(Bi,Sb) <sub>2</sub> Te <sub>3</sub>		1.41	Room temperature
Bi <sub>2</sub> Te <sub>2.7</sub> Se <sub>0.3</sub>		1.27	Room temperature
Bi <sub>0.4</sub> Sb <sub>1.6</sub> Te <sub>3</sub>		1.26	Room temperature
(Bi <sub>2</sub> Te <sub>3</sub> ) <sub>0.25</sub> (Sb <sub>2</sub> Te <sub>3</sub> ) <sub>0.75</sub>		1.80	723
Bi <sub>2</sub> Te <sub>2.85</sub> Se <sub>0.15</sub>		2.38	773
Bi <sub>0.5</sub> Sb <sub>1.5</sub> Te <sub>3</sub>		1.93	693
(Bi <sub>2</sub> Se <sub>3</sub> ) <sub>x</sub> (Bi <sub>2</sub> Te <sub>3</sub> ) <sub>1-x</sub>		1.87	713
Bi <sub>2</sub> Te <sub>2.85</sub> Se <sub>0.15</sub>	p-type	1.86	693
Bi <sub>2</sub> Te <sub>3</sub> /Sb <sub>2</sub> Te <sub>3</sub>		2.4	300
SiC/B4C+PSS		1.75	873
SnSe single crystal		2.6±0.3	923

In addition, with the development of the TE material technology, the cost of TE module has become much lower. In 2001, a piece of high quality TE cooling module (CP2-127-06-L1-4.5W) from Melcor, USA ([www.melcor.com](http://www.melcor.com)) costs US \$161, now the cost reduced to be \$59.8, a similar one costs only US \$24 from ATI (USA) ([www.analogtechnologies.com](http://www.analogtechnologies.com)). In China, it is even cheaper with a piece of Tecl-07103 Peltier Thermoelectric Cooling Module costing only US \$5.69 (<http://hebeiltd.en.made-in-china.com>). Therefore, cost should no longer be a problem for development of TE heating/cooling system.

## 2.2 Recent advance in thermoelectric module geometry and system design

The parameters that affect the performance of TE modules can be physical or nonphysical. The most important optimisation parameters for TE modules include TE element leg length, leg area ratio between n- and p-type legs, fill fraction, load resistance and module spacing (Twaha S et al, 2016). Thermal stresses in the legs and temperature distributions and their influence on module performance under designed operating conditions need to be investigated (Rabari R et al, 2014). Finite element can be used to solve such complexity using selected TE materials (Erturun U, 2014). The Math model has been developed for the thermodynamics and thermal stress analysis of TE system to optimum design or selection of the optimum module for the designed operating conditions (Al-Merbati S et al, 2013). Optimum thermoelement and module geometry can be determined by a compromise between the COP and heat pumping capacity to optimum design of the TE module for a specific application.

The standard simplified energy equilibrium model or zero dimensional model has been widely used for TE cooler and air-conditioning analysis and design (Riffat S B et al, 2004, Fraisse G et al, 2013). However, its accuracy is

limited due to gross simplifying assumptions: 1) thermoelectric material properties are temperature independent; 2) half of the Joule heat goes to the hot side while the other half goes to cold side. These assumptions could result in up to 10% error. One-dimensional thermoelement model solves detailed temperature distribution along thermoelement length. In one-dimensional model, temperature dependent parameters bring in two considerations. One is the temperature dependent Thomson effect. The other is that Thomson effect, Joule heat and heat conduction have to be considered together since the temperature distribution is no longer linear through the thermoelement (Huang M J et al, 2005; Mitrani D, 2009; Reddy B V K et al, 2013). Although a three-dimensional modelling captures temperature distribution both along and across the thermoelement, thus, it performs better than one-dimensional modelling, it is very computationally expensive and complicated (Wang X D et al, 2012). Therefore, one-dimensional thermoelement model should be an ideal tool for TEC analysis and design at present.

Commercially, a large amount of different types of modules are available, some of them are most suitable for heating/cooling applications, such as thermal cycling series module in ATI (USA) and CP series module (Lairdtech USA) for large heat pumping applications ([www.lairdtech.com/products/cp14-31-045-11-w45](http://www.lairdtech.com/products/cp14-31-045-11-w45)).

### 2.3 Recent advance in heat removal/dissipate systems

The power of the heat exchanger heat sinks in the hot and cold side of the TE modules, especially the hot side heat sink that is used to remove the high heat flux, is very important for enhancing the efficiency of the TE cooling/heating system. Researches can be found to investigate the heat sinks' geometry allocation of the heat transfer area and heat transfer coefficients of hot and cold side heat sinks (Zhao Y et al, 2012; Zhu L et al, 2013; Pan Y et al, 2007). The results obtained are useful for the optimal design and manufacture of heat sinks for TE cooling/heating systems.

Figure 3 shows some current commercial available high power TE heat sinks for electronic device cooling.



Figure 3: Various configurations of high power hot side heat sinks

### 3. THERMOELECTRIC COOLING SYSTEM WASTE HEAT UTILISATION

During the operation the thermoelectric cooling mode produces large amount of high density waste heat. Utilising the waste heat for domestic hot water/drying services would be an ideal way to enhance the overall efficiency of thermoelectric system operation and promote public adoption of the thermoelectric air conditioner. Research into the utilisation of the waste heat of thermoelectric system is rare (He W et al, 2013), and this system is ineffective in removal of the waste heat from the thermoelectric unit and results in a low cooling COP of 0.45.

However, utilisation of the waste heat for domestic applications has great potential to highly enhance overall COP of the thermoelectric system. The waste heat produced in the cooling mode of the thermoelectric system is high density, and for building applications our previous work found it has a suitable temperature of 60-70°C for producing domestic hot water (Riffat S B et al, 2004; Ma X, 2004).

Use of the microencapsulated phase change material slurry (MEPCM slurry) would be an ideal technology for effectively utilisation of waste heat produced in the thermoelectric cooling system. A MEPCM slurry can fulfil the three functions simultaneously in the thermoelectric space cooling system, i.e. heat absorption from the hot side of the TE modules, heat transportation through liquid cold plate and pipelines and heat storing in the heat storages. Furthermore, the high energy content of the slurry allows significant reductions to be made in the size of pipes, pumps and storage tanks. To keep the pump energy consumption low, it is important to choose a MEPCM slurry with good energy transportation capability, good heat transfer ability and lower pumping power requirement. The concentration of the MEPCM slurry will also affect the above aspects (Ma X et al, 2009).

In a thermoelectric cooling system, the waste heat produced on the hot side can be assessed by the second thermodynamics law, i.e.

$$\text{Equation 1: } Q_h = Q_c + Q_E$$

Where:

- $Q_h$  is the waste heat produced on the hot side
- $Q_c$  is the cooling energy produced on the cold side
- $Q_E$  is the electrical energy input

The Coefficient of Performance (COP) of the system for cooling is expressed as:

$$\text{Equation 2: } COP_c = Q_c / Q_E$$

The overall COP of the system when the waste heat is utilised in cooling mode can be expressed as:

$$\text{Equation 3: } COP_{overall} = (Q_h + Q_c) / Q_E = 2 \times COP_c + 1$$

As aforementioned in the Introduction section, the current most efficient TE space cooling system in research has an average cooling COP of 0.87, with the maximum cooling COP of 1.22 (Zhao D et al, 2004). If the waste heat produced in the system can be utilised for domestic hot water service, the overall average cooling COP can be 2.74, with the maximum overall system COP of 3.44, which could be competitive to the traditional vapour compression air conditioner system with a COP of 2 to 3. If a thermoelectric space cooling system could be well designed based on current advanced TE material, module and system design, the cooling COP could reach 2, by utilising the waste heat the overall COP can reach 5, which would be superior to the traditional one regarding to the energy efficiency.

#### **4. SIZE OF THE THERMOELECTRIC AIR CONDITIONER SYSTEM**

The TE air conditioner system is a compact flat unit. Previous work found that a 0.38m<sup>2</sup> of TE unit (with a cooling COP of 0.6 and heating COP of 1.12), which is smaller than a common room heating radiator, can satisfy the heating/cooling requirement of a 15m<sup>2</sup> room based on Scotland weather conditions (Ma X, 2004). With the development of the TE air conditioning technology, the cooling COP of the system would reach 2, as mentioned in section 3 (whereas the heating COP would be 3), the TE unit would be much smaller and the area of the above mentioned TE unit for a 15m<sup>2</sup> room in Scotland would have a potential to be reduced to only 0.11m<sup>2</sup>.

#### **5. EASY INTEGRATION INTO THE BUILDING STRUCTURE**

The thermoelectric system is very easy to be integrated into the building structure. This section proposes a novel multifunctional thermoelectric building energy façade system that integrates a thermoelectric heat pump unit into a double-skin façade to provide heating/cooling, heat recovery ventilation and domestic hot water or drying services, based on the waste heat utilisation. Various other building integration methods of the system are also shown schematically.

##### **5.1 A novel building integrated TE façade proposed**

The novel multifunctional thermoelectric façade is shown in Figures 4 and 5). This system smartly integrates a TE heat pump unit into a double-skin ventilated façade and is very compact. The system sets multifunction in one, it provides heating/cooling and ventilation for buildings, and the high density waste heat produced in the cooling mode (predicted >60°C) is directly utilised to provide domestic hot water or drying (clothing or other goods) services. The system has the capability of performing heat recovery ventilation or recovering heat from domestic waste water to use as a heat source of the TE heat pump in heating mode. Owing to the waste heat utilisation and domestic waste heat recovery, the system would have highly enhanced overall COP. In addition, a high power heat sink (which is most suitable for the TE's high density waste heat removal) or a micro encapsulated phase change slurry (PCS) system is used to effectively remove the waste heat on the hot side of the TE unit in cooling mode, which

reduce the temperature difference between the hot and cold side of the TE unit and therefore further enhance the COP.

There are two options of the façade system, i.e. air cooled system (option 1) and liquid cooled system (option 2), stated as follow:

Figure 4 shows Option 1, the key component of the façade is a flat TE heat pump unit integrated into the inner wall of the façade; the TE unit is consisted of TE modules, a finned encapsulated PCM and a high power heat sink (Figure 3). The ventilation fan is mounted in the gap of the double-skin facade. In cooling mode, heat from the building is extracted by the TE unit, this provides cooling to the room and the extra cooling energy is stored in the finned encapsulated PCM for use in the night time (when driven by PV) or high peak electricity period (when driven by mains power).

The cooled room exhaust air (may mixing with outdoor air) driven by the ventilation fan goes through the façade gap to effectively remove the waste heat produced by the TE unit, from high power heat sink on the hot side of the TE unit, and cools the hot side of TE modules to a lower temperature, which ensure the TE unit operating in higher performance. The waste heat is directly conducted to a drying chamber through flat duct (not shown in the Figure) for drying services. In heating mode, by changing the polarity of the DC power supply, the system will provide space heating. The heat sources of the TE heat pump are the warm room exhaust air (may mixing with some outdoor air) flowing through the façade gap, this allows the heat recovery ventilation. For both the cooling and heating modes, the extra cooling and heating energy provided by the TE unit are stored in the finned encapsulated PCM for use in the night time (when driven by PV) or high peak electricity period (when driven by mains power).

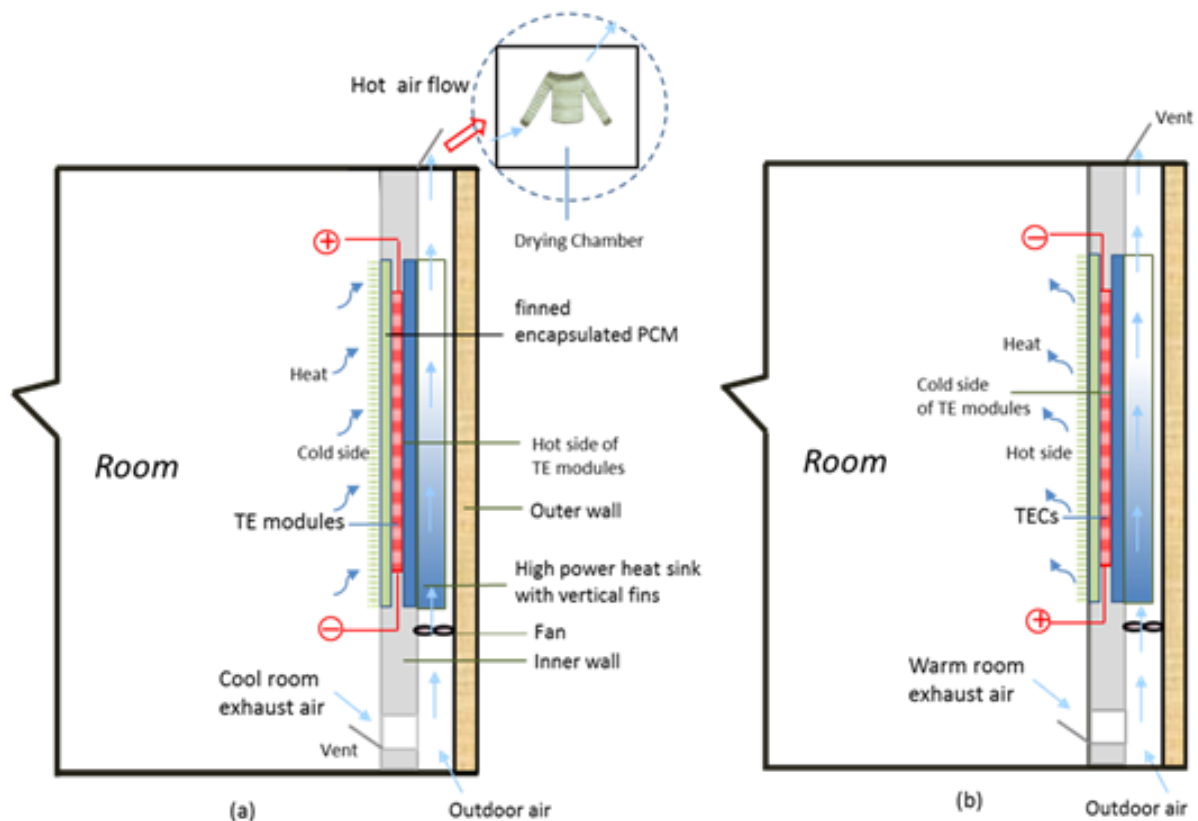


Figure 4: TE façade system-option 1 (a) cooling mode (b) heating mode

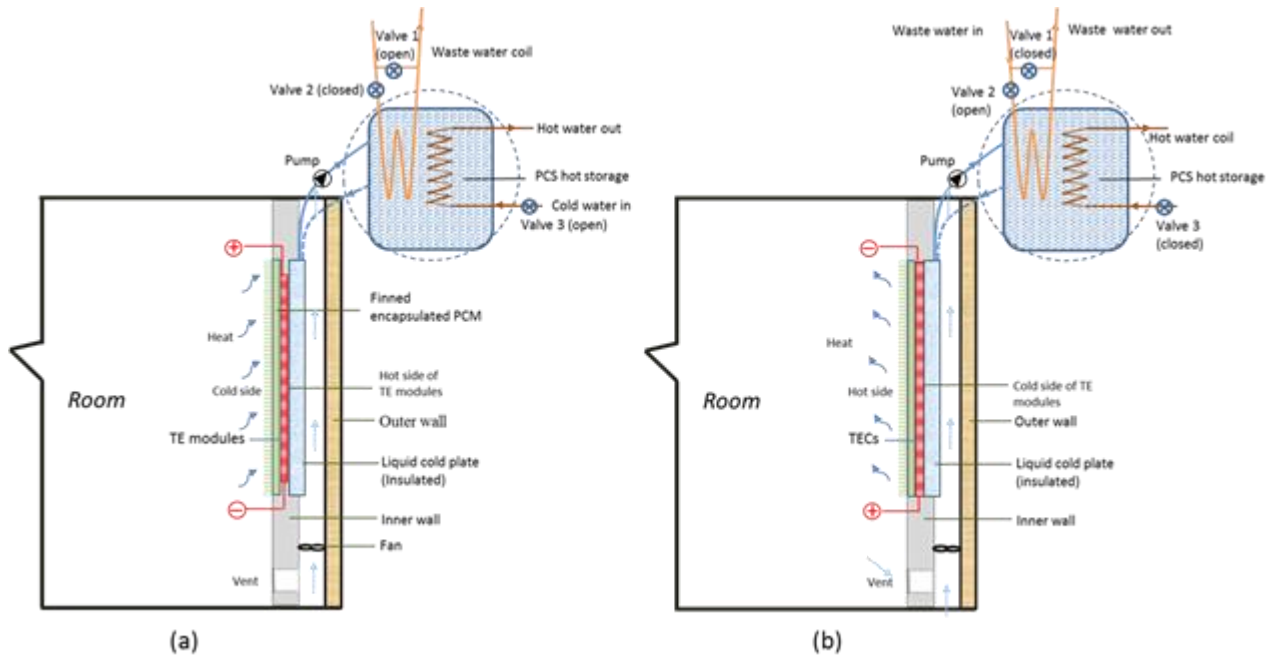


Figure 5: TE façade system-option 2 (a) cooling mode (b) heating mode

Figure 5 shows Option 2, instead of using the high power heat sink, the TE system uses a PCS system to effectively remove, transport and store the waste heat in cooling mode, the stored waste heat provides domestic hot water in a right temperature (predicted around 60-70oC, an auxiliary electric heater could be used in the storage if necessary). In heating mode, heat from waste water is stored in the PCS hot storage and is circulated by the PCS system to the cold side of the TE unit to be a heat source of the TE heat pump unit.

For the TE façade system in both Options, the room ventilation can be performed through the façade gap, the ventilation air movement inside the room can also promote the heating/cooling energy dissipating from the finned encapsulated PCM to the room. For the TE unit, a number of TE modules can be arranged to be one or more matrixes to form TE sub-units depending on the energy requirement of the room, with the partition in between to form the air flow channels in the façade gap.

The TE facade system can be used for residential and commercial buildings (e.g. school buildings/offices), for both new buildings and retrofitting buildings. The façade system can be driven by mains power or directly driven by solar PV panel and fuel cells, without need of converter, and so it can also be especially suitable for use for mobile spaces, such as mobile field office and houseboats, by forming a stand-alone system, to provide heating/cooling, ventilation and hot water or drying services for these small spaces.

## 6. VARIOUS BUILDING INTEGRATION METHODS OF TE AIR CONDITIONING UNIT

The TE air conditioner unit can be integrated into the building structure easily due to the small flat shape, compact structure and no direction restriction. Different methods for integration of the TE air conditioning unit into building structure are investigated. Except for integration into a double skin façade (Figures 4 and 5), the TE unit can be integrated into the ceiling, fireplace chimney and window frame. Figure 6 shows the integration of the TE air conditioning unit into ceiling. Figure 7 shows the integration of the TE air conditioning unit into fireplace chimney for retrofitting the buildings. Figure 8 shows the integration of the small scale TE air conditioning unit into the window frame.

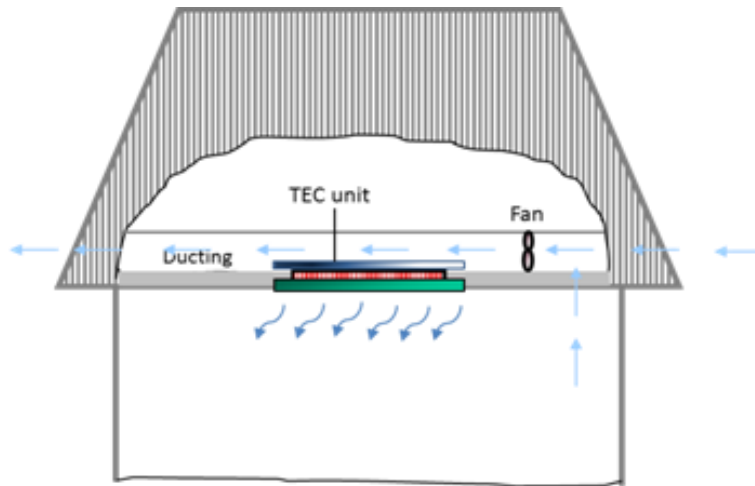


Figure 6: Integration of TE unit into ceiling

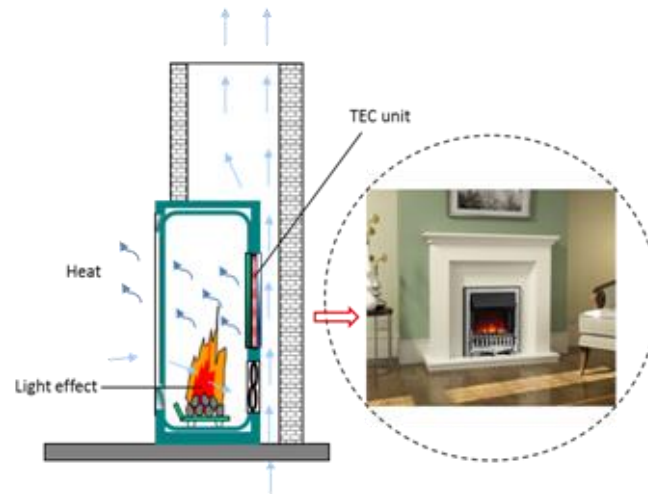


Figure 7: Integration of TE unit into fireplace chimney

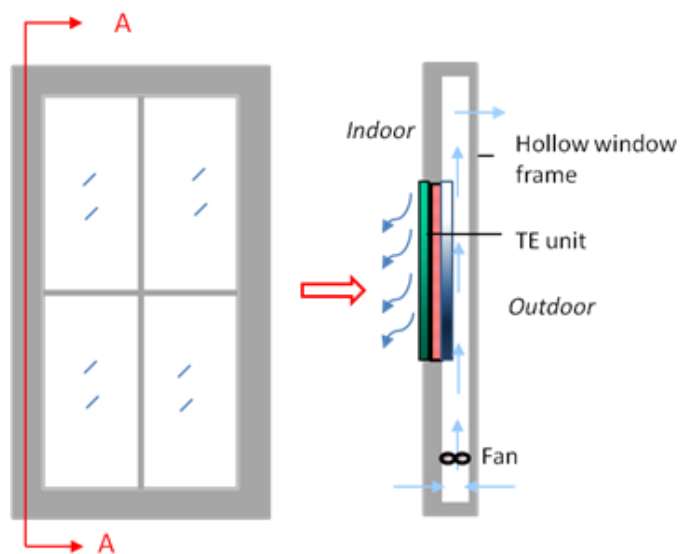


Figure 8: Integration of TE unit into window frame

## 7. CONCLUSIONS

Recent advances in TE technologies would provide a potential to greatly improve the COPs and reduce the costs of the TE air conditioning systems. This would promote the public acceptance of the TE air conditioners. The TE materials with higher Figure of merit have been reported, which would make domestic TE air conditioning system become practical. Furthermore, the advanced analytical models will provide an effective tool for optimum design of the TE modules and TE systems. In addition, effective utilisation of the waste heat produced in cooling mode will greatly improve the overall COP of the TE system. It is prospected that the TE air conditioner would be competitive and superior to the conventional vapour compression one regarding to the energy efficiency. The TE system has the advantage of easy integration into the building structure, which can also bring the benefit of heat recovery ventilation. Finally a novel building TE façade system is proposed, alternative methods of integration of the TE system into building structure are presented.

## 8. REFERENCES

- Alomair M, Alomair Y, Mahmood S, Abdulla H A, 2015, Theoretical and Experimental Investigations of Solar-Thermoelectric Air-Conditioning System for Remote Applications, *J. Thermal Sci. Eng. Appl* 7(2), 021013, Jun 01.
- Al-Merbaty S, Yilbas B S, Sahina Z, 2013. Thermodynamics and thermal stress analysis of thermoelectric power generator: Influence of pin geometry on device performance. *ApplThermEng*; 50(1):683–92.
- Bell L. E, 2008, Cooling, heating, generating power, and recovering waste heat with thermoelectric systems, *Science* 321, 1457-1461.
- Erturun U, Eremis K, Mossi K, 2014, Effect of various leg geometries on thermo- mechanical and power generation performance of thermoelectric devices. *Appl ThermEng*; 73(1):126–39.
- Fraisse G, Ramousse J, Sgorlon D, Goupil C, 2013, Comparison of different modelling approaches for thermoelectric elements. *EnergyConversManag*;65:351–6.
- Gillott M, Jiang L, Riffat S B, 2010, An investigation of thermoelectric cooling devices for small-scale space conditioning applications in buildings, *International Journal of Energy Research*. 34:776–786.
- Harman T.C., Walsh M.P., Laforge B.E., Turner G.W., 2005, Nanostructured thermoelectric materials, *J. Electron. Mater.* 34 (5), 19-22.
- He W, Zhou J, Chen C, Ji J, 2013, Experimental study and performance analysis of a thermoelectric cooling and heating system driven by a photovoltaic/thermal system in summer and winter operation modes, *Applied Energy* 107, 89–97.
- He W, Zhang G, Zhang X, Ji J, Li G, Zhao X, 2015. Recent development and application of thermoelectric generator and cooler. *Applied Energy*, 143:1–25.
- Huang M J, Yen R H, 2005, An-Bang Wang, The influence of the Thomson effect on the performance of a thermoelectric cooler, *Int. J. Heat Mass Transf.* 48, 413-418.
- Liu Z. et al, 2015, Experimental evaluation of an active solar thermoelectric radiant wall system, *Energy Conversion and Management* 94, 253–260.
- Ma X, 2004, Investigation of novel thermoelectric refrigeration systems. PhD thesis, University of Nottingham.
- Ma X, Omer S A, Riffat S B, Zhang Wei, 2009, Investigation of energy transportation capability of a phase change slurry through a cold storage-cooling coil system, *INTERNATIONAL JOURNAL OF ENERGY RESEARCH Int. J. Energy Res.* 33:999–1004.
- Mitrani, D, Salazar J, Turo A, Garcia M J, Chavez J A, 2009, One-dimensional modeling of TE devices considering temperature dependent parameters using SPICE, *Microelectron. J.* 40 (2009) 1398-1405.
- Ortlieb E, Nonel B, Lowery K, et al, 2017, Refrigerant Phase down Alternatives, and Factors Driving the Future of the Refrigerant Market, *The Magazine for Environmental Managers, A&WMA*, October.



- Park S H, Jo S, Kwon B, 2016, High-performance shape-engineerable thermoelectric painting, *Nature Communications*, Volume7, Article number: 13403.
- Pan Y, L Bi H, Chen J, 2007, Performance analysis and parametric optimal design of an irreversible multi-couple thermoelectric refrigerator under various operating conditions, *Applied Energy*, Volume 84, Issue 9, September, Pages 882-892.
- Rabari R, Mahmud S, Dutta A, 2014, Numerical simulation of nanostructured thermoelectric generator considering surface to surrounding convection, *International Communications in Heat and Mass Transfer* Volume 56, August, Pages 146-151.
- Reddy B V K, Barry M, Li J, Chyu M K, 2013, Mathematical modeling and numerical characterization of composite thermoelectric devices, *Int. J. Therm. Sci.* 67, 53-63.
- Riffat S.B., Ma Xiaoli, 2003, Thermoelectrics: a review of present and potential applications, *Applied Thermal Engineering* 23 913–935.
- Riffat S.B., Ma X, 2004, Improving the coefficient of performance of thermoelectric cooling systems: a review, *Int. J. Energy Res.* 28 753-768.
- Riffat S B, Ma, X, Qiu, G, 2004, Experimentation of a novel thermoelectric heat pump system, *International Journal of Ambient Energy*, Volume 25, Number 4.
- Tan G, Zhao D, 2015, Study of a thermoelectric space cooling system integrated with phase change material, *Applied Thermal Engineering* 86, 187-198.
- Twaha S, Zhu J, Yuying Yan, Bo Li, 2016. A comprehensive review of thermoelectric Technology: materials, applications, modelling and performance improvement, *Renewable and Sustainable Energy Review*, 65, 698-726.
- Wang X D, Huang Y X, Cheng C H, Lin D T W, Kang C H, 2012, A three-dimensional numerical modeling of thermoelectric device with consideration of coupling of temperature field and electric potential field, *Energy* 47, 488-497.
- Zhao D, Tan G, 2014. Experimental evaluation of a prototype thermoelectric system integrated with PCM (phase change material) for space cooling, *Energy* 68, 658-666.
- Zhao D, Tan G, 2014. A review of thermoelectric cooling: Materials, modelling and applications, *Applied Thermal Engineering* 66, 15-24.
- Zhou Y, Yu J, 2012, Design optimization of thermoelectric cooling systems for applications in electronic devices, *International Journal of Refrigeration*, Volume 35, Issue 4, June, Pages 1139-1144.
- Zhu L, Hongbo Tan H, Yu J, 2013, Analysis on optimal heat exchanger size of thermoelectric cooler for electronic cooling applications, *Energy Conversion and Management* Volume 76, December, Pages 685-690.

---

## #71: Performance analysis of sinter waste heat recovery system based on organic Rankine cycle

---

Junsheng FENG<sup>1</sup>, Guangtao GAO<sup>2</sup>, Gang PEI<sup>3</sup>, Hui DONG<sup>4</sup>

<sup>1</sup> University of Science and Technology of China, No.96, JinZhai Road, Baohe District, Hefei, Anhui, 230026, P.R.China, fjsheng@ustc.edu.cn

<sup>2</sup> University of Science and Technology of China, No.96, JinZhai Road Baohe District, Hefei, Anhui, 230026, P.R.China, gtgao@mail.ustc.edu.cn

<sup>3</sup> University of Science and Technology of China, No.96, JinZhai Road, Baohe District, Hefei, Anhui, 230026, P.R.China, peigang@ustc.edu.cn

<sup>4</sup> Northeastern University, NO. 3-11, Wenhua Road, Heping District, Shenyang, Liaoning, 110819, P. R. China, Dongh@smm.neu.edu.cn

*The efficient recovery and utilisation of sinter waste heat resource is quite important to reduce the energy consumption of sintering process. Due to the characteristics of low temperature sinter cooling flue gas without the dew point corrosion, the outlet flue gas of sinter waste heat boiler is introduced into the organic Rankine cycle (ORC) system. Based on the methods of theoretical analysis and numerical calculation, the variations of performance index of ORC system with the flue gas temperature at the outlet of evaporator under different evaporation temperature of working medium and pinch-point temperature difference in the evaporator are investigated by selecting the R245fa as the working medium of ORC system. The results show that, both the net put power and exergy efficiency of ORC system gradually decrease with the increase of flue gas temperature at the outlet of evaporator for a given evaporation temperature of working medium. When the pinch-point temperature difference in the evaporator is constant, both the net output power and exergy efficiency of ORC system tend to increase first and then decrease with the increase of flue gas temperature at the outlet of evaporator. In addition, with the increase of pinch-point temperature difference in the evaporator, the flue gas temperatures at the outlet of evaporator corresponding to the maximum net output power and exergy efficiency of ORC system all increase linearly. When the pinch-point temperature difference in the evaporator increases by 5°C, the flue gas temperature at the outlet of evaporator corresponding to the maximum net output power increases by 5°C, while the flue gas temperature at the outlet of evaporator corresponding to the maximum exergy efficiency increases by 10°C.*

*Keywords: sinter; waste heat recovery; organic Rankine cycle; performance analysis*

## 1. INTRODUCTION

The efficient recovery and utilisation of waste heat resources in the sintering process is one of the main ways to reduce the energy consumption of sintering process (Cai, 2007). Sinter waste heat resource accounts for about 70% of the total waste heat resources in the actual sintering process (Dong, 2011). Therefore, the efficient recovery and utilisation of waste heat resource in sinter cooling process plays an important role for energy conservation and emission reduction in the steel-making process. Aiming at the researches of heat transfer and waste heat recovery in sinter cooling process, several scholars have done a lot of work for sinter waste heat recovery, Zhang et al. (2013) and Tian et al. (2015) numerically studied the effects of multi-layer feeding and operation parameters on the efficiency of waste heat recovery in sinter cooling process. Liu et al. (2014, 2015) numerically analysed the effects of operational parameters of sinter annular cooler on the air temperature in bed layer and waste heat recovery quantity, and obtained the optimal operational parameters from both waste heat recovery and economic cost aspects.

In order to investigate waste heat recovery in sinter cooling process based on the mechanism analysis of flow and heat transfer in randomly packed bed with sinter particles, the experimental and numerical studies on the gas flow and gas solid heat transfer in sinter bed layer were conducted in our previous study, as reported by Feng et al. (2015, 2015a, 2016, 2016a, 2019, 2019a). At present, the sinter waste heat is taken away by the cooling air in the sinter vertical cooler and annular cooler, and then sent into the waste heat boiler for power generation (Cai, 2011). The temperature of cooling flue gas (cooling air) at the outlet of sinter waste heat boiler is under 200°C, which belongs to the category of low temperature waste heat resources (Jia, 2015). Compared with the traditional industrial flue gas waste heat boiler, the outlet cooling flue gas of sinter waste heat boiler does not contain corrosive gas, and can be recycled without considering the occurrence of dew point corrosion.

The organic Rankine cycle (ORC) is an effective method for the efficient recovery and utilisation of low temperature waste heat resources, which has many advantages, such as simple structure, convenient operation and high thermal efficiency, and so on, ORC has been a world-wide accepted technology of power generation by utilising the low temperature waste heat resources relatively compared to other dynamic energy conversion systems. According to the authors' knowledge, few researches have been conducted on the performance analysis of ORC system for the waste heat recovery and utilisation of low temperature cooling flue gas discharged from the sinter waste heat boiler. Therefore, the low temperature cooling flue gas at the outlet of sinter waste heat boiler is seen as the heat source fluid of ORC system in the present work, and the change of thermal performance of ORC system with the operational parameters is analysed in detail.

## 2. DESCRIPTION OF ORC SYSTEM

As shown in Figure 1(a), the basic ORC system consists of four components, namely evaporator, expander, condenser and pump. The  $T$ - $s$  diagram of ORC system without considering the overheating of working fluid is shown in Figure 1(b), the cycle process mainly involves four thermal processes, namely the isobaric heating process (5-1), adiabatic expansion process (1-2), isobaric condensation process (2-4) and adiabatic compression process (4-5).

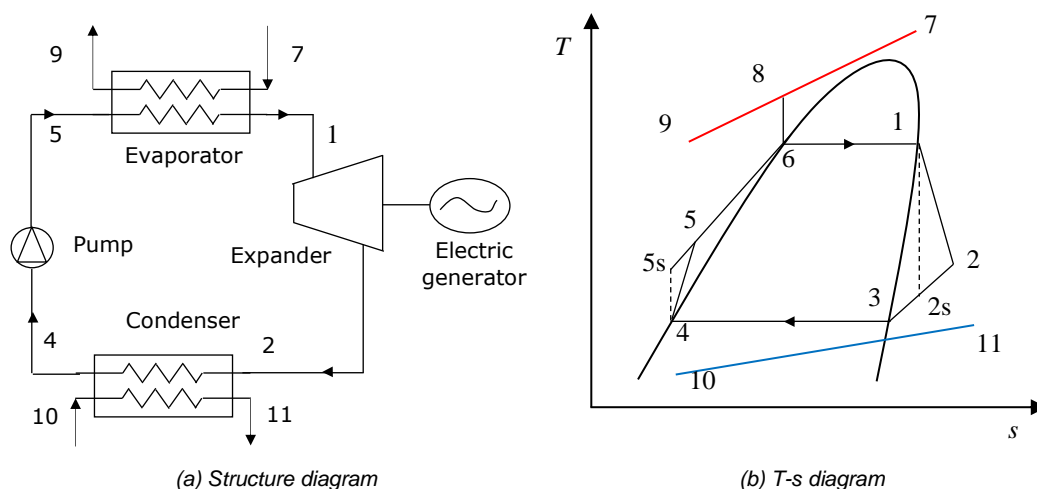


Figure 1: Structure and  $T$ - $s$  diagrams of ORC system

The working fluid in the evaporator is heated to the saturated vapour at high temperature and pressure through the heat exchange with the sinter cooling flue gas, and then the saturated vapour at high temperature and pressure

expands to do work in the expander. The saturated vapour at low temperature and pressure discharged from the outlet of expander is condensed to the saturated fluid in the condenser, and then the saturated fluid is sent into the evaporator for reuse through the pump.

The organic fluid is used as the working fluid in ORC system. The reasonable selection of organic working fluid has an important influence on the cycle efficiency, net output work and irreversible loss for the ORC system. The organic working fluid should have the characteristics of better saturated gas curve, lower critical temperature and pressure, higher latent heat of vaporisation, stronger thermal stability, non-flammable, environment-friendly, cheap and accessible (Maizza, 1996; Angelino, 1998). Based on the above requirements of organic working fluid, meanwhile considering the temperature range of sinter cooling flue gas, R245fa is selected as the working fluid of ORC system of sinter cooling flue gas waste heat.

### 3. ANALYSIS OF THERMAL PERFORMANCE

Based on the first and second laws of thermodynamics, and combined with the  $T$ - $s$  diagram of ORC system in Figure 1(b), the thermodynamic process of ORC system is described as follows.

In the isobaric heating process (5-1), the working fluid in ORC is heated at constant pressure in the evaporator. The heat transfer capacity from the thermal source to working fluid is calculated as:

$$\text{Equation 1: } Q_e = m_f (h_7 - h_9) = m_e (h_1 - h_5)$$

Where:

- $Q_e$  = heat transfer capacity from the thermal source to working fluid (kW)
- $m_f$  = flow rate of cooling flue gas (kg/s)
- $m_e$  = flow rate of working fluid (kg/s)
- $h_7$  = specific enthalpy of cooling flue gas at the inlet of evaporator (kJ/kg)
- $h_9$  = specific enthalpy of cooling flue gas at the outlet of evaporator (kJ/kg)
- $h_1$  = specific enthalpy of working fluid at the outlet of evaporator (kJ/kg)
- $h_5$  = specific enthalpy of working fluid at the inlet of evaporator (kJ/kg)

In the adiabatic expansion process (1-2), the expander converts heat into work. Considering the isentropic efficiency of expander, the work produced by the expander is described as:

$$\text{Equation 2: } W_t = m_e (h_1 - h_{2s}) \eta_t = m_e (h_1 - h_2)$$

Where:

- $W_t$  = work produced by the expander (kW)
- $h_{2s}$  = ideal specific enthalpy of working fluid at the outlet of expander (kJ/kg)
- $h_2$  = specific enthalpy of working fluid at the outlet of expander (kJ/kg)
- $\eta_t$  = isentropic efficiency of expander

In the adiabatic compression process (4-5), the pump converts electric power into work. Considering the isentropic efficiency of pump, the work required by the pump is described as:

$$\text{Equation 3: } W_p = m_e (h_{5s} - h_4) / \eta_p = m_e (h_5 - h_4)$$

Where:

- $W_p$  = work required by the pump (kW)
- $h_{5s}$  = ideal specific enthalpy of working fluid at the outlet of pump (kJ/kg)
- $h_4$  = specific enthalpy of working fluid at the outlet of condenser (kJ/kg)
- $h_5$  = specific enthalpy of working fluid at the outlet of pump (kJ/kg)
- $\eta_p$  = isentropic efficiency of pump

The net output work of ORC system is defined as:

$$\text{Equation 1: } W = W_t - W_p = m_e (h_1 - h_2 - h_5 + h_4)$$

Where:

- $W$  = net output work of ORC system (kJ/kg)

The exergy efficiency is defined as the ratio of net output work to maximum work obtained by the ORC system, and is given by:

$$\text{Equation 5: } \eta_e = \frac{W}{E_f} = \frac{m_e (h_1 - h_2 - h_5 + h_4)}{m_f c_f \left( T_7 - T_9 - T_0 \ln\left(\frac{T_7}{T_9}\right) \right)} = \frac{(h_1 - h_2 - h_5 + h_4)}{(h_1 - h_5) \left( 1 - \frac{T_0}{T_7 - T_9} \ln\left(\frac{T_7}{T_9}\right) \right)}$$

Where:

- $\eta_e$  = exergy efficiency of ORC system
- $E_f$  = exergy change of cooling flue gas in the evaporator (kW)
- $c_f$  = specific heat capacity of cooling flue gas (kJ/(kg K))
- $T_7$  = inlet temperature of cooling flue gas (K)
- $T_9$  = outlet temperature of cooling flue gas (K)
- $T_0$  = ambient temperature (K)

## 4. RESULTS AND DISCUSSION

The cooling flue gas at the outlet of sinter waste heat boiler is regarded as the heat source of ORC system in the present work, the temperature of which is under 200°C. The thermal process of ORC system shown in Figure 1(b) is calculated numerically, and the effects of evaporation temperature of working medium ( $T_1$ ) and pinch-point temperature difference in the evaporator ( $\Delta T = T_8 - T_6$ ) under different flue gas temperature at the outlet of evaporator on the thermal performance of ORC system are investigated in detail. The initial calculation parameters of ORC system are shown in Table 1.

Table 1: Initial calculation parameters of ORC system

Parameters	Values
Flow rate of cooling exhaust gas (kg·s <sup>-1</sup> )	190
Temperature of cooling exhaust gas (°C)	160
Inlet temperature of cooling water (°C)	20
Isentropic efficiency of pump	0.8
Isentropic efficiency of expander	0.85
Condensation temperature of working fluid (°C)	30
Pinch-point temperature difference of condenser (°C)	5
Ambient temperature (°C)	20

### 4. 1. Effect of evaporation temperature of working medium

Because of that the pinch-point temperature difference in the evaporator is greater than zero, the temperature range of outlet flue gas at the outlet of evaporator is also determined for the selected evaporation temperature of working fluid. The variation of net output work of ORC system with the outlet flue gas temperature under different evaporation temperature of working fluid is shown in Figure 2.

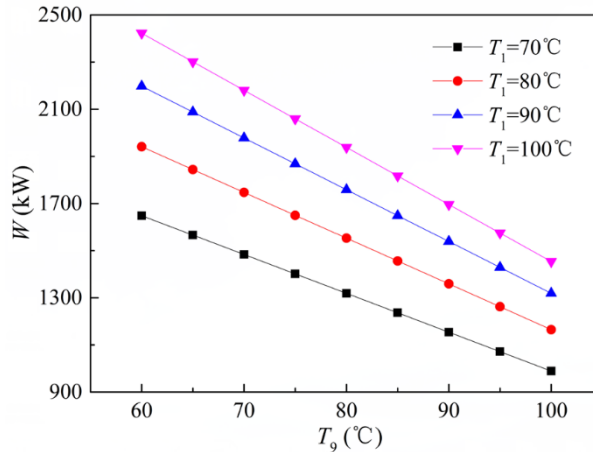


Figure 2: Effect of evaporation temperature of working medium on net output work

As can be seen from Figure 2, the net output work gradually decreases with the increase of outlet flue gas temperature for a given evaporation temperature of working fluid. When the outlet flue gas temperature is constant, the higher is the evaporation temperature of working fluid, the larger is the net output work of ORC system. This may be explained that, the increase of outlet flue gas temperature results in the decrease of heat transfer capacity between the cooling flue gas and the organic working fluid, the flow rate of working fluid decreases for a given evaporation temperature of working fluid, which results in the decrease of net output work of ORC system. With the increase of evaporation temperature of working fluid, the increase amplitude of net output work per unit flow rate of working fluid is larger than the decrease amplitude of flow rate of working fluid, so the net output work of ORC system gradually increase for a given outlet flue gas temperature.

The variation of exergy efficiency of ORC system with the outlet flue gas temperature under different evaporation temperature of working fluid is shown in Figure 3. As can be seen from Figure 3, the exergy efficiency gradually decreases with the increase of outlet flue gas temperature for a given evaporation temperature of working fluid. When the outlet flue gas temperature is constant, the higher is the evaporation temperature of working fluid, the larger is the exergy efficiency of ORC system. This may be explained that, because of that the evaporation temperature of working fluid is constant, the specific enthalpy of working fluid at critical point shown in Figure 1(b) is also constant. With the increase of outlet flue gas temperature, the energy level of cooling flue gas gradually increases, which results in the decrease of exergy efficiency of ORC system based on the Equation (5). When the outlet flue gas temperature is constant, the exergy change of cooling flue gas in the evaporator is also constant, the increase of net output work results in the increase of exergy efficiency of ORC system with the increase of evaporation temperature of working fluid.

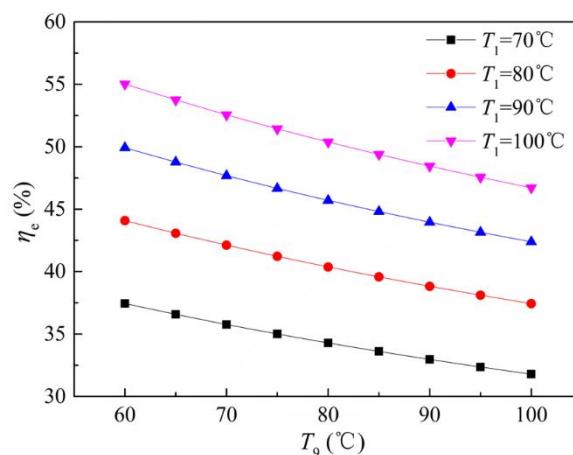


Figure 3: Effect of evaporation temperature of working medium on exergy efficiency

#### 4. 2. Effect of pinch-point temperature difference in evaporator

The variation of net output work of ORC system with the outlet flue gas temperature under different pinch-point temperature difference in the evaporator is shown in Figure 4.

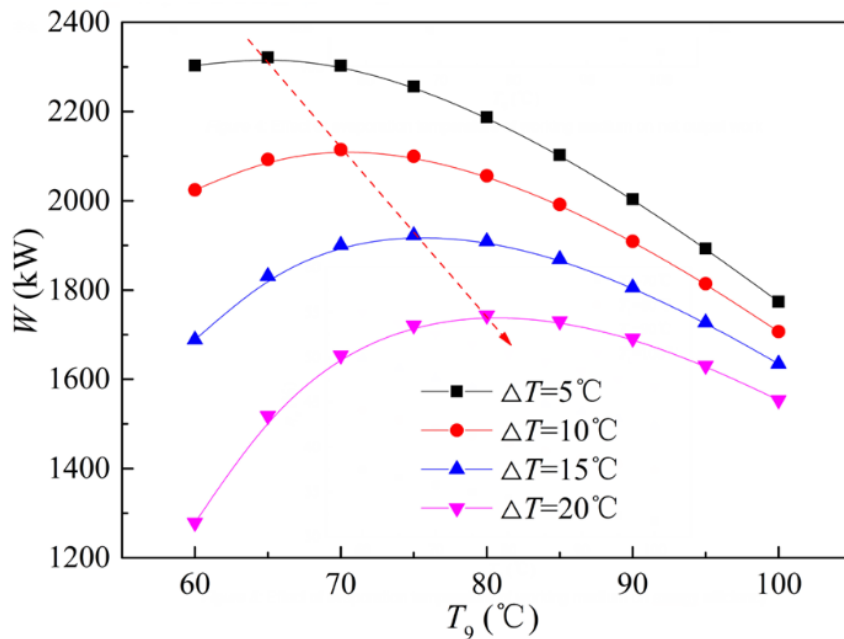


Figure 4: Effect of pinch-point temperature difference in evaporator on net output work

As can be seen from Figure 4, the net output work tends to increase first and then decrease with the increase of outlet flue gas temperature for a given pinch-point temperature difference in the evaporator. When the outlet flue gas temperature is constant, the higher is the pinch-point temperature difference in the evaporator, the smaller is the net output work of ORC system. This may be explained that for a given outlet flue gas temperature, the pinch-point temperature difference in the evaporator results in the decrease of evaporation temperature of working fluid, which leads to the decrease of net output work based on the research result of Figure 2. It is also obtained from Figure 4, the higher is the pinch-point temperature difference in the evaporator, the higher is the outlet flue gas temperature corresponding to the maximum net output power. When the pinch-point temperature difference in the evaporator increases by  $5^\circ\text{C}$ , the outlet flue gas temperature corresponding to the maximum net output power also increases by  $5^\circ\text{C}$ .

The variation of exergy efficiency of ORC system with the outlet flue gas temperature different pinch-point temperature difference in the evaporator is shown in Figure 5. As can be seen from Figure 5, the exergy efficiency gradually increases with the decrease of pinch-point temperature difference in the evaporator for a given outlet flue gas temperature. This may be explained that when the outlet flue gas temperature is constant, the exergy change of cooling flue gas in the evaporator is also constant, the increase of net output work results in the increase of exergy efficiency of ORC system with the decrease of pinch-point temperature difference in the evaporator.

It is also obtained from Figure 5, in the range of outlet flue gas temperature from  $60^\circ\text{C}$  to  $100^\circ\text{C}$ , only the exergy efficiency with the pinch-point temperature difference in the evaporator of  $5^\circ\text{C}$  tends to increase first and then decrease with the increase of outlet flue gas temperature, while the exergy efficiency with the other pinch-point temperature difference in the evaporator gradually increases. When the outlet flue gas temperature is greater than  $100^\circ\text{C}$ , the exergy efficiencies with the other three pinch-point temperature differences in the evaporator also tend to increase first and then decrease with the increase of outlet flue gas temperature. Furthermore, the higher is the pinch-point temperature difference in the evaporator, the higher is the outlet flue gas temperature corresponding to the maximum exergy efficiency. When the pinch-point temperature difference in the evaporator increases by  $5^\circ\text{C}$ , the outlet flue gas temperature corresponding to the maximum exergy efficiency increases by  $10^\circ\text{C}$ .

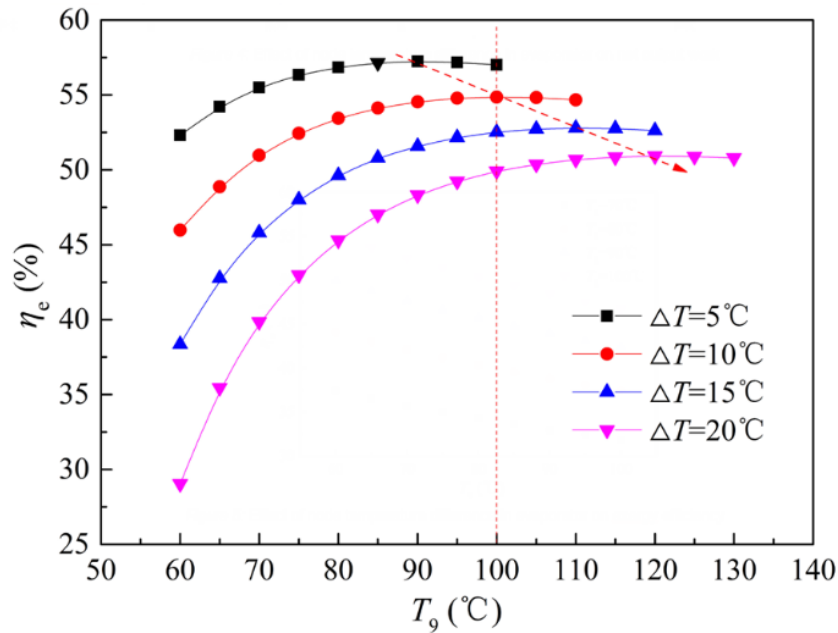


Figure 5: Effect of pinch-point temperature difference in evaporator on exergy efficiency

## 5. CONCLUSIONS

In the present work, R245fa is selected as the working fluid of ORC system for waste heat recovery of sinter cooling flue gas, and the thermal performance of ORC system is analysed in detail. The major findings are as follows.

(1) With the increase of outlet flue gas temperature, both the net output work and exergy efficiency of ORC system decrease for a given evaporation temperature of working fluid. When the outlet flue gas temperature is constant, the higher is the evaporation temperature of working fluid, the larger are the net output work and exergy efficiency of ORC system.

(2) The net output work and exergy efficiency of ORC system tend to increase first and then decrease with the increase of outlet flue gas temperature for a given pinch-point temperature difference in the evaporator. When the outlet flue gas temperature is constant, the lower is the pinch-point temperature difference in the evaporator, the larger are the net output work and exergy efficiency of ORC system.

(3) With the increase of pinch-point temperature difference in the evaporator, the outlet flue gas temperatures corresponding to the maximum net output power and exergy efficiency of ORC system all increase linearly. When the pinch-point temperature difference in the evaporator increases by  $5^\circ\text{C}$ , the outlet flue gas temperature corresponding to the maximum net output power increases by  $5^\circ\text{C}$ , while the outlet flue gas temperature corresponding to the maximum exergy efficiency increases by  $10^\circ\text{C}$ .

## 6. ACKNOWLEDGEMENT

This study was sponsored by National Natural Science Foundation of China (51274065, 51761145109), China Postdoctoral Science Foundation (2018M642538), Fundamental Research Funds for the Central Universities (WK2090130025), and Anhui Provincial Natural Science Foundation (1908085QE203).

## 7. REFERENCES

- Angelino G. 1998. Multicomponent working fluids for organic Rankine cycles (ORCs). *Energy*, 23(6), 449-463.
- Cai J J, Wang J J, Chen C X, Lu Z W. 2007. Waste heat recovery and utilization in iron and steel industry. *Iron and Steel*, 42 (6), 1-7.
- Cai J J, Dong H. 2011. Method and device of sinter waste heat recovery and utilization with vertical tank. *Chinese Patent*, 200910187381.8.



- Dong H, Lin H Y, Zhang H H, Cai J J, Xu C B, Zhou J W. 2011. Thermal test and analysis of sintering cooling system. *Iron and Steel*, 46 (11), 93-98.
- Feng J S, Dong H, Dong H D. 2015. Modification of Ergun's correlation in vertical tank for sinter waste heat recovery. *Powder Technology*, 280: 89-93.
- Feng J S, Dong H, Liu J Y, Liang K, Gao J Y. 2015a. Experimental study of gas flow characteristics in vertical tank for sinter waste heat recovery. *Applied Thermal Engineering*, 91: 73-79.
- Feng J S, Dong H, Gao J Y, Liu J Y, Liang K. 2016. Experimental study of gas–solid overall heat transfer coefficient in vertical tank for sinter waste heat recovery. *Applied Thermal Engineering*, 95: 136-142.
- Feng J S, Dong H, Gao J Y, Li H Z, Liu J Y. 2016a. Numerical investigation of gas-solid heat transfer process in vertical tank for sinter waste heat recovery. *Applied Thermal Engineering*, 107: 135-143.
- Feng J S, Zhang S, Dong H, Pei G. 2019. Frictional pressure drop characteristics of air flow through sinter bed layer in vertical tank. *Powder Technology*, 344: 177-182.
- Feng J S, Zhang S, Dong H, Pei G. 2019a. Effect of gas inlet parameters on exergy transfer performance of sinter cooling process in vertical moving bed. *Applied Thermal Engineering*, 152: 126-134.
- Jia G. 2015. Study on suitable operation parameters of waste heat boiler for vertical tank with sinter waste heat recovery. Shenyang, Northeastern University.
- Liu Y, Yang J, Wang J, Cheng Z L, Wang Q W. 2014. Energy and exergy analysis for waste heat cascade utilization in sinter cooling bed. *Energy*, 67(4): 370-380.
- Liu Y, Yang J, Wang J Y, Ding X G, Cheng Z L, Wang Q W. 2015. Prediction, parametric analysis and bi-objective optimization of waste heat utilization in sinter cooling bed using evolutionary algorithm. *Energy*, 90(1): 24-35.
- Maizza V, Maizza A. 1996. Working fluids in non-steady flows for waste energy recovery systems. *Applied Thermal Engineering*, 16(7), 579-590.
- Tian W Y, Zhang J Y, Dai C D, Long X Y. 2015. Recovery of waste heat from sinter cooling process: simulation and optimization. *Ironmaking and Steelmaking*, 42(2): 97-104.
- Zhang X H, Chen Z, Zhang J Y, Ding P X, Zhou J M. 2013. Simulation and optimization of waste heat recovery in sinter cooling process. *Applied Thermal Engineering*, 54(1): 7-15.

---

## #76: Mathematical modelling and performance analysis of a semi-transparent thin film PV glazing insulated with vacuum layer

---

Hasila JARIMI<sup>1\*</sup>, Daniel COOPER<sup>1</sup>, Qinghua LV<sup>2</sup>, Theo ELMER<sup>3</sup> and Saffa RIFFAT<sup>1</sup>

<sup>1</sup>The University of Nottingham, United Kingdom, Hasila.Jarim@nottingham.ac.uk

<sup>2</sup>Environmental Hubei Collaborative Innovation Center for High-efficient Utilization of Solar Energy, Hubei University of Technology, Hubei, Wuhan  
<sup>3</sup>Geo Green Power Limited, United Kingdom

*This paper presents a novel design of a semi-transparent thin-film PV glazing insulated with vacuum layer. The vacuum glazing unit proposed in this study consists of two parallel glass panes; thin-film PV glass of an a-Si type separated from a 4 mm hard low-e coated glass pane by an approximately 0.3 mm vacuum gap called PV VG-2L. A mathematical model was developed and solved in MATLAB. The simulation allows both thermal and electrical performance analysis. The developed model was validated against the experimental results. To carry out the experiment, PV VG-2L was developed using low-temperature high-level vacuum method. The thermal performance was evaluated indoors using an innovative air to air source thermoelectric (TEC)-driven calibrated hot box built at the Department of Architecture and Built Environment, the University of Nottingham by closely following ISO 12567 Standards. At temperature difference of 20 °C, the average measured total U-value was found at 1.6 W/m<sup>2</sup>K with the average temperature difference between the internal and external surface was 13 °C. From the analysis, the computed percentage difference for the glazing internal and external surface temperatures and U-value are 1.3%, 8.6% and 3.0% respectively. The theoretical and experimental results are concluded to be in good agreement and hence the model is proven valid. Using the validated mathematical model, the performance of PV VG-2L was simulated under real conditions. The promising U-value implies its range of potential applications can be improved depending on the energy needs and applications, such as for BIPV solar façade (PV curtain walling) in commercial buildings, greenhouses, skylight and conservatory. The next step or part two of the research will be on the proof of concept prototype development of the innovative thin-film PV glazing with vacuum insulated layer glazing and the experimental validation of the mathematical model*

Keywords: low-temperature; double thin film PV VG

## 1. INTRODUCTION

Windows and glazing installed in a building are important indicators of the energy efficiency of the building. In 2018, it has been reported that energy use in buildings is projected to increase by 32% between 2015 and 2040. Most of the increase is contributed mainly in emerging non-OECD countries, where population continues to shift from rural to urban areas (EIA 2017). The development of the glazing technology includes a single glazing with U-values which are typically very high, to double glazing technology and recently triple glazing technology. For double and triple glazing technology, the use of inert gasses such as Argon and Krypton are also introduced to reduce the heat transfer through the gap. However, the lowest heat transfer will occur when we have a vacuum layer in the gap. This is because vacuum layer means that the heat transfer mechanism that would occur between the glass sheets are mainly due to radiation and the thermal conduction of support pillars that are placed to support the glass sheets (Fang, Hyde et al. 2015). This type of glazing technology is known as vacuum glazing which significant advantage over the other glazing technologies being the low U-Value at a very low thickness.

### 1.1. Innovative vacuum glazing designs for building applications

In recent years, researchers have shown interest in the study of vacuum glazing technology. Innovative designs were developed and researched. Among them are; Bao, Liu et al. (2014) who have introduced a novel hybrid vacuum/triple glazing system in which a vacuum glazing unit is enclosed by two glass panels to form a triple glazing unit system. To eliminate additional loads due to pressure difference which can cause unwanted breakage, they have designed an equalised air pressure design to be on both sides of the vacuum glazing unit. Fang, Hyde et al. (2015) have performed simulation model using a finite volume model on thermal performance of triple vacuum glazing (TVG) sealed using indium alloy, and 4 mm thick glass panes. In their validated computer simulation work, the emissivity values of the glass sheets were varied from 0.18 to 0.03. The simulated centre U-values are reduced from  $0.41 \text{ Wm}^{-2}\text{K}^{-1}$  to  $0.22 \text{ Wm}^{-2}\text{K}^{-1}$  for a 0.4 m by 0.4 m size triple vacuum glazing. Memon (2017) introduced a triple vacuum glazing using Cerasolzer CS186 alloy as the edge sealant. From the 3D finite element model, the centre of glass U-value of  $0.33 \text{ Wm}^{-2}\text{K}^{-1}$  is found achievable. Memon and Eames (2017) investigated the building heating performance when retrofitted with the composite edge sealed triple vacuum glazing. An annual space-heating energy savings of 14.58% and 15.31% are expected to be achieved. Meanwhile, if single glazing windows are to be replaced with the designed triple vacuum glazing, a heat loss reduction of 12.92% and 2.69% are achievable. Research on vacuum glazing technology has also innovating towards integrating the technology with other advanced glazing technology. Fang, Hyde et al. (2010) have introduced an integration between electrochromic (EC) with vacuum glazing (VG) technology. The EC component was arranged facing the outdoor environment. For an incident solar radiation of  $300 \text{ W m}^{-2}$ , simulations shows that the EC layer is opaque and the inside temperature of the glass pane is higher than the indoor temperature. Meanwhile, for solar radiation of  $1000 \text{ W m}^{-2}$ , the outdoor glass pane temperature exceeds the indoor glass pane temperature, of which as a consequence heat is transferred from outdoors to indoors. Ghosh, Norton et al. (2017) integrated suspended particle device (SPD) with vacuum glazing. In their study, a strong correlation between the measures of the clearness of the atmosphere or clearness index was evaluated for south facing vertical glazing. For clearness index below 0.5, the SPD-vacuum glazing transmission was 17% and 1.1% for transparent and opaque states respectively. A group of researchers from China (Zhang, Lu et al. 2017) proposed an integration between a thin film PV glazing with a vacuum glazing. The glazing prototype was designed and manufactured in such a way that a lamination layer was sandwiched between the thin film PV glazing unit and a vacuum glazing unit, both are independently manufactured. According to the researchers, although semi-transparent photovoltaic windows can generate electricity in situ, they also increase the cooling load of buildings significantly due to the waste heat as a by-product. Experiment has been conducted and the results have indicated that the prototype can not only generate electricity, but also help reduce the cooling load as well as improve the indoor thermal comfort. Recently, researchers (Ghosh, Sundaram et al. 2018) investigated a combined semi-transparent multicrystalline PV vacuum glazing. In their research, both thermal and electrical performance have been investigated. They have found that the combination of multicrystalline PV cells with vacuum glazing provide low overall heat transfer coefficient, reduces solar heat gain, generates clean electricity and allows comfortable daylight.

### 1.2. Studies on support pillars

When a vacuum glazing is exposed to atmospheric pressure of approximately 1.01 kPa, in order to maintain the structure of the glazing or to prevent the separated glass sheets from collapsing, support pillars are very important to maintain the separation of the glass sheets (Collins and Simko 1998). However, the installation of these pillars creates thermal contact between the glass sheets. As a result, heat conduction occurs through the pillars which contributes to higher heat loss or low U-value of the system (Wilson, Simko et al. 1998, Eames 2008, Cuce and Riffat 2015). Theoretically, at fixed pillar radius and spacing, pillar materials with low value in thermal conductivity, will give low U-value. Therefore, there are researchers who have introduced the use of aerogel materials with thermal conductivity lower than  $0.01 \text{ W/mK}$  to support the vacuum glazing. For example, researchers, Schultz and Jensen (2008) have introduced an evacuated aerogel glazing. However, the vacuum level was in the range of medium vacuum level (approximately 10-1000 Pa) and in their design, the monolithic silica aerogel did not serve as the support pillars as in the typical vacuum glazing product. Also, one of the current authors, have published a

paper on the numerical analysis of vacuum glazing using aerogel as the support pillars (Cuce and Riffat 2015). 2D CFD analysis using ANSYS Fluent was developed and validated against manufacturer's data report of Pilkington. However, in their work, the atmospheric load analysis was not being considered and they have made assumptions that radiation heat transfer is negligible, and conduction is the only heat transfer mechanism occurring within the window.

The important parameters associated to the heat conduction through the support pillars are the pillars' diameter and the spacing between the glass sheets (height of the pillar) (Collins and Simko 1998). However at certain limit of vacuum spacing, the glass sheet will fracture since the pillars will not be able to withstand the weight of the glass with atmospheric pressure on it. Clearly, support pillars are very important components of a vacuum glazing. Table 1, summaries the literature which have discussed on the design choices and the influence of the pillars design to the U-value performance of the vacuum glazing. The design choices of the support pillar includes the materials used, the radius of the pillar and its separation. In terms of the materials used for the support pillars, materials which are commonly used or have been explored are solder glass, metals, and ceramics (Collins, Turner et al. 1995). All the aforementioned materials for the support pillars have high thermal conductivity property (i.e higher than 1 W/m<sup>2</sup>K)

Table 1: The summary of literature survey on the design choices and support pillars

Types of study	Pillar materials	Finding	Reference
Experiment and Numerical	Alumina and Inconel 718	The measured value of thermal conductance due to the pillar was found very similar with theoretical analysis. This is due to thermal conductivity of the pillars which are very high compared to the glass sheets.	(Collins, Turner et al. 1995)
Numerical analysis (Finite volume method)	Alumina and Inconel 718	The pillar separation and pillar radius must satisfy several different design constraint such as external mechanical constraint.	(Collins and Simko 1998)
Numerical model.		Allowable pillar diameter and spacing increases and conductance of pillar array decreases with increase in glass thickness. Variation in pillar radius, pillar separation and conductance of pillar array with changing in the glass pane thickness leads to changes in U-Value.	(Fang, Eames et al.)
Simple analytic and complex element model	Alumina and Inconel 718	Due to the high thermal conductivity of the pillar, they have concluded that the thermal resistance of a single support pillar can be accurately predicted using analytical equation.	(Wilson, Simko et al. 1998)
Transparent pillars using printing	support screen Low melting glass powder	This novel method to prepare a transparent spacer array for vacuum glazing is reliable and superior to the commonly used metal pillar array in terms of appearance and transmittance.	(Zhao, Luo et al. 2013)
Numerical model on transparent pillars	Aerogel support	The use of aerogel as support pillars was concluded to reduce the U value of a vacuum glazing	(Cuce and Riffat 2015)

This paper presents: a semi-transparent thin film PV glazing insulated with vacuum layer called PV VG-2L using a strong low thermally conductive aerogel Airloy® as the support pillars. This paper includes a brief review on the vacuum glazing technology with the focus on innovative glazing design and the research on the support pillars. The paper will then discussed the design concepts of the PV VG-2L by taking into consideration the mechanical constraint associated to the use of aerogel Airloy® as the support pillars. The mathematical model to predict the thermal performance and power production of the PV VG-2L were developed and numerically solved in MATLAB. To validate the model, a prototype was manufactured using a low temperature and high level vacuum oven and experimentally tested using an innovative air to air source thermoelectric (TEC)-driven calibrated hot box built at the Department of Architecture and Built Environment, the University of Nottingham by closely following ISO 12567 Standards. The discussion on the manufacturing process and the experimental validation of the mathematical model are also presented in the paper. Finally, the performance of the PV VG-2L was simulated under real conditions by considering installation at E.ON Research House during winter and summer conditions

## 2. THE DESIGN CONCEPT OF THE THIN FILM PV WITH VACUUM INSULATED LAYER USING AEROGEL SUPPORT PILLARS

The integration of photovoltaic technologies (PV) in the glazing element of a building envelope has a number of advantages over a conventional glazing system. In comparison to the typical high insulation materials used for

building envelope, electricity is generated while providing natural light with the combination of PV and glazing, thus reducing electricity consumption and demand during the day caused by artificial lighting. Windows and glazing are important indicators of the energy efficiency rating of a building. A conventional thin film PV glazing, has a U-value similar to the single glazing unit which is between 4-6 W/m<sup>2</sup>K depending on the type of thin film PV and its transparency. To improve the thermal performance of a thin film PV glazing, a combination with a double glazing unit is possible with the estimated U-value of 2.5-2.8 W/m<sup>2</sup>K depending on the gap size and the type of gas used to provide higher insulation in the air gap. This paper introduces the use of vacuum layer to improve the thermal performance of the PV glass. This means, in addition to power production, the PV glass have high insulating thermal performance.

As shown in Figure 1, different from the approach introduced by Zhang, Lu et al. (2017) in which the thin film PV glazing unit and a vacuum glazing unit are independently manufactured, the vacuum glazing unit proposed in this study consists of two parallel glass panes; thin film PV glass of a  $\mu$ C-Si/a-Si or an a-Si type separated from a 4 mm low-e coated glass pane by an approximately 0.3 mm vacuum gap called PV VG-2L. A thin tempered glass is used as the back cover. A slimmer feature of the thin film PV VG but with high insulating performance. Unlike the conventional vacuum glazing that uses highly thermal conductive materials the glass panes are supported by an array of support pillars made of strong and low thermally conductive aerogels of Airloy<sup>®</sup> with thermal conductivity less than 0.1 W/mK. To enhance the vacuum level, we use a non-evaporable chemical of saes group (2019). It is worth noting that, due to the vacuum layer, the convective and conductive heat transfer due to the gas particles is negligible and hence the thermal performance of the PV VG is significantly improved since heat will only be transferred via radiative heat transfer between the glass panes, conductive heat transfer through the support pillars and heat transfer through the edge sealing. In addition to that, the use of low thermally conductive support pillars will further reduce the heat transfer thus resulting in low U- value. To analyse the performance of the PV-VG system, the main constraints associated with the atmospheric pressure loading were considered to simulate the values for the safe pillar spacing and diameter. The constraints include:

- Surface tensile stress on the external glass surface,
- Hertzian conical fracture on the inner glass surfaces due to the support pillars,
- Maximum compressive stress that the pillar can take,
- The conductance of the pillar arrays less than 0.4 W/m<sup>2</sup>K.

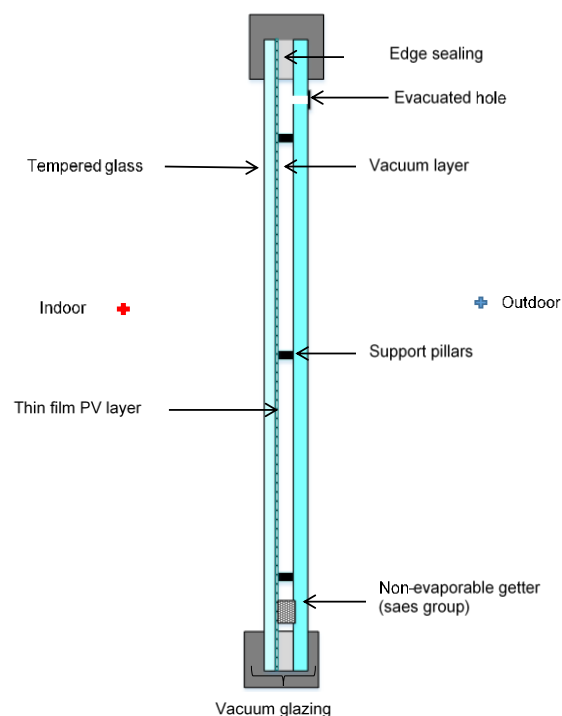


Figure 2: The schematics of the thin film photovoltaic glazing with vacuum insulated layer (PV VG) with getter

#### Hertzian conical crack

Based on the study of Hertz (Hertz 1881) the correlation between the pillar spacing and pillar radius for different types of pillar materials can be computed. Of particular interest for this project is the fracture behavior of the glass

sheets. Hertz observed that a conical stress fracture occurs when a hard sphere is pressed onto a glass surface. Meanwhile, Auerbach observed that the force  $P_c$  which cause the fracture was proportional to the radius of the indenter given in the following equation (Collins, Fischer-Cripps et al. 1992):

$$P_c = AR \quad (1)$$

Where  $A$  is known as Auerbach's constant, and has a value of  $\approx 10^5 Nm$  and  $R$  is the radius of the pillars or indenter. The equation can be rewritten as:

$$a^3 = \frac{4kPR}{3E} \quad (2)$$

Where  $a$  is the radius of the contact area between the indenter and the surface,  $E$  is the Young's Modulus and  $k$  is a function of the elastic properties of the material and has a value close to unity.

Rearrange  $R$  in terms of  $P_c$  and  $A$ , and substitute into (17) will give us (18),

$$P_c = \left(\frac{3AE}{4k}\right)^{1/2} a^{3/2} \quad (3)$$

Now, the force on each pillar can be written in terms of the pillar separation  $\lambda^2$  and the atmospheric pressure  $q$

$$P_c = q\lambda^2 \quad (4)$$

Combining equation (18) and (19) we can derive a relationship between pillar separation and pillar radius.

$$\lambda^2 = \left(\frac{3AE}{4k}\right)^{1/2} a^{3/4}/q \quad (5)$$

When aerogel is used as the support pillars, the following equation is obtained:

$$\lambda^2 = 161.34 a^{3/4} \quad (6)$$

#### *Maximum compressive strength*

It is very important to note that one of the main consequences of constructing a vacuum glazing using support pillars without enough strength is the production of stresses that will lead to failure of the vacuum glazing unit.

Thus, it is very important to restrict the level of compressive stress in the support pillars which is given by  $q\lambda^2/\pi a^2$  ( $q$  is the atmospheric pressure,  $\lambda$  is the pillar spacing, and  $a$  is the pillar radius) to values below the compressive strength of the materials of the support pillar themselves (Henshall, Eames et al. 2016). By taking into account the mechanical design constraints, the range of safe values for the pillar radius and spacing can be estimated graphically.

#### *The range of safe pillar spacing $\lambda$ , and radius $a$*

Based on the plotted graph – see figure 2, the optimum safe value for pillar spacing and pillar radius were determined. Although the pillar spacing for aerogel can be as far as 59 mm, the safe radius for the aerogel at that spacing is 0.8 mm. The value has exceeded the accepted value in avoiding visual obstruction (which should not exceed 0.5 mm (Ali, Hayat et al. 2016)). From the simulation results shows in Figure 2, radius of a pillar as 0.5 mm at pillar spacing of 36 mm as the optimum parameters for the aerogel pillars. Figure 2 shows that, at the optimum pillar spacing of 30 mm, the safe pillar radius to avoid conical crack is about 0.13 mm. However, in order to consider the compressive strength of the aerogel pillars, radius of 0.5 mm is chosen. The values, can be used to estimate the design parameters associated to the support pillars. However, it is possible to slightly apply larger separation in pillar separation in practice (Collins and Simko 1998). In this study we have employed several pillar spacing of 47 mm. In addition, to get low U-value, according to Collins and Simko (1998) the most insulating samples has glass to glass radiation of around 0.51 W/m<sup>2</sup>K. Therefore, total pillar conductance of 0.4 w/m<sup>2</sup>K should be considered in the design limit.

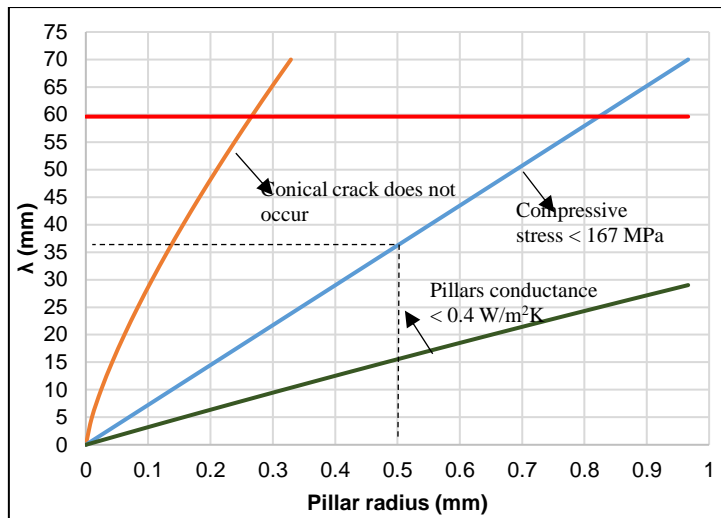


Figure 3: The curves to estimate the optimum pillar radius and spacing for aerogel pillar (glass thickness of 4 mm) for maximum tensile stress limited to 35 MPa.

### 3. THE MANUFACTURING OF PV VG-2L USING LOW TEMPERATURE HIGH LEVEL VACUUM OVEN METHOD

The first patent on the concept of the vacuum glazing was filed in 1913 by Zoller meanwhile the first vacuum glazing has been successfully fabricated at the University of Sydney in 1989 (Nippon Sheet Glass Spacia Co. 2003). Following to that, since 1994, the university has worked with Nippon Sheet Glass in commercialisation the product of which the first commercially available vacuum glazing technology, Pilkington Spacia was in the market in 1997 manufactured by Nippon Sheet Group (Glass 2016). To create the hermetic seal, the technique which has been proven successful is sealing using solder glass and the process involves heating the whole sample at temperature ranging between 350 °C to 650 °C. The evacuation was carried out via a pump out tube and a high level vacuum pump. Vacuum glazing available in the market using the aforementioned manufacturing methods are Pilkington Spacia™ by NSG, vacuum glazing by Qingdao Hengda Co.Ltd., and Beijing Synergy Vacuum Glazing Technology. Still at high temperature manufacturing technique, a manufacturer in China, has implemented the use of vacuum oven for both the evacuation and sealing process, and hence eliminating a protruding surface due to the pump out tube. With high temperature sealing, the use of low-emissivity (low-e) coated glass is limited. However, the use of low-e coated glass for one or both internal surfaces of the evacuated gap will reduce the radiative heat transfer between the glass panes. This will only possible if low temperature sealing (i.e. less than 200 °C) involves in the manufacturing process. In 2017, LandVac has introduced their vacuum glazing manufactured via low temperature method (LandVac 2018). At lab-scale, various studies have been conducted to investigate the manufacturing of vacuum glazing using low temperature method. Among them are (Fang, Hyde et al. 2014) who used Indium alloy, and (Memon, Farukh et al. 2015) who used Cerasolzer CS186 alloy which comprised of mainly 60% Sn and 35% Pb.

In this research, due to the temperature limitation of the thin film PV glass and the cost, we have used low-temperature method i.e. less than 200 °C to manufacture our prototype. Two types of Indium-based alloy with different melting temperature were utilised in this research. The application of Indium-based alloy, to create hermetic seal in vacuum was introduced back in 1952. It was due to the fact that, in high vacuum situation, materials like neoprene, silicon based adhesive would outgas and degrade the vacuum layer (Knudsen 1952). Additionally, Indium is a soft material that can flow under compression, have some ductility where it can be stretched and mould itself into the shape of the materials being sealed. It also has the ability to join materials that have a significant mismatched coefficients of thermal expansion under a thermal cycling which is in this case a thin film PV glazing and a glass pane (Hyde, Griffiths et al. 2000). It will address the stress-related issues due to edge sealing failure of vacuum glazing at huge temperature differentials (Arya and Hyde 2017).

#### 3.1. The manufacturing of PV VG-2L with one stage method: Seal (Edge) → Evacuate → Seal (Evacuated Hole)

The step by step method in the manufacturing of the prototype is as follows:

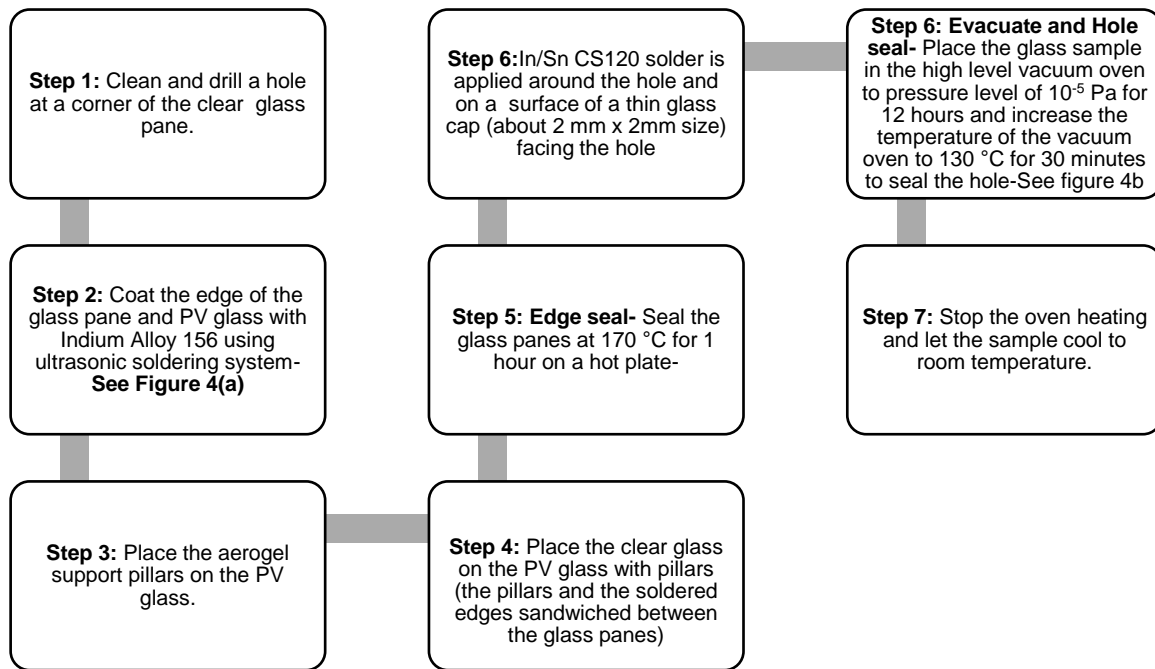


Figure 4: The PV VG- 2L prototype manufacturing process

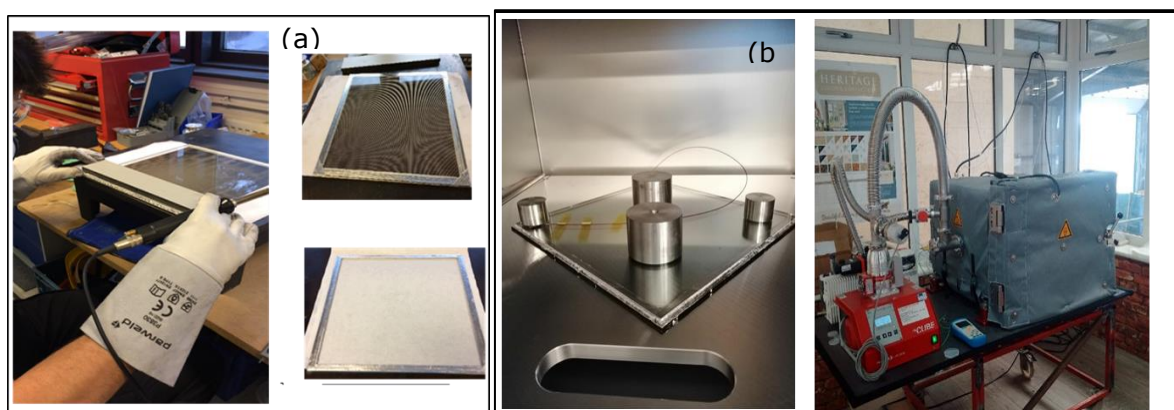


Figure 5: (a) Glass coated using the USS to remove the air pockets and oxide layer and (b) Sample placed in the vacuum oven

## 4. HEAT TRANSFER ANALYSIS

### 4.1. Analytical model of thin film PV glazing with vacuum insulated layer (PV VG)

A mathematical model which allows us to simultaneously simulate power production and the influence of solar radiation to the thermal performance of the PV VG is very important. The temperature nodes for the front glass facing outdoors, the thin film PV glass component, the edge facing indoors and the edge facing outdoors were denoted as  $g_1, g_2, T_{edge 1}$  and  $T_{edge 2}$  respectively. The design parameters of the presented PV VG may be analysed by taking into account all the parameters related to the individual component of a typical vacuum glazing unit which is the dominant in the design i.e. the heat transfer due to support pillars, edge seal and between the glass panes. In a research conducted by Wilson, Simko et al. (1998), the fact that the heat flow through the individual pillar can be estimated from a simple analytic model implies that the analysis using analytical model and complex finite element model are said to be very consistent to one another. Thus, it is unnecessary to undertake complex numerical modelling in order to determine the performance of vacuum glazing (Wilson, Simko et al. 1998). In addition, (Tom, Richard et al.) have concluded that a simplified 1-Dimensional model with only one spatial variable (i.e. distance  $x$  along the glass sheets, are very consistent with the complex three dimensional analysis. In this paper, the mathematical model will be developed based on analytical model of 1-D analysis and the model will be solved numerically in MATLAB. Energy balance equations as expressed in (7)-(11) were then developed. The absorbed solar radiation which not only influences the performance of the vacuum glazing component but also



the thin film PV component are included in the equations. The solution to the energy balance equation will provide useful information on the performance of the thin film PV glass and also in computing the temperature dependence heat transfer coefficients (HTCs). The calculated temperature dependent HTCs are then used to compute the centre U-value and the overall U-value of the designed PV VG. The absorbed solar radiation by the front glass cover and the thin film PV glass component were estimated by taking into consideration the effective absorptance transmittance product  $((\alpha\tau)_{eff})$  as in the work of (Han, Lu et al. 2019). The optical properties of the transparent front glass pane is characterised by the solar transmittance and the thin film PV glass properties by the solar absorptance. Due to multiple reflections occur between the front glass pane and the thin film PV glass component, the amount of the radiation reaching the thin film PV glass component will increase. However, the value will be influenced by the incidence solar angle of which, in this study, we have used the empirical equation that we have preliminary obtained based on the work by (Moralejo Vázquez 2014) to predict the value with the change in the incidence solar angle. Based on the heat transfer mechanism, the energy balance equations were developed. In order to simplify the analysis, the following assumptions have been made:

The temperature gradient only exist along the x-axis of the sheets (this has been proven in agreement with the complex 3-D modelling by Wilson, Simko et al. 1998

The heat transfer involved is assumed symmetrical. Therefore, we only consider a quarter of the PV VG- area in the heat transfer analysis.

In this study we have considered the lateral heat transfer through the glass slab in  $g1$  and  $g2$  in the x-direction. This is due to the fact that, the vacuum glazing is highly thermally insulated which makes the lateral heat transfer to become prominent.

Due to high thermal conductivity of the edge sealing, the edge seal is assumed as a thermal short circuit.

In general, the calculation of the heat transfer analysis only involves the heat convection and radiation from the internal and external surface to the ambient, heat conduction across the glass layer, heat conduction through the support pillars and edge sealing, heat exchange via radiation between the glass panes.

To simulate the performance of the PV VG-4L, the following energy balance equations were developed for each of the temperature nodes.

For  $g1$ :

$$\underbrace{S_{g1}}_1 + \underbrace{h_{a_g1}(T_{a_i} - T_{g1})}_2 = \underbrace{h_{g1_g2}(T_{g1} - T_{g2})}_3 + \underbrace{h_{g\_edge}(T_{g1} - T_{edge1})}_4 \quad (7)$$

1: The rate of the solar energy received by the PV glass component or glass facing indoors after transmission through glass 1 layer per unit area; 2: The rate of heat transfer between the indoor ambient to  $g1$  per unit area ; 3: The rate of heat transfer between  $g1$  to  $g2$  per unit area. The heat transfer includes heat conduction through the glass slabs of  $g1$ , which then followed by heat transfer in the vacuum gap which are due to the heat conduction of the gas particles (which decreases with the increase in vacuum level), heat transfer via radiation and heat conduction through the support pillars, and then followed by heat conduction through the glass slab  $g4$ .; 4: The rate of lateral heat conducted along the x- direction of the PV VG-2L from the centre of  $g1$ .

For  $T_{edge1}$ :

$$\underbrace{h_{k\_edge}\gamma_c(T_{g1} - T_{edge1})}_4 + \underbrace{h_{i\_edge}\gamma_{edge}(T_{a_i} - T_{edge1})}_5 = \underbrace{h_{edge}\gamma_{edge}(T_{edge1} - T_{edge2})}_6 \quad (8)$$

The heat transfer terms are defined as follows:

5: The rate of heat transfer between the indoor ambient to the edge area per unit glazing area (if not insulated); 6: The rate of heat transfer from edge 1 to edge 2 through thin film PV glass layer per unit area.

For  $T_{edge2}$ :

$$\underbrace{h_{edge}\gamma_{edge}(T_{edge1} - T_{edge2})}_6 = \underbrace{h_{k\_edge}\gamma_c(T_{edge2} - T_{g2})}_7 + \underbrace{h_{i\_edge}\gamma_{edge}(T_{edge2} - T_{a_o})}_8 \quad (9)$$

The heat transfer terms are defined as follows:

7: The rate of lateral heat conducted along the x- direction and y-direction of the PV VG-4L from the centre of the PV VG-4L. 8: The rate of heat transfer between the indoor ambient to the edge area per unit glazing area (if not insulated).

For  $g_2$ :

$$\underbrace{h_{g1\_g2}(T_{g1} - T_{g2})}_3 + \underbrace{h_{k\_edge}(T_{edge2} - T_{g2})}_7 + \underbrace{S_{g2}}_{10} = \underbrace{h_o(T_{g2} - T_{a,o})}_{11} \quad (10)$$

The heat transfer terms are defined as follows:

10: The rate of the solar energy received/absorbed by  $g_2$ ; 11: The rate of heat transfer from  $g_4$  to  $T_{a,o}$  per unit area.

To simulate the glazing's electrical performance, the following correlation developed by Schott (1985) and Evans (1981) is the most common correlation implemented by researches who study the PV/T –type solar collector such as Sarhaddi, Farahat et al. (2010) and Tonui and Tripanagnostopoulos (2007):

$$\eta_{eff} = \eta_{Tref} (1 - \beta_{ref}(T_{TF} - T_{ref})) \quad (11)$$

Where  $\beta_{ref}$  the temperature coefficient of the thin film PV is cells and  $\eta_{Tref}$  is the electrical efficiency at reference temperature (25°C). From the simulation, the values of the average temperature of the glass sheets (layers) were used to compute the heat transfer coefficients summarised in Table 1. By referring to figure 5 the centre thermal resistance  $R_{centre}$  and the edge thermal resistance  $R_{edge\_tot}$  can be computed as in equation (12) and (13) respectively.

$$R_{centre} = \frac{1}{h_{a_{g1}}} + \frac{1}{h_{g1\_g2}} + \frac{1}{h_{g2\_TF}} + \frac{1}{h_{TF\_g4}} + \frac{1}{h_o} \quad (12)$$

$$R_{edge\_tot} = \frac{1}{h_{edge}} + \frac{1}{h_{k\_edge}} + \frac{1}{h_{i\_edge}} \quad (13)$$

U-value is defined as the measure of heat transfer or thermal transmittance from a warm space of a building to the external cooler environment or vice versa. It reflects how well a glazing unit as a heat insulator. In this study, the centre U-value ( $U_{centre}$ ) and the total U-value ( $U_{total}$ ) may be computed using equation 14 and 15 respectively:

$$U_{centre} = \frac{1}{R_{centre}} \quad (14)$$

$$U_{total} = U_{centre}\gamma_c + U_{edge\_tot}\gamma_{edge} \quad (15)$$

In this study, to solve the energy balance equation, we have used the inverse matrix method. MATLAB is used to carry out the iteration process with Newton-Raphson iteration technique is employed to estimate the temperature and hence the temperature-dependant heat transfer coefficients of the variables.

Table 2: the definition of the symbol used

Symbol	Definition	Symbol	Definition
$S_{g1}, S_{g2}$	The absorbed solar radiation for $g_1$ and $g_2$ respectively.	$\gamma_c$	Correction factor due to the total area of the PV VG
$\gamma_{edge}$	Correction factor due to the total area of edge sealing	$h_{edge}$	Conductive heat transfer coefficient due to the edge sealing
$\delta_{edge}$	The edge sealing thickness	$h_{i,edge}$	Total heat transfer coefficient from the indoor ambient air to the uninsulated edge sealing area
$h_p$	Heat transfer coefficient through the support pillars	$h_{g1-g2}$	The total heat transfer coefficient from $g_1$ to $g_2$ of vacuum glazing
$h_{k\_edge}$	The lateral heat transfer to the glass edge	$k_{edge}$	Thermal conductivity through the edge sealing
$h_{a,g1}$	Total heat transfer coefficient from the internal ambient to $g_1$	$T_{a,i}$	Indoor ambient temperature
$h_o$	Total heat transfer coefficient from the external glass $g_4$ to the ambient	$T_{a,o}$	Outdoor ambient temperature

## 5. RESULTS AND DISCUSSIONS

### 5.1. U-value measurement using a TEC driven calibrated hot box

Figure 5a shows the manufactured PV VG-2L at 300 mm x 300 mm sample and overall thickness of 11 mm. The U-value of the prototypes were evaluated using the TEC-driven calibrated hot box (see Figure 5b) built at the University of Nottingham. Interested readers may refer to (Jarimi, Zhang et al. 2018) for further details. The sample was installed at the specimen area of the calibrated hot box. It was tested at temperature difference of 20 °C summarised in Table 2. The air speed in the hot and cold side were fixed at 0.3 m/s and 1.5 m/s respectively. Using the calibrated hot box, we could estimate the total heat transfer coefficient from the hot and cold surface. The values were then used as the input parameters for the computer simulation. To derive the absolute error, the Kline–McClintock second power law as given in NCEES (National Council of Examiners for Engineering and Surveying) (2001) is used. These errors were represented by the error bars of the associated curves. Additionally, the guideline in ISO 12567 was also being referred to evaluate the error from indoor testing.

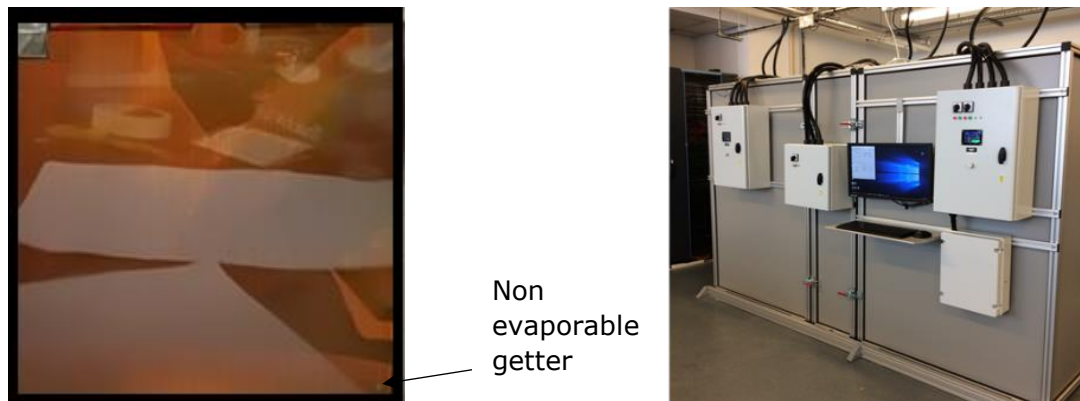


Figure 6: (a) The lab-scale manufactured PV VG-2L prototype and (b) TEC-driven calibrated hot box.

At average temperature difference of 20 °C, the average temperature difference between the glazing surface temperatures was 13.3 °C with the measured overall U-value of the prototypes was computed as 1.61 W/m<sup>2</sup>K. The thermal conductivity PV VG prototype at thickness of approximately 11 mm was measured to be as low 0.0176 W/mK which is in general comparable to heat insulation material with high insulating property such as aerogel. Nevertheless, in comparison to a vacuum glazing available in the market, the U-value is considered lower. This is due to the limitation in the fabrication process which has led to internal outgassing in the sample. From the modelling, it is estimated that the pressure level in the glass pane is approximately 1 Pa. Figure 6 shows the temperature variation with time for the hot and cold surface temperature of PV VG-2L at steady state condition. When compared with the result given by the mathematical model, Table 2 shows that the results were found to be in good agreement.

Table 3: A comparison between experimental and theoretical analysis when the sample was tested at hot air temperature of 28.5 °C and cold air temperature of 8.5 °C

T_hot (Experiment) (°C)	T_hot (Theory) (°C)	% (diff)	T_cold (Experiment) (°C)	T_cold (Theory) (°C)	% (diff)	U-value total (Experiment)	U-value total (Theory)	% (diff)
24.24	23.92	1.3%	10.95	11.14	8.6%	1.61	1.66	3.0%

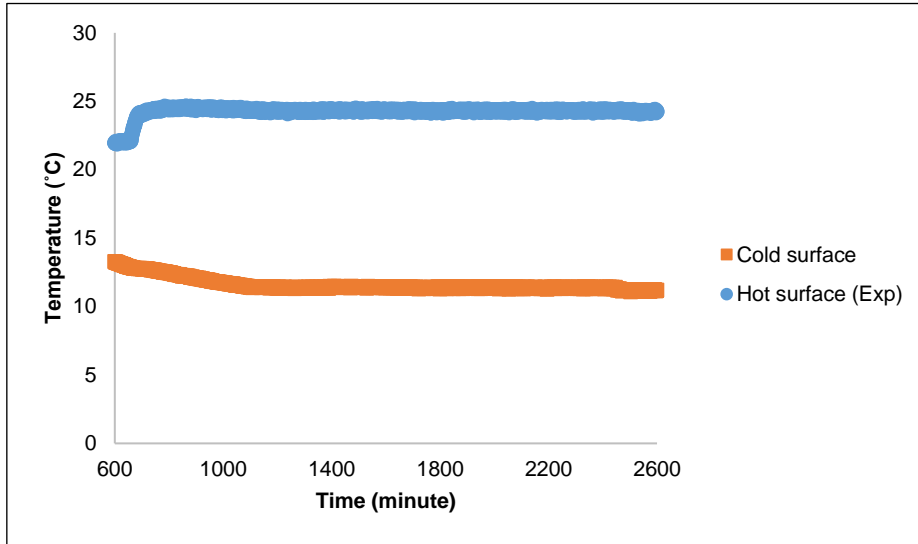


Figure 7: The temperature variation with time for the hot and cold surface temperature of PV VG-2L approaching and at steady state condition.

## 5.2. The advantage of low thermally conductive aerogel support pillars.

This research is also aiming to explore the potential of innovative support pillars for vacuum glazing using strong, high-temperature and low thermal conductivity aerogel pillars at 0.032 W/mK. To justify the idea, overall U value was computed and compared with the vacuum glazing using stainless steel as the support pillars at 20 W/mK in thermal conductivity. As mentioned earlier, materials with different compressive strength will have different design constraints due to mechanical stress. If stainless steel were to be applied as the support pillars, the safe pillar spacing and radius were chosen as 50 mm and 0.25 mm respectively. The performance of the thin film PV VG unit is compared with the variation in outdoor ambient conditions while indoor ambient conditions is fixed at 23 °C. Figure 7 shows that the U-value of PV-VG with stainless steel support pillar is approximately 40% higher in comparison to the U-value of PV-VG with aerogel support pillars. This leads to reduction in heat loss by almost 10 Watt per square meter of thin film PV Glazing unit. When applied as a building façade for high-storey building, at 30,000 square metre of BIPV for instance, the energy saving is as much as 300 kW.

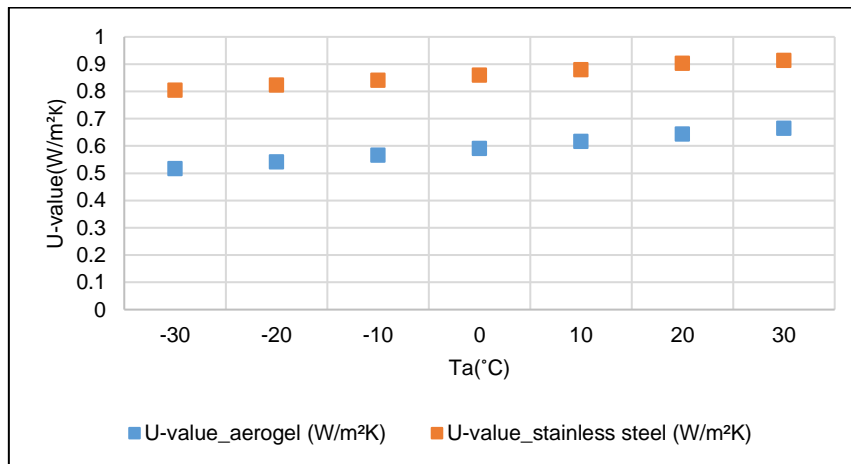


Figure 8: The comparison between the U-value of thin film PV VG using aerogel and stainless steel as the support pillars.

### 5.3. Simulated performance under real conditions

Using the validated mathematical model, the performance of the PV VG-2L was simulated under real conditions based on the recorded weather data on the 21<sup>st</sup> of June 2019 at E.ON 2016 research house at the University of Nottingham, United Kingdom with latitude of 52.9438° N, and longitude of -1.1934° W. During the day, when the PV component of the PV VG absorbed solar radiation, a fraction will be wasted in the form of heat which then reemitted or reradiated into the building internal space. This secondary heat source  $q_i$  factor when combined with the solar direct transmittance  $\tau_e$  of the glazing will give us the solar heat gain coefficient or solar gain factor ( $g$ -value) as shown in Equation (16).

$$g(\theta) = \tau_e(\theta) + q_i(\theta), \quad (16)$$

Figure 8(a) and (b) shows the variation in the average solar radiation and ambient temperatures; and the predicted average solar heat gain factor and the surface temperatures during the day from 12 p.m. to 5:40 p.m for a 1.5 m<sup>2</sup> PV VG-2L glazing unit at optimised design-i.e. with soft low-e coated glass ( $\varepsilon = 0.015$ ), electrical efficiency of 6%, and vacuum level of 0.01 Pa. The time range was selected due to the average recorded solar radiation which are higher than 200 W/m<sup>2</sup>. In general, the internal surface temperature of the glazing unit is mainly higher than the external surface temperature. This is owing to the position of the vacuum layer which is in front of the thin film PV layer. Therefore, the generated heat from the absorbed solar radiation can be easily transferred inside the building but insulated from the external glazing. This could be an advantage during winter and also countries like in the UK with average temperature ranges from 9–18 °C, but not very suitable for hot climate countries which require cooling almost throughout the year. However, due to the solar angle dependency of the solar heat gain, the value which is initially almost constant until 3 p.m. decreases almost quadratically towards sunset. Meanwhile, it was predicted as much as 300 W electrical power per 1.5 m<sup>2</sup> glazing will be produced in the day. Figure 9(b) shows the variation in the predicted U-value and surface temperatures during the night time (zero solar radiation). The estimated average U-value for the optimised sample is 0.62 W/m<sup>2</sup>K which is lower by almost 90% in comparison to a single thin film PV glazing.

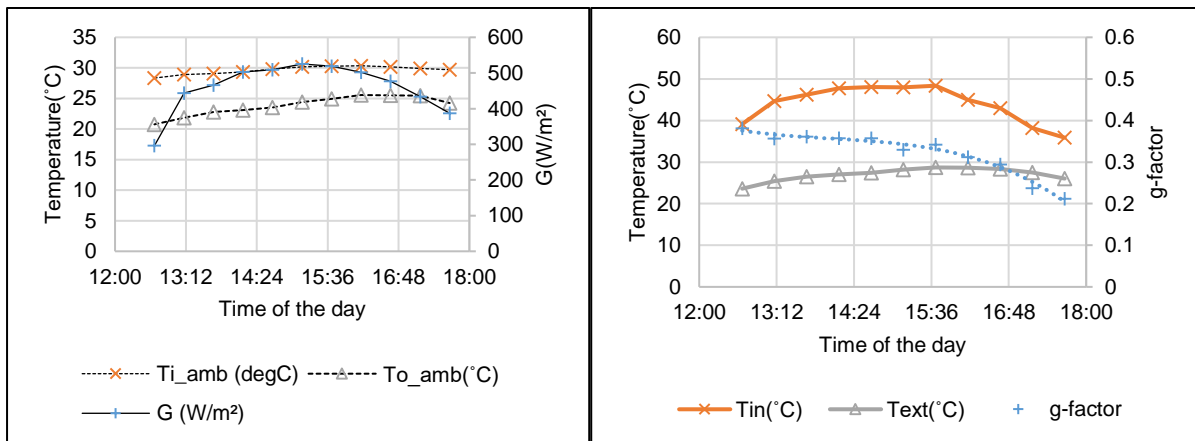


Figure 9: (a) Average outdoor ambient temperature ( $T_{o\_amb}$ ), indoor ambient temperature ( $T_{i\_amb}$ ) and solar radiation (b) Simulated variation in the external glazing surface temperature ( $T_{ext}$ ), internal glazing surface temperature ( $T_{int}$ ), and g-factor with time of the day

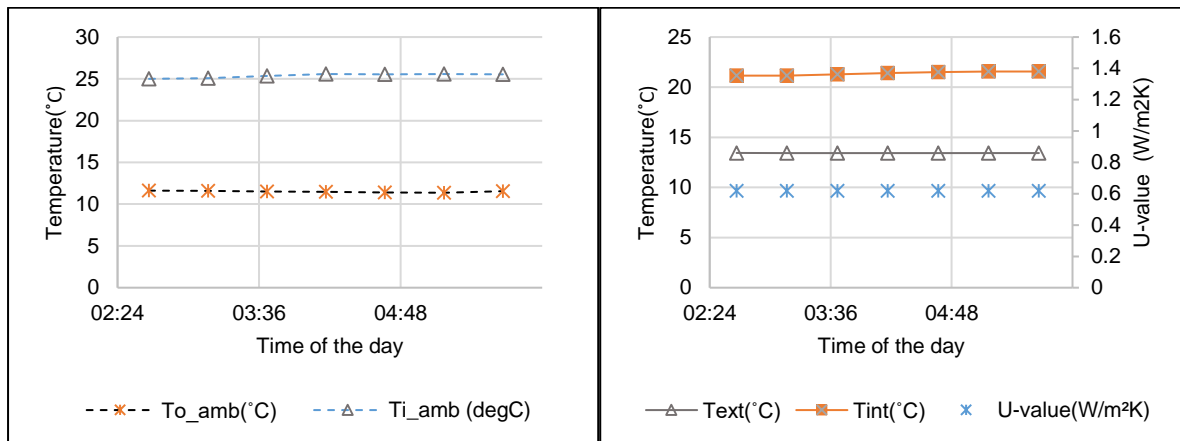


Figure 10: a) Average outdoor ambient temperature ( $T_{o\_amb}$ ), and indoor ambient temperature ( $T_{i\_amb}$ ) (b) Simulated variation in the external glazing surface temperature ( $T_{ext}$ ), internal glazing surface temperature ( $T_{int}$ ), and U-value with time of the day

## 6. CONCLUSIONS

An innovative semi-transparent thin film photovoltaic glazing insulated with vacuum insulated layer using strong and low-thermally conductivity aerogel material as the support pillar is presented in this paper. The design concept, novel manufacturing method, and analytical analysis were developed by taking into account the mechanical stress on the PV VG-2L. Experimental validation of the developed mathematical model was then performed and the performance of the PV VG -2L at optimum design parameters was compared with the design using stainless steel pillars and the performance was also simulated under real conditions to consider the absorbed solar radiation. The following conclusions can be drawn:

- The simulation results show that, the PV VG not only can produce power but has high insulation properties in which when compared to a single thin film PV glass the U-value is higher by almost 90%.
- In addition, in (Onyx Solar Energy S.L. 2018), in order to improve the thermal performance of the thin film PV glass, a combination with a double glazing unit is possible with the estimated U-value of 2.5-2.8 W/m<sup>2</sup>K depending on the type of gas used to provide the insulation in the air gap. Clearly, the vacuum layer introduced in the PV VG design presented in this paper is better in performance with the slim configuration of the glazing unit as an additional benefit.
- The use of aerogel support pillars will reduce U-value by almost 40% in comparison to the PV VG using stainless steel as the support pillars whilst producing useful power at the same time.
- The promising U-value implies its range of potential applications can be improved depending on the energy needs and applications, such as for BIPV solar façade (PV curtain walling) in commercial buildings, greenhouses, skylight and conservatory.

## 7. ACKNOWLEDGEMENT

The authors gratefully acknowledge Innovate UK's financial support through Newton Fund (Project reference no: 102882) and International Science & Technology Cooperation Program of China (No. 2016YFE0124300).

## 8. REFERENCES

Ali, H., N. Hayat, F. Farukh, S. Imran, M. S. Kamran and H. Ali (2016). Key design features of multi vacuum glazing for windows: A review.

Arya, F. and T. J. Hyde (2017). "Theoretical Study of Flexible Edge Seals for Vacuum Glazing." International Journal of Structural and Construction Engineering **11**: 1132-1137.

Bao, M., X. Liu, J. Yang and Y. Bao (2014). "Novel hybrid vacuum/triple glazing units with pressure equalisation design." Construction and Building Materials **73**(Supplement C): 645-651.

Collins, R. E., A. C. Fischer-Cripps and J. Z. Tang (1992). "Transparent evacuated insulation." Solar Energy **49**(5): 333-350.

Collins, R. E. and T. M. Simko (1998). "Current status of the science and technology of vacuum glazing." Solar Energy **62**(3): 189-213.

Collins, R. E., G. M. Turner, A. C. Fischer-Cripps, J. Z. Tang, T. M. Simko, C. J. Dey, D. A. Clugston, Q. C. Zhang and J. D. Garrison (1995). "Vacuum glazing—A new component for insulating windows." Building and Environment **30**(4): 459-492.

Cuce, E. and S. B. Riffat (2015). "Aerogel-Assisted Support Pillars for Thermal Performance Enhancement of Vacuum Glazing: A CFD Research for a Commercial Product." Arabian Journal for Science and Engineering **40**(8): 2233-2238.

Eames, P. C. (2008). "Vacuum glazing: Current performance and future prospects." Vacuum **82**(7): 717-722.

EIA (2017). International Energy Outlook 2017.

Evans, D. (1981). "Simplified method for predicting PV array output." Solar Energy **27**: 555–560.

Fang, Y., P. C. Eames, B. Norton and T. J. Hyde Effect of Glass Thickness on the Thermal Performance of Evacuated Glazing.

Fang, Y., T. Hyde, N. Hewitt, P. C. Eames and B. Norton (2010). "Thermal performance analysis of an electrochromic vacuum glazing with low emittance coatings." Solar Energy **84**(4): 516-525.

Fang, Y., T. J. Hyde, F. Arya, N. Hewitt, P. C. Eames, B. Norton and S. Miller (2014). "Indium alloy-sealed vacuum glazing development and context." Renewable and Sustainable Energy Reviews **37**: 480-501.

Fang, Y., T. J. Hyde, F. Arya, N. Hewitt, R. Wang and Y. Dai (2015). "Enhancing the thermal performance of triple vacuum glazing with low-emittance coatings." Energy and Buildings **97**: 186-195.

Fang, Y., T. J. Hyde, F. Arya, N. Hewitt, R. Wang and Y. Dai (2015). "Enhancing the thermal performance of triple vacuum glazing with low-emittance coatings." Energy and Buildings **97**(Supplement C): 186-195.

Ghosh, A., B. Norton and A. Duffy (2017). "Effect of atmospheric transmittance on performance of adaptive SPD-vacuum switchable glazing." Solar Energy Materials and Solar Cells **161**(Supplement C): 424-431.

Ghosh, A., S. Sundaram and T. K. Mallick (2018). "Investigation of thermal and electrical performances of a combined semi-transparent PV-vacuum glazing." Applied Energy **228**: 1591-1600.

Glass, N. S. (2016). "Glass in Buildings." Retrieved 6 April, 2017, from <http://www.nsg.com/en/sustainability/glassandclimatechange/glassinbuildings>.

Han, J., L. Lu, H. Yang and Y. Cheng (2019). "Thermal regulation of PV façade integrated with thin-film solar cells through a naturally ventilated open air channel." Energy Procedia **158**: 1208-1214.

Henshall, P., P. Eames, F. Arya, T. Hyde, R. Moss and S. Shire (2016). "Constant temperature induced stresses in evacuated enclosures for high performance flat plate solar thermal collectors." Solar Energy **127**: 250-261.

Hertz, H. (1881). On the contact of elastic solids. Journal für die reine und angewandte Mathematik **92**: 156-171.

Hyde, T. J., P. W. Griffiths, P. C. Eames and B. Norton (2000). Chapter 50 - Development of a Novel Low Temperature Dege Seal for Evacuated Glazing. World Renewable Energy Congress VI. A. A. M. Sayigh. Oxford, Pergamon: 271-274.

JARIMI, H., S. ZHANG, Q. XU, J. A. SANTANA, D. HARJUNOWIBOWO and S. RIFFAT (2018). An affordable small calibrated hot box suitable for thermal performance measurement of a glazing unit. 17th International Conference on Sustainable Energy Technologies 21st to 23rd August 2018, Wuhan, China.

Knudsen, A. W. (1952). "Metallic Vacuum-Tight Gasket." Review of Scientific Instruments **23**(10): 566-567.

LandVac. (2018). from <https://www.landvac.net/>.

Memon, S. (2017). "Experimental measurement of hermetic edge seal's thermal conductivity for the thermal transmittance prediction of triple vacuum glazing." Case Studies in Thermal Engineering **10**(Supplement C): 169-178.

Memon, S. and P. C. Eames (2017). "Predicting the solar energy and space-heating energy performance for solid-wall detached house retrofitted with the composite edge-sealed triple vacuum glazing." Energy Procedia **122**(Supplement C): 565-570.

Memon, S., F. Farukh, P. C. Eames and V. V. Silberschmidt (2015). "A new low-temperature hermetic composite edge seal for the fabrication of triple vacuum glazing." Vacuum **120, Part A**: 73-82.

Moralejo Vázquez, F. J. a. M. C., Nuria and Olivieri, Lorenzo and Caamaño Martín, Estefanía (2014). Optical characterisation of semi-transparent PV modules for building integration. 29th European Photovoltaic Solar Energy Conference and Exhibition (EU PVSEC 2014). Amsterdam, The Netherlands. : 1-9.

Nippon Sheet Glass Spacia Co., L. (2003). "Who invented SPACIA®?" Retrieved 6 April, 2017, from <http://www.nsg-spacia.co.jp/spacia/>.

Onyx Solar Energy S.L. (2018). "Calculate the glazing thermal transmittance." from <https://www.onyx-solar.com/utermical>.

saes group. (2019). "VACUUM NEG PUMPS & VACUUM SOLUTIONS." from <https://www.saesgetters.com/products-functions/functions/vacuum>.

Sarhaddi, F., S. Farahat, H. Ajam, A. Behzadmehr and M. Mahdavi Adeli (2010). "An improved thermal and electrical model for a solar photovoltaic thermal (PV/T) air collector." Applied Energy **87**(7): 2328-2339.

Schott, T. (1985). Operational temperatures of PV modules. 6th PV solar energy conference.

Tom, M. S., E. C. Richard, A. B. Fredric and K. A. Dariush Edge Conduction in Vacuum Glazing. Thermal Performance of the Exterior Envelopes of Buildings VI Conference, Clearwater Beach, FL.

Tonui, J. K. and Y. Tripanagnostopoulos (2007). "Air-cooled PV/T solar collectors with low cost performance improvements." Solar Energy **81**(4): 498-511.

Wilson, C. F., T. M. Simko and R. E. Collins (1998). "Heat conduction through the support pillars in vacuum glazing." Solar Energy **63**(6): 393-406.

Zhang, W., L. Lu and X. Chen (2017). "Performance Evaluation of Vacuum Photovoltaic Insulated Glass Unit." Energy Procedia **105**(Supplement C): 322-326.

Zhao, J., S. Luo, X. Zhang and W. Xu (2013). "Preparation of a transparent supporting spacer array for vacuum glazing." Vacuum **93**(Supplement C): 60-64.



---

## **#77: An innovative semi-transparent thin film PV vacuum glazing**

### **A brief report on potential market and cost analysis**

---

Ray LUKE<sup>1</sup>, Hasila JARIMI<sup>2</sup>, Saffa RIFFAT<sup>3</sup>

<sup>1</sup>Solar Ready Limited, United Kingdom, Ray.Luke@solar-ready.co.uk

<sup>2</sup>The University of Nottingham, United Kingdom, Hasila.Jarim@nottingham.ac.uk

<sup>3</sup>The University of Nottingham, United Kingdom, Saffa.riffat@nottingham.ac.uk

*This paper introduces an innovative vacuum glazing technology combined with thin film PV glass called thin film PV vacuum glazing (PV VG). In comparison to conventional vacuum glazing, PV VG not only has high thermal and sound insulating properties but can generate electrical power. The main aim of this paper is to discuss the economic and carbon saving analysis of the introduced technology with the significant distinction of the PV VG with other potential competing technology being emphasised. The market sectors related to the potential business opportunities and competing market are analysed to assess PV VG market potential and to understand the strength and weakness of PV VG. The PV VG technology which has been lab-scale proven, is aimed to be further upscale at both manufacturing and testing level.*

*Keywords: Innovative vacuum glazing; building applications*

## 1. INTRODUCTION

A novel thin film PV vacuum insulated glazing called PV VG has been designed, manufactured and tested by our research team. The product as shown in Figure 1, involves the integration of solar PV thin film glass into low profile vacuum glazing panel incorporating simplified manufacturing. The key innovation of PV-VG is combining vacuum glazing with laminated thin-film PV, providing a glazing product with the fundamental commercial advantage of installing, simultaneously, two major, energy saving technologies, thus reducing costs compared to installing each separately.

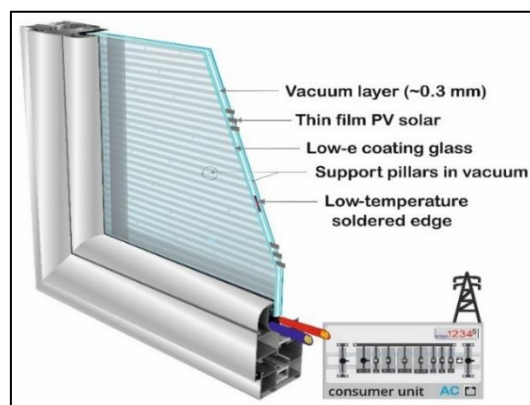

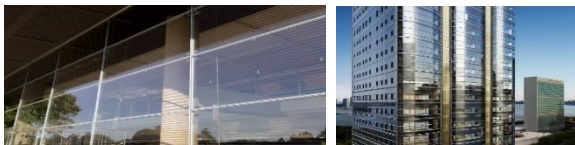


Figure 1: PV VG design and potential applications

The key innovations of the product are as follows:

- Generation of solar power by the amorphous or micro-silicon thin film;
- Reduction of the heat transfer into the building due to the thin film coating layer and therefore reducing cooling energy consumption in summer;
- Reduction of the U-value by vacuum layers lower energy consumption in winter;
- Support pillars that are not visually intrusive and therefore allow in daylight;
- PV lamination also allows daylight and vision unlike conventional crystalline silicon;
- Thin vacuum glazing reduces glass weight and window frame construction;
- Novel PV-VG panel manufacturing technology is introduced to reduce cost.

Table 1: The potential application of PV VG

Application	Artist impressions
<p><b>Solar Curtain Wall.</b> Aesthetics and energy generation with added thermal barrier. Photovoltaic curtain walls allow for buildings to generate additional power without compromising aesthetics, functionality and views. They also provide thermal comfort and avoid the greenhouse effect. The curtain wall method of glazing allows glass to be used in large uninterrupted areas creating consistent attractive facades. Photovoltaic windows are (semi) transparent modules that can be used to replace a number of architectural elements commonly made with glass or similar materials, such as windows and skylights. In addition to producing electric energy, these can create further energy savings due to superior thermal insulation properties and solar radiation control.</p>	
<p><b>Architectural decorative glass-</b> Transparent or translucent, for decoration but also privacy. Glass can be used to create building interiors which connect occupants with the external environment, combining unbroken views of the surrounding nature and high level of natural light with the comfort and safety of the internal environment. Our glass systems are developed for use in glass façades, walls or roofs, and for internal glazing applications</p>	

**Commercial refrigeration** -Good thermal barrier and no condensation. Refrigerators and freezers are important presentation areas for products and brands, and an unrestricted review is critical. Low reflective coatings increase the visibility of the product, whatever the lighting conditions and heated glass can be used to address the common issue of condensation. Energy efficiency is a key consideration for shops and supermarkets and our low-e coatings can be used to keep the cold inside.



## 2. MARKET POTENTIAL AND COMPETITOR

Global vacuum Glass Market for Building & Construction to Reach Around US \$7 Bn by 2026 (Transparency Market Research, 2019) '. Today's regulators and economics are demanding more from glass, the focus on energy efficiency and environmental impact are high on the agenda. Advances in low-e glass, windows now play a big part in energy conservation / comfort, minimising heat loss and internal condensation. A Payback analysis evaluating the top 3 best in market and 2 traditional methods of reducing heat loss in new build envelope. By combining low-emissivity glass and solar PV we can meet all energy saving requirements and still improve on the economic impact. Effectively, low-emissivity vacuum glass will reflect energy back into a building, to achieve much lower heat loss compared to ordinary double glazing and other cladding, the solar PV vacuum glazing will stop the heat from entering the building, thus reducing the heat/cooling load.

In terms of application, the vacuum insulated glass market for building & construction can be divided into residential, commercial, and industrial. The residential segment is anticipated to dominate the market during the forecast period. The residential segment is set to expand at a fast pace during the forecast period. Demand for vacuum insulated glass is lesser in the commercial segment than that in the residential buildings. Nevertheless, its demand is rising in industries due to its natural light purposes and noise cancellation properties. In terms of region, the global Vacuum Insulated Glass market for building & construction can be divided into North America, Europe, Asia Pacific, Latin America, and Middle East & Africa. North America and Europe hold prominent share of the vacuum insulated glass market for building & construction due to the presence of well-established buildings in these regions. North America also constitutes significant share of the market. The market in Asia Pacific is estimated to expand at a rapid pace due to the significant increase in construction and building activities in developing economies such as China and India. The market in Middle East & Africa and Latin America is expected to expand at a sluggish pace during the forecast period (Transparency Market Research, 2019).

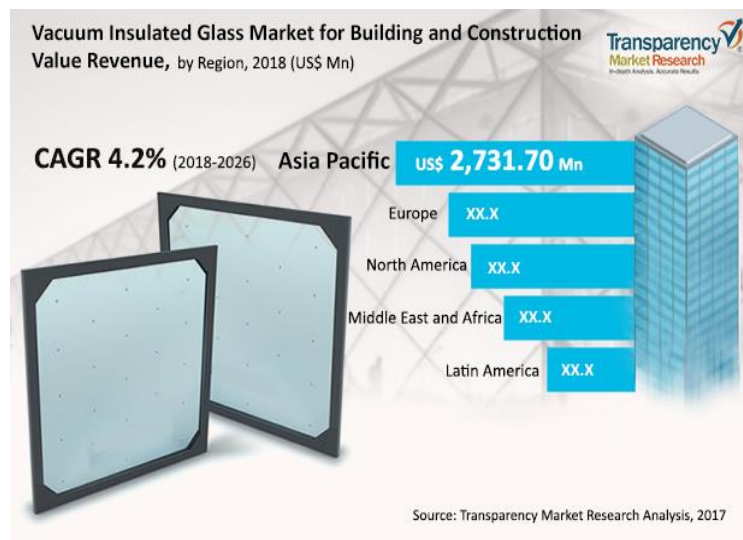


Figure 1: Vacuum insulate Glass Market for Building and Construction Value Revenue

Factors likely to drive uptake in the market for energy efficient, lighter, PV-VG products in the future include (Market Intelligence Report, 2014):

- Demand for reduction in heating/cooling costs of both dwellings/commercial buildings and greenhouses.
- Greenhouse gas reduction legislation
- Environmental legislation driving down CO<sub>2</sub> and NO<sub>x</sub> emissions

- Whole life-cycle costing
- International manufacturers seeking to compete for sales with improved products performance and efficiency

The market opportunities of the current thin film PV-vacuum glazing technology is also reflected by the BIPV glass market. Thus, it is worth to review the initial markets for BIPV glass which are to be found in skylights, facades, spandrels, curtain walls and atrium roofing where high levels of transparency are not required. More significant opportunities, if BIPV glass would achieve a transparency that is much closer to that of window/vision glass of which, at this stage, high levels of transparency in BIPV glass are not achievable without a loss of efficiency and, often, an increase in cost.

The market for BIPV glass is projected to grow to \$3.5 billion by 2020 and \$6.3 billion by 2022. This is due to involvement of large glass companies such as AGC, NSG/Pilkington, and BGT through partnerships with PV companies as well as with building product firms and installers. Two specific areas which seem to enhance the market are zero energy buildings and highly urban areas. From n-tech Research Issues (2015) the revenues for BIPV glass in zero-energy buildings will surge past \$800 million in 2018 and more than \$2.5 billion by 2022. In addition, n-tech expects BIPV glass will unlock residential building demand in a more medium-term timeframe, approaching \$200 million by 2018 and surpassing \$1.3 billion by 2022. In the UK industry, the country has a significant supply chain business such as NSG for the TCO coated glass (Louise, Stuart, & Rachael, 2013). From a mere 14 MW production in 2001 the market has grown to reach 2141 MW in 2009, at a CAGR of 58%. The market outlook for the coming decade appears promising as the major thin film producing countries - Japan, China, and the US - are announcing aggressive support for renewable energy expansion through incentives and regulations. It is predicted that in the long term the thin film PV technology will overcome crystalline technologies. From the Thin Film Photovoltaics Market, 2017-2030 report (Grandviewresearch, 2017), the solar energy sector attracted 56% of the total new investments (USD 286 billion) that were made in the renewable power and fuels industry. The prices of solar energy have plummeted by over 60% in the last 10 years. The market includes cadmium telluride (CdTe), copper indium selenide / gallium selenide (CIS / CIGS) and amorphous silicon (a-Si). It is expected that this generation of thin film photovoltaic technologies matures, they are likely to benefit from economies of scale, resulting in further cost reductions. Thin film photovoltaics was always an integral part of the PV industry. It is estimated that 80 companies with a total production capacity of 130 MW existed worldwide and their activities ranged from research to production of solar cells. About half of them were actually manufacturing and other 29 companies were involved in module production only. Among the companies, 41 companies used crystalline silicon (72 MW capacity), 2 ribbon silicon (1 MW capacity), 19 amorphous silicon (46 MW capacity), 3 CdTe (11 MW capacity), 5 CIS (research only), and 10 companies other concepts like III–V concentrator cells or spherical cells. In 2016, the worldwide production capacity of solar cells has increased about 500 times exceeding 68 GW in 2011 in which with thin films PV accounting for 11.5 GW or 17%. From the figures below, in general, there is an increase in the thin film PV module production in which CdTe has shown the greatest increase from 2013 to 2016.

The global solar PV glass market demand was also reported at 139.9 million square meters in 2015 and is expected to reach 856.3 million square meters by 2024, growing at a CAGR of 22.6% from 2016 to 2024 Utility emerged as the leading application segment and accounted for over 50% of total market volume in 2015. The segment is also expected to witness the highest growth of 23.9% over the forecast period. The huge market share of utility segment can be attributed to the various advantages offered, such as a contribution to sustainability, enhancement of branding and public relations effort, and reduction of the carbon footprint of facilities (Grandviewresearch, 2017). Europe was the leading regional market with demand share 51.4% in 2015. The region mainly benefitted from the favourable regulations prevailing particularly in Italy, Spain and Belgium. Meanwhile, Asia Pacific is expected to witness the highest growth of 22.7% over the forecast period. More than 45% of the manufacturers for solar PV glass are situated in China and Japan, which is expected to remain a key advantage for the regional market over the forecast period. Lower prices and favourable climatic conditions are also expected to benefit the regional market.

### 3. OUR PRODUCT

The PV-VG technology is widely applicable to residential, commercial and agricultural buildings world-wide. It is especially relevant to the development of low/zero-emission buildings, and to high-rise building skyscrapers which can have ~60% of their surfaces covered by glass. They are therefore ideal for electricity generation using the proposed PV-VG glazing, which can replace conventional windows. For example, fitting PV-VG on a 40 storey building can generate 3-4 times more electricity than a conventional PV system installed on the roof. Unlike conventional PV, PV-VG can generate power under low intensity daylight and can generate power from all four wall surfaces of the building. The application of PV-VG in buildings would reduce heat loss by over 60% compared to double glazed panel and about 50% compared to triple glazed panel. The capital cost of PV-VG as shown in Table 2, is about £158.40 /m<sup>2</sup> which is higher than double glazed thin film PV glass (£100/m<sup>2</sup>) by almost 60%. Despite this the annual energy cost saving and CO<sub>2</sub> reduction are about £16 and 80 kg, respectively. These values

have been calculated based on the assumption that heating of a UK house is provided by a gas boiler with 90% efficiency, the gas price is 4pence/kWh, and the carbon dioxide factor is 0.2 kgCO<sub>2</sub>/kWh. Consequently, the payback period for using PV-VG windows to replace double glazed windows is 0.75 year and 1 year to replace triple glazed windows. In addition, the power output of the PV glazing is in the range of 80-100 W/m<sup>2</sup> and the conversion efficiency is 9.7%. The wire and junction power box will be embedded into the frame of the window. The electric power could be used in the building or supplied to the grid, to benefit financially from the feed-in tariff.

Table 2: The estimated cost of thin film PV VG per square metre

Materials	Trade
4mm Glass - Toughened	£35.00
Electrically conductive edge sealant	£14.60
Aerogel support pillars	£10.00
Low-emissivity-coating	£22.80
soldering metal foils (Indium Alloy)	£50.00
Getter seal	£11.00
Induction sealing (foil)	£15.00
<b>Total cost per 1m<sup>2</sup></b>	<b>£158.40</b>

For upscaling, the joint-venture of the supply chains as summarised in Table 3 is possible.

Table 3: Potential supply chain and their roles

Company	PV VG component	Country of Origin
LandVac	Vacuum glazing manufacturer	China
Hanergy	Thin film PV glass manufacturer	China
Lisec	Production line manufacturers	Austria
University of Nottingham, Solar Ready and Geo Green Power	Product development and distribution team	United Kingdom

#### 4. CONCLUSIONS

It is important to note that the proposed advanced glazing unit is not yet in a position to challenge conventional residential windows where transparent (and not translucent) glazing is most often required. Nevertheless, in comparison to the conventional thin film PV glass or BIPV glass available in the market which has a typical U-value of 5, the thin film PV-VG unit will have a U-value between 0.7-1. In other words, in addition to power generation, the technology has high insulation property. From this project, the following key conclusions can be drawn:

- The demand for the technology is real.
- The timing for the innovative PV VG product is good.
- The competitors are slow to react to market demand
- Focusing on glass wall cladding gives us larger profit potential
- The proposed manufacturing partners are interested in innovation
- No other product has made it to market yet.
- By researching and refining manufacturing process we can compete with other established solutions and bring down cost by about 40% and failure rates.

## 5. REFERENCES

Grandviewresearch. Solar PV Glass Market Size Worth \$33.7 Billion By 2025 | CAGR: 30.9%. 2017 [cited 2018 5 December ]; Available from: <https://www.grandviewresearch.com/press-release/global-solar-pv-glass-market>.

Louise, J., I. Stuart, and R. Rachael. UK Solar Photovoltaic Roadmap. A strategy for 2020. 2013; Available from: [https://www.bre.co.uk/filelibrary/nsc/Documents%20Library/Not%20for%20Profits/KTN\\_Report\\_Solar-PV-roadmap-to-2020\\_1113.pdf](https://www.bre.co.uk/filelibrary/nsc/Documents%20Library/Not%20for%20Profits/KTN_Report_Solar-PV-roadmap-to-2020_1113.pdf).

Market Intelligence Report. 2014; Available from: <http://www.glassinthegulf.com/pdfs/MIR-Bowhead-Glass.pdf>

n-tech Research Issues (2015) New Report on BIPV Glass Market, Firm Forecasts Market Rising to \$3.5 billion by 2020. 2015 [cited 2018 18 March]; Available from: <http://www.prnewswire.com/news-releases/n-tech-research-issues-new-report-on-bipv-glass-market-firm-forecasts-market-rising-to-35-billion-by-2020-300185230.html>.

Transparency Market Research, T.M.R. Vacuum insulated glass for building & construction - Global industry analysis, size, share, growth, trends, and forecast, 2018-2026. 2019; Available from: <https://www.transparencymarketresearch.com/vacuum-insulated-glass-building-construction-market.html>

---

## #78: Research of air conditioning system in T3 terminal of Dunhuang Airport

---

Xiang HUANG<sup>1</sup>, Shengsheng DU<sup>2</sup>, Jingwen XUAN<sup>3</sup>, Kaixin HUANG<sup>4</sup>

<sup>1</sup> Heating, Gas Supply, Ventilating and Air Conditioning, School of urban planning and municipal engineering, Xi'an Polytechnic University, 710048 Shannxi China, killer370@126.com

<sup>2</sup> Heating, Gas Supply, Ventilating and Air Conditioning, School of urban planning and municipal engineering, Xi'an Polytechnic University, 710048 Shannxi China, 1394132407@qq.com

<sup>3</sup> Xi'an Polytechnic University, 710048 Shannxi China, janexjw123@163.com

<sup>4</sup> Heating, Gas Supply, Ventilating and Air Conditioning, School of urban planning and municipal engineering, Xi'an Polytechnic University, 710048 Shannxi China, hkx0309@163.com

*Dunhuang Airport in Gansu is an important transportation hub located in the northwest of China. The airport terminal is a spacious building with a large population flow and T3 terminal has recently been completed. It has the combined characteristics of lower outdoor wet-bulb temperature, a higher diurnal temperature range and abundant dry air energy in local summer air. In the design of the air conditioning system, a combination of evaporative cooling and traditional mechanical refrigeration is adopted to be a composite cooling system where the ability to switch operating methods allows a greatly reduced working time of mechanical refrigeration whilst simultaneously achieving the air conditioning function to meet the passengers' demands of fresh air volume and reducing initial investment and operating cost of the air conditioning system. This research involved testing the indoor supply-air parameters and environment comfort of the evaporative water chiller installed in the refrigeration station and the terminal. It was found that the supply-water temperature is 0.5°C higher than the ambient wet-bulb temperature, and the efficiency of the evaporative water chiller was 97.3%, indicating that the system can achieve a great economic and energy-saving effect. Meanwhile, the combination of these two cooling technologies provides a new direction for the design of air conditioning systems in dry areas. Finally, we analysed the possible reason for the phenomenon that the supply-water temperature is not below the wet-bulb temperature of ambient air and there might be scaling, air duct obstruction and operation mode problems in the system.*

*Keywords: terminal; air conditioning system; evaporative cooling; mechanical refrigeration; energy-saving economy*

## 1. INTRODUCTION

Investment and energy costs can be relatively high when only traditional mechanical refrigeration means of air-conditioning are considered, while the combination of evaporative cooling and traditional mechanical refrigeration cooling system can be alternated to greatly reduce the working time of mechanical refrigeration, to achieve the air conditioning function, meet the passengers' demand of fresh air, and reduce the initial investment and operating cost, making full use of local meteorological and environmental conditions. Most previous studies have shown little focus on the combination of these two technologies even in the application of airport air-conditioning. Thus, this paper introduces the structure, workflow, heat and mass transfer process of the air conditioning system in the Dunhuang Airport terminal in China, as well as the indoor supply-air parameters. The environment comfort of the evaporative water chiller installed in the refrigeration station and the terminal were tested, and the non-ideal state supply water temperature has been analysed in this paper.

## 2. ENGINEERING PROJECT SITUATION

Dunhuang Airport is located in Mogao Town, Dunhuang City, Gansu Province. It is a major hub airport in Gansu Province and for the west area. The newly built Terminal T3 is located on the west side of Terminal T2, it has a total construction area of 17380m<sup>2</sup> and the highest point of the building is 22.8m. The main building of the terminal consists of two floors. The first floor includes passengers' check-in, departure, arrival hall, baggage-claim hall, baggage sorting hall, long-haul flight waiting hall for passengers, VIP lounge, commercial catering, offices and facility room. The second floor includes the domestic passenger waiting hall, international passenger waiting hall, transfer area, commercial catering, offices and facility room.

## 3. WORKFLOW AND HEAT & MASS TRANSFER PROCESS OF THE SYSTEM

This project is located in the Dunhuang area of Gansu Province with lower outdoor wet-bulb temperature in the summer air conditioning and higher diurnal temperature range. Radiant floor cooling systems and evaporative cooling technology are applicable technologies here (Zhou, 2014: page 65-69) therefore the double-cold-source of high-temperature evaporative water chiller and screw chiller have been adopted in this terminal. The high-temperature indirect evaporative water chiller with low temperature difference and large flow rate of 690 kW per unit is selected in the terminal to handle the sensible heat of cooling load in large space areas such as departure halls, arrival halls, check-in halls, waiting halls and baggage claim halls, and the unit is shown in Figure 1.



Figure 1: High-temperature evaporative water chiller at refrigeration station of Dunhuang Airport

The double-cold-source of evaporative cooling and mechanical refrigeration are adopted in T3 terminal of the airport. The water system flow of the high-temperature evaporative water chiller is as follows: a high-temperature chilled water system adopts a variable primary flow system, the high-temperature evaporative water chiller produces high-temperature cold water which the supply/return water temperature is 17/20°C respectively, and then the secondary high-temperature cold water at 18°C is produced through the plate heat exchanger. In summer, the secondary high-temperature chilled water system uses a variable primary flow system. A part of the high-temperature cold water is supplied to the floor radiant coil system and the fan-coil unit in dry coil, the supply/return water temperature is 18/21°C respectively, and the chilled water system is adopted to handle the sensible heat of the departure hall, arrival hall, check-in hall, waiting hall and baggage claim hall in the terminal; a part of the high-temperature cold water is supplied to the terminal of the dry coil type of air-conditioner. The supply/return water temperature is 18/23°C respectively which can handle the fresh air load and all the latent heat load. The terminal of the air-conditioner includes two types of fresh air handling unit and fan-coil unit in dry coil. Two screw chillers with a cooling capacity of 427.5 kW per unit are selected in the terminal to handle the cooling loads of fresh air in large space area. A variable primary flow system is adopted in conventional chilled water system of air conditioner,



the cold source is guaranteed to meet the minimum flow rate required by the chiller, there is a variable flow system on the load side and supply/return water temperature is 7/12°C. The system is supplied to fan-coil unit in dry coil and evaporative air conditioner respectively.

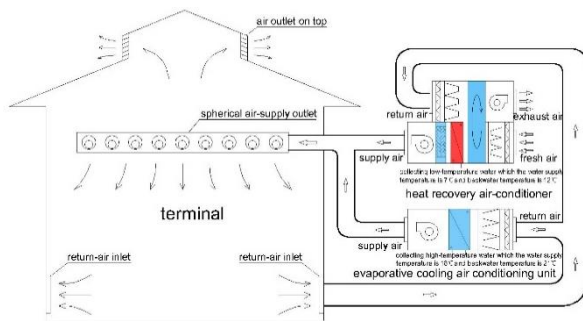


Figure 2: Operation mode when only the evaporative cooling air conditioning system is turned on

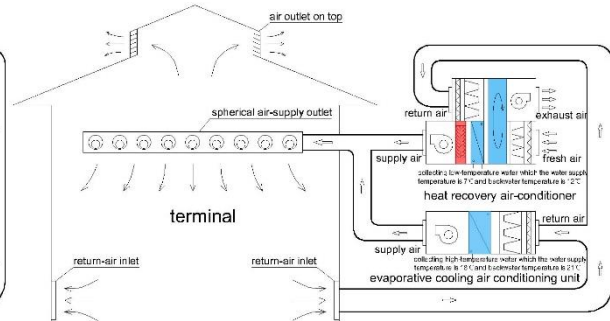


Figure 3: Operation mode when evaporative cooling air conditioning and mechanical refrigeration are both turned on

The form of air-conditioning system adopts the air-water system in the terminal (Huang, 2010), and independent temperature-humidity controls are used for the area. In the summer, the cooling form of the air-conditioning system is mainly evaporative cooling, combined with mechanical refrigeration. There are two operating conditions in this system: working condition a: in transition season and summer, the screw chiller and the heat recovery type of combined air handling unit with rotating wheels are closed, the high-temperature evaporative water chiller and evaporative fresh air handling unit are opened, as shown in Figure 2. Working condition b: in the summer rainy season, the outdoor air needs to be dehumidified, therefore, the mechanical cooling and combined air handling unit is turned on, as shown in Figure 3.

#### 4. TEST AND ANALYSIS OF EVAPORATIVE AIR CONDITIONING SYSTEM

In order to explore the actual effect of the air-water evaporative air conditioning system in the Dunhuang Airport terminal, we tested the indoor supply-air parameters and environmental comfort of the evaporative water chiller installed in the refrigeration station and the terminal on August 19-25th, 2018.

##### 4.1. Cold resource test

The heat and mass transfer process is shown in a psychrometric chart in Figure 4. The ambient air at state point o is cooled by the high-temperature cooling coil to the state point a that the wet-bulb temperature of the air is decreased from  $t_{wb, o}$  to  $t_{wb, a}$ , so that the temperature of the cold water is lower than the wet-bulb temperature  $t_{wb, o}$  is produced by the chiller. This air handling process is referred to drop enthalpy and cooling process. The lower wet-bulb temperature air at state point a is passed through the water-spraying zone below the filler under the effect of a fan and rises into the filler; the heat and mass transfer is conducted between counter flow of the air and thin water film on the surface of filler. Finally, it is exhausted into the atmospheric environment from the top of the water drenching filler. The handling process of the air at state point a can be divided into two stages in the water drenching filler section, the first stage is that the air at state point a is treated through the heat and mass transfer process to state point b, at this time, due to the evaporative cooling and conductive heat transfer in the air-side, the temperature of the air and water which are in contact with each other are decreased, the humidity ratio and relative humidity of the air are increased, and the dry bulb temperature is decreased to a minimum. It is said that the air treatment process at this stage is to increase enthalpy, cool and humidify; the second stage is that the air at state point b is treated through the heat and mass transfer process to state point c, and due to the heat loss through evaporation and conduction in the water-side, the temperature of the water in contact with the air is decreased, at the same time, the air state would follow the 100% saturation line of relative humidity. It is said that the air treatment process at this stage is to increase enthalpy, heat and humidity.

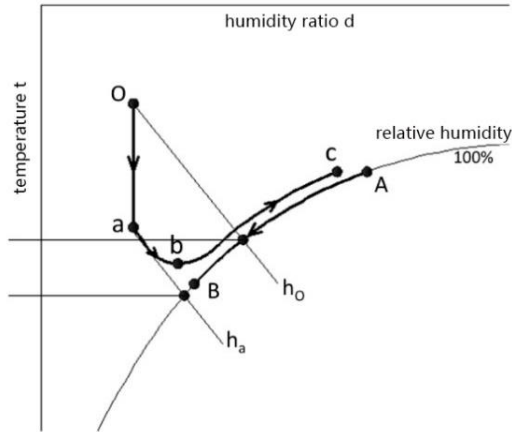


Figure 4: Psychrometric chart of heat and mass transfer process in evaporative water chiller

#### Performance evaluation of the chiller

The performance of the evaporative water chiller is usually evaluated through the following parameters:

Equation 14: Sub-wet bulb efficiency in indirect evaporative cooling section.

$$\eta_1 = \frac{t_{wb,o} - t_{wb,a}}{t_{wb,o} - t_{dp,o}} \times 100\%$$

Where:

- $\eta_1$  = the sub-wet bulb efficiency in indirect section
- $t_{wb,o}$  = the wet bulb temperature of ambient air (°C)
- $t_{wb,a}$  = the wet bulb temperature of the air after indirect evaporative cooling in the chiller (°C)
- $t_{dp,o}$  = the dew point temperature of ambient air (°C)

Equation 2: Efficiency of filler section.

$$\varepsilon_1 = \frac{t_o - t_B}{t_o - t_{wb,a}} \times 100\%$$

Where:

- $\varepsilon_1$  = the cooling efficiency of the filler section
- $t_o$  = the dry bulb temperature of ambient air (°C)
- $t_B$  = the supply water temperature of the filler section (°C)

Equation 3: Efficiency of evaporative water chiller.

$$\theta = \frac{t_o - t_B}{t_o - t_{wb,o}} \times 100\%$$

Where:

- $\theta$  = the whole cooling efficiency of the chiller

Equation 4: Approximation degree.

$$\epsilon = t_B - t_{dp,o}$$

Characterise the extent to which the temperature of supply water in the chiller is lower than the wet bulb temperature of the inlet air in the chiller.

Where:

- $\epsilon$  = the approximation degree

Equation 5: Cold depth.

$$\vartheta = t_{wb,o} - t_B$$

Characterise that the temperature of supply water in the chiller is lower than the wet bulb temperature of the inlet air.

Where:

- $\vartheta$  = the cold depth

The evaporative water chiller structure is shown in Figure 5:

- air side: the air entered into the chiller through the air inlet and was pre-cooling by the high-temperature cooling coil (inside of the coil is the high-temperature cold water produced by the evaporative water chiller). The wet bulb temperature of the air was reduced after precooling, the air then entered into the water drenching filler through the fan, the heat and mass transfer was conducted between counter flow of air and spraying water film, and was finally discharged from the top of the filler section;
- water side: a part of the cold water produced by the chiller was supplied to the end load for heat exchange, the other part was led into the cooling coil of air inlet to absorb the heat of the inlet air, and then the return water of the load was mixed with the outlet water of the cooling coil and was entered into the water distributor above the filler section, the water film was formed on the surface of the filler through the spraying nozzle, the heat exchange was conducted between the water film and air that the water was cooled, and cooling process was cycling, theoretically, the cold water produced by the evaporative water chiller can be lower than the wet bulb temperature of the ambient air.

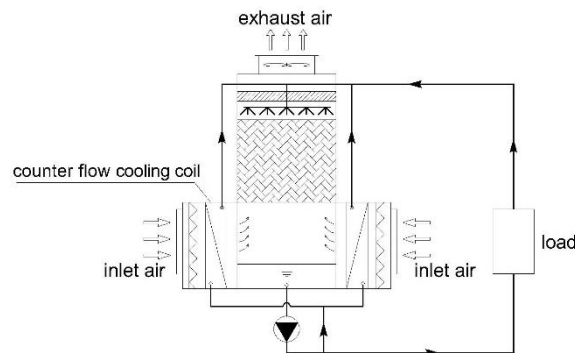


Figure 5: Structural schematic diagram of evaporative water chiller

## 5. DATA PROCESSING AND ANALYSIS

### 5.1. Test and analysis on evaporative water chiller

On August 22<sup>th</sup>, 2018, the evaporative water chiller was tested at 3p.m., during the same period of the day, the outdoor dry-bulb temperature in Dunhuang area was about 35°C, the relative humidity was about 18%, and the atmospheric pressure was 88100Pa. The outdoor and indoor design parameters are based on the "Design Code for Heating Ventilation and Air Conditioning of Civil Buildings" (Huang, 2016, Huang, 2017, GB50736-2012, 2012). The total designed cooling load for this project is 2044kW, the peak value appears at 6p.m., the designed cooling load for air-conditioning of every unit building area is 133 W/m<sup>2</sup>. The test results of the chiller's supply water temperature and efficiency are described below.

### Analysis of supply water temperature in evaporative cooling chiller

Through analysing the test parameters of the chiller, the ambient wet-bulb temperature is maintained at about 17.6°C during the test period, the ambient dew point temperature is maintained at about 7.3°C, and the supply water temperature of the evaporative water chiller is maintained at about 18.1°C, which is 0.5°C higher than the ambient wet-bulb temperature. The aim of the supply-water temperature below the ambient wet-bulb temperature has not reached.

Ideally, the supply water temperature of the chiller will be lower than the ambient air wet-bulb temperature, so the overall efficiency will be greater than 100%. However, according to the test, the overall efficiency of the evaporative water chiller was maintained at 97.3%, sub-wet bulb efficiency in indirect evaporative cooling section was maintained at 21%, and efficiency of filler section was maintained at 86.4% during the test period. The test results are shown as Figure 6, Figure 7. The efficiency of the chiller has not reached the ideal state. By checking the operation status of the chiller, it is found that there is a serious problem in the water spraying of filler section, which the details will be elaborated in Section 6: Problems and solutions.

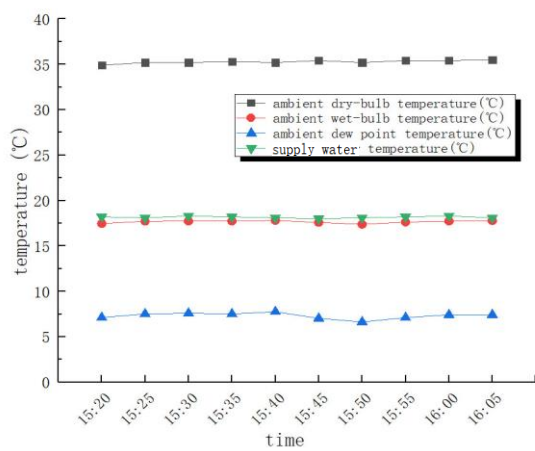


Figure 6: Variation diagram between supply water temperature and ambient parameters of the chiller

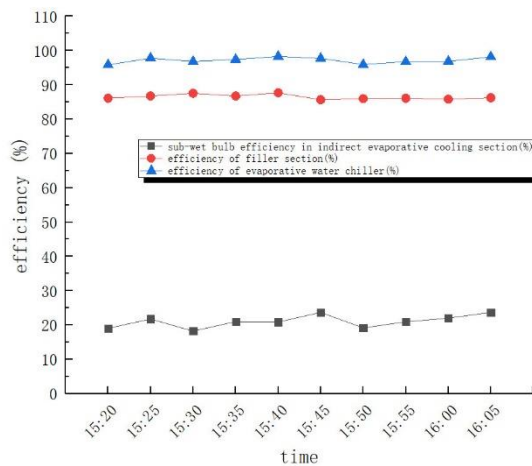


Figure 7: Variation diagram between efficiency of evaporative water chiller and time

## 5.2. Test Analysis of Terminal Environment

### Analysis of air supply parameters

The air supply temperature of the spherical air outlet in check-in hall on the first floor of the T3 terminal was tested, the air supply temperature was 22.8°C, and the thermal imaging of spherical air outlet is shown in Figure 8, and the air supply temperature of the spherical air outlet in the waiting area on the second floor of the T3 terminal was tested. The air supply temperature was 21.8°C and the thermal imaging of spherical air outlet is shown in Figure 9. The air supply temperature of T2 terminal was higher than T3 terminal. The reason was that the air conditioning system of the T2 terminal had just been turned on and had not reached a steady state. We consulted the staff that the air supply temperature of the spherical air outlet in the terminal is generally around 23°C.

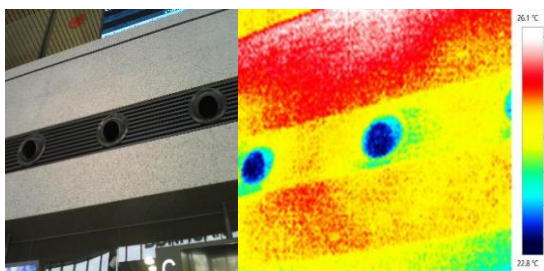


Figure 8: Thermal imaging of spherical air outlet in check-in hall on the first floor of the T3 terminal

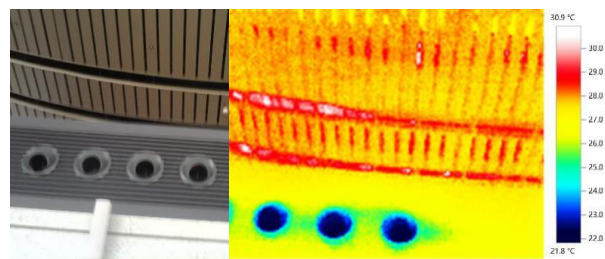


Figure 9: Thermal imaging of spherical air outlet in waiting area on the second floor of the T3 terminal

### Analysis of floor surface temperature

The floor surface temperature of the floor radiant cooling area in the T3 terminal was tested. The floor surface temperature of the check-in hall on the first floor of T3 terminal was 24°C and the thermal imaging is shown in Figure 10. The water supply temperature in the floor radiant coil was 19.3°C and the thermal imaging is shown in Figure 11. The floor surface temperature of the waiting area on the second floor of T3 terminal was 23.5°C and the thermal imaging is shown as Figure 12, whilst the water supply temperature in the floor radiant coil was 18.6°C and the thermal imaging is shown in Figure 13.

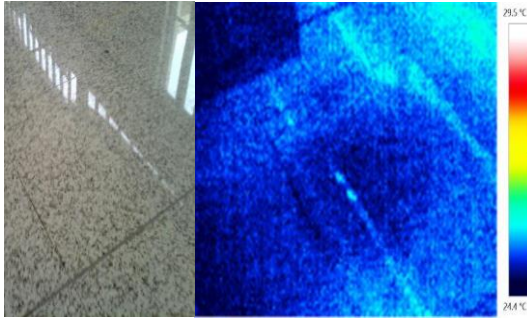


Figure 10: Thermal imaging of floor surface temperature

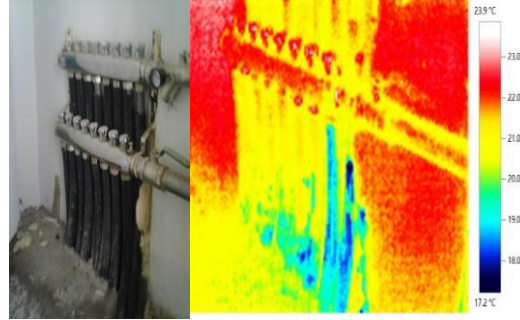


Figure 11: Thermal imaging of floor radiant coil manifold

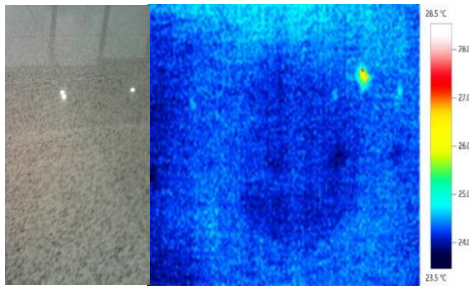


Figure 12: Thermal imaging of floor surface temperature

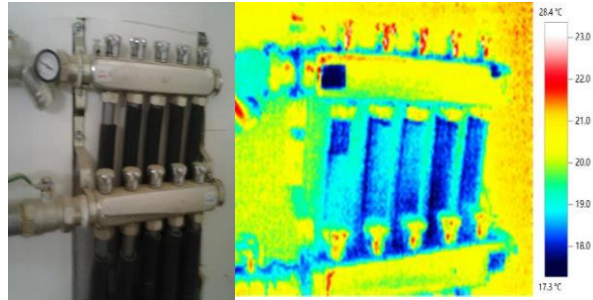


Figure 13: Thermal imaging of floor radiant coil manifold

### Analysis of indoor environment parameters

The environment parameters of the check-in hall in T3 terminal were tested and analysed: during the test period (14:00-15:00), the outdoor dry-bulb temperature was 36.7°C and the relative humidity was 18.1%. The environment temperature of the check-in hall was maintained at 26.3°C and the relative humidity was maintained at 39.6% which meets the thermal comfort requirements of the human body. The variation diagram is shown in Figure 14.

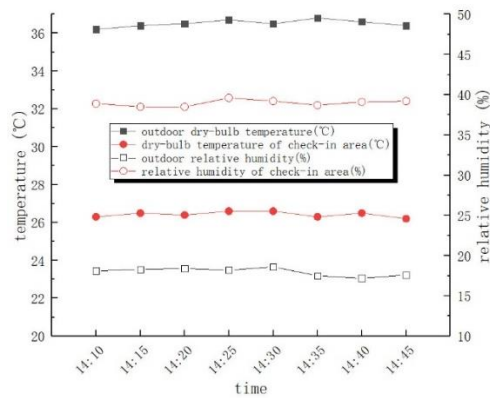


Figure 14: variation diagram between environment parameters of check-in hall in T3 terminal

### Analysis of indoor vertical gradient air parameters

The vertical gradient air parameters of the departure hall on the floor of T3 terminal were tested and analysed; the variation diagram is shown in Figure 15. On the same day, the atmospheric pressure in the Dunhuang area was 88380Pa and the results showed that when the vertical height was in the range of 0–6 meters, the dry-bulb temperature of the air increased with the increase of altitude, the temperature of the occupied zone (below 2 meters) was maintained at about 26°C, and the relative humidity of the air did not change significantly with increased height.

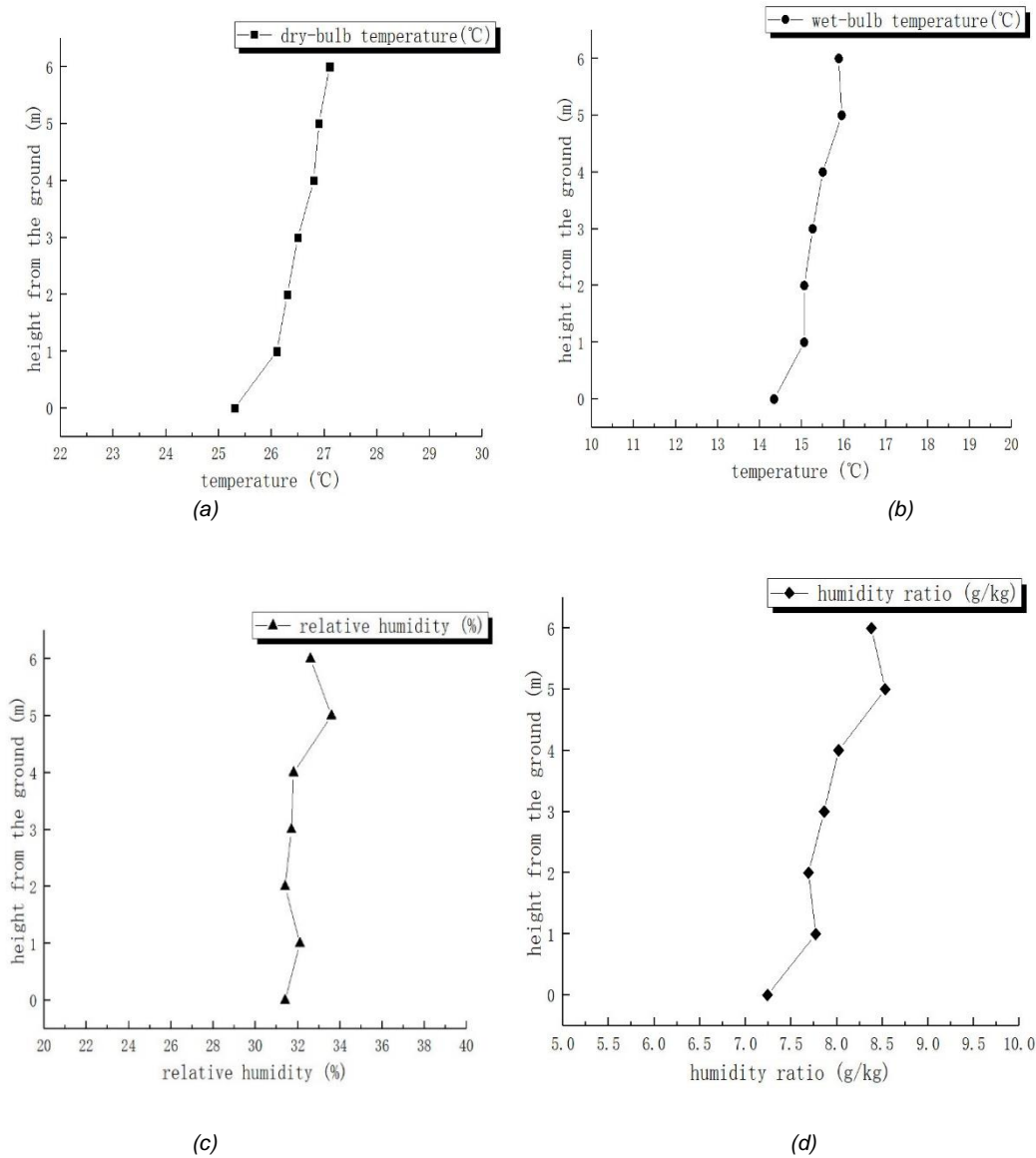


Figure 15: Vertical gradient air parameters variation diagram of the departure hall in T3 terminal

## 6. CONCLUSION

Firstly, during the test, it can be concluded that the air supply temperature of the spherical air outlet in the terminal is generally around 23°C, the floor surface temperature of the check-in hall of T3 terminal is around 24°C, the relative humidity was maintained at about 39.6%, and the environment temperature of the check-in hall was maintained at 26.3°C, which meets the thermal comfort requirements in humidity and temperature of the human body when composite evaporative cooling and mechanical refrigeration cooling system is working. Meanwhile, it was found that there was water leakage on the wall of the chiller. The leakage position was observed in the spray section of the evaporative water chiller and it was found that the main clogging problem most seriously occurred in the spray nozzle: only a few nozzles at the edge could spray water. This caused the pressure at the edge nozzle and the water pressure of the spray supply water to be too high causing an impact on the wall surface of the chiller.

The water overflowed from the gap of the wall of the chiller so that water loss occurred. In addition, the blocked nozzles brought on distribution inconsistency on the surface of filler section and there were a lot of dry areas which affected the supply water temperature of the chiller. On one hand, the water treatment device can be used to improve the water quality of circulating water; on the other hand, the circulating water of the chiller should be replaced regularly, and the nozzle clogging of the chiller should be checked and solved in time for regular maintenance to prolong the service life of the chiller (Huang, Liu, Yu, 2001:33-38, Du, Huang, 2017:59-62).

Secondly, the air duct obstruction is a general problem in ceiling type fan coil unit of Dunhuang Airport terminal, air supply duct of the fan coil and indoor air outlet are not in the same vertical direction, and there is a staggered arrangement between the air outlet of air duct and indoor air outlet, which causes the airflow rate of indoor supply air to be less than required and the fan-coil energy consumption is too high. On one hand, the reason for this problem is that the construction quality is not up to standard and match the design; on the other hand, the lack of construction supervision is showing up. As interior decoration has been completed, the renovation will have to be improved in the future.

Finally, the air conditioning system is an air-water conditioning system operated by combination of evaporative cooling and mechanical refrigeration. Most of the time, the evaporative cooling air conditioning system is turned on to meet the thermal comfort requirements of occupants. In extremely hot weather, mechanical refrigeration system can be turned on to assist with cooling. However, mechanical refrigeration system and evaporative cooling air conditioning system are often turned on at the same time in application (Huang, 2007:24-30, Huang, 2007:32-37+53, Huang, 2007:24-29+136). Although this measure can ensure that the indoor temperature and humidity requirements are within the specified range, the energy consumption of the entire system is very high. It is recommended to add the indoor and outdoor environment parameter monitoring and automatic control system to change the operating state through monitoring the real-time environment parameters indoors and outdoors. When only the evaporative cooling air conditioning system is turned on to meet the indoor thermal comfort, the system should be fully used. When evaporative cooling air conditioning system cannot meet the requirement, the mechanical refrigeration system can be turned on as well.

## 7. ACKNOWLEDGEMENT

This work was supported by a grant from the National key research and development program of China (Project No. 2016YFC0700404)

## 8. REFERENCES

Du S. S., Huang X., 2017. Preliminary study on evaporative air conditioning system for airport terminal in northwest China. *Refrigeration and Air-conditioning*, vol.17 (08), pp.59-62.

GB50736-2012, 2012. Design code of heating, ventilating and air conditioning for civil buildings. Beijing: China Architecture & Building Press.

Huang, X., 2010. Theory and application of evaporative air conditioning. Beijing: China Architecture & Building Press.

Huang, X., 2016. Design Guide of evaporative ventilation and air conditioning system. Beijing: China Architecture & Building Press.

Huang X., 2017. Air-conditioning engineering. 3rd Edition. Beijing: China Machine Press.

Huang X., Liu M., Yu X. Y., 2001. Analysis on application status of evaporative Cooling technology in xinjiang region of China. *Refrigeration and Air-conditioning*, vol.06, pp.33-38.

Huang X., 2007. Research progress on evaporative air conditioning technology at home and abroad (1). *Journal of HV&AC*, iss. (02), pp.24-30.

Huang X., 2007. Research progress on evaporative air conditioning technology at home and abroad (2). *Journal of HV&AC*, iss. (03), pp.32-37+53.

Huang X. 2007. Research progress on evaporative air conditioning technology at home and abroad (3). *Journal of HV&AC*, iss. (04), pp.24-29+136.

Zhou, M., 2014. Energy-saving technology of T3A terminal building in Xi'an Xianyang International Airport. *Construction Science and Technology*, vol.10, pp.65-69.

---

## #79: Thermodynamic analysis of a poly-generation system for electrical power, cooling and desalinated water

---

Ayman O. ABDELHAY<sup>1,2</sup>, Hassan E.S. FATH<sup>3</sup>, Sameh A. NADA<sup>4</sup>, Mohamed A. SHARAF<sup>5</sup>

<sup>1</sup>Faculty of Engineering, Egypt-Japan University of Science and Technology, New Borg El-Arab City, Alexandria, Egypt, ayman.osama@ejust.edu.eg

<sup>2</sup> Faculty of Engineering, Menoufia University, Shebin El-Kom, Menoufia, Egypt, ayman.osama@sh-eng.menofia.edu.eg

<sup>3</sup> Faculty of Engineering, Egypt-Japan University of Science and Technology, New Borg El-Arab City, Alexandria, Egypt, hassan.fath@ejust.edu.eg

<sup>4</sup> Faculty of Engineering, Egypt-Japan University of Science and Technology, New Borg El-Arab City, Alexandria, Egypt, sameh.nada@ejust.edu.eg

<sup>5</sup> Department of Engineering Science, Faculty of Petroleum & Mining Engineering, Suez University, Egypt, mohammed.eldeen@suezuniv.edu.eg, mwahab31@yahoo.com

Nowadays, designing new poly-generation systems is needed to meet the increasing community's demands of electrical energy, space cooling and fresh water. This should take more attention especially with the increasing conventional fossil fuel energy costs, freshwater shortage and CO<sub>2</sub> emission. This work presents the thermodynamic analysis of a sustainable poly-generation thermal system that can produce electricity, space cooling and desalinated water. The proposed system combines a Concentrated Solar Power (CSP), Steam Rankine Cycle (SRC), Multi Effect Distillation (MED) system and Absorption Refrigeration System (ARS). The system design target is to provide communities in remote areas with all needs of water, electricity and cooling using low-grade heat from green solar energy. In the solar field, solar irradiation is collected by Parabolic Trough Collectors (PTC) to heat the working fluid (Therminol-VP1 heat transfer oil). Thermal oil transfers the absorbed heat to the SRC that generates the required electrical power and provides both MED and ARS with a proper heating steam required depending on the demand loads. The developed model is used to design a pilot test unit of 10 kW electrical power, 1.7 m<sup>3</sup>/day of desalinated water and 3.6 TR cooling load capacity. Flow, heat, and exergy destruction rates for each component of the system are obtained. Performance parameters of the subsystems forming the plant are also evaluated. Results revealed that the PTC represent the most critical part in the system from the exergetic point of view as it experiences 84.65% of the total system exergy destruction the required PTC area is 83.12 m<sup>2</sup>. For the ARS unit, exergy loss is about 2.2 kW, 36.22% and 28.87% of this value occur in absorber and generator respectively. MED unit simulation results demonstrated that the gain ratio and specific heat transfer area are 2.29 and 144 m<sup>2</sup>/kg/s respectively. The exergy destruction in the MED unit is 1.8244 kW (66.43% in evaporators and 33.57% in condenser). The ARS coefficient of performance and second law efficiency were 0.7755 and 59.24% respectively.

Keywords: polygeneration; MED; CSP; absorption



## 1. INTRODUCTION

Earth has a huge amount of water but only 2.5% is pure water; the rest is salty. Consequently, to produce drinkable water from the available salty water, several desalination methods have been invented and used depending on the process energy, efficiency and cost. In the last decades, seawater desalination capacity has grown sharply and increased from 22 Mm<sup>3</sup>/day in 2000 to more than 90 Mm<sup>3</sup>/day in 2015 (Saldivia *et al.*, 2019). A considerable part of this production capacity is covered by thermal desalination techniques especially where relatively large water production capacity is required (Ettouney and El-Dessouky, 1999). Thermal desalination has high energy consumption compared to membrane processes: 130 million tons of oil fuel can be used for annual water production of 13 Mm<sup>3</sup>/day (Kalogirou, 1997; Kouhikamali and Mehdizadeh, 2011) producing huge amounts of CO<sub>2</sub> emissions. The utilisation of solar energy instead of fossil fuels to provide such desalination systems with the required energy can play a key role in decreasing the harmful environmental impact of CO<sub>2</sub> emissions and the rejected waste heat.

Applying the cogeneration systems to produce both fresh water and electricity driven by solar energy can solve both energy and water shortages, and decrease the unit cost of water and power as well (Palenzuela, Zaragoza and Alarcón-Padilla, 2015). Therefore, to cover the growing demand of potable water and electricity in an economical way, solar cogeneration systems for power and desalination can be utilised (Fernández-Izquierdo *et al.*, 2012). The multi-effect desalination (MED) method is considered to be one of the most convenient techniques to be coupled with solar systems due to its potential to be supplied by low-grade heat sources (lower than 70°C) together with having lower capital costs and pumping power compared to the other thermal desalination systems (Wang and Lior, 2006). Many articles have performed energy, exergy and economic analyses as well as studied the optimisation of MED to investigate and optimise different parameters that affect system design and performance (Ji *et al.*, 2007; Kamali and Mohebinia, 2008; Nafey, Fath and Mabrouk, 2008; Trostmann, 2009; Sayyaadi and Saffari, 2010; Shakib, Amidpour and Aghanajafi, 2011).

Solar MED systems (Thermal and Mechanical Vapor Compression, TVC, MVC), exergy and thermo-economical analyses have been investigated by Sharaf, Nafey and García-Rodríguez (2011a & 2011b). Comparisons between one purpose (water only) solar MED and dual-purpose (water and power) solar Organic Rankine Cycle (ORC)-MED systems have been carried out. Moreover, a comparison between Therminol-VP1 and Toluene oils as a heat transfer fluid for the solar field were also implemented. Results showed that the one purpose system is more economic than dual-purpose due to the higher gain ratio and lower Parabolic Trough Collector (PTC) area needed. Also, results revealed that increasing the number of MED evaporators reduces each of the solar field area, specific power consumption and unit product cost. System gain ratio can be increased by coupling the TVC to the MED system instead of increasing the number of MED effects.

Saldivia *et al.* (2019) presented a thermodynamic simulation model for a combined MED-solar steam generation plant (PTC collectors, a storage tank, and a steam generator) system under different operating conditions. The developed model showed a good agreement with the compared data obtained from Plataforma Solar de Almería (PSA) in Spain. Results showed that system water productivity increases linearly with solar radiation intensity. It was also concluded that the investigated model can be a powerful tool for the design and optimisation of solar MED systems.

MED system can be also driven by Linear Fresnel (LF) concentrating solar power instead of using PTCs. Concerning this, (Hamed *et al.*, 2016) investigated the effect of thermal energy storage, direct normal irradiance, and fuel cost on the performance of MED system supplied by LF solar field. Results displayed that the LF-MED without thermal energy storage can be more economical under certain weather conditions. On the other hand, three different configurations of LF-MED/TVC were studied techno-economically by (Askari and Ameri, 2016). System and water production costs were assessed in addition to the annual fuel savings and size of LF solar field. Results showed that the water production cost was 1.63 \$/m<sup>3</sup> but, it increases to 3.09 \$/m<sup>3</sup> in case of providing system with thermal storage. If the thermal storage duration increases from 6 h to 12 h, water production costs rises by about 42% and 65%, respectively.

In the last two decades, due to the dramatic growth in residential and commercial buildings, cooling loads have become a major consumer of electricity during the summer due to the use of traditional vapor compression air conditioning devices (Lee and Sherif, 2001). As the energy shortage increases year by year, application of heat-driven refrigeration systems could be considered as an appropriate alternative. Absorption systems are characterised by the possibility of utilising low-grade heat, which is rejected normally to the environment from the power cycles, to produce chilled water and/or hot water for both cooling and heating applications. In hot dry regions, it is reasonable to use systems that produce both chilled and pure water. Some articles studied the integration of air conditioning and HDH systems for building cooling and fresh water production (Nada, Elattar and Fouda, 2015b, 2015a; Elattar, Fouda and Nada, 2016; Fouda, Nada and Elattar, 2016). In addition, some research proposed the combination of Absorption Refrigeration System (ARS) and MED systems in which both systems work using a low temperature heat source. Aly (1995) introduced a novel hybrid system combining LiBr-H<sub>2</sub>O absorption system and 20 effects vertical stack MED distillation system for a capacity of 1.53 MGD of drinkable water with a GOR of 14.8

in addition to 3000 TR cooling. The performed analysis revealed that the proposed plant offers low cost water because the MED top brine temperature can be lowered to (30°C).

While, the hybrid single/double stage ammonia-water ARS combined with MED were investigated by (Alelyani *et al.*, 2017). The absorption system rectifier heat rejection which is supplied to the MED system. Thermodynamic and economic analyses were performed using Engineering Equation Solver (EES) software. The influence of concentration difference of strong and weak solutions, temperature of absorber and evaporator, and number of MED evaporators on the system gained ratio, cooling and water capacity, and exergy efficiency were studied. Results demonstrated that the exergy degradation of the proposed hybrid system is lower than stand-alone ARS or MED systems by about 55%. Coupling single and double stage ARS to the MED causes water production cost to decline by 30% and 9% respectively. Comparison between single and double stage ARS-MED and stand-alone ARS revealed that the cooling capacity decreases by 16% for the single-stage and remains constant for the two-stage system. The water unit product cost (UPC, \$/m<sup>3</sup>) has increases by 19% single-stage system and by 3% for the double-stage one while, the cooling UPC reduced by 44% due to the ARS-MED coupling.

Recently, several novel hybrid systems have been performed in order to face the problem of the increasing demands of energy, cooling, heating and freshwater issues. These systems are called poly-generation systems. Poly-generation systems aim also to decrease the environmental pollution related to the use of fossil fuels and the rates of CO<sub>2</sub> emissions through the partial or total replacement of fossil fuels by renewable energy sources. Furthermore, these integrated systems help in reducing the overall heat losses and increasing the amount of economic saving.

Some research works were found to deal with the poly-generation systems. (Calise, Dentice d'Accadia and Piacentino, 2014) introduced a poly-generation system combining photovoltaic/thermal (PVT) solar collectors, biomass fuelled heater, MED and ARS (single-stage LiBr-H<sub>2</sub>O) to generate electricity, potable water, heating and cooling. PVT produces both electricity to the main grid and heat supply for the ARS unit. The MED unit was provided by heat from the solar field and the biomass heater. Dynamic simulation was carried out using TRNSYS program. The conducted thermo-economic analysis indicated that the optimum solar field area for the ARS system is about 5.9 m<sup>2</sup>/kW. The storage tank volume was suggested to be 15 Litre/m<sup>2</sup> of solar field. Furthermore, the optimum number of effects of MED unit was 14. The most convenient temperatures at the solar field outlet temperatures in summer and winter was 85°C and 55°C respectively.

Calise *et al.* (2014) presented a hybrid MED-ARS (single-stage LiBr-H<sub>2</sub>O) powered by geothermal energy and concentrating photovoltaic/thermal solar collectors to produce electricity, thermal energy, cooling energy and fresh water simultaneously. The absorption chiller is powered by the thermal energy produced by the solar field (100°C). While, the MED system is driven by heat from the geothermal fluid (80°C). TRNSYS package was utilised to perform a dynamic simulation of the proposed system. Results showed that the energetic performance of the proposed system during summer is much better than during winter. The implemented economic analysis showed that the system profitability rises considerably with the hot water load increase. Simple payback period periods may increase to 10 years in case of lower utilisation of thermal energy, but full utilisation of energy and water causes the pay back periods to decrease significantly.

Calise *et al.* (2017) proposed the poly-generation combining MED, ORC and ARS supplied by energy from PTC solar field and geothermal wells. The studied system produces electricity, potable water in addition to cooling and heating energies. TRNSYS environment was used to implement one-year dynamic simulation using data of Pantelleria Island. Appropriate temperature for each component to avoid the very small temperature of the reinjected fluid to the geothermal wells was investigated. Electrical load was attained from measured data while heating and cooling loads were calculated by building dynamic simulation. Results showed that the studied system can supply 800 buildings with energy and water needs. The plant annual production was assessed to be 5120 MWh electricity, 1006 Mm<sup>3</sup> of pure water. Efficiency of the ORC was 15.30%, if the ORC uses (14.6%) solar energy and (85.4%) geothermal energy. The economic and environmental results indicated that the simple payback period was 8.5 while, the avoided fossil fuel and CO<sub>2</sub> emissions were estimated to be 3039 and 9451 tons respectively.

Sahoo *et al.* (2015) proposed a poly-generation system in which both biomass and solar energy were utilised to produce steam required for the electric power production (through steam turbine) and to supply an ARS with the required heat. Then, through a heat exchanger, the waste heat rejected from the ARS condenser is transmitted a multi effect humidification-dehumidification desalination system. Thermodynamics analysis of the proposed plant introduced poly-generation system that been carried out based on the Indian climatic condition (ambient temperature was assigned as 35°C). Analysis demonstrated that the proposed integration enhances the overall system efficiency and significantly decrease CO<sub>2</sub> emissions as well.

As there are too many systems that can separately produce power, cooling, heating and desalinated water, there will be a lot of integrations that can be suggested for study and investigation. This article represents an introduction of one of these new integrated systems. In this study, a poly-generation system driven by solar energy and

producing simultaneously electricity, cooling energy and pure water will be presented. The suggested system is an integration of concentrated solar power system (using PTCs), steam Rankine cycle (SRC), multi effect desalination (MED) system and absorption refrigeration system (ARS) as shown in Figure 1. The system design will be explored using energy and exergy concepts. Additionally, the simulation results will be presented.

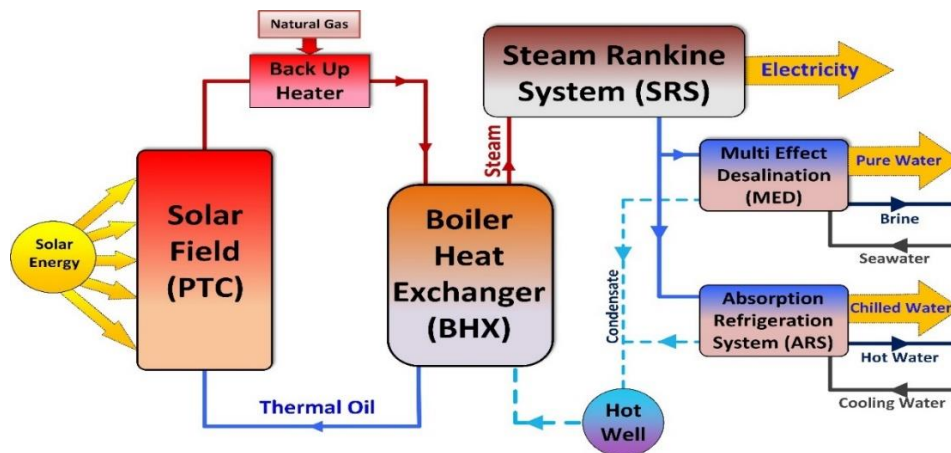


Figure 1: Flow diagram of the proposed Poly-generation System for Electricity, Cooling and Pure Water

## 2. AIM OF THE STUDY

In this research, steady-state energetic and exergetic design techniques of modelling were performed for a PTC-SRC-MED-ARS poly-generation system powered by solar energy. To the authors' knowledge, there are no articles available that deal with the proposed integration from this angle. The poly-generation plant introduced in this work is suitable for medium and high loads of electricity, cooling and potable water production. This may be reasonable for coastal and tourist spots along the solar beam areas like Middle East, North Africa (MENA) and GULF regions.

The studied system components are modelled and simulated depending on both first and second laws of thermodynamics using MATLAB environment. As a first step in modelling this system, the study was implemented depending on steady-state basis at a constant value of solar radiation intensity. This work aims to present and analyse the thermal design results gained for the proposed plant in order to produce 10 kW<sub>e</sub> power, 1.7 m<sup>3</sup>/day of pure water and 3.6 TR cooling. These small capacities have been chosen to suit a small plant that can be afterwards assembled and installed to study the proposed system feasibility. The energetic and exergetic results will be presented and discussed.

## 3. SYSTEM LAYOUT

As mentioned previously, the proposed layout combines three sub-systems, solar power system, absorption refrigeration system (ARS) and multi-effect distillation (MED) unit. The solar power system includes concentrated solar power cycle and steam Rankine cycle. Basically, the plant is driven by solar energy but, during night or in case of solar irradiation reduction, an auxiliary natural gas fuelled heater is utilised to stabilise the working fluid temperature. The proposed plant can generate electricity, space cooling and desalinated water continuously. The plant is mainly composed of the four units that can be described in detail through the following sections.

### 3.1. Solar field loop description & design data

Solar field loop combines a set of PTCs, Natural gas heater and boiler heat exchanger. Therminol-VP1 thermal oil is employed as a working fluid. It can stay as a liquid phase under 400°C (Sharaf Eldean and Soliman, 2015). Solar radiation is collected and concentrated on the thermal oil by parabolic trough collectors. Due to the continuous change in the solar radiation intensity, another energy source (gas fired heater) is used to compensate the decrease in the radiation intensity. Consequently, steady state condition for the boiler heat exchanger can be achieved. Through the boiler, heat gain is transferred from the thermal oil to the water side flowing in the Rankine cycle. In simulation solar intensity is assumed to be constant to accomplish the steady state condition. In order to design the solar field components (i.e. PTCs area, gas-fired heater and boiler capacity), input data shown in Table 1, **Error! Reference source not found.** was specified in the developed MATLAB program.

### 3.2. Steam Rankine loop description & design data

Steam Rankine loop generates the necessary electrical power for the consumers. In the boiler heat exchange, superheated steam is formed due to the heat transfer with thermal oil. Then, steam is expanded in the turbine producing mechanical power that is converted into electrical power in generator. At the turbine outlet, steam is assumed to be wet with 85% quality in order to decrease steam temperature at the turbine inlet and to increase the turbine life span. The back-pressure steam rejected from the turbine is exploited to drive both MED and ARS units instead of losing its energy through the condenser. The condensate rejected from the MED and ARS is collected in the condenser hot well and pumped again to the boiler. In case of MED and ARS part load, the remaining steam is condensed in the condenser. The design input data for the steam Rankine cycle is shown in Table 1.

Table 1: Design Data for Solar Field loop and Steam Rankine Cycle

Solar Field Loop			Steam Rankine Cycle		
Description	Value	Unit	Description	Value	Unit
Solar irradiation	750	W/m <sup>2</sup>	Electrical power output	10	kW
Boiler effectiveness	80%	-	Turbine efficiency	85%	-
Natural gas heater efficiency	70%	-	Turbine outlet steam dryness fraction	85%	-
Natural gas calorific value	42000	kJ/kg	Electrical generator efficiency	90%	-
Therminol-VP1 maximum temperature	350	°C	Pump efficiency	85%	-
			Condenser temperature difference	10	°C

### 3.3. MED unit description & design data

In the MED unit, turbine steam condenses completely inside the tubes of the first effect (evaporator). While the feed saline water (sprayed outside the tubes) boils and generate another amount of steam. The steam outlet of each effect serves as an energy source for the next effect. On the other hand, the rejected concentrated brine from each effect is directed to the next effect (at lower pressure) to generate more steam by flashing. Then at the end condenser, steam of the final effect condensed due to cooling by sea water. Part of the heated seawater is used as feed water to effects and the other part is returned back to the sea. The condensed pure water from each effect is collected as the required output desalinated water. The design data of MED system is summarised in Table 2.

### 3.4. ARS unit description & design data

The ARS unit is a single stage Water-LiBr type. This type is selected due to its better performance compared to ammonia-water solution (Horuz, 1998). Turbine steam condensation in the ARS generator results in boiling of Water-LiBr solution and separation of the refrigerant (water vapor). Then, weak solution is returned through a throttle valve to the absorber. In the ARS condenser, heat is removed from the refrigerant to the cooling water. Refrigerant is then throttled to fulfil the required temperature at the evaporator in which the chilled water acquires its low temperature needed for the cooling application. The evaporated refrigerant is cooled, condensed and mixed with the LiBr in the absorber forming a strong solution. Finally, the strong solution is pumped back to the generator and so on. To enhance the ARS performance, strong and weak solutions exchanges heat through liquid-liquid heat exchanger (Sözen, 2001). Input design data is displayed in Table 2.

Table 2: Design data for MED unit and ARS unit

MED unit			ARS unit		
Description	Value	Unit	Description	Value	Unit
Water production capacity	1700	kg/day	Cooling load	3.6	TR
Number of effects	3	-	Generator outlet temperature	88	°C
Heating steam temperature	69	°C	Absorber outlet temperature	30	°C
Feed seawater salt concentration	35000	ppm	Refrigerant outlet temperature from condenser	38	°C
Rejected brine salt concentration	65000	ppm	Evaporator temperature	4	°C
Feed seawater temperature	25	°C	Chilled water inlet temperature	12	°C
Effects feed water temperature	10	°C	Chilled water outlet temperature	6.5	°C
			Cooling water inlet temperature (to absorber)	25	°C
			Cooling water outlet temperature	35	°C
			Heat exchanger effectiveness	65%	-

#### 4. SIMULATION RESULTS AND DISCUSSION

A user-friendly graphical interface (GUI) for the proposed system has been developed using MATLAB toolbox environment. Through it, the required output capacities (electricity, cooling and water) and design initial values can be given as input data then, the simulation results can be calculated and displayed directly as shown in Figure 2. The presented simulation results are based on 10 kW electrical power, 1.7 m<sup>3</sup>/day and 3.6 TR cooling capacity. Results include streams flow rate, temperatures, performance parameters and exergy destruction of different system parts. The detailed simulation results are introduced in the following sections.

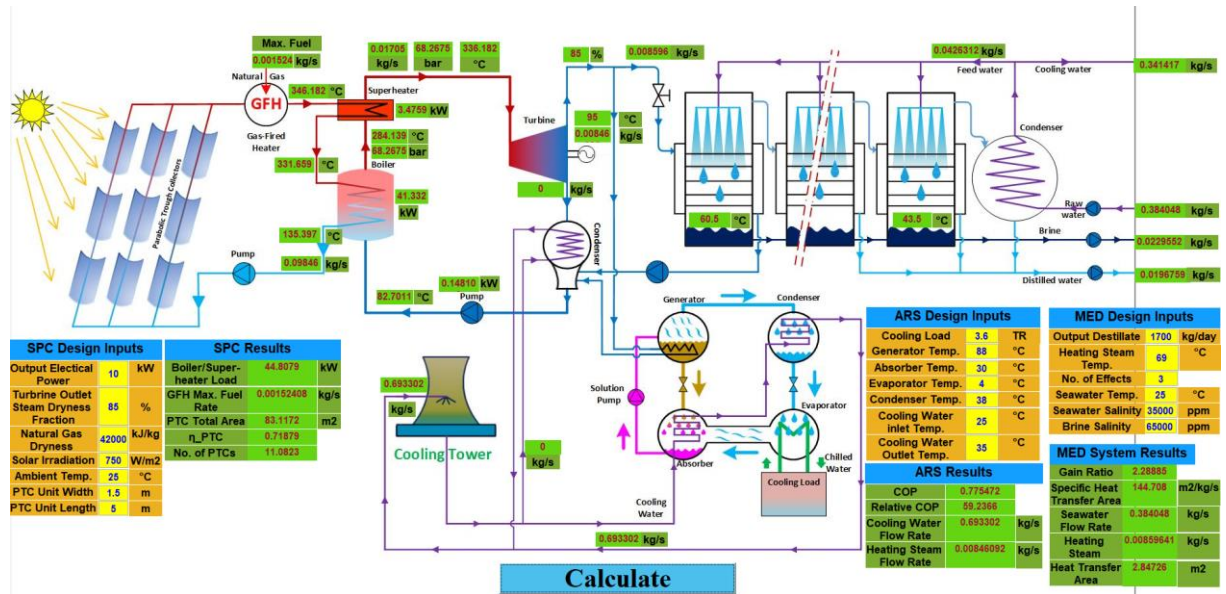


Figure 2: Developed GUI Simulation Results

#### 4.1. Solar power system simulation results

Solar Power System (SPS) combines the solar field and steam Rankine loops. Simulation results for the SPS are introduced in Table 5. Streams flow rate and components capacities are calculated. PTC thermal efficiency as well as the required PTC area are computed to be 71.88% and 83.12 m<sup>2</sup>. Exergy destruction analysis showed that the most critical part in the system that causes the highest percent of the exergy destruction is the PTCs. It represents 67.77% of the solar exergy input and 92.67% of the SPS exergy destruction as Table 5 demonstrates. In addition, PTC exergy loss accounts for 84.72% of the total system exergy destruction as can be seen in Figure 3.

Table 5: Energetic and Exergetic Results of Solar Power System

Description	Value	Unit	Description	Value	Unit
Turbine steam flow rate	0.0171	kg/s	Solar energy exergy input	58.0676	kW
Condenser maximum heat rate	32.9063	kW	Exergy destruction in turbine	1.5871	kW
Condenser maximum cooling water flow rate	0.7872	kg/s	Exergy destruction in boiler heat exchanger	1.4867	kW
Boiler heat exchanger capacity	44.8079	kW	Exergy destruction in hot well	0.0138	kW
Thermal oil flow rate	0.0985	kg/s	Exergy destruction in pump	0.0246	kW
Gas fired heater fuel capacity	0.0015	kg/s	Exergy destruction in PTC	39.3538	kW
PTC thermal efficiency	71.88%	-	Exergy destruction in solar power system	42.4660	kW
PTC area	83.1172	m <sup>2</sup>			

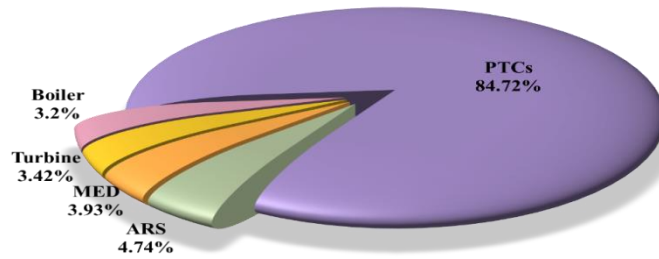


Figure 3: Plant Exergy Destruction analysis results by percentage

#### 4.2. MED simulation results

Simulation results for the MED unit generating 1.7 m<sup>3</sup>/day are presented in Table 6. Flow rates of inlet and outlet streams of the system are determined. Heat transfer area and exergy destruction of effects and condenser are evaluated. Then the system gain ratio (GR) (kg desalinated water/ kg heating steam) and specific heat transfer area (m<sup>2</sup>/kg/s desalinated water) are computed as 2.29 and 144 respectively. Total exergy destruction in the MED system is evaluated to be 1.8244 kW or 3.93% of the total plant exergy destruction (Figure 3). Exergy analysis, shown in Figure 4, also showed that each effect and condenser account for 22.14% and 33.57% of the MED total exergy destruction respectively.

Table 6: Energetic and Exergetic Results of MED Unit

Description	Value	Unit	Description	Value	Unit
Heating steam flow rate	0.0086	kg/s	Total heat transfer area for MED	2.8473	m <sup>2</sup>
Seawater flow rate	0.3840	kg/s	Exergy destruction per effect	0.404	kW
Feed flow rate to effects	0.0426	kg/s	Exergy destruction in condenser	0.6125	kW
Rejected brine flow rate	0.0230	kg/s	Total exergy destruction in MED	1.8244	kW
Heat transfer area per effect	0.8115	m <sup>2</sup>	Gain ratio	2.2889	-
Condenser heat transfer area	0.4129	m <sup>2</sup>	Specific heat transfer area	144.7077	m <sup>2</sup> /(kg/s)

#### 4.3. ARS simulation results

Table 5 illustrates thermodynamic simulation results of the ARS unit. Heat rates of ARS parts including generator, condenser, Absorber and heat exchanger are presented. Unfortunately, no available correlations were found in the literature to calculate the heat transfer area of these parts directly. Table 5 displays also mass flow rates of the heating steam, strong and weak solutions, cooling water and Chilled water. Exergy destruction for each part of the ARS were calculated. For the entire ARS, exergy destruction accounts for 2.2015 kW or 4.74% of the plant Exergy loss (Figure 3). While, the highest exergy loss experiences in the absorber and generator by 36.22% and 28.87% respectively (Figure 4). Therefore, a special attention must be considered in the design of these components. On the other hand, the exergy destruction in evaporator and condenser are 15.39% and 13.2% respectively. System coefficient of performance and second law efficiency were calculated to be 0.7755 and 59.24% respectively as mentioned Table 7.

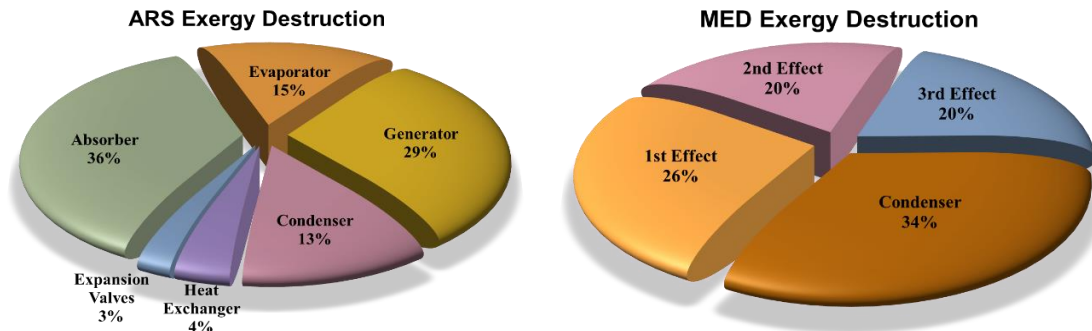


Figure 4: ARS and MED Exergy Destruction analysis results by percentage

Table 7: Energetic and Exergetic Results of ARS Unit

Description	Value	Unit	Description	Value	Unit
Generator Heat Rate	16.3224	kW	Exergy Destruction in Absorber	0.7973	kW
Condenser Heat Rate	13.348	kW	Exergy Destruction in Evaporator	0.3388	kW
Absorber Heat Rate	15.632	kW	Exergy Destruction in Generator	0.6355	kW
Heat Exchanger Rate of Heat	2.0927	kW	Exergy Destruction in Condenser	0.2906	kW
Steam Flow Rate of ARS	0.0085	kg/s	Exergy Destruction in Heat Exchanger	0.0852	kW
Chilled Water flow rate	0.545	kg/s	Exergy Destruction in Expansion Valves	0.0541	kW
Cooling Water Flow Rate	0.6933	kg/s	Total Exergy Destruction in ARS Unit	2.2015	kW
Refrigerant flow rate	0.0054	kg/s	Coefficient of Performance	0.7755	-
Strong Solution flow rate	0.0353	kg/s	Maximum Coefficient of Performance	1.3091	-
Weak Solution flow rate	0.0299	kg/s	Second Law Efficiency	59.24%	-

#### 4.4. Exergy analysis summary

Figure 5 presents the exergy balance diagram including the values of exergy input mainly with the solar energy, the exergy destruction of the whole plant and different system components, and the exergy output with the turbine mechanical power and with the outlet streams. The highest exergy destruction occurred in the PTC is due to the big difference between the highest exergy input, as it depends on the sun temperature (5800k), and the exergy output due to the heat transfer to the thermal oil. Consequently, in order to decrease the PTC exergy loss, the heat transfer between the solar radiation and the thermal oil has to be enhanced through new designs and investigations.

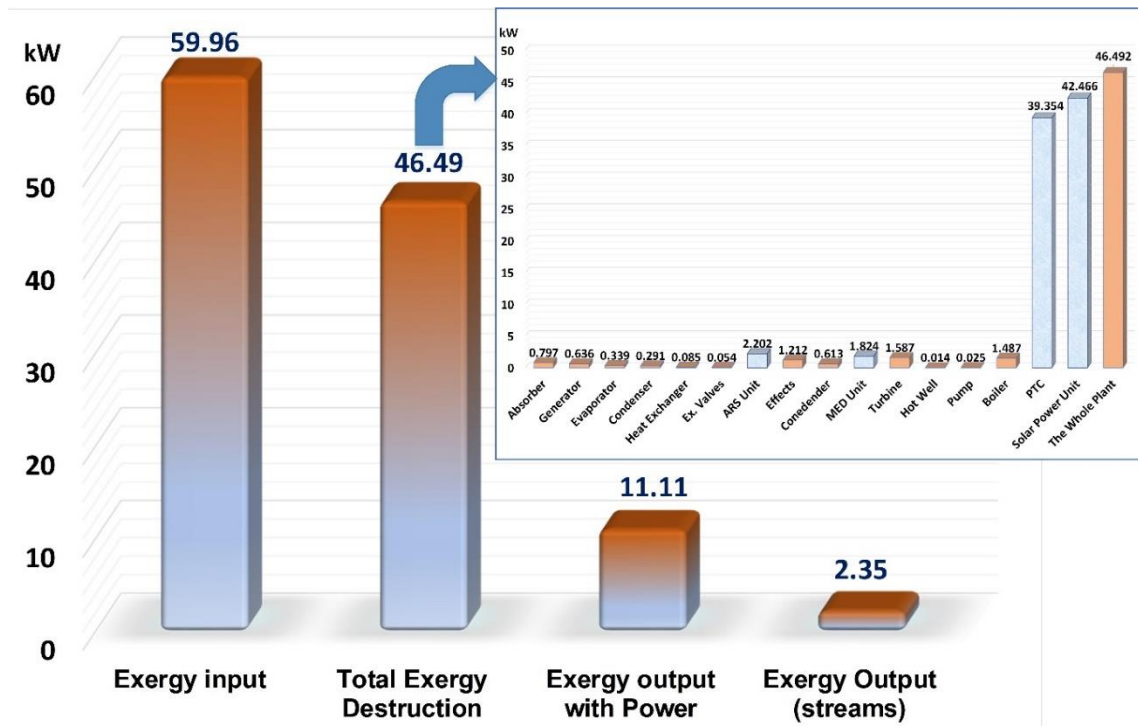


Figure 5: Exergy balance diagram

## 5. CONCLUSIONS

This study introduced a novel poly-generation capable to produce electrical power, cooling and desalinated water. The proposed plant is powered by concentrated solar power. System configuration combine PTC solar field, steam Rankine cycle, MED system and absorption chiller. System modelling depending on both first and second laws of thermodynamics is performed using MATLAB package. A case study of 10 kWe power, 1.7 m<sup>3</sup>/day of desalinated water and 3.6 TR cooling is applied to the simulation program.

Energetic and exegetic results have been presented and revealed that:

- The required PTC area for the studied plant is 83.12 m<sup>2</sup> with a thermal efficiency of 71.88%.
- PTC experiences the highest exergy destruction (39.3538 kW) compared to other system components. It represents about 84.65% of the total system exergy destruction and 67.77% of the solar exergy input.
- The MED gain ratio GR and specific heat transfer area are evaluated to be 2.29 and 144 respectively.
- MED system records an exergy loss of 1.8244 kW (22.14% in each effect and 33.57% in condenser).
- Absorption chiller coefficient of performance and second law efficiency are 0.7755 and 59.24%.
- The total rate of exergy destruction of the ARS is 2.2 kW. Most of this value occurs in absorber and generator (36.22% and 28.87% respectively).
- To overcome the high exergy destruction in the PTC, heat transfer to the thermal oil has to be modified through new designs and investigations.

## 6. REFERENCES

Alelyani, S. M. *et al.* (2017) 'Techno-economic analysis of combined ammonia-water absorption refrigeration and desalination', *Energy Conversion and Management*. Elsevier Ltd, 143, pp. 493–504. doi: 10.1016/j.enconman.2017.03.085.

Aly, S. E. (1995) 'A study of a new thermal vapor compression/multi-effect stack (TVC/MES) low temperature distillation system', *Desalination*, 103(3), pp. 257–263. doi: 10.1016/0011-9164(95)00078-X.

Askari, I. B. and Ameri, M. (2016) 'Techno economic feasibility analysis of Linear Fresnel solar field as thermal source of the MED/TVC desalination system', *Desalination*. Elsevier B.V., 394, pp. 1–17. doi: 10.1016/j.desal.2016.04.022.

Calise, F. *et al.* (2014) 'A novel renewable polygeneration system for a small Mediterranean volcanic island for the



combined production of energy and water: Dynamic simulation and economic assessment', *Applied Energy*. Elsevier Ltd, 135, pp. 675–693. doi: 10.1016/j.apenergy.2014.03.064.

Calise, F. *et al.* (2017) 'A novel hybrid polygeneration system supplying energy and desalinated water by renewable sources in Pantelleria Island', *Energy*. Elsevier Ltd, 137, pp. 1086–1106. doi: 10.1016/j.energy.2017.03.165.

Calise, F., Dentice d'Accadia, M. and Piacentino, A. (2014) 'A novel solar trigeneration system integrating PVT (photovoltaic/thermal collectors) and SW (seawater) desalination: Dynamic simulation and economic assessment', *Energy*. Elsevier Ltd, 67, pp. 129–148. doi: 10.1016/j.energy.2013.12.060.

Elattar, H. F., Fouda, A. and Nada, S. A. (2016) 'Performance investigation of a novel solar hybrid air conditioning and humidification-dehumidification water desalination system', *Desalination*. Elsevier B.V., 382, pp. 28–42. doi: 10.1016/j.desal.2015.12.023.

Ettouney, H. M. and El-Dessouky, H. (1999) 'A simulator for thermal desalination processes', *Desalination*, 125(1–3), pp. 277–291. doi: 10.1016/S0011-9164(99)00148-4.

Fernández-Izquierdo, P. *et al.* (2012) 'Experimental analysis of a multi-effect distillation unit operated out of nominal conditions', *Desalination*. Elsevier B.V., 284, pp. 233–237. doi: 10.1016/j.desal.2011.09.004.

Fouda, A., Nada, S. A. and Elattar, H. F. (2016) 'An integrated A/C and HDH water desalination system assisted by solar energy: Transient analysis and economical study', *Applied Thermal Engineering*. Elsevier Ltd, 108, pp. 1320–1335. doi: 10.1016/j.applthermaleng.2016.08.026.

Hamed, O. A. *et al.* (2016) 'Concentrating solar power for seawater thermal desalination', *Desalination*. Elsevier B.V., 396, pp. 70–78. doi: 10.1016/j.desal.2016.06.008.

Horuz, I. (1998) 'a comparison between ammonia - water and water - lithium bromide solutions in vapor absorption refrigeration systems', *International Communications in Heat and Mass Transfer*, 25(5), pp. 711–721.

Ji, J. G. *et al.* (2007) 'Simulation and analysis of a single-effect thermal vapor-compression desalination system at variable operation conditions', *Chemical Engineering and Technology*, 30(12), pp. 1633–1641. doi: 10.1002/ceat.200700303.

- Kalogirou, S. (1997) 'Survey of solar desalination systems and system selection', *Energy*, 22(1), pp. 69–81. doi: 10.1016/S0360-5442(96)00100-4.
- Kamali, R. K. and Mohebinia, S. (2008) 'Experience of design and optimization of multi-effects desalination systems in Iran', *Desalination*, 222(1–3), pp. 639–645. doi: 10.1016/j.desal.2007.01.182.
- Kouhikamali, R. and Mehdizadeh, M. S. M. (2011) 'Process investigation of different locations of thermo-compressor suction in MED-TVC plants', *Desalination*. Elsevier B.V., 280(1–3), pp. 134–138. doi: 10.1016/j.desal.2011.06.070.
- Lee, S. F. and Sherif, S. A. (2001) 'Thermodynamic analysis of a lithium bromide/water absorption system for cooling and heating applications', *International Journal of Energy Research*, 25(11), pp. 1019–1031. doi: 10.1002/er.738.
- Nada, S. A., Elattar, H. F. and Fouda, A. (2015a) 'Experimental study for hybrid humidification-dehumidification water desalination and air conditioning system', *Desalination*, 363, pp. 112–125. doi: 10.1016/j.desal.2015.01.032.
- Nada, S. A., Elattar, H. F. and Fouda, A. (2015b) 'Performance analysis of proposed hybrid air conditioning and humidification-dehumidification systems for energy saving and water production in hot and dry climatic regions', *Energy Conversion and Management*. Elsevier Ltd, 96, pp. 208–227. doi: 10.1016/j.enconman.2015.02.082.
- Nafey, A. S., Fath, H. E. S. and Mabrouk, A. A. (2008) 'Thermoeconomic design of a multi-effect evaporation mechanical vapor compression (MEE-MVC) desalination process', *Desalination*, 230(1–3), pp. 1–15. doi: 10.1016/j.desal.2007.08.021.
- Palenzuela, P., Zaragoza, G. and Alarcón-Padilla, D. C. (2015) 'Characterisation of the coupling of multi-effect distillation plants to concentrating solar power plants', *Energy*, 82, pp. 986–995. doi: 10.1016/j.energy.2015.01.109.
- Sahoo, U. *et al.* (2015) 'Scope and sustainability of hybrid solar-biomass power plant with cooling, desalination in polygeneration process in India', *Renewable and Sustainable Energy Reviews*. Elsevier, 51(May), pp. 304–316. doi: 10.1016/j.rser.2015.06.004.
- Saldivia, D. *et al.* (2019) 'Computational analysis for a multi-effect distillation (MED) plant driven by solar energy in Chile', *Renewable Energy*. Elsevier Ltd, 132, pp. 206–220. doi: 10.1016/J.RENENE.2018.07.139.
- Sayyaadi, H. and Saffari, A. (2010) 'Thermoeconomic optimization of multi effect distillation desalination systems', *Applied Energy*. Elsevier Ltd, 87(4), pp. 1122–1133. doi: 10.1016/j.apenergy.2009.05.023.
- Shakib, S. E., Amidpour, M. and Aghanajafi, C. (2011) 'A new approach for process optimization of a METVC desalination system', *Desalination and Water Treatment*, (October), pp. 84–96. doi: 10.5004/dwt.2012.2509.
- Sharaf Eldean, M. a and Soliman, a M. (2015) 'Study of Using Solar Thermal Power for the Margarine Melting Heat Process.', *Journal of solar energy engineering*, 137(2), pp. 0210041–2100413. doi: 10.1115/1.4028367.
- Sharaf, M. A., Nafey, A. S. and García-Rodríguez, L. (2011a) 'Exergy and thermo-economic analyses of a combined solar organic cycle with multi effect distillation (MED) desalination process', *Desalination*. Elsevier B.V., 272(1–3), pp. 135–147. doi: 10.1016/j.desal.2011.01.006.
- Sharaf, M. A., Nafey, A. S. and García-Rodríguez, L. (2011b) 'Thermo-economic analysis of solar thermal power cycles assisted MED-VC (multi effect distillation-vapor compression) desalination processes', *Energy*. Elsevier Ltd, 36(5), pp. 2753–2764. doi: 10.1016/j.energy.2011.02.015.
- Sözen, A. (2001) 'Effect of heat exchangers on performance of absorption refrigeration systems', *Energy Conversion and Management*, 42(14), pp. 1699–1716. doi: 10.1016/S0196-8904(00)00151-5.
- Trostmann, A. (2009) 'Improved approach to steady state simulation of multi-effect distillation plants', *Desalination and Water Treatment*, 7(1–3), pp. 93–110. doi: 10.5004/dwt.2009.701.
- Wang, Y. and Lior, N. (2006) 'Performance analysis of combined humidified gas turbine power generation and multi-effect thermal vapor compression desalination systems - Part 1: The desalination unit and its combination with a steam-injected gas turbine power system', *Desalination*, 196(1–3), pp. 84–104. doi: 10.1016/j.desal.2006.01.010.

---

## #80: Optimisation of battery capacity in a DC-power supply system of an office building

---

Lige ZHAO<sup>1</sup>, Rui YAN<sup>2</sup>, Fulin WANG<sup>3</sup>, Hong Jie CHEN<sup>4</sup>, Bin HAO<sup>5</sup>, Yutong LI<sup>6</sup>, Wei FENG<sup>7</sup>

<sup>1</sup>Beijing Key Laboratory of Indoor Air Quality Evaluation and Control, Department of Building Science, School of Architecture, Tsinghua University, Beijing 100084, China, 709825022@qq.com

<sup>2</sup>Beijing Key Laboratory of Indoor Air Quality Evaluation and Control, Department of Building Science, School of Architecture, Tsinghua University, Beijing 100084, China, yanruiqq135@163.com

<sup>3</sup>Beijing Key Laboratory of Indoor Air Quality Evaluation and Control, Department of Building Science, School of Architecture, Tsinghua University, Beijing 100084, China, flwang@tsinghua.edu.cn

<sup>4</sup>Beijing Key Laboratory of Indoor Air Quality Evaluation and Control, Department of Building Science, School of Architecture, Tsinghua University, Beijing 100084, China, sti70409@gmail.com

<sup>5</sup>Shenzhen Institute of Building Research, Shenzhen 518049, haobin@ibrcn.com China,

<sup>6</sup>Shenzhen Institute of Building Research, Shenzhen 518049, China, liyutong@ibrcn.com

<sup>7</sup>Lawrence Berkeley National Laboratory, Berkeley, CA, U.S.A, weifeng@lbl.gov

*Electricity is the most important power supply in urban areas but the huge difference between peak and trough demands still remain a serious problem which has led to a conspicuous decline of efficiency in electricity use and a waste of renewable energy such as wind power and solar power. Recently the development of DC-power supply systems and distributed storage provides a new solution for peak-load shifting and with a better capacity of renewable power uptake. In this paper, a DC-building in the low-carbon city of Shenzhen is used as a case-study and the battery capacity has been calculated and optimised with the simulation. The main conclusions are that the battery capacity determined by discarding a little part of solar power can be reduced by a significant degree and the distributed battery deployment by floor prevails over the centralised battery deployment.*

*Keywords: DC-power in buildings; distributed storage; peak-load shifting; renewable energy; battery capacity*

## 1. INTRODUCTION

With the enhancement of the economy and the rapid increase of urbanisation in China, electricity is the most important and main power in urban areas. Research shows that the proportion of electricity consumption to other energy types in Beijing is increasing annually and in 2012, it had risen to 38% (Wang, 2016). The proportion of civil buildings in cities is also rising, the electricity consumption of which utilises up to 40% of city electricity consumption (Beijing, 2018). The power load characteristic of civil buildings leads to huge differences in peaks and troughs. In some months, the peak electricity consumption could be four times that of the trough (Zhou, 2015), and this typical phenomenon has now been a widespread problem in big cities. This leads to a decline of efficiency in electricity use and a huge waste of renewable energy; sometimes the power grid has to discard part of the wind power or photovoltaic power (Shu, 2017). These issues will be a severe obstacle to the optimisation of China's energy structure and the economy.

Recently, however, the well developed technology of DC-power supply has provided a new method for dealing with this new phenomenon. To date, almost all electronic components are DC-power driven and in buildings, lighting, heating, ventilation and air-conditioning can all be powered by DC (Boeke, 2014). The burgeoning market of electric cars requires DC-power supply, too. In other words, nowadays the use of DC-power is more and more widespread, and renewable energy such as photovoltaic power generation and wind power are both DC power, so the adoption of DC power can reduce the conversion loss of renewable energy to a large extent (Frauhofer, 2013). However, there are still a number of problems which are all cannot be found in DC-power system, such as high transmission loss, harmonic pollution, voltage fluctuation and electromagnetic radiation pollution. DC systems, compared to the AC system, shows better reliability and safety (Xie, 2016, Deng, 2016). An American research institution, Navigant Research, forecasts that the global DC building market will reach \$9.7 billion by 2020, a 15-fold increase (Deng, 2016).

In view of various drivers described above, many successful studies of building DC-power distribution have been carried out around the world, and nearly all of them received remarkable results (Wu, 2014, Geary, 2012, Bjelovuk, 2010, Arghandeh, 2014, Wunder, 2014). Those experiments have shown the great advantages of building DC-power and distributed storage. The authors put forward the combination of all DC-power system in buildings and distributed electricity storage and carried out benefit analysis of this system (Wang, 2016). This scheme can play a good role in peak-load shifting of cities' power grids, saving 100 billion kWh of electricity every year, which is 2.0% of the total annual electricity consumption in China, and promoting the huge market of low-voltage electrical appliances, building micro-grid, battery and other industries. Based on this, some innovative buildings are attempting to use DC power. This paper studies such a DC building that will be built in Shenzhen low carbon city, compares the battery capacity in different types of power use mode, and puts forward the preliminary feasible scheme.

## 2. METHODOLOGY

The charge and discharge of the battery is to balance the mismatch between the power supply on the source side (the power grid or photovoltaic power generation) and the power consumption on the load side. The period of a charge and discharge cycle of the battery is 24 hours so as to achieve peak-load shift. The capacity of the battery is determined according to this cycle. For the purpose of peak-load shift, power from the grid can be constant, or demand-response mode, or the economic optimal power determined by time-of-use tariff (Li and Wang, 2017). This paper mainly focuses on constant power mode. The calculation is shown in the following steps.

Net building Load:

Equation 15: Net building Load.

$$P(t) = P_{load}(t) - P_{gen}(t)$$

Where:

- $P_{load}(t)$  = Power consumption load at time t, kW
- $P_{gen}(t)$  = Local power generation rate at time t, kW

Equation 16: Constant power taking from grid.

$$P_{set} = \alpha \frac{\int_0^T P(t) dt}{T}$$

Where:

- $P_{set}$  = Daily constant power taking, kW (when daily power generation is more than load,  $P_{set} = 0$ )
- $\alpha$  = coefficient in consideration of transmission loss

Daily required battery capacity:

For the purpose of balancing the mismatch between the power supplying side and the load side, the charging power or discharging power has to meet the following conditions: when  $P(t) > P_{set}$ , battery is discharged with the power of  $P(t) - P_{set}$ ; when  $P(t) < P_{set}$ , battery is charged with the power of  $P_{set} - P(t)$ . Supposing that the initial capacity is  $SOC_0$ , the battery's state of charge(SOC) at time  $t$  is:

Equation 3: State of charge. 
$$SOC(t) = SOC_0 + \eta \int_0^t [P_{set}(\xi) - P_\xi] d\xi$$

Where:

- $SOC(t)$  = State of charge at time  $t$ , kWh
- $SOC_0$  = Initial capacity, kWh
- $\eta$  = Coefficient in consideration of charging loss, normally less than 1

So the battery capacity is the difference value between the maximum of SOC and the minimum of SOC in 24 hours:

Equation 4: Daily battery capacity. 
$$Q(d) = maxSOC(t) - minSOC(t)$$

Where:

- $Q(d)$  = Battery capacity on date  $d$ , kWh
- $maxSOC(t)$  = The maximum of SOC in one day, kWh
- $minSOC(t)$  = The minimum of SOC in one day, kWh

The daily battery capacity can be determined by the formulas above, so according to the load and photovoltaic power generation over 365 days, the annual charging power can be calculated, and thus the daily battery capacity requirements can be calculated.

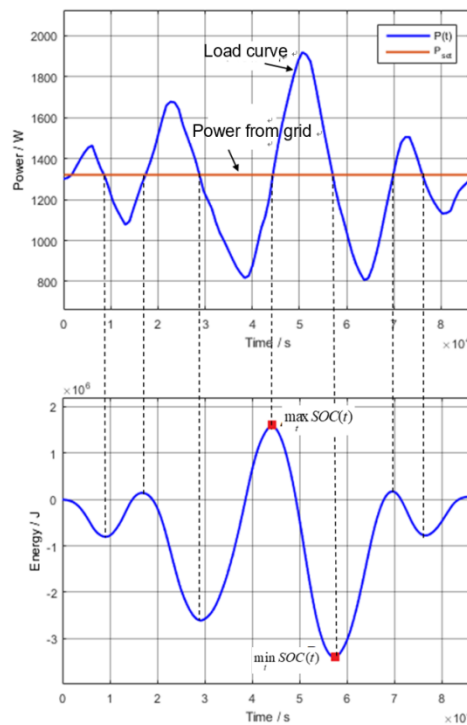


Figure 1: calculation of battery capacity

### 3. CASE STUDY

#### 3.1. Project introduction

The building is located in the core area of Shenzhen international low-carbon city. This project covers an area of 11037.76m<sup>2</sup>, with a total floor area of 62874.09m<sup>2</sup>. The main functions of the building include research, office, experiment, exhibition, education, residence, and cultural exchange. This project mainly aims at exploring the low-carbon living and working mode in the future, and solving the problem of the demonstration and promotion of net zero-energy building technology in hot summer and warm winter areas in China which can then be applied to similar climate areas around the world. The project not only makes technological innovation and breakthroughs in carbon emission control, environmental quality improvement, building industrialisation, and other aspects, but also serves as a model for green and low-carbon lifestyle construction, green community system exploration, and intelligent construction and operation.

The whole building is built in a modular design, separated into 4 parts: R1, R2, R3, and B. Part R is used for all kinds of laboratories, including zero carbon building R3, which has 6 floors and a total floor area of 4374m<sup>2</sup>. R3 is fully supported by DC-power supply, and powered by photovoltaic panels on the roof of R1 and R2, when lacking photovoltaic power generation, it also requires electricity from the power grid.



Figure 2: Case study building at Shenzhen Low-carbon center

#### 3.2. Building energy consumption simulation

The R3 building is simulated by DeST software designed by Building Energy-Saving Research Center in Tsinghua University. The building is cooled and heated by DC-driven variable frequency multi-split air-conditioning system, and the schedule of the air conditioning system is determined by the schedule of the staff and equipment in the office, which can be divided into two types: workdays and weekends. The equipment power intensity in the room is 15W/m<sup>2</sup>, and LED light power intensity is 6W/m<sup>2</sup>.

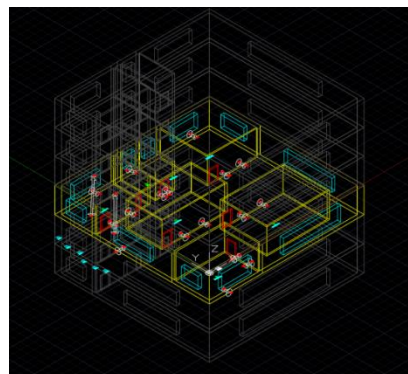


Figure 3: Simulation model of R3 building

### 3.3. Simulation of photovoltaic generation

The hourly PV power is calculated by hourly amount of solar radiation. The areas of the PV panels are  $S_1=370m^2$ ,  $S_2=800m^2$ :

Equation 5: PV power generation.

$$Q = (S_1 + S_2)\eta_1\eta_2I$$

Where:

- $Q$  = Hourly PV generation, kW
- $\eta_1$  = Incident photon-to-electron conversion efficiency, in this paper 14% is used
- $\eta_2$  = PV panels output efficiency, here 90% is used
- $I$  = Normal intensity of solar radiation,  $W/m^2$

### 3.4. Simulation results

Simulation results of building energy consumption

Table 1: R3 module energy consumption

	Total	HVAC	Lighting	Equipment
Building energy consumption $\times 10^4$ (kWh)	24.75	11.73	3.39	9.55
Energy consumption per unit area(kWh/m <sup>2</sup> )	56.58	26.83	7.76	21.83

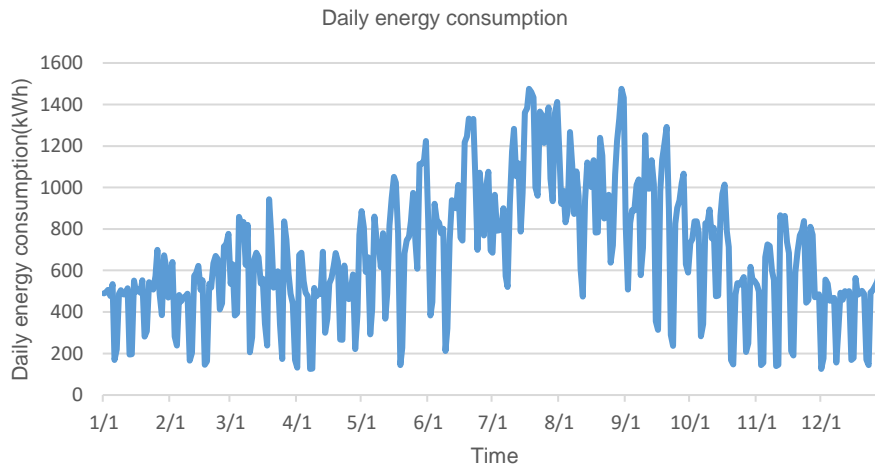


Figure 4: R3 building daily energy consumption

Simulation results of PV generation

The annual total photovoltaic power generation is 197,300 kWh, and the hourly power generation is shown in Figure 5:

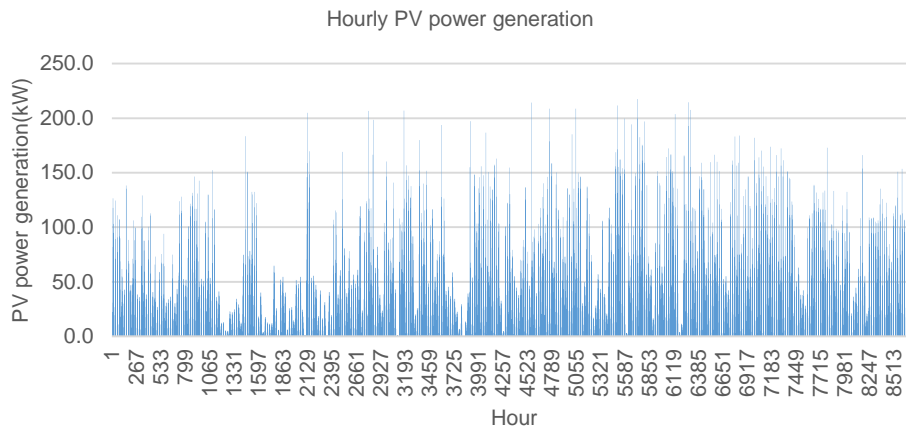


Figure 5: Hourly PV power generation

### Battery capacity

The maximum battery capacity is calculated to be 855.9kWh, and the annual average is 232.9kWh. The daily battery capacity fluctuates greatly. If the battery capacity meets the maximum power demand, it will cause a huge initial cost. The maximum capacity is shown in Table 2 when the unmet day is 0, 5, 10, 20 and 30.

Table 2: Battery capacity

Unmet days	0	5	10	20	30
Battery capacity (kWh)	855.9	671.6	591.6	514.1	406.9

Figure 6 shows a selected day when the calculated battery capacity is the maximum. It is conspicuous that the causes of excessive battery capacity is the large amount of PV power generation, far more than building energy consumption, thus leading to the accumulation of unnecessary battery power causing the waste of battery capacity. In order to solve this problem, we can adopt the strategy of returning power to the power grid or discarding PV power appropriately to reduce the battery capacity, preventing the waste of investment and reduce the maintenance cost of equipment.

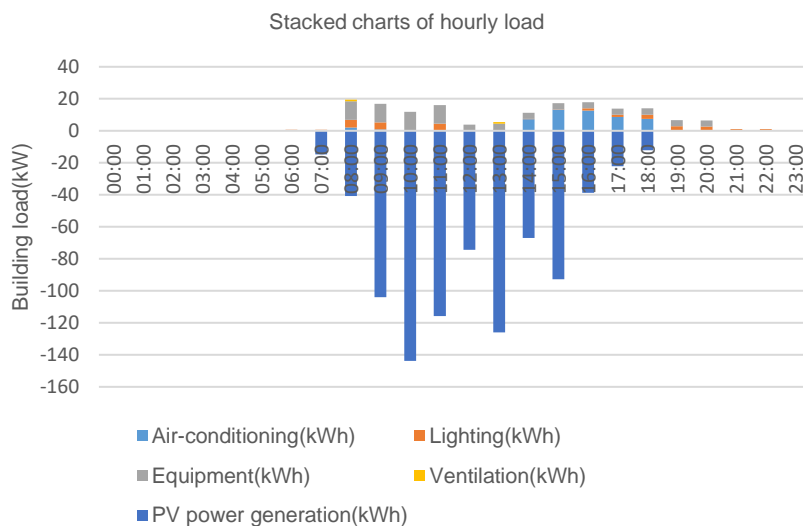


Figure 6: Building load the PV power generation on maximum battery capacity day

### 3.5. Regurgitation strategy

In order to verify the feasibility of the strategy above, the daily required battery capacity is also calculated. In this strategy, when the daily PV power generation is larger than the total building load of the day, the power taken from



the grid becomes negative, and the excess PV power generation is sent back to the grid, which can not only have a better uptake of the excess renewable power, but also supplement the power of the grid. The calculation results are shown in Figure 7. It can be intuitively seen that there is a significant decrease of peak value of battery capacity, the maximum required battery capacity is 526.5kwh, and the average value is 206.3kwh. The maximum capacity corresponding to the unmet days is given in Table 3.

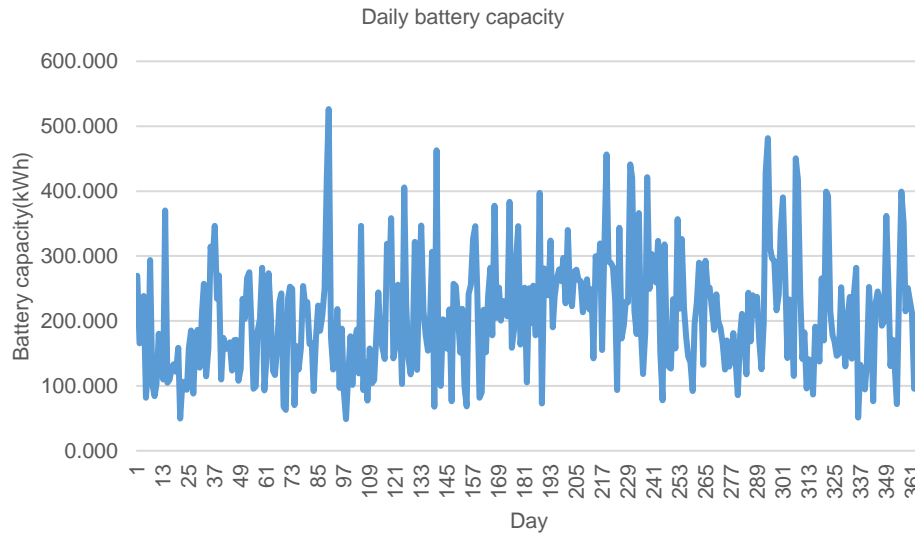


Figure 7: Daily battery capacity when adopting regurgitation strategy

Table 3: Battery capacity

Unmet days	0	5	10	20	30
Battery capacity(kWh)	526.5	441.1	416.9	366.1	343.7

### 3.6. Discarding PV power appropriately

On the infrequent days when photovoltaic power generation is too large, we can try to properly discard PV power. When the PV power generation is more than the total load of the building on a certain day, the charging power of the battery will be reduced to balance the charging and discharging amount on that day. Calculation results as shown in Figure 8, the battery capacity is 456.6 kWh, with an average of 163.2 kWh. Compared with two solutions stated before, it demonstrates the obvious superiority. On the other hand, the annual amount of PV power discarded is 20,000 kWh, only accounting for 10% of the total amount, which is relatively small, and if considering the decrease of initial investment, it will be the best strategy undoubtedly. The maximum capacity is shown in Table 4.

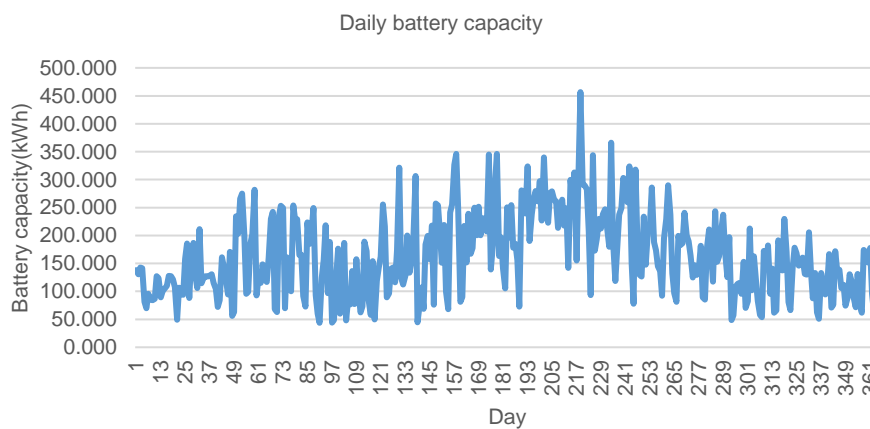


Figure 8: Daily battery capacity when discarding PV power properly

Table 4: Battery capacity

Unmet days	0	5	10	20	30
Battery capacity(kWh)	456.6	343.7	321.7	289.8	275.2

### 3.7. Comparison of three different strategy

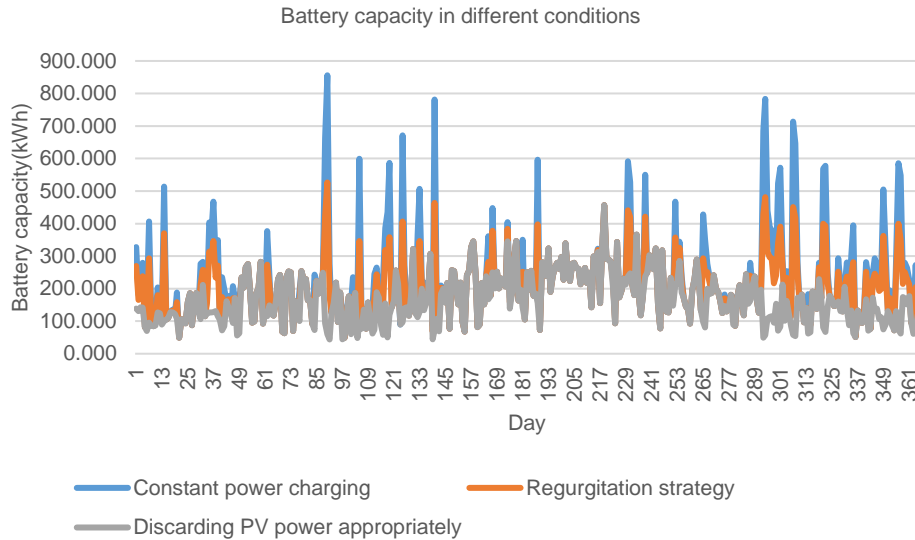


Figure 9: Battery capacity in three different strategy

Table 5: Comparison of battery capacities

	Capacity(kWh)		Capacity of different unmet days				
	Max	Min	0	5	10	20	30
Constant power charging(kWh)	855.8	232.9	855.9	671.6	591.6	514.1	406.9
Regurgitation strategy(kWh)	526.5	206.3	526.5	441.1	416.9	366.1	343.7
Discarding PV power appropriately(kWh)	456.6	163.2	456.6	343.7	321.7	289.8	275.2

We can easily draw conclusions from Figure 10 that in the second and the third strategy, battery capacities are much smaller than the initial one, both maximum and average capacities. When taking operability and initial cost into account, the third strategy is better than the first two strategies. Consequently, selection of battery capacity is paramount, achieving maximisation of economic benefits, reducing investment and maintenance costs, and saving resources.

### 3.8. Analysis of distributed storage

In the simulation and calculation above, we mainly talk about using only one battery in the whole building, which has its problems. The capacity of the battery is still large and, because the whole building is powered by just one battery, the system has poor flexibility. When a certain floor is out of service or a fault occurs, the system will be difficult to coordinate. In order to better realise the idea of distributed power storage, the battery can be distributed in each floor, each storage battery is responsible for the load of that floor, reducing the capacity and volume of the required storage battery. It is also more convenient for separate maintenance, at the same time enhancing the flexibility of the system, and better combined with the smart micro grid. The battery capacity of each floor of the building is shown in Table 6:

Table 6: Battery capacity by floor

Unmet days	0	5	10	20	30
F1	77.8	67.1	56.4	52.2	50.2
F2	81.3	61.9	57.8	53.5	51.1
F3	91.5	75.8	70.5	56.0	51.4
F4	81.1	62.1	58.3	53.3	51.4
F5	79.0	62.6	58.1	53.2	51.4
F6	80.4	64.1	59.3	54.5	51.3

It can be seen from Table 6 that the battery capacity of each floor can be controlled at a lower value by adopting the layered scheme. The comparison between this scheme and the scheme adopting one battery in the whole building is shown in the following table:

Table 7: Comparison of two schemes

Unmet days	0	5	10	20	30
The centralised one battery	456.6	343.7	321.7	289.8	275.2
Sum of 6 floors distributed batteries	491.1	393.6	360.4	322.7	306.8

Table 7 shows that in the scheme of layered storage battery, the sum of battery capacity is slightly larger than the previous plan, but considering the cost, the battery efficiency, volume, safety, reliability, charge and discharge and any other factors, we should choose the strategy of distributed energy storage. In doing so, charging and discharging system can be better controlled and managed, to realise the maximisation of economic benefit.

#### 4. CONCLUSION

This paper analysed the necessity and feasibility of building DC-power supply and distributed power storage by analysing the huge problems existing in the utilisation of electric energy in China. A case study building, which is the Low-carbon demonstration building in Shenzhen, China, was studied to determine the optimal battery capacity given different charging strategies. The conclusion was that the strategy of appropriately discarding PV power can reduce the required battery capacity, thus reducing the initial investment cost of batteries. Furthermore, two different energy storage schemes, i.e. centralised storage and distributed storage by floors, are compared. The scheme of distributed battery at each floor is superior because it can improve the flexibility and security of the system at a small increment of battery capacity and better match the concept of distributed energy storage.

#### 5. ACKNOWLEDGEMENT

This research is supported by National Key R&D Program of China, Research and Demonstration of Key Technology of Net-Zero Energy Building (Project Number 2016YFE0102300) and Innovative Research Groups of the National Natural Science Foundation of China (Grant number 51521005).

#### 6. REFERENCES

- Arghandeh, R., Woyak, J., Onen, A., Jung, J., Broadwater, R.P., 2014. Economic optimal operation of Community Energy Storage systems in competitive energy markets. *Applied Energy*, 2014, 135.
- Beijing Municipal Bureau of Statistics, 2018. Beijing Statistics Book 2017. China Statistics Press, 135. (In Chinese)
- Bjelovuk, G., 2010. American Electric Power's Utility-Scale Energy Storage. *Energy Storage and Renewables NARUC*. July 2010.
- Boeke, U., Ott, L., 2014. White Paper. Impact of a  $\pm 380V$  DC Power Grid Infrastructure on Commercial Building Energy Profiles.
- Deng, Y.N., 2016. Study and analysis of DC power supply system in intelligent buildings. *Advanced Technology*, 2016, No.02. (In Chinese)
- Frahofer, I. I. S. B., 2013. JTI-CP-ENIAC-2011-1 DCC+G.

Geary, D.E., 2012. Phasing out AC – Directly. 2012 IEEE Energytech, Cleveland, OH, 2012, 1-6.

Li A., Wang F. L., 2017. Optimal Design for the Battery Capacity of DC power Supply and Electricity Storage System in Buildings [J]. *Building Electricity*, 2017, 36(04):12-17. (In Chinese)

Shu, Y.B., Zhang, Z.G., Guo, J.B., 2017. Study of key factors of new energy consumption and study of solutions. *Proceedings of the CSEE*, 2017, 37(1): 1-8. (In Chinese)

Wang, F.L., Jiang, Y., 2016. Analysis of Key Technology and Benefits of DC power and Distributed Storage in Buildings. *Building Electricity*, 2016, 35(04):16-20. (In Chinese)

Wu, K., Li, H., 2014. Application of DC power in intelligent buildings. *Modern Building Electricity*, 2014, 5(06):13-17. (In Chinese)

Wunder, B., Ott, L., Szpek, M., Boeke, U., Weiß, R. 2014. Energy Efficient DC-Grids for Commercial Buildings. *2014 IEEE 36th International Telecommunications Energy Conference (INTELEC)*, Vancouver, BC, 2014, pp. 1-8.

Xie, Q.D., Qiu, X.Y., Ren, L., Liu, B., 2016. Capacity configuration module of hybrid energy storage system considering DC power distribution efficiency. *Electric Power Construction*, Vol.37, No.5. (In Chinese)

Zhou, E.Y., 2015. Study on urban residents' electricity model. Beijing: Tsinghua University bachelor thesis (In Chinese)

---

## #81: Spectral characteristics of nanometric absorber: a simple strategy to develop silicon nanostructures for efficient solar energy harvesting

---

Mohammad Kamal HOSSAIN<sup>1,2</sup>, Billel SALHI<sup>1</sup>, Ayman Wajeh MUKHAIMER<sup>3</sup>

<sup>1</sup> Center of Research Excellence in Renewable Energy (CoRERE), King Fahd University of Petroleum and Minerals (KFUPM), Dhahran 31261, Dhahran, Kingdom of Saudi Arabia, kamalhossain@kfupm.edu.sa

<sup>2</sup> Researcher at K.A.CARE Energy Research & Innovation Center at Dhahran, Dhahran, Kingdom of Saudi Arabia

<sup>3</sup> School of Engineering, RMIT University, GPO Box 2476, Melbourne VIC 3001, Australia

*Solar cells utilise a small portion of the solar spectrum depending on the technology used while solar radiation, being full of UV-VIS-IR wavelengths, does not leave absorbing and other layers unaffected. Only the photon energy that matches the absorbing layer contributes to effective power generation of solar cells. Higher and lower energy wavelengths induce thermalisation and absorption losses, which in turn introduce several consequences including heating and degradation in the cell level. Therefore, wavelength-sensitive engineered absorbing layers such as nanometric absorber-based solar cells hold huge potential. In this work, we have investigated and simulated four deterministic characteristics, viz. absorption depth profile; electromagnetic field; Poynting vector and exciton generation rate distribution at different incidents for silicon nanowire (Si-NW) systems. Flat silicon and Si-NW were considered as examples along with a comparative outlook. Such predictive studies facilitate the choice of technology and how to improve the cell efficiency using light-trapping techniques. Preliminary work has shown a simple strategy to achieve nanometric absorption using recent inventions granted to the Center of Research Excellence in Renewable Energy (CoRERE) at King Fahd University of Petroleum and Minerals (KFUPM). As-grown Si-NWs with coverage, ca.  $6.5 \times 10^9/\text{cm}^2$  were further characterised through scanning electron microscope. Such correlated demonstration as investigated in this work will open new avenues and possibilities to improve current nanowires-based optoelectronic devices, particularly thin film solar cells.*

*Keywords: optical characteristics; silicon nanowire; FDTD simulation; optical confinement; solar energy harvesting*

## 1. INTRODUCTION

Global energy demand has been projected to double by 2050. At present, nearly 80% of energy supply depends on fossil fuel, however depleting reserves will run out in 50-100 years. To mitigate this, solar energy, an eco-friendly, inexhaustible and cost-effective energy resource, can play a crucial role. The solar cell, a simple optoelectronic device, directly converts solar radiation into electricity using the photovoltaic effect (Saga 2010; Hoffmann 2006; Zeng 2019; Battersby 2019; Höger 2018). However, commercial and domestic adoption of photovoltaic has been a serious concern due to higher cost and lower efficiency. Silicon (Si) is very well studied and unprecedented material in the microelectronics era including solar energy harvesting using photovoltaic (PV) technologies. It has superior advantages such as stability, non-toxicity, low cost, abundance, etc. Conventional Si-based PV solar cells are not very efficient because of relatively low light absorption. Nanometric features add unique flavour and therefore Si nanowires (Si-NWs) have emerged as an extremely attractive candidate (Polman 2012; Yu 2014; Kelzenberg 2010; Boettcher 2010; Garnett 2010). Si-NWs show strong optical absorption compared to that of conventional planar PV solar cell. Apart from absorption, it has been reported that radial p-n junctions Si-NW solar cell provides short collection length for charge carriers, thus allowing the use of lower-quality Si materials and a way to reduce production cost substantially.

Although silicon (Si)-based solar cell is dominating current solar cell market the Shockley and Queisser efficiency limit (i.e. ~31% for Si) has become a great challenge. It implies that a small portion of solar spectrum contributes to electricity generation leaving huge amount of photon energy unused. Higher and lower energy photons induce thermalisation and absorption losses that comprises of nearly 50%. Such energy adds up several problems including heating and degradation in the cell level. Si-NWs, because of its nanometric features possesses great potential improve this efficiency constrain (Polman 2012; Kelzenberg 2010). Apart from strong optical absorption, Si-NWs bears other electrical characteristics that lead to reduced production cost. The contribution and vital role played by such Si-NWs can be further understood through predictive analysis of inherent optical characteristics such as absorption depth profile, electromagnetic field distribution, Poynting vector and exciton generation rate distribution. Absorption profile, energy flow, EM field distribution and exciton generation rate at 740 nm (1.8 eV for Si) in addition to spectral analysis of absorption depth profile for Si-NW system has been demonstrated previously (Li 2015; Krogstrup 2013; Salhi 2016; Hossain 2017; Hossain 2016). However further correlated spectral analysis amongst absorption depth profile, energy flow, electric field localisation and exciton generation rate distributions is indispensable

Here in this work, vertically aligned Si-NWs have been fabricated using metal nanoparticles catalysed chemical vapour deposition (CVD) technique. Optical and electrical characterisations have been carried out to understand the inherent properties of the as-fabricated Si-NWs. High-resolution scanning electron microscope (SEM) revealed the diameter of the as-grown Si-NWs to be in the range of 50 to 200 nm. Based on the experimental observations, a detailed simulation has been carried out to understand the mechanism how Si-NWs interact with solar spectral wavelengths and contribute to exciton generation rate distribution. Further detailed cross-sectional analyses as well as spectral generation rate distributions for different sizes of the Si-NW have been investigated. Such insights are not only indispensable to understand the mechanism behind but they also open out new possibilities in various applications.

## 2. MATERIALS AND METHOD

N-type Silicon wafer (resistivity  $<1\Omega\text{cm}$ ) was used to grow Si-NWs. The wafer was well-cleansed following standard procedure (i.e. 3:1 of concentrated  $\text{H}_2\text{SO}_4$  and 30%  $\text{H}_2\text{O}_2$  for 15 min at  $80^\circ\text{C}$ ) and was transferred to a sputtering chamber for metal layer deposition. Random sizes of the metal nanoparticles were achieved after annealing at different temperature (e.g.  $200^\circ\text{C}$ ,  $400^\circ\text{C}$  and  $600^\circ\text{C}$  for 3 hrs). Subsequently the specimen was transferred PECVD chamber to grow Si-NWs. A free-hand schematic has been shown in Figure 1 (a) illustrating the detailed steps and mechanism behind to achieve appropriate size and shape of metal nanoparticles as catalyst. If the initial metal nanoparticles are spherical, the as-grown nanowires will be cylindrical in shape. Therefore, it is important to fine-tune, optimise, and characterise before proceeding to nanowire growth. Insets (i)-(iv) represent specific steps involved in metal nanoparticles and nanowires growth, As-fabricated Si-NWs were characterised by SEM and high-resolution SEM. Optical and electrical characterisations have been carried out to understand the suitability of such Si-NWs in solar cell fabrications. Excitation generation rate distributions were extracted for different size of the Si-NWs at different spectral wavelengths using finite-difference time-domain analysis. A very similar model of Si-NW on c-Si wafer as was observed in this experiment was utilised in this simulation. Additional features such as absorption profile, energy transfer, and electromagnetic field distribution were carried out in the same simulation. As shown in Figure 1(b), a model of Si-NW on c-Si wafer was modelled in FDTD package of Lumerical Solution (ver 8.6). The geometry of the model was kept as close to those of as-grown Si-NWs as possible. Insets (i)-(iii) represent model dimensions, a bird's-eye view including source and monitor and spatial position of the monitors to extract optical characteristics. In this current work, we have focused on exciton generation rate distribution.

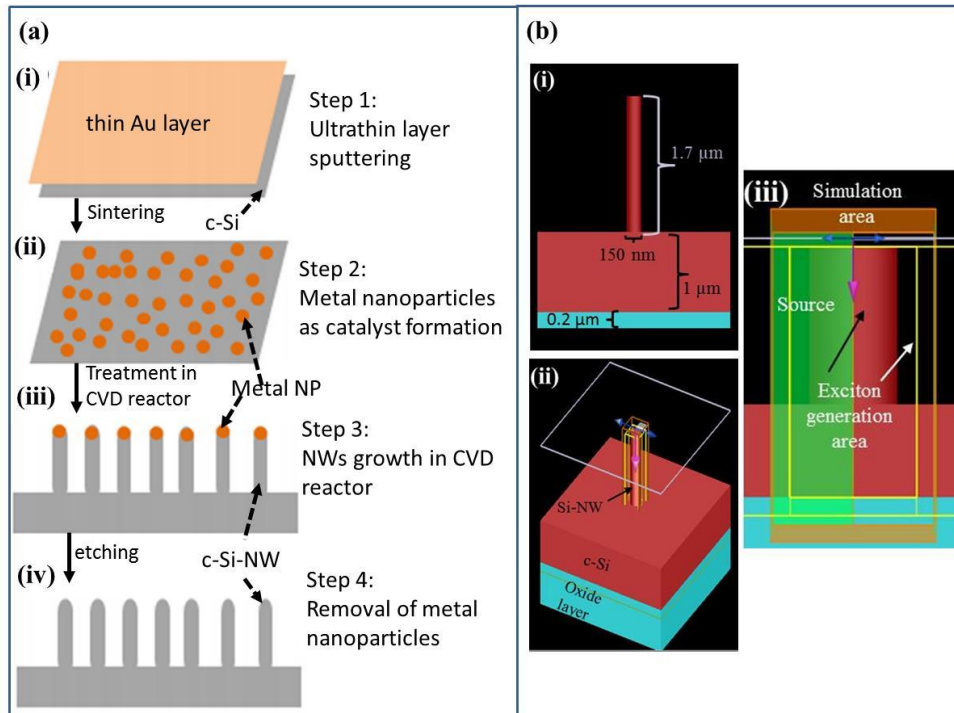


Figure 1: (a) Free-hand schematics illustrating the mechanism of Si-NWs growth; inset (i)-(iv) represent subsequent steps involved and (b) a typical model of Si-NW on c-Si wafer to extract optical characteristics particularly exciton generation rate distribution for different sizes of Si-NWs system at different solar spectral wavelengths.

### 3. RESULTS AND DISCUSSION

In metal nanoparticles directed nanowire growth, the dimensions, particularly size and shape, of nanoparticles play crucial role to determine the topography of the nanowires. Therefore, it is important to investigate the as-grown nanoparticles in full-fledge before proceeding to nanowire analysis. Figure 2 shows detailed topographic observations of as-grown metal nanoparticles of different size obtained in different treatments. Figure 2(a) represents metal nanoparticles of smaller sizes, whereas Figures 2(b) and (c) confirmed the size of nanoparticles in intermediate and bigger ones. Further lookout revealed that smaller nanoparticles are mostly in spherical sizes with diameter of 40-60 nm and lower inter-particle gaps as shown in inset of Figure 2(a). In such as coverage density of the metal nanoparticles was found to be higher. If these nanoparticles are used to grow Si-NWs, then density and diameter of the as-grown nanowires are expected to be higher and smaller respectively. Inset of Fig 2(a) represents the magnified view of the same as marked by dashed white square therein. A bit bigger, 90-110 nm and higher inter-particle gaps were observed as shown in inset of Figure 2(b). In such case coverage density of the metal nanoparticles was found to be lower. Si-NWs grown using these nanoparticles are expected to be bigger in diameter and smaller in coverage density. Inset of Fig 2(a) represents the magnified view of the same as marked by dashed white square therein. Further treatment revealed metal nanoparticles of 240-260 nm in diameter as shown in Figure 2(c). Inset of Figure 2(a) represents the magnified view of the same as marked by dashed white square therein.

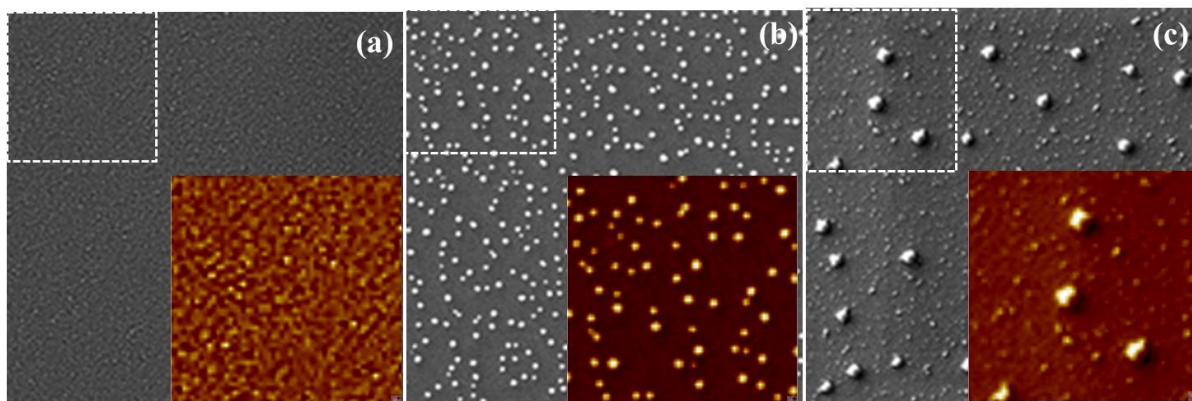


Figure 2: (a)-(c) SEM micrographs of metal nanoparticles growth in three different sizes starting from smaller to bigger ones respectively. Individual inset represents magnified view of the dashed squares shown therein.

Figure 3 shows SEM micrographs confirming the growth of vertical Si-NWs. As-grown Si-NWs were found to be in different diameters, positions and lengths. Diameter and position of Si-NWs are supposed to follow the diameter and position of initial catalyst, metal nanoparticles whereas length of the nanowires depends more in the interaction between precursor and metal nanoparticle itself. A high resolution FE-SEM image confirmed further that different dimension of nanowires possessed different sized of metal nanoparticles at the top as shown in inset (i) of Figure 3. Four typical metal nanoparticles are marked by white arrows for convenience. It is noteworthy that these particular four nanowires were clear evidence of Si-NWs of different diameters which were achieved by four different sizes of metal nanoparticles directed growth. Further to confirm the diameter of Si-NWs, a line profile along the line shown in inset (i) were extracted and shown in inset (ii). Corresponding nanowires were marked by 1, 2, 3 and 4 in inset (i) and inset (ii).

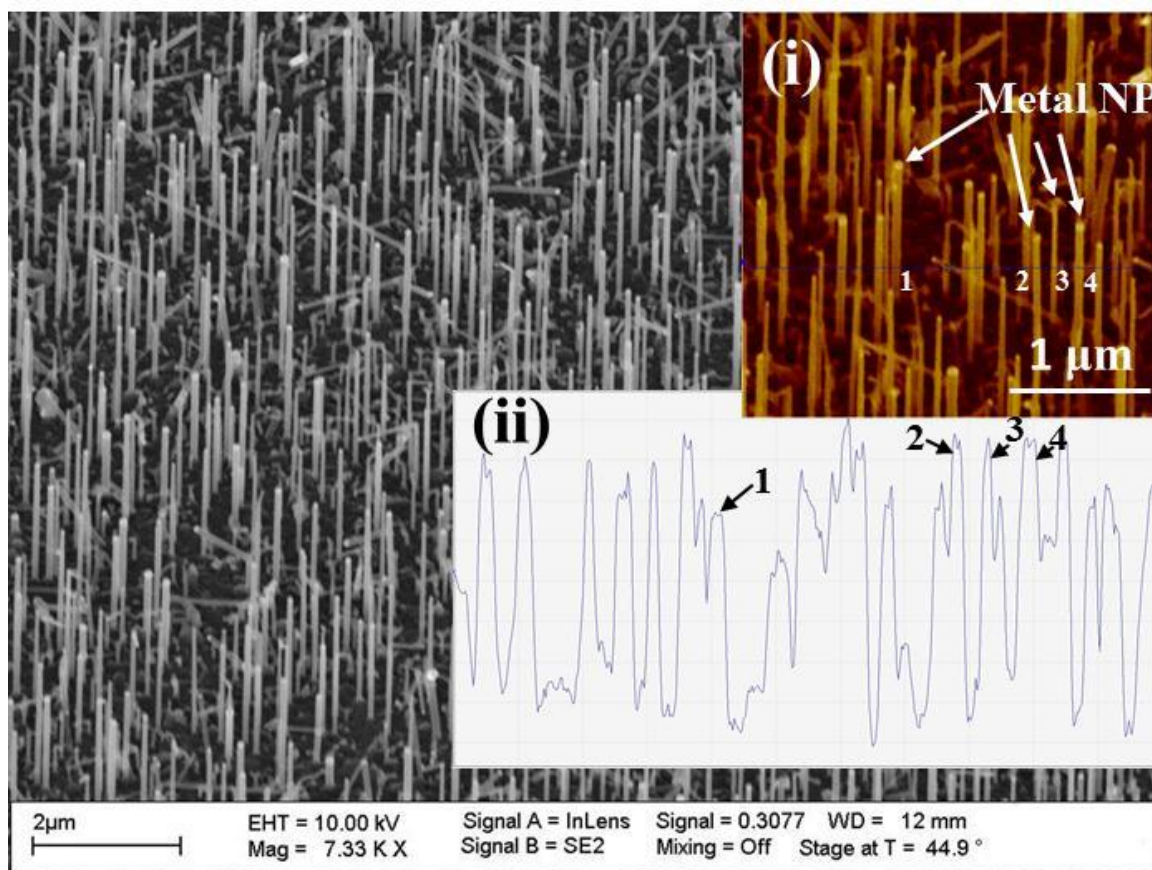


Figure 3: SEM micrograph confirming the growth of metal nanoparticles directed Si-NWs; inset (i): Magnified view of the dotted rectangle marked therein showing presence of metal nanoparticles at the top and inset (ii): Line profile along the line showed in inset (i) confirming four typical Si-NWs of different diameters.

Efficiency and heat build-up issue of solar cell is related to the photon absorption profile of the absorbing layer. In case of nanowire based solar cell, photon absorption can be confined and enhanced depending on solar spectrum and thus increase the light trapping in solar cell. As mentioned earlier, solar cell utilises a small portion of solar spectrum depending on the technology while absorbing layer and other layers including contact and encapsulation layer get affected with other unexpected solar wavelengths. Only the photon energy that matches with absorbing layer contributes to effective power generation of solar cell. Higher and lower energy wavelengths induce thermalisation and absorption losses which in turn introduce several consequences including heating and degradation in the cell level. Therefore, to reduce cost and increase efficiency, it is indispensable to understand the inherent behaviour of nanometric system in different solar spectrum. There are lot of studies so far reported and on-going that reflect the need of deep understanding particularly about nanometric features so that innovative and cost-effective route can be brought out in light to design efficient solar cell (Peng 2008; Peng 2010; Tang 2011; Tsakalakos 2007; Liu 2018; Maryasin 2018). Absorption profile, EM field distribution, Poynting energy and excitation generation rate distribution are inter-related and deterministic factors. Amongst the abovementioned characteristics, exciton generation rate distribution is the most important factor that determines the internal power conversion efficiency of the solar cell. Although all the properties were investigate in full including cross-sectional analysis at different solar spectrum starting from UV to visible to NIR, here in this communication the behaviour of such exciton generation rate distribution for different sizes of the nanometric system at two particular solar spectrums of interest are elucidated. Further details are expected to be in regular journal submission. Figures 4 (a)-(c) show exciton generation rate distributions of vertically aligned Si-NW of 50, 100, and 150 nm diameters



respectively at 700 nm solar spectral wavelength that coincides at the absorption band gap of n-type Si wafer (ca. 1.8 eV). At 700 nm wavelength of solar spectrum, 150 nm diameter of Si-NW was found suitable to hold higher exciton generation rate distribution. On the other side, Figures 1 (d)-(f) show exciton generation rate distributions of vertically aligned Si-NW of 50, 100, and 150 nm diameters respectively at 1100 nm solar spectral wavelength. It was observed that at 1100 nm wavelength of solar spectrum, 100 nm diameter of Si-NW was found suitable to hold higher exciton generation rate distribution. Such a correlated investigation amongst absorption profile, EM field distribution, Poynting energy and excitation generation rate distribution support to understand efficient nanometric system to increase photon trapping within the absorbing layer.

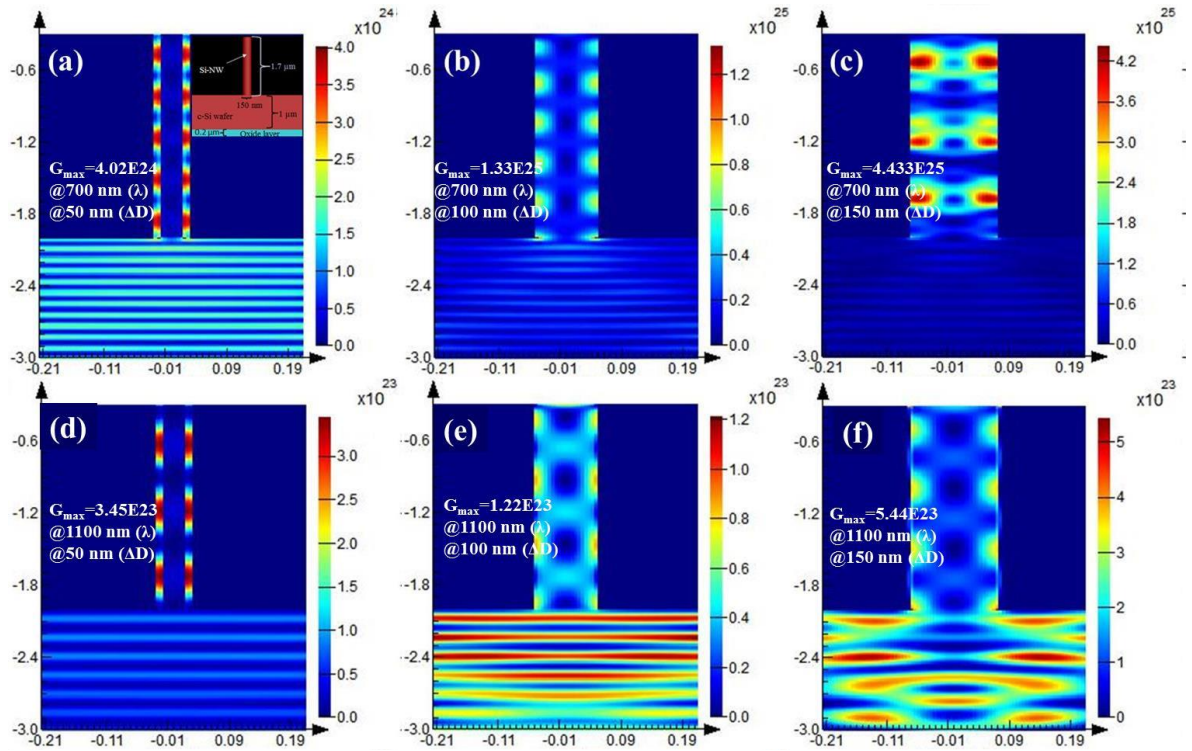


Figure 4: (a)-(c) Exciton generation rate distributions of vertically aligned Si-NW of 50, 100 and 150 nm diameters respectively at 700 nm solar spectral wavelength and (d)-(f) Exciton generation rate distributions of vertically aligned Si-NW of 50, 100 and 150 nm diameters respectively at 1100 nm solar spectral wavelength

#### 4. CONCLUSION

Considering the importance and huge potential of Si-NW based solar cell to reduce materials as well as process cost and increased solar to power conversion efficiency due to light trapping, a bi-directional investigations, improved process and simulative prediction, has been carried out and reported herewith. In terms of process, metal nanoparticles have been achieved with various sizes, but mostly spherical that acted as catalyst to grow nanoparticles directed Si-NWs. High resolution scanning electron microscope (SEM) revealed the diameter of the as-grown Si-NWs to be in the range of 50 to 200 nm, that coincide well with the dimension of metal nanoparticles. Based on the experimental observations; a detailed simulation has been carried out to understand the mechanism how Si-NWs of different dimension interact with solar spectral wavelengths and contribute to exciton generation rate distribution. Further detailed cross-sectional analyses as well as spectral generation rate distributions for different size of the Si-NW have been investigated. Such insights not only indispensable to understand the mechanism behind but also open up new possibilities in various applications.

Acknowledgement: Authors like to thank Center of Research Excellence in Renewable Energy (CoRERE), Research Institute, King Fahd University of Petroleum & Minerals, (KFUPM), Dhahran 31261, Saudi Arabia. Mohammad Kamal Hossain acknowledges the support provided by the King Abdullah City for Atomic and Renewable Energy (KACARE) for funding support through project KACARE182-RFP-07.

## 5. REFERENCES

- Battersby, S. (2019). News Feature: The solar cell of the future. *Proceedings of the national academy of sciences*, 116(1), 7-10.
- Boettcher S.W., Spurgeon J.M., Putnam M.C., Warren E.L., Turner-Evans D.B., Kelzenberg M.D., et al., 2010. Energy-conversion properties of vapor-liquid-solid-grown silicon wire-array photocathodes, *Science*, 327, 185.
- Garnett E., Yang P., 2010. Light trapping in silicon nanowire solar cells, *Nano lett.* 10, 1082.
- Hoffmann, W. (2006). PV solar electricity industry: Market growth and perspective. *Solar energy materials and solar cells*, 90(18-19), 3285-3311.
- Höger, I., Schaper, M., Mette, A., Lee, B. G., Fertig, F., Lantzsch, R., and Junghänel, M. (2018, August). Boosting module power by advanced interconnection and p-type Cz silicon solar cell efficiencies exceeding 22% in mass production. In *AIP conference proceedings* (Vol. 1999, No. 1, p. 110003). AIP Publishing.
- Hossain, M. K., Salhi, B., and Mukhaimer, A. W. (2017). Optical confinements in correlated spectral characteristics of vertically aligned silicon nanometric wires followed by a facile fabrication thereof. *Plasmonics*, 12(5), 1297-1304.
- Hossain, M. K., Salhi, B., Mukhaimer, A. W., and Al-Sulaiman, F. A. (2016). Fabrication and optical simulation of vertically aligned silicon nanowires. *Applied nanoscience*, 6(7), 1031-1036.
- Kelzenberg M.D., Boettcher S.W., Petykiewicz J.A., Turner-Evans D.B., Putnam M.C., Warren E.L., et al., 2010. Enhanced absorption and carrier collection in Si wire arrays for photovoltaic applications, *Nat. mater.* 9, 239.
- Krogstrup, P., Jørgensen, H. I., Heiss, M., Demichel, O., Holm, J. V., Aagesen, M., Nygard J. and Morral, A. F. (2013). Single-nanowire solar cells beyond the Shockley–Queisser limit. *Nature photonics*, 7(4), 306.
- Li, Y., Li, M., Song, D., Liu, H., Jiang, B., Bai, F., and Chu, L. (2015). Broadband light-concentration with near-surface distribution by silver capped silicon nanowire for high-performance solar cells. *Nano energy* 11, 756-764.
- Liu, Y., Sun, N., Liu, J., Wen, Z., Sun, X., Lee, S. T., and Sun, B. (2018). Integrating a silicon solar cell with a triboelectric nanogenerator via a mutual electrode for harvesting energy from sunlight and raindrops. *ACS nano*, 12(3), 2893-2899.
- Maryasin, V., Rafhay, Q., Bucci, D., Michallon, J., and Kaminski-Cachopo, A. (2018, August). Opto-electrical simulation of III-V nanowire based tandem solar cells on Si. In *AIP conference proceedings* (Vol. 1999, No. 1, p. 120001). AIP publishing.
- Peng, K. Q., Wang, X., Li, L., Wu, X. L., and Lee, S. T. (2010). High-performance silicon nanohole solar cells. *Journal of the American chemical society*, 132(20), 6872-6873.
- Peng, K., Wang, X., and Lee, S. T. (2008). Silicon nanowire array photoelectrochemical solar cells. *Applied physics letters*, 92(16), 163103.
- Polman A., Atwater H.A., 2012. Photonic design principles for ultrahigh-efficiency photovoltaics, *Nat. mater.* 11, 174.
- Saga, T. (2010). Advances in crystalline silicon solar cell technology for industrial mass production. *NPG Asia materials*, 2(3), 96.
- Salhi, B., Hossain, M. K., Mukhaimer, A. W., and Al-Sulaiman, F. A. (2016). Nanowires: a new pathway to nanotechnology-based applications. *Journal of electroceramics*, 37(1-4), 34-49.
- Tang, J., Huo, Z., Brittman, S., Gao, H., and Yang, P. (2011). Solution-processed core–shell nanowires for efficient photovoltaic cells. *Nature nanotechnology*, 6(9), 568.
- Tsakalagos, L., Balch, J., Fronheiser, J., Korevaar, B. A., Sulima, O., and Rand, J. (2007). Silicon nanowire solar cells. *Applied physics letters*, 91(23), 233117.
- Yu, L., S. Misra, J. Wang, S. Qian, M. Foldyna, J. Xu, et al., 2014. Understanding light harvesting in radial junction amorphous silicon thin film solar cells. *Sci. rep.* 4, 4357.
- Zeng, Y., Yang, Q., Wan, Y., Yang, Z., Liao, M., Huang, Y., and Wu, C. H. (2019). Numerical exploration for structure design and free-energy loss analysis of the high-efficiency polysilicon passivated-contact p-type silicon solar cell. *Solar energy*, 178, 249-256.

---

## #83: Performance optimisation of drag-type vertical axis wind turbine having twisted blades

---

Ahmed S. SAAD<sup>1</sup>, Ahmed ELWARDANY<sup>1,2</sup>, Shinichi OOKAWARA<sup>1,3</sup>, Mahmoud AHMED<sup>1</sup>

<sup>1</sup>Dept. of Energy Resources Engineering, Egypt-Japan University of Science and Technology, Alexandria 21934, Egypt, ahmed.salah@ejust.edu.eg (Ahmed S. SAAD),

<sup>2</sup>Mechanical Engineering Department, Faculty of Engineering, Alexandria University, Alexandria 21544, Egypt

<sup>3</sup>Dept. of Chemical Science and Engineering, Tokyo Institute of Technology, Tokyo 152-8552, Japan.

*The aim of this study is to enhance the performance of a twisted Savonius vertical axis wind turbine. The influences of various twist angles ( $\varphi$ ) ranged from  $0^\circ$  to  $180^\circ$  and the overlap ratios ( $\delta$ ) of 0 to 0.3 on the rotor performance have been investigated. Thus, the three-dimensional incompressible unsteady Reynolds-Averaged Navier-Stokes equations in conjunction with RNG  $k$ - $\epsilon$  turbulence model was utilised and numerically simulated. The numerical results were validated using the available experimental measurements. The predicted flow fields around the rotor were presented and analysed. Accordingly, results indicated that the Savonius rotor with a twist angle of  $45^\circ$  attained a maximum power coefficient ( $C_p$ ) of 0.194 at a tip speed ratio ( $\lambda$ ) of 0.8 and wind velocity of 6 m/s. The maximum value of power coefficient at a twist angle ( $\varphi$ ) of  $45^\circ$  increased with reducing the overlap ratio and it reached its maximum value of 0.223 at zero overlap ratio. The performance gain ( $C_p$ ) obtained by using the present optimised twisted Savonius rotor was 28 % compared to the conventional untwisted rotor which has  $C_p=0.174$ . Furthermore, the developed optimised rotor design significantly improved the static torque coefficient to ease the self-starting ability of the Savonius rotor.*

*Keywords: Savonius rotor; twisted blades; overlap ratio; end plates; power coefficient*

## 1. INTRODUCTION

Savonius rotor is a vertical axis wind turbine (VAWT) developed by the Finnish engineer, S.J Savonius, in the early 1920s (Savonius, 1931). This is the simplest VAWT with low cut-in wind speed, it usually consists of cylindrical halves facing opposite directions in such a way that they have formed almost an S-shape (for two-bladed rotor). Figure 1 shows characteristic parameters of a Savonius wind turbine with two semicircular profile blades. In Figure 1,  $d$  is the blade chord,  $e$  the blades overlap,  $D$  the rotor diameter and  $D_o$  is the end plate diameter. The illustrated turbine is submitted to a wind with undisturbed velocity  $V$ , and rotation rate represented by  $\omega$ . The basic working principle is based on the difference of the drag force between the convex and the concave surfaces of the rotor blades when they rotate around a vertical shaft. Thus, the main driving force of the Savonius rotor is drag force. However, at smaller rotor angles ( $\theta$ ) the contribution of lift force in the net torque generation has been reported by (Modi and Fernando, 1989 and Modi and Fernando, 1993). The rotor is a slow running device and has a relatively lower efficiency compared with other VAWTs as Darrieus rotor but on the other hand it has a good starting ability, wind acceptance from any direction, design simplicity and low cost (Menet, 2004, Eriksson, 2008, D'Alessandro, 2010, and Akwa, 2012).

The aspect ratio, overlap ratio, number of blades, end plates, number of stages and blade shape are the geometrical parameters that influence the performance of a Savonius rotor. It has been reported by several investigations that the performance of this rotor has increased significantly through optimisation of these parameters. It is reported that, the Savonius rotor has better performance with use of aspect ratio ( $AR=H/D$ ) within the range of 1.0-2.0 (Sheldahl, 1978, Ogawa, 1989, Saha, 2008, and Bhayo, 2017) while, the optimum value of overlap ratio ( $\delta=e/d$ ) lies between 0.15 and 0.25 which provide the best performance results (Fujisawa, 1992 and Akwa, 2011). The power coefficient of two-bladed rotor is higher than three-bladed rotor; however, a greater starting static torque has been shown by three-bladed rotor (Sheldahl, 1978). Using end plates at the rotor tips as shown in Figure 1 is the simplest method to improve the performance of Savonius rotor. The diameter ( $D_o$ ) of these end plates is to be taken as 1.1D (rotor diameter) (Fujisawa, 1996 and Jeon, 2015).

Conventional Savonius rotors have a negative torque at certain rotor angles and a large torque variation. To enhance the torque characteristics, multi-stage Savonius wind rotors have been proposed, but the use of a multi-stage rotor reduced the power coefficient as compared with single-stage rotor (Frikha, 2016 and Bhayo, 2017). Recently, some researchers have proposed helical Savonius wind rotors with different twist angles (Kamoji, 2009 and Damak, 2013). Helical Savonius wind rotors have a positive static torque coefficient for all rotor angles and better performance than conventional Savonius turbines. (Kamoji, 2009) performed an experimental investigation on a helical Savonius rotor with twist angle of  $90^\circ$ . It was reported that, the helical rotor has positive static torque coefficient at all the rotor angles. Another experimental study was achieved by (Damak, 2013) on a helical Savonius rotor with twist angle of  $180^\circ$ . The performance of the helical rotor was better than the conventional one.

It is obvious that many previous researchers have focused on investigating various shapes of Savonius wind rotor. However, a closer look at the design parameters clearly showed that there is a lack of clear analysis results that would indicate the effects of the twist angle on the performance of a Savonius rotor. Therefore, the main objective of the present study was to investigate the variation in the power coefficient, static torque coefficient and flow patterns of a Savonius rotor at different twist angles. Furthermore, the effects of various overlap ratios on the performance of the present proposed twisted Savonius rotor with optimised twist angle were investigated to improve its performance.

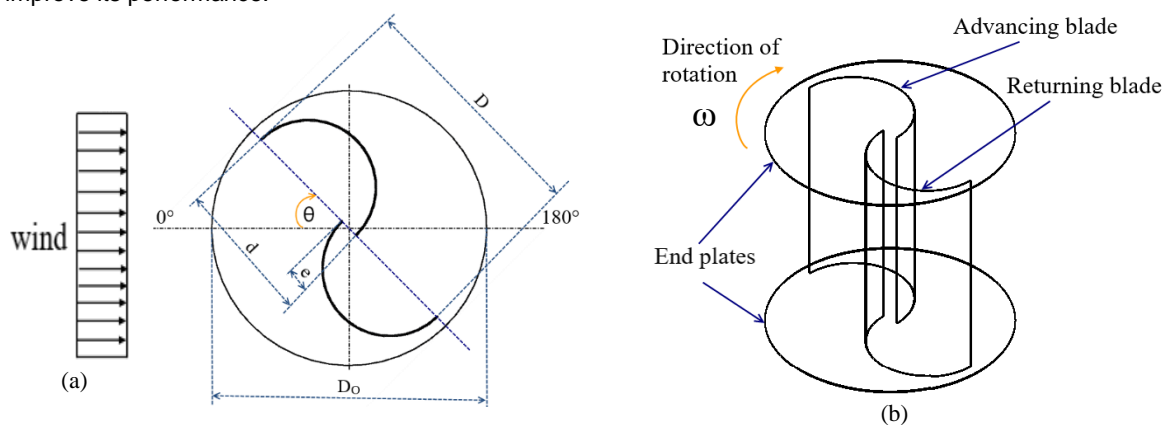


Figure 1: A schematic description and main geometric parameters of Savonius rotor (a) top view, (b) isometric view.

## 2. NUMERICAL ANALYSIS

In the present study, ANSYS Fluent 19.0 was used to compute the flow field around the Savonius wind rotor. The 3-D Unsteady Reynolds Averaged Navier-Stokes equations were solved using the SIMPLE algorithm. It was concluded in (Lee, 2016, Saad, 2017, and El-Askary, 2018) that the RNG  $k-\epsilon$  turbulence model has the ability to well predict the performance of the Savonius wind turbine, hence the RNG  $k-\epsilon$  turbulence model was used to close RANS equations in the present study. The computations have been performed to reach  $10^{-5}$  residuals of all governing equations except continuity equation which has an order of  $10^{-4}$  residuals.

For appropriate analysis, the sliding mesh model (Fluent, 2019) was selected to represent the rotation of the Savonius rotor. The computational domain was divided into two zones, the first one was the rotating zone around the rotor and the second was the remaining zone, as shown in Figure 2. The two zones were separated by an interface and the rotating zone was allowed to rotate with different rotational speeds while the second zone was kept fixed. The three-dimensional CAD model of the computational domain has been completed using Solid Works program, and the ANSYS ICEM program has been utilised for generating the computational grids. In the present study, the effect of the ground has not been considered. The inlet boundary was fed with a uniform velocity at 5D upstream of the rotor, and the outlet boundary was considered as an atmospheric pressure at the exit of the domain. The turbulence intensity considered in the present computation has been taken to be 5%. The top, bottom, and lateral sides of the domain were far from the centre of the rotor of about 5D. Thus, they were sufficiently far from the wake core, and were treated using "Neumann" boundary condition. The main grid shapes of the rotating rotor and surrounding outer domain are shown in Figure 2. The grid size in the range of 2 million cells has been used for all computations presented in the present investigation. For such a value of grid number, the non-dimensional near-wall grid distance ( $y^+$ ) was less than 5 over the rotor blades.

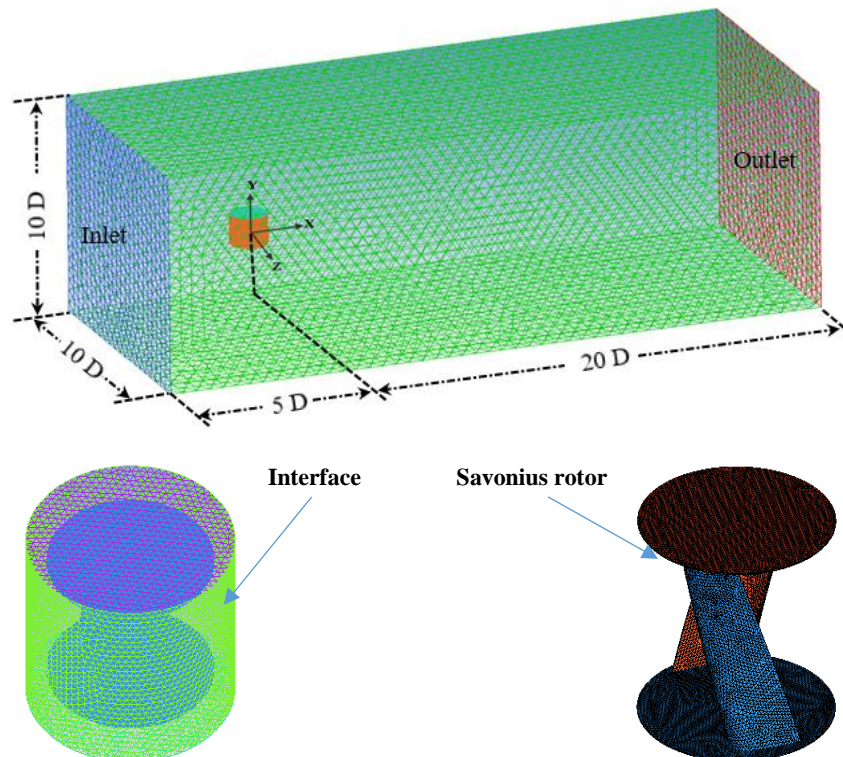


Figure 2: The computational domain and rotor volume mesh.

## 3. RESULTS AND DISCUSSION

### 3.1. Validation of the numerical method

To validate the numerical results, the predicted results obtained by the RNG  $k-\epsilon$  turbulence model were compared with the experimental results of (Fujisawa, 1992). The Savonius rotor tested by Fujisawa was 30 cm diameter with overlap ratio ( $\delta$ ) of 0.15 and aspect ratio (AR) of 1.0. The upstream wind speed was 6 m/s. Figure 3 shows the power coefficient comparison predicted by the present numerical and experimental results of (Fujisawa, 1992). It

can be noticed from that, there was good agreement between the present numerical using RNG  $k-\epsilon$  turbulence model and the available experimental results.

### 3.2. Effect of twist angle

The effect of twist angle on the performance the proposed twisted Savonius rotor was studied in order to improve the power coefficient and starting ability of the Savonius rotor. Figure 4 illustrates the twist angle ( $\phi$ ) which is the angle between the lower and upper ends of the rotor as well as the studied twist angles which are  $0^\circ$ ,  $30^\circ$ ,  $45^\circ$ ,  $90^\circ$ ,  $135^\circ$ , and  $180^\circ$ . All rotors have overall rotor diameter  $D = 400$  mm, thickness = 2 mm, aspect ratio  $AR = 1.0$  and overlap ratio  $\delta = 0.15$ . The diameter of end plates ( $D_o$ ) is taken to be 1.1 of rotor diameter ( $D$ ). The variation of the power coefficient with tip speed ratio for various twist angles ( $\phi$ ) at wind speed ( $V$ ) of 6 m/s is presented in Figure 5. It was observed that the increase in the twist angle up to optimum limit ( $\phi=45^\circ$ ), leads to significant gain in the power coefficient ( $C_p$ ), then  $C_p$  decreased with the increase in the twist angle. It was found that the highest power coefficient of 0.194 was achieved at twist angle of  $45^\circ$ . The twist angle  $\phi=180^\circ$  significantly decreased the power coefficient of the Savonius turbine.

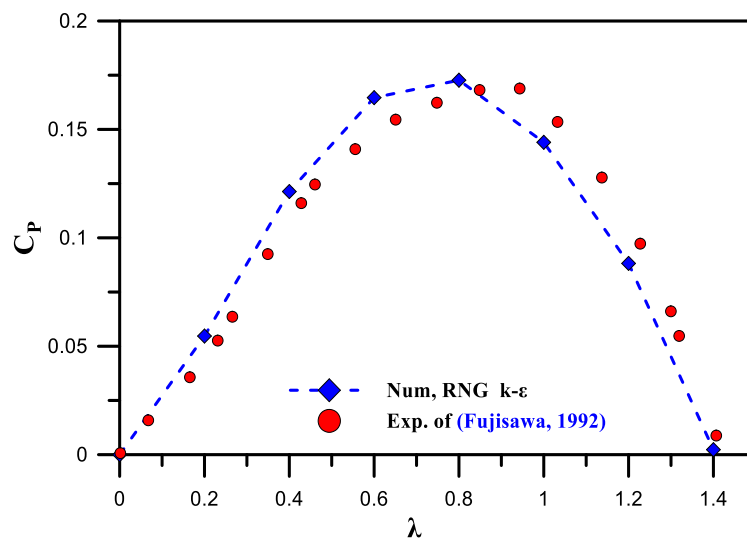


Figure 3: Comparison between the present numerical results and experimental results of (Fujisawa, 1992).

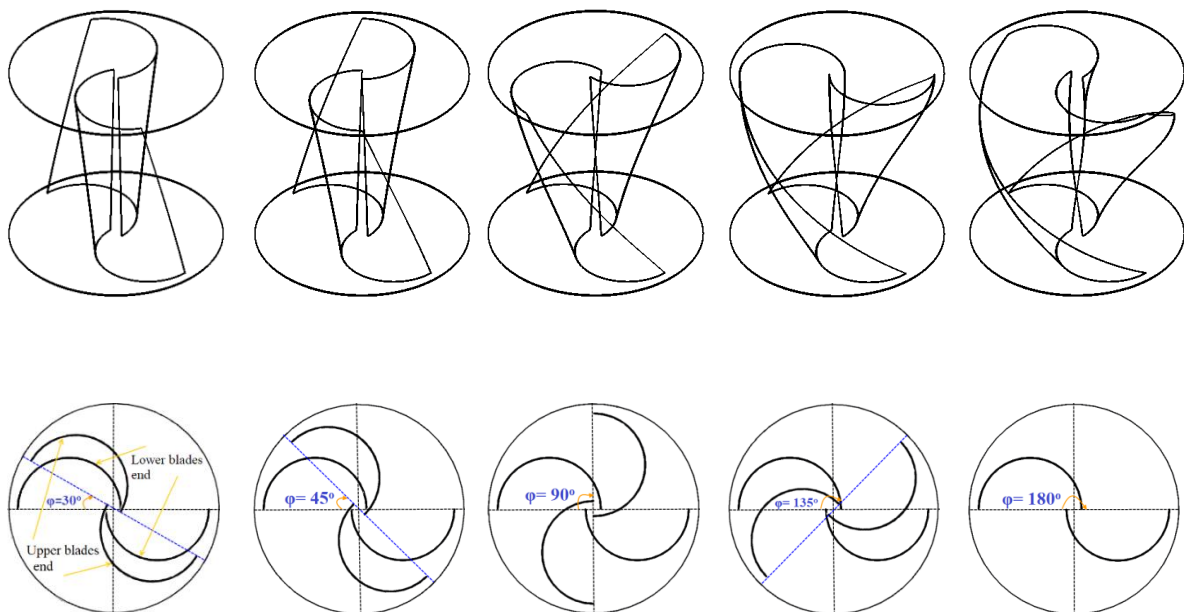


Figure 4: Isometric and top views of the tested Savonius rotors with various twist angle ( $\phi$ )

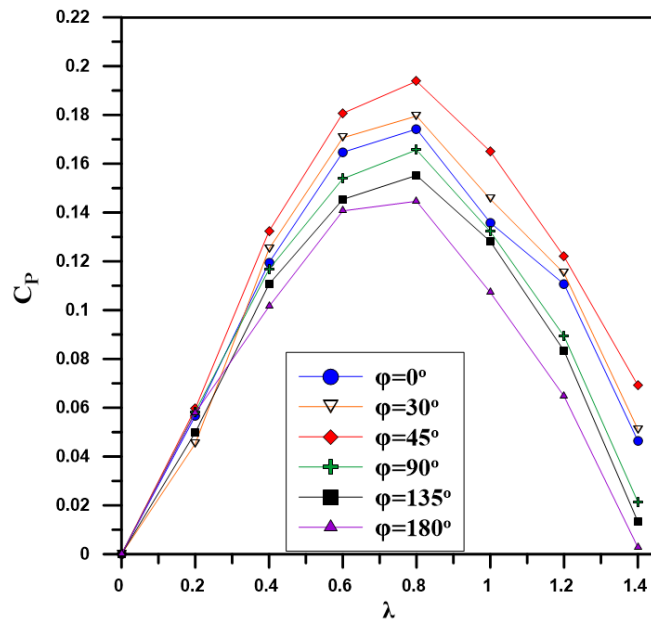


Figure 5: The variation of the average power coefficient with tip speed ratio for various twist angles ( $\phi$ ).

To explore the reasons of the performance improvements achieved by the present proposed twisted Savonius rotor with optimum twist angle of  $45^\circ$ , the torque coefficient ( $C_T$ ) within a complete cycle and static pressure contours are presented and compared with the Savonius rotor without twist. Figure 6 shows the variation of the instantaneous torque coefficient for the advancing blade, the returning blade, and entire rotor. The torque coefficient is presented during a complete cycle, from  $\theta = 0$  to  $360^\circ$ , at  $\lambda=0.8$  for the untwisted rotor ( $\phi=0^\circ$ ) and the twisted rotor ( $\phi=45^\circ$ ). The twisted rotor shows higher  $C_T$  by the returning and the advancing blades at the second and fourth quarters of the cycle, respectively as compared with the untwisted rotor. The torque coefficient of the untwisted rotor is slightly higher than that of the twisted rotor at the first and third quarters of the cycle. However, the torque coefficient of the entire rotor through the complete cycle shows higher average value for the twisted rotor.

The static pressure contours through five different sections across the rotor are presented in Figure 7 at rotor angle  $\theta = 0^\circ$ . The cross-section of the five sections is the same for untwisted rotor. Hence, the behavior of the pressure contours is almost the same for the five slices except small deviation due to the end plates. The incoming flow first impacts the convex surface of the advancing blade and gives up its momentum to the front part of the blade, which in turn increases the static pressure as shown in Figure 7-a. As the air travels along the upper part of the surface, the pressure decreases in that region. The air with lower energy then strikes the returning blade, which slightly increases the pressure on its concave surface. Similar behavior of the static pressure contours to the above discussed untwisted rotor is achieved for the twisted rotor at slice 1 as presented in Figure 7-b. However, due to the change in the blade orientation of the twisted rotor at the upper part of the blade, through slices 2 to 5, the pressure distributions are expected to be different. At these slices, the effect of the incoming flow in creating positive drag is higher. This attribute the high  $C_T$  of the twisted rotor as compared with the untwisted one, at rotor angle of  $0^\circ$ , as previously presented in Figure 6 (c). It is worth mentioning that the upper part of the twisted rotor, and due to twist, has a great share of the increase in the  $C_T$  of that rotor.

### 3.3. Effect of overlap ratio

The numerical analysis was extended to optimise the overlap ratio ( $\delta$ ) of the proposed twisted Savonius rotor with optimum twist angle of  $45^\circ$ . Overlap ratio ( $\delta=e/d$ ) is defined as the ratio of overlap distance between the two blades of the rotor ( $e$ ) to the blade chord length ( $d$ ), as shown previously in Figure 1. The studied values of overlap ratios were 0.1, 0.15, 0.2, 0.3 besides the case of the rotor without overlap ( $\delta=0$ ). All the tested rotors have an aspect ratio of 1.0 and the dimensions of the rotors with various overlap ratios are given in Table 1. It was observed from table 1 that the rotor diameter ( $D$ ) remained constant at all different overlap ratios to keep the Reynolds number  $Re = \frac{\rho V D}{\mu} = \text{constant}$ .

The variations of power coefficient ( $C_p$ ) with tip speed ratios for various overlap ratios ( $\delta$ ) at a wind speed of 6 m/s was shown in Figure 8. It was observed that the power coefficient of the twisted Savonius rotor decreased with the presence of overlap. The twisted Savonius rotor without overlapping ( $\delta=0.0$ ) has the highest values of  $C_p$  0.223 compared to the other tested overlap ratios. Unlike the conventional Savonius rotor which have better performance

at  $\delta=0.15-0.25$ , the present numerical results showed significant improvement for the performance of the twisted Savonius rotor without overlapping ( $\delta=0$ ).

Furthermore, Figure 9 illustrates the static torque coefficient ( $C_{TS}$ ) of the untwisted rotor with overlap ( $\varphi=0^\circ$ ,  $\delta=0.15$ ), twisted rotor with overlap ( $\varphi=45^\circ$ ,  $\delta=0.15$ ), and the twisted rotor without overlap ( $\varphi=45^\circ$ ,  $\delta=0$ ) obtained numerically by using the RNG  $k-\epsilon$  model over  $180^\circ$  degrees of rotor angles ( $\theta$ ) at wind speed of 6 m/s. It was observed that the twisted rotors always have positive  $C_{TS}$  values at all rotor angle unlike the untwisted rotor which has a negative value at rotor angle of  $\theta=138^\circ - 167^\circ$ . Hence, the twisted blades enhanced the self-starting ability of the Savonius rotor. The twisted rotor without overlap ( $\varphi=45^\circ$ ,  $\delta=0$ ) has the highest average  $C_{TS}$  compared to other studied rotors with positive values at all rotor angles which represent the high self-starting ability of this rotor.

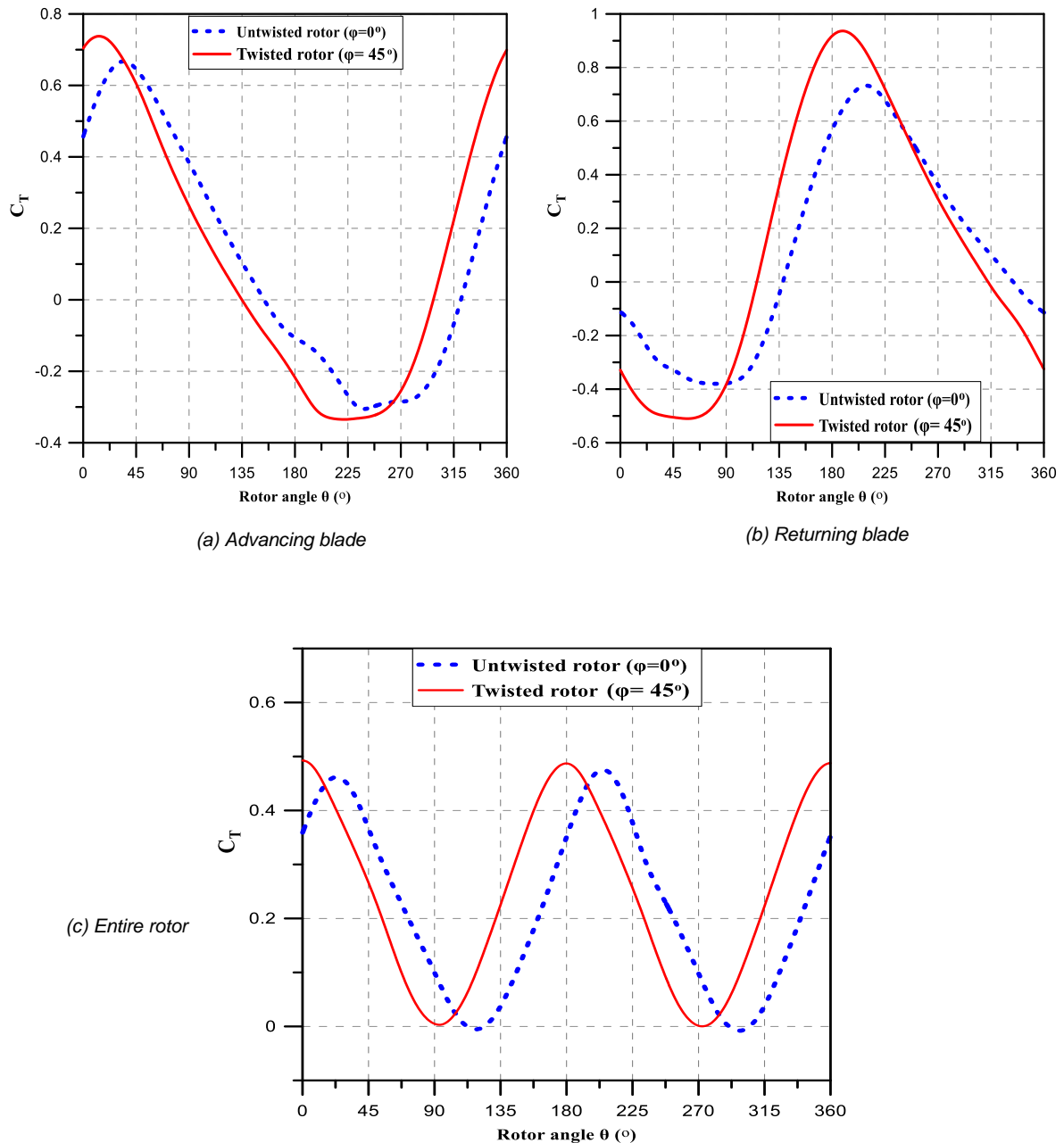


Figure 6: Torque coefficient over complete revolution for (a) Advancing blade, (b) Returning blade, and (c) Entire rotor.



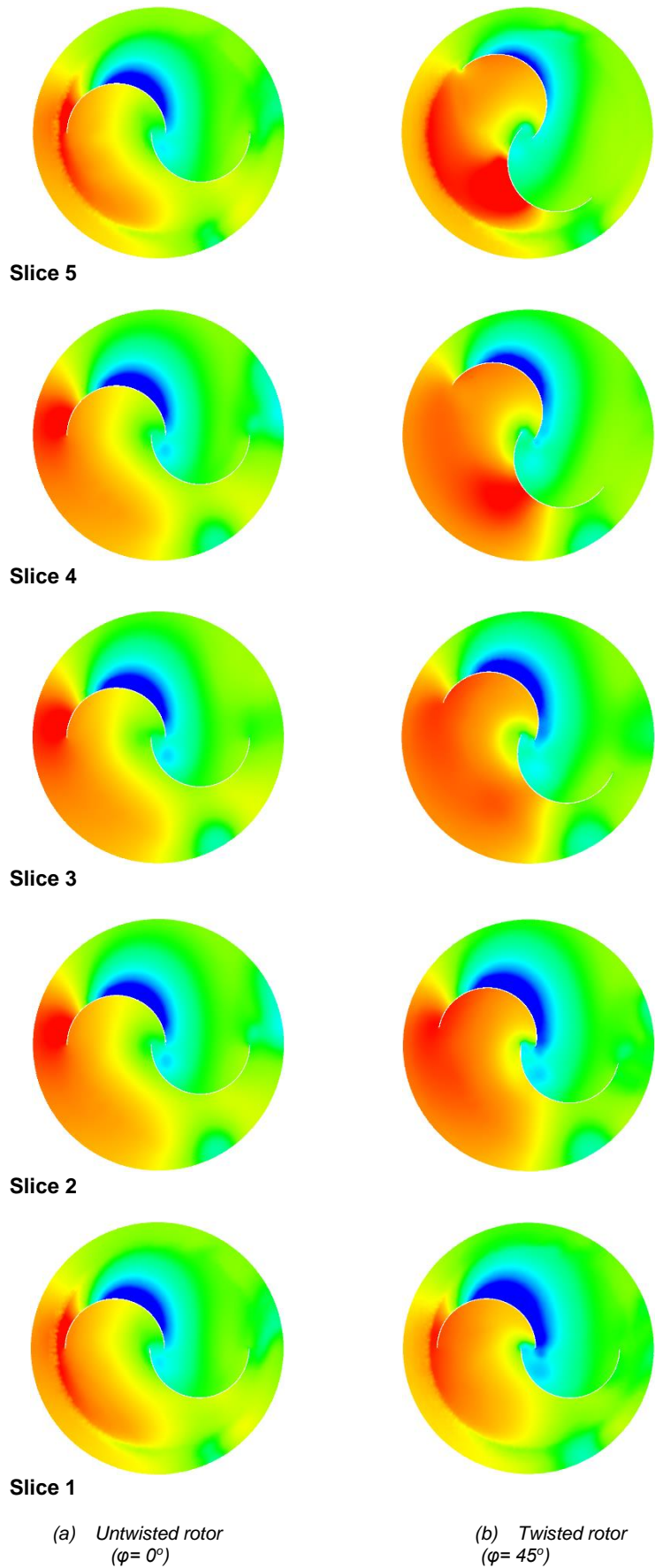
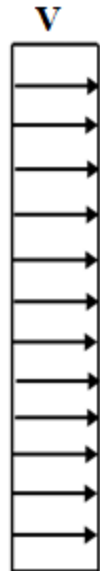
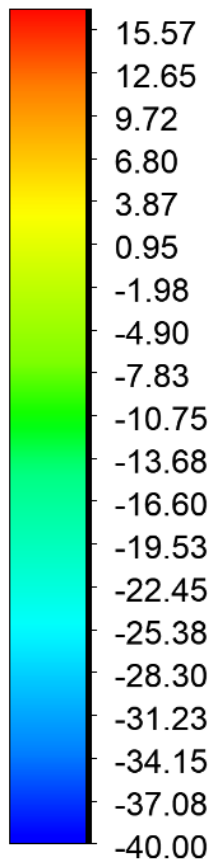
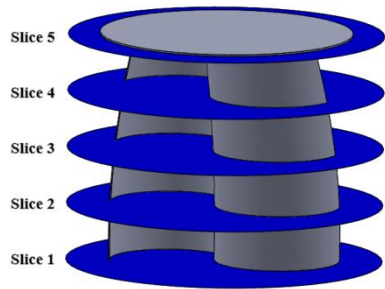


Figure 7: Sectional static pressure distribution around the blades at rotor angle  $\theta = 0^\circ$

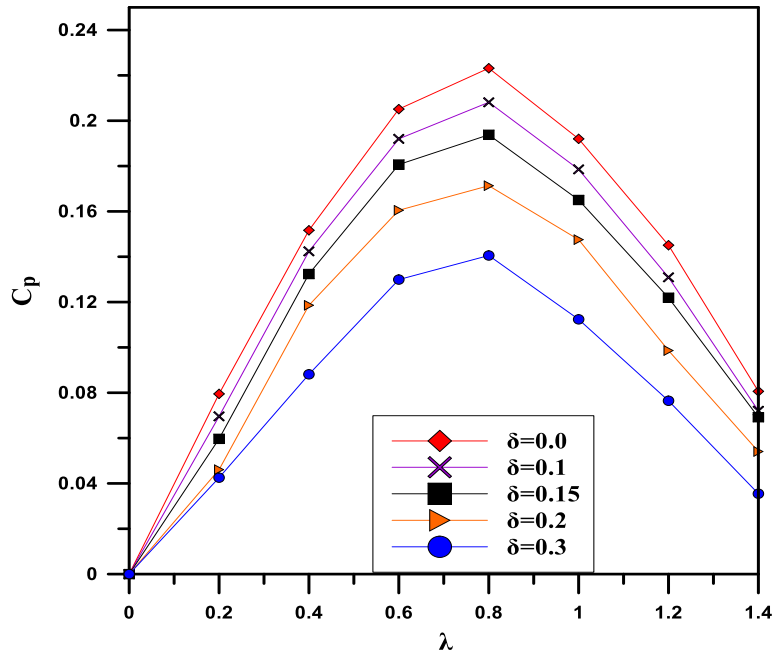


Figure 8: The variation of the average power coefficient with tip speed ratio for various overlap ratios ( $\delta$ ).

Table 1: Dimensions of the rotors with various overlap ratios

Overlap ratio	$\delta=0.0$	$\delta=0.1$	$\delta=0.15$	$\delta=0.2$	$\delta=0.3$
<b>Dimensions (mm)</b>					
<b>e</b>	0	20.7	32	43.8	46.4
<b>d</b>	197	207	213	219	232
<b>D</b>	400	400	400	400	400
<b>H</b>	400	400	400	400	400
<b>D<sub>o</sub></b>	440	440	440	440	440

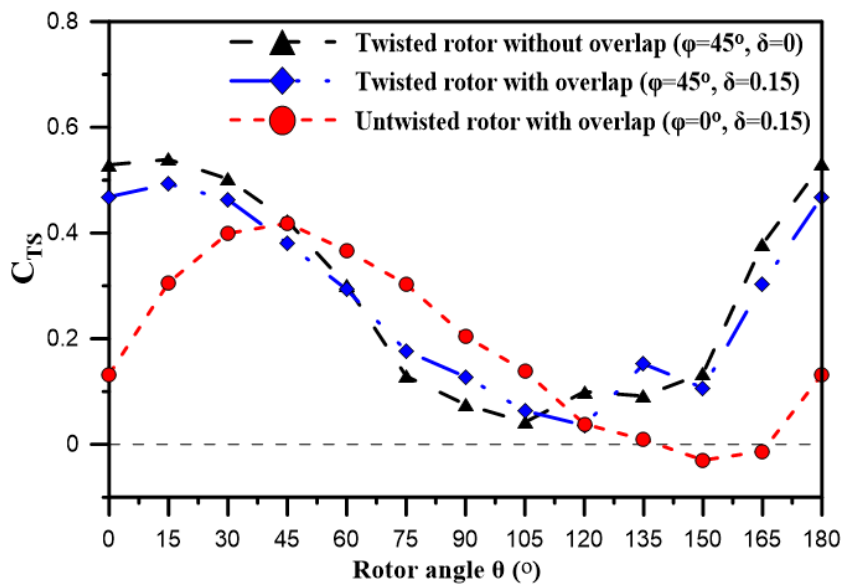


Figure 9: Static torque coefficient obtained numerically versus rotor angle of the studied Savonius rotors.

## 4. CONCLUSION

The performance of a Savonius wind rotor at various twist angles was numerically investigated. The simulations were performed using the 3-D incompressible unsteady Reynolds-Average Navier-Stokes equations along with the RNG  $k-\epsilon$  turbulence model. The numerical solution obtained using the RNG  $k-\epsilon$  model was found to give accurate results, as compared with published experimental measurements. The maximum power coefficient ( $C_{p, \max}$ ) increased with the increase in twist angle up to an optimum value of  $45^\circ$  and then decreased. The performance gain ( $C_p$ ) obtained by using the present twisted rotor with a twist angle of  $45^\circ$  is 11.5 % compared to the untwisted rotor which has  $C_p = 0.174$ . Furthermore, the effect of overlap ratio has been studied to optimise the performance of the proposed twisted design with optimum twist angle of  $45^\circ$ . Unlike the conventional untwisted Savonius rotor, the power coefficient of the twisted rotor with twist angle of  $45^\circ$  decreased with the presence of overlap. The twisted rotor without overlap has the highest  $C_p$  of 0.223 compared to the other tested overlap ratios. The performance gain ( $C_p$ ) obtained by using the present optimised twisted Savonius rotor with an optimum twist angle of  $45^\circ$  and without overlapping was 28 % compared to the conventional untwisted rotor which has  $C_p = 0.174$ . Furthermore, the optimised twisted rotor has the highest average  $C_{TS}$  with positive values at all rotor angle unlike the conventional untwisted rotor which has negative  $C_{TS}$  values at some rotor angles.

## 5. REFERENCES

- Akwa, J. V., Alves, G. and Petry, A. P., 2011. Discussion on the verification of the overlap ratio influence on performance coefficients of a Savonius wind rotor using computational fluid dynamics. *Renewable Energy*, 38, 141–149.
- Akwa, J. V., Vielmo, H. A. and Petry, A. P., 2012. A review on the performance of Savonius wind turbines. *Renewable and Sustainable Energy Reviews*, 16(5), 3054–3064.
- Bhayo, B. A. and Al-Kayiem, H. H., 2017. Experimental characterization and comparison of performance parameters of S-rotors for standalone wind power system. *Energy*, 138, 752–763.
- D'Alessandro, V., Montelpare, S., Ricci, R., and Secchiaroli, A., 2010. Unsteady Aerodynamics of a Savonius wind rotor: A new computational approach for the simulation of energy performance. *Energy*, 35(8), 3349–3363.
- Damak, A., Driss, Z. and Abid, M. S., 2013. Experimental investigation of helical Savonius rotor with a twist of  $180^\circ$ . *Renewable Energy*, 52, 136–142.
- Eriksson, S., Bernhoff, H. and Leijon, M., 2008. Evaluation of different turbine concepts for wind power. *Renewable and Sustainable Energy Reviews*, 12(5), 1419–1434.
- El-Askary, W. A., Saad, A.S., AbdelSalam, A.M., and Sakr, I.M., 2018. Investigating the performance of a twisted modified Savonius rotor. *Journal of Wind Engineering and Industrial Aerodynamics*, 182, 344–355.
- Fujisawa, N., 1992. On the torque mechanism of Savonius rotors. *Journal of Wind Engineering and Industrial Aerodynamics*, 40(3), 277–292.
- Fujisawa, N., 1996. Velocity measurements and numerical calculations of flow fields in and around Savonius rotors. *Journal of Wind Engineering and Industrial Aerodynamics*, 59(1), 39–50.
- Frikha, S., Driss, Z., Ayadi, E., Masmoudi, Z., and Abid, M. S., 2016. Numerical and experimental characterization of multi-stage Savonius rotors. *Energy*, 114, 382–404.
- Fluent, 2019. User's Guide Fluent 19.0. Fluent Incorporated, Lebanon, NH.
- Jeon, K. S. Jeong, J. I., Pan, J. K., and Ryu, K. W., 2015. Effects of end plates with various shapes and sizes on helical Savonius wind turbines. *Renewable Energy*, 79(1), 167–176.
- Kamoji, M. A., Kedare, S. B., and Prabhu, S. V., 2009. Performance tests on helical Savonius rotors. *Renewable Energy*, 34(3), 521–529.
- Lee, J. H., Lee, Y. T., and Lim, H. C., 2016. Effect of twist angle on the performance of Savonius wind turbine. *Renewable Energy*, 89, 231–244.

- Modi, V. and Fernando, M., 1989. On the performance of the Savonius wind turbine. *Journal of Solar Energy*, 111(1), 71–81.
- Modi, V. J. and Fernando, M., 1993. Unsteady aerodynamics and wake of the Savonius wind turbine: A numerical study. *Journal of Wind Engineering and Industrial Aerodynamics*, 46–47(C), 811–816.
- Menet, J. L., 2004. A double-step Savonius rotor for local production of electricity: A design study. *Renewable Energy*, 29(11), 1843–1862.
- Ogawa, T., Yoshida, H. and Yokota, Y., 1989. Development of Rotational Speed Control Systems for a Savonius-Type Wind Turbine. *Journal of Fluids Engineering*, 111(1), 53–58.
- Savonius, S. J., 1931. The S-Rotor and Its Applications. *Mechanical Engineering*, 53(5), 333-338.
- Sheldahl, R. E., Feltz, L. V. and Blackwell, B. F., 1978. Wind tunnel performance data for two- and three-bucket Savonius rotors. *Energy*, 2(3), 160–164.
- Saha, U. K., Thotla, S. and Maity, D., 2008. Optimum design configuration of Savonius rotor through wind tunnel experiments. *Journal of Wind Engineering and Industrial Aerodynamics*, 96, 1359–1375.
- Saad, A.S., AbdelSalam, A.M., Sakr, I.M., and El-Askary, W.A., 2017. Performance Analysis of a Helical Savonius Wind Turbine with Modified Rotor. *Proceedings of the 17<sup>th</sup> International Conference on Aerospace Sciences and Aviation Technology (ASAT – 17)*. Cairo, Egypt.

---

# #85: Heat transfer analysis of vacuum insulated windows compared to traditional fenestration technologies

## A thermal model analysis

---

Jorge Luis AGUILAR-SANTANA<sup>1</sup>, Hasila JARIMI<sup>2</sup>, Mariana VELASCO-CARRASCO<sup>3</sup>,  
Saffa RIFFAT<sup>4</sup>

<sup>1</sup>Department of Architecture and Built Environment, Faculty of Engineering, University of Nottingham, University Park, Nottingham, NG7 2RD UNITED KINGDOM,

<sup>1</sup>jorge.aguilarsantana@nottingham.ac.uk

<sup>2</sup>ezzhj@nottingham.ac.uk

<sup>3</sup>mariana.velascocarrasco@nottingham.ac.uk

<sup>4</sup>saffa.riffat@nottingham.ac.uk

*Evacuated glazing is novel window technology that have reported excellent heat transfer properties in recent years (as low as  $0.8\text{W}/\text{m}^2\text{K}$ ) when compared to single-layered solutions. Since window energy consumption accounts for up to 40% the total electricity consumed by buildings, the need of highly insulated solutions for windows is a priority particularly for recent international building codes.*

*This paper aims to represent a comprehensive approach to multi-layered technologies (double, triple, vacuum and photovoltaic vacuum glazing) under an office use environment. These simulations utilised a variety of climatic conditions (tropical, arid, temperate, continental and tundra) for assessing the glazing performance. EnergyPlus™ heat balance model was utilised for calculating the indoor to outdoor temperature performance, heat gain and loss of energy, heat transfer, visible transmittance and radiation impact.*

*Photovoltaic vacuum window reduced the summertime temperatures in office buildings by  $7.5^\circ\text{C}$  in Las Vegas,  $6.25^\circ\text{C}$  in London and  $5.39^\circ\text{C}$  in Beijing). For extreme temperature mitigation, photovoltaic vacuum glazing PV resulted the best option for locations in Kuala Lumpur, Las Vegas, London and Beijing. Vacuum glazing VG on the contrary was best suited for extreme cold conditions as those presented in Kuujuaq Canada. For energy saving assessment, triple glazing TG reduced heat gain rates by  $-41.8\%$  in Kuala Lumpur,  $-38.5\%$  in Las Vegas,  $-37.2\%$  in London,  $-38.9\%$  in Beijing and  $-33.2\%$  in Kuujuaq when compared against SG. Reduction on heat losses can be accounted by  $-83.8\%$ ,  $-83.7\%$ ,  $-82.9\%$ ,  $-81.6\%$  and  $-82.3\%$  in a similar array.*

*Vacuum insulated window demonstrated its ability to reduce heat transfer compared to traditional fenestration technologies, undoubtedly a more extensive use of this technology is forecasted in the near future when improvements in the manufacturing process make this technology to be widely available.*

*Keywords: heat transfer; multi-layered windows; evacuated windows; photovoltaic window*

## 1. INTRODUCTION

Windows are translucent building components utilised as connecting element between interior and exterior environments; they provide lighting, controlled ventilation and protection to exterior weather conditions. Overall, glazing components account for 20-40% of the total energy consumed by buildings (Ghosh & Norton, 2018). This consumption is primarily an effect of the temperature difference that windows are exposed to; it is directly related to the climate conditions of the location where they are installed and the loads demanded to provide thermal comfort.

Traditional single glazing has proved to be the least resilient glazing solution to extreme weather conditions, reporting a heat transfer coefficients or U-values of around  $5.74\text{W/m}^2\text{K}$  (Berkeley-Lab, 2017). In recent decades, several novel technologies have been developed to increase the heat insulation capacity aiming to reduce energy consumption; examples of these are double and triple glazing (Arici, et al., 2015), evacuated glazing (Son & Song, 2019) and photovoltaic vacuum glazing (Qiu, et al., 2019).

This paper aims to present an analysis of a series of heat transfer calculations using the EnergyPlus™ thermal model engine to describe the impact of these novel technologies under different climatic conditions. As stated by researchers and commercial manufacturers, U-values of multi-layered windows varies from  $1.5\text{W/m}^2\text{K}$  for double glazing (Pilkington™, 2016), to  $0.8\text{W/m}^2\text{K}$  for triple glazing (Pilkington™, 2018),  $1.0\text{W/m}^2\text{K}$  for vacuum glazing (Zhao, et al., 2007) and  $0.8\text{W/m}^2\text{K}$  in photovoltaic vacuum glazing (Ghosh, et al., 2018). This analysis would present a guideline of suitability and performance evaluation for urban concentrations.

## 2. METHODOLOGY

The approach of this study is in three stages, the first is aimed to calculate the optical and thermal characteristics of the window types, using Window™ software (Berkeley-Lab, 2017) and information presented by window manufacturers. The second stage is reserved for modelling an elemental office module, with a south-oriented window using the thermal model of EnergyPlus™ and variable climate conditions. Finally, a comprehensive analysis of the indoor-outdoor temperature performance is presented, including a heat gain and loss analysis, heat transfer, visible transmittance and radiation impact based on location performance.

### 2.1. Structure of glazing materials

For the representation of glazing characteristics, one sample of single glazing and four samples of multi-layered materials are included. Figure 1 represents the cross section of the single and multi-layered glazing types for buildings, including their solar heat gain coefficients (SHGC), visible transmittance (Tv) and heat transfer (U-value).

Addressing a standardisation of tests, the samples used a 3.9mm Optitherm™ clear glass (Pilkington, 2016) with thermal conductivity of  $1.0\text{W/mK}$  and emissivity coefficient of 0.025. Double-glazing incorporated a 15.0mm wide argon gap, while triple glazing included two of these gaps with identical material and size. For both vacuumed samples, a layer of LowE coating was included in the interior pane with the intention of reducing radiation rates to the indoor environment. The vacuum gap designed for both VG and PV was 0.3mm wide and included a square array of 25mm of steel pillars of 0.25mm in radius.

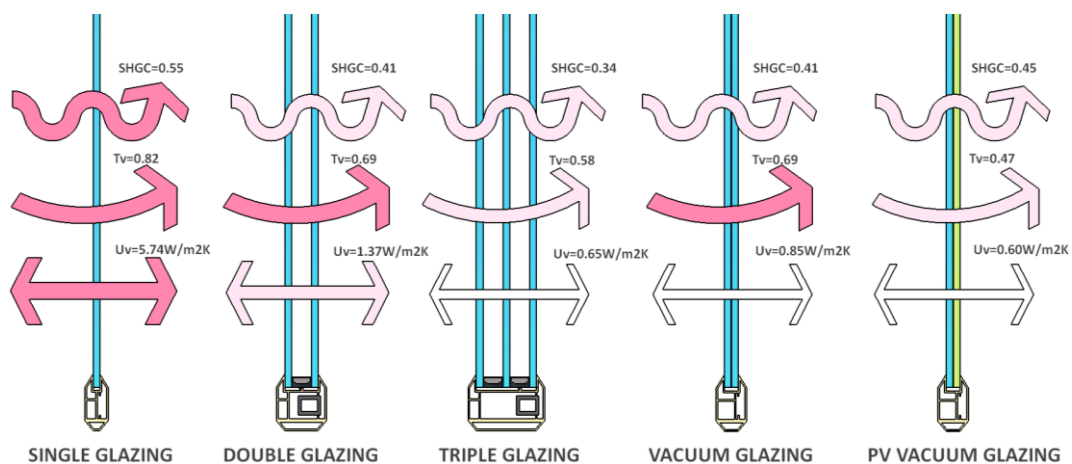


Figure 1: Section of glazing types and values utilised for the modelling process (SG, DG, TG, VG and PV accordingly).

Table 1: Glazing parameters for simulation model using Window simulation (Berkeley-Lab, 2017).

Window type	Number of glass layers	Thickness mm	U-value W/m <sup>2</sup> K	SHGC	Tvis
SG Single Glazing	1	3.9	5.74	0.54	0.82
DG Double Glazing Krypton	2	22.8	1.36	0.41	0.68
TG Triple Glazing Argon	3	41.7	0.65	0.34	0.58
VG Vacuum Glazing	2	7.8	0.85	0.41	0.68
PV Vacuum Photovoltaic	2	7.8	2.35	0.44	0.46

## 2.2. Simulation model

This mathematical study is based on an EnergyPlus™ simulation model (DOE, 2019) that utilises a window performance analysis, calculated using Window™ software (Berkeley-Lab, 2017). Initially, a series of glass panes were modelled with customised properties based in the Optitherm™S1Plus glass manufactured by Pilkington (Pilkington, 2016). Calculations on heat transfer, transparency and solar heat gain were established using the environmental condition NFRC 100-2010, these results are summarised and described in Table 1.

A compact office building of dimensions 3.00 x 3.00 x 3.00m was modelled (Fig. 2) replicating the real conditions of a reduced scale environment. This model included a window space of 2.25m<sup>2</sup> (1.5 x 1.5m) mounted on the south orientation. This fenestration was later interchanged for customised window technologies (SG, DG, TG, VG and PV). Larger cooling and heating loads are demanded in buildings with larger window-to-wall ratio (WWR). This specific simulation utilised a WWR of 6.25% in an office room of 9m<sup>2</sup>.

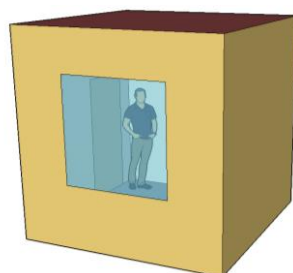


Figure 2: Building model for an office cubicle of 9m<sup>2</sup>.

Using the model on Figure 2, the setup for the simulations were carried out utilising the conduction heat transfer algorithm, adopting a full interior and exterior solar distribution (wind and solar exposure). The office schedule for lights, equipment and occupancy was employed. The exterior materials for wall elements were based on 100mm brick wall which included a 50mm insulation membrane (0.03W/m-K) and 19mm gypsum finishing. Additionally, 0.2m concrete slabs in floor and roof were modelled, finished with acoustic tiles for the roofing system and 25mm wood tiles on floor surfaces.

A derived input data file including the previous specifications was loaded into the comprehensive simulation model combining the cumulative data for the assigned weather conditions by using the EPW file for the locations summarised in Table 2. These urban locations were chosen in agreement to the five main climate groups defined by the Köppen-Geiger climate classification: Kuala Lumpur (group A, Tropical), Las Vegas (group B, Dry), London (Group C, Temperate), Beijing (Group D, Continental) and Kuujuaq (Group E, Polar).

Table 2: Climate parameters for the simulated conditions using the Köppen-Geiger classification.

Location	Köppen-Geiger climate classification	Climate type
Kuala Lumpur, MY	Af	Tropical Rainforest
Las Vegas, US	BWh	Arid Desert
London, GB	Cfb	Oceanic
Beijing, CN	Dwa	Hot Summer Continental
Kuujuaq, CA	ET	Tundra

A parametric analysis was executed considering the climate location on Table 2 and considering the five major window technologies in each simulation (single glazing SG, double glazing DG, triple glazing TG, vacuum glazing VG and photovoltaic vacuum glazing PV). This variety of climates and fenestrations aims to represent a wide variety of weather conditions and technologies to assess the suitability of each for a standardised guide of utilisation.

### 2.3. Temperature differential

This mathematical analysis is based in the zone and air system integration for energy and moisture balance, using a predictor-corrector approach. This analysis utilises the heat balance on the zone air solution scheme to calculate the energy balance for the EnergyPlus™ engine (DOE, 2017). This model is based in Equation 1, detailed as:

Equation 1: Zone air system integration for heat balance.

$$C_z \frac{dT_z}{dt} = \sum_{i=1}^{N_{sl}} \dot{Q}_i + \sum_{i=1}^{N_{surfaces}} h_i A_i (T_{si} - T_z) - \sum_{i=1}^{N_{zones}} \dot{m}_i C_p (T_{zi} - T_z) + \dot{m}_{inf} C_p (T_{\infty} - T_z) + \dot{Q}_{sys}$$

Where:

- $C_z \frac{dT_z}{dt}$  = energy stored in zone air
- $C_z = \rho_{air} C_p C_T$
- $\rho_{air}$  = density of zone air
- $C_p$  = specific heat of zone air
- $C_T$  = sensible heat capacity multiplier
- $\sum_{i=1}^{N_{sl}} \dot{Q}_i$  = sum of convective internal loads.
- $\sum_{i=1}^{N_{surfaces}} h_i A_i (T_{si} - T_z)$  = zone surfaces convective heat transfer
- $\sum_{i=1}^{N_{zones}} \dot{m}_i C_p (T_{zi} - T_z)$  = heat transfer due to interzone air mixing
- $\dot{m}_{inf} C_p (T_{\infty} - T_z)$  = heat transfer due to infiltration of outside air
- $\dot{Q}_{sys}$  = air systems output

This temperature differential utilised the output variables “Zone Mean Air Temperature” and “Zone Outdoor Air Drybulb Temperature” for the calculation of interior and exterior temperatures over a year. These variables are the sum of all exterior windows in a zone and the absolute value of the heat flow from all exterior windows (DOE, 2019).

### 2.4. Heat gain and heat loss

Considering that HVAC systems in the US consume up to 50% of the building energy and almost 20% of the total energy consumption (Pérez-Lombard, et al., 2008); cooling and heating losses are of great relevance for its impact on energy consumption. External loads on buildings are influenced importantly by the outdoor climate, meanwhile the internal loads are influenced by the occupant’s behaviour (Dotzauer, 2002). The heat gains presented in this model are in agreement with the recommended values by ASHRAE, which consider latent and sensible proportions. (ASHRAE, 2011). For this particular case, it includes the heat flow of frame, divider and glazing system to the zone (DOE, 2019).

Buildings are constrained to the cooling and heating loads to maintain thermal comfort, different climate conditions are expected to have a considerable impact on these loads. In accordance with that, cooling loads could be excessive if the solar radiation is extreme, having an impact in the overall solar heat gain coefficient. Heating loads on the other hand, depend directly on the building insulation materials and the heat transfer coefficient rated in the glass utilised. Given the fact that glass is very conductive on its own, it has reported U-values as high as 6.0W/m<sup>2</sup>K for single glazing; this is comparatively high when contrasted to other exterior materials such as solid wall, which reports U-values of 0.3W/m<sup>2</sup>K (Jelle, et al., 2012).

Output variables applied to subsurfaces that are in contact to exterior conditions are calculated in this section. In this particular case, Surface Window Heat Gain Energy and Zone Windows Total Heat Loss Energy were utilised. This calculation is equal to the sum of solar conductive gains/loss from the window glazing (DOE, 2019).

### 2.5. Heat transfer, visible transmittance and radiation heat rate

This section of the simulation effectively reports heat transfer of windows, incorporating the solar transparency and radiation rate; considering that they are the common standard for comparing commercially window attributes.



These calculations include the net heat flow through the window, solar transmittance of exterior windows, and heat transfer by solar radiation onto the interior face (DOE, 2019) reported in kWh for the span of a year. Output variables retrieved for this section included “Surface Window Net Heat Transfer Energy”, “Surface Window System Solar Transmittance” and “Zone Window Total Transmitted Solar Radiation Energy”.

### 3. RESULTS AND DISCUSSION

This research addresses the window contribution to heat transfer in office buildings, it presents an overview of the efficiency of window technologies under different climate conditions and estimate their differences in insulating capacity, heat gain/loss, visual and thermal properties (heat transfer, visible transmittance and radiation rate). The calculations are presented annually and per location, using data reported from weather stations managed by World Meteorological Organisations in each country (DOE, 2019).

#### 3.1. Temperature differential

The following results summarise the temperature difference of the window materials against the climatic conditions. Figure 3 presents the data for Kuala Lumpur, denoting the stable and warm temperature conditions of the location (26-28°C throughout the year), and the constant temperature at the interior of the building that falls in the range of 3.5-4.0 degrees higher than the exterior temperatures. SG is remarkably the least efficient of the solutions, failing to maintain a lower interior temperature and reaching the highest peak from all window samples (32.28°C in June). Annually, SG is 1.46%, 1.14%, 0.96% and 1.53% less efficient when compared to DG, TG, VG and PV respectively. Additional use of HVAC systems or passive strategies would be required to achieve thermal comfort in this location.

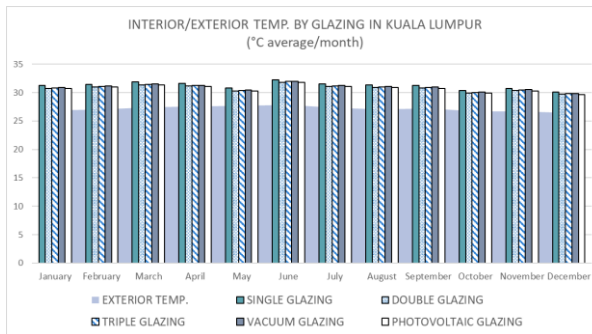


Figure 3: Temperature window-environment for Kuala Lumpur, MY

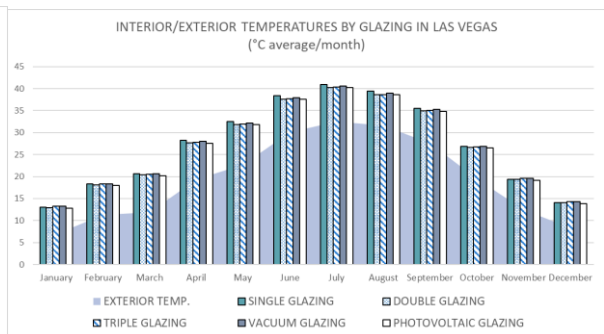


Figure 4: Temperature window-environment for Las Vegas, US

A group of more fluctuating range of temperatures is composed by Arid (Las Vegas), Oceanic (London) and Hot Summer (Beijing) locations; they follow a more similar and smoother curve in relation to their exterior temperatures; this behaviour is due in part to their relative distance to the tropics (>23.5°). From these three cities, Beijing was the only location reporting below-zero conditions (-3.82°C in January), meanwhile Las Vegas reported the highest temperatures during July (32.46°C). In regards of the performance of glazing solutions, PV vacuum glazing reduced the summertime temperatures for Las Vegas, London and Beijing; in 7.5°C, 6.27°C and 5.39°C, respectively. This effect on temperatures would have a considerable impact in the cooling loads of these three cities. Since Beijing has typical hot summer periods followed by cold winters, the temperature fluctuation is larger for this city, reporting a range of 30.25°C between its lowest and highest temperature.

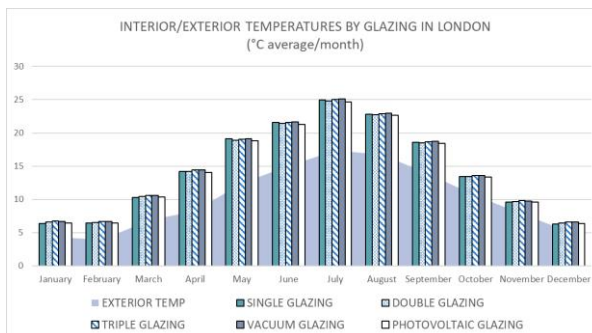


Figure 5: Temperature window-environment for London, GB

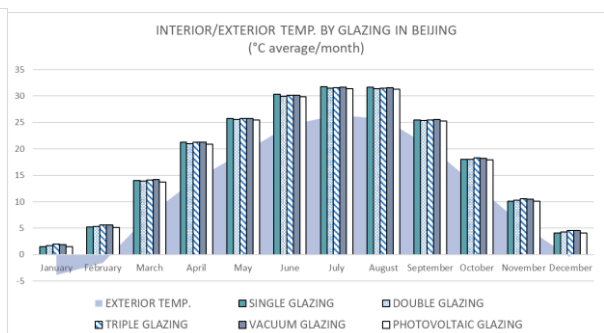


Figure 6: Temperature window-environment for Beijing, CN

For the particular sample simulated in climatic conditions of tundra (Kuujuuaq, CA); below zero temperatures are present during two-thirds of the year, markedly affecting the performance of samples during the year. For this reason, the best performance was achieved by vacuum glazing VG during summer and wintertime, increasing the extreme temperature conditions by 9.0°C and 5.44°C accordingly. Likewise, DG, TG and VG reported an improved interior temperature in this Canadian location in the ranges of 10.98%, 21.93% and 23.20% when compared to SG window sample.

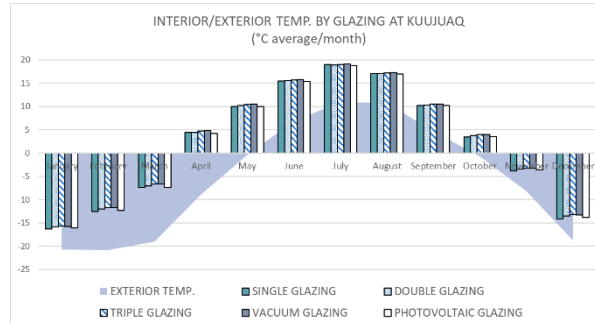


Figure 7: Temperature window-environment for Kuujuuaq, CA.

From these graphs (Figures 5 to 7) it is concluded that glazing temperature is significantly influenced by the climatic conditions that it is exposed to, particularly for severe hot/cold conditions. This affects the service range for the materials variability (Tmax-Tmin), which fluctuates in the intervals of 1.48°C, 25.52°C, 13.38°C, 30.25°C and 31.78°C as described by Kuala Lumpur, Las Vegas, London, Beijing and Kuujuuaq, respectively. This interpretation could explain why highly insulated solutions such as vacuum glazing VG and photovoltaic vacuum glazing PV had a better performance when exposed to extreme conditions, reducing such extreme conditions by 5.34% and 1.35% when compared against single glazing windows SG (Table 3).

Table 3: Exterior to interior temperature comparison for glazing types.

Temperature difference in Kuala Lumpur (°C)						
EXTERIOR TEMP.	SG	DG	TG	VG	PV	
SUMMER	27.89	32.28	31.82	31.94	31.99	31.78
WINTER	26.41	30.08	29.70	29.80	29.85	29.67
Temperature difference in Las Vegas (°C)						
EXTERIOR TEMP.	SG	DG	TG	VG	PV	
SUMMER	30.03	38.38	37.60	37.65	37.89	37.58
WINTER	8.27	14.05	14.02	14.29	14.27	13.85
Temperature difference in London (°C)						
EXTERIOR TEMP.	SG	DG	TG	VG	PV	
SUMMER	15.01	21.54	21.40	21.59	21.64	21.28
WINTER	5.11	6.30	6.47	6.59	6.56	6.38
Temperature difference in Beijing (°C)						
EXTERIOR TEMP.	SG	DG	TG	VG	PV	
SUMMER	24.49	30.31	29.96	30.10	30.17	29.88
WINTER	-0.47	4.12	4.31	4.58	4.52	4.12
Temperature difference in Kuujuuaq (°C)						
EXTERIOR TEMP.	SG	DG	TG	VG	PV	
SUMMER	6.83	15.46	15.53	15.70	15.84	15.37
WINTER	-18.80	-14.16	-13.56	-13.25	-13.35	-13.81

### 3.2. Heat gain and heat loss

Under this scenario and according to the data presented in Figure 8, the simulation case tested in Las Vegas US gives the major contributors to the heat gain energy in this model. The gains are condensed in the months from April to September for all the window technologies, having a major impact in the SG prototype, which recorded the highest heat gain during August (140.34kWh). On the other hand, the location with the substantially lowest heat gains was Kuujuaq with 3.62kWh during the month of June (TG sample). Likewise, the greatest heat losses are reported by the single glazing model (SG), this under Las Vegas and Kuujuaq climate (445.21kWh and 353.74kWh average per annum) overall. Triple, double and vacuum glazing recorded minor heat losses for the Kuala Lumpur climate (44.19kWh, 87.24kWh and 57.39kWh average yearly respectively).

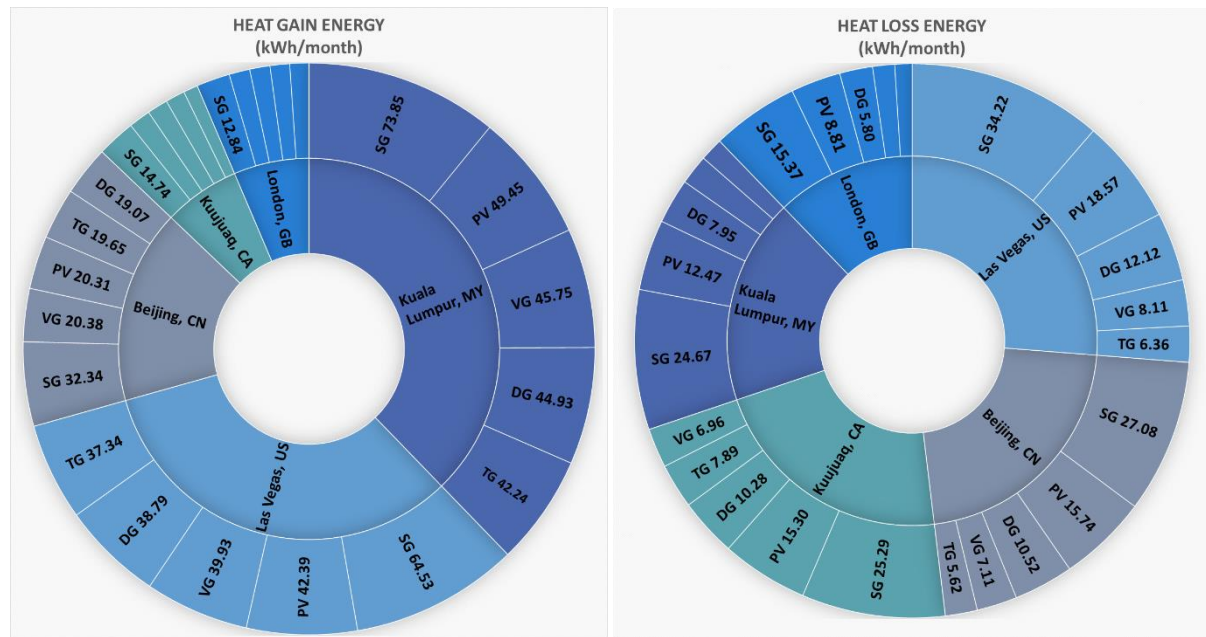


Figure 8: Impact of Heat Gain Energy (left) and Heat Loss Energy (right) of window systems in different climatic locations.

As shown in Figure 8, heat gain is predominantly covered by a substantial rate from Kuala Lumpur conditions, followed closely by Las Vegas and Beijing; tropical and arid climates will certainly have major gains and therefore TG and VG windows are then more suitable to reduce these rates. Moreover, heat losses are more equally distributed amongst locations, reporting the highest as for Las Vegas and Beijing cities. For both analysis the less impacting gain rates are presented by London, being TG (triple glazing) the more suitable solution for reducing losses in all the analysed environments.

It is worth noting that triple glazing windows (TG) reported the most reduction of heat gains in all the climate conditions, when compared to single glazing units (SG): -41.8% in Kuala Lumpur, -38.5% in Las Vegas, -37.2% in London, -38.9% in Beijing and -33.2% at Kuujuaq. This is mainly due to the fact that a double argon gap is slightly more efficient as an insulating material than vacuum glass with only one chamber. In this regard, triple glazing reported a saving on heat loss that accounts for -82.8% on average for all locations when it was compared to single glazing solutions (SG).

### 3.3. Heat transfer, visible transmittance and radiation heat rate

Heat transfer in the arid desert presented a substantial peak compared to other locations, as described by Figure 9. The highest heat transfer values are presented in the SG sample, especially during August (102.42kWh in Las Vegas); PV vacuum glazing reported the least impacting heat transfer with a minimum in Kuujuaq for the tundra climate (-18.66kWh for December), this means that the transfer of energy is conducted towards the environment in the winter extreme conditions. Overall, the PV vacuum window was reported as the most efficient technology for reducing heat transfer (-23.42% for Kuala Lumpur, -18.31% for Las Vegas, -12.98% for London, -20.1% for Beijing and -2.2% for Kuujuaq).

Using the optical properties of glazing as a comparison baseline, visible transmittance (Figure 10) reported a similar behaviour amongst the samples simulated, this is due to the optical properties of glazing that minimally change with the exposure to weather conditions. Comparably, the windows reported 0.17, 0.13, 0.10, 0.13 and 0.15 in the

visible transmittance factor for SG, DG, TG, VG, and PV respectively. The reduction of the factor on TG is proportional to the number of layers composing the sample (DG, TG, VG and PV), and the existence of LowE coatings for the VG and PV primordially.

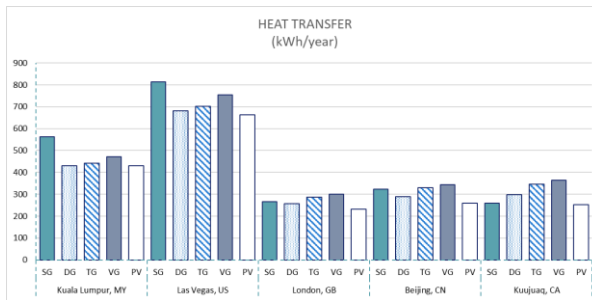


Figure 9: Heat transfer for different window technologies.

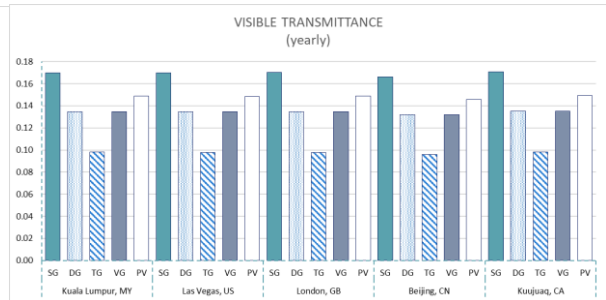


Figure 10: Visible transmittance for different window technologies.

In regards to the radiation heat rate described by the samples (Figure 11), the highest radiation rate was presented in Las Vegas location with 981.30kWh per year using single glazing, while the more decreased rate was reported in London using triple glazing windows (250.56 kWh per year). The radiation figures denoted a similar reduction in respect to the single glazing rates, decreasing -20.52% for DG, -42.18% for TG, -20.52% for VG and -12.37% for PV, respectively. The most radiated location overall was Las Vegas, followed by Kuala Lumpur, Beijing and London respectively. This result is proportional to the latitude of the locations, the last two being the northernmost of the samples simulated.

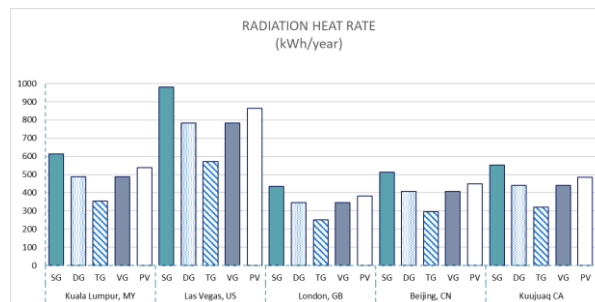


Figure 11: Radiation heat rate for different window technologies.

On the other hand, reductions of radiation heat rate by utilisation of photovoltaic vacuum glazing (PV) are present in all the conditions tested; delivering a decline of 12.36% in the radiation levels overall. Similarly, vacuum glazing solutions report an average reduction of 20.52% in relation to single glazing windows.

#### 4. CONCLUSIONS

For this mathematical model, a parametric temperature difference, heat transfer and optical analysis was conducted. This analysis was implemented for traditional window technologies against vacuum insulated fenestrations, and considering different climate conditions. Vacuum windows and photovoltaic vacuum windows resulted an excellent option for highly insulated materials for window elements, this due to its compact design, high insulating properties and adaptability to extreme weather conditions. A list of key findings from this research include:

- The influence of windows can be accounted for 20-40% of the total energy consumption in buildings while HVAC systems can consume up to 50%. Novel window technologies are an excellent solution to reduce this impact.
- For extreme temperature mitigation, photovoltaic vacuum glazing PV resulted the best option for locations in Kuala Lumpur, Las Vegas, London and Beijing. Vacuum glazing VG on the contrary was best suited for extreme cold conditions as those presented in Kuujuaq Canada.
- PV window reduced the summertime temperatures in office buildings by 7.5°C in Las Vegas, 6.25°C in London and 5.39°C in Beijing; this reduction was presented even for larger fluctuations of temperature like that presented in the Chinese capital (~30.25°C).
- In terms of temperature difference, the coldest climatic conditions in Canada resulted in better performance for DG, TG and VG, improving interior temperatures against SG by 10.98%, 21.93% and 23.20% respectively. This verifies the excellent thermal performance of evacuated glazing windows.

- For energy saving assessment, triple glazing TG reduced heat gain rates by -41.8% in Kuala Lumpur, -38.5% in Las Vegas, -37.2% in London, -38.9% in Beijing and -33.2% in Kuujuaq when compared against SG. Reduction on heat losses can be accounted by -83.8%, -83.7%, -82.9%, -81.6% and -82.3% in a similar array.
- The utilisation of a lower window-to-wall ratio can help to reduce heat gain energy in regions of warm summers, like those presented in Las Vegas. Likewise, the reduction of this ratio can diminish the heat losses in regions of cold winters like Beijing and Kuujuaq.
- Photovoltaic vacuum window was reported as the most efficient technology for reducing heat transfer in all the models simulated (-23.42% for Kuala Lumpur, -18.31% for Las Vegas, -12.98% for London, -20.1% for Beijing and -2.2% for Kuujuaq, correspondingly).
- Visible transmittance of windows reported values of 0.17 for SG, 0.13 for DG, 0.10 for TG, 0.13 for VG, and 0.15 for PV vacuum glazing. These results are proportional to the number of layers and dependant of the characteristics of coatings in samples.
- The highest radiation rate was presented in Las Vegas location with 981.30kWh per year using single glazing fenestration. From this particular sample, reductions of -20.52% (DG), -42.18% (TG), -20.52% (VG) and -12.37% for PV were reported.

This investigation has presented an insight of a sensitivity analysis using a widely approved validation scheme. Windows with thermal insulation or U-value reduction are recommended for locations with lower winter temperatures, like those presented in Kuujuaq and London; Implementation of double and triple glazing windows as well as vacuum glazing systems are recommended. Moreover, warmer weather conditions require a solar control technology that helps reducing the SHGC and solar radiation, the use of Low-E coatings and tinted glass has shown to be ideal incorporation under these circumstances.

Vacuum insulated window demonstrated its ability to reduce heat transfer compared to traditional fenestration technologies; certainly a more extensive use of this technology is forecasted in the near future, particularly when improvements in the manufacturing process and cost of assembly would convert these novel fenestration technologies a broadly available window solution.

## 5. ACKNOWLEDGEMENT

This research work was partially funded by the Mexican Council of Science and Technology (CONACYT) and the “Novel thin-film Photovoltaic Vacuum Glazing” project by InnovateUK; their full support is acknowledge by the authors.’

## 6. REFERENCES

- Arici, M., Karabay, H. & Kan, M., 2015. Flow and heat transfer in double, triple and quadruple pane windows. *Energy and Buildings*, Volume 86, pp. 394-402.
- ASHRAE, 2011. *Handbook - HVAC Applications*. Atlanta: American Society of Heating, Refrigerating and Air-Conditioning Engineers.
- Berkeley-Lab, 2017. *Window v7.6.4.0*, Berkeley: The Lawrence Berkeley National Laboratory.
- Cuce, E. & Cuce, P. M., 2016. Vacuum glazing for highly insulating windows: Recent developments and future prospects. *Renewable and Sustainable Energy Reviews*, Volume 54, pp. 1345-1357.
- DOE, U. D. o. E., 2017. *Engineering Reference*. Chicago: University of Illinois & Ernest Orlando Lawrence Berkeley National Laboratory.
- DOE, U. D. o. E., 2019. *EnergyPlus 9.1.0*, Berkeley: Department of Energy United States.
- DOE, U. D. o. E., 2019. *Input Output Reference*. Chicago: University of Illinois & Ernest Orlando Lawrence Berkeley National Laboratory.
- Dotzauer, E., 2002. Simple model for prediction of loads in district-heating systems. *Applied Energy*, 73(3-4), pp. 277-284.
- Ghosh, A. & Norton, B., 2018. Advances in switchable and highly insulating autonomous (self-powered) glazing systems for adaptive low energy buildings. *Renewable Energy*, pp. 1003-1031.

- Ghosh, A., Sundaram, S. & Mallick, T. K., 2018. Investigation of thermal and electrical performances of a combined semi-transparent PV-vacuum glazing. *Applied Energy*, Volume 228, pp. 1591-1600.
- Jelle, B. et al., 2012. Fenestration of today and tomorrow: A state-of-the-art review and future research opportunities. *Solar Energy Materials & Solar Cells*, Volume 96, pp. 1-28.
- Pérez-Lombard, L., Ortiz, J. & Pout, C., 2008. A review on buildings energy consumption information. *Energy and Buildings*, Volume 40, pp. 394-498.
- Pilkington, 2016. *Pilkington Optitherm™ Range*, Lancashire: NSG Group.
- Pilkington™, 2016. *Pilkington™ K Glass Range*, Lancashire: NSG Group.
- Pilkington™, 2018. *Pilkington Planar™*, Lancashire: NSG Group.
- Qiu, C., Yang, H. & Sun, H., 2019. *Investigation on the thermal performance of a novel vacuum PV glazing in different climates*. Hong Kong, 10th International Conference on Applied Energy, pp. 706-711.
- Son, H. & Song, T., 2019. Heat transfer and stress distribution in the central part of vacuum glazing. *Applied Thermal Engineering*, Volume 159.
- Zhao, J. F. et al., 2007. A modified pump-out technique used for fabrication of low temperature metal sealed vacuum glazing. *Solar Energy*, pp. 1072-1077.

---

## #87: Thermal performance evaluation for building application of phase change material blister panels

---

Mariana VELASCO-CARRASCO<sup>1</sup>, Ziwei CHEN<sup>2</sup>, Jorge Luis AGUILAR-SANTANA<sup>3</sup>  
Saffa RIFFAT<sup>4</sup>

<sup>1</sup> Department of Architecture and Built Environment, Faculty of Engineering, University of Nottingham, University Park, NG7 2RD, UK, mariana.velascocarrasco@nottingham.ac.uk

<sup>2</sup> Department of Architecture and Built Environment, Faculty of Engineering, University of Nottingham, University Park, NG7 2RD, UK, ziwei.chen@exmail.nottingham.ac.uk

<sup>3</sup> Department of Architecture and Built Environment, Faculty of Engineering, University of Nottingham, University Park, NG7 2RD, UK, jorge.aguilarsantana@nottingham.ac.uk

<sup>4</sup> Department of Architecture and Built Environment, Faculty of Engineering, University of Nottingham, University Park, NG7 2RD, UK, saffa.riffat@nottingham.ac.uk

*Phase Change Materials or PCMs are substances that can store high quantities of thermal energy due its high heat capacity; they have been used as an efficient way for passive cooling control, increasing the thermal inertia in building envelopes, reducing the energy demand while helping achieve thermal comfort. In this paper, a novel blister design is proposed to encapsulate the PCM for ceiling tile application. The feasibility of the blister design is assessed by experimental work. A set of three samples including Inertek 23 as the base fluid were tested; a base panel containing only pure PCM, a second composite sample, integrating aluminium wool at 3.77% and a third composite, using steel wool at a concentration of 2.3%. The results showed that the PCM blister panels are an effective solution for ceiling tile incorporation, reducing the indoor ambient temperature. The Base panel presented the lowest temperature range in both cases, proving that the enhancement particles have a positive effect over the PCM. The addition of steel enhancement proved to have the best thermal performance of all the panels, improving the temperature reduction 7 and 17% more in comparison to the pure PCM and aluminium panel respectively.*

*Keywords: energy storage; phase change materials; thermal performance*

## 1. INTRODUCTION

Energy storage is considered to be the best technological advancement for energy conservation (Anisur, et al., 2013). Phase change materials (PCMs) have the property to absorb, store and release large amounts of thermal energy by utilising the latent heat of the phase change; reducing the peak demand and improving the thermal comfort (Salunke & Shembekar, 2012), (Kalnæs & Jelle, 2015), (Wang, et al., 2019). The thermal performance of PCMs depends on the melting temperature, thermal conductivity, and energy storage density. Ideally, a PCM for thermal energy storage applications requires a rapid melting and solidification point (Ji, et al., 2014), (Ma, et al., 2013).

Paraffins, salt hydrates and fatty acids are the most popular PCMs having a wide temperature range within human thermal comfort, making them suitable for building applications. However, the PCMs can have low thermal conductivity; this factor is a main characteristic of the organic PCMs. Enhancing a PCM is an attractive technique to boost the performance of the material (Khodadadi, et al., 2013). In consequence, there are several solutions to improve the thermal conductivity and ability to promote energy exchange, such as the use of fins, heat pipes, micro and macro-encapsulation or the addition of nanoparticles with high thermal conductivity in the PCM base fluid as nano-enhanced PCM (Ma, et al., 2013), (Khodadadi, et al., 2013). Further methods propose the integration of metallic fins, foams wools and graphite (Ji, et al., 2014), (Wu, et al., 2013). A comprehensive review of PCM enhancement materials were revised by Velasco et al. finding that graphite, aluminium and carbon are the most frequently applied materials for organic PCM (Velasco-Carrasco, et al., 2018).

PCMs can be incorporated in active systems and passive systems. Passive design includes using the daytime solar energy for heating and cold night-time ambient energy for cooling (Arkar & Medved, 2007); active technologies use alternative units, such as heat pump systems, heat recovery, solar panels among others (Zhu, et al., 2009). The effects of adding PCM into building components have been widely investigated, for ceiling application Yahaya and Ahmad have studied a PCM mixture of lauric and stearic acid into a gypsum board, reducing the indoor temperature by 2°C (Yahaya & Ahmad, 2011). Other studies with a paraffin lightweight concrete as aggregate achieved a decrement of the indoor temperature by 2.9°C using a macroencapsulation (Memon, et al., 2015). The effects of an HVAC-PCM were studied by Saffari et al. using computational model in Madrid; finding that the PCM improve the cooling and heating energy performance in residential buildings (Saffari, et al., 2016).

There are two methods to integrate PCM in building elements. The first method, known as “shape-stabilised” considers the direct addition of the PCM into a building element, such as a gypsum wall (Silva, et al., 2016). In the majority of cases the PCMs need to be encapsulated for technical use, as otherwise the material would disperse from the location (Cabeza, et al., 2011). For this reason, the encapsulation method is the most used form of integration and has become a topic of analysis among researchers. The geometry of the encapsulation can take any shape; the most used ones are tubes, pouches, spheres and panels. The encapsulation geometry could potentially function as a heat enhancement method, improving the thermal conductivity of the PCMs (Amin & Belusko, 2014). Other benefit of the encapsulation is the capacity to counteract phase segregation, which is a regular phenomenon presented particularly in salt hydrates, in which the high storage density of the material disperse in layers, leading to the decline in the storage efficiency.

In a study conducted by Wei et al. it was demonstrated that among a sphere, cylinder, plate and tube; the sphere had the highest heat transfer rate, follow by the cylinder, plate and tube at last (Wei, et al., 2005). Zhang et al. investigated a microencapsulated PCM based on a silica shell to enhance the thermal conductivity. The study reported that the microcapsules indicate a high performance, achieving adequate phase change and improving the thermal conductivity (Zhang, et al., 2010). Similarly, Darkwa et al. studied the thermal performance of a high composite microencapsulated PCM board with three configurations: rectangular, triangular and pyramidal. The results showed that the thermal response time for the rectangular and triangular geometries were half that of pyramidal geometry. Furthermore, when compared with pure PCM the thermal conductivity increase over ten times. Nevertheless, a considerable reduction in the energy storage capacity was observed (Darkwa & Su, 2012).

Popular materials for encapsulation are polypropylene, polyolefin, polyamide, silica, polyurea, urea– formaldehyde, copper and aluminium (Salunke & Shembekar, 2012). For the salt hydrates, the corrosiveness with the metals reduces the encapsulation solutions, favouring plastic materials. Blant et al. proposed as basic encapsulation requirements: a heat transfer surface, structure stability, offer corrosion resistance and thermal stability (Bland, et al., 2017). It is seen in Table 1 potential encapsulation materials for PCMs.



Table 1: Potential containers materials for PCM encapsulation (Jacob & Bruno, 2015).

Group	Potential materials	Advantages	Disadvantages	Potential applications
Metallic	Steel (stainless and carbon), nickel/chromium/carbon/ruthenium	- High mechanical strength - Encapsulation by electroplating preformed, etc. - High thermal stability	- Potential corrosion - Higher cost	High temperature applications
Inorganic	Silicon dioxide, titanium dioxide, sodium silicate, calcium carbonate, silica	- High thermal stability - High thermal mechanical strength - Cheaper than metallic	- Porous shell can lead to leakage	High temperature applications Industrial processes application
Plastic	M-F, VTMS, UFR, BA-DVB, P(MMA-co-DVB), BMA-MMA copolymer, poly(urethane-urea), St-MMA, polystyrene	- Cheaper than metallic shells - Different encapsulation methods chemical and physical	- Relative low thermal stability - Low thermal conductivity	Application in building cooling and various industrial processes (food and paper manufacturing)

The classification for the encapsulation is based on the size of the container surrounding the PCM. Macroencapsulation covers diameters from 1mm onwards and is the *most used method for PCM encapsulation* (Jradi, et al., 2013). The microencapsulation covers from 1 $\mu$ m to 1mm and the nano is less than 1- $\mu$ m (Jacob & Bruno, 2015). *Microencapsulation represents higher complexity than macroencapsulation, nevertheless* the advanced technological developments have made it possible to encapsulate the PCM at the nano-scale, resulting in *higher heat transfer rates in comparison to macroencapsulation* (Hawladar, et al., 2003), (Khudhair & Farid, 2004).

The aim of this paper is to experimentally investigate the feasibility of a novel blister PCM panel for ceiling tile applications. As previously discussed, organic PCMs have low thermal conductivity; therefore, there is a substantial need to further enhance the thermal properties of the material. Two techniques including the addition of aluminium and steel wool were utilised for improving the thermal performance of the PCM. A set of three samples including Inertek 23 as the base fluid were tested: a base panel was created, containing only pure PCM, a second composite sample, integrating aluminium wool at 3.77% and a third composite, using steel wool at a concentration of 2.3%.

## 2. METHODOLOGY

### 2.1 Experimental setup

The study describes a set of experiments performed in the Environmental Climatic Chamber in the Marmot Laboratory, at the University of Nottingham. Three types of PCM blister panels were tested under the same environmental conditions. Previous studies have favoured the blister panel performance over other encapsulation methods, thus the blister panel was selected for further experimentation. Table 2 presents three panels selected for testing, the base panel contains pure PCM, and the second and third panel contain aluminium wool and steel wool respectively. The panels were allocated in a control box outside the environmental chamber, air from the environmental chamber was blown into the control box and the inlet, outlet, panel and ambient temperature were monitored throughout the test, as seen in Figure 1.

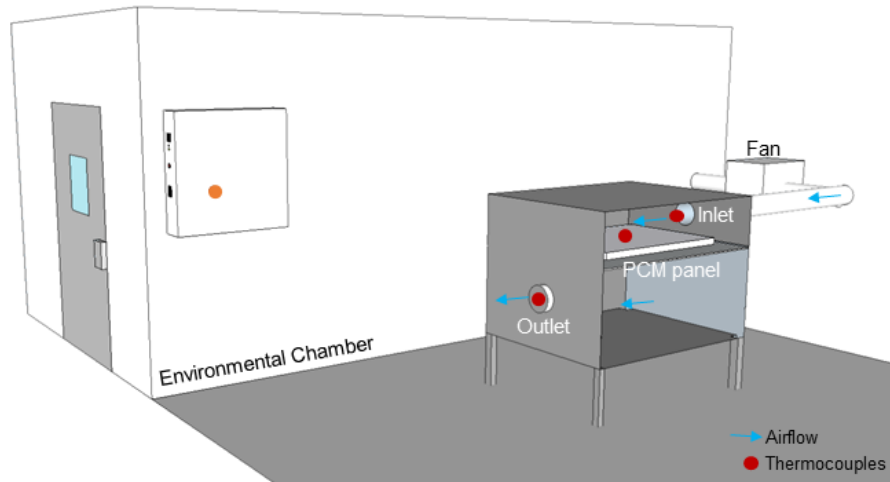


Figure 1: Schematic setup of the panel rig.

### 3.2 Material selection

The principle of microencapsulation is to create an envelope around the phase change material micro-particles, improving the heat transfer to the surroundings while avoiding phase segregation. INERTEK microcapsules have a size ranging from 5 to 25  $\mu\text{m}$ , the industrial reference is INERTEK 23 P. The PCM was selected based on its low melting point and thermal properties.

To enhance the thermal conductivity of the INERTEK 23 the addition of steel and aluminium wool was considered due to their low cost, light structure, and high thermal conductivity. Adding the wool particles prevents the material segregation, at the same time provides more contact area. The nano-enhanced PCM was prepared by using the two-step method, in which the enhancement material is produced and then added into the base fluid. The two-step method is economic and commonly applied. The dispersion of the material is random, the particles fluctuate in size, geometry, and volume; the proportion of the materials varies due to the manufacturing process. Table 2 contains the components selected for each panel.

Table 2: PCM blister panels composition.

Panel Name	PCM	Enhancement Material	$C_p$ (kJ/(kg K))	PCM mass (kg)	Enhancement mass (kg)	Total weight (kg)
Base Panel	INERTEK 23	-	-	0.538	-	0.538
Compound 1	INERTEK 23	Aluminium wool	0.91	0.371	0.014	0.385
Compound 2	INERTEK 23	Steel wool	0.49	0.390	0.009	0.399

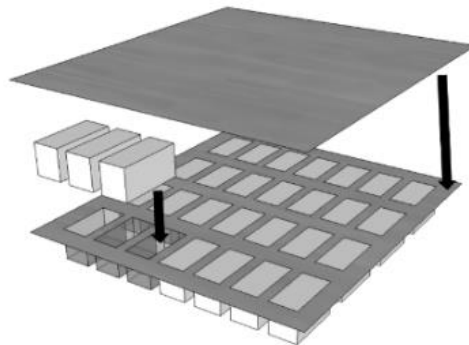


Figure 2: Schematic diagram of the blister panel.

The encapsulation material is a plastic blister measuring 15 x 15 x 2cm, the PCM is allocated into a plastic blister container and sealed with thermal conductive tape; the packaging was a weight of 14 gr per panel. A set of nine

panels was created for each scenario in order to simulate a 45cm x 45cm ceiling tile module (Figure 3). The control box has 70 x 67 x 73 cm the blister panels were allocated in the top section, over a metallic mesh surface. The inlet and outlet measure 18 cm in diameter and air coming from the Environmental Chamber was blown with the aid of an electric fan. Each test was repeated three times and the results average was noted.



Figure 3: Left- set of 9 blister panels Right- panel testing in the control box.

### 3. RESULTS

#### 3.1 Experimental results

Figure 4 shows the temperature range of the three blister panels, and the experiment was maintained during 19605 seconds (5.44 hrs). The environmental chamber temperature was constant at 28°C in all scenarios; the temperature was selected based on the enthalpy values and previous testing to ensure the melting process of the PCM. The temperature of the panels increased dramatically as the chamber initial temperature is higher than the PCM melting point. After the initial surge, it is seen that the Compound 1 and 2 reach a plateau at the 14585 second (4.05 hrs), while the Base panel maintains temperature increments for most of the testing period. The Compound 2 corresponding to the steel enhancement presents the highest temperatures among the panels, meaning that the panels is absorbing more heat as it melts. The Base panel has the lowest values reaching a maximum of 25.8°C.

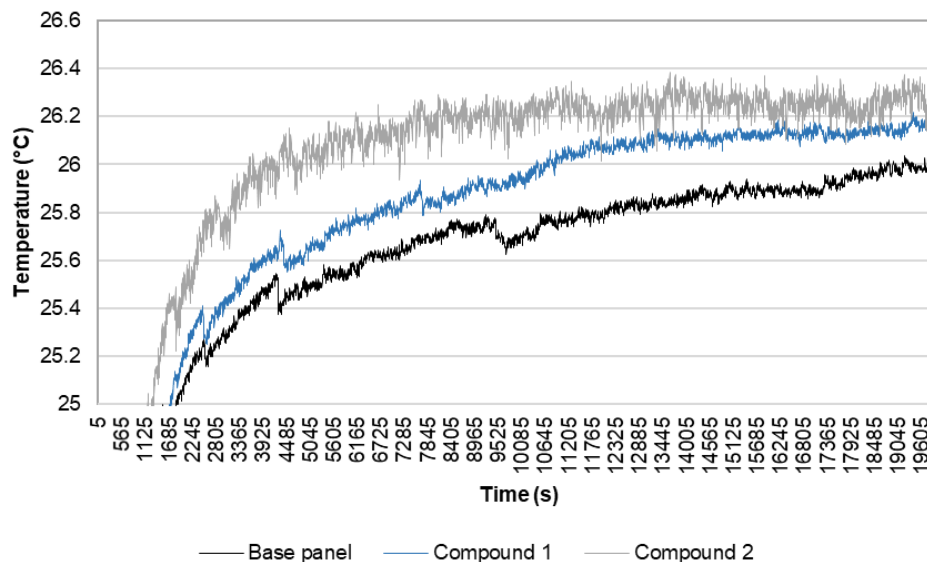


Figure 4: Test 1- Blister panels comparison at 28°C.

A second testing shows in Figure 5 the results for the temperature variation of the three panels. The experiment was maintained for 21085 seconds (5.8 hrs) with 2°C increments every two hours. The starting temperature was considered at 23°C while ending temperature was established at 27°C. The Base panel and Compound 1 presented similar trends, with a slightly higher temperature range in the aluminium mixture. The Compound 2 presents a minimal decrement in temperature in the first stage of the test, however the temperature levelled up once the second temperature increment is applied, and from this point onwards the temperature variation is considerably

higher than the other samples. In general, the test supports the conclusion that both compounds absorb more heat in comparison to the pure PCM panel.

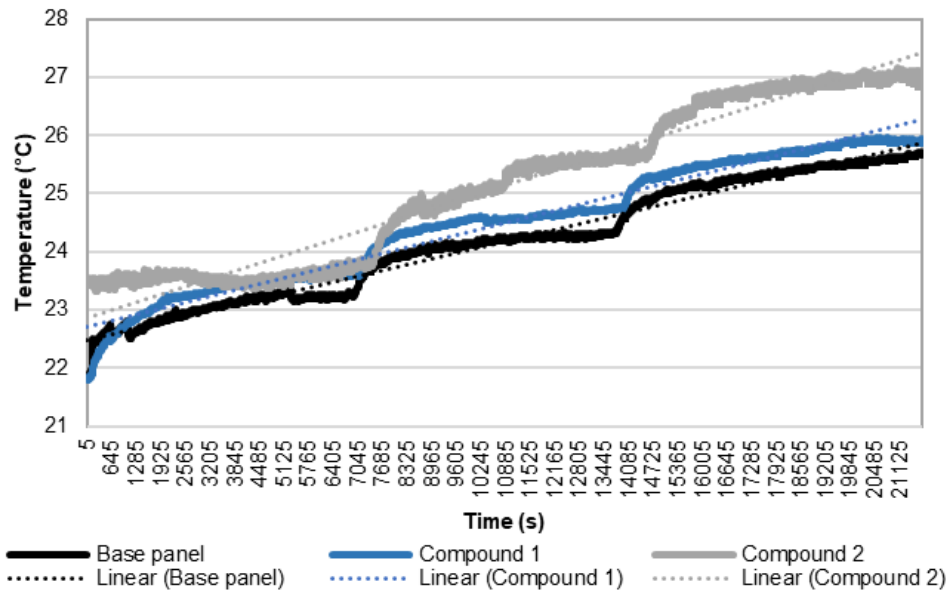


Figure 5: Test 2- Blister panels comparison with 2°C increments.

### 3.2 Discussion

The testing considers the performance of three blister panels with different material compositions. The temperature reduction and heat absorption varies for in all panels, for all cases the PCM panels have reduced the temperature by absorbing heat. Table 3 shows the heat absorption and average temperature drop for both tests.

Table 3: PCM blister panels heat absorption and average temperature drop.

	Mass (kg)	Average temperature drop (°C)		Average temperature drop (°C)	
		Q (kJ)	Average temperature drop (°C)	Q (kJ)	Average temperature drop (°C)
		Test 1		Test 2	
Base panel	0.538	0.986032	0.83308	0.406065	0.343076
Compound 1	0.371	0.621503	0.74976	0.326137	0.395609
Compound 2	0.390	0.771921	0.89507	0.31911	0.436361

The base panel considers pure INERTEK 23; this panel proved the highest heat absorption in comparison to the enhanced panels. Previous studies have concluded that the heat transfer performance depends strongly on the amount of PCM applied (Baby & Balaji, 2012). Among the tested panels, the Compound 2 presented the highest performance in relation to the average temperature reduction and the absorbed heat capacity despite having the 30% less amount of composite materials (PCM and steel wool) in comparison to the pure PCM.

Using the steel wool enhances the performance when compared to the pure INERTEK 23. In contrast the application of the aluminium wool has not given conclusive results, this could be mainly due of the amount of PCM inside the blister panel or/and the distribution of the particles in the base fluid. The enhancement in the heat transfer rate depends on the percentage of nanoparticles blend (Abdelrahman, et al., 2019). Further investigation is advice to establish the effect of the nano-enhanced particles with INERTEK 23.

### 4. CONCLUSIONS

In this research paper, the feasibility of the blister design for ceiling tile application was assessed by experimental work. INERTEK 23 with a melting point of 23°C was used as a feasible organic PCM for low-temperature thermal energy storage application. Aluminium and steel wool were selected as heat transfer materials due to their low cost, light structure, high thermal conductivity. A set of three samples were created for the experimentation; the panels consist on pure PCM, PCM/aluminium wool and PCM/steel wool mixture.

The main findings of the experimental study can be summarised as follows:

- In all cases, the blister panel was able to reduce the temperature of the control box. This shows the effectiveness of the blister encapsulation method, allowing the PCM to absorb the incoming heat and proving the feasibility for indoor application. For first test, the Base panel presented a temperature reduction of 0.83°C, while the Compound 1 had 0.74°C and 0.89°C for the Compound 2.
- This testing is represented a 45 x 45 cm ceiling tile, for building applications the amount of tiles would be considerably higher, meaning that the temperature reduction would be also expanded.
- Due to the manufacturing process and the structure of the enhancing material, the mass of the samples presented weight discrepancies, having a total mass of 0.538, 0.385, 389 kg, for the Base panel, Compound 1 and Compound 2 respectively. Significant work is still needed to explore the effects of the nano-enhancement particles to archive the optimal percentage distribution of materials.
- The Base panel presented the lowest temperature range in both cases, proving that the enhancement particles have a positive effect over the PCM.
- The highest temperature was achieved during the second test, where the Compound 2 reached a temperature of 27°C.
- The addition of steel enhancement proved to have the best thermal performance of all the panels; presenting the highest temperature reduction despite having the 30% less composite materials in comparison to the pure PCM.

## 5. ACKNOWLEDGEMENT

This work was supported in part by the Science and Technology Council of Mexico (Consejo Nacional de Ciencia y Tecnologia, CONACYT).

## 6. REFERENCES

- Abdelrahman, H., Wahba, M., Refaey, H. & Moawad, M. B. N., 2019. Performance enhancement of photovoltaic cells by changing configuration and using PCM (RT35HC) with nanoparticles Al<sub>2</sub>O<sub>3</sub>. *Solar Energy*, pp. 665-671.
- Amin, N. B. F. & Belusko, M., 2014. Effective thermal conductivity for melting in PCM encapsulated in a sphere. *Applied Energy*, Volume 122, pp. 280-287.
- Anisur, M., Mahfuz, M. K. M., Saidur, R. & Metselarr, I. M. T., 2013. Curbing global warming with phase change materials for energy storage. *Renewable and Sustainable Energy Reviews* , pp. 23-30.
- Arkar, C. & Medved, S., 2007. Free cooling of a building using PCM heat storage integrated into the ventilation system. *Solar Energy*, 81(9), pp. 1078-10878.
- Baby, R. & Balaji, C., 2012. Thermal management of electronics using phase change material based pin fin heat sinks. *Journal of Physics: Conference Series* , Volume 395, p. 012134.
- Bland, A., Khzouz, M., Statheros, T. & Gkanas, E., 2017. PCMs for residential building applications: A short review focused on disadvantages and proposals for future development. *Buildings*, Volume 7, p. 18.
- Cabeza, L. et al., 2011. Materials used as PCM in thermal energy storage in buildings - A review. *Renewable Sustainable Energy Reviews*, p. 1675–1695.
- Darkwa, J. & Su, O., 2012. Thermal simulation of composite high conductivity laminated microencapsulated phase change material (MEPCM) board. *Applied Energy*.
- Hawladar, M., Uddin, M. & Khin, M., 2003. Microencapsulated PCM thermal-energy storage system. *Applied Energy*, 74(1-2), pp. 195-202.
- Jacob, R. & Bruno, F., 2015. Review on shell materials used in the encapsulation of phase change materials for high temperature thermal energy storage. *Renewable and Sustainable Energy Reviews*, pp. 79-87.
- Ji, H. et al., 2014. Enhance thermal conductivity of phase change materials with ultrathin-graphite foams for thermal energy storage. *Energy and Environmental Science*, pp. 1185-1192.
- Jradi, M., Gillot, M. & Riffat, S., 2013. Simulation of the transient behaviour of encapsulated organic and inorganic phase change materials for low-temperature energy storage. *Applied Thermal Engineering* , pp. 211-222.

- Kalnæs, S. & Jelle, B., 2015. Phase change materials and products for building applications: A state-of-the-art review and future research opportunities. *Energy and Buildings*, pp. 150-176.
- Khodadadi, J., Fan, L. & Babaei, H., 2013. Thermal conductivity enhancement of nanostructure-based colloidal suspensions utilizes as phase change materials for thermal energy storage: A review. *Renewable and Sustainable Energy Reviews*, Volume 24, pp. 418-444.
- Khudhair, A. & Farid, M., 2004. A review on energy conservation in building applications with thermal storage by latent heat using phase change materials. *Energy Conversion and Management*, 45(2), pp. 263-275.
- Ma, Z., Lin, W. & Sohel, M., 2013. Nano-enhanced phase change materials for improved building performance. *Renew. Sustain. Energy Rev.*, pp. 1256-1268.
- Memon, S., Cui, H., Zhang, H. & Xing, F., 2015. Utilization of macro encapsulated phase change materials for the development of thermal energy storage and structural lightweight aggregate concrete.. *Applied Energy*, Volume 139, pp. 43-55.
- Microsystems, L., 2019. *Leica Microsystems*. [Online] Available at: [www.leica-microsystems.com](http://www.leica-microsystems.com)
- Saffari, M., Gracia, A., Ushak, S. & Cabeza, L., 2016. Economic impact of integrating PCM as passive system in buildings using Fanger comfort model. *Energy and Buildings*, pp. 159-172.
- Salunke, P. & Shembekar, P., 2012. A review on the effect of phase change material encapsulation on the thermal performance of a system. *Renewable and Sustainable Energy Reviews*, 16(8), pp. 5603-5616.
- Silva, T., Vicente, R. & Rodrigues, F., 2016. Literature review on the use of phase change materials in glazing and shading solutions. *Renewable and Sustainable Energy Reviews*, Volume 53, pp. 515-535.
- Velasco-Carrasco, M., Ziwei, C., Aguilar-Santana, J. & Riffat, S., 2018. Review on enhancement methods for phase change materials. *17 International Conference on Sustainable Energy Technologies*, Volume 3, pp. 130-138.
- Wang, H., Lu, W., Wu, Z. & G., Z., 2019. Parametric analysis of applying PCM wallboards for energy saving in high-rise lightweight buildings in Shanghai. *Renewable Energy*.
- Wang, X. M. A., 2007. Heat transfer characteristics of nanofluids: A review. *International Journal of Thermal Science*, pp. 1-19.
- Wei, J., Kawaguchi, Y., Hirano, S. & Takeuchi, H., 2005. Study on a PCM heat storage system for rapid heat supply. *Applied Thermal Engineering*, pp. 2903-2920.
- Wu, S. Y., Wang, H., Xiao, S. & Zhu, D., 2013. An investigation of melting/freezing characteristics of nanoparticle-enhanced phase change materials. *Journal of Thermal Analysis and Calorimetry*, 110(3), p. 1127–1131.
- Yahaya, N. & Ahmad, H., 2011. Numerical investigation of indoor air temperature with the application of PCM gypsum board as ceiling panels in buildings. *Procedia Engineering*, Volume 20, pp. 238-248.
- Yu, X. & Xie, H., 2012. A review on nanofluids: preparation, stability mechanisms and applications. *Journal of Nanomaterials*, pp. 1-17.
- Zhang, H., Wang, X. & Wu, D., 2010. Silica encapsulation of n-octadecane via sol-gel process: A novel microencapsulated phase-change material with enhanced thermal conductivity and performance. *Journal of Colloid and Interface Science*, pp. 246-255.
- Zhang, H., Wang, X. & Wu, D., 2010. Silica encapsulation of n-octadecane via sol-gel process: A novel microencapsulated phase-change material with enhanced thermal conductivity and performance. *Journal of Colloid and Interface Science*, pp. 246-255].
- Zhu, N., Ma, Z. & Wang, S., 2009. Dynamic characteristics and energy performance of buildings using phase change materials: A review. *Energy Conversion and Management*, 50(12), pp. 3169-3181.

---

## #88: Heat and mass transfer study for the dew-point evaporative cooler with porous layer in wet channel

---

Yuting LIU<sup>1</sup>, Jun Ming LI<sup>2</sup>

<sup>1</sup> Key Laboratory for Thermal Science and Power Engineering of Ministry of Education, Department of Energy and Power Engineering, Tsinghua University, Beijing 100084, China, liu-yt14@mails.tsinghua.edu.cn

<sup>2</sup> Key Laboratory for Thermal Science and Power Engineering of Ministry of Education, Department of Energy and Power Engineering, Tsinghua University, Beijing 100084, China, lijm@tsinghua.edu.cn

*This paper proposed a two-dimensional numerical model for the heat and mass transfer process in dew-point evaporative cooler with porous layer covering the wet surface. Water flows down along the wet surface covered by a fibrous layer which can intensify the water wettability and increase the wetting area, and transfers the heat and water vapour with secondary air in wet channel and heat with primary air in dry channel. The water downward flow in porous layer is governed by Darcy-Brinkman Equation and the heat and mass transfer in gas-liquid interface is derived from the molecular dynamics equation. The coupled momentum and heat and mass transfer equations for primary air, water and secondary air are solved by COMSOL. The distribution of temperature and heat distribution and the influence of porosity of the porous fibrous layer, inlet air velocity, working-to-primary air ratio and water inlet velocity and temperature on heat and mass transfer between the water and air are numerically studied and analysed. The numerical results showed that the influence of porosity of the porous layer is not significant, but the inlet air velocity and working-to-primary air ratio and water inlet velocity and temperature influence the cooling performance of dew-point evaporative cooler a lot.*

*Keywords: dew-point; evaporative cooler; experimental study; numerical study; optimization*

## 1. INTRODUCTION

Evaporative cooling is an energy-saving and environmentally friendly cooling technology where the heat is absorbed and the air cooled through water evaporation. Evaporative cooling methods can be divided into direct evaporative cooling (DEC) and indirect evaporative cooling (IEC) according to whether or not the product air is in contact with water. The IEC systems have an additional sensible heat exchange channel which is called the dry channel compared to DEC systems which have only a wet channel where the air contacts the water directly. Therefore, IEC systems have more applications than DEC systems because the product air (also called the supply air) is cooled without added moistures (Maheshwari, 2001). The air in the dry channel is called the primary air while the air in the wet channel is the secondary air or working air. The product air can be cooled to the wet-bulb temperature of the incoming air for an ideal system, but the actual wet-bulb efficiencies of DEC systems are 40-80% and the cooling capacities are largely dependent on the incoming air properties (Duan, 2012). The cooling efficiency can be improved by using dew-point evaporative cooling (also called M-cycle IEC) that improves the IEC design (Maisotsenko, 2003; Elberling, 2006; Xu, 2017). In this design, the secondary air (also called working air) is first cooled in the dry channel before entering the wet channel so that the product air temperature can be lowered to the dew point of the incoming air for an ideal design. The wet-bulb efficiencies of M-cycle IEC systems are 10-30% higher than those of IEC systems (Elberling, 2006).

The cooling efficiency and the temperature drop of the product air in the dew-point evaporative cooler are obviously influenced by the water wettability on the wet channel surface. The water wettability on the wet channel surface is mainly influenced by the wet surface material and many researchers studied the impacts of the wet surface materials on the evaporative cooler performance. Nowadays, many porous materials are used on the wet channel surface of dew-point evaporative coolers to enlarge the water wettability and improve the cooling efficiency of the dew-point evaporative cooler (Xu, 2017; Zhan, 2011; Liu, 2019; Zhao, 2009).

Many researchers have numerically studied the influence of various factors on the performance of dew-point evaporative coolers (Riangvilaikul, 2010; Anisimov, 2014; Zhao, 2008; Zhan, 2011a; Heidarinejad, 2015; Camargo, 2003), but for most of the numerical models, the influence of porous material and water film has not been considered, where the heat and mass transfer between the air and water is modelled using empirical correlations of convective heat and mass transfer coefficients. Because of these simplifications, the prediction accuracy for the dew-point evaporative cooler is not high enough and the influence of some factors like porous material and water flow are not clear.

In this study, a conjugate model including the flow and heat transfer between the primary air, secondary air and water film in porous medium is developed to study the heat and mass transfer process in dew-point evaporative cooler.

## 2. NUMERICAL MODEL

### 2.1. Mathematical equation

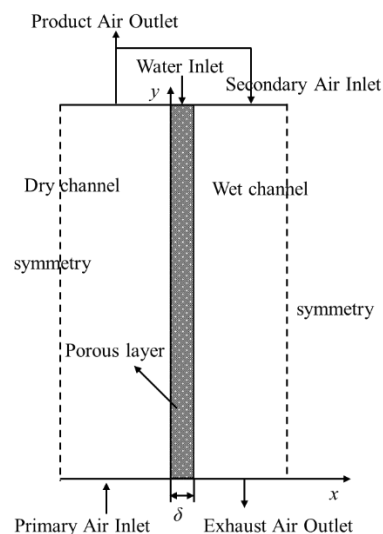


Figure 11: Physical model of the heat and mass exchanger for a dew-point evaporative cooler



As shown in *Figure 11*, the wet channel surface is covered with a thin porous layer to enlarge the water wettability where the liquid-saturated porous layer is assumed to be isotropic and homogeneous. The secondary air in wet channel is distributed from the primary air near the dry channel outlet and the primary air transfers heat to the liquid film and across to the secondary air, so the energy, momentum and diffusion equations for the primary air, the water film and the working air need to be solved simultaneously. The mathematical model for the heat and mass exchanger was based on the following assumptions:

- (1) The air and water flow is laminar and steady;
- (2) The local thermal equilibrium is valid in porous layer;
- (3) Dufour and Soret effects are negligible;
- (4) The liquid–gas interface is located at the surface of the porous layer.

The governing equations for the air and water film are as follows:

(a) Water film region

The water flow in porous layer is governed by Darcy-Brinkman equation as Equation 1, and the energy equation is shown as Equation 2, where the  $k_{\text{eff}}$  is the effective thermal conductivity for water in porous media and is calculated as Equation 3.

Darcy-Brinkman Equation:

$$\text{Equation 1: } \frac{1}{\varepsilon} \rho_f (\mathbf{u}_f \cdot \nabla) \frac{\mathbf{u}_f}{\varepsilon} = -\nabla p_f + \nabla \cdot \left[ \frac{1}{\varepsilon} (\mu_f (\nabla \mathbf{u}_f + (\nabla \mathbf{u}_f)^T) - \frac{2}{3} \mu_f (\nabla \cdot \mathbf{u}_f) \mathbf{I}) \right] - \left( \frac{\mu_f}{\kappa} \right) \mathbf{u}_f + \mathbf{g}$$

$$\text{Equation 2: } \rho_f c_{p,f} \mathbf{u}_f \cdot \nabla T_f + \nabla \cdot (-k_{\text{eff}} \nabla T_f) = 0$$

$$\text{Equation 3: } k_{\text{eff}} = \theta_{\text{pl}} k_{\text{pl}} + (1 - \theta_{\text{pl}}) k_f$$

(b) Primary air region

The outdoor air passes into the dew-point evaporative cooler from the bottom of dry channel and is cooled by the secondary air in wet channel along the dry channel, then part of primary air is extracted to the wet channel as secondary air and the other primary air is distributed to the indoor as the product air to cool the indoor room. The air flow equation and heat transfer equation are shown in Equations 4 and 5.

$$\text{Equation 4: } \rho_{a,p} (\mathbf{u}_{a,p} \cdot \nabla) \mathbf{u}_{a,p} = \nabla \cdot (-p_{a,p} \mathbf{I} + \mu_{a,p} (\nabla \mathbf{u}_{a,p} + (\nabla \mathbf{u}_{a,p})^T)) + \mathbf{g}$$

$$\text{Equation 5: } \rho_{a,p} c_{pa,p} \mathbf{u}_{a,p} \cdot \nabla T_{a,p} + \nabla \cdot (-k_{a,p} \nabla T_{a,p}) = 0$$

(c) Secondary air region

The secondary air is extracted from primary air near the product air outlet and flows along wet channel transferring heat and mass with water film in porous layer. The air flow equation, heat transfer equation and mass transfer equation are shown in Equations 6 to 8 respectively.

$$\text{Equation 6: } \rho_{a,w} (\mathbf{u}_{a,w} \cdot \nabla) \mathbf{u}_{a,w} = \nabla \cdot (-p_{a,w} \mathbf{I} + \mu_{a,w} (\nabla \mathbf{u}_{a,w} + (\nabla \mathbf{u}_{a,w})^T)) + \mathbf{g}$$

$$\text{Equation 7: } \rho_{a,w} c_{pa,w} \mathbf{u}_{a,w} \cdot \nabla T_{a,w} + \nabla \cdot (-k_{a,w} \nabla T_{a,w}) = 0$$

$$\text{Equation 8: } \mathbf{u}_{a,w} \cdot \nabla \omega + \nabla \cdot (-D \nabla \omega) = 0$$

## 2.2. Boundary conditions

(1) Primary air

For primary air inlet (at  $y=0$ ):

$$\text{Equation 9: } t_{a,p}(x, 0) = t_{a,in}; d_{a,p}(x, 0) = d_{in}; \mathbf{u}_{a,p}(x, 0) = \mathbf{u}_{a,in}$$

For primary air outlet (at  $y=l$ ):

$$\text{Equation 10: } p_{a,p} = 0; \nabla t_{a,p} = 0;$$

(2) Water film in porous layer

For water inlet (at  $y=l$ )

$$\text{Equation 11: } u_f(x,l) = u_{f,in}, t_f(x,l) = t_{f,in}$$

For water outlet (at  $y=0$ )

$$\text{Equation 12: } p_f = 0; \nabla t_f = 0;$$

(3) Secondary air

For secondary air inlet (at  $y=l$ )

$$\text{Equation 13: } t_{a,w}(x,l) = t_{a,p}(y=l); d_{a,w}(x,l) = d_m; u_{a,w}(x,l) = u_{a,in} \cdot r$$

Where  $r$  is the secondary air to primary air ratio, which means the air volume ratio extracted from dry channel to wet channel.

For secondary air outlet (at  $y=0$ )

$$\text{Equation 14: } p_{a,w} = 0; \nabla t_{a,w} = 0; \nabla \omega = 0$$

(4) Air-water interface (at  $x=\delta$ , and  $x=-W_{dry}$ )

Primary air and water film is separated by the heat transfer exchanger plate, and the thermal resistance of the plate can be neglected comparing the thermal resistance of primary air and water because the small thickness of the plate. So at interface of primary air and water ( $x=-W_{dry}$ ),

$$\text{Equation 15: } t_{a,p} = t_f$$

For the interface of water and secondary air (at  $x=\delta$ ),

$$\text{Equation 16: } t_i = t_{a,w} = t_f$$

$$\text{Equation 17: } q_f(x=\delta) = -k_f \left( \frac{\partial T_f}{\partial x} \right), q_f = q_{sensible} + q_{latent} = -k_{a,w} \left( \frac{\partial t_{a,w}}{\partial x} \right) + m_v \cdot h_{fg}$$

Where the  $m_v$  is the water vapour mass transfer flux from water to secondary air, and is calculated according to the kinetic theory as shown in Equation (18) (Harvie, 2000), where the  $\sigma$  is the accommodation coefficient, which means the probability that an impacting molecule will condense into the liquid upon contact with the surface and is usually defined using experimental results.

$$\text{Equation 18: } m_v = \frac{2\sigma}{2-\sigma} \sqrt{\frac{M}{2\pi R}} \left( \frac{P_{sat}(t_f)}{\sqrt{t_f}} - \frac{P_v}{\sqrt{t_{a,w}}} \right)$$

Where  $P_{sat}(t_f)$  is the water vapour saturation pressure at the temperature of  $t_f$ , and the  $P_v$  is the partial pressure of water vapour in secondary air at the interface.

For free surface of water and air, the shear stress in air is almost zero because the air viscosity is very small compared to water viscosity and the velocities of the water and air will not match. The  $v_{a,w}$  is caused by the mass transfer from water surface to secondary air and is at the magnitude of  $10^{-5}$  which can be neglected compared with air velocity of 2 m/s.

$$\text{Equation 19: } u_{a,w}(\delta, y) = 0; v_{a,w}(\delta, y) = m_v / \rho_v \approx 0$$

### 2.3. Numerical method

The coupled Equations 1 to 8 should be solved simultaneously using finite element method by COMSOL Multiphysics. The grid near the interface is refined as shown in *Figure 12*. The grid independence is checked before the calculation for models with different dimensions.

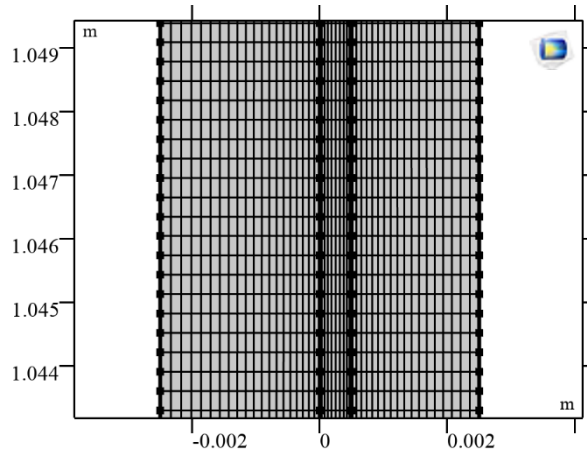


Figure 12: Grid of the model

## 3. RESULTS AND DISCUSSION

### 3.1. The influence of accommodation coefficient

The accommodation coefficient is usually defined by experimental results so this paper firstly investigated this influence on the numerical results. The relevance between the relative humidity at interface ( $x=\delta$ ) and different accommodation coefficients is shown in *Figure 13*. It shows that coefficient influences the numerical results a little because of the energy and mass conservation, increasing  $\sigma$  can decrease the difference between the water vapour saturation pressure and water vapour partial pressure at the interface, which is the drive of mass transfer but also can cause calculation unsteady. In this paper,  $\sigma=0.2$  is used in the following calculation.

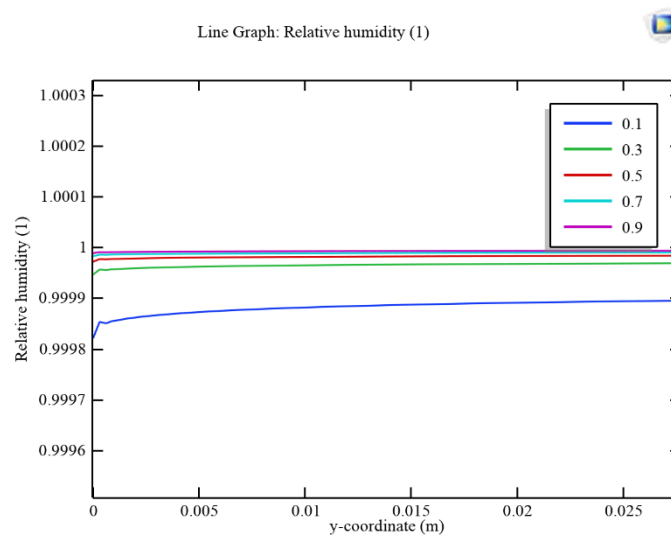


Figure 13: The influence of accommodation coefficient

### 3.2. The temperature and heat distribution

The temperature distribution for primary air, secondary air and water film is shown in *Figure 14*, from which, it can be seen that the temperature difference between the water boundaries is very small, so the thermal resistance of water film can be neglected compared to primary air and secondary air thermal resistance for dew-point evaporative cooler. Also, from the enlarged picture, it can be seen that the heat is transferred from water to primary air at near the top of cooler which could lead small temperature increase for primary air.

The latent and sensible heat transfer rate between the water and secondary air is shown in *Figure 15*, from which it can be seen that the latent heat transfer is much larger than sensible heat, and the heat transfer rate at near the water inlet is obviously larger than at other places, because at the water and secondary air inlet, the humidity of secondary air is smallest, so the difference of water vapour concentration between the saturation pressure at water temperature and water vapour partial pressure of secondary air is biggest, therefore the mass transfer rate is biggest which can be seen from *Figure 16*.

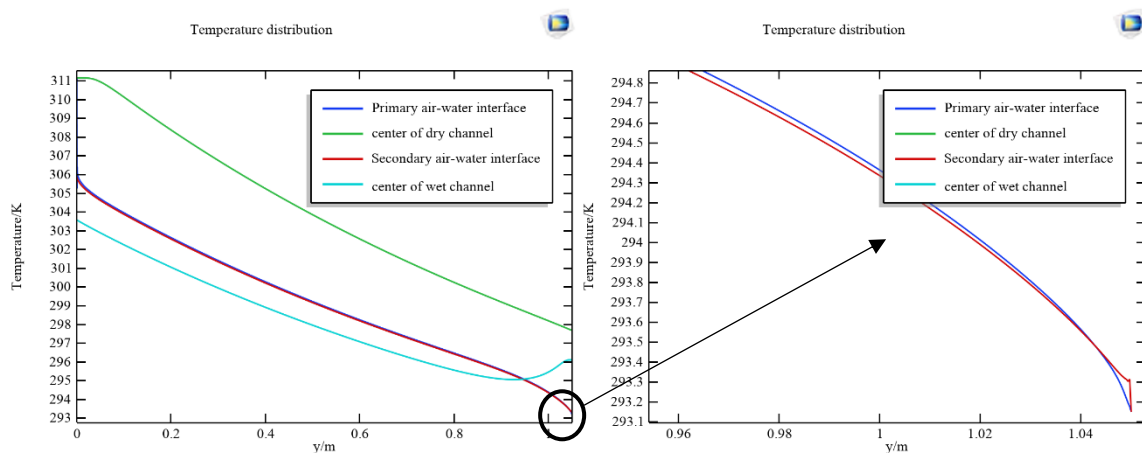


Figure 14: Temperature distribution

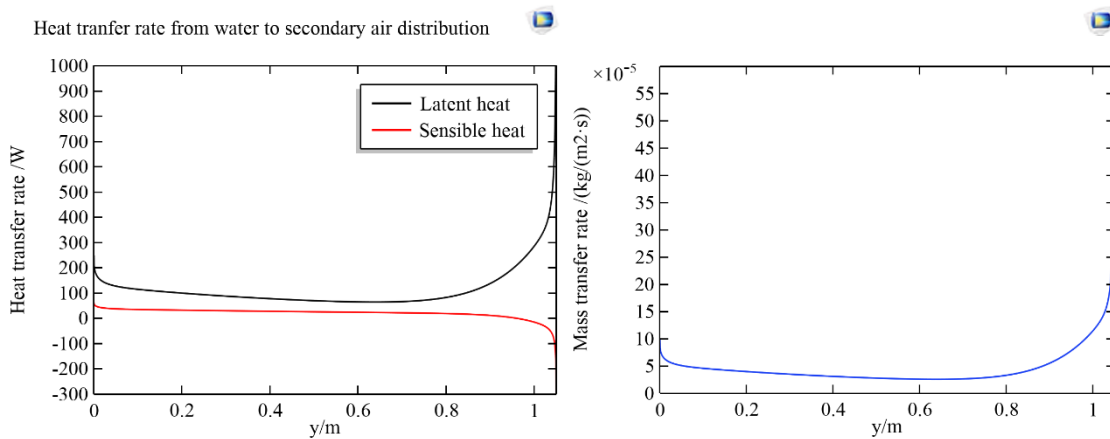


Figure 15: Heat transfer rate distribution

Figure 16: Mass transfer rate distribution

### 3.3. The influence of porosity

The influence of porosity of porous layer on primary air temperature is shown in *Figure 17*. It can be seen that the influence of porosity on the cooling efficiency of dew-point evaporative cooler is not significant. This is because the porosity of porous layer mainly influences the water flow and heat transfer coefficient, but the thermal resistance of water in porous layer is much smaller than the thermal resistance of primary air and secondary air as discussed in part 3.2. As a whole, the cooling efficiency is increased with increased porosity because the heat transfer coefficient will increase with porosity.

The influence of porosity for dew-point evaporative cooler is very different from falling liquid cooling as discussed in Nasr (2017), Terzi (2016) and Leu (2009) where the wall boundary condition is assumed to be temperature constant or heat flux constant.

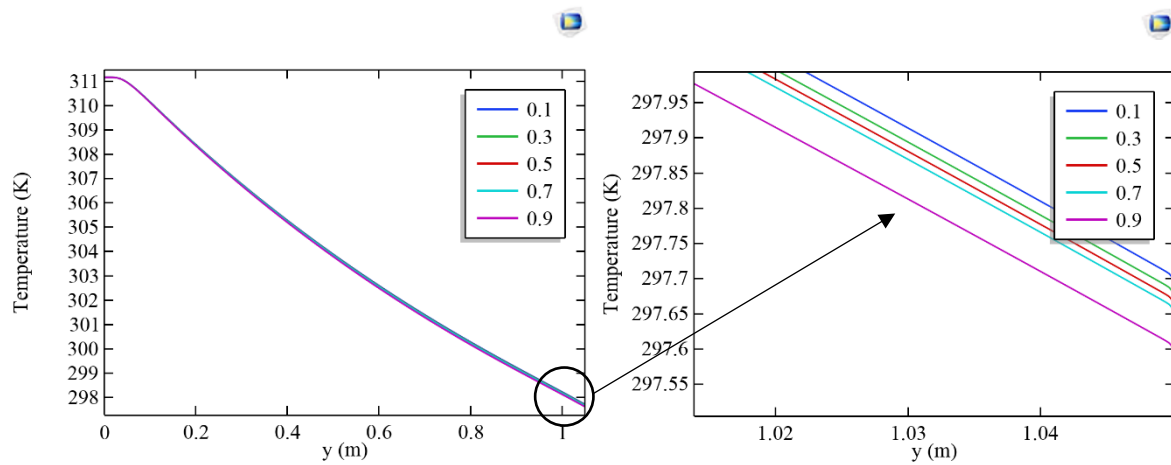


Figure 17: The influence of porosity on primary air temperature

### 3.4. The influence of inlet air velocity and working-to-primary air ratio

As discussed in 3.2 and 3.3, the cooling efficiency is mainly influenced by the primary air and secondary air, so the influence of inlet air velocity and working-to-primary air ratio is studied. From Figure 18, it can be seen that the primary air temperature is cooled more with lower air velocity, but at the same time, the cooling capacity will be lower because the product air flow volume is decreased. Therefore, the inlet air velocity should be chosen according to the requirement of cooling space.

The working-to-primary air ratio increasing means the air flow volume discharged to wet channel increasing, so the heat and mass transfer coefficients will be increased because the secondary air velocity is increased, but the cooling capacity will also be decreased because the air flow volume distributed to cooling space is decreased.

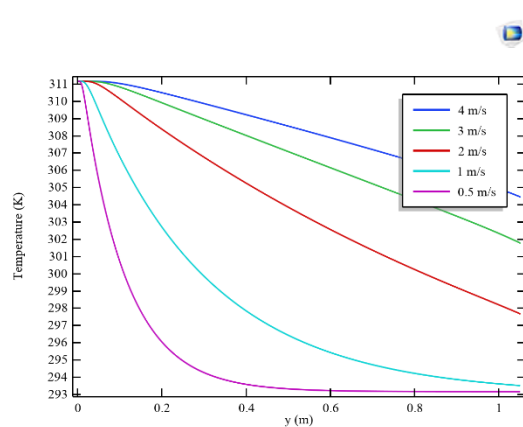


Figure 18: The influence of inlet air velocity

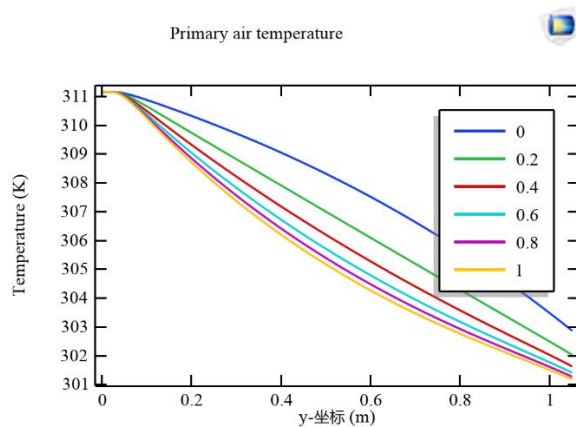


Figure 19: The influence of ratio

### 3.5. The influence of water inlet velocity and temperature

The influence of water inlet velocity and temperature is significant which can be seen from Figure 20 and Figure 21. Increasing the inlet water velocity and decreasing the inlet water temperature can improve the cooling efficiency of the dew-point evaporative cooler, because more heat can be transferred from the primary air to the water.

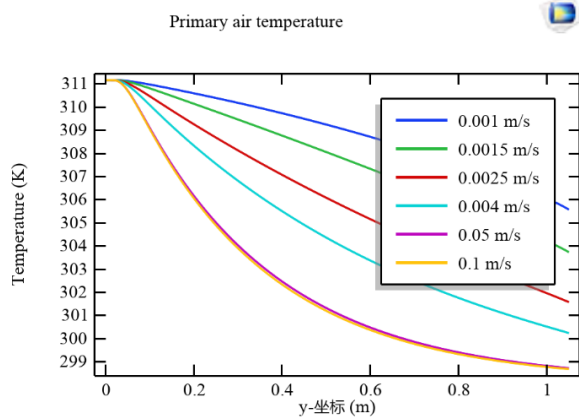


Figure 20: The influence of inlet water velocity

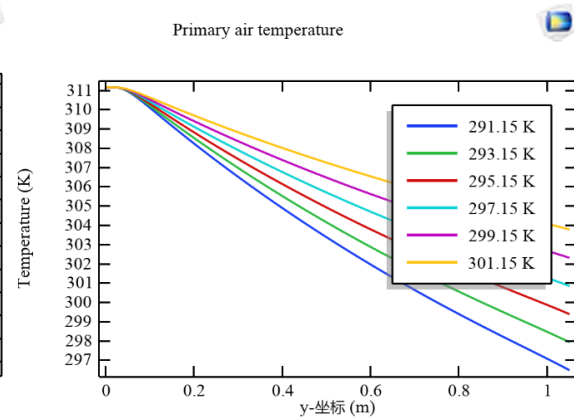


Figure 21: The influence of inlet water temperature

#### 4. CONCLUSION

A two-dimensional numerical model for the heat and mass transfer process in dew-point evaporative cooler with porous layer covering the wet surface is proposed and the coupled momentum and heat and mass transfer equations for primary air, water and secondary air are solved by COMSOL. The influence of porosity of the porous fibrous layer, inlet air velocity, working-to-primary air ratio and water inlet velocity and temperature on heat and mass transfer between the water and air are numerically studied and analysed. The numerical results showed that the influence of porosity of the porous layer is not significant, but the inlet air velocity and working-to-primary air ratio and water inlet velocity and temperature influence the cooling performance of dew-point evaporative cooler a lot. Decreasing inlet air velocity, increasing inlet water velocity and decreasing inlet water temperature can improve the cooling efficiency of dew-point evaporative cooler.

#### 5. NOMENCLATURE

$c_p$	Specific heat at constant pressure (kJ/(kg·K))
$d$	humidity (kg/kg)
$D$	Mass diffusivity, (m <sup>2</sup> /s)
$g$	gravity
$h_{fg}$	Latent heat of water (J/kg)
$k$	Thermal conductivity (W/m·K)
$M$	Molecular mass (kg/mol)
$m_v$	Mass transfer flux (kg/(m <sup>2</sup> ·s))
$l$	channel length (m)
$Nu$	Nusselt number
$p$	Pressure (Pa)
$q$	heat transfer flux (W/(m <sup>2</sup> ·s))
$R$	Universal Gas constant (J/(mol·K))
$r$	working-to-primary air ratio
$Re$	Reynolds number
$t$	Temperature (°C)
$T$	Temperature (K)
$u$	Velocity (m/s)
$W$	Channel width (m)

#### Greek symbols

$\varepsilon$	Porosity
$\sigma$	accommodation coefficient
$\kappa$	permeability
$\theta$	volume fraction of porous material
$\delta$	Thickness of porous layer (m)
$\mu$	Viscosity (kg/(m·s))
$\rho$	Density (kg/m <sup>3</sup> )
$\omega$	water vapour mass fraction

#### Subscripts

a	air
eff	effective
f	water film
g	gravity
i	interface
in	inlet
out	outlet
p	primary air
pl	porous layer
sat	saturation
v	water vapour
w	wet channel air (secondary air)

## 6. REFERENCES

- Anisimov, S., Pandelidis, D., & Danielewicz, J., 2014. Numerical analysis of selected evaporative exchangers with the maisotsenko cycle. *Energy Conversion and Management*, 88, 426-441.
- Camargo JR, Ebinuma CD, Cardoso S. A. 2003. Mathematical Model for Direct Evaporative Cooling Air Conditioning System. *Revista De Engenharia Térmica*. 2(2): 30-34.
- Duan, Z., Zhan, C., Zhang, X., Mustafa, M., Zhao, X., & Alimohammadisagvand, B., et al. 2012. Indirect evaporative cooling: past, present and future potentials. *Renewable and Sustainable Energy Reviews*, 16(9), 6823-6850.
- Elberling L. Laboratory Evaluation of the Coolerado Cooler-Indirect Evaporative Cooling Unit. Pacific Gas and Electric Company; 2006.
- Harvie DE, Fletcher DF. 2000. A Simple Kinetic Theory Treatment of Volatile Liquid-Gas Interfaces. *ASME. J. Heat Transfer*. 123(3):486-491.
- Heidarinejad, G., & Moshari, S., 2015. Novel modeling of an indirect evaporative cooling system with cross-flow configuration. *Energy and Buildings*, 92, 351-362.
- Leu, J. S., Jang, J. Y., & Chou, W. C., 2009. Convection heat and mass transfer along a vertical heated plate with film evaporation in a non-darcian porous medium. *International Journal of Heat and Mass Transfer*, 52(23-24), 5447-5450.
- Liu Y, Li JM, Yang X, Zhao X. 2019. Two-dimensional numerical study of a heat and mass exchanger for a dew-point evaporative cooler. *Energy*, 168:975-88.
- Maheshwari, G. P., Al-Ragom, F., & Suri, R. K., 2001. Energy-saving potential of an indirect evaporative cooler. *Applied Energy*, 69(1), 69-76.
- Maisotsenko V, Gillan LE, Heaton TL, Gillan AD. Method and Plate Apparatus for DewPoint Evaporative Cooler. F25D17/06; F28C1/00; F28D5/00ed. United States 2003.
- Nasr, A., & Al-Ghamdi, A. S., 2017. Numerical study of evaporation of falling liquid film on one of two vertical plates covered with a thin porous layer by free convection. *International Journal of Thermal Sciences*, 112(Complete), 335-344.
- Riangvilaikul B, Kumar S. 2010. Numerical study of a novel dew point evaporative cooling system. *Energy and Buildings*, 42(11):2241-50.
- Terzi, A., Foudhil, W., Harmand, S., & Jabrallah, S. B., 2016. Liquid film evaporation inside an inclined channel: effect of the presence of a porous layer. *International Journal of Thermal Sciences*, 109, 136-147.
- Xu P, Ma X, Zhao X, Fancey K., 2017. Experimental investigation of a super performance dew point air cooler. *Applied Energy*, 203:761-777.
- Zhan, C., Duan, Z., Zhao, X., Smith, S., Jin, H., & Riffat, S., 2011. Comparative study of the performance of the m-cycle counter-flow and cross-flow heat exchangers for indirect evaporative cooling – paving the path toward sustainable cooling of buildings. *Energy*, 36(12), 6790-6805.
- Zhan, C., Zhao, X., Smith, S., & Riffat, S. B., 2011a. Numerical study of a m-cycle cross-flow heat exchanger for indirect evaporative cooling. *Building and Environment*, 46(3), 657-668.
- Zhao, X., Li, J. M., & Riffat, S. B., 2008. Numerical study of a novel counter-flow heat and mass exchanger for dew point evaporative cooling. *Applied Thermal Engineering*, 28(14-15), 1942-1951.
- Zhao, X., Yang, S., Duan, Z., & Riffat, S. B., 2009. Feasibility study of a novel dew point air conditioning system for china building application. *Building and Environment*, 44(9), 1990-1999.

---

## #89: Solar gain mitigation in ventilated tiled roofs by using phase change materials

---

Michele BOTTARELLI<sup>1</sup>, Francisco Javier GONZÁLEZ GALLERO<sup>2</sup>, Ismael RODRÍGUEZ MAESTRE<sup>3</sup>, Gang PEI<sup>4</sup>, Yuehong SU<sup>5</sup>

<sup>1</sup> Dept. of Architecture, University of Ferrara, 44122 Ferrara, ITALY, michele.bottarelli@unife.it

<sup>2</sup> Escuela Politécnica Superior de Algeciras, University of Cádiz, 11202 Algeciras, SPAIN, javier.gallero@uca.es

<sup>3</sup> Escuela Politécnica Superior de Algeciras, University of Cádiz, 11202 Algeciras, SPAIN, ismael.rodriguez@uca.es

<sup>4</sup> Dept. of Thermal Science and Energy Engineering, University of Science and Technology of China, Hefei 230027, CHINA, peigang@ustc.edu.cn

<sup>5</sup> Dept. of Architecture and Built Environment, University of Nottingham, Nottingham NG7 2RD, UK, yuehong.su@nottingham.ac.uk

*International Energy Agency has recently warned about the fast growing of space cooling in buildings, especially in the hottest parts of the world. In this context, different passive cooling techniques, such as the use of phase change materials (PCM) in building envelope and Above Sheathing Ventilation (ASV) systems, have received an increased attention over the last years. PCMs have the capability to store solar radiation as latent heat and to increase thermal inertia of the building. Different experimental and numerical studies have demonstrated the ability of ASV in roofs to reduce solar heat gain. The efficiency of ASV systems, linked to external wind conditions, can be further improved by enhancing air permeability of tiles. Very few studies that combine PCM layers on the roof of the building together with ASV systems have been carried out, and none of them on ventilated roofs with increased air permeability. Thus, taken a model of an ASV system installed in an experimental mock-up (Ferrara, Italy) as a benchmark case, this work analyses the effect of including a PCM layer in two different configurations: first, laid on the roof deck (PCM1 case study) and secondly, suspended in the middle of the ASV channel (PCM2 case study). A 2D CFD (Computational Fluid Dynamics) model was considered to simulate airflow and heat transfer around and through the building envelope, under three days of extreme hot conditions in summer with high temperatures and low wind speed. Results showed slight differences in terms of mean temperatures at the different roof layers, although temperature fluctuations at deck in PCM1 case were smaller than half of those estimated for the benchmark case. PCM2 configuration achieved a reduction of about 10 Wh/m<sup>2</sup> (18%) in building energy load with respect to BM case over a 24h period. PCM1 got only 4%. Then, in this preliminary study authors have shown that, in terms of energy performance, a suspended PCM layer in the middle of the ASV channel would be a better measure than laid on the deck surface, although this last option would significantly decrease thermal stress of the insulation layer.*

*Keywords: passive cooling technique; ventilated pitched roof; phase change material; computational fluid dynamics*



## 1. INTRODUCTION

According to the International Energy Agency (IEA, 2019), building sector is responsible for nearly 40% of final global energy consumption worldwide, with major components in heating, cooling, ventilation, etc. Although IEA has identified some opportunities for global building energy demand to decline from now to 2040, due to a more efficient scenario, it has also warned about the fast growing of cooling in buildings. In fact, it has predicted that energy demand for space cooling will more than triple by 2050, an increase especially concentrated in the hottest parts of the world (IEA, Future of Cooling report, 2018).

In this context, different passive cooling techniques have received an increased attention over the last decades. A suitable selection of these techniques, which can be classified into heat protection, heat modulation and heat dissipation techniques (Santamouris and Kolokotsa, 2013), depends on many factors, such as climatic conditions, building space constraints and performance of the passive technique (Bhamare et al., 2019). In heat protection techniques, the building is protected from direct solar gains by using shading devices, active vegetation, etc. Regarding modulation techniques, the heat gain is modulated by the thermal inertia of the building structure. The integration of phase change materials (PCMs) in building envelope falls into this category. PCMs have high latent heat capacity and are able to absorb and release solar and infrared radiation through convection and radiation. They allow decreasing internal air temperature fluctuations (Sair et al., 2015) and reducing total discomfort hours and cooling energy loads (Sajjadian et al., 2015). It must be highlighted that that PCMs' performance depends on the quantity of the material and the temperatures during the day and night (Zalba et al., 2003). In heat dissipation techniques, excess heat of the building is released to a suitable environmental heat sink at a lower temperature. Within this group, roof ventilation, which uses environmental air as a heat sink, can also play an important role in lowering energy requirement for space cooling by increasing natural and forced air convection and reducing the heat transfer due to solar radiation.

Especially in hot climates, the roof plays an important role in comparison with other building elements due to its extension and exposure to the sun (Bortoloni et al., 2017). PCMs have been integrated in roofs in a variety of options with the aim of increasing thermal energy storage capacity of the building. Dong et al. (2015) developed a 3D heat transfer parametric study of a full-scale PCM roof, in which different influencing factors on thermal performance (solar radiation, transition temperature, roof slope, etc.) were investigated. They observed a strong temperature delay in the room with respect to the common case and that roof slope, PCM layer thickness and absorption coefficient of external surfaces were the most relevant factors. Pasupathy and Velraj (2008) presented a mathematical model that was experimentally validated in order to predict the thermal behaviour of a roof made of brick and concrete with a middle PCM layer. Authors concluded that a double PCM layer could limit temperature swings and be suitable for all seasons. Guichard et al. (2015) presented an experimental study on a complex roof with PCM inserted into an enclosed air space between the corrugated iron roof and plasterboard. The air layer between the iron roof and the PCM was not ventilated. Authors proved that the PCM was able to store thermal energy in the daytime and released it at night. Kosny et al (2012) showed an experimental roof configuration that consisted of a combination of photovoltaic (PV) laminates, air cavities, fiberglass insulation with reflected foil facing and PCM heat sink. Air cavities and air gap above the insulation layer provided above sheathing ventilation (ASV), which helped to reduce cooling loads during summer. Over 50% of saving in cooling energy demand was achieved.

Different studies based on experimental and numerical approaches have also investigated the performance of ASV systems. Thus, laboratory tests were carried out to assess airflow and temperature distribution in ASV as functions of solar radiation and size and shape of the air channel (Lee et al., 2009). A significant performance improvement over a standard ventilated roof was measured in full-scale models (Dimoudi et al., 2006). Numerical tools were used by other authors in order to estimate air distribution and heat transfer in ventilated roofs (Bottarelli et al. 2017). De With et al. (2009) developed a numerical algorithm to predict heat, air and moisture transport in the building envelope and quantified the thermal benefits, around 14%, of using a tiled roof over a traditional shingle roof. A reduction between 30 to 50% of heat flux into the attic was reported by other numerical studies when roof ventilation was considered (Miller et al., 2007; Ciampi et al., 2005, Gagliano et al., 2012). Miller et al. (2007) created a new algorithm to predict free laminar convection heat transfer in ventilated roofs and also applied a 2-D steady state CFD modelling, from which they made a correlation to estimate naturally induced airflow within the ventilated space. Ciampi et al. (2005) developed a 1D heat transfer steady state mathematical model based on thermal resistances circuits. Gagliano et al. (2012) used a 2D steady state CFD model to study the performance of the ventilated roof for different configurations and concluded that the best results were obtained when placing the insulation layer under the air layer. These numerical studies neglected the tile air permeability between the overlapping tiles and modelled ASV as an air duct. Air permeability was experimentally analysed by D'Orazio et al (2008) who concluded that, in the roofs studied, air permeability and the introduction of building elements which obstruct the flow could counter any differences in performance correlated with the cross section of the ventilation duct. The enhancement of ASV by tile air permeability was experimentally and numerically studied by Bottarelli et al. (2015), who achieved significant increase of ASV using new tile designs (European project LIFE HEROTILE, LIFE14CCA/IT/000939).

Recent studies generally focus on the combination of different passive cooling technologies in order to maximise the building cooling potential and energy saving capabilities (Roman et al. 2016). However, very few studies can

be found in scientific literature on the combination of ASV and PCMs. Furthermore, to the best of authors' knowledge, there are no studies on the use of ASV systems with increased air permeability together with PCM layers over the roof deck. Thus, the aim of the present work is to analyse the performance of this combination of passive techniques during hot periods in a Mediterranean site (Ferrara, Italy). Different configurations of ventilated roofs were simulated numerically by using CFD. First, a description of the methodology and case studies is given. Secondly, the numerical model is presented. Finally, the results obtained are analysed and discussed and conclusions drawn.

## 2. METHODOLOGY

The simulation of airflow and heat transfer in ventilated roofs is a complex problem that involves turbulence with a variety of length scales. Larger scales, which are related to wind and wind-building interaction, are connected to the small scales of the flow within the ASV and the tiny interstices among the overlapping tiles (Bortoloni et al., 2017). In order to solve this problem, CFD numerical simulations of the heat transfer mechanisms and airflow over a real building and through its ventilated pitched roof has been considered here. The commercial finite-element code COMSOL Multiphysics V5.3 was used. A reference or benchmark case study in which only the ASV was taken into account was used for comparison with other configurations that also included a PCM layer over the roof deck. The descriptions of the CFD model and study cases are given next.

### 2.1. CFD model

#### Domain

As the main interest is focussed on the natural ventilation channel and heat transfer exchange in the roof of the building, a 2D domain was considered as a section of a one floor building of infinite width, neglecting 3D effects of wind-building interaction. A sketch of the domain is shown in Figure 1 a). The building, for which only one half has been considered, is covered by a pitched roof with a slope of  $15^\circ$  and is included in a  $15\text{ m} \times 15\text{ m}$  external air environment. Details of the roof are given in Figures 1 b) and c) (benchmark case). The roof covering is made of Portuguese roof tiles laid on a batten and counter-batten system. In the present study, the batten and counter-batten system is not included in the model and tile shape is simplified such that the resulting ASV and tile models are shown in Figure 1 b) (Bortoloni et al., 2017). Air will flow into the ventilation channel at the eaves and through the gaps among the tiles, and mainly leaving out at the ridge.

Geometric values of the roof elements and properties of the building materials are described in Table 1 and Table 2, respectively.

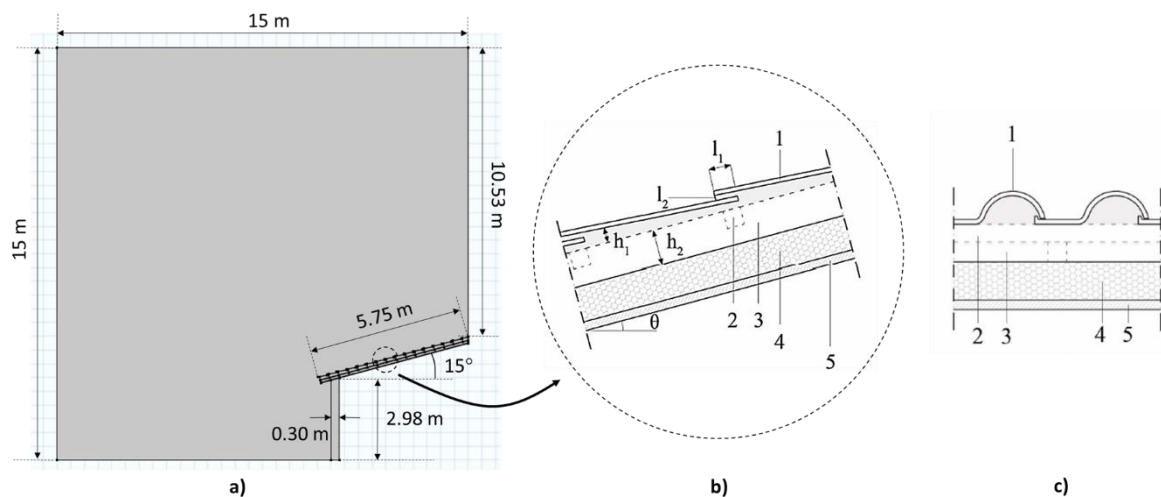


Figure 1. a) Sketch of the 2D model domain. b) Simplified 2D model of the tile and ASV channel (benchmark case).  $l_1$ , length of tile overlap;  $l_2$ , thickness of gap between overlapping tiles;  $h_1$ , thickness of the air layer under the tile;  $h_2$  thickness of the ventilation layer;  $\theta$ , tilt angle. c) Cross section of the Portuguese tile shape. 1, Tiles; 2, battens and resulting air layer; 3, counter-battens and resulting air layer; 4, insulation layer; 5, wooden board.

Table 1. Geometric characteristics of the ventilated roof.

Name	Description	Value (unit)
$l$	Tile thickness	0.01 (m)
$l_1$	Length of tile overlap	0.05 (m)
$l_2$	Distance between overlapping tiles	0.006 (m)
$h_1$	Thickness of air layer	0.015 – 0.03 (m)
$h_2$	Thickness of ventilation layer	0.08 (m)
$\theta$	Tilt angle	15 (°)

As it can be seen in Table 2, properties of the PCM ( $\text{Na}_2\text{CO}_3 \cdot 10\text{H}_2\text{O}$ , an hydrated salt) used in the present study are also given (Cabeza et al., 2011). Hydrated salts are often preferred in building applications due to their high latent heat combined to a low price. A mixture of a backfill material (20% of total volume) and the PCM is considered in the PCM layer that will be integrated in other ASV configurations. To represent time dependence of mixture density, conductivity and specific heat during the phase change, some specific relationships expressed in terms of normalised Dirac's pulse and different step functions were implemented (Bottarelli et al., 2015).

Table 2. Properties of building materials.

Material	Thickness (m)	Density ( $\text{kg}/\text{m}^3$ )	Thermal conductivity ( $\text{W}/\text{m}\cdot\text{K}$ )	Specific heat ( $\text{J}/\text{kg}\cdot\text{K}$ )	Latent heat ( $\text{J}/\text{kg}$ )	Melting temperature ( $^\circ\text{C}$ )
Wall	0.30	850	0.20	840	--	--
Rokwool insulation layer	0.08	130	0.037	1030	--	--
Wooden board	0.02	450	0.15	2100	--	--
Tiles	0.01	2000	1.00	800	--	--
PCM ( $\text{Na}_2\text{CO}_3 \cdot 10\text{H}_2\text{O}$ )	0.02	1485 (solid) 1442 (liquid)	0.554 (solid)	1783	246.5	32 (span $2^\circ\text{C}$ )
Backfill material	--	1200	0.8	1000	--	--

### Boundary conditions

The numerical study of the energy performance of the ASV system was developed for a period of three summer days with extreme hot conditions, that is, high air temperatures and high solar irradiance ( $\text{W}/\text{m}^2$ ) (Figure 2Figure). Minimum and maximum daily air temperatures were  $24.0^\circ\text{C}$  and  $38.3^\circ\text{C}$ , respectively. A time-dependent air temperature ( $T(t)$ ) was set as a boundary condition at the inlet of the fluid domain. Furthermore, solar irradiance, which reached a maximum value of  $800 \text{ W}/\text{m}^2$ , was set as an input time-dependent heat flux over the roof of the building. Roof surface had a hemispherical reflectance of 0.3.

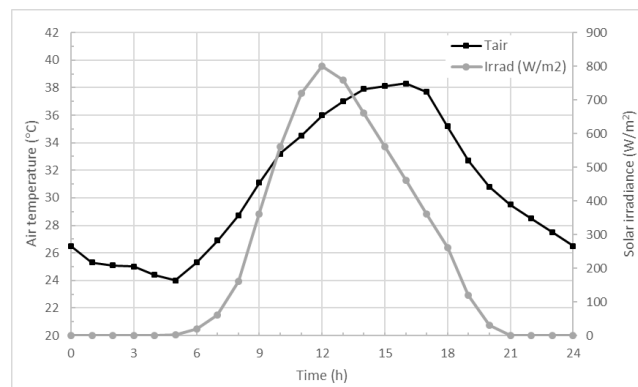


Figure 2. Air temperature and solar irradiance for one day of the simulation period.

A potential wind velocity profile was also set at the inlet, with a speed of  $1 \text{ m}/\text{s}$  ( $v_0$ ) at a reference level of  $10\text{m}$  ( $z_0$ ). This profile followed the following power law:

Equation 1: Wind speed profile

$$v(z) = v_0 \left( \frac{z}{z_0} \right)^\alpha$$

Where:

- $v(z)$  = wind speed at height  $z$  (m/s)
- $z$  = height (m)
- $v_0$  = wind speed at a reference height ( $z_0$ ) (m/s)
- $z_0$  = reference height ( $z_0$ ) (m)
- $\alpha$  = empirical non-dimensional exponent

The exponent  $\alpha$ , that depends on the surface roughness, was set to 0.3, a typical value for urban areas (Masters, 2004). Thus, low wind speed conditions, for which the efficiency of the ASV systems is smaller, will be analysed. Also these conditions would be more similar to the real ones in which the air in the streets does not flow in a direction perpendicular to building façade.

Constraints at other boundaries of the domain are described in Figure 2. Details of the different heat transfer mechanisms and conditions considered in the ventilated roof are shown in Figure 2 b). A constant room air temperature of 26°C and a heat transfer coefficient of 8 W/(m²K) were set on the ceiling and inside surface of the building wall. Grey body and surface-to-surface radiation models were used to calculate radiation heat transfer between surfaces in the ASV channel.

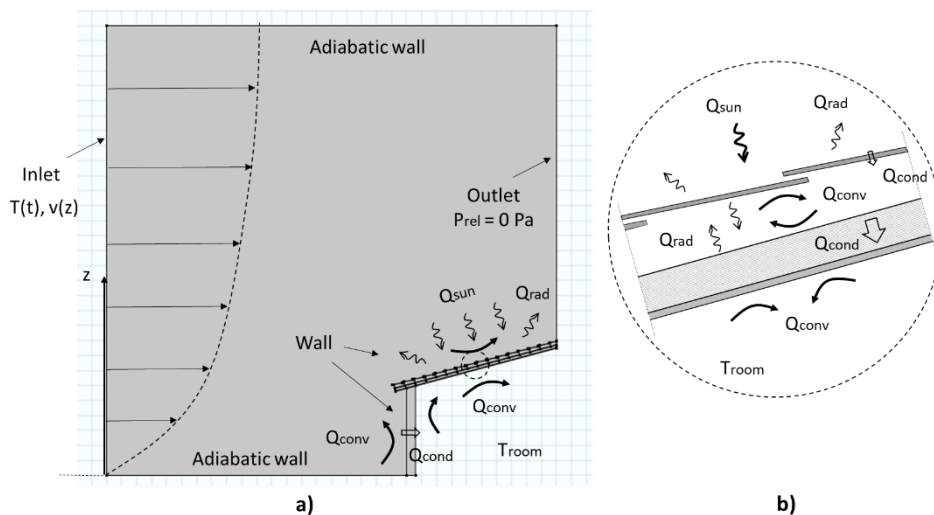


Figure 3. a) Description of boundary conditions in the whole domain. b) Details of boundary conditions on the roof.  $t$ , time;  $T$ , temperature;  $z$ , height;  $v$ , wind speed;  $Prel$ , relative pressure;  $Q_{sun}$ , solar irradiance;  $Q_{rad}$ , radiation heat flux;  $Q_{conv}$ , convective heat flux;  $Q_{cond}$ , conductive heat flux;  $T_{room}$ , fixed room air temperature.

### Mesh independence

An unstructured triangular mesh has been used with inflation layers (prismatic layers of increasing thickness) in the proximity to the wall-air interfaces in order to capture gradients within the mechanical and thermal boundary layers (Figure 4). Several runs of the initial CFD model were performed on different size meshes and their results were compared to analyse the grid independence of the solution. The average air speed at the cross-section in the middle of the ASV channel was used for comparison. Although there were no great differences (around 1.5% of relative variation) (Figure 5), meshes of near half a million elements were built for all the case studies developed.

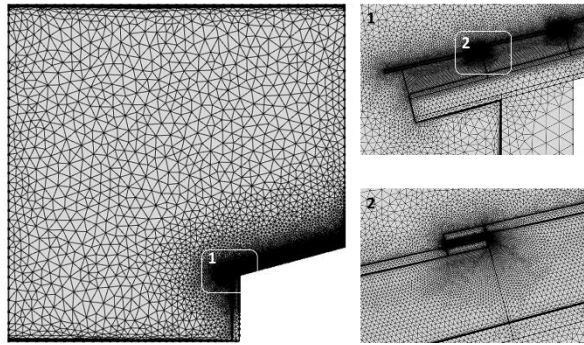


Figure 4. Details of the mesh used to represent the whole domain and ASV channel (benchmark case).

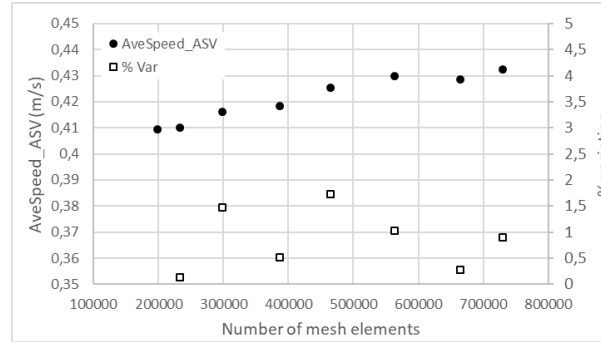


Figure 5. Mesh independence study. Average air speed at the cross section in the middle of the ASV channel was used for comparison (benchmark case).

### Turbulence model and solving strategy

k-ε model with standard wall functions were used to simulate turbulence within the fluid domain. The problem was solved in two stages. First, a steady state solution of the airflow was sought in the thermal conditions formerly described. Then, from the steady state airflow solution, the heat transfer transient problem was solved. This strategy can be justified considering that temperature differences along the roof are not very high and, consequently, airflow through the ASV channel is mainly dependent on external wind conditions. A relative tolerance of  $10^{-3}$  was set for residuals.

## 2.2. Case studies

Three case studies were considered: a benchmark case (from now on 'BM') described in section 2.1 and two configurations (PCM1 and PCM2) in which the ASV system was coupled with a PCM layer over the roof deck. In the last two cases, a 2 cm thick PCM layer was considered. In PCM1 configuration, the layer was laid on the roof deck while in PCM2 the layer was suspended in the middle of the ASV channel (Figure 5).

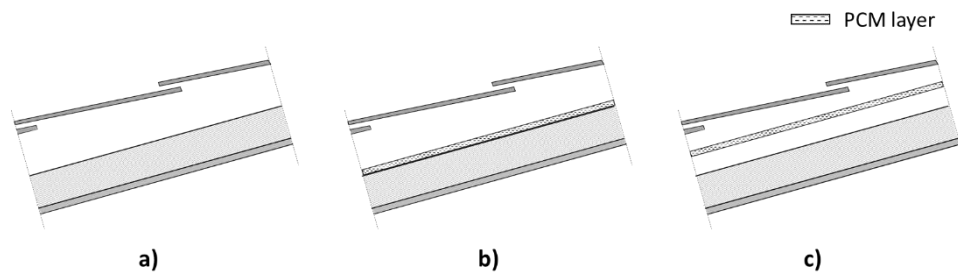


Figure 6. Cross sections of the ventilated roofs for the three case studies: a) benchmark case (BM); b) PCM layer laid on the roof deck (PCM1); c) PCM layer hanging in the middle of the ASV channel (PCM2).

Meshes with 497249, 487982 and 358988 elements were built for the BM, PCM1 and PCM2 case studies, respectively.

## 3. RESULTS AND DISCUSSION

Although authors have mainly focussed their attention on heat transfer through the different roof configurations, a study of velocity field has also been carried out in order to check the right performance of the numerical simulations. Thus, Figure 7 shows the airflow in the whole domain and through the ASV channel for the three case studies. In terms of velocity field, BM and PCM1 show a very similar behaviour, with a decay of air speed in the middle part of the channel and a slight increase towards the ridge. This dependence has been experimentally observed by Bortoloni et al. (2017). The highest values of air speed at the beginning can be explained by the action of the eave edge that channels air coming from below.

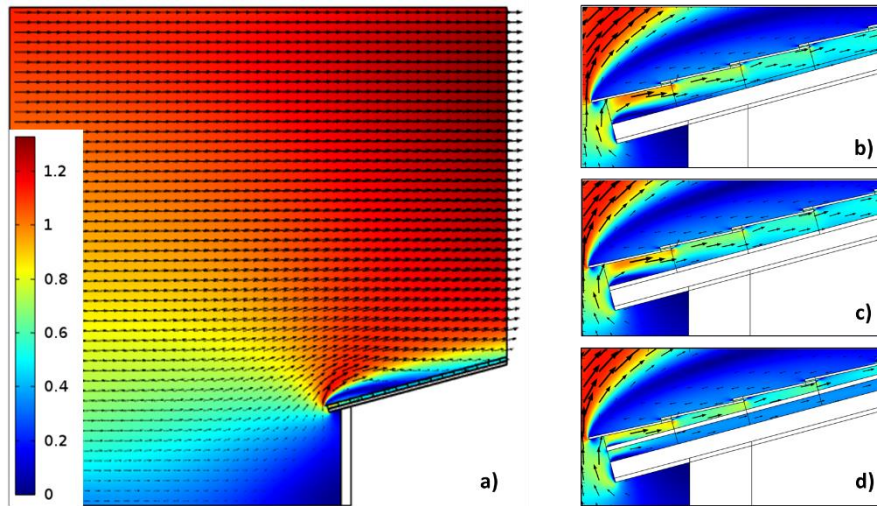


Figure 7. Surface and vector velocity plots. a) Full domain (BM). Details of the same plot for the different case studies b) BM c) PCM1 and d) PCM2.

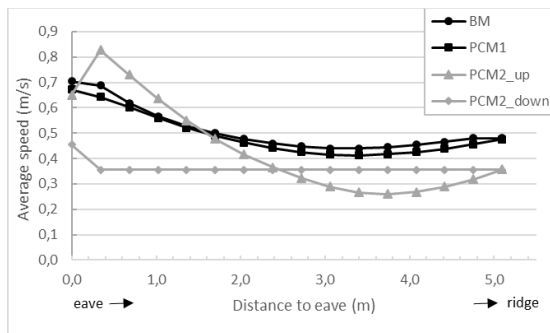


Figure 8. Average velocity at different cross sections along the ASV channel.

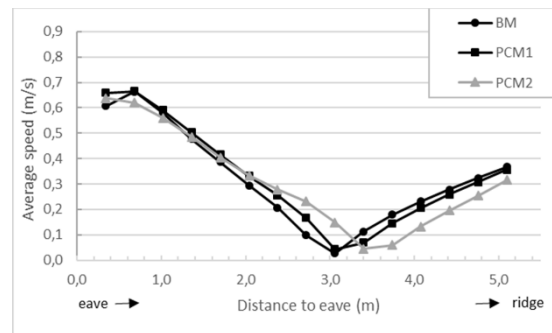


Figure 9. Average velocity at the outlet cross sections of the inter-tile gaps.

Regarding PCM2, airflow is split into two streams by the suspended PCM layer. It is interesting to note that, while the upper flow behaves similarly to the former two cases, the flow below the PCM layer shows an almost uniform velocity distribution. This is also shown in Figure 8 and can be explained again by the action of the eave edge and the irregularities caused by inter-tile gaps. The uniformity of velocity under the PCM layer is caused by the even distribution of surfaces. Figure 9 provides the values of the average velocity at the different outlet cross sections of the inter-tile gaps. A very similar trend is seen for the three cases with a steep decrease to nearly null velocity near the middle of the roof, which is related to the stagnation area in the wake of the outer flow and to an indoor-outdoor pressure balance.

Temperature has been estimated in many different locations of the building roof: on the ceiling (inner surface of the wooden board), at the interface between the wooden board and the insulation layer, over the insulation layer, on the PCM surfaces, etc. Thus, the average temperature of the ceiling and at the interface between the wooden board and the insulation layer are almost identical for the three cases, around 26.2°C and 26.7°C, respectively. Also, the average temperature at the outer surface of the insulation layer is very similar, with a value that ranges from 30.0°C (PCM2) to 30.6 °C (BM). At this interface, temperature variations seem to be smaller for the PCM1 configuration.

Regarding the heat transfer through the roof, mean values of heat flux for BM, PCM1 and PCM2 cases are 1.9, 1.7 and 1.5 W/m<sup>2</sup>, respectively. Thus, a 20% reduction is achieved with PCM2 configuration. Although a clear dampening is observed in the time dependence of heat flux, it seems PCM1 performance is not very good, probably because PCM is not able to release upwards the required amount of heat at night (Figure 10). In fact, the energy transferred to the room after a period of 24h is almost the same (a difference of around 4%) for BM and PCM1 configurations (Figure 11). In the same period, a reduction in building energy load of about 10Wh/m<sup>2</sup> (18%) is achieved by PCM2 configuration with respect to the benchmark case. This better performance of the PCM2 configuration may be explained by the ventilation of the two surfaces of the PCM layer, which enhances heat release.

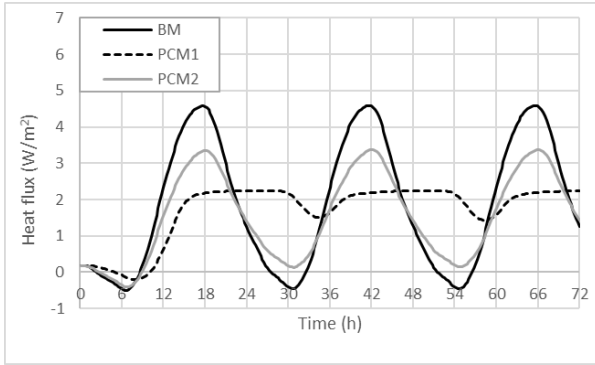


Figure 10. Time dependence of heat flux ( $W/m^2$ ) through the ceiling.

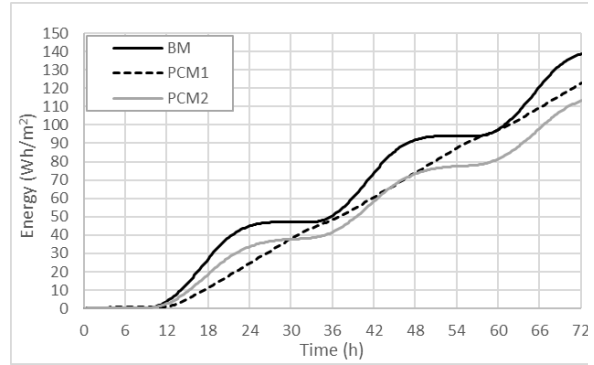


Figure 11. Time dependence of energy ( $Wh/m^2$ ) entering the room through the ceiling. Numerical integration of curves in Figure 11 for positive values of heat flux.

An interesting location, from the construction and refurbishment perspective, is the outer surface of the insulation layer because it degrades under extreme temperature conditions. Thus, surface temperature at different sections of the deck has been compared among the three case studies. The ASV channel was divided into 16 sections (related to the 16 tiles of the half of the roof). Thus, temperatures at section 1 (at the eave), 8 and 16 (at the ridge) on the deck surface have been analysed (Table 3). The smallest temperature fluctuations (half of those estimated for the BM case) and the lowest maximum temperature values were obtained with PCM1 configuration, that is, with the PCM layer right over the insulation layer.

Table 3. Temperature at different sections (1, 8 and 16) of the outer surface of the insulation layer.

	S1			S8			S16		
(°C)	BM	PCM1	PCM2	BM	PCM1	PCM2	BM	PCM1	PCM2
$T_{MEAN}$	30,5	30,2	30,4	30,6	30,1	30,0	31,2	30,6	29,9
$T_{MIN}$	24,3	25,0	24,4	24,3	25,4	24,6	24,4	25,5	24,9
$T_{MAX}$	37,1	31,6	36,9	37,5	31,4	35,0	39,1	31,5	33,5
$T_{MAX} - T_{MIN}$	12,8	6,6	12,6	13,2	6,0	10,4	14,7	6,0	8,6

As it can be seen from Figure 12, Figure 13 and Figure 14, temperature on the whole deck surface is almost constant for PCM1 configuration (32°C, the melting point of the PCM). Furthermore, the dampening effect of the PCM layer in PCM2 configuration increases far from the eaves.

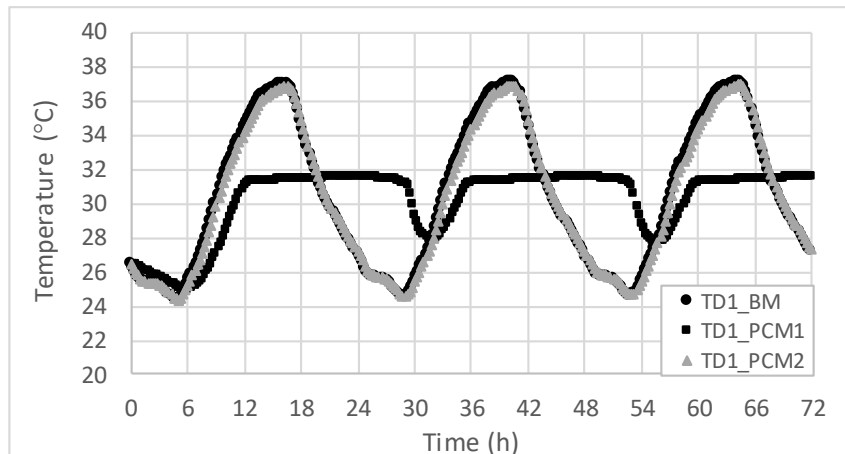


Figure 12. Temperatures at the first part (D1, close to the eave) on the deck (insulation layer) surface.

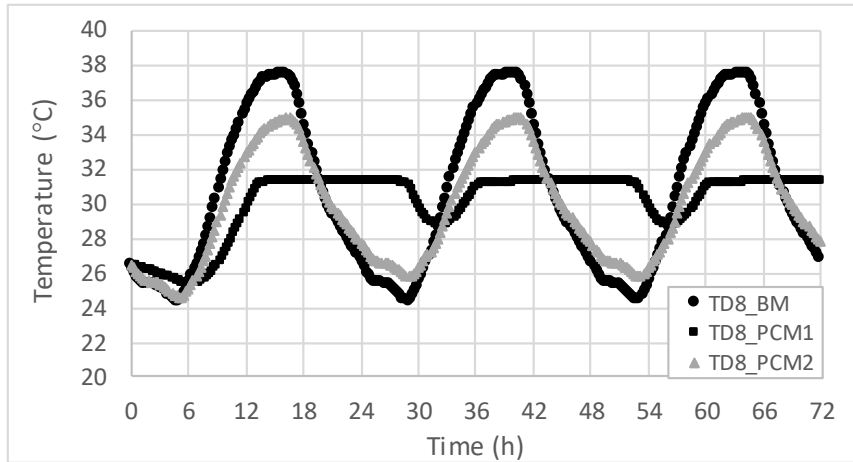


Figure 13. Temperatures at the middle part (D18) on the deck surface.

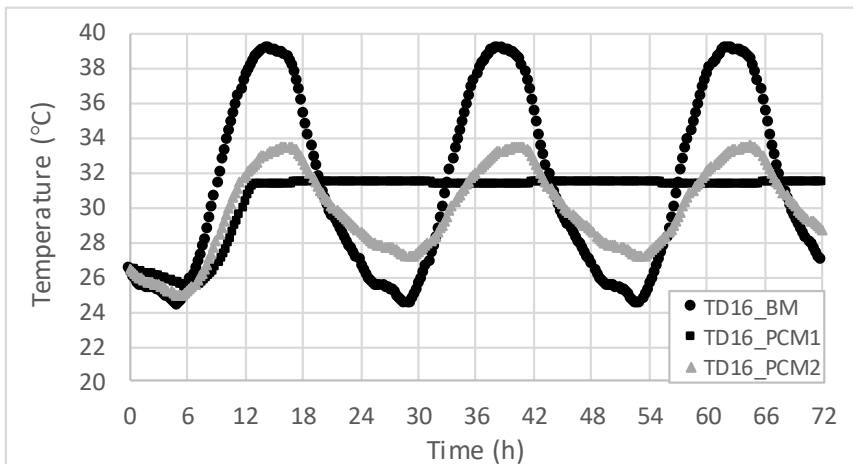


Figure 14. Temperatures at the last part (D16, close to the ridge) on the deck surface.

#### 4. CONCLUSIONS

In this work, the authors have studied the performance of a combination of two passive cooling techniques: ASV systems and the use of PCM on a pitched tiled roof of a building. They used CFD with finite elements (COMSOL, v5.3) to develop numerical simulations under extreme hot conditions in a Mediterranean site (Ferrara, Italy). Three case studies were considered: a benchmark case (BM) in which only the natural ventilation system on the building roof; a second study (PCM1) in which a PCM layer was laid over the roof deck; and a third one (PCM2) with the same PCM layer suspended in the middle of the ASV channel. Weather conditions were characterised by high temperatures and solar irradiance, with peak values of 38°C and 800W/m<sup>2</sup>, respectively. A typical urban potential wind profile with a reference value of 1m/s (at 10m) at the inlet of the domain was taking into account. This low values of air speed would also resemble real urban situations in which street wind is not usually perpendicular to building façade.  $k-\epsilon$  with wall functions were used to model turbulence. A mesh independence study, in which the average air speed at the cross-section in the middle of the ASV channel was used for comparison, was also developed.

It can be concluded that PCM1 case slightly reduces building energy load (about 4%) with respect to the BM case in a 24h period of time. In contrast, PCM2 configuration gets a reduction of about 18% (10Wh/m<sup>2</sup>) in the same period. A study of surface temperature on the insulation layer (deck) revealed that PCM1 case got an almost constant value, thus avoiding high fluctuations and delaying material degradation.

#### 5. REFERENCES

Bhamare, D.K., Rathod, M.K., Banerjee, J., 2019. Passive cooling techniques for building and their applicability in different climatic zones - The state of art. *Energy and Buildings*, 198, 467–490



- Bortoloni, M., Bottarelli, M., Piva, S., 2017. Summer thermal performance of ventilated roofs with tiled coverings. *Journal of Physics: Conference Series*, 796, 1-10.
- Bottarelli, M., Bortoloni, M., Zannoni, G., 2013. Prestazioni termiche estive di tetti ventilati a manto discontinuo, Conference proceedings, VII Italian Association of Energy Management Conference. Place: Publisher.
- Bottarelli, M., Bortoloni, M., Su, Y., Yousif, C., Aydin, A.A., Georgiev, A., 2015. Numerical analysis of a novel ground heat exchanger coupled with phase change materials. *Applied Thermal Engineering*, 88, 369-375.
- Bottarelli, M., Bortoloni, M., Zannoni, G., Allen, R., Cherry, N., 2017. CFD analysis of roof tile coverings. *Energy*, 137, 391-398
- Cabeza, L.F., Castell, A., Barrenechea, de Gracia, C.A., Fernández, A.I., 2011. Materials used as PCM in thermal energy storage in buildings: A review. *Renewable and Sustainable Energy Reviews*, 15, 1675-1695.
- Ciampi, M., Leccese, F., Tuoni, G., 2005. Energy analysis of ventilated and microventilated roofs. *Solar Energy*, 79, 183-192.
- De With, G., Cherry, N., Haig, J., 2009. Thermal Benefits of Tiled Roofs with Above-sheathing Ventilation. *International Journal of Building Physics*, 33, 171-194.
- Dimoudi, A., Androutsopoulos, A., Lykoudis, S., 2006. Summer performance of a ventilated roof component. *Energy and Buildings*, 38, 610-617.
- Dong, L., Yumeng, Z., Changyu, L., Guozhong, W., 2015. Numerical analysis on thermal performance of roof contained PCM of a single residential building. *Energy Conversion and Management*, 100, 147-156.
- D'Orazio, M., Di Perna, C., Principi, P., Stazi, A., 2007. Effects of roof tile permeability on the thermal performance of ventilated roofs: analysis of annual performance. *Energy and Buildings*, 40, 911-916.
- Gagliano, A., Patania, F., Nocera, F., Ferlito, A., Galesi, A., 2012. Thermal performance of ventilated roofs during summer period. *Energy and Buildings*, 49, 611-618.
- Guichard, S., Miranville, F., Bigot, D., Malet-Damour, B., Boyer, H., 2015. Experimental investigation on a complex roof incorporating phase-change material. *Energy and Buildings*, 108, 36-43.
- High Energy savings in building cooling by ROOf TILEs shape optimization toward a better above sheathing ventilation (Life Herotile Project). <http://www.lifeherotile.eu/it/>
- IEA, 2019. IEA website: <https://www.iea.org/topics/energyefficiency/buildings/>
- IEA, 2018. OECD/IEA. The future of cooling. Opportunities for energy-efficient air conditioning.
- Kosny, J., Biswas, K., Miller, W., Kriner, S., 2012. Field thermal performance of naturally ventilated solar roof with PCM heat sink. *Solar Energy*, 86, 2504-2514.
- Lee, S., Park, S.H., Yeo, M.S., Kim, K.W., 2009. An experimental study on airflow in the cavity of a ventilated roof. *Building and Environment*, 44, 1431-1439.
- Masters, G.M., 2004. Renewable and efficient electric power systems. New York: John Wiley and Sons.
- Pasupathy, A., Velraj, R., 2008. Effect of double layer phase change material in building roof for year round thermal management. *Energy and Buildings*, 40, 193-203.
- Roman, K.K., O'Brien, T., Alvey, J.B., Woo, O.J., 2016. Simulating the effects of cool roof and PCM (phase change materials) based roof to mitigate UHI (urban heat island) in prominent US cities. *Energy*, 96, 103-117.
- Santamouris, M., Kolokotsa, D., 2013. Passive cooling dissipation techniques for buildings and other structures: the state of the art, *Energy and Buildings*, 57, 74-94.

Sari A., Alkan C., Özcan A.N., 2015. Synthesis and characterization of micro/nano capsules of PMMA/capric-stearic acid eutectic mixture for low temperature-thermal energy storage in buildings. *Energy and Buildings*, 90, 106-113.

Sajjadian, S.M., Lewis, J., Sharples, S., 2015. The potential of phase change materials to reduce domestic cooling energy loads for current and future UK climates. *Energy and Buildings*, 93, 83–89.

Zalba, B., Marín, J.M., Cabeza, L.F., Mehling, H, 2003. Review on thermal energy storage with phase change materials, heat transfer analysis and applications. *Applied Thermal Engineering*, 23(3), 251-283.

---

## #93: Free piston Stirling engine response to the change in displacer's spring stiffness value

---

Muhammad I. RASHAD<sup>1</sup>, S.A. NADA<sup>1,2</sup>, Mahmoud ELZOUKA<sup>3</sup>

<sup>1</sup>Egypt Japan University of Science and Technology, New Borg El-Arab City, Alexandria, Egypt,  
mohamed.rashad@ejust.edu.eg

<sup>2</sup>Faculty of Engineering, Benha University, Benha, Egypt  
sameh.nada@ejust.edu.eg

<sup>3</sup>University of Nebraska-Lincoln, Lincoln, NE, USA

*This study aims to deduce the effect of the displacer spring's stiffness on the free piston Stirling engine (FPSE) performance. A combined dynamics and thermal model is developed and numerically solved without the need for linearisation using MATLAB Simulink™. The model takes into consideration the damping losses, pressure differences between the hot and cold spaces, collisions at stroke limits, losses due to flow in the annular clearance between the displacer and the cylinder's wall, fluid mixing and the effect of dead volumes. The proposed model estimates the operating frequencies, strokes of displacer and piston, dead volume, average output power, compression ratio, and total conversion efficiency. It was found that the displacer's spring stiffness has a significant effect on the engine's performance. For a given engine there is an optimum range for the displacer's spring stiffness that should be considered. Through the study, the stiffness value was changed gradually, and the engine's performance and cycle were observed. The maximum effect obtained was increasing the output average power by about 132.4% when changing the displacer's spring stiffness by 44.4% till the optimum value and then the average output power dropped afterwards. The output cycles and results are illustrated and discussed.*

*Keywords: Analysis; Stirling; Free piston; performance; Energy applications*

# 1. INTRODUCTION

The global energy demand is increasing extensively. Heading towards renewables is a must to face climate change. Utilising solar energy is an optimum solution for several countries to reduce the use of fossil fuels. The solar technologies can be classified into solar thermal and solar electric. Each classification has its own advantages and hence choosing the suitable technology depends on several aspects such as cost, the required capacity, and solar availability. Solar thermal technologies have the ability to be coupled energy storage system more efficiently and cheaper than solar electric (PV cells for example) especially in large scale power production. Consequently, large numbers of concentrated solar power plants that convert solar energy to electricity can be observed. (Kannan and Vakeesan, 2016). For residential scale (small scale) it is important to develop heat engines with convenient efficiency and at relatively low cost. Stirling engine is the most efficient heat engines, as it has the highest theoretical efficiency of heat engines. (Finkelstein, 1967) However, the actual ranges of efficiencies do not exceed a value of 65% of Carnot efficiency. (Thombare and Verma, 2008)

Stirling engine with different designs has been well covered in the literature. (Martini, 1978; Walker and Senft, 1985). The free piston Stirling engine (FPSE) has been well investigated as well. Qiu et al. (Qiu *et al.*, 2019) and Zhu et al. (Yu *et al.*, 2018) developed numerical models to investigate combined heating and power systems using FPSE. Their system was capable of providing electrical power and heat with efficiency up to 38%. Tavakolpour et al. (Tavakolpour-Saleh, Zare and Bahreman, 2017) developed a model for a new active FPSE engine; the engine was fabricated and tested for validation. The results of thermal efficiency showed a potential of up to 19.4 %. Karabulut (Karabulut, 2011) introduced a model of FPSE. His model worked with closed and open thermodynamic systems. It was deduced that FPSE with a closed thermodynamic cycle acts more stable operation at a smaller range of the hot end temperature and damping if compared to an open cycle engine. Zare et al. (Zare and Tavakolpour-Saleh, 2016) presented a genetic algorithm modelling for the FPSE based on frequency design. The parameters are introduced as unknown variables. These parameters are deduced based on required operating frequency using an optimisation scheme based on genetic algorithm.

The FPSE analysis is much more complicated. This is a result of the connection between the dynamics of the piston and displacer to the fluid processes and the direct effect of this connection on the thermal behaviour. Hence, accurate prediction of the system dynamics is essential to deal with the difficulties in the design process and to study the engine response at different parameters and conditions as well as to show and discuss the engine's potential to compete with the other solar technologies. All of these requirements are present in a relatively quick and accurate model. In this research, we propose a first-principle model for FPSE. The illustrated model can predict the engine's performance and output cycle. We also propose a completely hermetic configuration as shown in Figure 1. In this configuration we replace the piston-cylinder configuration (that is dominant in most of work found in the literature) by using an expansion bellow instead. The proposed configuration main advantages are no leakage, no friction due to relative motion and no mechanical sealing on moving parts.

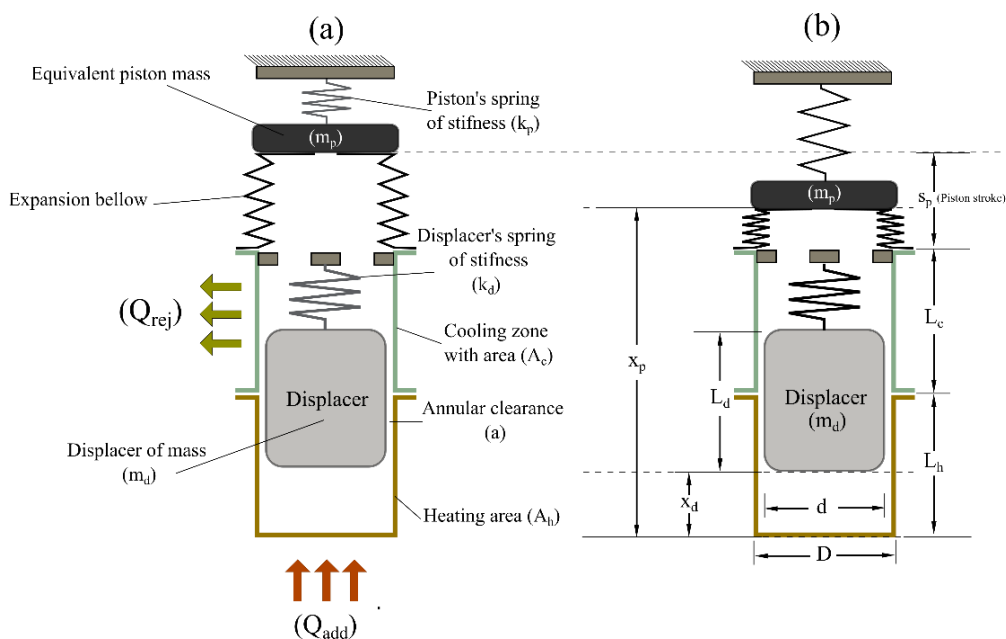


Figure 1: Engine schematic, (a) expanded, (b) contracted

The presented model takes into account the effects of damping losses, pressure difference, collisions, flow losses in the annular clearance, mixing and the most important the effect of dead volumes. The model predicts the operating frequency, strokes, dead volume (as in FPSE the dead volume varies during operation), average output power, compression ratio, total efficiency and output cycle. At the beginning the FPSE proposed model is presented. Then we illustrate the proposed engine performance and finally a comprehensive study on the engine's response to the variation in spring stiffness is presented along with the influences on the engine's output cycle. From the authors point of view the proposed configuration presents a new aspect for the hermetic design of FPSE that shows some potential for investigation. The simplified model will help in understanding more about the engine behaviour and response without much complications.

## 2. MODELLING AND ANALYSIS

In this section the analysis of the proposed configuration is demonstrated based on control volume analysis. The dynamic and thermal models are explained, the main governing equations of each model are illustrated. The positive direction of motion is assumed upwards through all of the analysis.

### 3.1. Engine dynamics

The main equations of the engine dynamics can be deduced in the differential form by balancing the engine's components, equating the external and effective forces as indicated in Figure 2 will give us Equations 1 and 2 which describe the acceleration of the piston and displacer respectively. The motion is described relative to a fixed reference which is the engine bottom in our case. Initially, the equivalent mass of the piston and the displacer are assumed at a starting position  $x_p$  and  $x_d$  respectively from the mentioned reference.

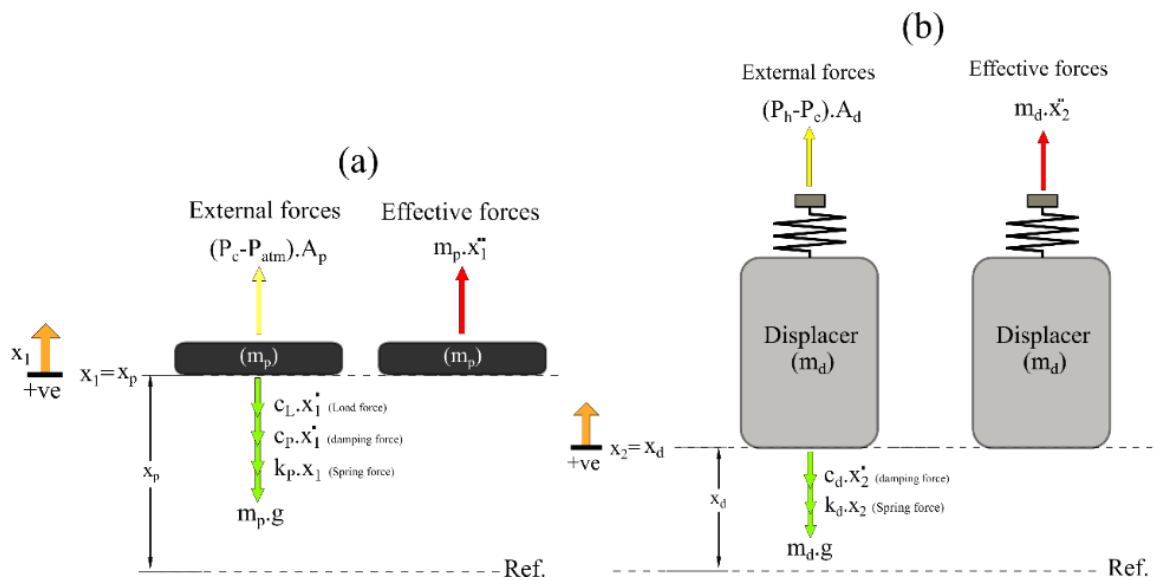


Figure 2: Forces balance, (a) equivalent mass balance, (b) displacer balance

Equation 1: Piston dynamics.

$$\ddot{x}_1 = \frac{(P_c - P_{atm})A_p}{m_p} - g - \frac{c_L \dot{x}_1}{m_p} - \frac{c_p \dot{x}_1}{m_p} - \frac{k_p x_1}{m_p}$$

Equation 2: Displacer dynamics.

$$\ddot{x}_2 = \frac{(P_h - P_c)A_d}{m_d} - \frac{c_d \dot{x}_2}{m_d} - g - \frac{k_d x_2}{m_d}$$

Where:

- $x_1, x_2$  = Equivalent mass and displacer displacement respectively. (m)
- $P_c, P_h, P_{atm}$  = Cold space pressure, hot space pressure and atmospheric pressure respectively. (Pa)
- $A_p, A_d$  = The Equivalent mass and displacer areas respectively. ( $m^2$ )
- $k_p, k_d$  = The spring stiffnesses of the equivalent mass and displacer respectively. (N/m)
- $m_p, m_d$  = The masses of the equivalent mass and the displacer respectively. (kg)
- $c_p, c_d, c_L$  = The damping coefficient of the equivalent mass, displacer and due to load respectively. (N.s/m)
- $g$  = Gravitational acceleration. ( $m/s^2$ )

### 3.2. Thermal Modelling

The thermal model deduces the instantaneous pressures, temperatures, and the mass flow rates. Open system analysis is adapted through the analysis. The engine space is divided into 2 control volumes as indicated in Figure 3. The universal gas law (state equation) and the first law of thermodynamics for open systems are applied separately on each volume. The mass flow rate is calculated from the conservation of mass. In the presented analysis the effect of the displacer movement and pressure difference are taken into account in calculating the total mass flow rate.

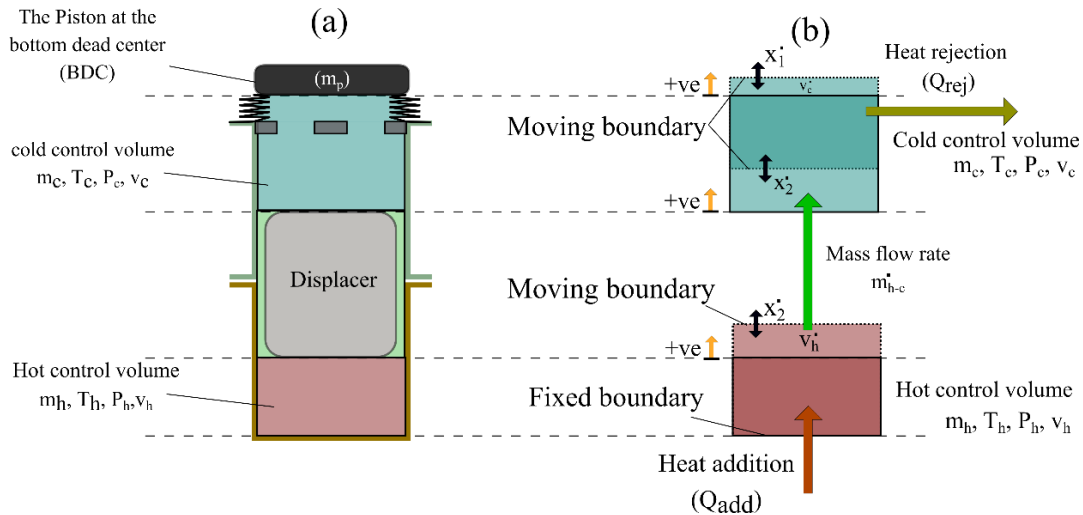


Figure 3: Volumes schematic, (a) Engine volumes, (b) Volume boundaries and balance

### 3.3. Calculating the instantaneous volumes and volumetric flow rates

As can be observed in Figure 3, the hot control volume is located at the lower part of the engine. While the cold control volume is located in the upper part. As a result of mass transfer between the two control volumes the system is considered an open system. The regenerator is assumed of zero dead volume for simplification. This can be valid for small sizes engines that operate at relatively low or medium temperatures. Using the velocities and displacements obtained from the dynamical model the instantaneous volumes and volumetric rates can be calculated as given by Equations 3, 4, 5 and 6.

Equation 3: Cold volume. 
$$V_c = (x_1)A_p - (L_d + x_2)A_d$$

Equation 4: Rate of change in cold volume. 
$$\dot{V}_c = \dot{x}_1 A_p - \dot{x}_2 A_d$$

Equation 5: Hot volume. 
$$V_h = x_2 A_d$$

Equation 6: Rate of change in hot volume. 
$$\dot{V}_h = \dot{x}_2 A_d$$

Where:

$V_c, V_h$  = Cold volume and hot volume respectively. ( $m^3$ )  
 $L_d$  = Displacer's length. (m)

### 3.4. Calculating the temperature and temperature rates

The cold and hot volume temperature rates  $\dot{T}_c$  and  $\dot{T}_h$  can be deduced as indicated in Equations 7 and 8 by applying the first law of thermodynamics for open system on each control volume separately. Through the analysis the regenerator is simplified. The heat stored in the regenerator can be obtained from Equation 9. The same equation can be used to obtain  $T_{out}$ . The temperature  $T_r$  can be assumed as the average temperature of  $T_h$  and  $T_c$ .

Equation 7: Cold space temperature. 
$$\dot{T}_c = \frac{1}{m_c C_V} ((C_P T_{origin} - C_V T_c) \dot{m}_{h-c} - P_c \dot{V}_c - Q_{rej})$$

Equation 8: Hot space temperature.

$$\dot{T}_h = \frac{1}{m_h C_V} (Q_{add} - \dot{m}_{h-c} (C_P T_{origin} - C_V T_h) - P_h \dot{V}_h)$$

Equation 9: Heat stored in the regenerator.

$$Q_{reg} = \dot{m} c_p (T_r - T_c) = \eta_{reg} \dot{m} c_p (T_h - T_{out})$$

Where:

$T_c, T_h$  = Cold and hot temperatures respectively. (K)

$C_v, C_p$  = The specific heat of air at constant volume and constant pressure respectively. (kJ/kg.K)

$m_c, m_h$  = air instantaneous mass in the cold and hot volume respectively. (Kg)

$Q_{rej}$  = The heat rejected from the upper cold part of the engine. (Watt)

$Q_{add}$  = Heat added at the receiver. (Watt)

$Q_{reg}$  = Heat stored in the regenerator. (Watt)

$\eta_{reg}$  = Regenerator efficiency.

$T_{origin}$  = The temperature of the transferred air between the 2 volumes. (K)

### 3.5. Calculating the pressures and pressure rates

By applying the ideal gas law, the pressure rates  $\dot{P}_c$  and  $\dot{P}_h$  can be evaluated. The equations can be obtained in the differential form as shown in Equation 10 and 11 which gives us the pressure of the cold and hot space respectively.

Equation 10: Cold space temperature.

$$\dot{P}_c = \frac{1}{V_c} (\dot{m}_{h-c} R T_c + m_c R \dot{T}_c - P_c \dot{V}_c)$$

Equation 11: Hot space temperature.

$$\dot{P}_h = \frac{1}{V_h} ((-\dot{m}_{h-c}) R T_h + m_h R \dot{T}_h - P_h \dot{V}_h)$$

Where:

$\dot{m}_{h-c}$  = mass flow rate from the hot to the cold volume. (kg/s)

$R$  = universal gas constant. (kJ/kg.K)

### 3.6. Calculating the mass flow rate

Obtaining the correct mass flow rate is of significant effect in FPSE. There are 2 major parameters that affect the mass flow rate, which are the instantaneous pressure difference between the cold and hot volumes and the displacer motion. In this study both effects are considered and combined to get the total mass flow rate. Firstly, the mass flow rate as a result of displacer motion which can be calculated from Equation 12. The air is assumed stationary inside the engine and the pressure is assumed constant through the whole engine, the negative sign is a result of assuming positive direction upwards. Secondly, the mass flow rate as a result of the pressure difference between the cold and the hot volumes which is calculated from Equation 13. In this case, the displacer is assumed stagnant. For any flow through orifice there is an equation that binds the pressure to flowrate. This relation depends mainly on the gas properties and the geometry of the orifice. In this investigation the Hagen-Poiseuille equation of the pressure drop through annular orifice is used. Finally, the total mass flow rate is calculated from Equation 14 by the summation of the 2 obtained value from Equations 12 and 13 at each time step.

Equation 12: Mass flow rate due to displacer movement.

$$\dot{m}_{(h-c)disp} = -(\dot{x}_2 A_d \rho_{origin})$$

Equation 13: Mass flow rate due to pressure difference.

$$\dot{m}_{(h-c)pressure} = \frac{\pi \Delta P_{disp} \rho_{origin} a^3 r}{6 \mu L_d}$$

Equation 14: Total mass flow rate.

$$\dot{m}_{h-c} = \dot{m}_{(h-c)disp} + \dot{m}_{(h-c)pressure}$$

Where:

$\dot{m}_{(h-c)disp}$  = mass flow rate as a result of displacer motion. (kg/s)

$\dot{m}_{(h-c)pressure}$  = mass flow rate as a result of pressure difference. (kg/s)

$\rho_{origin}$  = The density of the transferred air based on the direction of motion. (kg/m<sup>3</sup>)

$\mu$  = Air dynamic viscosity at the operating temperature. (kg/m.s)

$\Delta P_{disp}$  = Pressure difference across the displacer. (Pa)

$a$  = Clearance. (m)

$r$  = Cylinder bore diameter. (m)

### 3. RESULTS AND DISCUSSION

The parameters of the proposed engine are listed in Table 1. Generally, the engine is assumed to be subjected to constant heat flux of 250 Watt. Also, the cold side is assumed to have a perfect cooling that keeps it at about 300K which is above the assumed ambient temperature by 2 degrees.

Table 1: Proposed engine parameters

Geometry	
Cylinder diameter	$D = 0.1 \text{ m}$
Displacer length	$L_d = 0.135 \text{ m}$
Piston starting position from the reference	$x_p = 0.16 \text{ m}$
Displacer starting position from the reference	$x_d = 0.015 \text{ m}$
Hot section length	$L_h = 0.1 \text{ m}$
Clearance	$a = 0.001 \text{ m}$
Gas properties [air]	
Universal gas constant	$R = 287.05 \text{ J/kg. K}$
Specific heat at constant volume	$c_v = 718 \text{ J/kg. K}$
Specific heat at constant pressure	$c_p = 1005 \text{ J/kg. K}$
Dynamics parameters	
Piston mass	$m_p = 5 \text{ kg}$
Piston spring stiffness	$k_p = 20000 \text{ N/m}$
Piston damping coefficient	$C_p = 6 \text{ N.s/m}$
Displacer mass	$m_d = 0.18 \text{ kg}$
Displacer spring stiffness	$k_d = 2700 \text{ N/m}$
Displacer damping coefficient	$C_d = 8 \text{ N.s/m}$
Load coefficient	$C_{Load} = 40 \text{ N.s/m}$
Thermal parameters	
Heat added	$Q_{add} = 250 \text{ W}$
Initial pressure	$P_{ini} = 1.013 \times 10^5 \text{ Pa}$
Initial temperature	$T_{ini} = 298 \text{ K}$

Through the following section the proposed engine output performance is presented. At the beginning, the performance results are discussed. After that, the parameter of interest is changed over a certain range and the variation in the performance and output cycle is observed. In this study, the parameter of interest is the displacer's spring stiffness. The spring stiffness is changed from 1800 to 3400 N/m with a step of 400 N/m while keeping the rest of parameters constant at the given values in Table 1. At the end, the influence of the displacer's spring stiffness is demonstrated in correspondence to the equivalent mass stroke, the displacer stroke, the average hot temperature, the engine pressure, the instantaneous mass flow rate, the average output power, the output cycle illustrated on the PV-diagram and the actual dead volume during operation.



### 3.1. Engine performance

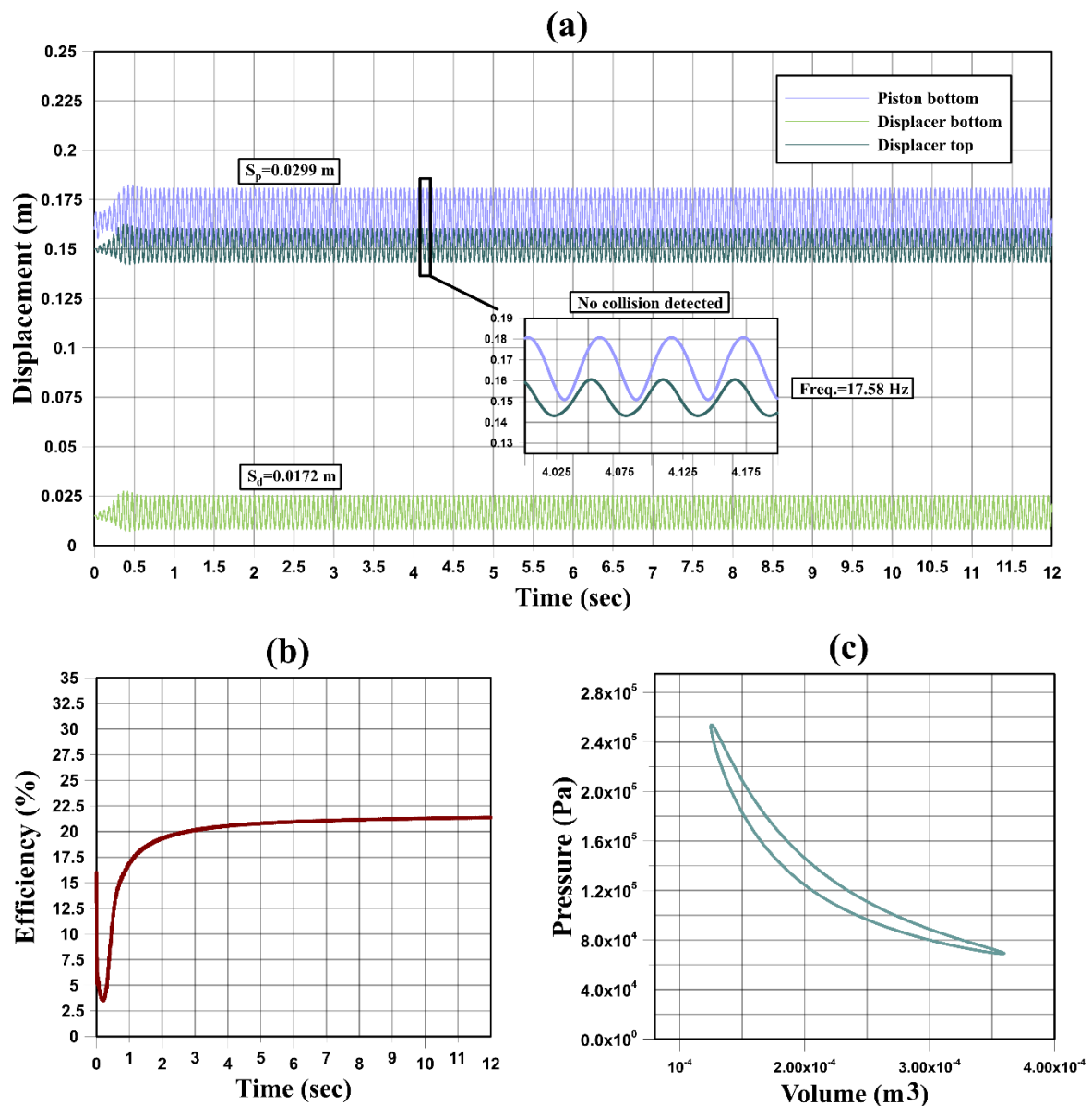


Figure 4: The engine performance, (a) Displacement diagram, (b) Engine's efficiency, (c) Engine's cycle

Figure 4 illustrates the overall performance of the proposed engine. The output displacement diagram can be shown in Figure 4a. The output displacement of the piston's equivalent mass bottom and the displacer top and bottom are clearly presented. From the figure it can be observed that engine reaches the steady state operation. It also indicates that no collisions between the displacer and the equivalent mass were detected. The engine achieved a steady state frequency of about 17.58 Hz. The strokes of the equivalent mass and displacer at steady state were found to be 0.0299 m and 0.0172 m respectively. Figure 4b shows that the engine achieved an efficiency of around 21.36% which is a convenient value for the assumption of air as working fluid and with no initial charging above the atmospheric pressure. The use of Helium with its thermal characterisation as a working fluid instead of air in addition to charging the engine over atmospheric pressure initially will enhance the performance of the engine. The output cycle at steady state can be seen in Figure 4c. The P-V diagram shows that the engine achieved a maximum pressure of  $2.53 \times 10^5$  Pa. The dead volume during operation can be concluded from the same figure as well. The dead volume during the engine steady operation was about  $1.24 \times 10^{-4}$   $\text{m}^3$ . The engine compression ratio was calculated to be 3.04. In general, the behaviour of the engine's cycle and performance were found to match the conventional Stirling cycle.

### 3.2. Displacer's spring stiffness ( $K_d$ )

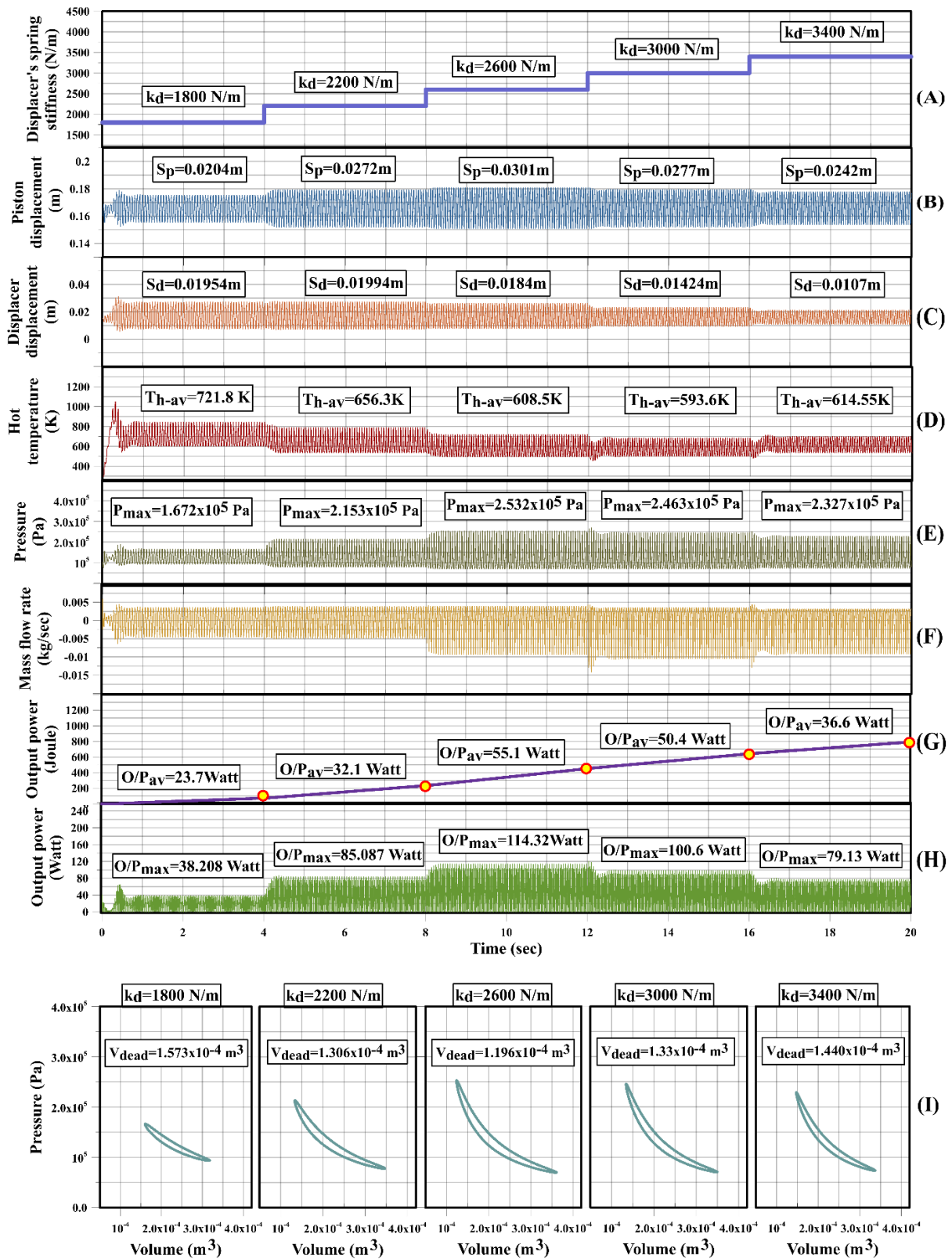


Figure 5: Engine response to variation in displacer's spring stiffness, (A) damping load coefficient, (B) piston displacement, (C) displacer displacement, (D) hot temperature, (E) engine's pressure, (F) mass flow rate, (G) output power in Joules, (H) output power in Watts, (I) engine output cycle.

In this section an investigation was carried out to analyse the engine response to the variation in the displacer's spring stiffness. As presented in Figure 5 the engine's model runs for 20 seconds. The value of the displacer's spring stiffness increases gradually every 4 seconds. As observed in Figure 5a, the stiffness starts at an initial value of 1800 N/m load coefficient and reaches a maximum value of 3400 N/m after 16 second. Which is nearly double the initial value. Figure 5b illustrates the effect of stiffness on the stroke of the equivalent mass. It is shown that the stroke increases gradually from 0.0204 m to 0.0301 on increasing  $K_d$  to about 2600 N/m. This means that the stroke increases by about 47.5% on increasing  $K_d$  by about 44.4%. After that the stroke decreases till it reaches a value of 0.0242 at the end of the 20 seconds. The effect on the displacer's stroke is presented in Figure 5c. It is found that after 2200 N/m the displacer's stroke is decreased significantly. As it dropped by about 85.9% from 0.0199 to 0.0107 m when  $K_d$  is increased from 2200 to 3400 N/m. Generally, decreasing the displacer stroke indicates lower performance as can be seen from Figures 5h and 5i. The hot side temperature as illustrated in Figure 5d tends to decrease till the value of 3000 N/m as it reduced by about 17.7% from 721.8K to 593.6K. This decrease can be justified by observing Figure 5f which indicates increase in the mass flow rate between the engine hot and cold spaces of the same range and, hence achieving better cooling. From Figure 5e the maximum pressure generated inside the engine appears increase till the value of 3000 N/m and it decreases afterwards. This can be confirmed by observing Figure 5i. The pressure increased by around 47.3% from  $1.672 \times 10^5$  Pa to  $2.463 \times 10^5$  Pa. The average output power and the instantaneous peak power shown in Figures 5g and 5h indicates that there is an optimum value for the displacer's spring stiffness for any given engine. In our study the optimum range is near the value of 2600 N/m. Another significant result is the sensitivity of the engine performance to the value of  $K_d$ , as the output power increased by 132.4% from 23.7 to 55.1 Watt on increasing the stiffness from 1800 to 2600 N/m. This result can be confirmed by tracing the enclosed area inside the curve in the PV-diagram illustrated in Figure 5i. From the same figure the dead volume during operation is shown to decrease by 23.9% to reach its minimum value which corresponds the optimum value of the stiffness and then increases afterwards.

#### 4. CONCLUSION

A new configuration for FPSE that implies the usage expansion bellows instead of piston cylinder is proposed. The main advantage for the new configuration is to eliminate leaking problem by turning the engine into fully hermetic. A simplified model that combines the engine dynamics and thermal modelling is developed. The model aims to avoid extreme simplicity or complexity in FPSE modelling. The model is numerically solved using Simulink™ without the need for linearisation. A given geometric parameter and operating conditions were introduced. The performance results were illustrated and discussed. The engine reached a steady state efficiency of 21.36% operating between 298K and 593K. The steady state frequency was found to be 17.5 Hz. The displacement diagram demonstrated that the engine achieved stable operation without any collisions detected. A comprehensive study that investigates the influence of the displacer's spring stiffness on the engine performance was conducted. It was concluded that for every given engine's parameter and operating conditions there is a certain optimum range for the spring stiffness to achieve highest performance condition in this study the optimum value was around 2600 N/m. Finally, the given model and configuration are considered a preliminary step that shows some potential for further investigation. Hence, more work and effort are needed in the future to enhance the model and to judge the reliability and lifetime of such configuration.

#### 5. REFERENCES

- Finkelstein, T. (1967) "Thermodynamic Analysis Of Stirling Engines.," *Journal Of Spacecraft And Rockets*, 4(9), Pp. 1184–1189. Doi: 10.2514/3.29049.
- Kannan, N. And Vakeesan, D. (2016) "Solar Energy For Future World: - A Review.," *Renewable And Sustainable Energy Reviews*, 62, Pp. 1092–1105. Doi: 10.1016/J.Rser.2016.05.022.
- Karabulut, H. (2011) "Dynamic Analysis Of A Free Piston Stirling Engine Working With Closed And Open Thermodynamic Cycles.," *Renewable Energy*. Doi: 10.1016/J.Renene.2010.12.006.
- Martini, W. R. (1978) *Stirling Engine Design Manual*. Us Department Of Energy, Office Of Conservation And Solar Applications ....
- Qiu, S. *Et Al.* (2019) "Development Of An Advanced Free-Piston Stirling Engine For Micro Combined Heating And Power Application.," *Applied Energy*. Elsevier, 235(June 2018), Pp. 987–1000. Doi: 10.1016/J.Apenergy.2018.11.036.
- Tavakolpour-Saleh, A. R., Zare, S. H. And Bahreman, H. (2017) "A Novel Active Free Piston Stirling Engine: Modeling, Development, And Experiment.," *Applied Energy*, 199, Pp. 400–415. Doi: 10.1016/J.Apenergy.2017.05.059.

Thombare, D. G. And Verma, S. K. (2008) "Technological Development In The Stirling Cycle Engines," *Renewable And Sustainable Energy Reviews*. Doi: 10.1016/J.Rser.2006.07.001.

Walker, G. And Senft, J. R. (1985) *Free Piston Stirling Engines, Free Piston Stirling Engines Se - 10*. Doi: 10.1007/978-3-642-82526-2\_10.

Yu, G. *Et Al.* (2018) "Modeling And Experimental Investigation Of A Free-Piston Stirling Engine-Based Micro-Combined Heat And Power System," *Applied Energy*, 226, Pp. 522–533. Doi: 10.1016/J.Apenergy.2018.05.122.

Zare, S. And Tavakolpour-Saleh, A. R. (2016) "Frequency-Based Design Of A Free Piston Stirling Engine Using Genetic Algorithm," *Energy*. Doi: 10.1016/J.Energy.2016.04.119.

---

## #96: Energy management of solar photovoltaic-battery energy systems in buildings

---

Jia LIU\*, Xi CHEN, Hongxing YANG

*Renewable Energy Research Group (REG), Department of Building Services Engineering,  
The Hong Kong Polytechnic University, Kowloon, Hong Kong, China  
\*Corresponding author: [jjia.liu@connect.polyu.hk](mailto:jjia.liu@connect.polyu.hk)*

*Recently, renewable energy is attracting much attention due to limited traditional energy sources and severe environmental issues caused by the over-consumption of fossil fuels. It is promising to use renewable energy for the power supply to buildings, as the building sector accounts for a large portion of global energy consumption with a constant increasing trend. In order to compensate for the intermittent and unpredictable disadvantage of renewable energy, the electrical energy storage technology such as the battery can be adopted to secure a reliable and sustainable power supply to buildings. This study aims to analyse and compare energy management strategies of an on-grid solar photovoltaic-battery system for a real building project in a typical hot summer and warm winter region. Three energy management strategies are developed for the building based on the Transient System Simulation Program (TRNSYS) including maximising the photovoltaic self-sufficiency, time-of-use electricity pricing and grid relieving. These three strategies are analysed and compared considering the technical aspects of the utility grid, PV system and building demand to find the most suitable energy management strategy for the building project. This study can provide theoretical references for the energy management and system operation to facility managers and building occupants. It can also serve as a demonstration case for designing on-grid photovoltaic-battery systems for near/zero energy buildings in hot summer and warm winter areas.*

*Keywords: Solar photovoltaic; Battery energy storage; Energy management strategy*

## 1. INTRODUCTION

Recently, the decreasing availability of fossil fuels and its negative implications on environment has aroused extensive attention in cutting down energy consumption and exploring alternative energy sources. The proportion of building energy consumption in the total energy use is 30% in China (Wan et al., 2011), 20-40% in developed countries (Pérez-Lombard et al., 2008) and up to 60% in Hong Kong (Luo et al., 2015). As promising substitutes for fossil fuels, solar and wind energy is widely utilised for the power supply in buildings in order to mitigate the energy crisis and environment pollution. Since renewable energy is usually intermittent, unpredictable (Ma et al., 2014b) and unmatched with building demand, corresponding electrical energy storage technologies should be combined for a stable and reliable power supply. The integrated electrical energy storage unit can not only adjust the power generated by photovoltaic (PV) panels or wind turbines to fit the building demand and enhance the energy efficiency but also regulate the frequency of the utility grid for on-grid renewable energy systems (Ma et al., 2014a). Electrical energy storage technologies can be sorted into a range of categories including the mechanical, electrochemical and electric storage. For buildings in urban areas, it is most likely to use the PV-battery energy storage (BES) system given the space limitation.

Much attention has been focused on the energy management of PV-BES systems in terms of the PV, battery, grid and system performance. For example, some researchers studied the energy management strategy considering the PV performance. The control strategy of the standalone PV-BES system is studied to track the maximum power point mode of PV panels and ensure the safe charging of battery cells, which is reported to be reliable and effective by a case study (Bonkile and Ramadesigan, 2019). Some efforts are made to improve the battery performance when studying the energy management strategies. An online energy management strategy is proposed for the lithium-ion battery applied in PV systems in order to minimise the battery degradation and reduce the energy cost. Its effectiveness is then validated by a baseline method (Feng et al., 2015). A control strategy focusing on the battery aging cost and building utility cost is proposed based on the model predictive control. The proposed approach is validated to be more competent compared with practical conventional strategies obtained by a one-month field test (Cai et al., 2019). Two novel control approaches are put forward to manage active battery charging used in PV systems including single-stage and two-stage charge controllers. It is proved that proposed methods are able to improve the total system efficiency due to the consideration of the dynamic performance of both PV arrays and battery cells (Saadeh et al., 2018). In terms of the grid integration with the PV-BES system, a novel energy management algorithm of the on-grid PV-BES system is proposed for a better grid integration and shorter payback period. It is reported that the proposed bi-directional power flow system can operate well in both maximum power point and limited power point modes, and it contributes to decreasing the size of home PV systems (Guichi et al., 2018). A complex control algorithm considering the model predictive control on voltage and power is studied for a microgrid PV-BES system to achieve a stable grid voltage outflow and balanced power flow. This developed energy management method is then verified by case studies with MATLAB (Hu et al., 2018). A distributed energy management approach is proposed for household PV-BES systems to prevent the grid from a high voltage based on a developed optimal scheduling algorithm. It is reported that the battery energy storage technology is powerful to solve the over-voltage problems without changing its primary function (Ranaweera et al., 2017).

Moreover, extensive research is found targeting the overall system performance when investigating the energy management strategy of PV-BES systems. For instance, Han et al. studied the hierarchical energy management of an off-grid PV system with battery and hydrogen as storage technologies using the simulation platform of HOMER to improve the economic and robust performance (Han et al., 2019). A decentralised energy management strategy is focused for a standalone alternating current PV-BES system based on the model predictive control method, which is feasible to stabilise the output voltage and level the load profile (Jayachandran and Ravi, 2019). A decentralised control method is also presented to manage the power flow of PV-BES systems to obtain high system stability and scalability. And the feasibility of the proposed approach is analysed with practical solar irradiation data (Kim and Bae, 2017). An innovative framework on the energy storage decision of battery used in PV systems is proposed based on smart meter data in order to evaluate different utility electricity price and feed-in tariff price. It is found that the utility price in the studied region is not economically feasible in terms of energy storage cost (Li et al., 2019). The impact of electric vehicles and heat pumps on the performance of household PV-BES systems are investigated based on 415 individual home data, showing that both technologies can improve the system self-consumption profitability (Klingler, 2018).

Although a large amount of research has been conducted on the energy management of PV-BES systems, few of them focused on developing energy management strategies for the PV-BES system in a practical building with a comprehensive concern of system performance indicators. In this study, different energy management strategies focusing on the PV self-sufficiency, time-of-use pricing and grid reliving respectively, are proposed and compared for the PV-BES system installed in a realistic building. The performance of these strategies of typical weeks in both summer and winter are analysed and discussed in detail. It can offer guidance to the operation and management of the PV-BES system in low energy building.

## 2. METHODOLOGY

### 2.1. PV-BES system in the practical building



Figure 1: Practical building with PV and battery energy storage system

A practical building equipped with the photovoltaic-battery energy storage (PV-BES) system in a typical hot-summer and warm-winter region is studied as shown in Figure 1. Both rooftop thin-film PV panels and facade thin-film PV panels are used with a total rated capacity of 13.12kW to convert solar energy into electricity. The lead-acid battery bank with a rated capacity of 45.6kWh is applied to store surplus solar energy during the solar energy shortage period. The detailed specification of the PV-BES system is shown as Table 1.

Table 1: Specification of the PV-battery energy system

Solar panels	ASP-S1-80W (CdTe)
Maximum power	80W
Open circuit voltage	118.5 V
Short circuit current	1.01 A
Voltage at max. power point	92 V
Current at max. power point	0.88 A
Maximum system voltage	1000 V
Rooftop cell number	149
Façade PV cell number	15
Battery storage	NP100-12FR (Lead-Acid)
Nominal capacity	100Ah/12 V
Number in series	38
Operational SOC ( $SOC_{min}$ - $SOC_{max}$ )	25%-90%(Cai et al., 2019)
Max. charging/discharging rate	0.2C
Charging efficiency	0.9

### 2.2. System simulation in TRNSYS

Transient System Simulation Program (TRNSYS) (University of Wisconsin-Madison, 2017) is widely acknowledged as an effective tool to simulate complex renewable energy systems based on the system energy conversion mechanism. It can be used to analyse the system performance from energy, cost and environment aspects (Roselli et al., 2019). TRNSYS consists of two major parts including the kernel part focusing on the system operation and component library providing extensive application modules. In this study, the renewable energy system containing five major elements namely the building load, PV panels, battery bank, utility grid and energy management strategy,

are established in the TRNSYS platform. According to the practical design configuration, the building load calculation involves the building envelop, air conditioning, and internal gains (i.e. lighting, equipment and indoor occupants). The developed modules in the TRNSYS library including Type 56, Type 117, Type 752, Type 655, Type 648 and other auxiliary components are adopted to build the overall system model. The used PV array model is determined according to the five-parameter empirical equivalent circuit model (De Soto et al., 2006, Duffie and Beckman, 2013). The PV self-sufficiency ratio is studied as shown in Equation 1:

$$\text{Equation 1: } PV \text{ self - sufficiency ratio} = \frac{P_{pv \text{ to load}} + P_{battery \text{ to load}}}{P_{load}}$$

Where:

- $P_{pv \text{ to load}}$  = power from PV generators to meet the load, kW
- $P_{battery \text{ to load}}$  = power from the battery bank to meet the load, kW
- $P_{load}$  = load demand of the building, kW.

The battery model is developed based on the energy balance mechanism using the state of charge (SOC) as the iteration indicator. The maximum charging SOC of the battery bank is 0.95, and the minimum SOC is 0.25 (Cai et al., 2019). The maximum charging/discharging rate of the lead-acid battery is 0.2 of its rated capacity and the charging efficiency is 0.9. In terms of the grid side, the standard deviation of the grid outflow is analysed to show the average grid stress as shown in Equation 2 (Voss et al., 2010):

$$\text{Equation 2: } Average \text{ grid stress}_{year} = Standard \ deviation(P_{grid \text{ to load}} + P_{grid \text{ to battery}})_{step}$$

Where:

- $P_{grid \text{ to load}}$  = power from the utility grid to meet the load, kW
- $P_{grid \text{ to battery}}$  = power from the utility grid to charge the battery, kW.

Three energy management strategies including maximising the PV self-sufficiency, time-of-use pricing and grid relieving are developed for the case building respectively. In the energy management strategy of maximising the PV self-sufficiency, the available PV power is firstly used to meet the building load and charge the battery, and the surplus PV power is then fed into the utility grid. If the PV power is not enough for the load, battery will be discharged to meet the load. And when the accessible battery capacity still cannot meet the load, the utility grid will act as the electricity back up. The energy management strategy of time-of-use pricing is based on the practical electricity regulation for the building located in Shen Zhen. During valley hours, the grid will satisfy the unmet load from the PV power, and charge the battery bank in a low electricity price. And when the peak time arrives, battery will be used to meet the unsatisfied load from the PV power to reduce the electricity bill. Since this building is not in operation during weekends, the PV power in weekends will charge the battery first and then feed into the grid. The electricity price in peak hours is about 0.15\$/kWh during 9:00-11:30, 14:00-16:30, 19:00-21:00, while it is about 0.1\$/kWh in flat hours during 7:00-9:00, 11:30-14:00, 16:30-19:00, 21:00-23:00. The electricity price in valley hours of 23:00-7:00 is approximately 0.04\$/kWh. While in the energy management strategy focusing on grid relieving, the grid feed-in power is limited as the 50% of rated PV power so that the exceeded part of PV feed-in power will be dumped to protect the utility grid from high power fluctuations. The grid power outflow is limited to charge the battery but always available to the load for securing the building electricity stability.

### 3. RESULT AND DISCUSSION

The annual operation performance of the system is evaluated, and the results of typical weeks in both summer and winter under three different strategies are compared. Figure 2 shows the power flow of typical weeks in summer and winter under the control of maximising the self-sufficiency strategy. The building load in summer is higher than that in winter because the ratio of air-conditioning load in summer is high in this hot-summer and warm-winter region. Therefore, the PV power is always not sufficient for the building load in weekdays in summer, and the electricity from the battery and grid should be used. While in winter, surplus PV power can usually be used to charge the battery. Average SOC in summer weekdays is smaller than that in winter weekdays, which means a higher battery degradation in summer.



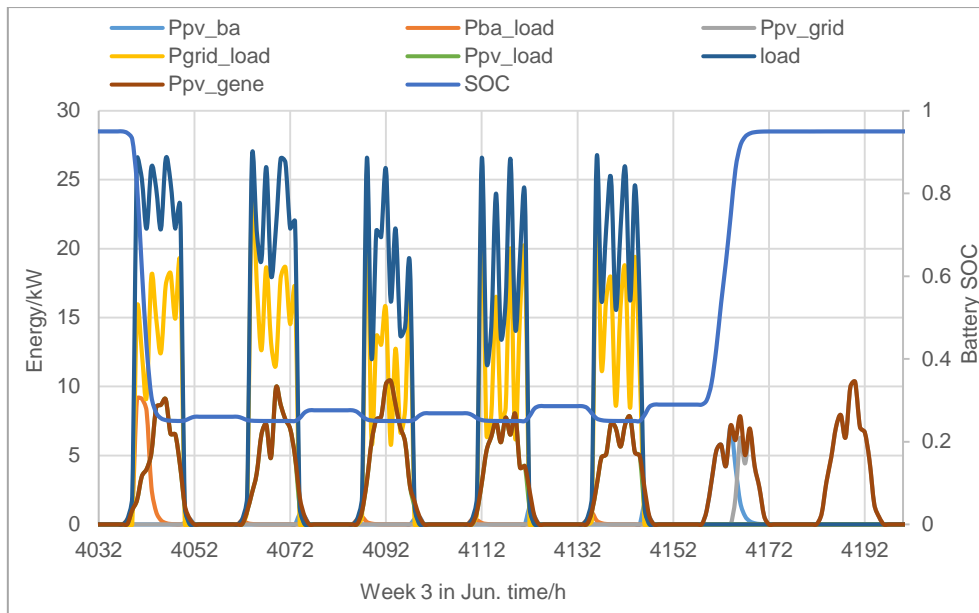


Figure 2(a): Power flow of week 3 in June of maximising self-sufficiency strategy

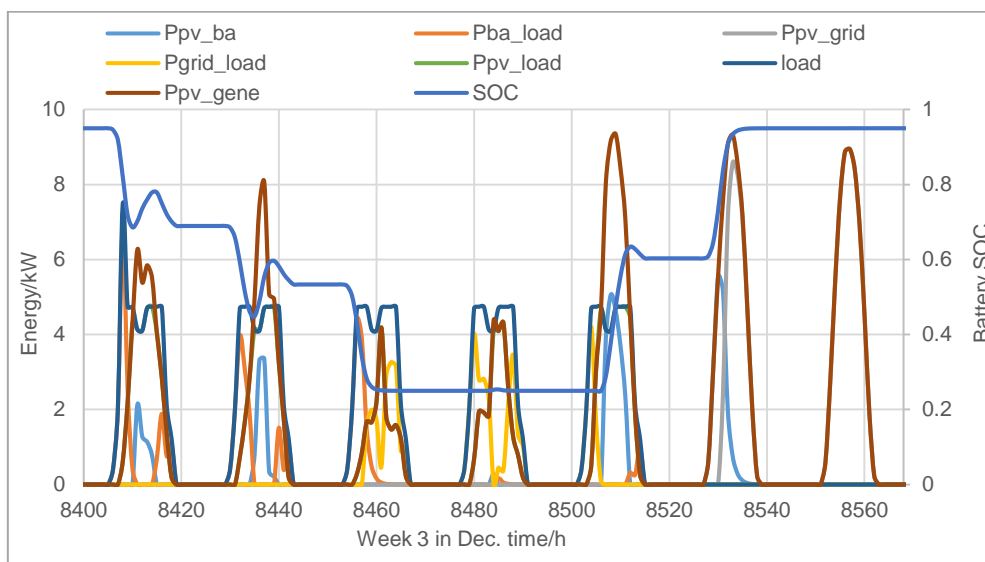


Figure 2(b): Power flow of week 3 in December of maximising self-sufficiency strategy

Figure 3 shows the power flow of typical weeks in summer and winter under the time-of-use pricing strategy. It is shown that during the peak time in weekdays, the battery will support the PV to meet the building load when it is not sufficient and the grid will charge the battery in a cheap cost during the valley period between 23:00pm to 7:00am. Therefore, the SOC distribution shows that the battery is frequently charged to the full state during the valley hours and discharged to meet the load in peak time. In winter when the building load becomes smaller, the battery will be not fully used even in the peak time because the PV power is relatively more. And when it is during weekdays, PV power will firstly charge the battery to maximum state and then feed into the grid, which earns the feed-in tariff.

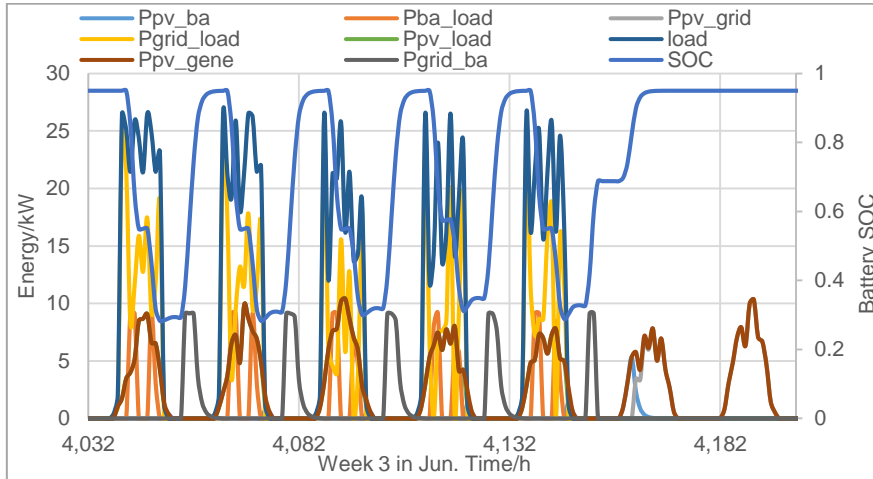


Figure 3(a): Power flow of week 3 in June of time-of-use pricing strategy

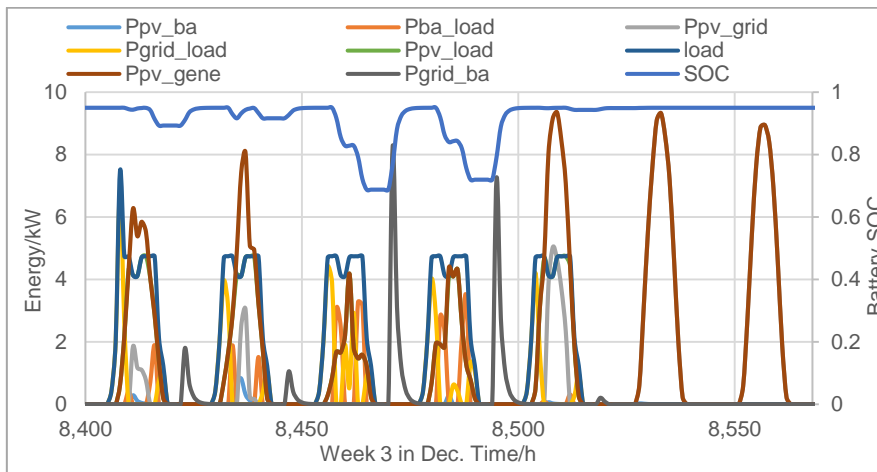


Figure 3(b): Power flow of week 3 in December of time-of-use pricing strategy

Figure 4 shows the power flow of typical weeks in both summer and winter under the grid relieving strategy. It shows that some part of PV power is dumped when exceeding the grid feed-in limit and some part of load will exceed the grid outflow limit but still met by the grid. The battery bank is fully used in summer but not in operation during the third week of December because the grid power and PV power is sufficient for the building demand.

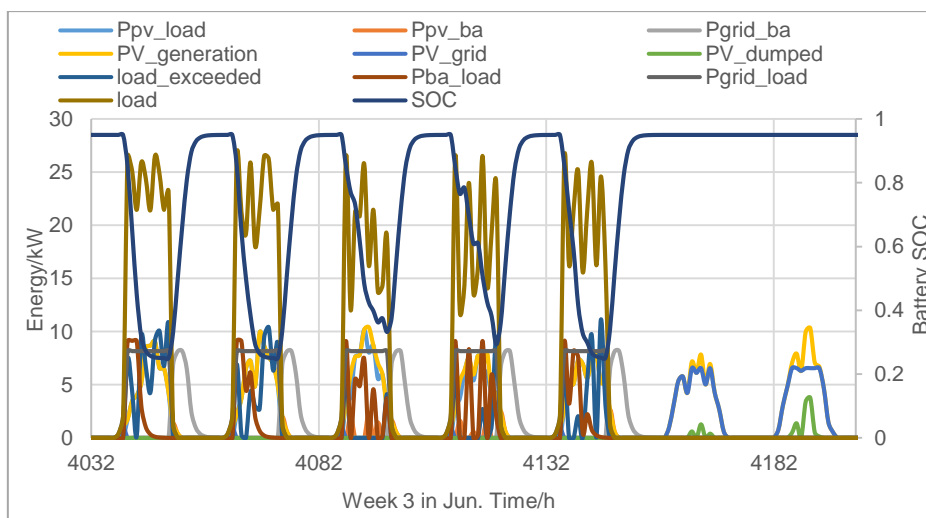


Figure 4(a): Power flow of week 3 in June of grid relieving strategy

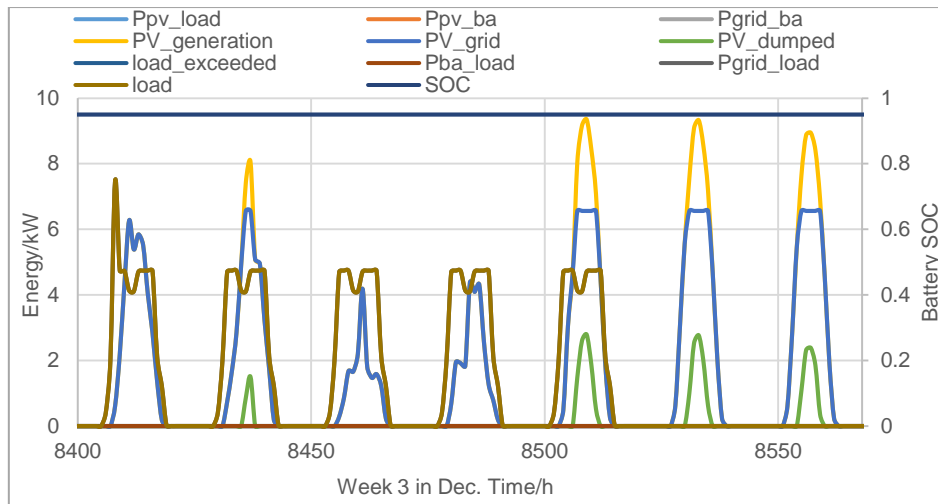


Figure 4(b): Power flow of week 3 in December of grid relieving strategy

Table 2 compares the self-sufficiency ratio and grid stress of these three strategies on an annual operation basis. It can be found that the maximising self-sufficiency strategy has the highest self-sufficiency ratio, but its standard deviation of grid out is the maximum with the largest grid stress. The standard deviation of grid out in the grid relieving strategy is the minimum for 4.241 with more centralised grid outflow distribution than other two strategies. But the self-sufficiency ratio in this strategy is the lowest for 0.649, which is about 25% lower than that in the maximising the self-sufficiency strategy. And the self-sufficiency ratio and standard deviation of the grid outflow in the time-of-use pricing strategy is the 0.824 and 4.832 respectively, which is the optimal in terms of the balanced performance of the energy self-sufficiency and grid stress.

Table 2. Comparison of three energy management strategies

Annually average	Self-sufficiency ratio	Standard deviation of grid out
Maximising self-sufficiency strategy	0.864	5.013
Time-of-use pricing strategy	0.824	4.832
Grid relieving strategy	0.649	4.241

#### 4. CONCLUSION

Three energy management strategies are developed for the PV-BES system installed in a practical building focusing on maximising the self-sufficiency, time-of-use pricing and grid relieving respectively. The building model is established in SketchUp and then imported into the TRNSYS platform to obtain the practical load demand of the envelope, air conditioning and internal gains based on the weather data in typical meteorological year. The major components of the PV-BES system including PV panels, battery bank, utility grid and energy management unit are established in the model to get the energy-balanced results. It is found that the power flow of the PV-BES system of a typical week in summer differs greatly from that in winter because of the load difference. The maximum annual self-sufficiency is about 0.864 under the maximising self-sufficiency strategy, while the minimum self-sufficiency is about 0.649 under the grid relieving strategy. The minimum standard deviation of grid out is 4.241 under the grid relieving strategy with smallest grid stress, which is 16% smaller than that in the maximising self-sufficiency strategy. The time-of-use strategy is the most appropriate for the building in terms of achieving a balanced system self-sufficiency and grid stress.

#### 5. REFERENCES

- Bonkile, M. P. & Ramadesigan, V. 2019. Power management control strategy using physics-based battery models in standalone PV-battery hybrid systems. *Journal of Energy Storage*, 23, 258-268.
- Cai, J., Zhang, H. & Jin, X. 2019. Aging-aware predictive control of PV-battery assets in buildings. *Applied Energy*, 236, 478-488.
- De Soto, W., Klein, S. & Beckman, W. J. S. E. 2006. Improvement and validation of a model for photovoltaic array performance. 80, 78-88.
- Duffie, J. A. & Beckman, W. A. 2013. *Solar engineering of thermal processes*, John Wiley & Sons.

- Feng, X., Gooi, H. B. & Chen, S. 2015. Capacity fade-based energy management for lithium-ion batteries used in PV systems. *Electric Power Systems Research*, 129, 150-159.
- Guichi, A., Talha, A., Berkouk, E. M. & Mekhilef, S. 2018. Energy management and performance evaluation of grid connected PV-battery hybrid system with inherent control scheme. *Sustainable Cities and Society*, 41, 490-504.
- Han, Y., Zhang, G., Li, Q., You, Z., Chen, W. & Liu, H. 2019. Hierarchical energy management for PV/hydrogen/battery island DC microgrid. *International Journal of Hydrogen Energy*, 44, 5507-5516.
- Hu, J., Xu, Y., Cheng, K. W. & Guerrero, J. M. 2018. A model predictive control strategy of PV-Battery microgrid under variable power generations and load conditions. *Applied Energy*, 221, 195-203.
- Jayachandran, M. & Ravi, G. 2019. Predictive power management strategy for PV/battery hybrid unit based islanded AC microgrid. *International Journal of Electrical Power & Energy Systems*, 110, 487-496.
- Kim, M. & Bae, S. 2017. Decentralized control of a scalable photovoltaic (PV)-battery hybrid power system. *Applied Energy*, 188, 444-455.
- Klingler, A.-L. 2018. The effect of electric vehicles and heat pumps on the market potential of PV + battery systems. *Energy*, 161, 1064-1073.
- Li, H. X., Horan, P., Luther, M. B. & Ahmed, T. M. F. 2019. Informed decision making of battery storage for solar-PV homes using smart meter data. *Energy and Buildings*, 198, 491-502.
- Luo, Y., Wang, M., Yang, H., Lu, L. & Peng, J. 2015. Experimental study of internally cooled liquid desiccant dehumidification: Application in Hong Kong and intensive analysis of influencing factors. *Building and Environment*, 93, 210-220.
- Ma, T., Yang, H. & Lu, L. 2014a. Feasibility study and economic analysis of pumped hydro storage and battery storage for a renewable energy powered island. *Energy Conversion and Management*, 79, 387-397.
- Ma, T., Yang, H., Lu, L. & Peng, J. 2014b. Technical feasibility study on a standalone hybrid solar-wind system with pumped hydro storage for a remote island in Hong Kong. *Renewable Energy*, 69, 7-15.
- Pérez-Lombard, L., Ortiz, J., Pout, C. J. E. & BUILDINGS 2008. A review on buildings energy consumption information. 40, 394-398.
- Ranaweera, I., Midtgård, O.-M. & Korpås, M. 2017. Distributed control scheme for residential battery energy storage units coupled with PV systems. *Renewable Energy*, 113, 1099-1110.
- Roselli, C., Diglio, G., Sasso, M. & Tariello, F. 2019. A novel energy index to assess the impact of a solar PV-based ground source heat pump on the power grid. *Renewable Energy*, 143, 488-500.
- Saadeh, O., Rabady, R. & Bani Melhem, M. 2018. New effective PV battery charging algorithms. *Solar Energy*, 166, 509-518.
- University of Wisconsin-Madison 2017. Transient System Simulation Program (TRNSYS 18).
- Voss, K., Sartori, I., Napolitano, A., Geier, S., Gonçalves, H., Hall, M., Heiselberg, P., Widén, J., Candanedo, J. A. & Musall, E. Load matching and grid interaction of net zero energy buildings. EURO SUN 2010 International Conference on Solar Heating, Cooling and Buildings, 2010.
- Wan, K. K. W., Li, D. H. W., Liu, D. & Lam, J. C. 2011. Future trends of building heating and cooling loads and energy consumption in different climates. *Building and Environment*, 46, 223-234.

---

## #97: Numerical study on trapezoidal solar pond based on a two-dimensional large eddy simulation model

---

Hongsheng LIU<sup>1</sup>, Dan WU<sup>2</sup>, Chungu QIAO<sup>1</sup>, Linsong JIANG<sup>1</sup>

<sup>1</sup> Key Laboratory of Ocean Energy Utilization and Energy Conservation of Ministry of Education, Dalian University of Technology, Dalian, 116024, China, lhsh@dlut.edu.cn

<sup>2</sup> Department of Mechanical and Power Engineering, Yingkou Institute of Technology, Yingkou 115014, China, 916974680@qq.com

*Thermal performance of a trapezoidal solar pond is numerically simulated by a two-dimensional unsteady model based on the large eddy simulation method. The temperature distributions of the Reynolds Averaged Navier-Stokes (RANS) and the Large Eddy Simulation (LES) are contrasted against the experimental data to verify the validation of the simulation. The characteristics of temperature, the velocity distribution and salt concentration are analysed. The results show that the overall temperature of the solar pond increases over the running time, and the maximum temperature (314K) appears in the lower convective zone. The velocity field is mainly distributed in LCZ, and the average velocity remains at the order of  $10^{-4}$ m/s. The salinity at the lower interface decreases linearly, while it decreases with a trend of fluctuating downward at the upper interface.*

*Keywords: solar pond; Two-dimensional model; large eddy simulation; temperature distribution*

## 1. INTRODUCTION

As a solar energy collecting and storing device, solar pond has been useful for industrial, domestic and agriculture heating purpose (Ranjan and Kaushik, 2014), such as salt production (Lesino and Saravia, 1991), house heating (Badran and Hamdan, 2004) and desalination (Othman et al., 2018), etc. A typical solar pond consists of three thermally distinct layers: the upper convective zone (UCZ), the non-convective zone (NCZ) and the lower convective zone (LCZ). The UCZ is a thin homogeneous layer with very low salinity water, which bears almost all the environmental influences on the surface of the solar pond. The middle layer or NCZ has salinity gradient with salinity increasing from top to bottom, and acts as a critical insulator to suppress the heat loss caused by the natural convection. The LCZ, also known as the energy storage zone, consists of high salinity brine and acts as a collection and reservoir of solar radiation.

Since the conception of solar pond was proposed (Weinberger, 1964) about 70 years ago, numerous experimental and theoretical studies on solar ponds have been extensively carried out to understand the thermal behaviour of the heat and mass transfer (Boudhief and Baccar, 2014), the thermal efficiency (Dehghan et al., 2013), the stability (Hull and Nielsen, 1989), the heat extraction (Elsebaei et al., 2013) and so on. In the recent years, the double diffusion theory of the heat and salt was explored and studied in depth. Kurt et al. (2006) developed a one-dimensional transient mathematical model to describe the heat and mass transfer behaviour of an experimental salt gradient solar-pond, and the differential equations were solved numerically using a finite-difference method. Accounting for the thermal extraction from the ponds, Njokua et al. (2017) proposed a numerical model to predict the time-varying temperature profiles, the energy and the exergy flows. Their computation results showed that the LCZ stores the most energy and has the highest storage efficiency. Boudhief et al. (2014) presented a numerical study on the properties of transient hydrodynamic, heat and mass transfer in a solar pond using the dimensionless governing equations of Navier–Stokes, thermal energy and mass transfer, which were solved numerically by a finite-volume method to provide the temperature, concentration and velocity fields in transient regime. Liu et al. (2015) established a turbidimetric model and a heat-salt double diffusion model of a trapezoidal solar pond, the influences of pond structure, the turbidity of the saltwater and the reflectivity on the surface of the solar pond were discussed.

In this paper, the working process of the solar pond is numerically simulated based on an experimental trapezoidal solar pond and its local meteorology. The solar radiation transmission, the diffusion of the heat and salt, heat loss and turbulence are considered in the two-dimensional simulation. The method of the large eddy simulation is employed to study the special micro-turbulence phenomenon in the solar pond. The validity of the numerical simulation is verified by the comparison between the experimental data and simulation results. The thermal performance and natural convection phenomenon in the solar pond are analysed, which will provide theoretical guides for application of the solar pond.

## 2. PHYSICAL MODEL OF TRAPEZOIDAL SOLAR POOL

A physical model of a mini trapezoidal solar ponds (Liu et al., 2015) with surface area of  $2.4 \times 2.4 \text{ m}^2$ , bottom area of  $1 \times 1 \text{ m}^2$  and depth of 1.2m, is developed by the CFD software of FLUNET. Figure 1 shows the schematic diagram of the energy transfer and stratification in the pool. The depth of the UCZ, NCZ and LCZ are 0.2m, 0.5m and 0.5m, respectively. Based on the same assumption as Liu et al.(2015), the solar pond is divided into 24 layers from top to bottom as shown in Figure 1, where the UCZ, NCZ and LCZ are corresponded to layers 1~4, 5~14 and 15~24, respectively.

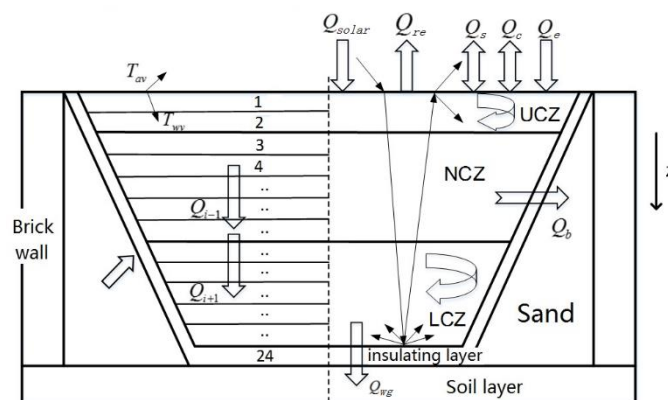


Figure 1: Solar pond energy transfer and layering diagram

## 2.1. Computational method

Combining the heat diffusion model with the salt diffusion model, the heat loss model, the solar radiation model, and the LES turbulence model, the heat transfer process in the pond is simplified as an unsteady state heat conduction with internal heat source, and the control equations are same with Njokua et al. (2017):

Equation 1: The continuity equation: 
$$\frac{\partial \bar{\rho}}{\partial t} + \frac{\partial (\bar{\rho} \tilde{u}_i)}{\partial x_i} = 0$$

Equation 2: The momentum equation: 
$$\frac{\partial (\bar{\rho} \tilde{u}_i)}{\partial t} + \frac{\partial (\bar{\rho} \tilde{u}_i \tilde{u}_j)}{\partial x_j} - \frac{\partial}{\partial x_j} (\mu_{sgs} \frac{\partial \tilde{u}_i}{\partial x_j}) = -\frac{\partial \bar{p}}{\partial x_i} + \frac{\partial \tau_{ij}^{sgs}}{\partial x_j}$$

Where:

- $\rho$  = the density of salt water (kg/m<sup>3</sup>)
- $u$  = flow velocity (m/s)
- $t$  = the length of time (s)
- “ $\sim$ ,  $\sim$ , sgs” represent the physical spatial filtering, the Favre filtering and the sub-grid, respectively.
- $p$  = denotes pressure (Pa).
- $\mu_{sgs}$  = the sub-grid dynamic viscosity of fluid (N·s/m<sup>2</sup>)

$\tau_{ij}^{sgs}$  is the sub-grid stress, which is used to characterise the effect of small scale vortex on the turbulent motion:

$$\tau_{ij}^{sgs} = \bar{\rho} (\overline{u_i u_j} - \overline{u_i} \overline{u_j}).$$

Equation 3: The energy equation: 
$$\frac{\partial (\bar{\rho} \tilde{h})}{\partial t} + \frac{\partial (\bar{\rho} \tilde{u}_i \tilde{h})}{\partial x_i} - \frac{\partial}{\partial x_i} (\frac{\mu_{sgs} c_p}{Pr_{sgs}} \frac{\partial \tilde{T}}{\partial x_i}) = \frac{\partial}{\partial x_i} (\lambda \frac{\partial \tilde{T}}{\partial x_i}) + \tilde{Q}_{solar} - \tilde{Q}_{loss}$$

Equation 4: The salt transport equation: 
$$\frac{\partial (\bar{\rho} \tilde{S})}{\partial t} + \frac{\partial (\bar{\rho} \tilde{u}_i \tilde{S})}{\partial x_i} = \frac{\partial}{\partial x_i} (\bar{\rho} \kappa_s \frac{\partial \tilde{S}}{\partial x_i})$$

Where:

- $h$  = denotes enthalpy (kJ)
- $c_p$  = isobaric specific heat capacity (J/Kg·K)
- $Pr_{sgs}$  = subgrid Planck number
- $S$  = the salt water concentration (%)
- $Q_{solar}$  = the solar radiation absorbed by water (kJ)
- $Q_{loss}$  = the heat loss in each layer (kJ)

$\frac{\partial}{\partial x_i} (\bar{\rho} \tilde{u}_i \tilde{S})$  is the convection term, representing the salinity flux from the flow of water in the pool.  $\frac{\partial}{\partial x_i} (\bar{\rho} \kappa_s \frac{\partial \tilde{S}}{\partial x_i})$  is the diffusion term, which represents the salinity flux caused by the change of salt gradient.

## 2.2. Model of solar radiation

The solar radiation absorbed by the saltwater at the depth  $z$  ( $Q_{solar}$ ) is calculated by the model of Date (2013):

Equation 5: 
$$Q_{solar} = (1 - \gamma)(1 - l)\phi_0 h(w, z)$$

Where:

- $\gamma$  = the percentage of the long wave radiation reflected on the surface (%)
- $l$  = the percentage of long wave radiation absorbed on the surface (%)
- $\phi_0$  = the solar radiation reached surface (attained by experiments) (W/m<sup>2</sup>)
- $h(w, z)$  = the radiation transmission at depth  $z$ , attained by the radiation transmission model (%)
- $w$  = the turbidity at depth  $z$  (NTU)

### 2.3. Model of heat loss

In the Equation (3), the heat loss in each layer ( $Q_{loss}$ ) denotes different heat loss in the surface, the middle layers and the bottom layer, respectively. For instance, on the surface of the pond,  $Q_{loss}$  represents the heat loss from the water surface ( $Q_{sur}$ ), while it represents the heat loss from the pond to the soil layer ( $Q_{soil}$ ) and the wall in the lowest layer and middle layers, respectively.

The net heat flux across the pond surface ( $Q_{sur}$ ) is the main part of the solar pond heat loss as shown in Figure 2:

$$\text{Equation 6:} \quad Q_{sur} = Q_l + Q_e + Q_s$$

$Q_l$  is the net long-wave radiation between the atmosphere and the pond surface determined by the cloud fraction, the relative humidity and the ambient temperature, which has been given by Elsebaï et al. (2013).  $Q_e$  is the evaporative heat flux across the pond surface considering the surface convection.

The sensible heat flux caused by the temperature difference between water and air on the surface,  $Q_s$ , has been described by Losordo (1991) as :

$$\text{Equation 7:} \quad Q_s = -1.57U(T_{sur} - T_a)$$

Where:

- $U$  is the wind speed over the surface (m/s)
- $T_a$  = temperature of the ambient air taken from the experimental data
- $T_{sur}$  = temperature of the water surface taken from the experimental data

$$\text{Equation 8: Heat loss from the sidewall:} \quad Q_w = A_w(T_w - T_a) / R$$

Where  $R$  is the thermal resistance of the wall ( $K \cdot m^2 / W$ ), which varies with the local position as the polystyrene foam board, the sand and the red brick.  $A_w$  is the heat transfer areas of the side wall.

The heat transferred from solar pond to the bottom soil can be represented as:

$$\text{Equation 9:} \quad Q_{soil} = A_{wg}(T_{wb} - T_{soil}) / R_{wg}$$

Where:

- $T_{wb}$  is the boundary temperature near the bottom( $^{\circ}C$ )
- $T_{soil}$  is the soil temperature lying at the depth of 0.15m below the pond ( $^{\circ}C$ )
- $A_{wg}$  is the area of the bottom( $m^2$ )
- $R_{wg}$  is the soil thermal resistance( $^{\circ}C \cdot m^2 / W$ ).

### 2.4. Computational method

In the present work, the energy equation is activated considering the convective heat transfer in the solar pond, the solar radiation transmission source term is induced by the user define function (UDF) which varies with time and depth. The semi-implicit pressure coupling method is used to couple the pressure and velocity, and a second order upwind difference is used to discrete the N-S equation. The Large eddy simulation method is employed to simulate the special micro turbulent flow in the trapezoidal solar pond. The salt mass fraction and temperature in the unit of calculation are extracted by user define function. Salt transport equation is built by the user defined scalar (UDS) considering the variation of density with the temperature and salinity.



### 3. RESULTS AND DISCUSSIONS

#### 3.1. Comparison between the RANS and LES

The calculated results based on the RANS and LES are compared with the experimental data (Liu et al., 2015) to valid the effectiveness of the numerical model. Figure 2 shows the temperature distribution of the simulated and experimental results in the solar pond on the 8th day. It can be found from Figure 2 that the temperature distribution of the RANS shows a different trend and a relatively large error with the experimental data, whose maximum temperature error is about 10°C in LCZ.

On the contrary, the temperature curve calculated by LES agrees with the experiment very well, the temperature error is below 2.5K and the maximum error ratio is about 6.5%. There are two possible reasons for this error: one is that the existing models of heat dissipation and radiation are not accurate enough to describe the actual operating conditions of the solar pond. The second possibility is that the temperature of the pond is easily affected by the transient change of the rain, the wind and other weather factors, which are not considered in the models. On the whole, the temperature distribution by LES shows a relative good consistency with the experiment.

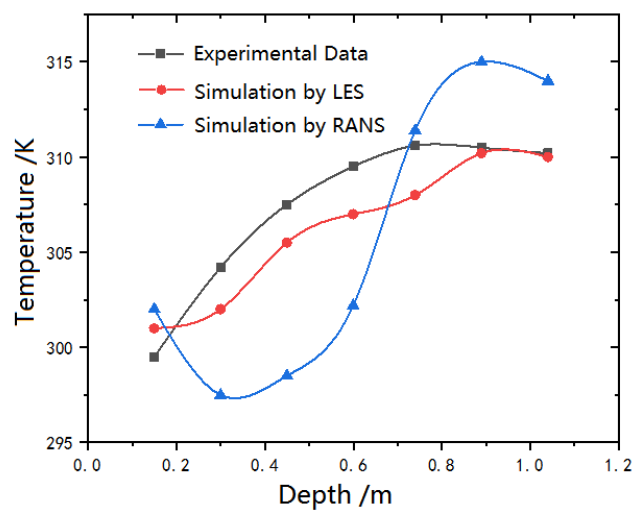


Figure 2: Comparison of simulation results and experimental results

Figure 3 shows the contrastive velocity nephogram of the RANS and LES at 2 pm on the 10th day. The left figure is the result of the RANS model and the right represents the LES model. As it can be seen from Figure 3, the velocity locates all over the solar pond in the RANS, and multiple vortices appear near the interface between the LCZ and NCZ, where the average velocity is about  $2.12 \times 10^{-5}$  m/s. As numerous existing studies have proved that the non-convective zone (NCZ) could restrict the flow of the salt water and keep a stable flow field in the solar pond, the velocity distribution based on the RANS is unreasonable. On the contrary, the vortices results based on the LES model mainly distributes in the LCZ, which is more suitable to the principle of solar pond and shows more reasonable velocity distribution.

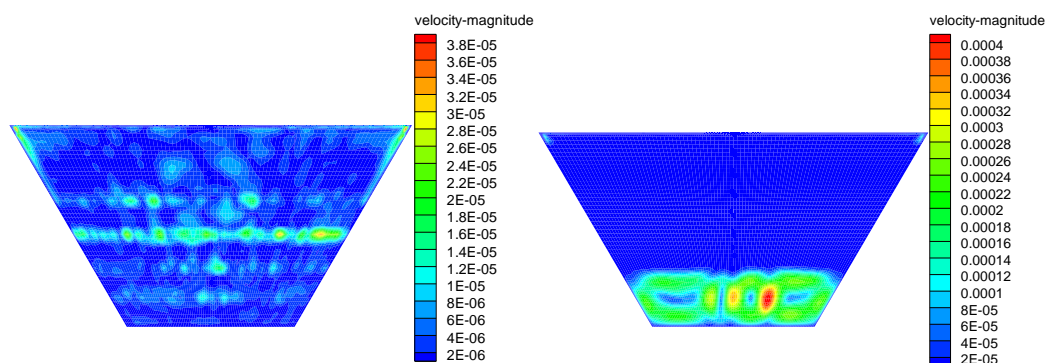


Figure 3: Comparison of the velocity nephogram of RANS (left) and LES(right)

### 3.2. Temperature variation of solar pool

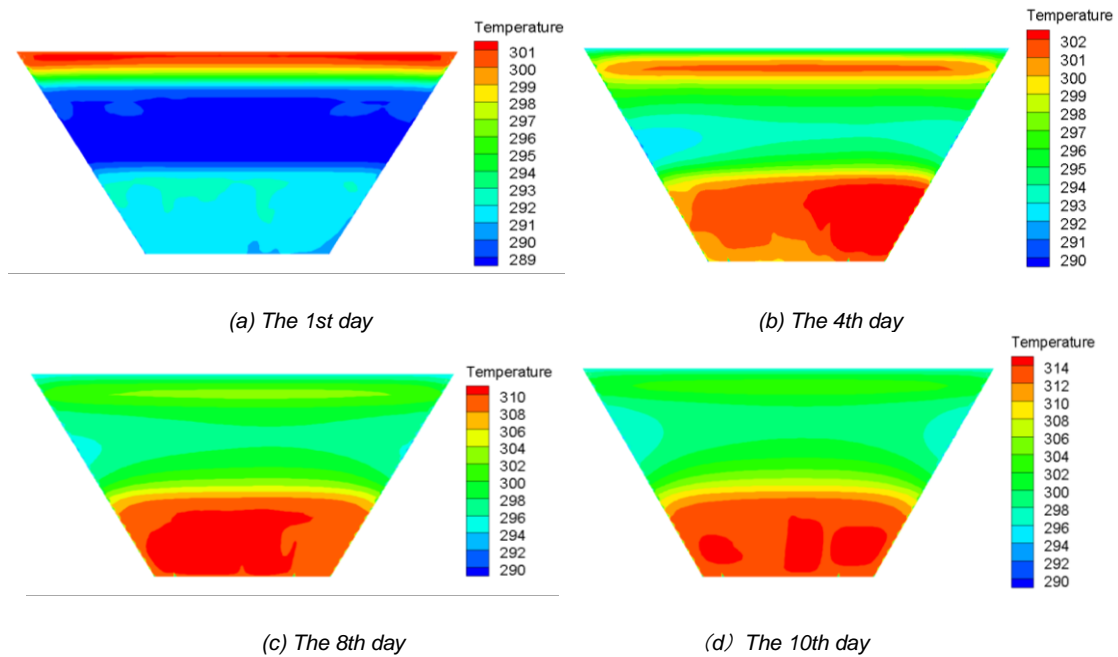


Figure 4: The temperature nephogram of the solar pool

Figure 4 shows the temperature nephogram of the solar pond at 12 o'clock on the 1st, 4th, 8th and 10th day. As it is shown in Figure 4, the average temperature of the 1st day reaches to 302K in the UCZ while it is only 289K in the NCZ and 293K in the LCZ, which indicates that the solar radiation is mainly absorbed by the surface of the pond at the initial stage. With the time running, the overall temperature of solar pond increases and high temperature zone moves to the LCZ. While a narrow hot zone occurs in the UCZ which is sensitive to the environment temperature and the solar radiation.

From the 1st to 10th day, the maximum temperature of LCZ increased from 286K to 314K. The temperature distribution in LCZ shows an irregular rule and an obvious thermal convection phenomenon occurs in the layer. Since the 8th day, an obvious disturbance occurs in the main high temperature zone of the LCZ, and the whole high temperature zone is decomposed into three local regions. The temperature comparison of the three layers shows that the temperature in NCZ is relative low, and the lowest temperature of the pond concentrates on the wall of the NCZ, because the convection in the NCZ is fairly faint and it could effectively prevent the heat loss of the LCZ.

Figure 5 presents the temperature change diagram of the centre point in the UCZ (0.15m), the NCZ (0.50m) and the LCZ (0.95m), respectively. As it can be seen in the figure, the overall temperature of the LCZ (0.95m) increases steadily at a rate of about 1.5K per day, because most of the solar radiation are absorbed and stored in the LCZ especially in the first 4 days. The temperature curve of the UCZ (0.15m) centre line is close to a harmonic distribution, which indicates that the temperature of the UCZ is crucially affected by the ambient temperature. The temperature variation in the NCZ (0.50m) shows a linear upward trend due to the non-convective effect by salt gradient. When the solar radiation turns weak, the temperature change is not evident in all of the three layers as in the 5th day.

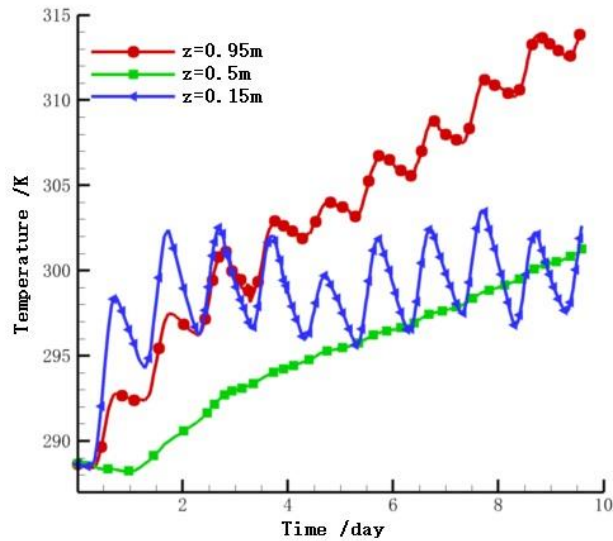


Figure 5: Temperature change diagram of the centre point at the same depth

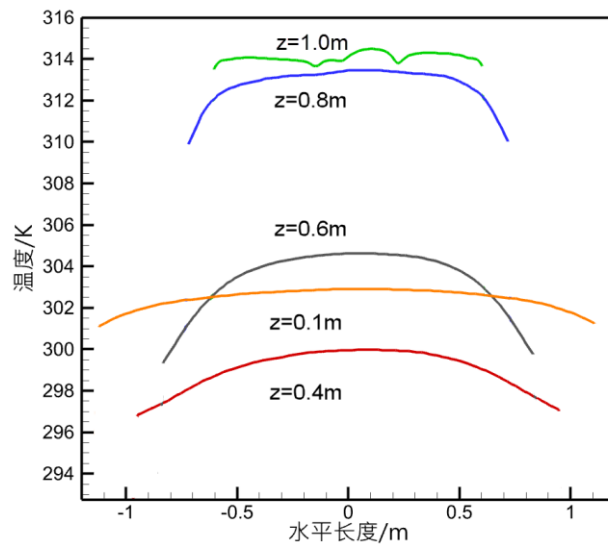


Figure 6: Temperature distribution at different depths of the solar pond

Figure 6 shows the temperature distribution at different horizontal positions at 14 o'clock on the 10th day. The horizontal position of the curves are in the depths of  $z = 0.2, 0.4, 0.6, 0.8$  and  $1.0$  m, respectively. It can be found that the temperature distribution shows a rule of high in centre and low on sides, and the lowest temperature in each layers locate in the wall sides due to the heat losses from the side wall. At the same level, the maximum temperature difference between the centre and the side reaches 4K at  $z = 0.6$  m (UCZ), while it is only 1.8 K at  $z = 1.0$  m (bottom). The temperature difference in the same horizontal level depends on the heat loss from the surface, the sidewall and bottom, which indicates that it is necessary to employ a two-dimensional model to study the thermal characteristics of solar pond.

### 3.3. Velocity distribution of solar pool

Figure 7 presents the velocity distribution cloud diagram of the trapezoidal solar pond at 14 o'clock of the 1st, 2nd, 6th and 10th day. Due to the effect of natural convection in the solar pond, the velocity regions are mainly distributed in the LCZ, and there also are some small and narrow velocity fields locate in the UCZ. It can be seen that the water velocity is small and distributed in a scattered manner in the first day, and there are almost no obvious vortex structures appears in the LCZ. Since the second day, the vortex structures turn obvious and envelop the LCZ and the average velocity maintains at  $10^{-4}$ m/s magnitude.

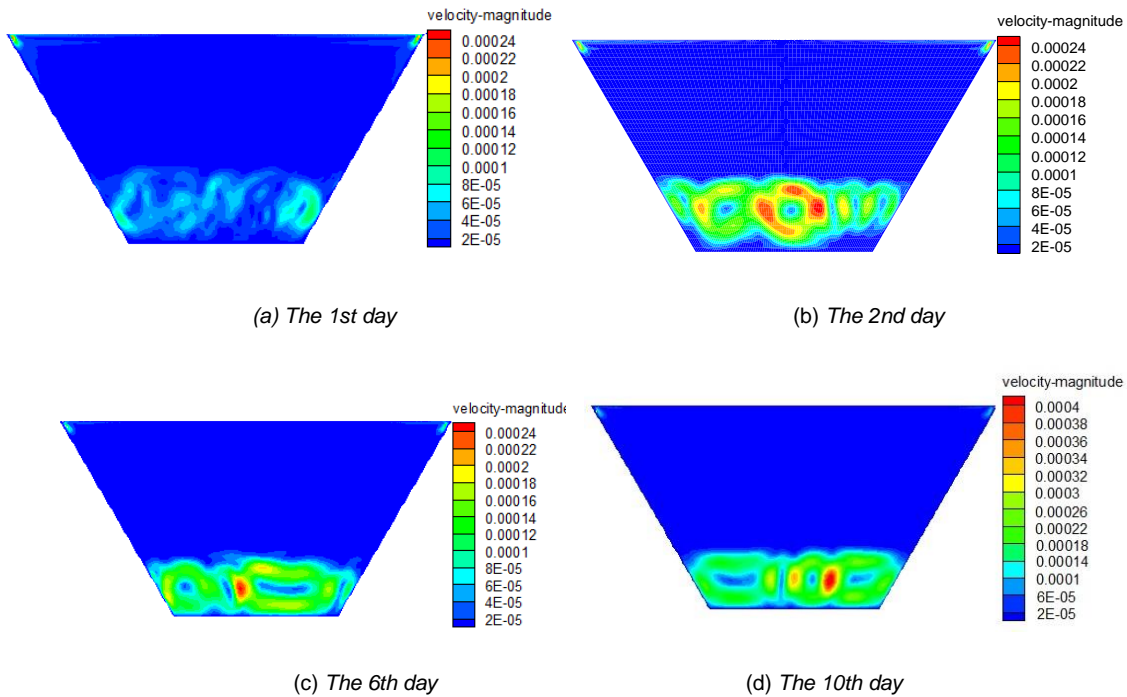


Figure 7: LES model solar pond velocity distribution cloud maps

Over time, several obvious vortices merge and split with each other in the LCZ. The structure of the vortices turns from disarray to orderliness. As it is shown in Figure 8, four distinct vortices appear in the LCZ on the 10th day and the vortices near the wall sides tend to expand inwards. The maximum velocity appears on the edge of a central vortex, which is about  $4 \times 10^{-4}$  m/s.

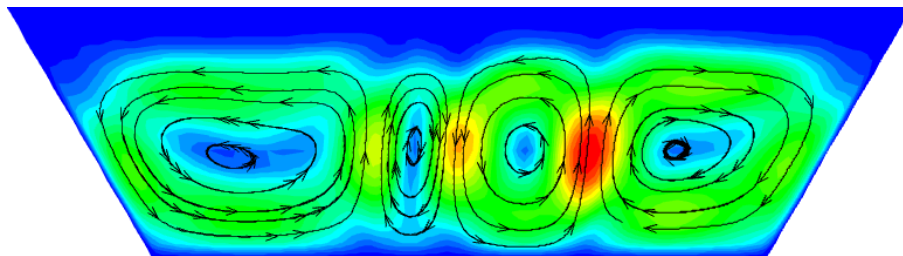


Figure 8: The vortices distribution on the 10th day

Figure 9 shows the variation of the average velocity of the UCZ, NCZ and LCZ at 14 o'clock. It can be seen that the average velocity of the LCZ is on the order of magnitude of  $10^{-5}$  m/s, which is much higher than that in the UCZ and NCZ. Although the average velocity in the LCZ fluctuates observably, it keeps constant and approximates to zero in the NCZ due to the limiting effect of salt gradient. As the velocity distribution in the UCZ mainly locates in a small and narrow zone with relative low speed, the mean bulk velocity is only on the order of  $10^{-6}$  m/s which is much lower than that in the LCZ.

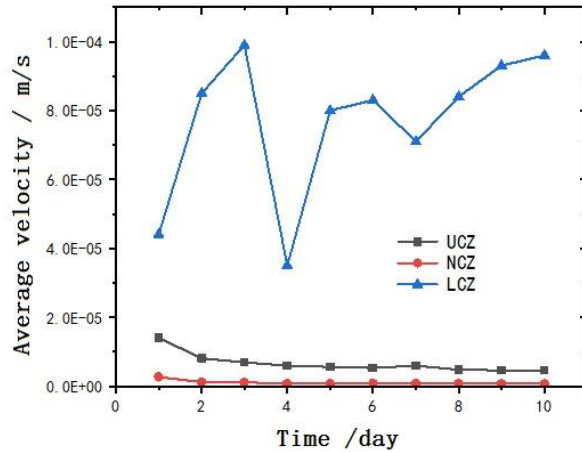


Figure 9: The change of the average velocity

### 3.4. Variation of the salinity at the interfaces within the solar pond

Figure 10 shows the variation of the salinity on the interface between the LCZ and NCZ ( $z=0.75\text{m}$ , lower interface), the NCZ and UCZ ( $z=0.25\text{m}$ , upper interface). It can be seen from Figure 10 that the salinity of the two interfaces present a descend trend, for instance, the descent rates of the salinity at the down interface decreases by 0.6% and it is 0.4% at the upper interface. The salinity declines by 0.15 percent in the first few hours on the both interfaces, because the initial salinity values of each layer are set to a given constant as in the experiment, the salinity spreads rapidly once the pond runs. After a transition of two days, the salinity on the lower interfaces decrease linearly, while it decreases with a trend of fluctuating downward on the upper interfaces.

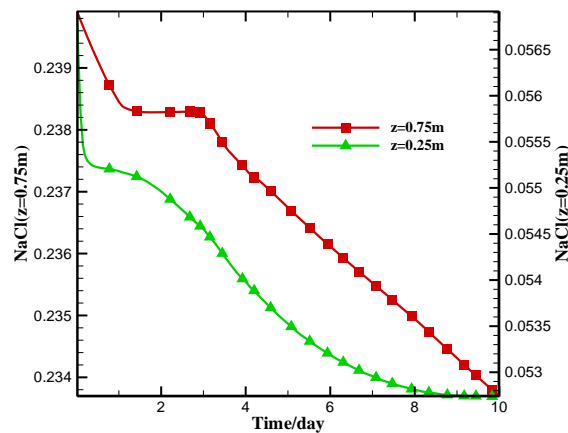


Figure 10: Variation of the salinity on the interface

## 4. CONCLUSION

In this paper, a two-dimensional model of a trapezoidal solar pond is built by the large eddy simulation method and the thermal performance of the solar pond is analysed. The results show that the LES method is more suitable for the special micro-turbulence phenomenon within the solar pond to predict the temperature and velocity distribution. With the time running, the overall temperature of solar pond increases, the high temperature zone moves from the UCZ to the LCZ, and the maximum temperature in the LCZ reaches 314K in the first 10 days. At the same level, the temperature show a rule of high in centre and low on sides which indicates that it is necessary to employ a two-dimensional model to study the thermal characteristics of the solar pond. The velocity regions in LCZ are mainly caused by the variation of the temperature field. Four distinct vortices with the velocity of  $10^{-4}\text{m/s}$  appear in the LCZ on the 10th day and the vortices near the wall trend to expand inwards. The salinity at the interfaces presents a descend trend effected by the natural convection in the pond.

## 5. ACKNOWLEDGEMENT

This work is supported by the National Natural Science Foundation of China (51606176, 51576029, 51476017).

## 6. REFERENCES

Badran A A, Hamdan M A, 2004. Comparative study for under-floor heating using solar collectors or solar ponds. *Applied Energy*, 77, 107-117.

Boudhraf R, Baccar M, 2014. Transient hydrodynamic, heat and mass transfer in a salinity gradient solar pond: A numerical study. *Energy Conversion and Management*, 79, 568-580.

Date A, Akbarzadeh A, 2013. Theoretical study of a new thermodynamic power cycle for thermal water pumping application and its prospects when coupled to a solar pond. *Applied Thermal Engineering*, 58, 511-512.

Dehghan A A, Alireza M, Mohsen M, 2013. Experimental investigation of energy and exergy performance of square and circular solar ponds. *Solar Energy*, 97: 273-284.

ElSebaei A A, Aboul-Enein S, Ramadan, et al, 2013. Thermal performance of shallow solar pond under open and closed cycle modes of heat extraction. *Solar Energy*, 95, 30-41.

Hull J R, Nielsen C E, 1989. Steady-state analysis of the rising solar pond, *Solar Energy*, 42, 365-377.

Kurt H, Ozkaymak M, Binark A K, 2006. Experimental and numerical analysis of sodium-carbonate salt gradient solar-pond performance under simulated solar-radiation. *Applied Energy*, 83, 324-342.

Lesino G, Saravia L, 1991. Solar ponds in hydrometallurgy and salt production. *Solar Energy*, 46, 377-382.

Liu H S, Jiang L S, Wu D, Sun W C, 2015. Experiment and Simulation Study of a Trapezoidal Salt Gradient Solar Pond. *Solar Energy*, 122, 1225-1234.

Losordo T M, Piedrahita R H, 1991. Modelling temperature variation and thermal stratification in shallow aquaculture ponds. *Ecological Modelling*, 54, 189-226.

Njokua H O, Agashia B E, Onyegegbu S O, 2017. A numerical study to predict the energy and exergy performances of a salinity gradient solar pond with thermal extraction. *Solar Energy*, 157, 744-761.

Othmana A A, Tawalbeh M, Assadb M E, et al, 2018. Novel multi-stageflash (MSF) desalination plant driven by parabolic troughcollectors and a solar pond: A simulation study in UAE. *Desalination*, 443, 237-244.

Ranjan K R, Kaushik S C, 2014. Thermodynamic and economic feasibility of solar ponds for various thermal applications: A comprehensive review. *Renewable and Sustainable Energy Reviews*, 32, 123-139.

Weinberger H, 1964. The physics of the solar pond. *Solar Energy*, 8, 45-56.

---

## #99: Small-scale solar driven mechanical vapour compression desalination system

---

Mohamed A. FARAHAT<sup>1</sup>, Hassan E. S. FATH<sup>2</sup>, Mahmoud AHMED<sup>3</sup>

<sup>1</sup>Egypt Japan University of Science and Technology (E-JUST), Borg Al-Arab, Alexandria, Egypt, [mohamed.farahat@ejust.edu.eg](mailto:mohamed.farahat@ejust.edu.eg)

<sup>2</sup>Egypt Japan University of Science and Technology (E-JUST), Borg Al-Arab, Alexandria, Egypt, [hassan.fath@ejust.edu.eg](mailto:hassan.fath@ejust.edu.eg)

<sup>3</sup>Egypt Japan University of Science and Technology (E-JUST), Borg Al-Arab, Alexandria, Egypt, [mahmoud.ahmed@ejust.edu.eg](mailto:mahmoud.ahmed@ejust.edu.eg)

*The objective of this present work was to develop, design and pilot test a small scale solar driven, high performance mechanical vapour compression (MVC) desalination unit with nano-filtration (NF) pre-treatment (Solar-NF-MVC). The system electrical and thermal energies was generated using the integration of photovoltaic (PV) and concentrated solar power (CSP) panels. CSP thermal energy was stored in a phase change material (PCM) exchanger for a start-up operation. Nano filtration (NF) membrane was used for feed water pre-treatment in order to increase the top brine temperature (TBT) up to 100°C. Therefore, the operation of the MVC unit could be at atmospheric pressure. This allowed the use of available components in the local market, besides reducing the size of the evaporator, vapour compressor, and vent ejector. Also, the unit air leakage was eliminated reducing corrosion and allowing the use of cheaper tubes material. A comprehensive mathematical model has been developed, programmed using MATLAB program, and was used as a tool for the system's design and operational performance analysis. Predicted results were verified using the available published data of similar operating systems. Then, the model was used for the detailed design of 1.0 m<sup>3</sup>/day pilot test unit locally manufactured and tested for its different operational scenarios including both start-up and steady-state operation.*

*Keywords: desalination; mechanical vapour compression (MVC); solar energy; nano-filtration (NF); engineering*

## 1. INTRODUCTION

Fresh water is the essence of life and is a basic human requirement for domestic, industrial and agricultural purposes. In Egypt, it is expected rapid development and population growth that will result in a large escalation of demand for fresh water. By 2025 the expected water consumption per capita will 500 m<sup>3</sup>/year (50% of the United Nations (UN) specified per capita). The intended application of desalination in Egypt is inline with the trends to ensure the provision of fresh drinking water to all citizens particularly in remote areas in which it is cheaper to desalinate saline water than transporting treated water to areas far (300 – 500 km) from the Nile (Egypt's main natural water resource). Although Multi-Stage Flash (MSF) and Multiple Effect Distillation (MED) have proven to be reliable and mature; however, they mainly suit large-scale units' capacity. different researches have been introduced combination between MVC and MSF and MED (Nafey, Fath and Mabrouk, 2006, 2008; A. A. Mabrouk, Nafey and Fath, 2007; Abdalnasser A. Mabrouk, Nafey and Fath, 2007) MVC desalination process has been attracted the attention of many researchers for small capacity (less than 5000 m<sup>3</sup>/day) units as reported by (Helal and Al-Malek, 2006) and (Ibrahimi, Arbaoui and Aoura, 2017). The main concept of MVC desalination unit is to recover the energy of vapour produced in the evaporator as the system heating steam after compression. MVC technology features also includes compactness, simple pretreatment, high thermal efficiency, high heat transfer coefficient, low pumping power and high operating flexibility (Al-Juwayhel, El-Dessouky, and Ettouney, 1997). However, MVC has some drawbacks as it needs electrical energy so it is not suitable for remote areas of limited electrical resources. Also, the limitation of TBT (60~70) °C needs large evaporator and vacuum system, which increases the capital and operational costs (CAPEX & OPEX).

Solar PV panels are being used nowadays to generate electricity in areas far from the electrical network. Heat builds up around PV cells reduces its efficiency, (Aly, 1983), where the electrical power generation is reduced by 0.4-0.5% for every 1°C above its rated output temperature which in most cases is 25°C. However, the collected heat can be recovered by cooling the PV panel (named as PV/T) using cooling medium such as air or water, (Aly and El-Fiqi, 2003), to increase the panel's efficiency and electricity generation, (Teo, Lee and Hawlader, 2012; Cuce and Cuce, 2014; Al Tarabsheh *et al.*, 2016; Giwa, Fath and Hasan, 2016; Mahmoud, Fath and Ahmed, 2018). The recovered thermal energy can be used as a driver for a different low-grade energy systems and offers a good choice towards a sustainable environment. PV/T recovered thermal energy can also be used to increase the water productivity of solar desalination process (Aly and El-Fiqi, 2003). PV/T cooling with its thermal energy recovery were used for humidification-dehumidification (HDH) desalination process, (Al Tarabsheh *et al.*, 2016). Ong *et al.*, (Ong *et al.*, 2012) used the higher temperature heat recovered from Concentrated PV (CPV) as a driver of the thermal systems in multi-effect membrane distillation (MEMD) process.

Concentrated Solar Power (CSP) are solar thermal systems used for different applications that can be used to store solar thermal energy as sensible or latent heat. This energy can be recovered to be used in any conventional thermal desalination plants (Hamed *et al.*, 2016). (Palenzuela *et al.*, 2011, 2015; Iaquaniello *et al.*, 2014; Hamed *et al.*, 2016) studied integration of CSP with desalination units and reported better thermodynamic efficiency that can reduce the total water production cost for lager and small-scale solar desalination plants.

The present market MVC technology has, however, the following drawbacks: -

- 1- Operation under Vacuum to limit TBT to below 70 C (to reduce scale formation). This leads to vapour high specific volume, and, therefore, -
  - a- Larger components as the evaporator, compressor, vacuum pump (ejector) etc
  - b- The need to use brine and product water special pumps to operate under vacuum suction pressure or place it much below the evaporator
  - c- High ingress air leakage that leads to larger air ejector and increases the chances of corrosion and the use of relatively expensive material, etc
- 2- Has higher specific water cost as compare to RO desalination

In the present work, these drawbacks will be addressed. In addition, the start-up and steady-state operation of a small scale solar-MVC system is presented as a standalone system. A comprehensive model is developed as a tool for the system's design and operational performance analysis. The model is, then, used for the detailed design of a 1.0 m<sup>3</sup>/day pilot test unit to be locally manufactured and test its different operational scenarios.

## 2. MVC PLANT DESCRIPTION & METHODOLOGY

Figure 22 illustrates the conceptual process diagram of the proposed solar-NF-MVC system. It consists of Two Main sub-systems, i- MVC desalination unit and ii- Solar Electrical / Thermal sub-system. Firstly, for MVC desalination unit, evaporator (1) working pressure will be near atmospheric pressure. Conventional mechanical vapour compressor (2) will be used to increase vapour enthalpy (and temperature) to the required heating steam value that will drive the evaporation process. The vapour is then condensed as distilled water (DW), where its thermal energy is recovered to pre-heat the feed water (FW) (3) and then stored in the DW tank (4). The thermal



energy of the rejected brine will also be recovered for FW preheating (5) and the brine is finally rejected to the brine tank (6). Secondly, Solar Electrical / Thermal system will supply electrical energy during MVC unit steady-state operation and thermal energy for the start-up process.

MVC start-up operation vapour will be initially generated from the solar PCM system. High pressure/temperature pre-treated FW leaves the PCM exchanger and enters the flash tank (7) and the generated vapour will enter the compressor to be compressed as the heating steam. Liquid water in the flash tank will be the FW to the evaporator. Step by step the start-up line will be switched off as it will be replaced by the main line for electrically driven MVC unit where the vapour generated from the evaporator will be re-circulated through the compressor.

Different pre-treatment components will be added to the FW sub-system to improve the overall system operational performance. These including, conventional filtration (F) (8), nanofiller (NF) (9) to eliminate the divalent molecules (Ca, Mg, SO<sub>4</sub>, etc.) and reduce the monovalent molecules (CO<sub>3</sub>). Membrane deaerator (Md) may also be used to eliminate the dissolved gasses and reduces its presence in the evaporator system. In addition, supporting and auxiliary components are added for the safe and efficient system operation (as pumps, tanks, valves measurements, and control system).

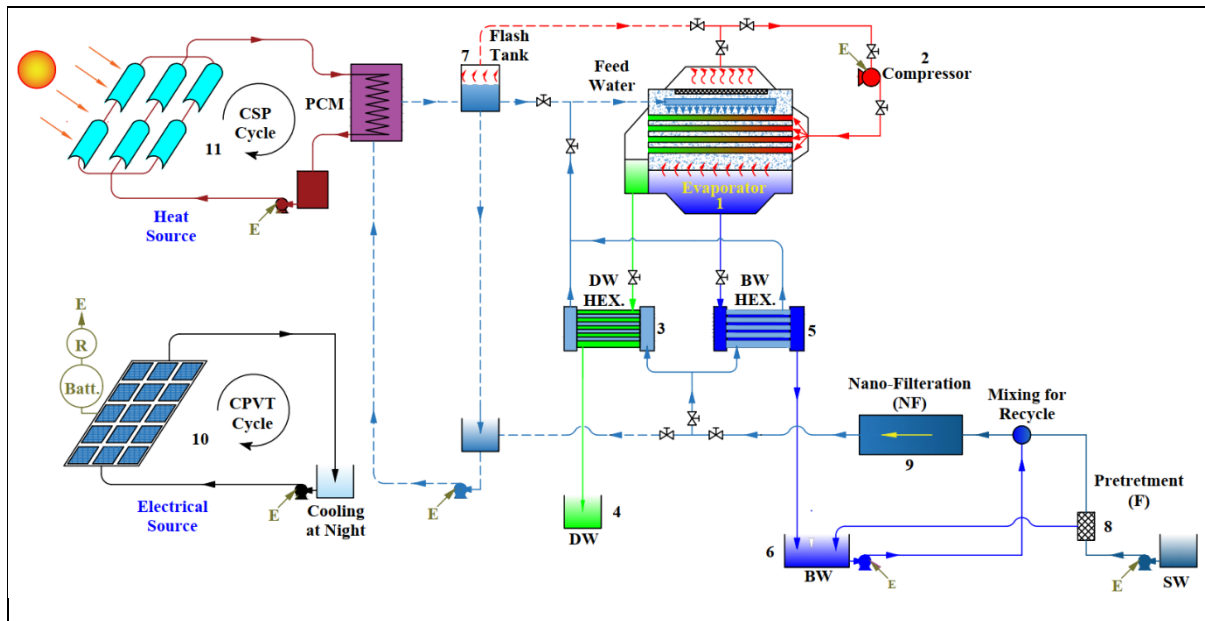


Figure 22: Conceptual Process Diagram of the Solar NF-MVC Desalination System

The solar system consists of the integration of PV/T (10) and CSP units (11). The integrated system generates both the electrical and thermal energies needed to drive the NF-MVC sub-systems. The solar system includes PCM for thermal energy storage for start-up in order to maintain the 24/7 system operation and at near constant temperature. The electrical energy generated will be stored in batteries (Batt) and to drive all mechanical and control devices via the rectifiers (R). Thermal oil will be used as the working fluid in the solar loop.

### 3. MODEL DEVELOPMENT

A Mathematical model has been developed and is programmed, using MATLAB, by applying energy, material and salinity balanced equations. (Ettouney, 2006) presented a detailed design model for a single MVC desalination system. The mass and salinity balance equations are solved to calculate the flow rates of the system.

Equation 17: Mass Balance.

$$M_f = M_d + M_b$$

Equation 18: Salinity Balance.

$$M_f = M_d \left( \frac{X_b}{X_b - X_f} \right)$$

Where:

- $M_f$  = Feed water mass flow rate (kg/s)
- $M_d$  = distilled water mass flow rate (kg/s)
- $M_b$  = Brine water mass flow rate (kg/s)
- $X_f$  = Feed water salinity (ppm)
- $X_b$  = Brine water salinity (ppm)

For the temperatures along with the whole system components, energy balance equations are applied for evaporator and both brine and distillate preheaters.

Equation 19: Evaporator energy balance. 
$$M_f C_p (T_b - T_f) + M_d L_v = M_d L_d + M_d C_p (T_s - T_d)$$

Equation 4: Brine and distilled water preheater energy balance. 
$$M_f C_p (T_f - T_{cw}) = M_d C_p (T_d - T_o) + M_b C_p (T_b - T_o)$$

Where:

- $T_{cw}$  = Sea water temperature. (°C)
- $T_f$  = Feed water to the evaporator temperature. (°C)
- $T_b$  = Brine water temperature. (°C)
- $T_d$  = Distilled water temperature. (°C)
- $T_s$  = Superheated water after the compressor temperature. (°C)
- $T_o$  = ambient temperature. (°C)
- $C_p$  = Specific heat at constant pressure, kJ/kg.°C
- $L_v$  = Latent heat for evaporation at vapour temperature in evaporator, kJ/kg
- $L_d$  = Latent heat for evaporation at distilled water temperature, kJ/kg

In order to obtain the full design data, the heat transfer area for the evaporator and both brine and distilled water preheaters are calculated as follows;

Equation 5: Evaporator heat transfer area. 
$$A_e = \frac{M_d L_d + M_d C_p (T_s - T_d)}{U_e (T_d - T_b)}$$

Equation 6: Brine preheater heat transfer area. 
$$A_d = \frac{M_d C_p (T_d - T_o)}{U_d (LMTD)_d}$$

Equation 7: Distilled preheater heat transfer area. 
$$A_b = \frac{M_b C_p (T_b - T_o)}{U_b (LMTD)_b}$$

Where:

- $A_e$  = Evaporator heat transfer area. (m<sup>2</sup>)
- $A_b$  = Brine preheater heat transfer area. (m<sup>2</sup>)
- $A_d$  = Distilled preheater heat transfer area. (m<sup>2</sup>)
- $U_e$  = Evaporator overall heat transfer coefficient. (kW/m<sup>2</sup>.°C)
- $U_b$  = Brine preheater overall heat transfer coefficient. (kW/m<sup>2</sup>.°C)
- $U_d$  = Distilled preheater overall heat transfer coefficient. (kW/m<sup>2</sup>.°C)
- $LMTD_d$  = Distilled preheater Logarithmic mean temperature difference. (°C)
- $LMTD_b$  = Brine preheater Logarithmic mean temperature difference. (°C)

For PV/T the efficiency is assumed to be 0.15 while the CSP efficiency is calculated as reported by (Sharaf Eldean and Soliman, 2014). The PV/T efficiency and the CSP efficiency and area are calculated as follows;

Equation 8: CSP efficiency. 
$$\eta_{CSP} = \eta_o - a_1 (T_{PTC} - T_o) - a_2 \left( \frac{T_{PTC} - T_o}{G} \right) - a_3 \left( \frac{T_{PTC} - T_o}{G} \right)^2$$

Equation 9: CSP Area. 
$$A_{CSP} = \frac{Q_u}{\eta_{PTC} G}$$

Equation 10: PV/T Area. 
$$A_{PV/T} = \frac{P_t}{\eta_{PV} G}$$

Where:

- $\eta_{PTC}$  = PTC efficiency.
- $\eta_o = 0.75$
- $T_{PTC}$  = Average PTC temperature (°C).
- $a_1 = 4.5 \times 10^{-6}$
- $a_2 = 0.039$
- $a_3 = 3 \times 10^{-4}$
- $Q_u$  = Useful energy in PTC (W)

- $G$  = solar flux ( $w/m^2$ )
- $P_t$  = total electrical power (W)
- $\eta_{PV/T}$  = PV/T efficiency.

## 4. RESULTS AND DISCUSSIONS

### 4.1. Model validation

The present model has been validated by comparing its results with published data of (Ettouney, 2006); Figure 23. The figure shows a comparison between superheated vapour temperature and specific power variation with brine temperature. The comparison is carried out at different temperature difference between DW and BW. It can be depicted that there is a good agreement between the present work results and published data.

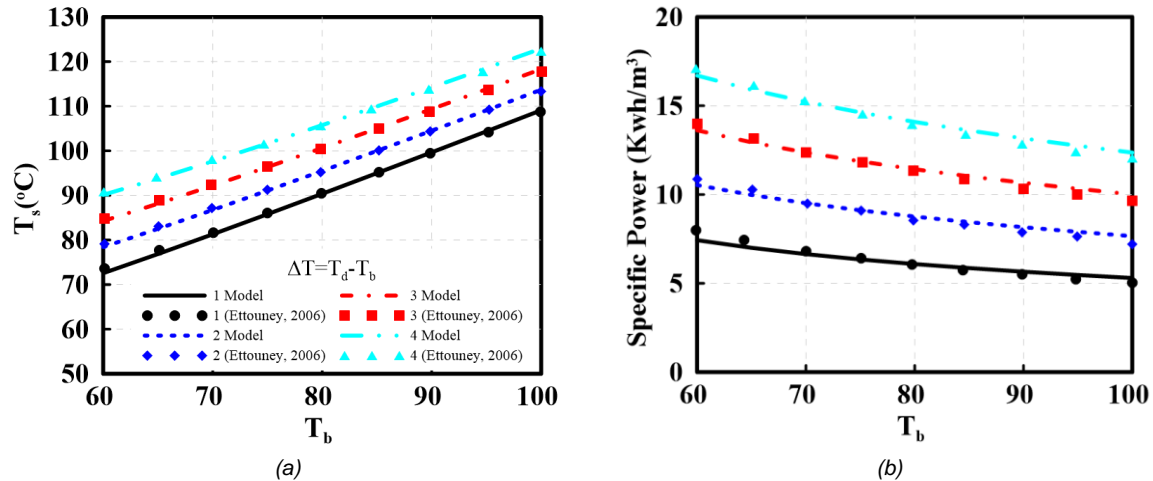


Figure 23: Comparison between the present Model results and the published data of Ettouney, 2006 , (a) Superheated vapour temperature, (b) Specific Power

### 4.2. Model results and discussion

The presented simulation model results are reported depending on the weather condition of Borg EL-Arab city, Alexandria, EGYPT. All results discussion will be for the selected case study values shown in Table 4.

Table 4: Input Data to Present Simulation Model

Parameter	Unit	Value
Distilled Water Flow Rate	$m^3/day$	1
System working time	hr	24
Sea Water Salinity	ppm	40000
Brine Water Salinity	ppm	80000
Sea Water Temperature	$^{\circ}C$	30
Ambient Temperature	$^{\circ}C$	30
Distilled /Bine Temperature Difference	$^{\circ}C$	1~4
Start-up Time	hr	0.5
Compressor Efficiency	%	70

The effect of FW temperature on the MVC desalination system performance will be presented. The presented results are at specified different temperature difference between DW and BW.

Figure 243 illustrates the effect of FW temperature on the MVC system' required power and specific power consumption. It can be depicted that, increasing FW temperature will reduce power consumption as working under vacuum will be eliminated so less power will be needed. On the other hand, the power will increase as distillate-brine temperature difference increased because of more superheating will be required for distilled vapour and that means more power. Depending on that, working at higher FW temperature with a lower distillate-brine temperature difference will be selected.

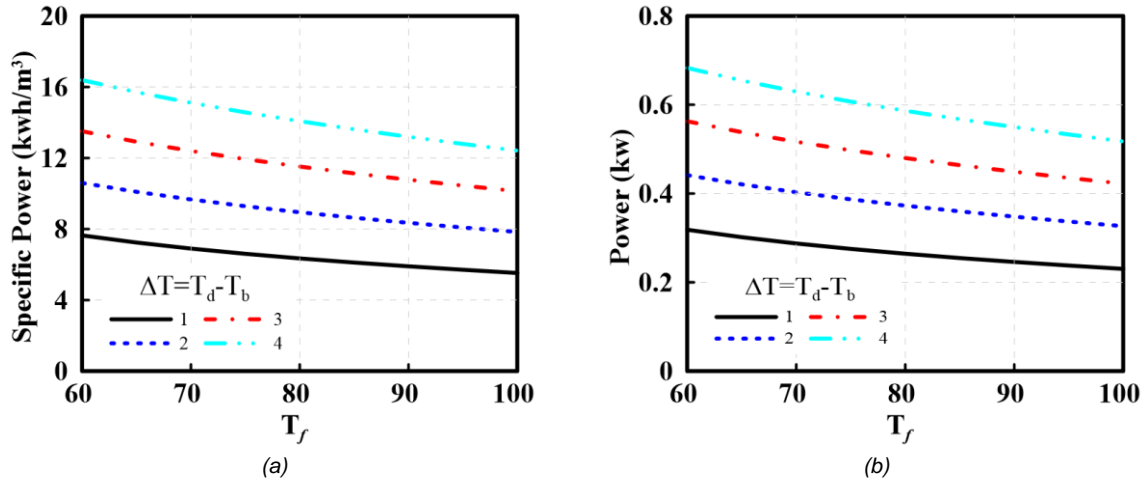


Figure 24: effect of FW temperature on the power and specific power consumption at different temperature difference, (a) Power, (b) Specific Power

Selecting high-temperature FW will affect the evaporator and brine and distilled heaters surface areas as presented in Figure 25. The areas of brine and distilled heaters will be increased with the increase of FW temperature. This is because of the amount of higher energy required to reach FW high temperature and, therefore, it requires more heating surface area. As FW goes through the evaporator with high energy, the evaporator heating surface area will be decreased.

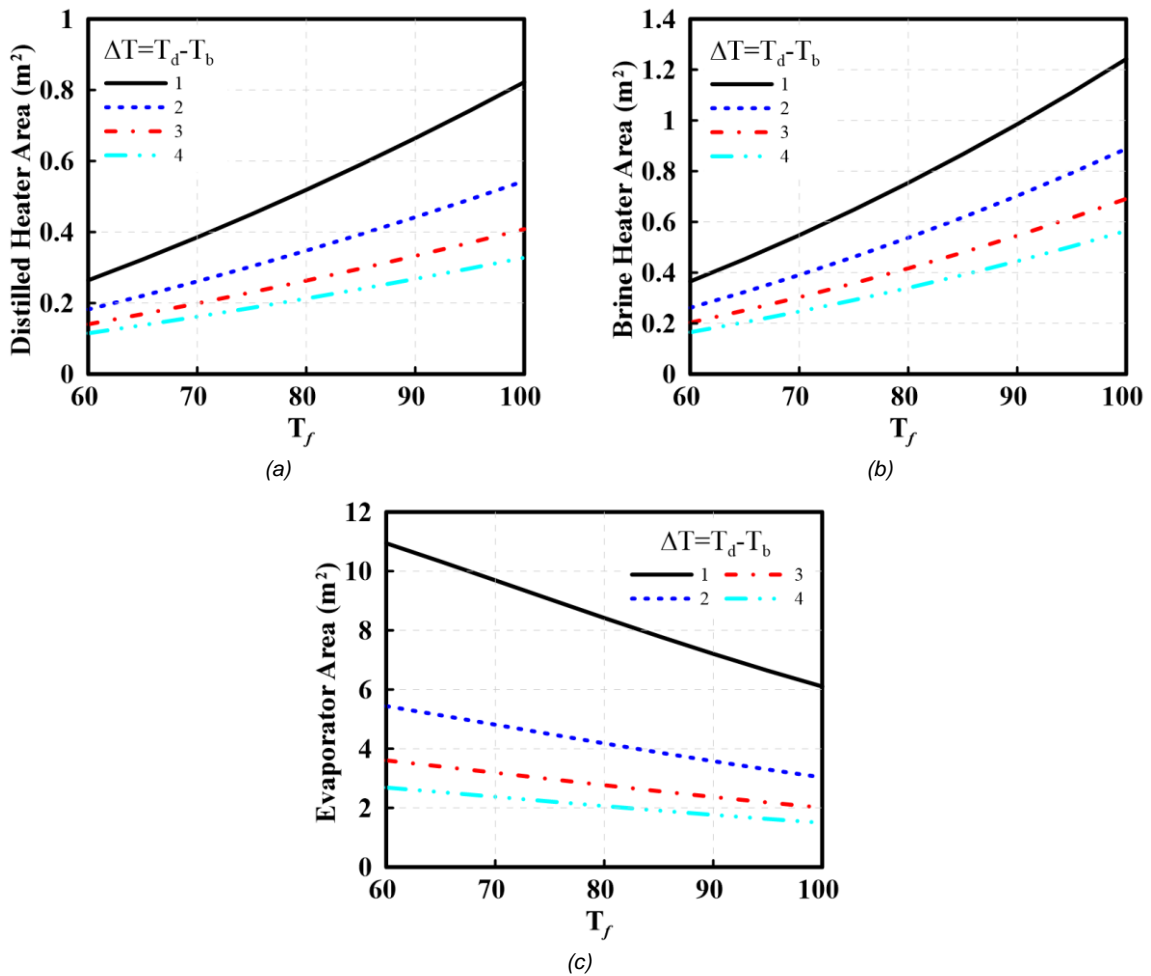


Figure 25: Effect of FW temperature on the evaporator, brine, and distilled heaters surface areas at different distillate-brine temperature difference, (a) distilled heater, (b) brine heater, (c) evaporator

Figure 26 illustrates the change of Gain Output Ratio (GOR) with FW temperature at different temperature difference. It is mainly observed that increasing the FW temperature has no significant change on the GOR. Also, the change in temperature difference has a slight change which can be neglected. For instance, at a temperature difference of 2 °C GOR changed from 0.54 to 0.52 with the change of FW temperature difference from 60 °C to 100 °C respectively. Also, at FW temperature of 80 °C, GOR changes from 0.518 to 0.547 with temperature difference 1.4 °C.

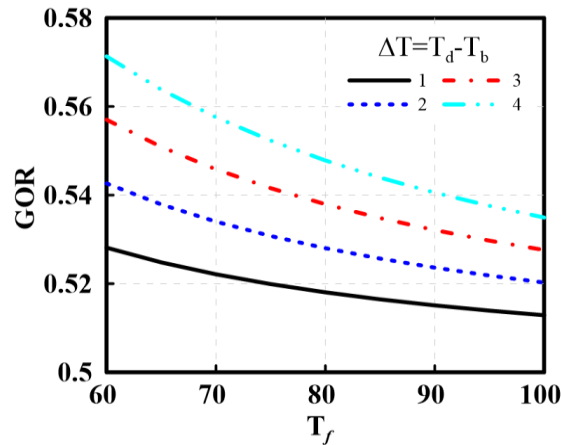


Figure 26: Effect of feed water temperature on the GOR at different distillate-brine temperature difference.

Figure 27 shows the change of PV and Parabolic Trough Collector (PTC) CSP areas with distillate-brine temperature difference. Such a figure is represented at different temperature difference. The present data is calculated on 21 May by using ASHRAE model for solar intensity prediction. As the total solar energy, sunshine time and average solar intensity are calculated over that day. It can be depicted that the PV area is reduced with the increase of FW temperature because of the decrease of power required. Also, the same change of power with temperature difference is detected for PVT area. About PTC area there is no significant effect of the temperature difference. But a sharp increase is observed with the increase of FW temperature. This increase happened as for high FW temperature, a large amount of energy is required and therefore a large heating area.

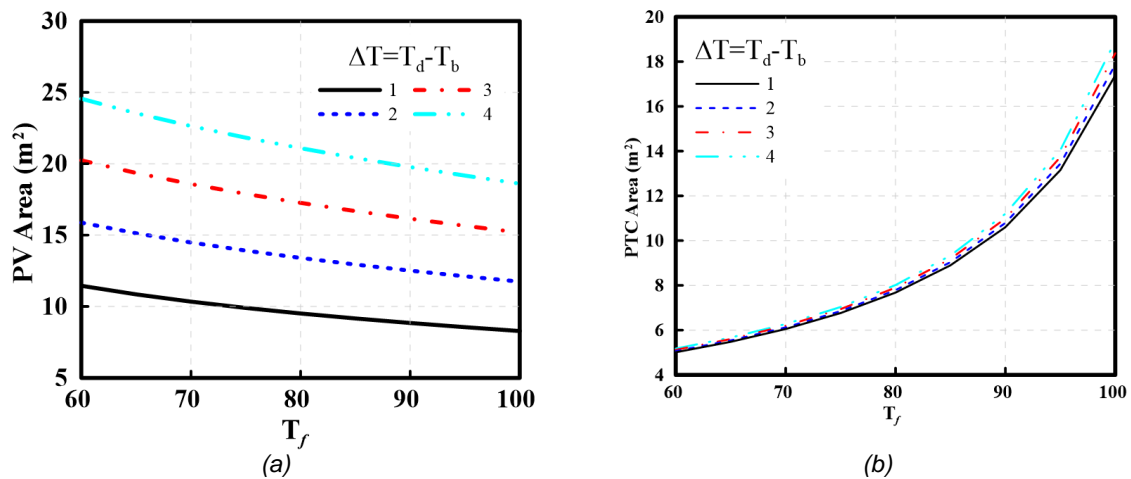


Figure 27: effect of feed water temperature on PV and PTC areas at different temperature difference, (a) PV, (b) CSP

(NOTE Correct CSP instead of PTC in the 6 (b))

A long-term study has been carried out during the whole seasons. Figure 28 shows the change of PV/T, CSP areas along the year for Borg EL Arab, Alexandria, EGYPT. Mainly it can be depicted that the PV/T and CSP areas change according to solar intensity as it shows high values in the first few months of the year (wintertime) then it gradually decreased till June then it increased again at the end of the year. About temperature difference, it has no significant effect on CSP area. Unfortunately, it has a great effect on the PV area. As with the increase in temperature difference, there is an increase in PV/T and CSP areas for any selected time. So, it is recommended to work at low-temperature difference between distilled and brine water.

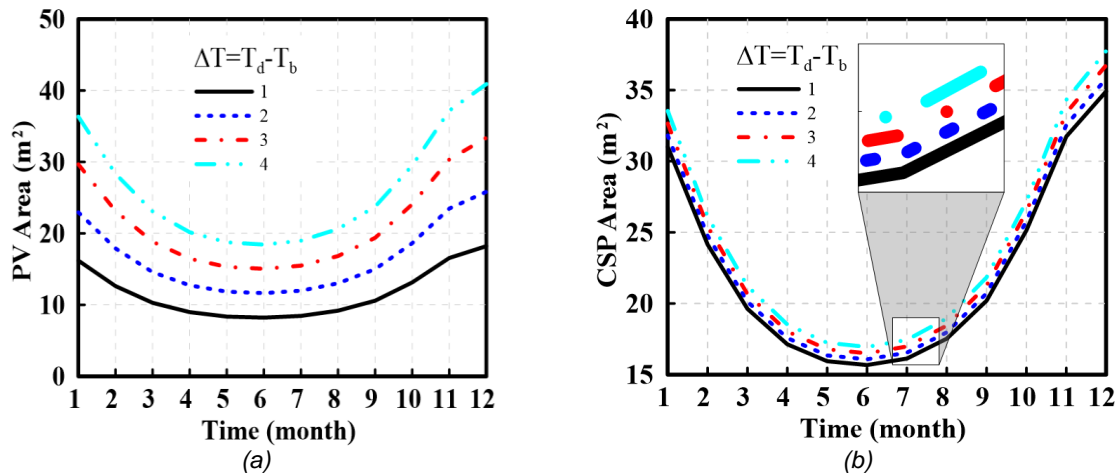


Figure 28: variation of PV/T and CSP areas along the year at different temperature differences, (a) PV/T area, (b) CSP area.

Figure 29 illustrates the change of the system efficiency along the year at different temperature difference. The whole system efficiency has been calculated according to the amount of solar power that is used for 1.0 m<sup>3</sup>/day product water of the pilot unit. The efficiency increased from January till June where it reaches its maximum value. Then it is reduced to its minimum value in December. The efficiency is clearly affected by temperature distillate-brine difference. As its highest values are obtained at the lowest temperature difference values. At temperature difference 1.0 °C the maximum and minimum efficiency values are about 35% and 22% respectively.

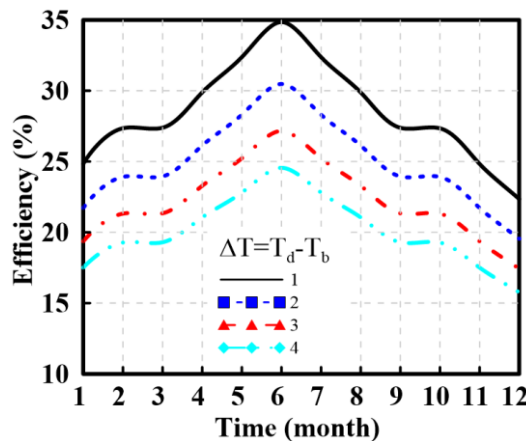


Figure 29: proposed system efficiency along the year at different temperature differences.

Use better curve fitting

## 5. CONCLUSION

A solar driven desalination system is proposed to produce a standalone MVC desalination unit. The system consists of a conventional MVC desalination unit, PV/T system as an electrical energy source and CSP system with PCM to store solar thermal energy as the heat source for the start-up process. The steady state and start-up processes are investigated. A comprehensive model is developed as a tool for the system's design and operational performance analysis for 1.0 m<sup>3</sup>/day production. The proposed system working at atmospheric pressure will have some benefits. This will allow the use of available components in the local market, besides reducing the size of the evaporator, vapour compressor, and vent ejector. Also, the unit air leakage will be eliminated that will reduce corrosion and allow the use of cheaper material. Mainly, working at high FW temperature will increase the CSP and PV/T required areas. Also, working at a low distillate-brine temperature difference will be more efficient. The total efficiency for the system is calculated with the highest and lowest values are about 35% and 22% respectively at 1.0 °C temperature difference.

## 6. NOMENCLATURE

<i>Batt.</i>	<i>Batteries</i>	<i>MEMD</i>	<i>Multi-Effect Membrane Distillation</i>
<i>BW</i>	<i>Brine Water</i>	<i>MSF</i>	<i>Multistage Stage Flash</i>
<i>CAPEX</i>	<i>Capital Expenditure</i>	<i>MVC</i>	<i>mechanical vapour compression</i>
<i>CSP</i>	<i>concentrated solar power</i>	<i>NF</i>	<i>Nano-Filtration</i>
<i>DW</i>	<i>Distilled Water</i>	<i>PCM</i>	<i>Phase Change Material</i>
<i>F</i>	<i>Filter</i>	<i>PV</i>	<i>Photovoltaic</i>
<i>FW</i>	<i>Feed Water</i>	<i>PVT</i>	<i>Photovoltaic-Thermal</i>
<i>HDH</i>	<i>Humidification-Dehumidification</i>	<i>R</i>	<i>Rectifiers</i>
<i>LMTD</i>	<i>Logarithmic mean temperature difference</i>	<i>RO</i>	<i>Reverse Osmosis</i>
<i>MD</i>	<i>Membrane De-aerator</i>	<i>TBT</i>	<i>Top brine temperature</i>
<i>MED</i>	<i>Multiple Effect Distillation</i>	<i>UN</i>	<i>United Nations</i>

## 7. ACKNOWLEDGEMENT

The authors would like to acknowledge Egypt' Science and Technology Development Fund (STDF) for funding the project # 30457.

## 8. REFERENCES

- Al-Juwayhel, F., El-Dessouky, H. and Ettouney, H. (1997) 'Analysis of single-effect evaporator desalination systems combined with vapor compression heat pumps', *Desalination*, 114(3), pp. 253–275. doi: 10.1016/S0011-9164(98)00017-4.
- Aly, G. (1983) 'COMPUTER SIMULATIONS OF MULTIPLE-EFFECT FFE-VC SYSTEMS FOR WATER DESALINATION', *Desalination*, 45, pp. 119–131.
- Aly, N. H. and El-Fiqi, A. K. (2003) 'Mechanical vapor compression desalination systems - A case study', *Desalination*, 158(1–3), pp. 143–150. doi: 10.1016/S0011-9164(03)00444-2.
- Cuce, E. and Cuce, P. M. (2014) 'Improving thermodynamic performance parameters of silicon photovoltaic cells via air cooling', *International Journal of Ambient Energy*, 35(4), pp. 193–199. doi: 10.1080/01430750.2013.793481.
- Ettouney, H. (2006) 'Design of single-effect mechanical vapor compression', *Desalination*, 190(1–3), pp. 1–15. doi: 10.1016/j.desal.2005.08.003.
- Giwa, A., Fath, H. and Hasan, S. W. (2016) 'Humidification-dehumidification desalination process driven by photovoltaic thermal energy recovery (PV-HDH) for small-scale sustainable water and power production', *Desalination*. Elsevier B.V., 377, pp. 163–171. doi: 10.1016/j.desal.2015.09.018.
- Hamed, O. A. *et al.* (2016) 'Concentrating solar power for seawater thermal desalination', *Desalination*. Elsevier B.V., 396, pp. 70–78. doi: 10.1016/j.desal.2016.06.008.
- Helal, A. M. and Al-Malek, S. A. (2006) 'Design of a solar-assisted mechanical vapor compression (MVC) desalination unit for remote areas in the UAE', *Desalination*, 197(1–3), pp. 273–300. doi: 10.1016/j.desal.2006.01.021.
- Iaquaniello, G. *et al.* (2014) 'Concentrating solar power (CSP) system integrated with MED-RO hybrid desalination', *Desalination*. Elsevier B.V., 336(1), pp. 121–128. doi: 10.1016/j.desal.2013.12.030.
- Ibrahimi, M., Arbaoui, A. and Aoura, Y. (2017) 'Design analysis of MVC desalination unit powered by a grid connected photovoltaic system', *Energy Procedia*. Elsevier B.V., 139(4), pp. 524–529. doi: 10.1016/j.egypro.2017.11.248.
- Mabrouk, A. A., Nafey, A. S. and Fath, H. E. S. (2007) 'Analysis of a new design of a multi-stage flash-mechanical vapor compression desalination process', *Desalination*, 204(1–3 SPEC. ISS.), pp. 482–500. doi: 10.1016/j.desal.2006.02.046.
- Mabrouk, A. A., Nafey, A. S. and Fath, H. E. S. (2007) 'Thermoeconomic analysis of some existing desalination processes', *Desalination*, 205(1–3), pp. 354–373. doi: 10.1016/j.desal.2006.02.059.

Mahmoud, A., Fath, H. and Ahmed, M. (2018) 'Enhancing the performance of a solar driven hybrid solar still/humidification-dehumidification desalination system integrated with solar concentrator and photovoltaic panels', *Desalination*. Elsevier, 430(December 2017), pp. 165–179. doi: 10.1016/j.desal.2017.12.052.

Nafey, A. S., Fath, H. E. S. and Mabrouk, A. A. (2006) 'A new visual package for design and simulation of desalination processes', *Desalination*, 194(1–3), pp. 281–296. doi: 10.1016/j.desal.2005.09.032.

Nafey, A. S., Fath, H. E. S. and Mabrouk, A. A. (2008) 'Thermoeconomic design of a multi-effect evaporation mechanical vapor compression (MEE-MVC) desalination process', *Desalination*, 230(1–3), pp. 1–15. doi: 10.1016/j.desal.2007.08.021.

Ong, C. L. *et al.* (2012) 'A novel concept of energy reuse from high concentration photovoltaic thermal (HCPVT) system for desalination', *Desalination*. Elsevier B.V., 295, pp. 70–81. doi: 10.1016/j.desal.2012.04.005.

Palenzuela, P. *et al.* (2011) 'Simulation and evaluation of the coupling of desalination units to parabolic-trough solar power plants in the Mediterranean region', *Desalination*, 281(1), pp. 379–387. doi: 10.1016/j.desal.2011.08.014.

Palenzuela, P. *et al.* (2015) 'Comparison between CSP+MED and CSP+RO in Mediterranean Area and MENA Region: Techno-economic Analysis', *Energy Procedia*. Elsevier B.V., 69, pp. 1938–1947. doi: 10.1016/j.egypro.2015.03.192.

Sharaf Eldean, M. A. and Soliman, A. M. (2014) 'Study of Using Solar Thermal Power for the Margarine Melting Heat Process', *Journal of Solar Energy Engineering*, 137(2), p. 021004. doi: 10.1115/1.4028367.

Al Tarabsheh, A. *et al.* (2016) 'Performance of photovoltaic cells in photovoltaic thermal (PVT) modules', *IET Renewable Power Generation*, 10(7), pp. 1017–1023. doi: 10.1049/iet-rpg.2016.0001.

Teo, H. G., Lee, P. S. and Hawlader, M. N. A. (2012) 'An active cooling system for photovoltaic modules', *Applied Energy*. Elsevier Ltd, 90(1), pp. 309–315. doi: 10.1016/j.apenergy.2011.01.017.



---

## **#100: To develop a holistic and affordable toolkit to identify potential energy savings in an existing building: a case study in Taiwan**

---

Diane SCOBORIA<sup>1</sup>, Nataly MARTINEZ OBANDO<sup>2</sup>, Shin-Ku LEE<sup>3</sup>, Benson LAU<sup>4</sup>

<sup>1</sup> Energy Engineering Program, National Cheng Kung University, Tainan 701, Taiwan, R.O.C.,  
diane.scoboria@gmail.com

<sup>2</sup> Energy Engineering Program, National Cheng Kung University, Tainan 701, Taiwan, R.O.C.,  
Martineznataly201@gmail.com

<sup>3</sup> Research Center for Energy Technology and Strategy, National Cheng Kung University, Tainan 701, Taiwan,  
R.O.C., sklee1015@gmail.com

<sup>4</sup> School of Architecture + Cities, University of Westminster, 35 Marylebone Road, London, NW1 5LS,  
United Kingdom, B.Lau@westminster.ac.uk

*Taiwan is a mountainous island where buildings must withstand earthquakes and typhoons while also achieving energy efficiency. This case study looks at a university building in the town of Tainan and proposes small but critical improvements to increase energy efficiency that would not require drastic building renovations. We used readily available tools including eQUEST, thermal infrared cameras, and U-value testers to determine energy efficiency improvements. In addition, we considered the daily use of the building, its occupational schedule, and zones with and without air conditioning. We evaluated the lighting, insulation, window materials and window shading. Comparisons were then made between the baseline design and the actual building energy consumption data to improve the accuracy of the findings.*

*Our results show that a 16% improvement in energy efficiency can be achieved by increasing the standard AC temperatures, changing the lighting as well as by modifying the windows and shading. While insulation is critical in cold weather environments, we determined it is a minor factor in hot, humid environments. Most methods used in this study are appropriate for homeowners and small businesses to identify the energy efficiency methods appropriate for their climate and houses.*

*Keywords: Energy efficiency improvements, existing building, eQUEST*

## 1. INTRODUCTION

Buildings are not just structures with walls and supporting roofs. They are places where we spend most of our time. Places of safety and protection for people and objects we care about. Unfortunately, they come at a price, with buildings consuming over 30% of the total energy in Taiwan. Therefore, the more energy we use, the more the nation relies on coal-fired power plants that severely contribute to carbon dioxide and other greenhouse gasses, which is a primary cause of climate change.

Maintaining our standard of living while reducing energy use is challenging yet essential. In this study, we used readily available tools, including eQUEST, thermal infrared cameras, and U-value testers, to analyse energy efficiency improvements. These tools were used to assess the building of the Department of Aeronautics and Astronautics at the National Cheng Kung University (NCKU) in Tainan, Taiwan. Moreover, different energy use scenarios using energy simulations were examined.

Energy simulations have become important tools to improve energy efficiency. While there are various programs on the market today, one of the most commonly used is eQUEST, designed by the US Department of Energy, which is user-friendly because it was designed for the general public. Meanwhile, more advanced features are available through the professional-level program, Energy Plus, including solar thermal, wind turbines and electrical storage. Other programs on the market include Trace 700 and IES-VE by Trane and Don McLean, respectively (Smith 2016).

Among the many studies conducted to examine energy simulations, one study from the University of Massachusetts used several simulation programs to analyse the energy efficiency of a university dormitory. Findings showed that eQUEST was the most robust tool for calculating energy use and heating loads, beating both IES-VE and GBS. In this study, the energy and gas consumption was estimated with a high degree of accuracy, within 3% of actual use (Mostafavi, Farzinmoghadam and Hoque, 2013). Meanwhile, the zero-energy office building for Pusat Tenaga Malaysia only uses 40 kWh/m<sup>2</sup> every year through a combination of an energy-efficient building envelop design with insulation, double glazed windows with low-emissive coating, floor slab cooling, energy-efficient equipment and daylight lighting. In combination with photovoltaic solar panels, it produces enough energy to support itself, showing that energy-efficient buildings are possible (Kristensen et al. 2007).

Insulation plays a strikingly different role in places with cold climates compared with hot, humid climates like Taiwan. In cold climates, insulation is crucial in building design and is key to improving human comfort. In contrast, it plays a lesser role in warm climates, where the difference between the exterior and internal temperatures is less significant. A study by the US Department of Energy examined housing renovations in Florida, a hot, humid climate. While roof insulation was identified as one of the 13 key strategies for energy savings, they pointedly did not include increasing wall insulation because it is a less effective tactic. This finding was supported by Pongsuwan (2009) in a study of architecture in Bangkok, Thailand, where controlled studies of common building materials found that the rate of heat penetration is highest through the ceiling. On the other hand, the penetration was less for walls regardless of the direction they faced. The heat transfer rate through the 4-inch (10.16 cm) brick walls in the north, south, east and west directions were approximately 36, 47, 60 and 70 watt/m<sup>2</sup>, respectively. All of these were less than the heat transfer rates through the roof (up to 126 watt/m<sup>2</sup>), validating the importance of ceiling insulation over wall insulation. These findings support our results about downplaying the importance of insulation in hot climates.

Thermal infrared imaging is commonly used to gather information about existing buildings and identify potential improvements. It is used to determine heat leaks through building envelopes, missing insulation, thermal bridges, moisture sources and air leakage as well as to detect problems with the HVAC systems (Balaras and Argiriou, 2002). In 2001, a study examined the use of infrared imaging to successfully identify the impact of metal studs as thermal bridges in a library building in Toronto, Canada. Results showed that the average wall temperature between the metal studs is between 17.5°C and 19°C, while the temperature at the steel studs was significantly lower (16°C) (Taileb and Dekkiche, 2015). This shows one of the many benefits of thermal infrared imaging in the construction and renovation industry.

## 2. METHODOLOGY

In this study, we designed a method to analyse buildings and determine the best energy-saving strategies. Considering the hot, humid summers of Taiwan, optimizing energy saving can be a challenge. Taiwan is a small island located in the western Pacific Ocean, separated from mainland China by the 180 km wide Taiwan Strait. On the southern end of the island, just south of the Tropic of Cancer, lies the city of Tainan at 22°59'26.99"N, 120°12'47.99"E. Tainan has a reputation for bright, sunny weather where every year, it has over 180 days when temperatures reach over 30°C and annually receives over 2,180 hours of sunshine. Midsummer temperatures reach a monthly average high of 32.9°C with around 80% humidity. In midwinter, it cools down considerably to a

monthly average low of 14.1°C with snow occasionally dusting the top of the mountains in neighbouring counties (Central Weather Bureau). Therefore, buildings in Tainan must be built to accommodate this hot, humid climate.

The Department of Aeronautics and Astronautics at NCKU already incorporates different energy-efficient principles with its southern orientation, window overhangs and ample natural lighting. The building has a non-air conditioned lobby and courtyard, which are shaded but well ventilated, making them energy efficient and comfortable except in the hot summer months. The 2,420 m<sup>2</sup> building was established in 1985 and consists of four floors, a terrace, and a basement where most of the labs are located. Moreover, it is home to 60.9% air conditioned classrooms, laboratories and offices as well as 39.1% of non-air conditioned study areas and hallways.

This building was selected for this study to see if eQUEST could be used to identify any additional energy saving for a building which already incorporates many energy efficient principles. In addition, there were practical considerations including its availability during the entire study period, the lack of costs or permissions needed to access it, and the availability of a rough floorplan with all its dimensions. The eQUEST software was selected because of its widespread availability, industry acceptance as a reliable tool, and the free accessibility of its program. All these factors make it a useful tool when promoting an everyday energy solution.



Figure 1: The south side of the Department of Aeronautics and Astronautics, NCKU



Figure 2: The west side of the Department of Aeronautics and Astronautics, NCKU

This study focused on how to implement improvements in laboratories, offices and classrooms. The classrooms have a footprint of around 60 m<sup>2</sup>, three sets of windows with clear, single-layer glass, one air conditioner, 40 fluorescent light bulbs (18W), 50 table-chairs and two doors. The major electricity consumer is the air conditioner, while minor consumers include lighting and miscellaneous equipment such as projectors, a teaching computer, and outlets used by students to charge their laptops and smartphones.

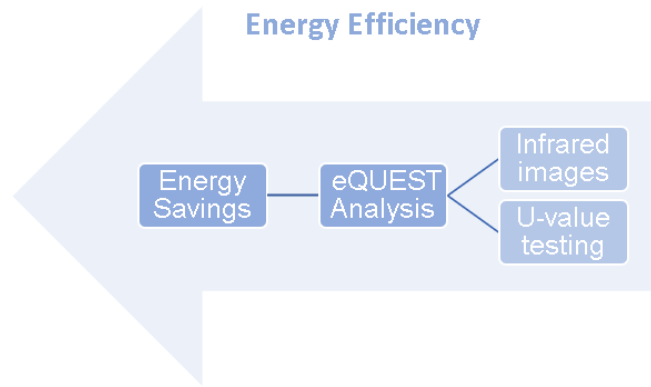


Figure 3: Project flowchart

Readily available tools like thermal infrared cameras and U-value testers were used to collect information about the study site. Meanwhile, we employed eQUEST to design and simulate the building energy use and perform a detailed analysis of potential energy savings.

### 2.1. Infrared Cameras

Thermal infrared cameras detect infrared radiation and translate it into a thermal image, making them useful tools to determine heat sources. As a key element to reducing the air conditioning needs in a building, the technology has been made simpler and more accessible with recent developments. The most reliable results are produced by selecting the appropriate emissivity level, which shows how well a material radiates thermal radiation. In this study, we used the Flir C2 infrared camera that produces both infrared images called thermograms (Figure 4a) and standard images (Figure 4b). The camera operates in a range of  $-10^{\circ}\text{C}$  to  $150^{\circ}\text{C}$ , which is well within the temperature range of the building, with an accuracy of  $\pm 2^{\circ}\text{C}$  at  $25^{\circ}\text{C}$  (Flir 2019).



Figure 4a: Infrared thermogram showing heat sources in the department



Figure 4b: The same photo without infrared

The temperatures inside and outside the classrooms were measured in two sessions on November 20, 2018 around 8:00 p.m. and the following day at 10:00 a.m. We realized that heat transfer will change depending on the season, but the temperature was warm during the day ( $25^{\circ}\text{C}$ ) even in November, so the temperature difference between the inside and outside was noticeable. In future studies, it would be preferable to take the infrared images during the season where the temperature difference is at its extreme, which, in Tainan, is the hot summer months.

Results showed that the windows are a major source of heat transfer, conducting the heat out at night (Figure 5a) and in during the day (Figure 5b).



Figure 5a: Windows in the classrooms dissipate heat at night



Figure 5b: Windows increase the temperature during the day

In addition, the exterior walls of the building become hot during the day, and it was theorized that they contribute to the heat build-up in the classrooms (Figure 6).

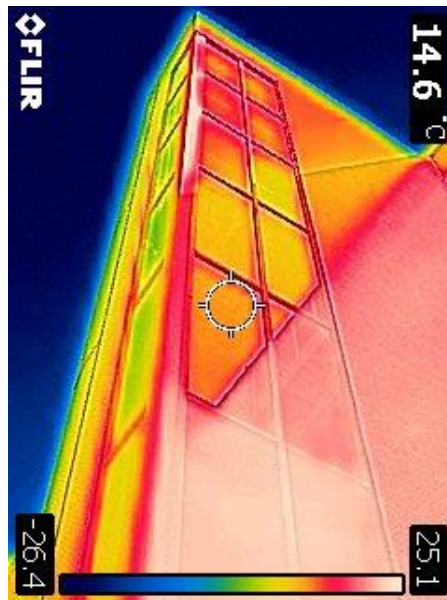


Figure 6: Exterior walls with southern and western exposure become hot during the day and likely conduct heat into the building.

From analysing infrared images we listed the high-priority heat transfer concerns for this building: windows, window overhangs (and fins), and insulation in the walls and lighting. This helped us identify what to prioritize in the eQUEST energy simulation.

## 2.2. Insulation Test

A Temperature Flux was used to determine the insulation on the southern exposure of the building. Wall insulation, usually recorded as U value, affects heat transfer within the walls of a building. In cold climates, one of the most effective ways to reduce heat loss is by increasing the insulation in the walls and roof. The device measured the wall temperature on both the interior and exterior surfaces, and a thermometer measured the atmospheric temperature inside and outside the classroom. On the test day, the inside atmospheric temperature was 25°C while the outside was 28°C. The wall temperatures recorded for the inside and outside were at 26°C and 28°C, respectively.

Unfortunately, given that the inside and outside temperatures were close in value on the test day, we determined that the level of error was too high to provide usable U value data. The tool and process, however, can be used in situations where there is a larger temperature difference between the two sides of the wall. After the U-value is determined, the insulation data can be used to accurately design the building in eQUEST.

### 2.3. eQUEST Analysis

eQUEST is an energy simulation tool that allows us to input building information and generate an analysis of how the building consumes energy. Designed by the US Department of Energy, the software is available for free. It provides professional-level results with an affordable level of effort. The software is designed to predict monthly energy use and energy costs for the building using measurements, insulation, HVAC systems and use schedules as well as external information like the local climate data. Using this tool, we can quantify energy savings and determine the cost-effectiveness of individual measures.

We divided the project into three areas: simplifying the structure of the building, inputting building characteristics and simulating energy efficiency scenarios.

First, we simplified the model of the building using eQUEST to simulate its structure. To simplify the project, we did not consider the basement because electricity needs vary significantly from the rest of the building. The basement is where the large equipment is housed and where the experiments of our department are conducted, which results in different energy use requirements. The weather data of Hainan, China, were used for software simulations; thus, minor errors should be expected, such as overestimating cooling expenditures throughout the year.

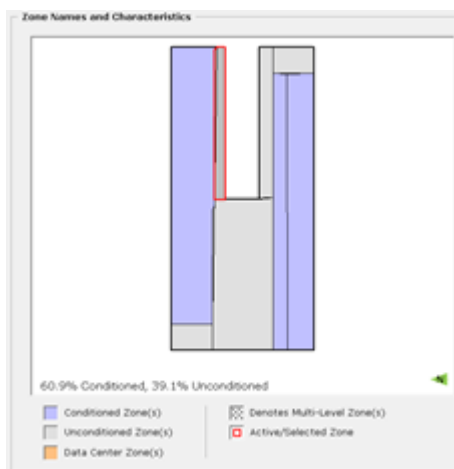


Figure 7a: The eQUEST zones

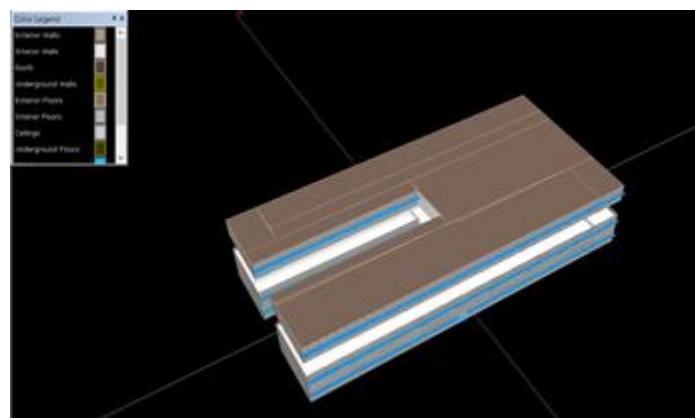


Figure 7b: The entire structure in eQUEST

The second step was to input building characteristics based on measurable building features (overhangs, fins, windows, AC types) and regional standards, where actual building data were unavailable. The parameters that we considered were based on everyday use and included the occupational schedule, which leaves many classrooms vacant during the summer months. The model consisted of four floors from which we divided into air conditioned (AC) and non-air conditioned (non-AC) zones, including bathrooms, halls, storage and the lobby.

The third step was to analyse different scenarios using the eQUEST Energy Efficiency Measure Wizard. This allowed us to determine the best method and the combination of methods to improve building energy efficiency. We initially looked at the concerns identified in the thermal infrared test (windows, window overhangs, insulation in walls and lighting), but then expanded our analysis to other potential factors.

### 3. RESULTS

The most effective energy savings were achieved by changing the thermostat setpoint, followed by modifying the lighting and windows.

Significant energy savings can be achieved by changing the standard thermostat temperature (T<sub>sat</sub> management). Thermal comfort is subjective, it depends on the gender of the subject and the region where they live. Maykot (2018) found that women prefer an air conditioned environments 0.8°C warmer than men. Kantor (2014) found that while Taiwanese men feel that 27.5°C is a neutral temperature, they prefer cooler environments (23.5°C). We analysed energy savings based on these temperature setpoints (Table 1).

Table 1: Energy savings based on minimum AC thermostat setpoints

	Minimum AC thermostat setpoint		Energy Savings (%)
Men prefer	23.5°C	74.3°F	-1%
Baseline	24.0°C	75.2°F	0%
Women prefer	24.3°C	75.7°F	1%
<b>Compromise</b>	<b>26.0°C</b>	<b>78.8°F</b>	<b>6%</b>
Neutral for men	27.5°C	81.5°F	9%
Neutral for women	28.3°C	82.9°F	12%

The preferred temperatures (Table 1) result in little or negative energy savings. On the other hand, the neutral temperatures provide significant energy savings but are unlikely to be adopted in most Taiwanese offices. A more likely solution is to select a setpoint between the preferred and neutral temperatures. A reasonable compromise may be possible around 26°C. A study out of Singapore found that as the setpoint is increased from 23°C to 26°C, thermal comfort can be maintained if study participants are given personal fans (Schiavon et al., 2017). Moreover, in addition to increasing energy efficiency, the participants showed the best cognitive performance with this combination of settings. By adopting this setpoint, the department would achieve 6% energy savings which amounts to over 70,000 kWh per year.

Additional improvements increased the energy efficiency to 16% (Table 2). While changing the thermostat setpoint made the largest impact, it was followed close behind by reducing the lighting load by minimizing corridor and lobby lighting when unoccupied. Changing the glass to reflective glass played a substantial role, while a more moderate improvement was seen by increasing the window shading and fins from 1 to 1.3 meters. Window overhangs and fins reduce the sunlight hitting the windows thereby reducing thermal radiation.

Table 2: Energy savings

	Energy Savings (kWh/year)	Energy Savings (%)
Window Glass	44,006	4%
Lighting	56,828	5%
Thermostat setpoint	70,978	5%
Window Shading & Fins	24,610	2%
<b>TOTAL</b>	<b>196,422</b>	<b>16%</b>

Surprisingly, insulation plays a minimal role in hot, humid climates. Adding 7.6 cm of polystyrene (R-12) insulation showed only a 1,500 kWh improvement per year, while adding roof insulation had no effect.

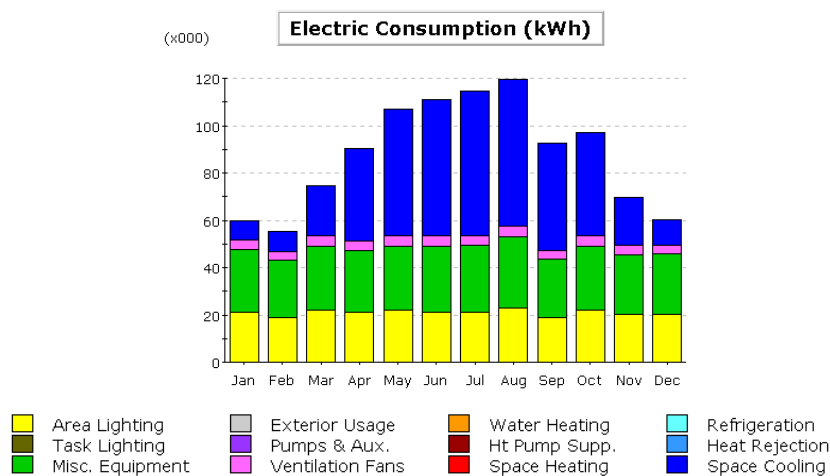


Figure 8: Monthly electric consumption shows increased air conditioning needs in summer months

This study found that renovations will provide 16% energy savings which translates to just over 196,000 kWh per year. Given that Tainan relies on coal fired power plants for electricity, this reduction in energy translates to a reduction of 109,000 kg of CO<sub>2</sub>, which is the primary cause of climate change in the world today. Moreover, by applying these improvements to the department, the electricity bill decreases by 510,000 NT (\$16,200 USD) per year. While some of these savings will have to be spent on building renovations, the long-term energy savings will continue for the lifetime of the building.

#### 4. CONCLUSION

While the Department of Aeronautics and Astronautics was designed to be energy efficient, there are still areas for improvement. For that reason, this study explores how these problems can be addressed using thermal infrared cameras, u-value testers and eQUEST simulation software. Using these methodologies, the thermal infrared camera and eQUEST results are reasonable for the climate and the existing building structure. However, the u-value test data were neglected because the difference in temperature was insufficient and would have introduced a significant error. To get valid results, the test should be conducted when there is a large difference between indoor and outdoor temperatures. Furthermore, this study analysed various energy efficiency scenarios. The improvements came from increasing the AC temperature to 26°C, adding personal fans, changing the lighting, upgrading the windows and expanding shading and fins. Overall, this study created a methodology that can be used not only for university buildings but also for homeowners and small businesses.

#### 5. REFERENCES

- Balaras, C.A. & Argiriou, A.A. 2002. 'Infrared thermography for building diagnostics.' *Energy and Buildings*, vol. 34, pp. 171–183.
- Flir, 2019. 'Flir C2 compact digital camera,' viewed 5 June 2019, available at <<https://www.flir.com/products/c2/>>
- Central Weather Bureau, Government of Taiwan, viewed 10 June 2019, available at <<https://www.cwb.gov.tw>>
- Kantor, N., Tsai, K.T., Egerhazi, L. & Lin, T.P. 2014. 'Outdoor thermal comfort requirements of Taiwanese and Hungarians in the warm months,' *American Meteorological Society*. 30 September 2014. Cleveland: AMS100.
- Kristensen, P.E., Tang, C.K., Reimann, G. & Ismail, A.Z., 2007. 'Design strategies for energy efficiency in hot and humid climate: the case of the ZEO building,' *International Conference on Sustainable Building Asia*. pp. 27–29 June 2007. Seoul: ICONDA.
- Maykot, J.K., Rupp, R.F., & Ghisi, E. 2018. 'A field study about gender and thermal comfort temperatures in office buildings,' *Energy and Buildings*, vol. 178, pp. 254–264.
- McIlvaine J., Sutherland, K. & Martin, E. 2013. *Energy retrofit field study and best practices in a hot-humid climate*. Florida: US Department of Energy. Available at <<https://www.nrel.gov/docs/fy13osti/57827.pdf>>
- Mostafavi, N., Farzinmohadam, M. & Hoque, S. 2013. 'Envelope retrofit analysis using eQUEST, IESVE revit plug-in and green building studio: A university dormitory case study.' *International Journal of Sustainable Energy*, vol. 34, no. 9, pp. 1–20.
- Pongsuwan, S. 2009. 'The miracle of insulation in hot-humid climate building.' *International Journal of Renewable Energy*, vol. 4, no. 1, pp. 47–49.
- Schiavon, S., Yang, B., Donner, Y., Chang, V.W., & Nazaroff, W.W. 2017. 'Thermal comfort, perceived air quality, and cognitive performance when personally controlled air movement is used by tropically acclimatized persons.' *Indoor Air*, vol. 3, pp. 690-702.
- Smith, M. 2016. *The energy modeling breakdown*. Available at <<https://www.verdicalgroup.com/the-energy-modeling-breakdown/>>
- Taileb, A. & Dekkiche, H. 2015. 'Infrared imaging as a means of analyzing and improving energy efficiency of building envelopes: the case of a LEED gold building.' *Procedia Engineering*, vol. 118, pp. 639–646.



- Abdelrahman, H., Wahba, M., Refaey, H. & Moawad, M. B. N., 2019. Performance enhancement of photovoltaic cells by changing configuration and using PCM (RT35HC) with nanoparticles Al<sub>2</sub>O<sub>3</sub>. *Solar Energy*, pp. 665-671.
- Amin, N. B. F. & Belusko, M., 2014. Effective thermal conductivity for melting in PCM encapsulated in a sphere. *Applied Energy*, Volume 122, pp. 280-287.
- Anisur, M., Mahfuz, M. K. M., Saidur, R. & Metselarr, I. M. T., 2013. Curbing global warming with phase change materials for energy storage. *Renewable and Sustainable Energy Reviews*, pp. 23-30.
- Arkar, C. & Medved, S., 2007. Free cooling of a building using PCM heat storage integrated into the ventilation system. *Solar Energy*, 81(9), pp. 1078-10878.
- Baby, R. & Balaji, C., 2012. Thermal management of electronics using phase change material based pin fin heat sinks. *Journal of Physics: Conference Series*, Volume 395, p. 012134.
- Bland, A., Khzouz, M., Statheros, T. & Gkanas, E., 2017. PCMs for residential building applications: A short review focused on disadvantages and proposals for future development. *Buildings*, Volume 7, p. 18.
- Cabeza, L. et al., 2011. Materials used as PCM in thermal energy storage in buildings - A review. *Renewable Sustainable Energy Reviews*, p. 1675–1695.
- Darkwa, J. & Su, O., 2012. Thermal simulation of composite high conductivity laminated microencapsulated phase change material (MEPCM) board. *Applied Energy*.
- Hawladar, M., Uddin, M. & Khin, M., 2003. Microencapsulated PCM thermal-energy storage system. *Applied Energy*, 74(1-2), pp. 195-202.
- Jacob, R. & Bruno, F., 2015. Review on shell materials used in the encapsulation of phase change materials for high temperature thermal energy storage. *Renewable and Sustainable Energy Reviews*, pp. 79-87.
- Ji, H. et al., 2014. Enhance thermal conductivity of phase change materials with ultrathin-graphite foams for thermal energy storage. *Energy and Environmental Science*, pp. 1185-1192.
- Jradi, M., Gillot, M. & Riffat, S., 2013. Simulation of the transient behaviour of encapsulated organic and inorganic phase change materials for low-temperature energy storage. *Applied Thermal Engineering*, pp. 211-222.
- Kalnæs, S. & Jelle, B., 2015. Phase change materials and products for building applications: A state-of-the-art review and future research opportunities. *Energy and Buildings*, pp. 150-176.
- Khodadadi, J., Fan, L. & Babaei, H., 2013. Thermal conductivity enhancement of nanostructure-based colloidal suspensions utilizes as phase change materials for thermal energy storage: A review. *Renewable and Sustainable Energy Reviews*, Volume 24, pp. 418-444.
- Khudhair, A. & Farid, M., 2004. A review on energy conservation in building applications with thermal storage by latent heat using phase change materials. *Energy Conversion and Management*, 45(2), pp. 263-275.
- Ma, Z., Lin, W. & Sohel, M., 2013. Nano-enhanced phase change materials for improved building performance. *Renew. Sustain. Energy Rev.*, pp. 1256-1268.
- Memon, S., Cui, H., Zhang, H. & Xing, F., 2015. Utilization of macro encapsulated phase change materials for the development of thermal energy storage and structural lightweight aggregate concrete.. *Applied Energy*, Volume 139, pp. 43-55.
- Microsystems, L., 2019. *Leica Microsystems*. [Online]  
Available at: [www.leica-microsystems.com](http://www.leica-microsystems.com)
- Saffari, M., Gracia, A., Ushak, S. & Cabeza, L., 2016. Economic impact of integrating PCM as passive system in buildings using Fanger comfort model. *Energy and Buildings*, pp. 159-172.
- Salunke, P. & Shembekar, P., 2012. A review on the effect of phase change material encapsulation on the thermal performance of a system. *Renewable and Sustainable Energy Reviews*, 16(8), pp. 5603-5616.

- Silva, T., Vicente, R. & Rodrigues, F., 2016. Literature review on the use of phase change materials in glazing and shading solutions. *Renewable and Sustainable Energy Reviews*, Volume 53, pp. 515-535.
- Velasco-Carrasco, M., Ziwei, C., Aguilar-Santana, J. & Riffat, S., 2018. Review on enhancement methods for phase change materials. *17 International Conference on Sustainable Energy Technologies*, Volume 3, pp. 130-138.
- Wang, H., Lu, W., Wu, Z. & G., Z., 2019. Parametric analysis of applying PCM wallboards for energy saving in high-rise lightweight buildings in Shanghai. *Renewable Energy*.
- Wang, X. M. A., 2007 . Heat transfer characteristics of nanofluids: A review. *International Journal of Thermal Science*, pp. 1-19.
- Wei, J., Kawaguchi, Y., Hirano, S. & Takeuchi, H., 2005. Study on a PCM heat storage system for rapid heat supply. *Applied Thermal Engineering*, pp. 2903-2920.
- Wu, S. Y., Wang, H., Xiao, S. & Zhu, D., 2013. An investigation of melting/freezing characteristics of nanoparticle-enhanced phase change materials. *Journal of Thermal Analysis and Calorimetry*, 110(3), p. 1127–1131.
- Yahaya, N. & Ahmad, H., 2011. Numerical investigation of indoor air temperature with the application of PCM gypsum board as ceiling panels in buildings. *Procedia Engineering*, Volume 20, pp. 238-248.
- Yu, X. & Xie, H., 2012. A review on nanofluids: preparation, stability mechanisms and applications. *Journal of Nanomaterials*, pp. 1-17.
- Zhang, H., Wang, X. & Wu, D., 2010. Silica encapsulation of n-octadecane via sol-gel process: A novel microencapsulated phase-change material ith enhanced thermal conductivity and performance. *Journal of Colloid and Interface Science*, pp. 246-255.
- Zhang, H., Wang, X. & Wu, D., 2010. Silica encapsulation of n-octadecane via sol-gel process: A novel microencapsulated phase-change material ith enhanced thermal conductivity and performance. *Journal of Colloid and Interface Science*, pp. 246-255].
- Zhu, N., Ma, Z. & Wang, S., 2009. Dynamic characteristics and energy performance of buildings using phase change materials: A review. *Energy Conversion and Management*, 50(12), pp. 3169-3181.

---

## #102: Numerical study of the effect of surface wettability on droplet impact on a spherical surface

---

Xiaohua LIU<sup>1\*</sup>, Kaimin WANG<sup>1</sup>, Yaqin FANG<sup>1</sup>, R. J. GOLDSTEIN<sup>2</sup>, Shengqiang SHEN<sup>1</sup>

<sup>1</sup> Key Laboratory of Ocean Energy Utilization and Energy Conservation of Ministry of Education, Dalian University of Technology, 116024, Dalian, China

<sup>2</sup> Department of Mechanical Engineering, University of Minnesota, MN 55455, USA

\*Corresponding author: lxh723@dlut.edu.cn

*The phenomena of droplet impact are widely found in nature and industrial field, surface wettability plays a significant part on the dynamic characteristics of the droplets after impacting. In this paper, effect of surface wettability on the dynamic characteristics of droplet after impacting spherical surfaces is explored, through two-dimensional numerical simulation with Coupled Level-Set and Volume-of-Fluid (CLSVOF) method. The degree of surface wettability is represented by the contact angle (CA). It is found that when the impact velocity is a constant, with the increase of the contact angle, the liquid film is more prone to break up and rebound after impacting a spherical surface. The maximum spreading factor and time needed to reach the maximum spreading factor both decrease with the increase of the contact angle. The Rebound height and rebound time increase with the increase of the contact angle. In a word, the increase of the contact angle hinders droplet spread, but promotes droplet break-up and rebound, somehow. When the contact angle is a constant, with the impact velocity increasing, the maximum spreading factor increases while the time needed to reach the maximum spreading factor decreases. It is also found that when the contact angle is a constant, the time needed to reach the maximum spreading factor increases with the curvature ratio,  $\varepsilon$ . When the contact angle is between 30 and 150°, the maximum spreading factor increases with curvature ratio, while when the contact angle ranges from 0 to 30°, the maximum spreading factor decreases with the increase of the curvature ratio.*

*Keywords: droplet impact; surface wettability; spreading factor; impact velocity; curvature ratio*

## 1. INTRODUCTION

Droplet impact on a solid surface or liquid film occurs frequently in nature or industrial fields. Droplet impact phenomenon can be observed in the following practical applications. During the cooling process inside a spray cooling tower, water droplets impact onto heated tubes. In a trickle bed reactor, when gas and liquid droplets flow downward, the droplets impact with catalyst. In pharmaceutical manufacturing, solid particles are brought into a reactor and impact with liquid. In an IC engine, petrol or diesel fuel is injected onto a piston crown. Typical applications are also found in the evaporators of multi-effect distillation seawater desalination system. The seawater droplets impact outside surface of horizontal tube during film evaporation.

The surface wettability has a significant effect on droplet impact. Li et al. (2009; 2013) experimentally studied droplets impact process with different temperatures (50-120°C) and wettability. Results indicate that on part of hydrophobic surfaces, the droplet retract height increases with surface temperature, while on hydrophilic and super-hydrophobic surfaces, this rule disappears. The dynamic characteristics of droplet were also studied when impacting the surface where wettability had radial and axial symmetry gradient distribution. Shen et al. (2009; 2013) did numerical simulation of deformation process after droplet impacting a flat surface. The results show that with the decrease of the contact angle, the droplet spreading factor increases, and the oscillation frequency of droplet slows down, reaching equilibrium sooner. Volume-of-Fluid (VOF) method was applied to explore droplet spreading process with different wettability on an inclined surface. Under the same conditions, a non-wetting surface results in partial crushing of droplet. Antonini et al. (2012) experimentally studied surface wettability effects on the characteristics of water droplet impact. When Weber number is between 30 and 200, wettability affects both droplet maximum spreading distance and spreading characteristic time. When Weber number is higher than 200, wettability effect is secondary for the increasing of inertial force. Quan et al. (2009) first used a pseudopotential model of the Lattice Boltzmann method and proved that retract speed and rebound tendency both increase with better wettability. VOF method was used by Liang et al. (2013) to simulate the individual droplet dynamic behavior when droplets impact different wettability surfaces with different impact velocities. Calculation results show that a hydrophobic surface leads to droplet rebound. The maximum spreading factor increases with decreasing contact angle, and time used to reach the maximum spreading factor reduces accordingly. Wang et al. (2013) studied the effect of contact angle on the droplet impact on dry spherical surfaces by CLSVOF method. It was shown that the increase of the contact angle hinders droplet spreading but promotes retracting (Liu 2017). The liquid film oscillates when the contact angle is relatively small. The oscillation period decreases with increasing the contact angle, while it increases with increasing impact velocity (Yan 2018). Kim et al. (2013) carried out the experiment with liquid drops impacting solid surfaces where a super-hydrophilic annulus was set on a super-hydrophobic base. The liquid film covering the super-hydrophobic region is arrested by the hydrophilic annulus and spontaneously ruptures into a water ring. Kannan et al. (2008) experimentally explored the droplet impact behavior on a hydrophobic grooved surface. The result indicates that trough structure changes the shape of film spreading on the groove surface, and enhancing hydrophobicity of groove surface would be more conducive to droplet rebound.

Mitra et al. (2013) completed a theoretical and experimental study on the effect of a spherical surface with high thermal conductivity on super-cooled droplet impact process. The surface temperature ranges from 20 to 250°C. They pointed out that when the surface temperature was below or close to the saturation temperature, wetting contact occurred. When the surface temperature was higher than the saturation temperature, non-wetting contact occurred. In the non-wetting contact circumstance, surface temperature decreases slowly. Collision of a droplet onto a still spherical particle was experimentally investigated by Banitabaei et al. (2017) during which the effect of wettability on collision was studied. It was found that for droplet impact onto a hydrophilic particle, the droplet is neither disintegrated nor stretched enough to form a liquid film after impact in the entire velocity range studied. However, on a hydrophobic particle, when Weber number achieves about 200 or larger, a liquid film forms after impact. With the Weber number increasing, the lamella length and cone angle increases accordingly. Another main conclusion is that increasing the contact angle from hydrophilic to hydrophobic zone has a considerable effect on geometry of the liquid film and lamella formation. However, when the contact angle exceeds a threshold value of 110°, increasing of the contact angle has little effect on lamella geometry. A similar lamella formed after droplet impacting a small disk was observed by Rozhkov et al. (2002) with a high-speed photography technique.

In conclusion, the research of surface wettability effects on droplet impacting process had a certain foundation. However, these researches mostly focused on flat surfaces, and furthermore, parameters, such as impact velocity, droplet size and spherical curvature, needed to be investigated further. In this paper, a two-dimensional numerical simulation with CLSVOF method is used to explore droplet dynamic characteristics of impacting process on spherical surfaces. Impact velocity and curvature ratio are mainly studied when droplets impact spherical surfaces with different wettability.

## 2. PHYSICAL AND MATHEMATICAL MODEL

### 2.1. Physical model

Shown in Figure 1, a droplet impacts a spherical Surface with a certain initial velocity, and the impact direction is parallel with the centre line of droplet and sphere. The moment when the droplet contacts the sphere is considered as the zero moment.

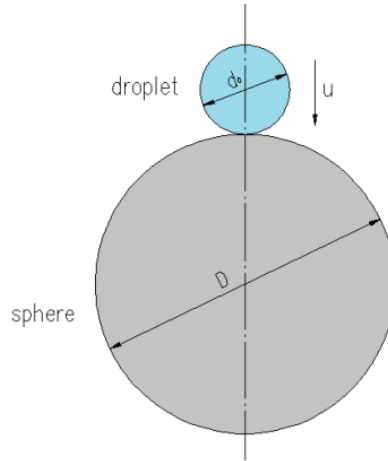


Figure 1: Physical model of droplet impact a spherical surface

### 2.2. Mathematical model

In this paper, a numerical simulation is accomplished by ANSYS FLUENT14.5 software. Droplet impacting a spherical surface is a transient process. CLSVOF method is used by coupling VOF with Level-Set methods together and the advantage of which is that parameters describing phase interface with higher sharpness can be given out accurately. On the basis of mass and momentum conservation, two-dimensional laminar axisymmetric model and Pressure Implicit with Splitting of Operators (PISO) algorithm which has faster convergence speed are used. Liquid droplet is considered incompressible and calculation area is isothermal during the impact process.

For the liquid, the control equations of mainstream field are shown as follows (Liang 2012).

Equation 1: 
$$\nabla \mathbf{v} = 0$$

Equation 2: 
$$\frac{\rho \partial \mathbf{v}}{\partial t} + \rho \mathbf{v} \bullet \nabla \mathbf{v} = -\nabla p + \nabla \bullet \mathbf{v} \left[ \nabla \mathbf{v} + (\nabla \mathbf{v})^T \right] - \sigma \kappa \delta(\phi) \nabla \phi + \rho \mathbf{g}$$

Where:

- $\mathbf{v}$  = velocity vector
- $\rho$  = density
- $p$  = pressure
- $\sigma$  = surface free energy
- $\mathbf{g}$  = the gravitational acceleration
- $\kappa$  = the interface curvature which can be calculated with Equation (3).

Equation 3: 
$$\kappa = \nabla \bullet \frac{\nabla \phi}{|\nabla \phi|}$$

Where  $\delta(\phi)$  can be calculated with the following formula:

Equation 4: 
$$\delta(\phi) = \begin{cases} \frac{1 + \cos(\pi\phi/a)}{2a} & |\phi| < a \\ 0 & |\phi| \geq a \end{cases}$$

Where:

- $a = 1.5\omega$ , and
- $\omega$  = minimum mesh size.

Other relevant dimensionless numbers are defined as follows:

Equation 5: 
$$T^* = t \cdot u / d_0$$

Equation 6: 
$$D^* = d / d_0$$

Equation 7: 
$$H^* = h / d_0$$

Equation 8: 
$$\varepsilon = d_0 / D$$

Where:

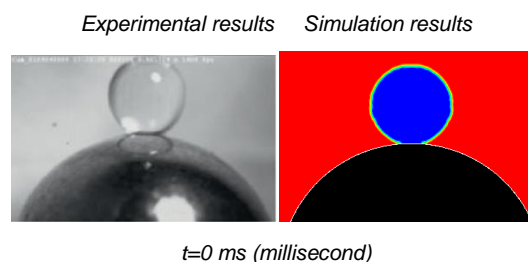
- $T^*$  is the dimensionless time
- $t$  is time
- $u$  is the impact velocity, the ratio of the droplet falling distance to the time interval of which, in this paper, the impact velocity is the velocity when droplet collide with the surface the first time
- $d_0$  is the initial diameter of the droplet
- $D^*$  is the spreading factor
- $D$  is the diameter of the solid sphere
- $d$  is the liquid film spreading diameter along the sphere
- $h$  is the liquid film central height (when liquid film rebounds into air)
- $h$  represents the vertical distance from the highest point of liquid to the highest point of sphere
- $H^*$  is the dimensionless liquid film central height
- $\varepsilon$  is the curvature ratio.

The droplet is water. Non-slip boundary condition is used with constant temperature and the wall is considered smooth without roughness.

### 3. RESULTS AND DISCUSSION

#### 3.1. Simulation model verification

Using the experimental results from Mitra et al. (2013), the simulation model used in this paper is verified. Comparison is shown in Figure 2. The initial droplet diameter is 3.1 mm (millimeter), spherical diameter is 10 mm, contact angle is 90° and the impact velocity is 0.431 m/s.



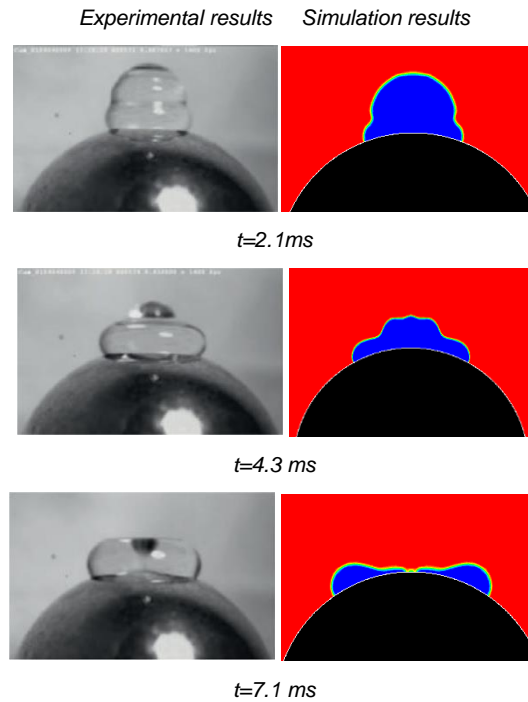
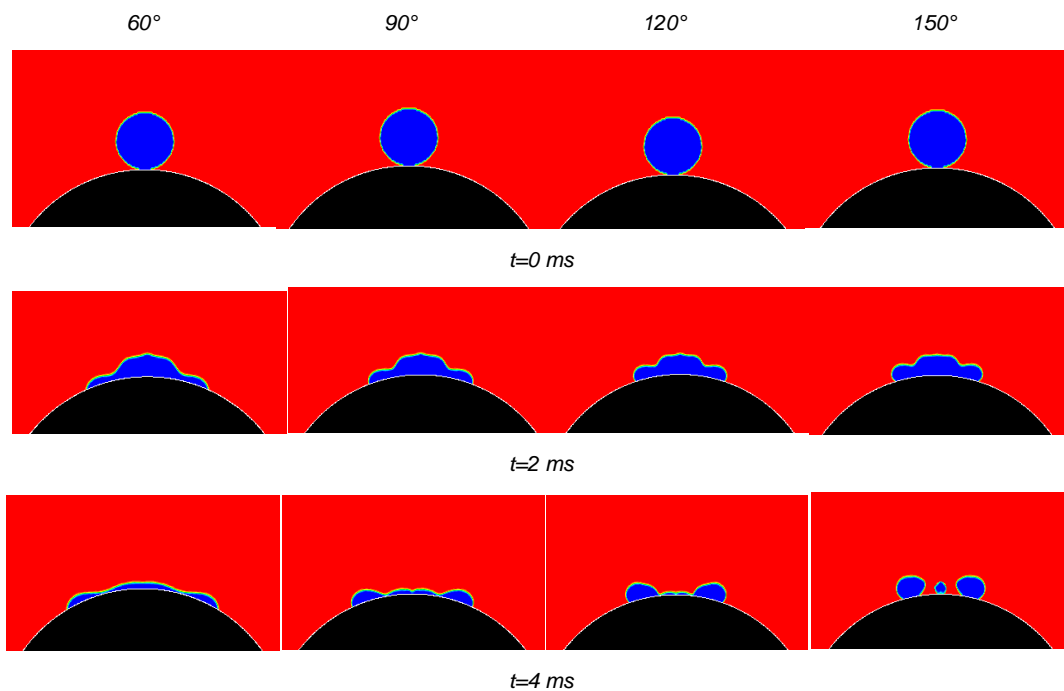


Figure 2: Droplet spreading characteristics

According to Figure 2, we can find that two-dimensional numerical simulation results are consistent with the experimental results at most stages of collision. At the later time, there just presents a little retraction lags by two-dimensional simulation results.

### 3.2. Simulation results and analysis

The contact angle (CA) is an important parameter to present surface wettability. When CA is less than  $90^\circ$ , the surface is hydrophilic. While CA is between  $90$  and  $150^\circ$ , the surface is hydrophobic. When CA is greater than  $150^\circ$ , the surface is super-hydrophobic. The phase diagram of droplet impact a spherical surface is shown in Figure 3. The curvature ratio is 0.2, the impact velocity is 0.7 m/s, and CA is  $60^\circ$ ,  $90^\circ$ ,  $120^\circ$ , and  $150^\circ$ , respectively.



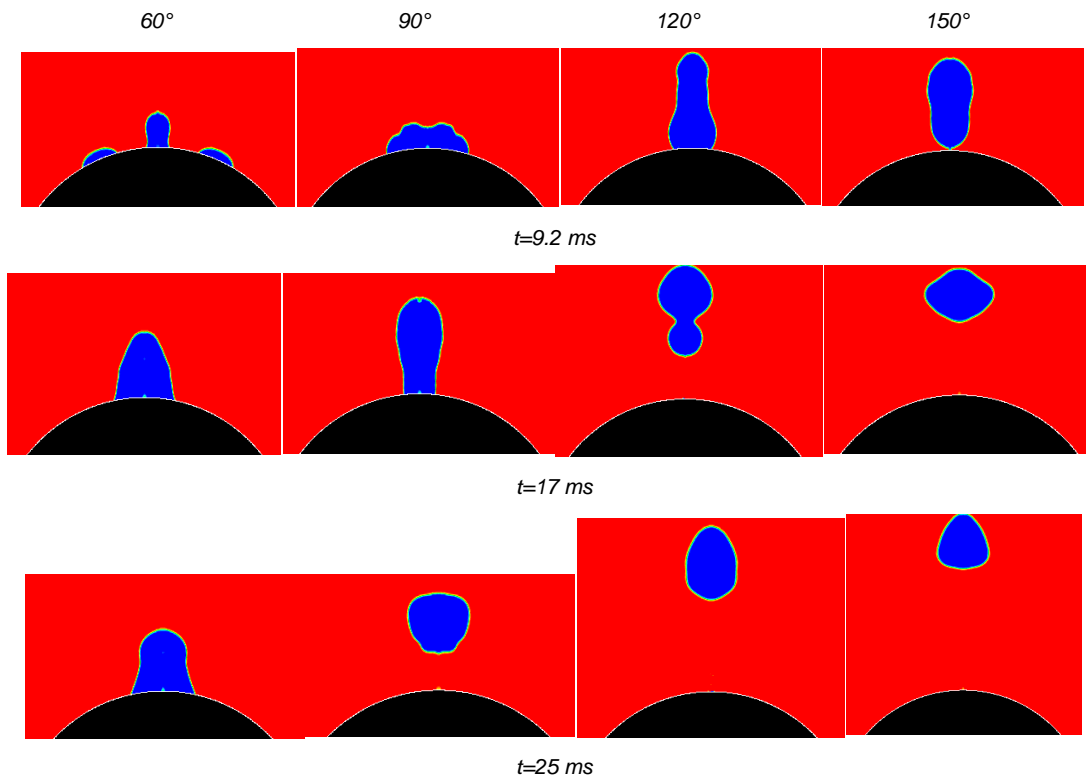


Figure 3: Phase diagram of droplet impact on surfaces with different CA

As shown in Figure 3, the dynamic characteristics of droplet after impact are different with different surface wettability. When surface wettability becomes worse, liquid film is more prone to break and rebound. When surface energy is great enough after droplet spreading, rebound will occurs. When CA is  $90^\circ$ , centre sag appears at 9.2 ms; when droplet impacts a spherical surface with CA of  $120^\circ$ , droplet rebounds and forms into gourd-shape at 17 ms.; when CA is  $150^\circ$ , complete rebound takes place, and the rebound height is higher than that with CA of  $120^\circ$  at 17 ms.

The Spreading factor ( $D^*$ ) and the dimensionless liquid film central height ( $H^*$ ) with different surface wettability changes with dimensionless time, as shown in Figure 4 and 5, where  $\epsilon$  is 0.2,  $u$  is 0.7 m/s, and CA is  $60^\circ$ ,  $90^\circ$ ,  $120^\circ$  and  $150^\circ$ , respectively.

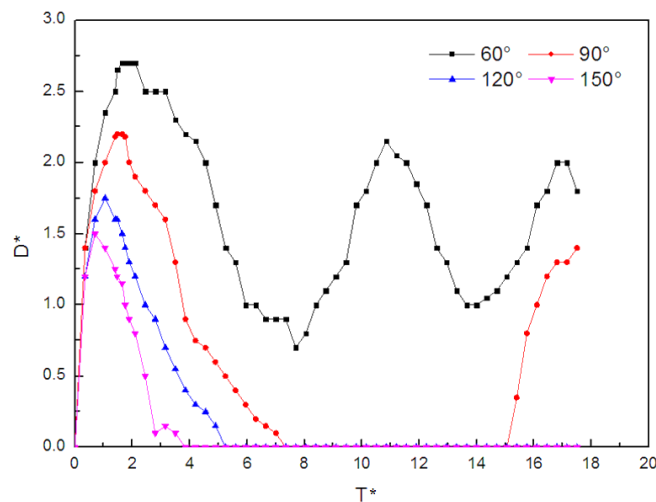


Figure 4: The change of the spreading factor over dimensionless time with different CA



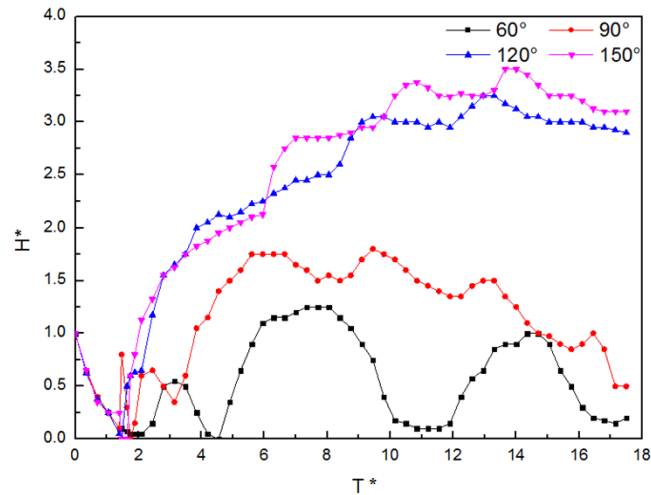


Figure 5: The change of the dimensionless liquid film central height over dimensionless time with different CA

As shown in Figure 4, with the decrease of CA, the maximum spreading factor becomes greater, and longer time is needed to reach maximum spreading factor. Figure 5 shows that the greater the contact angle is, the higher the droplet rebound height and the longer the rebound time are. The main reason is that more surface energy converts into kinetic energy under a larger contact angle. When CA is 60°, droplet partial rebound occurs after droplet reaches the maximum spreading factor, the droplet retract makes droplet gathering and then the liquid film oscillates on the surface. The spreading factor and the dimensionless film central height attenuate gradually during oscillation. When CA is 90°, the droplet also partially rebounds after droplet reaching the maximum spreading factor, then complete rebound happens after further retract. When CA is 120° or 150°, complete rebound occurs after spreading, the larger the contact angle is, the earlier the droplet leaves from the surface.

With different impact velocities, the relationship between CA and the maximum spreading factor ( $D^*_{max}$ ) is shown in Figure 6. The relationship between CA and time needed to reach the maximum spreading factor ( $t_{max}$ ) is shown in Figure 7. The curvature ratio is 0.2. The impact velocity is 0.431, 0.7 and 1 m/s, respectively.

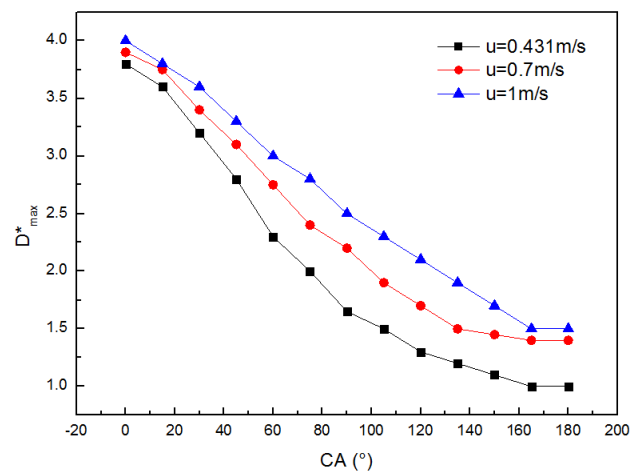


Figure 6: Relation between CA and the maximum spreading factor with different impact velocities

Figure 6 shows that with the decrease of contact angle, maximum spreading factor becomes greater after droplets impact. This is because a good hydrophilicity is beneficial to droplet spreading. For the same contact angle, maximum spreading factor increases with the impact velocity. The reason is that greater initial kinetic energy helps droplet to spread further.

As shown in Figure 7, with the same impact velocity, the greater the contact angle is, the shorter the time needed to reach maximum spreading factor is. Under the same contact angle, the smaller the impact velocity is, the longer the time needed to reach maximum spreading factor is.

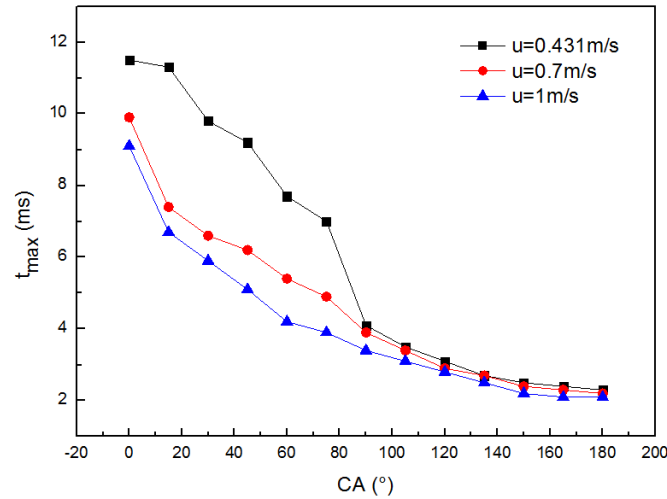


Figure 7: Relation between CA and time needed to reach maximum spreading factor with different impact velocities

Under different curvature ratio, the relationship between CA and maximum spreading factor ( $D_{max}^*$ ) is shown in Figure 8. The relationship between CA and time needed to reach maximum spreading factor ( $t_{max}$ ) is shown in Figure 9. The impact velocity is 0.7m/s, and curvature ratio is 0.15, 0.2, and 0.25, respectively.

As shown in Figure 8, under the same curvature ratio, the maximum spreading factor decreases with increasing contact angle. When CA ranges from 30° to 150°, the maximum spreading factor increases with curvature ratio. This is because the larger the curvature ratio becomes, the greater the influence of gravity on spreading process is. When CA ranges from 0 to 30°, the maximum spreading factor decreases with increasing curvature ratio. The reason is that maximum spreading diameter increases with curvature ratio while droplet diameter also increases with curvature ratio when sphere diameter is constant. The function of increasing droplet diameter is greater than that of maximum spreading diameter, so maximum spreading factor decreases with increasing curvature ratio for CA ranging from 0 to 30°.

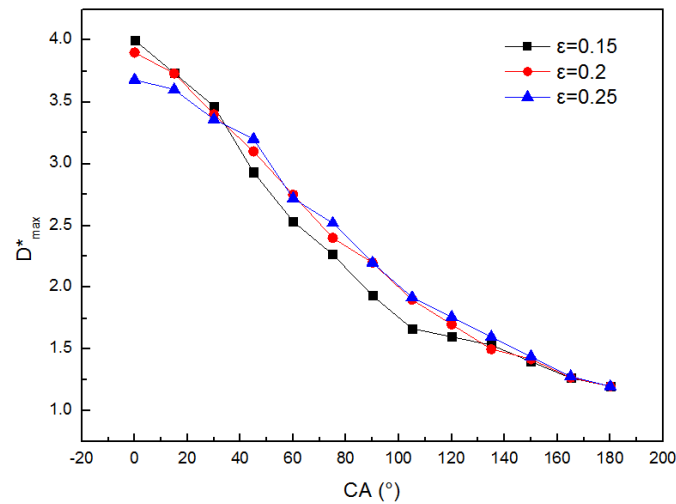


Figure 8: Relation between CA and maximum spreading factor with different curvature ratios

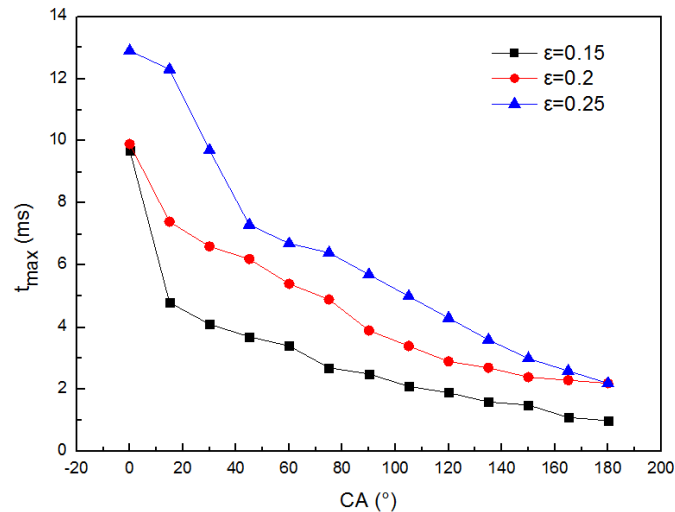


Figure 9: Relation between CA and time needed to reach maximum spreading factor with different curvature ratios

Figure 9 shows that under the same curvature ratio, when CA increases, time needed to reach the maximum spreading factor decreases. This is because under the impact velocity of 0.7 m/s, wettability affects both droplet maximum spreading distance and spreading characteristic time significantly (Antonini 2012). Under the same contact angle, when curvature ratio increases, time needed to reach the maximum spreading factor increases. This is mainly because the greater maximum spreading diameter needs more time to reach maximum spreading factor when the contact angle is a constant.

#### 4. CONCLUSION

Using two-dimensional numerical simulation with CLSVOF method, effect of surface wettability on droplet dynamic characteristics after impacting sphere is explored. The conclusions are as follows:

(1) With larger contact angle or more hydrophobic surfaces, liquid film is more prone to break and rebound after droplet impact. The rebound height and rebound time increase with contact angle. When complete rebound occurs, the larger the contact angle is, the earlier the droplet leaves the surface. Droplet spreading factor and time used to reach the maximum spreading factor increase with decreasing contact angle.

(2) With increasing the impact velocity, the maximum spreading factor increases and time used to reach the maximum spreading factor decreases.

(3) The greater the curvature ratio is, the longer time needed to reach the maximum spreading factor. Within the range of contact angle from 30 to 150°, the bigger the curvature ratio is, the greater the maximum spreading factor is. But within the range of the contact angle from 0 to 30°, the bigger the curvature ratio is, the smaller the maximum spreading factor is.

#### 5. ACKNOWLEDGEMENT

This work was supported by the National Natural Science Foundation of China (No. 51476017) and Department of Mechanical Engineering, University of Minnesota.

#### 6. REFERENCES

Antonini C., Amirfazli A., Marengo M., 2012. Drop impact and wettability: from hydrophilic to super-hydrophobic surfaces. *Phys. Fluids.*, 24(10), 102104.

Banitabaei S.A., Amirfazli A., 2017. Droplet impact onto a solid sphere: Effect of wettability and impact velocity. *Phys. Fluids.*, 29, 062111.

- Kannan R., Sivakumar D., 2008. Drop impact process on a hydrophobic grooved surface, *Colloids Surf., A*, 317(1-3), 694-704.
- Kim S., Moon M.W., Kim H.Y. 2013. Drop impact on super-wettability-contrast annular patterns. *J. Fluid Mech.*, 730, 328-342.
- Li X.Y., Ma X.H., Lan Z., 2009. Behavioral patterns of drop impingement onto rigid substrates with a wide range of wettability and different surface temperatures, *AIChE J.*, 55(8), 1983-1992.
- Li X.Y., Mao L.Q., Ma X.H., 2013. Dynamic behavior of water droplet impact on microtextured surfaces: the effect of geometrical parameters on anisotropic wetting and the maximum spreading diameter, *Langmuir*, 29(4), 1129-1138.
- Liang C., Wang H., Zhu X., Chen R., Ding Y.D., Liao Q., 2013. Numerical simulation of droplets impact on surface with different wettability. *CIESC J.*, 64(8), 2745-2751.
- Liang G.T., Shen S.Q., Yang Y., 2012. CLSVOF simulation for splashing of single drop impact on flat liquid film. *J. of Therm. Sci. Technol.*, 11(1), 8-12.
- Liu X.H., Zhao Y.M., Shi Chen, Shen S.Q., Zhao X.Y., 2017. Numerical research on the dynamic characteristics of a droplet impacting a hydrophobic tube. *Phys. Fluids.*, 29(6), 062105.
- Mitra S, Sathe M.J., Doroodchi E., Utikar R., Shah M.K., Pareek V., Joshi J.B., Evans G.M., 2013. Droplet impact dynamics on a spherical particle. *Chem. Eng. Sci.*, 100, 105-119.
- Quan S.L., Li S., Li W.Z., Song Y.C., 2009. A simulation of impact of droplets on solid surfaces by using the Lattice Boltzmann method. *Chin. J. Comput. Mech.*, 26(5), 627-632.
- Rozhkov A., Prunet-Foch B., Vignes-Adler M., 2002. Impact of water drops on small targets, *Phys. Fluids.*, 14(10), 3485-3501.
- Shen S.Q., Li Y., Guo Y. L., 2009. Numerical simulation of droplet impacting on isothermal flat solid surface. *J. Eng. Therm. Phys.*, 30(12), 2116-2118.
- Shen S.Q., Yu H., Guo Y.L., Liang G.T., 2013. Numerical simulation for splashing of single drop impact on spherical liquid film. *J. Therm. Sci. Technol.*, 12(1), 20-24.
- Wang Y.L., 2013. Numerical study on droplet impacting spherical surfaces. Dalian, DLUT.
- Yan Z., Li Y., Li C., Zhang W.H., Yuan H., Mei N., 2018. Numerical simulation study of droplet impact on various solid surfaces. *J. Therm. Sci. Tech.* 17(1), 8-14.

---

## #105: Synergistic combination of anaerobic digestion and gasification

---

Ee Yang LIM<sup>1</sup>, Yen Wah TONG<sup>2</sup>

<sup>1</sup> Department of Chemical and Biomolecular Engineering, National University of Singapore, 4 Engineering Drive 4, S117576 Singapore, ee\_yang@u.nus.edu

<sup>2</sup> Department of Chemical and Biomolecular Engineering, National University of Singapore, 4 Engineering Drive 4, S117576 Singapore, chetyw@nus.edu.sg

*Biochar from pyrolysis has been proposed as one of the solutions to enhance methane production and improve stability in anaerobic digestion. However, there is a lack of study on the use of biochar from the gasification process. Biochar from the gasification process is typically considered as waste output and has no market due to potential higher ash content and heavy metals. However, the combination of anaerobic digestion and gasification has the potential of larger energy recovery from waste materials compared to the pyrolysis process. The aim of this study is to evaluate the performance of the application of biochar produced from the gasification process in an anaerobic digester to enhance methane production and its impact during high organic loading. Tests were performed under different amount of biochar ranging from 4.0 g to 12.0 g. The 1 L reactors were fed semi-continuously with food waste at 3 g-VS L<sup>-1</sup> day<sup>-1</sup> and subsequently at 6 g-VS L<sup>-1</sup> day<sup>-1</sup>. The optimal biochar loading was determined to be 4 g and improved methane yield by 27%. 12 g biochar did not improve methane yield at 3 g-VS L<sup>-1</sup> day<sup>-1</sup> organic loading rate but provided better stability during high organic loading. The biochar's ash content released into the reactor did not reach the inhibitory level, therefore are not the contributing factor for lower performance. Methane content of the reactors without biochar dropped below 10% within 4 days of organic loading shock, while reactors with biochar, sustained production above 10% methane content. The application of biochar from the gasification process enhanced biogas production and process stability. This provides a possible pathway for a synergistic combination of anaerobic digestion and gasification of waste for energy recovery and reduction in ash/waste disposal.*

Keywords: anaerobic digestion; gasification; biochar; biogas

## 1. INTRODUCTION

Rapid urbanisation has resulted in increasing generation of municipal solid waste (MSW) which causes social and environmental problems (Xue, Cao and Li, 2015). World-wide production of municipal solid waste (MSW) had been predicted to grow to 2.2 billion tonnes $\cdot$ year<sup>-1</sup> by 2025, of which the largest component is food waste (FW) (Clarke, 2018). In Singapore, according to the statistics provided by National Environment Agency (NEA), 763,100 tonnes of FW were generated in 2018, of which, only 17% was recycled (Singapore NEA, 2018). Besides FW, another significant 521,200 tonnes of horticultural waste, or yard waste (YW) were generated. The wastes were generally incinerated in a waste-to-energy (WTE) plant and thereafter, sent to a landfill. With the growing amount of waste and limited space, the landfill will be filled up by 2035 (MEWR | Landfill, 2019). Anaerobic digestion (AD) is an alternative to incineration to manage organic waste, such as FW and YW. It was reported that AD provides more electricity and improvement in most environmental impact categories compared to incineration (Tong *et al.*, 2018).

AD is a biological process comprising mainly of four steps, i.e. hydrolysis, acidogenesis, acetogenesis and methanogenesis (Zhang *et al.*, 2014). It reduces the organic waste to biogas (comprises mainly CO<sub>2</sub> and CH<sub>4</sub>) and digestate which can be used for fuel and fertilizers respectively. Although AD is a matured technology, it faces challenges such as accumulation of volatile fatty acids (VFA) and other inhibitory compounds. The dynamic nature of wastes also presents other challenges such as process instability and performance deterioration when there is fluctuations in the organic loading rate (OLR) (Regueiro, Lema and Carballa, 2015). YW is also difficult to handle in AD due to its high cellulose and hemicellulose content (Zhang, Loh and Zhang, 2018), which necessitates pre-treatment prior to AD.

In parallel to biological treatment, thermochemical conversion processes, such as gasification and pyrolysis, are also becoming more important to handle such difficult biomass (Pecchi and Baratieri, 2019). Gasification can convert these waste biomasses to syngas (mainly CO and H<sub>2</sub>), for utilisation in chemical synthesis or fuel (Yu and Smith, 2018). However, it also produces solid carbonaceous char or biochar that are typically considered as waste due to the potential of higher ash content, poisonous organic compounds and heavy metals (Pecchi and Baratieri, 2019).

Instead of disposal, one possible approach is to find a more economical and environmentally friendly way to re-utilise the biochar (You *et al.*, 2017). Many recent studies have reported that methane production of AD is improved with the amendment of carbon materials (CM) such as granular activated carbon, carbon nanotubes, and biochar (Zhao *et al.*, 2017; C. Wang *et al.*, 2018; Zhang *et al.*, 2018). It is suggested that biochar can improve AD system with its buffering capacity, promoting granulation (C. Wang *et al.*, 2018) and facilitating Direct Interspecies Electron Transfer (DIET) based syntrophy (You *et al.*, 2017). It is also suggested to alleviate stress of ammonium by adsorption (Lü *et al.*, 2016). In addition, biochar is being used for carbon sequestration and soil amendment to improve soil ecosystem (Lehmann, Gaunt and Rondon, 2006; Woolf *et al.*, 2010; Field *et al.*, 2013) and since the discharged digestate can be used as fertilizers, the use of biochar in AD is not required to be recovered. This provides significant advantage of utilisation of biochar over other carbonaceous materials for AD system amendment, turning waste into a resource.

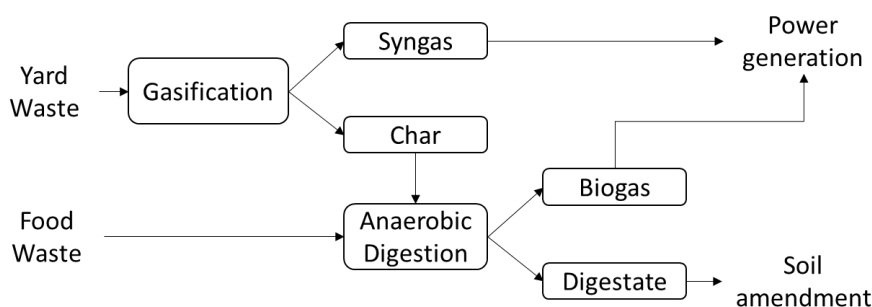


Figure 1: Schematic for synergetic management of food waste and other biomasses

However, to date, most application of biochar comes from pyrolysis process (Masebinu *et al.*, 2019). Although they are easily and commercially available as compared to biochar from gasification, their results might not be comparable as char from gasification and pyrolysis are physically and chemically different (Brewer *et al.*, 2009). Currently, there are only two works (Shen *et al.*, 2016; Linville *et al.*, 2017) that utilised biochar from gasification for AD but are limited to only batch process. The main goal of this study was to investigate the long-term effect of different dosage and possible inhibitory effects of biochar addition in a semi-continuous AD process during normal and high organic load phase of operation. Therefore, in this work, the feasibility study presents a potential pathway

for a synergistic combination of AD and gasification for waste management, recovering of energy and reduction in disposal.

## 2. MATERIALS & METHODS

### 2.1. Inoculum & Substrates

The seed sludge was obtained from an AD plant in Ulu Pandan Water Reclamation Plant, Singapore. FW was collected from a canteen in National University of Singapore, which comprise mainly of meat, noodles, rice and vegetables. The FW was first sorted to remove large bones and non-biodegradable waste and subsequently homogenised using a blender. It was then stored at -20°C freezer until used. The characteristics of FW and sludge are shown in Table 1. Biochar was obtained from a previous gasification experiment. Briefly, the waste wood pellets were fed into a small-scale downdraft gasifier using air as the gas agent at 800°C (Shen *et al.*, 2019). Table 2 presents the elemental analysis of the biochar.

Table 1: Characteristics of FW & Sludge

Parameter	Unit	Food waste	Sludge
pH	-	-	7.74
Total solids (TS)	% of wet weight	33.10 ± 0.15	5.16 ± 0.51
Volatile solids (VS)	% of wet weight	31.43 ± 0.08	1.44 ± 0.12
VS/TS ratio	-	0.95	0.28
Carbon content	% of TS	51.48 ± 1.91	-
Nitrogen content	% of TS	3.10 ± 0.05	-
C/N ratio	-	16.61	-

Table 2: Elements in biochar from air gasification

Ash (%)	pH	Elemental Analysis (wt%)							
		C	H	Ca	Fe	Mg	Na	P	K
18.88 ± 0.66	10.73 ± 0.02	72.37 ± 0.21	0.64 ± 0.17	3.54 ± 0.65	0.04 ± 0.01	1.23 ± 0.18	0.41 ± 0.18	0.25 ± 0.05	4.91 ± 0.14

### 2.2. Reactors & Operations

1 L reactors with working volume of 0.8 L were setup with 0, 4, 8 and 12 g of 150 µm biochar. The reactors were fed with 3 g-VS L<sup>-1</sup> of food waste every day for 10 days and operated under mesophilic condition (36 ± 1°C). After that, the reactors were subjected to organic overload at 6 g-VS L<sup>-1</sup> every day until the reactors stopped generating biogas. The hydraulic retention time (HRT) was maintained at 20 days throughout the experiment. Experiments were conducted in duplicates.

### 2.3. Analytical Methods

Ammonia concentration were determined every 3 days using HACH calorimeter (HACH, DR900, USA) and pH were determined every day using a pH probe (Agilent 3200 M, USA). The total solid (TS) and volatile solid (VS) were determined by the initial and final weights of the samples after placing them in an oven at 105 °C overnight and a furnace at 550 °C for 4 hours respectively. A gas chromatograph (Clarus 580 Arnel, PerkinElmer, USA) equipped with a thermal conductivity detector was used to determine hydrogen (H<sub>2</sub>), carbon dioxide (CO<sub>2</sub>), and methane (CH<sub>4</sub>) concentration of the biogas. The liquid portion of the samples were collected by centrifuging the digestate samples at 10,000 rpm for 10 minutes. The total volatile fatty acids (VFA) and alkalinity were determined using SI Analytics titrator (SI Analytics, Titroline 5000, Germany) according to the manufacturer's instructions. The liquid samples were filtered with a 0.2 µm syringe filter before determination of the metal released into the digestate samples using an Inductively Coupled Plasma-Optical Emission Spectrometer (ICP-OES) (Optima 5300DV, Perkin Elmer, USA).

## 3. RESULTS & DISCUSSIONS

### 3.1. Impact on AD Performance

The effects of different dosage of biochar on the waste-to-energy performance of AD of FW was investigated. The organic loading rate were subsequently increased to simulate an organic loading shock. The experiment was terminated when the biogas methane content of most reactors dropped below 10%. Figure 2 shows the changes of cumulative methane volume and pH respectively. The specific methane yield is a major indicator of energy conversion efficiency (Zhang *et al.*, 2017). As shown in Figure 2A, 4g BC achieved overall highest methane

production which worked out to be  $0.47 \text{ L g-VS}^{-1} \text{ day}^{-1}$  as compared to a methane yield of  $0.37 \text{ L g-VS}^{-1} \text{ day}^{-1}$  in AD reactor without biochar, an overall 27% improvement. The amount of biochar amended could also have detrimental effect on the methane production as seen in Figure 2. 12 g of BC resulted in lower methane yield than the reactors without biochar initially but improved after Day 9. A previous study on batch AD amended with biochar also showed detrimental effect at higher dosage (Shen *et al.*, 2016). A previous study on the dosage of biochar on ammonium revealed that removal efficiency gradually decreased as dosage increases more than 1 g (Kizito *et al.*, 2015). The authors suggested that as the mass of the solid increases, the overlapping of absorbent layers shielded available active sites on the absorbent. Similarly, increasing activated carbon mass also resulted in decreasing adsorbate uptake (Long *et al.*, 2008). It was also observed that the gasification biochar tends to agglomerate in the presence of the AD sludge. Therefore, the increased in lag phase for higher dosage could be related to poor mass transfer with higher dosage of biochar. On Day 11, reactors containing 8 g biochar achieved a methane yield of  $0.47 \text{ L g-VS}^{-1} \text{ day}^{-1}$ . As the lag phase of high dosage biochar appeared to be longer, providing longer period for the acclimatisation of the AD reactors could improve the reactors overall performance and stability. One major limitation was that the amount of biochar remaining in the AD reactors could not be quantified and it was assumed to be homogenous and therefore removed at a known calculated rate. The biochar “loss” was replenished during food waste addition.

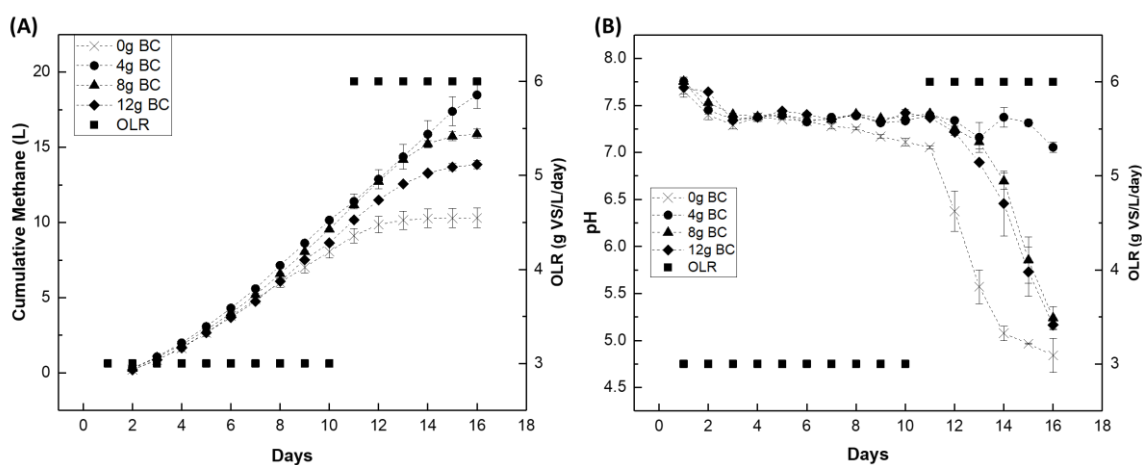


Figure 2: Impact of different dosage of biochar on (A) Cumulative Methane Volume; (B) pH.

The ammonia concentration for all reactors were  $1.48 \pm 0.1 \text{ g/L}$  and it remained below  $1.7 \text{ g/L}$ , indicating that there was no resulting ammonium inhibition throughout the operation (Zhang *et al.*, 2014). There were also no significant changes to the ammonium concentration when biochar was added, indicating that the adsorption of ammonium by the biochar was minimal. This was in accordance with  $2\text{-}3 \text{ mg-N/g-biochar}$  reported by Lü *et al.*, 2016, indicating negligible adsorption. However, the alkalinity of the biochar (pH 10.73) could contribute by shifting the ammonium towards cytotoxic ammonia (Mumme *et al.*, 2014). Higher dosage of biochar may increase the microorganism's exposure to the cytotoxic ammonia. The signs of inhibition disappeared over time and a possible explanation could be the formation of biofilms which are more resistant to adverse effects than suspended microorganisms (Sossa *et al.*, 2004).

The initial pH ranges from 7.40 to 7.65 which did not show significant pH buffering effect of biochar, except for 12 g of biochar. There were significant differences after a period of feeding for all biochar dosage and it became obvious when pH of reactors without biochar began to drop from 7.33 to 7.06 on Day 7 to Day 10 while the reactors with biochar maintained between 7.33 and 7.41. During high OLR phase, reactors without biochar collapsed rapidly on Day 11. The pH buffering effect of biochar could be observed during this period as AD amended with biochar showed a much gradual collapsed.

### 3.2. Impact on VFA & Alkalinity

From Figure 3, the alkalinity concentration was observed to increase as the biochar dosage increased. This indicated that biochar's buffering effect played an important role in times of instability. The buffering capacity of biochar resulted in more stable pH during high OLR, but it was not enough to sustain the rapid accumulation of VFA, except biochar amended with 4 g BC, which resulted in pH dropping below the optimal range.

VFA concentration, as shown in Figure 3A, of 4 g of biochar amended reactors were lower throughout the experiment and produced more biogas, which could indicate better microbial utilisation. The results followed a similar trend to another study by Wang *et al.*, 2018, where they reported that there was lesser abundance of



heterotrophic methanogens which implied that interspecies hydrogen transfer was not improved but the abundance of acetoclastic methanogens and the enrichment of *Bacteroidetes* genera could indicate potential DIET mechanism. Biochar addition was also shown to decrease the diversity of the microbial communities but VFA degradation and methane production were significantly improved (G. Wang *et al.*, 2018). Thus, it was suggested that biochar addition during stable operations likely to facilitate DIET based syntrophy and promoted the growth of these predominant microbes, which ultimately improved the overall stability during high OLR.

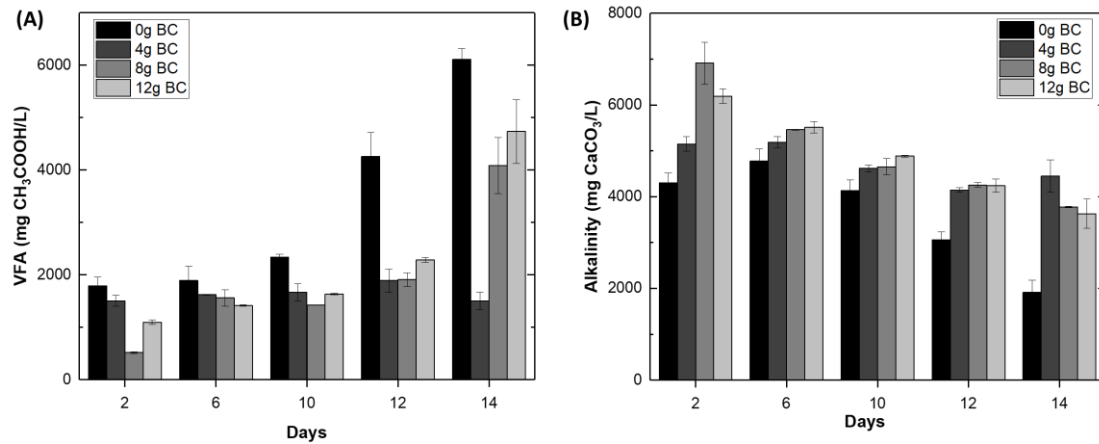


Figure 3: Impact of different dosage of biochar on (A) VFA; (B) Alkalinity.

The VFA concentration for the 0 g biochar reactors increased by 1.8 times on Day 12 when high OLR was implemented on Day 10. The increase in VFA led to a rapid decrease in pH and biogas production. VFA concentration in reactors with 8 g and 12 g of biochar increased by 2 times from Day 12 to Day 14 but it did not result in immediate collapse of methane production. From this trend, it could be deduced that biochar facilitated the formation of biofilm which was more resistance towards inhibitory agents (Sossa *et al.*, 2004; Mumme *et al.*, 2014). However, the consumption by DIET syntrophy microbial was still slower than the accumulation of VFA which resulted in non-optimal pH for the methanogens. It ultimately led to inhibition of the methane production. VFA is one of the common inhibitors (Chen, Cheng and Creamer, 2008) but its accumulation could prove too late for remediation.

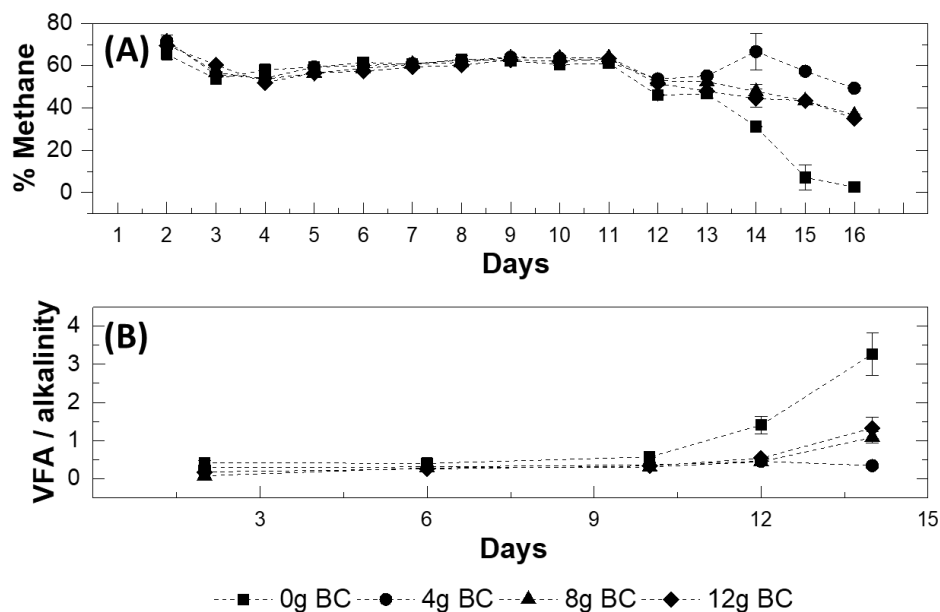


Figure 4: Impact of biochar dosage on (A) % methane; (B) VFA/alkalinity ratio

From Figure 4, biochar addition did not improve the methane concentration of the reactors and maintained on average of 61%. However, when OLR was increased, the methane concentration of reactors without biochar dropped more than 20% and collapsed rapidly thereafter. Hydrogen were also present in the reactors without

biochar during this period (results not shown). The reactors with biochar experienced a drop of about 10% but sustained a methane concentration of about 40% to 57%. Methane concentration was not a good indicator of showing process instability as it did not show any early warning signs of deterioration. However, a common early warning indicator is the VFA/alkalinity ratio which describes the process stability (Bong *et al.*, 2018). It was suggested that a ratio between 0.3 and 0.4 could indicate healthy reactor while a value above 0.6 would indicate a stress and/or overloaded reactor. The ratio for reactors without biochar increased to  $0.57 \pm 0.02$  on Day 10 and increased to 1.41 on Day 12. Reactors with 4 g of biochar maintained a ratio below 0.6 throughout the experiment while the higher dosage reactors exceeded 0.6 on Day 14. This showed that with the addition of biochar, the indicator could still potentially be used as one of the tools for monitoring reactor stability. A more frequent measurement would reveal whether the VFA/alkalinity ratio could be used as an early warning indicator.

### 3.3. Impact of Alkali Metal Content

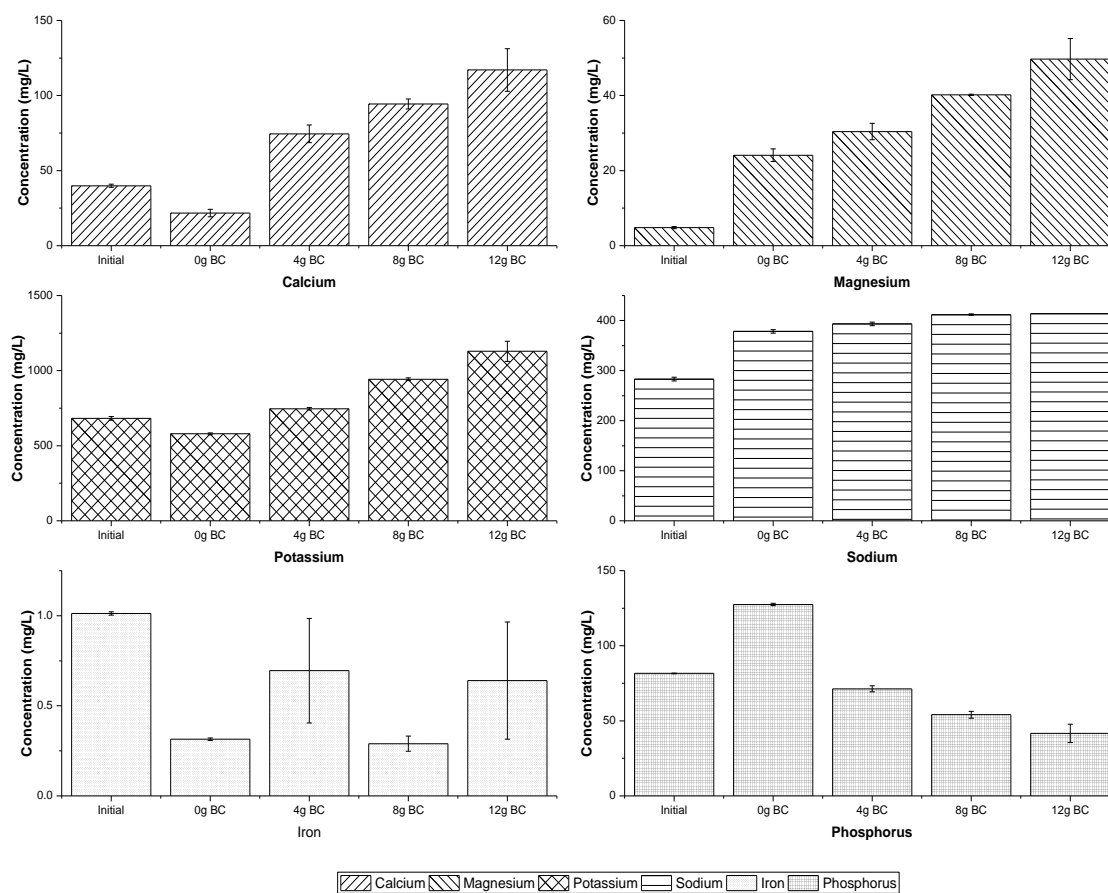


Figure 5: Alkali metal concentration in liquid fraction of reactors

There were a number of reports on CM inhibiting methane production (Martins *et al.*, 2018). For higher biochar dosage, it was suggested that the presence of some metals element might have inhibited the AD system (Linville *et al.*, 2017). It was reported that calcium and potassium exhibit inhibitory effect on AD at concentration of 300 mg/L and 400 mg/L respectively (Romero-Güiza *et al.*, 2016). 8g biochar and above loading contains metal concentration that exceeds these values. Based on Table, the calcium and potassium concentration loaded into the AD were  $354 \pm 65$  mg/L and  $491 \pm 14$  mg/L respectively. However, according to the analysis in Figure 5, only potassium appears to exceed the inhibitory level for all the reactors. Base on the results, the alkali metal concentrations released into the AD increases as biochar dosage increases, except for phosphorous. Interestingly, more biochar reduces the concentration of phosphorous which could indicate precipitation or sorption (Bornø, Müller-Stöver and Liu, 2018). This could help enrichment of the macro- and micronutrients in the digestate for use in fertilizers but at the same time reduce the availability to AD. In other studies, the authors added bottom ashes and/or fly ashes to AD reactors and studied on their effects on AD performance (Banks and Lo, 2003; Lo, 2005; Lo *et al.*, 2010). It was reported that the ash had acid neutralising capacity which maintained alkalinity and promoted biogas production and at the same time, there was no evidence to suggest that heavy metals would be leached

out. In this study, metal constituents from biochar were released into the AD reactors which directly impacted on the alkalinity. These reactors showed better buffering and stability at higher OLR, therefore, the released alkali metals from biochar have demonstrated, in this experiment, to be likely beneficial to the AD and did not exert any detrimental effects on the systems.

### 3.4. Overall Impact of Gasification Biochar on AD

Overall, it was shown that gasification biochar could enhance the AD performance and act as a stabilising agent for AD. The addition of biochar was able to mitigate the food waste induced instability by (1) providing buffering capacity, (2) immobilisation of bacteria cells and (3) facilitating DIET. This could be observed when the gasification biochar maintained the pH above 7.4 when food waste was added over a period of 10 days whereas the reactors without biochar started experiencing slight acidification. This was mainly contributed by the high ash content ( $18.88 \pm 0.66\%$ ), specifically, the calcium, potassium and phosphorous. The gasification biochar produced had a relatively low H/C and O/C ratio of 0.11 and 0.08 respectively. This indicates that it is chemically stable due to the fixed carbon aromatic rings (You *et al.*, 2017). The high degree of carbonisation provided suitable environment to facilitate DIET. Due to the extremely low O/C ratio, the biochar most probably has minimal polarity and high hydrophobicity (Moreno-Castilla, 2004). This could explain the better CO<sub>2</sub> sorption during high OLR which led to higher CH<sub>4</sub> concentration as compared to reactors without biochar. At the same time, high dosage of gasification biochar could (1) increase exposure to cytotoxic ammonia, (2) precipitation or sorption which reduce availability of macro- and micronutrients, and (3) reduced active sites due to agglomeration of the biochar.

Ultimately, the pH of reactors was governed by the VFAs and although biochar provided the buffer necessary for a stable AD operation, it could not prevent the acidification of the reactors if the VFAs continues to accumulate. Therefore, proper monitoring, such as through the VFA/alkalinity ratio, and pH, and managing the VFA accumulation through adjusting of the OLR, and HRT is important. The addition of biochar provided buffering and time for operators to make the necessary correction to prevent severe and irreversible acidification. It is important to note that the long-term continuous addition of biochar remains unclear as there is currently no way to determine the amount of biochar removed or remained in the reactors. The application of biochar in semi-continuous lab-scale reactors appeared to be homogenous and therefore the biochar “loss” could be determined theoretically. Therefore, the application in large-scale AD remains to be seen.

Finally, it was suggested in a previous study of a 1000 L pilot scale reactor that activated carbon supplementation strategy could be economically feasible (Zhang, Zhang and Loh, 2018). As such, the use of biochar produced from waste material could be a perfect substitute supplement and at the same time, providing a synergistic strategy to manage different types of waste. Therefore, for a more holistic study, a detailed economic and environmental feasibility of application of gasification biochar in AD using life cycle assessment (LCA) could be performed.

## 4. CONCLUSIONS

This study investigated the potential use of gasification char for continuous application in an anaerobic digester. The results suggested that biochar facilitated the DIET pathway which enhanced the methane productivity and provided better stability during high OLR. The application of 4 g of biochar (equivalent to 5 g/L) was shown to be optimal, enhancing the methane yield by 27%. However, higher dosage of biochar resulted in inhibitory effects which was likely related to exposure to cytotoxic ammonia, reduced active sites and precipitation. VFA accumulation remains a key issue to be addressed in the AD of food waste and the addition of biochar at high OLR could only improve stability to a certain extent. The buffering capability of biochar played a key role during high OLR which was contributed by the alkali metal content in the biochar towards the alkalinity of the AD. The use of VFA/alkalinity ratio as an early warning indicator appears to be useful and not affected by the addition of biochar. Overall, the results suggested that the synergistic combination of a biological and thermochemical process to recover energy from different difficult to handle wastes can improve the whole process stability, speed and potentially reduce final waste output.

## 5. ACKNOWLEDGEMENT

This work was supported by the National Research Foundation, Prime Minister's Office, Singapore under its Campus for Research Excellence and Technological Enterprise (CREATE) programme. The authors thank Dr Ye Shen from the Energy and Environmental Sustainability for Megacities (E2S2) program under CREATE for his help in facilitating some of the work. Ee Yang Lim acknowledges the Ph.D. scholarship supported by NUS Environmental Research Institute (NERI).

## 6. REFERENCES

- Banks, C. J. and Lo, H. (2003) 'Assessing the effects of municipal solid waste incinerator bottom ash on the decomposition of biodegradable waste using a completely mixed anaerobic reactor', *Waste Management & Research*, 21(3), pp. 225–234. Available at: <https://journals.sagepub.com/doi/10.1177/0734242X0302100306>.
- Bong, C. P. C. *et al.* (2018) 'The characterisation and treatment of food waste for improvement of biogas production during anaerobic digestion – A review', *Journal of Cleaner Production*, 172, pp. 1545–1558. doi: 10.1016/j.jclepro.2017.10.199.
- Bornø, M. L., Müller-Stöver, D. S. and Liu, F. (2018) 'Contrasting effects of biochar on phosphorus dynamics and bioavailability in different soil types', *Science of the Total Environment*, 627, pp. 963–974. doi: 10.1016/j.scitotenv.2018.01.283.
- Brewer, C. E. *et al.* (2009) 'Characterization of biochar from fast pyrolysis and gasification systems', *Environmental Progress & Sustainable Energy*. John Wiley & Sons, Ltd, 28(3), pp. 386–396. doi: 10.1002/ep.10378.
- Chen, Y., Cheng, J. J. and Creamer, K. S. (2008) 'Inhibition of anaerobic digestion process: a review.', *Bioresource technology*, 99(10), pp. 4044–64. doi: 10.1016/j.biortech.2007.01.057.
- Clarke, W. P. (2018) 'The uptake of anaerobic digestion for the organic fraction of municipal solid waste – Push versus pull factors', *Bioresource Technology*, pp. 1040–1043. doi: 10.1016/j.biortech.2017.10.086.
- Field, J. L. *et al.* (2013) 'Distributed biochar and bioenergy coproduction: a regionally specific case study of environmental benefits and economic impacts', *GCB Bioenergy*. John Wiley & Sons, Ltd (10.1111), 5(2), pp. 177–191. doi: 10.1111/gcbb.12032.
- Kizito, S. *et al.* (2015) 'Evaluation of slow pyrolyzed wood and rice husks biochar for adsorption of ammonium nitrogen from piggery manure anaerobic digestate slurry', *Science of the Total Environment*, 505, pp. 102–112. doi: 10.1016/j.scitotenv.2014.09.096.
- Lehmann, J., Gaunt, J. and Rondon, M. (2006) 'Bio-char sequestration in terrestrial ecosystems - A review', *Mitigation and Adaptation Strategies for Global Change*, pp. 403–427. doi: 10.1007/s11027-005-9006-5.
- Linville, J. L. *et al.* (2017) 'In-situ biogas upgrading during anaerobic digestion of food waste amended with walnut shell biochar at bench scale', *Waste Management and Research*. SAGE Publications Ltd, 35(6), pp. 669–679. doi: 10.1177/0734242X17704716.
- Lo, H. M. (2005) 'Metals behaviors of MSWI bottom ash co-digested Anaerobically with MSW', *Resources, Conservation and Recycling*, 43(3), pp. 263–280. doi: 10.1016/j.resconrec.2004.06.004.
- Lo, H. M. *et al.* (2010) 'Modeling biogas production from organic fraction of MSW co-digested with MSWI ashes in anaerobic bioreactors', *Bioresource Technology*, 101(16), pp. 6329–6335. doi: 10.1016/j.biortech.2010.03.048.
- Long, X. *et al.* (2008) 'Adsorption of ammonia on activated carbon from aqueous solutions', *Environmental Progress*. John Wiley & Sons, Ltd, 27(2), pp. 225–233. doi: 10.1002/ep.10252.
- Lü, F. *et al.* (2016) 'Biochar alleviates combined stress of ammonium and acids by firstly enriching Methanosaeta and then Methanosarcina', *Water Research*, 90, pp. 34–43. doi: 10.1016/j.watres.2015.12.029.
- Martins, G. *et al.* (2018) 'Methane Production and Conductive Materials: A Critical Review', *Environmental Science and Technology*, pp. 10241–10253. doi: 10.1021/acs.est.8b01913.
- Masebinu, S. O. *et al.* (2019) 'A review of biochar properties and their roles in mitigating challenges with anaerobic digestion', *Renewable and Sustainable Energy Reviews*, pp. 291–307. doi: 10.1016/j.rser.2018.12.048.
- MEWR | Landfill (2019) *Ministry of the Environment and Water Resources [SG]*. Available at: <https://www.mewr.gov.sg/topic/landfill> (Accessed: 29 March 2019).
- Moreno-Castilla, C. (2004) 'Adsorption of organic molecules from aqueous solutions on carbon materials', *Carbon*, 42(1), pp. 83–94. doi: 10.1016/j.carbon.2003.09.022.
- Mumme, J. *et al.* (2014) 'Use of biochars in anaerobic digestion', *Bioresource Technology*, 164, pp. 189–197. doi: 10.1016/j.biortech.2014.05.008.
- Pecchi, M. and Baratieri, M. (2019) 'Coupling anaerobic digestion with gasification, pyrolysis or hydrothermal carbonization: A review', *Renewable and Sustainable Energy Reviews*, pp. 462–475. doi: 10.1016/j.rser.2019.02.003.

- Regueiro, L., Lema, J. M. and Carballa, M. (2015) 'Key microbial communities steering the functioning of anaerobic digesters during hydraulic and organic overloading shocks', *Bioresource Technology*, 197, pp. 208–216. doi: 10.1016/j.biortech.2015.08.076.
- Romero-Güiza, M. S. *et al.* (2016) 'The role of additives on anaerobic digestion: A review', *Renewable and Sustainable Energy Reviews*, pp. 1486–1499. doi: 10.1016/j.rser.2015.12.094.
- Shen, Y. *et al.* (2016) 'Towards a sustainable paradigm of waste-to-energy process: Enhanced anaerobic digestion of sludge with woody biochar', *Journal of Cleaner Production*, 135, pp. 1054–1064. doi: 10.1016/j.jclepro.2016.06.144.
- Shen, Y. *et al.* (2019) 'CO<sub>2</sub> gasification of woody biomass: Experimental study from a lab-scale reactor to a small-scale autothermal gasifier', *Energy*, 170, pp. 497–506. doi: 10.1016/j.energy.2018.12.176.
- Singapore NEA (2018) *Waste Statistics and Overall Recycling*, Singapore National Environment Agency. Available at: <https://www.nea.gov.sg/our-services/waste-management/waste-statistics-and-overall-recycling> (Accessed: 29 March 2019).
- Sossa, K. *et al.* (2004) 'Effect of ammonia on the methanogenic activity of methylaminotrophic methane producing Archaea enriched biofilm', *Anaerobe*, 10(1), pp. 13–18. doi: 10.1016/j.anaerobe.2003.10.004.
- Tong, H. *et al.* (2018) 'A comparative life cycle assessment on four waste-to-energy scenarios for food waste generated in eateries', *Applied Energy*, 225, pp. 1143–1157. doi: 10.1016/j.apenergy.2018.05.062.
- Wang, C. *et al.* (2018) 'Role of biochar in the granulation of anaerobic sludge and improvement of electron transfer characteristics', *Bioresource Technology*, 268, pp. 28–35. doi: 10.1016/j.biortech.2018.07.116.
- Wang, G. *et al.* (2018) 'Synergetic promotion of syntrophic methane production from anaerobic digestion of complex organic wastes by biochar: Performance and associated mechanisms', *Bioresource Technology*, 250, pp. 812–820. doi: 10.1016/j.biortech.2017.12.004.
- Woolf, D. *et al.* (2010) 'Sustainable biochar to mitigate global climate change', *Nature Communications*, 1(5). doi: 10.1038/ncomms1053.
- Xue, W., Cao, K. and Li, W. (2015) 'Municipal solid waste collection optimization in Singapore', *Applied Geography*, 62, pp. 182–190. doi: 10.1016/j.apgeog.2015.04.002.
- You, S. *et al.* (2017) 'A critical review on sustainable biochar system through gasification: Energy and environmental applications', *Bioresource Technology*, 246, pp. 242–253. doi: 10.1016/j.biortech.2017.06.177.
- Yu, J. and Smith, J. D. (2018) 'Validation and application of a kinetic model for biomass gasification simulation and optimization in updraft gasifiers', *Chemical Engineering and Processing - Process Intensification*, 125, pp. 214–226. doi: 10.1016/j.cep.2018.02.003.
- Zhang, C. *et al.* (2014) 'Reviewing the anaerobic digestion of food waste for biogas production', *Renewable and Sustainable Energy Reviews*. Pergamon, 38, pp. 383–392. doi: 10.1016/J.RSER.2014.05.038.
- Zhang, J. *et al.* (2017) 'Enhanced anaerobic digestion of food waste by adding activated carbon: Fate of bacterial pathogens and antibiotic resistance genes', *Biochemical Engineering Journal*, 128, pp. 19–25. doi: 10.1016/j.bej.2017.09.004.
- Zhang, J. *et al.* (2018) 'Recent achievements in enhancing anaerobic digestion with carbon- based functional materials', *Bioresource Technology*, 266, pp. 555–567. doi: 10.1016/j.biortech.2018.07.076.
- Zhang, L., Loh, K. C. and Zhang, J. (2018) 'Food waste enhanced anaerobic digestion of biologically pretreated yard waste: Analysis of cellulose crystallinity and microbial communities', *Waste Management*, 79(October), pp. 109–119. doi: 10.1016/j.wasman.2018.07.036.
- Zhang, L., Zhang, J. and Loh, K. C. (2018) 'Activated carbon enhanced anaerobic digestion of food waste – Laboratory-scale and Pilot-scale operation', *Waste Management*, 75, pp. 270–279. doi: 10.1016/j.wasman.2018.02.020.
- Zhao, Z. *et al.* (2017) 'Towards engineering application: Potential mechanism for enhancing anaerobic digestion of complex organic waste with different types of conductive materials', *Water Research*, 115, pp. 266–277. doi: 10.1016/j.watres.2017.02.067.

---

## #108: Simulation study and comparative analysis of solar-air dual source heat pump system

---

Jingyong CAI, Jie JI\*

*University of Science and Technology of China, Huangshan Road NO.443, Hefei, China*

*\*Corresponding author: jijie@ustc.edu.cn*

*The concept of solar-air dual source heat pump has been proposed to overcome the limitations of single source heat pump system. In this paper, a comparative investigation is presented among three types of solar-air dual source heat pump with different heat source configurations: solar-air series source heat pump (SA-SHP), solar-air parallel source heat pump (SA-PHP) and air-solar series source heat pump (AS-SHP). The impact of solar irradiation and ambient temperature has been discussed. Based on the results of parametric analysis, the optimal working condition for each system has been identified. The results indicate that SA-SHP is suitable for working under the environment with low solar irradiation, AS-SHP shows the best performance under the condition with low ambient temperature and high solar irradiation, and SA-PHP can achieve the optimal state at high ambient temperature or high solar irradiation.*

*Keywords: dual source heat pump; solar energy; air source; heat source; space heating*

## 1. INTRODUCTION

With the improvement of living standard, space heating in winter has become increasingly demanding, but it also brings environmental and energy issues due to the consumption of fossil fuel (Bellos, 2016). Therefore, seeking energy-efficient, environmental friendly and economical heating supply method is of great significance. Due to the capability of utilising low-grade energy, heat pump can produce huge economic and environmental benefits, with the potential to become an ideal solution for heating supply (Chua, 2010).

To overcome the limitation of single-source heat pump, the concept of solar-air dual source heat pump has been proposed and discussed by numerous scholars. Dong et al. (2017) developed a finned tube evaporator painted with solar selective absorption coating (SSAC) for solar integrated air source heat pump to enhance its capability to absorb solar irradiation. Qiu et al. (2018a) studied the heat transfer characteristics of the finned tube heat exchanger painted with SSAC, and the results suggested that the rise of solar irradiation would lead to the reduction of fin efficiency and convective heat transfer capacity. Kim et al. (2018) designed a novel hybrid solar collector with the assistance of air-source receiver and solar thermal receiver. The performance of different kinds of SAHP with the hybrid solar collector was compared, and the results showed that the hybrid collector could extend the annual running time of SAHP system to improve the overall economic benefits. For the heat pump system with a hybrid source evaporator consisting of bare plate and spiral-finned tube, Li et al. (2015) investigated the system performance working with different kinds of refrigerant. It was revealed that the impact of the type of refrigerant was not significant. Different thermodynamic cycles have been developed to enhance the utilisation of hybrid heat source. Deng et al. (2016) modified the DX-SAHP by connecting a finned tube heat exchanger in parallel with the solar collector. The study revealed that the modified system could operate more efficiently under low solar irradiation. Cai et al. (2016) investigated the performance of a hybrid source heat pump with air source evaporator and solar evaporator connected in series, which showed superior performance than single source heat pump. Qiu et al. (2018b) proposed a novel system integrated of solar energy and ASHP, which can effectively utilise medium solar radiation in cold regions.

Although various schemes of dual source heat pump system have been proposed, previous studies mainly focus on the operation characteristics of specific system. The operation performance and suitable working conditions for different dual source heat pump systems have not been discussed and compared. Solar-air series source heat pump (SA-SHP), solar-air parallel source heat pump (SA-PHP) and air-solar series source heat pump (AS-SHP) with the identical components and different heat source configurations have been presented and compared in this paper. The impact of environmental parameters has been discussed to identify the optimal working condition for each system.

## 2. SYSTEM DESCRIPTION

The schematic of SA-SHP, SA-PHP and AS-SHP is shown in Figure 1. The main components of each system include air source evaporator, solar evaporator, compressor, condenser and capillary. In particular, two solenoid valves located at the inlet of each evaporator in SA-PHP can adjust the distribution of refrigerant. Air source evaporator and condenser are composed of finned-tube heat exchanger to exchange heat with the indoor or outdoor environment. Solar evaporator is consisted of bare plate collector coated with SSAC which can effectively collect solar irradiation.

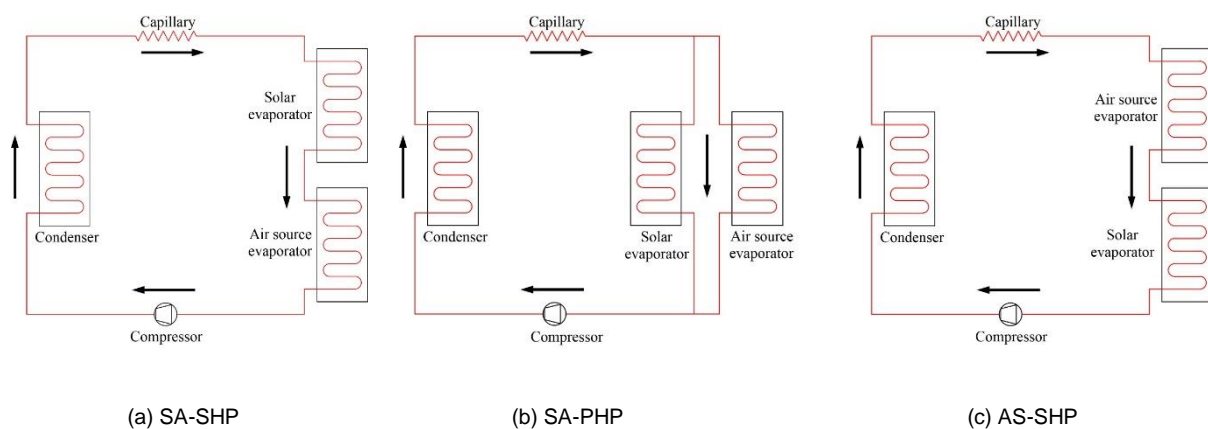


Figure 1: The schematic of solar-air hybrid source heat pump water heater

The difference of SA-SHP, SA-PHP and AS-SHP lies in the pattern of heat source, and the corresponding working principles are as follows:

- (1) SA-SHP: the refrigerant absorbs energy from solar evaporator and air source evaporator in sequence.
- (2) SA-PHP: the refrigerant has been divided into two branches and is vaporised in air source evaporator and solar evaporator simultaneously.
- (3) AS-SHP: the working fluid initially evaporates in air source evaporator and then the solar evaporator acts as the supplement heat source.

After the working fluid is vaporised in the evaporator, it is compressed into the vapour with high temperature and pressure in compressor. Then it enters the condenser and releases heat to the indoor environment. The working fluid becomes liquid after the condensation process, and flows into the capillary. The refrigerant becomes the liquid with low temperature and pressure after throttling and returns the evaporator.

The heat transfer characteristics of air source evaporator and solar evaporator are different, so the performance of in SA-SHP, SA-PHP and AS-SHP will display different operation behaviour due to the different heat source configurations. Therefore, it is necessary to discuss and compare the performance of SA-SHP, SA-PHP and AS-SHP under different working conditions. To ensure the comparability of SA-SHP, SA-PHP and AS-SHP, the geometric sizes of the components in each system are identical. In space cooling mode, the solar evaporator is bypassed and air source evaporator is used for heat dissipation, so the thermodynamic cycle and configuration of SA-SHP, SA-PHP and AS-SHP will be identical. Therefore, the space cooling performance will not be discussed in the paper.

### 3. MODELLING AND EVALUATION

#### 3.1. Mathematical modelling

To compare the performance of SA-SHP, SA-PHP and AS-SHP, a mathematical model based on distributed parameter approach is developed to simulate the behavior of the above systems, based on the following hypothesis: (1) The flow of refrigerant is one dimensional and homogeneously mixed. (2) The pressure drop of working fluid is not taken into consideration. (3) The compression process in compressor is supposed to be polytropic. (4) The expansion process in capillary is assumed to be isenthalpic.

*For solar evaporator*

Equation 1: The energy balance equation for the refrigerant pipeline.

$$\rho_p c_p \frac{\partial T_p}{\partial t} = k_p \frac{\partial^2 T_p}{\partial z^2} + \frac{1}{A_p} \left[ \pi D_{p,i} \alpha_{ref,p} (T_{ref} - T_p) + W U_{sol} (T_a - T_p) + \beta I W \right]$$

Where:

- $\rho_p$  = density of refrigerant pipe (kg/m<sup>3</sup>)
- $c_p$  = specific heat of refrigerant pipe (kJ/(kg·K))
- $T_p$  = temperature of refrigerant pipe (K)
- $t$  = time (s)
- $k_p$  = heat conductivity of refrigerant pipe (W/(m·K))
- $A_p$  = cross section area of refrigerant pipe (m<sup>2</sup>)
- $D_{p,i}$  = inner diameter of refrigerant pipe (m)
- $W$  = tube pitch of solar evaporator (m)
- $I$  = solar irradiation (W/m<sup>2</sup>)
- $\alpha_{ref,p}$  = convective heat transfer coefficient between the refrigerant and pipeline (W/(m<sup>2</sup>·K))
- $U_{sol}$  = heat transfer coefficient of solar evaporator (W/(m<sup>2</sup>·K))
- $T_a$  = temperatures of the ambient (K)
- $T_{ref}$  = temperature of refrigerant (K)
- $\beta$  = specific latent enthalpy of water



For air source evaporator

Equation 2: The energy balance equation for the refrigerant pipeline. 
$$\rho_p c_p \frac{\partial T_p}{\partial t} = k_p \frac{\partial^2 T_p}{\partial z^2} + \frac{1}{A_p} [\pi D_{p,i} \alpha_{ref,p} (T_{ref} - T_p) + \pi D_{p,o} \alpha_{a,p} (T_a - T_p)]$$

Where:

- $D_{p,o}$  = outer diameter of the refrigerant pipe (m)
- $\alpha_{a,p}$  = convective heat transfer coefficient between the air and pipeline (W/(m<sup>2</sup>.K))

For compressor

Equation 3: The mass flow rate of refrigerant in compressor 
$$m_{ref,com} = \lambda \frac{n V_{com}}{v_{suc}}$$

Where:

- $m_{ref,com}$  = mass flow rate of refrigerant in compressor (kg/s)
- $\lambda$  = volumetric efficiency
- $V_{com}$  = displacement of compressor (m<sup>3</sup>)
- $n$  = rotating speed of compressor (rad/s)
- $v_{suc}$  = specific volume of refrigerant at the suction of compressor (m<sup>3</sup>/kg)

Equation 4: The power consumption of compressor

$$P_{com} = n \frac{P_{suc} V_{com}}{\eta_{com}} \frac{\gamma}{\gamma - 1} \left[ \left( \frac{P_{dis}}{P_{suc}} \right)^{\frac{\gamma - 1}{\gamma}} - 1 \right]$$

Where:

- $P_{com}$  = power consumption of compressor (kW)
- $\eta_{com}$  = total operation efficiency of compressor
- $\gamma$  = polytropic index
- $p_{suc}$  = suction pressure (Pa)
- $p_{dis}$  = discharge pressure (Pa)

Equation 5: The energy balance equation for compressor

$$M_{com} c_{com} \frac{\partial T_{com}}{\partial t} = P_{com} - m_{ref,com} (h_{com,out} - h_{com,in}) - U_{com} A_{com} (T_{com} - T_a)$$

Where:

- $M_{com}$  = mass of compressor (kg)
- $c_{com}$  = specific heat of compressor (kJ/(kg.K))
- $T_{com}$  = temperature of compressor (K)
- $A_{com}$  = external surface area of compressor (m<sup>2</sup>)
- $U_{com}$  = total heat transfer coefficient between the compressor and the environment (W/(m<sup>2</sup>.K))
- $h_{com,out}$  = the specific enthalpy of refrigerant of refrigerant at the outlet of compressor (kJ/kg)
- $h_{com,in}$  = the specific enthalpy of refrigerant of refrigerant at the inlet of compressor (kJ/kg)

For capillary

Equation 6: The mass flow rate of refrigerant in capillary.

$$m_{ref,cap} = C_1 D_{cap,i}^{C_2} L_{cap}^{C_3} T_{con}^{C_4} 10^{C_5 \times \Delta T_{cap,in}}$$

Where:

- $m_{ref,cap}$  = mass flow rate of refrigerant in capillary (kg/s)
- $D_{cap,i}$  = inner diameter of capillary (m)
- $L_{cap}$  = length of capillary (m)
- $T_{con}$  = condensing temperature (K)

- $T_{cap,in}$  = supercool degree of refrigerant at the inlet of capillary (K)
- $C_1 \sim C_5$  = empirical constant

For condenser

Equation 7: The energy balance equation for the refrigerant pipeline.

$$\rho_p c_p \frac{\partial T_p}{\partial t} = k_p \frac{\partial^2 T_p}{\partial z^2} + \frac{1}{A_p} \left[ \pi D_{p,i} \alpha_{ref,p} (T_{ref} - T_p) + \pi D_{p,o} \alpha_{a,p} (T_a - T_p) \right]$$

### 3.2. Performance analysis

Equation 9: The evaporating capacity of solar evaporator.

$$Q_{eva,sol} = m_{ref,sol} (h_{sol,out} - h_{sol,in})$$

Where:

- $m_{ref,sol}$  = mass flow rate of refrigerant in solar evaporator (kg/s)
- $h_{sol,out}$  = the specific enthalpy of refrigerant of refrigerant at the outlet of solar evaporator (kJ/kg)
- $h_{sol,in}$  = the specific enthalpy of refrigerant of refrigerant at the inlet of solar evaporator (kJ/kg)

Equation 10: The evaporating capacity of air source evaporator.

$$Q_{eva,air} = m_{ref,air} (h_{air,out} - h_{air,in})$$

Where:

- $m_{ref,air}$  = mass flow rate of refrigerant in air source evaporator (kg/s)
- $h_{air,out}$  = the specific enthalpy of refrigerant of refrigerant at the outlet of air source evaporator (kJ/kg)
- $h_{air,in}$  = the specific enthalpy of refrigerant of refrigerant at the inlet of air source evaporator (kJ/kg)

Equation 11: The ratio of evaporation capacity in air source evaporator to the overall evaporation capacity.

$$R_{air} = \frac{Q_{eva,air}}{Q_{eva,sol} + Q_{eva,air}}$$

Equation 12: The heating capacity of each system.

$$Q_{con} = m_{ref,con} (h_{con,in} - h_{con,out})$$

Where:

7.  $m_{ref,con}$  = mass flow rate of refrigerant in condenser (kg/s)
8.  $h_{air,out}$  = the specific enthalpy of refrigerant of refrigerant at the outlet of condenser (kJ/kg)
9.  $h_{air,in}$  = the specific enthalpy of refrigerant of refrigerant at the inlet of condenser (kJ/kg)

Equation 13: The total power consumption of each system.

$$P_{sys} = P_{com} + P_{fan,id} + P_{fan,od}$$

Where:

10.  $P_{fan,id}$  = power consumption fan at the indoor(kW)
11.  $P_{fan,od}$  = power consumption fan at the outdoor(kW)

Equation 14: The coefficient of performance (COP) of each system.

$$COP = \frac{Q_{con}}{P_{sys}}$$

## 4. RESULTS AND DISCUSSION

### 4.1. Impact of solar irradiation

The performance of SA-SHP, SA-PHP and AS-SHP has been compared with solar irradiation ranging from 100W/m<sup>2</sup> to 800W/m<sup>2</sup> at the outdoor ambient temperature of 10°C and indoor ambient temperature of 20°C.

Figure 2 shows that as the solar irradiation rises, for SA-SHP, SA-PHP and AS-SHP, the  $Q_{eva,sol}$  increases, while  $Q_{eva,air}$  declines. In terms of  $Q_{eva,sol}$ , the value in SA-SHP is the highest, followed by SA-PHP, and the value in AS-SHP is the lowest. The reason is that the refrigerant in AS-SHP enters air source evaporator at first, so the vapor quality at the inlet of solar evaporator in AS-SHP is higher than that of SA-PHP and SA-SHP, leading to the degradation of heat transfer in solar evaporator. For  $Q_{eva,air}$ , the value in AS-SHP is the highest, followed by SA-PHP, and the value in SA-SHP is the lowest. It is noteworthy that with solar irradiation rising above  $500\text{W/m}^2$ ,  $Q_{eva,air}$  in SA-SHP reduces below 0. It is because that in the air source evaporator of SA-SHP the evaporation temperature exceeds the ambient temperature after the refrigerant absorbing energy via solar evaporator, leading to the heat loss to ambient. Overall,  $Q_{eva}$  in SA-SHP, SA-PHP and AS-SHP increases with the rise of solar irradiation, as shown in Figure 2(b). The  $Q_{eva}$  in SA-PHP is the highest, followed by AS-SHP, and the value in SA-SHP is the lowest. Figure 2(b) also indicates that the contribution of air source evaporator to the overall  $Q_{eva}$  in SA-SHP, SA-PHP and AS-SHP declines as the solar irradiation increases.  $R_{air}$  is the highest in AS-SHP, followed by SA-PHP, and the value in SA-SHP is the lowest. With the solar irradiation rising from  $100\text{W/m}^2$  to  $800\text{W/m}^2$ , for SA-SHP,  $R_{air}$  drops from 0.52 to -0.16, the value in SA-PHP declines from 0.49 to 0.17, and the value in AS-SHP decreases from 0.57 to 0.38.

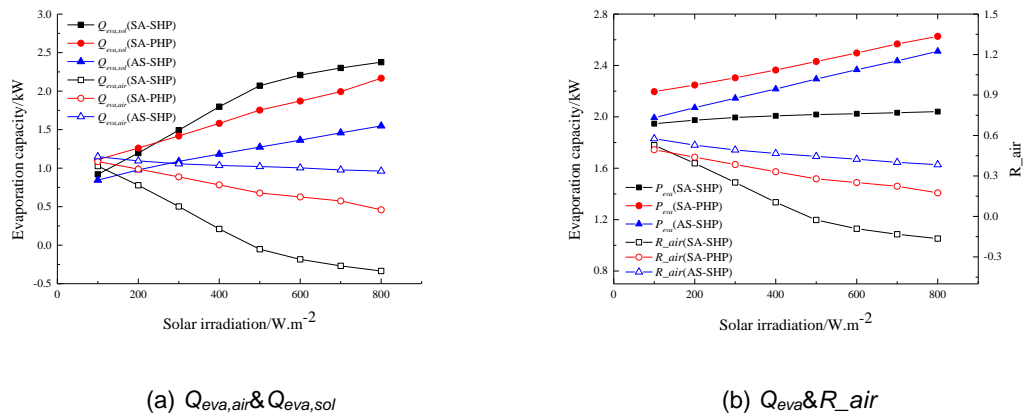


Figure 2: Impact of solar irradiation on the evaporating capacity

The variation of input power and heating capacity in SA-SHP, SA-PHP and AS-SHP under different solar irradiances is shown in Figure 3. It can be observed that as solar irradiation increases, both  $P_{sys}$  and  $Q_{con}$  of SA-SHP, SA-PHP and AS-SHP rise. The  $Q_{con}$  of SA-PHP is the highest, followed by AS-SHP, and the value in SA-SHP is the lowest. With the solar irradiation rising from  $100\text{W/m}^2$  to  $800\text{W/m}^2$ , the  $Q_{con}$  in SA-SHP rises from 2.46kW to 2.58kW, the value in SA-PHP rises from 2.71kW to 3.26kW, and the value in AS-SHP increases from 2.52kW to 3.06kW. In terms of  $P_{sys}$ , when solar irradiation increases from  $100\text{W/m}^2$  to  $800\text{W/m}^2$ , SA-PHP displays the maximum increment, rising from 0.55kW to 0.64kW, followed by AS-SHP, rising from 0.57kW to 0.61kW, and the increment in SA-SHP is the least, rising from 0.57kW to 0.59kW.

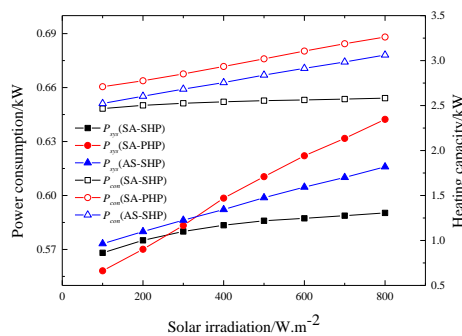


Figure 3: Impact of solar irradiation on power consumption and heating capacity

The variation of the COPs in SA-SHP, SA-PHP and AS-SHP at specified solar irradiation is shown in Figure 4. It can be observed that the COPs of SA-PHP and AS-SHP can be improved significantly as the solar irradiation increases, while the COP of SA-SHP is stable under different solar irradiances. When solar irradiation increases from  $100\text{W/m}^2$  to  $800\text{W/m}^2$ , the COP of SA-SHP rises from 4.34 to 4.37, the value in SA-PHP increases from 4.85

to 5.06, and the value in AS-SHP rises from 4.40 to 4.97. It can be concluded that the rise of solar irradiation is beneficial for the performance improvement in SA-PHP and AS-SHP significant, while the effect for SA-SHP is limited.

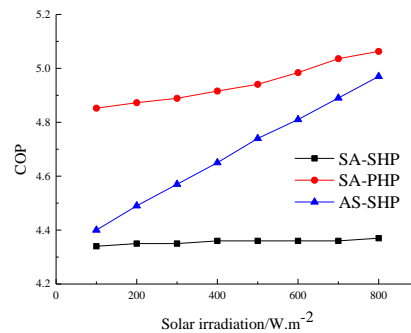


Figure 4: Impact of solar irradiation on COP

#### 4.2. Impact of ambient temperature

The performance of SA-SHP, SA-PHP and AS-SHP has been compared with the outdoor ambient temperature ranging from  $-10^{\circ}C$  to  $10^{\circ}C$  at the solar irradiation of  $200W/m^2$  and indoor ambient temperature of  $20^{\circ}C$ .

The variation of evaporation capacity of SA-SHP, SA-PHP and AS-SHP under different outdoor ambient temperatures is illustrated in Figure 5. It can be observed that for SA-SHP and SA-PHP, both  $Q_{eva, sol}$  and  $Q_{eva, air}$  rise as the outdoor ambient temperature increases. However, the  $Q_{eva, sol}$  in AS-SHP decreases at the ambient temperature above  $5^{\circ}C$ , due to the decline of heat gain from the ambient caused by the rise of refrigerant temperature at the inlet of solar evaporator. For SA-SHP, SA-PHP and AS-SHP, the contribution of air source evaporator to the overall  $Q_{eva}$  increases as the outdoor ambient temperature rises, and the value in AS-SHP is the highest. With the outdoor ambient temperature rising from  $-10^{\circ}C$  to  $10^{\circ}C$ , for SA-SHP,  $R_{air}$  rises from 0.23 to 0.39, the value in SA-PHP increases from 0.22 to 0.39, and the value in AS-SHP rises from 0.21 to 0.52.

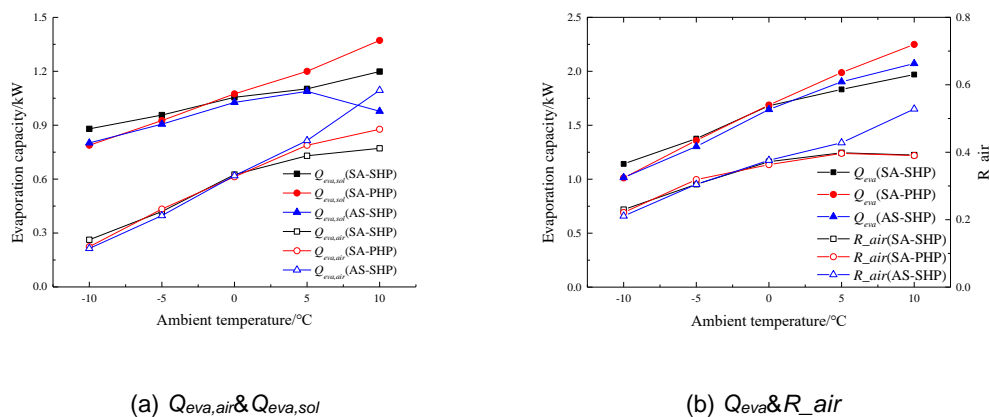


Figure 5: Impact of ambient temperature on evaporation capacity

For SA-SHP, SA-PHP and AS-SHP, the  $P_{sys}$ ,  $Q_{con}$  and COP increase as the outdoor ambient temperature rises, as shown in Figure 6~7. The  $P_{sys}$  of each system is relatively close, and the  $Q_{con}$  of SA-PHP is the highest at the outdoor ambient temperature above  $-5^{\circ}C$ . It can be observed that the COPs of SA-SHP, SA-PHP and AS-SHP are close at the ambient temperature of  $0^{\circ}C$ . The COP of SA-SHP is the highest, followed by SA-PHP and AS-SHP at the outdoor ambient temperature below  $0^{\circ}C$ . When the outdoor ambient temperature is above  $0^{\circ}C$ , the SA-PHP has the highest COP, followed by AS-SHP, the COP of SA-SHP is the lowest. When outdoor ambient temperature

increases from -10 to 10, the COP of SA-SHP increases from 3.51 to 4.34, the value in SA-PHP rises from 3.39 to 4.87, and the value in AS-SHP rises from 3.26 to 4.49.

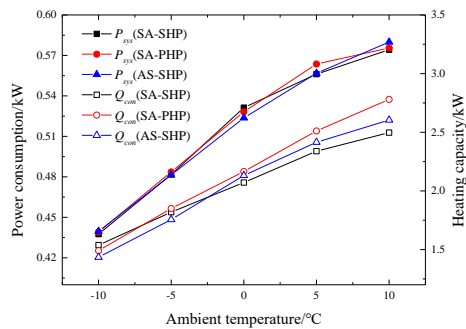


Figure 6: Impact of ambient temperature on power consumption and heating capacity

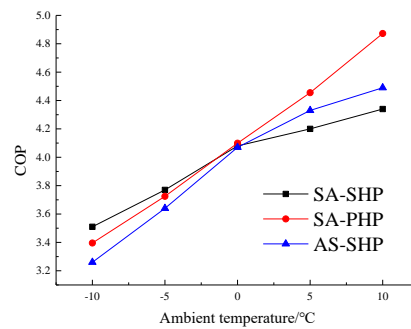


Figure 7: Impact of outdoor ambient temperature on COP

### 4.3. Optimal working condition

From the above results, it can be concluded that SA-SHP, SA-PHP and AS-SHP display different operation characteristics. To identify the optimal working condition for each system, the COP of SA-SHP, SA-PHP and AS-SHP has been compared under solar irradiation of 100W/m<sup>2</sup> ~800W/m<sup>2</sup> and ambient temperature of -10°C~10°C. A matrix has been employed to illustrate the optimal working condition range for each system, each grid is filled in the system with the highest COP, as shown in Figure 8.

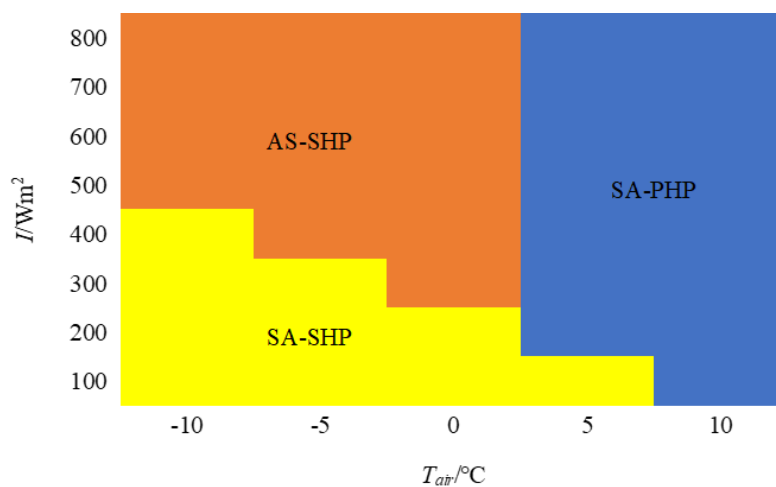


Figure 8: Optimal working condition for each system

For SA-SHP, due to the air source evaporator will dissipate energy to the ambient under high solar irradiation, it is suitable for working under the environment with low solar irradiation. Under the condition with low ambient temperature and high solar irradiation, AS-SHP shows the best performance, as the solar evaporator can act as the supplement heat source for the incompletely vaporised working fluid. SA-PHP can achieve the optimal performance under the condition with high ambient temperature or high solar irradiation. It is because that for SA-SHP and AS-SHP, the outlet parameter of the evaporator at the front will affect the heat transfer of the evaporator at the rear, while, in SA-PHP the problem can be reduced or avoided.

## 5. CONCLUSION

In this paper, solar-air series heat pump (SA-SHP), solar-air parallel heat pump (SA-PHP) and air-solar series heat pump (AS-SHP) with the identical components and different heat source configurations have been presented and compared in this paper. The impact of environmental parameters has been discussed to identify the optimal working condition for each system. The conclusions are summarised as follows:

(1) The impact of solar irradiation on SA-SHP, SA-PHP and AS-SHP is significantly different. COPs of SA-PHP and AS-SHP can be improved significantly as the solar irradiation increases, while the COP of SA-SHP is stable under different solar irradiations. The difference between the performances of each system is not obvious at specified ambient temperatures and the COPs of SA-SHP, SA-PHP and AS-SHP are close at the ambient temperature of 0°C.

(2) For SA-SHP, due to the air source evaporator will dissipate energy to the ambient under high solar irradiation, it is suitable for working under the environment with low solar irradiation. Under the condition with low ambient temperature and high solar irradiation, AS-SHP shows the best performance, as the solar evaporator can act as the supplement heat source for the incompletely vaporised working fluid. SA-PHP can achieve the optimal performance under the condition with high ambient temperature or high solar irradiation.

## 6. REFERENCES

- Bellos, E(s), 2016. Energetic and financial evaluation of solar assisted heat pump space heating systems. *Energy Conversion and Management*. 120, 306-19.
- Cai, J(s), 2016. Performance analysis of a novel air source hybrid solar assisted heat pump. *Renewable Energy*. 139, 1133-45.
- Chua, K.J(s), 2010. Advances in heat pump systems: A review. *Applied Energy*. 87, 3611-24.
- Deng, W(s), 2016. Simulation analysis on dynamic performance of a combined solar/air dual source heat pump water heater. *Energy Conversion and Management*. 120, 378-87.
- Dong, X(s), 2017. Experimental investigation on heating performance of solar integrated air source heat pump. *Applied Thermal Engineering*. 123, 1013-20.
- Kim, T(s), 2018. A comparative investigation of solar-assisted heat pumps with solar thermal collectors for a hot water supply system. *Energy Conversion and Management*. 172, 472-84.
- Li, S(s), 2015. Comparison analysis of different refrigerants in solar-air hybrid heat source heat pump water heater. *International Journal of Refrigeration*. 57, 138-46.
- Qiu, G(s), 2018a. Theoretical study on the heat transfer characteristics of a plain fin in the finned-tube evaporator assisted by solar energy. *International Journal of Heat and Mass Transfer*. 127, 847-55.
- Qiu, G(s), 2018b. A novel integrated heating system of solar energy and air source heat pumps and its optimal working condition range in cold regions. *Energy Conversion and Management*. 174 (2018) 922-31.

---

## #109: Measurement and analysis of thermal environment in transition space of veranda

Taking a building in the hot summer and cold winter area as an example

---

Huang YANYAN<sup>1</sup>, Chen YUNLONG<sup>2</sup>, Liu WEICHANG<sup>3</sup>

<sup>1</sup> School of Civil Engineering and Environment, Hubei University of Technology, Hongshan District, Wuhan City, Hubei Province, tracybaifercyl@gmail.com

<sup>2</sup> School of Civil Engineering and Environment, Hubei University of Technology, Hongshan District, Wuhan City, Hubei Province, 756677874@qq.com

<sup>3</sup> School of Civil Engineering and Environment, Hubei University of Technology, Hongshan District, Wuhan City, Hubei Province, 990390881@qq.com

*With the emphasis on building energy conservation in China, people's demands for quality of life and the comfort of building thermal environment have become the focus of attention. As a transitional space, the veranda has an important impact on the indoor thermal environment and building energy consumption. The main purpose of this study is to explore the thermal environment characteristics of the veranda space and its impact on the indoor thermal environment. Taking a building veranda in the hot summer and cold winter area as the research object, the measured data of indoor and outdoor thermal environment (temperature, humidity, wind speed, etc.) under different working conditions were collected. Through the data sorting and analysis, the thermal environment characteristics of the veranda space, the orientation of the veranda, the enclosure structure, the opening method of the doors and windows, the vegetation shading and other factors affect the indoor thermal environment. The measured results show that the transition space of the veranda has good thermal insulation effect in summer and can play an important role in reducing building energy consumption.*

*Keywords: Hot summer and cold winter area, Insulation effect, Veranda transition space, Measured and analysed*

## 1. INTRODUCTION

In today's society where urbanisation is rapidly increasing and energy-saving design is becoming more and more urgent, the importance of research on building thermal environment is self-evident. The outer corridor serves as a transitional space between the interior and exterior of the building and plays an important role in transportation and guidance. However, at present, the role of the outer corridor as a heat buffer space is not paid enough attention. The thermal environment of the outer corridor and its influence on the indoor thermal environment are studied in order to clarify the influence mechanism of the thermal environment of the outer corridor and make better use of the outer corridor (Huang, 2014). Helping the indoor environment to achieve energy conservation will improve the indoor thermal environment, thereby improving the thermal comfort of the human body.

In the process of building design, the thermal environment data of space is often based on software simulation, which is in the hypothetical stage of McKinsey's black box theory, and has not been tested by practice. In order to verify whether the actual thermal environment is consistent with the state of the software simulation, how to amend it to help the new building to use the software simulation method to adjust the building shape to improve the thermal environment at the beginning of the design (Huang, 2014). This paper mainly discusses the actual measurement. The actual measurement team measured the existing transition space of the veranda and verified whether the thermal environment effect assumed in the design was achieved based on the existing thermal environment data (Martin, 1999). In addition, we used the measured method to analyse the thermal environment of the transition space of the outer corridor, and studied the influence of the orientation of the veranda, the enclosure structure, the opening method of the doors and windows, the vegetation shading and other factors on the indoor thermal environment, and explored the influence law.

## 2. INTRODUCTION TO THE ACTUAL MEASUREMENT OF THE TRANSITION SPACE OF THE VERANDA

Hubei University of Technology is located in the southwest of Wuhan, west of Hongshan District, and south of Nanhu Avenue. The site was selected at the Civil Engineering Building of Hubei University of Technology. It is located in the northeast of the campus (Figure 1) and is a modernist building built in the 21st century. The whole building has a concave shape, frame structure, bird's eye view plane as shown in Figure 2, the north side of the building is the old building (the north building), which was built in 2001; the south side of the building is the new building (the south building), which was expanded in 2016.

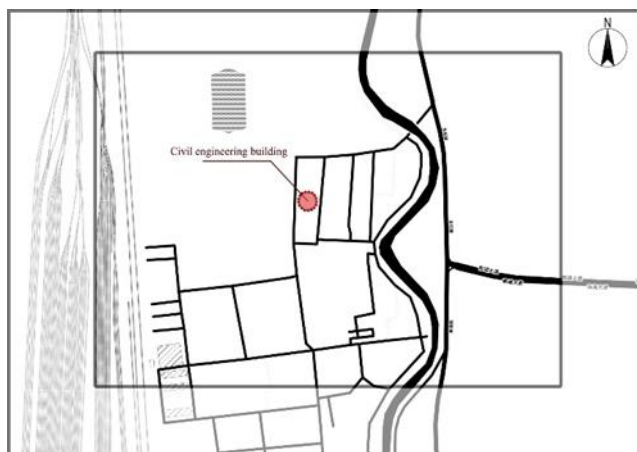


Figure 1: Location map of the civil engineering building of Hubei University of Technology



Figure 2: Aerial view of the civil building

According to meteorological data, the climate of the measured building is typical of hot summer and cold winter climate. The actual location is measured in the outer corridor space connecting the north and south buildings (Figures 3 and 4), and the west side is the conference room. The outer corridor is 27.5m long, 4.6m wide and 3.3m high. The outer wall adopts ordinary concrete hollow block (polystyrene granule insulation mortar), and the east side adopts large-area transparent curtain wall with a window-to-wall ratio of 0.09 and an average shading coefficient of 0.81. The west window and wall ratio is 0.07, and the average shading coefficient is 0.68, which meets the corresponding requirements of the "Public Building Energy Efficiency Design Standard" (GB50189-2005).



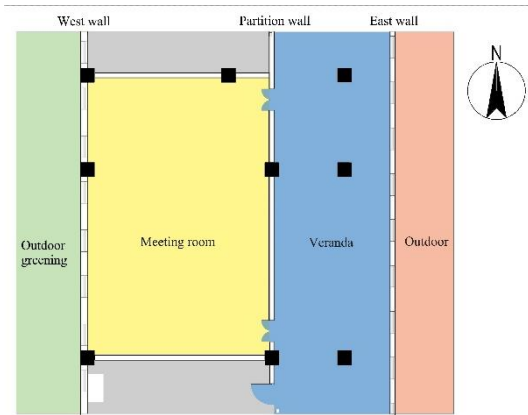


Figure 3: Plane transition space plan



Figure 4: Real shot of the transition space of the veranda

## 2.1. Measured summary

The actual team selected the actual survey from July 30th to August 2nd. According to the weather station, these days are the hottest “three days” in Wuhan. The wind speed is small, the temperature is high, and the average temperature is close to 30°C. Sunny, occasional cloud cover, strong solar radiation, is a typical summer hot climate.

The experimental team used small meteorological stations, hot wire anemometers, ibuttons, infrared thermometers, infrared thermal imagers and other related measuring instruments to collect the surface temperature, glass window surface temperature, and veranda of each wall of the transition space in the measured time. Internal and external air temperature and humidity and wind speed data, after the data collection is completed, the relevant thermal environment data are analysed. The specific measured instruments, test contents, and instrument related parameters are shown in the table (Table 1).

Table 1: Measured instruments and related parameters

Measuring instrument	Instrument model	Measurement content	Measuring range	Placement position
Ibutton	DS1921G	Wall and window skin temperature	-40~85°C	Wall window surface
Hot wire anemometer	TES1340	Air point wind speed	0~40m/s	Air measurement points inside and outside the gallery
		Air point temperature	-40~85°C	
		Air point humidity	0~100%	
Infrared Thermometer	FLUKE-F63	Wall window skin temperature	-40~85°C	Handheld measurement
Infrared thermal imager	FLUKE-Tis75	Measuring point temperature distribution	-40~85°C	Handheld measurement
Weather station	QS-3000	Background solar radiation	0~2000W/m <sup>2</sup>	The south floor of the civil building
		Background meteorological temperature	-40~80°C	
		Background relative humidity	0~100%	

## 2.2. Measured content and method

This test is to set the measured points A(a), B(b), C(c), D(d), E(e), F(f) from the east to the west respectively, and A to F for the surface of the wall, a to f are glass surface measuring points. In order to test the indoor thermal environment more accurately, the actual measurement team arranged the air temperature and humidity and wind speed measurement points in the veranda and the number 1 to 8 in the conference room. The specific measured points are arranged as shown in Figures 5 and 6 and in Table 2. In addition, all measuring points are selected from the same physical height of 1.5m from the third floor. This height is close to the human thermal comfort, and the measured thermal environment data is more informative.

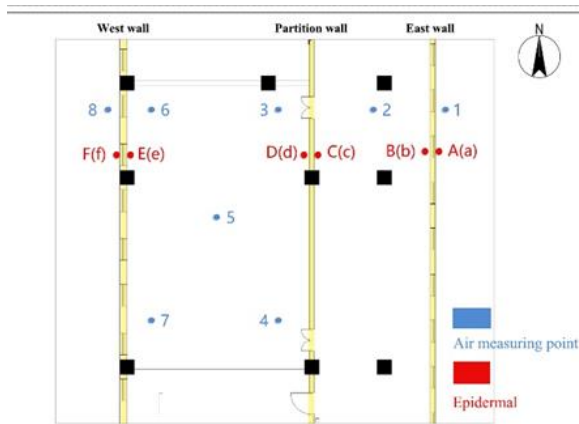


Figure 5: Survey point layout



Figure 6: Survey point layout real shot

Table 2: Each measured point and instrument layout

Measuring instrument	Measuring position	Placement height	Measurement content
Infrared Thermometer	A~F, a~f	1.5m from the ground Handheld measurement	Epidermal temperature
Infrared thermal imager		Handheld measurement	Temperature distribution around the measuring point
Hot wire anemometer	Measuring point 1~8	1.5m from the ground	Air measuring point temperature, humidity, wind speed

The measured time is from July 30th to August 2nd for a total of four days. The actual measurement team sets 30 and 31 days to open the door and open the window. Simulate the semi-enclosed veranda; set the opening and closing windows for 1, 2 and 2 days. Working condition 2, simulating a closed veranda, studying the influence of two different forms of veranda transition space on the thermal environment. Both working conditions were tested for two days to ensure that the experimental data did not cause errors due to uncertain factors. The data within the same time period of 2 days under each working condition was averaged and the final average value was determined for analysis and reference.

### 3. COMPARATIVE ANALYSIS OF MEASURED DATA

#### 3.1. Analysis of air temperature inside and outside the gallery

First of all, the actual measurement team selected the temperature data of the outer wall outside the measuring point, the outer measuring point in the outer wall, the measuring point in the outer wall 2 and the measuring point 3 in the partition wall on July 30 and 31, to study the air inside and outside the outer corridor. Temperature condition. The temperature conditions of each measuring point are shown in the following table (Table 3):

Table 3: Working conditions: air temperature conditions inside and outside the measuring point 1, 2, 3

Measuring point number	Measuring point 1	Measuring point 2	Measuring point 3
Average temperature	30.6°C	32.0°C	32.1°C
Maximum temperature	35.3°C	33.6°C	33.6°C
lowest temperature	29.3°C	30.6°C	30.6°C

It can be seen from the data in the table that the average temperature of the outdoor measuring point is 1.5°C lower than the temperature of the measuring point in the building, but the highest temperature is 1.7°C higher and the lowest temperature is 1.3°C lower. It can be preliminarily concluded that the window is opened when the working condition is opened. In this case, the semi-enclosed veranda has a certain influence on the indoor temperature, which is expressed in the average temperature and the lowest temperature is higher than the outdoor, and the highest temperature is lower than the outdoor.

Under normal circumstances, the outdoor temperature change is larger than the fluctuation within the building, and the influence of the outer gallery on the temperature stability in the building. We have scatter the temperature data of the above points, and the results are shown in Figure 7:

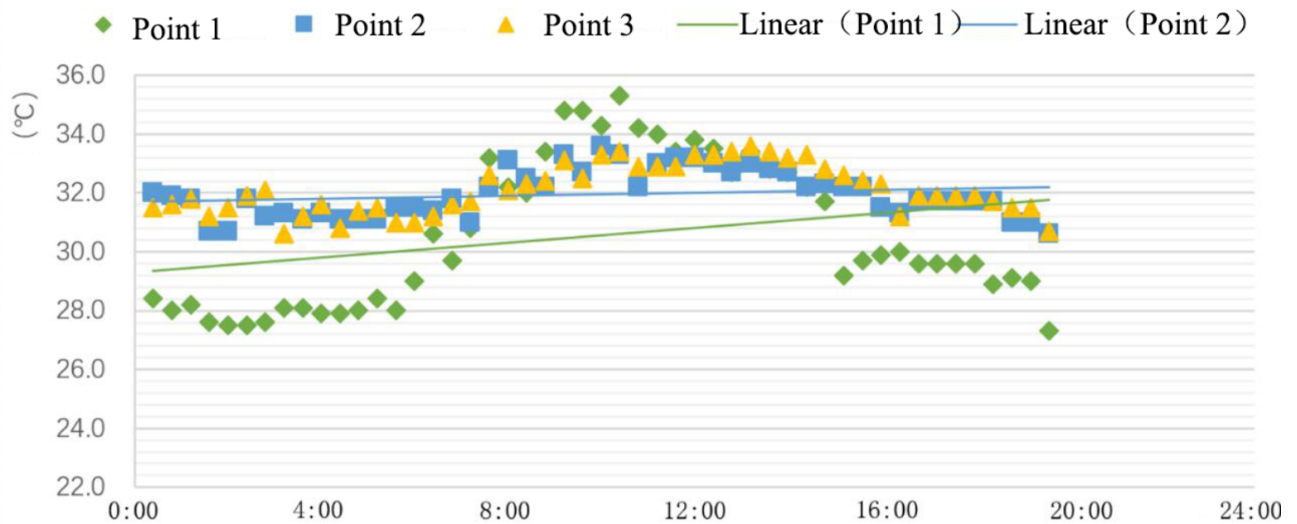


Figure 7: Distribution of the temperature conditions of the measuring point 1, 2, 3

It can be seen from the scatter distribution in the figure that the temperature of the measuring point 2 and the measuring point 3 is about 3.5°C higher than the measuring point 1 in the period from 0:00 to 8:00, and then the solar radiation is enhanced, 8:00. Until 12:00, the temperature of the measuring point 1 exceeds the measuring point 2 and the measuring point 3 by about 1.5°C, and then gradually approaches to the same. After 16:00, the temperature of the measuring point 1 is lower than the measuring points 2 and 3. Comparing the trend line of summer measurement point 1 and measurement point 2, it can be found that the change trend of measurement point 1 is larger than that of measurement point 2, and the temperature scatter distribution is also looser; the change trend of measurement point 2 and measurement point 3 is almost the same. In some time periods, the scatter points almost coincide, and the temperature of the veranda is very close to the temperature in the conference room under the condition of opening the door.

### 3.2. Analysis of skin temperature of east wall and partition wall

In order to verify whether the change reflected by the temperature data of the air inside and outside the outer corridor is reliable, the actual team selected the wall surface temperature data of the inner and outer measuring points A and B of the east wall and the measuring points C and D inside and outside the partition wall for comparison. To more fully analyse the impact of the presence of the veranda on the indoor thermal environment. The actual measurement team selected the temperature data of the test points A, B, C, and D on July 30 and 31 to compare the temperature conditions as shown in the following table (Table 4):

Table 4: Working conditions - East wall measuring points A, B and partition wall measuring points C, D air temperature conditions

Measuring point number	A	B	C	D
Average temperature	36.0°C	34.8°C	34.1°C	33.5°C
Maximum temperature	46.0°C	36.0°C	35.0°C	34.5°C
lowest temperature	31.0°C	32.0°C	33.0°C	32.5°C

It can be seen from the data in the table that the average temperature and maximum temperature of the wall surface are gradually decreasing from east to west, and the temperature difference between the wall and the outside is large. The average temperature of A and B is 1.2°C, and the maximum temperature is 10°C. The temperature of the B and C measuring points of the two walls in the outer gallery is similar. It can be seen that the wall body is very obvious for the thermal insulation of the building, and the temperature of the wall skin is more affected by the air heat radiation, and its thermal conductivity is poor. It is preliminarily concluded that the outer gallery has a positive impact on the thermal environment inside the building.

In order to confirm our inference, the temperature curves of the four measuring points within 24 hours were selected for comparison, as shown in the following figure (Figure 8):

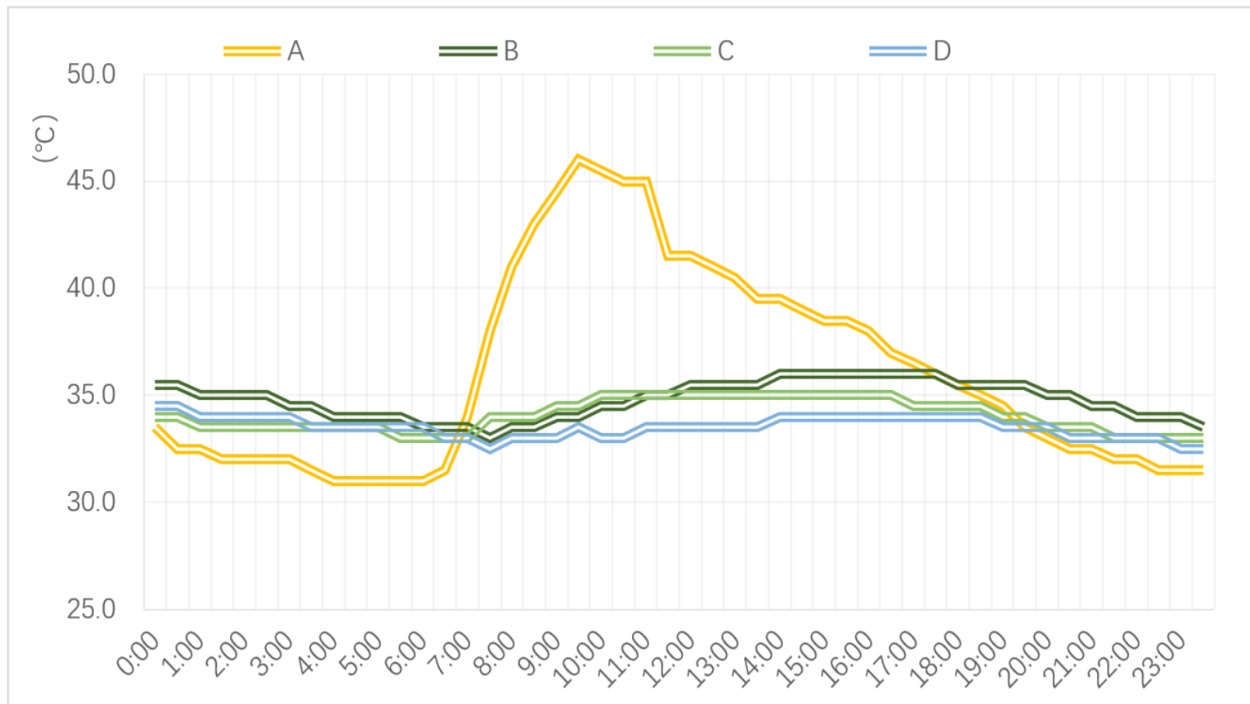


Figure 8: Temperature profile of working conditions, measuring points A, B, C, D

According to the curve in the figure, the temperature change inside and outside the partition wall still shows the trend of first stable and then rising and then decreasing. Compared with the east wall, the temperature of the inner and outer surfaces of the partition wall is significantly lower, and the variation range is smaller. The highest temperature is C measurement. The point is 35°C, the lowest is 32.5°C. The temperature change in the D partition is more stable, with a variation of only 2°C within 24 hours.

### 3.3. Analysis of air temperature inside and outside the working environment and working conditions

The door and window switch mode set by the working condition is to open the door and open the window, and the working condition three is to open the door and close the window. The test time for the third working condition is August 3 and 4, the weather is shower, the temperature is 27~34°C, and the westerly wind is 2.

In order to study the influence of the interface form on the closed and semi-enclosed thermal environment of the outer gallery, the external wall measurement point 1 and the outer corridor measurement point 2 were selected. The corresponding measurement conditions 1 and the working condition three temperature conditions are shown in the table (Table 5). Show:

Table 5: Working conditions 1 and working conditions: Three air temperature conditions inside and outside the east wall

	Measuring point 1	Measuring point 2
average temperature	30.60°C	32.00°C

Working condition one	Maximum temperature	35.30°C	33.60°C
	lowest temperature	27.30°C	3.060°C
	average temperature	32.96°C	32.30°C
Working condition three	Maximum temperature	42.20°C	34.10°C
	lowest temperature	28.20	30.10

It can be seen from the average temperature inside and outside the east wall of the working condition and the working condition that the outdoor temperature rises by 2.36°C, the temperature inside the outer gallery only rises by 0.3°C, and the outdoor maximum temperature rises. 6.9°C and only 1.5°C in the outer gallery. It can be preliminarily concluded that the closed gallery has a better thermal insulation effect in the summer than the semi-enclosed veranda.

Since the effect of the opening of the window on the summer heat insulation is obvious, the actual measurement team selected the temperature data of the working condition 1 and the working condition three measuring points 1 and 2 to draw a 24-hour temperature change curve, as shown in Figure 9:

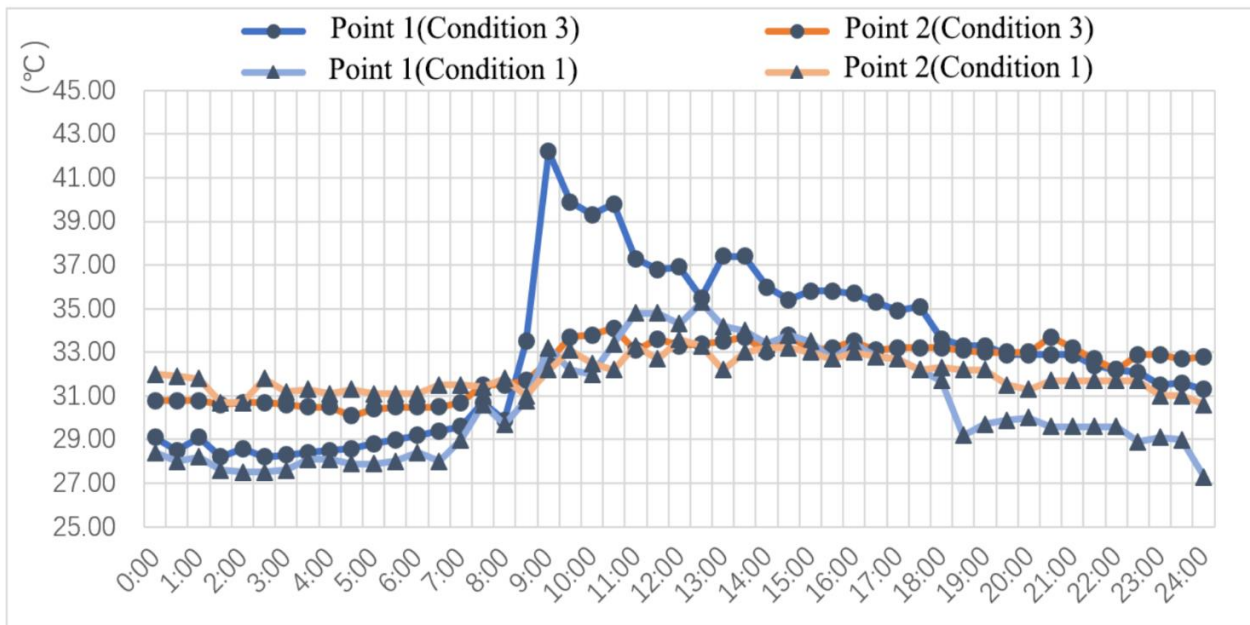


Figure 9: Working condition 1 comparison case 2 measuring point 1, 2 temperature condition curve

Through the curve in the figure, it is more intuitive to see the temperature changes of the working conditions and the working conditions of each measuring point: it can be seen that due to the weather change, the working condition 1 of the measuring point 1 and the three curves of the working condition are greatly different. The temperature curve of the measuring point 2 in the gallery has almost no change under two different working conditions, and the temperature difference is almost at about 1°C.

#### 4. LAYOUT AND SPECIFICATIONS

(1) Under the condition of opening the window, the outdoor temperature change in summer is larger than that in the room, and the temperature stability is worse. The transition space of the outer gallery plays a certain role in regulating the indoor temperature. The outer gallery and indoor temperature are stable, but the overall temperature is high. .

(2) As a transitional space, the outer corridor can play an important role in regulating the indoor thermal environment in summer: in the case of the east wall being exposed to the sun, the transition space of the outer corridor can act as a double skin of the building, while radiating heat to the sun. Ample buffer space makes the indoor and outdoor skin temperature difference up to 10 °C.

(3) The closed veranda formed by the closed window has a greater influence on the thermal environment of the veranda in the summer than the semi-enclosed veranda, which is more conducive to the insulation of the outer corridor and is not affected by external temperature changes.

## **5. REFERENCES**

Huang, Y., Wang, J., Zhang, H., 2014. Analysis of external sunshade design and shading effect of large space buildings - Taking Taiyuan South Railway Passenger Station as an example [J]. Journal of Hubei University of Technology, 02:33-36.

Huang, Y., Chen, H., Yuan, L., 2014. Measurement and Analysis of Thermal Insulation Effect of Building Skin Energy Saving Reconstruction in Summer Hot Areas [J]. Journal of Guilin University of Technology, 02:278-282.

Treberpung, M., Neues Bauen mit der Sonne.1999. Anstzezeuinerk limagerechten Architektur [M].Springer Wien Newyork.:36.

---

# #111: Priority and urgency between geothermal and solar photovoltaic in Indonesia's electricity power generation

---

Tabratas THAROM<sup>1,2</sup>, Hendro Sasongko HADI<sup>3</sup>, Pablo COLLAZZO<sup>4</sup>

<sup>1</sup>Grenoble Ecole de Management, 38000 Grenoble France, [ttharom@gmail.com](mailto:ttharom@gmail.com)

<sup>2</sup>Uzma Engineering Sdn. Bhd., 47820 Selangor Malaysia, [tabratas.tharom@uzmagroup.com](mailto:tabratas.tharom@uzmagroup.com)

<sup>3</sup>Global Guru Indonesia, Jakarta Indonesia, [hendroshadi@gmail.com](mailto:hendroshadi@gmail.com)

<sup>4</sup>Grenoble Ecole de Management, 38000 Grenoble France, [pablo.collazzo@grenoble-em.com](mailto:pablo.collazzo@grenoble-em.com)

*Indonesia has a large and varied potential for renewable energy. As a country on the equator, every location in Indonesia is exposed to sunlight throughout the year, therefore Indonesia has plenty of solar energy potential. In terms of geothermal energy resources, Indonesia is also located in the ring of fire which surrounds the Pacific Ocean, with plenty of rock that can supply such energy in the huge potential amount. Both solar and geothermal energy have different characteristics and challenges, and different technological comparison and related policy for each energy type. Geothermal Power Plant (GPP) business is emphasised on drilling work, which is associated to the same risky exploration of oil and gas sector. This highly risky exploration cost is the main decisive factor to invest. GPP is operated to serve base load due to its high capacity factor. Meanwhile Solar Photovoltaic Power Plant (SPP) could be installed and operated in relatively short time, but the price of electrical energy storage for compensating its low capacity factor, could make the investment cost soars. This paper uses SWOT to assess the conditions of GPP and SPP. Policy Gap Analysis is also used for assessing the lack of regulations for GPP and SPP. Policy Gap Analysis review is based on trilemma energy and business model canvassing for firm's strategies. Based on the differences and characteristics of both energy resources, this paper aims to assess the feasibility of GPP by comparing it to SPP in order to define the most feasible way to conduct GPP and SPP with the urgency and priority criteria upon SWOT and Policy Gap Analysis.*

*Keywords: geothermal; Indonesia; power plant; solar photovoltaic; SWOT; Policy Gap analysis; trilemma energy; firm's strategies*

## 1. INTRODUCTION

Geothermal Power Plants (GPP) and Solar Photovoltaic Power Plants (SPP) are two renewable energy systems known for their huge potential for electricity production, especially in Indonesia because of its location along the geothermal ring of fire and the equator. Each have different technical characteristics and investment profiles, especially within their technology, risk investment characteristic and operation with specific related policy.

GPP has the cheapest generation cost for renewable electricity after hydro power and has been considered as the base-load in Indonesia for a long time. GPP is characterised by highly risky exploration costs, large investment and longer payback periods for investments. The exploration phase is widely considered to be the most critical phase due to its high risk and uncertainty with the investor having to invest a considerable capital upfront for exploration (Purba *et al.*, 2019). These obstacles recently lead the Government of Indonesia to initiate incentives to make GPP more attractive to investors, for example Preliminary Survey and Exploration Assignment (PSPE) and Government Drilling. PSPE activities cover geological survey, geochemist survey, geophysics survey, and exploration well drilling (DGNREEC MEMR Republic of Indonesia, 2019). As with the PSPE incentive, Geothermal Working Area will be given as direct assignment mechanism (Permana, 2017). PSPE programs aim to reduce exploration risk by collecting and analysing the data to ease the exploration risk, which in turn will make the investment more credible and bankable in the early stage of the GPP project. The Government Drilling program is meant to reduce the investment risk in initial stages of development by data addition and exploration drilling in Greenfield Area (DGNREEC MEMR Republic of Indonesia, 2019). Costs and risk allocation in geothermal exploration and wellfield development in Indonesia are shown in Table 1 where geothermal wells in Indonesia are usually 1,000 to 2,800 meters in depth and the drilling success rate appears to range from 63% to 73% (Purba *et al.*, 2019).

Table 1: Cost and risk allocation in geothermal exploration and wellfield development. (excludes cost of bidding and licensing, permitting, and other company overheads) (Purba *et al.*, 2019)

Stage	Cost (thousand USD)	Cost Percentage from Total Project	Risk Allocation	
1. Regional Reconnaissance: Selection of Prospects for Exploration.	250 – 500	~1%	Typically borne by government agency, may be borne in part by private developer.	
2. Detailed Surface Exploration: Geology, Geochemistry, and Geophysics.	1,000 – 5,000	2 – 6%	Often borne by government agency, usually augmented or borne largely by private developer.	
3. Drilling Temperature Gradient Holes: 3 to 5 wells, @200 to 500 depth.	300 – 2,000	~1%	Occasionally borne by government agency, usually borne by private developer.	
4. Drilling Deep Exploratory Hole: 1 -3 wells @1.5 to 2.8 km depth.	7,000 – 23,000	3 – 7%	Occasionally borne by government agency, usually borne by private developer.	
5. Long-term flow testing and numerical simulation of reserves (produces bankable document)	500 – 1,000	> 1%	Very rarely borne by government agency, almost always borne by private developer.	
Total Exploration Cost	9,050 ~ 28,000	~7 – 15%		
	Power Plant Size (MW)			
	20	50	100	
6. Drilling of The Development Wellfield: Production, Injection, and Unsuccessful Holes @80% success rate and 7 MW output / well	32,000 – 36,000	50,000 – 64,000	100,000 – 108,000	Very rarely borne by government agency, almost always borne by private developer.
Total Power Plant Cost	41,050 – 62,500	50,000 – 64,000	69,500 – 90,950	85 – 92%
Total Cost (Million USD / MW)	1.08 – 1.35	1.38 – 1.80	2.05 – 3.12	

But there are drawbacks in SPP as well with low capacity due to being highly dependent on local radiation levels and weather, necessitating the need to introduce energy storage to back-up the power to compensate this low capacity factor. The energy storage price is still relatively high, although this is gradually decreasing. Based on



IRENA Report on 2018, in 2017, Solar Photovoltaic (PV) modules are more than 80% cheaper than in 2009 (IRENA, 2018).

The current structure of the electricity business in Indonesia is “Vertically Integrated plus IPP”. It means that the supply of electricity starting from power generation, transmission, and distribution, and electricity sales to public is carried out by one utility, namely PT PLN (Persero) – a state-owned company also known as a Public Service Obligation (PSO) company in Indonesia for electricity sector, which as “Off-Taker” of electricity business. The competition in the electricity business in Indonesia only occurs in the power generation side through private power generation, called Independent Power Producer (IPP) (Sommeng and Anditya, 2018). But, in PLN’s business area, the electricity is produced not only from IPP but also from PLN’s owned power generation, PLN’s rented power generation, and energy transaction from excess power and collaboration with other business area, such as Private Power Utility (PPU). In 2018, SPP average generation cost in PLN’s business area, was still high and the most expensive of other type of power plants, see Table 2 (Coorporate Secretary PT PLN (Persero), 2019).

Table 2: Average Generation Cost (Rp / kWh) in PT PLN (Persero)’s Business Area (Coorporate Secretary PT PLN (Persero), 2019)

Year	Type of Power Plant							Average
	Hydro	Steam	Diesel	Gas	Geothermal	Combined Cycle	Solar Power Plant	
2018	352.39	831.46	2,228.71	5,781.99	2,350.98	1,298.72	7,672.68	1,160.89

As on Regulation of MEMR Republic of Indonesia Number 50 Year 2017 jo. Number 53 Year 2018, PLN is obligated to operate power plants utilising renewable energy sources for a capacity up to 10 MW on a must-run basis, through a direct selection mechanism based on capacity quota (MEMR Republic of Indonesia, 2017). The cost and risk, including related policy for GPP and SPP, unavoidably must be addressed to compare GPP and SPP. The SWOT analysis is applied due to the need of these renewable resources mapping side by side applying the same criteria to find the most feasible option.

It is important for Indonesia to accelerate GPP since fossil fuels cause environmental damage. GPP also is the most stable and the most reliable renewable energy resource to back-up the national grid and especially large hydro power during drought season. The SWOT methodology is chosen because it could map the position of GPP and SPP internally and externally, as well as their relative priorities. Therefore the recommendation and solution could be made based on the position in the SWOT quadrant.

## 2. LITERATURE REVIEW

In comparing GPP and SPP, the authors considered the technological and economic aspects which include related policy and regulations applied in Indonesia. In economic aspects, based on IRENA report on 2018, Levelized Cost of Electricity (LCOE) for geothermal projects, between 2007 and 2014, varied from as low as USD 0.04 / kWh for second-stage development of an existing field to as high as USD 0.14 / kWh for greenfield developments (IRENA, 2018). For comparison data in 2018 for global and PLN’s business area in renewable energy power generation cost see Table 3. From Table 3, the average generation cost from GPP and SPP in PLN’s business area is higher than the LCOE global data. However, the basic cost of electricity production in PLN’s business area is almost the same with the LCOE global data.

Table 3: Renewable Energy Power Generation Cost in 2018

Type of Power Plant	Global Data Source: (IRENA, 2019)		PT PLN (Persero)’s Business Area Source: (Coorporate Secretary PT PLN (Persero), 2019)		
	Weighted-Average Cost of Electricity – Levelized Cost of Electricity (LCOE) (USD / kWh)	Cost of Electricity: 5 <sup>th</sup> and 95 <sup>th</sup> Percentiles (USD / kWh)	Rp / kWh	Average Generation Cost USD / kWh (Assumption: 1 USD = Rp14,249.67 – Average JISDOR’s rate in 2018)	Basic Cost of Electricity Production (According to The Audit Board of The Republic of Indonesia (BPK RI)’s Audit)
Bioenergy	0.062	0.048 – 0.243	N/A	N/A	Rp1,406.00 / kWh or USD 0.10 / kWh <sup>1)</sup>
Geothermal	0.072	0.060 – 0.143	2,350.98	0.16	) Notes: 1) 1 USD = Rp14,249.67 – Average JISDOR’s rate in 2018
Hydro	0.047	0.030 – 0.136	352.39	0.02	
Solar	0.085	0.058 – 0.219	7,672.68	0.54	2) For all types of power plant, include fossil and new energies power plant
Photovoltaics					
Concentrating Solar Power	0.185	0.109 – 0.272	N/A	N/A	
Offshore Wind	0.127	0.102 – 0.198	N/A	N/A	
Onshore Wind	0.056	0.044 – 0.100	N/A	N/A	

The general comparisons of payback time, construction periods, capacity factors, efficiency and environmental impacts from various types of power generation can see in Table 4.

Table 4: General Comparison from Various Types of Power Generation (Li, 2015)

Type of Power Plant	Payback Time (Year) <sup>1)</sup>	Construction (Year)	Capacity Factor (%)	Efficiency (%)	CO <sub>2</sub> <sup>2)</sup>	Water <sup>3)</sup>	Land <sup>4)</sup>
Solar Photovoltaic	1 – 2.7	0.3 ~ 0.5	8 – 20	4 - 22	90	10	28 - 64
Wind	0.4 – 1.4	< 1	20 – 30	24 - 54	25	1	72
Hydro	11.8 (small) 0.5 (large)	1 10 ~ 20	20 – 70	> 90	41	36	750
Geothermal	5.7	3-5	90+	10 - 20	170	12 - 300	18 - 74
Coal	3.18	1 ~ 3	N/A	32 - 45	1,004	78	N/A
Gas	7	2 ~ 3	N/A	45 - 53	543	78	N/A

Note:

<sup>1)</sup> The payback time depends on financial and economic term and condition

<sup>2)</sup> Average greenhouse gas emissions expressed as CO<sub>2</sub> equivalent for individual energy generation technologies: CO<sub>2</sub> equivalent g/kWh

<sup>3)</sup> Water consumption in kg/kWh of electricity generation

<sup>4)</sup> Units: km<sup>2</sup>/TWh

A typical value for commercially available solar photovoltaic modules today is 15 – 17% with high-end products already above 20% when measured at Standard Test Conditions (STC). The module area needed to deliver 1 kW<sub>P</sub> of peak generation capacity can be calculated as 1 / efficiency of a solar module and equals 6.25 m<sup>2</sup> by today's standard solar photovoltaic modules. In Indonesia's study case, ground-mounted SPP may be located very close to each other, since shadow impact is not an issue. The ground mounted 1 MW<sub>P</sub> SPP at Cirata, West Java, occupies 8.65 m<sup>2</sup> per kW<sub>P</sub> (1,040 kW<sub>P</sub> using 0.9 Hectare area). The space requirement for solar photovoltaic modules per MW<sub>P</sub> is significantly more than for thermal power plants. SPPs have relatively high initial costs and a low capacity factor (National Energy Council (DEN), 2017) but, SPP investment is risky but the investment / preconstruction costs and risks are not as heavy as the geothermal energy.

Geothermal is distinct from variable renewables, such as wind and solar, because it can provide consistent electricity throughout the day and year. GPP has a small ecological footprint but there is no security of success before the first well is drilled and the reservoir has been tested: GPP has high initial costs. SPPs are modular, easy to install, and can be integrated in buildings without require incremental ground space whilst with GPP's, the best reservoirs not always located near cities, need access to base-load electricity demands, and the pipelines to transport the geothermal fluids will have an impact on the surrounding area. For the environmental aspects, steam from geothermal fields contains Non-Condensable Gas (NCG) such as CO<sub>2</sub>, H<sub>2</sub>S, NH<sub>3</sub>, N<sub>2</sub>, CH<sub>4</sub>, and H<sub>2</sub>. Among them, CO<sub>2</sub> is the largest element within the NCG's discharged. NCG concentrations from each geothermal field are different. In Indonesia's study case, NCG emissions from Wayang Windu field are 1.1% and emissions from Kamojang field are 0.98%. Both of the fields produce dry steam. Ulubelu (two-phase steam) field gas NCG concentrations of 0.68%. The average NCG emissions from the three fields is 0.92%. The emissions of CO<sub>2</sub> range from 42 to 73 g/kWh with an average value of 62.90 g/kWh. For H<sub>2</sub>S, the values range between 0.14 to 2.54 g/kWh with an average value of 1.45 g/kWh. On the other side, SPP is noiseless and does not generate any emissions during operation. However, some thin-film technologies, as a type of solar photovoltaic module, do contain small amounts of cadmium and arsenic and the best perovskite absorbers contain soluble organic lead compounds, which are toxic and environmentally hazardous at a level that calls for extraordinary precautions (National Energy Council (DEN), 2017).

In order to ease geothermal risk, the Exploration Risk Insurance (ERI) could be initiated in the early state of GPP development for insuring the output of a reservoir. In financing geothermal projects, institutional investors and large IPP's can invest in the late stage of GPP development, such as power plant engineering and construction, commissioning, and operation. The probability of failure for geothermal wells is increasing proportionally with the electricity generation capacity, regardless of the exploration or the development stage (Munich RE, 2015).

By applying SWOT analysis, the Wielkopolskie region in Poland could emphasise on simple legal regulations, increase subsidies, introduce guaranteed green certificate prices, and educate the public, investors, developers, and decision-makers, despite of having a large renewable energy potential (Iglinski *et al.*, 2015). Since 2005, in Poland, the main mechanism to support the production of electricity from renewable sources is the system of so-called green certificates. The moment of generation of green certificates is the same as the moment of issuing certificates of origin to a company generating electricity in the renewable energy source. Green certificates have no material form. The system of certificates of origin (so-called green certificates) has been defined in detail in the Regulation of the Minister of Economy of August 14, 2008 (as amended) on the detailed scope of obligations in obtaining and presenting for redemption the certificates of origin, the substitute fee, purchase of electricity, and heat produced from renewable energy sources and the obligation to confirm the data on the amount of electricity generated from renewable energy source (Green Energy Poland S.A., 2010).

SPP only produces electricity when the sun is shining so, in order to increase the capacity factor of SPP, it will be necessary to regulate the need for electric energy storage systems. For on-grid types of SPP, the output of SPP installations can only be adjusted negatively (reduce feed-in) according to demand as production basically follows the daily and yearly variations in solar irradiation (National Energy Council (DEN), 2017). In a study case in Southeast Sulawesi, by incorporating the tracking system in SPP, it can achieve the highest electricity generation than fixed optimum angle and monthly optimum angle throughout the year but the highest investment cost will be achieved. In fact, the SPP with the tracking system will have high installation costs per plant (Rachman *et al.*, 2015). Increasing solar irradiation will also make the power output of solar photovoltaic modules increase. The amount of solar irradiation at solar photovoltaic can be increased by reflector. It produces reflected light that will be exposed to the solar photovoltaic module. Thus, the solar photovoltaic module has two sources of sunlight. One of research results showed that by direct measurement of solar photovoltaic module's characteristic, reflectors can boost the performance of solar photovoltaic modules to generate electricity around 20 – 30% but it also increases the value of short circuit current from the solar photovoltaic module (Setiawan and Dewi, 2013). As we know, if the electricity generation from SPP can achieve the maximum optimum value, power generation cost per kWh will be reduce proportionally. This lower electricity generation cost from SPP, however could not compete to existing GPP cost because the incremental of investment cost will be happened when we use the optimum solution of SPP.

From geothermal, Government of Indonesia achieve renewable energy non-tax state revenue, in 2018 non-tax state revenue from geothermal reaching around Rp2.3 trillion or 326% of 2018 state budget target of Rp700 billion (MEMR Republic of Indonesia, 2019a). Not only as power generation but also heat energy from geothermal energy can be utilised for direct use, for example heat energy contained in the hot water geothermal manifestation in the Bakan Village, North Sulawesi can be directly utilised directly for drying agriculture products, such as cacao and coconut. Heat energy of 176.94 kJ/s which is released by hot spring with 2 m<sup>3</sup>/hour discharge and temperature of 72.5 Celsius degrees which is passed into heat exchanger can raise the temperature of the drying chamber from 32 Celcius degrees to 50 Celcius degrees (Sukaryadi, 2013). In Lahendong, direct uses of geothermal energy has been established for processing palm sugar at the Masarang Sugar Factory since 2004. This was realised through the collaboration between PT Pertamina Geothermal Energy (PGE) and the Masarang Foundation, which is a community empowerment program, using brine from the separator. This activity helped increase the income of around 6,285 sugar palm farmers in the region. The use of geothermal energy also helps prevent natural damage due to illegal logging in the forest because farmers have used firewood to process palm sugar so far (Energift, 2016). Government regulation for direct uses of geothermal energy is still on progress. This regulation draft needs to be finalised to give legal certainty and to stimulate investment climate on geothermal industry for direct use (DGNREEC MEMR Republic of Indonesia, 2019). With some actions those have been taken by Government of Indonesia, Indonesia's geothermal utilisation is around 2000 MW, the second largest in the world, with a ranking following the Philippines and projected to be ranked first, beating America, in 2020 (MEMR Republic of Indonesia, 2019b). For SPP, based on PLN's Electricity and Supply Business Plan 2019 – 2028 (RUPTL PT PLN (Persero) 2019 – 2028), to maintain the new and renewable energy in energy mix for power generation sector of 23.2% in 2026 – 2028, it is necessary to add a SPP rooftop around 3,200 MW<sub>P</sub>. This target can be achieved with community participation and government support in developing new and renewable energy in power generation sector, especially on SPP rooftop that price is expected to decline further in the future.

The lack of attractiveness in Indonesia's Renewable Energy is shown by the result of EY's Renewable Energy Country Attractiveness Index (RECAI) 2019. The index measures factor driving market attractiveness for renewable energy in a world where renewable energy has gone beyond decarbonisation and reliance on subsidies. The result Indonesia sits on 40<sup>th</sup> position in 2019, the last as the least attractive country (Ernst & Young LLP, 2019). But, The Ministry of Energy and Mineral Resources (MEMR) Republic of Indonesia, c.q. Directorate General of Electricity as the regulator in the electricity sector in Indonesia is always committed to encouraging increasing renewable energy generation development in the electricity sector while maintaining the principle of Energy Trilemma balance and making policies and regulations conducive by involving the participation of all stakeholders to accommodate all the potential available primary energy to be developed for sustainability of electricity supply and create affordable electricity tariff for the entire Indonesian community (Sommeng and Anditya, 2018).

### 3. ANALYSIS

Based on the literature review, the authors compare GPP and SPP in Indonesia by using SWOT analysis as follows. For the strength, the analysis is in Table 5:

Table 5: Strength Analysis

	GPP	SPP
Energy Reliability	High CF	Low
Revenue Stream	Heating and electric energy	Electric energy only

For the strength, the conclusions are:

- GPP is more reliable than SPP in term of capacity factor
- GPP could sell heat energy beside electric energy
- GPP is the source of reliable energy and income, which is better than SPP.
- In the views of authors, the GPP is better than SPP as the source of reliable energy and revenue stream.

For the weakness, the analysis is as in Table 6:

Table 6: Weakness Analysis

	GPP	SPP
Electricity Generation Cost	Low for 2 <sup>nd</sup> development stage, high for greenfield	Moderate
Investment Risk	High	Moderate
Payback Period	Long	Moderate
Key People/HR	Hard	Moderate
Insurability/Bankability	Hard	Moderate
Technology Risk	High	High

For the weakness, the conclusions are:

- GPP for greenfield is high investment.
- In the views of authors, GPP is riskier than SPP for investment, payback period (long period is riskier), key people development/recruitment, insurability/bankability and technology implementation.

For the opportunity, the analysis is as in Table 7:

Table 7: Opportunity Analysis

	GPP	SPP
Customer diversification	Direct uses (brine water utilisation) and indirect uses (electricity production)	Only for electricity High: SPP Rooftop, SPP integrated in buildings or new modern home cluster, SPP integrated with internet
Market expansion	Limited but there are new industrial segment of customer to generate more income	broadband and bank instalments (Green Smart Power PT PLN (Persero)), SPP for rural areas.

For the opportunity, the conclusions are:

- GPP has the chance to have customer diversification such for direct uses.
- SPP has market expansion throughout Indonesia as the equatorial country and Government of Indonesia has been stipulated SPP rooftop regulation.
- In the views of authors, the GPP has more market potential because of its direct uses by utilising brine water, but SPP could penetrate all the market region since Indonesia is the equatorial country.

For the threat, the analysis is as in Table 8:

Table 8: Threat Analysis

	GPP	SPP
Insurability Risk	Highest	Less Risky
Bankability	Highest	Moderate
Competition for HR/business switching from oil and gas sectors	High	No
Energy storage/reserve power back-up for realibility	None	Yes

For the threat, the conclusions are:

- GPP has highest risk due to insurability and bankability, especially in earlier stage / exploration stage, compared to SPP and all kinds of renewable energy.
- GPP competition to other energy business especially from oil/gas sectors is hard especially for human resource and business intention.

- GPP cost of electricity reduction is not as competitive as SPP.
- SPP will lose its competitiveness if the energy storage and reserve power back-up are applied due to its high investment.
- In the views of authors, the GPP is the riskiest project, therefore both GPP and SPP need to mitigate it carefully.

The complete SWOT analysis is as in Table 9:

Table 9: Complete SWOT Analysis

<b>Strengths</b>	<b>Weakness</b>
*GPP ^ SPP	*GPP ^ SPP
<b>Opportunities</b>	<b>Threats</b>
*GPP ^ SPP	*GPP ^ SPP

It is clear that GPP dominates all aspects of SWOT

### 3.1. Policy gap analysis

The Geothermal Energy Market crucial conditions:

- The Indonesia electric policy is based on the energy affordability. To support the affordability, Gol uses tax incentives or subsidy which means burden on national economic security. To avoid such heavy burden, Gol set the standard of electric price for electric power purchase called BPP. Any electric energy produced by Independent Power Producer (IPP) has been limited to 85 % of BPP as electric power purchase price for SPP and 100 % of BPP for GPP. It is viewed as a burden from IPP, but there is opportunity to have more efficiency in order to reduce the production cost.
- Gol offers PLN as national state owned company to run geothermal energy business including PSPE incentives to ease exploration risk. This initiatives could cause IPP demotivated to explore geothermal energy although Gol had already stated and describe the criteria for it.
- There is no insurance company to cover the exploration risk
- Lack of data inquiry to provide insurance requirement of documentations
- Power Purchase Agreement (PPA) is non-bankable since there is no guaranteed proven reserve to support the needs of national electric operator (PLN)

Regulations for easing the crucial condition:

- Gol should have incentives rule to boost cost efficiency of renewable energy
- Gol should have clear criteria and rules to the share of geothermal energy business between PLN and IPP as energy producer and buyer and provide clear and condusive communication.
- Gol should have Insurance backup to insure the exploration risk and coordinate and regulate the related team such as developer, bank, and geothermal insurance company as integrated team to provide such data and fund to support insurance requirement and inquiry

The SPP energy market crucial conditions:

- SPP interconnection to electric grid is still the problem due to electric storage/reserve power availability to back up SPP intermittency
- SPP electricity generation cost is still high

Regulations for easing the crucial condition

- Gol should boost the soft loan, grant, incentives and regulation to reduce the cost of energy storage and the reserve power development for back up variable renewable energy such as SPP into the electric grid.
- Incentives for cost reduction through invention or efficiency

#### 4. FINDINGS AND RECOMMENDATIONS

Tables 10 and 11 contain the findings and pending matters to conduct either GPP or SPP in Indonesia. For SPP, the solution and recommendation are as following:

*Table 10: SPP Findings and Pending Matters*

	Developer	Government of Indonesia	Pending Matters
Energy Reliability	Unfavoured	Favoured	Dependency on local radiation and weather, impacts to the capacity factor and grid stability
Revenue Stream	Moderate	Moderate	-
Electricity Generation Cost	Moderate	Moderate	Regulator must be able to maintain the interests of renewable energy developers, because the current structure of electricity business in Indonesia.
Investment Risk	Moderate	Moderate	-
Payback Period	Moderate	Moderate	-
Key People/HR	Moderate	Moderate	-
Insurability/Bankability	Moderate	Moderate	-
Technology Risk	Moderate	Moderate	New incentives to stimulate technology to reduce the price
Customer diversification	Moderate	Moderate	-
Market expansion	High	High	New incentives to expand the market

The solution and recommendation for SPP are as following:

- SPP is far less reliable than GPP. SPP is highly dependent on local radiation level and weather.
- To conduct SPP project properly:
  - More incentives for SPP to reduce the cost.
  - More incentives for SPP to construct all over the grid which is technically feasible because of its location in equatorial line
  - Incentives and funding for energy storage and reserve power in electric grid for supporting energy reliability
- Market expansion of SPP is widely open, since Indonesia is an equatorial country, thus it is ideal to answer energy equity especially electricity accessibility in Trilemma Energy question.

For GPP, the solution and recommendation are as following:

*Table 11: GPP Findings and Pending Matters*

	Developer	Government of Indonesia	Pending Matters
Energy Reliability	Favour	Favour	PSPE and Government Drilling is still on progress.
Revenue Stream	Compensate Electric Loss	New Income Taxation and Production Bonus Potential for Local Government	PSPE and Government Drilling is still on progress.
Electricity Generation Cost	Favourable for second stage	Hard for development in Greenfield's Area	Regulator must be able to maintain the interests of renewable energy developers, because the current structure of electricity business in Indonesia.
Investment Risk	High	High	PSPE and Government Drilling is still on progress.
Payback Period	Long	High	New Update for Fiscal Incentives.
Key People/HR	Difficult	Difficult	-
Insurability/Bankability	Low	Low	PSPE and Government Drilling is still on progress.
Technology Risk	High	High	New incentives to stimulate technology to reduce the price
Customer diversification	Lucrative	Lucrative for taxation	Government Regulation on Geothermal for Direct Uses is not finished yet.

	Developer	Government of Indonesia	Pending Matters
Market expansion	Limited	Limited	Government Regulation on Geothermal for Direct Uses is not finished yet.
Insurability Risk	High	High	Government Drilling program and PSPE is still on progress.
Bankability	Low	Low	Government Drilling program and PSPE is still on progress.
Competition for HR/business switching from oil and gas sectors	High	High	The New Assessment Process and Regulation from Oil / Gas Drilling Expertise to Geothermal Drilling Expertise

The solution and recommendation for GPP are as following:

- GPP is the more reliable than SPP with high risk in technical and economic considerations, thus it is ideal to answer energy security in trilemma energy question
- To conduct GPP project properly:
  - PSPE and Geothermal Drilling must be done properly and fairly to guarantee proven reserve in order to have insurable and bankable project in integrated team such as developer and bank.
  - More incentives on new GPP greenfield.
  - Direct uses from geothermal energy should be eased to sell, so the developer will get additional income and attractive payback period.
  - The incentives to focus on geothermal energy should attract the developer from switching to oil and gas sector
- Human Resource must be maintained carefully, since there is a competition to recruit drilling expert and other related expertise between GPP and oil gas sector due to its job almost similar.
- Criteria, regulation and position between PLN and IPP should be constructed clearly
- The integrated team of developer, bank should be regulated and coordinated by Gol in order to provide data and fund to support insurance requirement and inquiry for proven reserve.
- Gol should have Insurance backup to insure the exploration risk and coordinate and regulate the related team such as developer, bank to provide such data and fund to support insurance requirement and inquiry

Based on SWOT and Policy Gap Analysis above based on trilemma energy foundation, the recommended priority and criteria for GPP and SPP could be summarised as follows:

- In the long term conditions (over 5 years of exploration and construction period), GPP fits to provide energy security and affordability
- Whilst, in the short term conditions, SPP fits to provide energy accessibility.
- SPP fits to remote area and the share of SPP in electric grid should be supported by energy storage or reserve power availability
- IPP should invest in GPP for long term goal
- IPP should invest in SPP for short term in on-grid system which has been provided its reliability in the case of intermittency (sufficient backup power generation or electric energy storage)

## 5. REFERENCES

Coorporate Secretary PT PLN (Persero) (2019) *PLN Statistics 2018*. Edited by Coorporate Secretary PT PLN (Persero). Jakarta. Available at: <https://www.pln.co.id/statics/uploads/2019/07/STATISTICS-English-26.7.19.pdf> (Accessed: 29 July 2019).

DGNREEC MEMR Republic of Indonesia (2019) *The Achievement of Directorate General of New, Renewable Energy, and Energy Conservation February 2013 - February 2019*. Jakarta. Available at: <https://drive.esdm.go.id/wl/?id=FR8x6zWfLWx43U8LuAJ2HcAtTtJ5gAxl> (Accessed: 25 July 2019).

Energift (2016) *Pemanfaatan Panas Bumi untuk Industri - Panas Bumi Sulawesi Utara*. Available at: <http://panasbumi.sulutprov.go.id/id/2016/09/02/industri-kecil-dan-menengah/> (Accessed: 30 July 2019).

Ernst & Young LLP (2019) *Renewable Energy Country Attractiveness Index*. Available at: [https://www.ey.com/Publication/vwLUAssets/ey-RECAI-Index-53-scores-ladder/\\$FILE/ey-RECAI-Index-53-scores-ladder.pdf](https://www.ey.com/Publication/vwLUAssets/ey-RECAI-Index-53-scores-ladder/$FILE/ey-RECAI-Index-53-scores-ladder.pdf) (Accessed: 30 July 2019).

Green Energy Poland S.A. (2010) *Green Certificates – Mechanism of Action, The Price, The Principles of Turnover*. Available at: <http://gepsa.pl/en/322-2/> (Accessed: 30 July 2019).

Iglinski, B. *et al.* (2015) 'SWOT Analysis of The Renewable Energy Sector in Poland. Case Study of Wielkopolskie Region', *Journal of Power Technologies*, 95(Renewable and Sustainable Energy), pp. 143–157. Available at: <http://papers.itc.pw.edu.pl/index.php/JPT/article/download/669/668> (Accessed: 30 July 2019).

IRENA (2018) *Renewable Power Generation Costs in 2017*, International Renewable Energy Agency. Abu Dhabi. Available at: [https://www.irena.org/-/media/Files/IRENA/Agency/Publication/2018/Jan/IRENA\\_2017\\_Power\\_Costs\\_2018.pdf](https://www.irena.org/-/media/Files/IRENA/Agency/Publication/2018/Jan/IRENA_2017_Power_Costs_2018.pdf) (Accessed: 28 September 2018).

IRENA (2019) *Renewable Power Generation Costs in 2018*, International Renewable Energy Agency. Abu Dhabi. Available at: [https://www.irena.org/-/media/Files/IRENA/Agency/Publication/2019/May/IRENA\\_Renewable-Power-Generations-Costs-in-2018.pdf](https://www.irena.org/-/media/Files/IRENA/Agency/Publication/2019/May/IRENA_Renewable-Power-Generations-Costs-in-2018.pdf) (Accessed: 29 July 2019).

Li, K. (2015) 'Update on Comparison of Geothermal with Solar and Wind Power Generation Systems', in *Proceedings World Geothermal Congress*. Melbourne, pp. 19–25. Available at: <http://www.ladeltascience.com/earth/volcano/volcano.html> (Accessed: 29 July 2019).

MEMR Republic of Indonesia (2017) *Regulation of MEMR Republic of Indonesia Number 50 Year 2017 on Utilization of Renewable Energy Sources for Power Supply*. Jakarta. Available at: [https://jdih.esdm.go.id/peraturan/Permen ESDM Nomor 50 Tahun 2017 \(Terjemahan\).pdf](https://jdih.esdm.go.id/peraturan/Permen ESDM Nomor 50 Tahun 2017 (Terjemahan).pdf) (Accessed: 26 July 2019).

MEMR Republic of Indonesia (2019a) 'Booklet Energi Berkeadilan Q4 2018 English (Update May-2019).pdf'. Jakarta, p. 54. Available at: [file:///C:/Users/pingu/Downloads/Booklet Energi Berkeadilan Q4 2018 English \(Update May-2019\).pdf](file:///C:/Users/pingu/Downloads/Booklet%20Energi%20Berkeadilan%20Q4%202018%20English%20(Update%20May-2019).pdf).

MEMR Republic of Indonesia (2019b) *Respon Atas Potensi Isu Negatif Sektor Energi dan Sumber Daya Mineral*. Available at: <https://drive.esdm.go.id/wl/?id=2QG6JR27rreD8TgDC7o7pv8yCn4gBhwm> (Accessed: 30 July 2019).

Munich RE (2015) *Exploration Risk Insurance - Munich Re's Experience in Turkey*. Available at: <https://www.irena.org/-/media/Files/IRENA/Agency/Events/2015/Oct/5/S34GeothermalExplorationInsuranceTurkeyMunichRE.pdf?la=en&hash=4E90B16528F46D6BE7DEBB035B2E2A9B558EF701> (Accessed: 30 July 2019).

National Energy Council (DEN) (2017) *Technology Data for the Indonesian Power Sector*. Jakarta. Available at: <https://www.den.go.id/index.php/publikasi/download/55>.

Permana, N. Y. (2017) *Luncurkan Program PSPE, Investasi Panas Bumi Menggeliat - Kementerian ESDM Republik Indonesia*. Available at: <http://ebtke.esdm.go.id/post/2017/07/12/1706/luncurkan.program.pspe.investasi.panas.bumi.menggeliat> (Accessed: 25 July 2019).

Purba, D. P. *et al.* (2019) 'Key Considerations in Developing Strategy for Geothermal Exploration Drilling Project in Indonesia', in *Proceedings, 44th Workshop on Geothermal Reservoir Engineering*. California, p. 12. Available at: <https://pangea.stanford.edu/ERE/db/GeoConf/papers/SGW/2019/Purba.pdf> (Accessed: 25 July 2019).

Rachman, A. *et al.* (2015) 'International Journal of Energy Economics and Policy.', *International Journal of Energy Economics and Policy*, 5(4), pp. 918–925. Available at: <https://www.econjournals.com/index.php/ijeep/article/download/1227/909> (Accessed: 30 July 2019).

Setiawan, E. A. and Dewi, K. (2013) 'Impact of Two Types Flat Reflector Materials on Solar Panel Characteristics', *International Journal of Technology (IJTech)*, 4(2), pp. 188–199. Available at: <http://www.ijtech.eng.ui.ac.id/old/index.php/journal/article/view/108>.

Sommeng, A. N. and Anditya, C. (2018) 'Boosting Renewable Power Generation in Indonesia Electricity Sector: A Policy Action by The Government', in E. Kusriani, F.H. Juwono, A. Y. and E. A. S. (ed.) *E3S Web of Conferences*. Bali: EDP Sciences, p. 9. doi: 10.1051/e3sconf/20186702060.

Sukaryadi, D. (2013) 'Menjemur Produk Pertanian dengan Air Panas Bumi (Hot Spring) di Desa Bakan, Bolaang Mongondow, Sulut', in *13th Indonesia International Geothermal Convention and Exhibition 2013*. Jakarta, p. 8.



---

## #112: Liquid propellant: catalyst pack pressure drop effect of 50 N green thruster

---

Muhammad Shahrul Nizam SHAHRIN, Norazila OTHMAN\*, Mastura AB WAHID,  
Mohammad Nazri M. JAAFAR

*Aeronautics Laboratory, School of Mechanical Engineering, Faculty of Engineering, Universiti Teknologi  
Malaysia, 81310, Johor Bahru, Johor, Malaysia*  
\*Corresponding author: norazila@mail.fkm.utm.my

*Catalyst pack pressure drop ( $\Delta P_{cp}$ ) is an important design parameter to know the performance of thruster. Based on this problem, the aim of this study is to determine the performance of 50 N green thruster from catalyst pack pressure drop value in term of group parameter. A group of parameter is affecting catalyst pack pressure drop is involving parameter such as catalyst pack heating temperature ( $T_{cp}$ ), injection pressure ( $\Delta P_{in}$ ), inversely proportional of mass flux ( $\phi$ ) (catalyst pack pressure drop is known to be a function of mass flux) and the injector ( $D_i$ ) or nozzle throat diameter ( $D_t$ ). Experimental investigations are carried out under the controlled conditions in Liquid Propulsion Laboratory located in Aeronautics Laboratory, Universiti Teknologi, Malaysia. Tests are performed under the catalyst packs heating temperature in range 75°C to 200°C, the compaction pressure for catalyst pack are 6.0 MPa and 9.3 MPa, the injection pressure in range of 29 Bar to 37 Bar and two different injector diameter, 1.045 mm and 1.367 mm, and nozzle throat diameter, 4.574 mm and 3.588 mm. From the study, the effect of each operating parameters denotes that the effect of catalyst pack pressure drop (function of mass flux) affects the decomposition efficiency is identified. The small diameter injector of 1.045 mm with large nozzle throat diameter 4.574 mm, compaction pressure about 9.3 MPa and injection pressure about 37 Bar are achieved the optimum thruster configuration setting for approximate 50 N thrust production. However, the effect of large injector diameter and small nozzle throat diameter will decline in decomposition efficiency in this study. Additionally, the effect of catalyst pack heating temperature on the catalyst pack pressure drop ( $\Delta P_{cp}$ ) does not lead to any correlation to the decomposition efficiency and thruster performance.*

*Keywords: catalyst pack; heating temperature; injection pressure drop; injector, mass flux; nozzle throat; thruster*

## 1. INTRODUCTION

Propellant is significant used on a variety of rocket, spacecraft, micro and mini satellites, tactical missiles and even reusable launch vehicle. They are in a form of bi-propellant or monopropellant liquid propulsion fuel and solid propulsion fuel. Hydrazine and its based propellant are one of the champion in the propulsion system application as it has become the liquid monopropellant of choice for few decades (Anflo & Grönland, 2012). Other than hydrazine, propellant such as ammonium perchlorate also are being replaced as the current trend for solid propellant and direction in a green space propulsion (Gohardani et al., 2014). As the toxicity and carcinogenic behaviour of such kind of propellants, a greener propellant had become an alternative in the thruster application such as Hydrogen Peroxide (H<sub>2</sub>O<sub>2</sub>), Hydroxylammonium Nitrate (HAN), and Hydrazium Nitroformat (HNF), and Ammoniumdinitramide (ADN) (Anflo & Grönland, 2012) for liquid propellant specifically.

In addition, propulsion technologies categorised into few section depend on the mission and uses of that particular propulsion technologies such as to be used as escape propulsion, in-space and outer space propulsion (Salgado, Belderrain, & Devezas, 2018). Common propulsion technologies are chemical based propulsion, it can be in form of solid, liquid, hybrid and green propellants, and non-chemical propulsion such as plasma (electric or ionic propulsion), solar sail and tether propulsion (Salgado et al., 2018). More advanced propulsion technology also developed such as thermo-nuclear based propulsion, laser and also fusion propulsion (Salgado et al., 2018). Solid propellant usually used in launch vehicles especially in booster engine such that in Space Shuttle, Delta IV, Atlas V, Ariane 5 and also in intercontinental ballistic missiles (ICBM) (Salgado et al., 2018). Solid fuel has a good record and performance, and very reliable propellant but main disadvantages are that the thrust output cannot be controlled, and cannot be switched off once it had burnt (Salgado et al., 2018) as shown in Figure 1.

In contrast, liquid propellant use liquid materials as oxidiser hence the name. Two main types of liquid propellant are using bi-propellant and monopropellant. Usually, it consists of fuel and oxidiser where both are stored in separate tank and will be pumped into the combustion chamber where burning occurs is called bi-propellant system (Salgado et al., 2018). While monopropellant system that is using in this study consists of propellant tank and catalyst where when both undergo reaction at high pressure, a decomposition of the propellant take place in the thruster engine as shown in Figure 2. The thruster produces the thrust, the work done (thrust) that obtained from the variation parameter set such as reaction pressure, decomposition of monopropellant based high grade hydrogen peroxide (Hg-H<sub>2</sub>O<sub>2</sub>), diameter of injector (orifice) and even diameter of nozzle throat. Therefore, the investigation of this parameter is important.

Thus, the aim of this paper is to investigate the potential operating parameter for thruster performance analysis using a high-grade H<sub>2</sub>O<sub>2</sub> (Hg-H<sub>2</sub>O<sub>2</sub>). Therefore, the scope of this study achieves from the background of study, which is from green propellant candidates' characteristics, catalyst and catalyst bed. Next, the methodology is experimental setup, the preparation of Hg-H<sub>2</sub>O<sub>2</sub>, decomposition of Hg-H<sub>2</sub>O<sub>2</sub> and performance evaluation based on theoretical calculation about the thruster design. Thus, it helps in choosing the suitable operating parameter for expected thrust. In addition, the result and discussion were stated to prove that, the knowledge establishes for this study and finally yet important is conclusion.

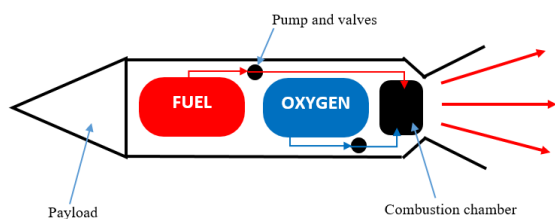


Figure 1: Liquid propulsion

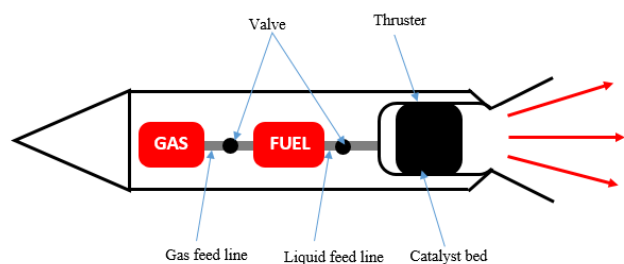


Figure 2: Monopropellant system

## 2. BACKGROUND OF STUDY

Green liquid propellant has emerged onto the surface of featured propellant of choice due to awareness on environmental aspect, as well as an opportunity to save cost at better or at least similar performance and other several things that were taken into consideration (Gohardani et al., 2014). Most of the studies done on green propulsion system usually aims to provide replacement or alternative to the toxic and carcinogenic propellant such as hydrazine (Amri, Gibbon, & Rezoug, 2013; An & Kwon, 2009; Baek, Jung, Kang, & Kwon, 2018; Essa et al., 2017; Florczuk & Rarata, 2017; Gohardani et al., 2014; Guerrieri, Silva, Cervone, & Gill, 2017; S. L. Lee & Lee, 2009; Okninski et al., 2017; Salgado et al., 2018; Scharlemann et al., 2013; Schmidt & Wucherer, 2004). Liquid

green propellant possesses the characteristics and versatility in replacing hydrazine based propellant. However, green propellant must show that it has the potential benefits for the end users (Anflo & Grönland, 2012). The potential benefits of a green propellant system are binary, to have a better performance at shortened lead time and reduced overall cost (Anflo & Grönland, 2012). The better performance of green propellant has characteristics such as high specific impulse, high pulse mode performance, and blow down capability. Instead, not only on environmental issue, green propellant is expected to have a required performance, easier to work with and eventually reduce the overall cost due to simplification in term of safety, handling procedure, and storage. On the environmental issue, hydrazine is no single handed being responsible for the raise of the green propellant trend. However, hydrazine derivatives and other type of propellants such as MMH, UDMH, A-50 (hydrazine and UDMH at 50/50 mixture), and also oxidisers such as NTO, MON, RFNA and WFNA (Florczuk & Rarata, 2017; Schmidt & Wucherer, 2004). These type of propellants are the combinations of the very toxic, corrosive and difficult in storage fuels and oxidisers (Florczuk & Rarata, 2017).

Cost of spacecraft fuelling and launch vehicles consist of six criteria, which are, (i) cost of propellant, (ii) cost of labour to move propellant from the shipping container to the spacecraft, (iii) cost of health surveillance of the fuelling personnel, (iv) depreciation of Ground Service Equipment (GSE), (v) decontamination of transfer lines, and (vi) cost of disposal residuals. In which all these cost listed are envisioned to have certain degree of different for green and non-green propellants (Schmidt & Wucherer, 2004). If the green propellant manages to be in a way that performance to the cost ratio higher than the typical liquid propellant then, it has a bright future in the industries and environment. Besides being a less toxic, green propellants have advantages over hydrazine in term density and freezing point such as summarised in Table 1 with small tolerance in specific impulse.

Table 1: Performance of established monopropellants (Baek et al., 2018)

Characteristics	HAN-based	AND-based	98 wt % H <sub>2</sub> O <sub>2</sub>	Hydrazine
Freezing point, °C	-100	-7	-1.4	2
Density, g/cm <sup>3</sup>	1.4	1.2	1.4	1
Vacuum I <sub>sp</sub> , s	253	253	186	225
Adiabatic decomposition temperature, °C	1749	1780	952	850
Toxicity	Low	Low	Low	High

These challenging aspects in research and development show that the task such as green propellant candidates is first important material that contributes the production of green propellant. Second is catalyst, decomposition of liquid propellant support to complete the combustion. In addition, the challenging from catalyst bed also measured for the potential amount of thrust that produces from thruster.

## 2.1. Green propellant candidates

Table 2 shows the green propellant candidates. The reduction in toxicity, reliable performance potential, easier to handle and store and, for some cases where a big reduction in purchasing cost (Scharlemann et al., 2013). 10 of propellant form the list had been experimentally tested which are AND based, AN based, hydrogen peroxide, ethanol, heptane, kerosene (Jet-A1), d-Limonene, octane, turpentine and solid fuel (Scharlemann et al., 2013). Current works in replacing hazardous propellants such as hydrazine and ammonium perchlorate represents or an effort of identification the green propellants that result in less harmful environmental impact one of the ongoing trends in green propulsion (Gohardani et al., 2014). Less toxic option for replacing monopropellant hydrazine which are hydrogen peroxide, nitrous oxide fuel blends and ionic liquids (Gohardani et al., 2014).

Hydrogen peroxide can be used as monopropellant as well as an oxidiser in bi-propellant system. Hydrogen peroxide is thermodynamically unstable, very reactive and decomposes slowly even in its most stabilised form but possess a theoretically lower specific impulse than that of hydrazine (Gohardani et al., 2014). However, hydrogen peroxide blended ethanol have a feasibility as a high performance green monopropellant which possess equal or better performance than hydrazine (Baek et al., 2018). Kamil Sobczak et al. stated that high grade hydrogen peroxide not only as an oxidiser but also serves as fuel ignition in bipropellant system and also stated three main advantages of the concept are, (1) green, non-toxic and easy to handle, (2) performance comparable to conventional MMH/MON propulsion, and (3) self-ignition and unlimited restart-ability (Sobczak et al., 2017).

Table 2: Green propellant candidates (Scharlemann et al., 2013)

Monopropellant/oxidiser	Fuel
Ammonium dinitramide (ADN)	Butane
Ammonium nitrate (AN)	Dibutyl ether
Hydroxylammonium nitrate (HAN)	Diethylenetriamine
HAN-ADN-HNF-AN	Dimethylether
Hydrazinium nitroformate (HNF)	Ethanol
Hydrogen peroxide	Heptane
Nitrous oxide	Isopropyl alcohol
	Kerosene (Jet-A1)
	d-Limoene
	Methane
	Octane
	HTPB
	PMMA

## 2.2. Catalyst

Catalyst plays an important role in monopropellant, liquid bi-propellant and hybrid thrusters (Okiniski et al., 2017). The decomposition of liquid non-hypergolic propellant depends on the competency of the catalyst bed system (Essa et al., 2017; J. Lee & Kwon, 2013; Okninski et al., 2017). The working principle of this system requires a catalytic decomposition through a metal-based catalyst which made catalyst became a paramount parameter, thus numerous studies have focused on catalyst reactor design, catalyst reactivity and supports, catalyst additives, and catalyst poisoning (Jang, Kang, & Kwon, 2015). As an example, the decomposition of hydrogen peroxide can be catalysed by few types of catalytic material such as platinum, palladium, iridium, silver, silver oxide, potassium permanganate and few other that interchangeable depend on type of the thruster and mission requirement. The catalyst in the monopropellant is one of the major contributing factors for the efficiency of the thruster itself with respect to the green liquid propellant that is used. Catalyst contributes to the decomposition of the liquid propellant where these factors including injection pattern, material of catalyst, physical/geometrical characteristics of the catalyst (pellets, gauges, foams, powder, honeycomb, etc.) nature of carrier material, nature of active catalysts, manufacturing process variations, lifetime, and many others (Kang, Lee, Kang, & Kwon, 2017; Scharlemann et al., 2013). Many studies had been done with regards to develop the most efficient catalyst for the liquid green propellant. In this study, a silver strip is used as catalyst material.

## 2.3. Catalyst bed

Catalyst bed or catalyst pack is made of any catalytic material that when mixed with the liquid propellant produces a decomposition reaction. The catalyst bed need to have the ability of rapid and repeatable performance over a multitude of operational cycles based on particular mission strategy (Essa et al., 2017). The performance of catalyst is depending on two most important things that are surface area of the catalyst bed and pressure drop inside the catalyst bed. A high performing catalyst bed has high surface area per unit volume and a low-catalyst pack pressure drop. Both criteria are contradicting each other and necessary design trade-off must be considered. High surface area of the catalyst bed provides a better opportunity for the propellant to react with the catalyst. However, higher surface area means that the catalyst bed must be tightly-packed which eventually usually led to higher pressure drops (Essa et al., 2017). In this study, about 200 pieces of silver strips is compressed to form the catalyst bed. The compaction pressure is 6.0 MPa and 9.3 MPa.

## 3. METHODOLOGY

In this study, the methodology is explaining for working mechanism of monopropellant thruster for experimental task, the preparation of Hg-H<sub>2</sub>O<sub>2</sub> and the decomposition reaction between H<sub>2</sub>O<sub>2</sub>/catalyst. Figure 3 shows the cross-section views of basic monopropellant thruster used in this study.

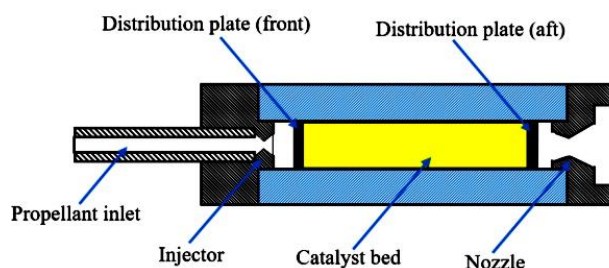


Figure 3: monopropellant thruster cross-sectional view

### 3.1. Working mechanism of monopropellant thruster

Monopropellant typed thruster engine are regularly used as the attitude and altitude control for spacecraft such as satellites and also launch vehicles (Jang et al., 2015). Monopropellant thruster work by generates high temperature, high speed, gases by decomposition of single propellant. The propellant is injected into a catalyst bed containing catalyst from silver strips shows in Figure 4. The decomposition process occurs and producing thrust that channelled throughout the nozzle.

Typical component of monopropellant thruster consists of a propellant tank, injector, catalyst bed, distributor plates and nozzles as shown in Figure 5. Liquid propulsion system can be categorised into pump fed system or pressure fed system (Ul-Haq, Khan, & Mehmood, 2017). The pressurised gas usually nitrogen, are used to deliver pressure into the propellant tank when the valve is released. High-pressure propellant injects into the catalyst bed when the valve releases where both valves controlled to get the required injection pressure, in this study the injection pressure is 29 Bar and 37 Bar. Upon decomposition of hydrogen peroxide that occurs inside the catalyst bed, a pressure drops happened along the catalyst bed and to prevent the catalyst bed from breaking, catalyst is blocked with distributor at the end of the reaction chamber. Distributor usually made of metal plate with holes. Decomposed hydrogen peroxide passes through these holes of the distributor into the nozzle.



Figure 4: Silver strips ready for compaction process.

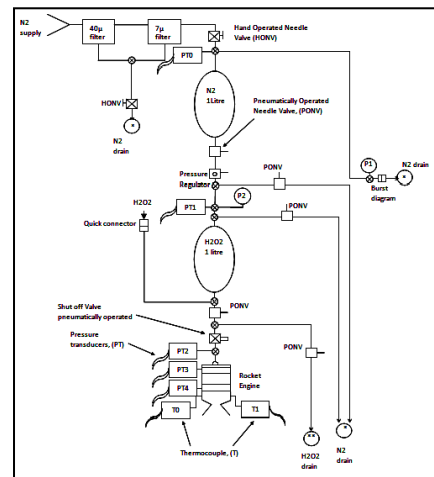


Figure 5: Line diagram of the test facility.

### 3.2. Preparation of high-grade hydrogen peroxide

Hydrogen peroxide used for catalytic decomposition in thruster engine are made of high-grade hydrogen peroxide, Hg-H<sub>2</sub>O<sub>2</sub> with concentration of about 90 % that usually called as High Test Peroxide (HTP) (Jo, 2017; Kang et al., 2017; S. L. Lee & Lee, 2009; Ul-Haq et al., 2017). Hg-H<sub>2</sub>O<sub>2</sub> are highly concentrated and highly purified when most of the additives is removed during the process of preparing it as shown in Figure 6. Additives found in hydrogen peroxide are actually the stabilisers used by the manufacturers to stabilise hydrogen peroxide that is diluted at certain concentration. Concentration of hydrogen peroxide, temperature, pH value, impurities, and stabilisers give significant implication on the rate of decomposition (Othman, 2011). Figure 6 shows the production of high-grade hydrogen peroxide using rotary evaporator machine in Liquid Propulsion Laboratory Universiti Teknologi Malaysia.

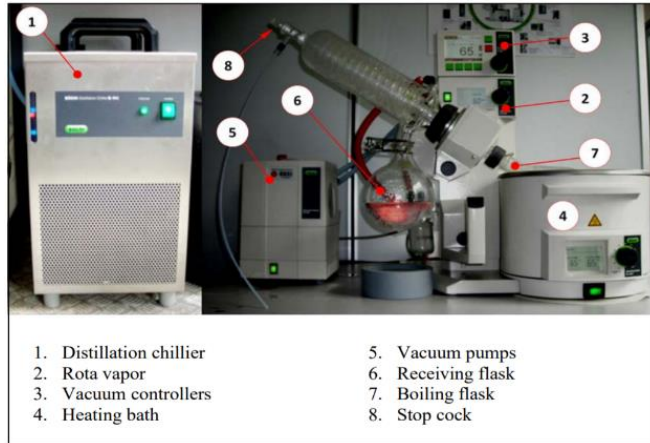


Figure 6: the instrumentation of the rotary evaporator machine for preparing the high-grade hydrogen peroxide.

### 3.3. Decomposition of hydrogen peroxide

The decomposition of high-grade hydrogen peroxide fused with the catalyst. In this study, silver strips is used as shown in Figure 4 it was prepared by compressed them for specific pressure and then, it was placed inside the catalyst bed. At high pressure, the reaction of both materials that breaks the bonding in peroxide chain produces decomposed into water in form of steam, oxygen gas and releasing heat from the exothermic reaction. High pressure and high temperature gas are channelled through nozzle and thrust is produced. Following reaction is achieved as given in Equation 1.



Where:

- $H_2O_2$  = Hydrogen peroxide
- $H_2O$  = Water
- $O_2$  = Oxygen

Based on the Equation (1), the energy released in form of heat during the decomposition process of high grade hydrogen peroxide reached temperature of about 1000K (Jo, 2017; S. L. Lee & Lee, 2009; Li, Ge, Wei, & Li, 2016; Othman, 2011; Ul Haq et al., 2017). The thruster performance depends on the capability of the catalyst bed (silver strips quantity as shown in Figure 6) to decompose all the hydrogen peroxide in monopropellant system (Essa et al., 2017). According to Sungyong An et al., the decomposition capacity of the catalyst bed is a central parameter in designing a thruster for a larger thruster design and since the mass flux as given in Equation 2. It indicates the decomposition capacity of catalyst bed but it does not show the overall capacity of the catalyst because the length parameter of the catalyst bed is absent (An & Kwon, 2009). Sungyong An et al. also state that instead of mass, the decomposition capacity as shown in Equation 3 is more accurate in describing the capacity of catalyst bed where the rate of decomposition of the propellant was assumed to be proportional to the volume of the catalyst bed and inversely proportional to the propellant mass flow rate (An & Kwon, 2009).

Equation 2: Decomposition capacity of catalyst bed

$$G = \frac{\dot{m}}{A} = \frac{\text{propellant mass flow rate}}{\text{cross-sectional area}}$$

Equation 3: Mass flux,  $\Phi_2$

$$\text{Decomposition capacity} = \frac{\text{propellant mass flow rate}}{\text{catalyst bed volume}}$$

### 3.4. Performance evaluation methods for thruster design

The main focus of the thruster performance evaluation is based on the characteristic velocity,  $C^*$ , as shown in Equation (4) and Equation (5). It is one of the parameter that reflect the performance of catalyst bed (Essa et al., 2017).  $R_u$  is the universal gas constant,  $T_c$ ,  $P_c$ , and  $A_t$  are measured nozzle temperature, nozzle entry stagnation pressure, and nozzle throat area,  $\dot{m}$  is the propellant mass flow rate,  $\bar{M}$  is the molar mass of propellant decomposition and  $\gamma$  is the ratio of specific heats (Essa et al., 2017; Othman, 2011). If the thruster is under ideal

(isentropic) conditions, both  $C^*$  values could be similar but due to non-ideal in the thruster operation and errors in the measured quantities, then the two values distinct by a slight amount are common (Essa et al., 2017). Theoretical maximum value of  $C^*$ , for monopropellant system is achieved after the propellant is totally decomposed or reacted under isentropic conditions (Essa et al., 2017). The performance of the catalyst bed is calculated by projecting the value of  $C^*$  efficiency (Essa et al., 2017). The real value of  $C^*$  predicted from the experimental assessments, divided by the theoretical maximum value gives the  $C^*$  efficiency value as shown in Equation 6 (An & Kwon, 2009; Essa et al., 2017). The decomposition of propellant with good performing catalyst bed usually have a  $C^*$  efficiency of 90% or more (Essa et al., 2017; Othman, 2011).

Equation 4: Theoretical characteristic velocity

$$C_{theo}^* = \sqrt{\frac{1}{\gamma} \left( \frac{\gamma + 1}{2} \right)^{\frac{\gamma + 1}{\gamma - 1}} \frac{R_u T_c}{\bar{M}}}$$

Equation 5: Experiment characteristic velocity

$$C_{exp}^* = \frac{P_c A_t}{\dot{m}}$$

Equation 6: Efficiency of characteristic velocity

$$\eta_{C^*} = \frac{C_{exp}^*}{C_{the}^*} \cdot 100$$

Thrust level,  $F$ , and the specific impulse,  $I_{sp}$ , can be calculated as shown in Equation 7 to 9 for defined thruster geometry, chamber pressure and ambient conditions (Amri et al., 2013; An & Kwon, 2009).  $C_F$  is vacuum thrust coefficient and  $g_0$  is gravitational constants.

Equation 7: Theoretical thrust

$$F_{theo} = A_t P_0 \gamma \left[ \left( \frac{2}{\gamma - 1} \right) \left( \frac{2}{\gamma + 1} \right)^{\frac{\gamma + 1}{\gamma - 1}} \left( 1 - \left( \frac{P_e}{P_0} \right)^{\frac{\gamma - 1}{\gamma}} \right) \right]^{\frac{1}{2}} + (P_e - P_a) A_e$$

Equation 8: Experiment thrust

$$F_{expt} = P_4 A_t C_F$$

Equation 9: Specific Impulse

$$I_{sp} = \frac{F_{theo/expt}}{\dot{m} g_0}$$

#### 4. RESULTS AND DISCUSSION

The fabricated 50 N thruster is designed based on Equation 7, however the experiment is necessary to know the performance of this thruster to investigate the operating group parameter that was set as shown in Table 3. The test rig set-up as shown in Figure 5 was connected with four-pressure transducer labelled as  $P_1$ ,  $P_2$ ,  $P_3$  and  $P_4$  and shown in Figure 7. The optimum pressure drop catalyst pack ( $P_3 - P_4$ )  $\Delta P_{cp}$  effects depends on mass flux as shown in Equation 3 through the catalyst bed as bed loading to produce the complete decomposition. The mass flow rate depends on characteristic velocity as shown in Equation 5 is important for mass flux and uses the value of  $P_4$  for experimental results. Therefore, the 30 successful hot tests had been conducted using the 50 N thruster to know the effect of pressure drop across the catalyst pack.

Table 3: Summary of tests

Diameter of injector ( $D_i$ ), mm	Diameter of nozzle ( $D_t$ ), mm	Compaction pressure ( $P_{cp}$ ), MPa	Injection pressure ( $P_2$ ), bar	Catalyst pack heating temperature ( $T_{cp}$ ), °C	Purpose
Series I					
1.367	3.588	6	~29	90,150, 200	To study the effect of injection pressure and temperature.
Series II					
1.367	4.574	9.29	~37 and ~29	75 and 150	To study the effect of injection pressure, engine temperature and compaction pressure between series I and II
Series III					
1.045	4.574	9.29	~37 and ~29	75 and 150	To study the effect of injection pressure, engine temperature and the effect of change diameter of injector between series II and III.

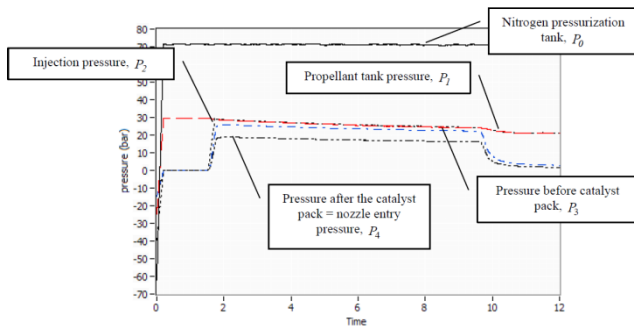


Figure 7: Pressure plot during experiment.

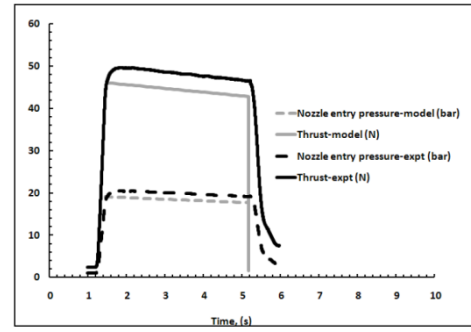


Figure 8: Thrust plot comparison between theory and experiment.

From the series-I, low injector pressure will cause atomisation, feed-system linked instabilities, and effect of catalyst-pack pressure drop is low will significantly produce the low thrust. Therefore, this test decides to increase the catalyst-pack-compaction pressure,  $P_{cp}$  to 9.29 MPa. The series-II and III experiments were conducting for 9.29 MPa catalyst-pack compaction pressure,  $P_{cp}$  and injector diameters of 1.367 mm (series I and II) and 1.045 mm (series-III). For both series II and III, the nozzle throat diameter is 4.574mm, while the series I is 3.588mm for throat diameter.

From the series-II experiments, the injector pressure drop,  $\Delta P_{in}$  ( $P_2-P_3$ ) is low only around 4 to 2.5 bar, but the pressure drop across the catalyst pack,  $\Delta P_{cp}$  is in the acceptable range of 5.5 bar to 8.0 bar. However, the thrust values obtained are close to 50 N. In series-III experiment, the injector diameter was decreased to 1.045 mm. The series-III experiments demonstrate acceptable pressure drops across the injector and catalyst pack. The thrust delivered is also around 50 N. Therefore, comparing experimental results obtained so far from the series-III thruster configuration ( $D_i = 1.045$  mm,  $D_t = 4.574$  mm, and compaction pressure,  $P_{cp} = 9.29$  MPa) is felt to be the most suitable. As an example thrust plot comparison between theoretical and experiment series-III (one result only) as shown in Figure 8.

The pressure drop across the catalyst pack,  $\Delta P_{cp}$  is an important design parameter and this is known to be a function of mass flux,  $\Phi$ . The variations of  $\Delta P_{cp}$  with respect to  $\Phi_2$  for test series I, II III is given in Figure 9(a) for different catalyst-pack heating temperatures. Since, the hot test was conducted with two different catalyst-pack heating-temperature,  $T_{cp}$ , there are two mass fluxes that can be calculated.  $\Phi_1$  is based on the mass flow rate through the injector and  $\Phi_2$  is based on the choked mass flow rate through the nozzle throat. In this study only  $\Phi_2$  was explained. Since the choked mass flow rate through the nozzle represents the effective component of thrust production,  $\Phi_2$  is taken as an effective mass flux. The effect of catalyst-pack heating-temperatures on the  $\Delta P_{cp}$  does not lead to any correlation. In one case, a lower heating temperature has a higher  $\Delta P_{cp}$  while in another case it is in the opposite.

The  $\eta_c$  is known to be proportional to catalyst-pack heating-temperature,  $T_{cp}$ , square root of injector pressure drop  $\sqrt{\Delta P_{in}}$  (which is inversely affects the atomised droplet size of propellant), inversely proportional to mass flux  $\Phi_2$ , and injector diameter  $D_i$  (atomised droplet size is proportional to injector diameter). For simplicity group these

variables in the simple form as  $\frac{T_{cp}\sqrt{\Delta P_{in}}}{\Phi_2 D_i}$ .  $T_{cp}$  is in degree Celsius,  $\Delta P_{in}$  is in bar,  $\Phi$  is in kg/(m<sup>2</sup>s) and  $D_i$  is in

mm. The variation of  $\eta_c$  with respect to  $\frac{T_{cp}\sqrt{\Delta P_{in}}}{\Phi_2 D_i}$  is given in Figure 9(b). Ignition time delay,  $\Delta t_{in}$  could have

significant relationship with  $\frac{T_{cp}\sqrt{\Delta P_{in}}}{\Phi_2 D_i}$ . The variations of  $\Delta t_{in}$  with respect to  $\frac{T_{cp}\sqrt{\Delta P_{in}}}{\Phi_2 D_i}$  for all the 30 tests are

plotted in Figure 9(c). Despite the scattering of the points, the general trend of the experimental results indicates that  $\Delta t_{in}$  will decrease with increasing of  $\frac{T_{cp}\sqrt{\Delta P_{in}}}{\Phi_2 D_i}$ . Based on the trend of series -I, II and III, it was proven that



the catalyst pack pressure drop  $\Delta P_{cp}$  leads the effect to the mass flux value in group of operating parameter  $\frac{T_{cp}\sqrt{\Delta P_{in}}}{\Phi_2 D_i}$ . The higher  $\Delta P_{cp}$ , the higher value of  $\frac{T_{cp}\sqrt{\Delta P_{in}}}{\Phi_2 D_i}$  and the higher thrust as shown in Figure 8.

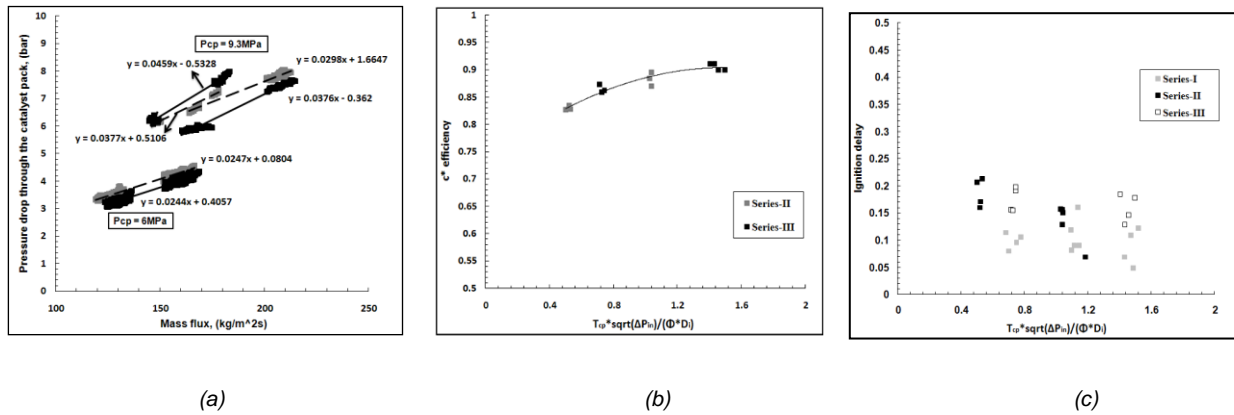


Figure 9: (a) Series-I, II and III pressure drop through the catalyst pack versus mass flux. (b)  $C^*$  efficiency versus

$$\frac{T_{cp}\sqrt{\Delta P_{in}}}{\Phi_2 D_i}. \text{ (c) Ignition delay versus } \frac{T_{cp}\sqrt{\Delta P_{in}}}{\Phi_2 D_i}$$

## 5. CONCLUSION

Green liquid propellant has a bright future in a propulsion application where it can tackle environmental issue, workability issue and at the same time having a performance required for a certain mission. The hydrogen peroxide is alternative green propellant for monopropellant. Conclusion in this study was: i) 50N rocket thruster using hydrogen peroxide monopropellant had been designed, ii) A total of 30 successful rocket firings had been conducted using concentrated and distillate rocket grade hydrogen peroxide and by varying the injector diameter, nozzle throat diameter, catalyst pack compaction pressures, and catalyst-pack heating-temperatures, iii) Method of calculating rocket thruster performance has been developed, iv) Thruster performances of the tested thruster are presented, v) The project has achieved optimum thruster configuration for the production of around 50N thrust with optimum value of catalyst-pack pressure drop for the configuration;  $D_i = 1.045\text{mm}$ ,  $D_t = 4.574\text{mm}$ ,  $P_{cp} = 9.29\text{MPa}$ , and  $p_2 = 37\text{bar}$ , and vi) The project has achieved  $\eta_c^*$  around 0.90 that is close to the industrial values. A

group parameter that affects  $\eta_c^*$  and ignition delay  $\Delta t_{in}$  had been identified as  $\frac{T_{cp}\sqrt{\Delta P_{in}}}{\Phi_2 D_i}$ .

## 6. ACKNOWLEDGEMENT

This work was supported by Ministry of Higher Education under the Fundamental Research Grant Scheme with awards research grant No. 5F099 and School of Mechanical Engineering, Faculty of Engineering, Universiti Teknologi Malaysia for the available facility and supervision.

## 7. REFERENCES

- Amri, R., Gibbon, D., & Rezoug, T. (2013). The design, development and test of one newton hydrogen peroxide monopropellant thruster. *Aerospace Science and Technology*. <https://doi.org/10.1016/j.ast.2012.02.002>
- An, S., & Kwon, S. (2009). Scaling and Evaluation of Pt/Al<sub>2</sub>O<sub>3</sub> Catalytic Reactor for Hydrogen Peroxide Monopropellant Thruster. *Journal of Propulsion and Power*. <https://doi.org/10.2514/1.40822>
- Anflo, K., & Grönland, T.-A. (2012). *Towards Green Propulsion for Spacecraft with ADN-Based Monopropellants*. <https://doi.org/10.2514/6.2002-3847>
- Baek, S., Jung, W., Kang, H., & Kwon, S. (2018). Development of High-Performance Green-Monopropellant Thruster with Hydrogen Peroxide and Ethanol. *Journal of Propulsion and Power*. <https://doi.org/10.2514/1.b37081>

- Essa, K., Hassanin, H., Attallah, M. M., Adkins, N. J., Musker, A. J., Roberts, G. T., Smith, M. (2017). Development and testing of an additively manufactured monolithic catalyst bed for HTP thruster applications. *Applied Catalysis A: General*, 542. <https://doi.org/10.1016/j.apcata.2017.05.019>
- Florczuk, W., & Rarata, G. P. (2017). *Performance evaluation of the hypergolic green propellants based on the HTP for a future next generation spacecrafts*. <https://doi.org/10.2514/6.2017-4849>
- Gohardani, A. S., Stanojev, J., Demairé, A., Anflo, K., Persson, M., Wingborg, N., & Nilsson, C. (2014). Green space propulsion: Opportunities and prospects. *Progress in Aerospace Sciences*. <https://doi.org/10.1016/j.paerosci.2014.08.001>
- Guerrieri, D. C., Silva, M. A. C., Cervone, A., & Gill, E. (2017). Selection and Characterization of Green Propellants for Micro-Resistojets. *Journal of Heat Transfer*. <https://doi.org/10.1115/1.4036619>
- Heo, S., Jo, S., Yun, Y., & Kwon, S. (2018). Effect of dual-catalytic bed using two different catalyst sizes for hydrogen peroxide thruster. *Aerospace Science and Technology*, 78. <https://doi.org/10.1016/j.ast.2018.03.032>
- Jang, D., Kang, S., & Kwon, S. (2015). Preheating characteristics of H<sub>2</sub>O<sub>2</sub> monopropellant thruster using manganese oxide catalyst. *Aerospace Science and Technology*, 41. <https://doi.org/10.1016/j.ast.2014.12.010>
- Jo, S. (2017). Response characteristics of H<sub>2</sub>O<sub>2</sub> monopropellant thrusters with MnO<sub>2</sub>-mixed PbO catalyst. *Aerospace Science and Technology*, 60. <https://doi.org/10.1016/j.ast.2016.10.022>
- Kang, H., Lee, D., Kang, S., & Kwon, S. (2017). Effect of H<sub>2</sub>O<sub>2</sub> injection patterns on catalyst bed characteristics. *Acta Astronautica*, 130. <https://doi.org/10.1016/j.actaastro.2016.10.023>
- Lee, J., & Kwon, S. (2013). Reduction of Catalyst Volume by Using Metal Mesh in Small-Scale H<sub>2</sub>O<sub>2</sub> Thrusters. *Journal of Propulsion and Power*. <https://doi.org/10.2514/1.b34667>
- Lee, S. L., & Lee, C. W. (2009). Performance characteristics of silver catalyst bed for hydrogen peroxide. *Aerospace Science and Technology*. <https://doi.org/10.1016/j.ast.2008.02.007>
- Li, S., Ge, Y., Wei, X., & Li, T. (2016). Mixing and combustion modeling of hydrogen peroxide/kerosene shear-coaxial jet flame in lab-scale rocket engine. *Aerospace Science and Technology*. <https://doi.org/10.1016/j.ast.2016.07.008>
- Okninski, A., Valencia Bel, F., Surmacz, P., Sobczak, K. M., Rarata, G. P., Wolanski, P., & Bartkowiak, B. (2017). *Experimental Evaluation of a Catalyst Bed Based on Mn x O y /Al 2 O 3 Catalyst for Decomposition of 98% Hydrogen Peroxide*. <https://doi.org/10.2514/6.2017-4923>
- Othman, N. (2011). *Design and Development of 50-N Hydrogen Peroxide Monopropellant Rocket Thruster*. Universiti Teknologi Malaysia.
- Salgado, M. C. V., Belderrain, M. C. N., & Devezas, T. C. (2018). Space propulsion: A survey study about current and future technologies. *Journal of Aerospace Technology and Management*, 10, 1–23. <https://doi.org/10.5028/jatm.v10.829>
- Scharlemann, C., Pirault-Roy, L., Brahmi, R., Batonneau, Y., Kharchafi-Farhat, G., Farhat, K., ... Saouabé, M. (2013). Green Propulsion: Catalysts for the European FP7 Project GRASP. *Topics in Catalysis*. <https://doi.org/10.1007/s11244-013-0223-y>
- Schmidt, E. W., & Wucherer, E. J. (2004). Hydrazine(S) vs. nontoxic propellants - Where do we stand now? *European Space Agency, (Special Publication) ESA SP*.
- Sobczak, K. M., Wolanski, P., Okninski, A., Bartkowiak, B., Surmacz, P., Kublik, D., ... Valencia Bel, F. (2017). *Test Campaign of a Green Liquid Bi-propellant Rocket Engine Using Catalytically Decomposed 98% Hydrogen Peroxide as Oxidizer*. <https://doi.org/10.2514/6.2017-4926>
- UI Haq, N., Khan, R. A., & Mehmood, R. (2017). Design, development and testing of 1N Hydrogen Peroxide thruster. *Proceedings of 2017 14th International Bhurban Conference on Applied Sciences and Technology, IBCAST 2017*, 599–607. <https://doi.org/10.1109/IBCAST.2017.7868112>.

---

## #117: Research on air-conditioner energy saving control method based on Q-learning and adaptive constraint network

---

Chong CHEN<sup>1</sup>, Dong YUE<sup>2</sup>, Shaobing LI, Dechao SONG, Pengfei WANG,  
Jiabi DENG

<sup>1</sup>Gree Electric Co Ltd, Internet of Things Research Institute, Zhuhai China, harry.chen@leayun.cn

<sup>2</sup>Gree Electric Co Ltd, Internet of Things Research Institute, Zhuhai China, 996154062@qq.com

*In order to solve the problem of air-conditioner's high energy consumption during operation under traditional PID control, this paper proposes an air-conditioner energy-saving control method based on Q-learning and adaptive constraint network. Firstly, standard reward matrix is constructed according to the "expert system" and "reward function", and the air-conditioner operating parameters corresponding to matrix elements are divided into A and B datasets. Secondly, initialising radial basis function (RBF) neural network model and training constrain network with A datasets. Besides, using B datasets doesn't verify model performance until accuracy rate is over 90% and this model is regarded as Standard Comfort Energy-saving Constraint Network (SCECN). Finally, air conditioner operation strategy is formulated by combining Q-learning algorithm of reinforcement learning with actual reward matrix that is constructed according to SCECN. If this strategy dissatisfies needs of user, SCECN will be updated by actual feedback data and defined as Self-Adaptive Comfort and Energy Constraint Network (SACECN). Experiments show: comparing with traditional control logic of air-conditioner, the algorithm saves up to 18.3% electric energy when air-conditioner operates.*

*Keywords: expert system; radial neural network; reinforcement; learning; constraint model*

# 1. INTRODUCTION

The optimised energy-saving control of air-conditioner does not only improve the utilisation of current resources, but also provides new research ideas for real-time regulation of indoor temperature. At present, the traditional PID air-conditioner control strategy being based on personal experience and lacking self-adaptive ability is unable to meet the control requirements of different working-conditions and consumes much energy, so it is expedite to develop air-conditioner control strategy with strong generalisation ability, energy saving and high efficiency. K.R. Selvaraj (2017) proposed a Smart-Learning Network Controller for Centralised Air-Condition Systems Using Model-View-Controllers Model, this model uses machine learning algorithms to predict user's thermal comfort and adjust air-conditioner temperature to provide ideal thermal comfort and indoor air quality at the lowest vital cost. Guo Yao (2018) proposed an optimised air-conditioner control method for central hospital based on annealing algorithm. The method firstly establishes the optimisation system by constructing function of the energy consumption cost of each component of air conditioner and the over-all energy consumption, then annealing algorithm is used for calculating real-time deviation between sample measurement value and predicted value of the optimised system. The deviation is used for adjusting the optimal strategy what realises energy-saving optimisation control of air-conditioner. Shi Jianhua (2016) proposed an energy-saving fuzzy control method of central air-conditioner system being based on dynamic rule base. When dynamic fuzzy rule gradually changes, the method approximates the best value under different load conditions by adjusting the cooling water flow and the cooling tower air. Only in this way can it save energy consumption. Cui Zhiguo (2018) proposed a control method of air-conditioner system based on data mining technology. The method firstly carries data-preprocessing by KNN, PCA algorithm, then it builds model of cold source system based on actual data, finally machine learning algorithms are used for predicting burden. By this way, it achieves saving-energy too.

However, there are few studies on the field of household inverter air conditioners in term of optimising energy-saving control. In view of this study-environment, the paper proposes an energy-saving optimisation control algorithm based on Q-learning and adaptive constraint network for household inverter air conditioners.

## 2. INTRODUCTION OF RADIAL BASIS NEURAL NETWORK AND Q-LEARNING

### 2.1. Radial Basis Neural Network

Multivariate interpolation radial basis function (RBF) neural network proposed by Powell provides a solution to the problem that low-dimensional data is linear inseparability. The network consists of an input layer, a hidden layer, and an output layer, it is shown in Figure 1:

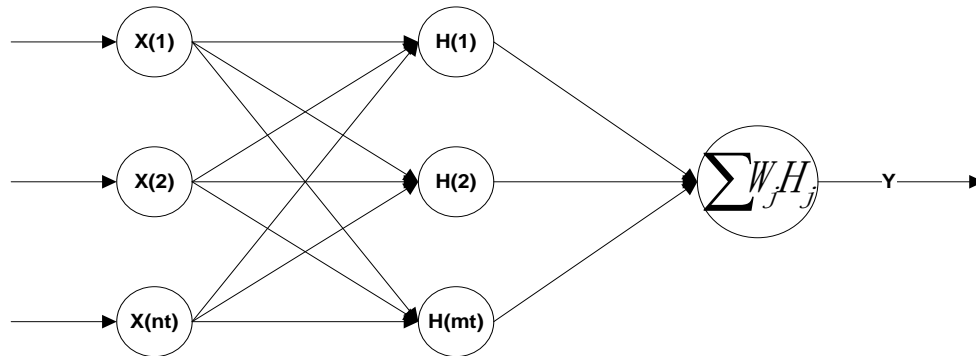


Figure 1: RBF neural network structure

The meaning of the variables in the figure:  $X_R=[x_1,x_2,\dots,x_{nR}]^T$  is the input vector,  $H_R=[h_1,h_2,\dots,h_{mR}]^T$  is the radial basis vector,  $nR$  and  $mR$  are the number of input vector node and the hidden node respectively. The basis function of hidden layer uses a Gaussian function, it is shown in Equation 1:

Equation 1: 
$$h_j = \exp\left(-\frac{\|X_R - C_j\|^2}{2b_j^2}\right) \quad j = 1, 2, \dots, mR$$

Where:

- $h_j$  = Gaussian function of the  $j$ th hidden node
- $C_j$  = central vector of the  $j$ th hidden node
- $B_R$  = base width vector

In order to construct a reasonable network which is suitable with problem scale and avoid the problem of slow running speed due to the redundancy of neurons, this paper realises the network structure initialisation by using the dynamic network structure optimisation SORBF algorithm which was proposed by Luo Wenfa (2018). As is shown in Figure 2:

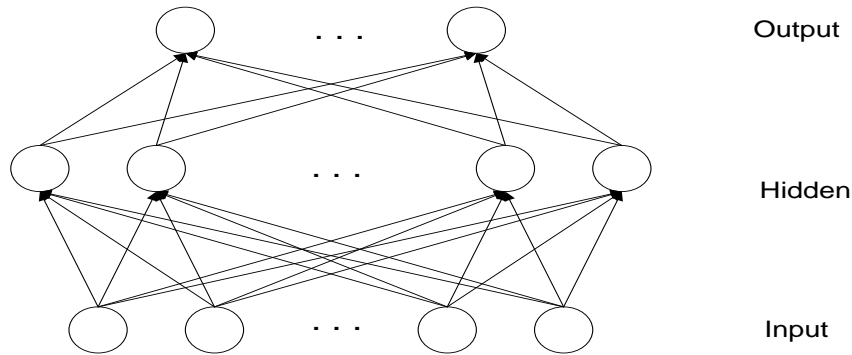


Figure 2: RBF network structure

In network structure: Input is the air-conditioner operating parameters such as indoor ambient temperature, outdoor ambient temperature, set temperature, indoor evaporator intermediate temperature, and outdoor condenser intermediate temperature. Output is the operating frequency of compressor, the opening of the electronic expansion valve and the speed of external fan. According to adaptive adjustment, hidden layer contains 258 neurons.

## 2.2. The theory of Q-learning

A key assumption of Q-learning is that the interaction between agent and environment can be regarded as a Markov decision process (Zhang, 2013), which is consisted by the  $S=\{s_1, s_2, \dots, s_n\}$  sets which are finite and discrete environmental states, the  $A=\{a_1, a_2, \dots, a_n\}$  sets which are finite and discrete learner actions, scalar enhanced signal  $r$  and learner strategy  $\pi: S \rightarrow A$ .

In each iteration, Agent senses environmental state  $s \in S$  and selects action  $a \in A$  to act on the environment according to the current policy  $\pi$ . The environment state is changed to  $s' \in S$  by this way, and an enhanced signal (reward)  $r(s)$  that is generated is feedback to learner. Then the learner updates strategy and proceeds to next iteration. The Q function which is optimised by continuous reflection learning finds the best strategy for each state  $\pi^*(s) \in A$ , it is shown in Equation 2:

$$\text{Equation 2: } V^\pi(s) = E(\sum_{t=0}^{\infty} \gamma^t * r(s_t, \pi(s_t)) | s_0 = s)$$

Where:

- $\gamma \in (0,1)$  = constant-time discount factor what reflects the importance of future returns relative to current returns

According to the Bellman optimal criterion, the maximum value of Equation 3 is:

$$\text{Equation 3: } V^*(s) = \max V^\pi(s) = \max [R(s, a) + \gamma \sum_{s' \in S} P_{s,s'}(a) * V^*(s')]$$

Where:

- $R(s,a)$  = mathematical expectation of  $r(s_t, a_t)$
- $P_{s,s'}(a)$  (a) = transition probability that s state reaches  $s'$  state under action a.

The idea of Q-learning is not to estimate the environment model, but it can find the optimal strategy by simple Q-value iteration in the case of unknown  $R(s, a)$  and  $P_{s,s'}(a)$ , which meets the Equation 4.

Associating each pair of states and actions  $(s, a)$  under strategy  $\pi$  with a Q value:

$$\text{Equation 4: } Q^\pi(s, a) = R(s, a) + \gamma \sum_{s' \in S} P_{s,s'}(a) * V^\pi(s')$$

From Equation 3 and Equation 4, you can get Equation 5:

$$\text{Equation 5: } \pi^*(s) = \arg \max Q^*(s, a)$$

Q learning obtains  $Q^*(s, a)$  by the following Equation 6 (Gosavi, 2009):

$$\text{Equation 6: } Q_{t+1}(s, a) = (1 - \alpha)Q_t(s, a) + \alpha(r_t + \gamma \max_{a'} Q_t(s', a'))$$

- Where:
- $\alpha = (1 + \text{visit}(s, a))^{-1}$  = learning rate,  $\alpha \in (0, 1]$
- $\text{visit}(s, a)$  = total number of visits of state action pair (s, a)

With  $t \rightarrow \infty$ , if the Q value of each pair (s, a) can be updated all the time and  $\alpha$  decreases to 0, then  $Q_t(s, a)$  will converge to the optimal with probability 1.

### 3. INTELLIGENT CONTROL ALGORITHM BASED ON Q-LEARNING AND ADAPTIVE CONSTRAINT NETWORK

In order to overcome the high energy consumption of traditional air-conditioner control methods, this paper proposes an air-conditioner intelligent control algorithm being based on Q-learning and adaptive constraint network by combining RBF network with reinforcement learning theory. The specific algorithm steps are as follows:

When air-conditioner operates, the reward matrix RCE is constructed according to the ‘‘Expert system’’ and ‘‘Reward function’’. Then, operating parameters of air-conditioner corresponding to reward matrix element are divided into the A and B datasets. Tabulation planning is as shown in Table 1:

Table 1: Tabulation Planning

	$41 < T2 \leq 44$	$38 < T2 \leq 41$	$35 < T2 \leq 38$	$32 < T2 \leq 35$	$29 < T2 \leq 32$
$T1 < 16$					
$16 \leq T1 < 19$					
$19 \leq T1 < 22$					
$22 \leq T1 < 25$					
$25 \leq T1 < 28$					

$$\text{Reward Function: } \text{Reward} = \alpha * |\Delta T_{indoor}| + \beta * |\Delta T_{outdoor}|$$

Where:

- $\Delta T_{indoor}$  = difference between indoor temperature(T1) and set temperature in the current environment
- $\Delta T_{outdoor}$  = difference between outdoor temperature(T2) in the current environment and outdoor working conditions in table
- $\alpha \setminus \beta$  = expert experience weights for different environment and different types of air conditioner

The exploration of the reward matrix elements is carried out in the above range of working conditions, and the algorithm combines Monte Carlo’s idea with reward function being based on expert experience searches optimal control strategy under every working condition;

According to the scale and characteristics of the problem, the SORBF algorithm is used for initialising the radial basis neural network model and A datasets is used for training neural network, then verifying constraint network with B datasets;

*Using the validated constraint network and the Q-learning strategy of reinforcement learning is to make the optimal strategy decision for air-conditioner operation;*

Constructing the reward matrix RCE’ under actual conditions with constraint network;

*Learning Q table combining obtained reward matrix RCE’ with Equation 7:*

$$\text{Equation 7: } Q(s, a) = R(s, a) + \theta * \max\{Q(s_{next}, a_{next})\}$$

Where:

- Q = same scale as R
- s = current state,  $s_{next}$  represents the next possible action
- a = current action,  $a_{next}$  represents the next possible action
- $\theta$  = greedy factor which is setted 0.8
- $Q(s,a)$  = maximum expected benefit that be obtained by performing a action under s state

Making optimal control strategy decisions for air-conditioner operations by using the maximum expected matrix Q and a Equation 8;

Equation 8:  $Q(s, a) = \max\{Q(s, a_{next})\}$

The algorithm flow is shown in Figure 3:

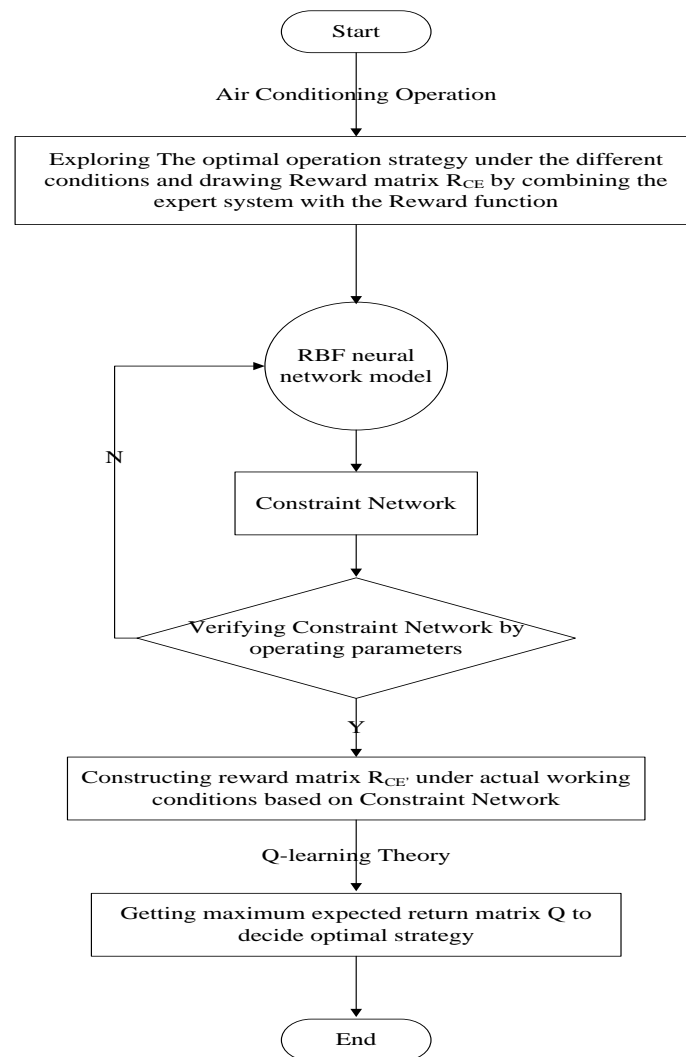


Figure 3: Air-conditioner intelligent control algorithm flow

#### 4. EXPERIMENTAL RESULTS AND ANALYSIS

Taking 2.6KW air-conditioner as the experimental object, it is controlled by traditional PID logic control method and the intelligent control algorithm proposed in this paper respectively. In terms of this experimental object, I set  $\alpha=0.75$ ,  $\beta=0.25$  and  $\Theta=0.8$ . The specific operation data is shown in Figure 4 and Figure 5 (the red line indicates data curve under traditional PID logic control, the blue line indicates data curve under controlling of the intelligent algorithm):

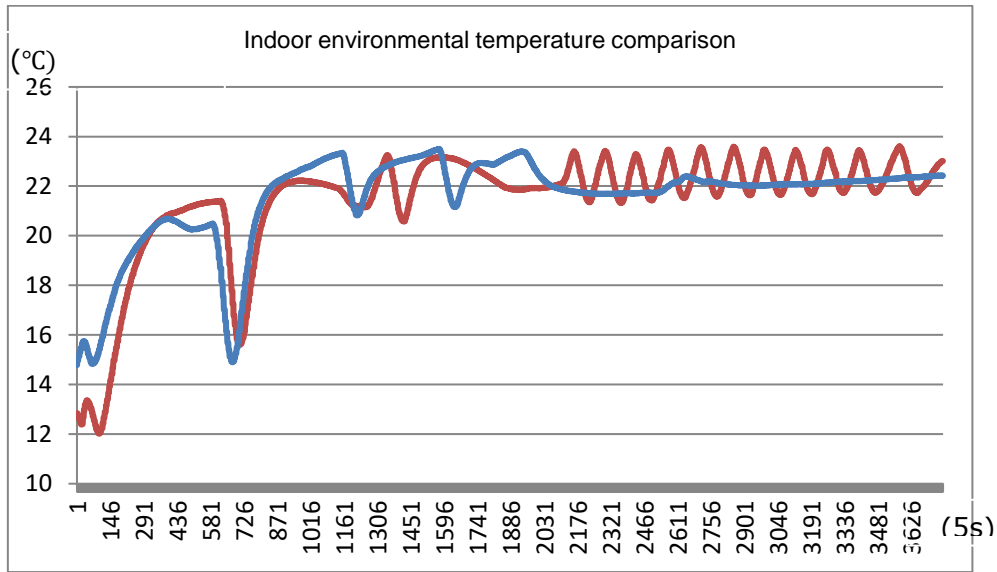


Figure 4: comparison of indoor ambient temperature

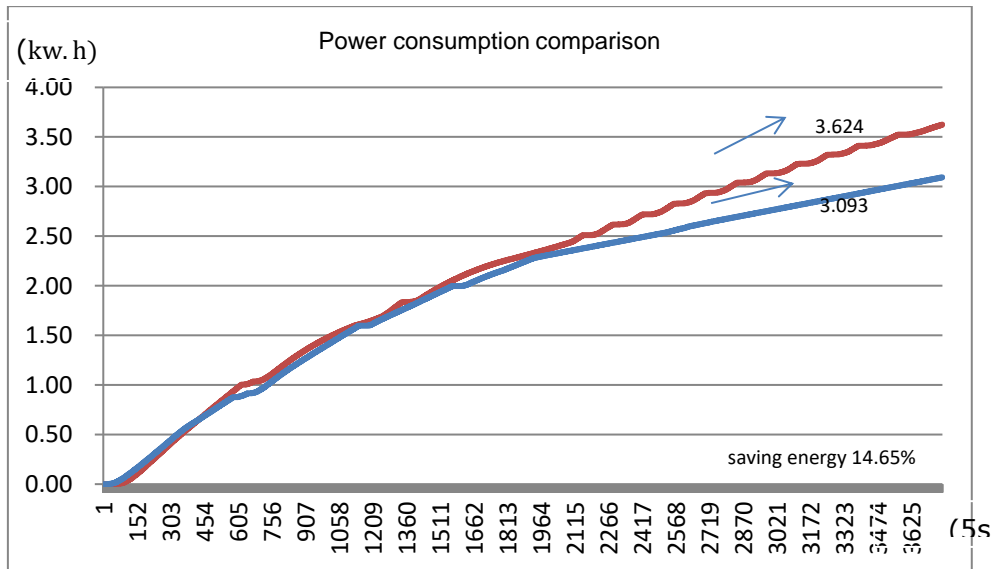


Figure 5: comparison of total electricity consumption

It can be seen from the figure that when the set temperature (set\_T) is 25 degrees and air conditioner continuously runs for 3.5 hours, the total power consumption is 3.093 degrees when air conditioner is controlled by intelligent algorithm, the total power consumption is 3.624 degrees when air conditioner is controlled by traditional PID algorithm. From data, intelligent algorithm saves about 14.65% electric-energy.

Under other working conditions (set\_T,in\_T,out\_T), this paper also verifies performance of proposed algorithm. The specific results are shown in Table 2:

Table 2: comparison of saving-energy effects between proposed algorithm and traditional PID control under different working conditions

	Traditional PID	Proposed	Energy-saving
(25, 15, 5)	1.906	1.558	16.684%
(25, 15, 2)	0.748	0.634	15.53%
(25, 15, -7)	0.482	0.417	13.49%
(25, 15, -10)	4.001	3.269	18.3%



## 5. CONCLUSION

In order to solve the defects of traditional air-conditioner logic which consists of hysteresis in steady-state control, temperature fluctuation, poor comfort and high energy consumption, this paper proposes an air-conditioner control method which combines Q-learning which is based on reinforcement learning theory with adaptive-constraint network which is based on radial basis neural network. Experiments show that compared with the traditional air-conditioner control method, the algorithm achieves up to 18.3% energy-saving effect under the premise of ensuring user comfort.

## 6. REFERENCES

- Gosavi, A, 2009. Reinforcement Learning: a tutorial survey and recent advances [J]. *Inform Journal on Computing*. 21(2):178-192.
- Selvaraj, K.R., 2017. Smart-Learning Network Controllers for Centralized Air-Condition Systems Using Model View Controller Model [J]. *International Visual Informatics Conference*. 10:737-749.
- Guo, W. et al, 2018. Research on Hospital Central Air-conditioner Optimization Control Based on Annealing Algorithm [J]. *Computer and Digital Engineering*. 340(2):293-297.
- Shi, J. et al, 2016. Research on energy-saving fuzzy control algorithm of central air-conditioner system based on dynamic rule base [J]. *Wuhan Vocational and Technical College*. 10.
- Cui, Z. et al, 2018. Research on control method of air-conditioner system based on data mining technology [C]. *China Academy of Building Research*.
- Luo Wenfa et al, 2018. Self-learning stability control algorithm for neural networks based on dynamic network structure optimization [J]. 4.
- Zhang K., Li Gu, Yang Baiwei, 2013. Q-learning based opportunistic spectrum access channel selection algorithm [J]. *Journal of Computer Applications*. 30(5).

---

# #119: Life cycle assessment of wood pellet from para-rubber tree residues

Cradle to grave

---

Piyarath SAOSEE<sup>1,2</sup>, Boonrod SAJJAKULNUKIT<sup>1,3</sup>, Shabbir H. GHEEWALA<sup>1,3</sup>

<sup>1</sup>The Joint Graduate School of Energy and Environment (JGSEE), King Mongkut's University of Technology Thonburi, Bangkok 10140, Thailand, piyarath25@gmail.com

<sup>2</sup>Organization Strategy Management Division, National Science and Technology Development Agency (NSTDA), Klong Luang, Pathumthani 12120, Thailand

<sup>3</sup>Centre of Energy Technology and Environment, Ministry of Education, Thailand

*This study focuses on the Life Cycle Assessment (LCA) of wood pellets made from para-rubber tree residues. The scope of the study is cradle to grave, covering para-rubber tree plantation, wood pellet production, and heat production by a boiler (capacity 3 t/h). The environmental impacts were assessed throughout the para-rubber tree wood pellet production chain, including the comparison of wood pellets with conventional biomass and fossil fuels. The SimaPro software (v. 8.5.2.0) was used for the LCA and the ReCiPe2016 Midpoint/Endpoint method (version 1.02) was chosen to evaluate the environmental impacts of heat production from para-rubber tree wood pellets. The contribution of heat production is more than 65% to many of the environmental impact categories considered including stratospheric ozone depletion, ozone formation, fine particulate matter formation, terrestrial acidification, freshwater eutrophication, and human non-carcinogen toxicity. Moreover, the contribution of transportation is over 60% in global warming, terrestrial ecotoxicity, marine ecotoxicity, human carcinogen toxicity, and fossil resource scarcity. As anticipated, the life cycle greenhouse gas emissions or global warming for heat production from para-rubber tree wood pellet (including wood pellet and waste wood) are lower than fossil fuels (coal, natural gas, diesel and residue fuel oil). The greenhouse gas emissions of the former are almost twenty times lower than their fossil equivalents. Most of the other impact categories are also lower for the wood pellets except for freshwater eutrophication, land use, mineral resource scarcity, and water consumption which are higher. The result of comparison of endpoint impacts of 1 GJ heat production from wood pellet, conventional biomass and fossil fuels shows that the wood pellets have lower impacts than the fossil fuels (coal, natural gas, diesel and residue fuel oil) for human health (15.76 DALY), ecosystem quality (11.54 species.yr) as well as resource scarcity (9.18 USD2013).*

*Keywords: para-rubber tree; life cycle assessment; wood pellet; heat production; fossil fuel*

## 1. INTRODUCTION

Wood pellets are made from wood waste and are used for producing heat and electricity. Several countries use the wood pellets to substitute fossil fuels to drive their policies to reduce emission of greenhouse gases. The global trend of wood pellet market has increased significantly, on average 14% per year since 2011 (Thrän *et al.*, 2017). The world trade of wood pellet in 2018 was evaluated at 23.8 million tonnes, an enormous 26% increase from 2017 at 18.9 million tonnes. This resulted from Denmark, South Korea and Japan importing at least 40% higher, especially Japanese wood pellet imports more than doubling (Walker and Strauss, 2019). Likewise, the wood pellet import of EU has grown rapidly which accounted for 51% of global wood pellets production and 75% global share of wood pellet consumption. The main sources to supply EU are projected to be Russia, Canada, and particularly, the US (Jonsson and Rinaldi, 2017). South Korean imports wood pellet reached 3.4 million tonnes, with more than 95% of that volume coming from Southeast Asia; 63.8% wood pellets imported from Vietnam (Walker and Strauss, 2019). The cost of pellets becomes a barrier in China because it is significantly higher than the cost of coal. Using wood pellet in China still is impractical due to unstable heat values of pellet, limited supplies, the lack of product and heating equipment standards (Wang *et al.*, 2017).

In 2018, Thailand exported 289,310 tonnes wood pellets, especially to South Korea (Thai Customs, 2019). As the Thai government encourages the use of wood pellets in the Thai industry to lessen reliance on imported fuels, they launched a project to support 30% to 50% of the cost to replace factory boilers with ones capable of utilising wood pellets (Department of Alternative Energy Department and Efficiency and King Mongkut's Institute of Technology Ladkrabang, 2016). The South of Thailand has a lot of suitable areas which can grow para-rubber tree. Para-rubber tree became an important economic crop. The products of a para-rubber tree are latex and wood. The wood of the para-rubber tree is processed and transformed to furniture. Accordingly, the para-rubber tree residue from the sawmill and furniture industry is chosen to produce wood pellets. Wattana *et al.* (2017) studied the characterisation of mixed biomass pellets made from oil palm and para-rubber tree residues to further improve quality of the wood pellets. Although the consumption of wood pellets in Thailand, mostly industrial boilers, is higher each year, especially for manufactures of public companies, the power plants still use other biomass such as wood chips and rice husk because these are cheaper (Kotrba, 2016). Hence, this study would like to evaluate the environmental impacts from the use of wood pellets from para-rubber residue for heat production.

The result of examining the environmental implications of co-firing coal and wood pellets in South-eastern United States indicated that co-firing with wood pellets could be a viable interim solution for the aging fleet of coal-fired power plants within South-eastern United States, particularly if stricter emission regulations and renewable portfolio standards are implemented (Morrison and Golden, 2017). A study in China found that the wood pellet combustion reduced greenhouse gas, SO<sub>2</sub>, NO<sub>x</sub> and particulate matter emissions (Wang *et al.*, 2017). The study on the life cycle analysis of small scale pellet boilers showed that the environmental impact reduction in 10 kW wood pellet boiler as compared to fossil fuel boilers was mainly due to their reduced impact on climate, natural land transformation, and fossil depletion (Monteleone *et al.*, 2015).

Life Cycle Assessment (LCA) is the environmental perspectives and potential impacts study throughout a life cycle of a product from raw material acquisition through production, use, and disposal (Huijbregts *et al.*, 2016). LCA reduces the risk of problem-shifting from one phase to another phase (Finnveden *et al.*, 2009). It is an important tool which can consider opportunities to improve the environmental performance of products, inform decision-makers in industry, government or non-government organisations, implement an ecolabelling scheme, make an environmental claim, or produce an environmental product declaration (ISO14040, 2006). Hence, the objective of this study focuses on the LCA of wood pellets made from para-rubber tree residues. The scope of the study is cradle to grave, covering para-rubber tree plantation, wood pellet production, and heat production by a boiler (capacity 3 t/h). The environmental impacts were computed across the para-rubber tree wood pellet production chain, and also compared with conventional biomass and fossil fuels.

## 2. MATERIALS AND METHODS

### 2.1. Goal and scope definition

The goals of this study are to evaluate the environment impacts of wood pellet made from para-rubber tree residues (cradle to grave), and to compare with conventional biomass and fossil fuels. The result of this study will be analysed for environmental impacts hotspot which is useful for entrepreneurs planning and developing wood pellet production. It is also useful for users in choosing suitable fuels for heat production with reduced environmental impacts. Moreover, the government can apply information from this study for establishing guidelines. The functional unit of this study is one gigajoule (GJ) of heat which is produced from a 3 t/h boiler using para-rubber residues wood pellets, conventional biomass or fossil fuels.

The system boundary (Figure 1) consists of three main parts: the raw material source, wood pellet production and heat production. Firstly, the raw material, the para-rubber tree residues, starts from sprout preparation, para-rubber

tree plantation, cutting and rubber wood sawing and processing. The para-rubber trees are cut at the age of 25 years when their yield of latex is reduced. After cutting, the rubber trees are divided into three parts; roots, logs and branches. In this study, roots are ignored since they are full of soil and difficult to manage. Subsequently, the rubber wood logs are sent to the sawmill for plank wood processing. The planks are dried and treated by some chemicals to protect them from insects. Some branches and barks are used as fuel for the drying process. Most of the barks and fresh sawdust are sent to the wood pellet factory. Secondly, the wood pellet production comprises of pretreatment, drying, comminution, pelletisation, cooling and storage. Finally, the wood pellets are used as fuel to produce heat in the 3 t/h boiler. Transportation has 3 steps (Figure 2): (1) Transportation from processed plantation area to rubber wood factory is 100 kilometres distance by 10-wheel truck, with 16 tonnes of rubber wood log (100% loading) 0% loading as return trip is, (2) Transportation from processed rubber wood factory to wood pellet factory, is 100 kilometres distance by 10-wheel truck, with 16 tonnes of sawdust and bark (75% loading) and return trip is 0% loading, and (3) Transportation from wood pellet factory to users, is 250 kilometres by 18-wheel truck, with loading 32 tonnes of wood pellets and return trip is 0% loading. All these trucks use diesel for fuel. Transportation of workers to and from the factory is not included in the system boundary.

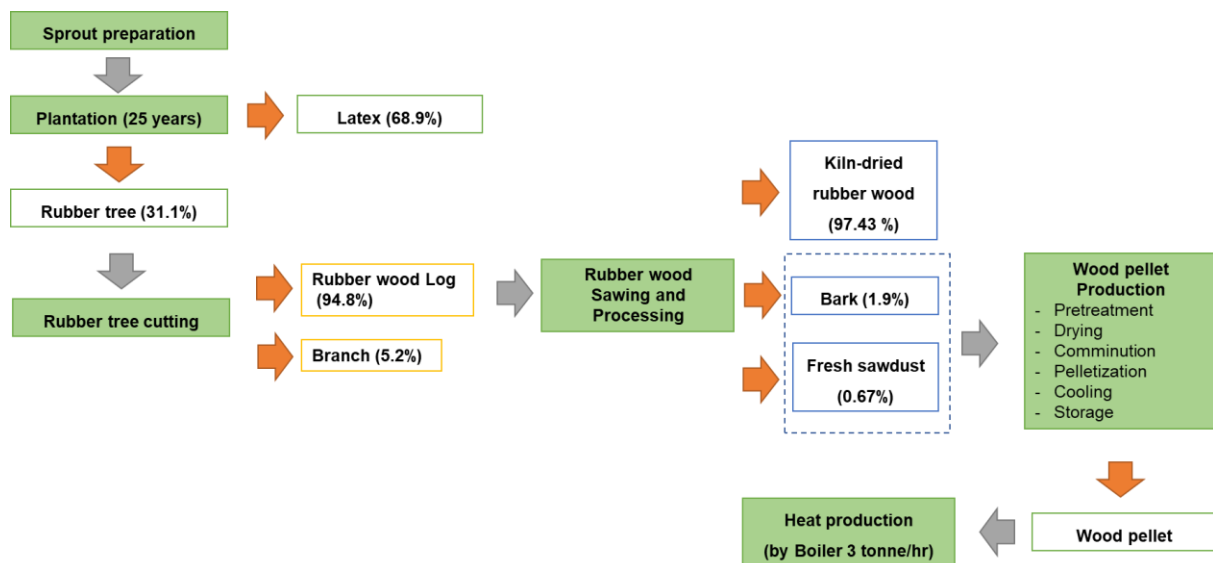


Figure 1: System boundaries for the cradle to grave life cycle assessment of wood pellet production and utilisation, including economic allocation of para-rubber wood

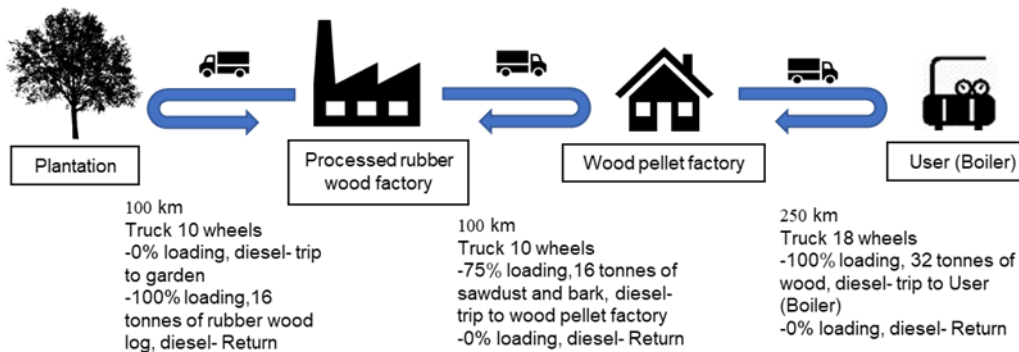


Figure 2: Transportation relation with wood pellet production and utilisation

## 2.2. Inventory analysis

The para-rubber sprout preparation, plantation and cutting data are referred from the project on assessment of water footprint in the rubber plantations in the new areas in the south of Thailand (Musikavong *et al.*, 2015). This data is collected from 12 provinces in southern Thailand. The data of para-rubber wood processing is referred from the report about the water footprint of rubber wood products (Ketdecha, 2013). The secondary data, especially for para-rubber wood processing, were checked via mass and energy balances. They were also reconfirmed in consultation with the factory staff.

The life cycle inventory data of wood pellet production is collected from a wood pellet factory in the south of Thailand. They use para-rubber tree residue (70% fresh sawdust and 30% bark) for raw material to produce the wood pellets. Machines of this factory have one chopper, one hammer mill, one screener, one rotary drum dryer, three pellet mills, one cyclone and one cooler. Production capacity of this factory is 110 tonnes per day. Electricity consumption is measured while the production is in operation. The efficiency of heat production by the 3 t/h boiler was determined during the project to support the cost to replace factory boilers with ones capable of utilising wood pellets. Air emission data from wood pellet combustion is from the U.S. Life Cycle Inventory Database.

Economic allocation is used to share the environmental burden between the two co-products from the process of the para-rubber tree plantation: latex and wood (Figure 1). As the allocation is based on the market value of the co-products, most proportion is shared by the latex (68.9%) as it is the main product having higher price.

### 2.3. Impact assessment

The SimaPro software (v. 8.5.2.0) is used for the LCA and the ReCiPe2016 Midpoint/Endpoint method (version 1.02) was chosen to analyse the environmental impacts of heat production from para-rubber tree wood pellets. The software is designed to be a source of science-based information, providing full transparency and avoiding black-box processes (SimaPro, 2019). This study concentrates on the following 17 impact categories of midpoints: global warming potential, stratospheric ozone depletion, ozone formation (human health), ozone formation (terrestrial ecosystems), fine particulate matter formation, terrestrial acidification, freshwater eutrophication, marine eutrophication, terrestrial ecotoxicity, freshwater ecotoxicity, marine ecotoxicity, human carcinogenic toxicity, human non-carcinogenic toxicity, land use, mineral resource scarcity, fossil resource scarcity, and water consumption. The endpoints are resources scarcity, ecosystem quality and human health.

## 3. RESULTS AND DISCUSSION

### 3.1. Comparison of environmental impacts throughout the para-rubber tree wood pellet life cycle

The contribution of heat production (Figure 3) is more than 65% to many of the environmental impact categories considered including stratospheric ozone depletion, ozone formation, fine particulate matter formation, terrestrial acidification, freshwater eutrophication, and human non-carcinogen toxicity. Moreover, the contribution of transportation is over 60% in global warming, terrestrial ecotoxicity, marine ecotoxicity, human carcinogen toxicity, and fossil resource scarcity.

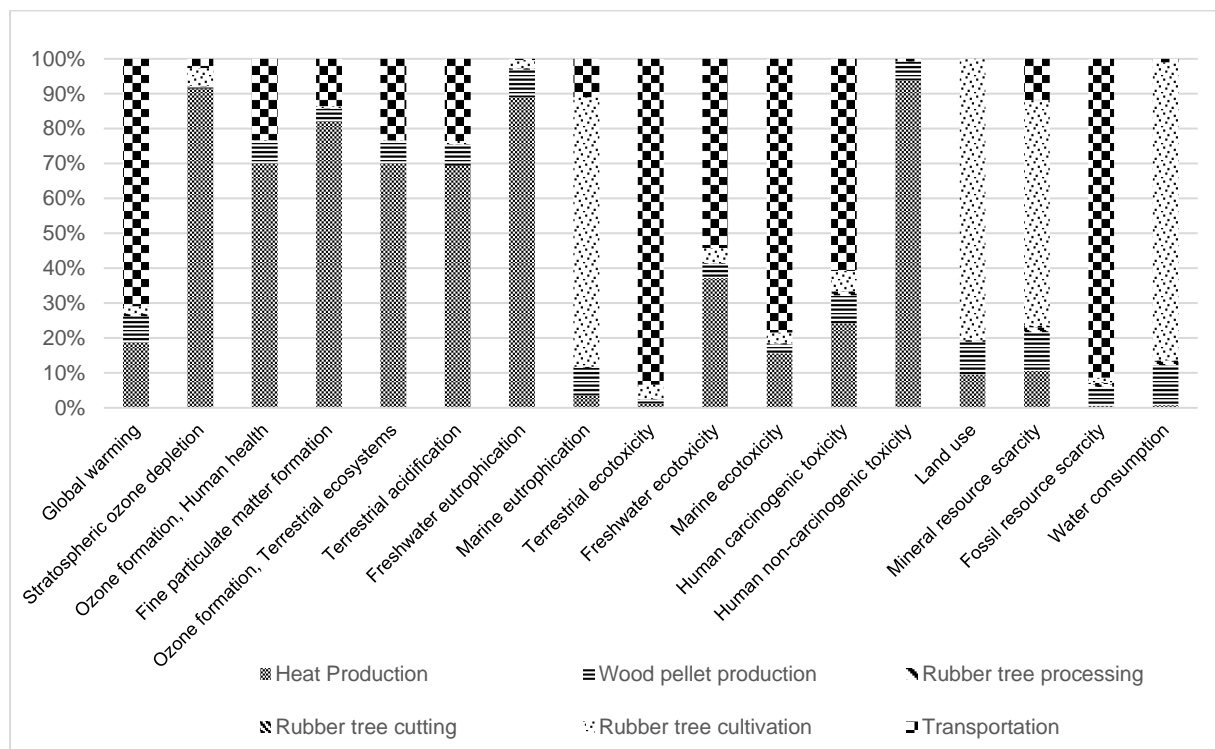


Figure 3: Contribution of para-rubber wood pellet life cycle phases impact on the ReCiPe Midpoint subcategories

The para-rubber tree cultivation contributes to the higher value of marine eutrophication, land use, mineral resource scarcity and water consumption because the cultivation process uses some water and a large amount of fertilizer. Water consumption of wood pellet production originates from the firewood (in drying process) which includes branches and bark of para-rubber tree.

### 3.2. Comparison of environmental impact of 1 GJ heat production from wood pellet, conventional biomass and fossil fuels

The result of comparison of the endpoint impacts of 1 GJ heat production from wood pellet, conventional biomass and fossil fuels (Figure 4) shows that the wood pellet generally has much lower impacts than the fossil fuels (coal, natural gas, diesel and residue fuel oil) in human health (15.76 DALY), ecosystem quality (11.54 species.yr) and resource scarcity (9.18 USD2013). The damage to human health of unspecified wood waste is higher than fossil fuels except for lignite. This result is related with the Human carcinogen toxicity of wood waste (Figure 5) which is higher than all fuels. Although ecosystem quality and resource scarcity of wood pellets are lower than fossil fuels, these are higher than wood waste as wood pellet production uses energy from fossil fuels and growing para-rubber tree uses fertilizers. The performance of para-rubber wood pellets for heat production is better than fossil fuels in all the endpoint impact categories –human health, ecosystem quality and resource scarcity. The damage to resource availability indicates that natural gas and oil (9-12 USD2013) are less readily available than coal (2-4 USD2013).

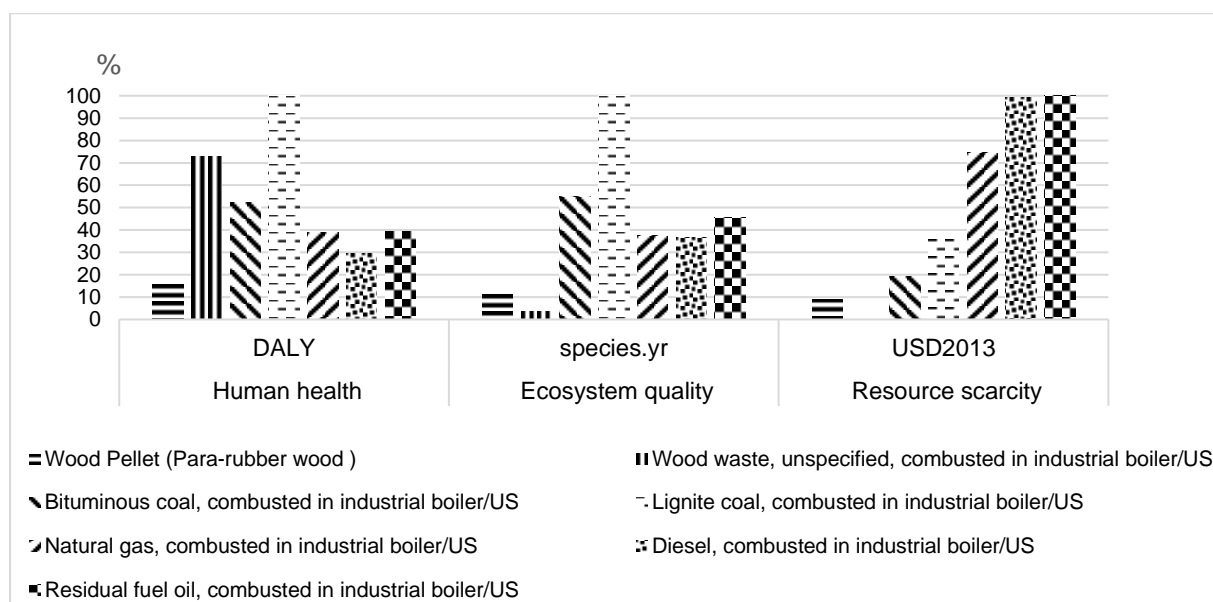


Figure 4: Comparative analysis of waste wood, and fossil fuel endpoint impact profiles

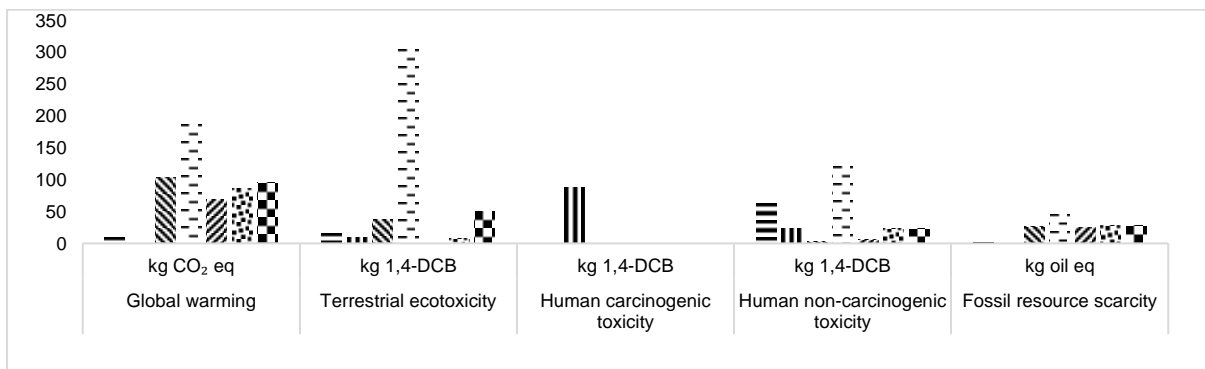
The midpoint impact categories (Figure 5) of 1 GJ heat from the wood pellets is lower than fossil fuels except for Freshwater eutrophication, Land use, Water consumption, and Mineral resource scarcity which are higher. The life cycle greenhouse gas emissions or Global warming for heat production from para-rubber tree wood pellet (including wood pellet and waste wood) are lower than fossil fuels. The greenhouse gas emissions of the former are almost twenty times lower than their fossil equivalents. The reason for lower in the greenhouse gas emission is that wood pellet and wood waste uptake a lot of CO<sub>2</sub> as the tree was growing. However, the greenhouse gas emission of the wood pellet is more than wood waste due to the consumption of energy for wood pellet production. In a case study in China, 1 GJ of heat from wood pellet combustion released 11.76 kgCO<sub>2</sub>-eq of greenhouse gases, which is approximately 94% less than emissions from coal heating systems (Wang *et al.*, 2017) while 1 GJ of heat production from para-rubber tree wood pellet in this study released only 10.73 kgCO<sub>2</sub>-eq.

The toxicity potential, shown in kg 1,4-dichlorobenzene equivalent, is used for Human toxicity, Terrestrial ecotoxicity, Fresh toxicity and Marine toxicity. This study indicates that all toxicity categories of wood pellet are low except human non-carcinogenic toxicity which arises from wood ash of combustion for drying process and heat production. Therefore, disadvantage of using wood for fuel is high quantity of ash (3% of fuel), to decrease human non-carcinogenic toxicity should try to capitalise on wood ash like a component of cement or fertilizer for acid soil (Tosti *et al.*, 2019; Asquer *et al.*, 2019).

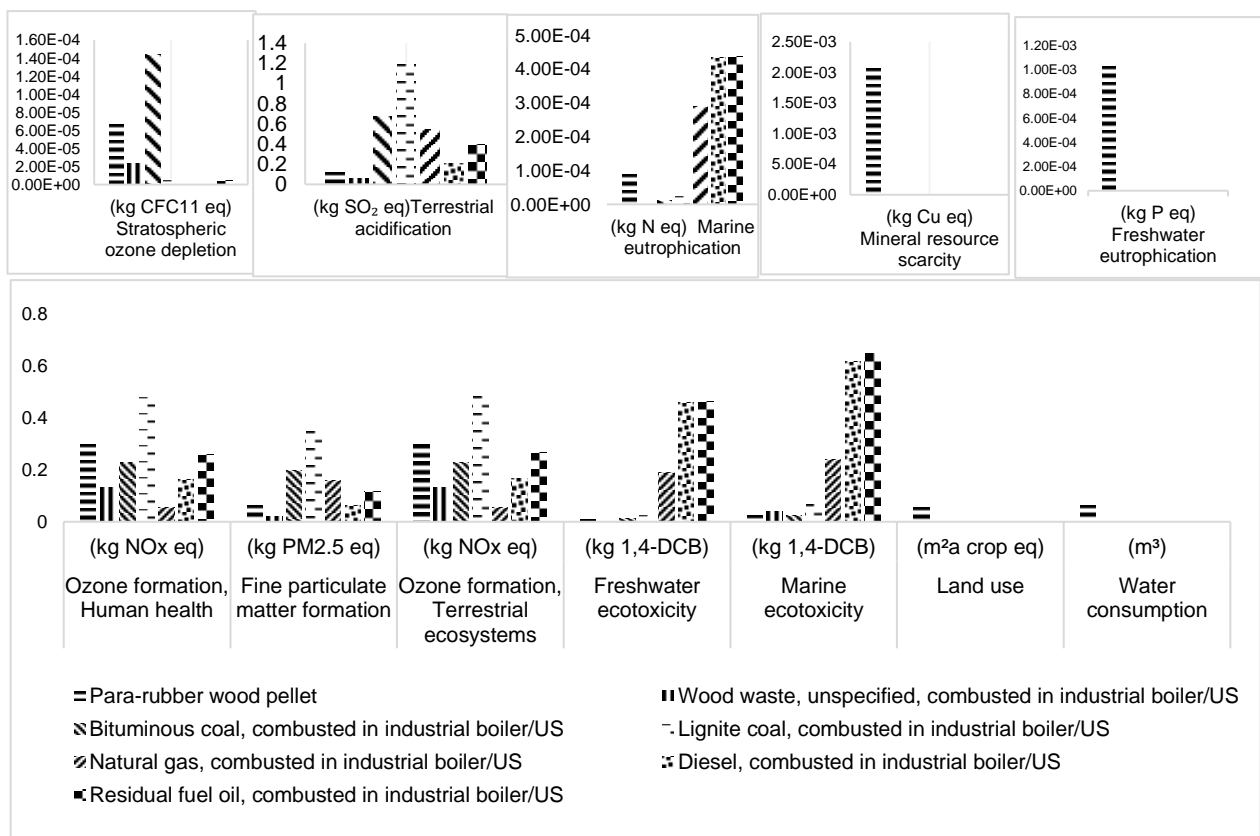
The environmental impact from emissions to air indicates that Fine particulate matter formation from wood pellet is lower than fossil fuels except for natural gas, which indicates that using wood pellets to replace oil or coal will reduce the quantity of particulate matter smaller than 2.5 micron which has been causing concerns in Thailand of smog and human health. Meanwhile, Stratosphere ozone depletion of wood pellet is higher than all except bituminous; increasing of Stratosphere ozone depletion results from nitrogen fertilizer which was used in para-rubber plantation. Ozone formation value of wood pellets is similar to coal, diesel, and fuel oil because of the process of heat production, wood pellet production (using firewood in combustion for drying raw material) and transportation (using diesel for truck).

Terrestrial acidification value of 1 GJ heat from wood pellet is significantly lower when compared with coal and oil as a result of the wood not having sulphur content; but it still has a nominal value of 0.13 kg SO<sub>2</sub> eq arising from the use of grid electricity in wood pellet production and diesel in transportation. The use of fertilizers releases N and P to the environment which are responsible for eutrophication. Freshwater eutrophication, which is mainly from P release, is 0.001 kg P eq for wood pellets and it is not even visible for the other fuels. On the other hand, Marine eutrophication of wood pellets, mainly from N release, is 9.14x10<sup>-5</sup> kg N eq which is less than natural gas, diesel and fuel oil. The Marine eutrophication for the fossil fuels is from NO<sub>x</sub> of fossil fuels burning, NO<sub>x</sub> is redeposited to land and water through wet deposition.

Land use and Water consumption for 1 GJ heat production from para-rubber wood residue are 0.06 m<sup>2</sup>a crop eq and 0.07 m<sup>3</sup> respectively, while for wood waste and fossil fuels are zero. This result relates with activity of para-rubber plantation which uses land and water for the cultivation of para-rubber trees.



The reason why Fossil scarcity of wood pellet is the lowest, is because wood pellet made from plants, which are renewable. Mineral scarcity of wood pellet is 0.002 kg Cu eq because of changing saw blades in the sawing process.



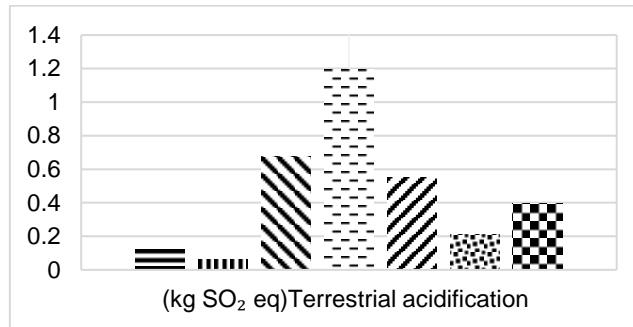


Figure 5: Overall comparison of the midpoint impacts of wood pellets, waste wood, and fossil fuels

### 3.3. Policy recommendations for improvement of wood pellet production and consumption

To improve wood pellet production and consumption in Thailand, several policy recommendations are identified as follow.

#### *Reducing over-use of fertilizers and herbicides*

Marine eutrophication of wood pellets (Figure 5) is higher than wood waste, bituminous and lignite. In the para rubber tree cultivation process, farmers still use chemical fertilizers two times per year. Although the government supported the innovation for calculating quantity of fertilizers in relation to soil quality, this project was not widely adopted for para rubber cultivation. Hence, the government should promote and reactivate this project to reduce over-use of fertilizers. At present, para rubber tree cultivation in Thailand still uses herbicides such as glyphosate and paraquat to remove weeds. Although these herbicides have been banned for use in cultivation in several countries (Sustainable pulse, 2019), the Thai government has announced a limit on using these herbicides. The Ministry of Agriculture and Cooperatives supports registration and training of farmers who need to use them. To be safe for farmers, a long term plan for decreasing use of hazardous herbicides should be prepared, including research on organic herbicides which are environmental-friendly.

#### *Management of energy use throughout life cycle of wood pellets*

The energy use throughout the life cycle of wood pellets has three parts; wood waste for combustion in drying process, diesel for vehicles, and electricity consumption of wood pellet factory. Section 3.1 shows that the contribution of transportation is over 60% in Global warming, Terrestrial ecotoxicity, Marine ecotoxicity, Human carcinogen toxicity, and Fossil resource scarcity. Hence, it is an important to convince entrepreneurs to use renewable energy in this phase. For transportation, diesel can be substituted by biodiesel. Nevertheless, efficient use of energy in the factory is the first activity entrepreneurs can do. The government must rapidly create some strategies to convince entrepreneurs to participate in using clean energy and using energy efficiently.

#### *Planning for logistics*

The transportation has been modeled in this study (Figure 2) following the actual situation. Setting of wood pellet factories is near raw material source and users, leading to reductions in cost and fuel use. The return trip of transport are still empty. If entrepreneurs can plan the return trips to carry back some material, the cost of transportation as well as the environmental impacts will decrease.

#### *Pollution control*

Ozone formation, stratospheric ozone depletion and Fine particulate matter formation of wood pellets is higher than wood waste and some fossil fuels. Emissions to air originate from the drying process of wood pellet production and heat production. Therefore, controlling air pollution emissions by efficient equipment is important. Pollution control must be conscientiously investigated by the relevant government agencies.

## 4. CONCLUSIONS

The result of LCA through all production processes and transportation indicate that heat production process contributes to more than 65% for stratospheric ozone depletion, ozone formation, fine particulate matter formation,



terrestrial acidification, freshwater eutrophication, and human non-carcinogen toxicity. Source of air pollution comes from combustion, so to control air pollution emission by efficient equipment is important.

In addition, the contribution of transportation is over 60% in global warming, terrestrial ecotoxicity, marine ecotoxicity, human carcinogen toxicity, and fossil resource scarcity. In this study, the fuel for transportation is diesel; if possible, changing from diesel to biodiesel or bioenergy could likely decrease the impacts from transportation. Meanwhile, distance management of raw material source and wood pellet users could also be important.

From the LCA results of comparison among wood pellets with fossil fuels, it can be concluded that in terms of global warming, stratosphere ozone depletion, ozone formation, fine particulate matter formation, terrestrial ecotoxicity, human carcinogenic toxicity, human non-carcinogenic toxicity, fossil resource scarcity, terrestrial acidification, fresh ecotoxicity, marine ecotoxicity and marine eutrophication, wood pellets are better than fossil fuels while fossil fuels are better than wood pellets for freshwater eutrophication, land use, mineral resource scarcity, and water consumption. These results are understandable because biomass-based fuels are expected to have higher values for land, water and nutrient-related impacts due to agriculture.

Although, several environmental impacts of wood pellet are better than fossil fuel, source of raw material for wood pellet production will be consider about using over fertilizer and herbicide which directly affect eutrophication and stratosphere ozone depletion. Moreover, consumption of fossil fuel (particularly during transportation) should specially be considered for changing to renewable energy.

## 5. ACKNOWLEDGEMENT

The authors gratefully thank the Joint Graduate School of Energy and Environment at King Mongkut's University of Thonburi and the Energy Policy and Planning Office, Ministry of Energy, Thailand for financial support. In addition, we would like to thank the staff at the wood pellet factory for kindly providing information.

## 6. REFERENCES

Asquer, C., Cappai, G., Carucci, A., De Gioannis, G., Muntoni, A., Piredda, M. and Spiga, D. (2019) 'Biomass ash characterisation for reuse as additive in composting process', *Biomass and Bioenergy*. 123, pp. 186–194.

Department of Alternative Energy Department and Efficiency and King Mongkut's Institute of Technology Ladkrabang. (2016) *Using wood pellet for small boiler in industry*, Bangkok: Department of Alternative Energy Department and Efficiency. Bangkok.

Finnveden, G., Hauschild, Michael Z., Ekvall, T., Guinée, J., Heijungs, R., Hellweg, S., Koehler, A., Pennington, D. and Suh, S. (2009) 'Recent developments in Life Cycle Assessment', *Journal of Environmental Management*. 91(1), pp. 1–21.

Huijbregts, M., Steinmann, Z. J. N., Elshout, P. M. F. M., Stam, G., Verones, F., Vieira, M. D. M., Zijp, M. and Zelm van, R. (2016) *ReCiPe 2016*, National Institute for Public Health and the Environment.

ISO14040 (2006) *Environmental management — Life cycle assessment — Principles and framework*, International Standard Organization.

Jonsson, R. and Rinaldi, F. (2017) 'The impact on global wood-product markets of increasing consumption of wood pellets within the European Union', *Energy*. 133(2017), pp. 864–878.

Ketdecha, N. (2013) *The water footprint of rubber wood products case study: Nakhon Si Thammarat and Chanthaburi Province*. Thammasart University.

Kotrba, R. (2016) *Asian wood pellet producer market snapshot*, *Biomass Magazine*. Available at: <http://biomassmagazine.com/articles/13880/asian-wood-pellet-producer-market-snapshot> (Accessed: 15 March 2019).

Monteleone, B., Chiesa, M., Marzuoli, R., Verma, V. K., Schwarz, M., Carlon, E., Schmidl, C. and Ballarin Denti, A. (2015) 'Life cycle analysis of small scale pellet boilers characterized by high efficiency and low emissions', *Applied Energy*. 155(2015), pp. 160–170.

- Morrison, B. and Golden, J. S. (2017) 'Life cycle assessment of co-firing coal and wood pellets in the Southeastern United States', *Journal of Cleaner Production*. 150, pp. 188–196.
- Musikavong, C., Hanpongkittikun, A., Sdoodee, S., Suksaroj, C. and Jungcharoentharn, N. (2015) *Assessment water footprint in the rubber plantations in the new area of the South of Thailand*. Bangkok.
- Thai Customs (2019) *Statistic report*. Available at: [http://www.customs.go.th/statistic\\_report.php?tab=by\\_statistic\\_code](http://www.customs.go.th/statistic_report.php?tab=by_statistic_code) (Accessed: 1 May 2019).
- Thrän, D., Peetz, D. and Schaubach, K. (2017) *Global wood pellet industry and trade study 2017. IEA Bioenergy Task 40, IEA Bioenergy Task 40*. IEA Bioenergy. Available at: [http://task40.ieabioenergy.com/wp-content/uploads/2013/09/IEA-Wood-Pellet-Study\\_final-2017-06.pdf](http://task40.ieabioenergy.com/wp-content/uploads/2013/09/IEA-Wood-Pellet-Study_final-2017-06.pdf).
- Tosti, L., Zomerren, A., Pels, Jan R., Dijkstra, Joris J. and Comans, Rob N.J. (2019) 'Assessment of biomass ash applications in soil and cement mortars', *Chemosphere*. 223, pp. 425–437.
- Walker, S. and Strauss, W. (2019) *2019 Global Wood Pellet Markets Outlook*. Available at: <https://www.canadianbiomassmagazine.ca/pellets/2019-wood-pellet-markets-outlook-7190> (Accessed: 20 April 2019).
- Wang, C., Chang, Y., Zhang, L., Pang, M. and Hao, Y. (2017) 'A life-cycle comparison of the energy, environmental and economic impacts of coal versus wood pellets for generating heat in China', *Energy*. 120, pp. 374–384.
- Wattana, W., Wattana, W., Phetklung, S., Jakaew, W., Chumuthai, S., Sriama, P. and Chanurai, N. (2017) 'Characterization Mixed Biomass Pellet Made from Oil Palm and Para-rubber Tree Residues', *Energy Procedia*. 138, pp. 1128–1133.
- PRé Consultants B.V., (2019) About SimaPro. Available at: <https://simapro.com/about/> (Accessed: 25 July 2019).
- Sustainable pulse. (2019) *Glyphosate Herbicides Now Banned or Restricted in 17 Countries Worldwide*. Available at: <https://sustainablepulse.com/2019/05/28/glyphosate-herbicides-now-banned-or-restricted-in-17-countries-worldwide-sustainable-pulse-research/#.XTsTpugza00> (Accessed: 28 May 2019).

---

## #120: Investigating supercritical CO<sub>2</sub> power cycle and potential of improvement of turbine leakage characteristics by using barrier gas

---

Hafiz Ali MUHAMMAD<sup>1,2</sup>, Junhyun CHO<sup>2</sup>, Gilbong LEE<sup>2</sup>, Beomjoon LEE<sup>2</sup>, Young-Jin BAIK<sup>1,2,\*</sup>

<sup>1</sup>Dept. of Renewable Energy Engineering, University of Science and Technology, Daejeon 305-350, South Korea

<sup>2</sup>Energy Efficiency and Materials Research Division, Korea Institute of Energy Research, Daejeon 305-343, South Korea

\*Corresponding author: twinjin@kier.re.kr

*Supercritical CO<sub>2</sub> power cycle, which has gained a tremendous interest in recent year owing to its compactness and enhanced efficiency, was investigated in this study. In the present study, leakage characteristics of the 500 °C-class sub-miniature supercritical carbon dioxide turbine with Labyrinth seals were investigated for CSP (Concentrated Solar Power) generation. In contrast to previous studies, a new leakage management scheme using barrier gas was proposed and simulated. The modelling of the labyrinth seals was validated against the published results. Subsequently, multivariate optimisations based on the genetic algorithm were carried out to maximise the improvement of the leakage characteristics. Results show that the power demand for the recovery of leakage by the proposed scheme can be reduced by up to 15% compared to the power demand according to the conventional scheme under the simulation conditions considered in the present study.*

*Keywords: supercritical CO<sub>2</sub>; turbine; seal leakage; barrier gas*

## 1. INTRODUCTION

The thermodynamic community has been working on increasing the share of renewable energy in World's global energy mix and to increase the efficiency of energy conversion systems. To this extent supercritical CO<sub>2</sub> (sCO<sub>2</sub>) cycle has been rigorously investigated in the past, as it is capable of generating power with improved efficiency and can utilise renewable energy resource as the heat source (Li et al, 2017; Kumar and Srinivasan, 2016). Supercritical carbon dioxide (sCO<sub>2</sub>) power generation is a highly efficient miniaturised power production technology. Unlike conventional power generation, it generates electricity by rotating the turbine using sCO<sub>2</sub> at high temperature and pressure. It is also suitable for condensing solar power generation (CSP) application because of its compatibility with the existing heat storage systems and its potential to be operated using dry –cooling since there is no phase change involved during the heat transfer process (Brun et al, 2017). For this reason, sCO<sub>2</sub> power generation studies are actively being conducted with the aim of applying CSPs as the heat source. Figure 1 shows a recompression sCO<sub>2</sub> cycle schematics with CSP as the heat source (Ma and Turchi, 2011). The United States is a technology leader in this field, and through a large research program called 'SunShot', it is pursuing research on sCO<sub>2</sub> power generation cycle, turbomachinery, heat exchanger and material development with the goal of achieving LCOE of 6cent / kWh by 2020 (U.S. DOE, 2012). NREL has been working on improving the efficiency of sCO<sub>2</sub> based power generation systems over conventional steam based systems (Glatzmaier, 2011; Turchi et al, 2012; Neises, 2013). (Sullivan and Zidan, 2016) has worked on the development of high temperature solar cell collectors while (Pint et al, 2017) studied the material compatibility in high temperature sCO<sub>2</sub> environment. Research is also being conducted on how to lower the LCOE of sCO<sub>2</sub> based system for CSP (Schmitt et al, 2017). In addition, basic research on sCO<sub>2</sub> power generation cycle and compressor is being carried out in Europe (Crespi et al, 2017; Monge et al, 2014).

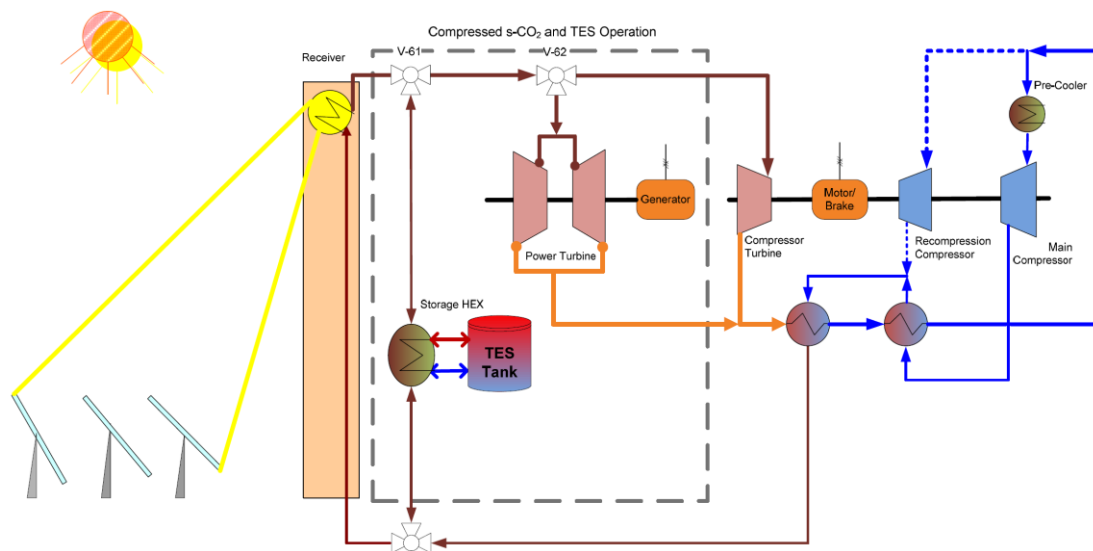


Figure 1: Concentrating solar power (CSP) generation based sCO<sub>2</sub> cycle schematics.

Like any conventional power generation cycle, the sCO<sub>2</sub> power generation system consists of various elements, of which the turbine is one of the critical device that produce power using high temperature and high pressure working fluid. A typical power generating turbine has fixed and rotating components, separated by the seal. The sealing technology is necessary to limit the amount of leakage of the working fluid through the gap between the rotating and the fixed components. Any amount of leakage that occurs through the turbine needs to be replenished by an additional process to sustain continuous operation. Supplementing the leaked flow to the main cycle is energy intensive process and reduces the net power production of the overall system. Therefore, to maximise the cycle efficiency it is essential to minimise the leakage amount.

In the early stage of sCO<sub>2</sub> power generation research, extensive research has been carried out to develop a turbine with a closed structure that can prevent such leakage (Convoy et al, 2013; Clementoni et al, 2016). However, in such a structure, the problem of bearing reliability arises due to large axial forces because of high rotational speed of the shaft. Also, due to the high density of sCO<sub>2</sub>, the close hermetic structure of turbomachinery, leads to excessive windage losses (Pasch et al, 2012). The windage losses can significantly reduce the sCO<sub>2</sub> cycle efficiency and recent studies show it still has been a daunting challenge to overcome (Moore et al, 2014; Thatte et

al, 2016). Alternatively, some researchers adopted open turbine structure and have investigated energy efficient ways for leakage supplement system (Muhammad et al, 2019).

In this study, leakage characteristics of a small 500°C sCO<sub>2</sub> turbine using a labyrinth seal were investigated which is expected to be applicable in the field of condensing solar power generation. A base case with labyrinth seal is established and its performance in terms of required reinjection power for leakage supplement system was quantified. To improve the leakage characteristics, unlike previous studies, a novel barrier gas utilisation method was proposed, modelled and simulated in the MATLAB environment. In order to maximise the improvement effect compared to the base case, multivariate optimisation using pattern search algorithm (PSA) was performed. The objective function is selected as the reinjection power and is minimised using PSA in the MATLAB.

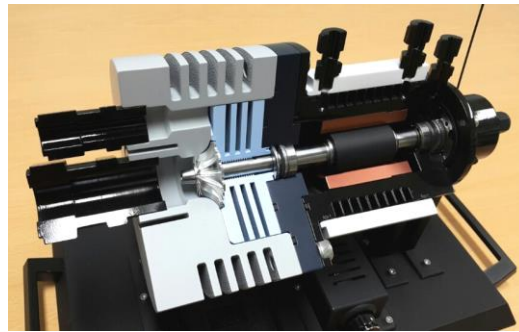


Figure 2(a): A model of 500°C ultra-small sCO<sub>2</sub> turbine (Baik et al, 2018).

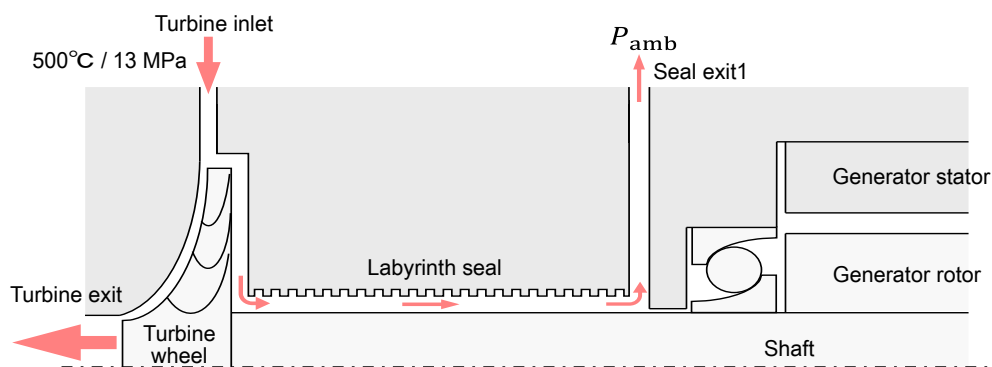


Figure 2(b): Schematics of 500°C ultra-small sCO<sub>2</sub> turbine.

## 2. MODELLING AND SIMULATION

Figure 2 shows a model and schematic diagram of a 500°C ultra-small sCO<sub>2</sub> turbine-generator considered in this study. The high pressure CO<sub>2</sub> heated by the solar heater to the high temperature passes through the turbine inlet and accelerates through the nozzle to rotate the turbine wheel. After rotating the turbine wheel and expanding to the low temperature and low pressure state, it is discharged to the turbine outlet. The generator rotor attached with the turbine shaft rotates to generate power through the stator of the generator. At the time of power generation, some amount of working fluid leaks through the gap between the rotating turbine wheel / shaft and the fixed casing / body at the rear of the turbine wheel, towards the generator at atmospheric pressure. In the event of leakage, an external process is required to replenish the same amount of CO<sub>2</sub> or collect the leaked CO<sub>2</sub> from the seal and inject it back into the main cycle for continuous operation.

The leakage generated from the labyrinth seals was calculated by the Hodkinson model given in Equation 1 which takes into account the compressibility effect by employing an expansion coefficient (Suryanarayanan, 2009, p. 7; Hodkinson, 1939). The leakage amount was expressed as:

Equation 1(a): Leakage through labyrinth seals.

$$\dot{m} = A * \alpha * \Psi * \Upsilon * \sqrt{d_{In} * P_{In}}$$

Equation 1(b): Expansion coefficient.

$$\Psi = \sqrt{\frac{1 - \left(\frac{P_e}{P_{In}}\right)^2}{N - \ln(P_e/P_{In})}}$$

Equation 1(c): Kinetic energy carry over coefficient.

$$\Upsilon = \sqrt{\frac{1}{1 - \frac{N-1}{N} \frac{c/S}{c/S+0.02}}}$$

Where:

- $\dot{m}$  = leakage mass flow rate (kg/s).
- A = Annulus area for leakage flow (m<sup>2</sup>).
- $\alpha$  = 0.72 (an experimentally determined coefficient similar to discharge coefficient).
- $\Psi$  = Expansion coefficient.
- C = Seal and rotor clearance shown in Figure 4.
- S = Seal pitch shown in Figure 4.
- N = Number of teeth.
- $d_{in}$  &  $P_{in}$  = Seal inlet density (kg/m<sup>3</sup>) pressure (Pa).
- $P_e$  = Seal outlet pressure which is ambient pressure in the Figure 2 (Pa).

## 2.1. Model validation

The amount of leakage predicted by the Hodkinson model given in Equation 1 was compared with the experimental results of (Yuan et al, 2015). (Yuan et al, 2015) conducted experiments on two teeth labyrinth seals with sCO<sub>2</sub> as working fluid. The boundary conditions and seal geometrical parameters taken in their experiments are tabulated in Table 1. The Figure 4 shows the comparison between the experimental and this study results for non-choked flow conditions. From Figure 4, we concluded the model used in this study predicted the leakage flow rate of sCO<sub>2</sub> through labyrinth seals with reasonable accuracy.

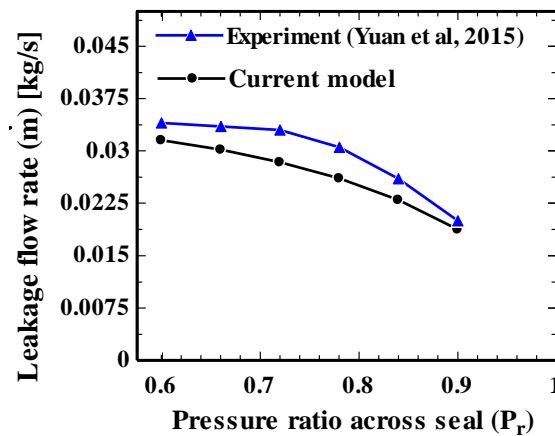


Figure 3: Model prediction comparison with experimental results.

Table 1: Labyrinth seal geometry for comparison (Yuan et al, 2015).

Parameter	Values
Seal inlet pressure ( $P_{in}$ )	10 [MPa]
Seal inlet density ( $d_{in}$ )	475 [kg/m <sup>3</sup> ]
Pressure ratio across seal ( $P_r$ )	0.6—0.9
Seal clearance (c)	0.105 [mm]
Seal pitch (P)	2.54 [mm]
Number of teeth (N)	2

## 2.2. Labyrinth seals for small scale sCO<sub>2</sub> turbine with barrier gas utilisation

In our study we initially established as a base case for labyrinth seals without barrier gas. The labyrinth seal geometrical parameters considered in this study are shown in Figure 4.

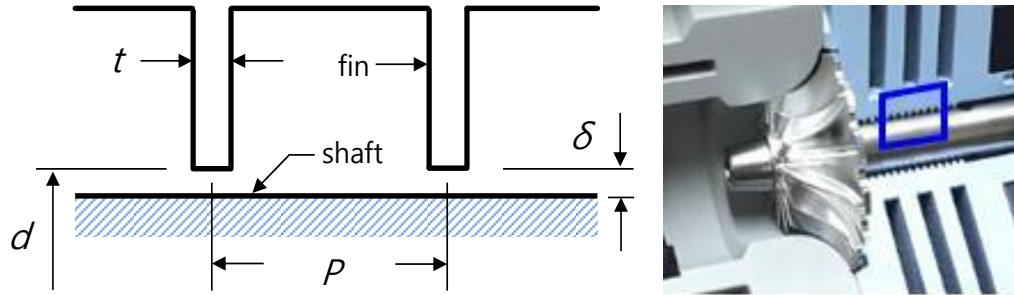


Figure 4: Labyrinth seal geometry for sCO<sub>2</sub> turbine (Baik et al, 2018).

To improve the leakage characteristics, we proposed and investigated a barrier gas method. The aim was to reduce the leakage amount by injecting a barrier gas at high pressures. To utilise the barrier gas schematics the labyrinth seals were divided into three parts A, B and C and an additional flow path was formed as shown in Figure 5. When the high pressure barrier gas was injected, the pressure ratio across seal exit 2 in part A decreases, which led to the decrease in the leakage flow rate ( $\dot{m}_A$ ) from the turbine rear wheel. The mass flow rate of the barrier gas injected divided itself in two paths and partly flowed towards seal exit 2 and the remaining was collected at seal exit 1. The sum of  $\dot{m}_A$  and  $\dot{m}_B$  collected at seal exit 2 is at higher pressure ( $P_{ex}$ ) compared to ambient pressure. In this method, unlike the conventional sealing method, it is necessary to collect the CO<sub>2</sub> discharged at two places to re-inject to the main cycle, but the power required for the re-injection pressurisation process can be minimised by controlling the pressure of the barrier CO<sub>2</sub> and the lengths of the seals.

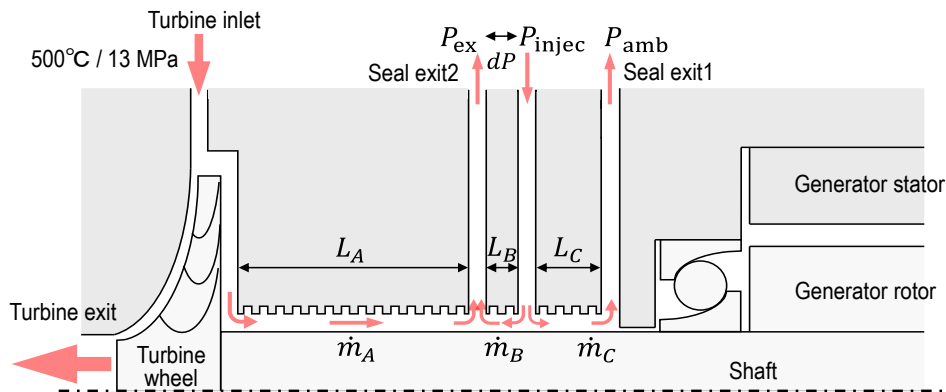


Figure 5: Conceptual diagram of seal with barrier gas utilisation.

The amount of leakage gathered was later compressed to the low pressure level of the cycle and is subsequently reinjected to the main cycle. The power consumed during rejection is given by:

Equation 2: Reinjection power.

$$\dot{W} = [(\dot{m}_A + \dot{m}_B) * (h - h_{l,ex})] + \dot{m}_C * (h - h_{l,amb})$$

Where:

- $\dot{W}$  = Reinjection power (W)
- $h$  = Enthalpy after compression,  $h=f(P_{low}, \eta)$ . The compressor efficiency ( $\eta$ ) was taken as 0.80.
- $h_{l,ex}$  = Enthalpy of leakage at  $P = P_{ex}$  and  $T=T_o$
- $h_{l,amb}$  = Enthalpy of leakage at  $P = P_{amb}$  and  $T=T_o$

In the labyrinth seal design shown in Figure 5, four important design factors were chosen as the most influencing parameters. The first three factors were the length of each seal ( $L_A$ ,  $L_B$ , and  $L_C$ ), and the last factor is the pressure of the barrier CO<sub>2</sub> ( $P_{injec}$ ). It is obvious increasing the length of seal reduces the leakage flow rate across the

respective seal. However, since the internal space of the turbine was limited, optimum design for each seal length in a given space was required to optimise the seal performance. Given the conditions and schematics shown in Figure 5, increasing the barrier gas pressure can reduce the amount of leakage from the back of the turbine wheel and increase the discharge pressure ( $P_{ex}$ ), thereby reducing the power required for the re-injection of  $CO_2$  discharged into the flow path between the seals A and B at seal exit 2. However, there is a possibility that the re-injection power required for the pressurisation of the  $CO_2$  discharged through the seal exit 1 can increase. Therefore, an optimum value of  $P_{Injec}$  was required to minimise the power  $\dot{W}$  formulated in Equation 2.

The system was assumed to be in a steady state and the heat loss was neglected. The geometrical parameters of the seal taken from (Baik et al, 2018) were: thickness 't' of the pin forming the seal was taken as 0.1 mm, the pin spacing 'P' was 1 mm, the gap ' $\delta$ ' was 0.06 mm, rotor diameter 'd' was 8 mm, the rear temperature and pressure ( $P_{low}$ ) of the wheel are 435°C. and 7.7 MPa, respectively, and the rear end of the seal is atmospheric pressure (101.325 kPa). The temperature of the barrier  $CO_2$  injected into the flow path between the seals B and C was set to the atmospheric temperature (30°C). The total length of the seal was 30 mm, and it was assumed that the size of the space for forming the passage between the seals was negligible. The physical properties of carbon dioxide were obtained using REFPROP 9.0 (Lemmon et al, 2010).

### 3. RESULTS AND DISCUSSIONS

#### 3.1. Variation of leakage characteristics with design factors

Under the above calculation conditions, the leakage flow rate using conventional method shown in Figure 2(b) was 7.49 g/s and the reinjection power required to inject it back was 3.68 kW. In the proposed design shown in Figure 5, the variation of reinjection power with four design factors (independent variables) was investigated. Figure 6 indicates the change in leakage characteristics according to the variation of each design factor when the difference between the pressure of the barrier  $CO_2$  and the  $P_{ex}$  is 10 kPa. In Figure 6(a), the re-injection power of  $CO_2$  discharged into the seal exit 2 (Seal exit2) reduces with the increase in the  $L_A$ , while the re-injection power of the leaked  $CO_2$  gathered at seal exit 1 consequently increases. Figure 6(b) shows increasing  $L_B$ , increases the required compression power at both seal exits. The plausible reason is increasing  $L_B$  decreases both  $L_A$  and  $L_C$ . And although the  $\dot{m}_B$  decreases, however the sum of  $\dot{m}_A$  and  $\dot{m}_B$  at seal exit 2 increases which will increase the reinjection power at seal exit 2. The reinjection power at seal exit 1 increases due to the increase in  $\dot{m}_C$  because of the reduction in  $L_C$ . Figure 6(c) shows an optimum value of  $L_C$  exists which minimise the total reinjection power. Finally, Figure 6(d) presents the variation of objective function with  $P_{Injec}$ . When the barrier gas is at lower pressures, it failed to act as the barrier and hence the reinjection power at seal exit 2 are high at lower injection pressures. On the other hand, excessively increasing the  $P_{Injec}$  will drastically increase the  $\dot{m}_C$  and thereby increasing the required reinjection power at seal exit 1 as can be seen in Figure 6(d). Therefore, finding the optimum value of  $P_{Injec}$  is critical to optimise the leakage characteristics of the proposed design.

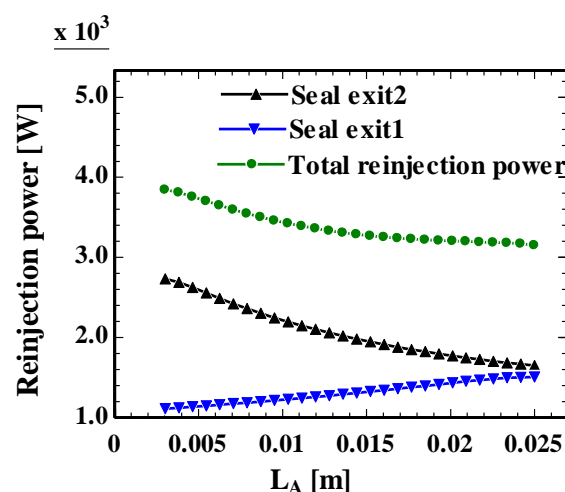


Figure 6(a): Variation of leakage characteristics with design factor  $L_A$  ( $L_B=L_C$  and  $P_{Injec} = 1MPa$ ).



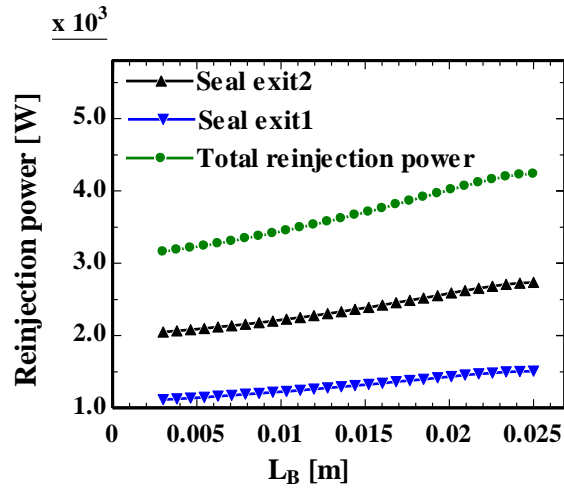


Figure 6(b): Variation of leakage characteristics with design factor  $L_B$  ( $L_A=L_C$  and  $P_{injec} = 1MPa$ ).

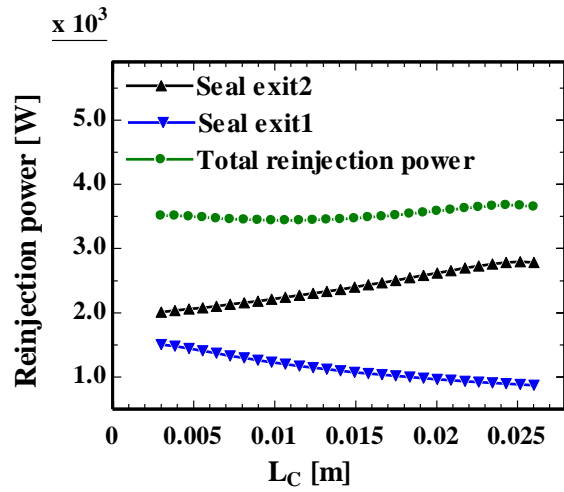


Figure 6(c): Variation of leakage characteristics with design factor  $L_C$  ( $L_A=L_B$  and  $P_{injec} = 1MPa$ ).

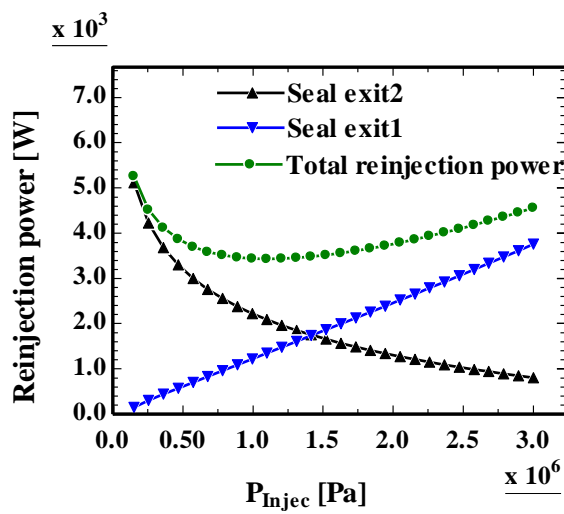


Figure 6(d): Variation of leakage characteristics with design factor  $P_{injec}$  ( $L_A=L_B=L_C$ ).

### 3.2. Optimisation of design factors using multivariate optimisation algorithm

As described above, the leakage characteristics of the present invention vary depending on a number of design factors. Therefore, in order to optimise the leakage characteristics, an optimal combination of these should be found. PSA is a suitable optimisation technique for multivariable functions and was adopted in our study (Lewis and Torczon, 2002). It has an advantage that it can be applied without information about the gradient of the objective function. In this study, we implemented PSA using Global Optimisation Toolbox of Matlab, 2017. The bounds on the independent variables are given in Table 2. Minimum length of each seal is selected as 2 mm so that each seal has at-least two teeth. The bound on the  $P_{Injec}$  is governed by the ambient pressure and the low pressure level of the cycle.

Table 2: Bounds of independent variables.

Parameter	Bound
Total length ( $L_A+L_B+L_C$ )	= 30 mm
Individual lengths ( $L_A, L_B$ & $L_C$ )	$\geq 2$ mm
$P_{Injec}$	$dP+101.325 \text{ kPa} < P_{Injec} < 7.7 \text{ MPa}$

The optimal combination of the four design factors, i.e.  $L_A$ ,  $L_B$ ,  $L_C$  and  $P_{Injec}$  are 20 mm, 2 mm, 8 mm and 873.86 kPa, respectively assuming 1 kPa of the difference between the pressure of the barrier  $\text{CO}_2$  and the seal 2 discharge pressure ( $P_{ex}$ ). The PSA optimisation results with respect to iteration number are shown in Figure 7. The algorithm terminates when the difference in objective function value was less than  $1\text{E-}6$  for the successive iterations. At the optimal conditions the leakage from the rear of the turbine wheel was 9.05 g / s, and the flow rate of the barrier  $\text{CO}_2$  was:  $\dot{m}_B$  0.17 g / s, and  $\dot{m}_C$  was 2.17 g / s. The power required to reinject the leakage gathered at seat exit 2 and seal exit 1 was 1.74 kW and 1.06 kW, respectively. The total required power in the proposed schematics was therefore 2.81 kW which is about 23.6% less compared to 3.68 kW for the conventional method.

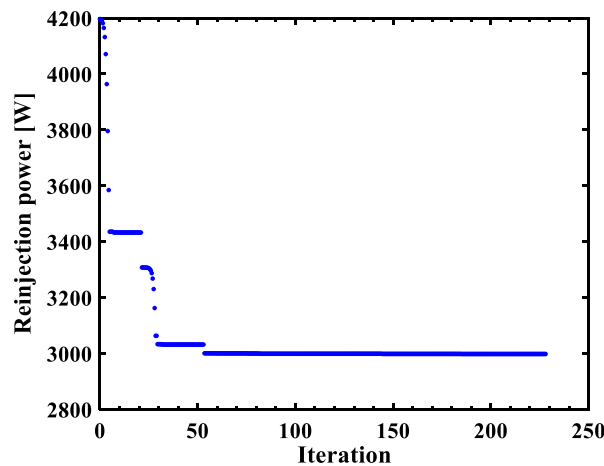


Figure 7: ReInjection power (objective function) variation with successive iterations of PSA.

## 4. CONCLUSIONS

This study was carried out as a preliminary investigation of leakage characteristics of supercritical  $\text{CO}_2$  turbine at  $500^\circ\text{C}$ , which is expected to be applicable to the field of concentrating solar power generation in the future. The study proposed and modelled a new barrier gas utilisation scheme to reduce the power associated with leakage supplement system for  $\text{sCO}_2$  turbine. In order to maximise the improvement effect, multivariate optimisation using pattern search algorithm was performed. As a result, it was observed that the power demand for the reinjection of  $\text{CO}_2$  could be reduced by 23.6% under the simulated conditions of this study, compared with the conventional method.

## 5. REFERENCES

- Baik, Y. J., Cho, J., Shin, H. K., Cho, J., Roh, C. W., Choi, B., Lee, B., Lee, G., Ra, H., 2018. Potential for Improvement of Leakage Characteristics by Using Barrier Gas in a Subminiature Supercritical Carbon Dioxide Turbine. *The Korean Solar Energy Society*.
- Brun, K., Friedman, P., and Dennis R., 2017. *Fundamentals and Applications of Supercritical Carbon Dioxide (sCO<sub>2</sub>) Based Power Cycles*. Woodhead Publishing.
- Clementoni, E., Cox, T., and King M., 2016. Steady-state power operation of a supercritical carbon dioxide Brayton cycle with thermal-hydraulic control. *ASME TurboEXPO 2016*, GT2016-56038.
- Convoy, T., Pasch, J., and Fleming, D., 2013. Control of a Supercritical CO<sub>2</sub> Recompression Brayton Cycle Demonstration Loop. *ASME Journal of Engineering for Gas Turbines and Power*, 135, 111701.
- Crespi, F., Sanchez, D., Rodriguez, J. M., and Gavagnin G., 2017. Fundamental Thermo-Economic Approach to Selecting sCO<sub>2</sub> Power Cycles for CSP Applications. *Energy Procedia*, 129, pp. 963-970.
- Glatzmaier, G., 2011. Summary Report for Concentrating Solar Power Thermal Storage Workshop-New Concepts and Materials for Thermal Energy Storage and Heat-Transfer Fluids. NREL/TP-5500-52134.
- Hodkinson, B., 1939. Estimation of the Leakage through a Labyrinth Gland. *Proc. Inst. Mech. Engrs*, 141, pp. 283-288.
- Kumar, P., Srinivasan, K., 2016. Carbon dioxide based power generation in renewable energy systems. *Applied Thermal Engineering*, 109, pp. 831-840.
- Lemmon, E. W., Huber, M. L. and McLinden, M. O., 2010. NIST Standard Reference Database 23: Reference Fluid Thermodynamic and Transport Properties-REFPROP. Version 9.0, National Institute of Standards and Technology, Standard Reference Data Program, Gaithersburg.
- Lewis, R. M. and Torczon, V., 2002. A globally convergent augmented Lagrangian pattern search algorithm for optimization with general constraints and simple bounds. *SIAM Journal on Optimization*, 12, pp. 1075-1089.
- Li, M.J., Zhu, H.H., Guo, J.Q., Wang, K., Tao, W.Q., 2017. The development technology and applications of supercritical CO<sub>2</sub> power cycle in nuclear energy, solar energy and other energy industries. *Applied Thermal Engineering*, 126, pp. 255-275.
- Ma, Z., and Turchi, C., 2011. Advanced Supercritical Carbon Dioxide Power Cycle Configurations for Use in Concentrating Solar Power Systems. *Supercritical CO<sub>2</sub> Power Cycle Symposium* May 24-25 Boulder, Colorado.
- MATLAB Version R2017b, 2017, The MathWorks Inc.
- Monge, B., Sanchez, D., Savill, M., and Sanchez T., 2014. The 4th International Symposium - Supercritical CO<sub>2</sub> Power Cycles, September 9-10, 2014, Pittsburgh, Pennsylvania.
- Moore, J., Brun, K., Evans, N., Bueno, P., and Kalra, C., 2014. Development of a 1 MWe supercritical CO<sub>2</sub> Brayton cycle test loop. *The 4th international symposium-Supercritical CO<sub>2</sub> power cycles*, Pittsburgh, Pennsylvania.
- Muhammad H.A., Lee B., Lee G., Cho J., Baik Y.J., 2019. Investigation of leakage reinjection system for supercritical CO<sub>2</sub> power cycle using heat pump. *Renewable Energy*, 144, pp. 97-106. <https://doi.org/10.1016/j.renene.2018.10.059>
- Neises, T., 2013. A Comparison of Supercritical Carbon Dioxide Power Cycle Configurations with an Emphasis on CSP Applications. NREL/PR-5500-60654, *SolarPACES* Las Vegas, NV.
- Pasch, J., Conboy, T., Fleming, D. and Rochau, G., 2012. Supercritical CO<sub>2</sub> Recompression Brayton Cycle: Completed Assembly Description. SAND2012-9546.

Pint, B. A., Brese, R. G., and Keiser, J. R., 2017. Effect of Pressure and Thermal Cycling on Compatibility in CO<sub>2</sub> for Concentrated Solar Power Applications. *Proceedings of ASME Turbo Expo 2017: Turbomachinery Technical Conference and Exposition* GT2017-65066, Charlotte, NC, USA.

Schmitt, J., Wikes, J., Allison, T., and Bennett J., 2017. Lowering the Levelized Cost of Electricity of a Concentrating Solar Power Tower with a Supercritical Carbon Dioxide Power Cycle. *Proceedings of ASME Turbo Expo 2017: Turbomachinery Technical Conference and Exposition* GT2017-64958, Charlotte, NC, USA.

Sullivan, S., and Zidan, R., 2016. High-Efficiency Low-Cost Solar Receiver for Use in a Supercritical Co<sub>2</sub> Recompression Cycle. *CSP Program Summit* 2016.

Suryanarayanan, S., 2009. Labyrinth seal leakage equation. Master Thesis, *Texas A&M University*.

Thatte, A., Loghin, A., Martin, E., Dheeradhada, V., Shin, Y., and Ananthasayanam, B., 2016. Multi-Scale Coupled Physics Models and Experiments for Performance and Life Prediction of Supercritical CO<sub>2</sub> Turbomachinery Components. *The 5th International Symposium - Supercritical CO<sub>2</sub> Power Cycles*, San Antonio, Texas.

Turchi, C., Ma, Z., and Dyreby, J., 2012. Supercritical Carbon Dioxide Power Cycle Configurations for Use in Concentrating Solar Power Systems. *ASME Turbo Expo 2012*, Copenhagen, Denmark.

U.S. Department of Energy, 2012, SunShot Vision Study.

Yuan, H., Pidaparti, S., Wolf, M., Edlebeck, J., Anderson, M., 2015. Numerical modelling of supercritical carbon dioxide flow in see-through labyrinth seals. *Nuclear Engineering and Design*, 293, pp. 436-446.

---

## #121: Experimental study on the effect of orientation of vapour grooves on the thermal performance of a novel plate loop heat pipe

---

Sheng DU<sup>1</sup>, Quan ZHANG<sup>2</sup>\*, Peilin HOU<sup>3</sup>, Sikai ZOU<sup>4</sup>, Chang YUE<sup>5</sup>, Zhengyong SHA<sup>6</sup>

<sup>1</sup>College of Civil Engineering, Hunan University, Changsha, Hunan 410082, China, 501744567@qq.com.

<sup>2</sup>College of Civil Engineering, Hunan University, Changsha, Hunan 410082, China, quanzhang@hnu.edu.cn.

<sup>3</sup>College of Civil Engineering, Hunan University, Changsha, Hunan 410082, China, 501744567@qq.com.

<sup>4</sup>College of Civil Engineering, Hunan University, Changsha, Hunan 410082, China, 296974421@qq.com.

<sup>5</sup>College of Civil Engineering, Hunan University, Changsha, Hunan 410082, China, 190400441@qq.com.

<sup>6</sup>Xiangjiang Technology Co. Ltd, Yangzhong, Jiangsu 21200, China, 18705283333@139.com.

\* Corresponding Author: quanzhang@hnu.edu.cn (Quan Zhang)

*Due to the stability, efficiency and reliability of the loop heat pipe (lhp) with plate evaporator, it has prominent merit in the cooling of electronic devices. In this paper, a novel lhp without compensation chamber is experimentally studied, and the effect of the location of vapour grooves on the thermal performance of the lhp is analysed, including start-up process, cycle operating performance, temperature distribution and thermal resistance. The results show that the lhp cannot start up thoroughly when heat load is lower than 70w at location b, and the operating temperature is higher than location a. When heat load is over 70w, the lhp start up entirely. When heat load is 150w, the maximum temperature of heating surface and evaporator at location b are 83.3°C and 63.9°C respectively, lower than those of location a, which are 86.5°C and 69.68°C. The infrared thermal image of the lhp shows that the whole temperature of lhp increase with increasing heat load and heat sink temperature. In addition, when heat load is over 100w, the temperature of lhp at location b is lower than that of location a, which indicates the lhp operates better in high-load condition.*

*Keywords: loop heat pipe; vapour grooves; infrared thermal image; whole temperature distribution; liquid line wick*

## 1. INTRODUCTION

The two-phase heat transfer devices have prominent merits in cooling and heat dissipation, it is widely used in thermal control of aerospace, telecommunication and data centre (Ling *et al*, 2015; Ling *et al*, 2016; Yue *et al*, 2018; Zhang *et al*, 2017). Especially, due to the compact structure, high heat transfer capacity and stable operating performance of the loop heat pipes (LHPs), its utility in energy saving of cooling system for data centre have been studied by many researchers (Zhang *et al*, 2017). Generally, the LHPs with plate evaporator are the most suitable type for cooling of CPU and other electronic devices (He *et al*, 2016). According to the different location of the compensation chamber (CC), there are two types of plate evaporators. The first evaporator has an integral CC, which is located on the top of the evaporator. For the second evaporator, its CC located at the bottom of the evaporator.

For the latter evaporator, the influences of structure, material of the wick, parameters of vapour grooves on the thermal performance of the LHPs have been studied by many researchers. Zhang (Zhang *et al*, 2012) investigated the temperature oscillation during the start-up process and cycle load operation, the results shown that the temperature oscillation was caused by insufficiency of driving force and phase change of fluid in compensation chamber. Wang (Wang *et al*, 2012) tested the effects of the location of condenser and operating orientation on the performance of the LHP, he found that lower distance between evaporator and condenser, as well as antigravity operating orientation have positive influence in decreasing the temperature of evaporator. A plate evaporator with bifacial wick was designed by Joung (Joung *et al*, 2008), the thermal characteristics of the LHP at horizontal orientation were experimentally tested. The results indicated that the LHP can start up successfully and self-regulated great in variable heat loads. In addition, the operating temperature and working range of the LHP decreases with increasing filling rate. Chernysheva (Chernysheva *et al*, 2014) studied the influence of temperature of cooling water on performance of the LHP and established a relative mathematical model to predict LHPs' operating temperature. It shown that the operating temperature changed little when cooling temperature was below 40°C, which was because the LHP worked at variable conductance mode. Wang (Wang *et al*, 2018) evaluated the potential of the utility of enhanced boiling structure of the LHP, he also compared the influence of micro-cone structured substrate and polished copper substrate on thermal performance of the LHP. Kiseev (Valery *et al*, 2010) studied the thickness of the evaporator wick, size of vapour grooves, materials and porosity of wick in details. Chen (Chen *et al*, 2012) found the thermal performance of the LHP increased with increasing porosity of wick, and the operating temperature decreased with increasing porosity.

However, in existing researches, the location of heating surface is not clear, and the orientation of the vapour grooves has essential influence on LHPs' capacity. In this paper, the effect of the orientation of the vapour grooves on the thermal performance of the LHP was experimentally studied, including start-up process, cycle load operation and thermal resistance.

## 2. EXPERIMENTAL SETUP

The schematic of the tested LHP is shown as Figure 1. The LHP is made of copper and pure water, its main parameters are listed in Table 1. Especially, the compensation chamber is removed from the evaporator to compress the size of the LHP. Meanwhile, a section of liquid line is filled with sintered copper wick to enhance the backflow of the working fluid and insulate heat leakage from evaporator to liquid line.

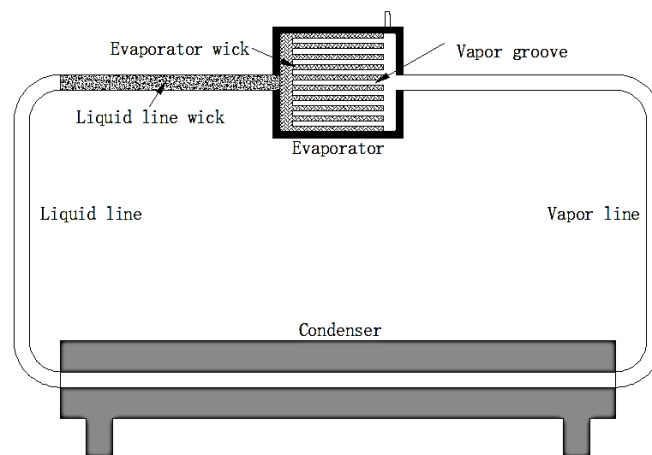


Figure 1: Schematic of the investigated loop heat pipe.

Table 1: Main design parameters of the LHP.

Evaporator		Wick in evaporator	
length*width*thickness	50mm*43mm*8mm	Copper powder particle size	100-125 $\mu\text{m}$
Wall thickness	1mm	Porosity	61%
Vapour/Liquid line		Wick in liquid line	
Diameter (outer/inner)	6mm/5mm	Copper powder particle size	100-125 $\mu\text{m}$
Tube thickness	0.5mm	Porosity	61%
Length	280mm	Length	100mm
Condenser		grooves	
Diameter (outer/inner)	6mm/5mm	Length*width*height	35mm*2mm*2mm
Tube thickness	0.5mm	number	12
Length	200mm	Interval	2mm

In this study, there are two orientations of the vapour grooves, as shown in Figure 2. The vapour groove is on the top of the evaporator at Condition A, while the heat source (ceramic heating chip with size of 35mm x 35mm) is under the evaporator. For Condition B, the vapour grooves and heat source are both under the evaporator and connected directly. There are ten thermocouples to measure the temperature during the tests. The heat load is controlled by a power meter and a voltage regulator, the data is record with Agilent 34970A data acquisition module.

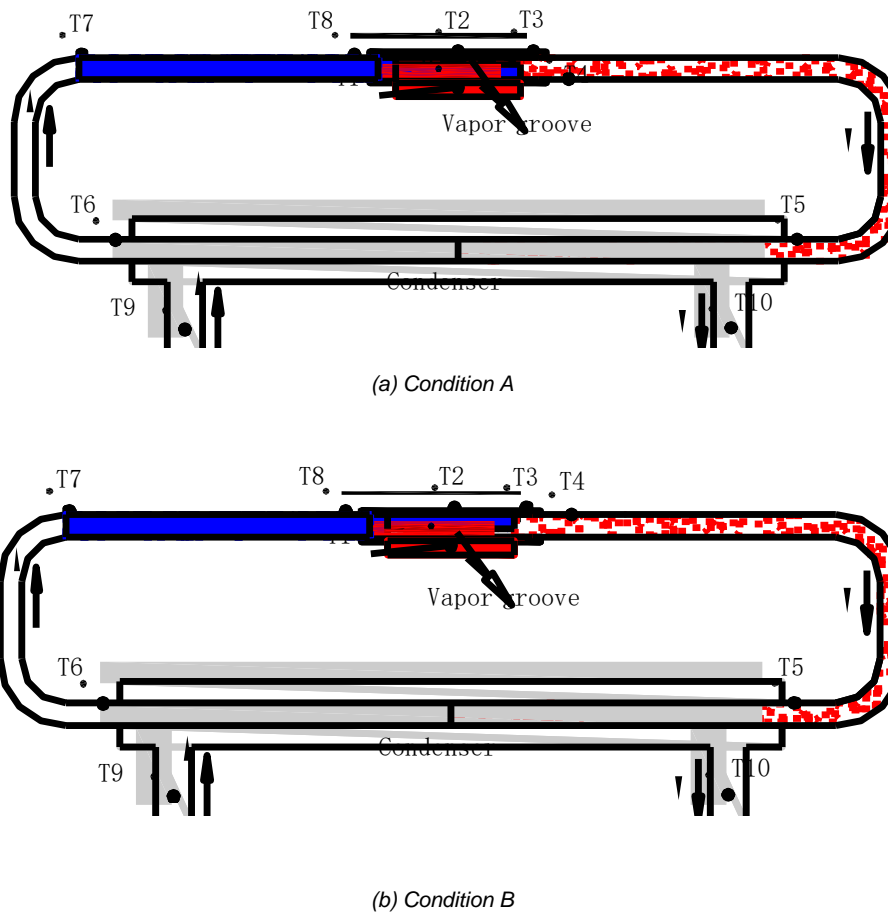


Figure 2: Orientations of vapour grooves and location of thermocouples.

### 3. RESULTS AND DISCUSSION

#### 3.1 Start-up process

The start-up process of the LHP at Condition A and Condition B are shown in Figure 3 and Figure 4, respectively. It is obvious that the LHP can start up smoothly and immediately at Condition A. When the evaporator is heated by ceramic chip, the temperatures of each components increase rapidly, then the temperatures reach the stable state and close to constant. In the meantime, no temperature oscillation and overshoot are occurred in the startup process of the LHP.

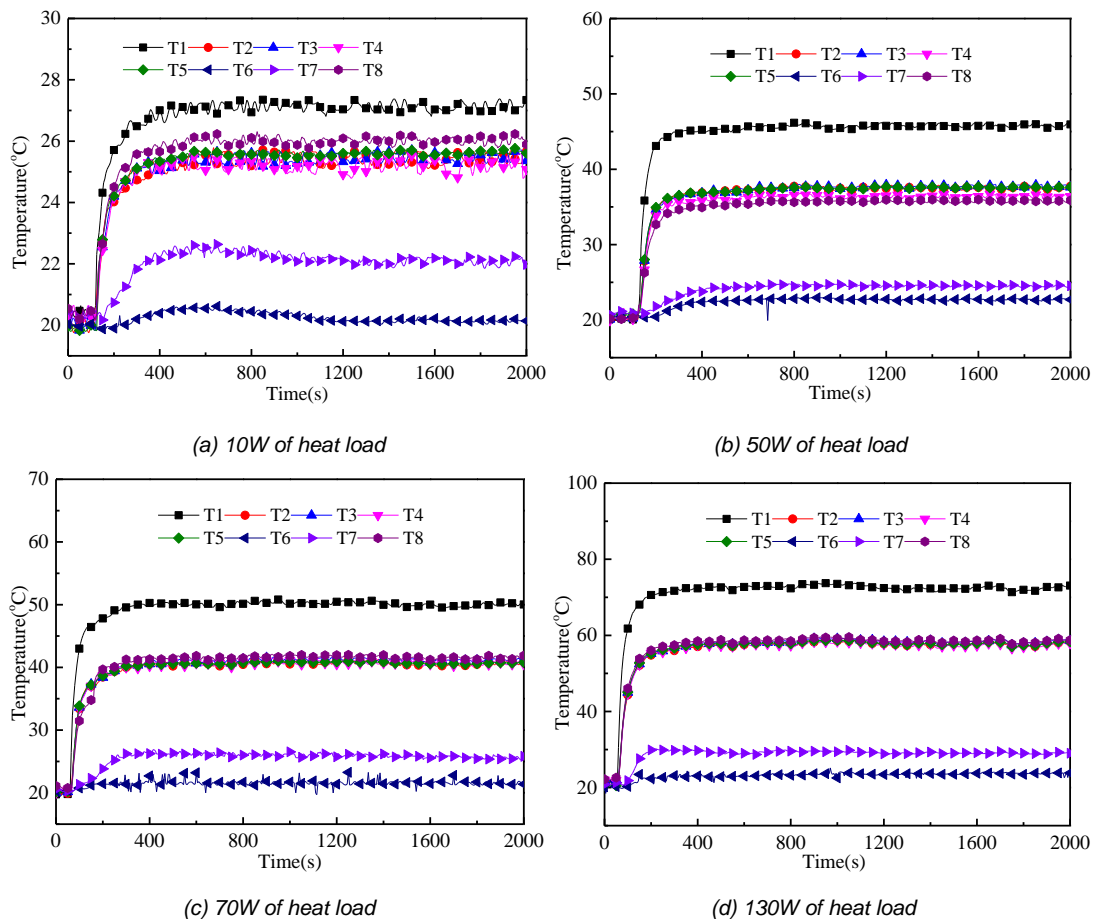


Figure 3: Startup process of the LHP at Condition A.

However, the temperature at Condition B with heat load of 10W and 50W are much higher than those at Condition A, and the overshoot occurs at the Condition B with heat load of 70W, while the LHP starts up smoothly at heat load of 130W. These indicate that the LHP didn't start up evenly at heat load of 10W and 50W. When heat load is 70W, the occurrence of overshoot account for the heat and pressure accumulation in the evaporator, which are the dynamic to promote the cycle of the working fluid inside the LHP. While when heat load is 130W, the LHP gains sufficient power to start up directly, hence no temperature oscillation and overshoot are observed.



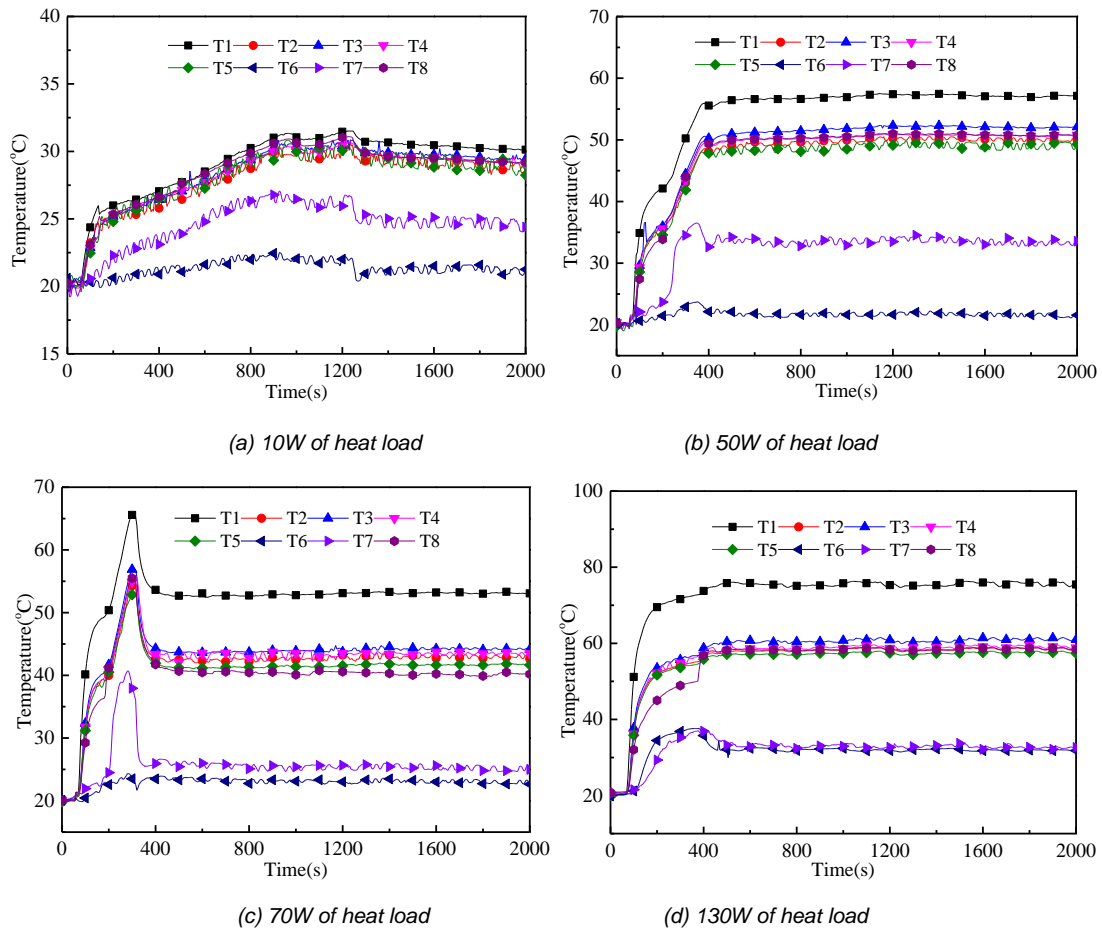
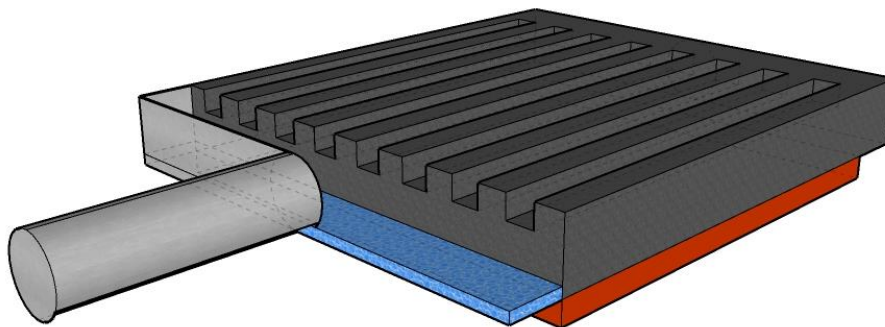
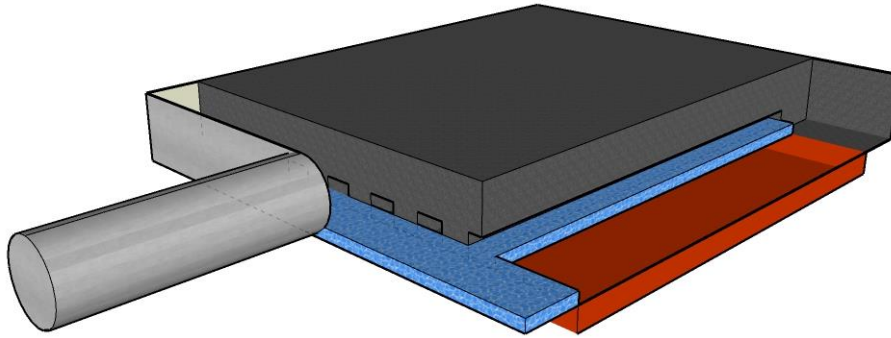


Figure 4: Startup process of the LHP at Condition B.

There are two reasons accounting for this phenomenon: (1) The liquid working fluid in vapour grooves at Condition B could affect the start-up process of the LHP. As shown in Figure 5(a), only a few liquid working fluids gather in the vapour grooves at Condition A. The working fluid evaporates rapidly at the surface between the wick and vapour grooves, the pressure of evaporator increases which pushes the flow of working fluid in condenser and liquid line. The LHP can start up quickly and reach the steady state. However, when the LHP operates at Condition B, as shown in Figure 5(b). The liquid working fluid accumulates in the vapour grooves initially, whose temperature rises when the evaporator is heated by ceramic chip, delaying the evaporation process. When the liquid in vapour grooves entirely dry out, the LHP could begin to operate and dissipate heat from the ceramic chip. (2) The operation of the LHP is influenced by the heat leakage from evaporator to liquid line. The heat leakage and the cooling capacity of the backflow fluid from condenser reach a counterbalance. When heat load is low, the evaporation rate in vapour grooves is low, which causes the insufficiency of the backflow fluid, and the LHP cannot operate smoothly and efficiently. With the increasing heat load, the liquid fluid in vapour grooves evaporates faster. The vapour pressure in evaporator is able to drive the circulation of the working fluid in the LHP, and the LHP begins to work and transfer heat from evaporator to condenser.



5 (a) Condition A



5 (b) Condition B



Figure 5: Schematic of evaporator at different orientations.

### 3.2. Operating performance

The heating surface temperature (T1) and the vapour temperature (T3), are of great importance to reflect the performance of the LHP. The temperatures of T1 and T3 at different heat sink temperatures are shown in Figure 6. When heat sink temperature is 10°C and 20°C, T1 and T3 increase with increasing heat load firstly, meanwhile, T1 and T3 at Condition B are higher than those of at Condition A. When heat load reaches 70W, T1 and T3 at Condition B drop suddenly and then increase gradually with increasing heat load. What's more, when heat load ranges from 70W to 150W, T1 and T3 at Condition B are lower than those of at Condition A. When heat sink temperature is 30°C, T1 and T3 at Condition B are always lower than those of at Condition A.

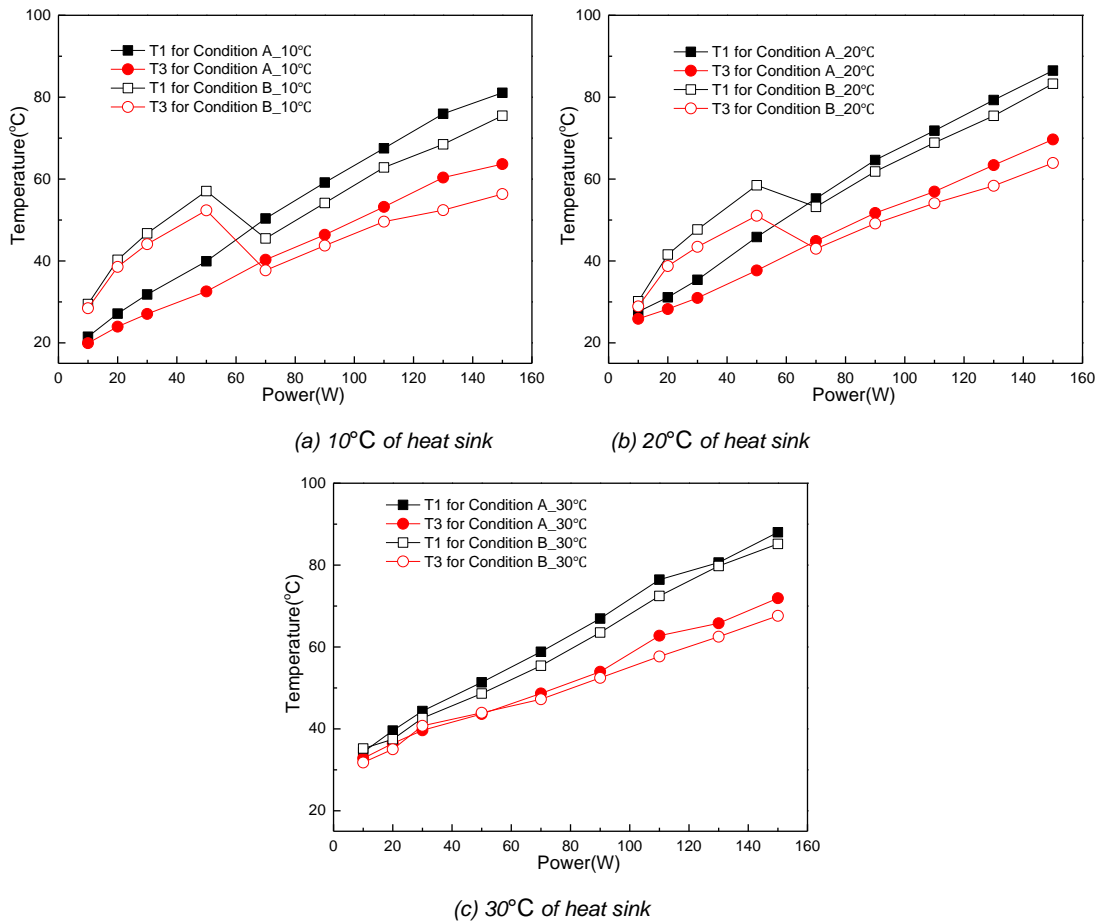


Figure 6: Temperature of T1 and T3 at different heat sink temperatures.

The temperature of liquid line wick inlet (T7) and evaporator inlet (T8) are another two important parameters to evaluate the thermal capacity of the LHP. As shown in Figure 7, the values of T7 and T8 at Condition B have the same changing regulation with T1 and T3. When heat load ranges from 10W to 50W and heat sink temperature is 10°C and 20°C, T7 and T8 increase obviously with increasing heat load, and in the meantime, T7 and T8 at Condition A are lower than those of at Condition B. A sudden drop up is also occurred when heat load reaches 70W, after which, T7 and T8 keep rising when heat load increases from 70W to 150W. In addition, when heat load is over 70W, temperatures at Condition B are always lower than those of at Condition A.

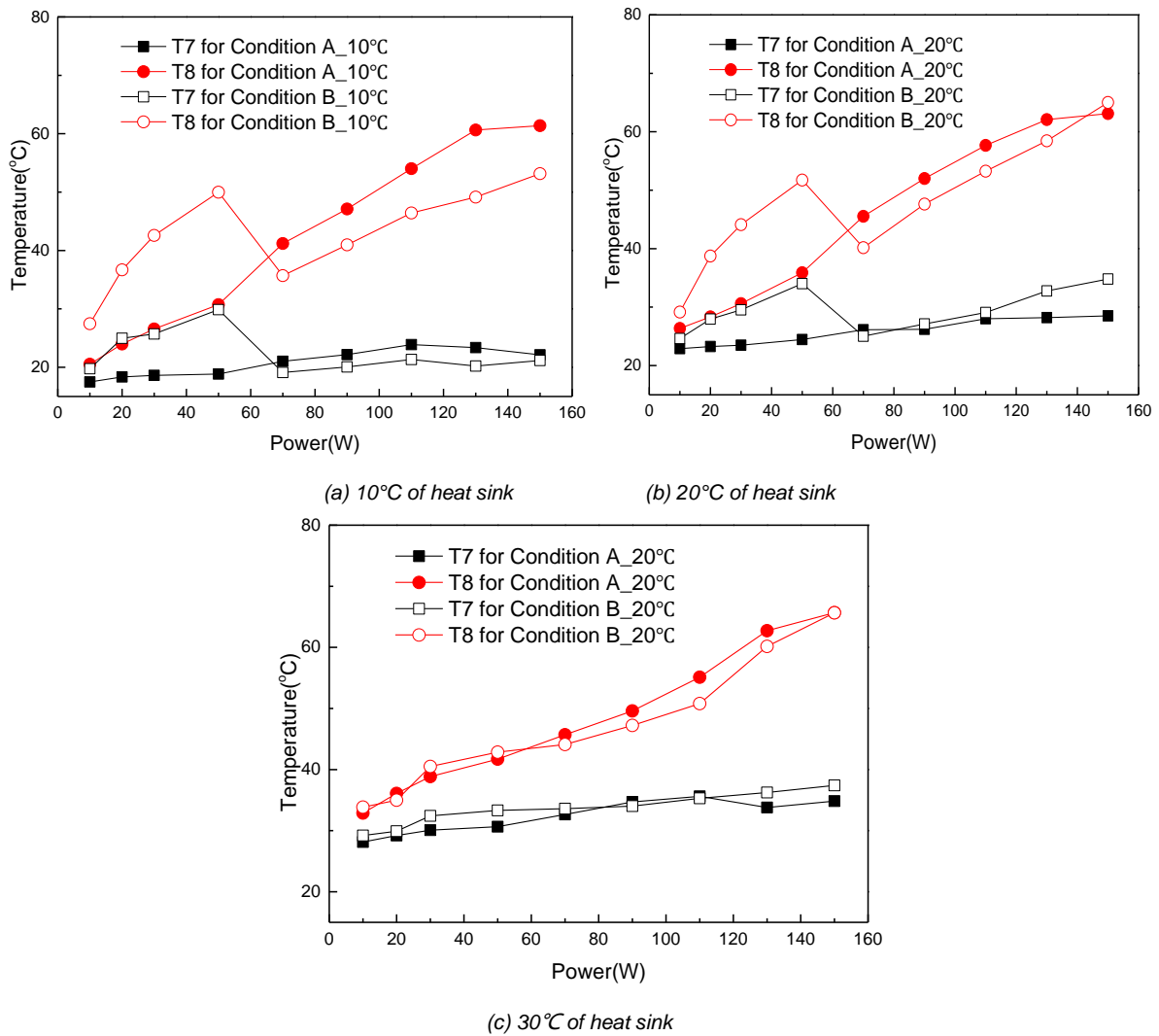


Figure 7: Temperatures of T7 and T8 at different heat sink temperatures.

In order to measure the whole temperature distribution when the LHP operates, the IR imaging technology is used to record the images. The IR images are shown in Figure 8. For the Condition A, it is obvious that the whole temperature of the LHP increases with increasing heat load, while a sudden temperature drop occurred at Condition B when heat load reaches 70W. Hence, the LHP can only operate evenly and efficiently at high heat load. For the influence of heat sink temperature, as shown in Figure 9, the whole temperature of the LHP increases with increasing heat sink temperature. In addition, the evaporator of the LHP shows a great thermal equilibrium.

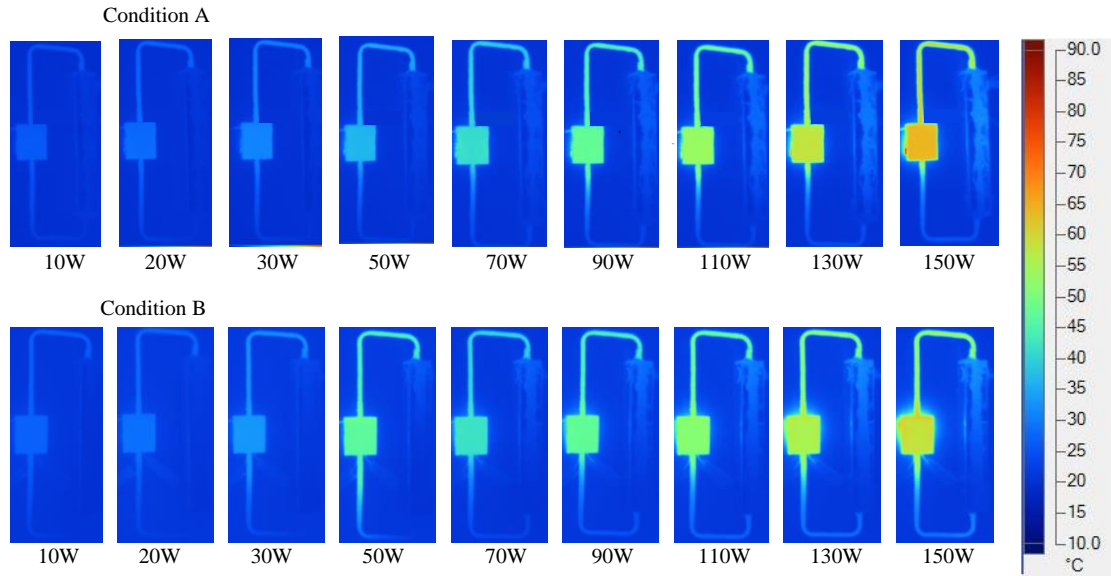


Figure 8: IR images of the LHP

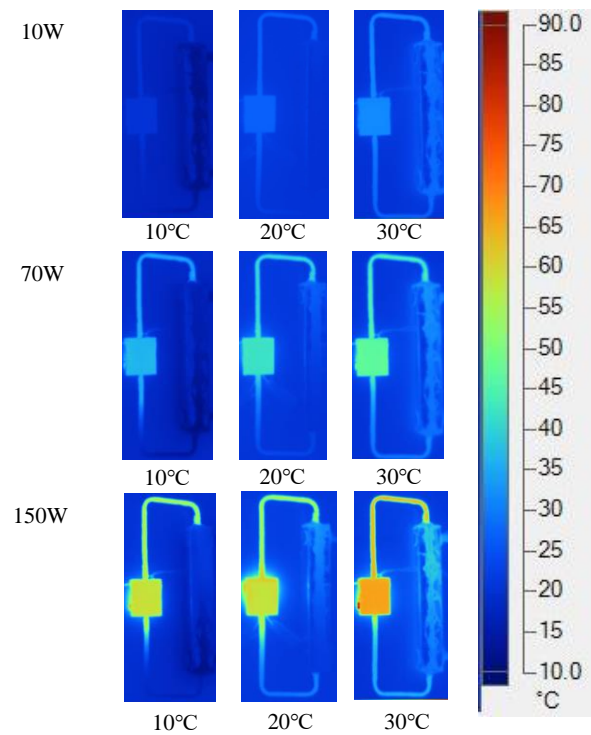


Figure 9: IR images of the LHP at different heat sink temperatures.

### 3.3. Thermal resistance

The thermal resistance is one of most significant characteristic to reflect the heat transfer capacity of the LHP, especially, the evaporator thermal resistance (ETR, thermal resistance between evaporator and heat source) and the loop thermal resistance (LTR, thermal resistance between heat sink and heat source). The ETR and LTR at Condition A and Condition Bare shown in Figure 10. When the heat load ranges from 10W to 50W and heat sink temperatures are 10°C and 20°C, the LHP cannot operate smoothly, the LTR at Condition B is much higher than that of at Condition A. However, when the LHP start up evenly, the LTR at Condition B is always slightly lower than the LTR at Condition A. But for ETR, it is clear that the heat load and heat sink temperature have little impact on its value, and the ETR at Condition A and Condition B are nearly equivalent.

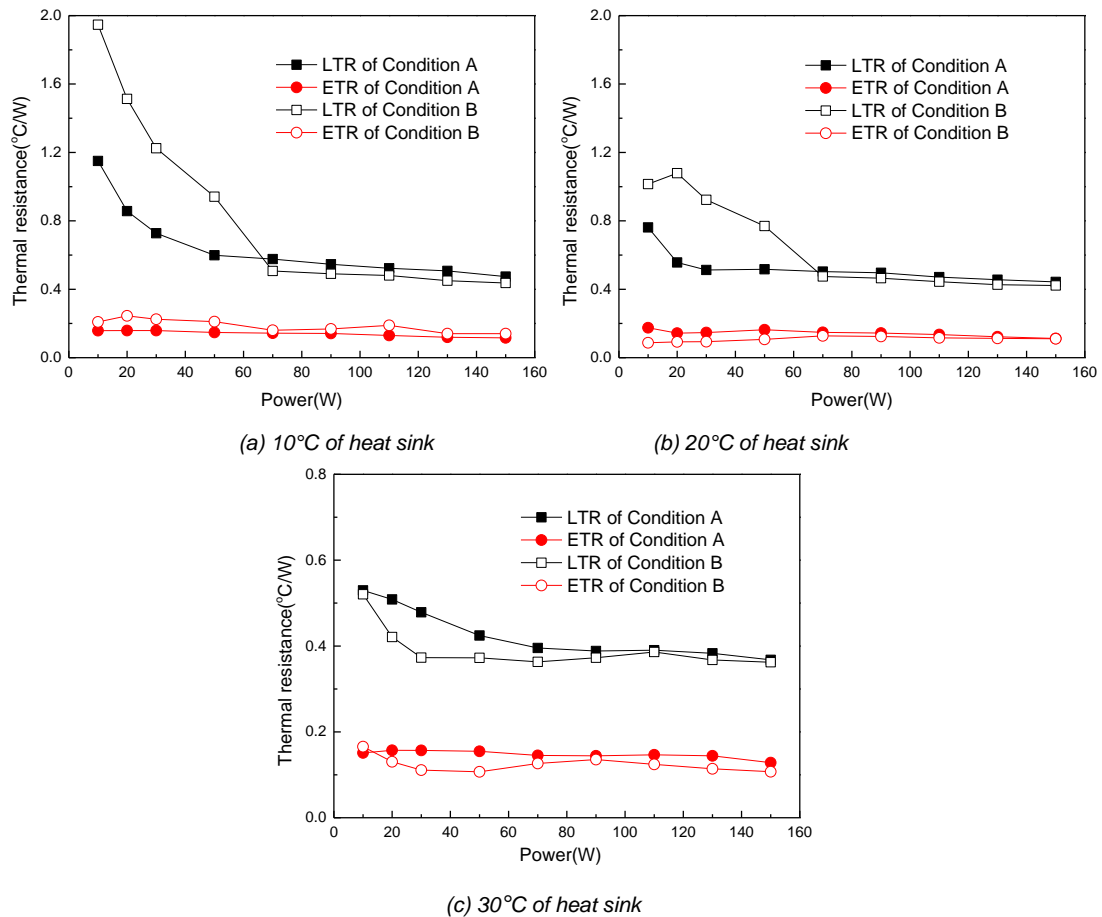


Figure 10: ETR and LTR of the LHP.

#### 4. CONCLUSIONS

A serious studies are conducted in this paper, the effect of the orientation of vapour grooves on the thermal performance of a novel LHP is analysed in details. Especially, the IR imaging technology is used to observe the whole temperature distribution of the LHP. The main conclusions are as following:

- The LHP at Condition B cannot start-up evenly and operate efficiently when heat load ranges from 10W to 50W at heat sink temperature of 10°C and 20°C, its operation temperature, thermal resistance and heat transfer capacity is obvious lower than those of at Condition A.
- When heat load is over 70W or the heat sink temperature is 30°C, the LHP at Condition B shows a better operating performance than at Condition B, its operation temperature is lower than that of at Condition A.
- The LHP at Condition B can operate more smoothly and efficiently at high heat load (especially over 100W) and high heat sink temperature (especially over 30°C).

#### 5. ACKNOWLEDGEMENT

This work was supported by International Science and Technology Cooperation Project of China (2017YFE0105800) and National Natural Science Foundation of China (NSFC) (Grant No. 51878254).

#### 6. REFERENCES

- Chen, BB, Liu, ZC, Liu, W, Yang, JG, Li, H, Wang, DD, 2012 Operational characteristics of two biporous wicks used in loop heat pipe with flat evaporator, *International Journal of Heat and Mass Transfer*, 55: 2204-2207.
- Chernysheva, MA, Yushakova, SI, Maydanik, YF, 2014, Cooper-water loop heat pipes for energy-efficient cooling systems of supercomputers, *Energy*, 69: 534-542.

- He, S, Liu ZC, Zhao, J, Jiang, C, Yang, JG, Liu W, 2016, Experimental study of an ammonia loop heat pipe with a flat plate evaporator, *International Journal of Heat and Mass Transfer*, 102:1050-1055.
- Joung, W, Yu, T, Lee, J, 2008, Experimental study on the loop heat pipe with a planar bifacial wick structure, *International Journal of Heat and Mass Transfer*, 51: 1573-1581.
- Ling, L, Zhang, Q, Yu, YB, Wu, YN, Liao, SG, 2015, Study on thermal performance of micro-channel separate heat pipe for telecommunication stations: Experiment and simulation, *International Journal of Refrigeration*, 59: 198-209.
- Ling, L, Zhang, Q, Yu, YB, Liao, SG, Sha, ZY, 2016, Experimental study on the thermal characteristics of micro channel separate heat pipe respect to different filling ratio. *Applied Thermal Engineering*, 102: 375-382.
- Valery, MK, Valeri, VV, Issam, M, 2010, Experimental optimization of capillary structures for loop heat pipes and heat switches, *Applied Thermal Engineering*, 30: 1312-1319.
- Wang, SF, Huo, JP, Zhang, XF, Lin, ZR, 2012, Experimental study on operating parameters of miniature loop heat pipe with flat evaporator, *Applied Thermal Engineering*, 40: 318-325.
- Wang, XL, Wei, JJ, Deng, YP, Wu, Z, Sundén, B, 2018, Enhancement of loop heat pipe performance with the application of micro/nano hybrid structures, *International Journal of Heat and Mass Transfer*, 127: 1248-1263.
- Yue, C, Zhang, Q, Zhai, ZQ, Ling, L, 2018, CFD simulation on the heat transfer and flow characteristics of a microchannel separate heat pipe under different filling ratios, *Applied Thermal Engineering*, 139: 25-34.
- Zhang, XF, Huo, JP, Wang, SF, 2012, Experimental investigation on temperature oscillation in a miniature loop heat pipe with flat evaporator, *Experimental Thermal and Fluid Science*, 37: 29-36.
- Zhang, HN, Shi, ZC, Liu, KT, Shao, SQ, Jin, TX, Tian, CQ, 2017, Experimental and numerical investigation on a CO<sub>2</sub> loop thermosyphon for free cooling of data centers, *Applied Thermal Engineering*, 111: 1083-1090.
- Zhang, HN, Shao, SQ, Jin, TX, Tian, CQ, 2017, Numerical investigation of a CO<sub>2</sub> loop thermosyphon in an integrated air conditioning system for free cooling of data centers, *Applied Thermal Engineering*, 126: 1134-1140.

---

## #124: Exploitation of low-grade renewable energy using heat pump technology in China

---

Pai WANG<sup>1</sup>, Yitai MA<sup>2</sup>, Qichao ZHANG<sup>3</sup>, Minxia LI<sup>4</sup>, Baomin DAI<sup>5</sup>

<sup>1</sup> Key Laboratory of Efficient Utilization of Low and Medium Grade Energy, MOE, Tianjin University, Tianjin, 300072, China, paiwang@tju.edu.cn

<sup>2</sup> Key Laboratory of Efficient Utilization of Low and Medium Grade Energy, MOE, Tianjin University, Tianjin, 300072, China, ytma@tju.edu.cn

<sup>3</sup> Key Laboratory of Efficient Utilization of Low and Medium Grade Energy, MOE, Tianjin University, Tianjin, 300072, China, 15022282120@163.com

<sup>4</sup> Key Laboratory of Efficient Utilization of Low and Medium Grade Energy, MOE, Tianjin University, Tianjin, 300072, China, tjmxli@tju.edu.cn

<sup>5</sup> Tianjin Key Laboratory of Refrigeration Technology, Tianjin University of Commerce, Tianjin, 300134, China, dbm@tju.edu.cn

*In order to cope with the problems of energy shortages and environmental pollution, heat pumps have been widely used for the exploitation of low-grade renewable energy. But there is little existing Chinese legislation that considers heat pumps as a kind of renewable energy technology, and the calculation method of renewable energy exploited by heat pumps in China is not clear enough. Thus, the importance of incorporating heat pump technology into renewable energy has been clarified in this paper. The current status and legislation of renewable energy and heat pumps in the EU (European Union) and China were introduced. The comparison found that the legislation in China is far behind from that in the EU. Calculation methods of the primary energy utilisation magnification ( $\alpha$ ) and the renewable energy contribution rate ( $\beta$ ) were used to illustrate the importance of heat pumps in renewable energy development. According to the actual situation in China, a new formula of  $\beta$  was proposed. The results show that the primary energy utilisation magnification of heat pumps to coal-fired boilers is nearly 2 and the renewable energy contribution rate is 67% to 71% in EU while the value of it is 61% to 75% in China. These results will promote the development of heat pumps and renewable energy in China.*

**Keywords:** heat pump; renewable energy; legislation; primary energy utilisation magnification; renewable energy contribution rate

## 1. INTRODUCTION

Since the beginning of the new century, the state of energy and the environment in China has become worrying. China has been the largest carbon emitter in the world since 2007 and the largest energy consumer since 2009 (Chen, 2013). The energy structure is dominated by coal, the burning of which severely pollutes the environment and this situation will not substantially change in the near future. The control of carbon emissions will be difficult. The coal-dominated energy structure, including direct combustion with outdated coal-fired equipment, has been a serious source of air pollution in China. Meanwhile, the uneven distribution of energy resources is also of concern (Liu, 2011). Coal resources are mainly located in the North and Northwest. However, the main energy consumption areas are concentrated in south-eastern coastal areas where the economy is the most developed. There is an obvious mismatch of resource storage and energy consumption. Mass transportation over long distances of coal from the North to South, as well as electricity delivery from the West to East, is the main energy flow characteristic and energy transport pattern of China (China Government, 2007). Exploitation of renewable energy and reduction of fossil fuel utilisation are imminent.

In 2005, the National People's Congress of China passed the Renewable Energy Law marking China's renewable energy development moving into the fast lane (Zhang, 2016). In particular, China put forward the target to increase the proportion of renewable energy to 15% by 2020 and to 20% by 2030 (National Development and Reform Commission, 2016). By 2030, China's total energy consumption may reach 45 - 50 billion tons of standard coal, of which 20% will be from non-fossil energy, mainly renewable energy. Achieving the target will be very challenging. Annual increases of total energy consumption and renewable energy consumption are shown in Figure 1, in which the dash lines are the predicted values. To increase the proportion of renewable energy, in addition to the general renewable energy, heat pump technology should be taken seriously (Bayer, 2012).

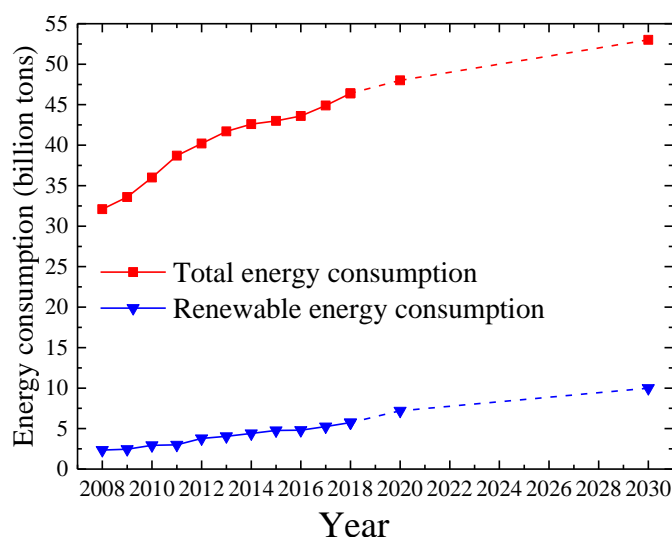


Figure 1: Annual changes of total energy consumption and renewable energy consumption (National Development and Reform Commission, 2016; National Energy Administration, 2016; National Energy Administration, 2015)

Research on heat pumps and renewable energy typically shows the coupling relationship, that is, power supplied to heat pumps is from renewable energy. Poppi *et al.* reviewed the investigations on solar heat pump systems and drew the conclusion that solar heat pump systems increased the share of renewable energy and reduced electric energy demand in residential heating applications (Poppi, 2018). Østergaard *et al.* investigated the introduction of heat pumps into integrated fluctuating renewables and the overall system costs (Østergaard, 2019). Stanek *et al.* analysed a heat pump system with renewable energy providing electricity and presented the ecological benefits (Stanek, 2019). Wanjiru *et al.* introduced an optimal control strategy for heat pump integrated with renewable energy and found that this control strategy led to significant savings on energy (Wanjiru, 2017a). Also, Wanjiru *et al.* advanced the previously developed control model to operate a heat pump water heater using integrated renewable energy systems (Wanjiru, 2017b). Calotă *et al.* analysed the potential of heat recovery in which the power delivered by the solar panels can be used for a lithium-bromide absorption system (Calotă, 2017).

As can be seen from the above research, heat pumps can reduce fossil energy consumption and save energy. But research on the direct relationship between heat pumps and renewable energy is lacking. This paper discusses the importance of developing heat pumps and incorporating heat pumps into renewable energy. The present situations and legislation of heat pumps and renewable energy in the EU and China are presented. Two methods



were used to illustrate the heat pump energy-saving principle and the importance of heat pumps in renewable energy development. Results show that power plants burning one ton of coal to generate power for heat pumps equates to fossil fuel boilers burning nearly two tons of coal. In accordance with the actual situation in China, a new formula of the renewable energy contribution rate ( $\beta$ ) is proposed: 61% to 75% of the heat supplied by heat pumps is renewable energy.

## 2. THE IMPORTANCE OF DEVELOPING HEAT PUMPS

### 2.1. Alleviating environmental pollution problems in China

In 2020, China will basically realise the well-off society. Good air quality is strictly required. Moreover, Winter Olympic Games will be held in 2022, and China has promised the IOC that the "Olympic Blue" is prolonged. So the reduction of PM2.5 emission has become a key task. It is the main measure to improve air quality and reduce PM2.5 concentration by using high-efficient electric transmission instead of coal transportation. In a word, to improve air quality, under the mature electrification conditions, using heat pumps to replace coal-fired boilers and loose coal is the correct path.

### 2.2. Achieving the renewable energy goals

The National Energy Board issued the 13<sup>th</sup> Five-Year Plan for Renewable Energy (National Development and Reform Commission, 2016). It proposed that the proportion of renewable energy to total energy consumption should reach 15% by 2020 and 20% by 2030. The General Office of the State Council issued the Energy Development Strategy Action Plan (2014-2020) (State Council, 2014) proposing that, by 2020, total energy consumption should be controlled at about 4.8 billion tons of standard coal. Renewable energy replace 720 million tons of standard coal.

Total energy consumption and the proportion of renewable energy in China are shown in Table 1. In the future, both the numerator and the denominator of the renewable energy proportion will increase. Only when the increasing speed of the numerator is greater than that of the denominator, can the goal of achieving the proportion of renewable energy reaching 15% by 2020 and 20% by 2030 be achieved. In reality, total energy consumption is increasing year by year, while the development of renewable energy is facing a series of problems. Due to the restriction on seasonal conditions, the speed of development of hydropower will slow down. Additionally, with the increase of total installed capacity of wind power, the impact of wind power volatility on the power grid has become more apparent, and the "abandoning wind" phenomenon is serious (Yin, 2019). According to the statistics of the National Energy Administration, the total number of abandoned wind power in China has reached 49.7 billion kWh in 2016. The abandonment of electricity in winter accounts for 67% of the total annual abandonment of electricity, and in the north-eastern region, the abandonment of electricity in winter accounts for 90% of the total annual abandoned wind power (Wu, 2018). Figure 2 shows the tendency of proportion of renewable energy in China. It can be found that, the amount of renewable energy developed by heat pumps is developing rapidly compared to other methods. Based on the past statistical data and future plans, such as the 13<sup>th</sup> Five-Year Plan, the target of renewable energy is difficult to achieve by only developing hydropower, wind power and photo-electric unless the heat pump is considered as a kind of renewable energy technology. What's more, heat pumps can supply heat by consuming electricity, which can reduce the gap between the supply thermoelectric ratio and the required thermoelectric ratio to a certain extent, thereby alleviating the abandoning wind phenomenon.

*Table 1: Total energy consumption and the proportion of renewable energy in China*

Year	Total Energy consumption / billion tons of coal	Renewable energy /billion tons of coal	The proportion of renewable energy /%
2015	43	4.56	10.6
2016	43.6	4.8	11
2017	44.9	5.25	11.7
2018	46.4	5.74	12.37
2020	48	7.2	15
2030	53	10.6	20

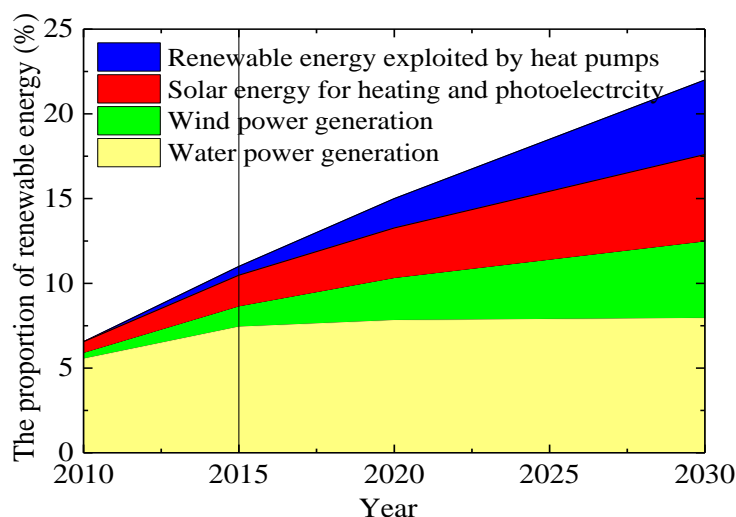


Figure 2: The proportion of renewable energy in China

### 3. THE STATE OF RENEWABLE ENERGY POLICIES

#### 3.1. Renewable energy policies in the EU

The EU has identified that all the energy exploited by heat pumps is renewable energy (Union European, 2009). In 2009, the EU adopted air-source heat pumps into the renewable energy through regulation. In 2013, the EU determined how to calculate the amount of renewable energy in heat pump technology. The renewable energy regulations and policies in the EU are shown in Table 2.

Table 2: Regulations and policies of renewable energy and heat pumps in the EU

Name	Publication date	Main contents
Renewable Energy Source Directive (DIRECTIVE 2009/28/EC)	2009	Air-source heat pumps were included into renewable energy. And the renewable energy target by 2020 was determined.
NREAPs-National Renewable Energy Action Plans	2013	The specific renewable energy development plans were identified.
Commission decision on establishing the guidelines for member states on calculating renewable energy from heat pumps (2013/114/EU)	2013	How to calculate the amount of renewable energy in heat pump technology was determined.

#### 3.2. Renewable energy policies in China

In China's Renewable Energy Law, renewable energy refers to wind energy, solar energy, hydropower, biomass energy, geothermal energy, ocean energy and other non-fossil sources of energy. Some low grade energy sources, such as air heat source, surface water heat source and shallow soil heat source are not included in renewable energy. But essentially, these energy sources are generated by solar energy and should be part of renewable energy. By introducing heat pumps, these low grade energy sources can be effectively utilised. Air heat source can be exploited by air-source heat pumps; water heat source can be exploited by water-source heat pumps; shallow soil heat source can be exploited by ground-source heat pumps. In the average range, two-thirds of the heat pump installed capacity represents renewable energy installed capacity. Thus, heat pumps should be a part of renewable energy in the national statistics.

However, at the national level, China has not classified heat pumps as renewable energy in the Renewable Energy Law. But some state institutions have already been aware of the importance of heat pumps. The Ministry of Housing and Urban-Rural Development of the People's Republic of China issued *Guidelines for including air thermal energy into the renewable energy category* and the National Energy Administration issued the *Opinions on Promoting Renewable Energy Heating (Draft for Soliciting Opinions)*, both of which classified heat pumps as renewable energy.

What is more, some provinces and cities have included heat pumps into renewable energy, as shown in Table 3. However, these national institutions and local government only classified heat pumps as renewable energy equipment or classified air-source energy and geothermal energy into renewable energy. How to calculate the amount of renewable energy in heat pump technology was not determined. Comparatively, regulations in the EU are better.

Table 3. Regulations and policies of renewable energy and heat pumps in China

Province	Names	Date	Main contents
Zhejiang	Application Standard for Renewable Energy of Civil Building	2015.3.1	Air-source heat pumps and ground-source heat pumps were included into renewable energy.
Shandong	Implementation Opinions of the General Office of the People's Government of Shandong Province on Promoting Heating in Rural Areas	2016.11.24	Air-source energy and shallow geothermal energy were included into renewable energy.
Shanxi	Implementation Opinions on Comprehensively Accelerating the Construction of Urban Central Heating and Promoting Clean Heating in Winter	2017.6.20	Air-source heat pumps and water-source heat pumps were included into renewable energy.
Beijing	The 13th Five-year Energy Development Plan of Beijing City	2017.7.19	Heat pumps were included into renewable energy.
Guangdong	Design Standard for Energy Efficiency of Public Buildings (Draft for Soliciting Opinions)	2019.3.18	Air-source heat pumps were included into renewable energy.
Tianjin	Catalogue of promoting, restricting and prohibiting energy-saving technology, materials and equipment of Tianjin	2019.3.22	Ground-source heat pump equipment and air-source heat pump equipment were included in renewable energy equipment.
Jilin	Catalogue of energy-saving technology and promoting, restricting and prohibiting production of Jilin Province	2019.4.30	Air-source energy and geothermal energy were included into renewable energy.

#### 4. METHODS TO VALUE THE HEAT PUMP ENERGY-SAVING PRINCIPLE

To illustrate the importance of heat pumps in renewable energy development, calculation methods of the primary energy utilisation magnification ( $\alpha$ ) and the renewable energy contribution rate ( $\beta$ ) were used.

##### 4.1. The primary energy utilisation magnification

Generally, the primary energy utilisation magnification of heat pumps to fossil fuel is setting as following:

Equation 1: 
$$\alpha = \frac{PER}{\eta_b}$$

Where:

- PER = the primary energy efficiency of heat pumps
- $\eta_b$  = the energy efficiency of fossil fuel boilers

The primary energy efficiency of heat pumps is formulated as below.

Equation 2: 
$$PER_h = \frac{Q_h}{Q_p} = \frac{Q_h}{W / \eta_p \eta_{pt}} = COP_h \times \eta_p \times \eta_{pt}$$

Where:

- $Q_h$  = heat load of heat pumps
- $Q_p$  = heat load of power plant
- $W$  = power input
- $\eta_p$  = efficiency of power plant
- $\eta_{pt}$  = efficiency of power transmission
- $COP_h$  = coefficient of performance of heat pumps

Take the year of 2017 as an example. According to the data from the National Energy Administration in 2017, the national average coal consumption of coal-fired power plants was 309g/(kWh). The average efficiency of power generation was 40.2%. National power network transmission line loss rate was 6.4% (National Energy Administration, 2018). So, the comprehensive efficiency was 37.63%. Assuming the average (or seasonal) COP of heat pumps was 3 - 3.5, the primary energy efficiency of heat pumps was 112.89% - 131.71%. What's more, with the improvement of power generation efficiency and the reduction of power network transmission line loss, the primary energy efficiency of heat pumps will continue increasing.

The energy efficiency of fossil fuel boilers is formulated as below.

$$\eta_b = \frac{Q_b}{Q_c}$$

Equation 3:

Where:

- $Q_b$  = heat load of boiler
- $Q_c$  = heat load of coal

Coal is far transported from coal mines through loading, electric railways, transiting, storage, stacking, short-distance transportation, unloading, and so on. In this process, a great deal of work is done by machine, while the mechanical power is obtained from coal power generation. In this way, the transportation of coal from mines to fossil fuel boilers also consumes coal.

Assuming that the energy efficiency of coal transportation and transition is 80%, in this case, formula 4 is the real energy efficiency of fossil fuel boilers.

$$\eta_b = \frac{Q_b}{Q_c / \eta_{ct}} = \frac{Q_b}{Q_c} \times 80\%$$

Equation 4:

Where:

$\eta_{ct}$  = efficiency of coal transmission

Reconsidering that the energy efficiency of fossil fuel boilers is 80%, the primary energy efficiency of coal-fired boilers is just 64%.

Based on the above analysis, the primary energy efficiency of heat pumps is 112.89% - 131.71%, while the primary energy efficiency of fossil fuel boilers is 64%. It can be drawn out that  $\alpha=1.76\sim 2.06$ . With the improvement of power generation efficiency and the reduction of power network transmission line loss, the value of  $\alpha$  will continue increasing.

For example, it is assumed that the annual heating period is 120 days and the heat requirement is 60W per square meter. When the COP of heat pump is 3, the primary energy efficiency of heat pumps is 112.89%. The calorific value of standard coal is 29307.6kJ. The coal consumption of heat pump is:

$$\frac{\frac{60}{112.89\%} * 120 * 24 * 3600}{29307.6 * 1000} = 18.80 \text{ kg}$$

The primary energy efficiency of coal-fired boilers is 64%. The coal consumption of coal-fired boilers is:

$$\frac{\frac{60}{64\%} * 120 * 24 * 3600}{29307.6 * 1000} = 33.17 \text{ kg}$$

It can be seen that by using heat pumps, about 14.37kg standard coal will be saved per square meter. It means that power plants burning 1 ton of coal to generate power for heat pumps equates to fossil fuel boilers burning nearly 2 tons of coal. And the emissions of coal-fired power plants are much smaller than ordinary small-and-medium sized fossil fuel boilers.

#### 4.2. Renewable energy contribution rate of heat pumps

The calculation method of renewable energy exploited by heat pumps in China is not clear enough, which can be learned from the EU and revised according to Chinese national conditions.

##### *Renewable energy contribution rate of heat pumps in the EU*

The EU has included the calculation of heat pumps renewable energy contribution rate in the law. In the Annex VII of DIRECTIVE 2009/28/EC (Union European, 2009), the minimum seasonal performance factor of air-source heat pumps was regulated.

Equation 5:

$$SPF > 1.15 \times \frac{1}{\eta_{pepg}}$$

Where:

- SPF = seasonal performance factor
- $\eta_{pepg}$  = efficiency of primary energy power generation

According to Eurostat, the higher the efficiency of primary energy power generation is, the lower the *SPF* of heat pumps is requested. The actual *SPF* is generally between 2.4 and 2.6, as shown in Table 4.

Table 4. Calculated *SPF* due to the limitation of renewable energy in the EU (Fang, 2015)

Year	Primary generation efficiency $\eta_{pg}/\%$	<i>SPF</i>
2006	44.1	2.61
2007	43.9	2.62
2008	44.7	2.57
2009	45.1	2.55
2010	45.5	2.53

In the EU formula, removing the value of electricity, the remaining part is the renewable energy exploited by heat pumps. The calculation formulas are as follows.

Equation 6:

$$E_{RES} = Q_{usable} \left(1 - \frac{1}{SPF}\right)$$

Equation 7: 
$$Q_{\text{usable}} = H_{\text{HP}} \times P_{\text{rated}}$$

Where:

- $E_{\text{RES}}$  = renewable energy that heat pump exploited
- $Q_{\text{usable}}$  = total heat output of heat pump
- $H_{\text{HP}}$  = full-load operating hours
- $P_{\text{rated}}$  = installed capacity of heat pump

The renewable energy contribution rate of heat pumps in Europe is:

Equation 8: 
$$\beta_{\text{EU}} = \frac{E_{\text{RES}}}{Q_{\text{usable}}} = 1 - \frac{1}{\text{SPF}}$$

*Renewable energy contribution rate of heat pumps in China*

The proportion of renewable energy to primary energy consumption in China is calculated by the following equation:

Equation 9:

$$\text{Proportion of the renewable energy} = \frac{\text{Utilization of the renewable energy(standard coal)}}{\text{Total energy consumption (standard coal)}} \times 100\%$$

In the statistical calculation, any energy, whether it is for power generation or direct heat (thermal) utilisation, must be converted into the equivalent amount of primary energy standard coal. The standard coal that equates to the power generation of renewable energy can be calculated by the national average efficiency of coal-fired power plants.

For example, in the year of 2009, the national average efficiency was 36.4%, while the national average coal consumption for power generation was 341g/(kWh) (Zhou, 2011). With the increase of power generation efficiency, the conversion value should change. For instance, in 2013, national average efficiency was 38.7% while the national average coal consumption was 321g/(kWh) (China Electricity Council, 2013). At the end of 2015, the State Council issued that the average coal consumption of all power plants on service should be less than 310g/(kWh). For newly built power plants, the average coal consumption should be less than 300g/(kWh) (China Government, 2015). According to the EU standards, the *SPF* of heat pumps exploiting renewable energy in China can be calculated, as shown in Table 5.

*Table 5: Calculated SPF due to the limitation of renewable energy in China*

Year	Coal consumption for power	Power generation	<i>SPF</i>
	generation /g·(kWh) <sup>-1</sup>	efficiency $\eta_{\text{pg}}$ /%	
2015	315	39.4	2.92
2016	312	39.9	2.88
2017	309	40.2	2.86
2018	307	40.5	2.84
Newly built plants	<300	>41.4	<2.78

Compared with the power generation efficiency in the EU, the efficiency in China is 6% lower. As a result, the *SPF* value of heat pumps in China should be 0.4-0.5 times higher than that in the EU. It shows that if following the EU standards, the *SPF* of heat pumps in China should be higher.

According to the actual situation in China, the calculation formula of heat pumps renewable energy contribution rate is presented in this paper. Compared with coal-fired boilers, the extra heat of heat pumps is renewable energy.

$$E_{RES} = Q_{usable} \left( \frac{1}{\eta_{ct}\eta_b} - \frac{1}{\eta_p\eta_{pt}SPF} \right)$$

Equation 10:

Therefore, the renewable energy contribution rate of heat pumps in China is:

$$\beta_{China} = \frac{E_{RES}}{Q_{usable}} = \frac{1}{\eta_{ct}\eta_b} - \frac{1}{\eta_p\eta_{pt}SPF}$$

Equation 11:

The calculation results of the renewable energy contribution rate of heat pumps in the EU and China are shown in Table 6. The EU formula is simpler and the rate is only affected by *SPF*. The contribution rate is higher when the *SPF* is higher. The Chinese formula is a little complicated and the rate is affected by coal transportation efficiency, power transmission efficiency, fossil fuel boilers efficiency, power plants efficiency, and *SPF*. Generally, coal transportation efficiency, power transmission efficiency and fossil fuel boilers efficiency are regarded as constants. Power plants efficiency is related to *SPF*. So, it can be assumed that the contribution rate in China is affected only by *SPF* also. When the *SPF* is smaller,  $\beta$  is also smaller. When the *SPF* increases, the  $\beta$  should increase more. In general, when the *SPF* is between 3 and 3.5, 67% to 71% of the heat pump heat load in the EU is renewable energy, and 61% to 75% of the heat pump heat load in China is renewable energy.

Table 6: The renewable energy contribution rate of heat pumps in the EU and China

<i>SPF</i>	$\beta_{China}$ formula 11	$\beta_{EU}$ formula 8
2.5	0.42	0.6
3	0.61	0.67
3.5	0.75	0.71

## 5. CONCLUSION

The coal-dominated energy structure, as well as direct combustion with outdated coal-fired equipment, has become a source of air pollution in China. Exploitation of renewable energy and reduction of fossil fuel utilisation are imminent. In addition to the general renewable energy, heat pump technology should be taken seriously.

This paper discussed the importance of developing heat pumps and incorporating heat pumps into renewable energy. To improve the air quality, heat pumps in place of coal combustion will play an important role. Also, heat pumps contribute to achieving the renewable energy development targets. On the one hand, wind abandonment phenomenon will be reduced by using heat pumps. On the other hand, the target of renewable energy is difficult to achieve by only developing hydropower, wind power and photoelectric unless the heat pump is considered as a kind of renewable energy technology.

The legislation and policies in the EU are better as they adopted air-source heat pumps into the renewable energy through regulation and the EU determined how to calculate the amount of renewable energy in heat pump technology. However, in China, renewable energy only refers to wind energy, solar energy, hydropower, biomass energy, geothermal energy, ocean energy and other non-fossil sources of energy. In the Renewable Energy Law, heat pumps are not included into renewable energy. Although some state institution and provinces have already been aware of the importance of heat pumps, how to calculate the amount of renewable energy in heat pump technology is not determined.

To illustrate the importance of heat pumps in renewable energy development, calculation methods of the primary energy utilisation magnification ( $\alpha$ ) and the renewable energy contribution rate ( $\beta$ ) were used. Results show that power plants burning 1 ton of coal to generate power for heat pumps equates to fossil fuel boilers burning nearly 2 tons of coal. And the calculation method of renewable energy exploited by heat pumps in China is not clear enough, which can be learned from the EU and revised according to Chinese national conditions. According to the actual situation in China, a new formula of  $\beta$  was proposed. 61% to 75% of the heat supplied by heat pumps is renewable energy.

These results will promote the development of heat pumps and renewable energy in China.

## 6. REFERENCES

- Bayer P, Saner D, Bolay S, Rybach L, Blum P. 2012. Greenhouse gas emission savings of ground source heat pump systems in Europe: A review. *Renewable and Sustainable Energy Reviews*; 16:1256-1267.
- Calotă R, Girip A, Ilie A, Cîrstolovean L. 2017. Hybrid Absorption Heat Pump System Using Renewable Energy. *Procedia Engineering*, 181, 738-745.
- Chen S. *Energy*. 2013. Environment and economic transformation in China. Britain: Routledge.
- China Electricity Council. 2013. Annual development report of China electric power industry. Beijing: China Market Press.
- China Government. 2015. Li Keqiang Chaired a Meeting of the State Council. [http://www.gov.cn/guowuyuan/2015-12/02/content\\_5019050.htm](http://www.gov.cn/guowuyuan/2015-12/02/content_5019050.htm); [accessed 13 May 2018].
- China Government. 2007. China's energy conditions and policies. Governmental report. [http://www.gov.cn/zwggk/2007-12/26/content\\_844159.htm](http://www.gov.cn/zwggk/2007-12/26/content_844159.htm).
- Fang Q, Song Z, Gao Q, Zhao H, Chen N, Xu H, Sun Y. 2015. Study Report of Air Source Heat Pump Industry of China in 2015. 2015 China Heat Pump Alliance Annual Conference & Asian Air-source Heat Pump Forum.
- Liu W, Lund H, Mathiesen BV, Zhang X. 2011. Potential of renewable energy systems in China. *Applied Energy*; 88:518-525.
- National Development and Reform Commission. 2016. The 13th Five-Year Plan for Renewable Energy Development. Governmental report. [http://ghs.ndrc.gov.cn/ghwb/gjjgh/201706/t20170614\\_850909.html](http://ghs.ndrc.gov.cn/ghwb/gjjgh/201706/t20170614_850909.html).
- National Energy Administration, China National Renewable Energy Centre, Chinese Wind Energy Association, Chinese Renewable Energy Industries Association. 2015. Renewable Energy 2015. Governmental report. <http://www.cnrec.org.cn/cbw/zh/2015-10-23-488.html>.
- National Energy Administration. 2018. 2017 Annual Report on National Power Reliability. [http://zfxgk.nea.gov.cn/auto79/201806/t20180606\\_3191.htm](http://zfxgk.nea.gov.cn/auto79/201806/t20180606_3191.htm).
- Østergaard P A, Jantzen J, Marcinkowski H M, Kristensen M. 2019. Business and socioeconomic assessment of introducing heat pumps with heat storage in small-scale district heating systems. *Renewable Energy*.
- Poppi S, Sommerfeldt N, Bales C, Madani H, Lundqvist P. 2018. Techno-economic review of solar heat pump systems for residential heating applications. *Renewable and Sustainable Energy Reviews*, 81, 22-32.
- Stanek W, Simla T, Gazda W. 2019. Exergetic and thermo-ecological assessment of heat pump supported by electricity from renewable sources. *Renewable energy*, 131, 404-412.
- State Council. 2014. Strategic Action Plan for Energy Development (2014—2020). Governmental report. [http://www.nea.gov.cn/2014-12/03/c\\_133830458.htm](http://www.nea.gov.cn/2014-12/03/c_133830458.htm).
- Union European. 2009. Directive 2009/28/EC of the European Parliament and of the Council of 23 April 2009 on the promotion of the use of energy from renewable sources and amending and subsequently repealing Directives 2001/77/EC and 2003/30/EC. *Official Journal of the European Union*, 2009, 5: 2009.
- Wanjiru E M, Sichilalu S M, Xia X. 2017a. Optimal operation of integrated heat pump-instant water heaters with renewable energy. *Energy Procedia*, 105, 2151-2156.
- Wanjiru E M, Sichilalu S M, Xia X. 2017b. Model predictive control of heat pump water heater-instantaneous shower powered with integrated renewable-grid energy systems. *Applied energy*, 204, 1333-1346.
- Wu Y, Yin S, Fu L, Jiang Y. 2018. Thermoelectric synergy to improve cogeneration flexibility, *District Heating*, 2018 (1): 32-38.



Yin S, Xia J, Jiang Y. 2019. Analysis of the characteristics of supply thermoelectric ratio and demand thermoelectric ratio in northern China, *District Heating*, 2019 (1): 3.

Zhang D, Cao H, Zou P. 2016. Exuberance in China's renewable energy investment: Rationality, capital structure and implications with firm level evidence. *Energy Policy*; 95:468-478.

Zhou Y. 2011. The Development and Prospect of Coal-Fired Power Generation Energy-Saving Technologies in China. *Sino-Global Energy*, 2011; 16:91-95.

---

## #127: Life cycle assessment of microalgae-based pig production system

---

Liang-Chiung CHENG<sup>1</sup>, Wei WU<sup>2</sup>

<sup>1</sup> Department of Chemical Engineering National Cheng Kung University, No.1, Dasyue Rd., East Dist., Tainan City 70101, Taiwan (R.O.C.), ciera1107@gmail.com

<sup>2</sup> Department of Chemical Engineering National Cheng Kung University, No.1, Dasyue Rd., East Dist., Tainan City 70101, Taiwan (R.O.C.), weiwu@gs.ncku.edu.tw

*The pig manure produced by intensive pig farming is known to have significant impacts on the environment. The nitrogen and phosphorus compounds in the manure contaminate the soil and bodies of water. However, these nutrients can also become a good source to cultivate microalgae. The aim of the present work was to evaluate the environmental impact of microalgae-based pig production systems using high-rate algal ponds (HRAPs) through mass balances, energy balances and life cycle assessment (LCA). The system involved simultaneous treatment of piggery wastewater using microalgae, co-anaerobic digestion of pig manure and microalgal biomass, biogas cogeneration, and substitution of pig feed. The organic residues from the anaerobic digestion could be applied as organic fertilizers to farmland replacing mineral fertilizers. The environmental performances of four scenarios including (i) conventional application; (ii) anaerobic digestion (AD) only; (iii) AD and HRAPs; and (iv) co-AD and HRAPs were compared. As shown in the results of the analysis, the pig feed production contributed to the most environmental impact in all scenarios. For the overall system in four scenarios, the impact generated by the suggested system (scenario 3) can reduce the CO<sub>2</sub>e by up to 54% compared to the conventional system (scenario 1). Additionally, the sensitivity analysis of each scenario indicated that substituting pig feed to microalgae became the main factor in improving GHG performance.*

*Keywords: high rate algae ponds; wastewater treatment; life cycle assessment; microalgae; piggery wastewater*

## 1. INTRODUCTION

Intensive livestock production is known to have a significant impact on the environment. This is because the livestock supply chain requires significant inputs of feed, energy and water, the production of CH<sub>4</sub>, NH<sub>3</sub> and other emissions to air, and pollution risks results from inefficient waste management methods. Although literature consistently reports that feed production produces the greatest environmental impacts, wastewater management becomes problematic on a localized scale for pig production. The pig manure produced by intensive pig farming is known to have significant impacts on the environment. The nitrogen and phosphorus compounds in the manure contaminate the soil and bodies of water. This is due to potential leaching and escape of nitrogen (N) and phosphorus (P) to fresh-water and ground-water resources, and acidification risks from NH<sub>3</sub> if waste matter are managed poorly. However, these nutrients can also become a good source to cultivate microalgae. Microalgae have been promoted as one of the more promising third generation biofuels for their ability to divide rapidly, grow in low quality water, absorb CO<sub>2</sub>, and grow on non-arable land. Owing to photosynthetic oxygenation, microalgae based wastewater treatment shown to have an enormously lower carbon footprint than conventional alternatives using mechanical aeration. Atmospheric carbon fixation can even support climate change mitigation if the biomass photosynthesized is used for bioenergy production or converted the biomass into biochar for long-term carbon storage.

The aim of the present work was to evaluate the environmental impact of microalgae-based pig production system using high-rate algal ponds (HRAPs) through mass balances, energy balances and life cycle assessment (LCA). The system involved simultaneous treatment of piggery wastewater using microalgae, co-anaerobic digestion of pig manure and microalgal biomass, biogas cogeneration, and substitution of pig feed. The organic residues from the anaerobic digestion could be applied as organic fertilizers to farmland replacing mineral fertilizers. The environmental performances of four scenarios including (i) conventional application; (ii) anaerobic digestion (AD) only; (iii) AD and HRAPs; and (iv) co-AD and HRAPs were compared. Figure 1 shown the pig supply chain system boundaries in this study.

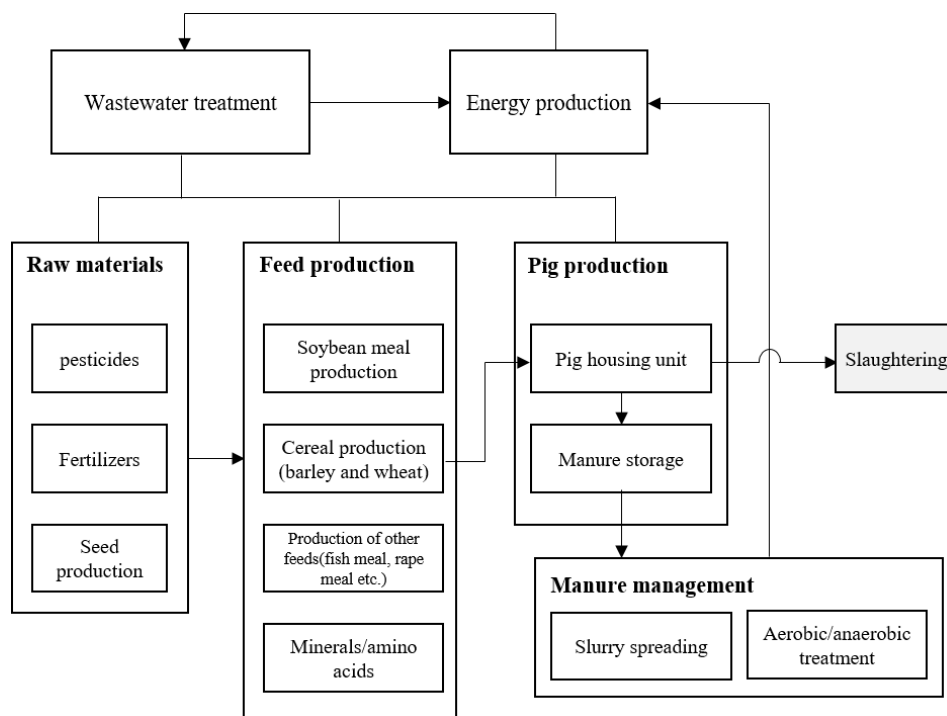


Figure 1: Pig supply chain system boundaries

## 2. MATERIALS AND METHODS

### 2.1. Goal and scope

The goal of this study was to construct an inventory and then estimate the environmental impact of microalgae-based pig production system using HRAPs to treat the wastewater in Europe. Moreover, as feed production was identified as the main hotspot in the production chain, piggery wastewater-grown microalgae were proposed as an alternative to substitute for feed in order to mitigate the environmental impacts related to the entire system.

The study was performed through a cradle-to-farm gate perspective. Hence, further stages such as slaughtering, packaging, distribution and meat consumption were excluded from the assessment. Although most of the previous LCA studies involving pig meat production include the slaughtering stage within the system boundaries, the hotspots in all these studies were recorded in the stages before the slaughterhouse.

### 2.2. Functional unit

This study was focused on feeder pigs and the functional unit was defined as “1000 kg live weight of pig at farm gate”, which is the average live weight of pigs before slaughterhouse in this study. A factor of 0.75 is used in order to convert from live weight to slaughter weight, i.e. 1000 kg live weight equals to about 750 kg slaughter weight.

### 2.3. Four scenarios

As shown in Figure 2, the foreground system of scenario 1 (business as usual) describes pig farming, raw manure in-house and outside storage, and transport and then spreading to agricultural land.

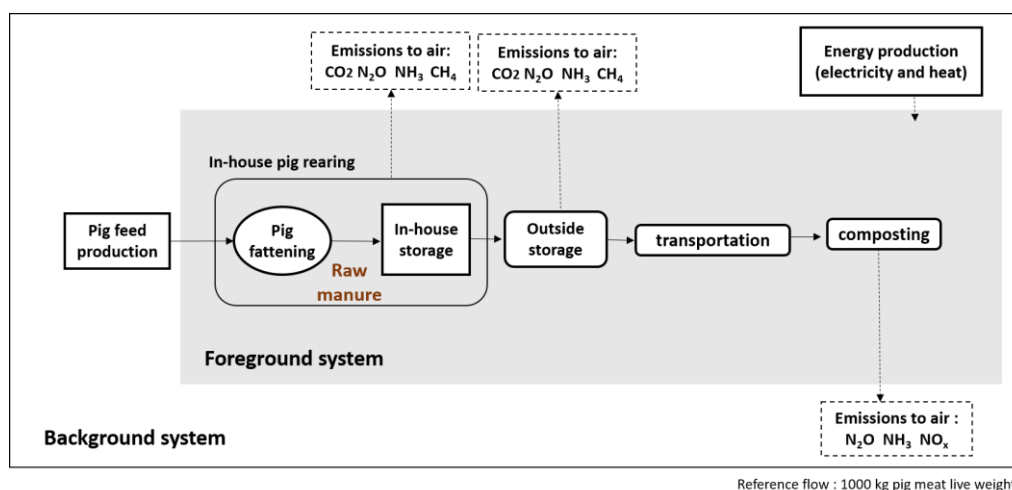


Figure 2: System boundary of scenario 1

As the foreground system for scenario 2, anaerobic digestion, the fresh pig manure, after being excreted by pigs, went through only in-house storage, and then the manure was pumped into an anaerobic digester. After the digestion, the digestate, both liquid and solid part, was transported and applied to agricultural fields (Figure 3).

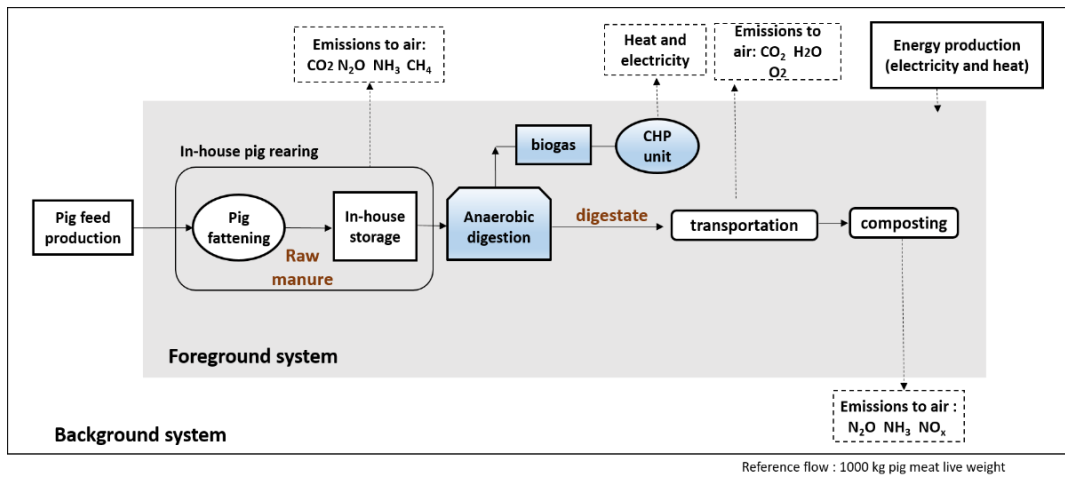


Figure 3: System boundary of scenario 2

In scenario 3 (HRAP), the fresh pig manure went through only in-house storage and then was pumped into an anaerobic digester as well. After the digestion, the liquid digestate was sent to high rate algae ponds (HRAPs) and the solid digestate was transported and spread to agricultural fields. Furthermore, the microalgae, grown in HRAPs, underwent primary harvesting (i.e. gravity settler and centrifugation) and then all the microalgae were incorporated in the pig meal (Figure 4).

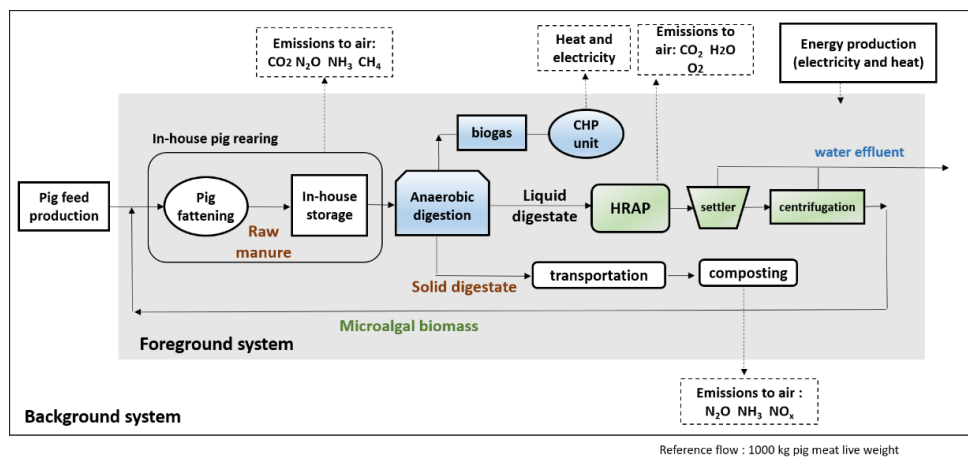


Figure 4: System boundary of scenario 3

Scenario 4 (HRAP and co-digestion) is nearly the same as scenario 3. The only difference between the two is that not all the liquid digestate-grown microalgae were substituted for pig feed. Part of the biomass was sent back into the anaerobic digester to co-digest with the manure in order to generate more energy (Figure 5).

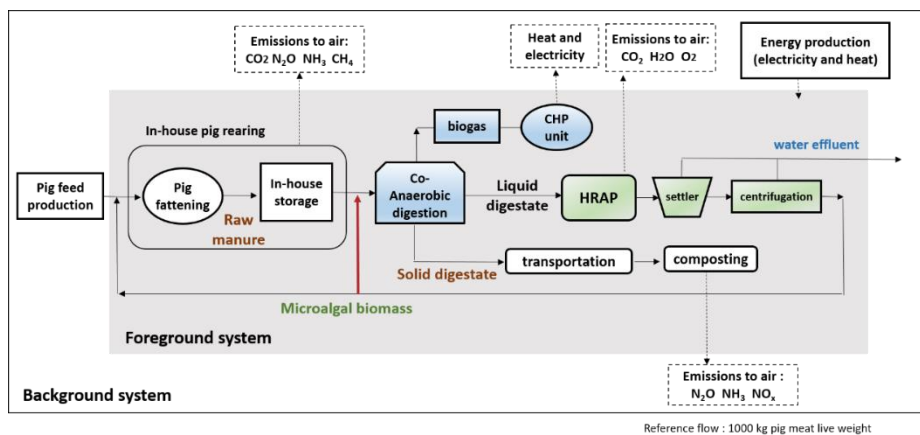


Figure 5: System boundary of scenario 4

## 2.4. Pig production

Feed supply for each scenario was analysed and inventoried in detail. Primary data about the feed formula and composition was provided by (Nguyen et al., 2010). Pig housing consumes on average 19.5 kWh electricity and 23.9 MJ heat per slaughter pig (Dalgaard et al., 2007). Pumping and stirring slurry from in-house to outside storage consumes 4.6 kWh per 1000 kg slurry ex-housing (Wesnæs et al., 2009). The calculations related to manure characteristics are presented in Table 1.

Table 1: Calculations related to manure characteristics

Manure composition (kg)	Ex-animal <sup>(a)</sup>	Ex-housing
Mass	A	A - total emission in in-house storage = B
DM (dry matter)	D	$D \times 0.95 = E$ <sup>(c)</sup>
VS (volatile solid)	G	$G - (D - E) = H$ <sup>(e)</sup>
Nitrogen (N)	(Feed weight $\times$ N content of feed) - nitrogen in meat = J	J - nitrogen loss in in-house storage = K
Phosphorous (P)	(Feed weight $\times$ P content of feed) - nitrogen in meat = M	M
Manure composition (kg)	Ex-storage	Ex-digestion
Mass	$B \times 1.086 = C$ <sup>(b)</sup>	C - biogas produced = N
DM (dry matter)	$C \times 0.061 = F$ <sup>(d)</sup>	F - biogas produced = O <sup>(g)</sup>
VS (volatile solid)	$F \times 0.8 = I$ <sup>(f)</sup>	I - biogas produced = P <sup>(g)</sup>
Nitrogen (N)	K - nitrogen loss in outside storage = L	L
Phosphorous (P)	M	M

a) Data from (Nguyen et al., 2010)

b) Based on DJF (2008a): 8.6% rain water coming during ex-storage

c) Based on DJF (2008b) and Poulsen et al. (2001):  $DM_{ex-housing} / DM_{ex-animal} = 0.90$  (more than 1 month in housing units);  $DM_{ex-storage} / DM_{ex-housing} = 0.95$  (DM loss when manure is stored in housing units for less than 1 month (15 days) is assumed to be 5% (i.e. half of that in the base case), which is seen as a conservative limit)

d) Based on DJF (2008a): dry matter content of manure ex-storage = 6.1%

e) Assumption: the loss of DM is originated primarily from the loss of VS

f) Sommer et al. (2008): VS content of DM ex-storage = 80%

g) Change in dry matter is equal to change in total mass and volatile solid

## 2.5. Emissions

Direct emissions to the atmosphere resulting from the pig farming and manure utilization were calculated. In most cases, livestock emissions cannot be measured with reasonable accuracy, so they are often obtained by using some modelling techniques. Current LCA studies on livestock products often use Intergovernmental Panel on Climate Change (IPCC) Guidelines to obtain default factors to estimate emissions of methane (CH<sub>4</sub>) and nitrous oxide (N<sub>2</sub>O). According to IPCC, CH<sub>4</sub> emissions to air from both enteric fermentation and manure storage. In addition, the levels of CH<sub>4</sub> and N<sub>2</sub>O generated in a specific manure management system are affected by many factors, e.g. the climatic condition, the duration of manure storage in housing units, in-house or outside storage, with or without a cover. Also, indirect N<sub>2</sub>O, NH<sub>3</sub>, NO<sub>x</sub> emissions derived from pig farming and manure management were considered in this study.

## 2.6. Waste management and utilisation

The anaerobic digestion considered in this study operated at mesophilic temperatures (around 37°C). It is assumed that the biogas produced is composed of 65% CH<sub>4</sub> and 35% CO<sub>2</sub>. Parameters used are presented in Table 2.

Table 2: Parameters used regarding anaerobic digestion

Parameters	Values	Reference
Digester electricity consumption (kW / tonne manure ex-housing)	2	(Nguyen et al., 2010)
Digester heat consumption (kW / tonne manure ex-housing)	13	(Nguyen et al., 2010)
Methane yield (m <sup>3</sup> CH <sub>4</sub> /kg VS)	0.356	(Møller, Sommer, & Ahring, 2004)
Efficiency (%)	0.85	assume

The produced biogas is burned in a biogas engine to co-generate heat and power (CHP). It is assumed that the biogas plant is connected to the district heating grid and therefore the heat source is displaced. The Agri-footprint process “Heat, from residue, heating systems from NG, consumption mix, at consumer, EU-27 S System” was used to model this. The electricity produced from the biogas can avoid electricity production. This was modelled through the Agri-footprint process “Electricity mix, AC, consumption mix, at consumer, < 1kV EU-27 S System”. The composting matters (i.e. slurry and digestate produced) were assumed to substitute a certain amount of artificial fertilizers and counted for the displaced fertilizer production and application. Mineral fertilizer equivalent (MFE) for N in slurry, which is the most important nutrient element in manure, has been derived approximately as 75% based on field experiments. More specifically, the MFE of slurry N is 75%, meaning that every 100 kg of N in pig slurry applied to a crop should replace 75 kg N in fertilizers. MFE for N in the digestate was higher than the raw one, 80% versus 75%. Although the value of MFE, depending on the environmental regulation in a particular geographic area, may not always be the case, but can serve as a benchmark for resource conservation (Nguyen et al., 2010). On the other hand, there is no clear restriction about P in manure. The MFE values for P in manure are considered 100% in most cases.

### 3. LIFE CYCLE ASSESSMENT

Calculations are performed in SimaPro 8.3 using data from ecoinvent 3 and Agri-footprint data base. (Method: IPCC 2013 GWP 100a) The carbon dioxide equivalent result is shown in Figures 6 and 7.

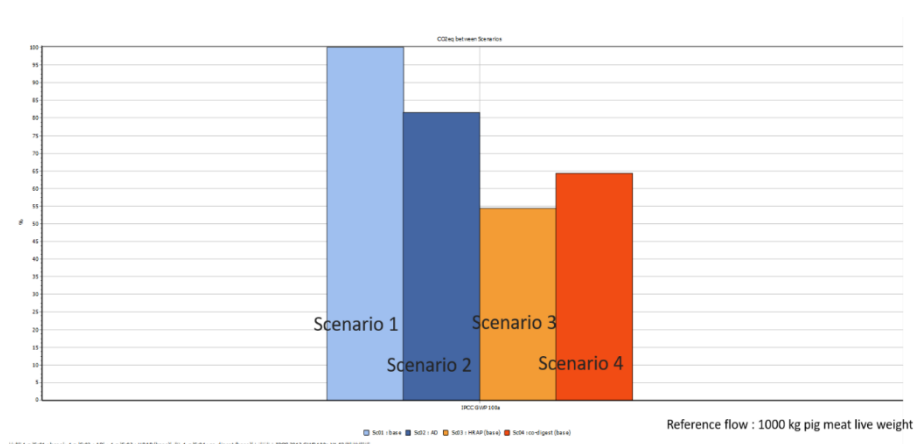


Figure 6: System boundary of scenario 3

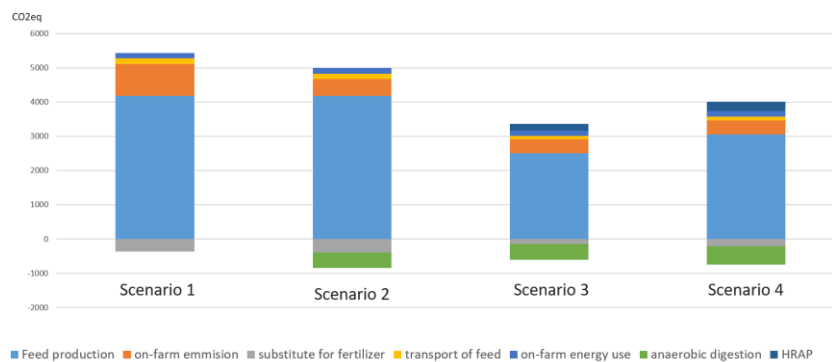


Figure 7: System boundary of scenario 3

#### **4. CONCLUSION**

Using microalgae to substitute pig feed can reduce greenhouse gas (GHG) emissions effectively. However, using microalgae to co-digest with pig manure is not the most effective way. Economic analysis should be done to further analyse the system.

#### **5. REFERENCES**

Dalgaard, R., Halberg, N., & Hermansen, J. E. (2007). Danish pork production: an environmental assessment.

DJF (Danmarks Jordbrugs Forskning), 2008a. Normtal 2008. Gældende pr. 1. August 2008. (Normtal for kvælstof, fosfor og kalium i husdyrgødning).

IPCC, 2006. Guidelines for National Greenhouse Gas Inventories. Eggleston, H.S., Buendia, L., Miwa, K., Ngara, T., Tanabe, K. (Eds.), Prepared by the National Greenhouse Gas Inventories Programme, Published: IGES, Japan.

Møller, H. B., Sommer, S. G., & Ahring, B. K. (2004). Methane productivity of manure, straw and solid fractions of manure. *Biomass and bioenergy*, 26(5), 485-495.

Nguyen, T. L. T., Hermansen, J. E., & Mogensen, L. (2010). Fossil energy and GHG saving potentials of pig farming in the EU. *Energy Policy*, 38(5), 2561-2571.

Wesnæs, M., Wenzel, H., & Petersen, B. M. (2009). Life cycle assessment of slurry management technologies. *Miljøstyrelsen*.